PROCEEDINGS OF 14th INTERNATIONAL EXERGY, ENERGY, AND ENVIRONMENT SYMPOSIUM

Editors
Professor İbrahim Dinçer
Professor M.Ziya Sogut

December 24-27, 2023

İstanbul/Türkive

14th INTERNATIONAL EXERGY, ENERGY, AND ENVIRONMENT SYMPOSIUM

December, 24-27, 2023

ORGANIZERS

SUPPORTERS

14th INTERNATIONAL EXERGY, ENERGY, AND ENVIRONMENT SYMPOSIUM

PROCEEDINGS BOOK

ORGANIZERS

December 24-27, 2023

İstanbul/Türkiye

Copyright

Piri Reis University, Istanbul, Turkey
Post Office District, Eflatun St. No:8, 34940 Tuzla/İSTANBUL

EDITED BY:
M.Ziya Sogut

E-ISBN : 978-625-98546-0-1
Published January, 2024
Not sold for money

MESSAGE FROM THE FOUNDING CHAIR

The 14th International Exergy, Energy and Environment Symposium (IEEES) is a multidisciplinary international symposium where energy and environmental issues, along with the effects of global climate change are addressed at an advanced level. In the symposium all aspects of structural problems are discussed, including evidence, causes, impacts and potential solutions. This symposium aims at providing an effective platform for sharing research-based technical knowledge, disseminating high-quality research results, presenting new approaches, strategies, policies and scientific developments, and supporting future priorities for a more sustainable development and environment. Technology change covers a wide range of disciplines such as innovative solutions, process engineering, effects of climate change, climate change modeling and simulations, energy and environmental policies, energy resources and conversion technologies, renewable energy sources, emission reduction, waste management, ecosystem and biodiversity, sustainable development, etc.

IEEES has been successfully organized as a leading Symposium in its field since 2003 and IEEES-14 was held as the 14th event of this symposium at Piri Reis University, Istanbul, Turkey. This event, held in different parts of the world, continues to develop its international profile. The scientific aspect of IEEES-14 includes sessions featuring keynote speakers, invited speakers, and parallel sessions in which research-based scientific papers are presented. In addition, poster presentation sessions and sector-specific sessions, where industry participants will share their original high-quality work, have also been included.) A welcome reception, gala dinner, and corporate events are planned for the social part of IEEES-14.

All papers submitted to the symposium have undergone an effective peer-review process befitting the quality of the symposium.Papers accepted for presentation are published in the IEEES-14 proceedings book. After the symposium, high-quality papers will be reviewed for publication in special issues of reputable international journals and as edited books. Within the scope of the symposium, all papers and results that were discussed among the panelists and participants were evaluated for a symposium final report. 432 participants from 27 different countries attended to this event. IEEES-14 was held successfully and the outcomes obtained from this symposium have been assessed as a milestone where energy and environmental sustainability will be taken into account for researchers, academicians, and decision-makers.

Prof. Dr. İbrahim DİNÇER
IEEES-14, Founding Chair

MESSAGE FROM THE SYMPOSIUM CHAIR

Today, energy and environmental issues that directly trigger and impact climate change increase the need for strategic models that will enhance societal sustainability day by day. Global warming, which occurs as a result of pollution caused by human-induced and fossil fuel consumption, increases the Earth's average surface temperature, and its impact continues to adversely affect life forms day by day. Since the industrial revolution, while greenhouse gas emissions, mostly released by burning fossil fuels such as coal, oil and natural gas continue to pollute the world, clean fuels such as hydrogen that will reshape a carbon-free future and their system solutions are increasing their effectiveness day by day. Energy and environmental sustainability are multidisciplinary and comprehensive in terms of frameworks and impacts. Today's emerging green call and decarbonization issues include basic focuses such as the environment, people, society and ecosystem. The 14th International Exergy, Energy, and Environment Symposium (IEEES-14), organized and conducted within this framework, took place in Istanbul, Turkey, from December 24 to 27, 2023. The event was organized and collaborated on by Piri Reis University, Ontario Tech University, the Chamber of Shipping, and the Hydrogen Technologies Association. Turkish Lloyd, Shipbuilders' Association (GISBIR), Tuzla Municipality, Emar EVD, Turkish Economy Bank, and Turkish Airlines provided strong support for the symposium, which was conducted as a multinational event with scientific presentations.

The 14th International Exergy, Energy and Environment Symposium (IEEES-14) aimed to bring together academicians, researchers, scientists, technocrats and practicing engineers working in various disciplines from energy to the environment. The symposium includes opening speeches, guest speeches, oral and wall presentations, and special sessions on sectoral topics. As part of the symposium themes, there have been more than 40 parallel sessions from various disciplines. IEEES-14 has been based on energy and environmental sustainability as an effective platform to disseminate the ideas, experiences and knowledge of researchers and engineers working on sustainable energy and environmental systems worldwide. IEEES-14 has covered a wide range of current topics such as Renewable Energy Technologies, Solar Energy, Oil and Gas Technologies, Smart Grids, Green and Electric Transportation, Alternative and Clean Fuels, Hydrogen and Fuel Cell Technologies, Nuclear Energy, Desalination Technologies, Wastewater Treatment, and Environmental Technologies. The symposium aims to increase the visibility and advancement of cleaner technologies such as green energy, renewable energy, and environmental science. In addition, topics such as smart cities, green buildings, energy management systems, and decarbonization have also been included. Societal and environmental threats have also been addressed by revealing challenges of life cycle assessment, CO_2 reduction technologies, biological waste utilization, wastewater treatment, challenges in nuclear energy, and transportation fuels. IEEES-14 includes 6 keynote presentations, 6 invited speaker participations, over 40 parallel sessions, and more than 30 poster presentations. Within the scope of IEEES-14, a total of 163 presentations were delivered from 27 different countries. IEEES-14 has been a successful symposium, opening new perspectives that support energy and environmental sustainability with the insights it presented on academic and social platforms. I extend my heartfelt gratitude to the strong support provided by Piri Reis University Rectorate and its Rector Prof. Dr. Nafiz Arıca, the Organizing Institutions, Supporting Organizations, the Organization Committee, and the members of the organizing board, as well as the Founding Chair Prof. Dr. İbrahim Dinçer, for making this event possible. I sincerely thank our sponsors for their assistance, support, and collaboration. Finally, I would like to express my heartfelt gratitude to all participants whose contributions and support have led to the great success of the symposium.

Prof. Dr. M.Ziya SOGUT
IEEES-14, Symposium Chair

CONTENT

COMMITTEES

Istanbul, Turkey, 24-27 December, 2023

Editor:

İbrahim Dinçer

Mehmet Ziya Sogut

Honorary Chair

Arıca, Nafiz / Rector of Piri Reis University, Türkiye

Founding Chair

Dinçer, İbrahim / President of HTA in Türkiye / Canada

Symposium Chair

Sogut, M. Ziya / Piri Reis University,Türkiye

Symposium Co-Chair

Helvacıoğlu, Ş. / Piri Reis University, Türkiye

Technical Chair

Colpan, C.O. / Dokuz Eylül University, Türkiye

Executive Committee Members:

Erdoğan, O.	Turk Loydu, Piri Reis University, Türkiye
Abd Rahim Bin Abu Talip	University Putra, Malaysia
Karakoç, T.H.	HTA, Türkiye
Khalid, F.	Indian Institute of Technology Guwahati, India
Khanmohammadi, S.	Kermanshah University of Technology, Iran
Kızılkan, Ö	Isparta University of Applied Science, Türkiye
Muhsin, K.	Uludağ University, Türkiye
Midilli, A.	HTA, Türkiye
Nizetic, S.	University of Split, Crotia
Özkaynak, S.	Piri Reis University, Türkiye
Ratlamwala, T.A. Hussain	National University of Sciences and Technology, Pakistan
Rohács, J.	DNV
Saghir, Z.	Toronto Metropolitan University, Toronto, Ontario
Utlu, Z.	University of Haliç, Türkiye

Yamaguchi, H. Doshisha University, Japan

Scientific Committee Members:

Al-Alami, A.H. – UAE
Afzal, M. – Canada
Alsanius, B. – Sweden
Al-Kassir, A. – Spain
Al-Taweel, A. – Canada
Aydin, D. – Cyprus
Bortoli, D. – Portugal
Caldwell, C. – Canada
Caman, M. E. – Türkiye
Carneiro, J. – Portugal
de Castro, M. – Spain
Cengel, Y. – USA
Chamchine, A. – United Kingdom
Cheema, M. – Canada
Corscadden, K. – Canada
Cuadros, F. – Spain
Collares-Pereira, M. – Portugal
Colpan, C. O. – Türkiye
Devrim, Y. – Türkiye
Dincer, I. – Canada
Dogan, F. – USA
Fredeen, A. – Canada
Freewan, A. – Jordan
Ghaly, A. E. – Canada
Grammelis, P. – Greece
Gregorio, G. – Philippines
Grob, G. R. – Switzerland
Hamdullahpur, F. – Canada
Hammond, G. P. – UK
Hayman, P. – Australia
He, S. – Canada
Helvacıoglu, I., Türkiye
Hepbasli, A. – Türkiye
Harris, P. G. – Hong Kong
Imai, H. – Japan
Jarimi, H. – Malaysia
Jones, I. S. F. – Australia
Joyce, A. – Portugal
Kacira, M. – USA
Karakoc, T. H. – Türkiye
Karaosmanoglu, F. – Türkiye
Kilicarslan, A. – Türkiye
Kılıç, M – Türkiye
Kılkıs, B – Türkiye
Kwak, H. – Korea
Lahèrrere, J. – France
Leal, W. – Germany
Lee, W. S. – USA
Levizzani, V. – Italy
Li, X. – Canada
Lucio, P. S. – Brazil
Lund, P. – Finland
Mello, L. F. – Brazil
Midilli, A. – Türkiye
Naterer, G. F. – Canada
Nguyen, N. T. V. – Canada
Niu, H. Canada
Nobre, C. – Brazil
Oliveira, A. – Portugal
Oki, T. – Japan
Ozkan, M. – USA
Pachauri, R. K. – India
Prasher, S. – Canada
Riffat, S. – UK

Rosa, R. – Portugal

Rosen, M. A. – Canada

Ross, N. – Canada

Rudra, R. – Canada

Sá da Costa, A. – Portugal

Sawa, T. – Japan

Sarıkoç, S. – Türkiye

Schaffer, D. – Italy

Schmidt, D. – Germany

Sen, Z. Türkiye

Sogut, M.Z. – Türkiye

Stewart-Clark, S. – Canada

Veziroglu, T. N. – USA

Xu, C. C. – Canada

Yan, J. – Sweden

Tasdemir, A. – Türkiye

Yuksel, B. – Türkiye

Zhang, X. R. – ChinaZheng, Y. – Canada

Organizing Committee Members:

Koray, M.	Piri Reis University, Türkiye
Demir, M.E.	Istanbul Technical University, Türkiye
Güler, E.	Piri Reis University, Türkiye
Musaoğlu, M.T.	Amasya Üniversitesi, Türkiye
Çetin, O.	Piri Reis University, Türkiye
Dalkıran, A.	Isparta Applied Science University, Türkiye
Güner, U.	Piri Reis University, Türkiye
Gürbüz, G.	Piri Reis University, Türkiye
Yılan, S.	Piri Reis University, Türkiye
Narin, D.	Piri Reis University, Türkiye

PARTICIPANTS

Ali Tetbirt	UDES, Algeria
Aminu Yusuf	Istanbul University-Cerrahpasa
Abdel Illah Nabil Korti	University de Tlemcen
Abdelatif Takilate	Centre de developpement des energies renouvelables
Abdelkader Aissat	University of Blida 1
Abdelmalek Elhadi	University of Mohamed Boudiaf, Msila, Algeria.
Abdesselam Bouloufa	Ferhat Abbas Sétif-1 University
Abdullah Muratoğlu	Batman University
Abhilash Suryan	College of Engineering Trivandrum
Adda Asma	Medea university
Adnan Midilli	Istanbul Technical University
Ahcene Karaali	Université Frères Mentouri Constantine 1
Ahmad Zikri	Bursa Uludag University
Ahmet Durmayaz	Istanbul Technical University
Ahmet Kilicaslan	Ontario Tech University
Ahmet Taşdemir	Piri Reis University
Aicha Sebti	UDES, Algeria
Aissa Mohamed	CDER/URAER, Algeria
Aissa Bouchelaghem	Ferhat Abbas Sétif-1 University
Ali Burak Göğebakan	TCDD Technical
Ali Çelik	Erzurum Technical University
Ali Oral	Balikesir University
Ali Cherif	The University of Texas
Ali Khalvati	Viona Consulting
Alkın Erdal Demirhan	Istanbul Technical University
Alper Gülmez	Arçelik
Amar Berkaache	Msila University
Amar Manser	CRTSE, Algeria
Amel Berkane	Tipaza University Center
Amel Mameche	Sonatrach

Aminu Yusuf	Istanbul University-Cerrahpasa
Amokrane Samira	Université des Sciences et de la Technologie Houari Boumediene
Amor Gama	CDER/URAER, Algeria
Amor Fezzani	URAER EPST CDER, Algeria
Anatolii N Startsev	Boreskov Institute of Catalysis
André Mariano	UFPR, Algeria
Aneesh Vasudev	University of Vaasa
Anil Erdogan	Vestel Home Appliances
Anne Oliveira	UFPR, Algeria
Anoop Shukla	Amity University Uttar Pradesh
Antar Beddar	URAER EPST CDER, Algeria
Arif Hepbaşlı	Yasar University
Arif Karabuga	Haliç University
Assem Andurakhmanova	Yildiz Technical University
Assia Boukezzata	CRTSE, algeria
Assia Djebri	University of Sciences and Technology Houari Boumediene
Atef Mohany	Ontario Tech University
Atoui Sakina	UDES, Algeria
Aysegul Goren	Ontario Tech University
Ayşegül Abusoğlu	Istanbul Technical University
Aytunc Erek	Dokuz Eylül University
Azzedine Boutelhig	CDER, Algeria
Bachir Dadda	URAER, Algeria
Barış Yılmaz	Lakehead University
Bekhedda Kheira	CRTSE, Algeria
Belgassim Boutra	UDES, Algeria
Ben Baby	University of Palermo
Bendjebbas Hichem	UDES/CDER, Algeria
Benmouhoub Dahbia	USTHB, Algeria
Benziada Mébrouk	CDER, Algeria
Berk Kurt	Hidropar Movement Control Technology Center

Berkay Tahirağaoğlu	Bursa Uludağ University
Billel Allouche	Frères Mentouri Constantine 1 University
Boualem Bendib	UDES, Algeria
Boubekeur Boudine	Université Constantine 1
Bouleklab Mohamed Cherif	Constantine 1 University
Burak Muratçobanoğlu	Erzurum Technical University
Burak Vardar	Dokuz Eylül University
Burcu Kiren	Eskişehir Technical University
Burcu Yılmazel	Eskişehir Technical University
Busra Ozkok	Konya Technical University
Bülent İbrahim Turan	Muğla Sıtkı Koçman University
Büşra Namaldı Kömürcü	Erciyes University
Büşra Osma	Piri Reis University
Can Coskun	Izmir Democracy University
Can Ozgur Colpan	Dokuz Eylül University
Can Tuncer	Gesbey Enerji Türbini Kule Üretim San. ve Tic. A.Ş., Ar&Ge Merkezi
Canan Ağlan	Marmara University
Cemil Alkan	Tokat Gaziosmanpasa University
Cemil Koyunoğlu	Yalova University
Cengizhan Gök	1st Air Maintenance Factory Directorate
Ceren Şengül	Gazi University
Chaimae Younes	Energy and Materials Team – Innovative Technologies Laboratory
Chandra Prakash Gupta	National Institute of Technology Warangal
Chekirou Wassila	Université Frères Mentouri Constantine 1
Chems-Eddine Chitour	ENP
Cihan Emre Şahin	Istanbul Technical University
Çağla Cergibozan	Dokuz eylül University
Daining Fang	Beijing Institute of Technology
Davut Ertekin	Bursa Technical University
Delia Teresa Sponza	Dokuz Eylül University
Demet Yılmaz	Suleyman Demirel University

Deniz Ulusarslan	Yildiz Technical University
Dibakar Rakshit	Indian Institute of Technology Delhi
Didem Sena Aksu	Izmir Democracy Universty
Dinesh Bejjanki	National Institute of Technology Warangal
Djamel Eddine Ameziani	USTHB
Djamel Zeriri	Sonatrach
Dogan Erdemir	Ontario Tech University
Dogukan Mızrak	Dokuz Eylül University
Du Jianguo	Jiangsu University
Duygu Erten	TURKECO
Duygu Gündüz Han	Istanbul Medeniyet University
Duygu Ülker	Istanbul University
Ebru Erunal	Çukurova University
Edwin Geo Varuvel	Istinye University
Elangkathir V	Annamalai University
Elayaperumal A	CEG Campus, Anna University
Elif Gezginci	Konya Technical University
Emanuele Nadalon	University of Trieste
Emine Nokay	IZTECH
Emir Ejder	Istanbul Technical University
Emre Kaçmaz	Eskisehir Technical University
Emre Mandev	Erzurum Technical University
Emrehan Gürsoy	Karabük University
Engin Gedik	Karabuk University
Enver Yalçın	Balikesir University
Eren Cankılıç	Dokuz Eylül University
Eren Küpcü	Graduate School of Bursa Technical University
Ergün Demirel	Piri Reis University
Erkan Dursun	Marmara University
Erol Pehlivan	Konya Technical University
Ersin Akyüz	Balıkesir University
Ersin Alptekin	Dokuz Eylül University

Esin Varol	Eskisehir Technical University
Faraz Afshari	Erzurum Technical University
Fathia Chekired	UDES/CDER, Algeria
Fathima Ancy M	College of Engineering Trivandrum
Fatih Bouzeffour	UDES/CDER, Algeria
Fatih Özcan	Bursa Uludag University
Fatih Yılmaz	Isparta University of Applied Sciences
Fatiha Souahi	ENP
Fatma Zohra Tighilt	CRTSE, Algeria
Fazıl Erinç Yavuz	Renta Elektrikli Ev Aletleri San ve Dış Tic.
Fazlı Okan Bovatekin	Dokuz Eylül University
Ferhat Djawad Boumediene	Université des Sciences et de la Technologie Houari
Ferhat Yahi	UDES, Algeria
Feriel Sahoui	USTHB
Fevzi Yaşar	Batman University
Fidelis Abam	University of Calabar
Fouad Aissaoui	Tipaza university center
Funda Yercan	Piri Reis University
Gabriela Conor	UFPR
Gamze Nalçacı	ODTÜ/METU
Gamze Soyturk	Isparta University of Applied Sciences
Gizem Başaran Dindaş	Gebze Technical University
Goutam Khankari	Damodar Valley Corporation Kolkata
Gökhan Sefer	Gebze Technical University
Gökhan Sevilgen	Bursa Uludağ University
Görkem Berkay Ergeç	Izmir Democracy Universty
Gözde Nalçacı	Gazi University
Guesmla Seyfeddine	University of Concordia
Gülcan Koca	Gazi University
Gülçin Yıldırım Çimşir	Istanbul Technical University
Güldem Elmas	Istanbul University-Cerrahpaşa
Gülşah Elden	Erciyes University

Gülşen Akın Evingür	Piri Reis University
Hadi Genceli	Yıldız Technical University
Hadj Mekatel Boumediene	Université des Sciences et de la Technologie Houari
Hafida Lebik	UDES, Algeria
Haider Muften	Al-Ghanimi
Hakim Merarda	UDES, Algeria
Hale Demirtepe	Izmir Institute of Technology
Halil Çeçen	Nuh Naci Yazgan University
Hamamda Smail	Constantine 1 University
Hanane Aburideh	UDES, Algeria
Hani Zeidan	Çukurova University
Hannah Klatzke	University of Detroit Mercy
Hasan Güneş	Istanbul Technical University
Hasan Göler	Piri Reis University
Hatice Eser Ökten	Izmir Institute of Technology
Hayet Lallali	CRTSE, Algeria
Hayet Tizi Boumediene	University of Sciences and Technology Houari
Haythem Sahli National Engineering School of Tunis	Research Laboratory Energetic and Environment -
Hazal Gergeroğlu	CIC nanoGUNE
Hechemi Rahmani	UDES, Algeria
Hilal Akci	Ontario Tech University
Hocine Guellil	ETAP Laboratory, University of Tlemcen
Hocine Belmili	CDER, Algeria
Houda Tassoult	UDES, Algeria
Hüseyin Cengiz Yatmaz	Gebze Technical University
Hüseyin Gençer	Piri Reis University
Ibrahim Karaçaylı	Ege University
Ibrahim Dincer	Ontario Tech University
Idriss Hadj Mahammed	URAER EPST CDER, Algeria
Imene Ameur	University of Constantine 1

Iryna Shkilniuk	National Technical University of Ukraine “Igor Sikorsky Kyiv Polytechnic Institute”
Isares Dhuchakallaya	Thammasat University
İsmail Ekmekci	Istanbul Ticaret University
İsmail Özdemir	Istanbul Gedik University
Jari Hyvönen	Wärtsilä Finland Oy
Jay Dhariwal	IIT Delhi
José Vargas	UFPR
Kaan Erdem	Istanbul Medeniyet University
Kacem Gairaa	URAER EPST CDER, algeria
Kaddour Abdelmadjid	URAER/CDER, Algeria
Kahina Lasmi	CRTSE, Algeria
Kamala Thota	NIT Warangal
Kamil Erkan	Marmara University
Karthikeyan M	CEG Campus, Anna University
Kemal Ege Sural	Istanbul Technical University
Khaled Hamdani	CRTSE, Algeria
Kiran Donthula	National Institute of Warangal
Kubilay Karayel	Ontario Tech University
Kumaravel S	Annamalai University
lamine Aoudjit	UDES, Algeria
Lekshmipriya J	College of Engineering Trivandrum
Lutfiye Altay	Ege University
Lyes Nasseri	USTHB
Maamar Hamdani	URAER/CDER, Algeria
Maamar Ouali	UDES, Algeria
Maciej Mikulski	University of Vaasa
Mahdi Mokrane	UDES, Algeria
Mahfoud Djezzar	Frères Mentouri Constantine 1 University
Mahmoud Ghannam	Ford Motor Company
Malika Ouagued	University Hassiba Benbouali of Chlef
Manel Drici	Badji Mokhtar Annaba
Manohar Kakunuri	National Institute of Technology Warangal

Manoj Babu A	Dr.MGR Educational and research Institute
Marco Ferraro	CNR-ITAE
Marco Beccali	University of Palermo
Maryam Karami	Kharazmi University
Mato Knez	CIC nanoGUNE
Mauro Reini	University of Trieste
Mehmet Akif Ceviz	Erzurum Technical University
Mehmet Akif Ezan	Dokuz Eylül University
Mehmet Akman	Muğla Sıtkı Koçman University
Mehmet Furkan Koparan	Dokuz Eylül University
Mehmet Gursoy	Ontario Tech University
Mehmet İshak Yüce	Gaziantep University
Mehmet Ziya Sogut	Piri Reis University
Melchiorre Casisi	University of Trieste
Melda Çarpınlıoğlu	Gaziantep University
Merve Yılmaz	Marmara University
Merve Altuntas	Erciyes University
Metin Gül	Balıkesir University
Mezidi Ahmed	UDES/CDER, Algeria
Mikail Rıza Onat	Istanbul Technical Uiversity
Miloud Sebais	University of Constantine 1
Mine Sertsöz	Eskisehir Technical University
Ming Liang	Ford Motor Company
Mohamed Ait OumeraciI	USTHB
Mohamed Ali Djebiret	UDES, Algeria
Mohammad Hasan Khoshgoftar Manesh	University of Qom
Mohammed Ayad	UDES/EPST CDER, Algeria
Mohand Berdja	UDES, Algeria
Mohit Barthwal	Indian Institute of Technology Delhi
Morteza Khoshvaght-Aliabadi	Korea University
Moslem Sharifishourabi	Ontario Tech University
Mouloud Guermoui	URAER/EPST CDER, Algeria

Mouna Elakhdar	Research Laboratory Energetic and Environment - National Engineering School of Tunis
Mourad Houabes	High National School of Technology and Industry
Muhammad Ishaq	Ontario tech University
Muhammed Baştuğ	Izmir Institute of Technology
Muhammed Bozelli	HKTM
Muhammed Budak	Marmara University
Muhammet Çelik	Aksaray University
Muhammet Sefa Odabaşı	Bursa Uludağ University
Muhsin Kılıç	Uludag University
Murat Ayar	Eskisehir Technical University
Murat Emre Demir	Istanbul Technical University
Murat Köseoğlu	Gedik Universty
Murat Mustafa Savrun	Adana Alparslan Türkeş Science and Technology University
Murat Ozturk	Isparta University of Applied Sciences
Murat Uysal	Teksan Generator
Murilo Rampi	UFPR, Algeria
Mustafa Esen Marti	Konya Technical University
Mustafa Özden	Bursa Technical University
Mustafa Serdar Genç	Erciyes University
Mustafa Tolay	Tolay Energy
Mustafa Umut Karaoğlan	Dokuz Eylül University
Mustafa Yılmazoğlu	Gazi University
Mustafa Yılmaz	Marmara University
Mümine Gerçek Şen	Izmir High Technology University
Nadia Metidji	UDES/CDER
Nadim Karoune	University Freres Mentouri Constantine 1
Nagihan Ersoy	Manisa Celal Bayar University
Nahman Boukheit	Université Frères Mentouri Constantine 1
Naoual Seddaoui	UDES, Algeria
Naresh Thota	National Institute of Technology Warangal
Nazım Taş	Istanbul Technical University

Nazlı Deniz Ünal	Gazi University
Nazmi Ekren	Marmara University
NIitesh Kumar Choudhary	National Institute of Technology Durgapur
Nibou Djamel Boumediene	Université des Sciences et de la Technologie Houari
Nicholas Melenek	UFPR
Nihad Dukhan	University of Detroit Mercy
Noreddine Boudechiche	Khemis Miliana University
Nurdan Akdemir	Erzincan University
Nurdan Yıldırım	Yaşar University
Nuri Kayansayan	Dokuz Eylül University
Oğuzhan Arabacı	Istanbul Technical University
Oğuzhan Gündüz	Marmara University
Okan Gök	Dokuz Eylül University
Oktay Cetin	Piri Reis University
Omar Alharasees	Budapest University of Technology and Economics
Omer Kemal Kinaci	Istanbul Technical University
Onder Kızılkan	Isparta University of Applied Sciences
Onur Otlu	Yıldız Technical University
Oral Erdoğan	Piri Reis University
Orçun Şenler	
Osama Khan Islamia	Department of Mechanical Engineering, Jamia Millia
Ouahiba Halimi	University of Constantine 1
Ouiza Allalou	USTHB
Oya Bakar	Teksan Generator
Ozan Gül	Bingol University
Ozgur Balli	TAI
Ömer Faruk Güler	Afyon Kocatepe University
Özlem Boydak	Istanbul Medeniyet University
Özüm Çallı	Istinye University
Parisa Heidarnejad	Istanbul Gedik University
Prasanth P Nair	IIT Gandhinagar

Praveen Kumar Bommineni	National Institute of Technology Warangal
Premkumar P	Annamalai University
Puttapati Sampath Kumar	National Institute of Technology Warangal
Rabah Gomri	University Freres Mentouri Constantine 1
Rafik Elhadi	CRAPC
Rahmani Lazhar	Ferhat Abbas University SETIF-1 Algeria
Rahul Sharma	IIT Delhi
Rajkumar P	Annamalai University
Ramsagar Vooradi	National Institute of Technology Warangal
Ramya Araga	National Institute of Technology Warangal
Rania Hammemi	Research Laboratory Energetic and Environment - National Engineering School of Tunis
Rania Mahdadi	Ferhat Abbas Sétif-1 University
Resat Selbas	Isparta University of Applied Sciences
Rinat Zhanbayev	National Engineering Academy of the Republic of Kazakhstan
Ronelly De Souza	University of Trieste
Rukiye Öztekin	Dokuz Eylül University
S. Atalay Keleştemur	Istanbul Gedik University
Saadallah Soror	University of Constantine 1
Sabri Alkan	Bandırma Onyedi Eylül University
Sabri Boulouma	UDES, Algeria
Sabrina Boualit	URAER EPST CDER, Algeria
Sabrina Sam	CRTSE
Sadek Igoud	Solar Equipments Development Unit
Said Benkaciali	URAER EPST CDER
Sakıp Tüzköz	Gesbey Enerji Türbini Kule Üretim San. ve Tic. A.Ş., Ar&Ge Merkezi
Salah Bezarı	Applied Research Unit in Renewable Energies
Salih Aksu	Gesbey Enerji Türbini Kule Üretim San. ve Tic. A.Ş., Ar&Ge Merkezi
Salih Bilgiç	Dokuz Eylül University
Salima Laouar	Applied Research Unit for Renewable Energies
Samia Belhousse	CRTSE

Samira Kaci	CRTSE
Samiye Adal	Afyon Kocatepe University
Sarah Djelti	UDES, Algeria
Sarah Mahidine	UDES, Algeria
Sarath Babu Anne	NIT Warangal
Saravanan CG	Annamalai University
Sebahattin Unalan	Erciyes University
Sebastian George Colleoni	Haier Europe
Sedat Ballikaya	Istanbul University-Cerrahpasa
Selçuk Ekici	Igdir University
Selim Can Bozkır	Dokuz Eylül University
Selma Ergin	Istanbul Technical University
Selmane Allouche	University of Constantine1
Sena Erkent	Suleyman Demirel University
Sennur Alay Aksoy	Süleyman Demirel University
Sera Ayten Çetinkaya	Dokuz Eylül University
Serap Goksu	Recep Tayyip Erdoğan University
Serdar Sanlı	
Sevınc Sırdas	Istanbul Technical University
Seyed Hamed Pour Rahmati Khalejan	Hidropar Motion Control Technology Center
Seyedeh Somayeh Nasiri Gahraz	Kharazmi University
Shailesh Singh Sikarwar	National Institute of Technology Warangal
Sibel Uygun Batgi	Ontario Tech University
Sihem Bouanik	CRTSE
Simge Özkayalar	Dokuz Eylül University
Sinan Burhan	Marmara University
Snigdha Saha	National Institute of Technology Warangal
Sriram Chandran R	Indian Institute of Science
Subaash R	CEG Campus, Anna University
Sujit Karmakar	NIT Durgapur
Suresh Lal S R	College of Engineering Trivandrum

Süleyman Karsli	Gebze Technical University
Sümeyya Ayça	Istanbul Health and Technology University
T. Hikmet Karakoç	Istanbul Ticaret University
Taha Aydın	Yıldız Technical University
Taha Buğra Sari	
Tahar Tayebi	Bachir El Ibrahimi University Bordj Bou Arreridj
Tamer Çınar	SIGMA A.Ş
Tarek Ibnou Ziad Berrama Boumediene	University of sciences and technology Houari
Tayfun Tanbay	Bursa Technical University
Toufik Smail	UDES/CDER, Algeria
Toufik Zarede	UDES/CDER, Algeria
Tuba Tezer	Balıkesir University
Tuba Okutucu Özyurt	Istanbul Technical University
Tunahan Akış	Dokuz Eylül University
Uğur Demir	Piri Reis University
Utku Kale	Budapest University of Technology and Economics
Vanessa Kava	UFPR
Vasıf Can Yıldıran	Istanbul Technical University
Vedagiri Praveena	SRM Institute of Science and Technology
Venkata Suresh Patnaikuni	National Institute of Technology Warangal
Wassila Yazid	UDES, Algeria
Weili Song	Beijing Institute of Technology
Xuecheng Chen	West Pomeranian University of Technology
Yağmur Nalbant Atak	Atılım University
Yasir Ahmed Solangi	Jiangsu University
Yettou Fatiha	URAER-CDER, Ghardaia
Yiğithan Çalı	Vestel White Goods Company
Yorken Chrisha C	College of Engineering Trivandrum
Yunus Mert Becermen	Arçelik
Yunus Babacan	Erzincan University
Yusuf Taha Ismailoglu	Yildiz Technical University
Zafer Metin Ataş	Gebze Technical University

Zafer Utlu	Halic University
Zafer Erbay	Adana Alparslan Türkeş Science and Technology University
Zahra Sadaoui	University of Sciences and Technology Houari Boumediene
Zeang Zhao	Beijing Institute of Technology
Zehra Sakınç	Gaziantep University
Zehra Yumurtacı	Yıldız Technical University
Zehra Karagöz	Marmara University
Zeineddine Ouili	Université Constantine 1
Zergane Said	Université of Msila
Zeynep Durmuş Arsan	IZTECH
Zouhira Hireche	USTHB
Zuhal Oktay	Izmir Democracy University

SCIENTIFIC PAPER LIST

Paper no	Paper Title	Authors
IEEES-001	Sizing and Performance Evaluation of Photovoltaic System Coupled With Electrolyzer Hydrogen Production in Algeria	Malika Ouagued
IEEES-002	Future Methanol Cost Projections in Specific Regions: A Comprehensive Study	Metin Gül, Ersin Akyüz
IEEES-003	Preliminary Study on a Transient Freezer Model with Phase Change Material (PCM)	Mehmet Furkan Koparan, Okan Gök, Ersin Alptekin, Mehmet Akif Ezan, Aytunç Erek
IEEES-004	Sustainable Solar Energy: Repurposing Discarded Materials in Parabolic Concentrator Fabrication	Emre Mandev, Mehmet Akif Ceviz, Ali Çelik, Burak Muratçobanoğlu, Faraz Afshari
IEEES-005	Assessment of the Effect of Lint Accumulation in the Heater Channel on the Performance of the Water Cooled Washing Drying Machines in Different Operating Conditions	Nazım Taş, Ayşegül Abuşoğlu
IEEES-006	Thermodynamic and Parametric Analysis of a Double Adsorptive Solar Cooling Cycle	Wassila Chekirou, Nahman Boukheit, Ahcene Karaali
IEEES-007	Effect of Adsorbent/Adsorbate Working Pairs on Solar Adsorption Cooling Performance's	Wassila Chekirou, Nahman Boukheit, Ahcene Karaali
IEEES-008	A Year-Round Dynamic Simulation of a Solar Trigeneration System in Hot and Humid Climate	Maryam Karami, Seyedeh Somayeh Nasiri Gahraz
IEEES-009	Acetate Cellulose Modified Nanofiltration Membrane Efficiency and Performance	Aburıdeh Hanane, Zıouı Djamila, Tıgrıne Zahia, Hout Sarra, Belgroun Zoubir, Abbas Mohamed
IEEES-010	Fabrication and Photocatalytic Activity of Undoped and Mg doped ZnO	Boudıne Boubekeur, Ameur Imene, Halımı Ouahiba, Sebaıs Miloud
IEEES-011	Hydrogen as the Fuel of the Future and Hydrogen-Powered Aircraft	Cengizhan Gok, Selcuk Ekici, Ozgur Balli, T.Hikmet Karakoc
IEEES-012	Performance Improvement of PV Generator Using a Sun Tracking System	Sakina Atoui, Fouad Aissaoui, Amel Berkane, Ayad Mohammed, Djamila Ghribi, Said Boudjana
IEEES-013	Numerical Investigation of The Effect of Forced Air/nanofluid Pairs on PV/T System Performance	Gökhan Sefer, Süleyman Karsli
IEEES-014	Exergy-Based Performance Assessment of an Ejector-Enhanced Auto-Cascade Refrigeration Cycle	İbrahim Karacayli, Lutfiye Altay, Arif Hepbasli
IEEES-015	Effects of H2 admixture on RCCI combustion dual-fuel marine engines: A model-based study	Aneesh Vasudev, Maciej Mikulski, Jari Hyvönen

IEEES-016	The Management of Electrical and Thermal Energy in a House at Different Climates Algeria	Mezidi Ahmed, Tassoult Houda, Bendjebbas Hicham
IEEES-017	Comparative Analysis of Energy Storage Methods for a Parabolic Through Collector Solar Power System	Ömer Faruk Güler
IEEES-018	Greenhouse Heating with Low Enthalpy Solar and Geothermal Energy	Ömer Faruk Güler
IEEES-019	Integrating Phase Change Materials (PCMs) Into Cotton Ring Spun Yarn Structure For Thermo-Regulating Function	Demet Yılmaz, Sennur Alay Aksoy
IEEES-020	Shading Strategies as Energy Efficient Retrofit Measures in Residential Buildings: Implementations for Adaptation to Future Climate Change	Mümine Gerçek Şen
IEEES-021	Photovoltaic-Phase Change Materials-Thermoelectric System Coated With Radiative Cooling	Aminu Yusuf, Sedat Ballıkaya
IEEES-022	The improvement of the Mebeverine Hydrochloride photocatalytic degradation by using combined Activated Carbon/ZnO under sunlight	Assia Djebri, Ouiza Allalou, Noreddine Boudechiche, Zahra Sadaoui
IEEES-023	Production of Microencapsulated Thermochromic Systems in Poly(methyl methacrylate-co-methacryl amide) Shell and Application to Polyester Fabric for Thermal Management	Sennur Alay Aksoy, Simge Özkayalar, Cemil Alkan
IEEES-024	A Study On The Comparıson Of Battery Parameters Of An Electrıc Bus Accordıng To Passenger Occupancy	Muhammet Sefa Odabaşı, Berkay Tahirağaoğlu, 3gökhan Sevilgen
IEEES-025	Sustainable Efficiency based Development of A Painting Robot Machine Simulating Operator Movements for Wind Turbine Tower Painting Process	Sakıp Tüzköz, Salih Aksu, Can Tuncer, Ali Oral, Enver Yalçın
IEEES-026	Parameters of Renewable Energy Use in Rail Systems	Mine Sertsöz
IEEES-027	Hydrogen Energy In Transportatıon	Ali Burak Gögebakan1 Mine Sertsöz
IEEES-028	Investigation of Optimal PV Panel Angle for Güney/Denizli	Muhammed Rıza Bozelli, Berk Kurt
IEEES-029	Dissociation of Methane for Hydrogen Production in a Solar Reactor	Rabah Gomrı, Cheima Hadef, Belkcem Nezzarı
IEEES-030	Examination of the Impact of Electric Vehicles on Line Losses in the IEEE 14-Bus System	Ozan Gül
IEEES-031	Examination of the Impact of Electric Vehicles and Cryptocurrency Mining Operations on Line Losses in the IEEE 14-Bus System with Renewable Energy Sources	Ozan Gül
IEEES-032	Examination of the Impact of Renewable Energy Sources on Line Losses in the IEEE 14-Bus System	Ozan Gül
IEEES-033	Development of Metal Loaded Minerals as Heterogeneous Catalysts in the Degradation of Dye Solutions	Zafer Metin Ataş, Gizem Başaran Dindaş, Hüseyin Cengiz Yatmaz

IEEES-034	CO2 Removal by Calcined Eggshell	Sena Erkent, Barış Gürel, Karani Kurtuluş, Savaş Özün, Murat Varol, Kamil Ekinci, Sema Yurdakul
IEEES-035	Numerical Investigation of the Effect of Different Boundary Conditions and Geometrical Properties on CO2 Removal Efficiency in the Retention of CO2 from Flue Gas in a CO2 Capture Column With Calcined Eggshell By Carbonation Reaction	Barış Gürel, Karani Kurtuluş, Savaş Özün, Murat Varol, Kamil Ekinci, Sena Erkent, Sema Yurdakul
IEEES-036	A Computational Investigation Into the Leakage and Dispersion of Hydrogen in Enclosed Areas	Lekshmipriya J, Abhilash Suryan, Prasanth P Nair
IEEES-037	Evaporative Coolıng Of Solar Photovoltaıc Panels: A Computatıonal Study	Fathima Ancy M, Abhilash Suryan, Prasanth P Nair, Sriram Chandran R
IEEES-038	Analysis of Wind Flow around Major Buildings in the Campus of College of Engineering Trivandrum	Yorken Chrisha C, Abhilash Suryan, Prasanth P Nair, Suresh Lal S R
IEEES-039	Investigation on combustion, performance and emission characteristics of Waste Cooking oil – diesel blends with hydrogen in CI engine – A dual fuel approach	Kiran Suresh, Leenus Jesu Martin, Edwin Geo Varuvel
IEEES-040	Thermodynamic Analysis of Desalination System on Combined Cycle Power Plants Through Throttling Process Method by Using a Vapor Compressor	Ahmad Zikri, Muhsin Kilic, Fatih Ozcan
IEEES-041	Dynamic Modeling of a Compressed Natural Gas Refueling Station	Fatih Ozcan, Muhsin Kiliç,
IEEES-042	Green Synthesis of Encapsulated Nano Silver Biochar Composite for Malachite Green Removal from Aqueous Solution: Novel Synthesis and Optimization	Erol Pehlivan, Elif Gezginci, Busra Ozkok
IEEES-043	Co-Pyrolysis of Walnut Shell and Waste Rubber Blend to Produce Sustainable Bio-based Materials	Burcu Kiren, Esin Apaydın Varol
IEEES-044	Experimental Studies on Energy and Exergy-based Assessments of a Freezer	Burak Vardar, Fazli Ozan Bovatekin, Yunus Mert Becermen, Okan Gök, Ersin Alptekin, Mehmet Akif Ezan, Aytunç Erek
IEEES-045	3D Steady-State Numerical Modeling of a Static Freezer	Salih Bilgiç, Eren Cankılıç, Alper Gülmez, Okan Gök, Ersin Alptekin, Mehmet Akif Ezan, Aytunç Erek
IEEES-046	Analyzing the Lean Burn Combustion Stability by Hydrogen Induction in Gasoline Direct Injection Engine	Jerome Stanley M, Leenus Jesu Martin M, Edwin Geo Varuvel
IEEES-047	Energy and Exergy Analysis of CLC Based Biomass Fired Power Plant With Different Oxygen Carriers	Shailesh Singh Sikarwar, Ramsagar Vooradi, Venkata Suresh Patnaikuni,

		Manohar Kakunuri Surname
IEEES-048	Impact of Biofuels on Maritime Decarbonization and Vessel Performance	Emir Ejder, Hasan Göler, Ergün Demirel
IEEES-049	A Effective Moisture Diffusivity of a Hybrid Double Pass Collector-Solar Dryer For Tomato Slices Drying	Korti A.N., Guellil H.
IEEES-050	Production of Microencapsulated Thermochromic Systems Based on Fluoran Dye and Investigation of Their Thermal Properties	Cemil Alkan, Simge Özkayalar, Sennur Alay Aksoy
IEEES-051	Biogas Renewable Energy: Conversion of Solid Waste To Energy In The Marmara Region	Muhammed Ömer Budak, Canan Ağlan Gökler
IEEES-052	Applications of Fresnel Concentrated Solar Power System and their Impact Towards Environment	Houda Tassoult, Ahmed Mezidi
IEEES-053	Impact of Natural Gas Composition on the Energy-Exergy-Environmental Performance of a Combined Cycle Power Plant	Tayfun Tanbay, Ahmet Durmayaz
IEEES-054	Development of a VIV System for Hydrokinetic Energy Harvesting and Pumped Hydro Storage	Alkın Erdal Demirhan, Murat Emre Demir, 1ömer Kemal Kınacı
IEEES-055	Harnessing Wind Energy: Solid Sails in Maritime Transport for Sustainable Energy Utilization	Cihan Emre Şahin, Murat Emre Demir
IEEES-056	“Effects of Distance and Absorber Shape on the Energetic and Exergetic Performance of a Solar Collector”	Hocine Guellil, Abdelıllah Nabil Korti
IEEES-057	Thin Films in Solar Cell Applications	Büşra Osma, Gülşen Akın Evingür
IEEES-058	Waste Management on Oil Spill Emergency Response in Turkish Coastal Waters	Duygu Ülker
IEEES-059	Thermodynamic Analyses Of A Organic Rankine Cycle (ORC) With Working Fluids R245FA, R245CA And R1233ZD In A Multigenerational Hybrid System	Özlem Boydak, İsmail Ekmekçi, Mustafa Yılmaz
IEEES-060	Need of a Policy and Strategy on Intelligence versus Artificial Intelligence in Engineering Education?	Melda Ozdınc Carpınlıoglu
IEEES-061	Efficiency Increasing Coatings on Photovoltaic Panels (PV)	Merve Yılmaz, Erkan Dursun, Zehra Karagöz, Nazmi Ekren, Oğuzhan Gündüz
IEEES-062	Techno-Economic Analysis of the Distribution Network for the European Market of Green Ammonia Produced From Offshore Wind Farms to be Installed Off the Coast of Northern Europe	Mikail Rıza Onat, Murat Emre Demir
IEEES-063	Assessing the Bilateral Impacts in a Changing Climate in terms of Shipping Sector	Duygu Ülker, Serap Goksu
IEEES-064	Numerical Investigation in a Dishwasher Hub: Reducing Pressure Difference and Pump Power	Fazıl Erinç Yavuz, Vasıf Can Yıldıran, Sebastian George Colleoni

IEEES-065	Energy Footprint of Gypsum Plasterboard Production Plant	Zehra Sakınç, Abdullah Muratoğlu, Mehmet İshak Yücel
IEEES-066	An Assessment of A Novel Hybrid Photoelectrochemical-Conventional Hydrogen Generator	Mehmet Gursoy, Ibrahim Dincer.
IEEES-067	Design and Implementation of Lighting and Household Loads Monitoring System based on Power Line Carrier Communication	Fathia Chekired, Ali Laldji, Imed Eddine Drioueche, Younes Nezzari, Fethi. Akel, Aissa Meflah, Slimane Kerrouchi, Laurent Canale
IEEES-068	A Novel Approach for Estimating Chemical Exergy Values of Biomass Mixtures Using Artificial Neural Networks	Dogan Erdemir, Ibrahim Dincer
IEEES-069	Capacity Potential and Cost Assessment for Hydrogen Production from Marine Sources	G. Kubilay Karayel, Ibrahim Dincer
IEEES-070	Performance Study of a Desiccant Dehumidification Wheel	Fatih Bouzeffour, Walid Taane, Mouna Kassim, Zahra Neffah, Djelloul Belkacemi
IEEES-071	Development of Electrolytic Cation Exchange Reactor Module for Generation of Hydrogen Gas Using Ocean Water	Hilal Sayhan Akci Turgut, Ibrahim Dincer.
IEEES-072	Integrating Ultrasound Technology for Wastewater Treatment and Hydrogen Production into an Energy System: Analysis and Assessment	Moslem Sharifishourabi, Ibrahim Dincer, Atef Mohany
IEEES-073	Theoretical Investigation of Solar Energy Assisted Cooling in Refrigerated Trailers	Yusuf Taha İsmailoğlu, Deniz Ulusarslan
IEEES-074	Study of boiling heat transfer coefficient during evaporation of CO2	Rabah Gomrı, Nadim Karoune
IEEES-075	Microalgae Derived Biostimulants for Sustainable Agriculture Exergoeconomic Analysis	N. Melenek, M. Gasparin, G. Conor, A. C. D. Oliveira, K. Melenek, A. B. Mariano, V. M. Kava, J. V. C. Vargas.
IEEES-076	Design of an Electro Bio-membrane Reactor for Simultaneous Biohydrogen Production, Desalination, and Bacterial Energy Generation	A. Yagmur Goren, Ibrahim Dincer, Ali Khalvati
IEEES-077	Analysis of PEM Fuel Cell System Efficiency Using Machine Learning Algorithms	Emre Kacmaz, Burcu Yılmazel
IEEES-078	Implementation of Salp Swarm algorithm for optimal energy dispatching in microgrids	Boulouma Sabri, 1seddaoui Naoual, Belmili Hocine, Bendib Boualem
IEEES-079	Projections for Türkiye's Net Zero Carbon Target by 2053	Ceren Şengül, Mustafa Zeki Yılmazoğlu

IEEES-080	Investigation of the Effects of Heat Pump Applications on Cultural Heritage Buildings: A Case Study on Gazi University Rectorate Building	Nazlı Deniz Ünal, Mustafa Zeki Yılmazoğlu,
IEEES-081	Integration of Hydrogen Technologies into Buildings in Historic Urban Areas	Emine Sacha Nokay, Zeynep Durmuş Arsan,
IEEES-082	PV Parameter Estimation Using Remora Optimization Algorithm	Gamze Nalçacı
IEEES-083	Retrofitting Office Buildings on Global Warming Case Study: Turkey	Gözde Nalçacı, Gamze Nalçacı
IEEES-084	LBM simulation of thermal comfort in a room cooled by displacement ventilation: effect of Inlet-outlet layouts	Nasserı Lyes, Hıreche Zouhira, Ameziani Djamel Eddine
IEEES-085	An Uninterrupted Hydrogen and Wind-Solar Renewable Energy System Design and Multi-Objective and Multi-Constrained Optimization Approach for Hybrid Renewable Energy Systems	Tuba TEZER
IEEES-086	Comparison of Lithium-sulfur and Lithium Iron Phosphate Batteries for Present and Prospective Battery Management System of Electric Vehicles	Gamze Nalçacı
IEEES-087	Design and Analysis of a Floating Photovoltaic Based Ammonia Production System	Sibel Uygun Batgi, Ibrahim Dincer
IEEES-088	Impact of Reaction Parameters on Biodiesel Yield and Fuel Characteristics: A Case Study on Algal Oil	Cemil Koyunoğlu, Fevzi Yaşar
IEEES-089	Exergy and pinch analyses for integration of Cu-Cl cycle with solid oxide fuel cell	Muhammad Ishaq, Ibrahim Dincer
IEEES-090	Investigation of the Relationship Between the Topography and the Fluid Circulation Depth on the Geothermal Systems of Central Anatolia Region	Sinan Burhan, Kamil Erkan
IEEES-091	The Refrigerant Amount Optimization Study for the Household Refrigerator Performance	Selim Can Bozkır, Yiğithan Çalı
IEEES-092	Analysis of Cyber Risk Management Frameworks for The Maritime Industry	Atalay Keleştemur, Güldem Elmas, İsmail Özdemir, Ahmet Murat Köseoğlu
IEEES-093	Kinetic Analysis and Simulation of Rice Husk Char Gasification in H2O and CO2 Atmospheres for Enhanced Syngas Production	Cemil Koyunoğlu, Mustafa Tolay
IEEES-094	The Usage of Electric Transport Vehicles in the Logistics Industry	Ahmet Murat Köseoğlu, İsmail Özdemir
IEEES-095	Thermodynamic Performance Analysis of Different Phase Change Materials for Cold Thermal Energy Storage	Merve Altuntas, Dogan Erdemir, Sebahattin Unalan
IEEES-096	Smart Greenhouse System and Control of Necessary Parameters for Accelerating Plant Growth-I	Nurdan Akdemir, Yunus Babacan
IEEES-097	Smart Greenhouse System and Control of Necessary Parameters for Accelerating Plant Growth-II	Nurdan Akdemir, Yunus Babacan
IEEES-098	Smart Greenhouse System and Control of Necessary Parameters for Accelerating Plant Growth-III	Nurdan Akdemir, Yunus Babacan

IEEES-099	Potential Use of Hydrogen Pentoxide and Hydrogen Peroxide in Transportation Sector: An LCA Study	Assem Abdurakhmanova, Ibrahim Dincer
IEEES-100	A Comprehensive Analysis of the Thermal and Heat Transfer Characteristics of the Melting of Capric Acid As A Phase Change Material In a Rectangular Thermal Storage Unit	Md. Imran Alam, Munawar Nawab Karimi, Osama Khan, Ashok Kumar Yadav, Anoop Kumar Shukla, Sabri Alkan
IEEES-101	Experiments review of solar wastewater treatment (SOWAT)	Sadek Igoud, Belgassim Boutra, Lamine Aoudjit, Aïcha Sebti, Fatiha Souahi, Chems-Eddine Chitour, Djamel Zeriri, Amel Mameche
IEEES-102	Intelligent Control of DC-DC Boost Converter for Hydrogen and Fuel Cell Systems: An Artificial Neural Network Approach	Mustafa Özden, Davut Ertekin
IEEES-103	Active Balancing with Bidirectional Energy Transfer: A Flyback Converter Solution for Lithium-Ion Cells	Eren Küpcü, Davut Ertekin
IEEES-104	Fabrication of a Graphene-Based Nanohybrid Interlayer For Improved Li-S Cells Via Atomic Layer Deposition	Hazal Gergeroglu, Mato Knez, Mehmet Ziya Söğüt
IEEES-105	Simultaneous Biohydrogen Production from Energetic Poplar and Waste Minimization Using Membraneless Microbial Electrolysis Cell	A. Faruk Kılıcaslan, A. Yagmur Goren, Ibrahim Dincer, Ali Khalvati
IEEES-106	Exergy-Based Analysis of Polymer Recycling in the Automotive Sector	Cemil Koyunoğlu, Tamer Çınar
IEEES-107	Energy and Exergy Analysis of Steam Co-gasification of Olive Husk and Polypropylene: An Aspen Plus Modeling Study	Duygu Gündüz Han, Kaan Erdem, Adnan Midilli
IEEES-108	Smart Control for Sustainable Power: A Step-Up Converter with Artificial Neural Network Regulation in Hydrogen and Fuel Cell Technology	Davut Ertekin, Mustafa Özden
IEEES-109	Life Cycle Analysis of Power Supply Selection for a Chloralkali Production Plant	Sümeyya Ayça, Ibrahim Dincer
IEEES-110	Decarbonisation Targets and Actions in Turkish Maritime Sector Within the Framework of the Financing Agreement for the Annual Action Plan in favor of Türkiye for 2021	Halil Çeçen
IEEES-111	Review of the Current Developments About Reducement of the Greenhouse Gas Emissions from Maritime Activities According to Turkish Climate Change Bill	Halil Çeçen
IEEES-112	Goal Programming-Based Bi-Objective Optimization Model in Empty Container Logistics	Hüseyin Gençer, Sevda Dede
IEEES-113	Multi-Objective Optimization in Container Port Operations	Hüseyin Gençer
IEEES-114	Energetic and Exergetic Performance Analysis of the Solar Tower-Based Integrated Plant Combined With Helium-Based Brayton Cycle and HTSE For Power and Hydrogen Generation	Fatih Yılmaz, Murat Ozturk, Resat Selbas

IEEES-115	Assessment of the Current Developments Regarding the Reduction of Maritime Transport CO2 Emissions Within the Framework of the Acquis Communautaire	Halil Çeçen
IEEES-116	Demoeconomics: The Relationship Between Energy and Demoethical Values	Rinat A. Zhanbayev, Muhhamad Irfan, Daniil G. Maksimov, Anna V. Shutaleva, Makpal Kozhakanova
IEEES-117	Electrochemical Disinfection of Secondary Effluent Using a Low Cost Stainless Steel Electrodes	Hafida Lebik, Rafik Elhadi, Sarah Mahidine, Wassila Yazid, Sarah Djelti, Belgassim Boutra
IEEES-118	Re-defining and conceptualizing the Energy Footprint as a Sstandalone Indicator	Abdullah Muratoglu,
IEEES-119	Insights Into a Sustainable Campus: Piri Reis University	Duygu Erten, P.E.Aıa, Breeam Fellow
IEEES-120	Exergy-based Performance Analysis and Assessment of Geothermal District Cooling Systems	Nurdan Yildirim, Arif Hepbasli,
IEEES-121	Evaluating Sustainable Aviation Fuels: A Comparative Analysis of Expert Groups	Omar Alharasees, Serdar Sanlı, Utku Kale
IEEES-122	Hydrogen-Powered Aviation: Shaping Sustainable Future Skies	Omar Alharasees, Serdar Sanlı, Utku Kale
IEEES-123	Adaption of Fuel-Cell Energy in Aviation Infrastructure	Omar Alharasees, Utku Kale
IEEES-124	A Strategy on Off-Shore Alternative Fuel Production	Onur Otlu, Adnan Midilli, Zehra Yumurtacı
IEEES-125	Thermal Analysis for Different Discharge Rates in A Li-Ion Battery Package	Büşra Namaldı Kömürcü, Muhammet Çelik, Gülşah Elden, Mustafa Serdar Genç
IEEES-126	Design and Analyses of Double Flash Geothermal Power Plant Combined ith Reheat-Transcritical CO2 Rankine Cycle for Power, Hydrogen, Hot Water, and Freshwater Generation	Fatih Yılmaz, Murat Ozturk, Resat Selbas
IEEES-127	Experimental and Numerical Analysis on Prasmatic LFP Battery Surface Temperature Distribution	Oya Bakar, Murat Uysal, Barış Yılmaz
IEEES-128	Green Synthesis of ZnO nanoparticles for effecticve photocatalyric degradation of Malacgite Green under UV ligt and Sun-Light: A Comparative Study	Mohammed Aıt Oumeracı, Tarek Berrama, Hayet Tızı, Fariel Sahoui
IEEES-129	Energetic and Exergetic Analysis of a Marine-Type ORC WHRS using Zeotropic Mixtures	Mehmet Akman, Selma Ergin
IEEES-130	Comparison study of four typical ORC configurations integrated with hydrogen production unit for the exploitation of medium temperature geothermal sources	Taha Aydin, Hadi Genceli, Parisa Heidarnejad
IEEES-131	Adsorption of Co (II) ions onto NaX and NaA zeolites	Ferhat Djawad, Nıbou Djamel, Hadj Mekatel, Amokrane Samira.

IEEES-132	Development of a Dynamic t-CO2 Rankine Cycle Model with Heat Recovery System for Daily-Based Performance Assessment	Tunahan Akış, Mehmet Akif Ezan, Nuri Kayansayan, Önder Kızılkan, Çağla Cergibozan, Can Özgür Çolpan
IEEES-133	Thermodynamic Analysis of the Parabolic Dish Collector Based Hydrogen Production System	Arif Karabuga, Zafer Ulu
IEEES-134	Smart Micro-grids as Improving Solution for supplying Agriculture Farms	H. Belmili, S. Boulouma, L. Baghli, B. Bendib, A. Mecharnane
IEEES-135	Comparative Evaluation of Solar Exergy Models for Various Regions in Turkey	Seyed Hamed Pour Rahmati Khalejan
IEEES-136	Efficiency Optimization of Solar Assisted Absorption Refrigeration Systems	Gülçin Yıldırım Çimşir, Tuba Okutucu Özyurt
IEEES-137	Robust Grid Synchronization PLL Algorithms for Harmonic Distored and Unbalanced 3-Phase Grid Conditions	Smail Toufik, Boulouma Sabri, Seddaoui Nawel, Rahmani Hachemi
IEEES-138	Study the Flame Charecteristics of Gasoline Propanol Blends for SI Engine	Kumaravel S., Saravanan C. G., Premkumar P., Edwin Geo V, Manoj Babu A, Elaya Perumal A.
IEEES-139	A Concept Design Study for the Energy-Efficiency of Bulk Carriers	Mehmet Akman, Bülent İbrahim Turan, Ahmet Taşdemir, Mehmet Ziya Söğüt
IEEES-140	Analysis of Thermally Coupled Fuel Cell and Metal Hydride Hydrogen Storage Tank System for Lightweight Vehicles	Sera Ayten Çetinkaya, Mehmet Akif Ezan, Mustafa Umut Karaoğlan, C. Ozgur Colpan
IEEES-141	Structural and Thermal Characterization of Polyethylene-based Nanocomposites containing Multi-walled Carbon Nanotubes	Soror Saadallah, Kelthoum Saadallah, Mohamed Cherif Bouleklab, Smail Hamamda
IEEES-142	Polystyrene ZIF-8 Metal-Organic Framework Composite Nanofibrous Membrane for Oil/Water Separation	Kamala Thota, ,Ramya Araga, Manohar Kakunuri, Sharath Babu Anne
IEEES-143	Assessment of the Life Cycle and Energy, Exergy use of Various Tomato Products Supply Chain in the Food Sector Under Various Improvement Scenarios	Samiye Adal, Zafer Erbay
IEEES-144	A Study on the Elimination of Heavy Metal Pollution with Soma Thermal Power Plant Fly Ash	Nagihan Ersoy, İsmail Ekmekçi
IEEES-145	Evaluation of Wind Energy and Atmospheric Stability in Edincik	Sevinc A. Sirdas, Kemal Ege Sural

Symposium Program

IEEES-14
December
24, 2023

Piri Reis University Sea
Campus B block

10:30	**Registration**	Piri Reis University, B Block Chair: Dr. M.Ziya Sogut
13:45 - 15:15	**Wall Presentations**	Preparing of wall paper presentation **Cemil Koyunoğlu, Mustafa Tolay** "Kinetic Analysis and Simulation of Rice Husk CharGasification in H_2O and CO_2 Atmospheres for Enhanced Syngas Production" **Yorken Chrisha C., Abhilash Suryan, Suresh Lal S R, Prasanth P Nair** "Analysis of WindFlow around Major Buildings in an Academic Campus in India" **Demet Yılmaz, Sennur Alay Aksoy** "Integrating Phase Change Materials (PCMs) IntoCotton Ring Spun Yarn Structure For Thermo-Regulating Function" **Sevinç Sırdaş, Kemal Ege Sural** "Evaluation of Wind Energy and Atmospheric Stability inEdincik" **Gökhan Sefer, Süleyman Karsli** "Numerical Investigation of the Effect of Forced Air/nanofluid Pairs on Pv/t System Performance" **Sevinç Sırdaş, Oguzhan Arabaci** "Effects of Climate Change and Global Oscillations onPrecipitation Variability" **Mahdi Mokrane, Maamar Ouali, Ferhat Yahi, Mohamed Ali Djebiret, Ali Tetbirt, Mohand Berdja** "Enhancing Household Refrigerator Efficiency through the Integration ofPhase Change Materials: An Experimental and Statistical Analysis" **Ferhat Djawad, Nibou Djamel, Hadj Mekatel, Amokrane Samira** "Adsorption of Co (II)ions onto NaX and NaA Zeolites"

IEEES-14
December 25, 2023

Piri Reis University Sea Campus, B Block

(Program Presenter: Dilara Narin)

08:00-09:00		Registration
09:00- 09:15		Opening Ceremony; Performer :….....
09.15 – 09:30	09:15-09:20	**Dr. M.Ziya Sogut (Symposium Chair)**
	09:20-09:30	**Dr. Nafiz Arıca (Rector of Piri Reis University)**

KEYNOTE TALK -1		
09:30 - 11:00		Session Chair: **Dr. Yunus Çengel**
	Keynote Talk 1	**Dr. İbrahim Dinçer** "The Role of Exergy in Integrated Energy Systems"
	Keynote Talk 2	**Dr. Mihri Özkan** "Direct Air Capture of CO_2 and Its Use for Synthetic Aviation Fuels: The Promise of Greener Skies"
11:00-11:30		**Coffee Break**
11:30-13:00		**KEYNOTE TALK -2**
11.30 - 13.00		Session Chair: **Dr. Arif Hepbaşlı**
	Keynote Talk 3	**Dr. Donghai Wang** "Development and Application of Functional Materials for Next-Generation Electrochemical Energy Storage Technologies"
	Keynote Talk 4	**Dr. Cengiz Özkan** "Prospects in Global Vehicle Electrification Over the Next Decade"
13:00-14:00		**Lunch / Coffee Break**
14:00-15:00		**Sectorial Session (Seminar 1)**
14.00 - 15.00		Session Chair: Dr. Murat Koray
	14:00-14:10	Heliplat
	14:10-14:20	GİSBİR
	14:20-14:30	STM
	14:30-14:40	Artı Denizcilik
	14:40-14:50	Vizyon Inovatif Yalıtım
	14:50-15:00	TMS Group

Technical Session-1 (Room 1)		
14:00 - 15:30	**Energy Systems and Technologies: PV & Solar-Based Systems**	**Session Chair: Dr. Cüneyt Ezgi** **Davut Ertekin, Eren Küpcü** Active Balancing with Bidirectional Energy Transfer: A Flyback Converter Solution for Lithium- Ion Cells **Houda Tassoult, Mezidi Ahmed** Applications of Fresnel Concentrated Solar Power System and their Impact Towards Environment **Abdullah Muratoğlu** Re-defining and Conceptualizing the Energy Footprint as a Standalone Indicator **Oya Bakar, Barış Yılmaz, Murat Uysal** Experimental and Numerical Analysis on Prismatic LFP Battery Surface Temperature Distribution **Nazım Taş, Ayşegül Abusoğlu** Assessment of the Effect of Lint Accumulation in the Heater Channel on the Performance of the Water Cooled Washing Drying Machines in Different Operating Conditions
Technical Session-2 (Room 2)		
14:00 - 15:30	**Energy & Exergy Analysis and Applications**	**Session Chair: Dr. Hadi Genceli** **Tunahan Akış, Mehmet Akif Ezan, Nuri Kayansayan, Önder Kızılkan, Çağla Cergibozan, Can Özgür Çolpan** Development of a Dynamic t-CO_2 Rankine Cycle Model with Heat Recovery System for Daily-Based Performance Assessment **Maryam Karami, Seyedeh Somayeh Nasiri Gahraz** A Year-round Dynamic Simulation of a Solar Trigeneration System in Hot and Humid Climate **Ibrahım Karacaylı, Lutfiye Altay, Arif Hepbasli** Exergy-Based Performance Assessment of an Ejector-Enhanced Auto-Cascade Refrigeration Cycle

Technical Session-3 (Room 3)		
	Sustainability and	**Session Chair: Dr. Nader Javani**
		Metin Gül, Ersin Akyüz Future Methanol Cost Projections in Specific Regions: A Comprehensive Study
		Fathia Chekired Design and Implementation of Lighting and Household Loads Monitoring System based on Power Line Carrier Communication

		Sabri Boulouma, Naoual Seddaoui, Rahmani Lazhar, Hocine Belmili, Boualem Bendib Implementation of Salp Swarm Algorithm for Optimal Energy Dispatching in Microgrids **Ömer Faruk Güler** Comparative Analysis of Energy Storage Methods for a Parabolic Through Collector Solar Power System **Seyed Hamed Pour Rahmati Khalejan** Comparative Evaluation of Solar Exergy Models for Various Regions in Turkey
Technical Session-4 (Room 4)		
14:00 - 15:30	**Green Transition and Decarbonization: Transportation Vehicles**	**Session Chair: Dr. Elayaperumal Annamalai** **Halil Çeçen** Review of the Current Developments About Reducement of the Greenhouse Gas Emissions from Maritime Activities According to Turkish Climate Change Bill **Murat Ayar** Investigating Fuel Consumption Disparities Between Nonstop and Connecting Flights **Sinan Burhan, Kamil Erkan** Investigation of the Relationship Between the Topography and the Fluid Circulation Depth on the Geothermal Systems of Central Anatolia Region **Fazıl Erinc Yavuz, Vasif Can Yildiran, Sebastian George Colleoni** Numerical Investigation in a Dishwasher Hub: Reducing Pressure Difference and Pump Power **Onur Otlu, Adnan Midilli, Zehra Yumurtacı** A Strategy on Off-Shore Alternative Fuel Production
Technical Session-5 (Room 5)		
		Session Chair: Dr. Edwin Geo Varuvel **Boubekeur Boudıne, Imene Ameur, Miloud Sebais, Ouahiba Halimi, Zeineddine Ouili** Fabrication and Photocatalytic Activity of Undoped and Mg Doped ZnO **Hanane Aburideh** Acetate Cellulose Modified Nanofiltration Membrane Efficacity and Performance **Burak Vardar,** Fazlı Okan Bovatekin, Yunus Mert Becermen, Okan Gök, Ersin Alptekin, Mehmet Akif Ezan, Aytunc Erek, Experimental Studies on Energy and Exergy-based Assessments of a Freezer **Salih Bilgiç,** Eren Cankılıç, Alper Gülmez, Okan Gök, Ersin Alptekin, Mehmet Akif Ezan, Aytunç Erek 3D Steady-State and Transient Numerical Studies of a Static Freezer **Zahra Sadaoui, Noreddine Boudechiche, Ouiza Allalou, Assia Djebri** The Improvement of the Mebeverine Hydrochloride Photocatalytic Degradation by Using Combined Activated Carbon/ZnO Under Sunlight
15:30- 15:45		**Coffee Break**
Technical Session-6 (Room 1)		
16:45 - 18:15	**Energy Systems and Technologies:** **PV & Solar-Based Systems**	**Session Chair: Dr. Ahmet Taşdemir** **Muhammed Bozelli, Berk Kurt** Investigation of Optimal Panel Angle for Denizli/Güney

		Rabah Gomri Dissociation of Methane for Hydrogen Production in a Solar Reactor **Hani Zeidan, Mustafa Esen Marti, Ebru Erunal** Synthesis and Characterization of Novel CeO2/SiO2 Composites and Their Use in Removal of Cationic and Anionic Dyes **Mezidi Ahmed, Houda Tassoult, Bendjebbas Hichem** The Management of Electrical and Thermal Energy in a House at Different Climates Algeria **Hocine Belmili** Smart Micro-grids as Improving Solution for Supplying Agriculture Farms
Technical Session-7 (Room 2)		
16:45 - 18:15	**Energy & Exergy Analysis and Applications**	**Session Chair: Dr. Nader Javani** **Atoui Sakina, Fouad Aissaoui, Amel Berkane, Mohammed Ayad** Performance Improvement of Pv Generator Using a Sun Tracking System **Arif Karabuga, Zafer Utlu** Thermodynamic Analysis of the Parabolic Dish Collector-Based Hydrogen Production System **Sümeyya Ayça, İbrahim Dinçer** Life Cycle Analysis of Power Supply Selection for a Chloralkali Production Plant **Aminu Yusuf, Sedat Ballikaya** Photovoltaic-phase Change Materials-thermoelectric System Coated With Radiative Cooling **Vasif Can Yildiran, Hasan Günes** An Investigation of the Impact of the Cooling Air Diffusers on Drying Performance in a Condenser Tumble Dryer
Technical Session-8 (Room 3)		
16:45 - 18:15	**Sustainability and Environmental Management: Fuels**	**Session Chair: Dr. Dogan Erdemir** **Emine Sacha Nokay, Zeynep Durmuş Arsan** Integration of Hydrogen Technologies into Buildings in Historic Urban Areas **Edwin Geo Varuvel** Analyzing the Lean Burn Combustion Stability by Hydrogen Induction in Gasoline Direct Injection Engine **Kumaravel S, Saravanan C G, Premkumar P, Edwin Geo Varuvel, Manoj babu A, Elayaperumal A** Study the Flame Characteristics of Gasoline Propanol Blends for SI Engine

Technical Session-9 (Room 4)		
16:45 - 18:15	**Green Transitionand Decarbonization :Transportation Vehicles**	**Session Chair: Murat Emre Denir** **Cengizhan Gök, Selcuk Ekici, Ozgur Balli, Tahir Hikmet Karakoc** Hydrogen as the Fuel of the Future and Hydrogen-powered Aircraft **Assem Abdurakhmanova, Ibrahim Dincer** Potential Use of Hydrogen Pentoxide and Hydrogen Peroxide in Transportation Sector: an LCA Study **Tarek Ibnou Ziad Berrama, Mohamed Ait Oumeraci, Feriel Sahoui, Hayet Tizi** Green synthesis of ZnO Nanoparticles for effective photocatalytic degradation of Malachite Green under UV light and Sun-light: a comparative study
Technical Session-10 (Room 5)		
16:45 - 18:15	**Energy Efficient materials**	**Session Chair: Dr. Murat Uyar** **Lekshmipriya J, Abhilash Suryan, Prasanth P Nair** A Computational Investigation, Into the Leakage and Dispersion of Hydrogen, in EnclosedAreas **Nihad Dukhan, Hannah Klatzke, Ming Liang, Mahmoud Ghannam** Effect of Metal Foam Bonding to Solid Substrate for Cooling Electronic Systems: Brazing vs. Thermal Epoxy **Sadek Igoud, Belgassim Boutra, lamine Aoudjit, Aicha Sebti, Fatiha Souahi, Chems-Eddine Chitour, Djamel Zeriri, Amel Mameche** Experiments Review of Solar Wastewater Treatment (SOWAT)

IEEES-14
December 26, 2023

Piri Reis University Sea Campus, B Block

(Program Presenter: Dilara Narin)

KEYNOTE TALK		
09.00 – 10:30		Session Chair: **Dr. Ali Cemal Benim**
	Keynote Talk 5	**Dr. Abdul-Ghani Olabi (Online)** “Digital Twin & Artificial Intelligent for Renewable Energy & Energy Storage Systems”
	Keynote Talk 6	**Dr. Yunus Çengel** “Energy and Exergy Efficiencies of Geothermal Power Plants”
10.30 – 11:00		**Coffee Break**
INVITED TALK		
11:00-12:30		Session Chair: **Dr. Özgür Çolpan**
	Invited Talk 1	**Dr. Adnan Midilli**
	Invited Talk 2	**Dr. Ali Cemal Benim**
	Invited Talk 3	**Dr.Birol Kılkış-Online**

12:30-13:00		**Sectorial Session-2 (Room-1)**
12.30 - 13.00		Session Chair: **Dr. Oktay Çetin**
	12:30-12:40	Hydroworks Mühendislik
	12:40-12:50	Seapower Electrical Systems
	12:50-12:55	Berkin Engineering
	12:55-13:00	Alfa Laval
	13:00-13:10	Yaf Diesel
12:30-13:00		**Wall Paper Presentation**
		Session Chair: Dr. M.Ziya Sogut
		Fatih Özcan, Muhsin Kilic "Prediction of Thermodynamic Properties for Compressed Natural Gas Mixtures"
		Gözde Nalçacı, Gamze Nalçacı "Retrofitting Office Buildings on Global Warming Case Study: Turkey"
		Halil Çeçen "Assessment of the Current Developments Regarding the Reduction of Maritime Transport CO2 Emissions Within the Framework of the Acquis Communautaire"
		Chekirou Wassila, Nahman Boukheit, Ahcene Karaali " Effect of Adsorbent/adsorbate Working Pairs on SolarAdsorption Cooling Performance’s"
		Hocine Guellıl, Korti Abdel Illah Nabil "Effects of Distance and Absorber Shape on the Energetic and Exergetic Performance of a Solar Collector"
		Mekatel Elhadj, Belmedani Mohamed, Bentaieb Noureddine "A New Heterosystem ZnO/NaX Zeolite for the Removal of Blue Basic Dye 41 by Photocatalysis Under Solar Irradiation"
		Büşra Namaldı Kömürcü, Muhammet Çelik, Gülşah Elden, Mustafa Serdar Genç Thermal Analysis for Different Discharge Rates in A Li-Ion Battery Package
		Hafida Lebik, Rafik Elhadi, Sarah Mahidine, Wassila Yazid, Sarah Djelti Electrochemical Disinfection of Secondary Effluent Using a Low Cost Stainless Steel Electrodes

13:00-14:00		Lunch / Coffee Break
Technical Session-11 (Room 1)		
14:00 - 15:00	**Energy Systemsand Technologies: PV & Solar Based Systems**	**Session Chair: Dr. Houda Tassoult** **Abdel Illah Nabil Korti, Hocine Guellil** An Effective Moisture Diffusivity of a Hybrid Double Pass Collector-Solar Dryer For Tomato Slices Drying **Fathima Ancy M, Abhilash Suryan, Prasanth P Nair, Sriram Chandran R** Evaporative Cooling of Solar Photovoltaic Panels: a Computational Study **Taha Buğra Sari, Orçun Şenler, Murat Mustafa Savrun** Power Grid Schemes of Marine Vehicles with Electric Propulsion
Technical Session - 12(Room 2)		
14:00 - 15:00	**Energy & Exergy Analysisand Applications**	**Session Chair: Dr. İsmail Ekmekçi** **Uğur Demir** Evaluation of Operational Factors for The Energy Efficieny Optimization of High-Speed Roro Vessels by Trim Optimization **Gülçin Yıldırım Çimşir, Tuba Okutucu Özyurt** COP Improvement of Solar Assisted Absorption Refrigeration Systems **Ahmad Zikri, Muhsin Kilic, Fatih Özcan** Thermodynamic Analysis of Desalination System on Combined Cycle Power Plants Through Throttling Process Method by Using a Vapor Compressor
Technical Session-13 (Room 3)		
14:00 - 15:00	Sustainability and Environmental Management: Waste Solid	**Session Chair: Dr. Belmedani Mohamed** **Duygu Erten** Insights Into a Sustainable Campus: Pir i Reis University **Cemil Koyunoğlu, Fevzi Yaşar** Impact of Reaction Parameters on Biodiesel Yield and Fuel Characteristics: A Case Study on Algal Oil

Technical Session-14 (Room 4)		
14:00 - 15:00	**Energy Systems and Technologies: Renewable Sources**	**Session Chair: Dr. Nurdan Yıldırım** **Mine Sertsöz** Parameters of Renewable Energy Usege in Rail Systems **Hüseyin Gençer** Multi-Objective Optimization in Container Port Operations **Mehmet Furkan Koparan, Mehmet Akif Ezan, Okan Gök, Ersin Alptekin, Aytunç Erek** Preliminary Study on a Transient Freezer Model with PCM
Technical Session-15 (Room 5)		
14:00 - 15:00	**Energy efficient materials**	**Session Chair: Dr. Can Coşkun** **Özüm Çallı, Vedagiri Praveena, Edwin Geo Varuvel** "Combined Effects of Nozzle Hole Variation and Piston Bowl Geometry Modification on Performance Characteristics of a Diesel Engine with Energy and Exergy Approach" **Zafer Metin Ataş, Gizem Başaran Dindaş, Hüseyin Cengiz Yatmaz** Development of Metal Loaded Minerals as Heterogeneous Catalysts for the Degradation of Dye Solutions **Hazal Gergeroglu, Mato Knez, Mehmet Ziya Sogut** Fabrication of a Graphene-based Nanohybrid Interlayer for Improved Li-S Cells via Atomic Layer Deposition
Technical Session-16 (Room 1)		
		Session Chair: Dr. Orhan Özgür Aybar **Yusuf Taha Ismailoglu, Deniz Ulusarslan** Theoretical Investigation of Solar Energy-Assisted Cooling in Refrigerated Trailers
Technical Session-17 (Room 2)		
		Session Chair: Dr. Hocine Belmili

15:00 - 16:00	**Energy & Exergy Analysis and Applications**	**Edwin Geo Varuvel** Investigation on Combustion, Performance and Emission Characteristics of Waste Cooking Oil – Diesel Blends With Hydrogen in CI Engine – a Dual Fuel Approach **Lyes Nasserı, Zouhira Hireche, Djamel Eddine Ameziani** LBM Simulation of Thermal Comfort in a Room Cooled by Displacement Ventilation: Effect ofInlet-outlet Layouts **Murat Koseoglu, İsmail Özdemir** The Usage of Electric Transport Vehicles in the Logistics Industry **Mehmet Akman, Selma Ergin** Energetic and Exergetic Analysis of a Marine-Type ORC WHRS Using Zeotropic Mixtures **Fatih Özcan, Muhsin Kılıç** Dynamic Modeling of a Compressed Natural Gas Refueling Station
Technical Session-18(Room 3)		
15:00 - 16:00	**Sustainability and Environmental Management: Waste Solid Recycle**	**Session Chair: Dr. Fatih Yılmaz** **İsmail Ekmekci, Nagihan Ersoy** A Study on the Elimination of Heavy Metal Pollution with Soma Thermal Power Plant Fly Ash **Muhammed Baştuğ, Hatice Eser Ökten, Hale Demirtepe** Heavy Metal Phytoremediation Using Energy Crops in Surface Soil of an Industrial Zone
Technical Session-19 (Room 4)		
15:00 - 16:00	**Energy Systems and Technologies: Renewable Sources**	**Session Chair: Dr. Duygu Erten** **Merve Altuntas, Dogan Erdemir, Sebahattin Unalan** Thermodynamic Performance Analysis of Different Phase Change Materials for Cold Thermal Energy Storage **Cihan Emre Şahin, Murat Emre Demir** Harnessing Wind Energy: Solid Sails in Maritime Transport for Sustainable Energy Utilization **Nazlı Deniz Ünal, Mustafa Yılmazoğlu** Investigation of the Effects of Heat Pump Applications on Cultural Heritage Buildings: A Case Study on Gazi University Rectorate Building **Mine Sertsöz, Ali Burak Göğebakan** Hydrogen Energy in Transportation Vehicles
Technical Session-20 (Room 5)		
15:00 - 16:00	**EnergyEficientmaterials**	**Session Chair: Dr. Şebnem Helvacıoğlu** **Erol Pehlivan, Elif Gezginci, Busra Ozkok** Green Synthesis of Encapsulated Nano Silver Biochar Composite for Malachite Green Removal from Aqueous Solution: Novel Synthesis and Optimization **Saadallah Soror, Hamamda Smail, Bouleklab Mohamed Cherif** Structural and Thermal Characterization of Nanocomposites Based on Multi-walled Carbon Nanotubes (MWNT) and Polyethylene

Technical Session-21 (Room 1)		
16:30 - 17:45	**Energy Systems and Technologies: Renewable Sources**	**Session Chair: Dr. Edwin Geo Varuvel** **Ömer Faruk Güler** Greenhouse Heating with Low Enthalpy Solar and Geothermal Energy **Ozan Gül** Examination of the Impact of Renewable Energy Sources on Line Losses in a 14-Bar System **Alkın Erdal Demirhan, Murat Emre Demir, Omer Kemal Kinaci** Development of a VIV System for Hydrokinetic Energy Harvesting and Pumped Hydro Storage **Hilal Akci, Ibrahim Dincer** Development of Electrolytic Cation Exchange Reactor Module for Generation of Hydrogen Gas Using Ocean Water
Technical Session -22(Room 2)		
16:30 - 17:45	**Energy & Exergy Analysis and Applications**	**Session Chair: Dr. Mehmet Akman** **Ramsagar Vooradi, Shailesh Singh Sikarwar, Venkata Suresh Patnaikuni, Manohar Kakunuri** Energy and Exergy Analysis of CLC Based Biomass Fired Power Plant With Different Oxygen Carriers **Samiye Adal, Zafer Erbay** Assesment of The Lıfe Cycle And Energy, Exergy Use of Varıous Tomato Products Supply Chaın in The Food Sector Under Varıous Improvement Scenarios **Nurdan Yildirim, Arif Hepbasli** Exergy-based Performance Analysis and Assessment of Geothermal District Cooling Systems
Technical Session -23(Room 3)		
16:30 - 17:45	**Sustainability and Environmental Management: Climate Change**	**Session Chair: Dr. Hazal Gergeroğlu** **Can Coskun, Görkem Berkay Ergeç, Didem Sena Aksu, Zuhal Oktay** Simplified Method for Predicting Hourly Global Solar Radiation Distribution **Hüseyin Gençer** Goal Programming-Based Bi-Objective Optimization Model in Empty Container Logistics **Sevinc Sirdas, Kemal Ege Sural** Global Warming and Thunderstoms in South Aegean Region of Turkiye

Technical Session-24 (Room 4)		
16:30 – 17:45	**Energy Systems and Technologies**	**Session Chair: Dr. Murat Köseoğlu** **Mikail Rıza Onat, Murat Emre Demir** Techno-economic Analysis of the Distribution Network for the European Market of GreenAmmonia Produced From Offshore Wind Farms to Be Installed Off the Coast of Northern Europe **Fatıh Bouzeffour** Performance Study of a Desiccant Dehumidification Wheel **Oktay Cetin, Mehmet Ziya Sogut, Funda Yercan,** Assesment of Environmental Pollution Entropy-based Approach of Container Ships in the Ice-covered Arctic Waters
Technical Session-25 (Room 5)		
16:30 - 17:45	**Energy efficient materials**	**Session Chair: Dr. Şebnem Helvacıoğlu** **Sarath Babu Anne, Kamala Thota, Manohar Kakunuri, Ramya Araga** Polystyrene ZIF-8 Metal-Organic Framework Composite Nanofibrous Membrane for Oil/Water Separation

IEEES-14
December
27, 2023

Piri Reis University Sea Campus, B Block
(Program Presenter: Dilara Narin)

KEYNOTE TALK		
09.30 – 10:15		Session Chair: **Dr. Zafer Utlu**
	Keynote Talk 7	**Dr. Arif Hepbaşlı** "Exergy Management Matrix: Proposal and an Acrostic Approach"
INVITED TALK		
		Session Chair: Prof. Dr. Chekirou Wassila
10:20 – 11:30	Invited Talk-4	**Dr. Levent Kurnaz**
	Invited Talk- 5	**Dr. Derek Baker**
11:30 – 12:00		**Coffee Break**
12:00-13:30		**Sectorial Session-3 (Room1)**
		Session Chair: Dr. Hüseyin Gencer
12.00 - 13.10	**12:00-12:10**	PLT Mühendislik
	12:10-12:20	BMA Technology
	12:20-12:30	BTM Co.
	12:30-12:40	COLREG
	12:40-12:50	MAR-CA
	12:50-13:00	Atomar Denizcilik ve Taşımacılık
	13.00-13:10	Oceanist Engineering
12:30-13:00		**Wall Paper Presentation**
		Session Chair: Dr. Ozan Gül

Mohammad Hasan Khoshgoftar Manesh "Proposed an Innovative Polygeneration Structure for Power, Cooling,Heating, Fresh Water, Hydrogen, Carbone Dioxide and Ethanol Production"

Nurdan Akdemir, Yunus Babacan " Smart Greenhouse System and Control of Necessary Parameters forAccelerating Plant Growth-III"

Ozan Gül "Examination of the Impact of Electric Vehicles on the 14-Bar System's Line Losses"

Abdesselam Bouloufa, Rania Mahdadi, Aissa Bouchelaghem "SnO2:F Transparent Conducting Oxide PropertiesThin Film for Perovskite Solar Cell "

Chekirou Wassila, Nahman Boukheit, Ahcene Karaali "Thermodynamic and parametric analysis of a doubleadsorptive solar cooling cycle"

Toufik Smail, Sabri Boulouma, Nawel Seddaoui, Hechemi Rahmani "Robust Grid Synchronization PLL Algorithmsfor Harmonic Distorted and Unbalanced 3-Phase Grid conditions"

Mehmet Ziya Sogut, Oral Erdoğan "Assessment of the Economic and Environmental Impacts of Circular Processesin Green Port Transition and Entropy Management"

Omar Alharasees, Utku Kale "Hydrogen-Powered Aviation: Shaping Sustainable Future Skies"

Mehmet Gursoy, Ibrahim Dincer "An Assessment of A Novel Hybrid Photoelectrochemical-Conventional Hydrogen Generator"

Muhammad Ishaq, İbrahim Dincer "Exergy and pinch analyses for integration of Cu-Cl cycle with solid oxide fuel cell"

Aysegul Goren, Ibrahim Dincer, Ali Khalvati "Design of an Electro Bio-membrane Reactor for Simultaneous Biohydrogen Production, Desalination, and Bacterial Energy Generation"

Ahmet Kilicaslan, Aysegul Goren, Ibrahim Dincer, Ali Khalvati "Simultaneous Biohydrogen Production from Energetic Poplar and Waste Minimization Using Membraneless Microbial Electrolysis Cell"

Moslem Sharifishourabi, Ibrahim Dincer, Atef Mohany "Integrating Ultrasound Technology for Wastewater Treatment and Hydrogen Production into an Energy System: Analysis and Assessment"

Emre Mandev, Mehmet Akif Ceviz, Ali Çelik, Burak Muratçobanoğlu, Faraz Afshari Sustainable Solar Energy: Repurposing Discarded Materials in Parabolic Concentrator Fabrication

Murat AYAR Investigating Fuel Consumption Disparities Between Nonstop and Connecting Flights

Sera Ayten Çetinkaya, Mehmet Akif Ezan, Mustafa Umut Karaoğlan, Can Ozgur Colpan Analysis of Thermally Coupled Fuel Cell and Metal Hydride Hydrogen Storage Tank System for Lightweight Vehicles

Duygu Gündüz Han, Kaan Erdem, Adnan Midilli "Energy and Exergy Analysis of Steam Co-gasification of Olive Husk and Polypropylene: An Aspen Plus Modeling Study"

Sena Erkent "Numerical Investigation of the Effect of Different Boundary Conditions and Geometrical Properties on CO2 Removal Efficiency in the Retention of CO2 from Flue Gas in a CO2 Capture Column With Calcined Eggshell By Carbonation Reaction"

Omar Alharasees, Serdar Sanlı, Utku Kale Hydrogen-Powered Aviation: Shaping Sustainable Future Skies

Omar Alharasees, Serdar Sanlı, Utku Kale Hydrogen-Powered Aviation: Shaping Sustainable Future Skies

Emre Kaçmaz, Burcu Yilmazel Analysis of PEM Fuel Cell System Efficiency Using Machine Learning Algorithms

Sibel Uygun Batgi, İbrahim Dinçer Design and Analysis of a Floating Photovoltaic Based Ammonia Production System

Sennur Alay Aksoy, Demet Yılmaz "Integrating Phase Change Materials (PCMs) Into Cotton Ring Spun Yarn Structure For Thermo-Regulating Function"

Sennur Alay Aksoy, Cemil Alkan, Simge Özkayalar
"Production of Microencapsulated Thermochromic Systems in Poly(methyl methacrylate-co-methacryl amide) Shell and Application to Polyester Fabric for Thermal Management"

Cemil Alkan, Simge Özkayalar, Sennur Alay Aksoy
"Production of Microencapsulated Thermochromic Systems Based on Fluoran Dye and Investigation of Their Thermal Properties"

Davut Ertekin, Mustafa Özden "Smart Control for Sustainable Power: A Step-Up Converter with Artificial Neural Network Regulation in Hydrogen and Fuel Cell Technology"

Davut Ertekin, Mustafa Özden
"Intelligent Control of DC-DC Boost Converter for Hydrogen and Fuel Cell Systems: An Artificial Neural

		Network Approach” **Sena Erkent** “CO2 Removal by Calcined Eggshell”
13:00-14:00		**Lunch / Coffee Break**
		Technical Session-26 (Room 1)
		Session Chair: Dr. A.Sarath Babu **Enver Yalçın, Ali Oral, Can Tuncer, Salih Aksu, Sakıp Tüzköz** Sustainable Efficiency based Development of A Painting Robot Machine Simulating OperatorMovements for Wind Turbine Tower Painting Process **Fatih Yilmaz, Murat Ozturk, Resat Selbas** Design and Analyses of Double Flash Geothermal Power Plant Combined With Reheat-transcriticalCO2 Rankine Cycle for Power, Hydrogen, Hot Water, and Freshwater Generation **Praveen Kumar Bommineni, Venkata Suresh Patnaikuni, Snigdha Saha** 3-D Numerical Analysis of Vanadium Redox Flow Battery with Serpentine Flow Field **Tuba Tezer** An Uninterrupted Hydrogen and Wind - Solar Renewable Energy System Design and Multi- objective and Multi-constrained Optimization Approach for Hybrid Renewable Energy Systems
		Technical Session -27 (Room 2)
14:00 - 15:00	**Energy & Exergy Analysisand Applications**	**Session Chair: Dr. Ramsagar Vooradi** **Tayfun Tanbay, Ahmet Durmayaz** Impact of Natural Gas Composition on the Energy-Exergy-Environmental Performance of a Combined Cycle Power Plant **Malika Ouagued** Sizing and Performance Evaluation of Photovoltaic System Coupled With Electrolyzer HydrogenProduction **Özlem Boydak, Ismail Ekmekci, Mustafa Yılmaz** Thermodynamic Analyses Of A Organic Rankine Cycle (ORC) With Working Fluids R245FA, R245CA And R1233ZD In A Multigenerational Hybrid System **Dogukan Mızrak, Yağmur Nalbant Atak, Anil Erdogan, Can Ozgur Colpan** Performance Assessment of Power and Synthetic Methane Production from Geothermal Energy

Technical Session-28 (Room 3)		
14:00 - 15:00	**Sustainability and Environmental Management: Bio-**	**Session Chair: Dr. Mehmet Akman** **Burcu Kiren, Esin Varol** Co-Pyrolysis of Walnut Shell and Waste Rubber Blend to Produce Sustainable Bio-based Materials **Naresh Thota, Chandra Prakash Gupta** Natural Gas Production by Anaerobic Digestion Process From Different Food Wastes: a Simulation Study **Nicholas Melenek, Murilo Rampi, Gabriela Conor, Anne Oliveira, André Mariano, Vanessa Kava, José Vargas** Mıcroalgae Derived Biostimulants for Sustainable Agriculture Exergoeconomic Analysis
Technical Session-29 (Room 4)		
14:00 - 15:00	**Green Transition and Decarbonization**	**Session Chair: Dr. Ergün Demirel** **Mümine Gerçek Şen** Shading Strategies as Energy Efficient Retrofit Measures in Residential Buildings: Implementations for Adaptation to Future Climate Change **Ozan Gül** Examination of The Impact Of Electric Vehicle and Cryptocurrency Mining Operations On Line Losses in a 14-Bar System With Renewable Energy Sources
Technical Session-30 (Room 5)		
14:00 - 15:00	**Sustainability and Environmental Management: Bio-based Production**	**Session Chair: Dr. Sevinç A. Sırdaş** **Rabah Gomri, Nadim Karoune** Study of Boiling Heat Transfer Coefficient During Evaporation of CO2 **Onder Kızılkan, Gamze Soyturk** Thermodynamic Analysis Of Multi-Energy Integrated System Combining Geothermal, Green Hydrogen, and Cold Energy Storage
Technical Session -31 (Room 1)		
15:00 - 16:00	**Energy Systems and Technologies**	**Session Chair: Dr. Cemil Koyunoğlu**
Technical Session-32(Room 2)		
		Session Chair: Dr. Fatih Yılmaz

15:00 - 16:00	**Energy & Exergy Analysis and Applications**	**Zehra Sakınç, Abdullah Muratoğlu, Mehmet İshak Yüce** Energy Footprint of Gypsum Plasterboard Production Plant **Selim Can Bozkır, Yiğithan Çalı** The Refrigerant Amount Optimization Study for the Household Refrigerator Performance **Fatih Yilmaz, Murat Ozturk, Resat Selbas** Energetic and Exergetic Performance Analysis of the Solar Tower-based Integrated Plant Combined With Helium-based Brayton Cycle and HTSE for Power and Hydrogen Generation
Technical Session-33 (Room 3)		
15:00 - 16:00	**Green Transitionand Decarbonization :Policies & Strategies**	**Session Chair: Dr. Önder Kızılkan** **Gamze Soyturk, Onder Kizilkan** Conceptual Design and Analysis of A Solar Energy Based Multi-Generation System With HeliumGas Cycle, Green Ammonia and Hydrogen Production **Duygu Ülker, Serap Goksu** Assessing the Bileteral Impacts in a Changing Climate in terms of Shipping Sector

Technical Session-34 (Room 4)		
15:00 - 16:00	**Energy Efficient materials**	**Session Chair: Dr. Hüseyin Gencer** **Taha Aydin, Hadi Genceli, Parisa Heidarnejad** Comparison study of four typical ORC configurations integrated with hydrogen production unit for the exploitation of medium temperature geothermal sources **Emir Ejder, Hasan Göler, Ergün Demirel** Impact of Biofuels on Maritime Decarbonization and Vessel Performance **Murat Koseoglu, S. Atalay Keleştemur, Güldem Elmas, İsmail Özdemir** Analysis of Cyber Risk Management Frameworks for The Maritime Industry
Technical Session-35 (Room 5)		
15:00-16:00	**Energy Systems and Technologies**	**Session Chair: Dr. Zhanbayev Rinat**
16:00-16:30		**Coffee Break**

Technical Session-36 (Room)		
16:30 - 17:30	**Energy Systems and Technologies:Battery & Electricity Based Systems**	**Session Chair: Dr. Cemil Koyunoğlu** **Cemil Koyunoğlu, Tamer Çınar** Exergy-Based Analysis of Polymer Recycling in the Automotive Sector **Muhammet Sefa Odabaşı, Berkay Tahirağaoğlu, Gökhan Sevilgen** A Study in The Comparison of Battery Parameters of an Electric Bus According to Passenger Occupancy
Technical Session-37 (Room 2)		
16:30 - 17:30	**Energy & Exergy Analysis and Applications**	**Session Chair: Dr. Hadi Genceli** **Gülcan Koca** A Case Study for Marmara Region: Energy and Efficiency Analysis for SMR and Solar PTC Hybrid System **Dogan Erdemir, Ibrahim Dincer** A Novel Approach for Estimating Chemical Exergy Values of Biomass Mixtures Using ArtificialNeural Networks
Technical Session-38 (Room 3)		
16:30 - 17:30	**Sustainability and Environmental Management: Water Treatment**	**Session Chair: Dr. OKTAY ÇETİN** **Duygu Ülker** Waste Management on Oil Spill Emergency Response in Turkish Coastal Waters
Technical Session-39 (Room 4)		
16:30 - 17:45	**Green Transition and Decarbonization: Policies &**	**Session Chair: Dr. OKTAY ÇETİN** **Halil Çeçen** Decarbonisation Targets and Actions in Turkish Maritime Sector Within the Framework of the Financing Agreement for the Annual Action Plan in favor of Türkiye for 2021 **Ceren Şengül, Mustafa Yılmazoğlu** Projections for Türkiye's Net Zero Carbon Target by 2053 **Melda Carpınlıoglu** Need of a Policy and Strategy on Intelligence versus Artificial Intelligence in Engineering

	Strategies	Education?

Technical Session-40 (Room 5)		
16:30 - 17:45	**Energy Efficient materials**	**Session Chair: Dr. Murat Emre Demir** **Gülşen Akın Evingür, Büşra Osma** Thin Films in Solar Cell Applications **Merve Yılmaz, Erkan Dursun, Zehra Karagöz, Nazmi Ekren, Oğuzhan Gündüz** Efficiency Increasing Coatings on Photovoltaic Panels (PV) **Emrehan Gürsoy, Engin Gedik** Entropy Generation Induced by AC and DC Magnetic Fields on MWCNT-Fe3O4/Water HybridNanofluid Flowing in U-tube **Mehmet Akman, Bülent İbrahim Turan, Ahmet Taşdemir, Mehmet Ziya Sogut** A Conceptual Framework for Energy-Efficient Design of Bulk Carriers

Closing Remarks

KEYNOTE SPEAKERS

Professor Ibrahim Dincer

PROFESSOR OF MECHANICAL ENGINEERING, ONTARIO TECH UNIVERSITY, CANADA

Professor Ibrahim Dincer is a full professor of Mechanical Engineering in Ontario Tech University, Canada. Renowned for his pioneering works in the area of sustainable energy technologies, he has authored and co-authored many books and book chapters, a number of journals and conference papers and numerous technical reports. Dr. Dincer has chaired many national and international conferences, symposia, workshops and technical meetings and has delivered many plenary, keynote and invited lectures. He is a recipient of several research, teaching and service awards, and has been actively working in the areas of hydrogen and fuel cell technologies.

Professor Abdul-Ghani Olabi

THE DIRECTOR OF SUSTAINABLE ENERGY AND POWER SYSTEMS RESEARCH CENTRE AT THE UNIVERSITY OF SHARJAH

Prof Olabi is the Director of Sustainable Energy and Power Systems Research Centre at the University of Sharjah "UoS". For the previous three years, he was the Head of Sustainable and Renewable Energy Engineering Department, before joining UOS, he was the director and founding member of the Institute of Engineering and Energy Technologies at the University of the West of Scotland. For the last 35 years, Prof Olabi worked at different national and international institutes such as; National Research Centre-Italy "CNR", Research Centre of FIAT-Italy "CRF", Dublin City University "DCU", Institute of Engineering and Energy Technologies "IEET" at UWS, and Aston University. Prof Olabi is an Academic Expert Reviewer, he acted as member and chairman for a number of accreditation panels.

Prof Olabi has supervised postgraduate research students (40 PhD) to successful completion. He has published large number of peer-reviewed papers concerning on Renewable Energy and Energy Storage Systems, particularly, hydrogen and Fuel Cell. In the last few years, Prof Olabi has patented 5 innovative projects regarding innovative generation of PEM Fuel Call and Supercapacitor.

Professor Yunus Cengel

EMERITUS AT THE UNIVERSITY OF NEVADA, RENO, USA.

Yunus Çengel is a Professor Emeritus at the University of Nevada, Reno, USA. He received his Ph.D. in Mechanical Engineering from North Carolina State University and served as a faculty member at the University of Nevada, Reno since 1984. He was the Director of the Industrial Assessment Center and served as a consultant in the areas of energy efficiency, renewable energy, and energy policies. Professor Çengel is the author or coauthor of several widely adopted engineering textbooks such as Thermodynamics: An Engineering Approach, Heat and Mass Transfer: Fundamentals and Applications, and Fluid Mechanics: Fundamentals and Applications, all published by McGraw-Hill

Professor Arif Hepbaşlı

ENERGY SYSTEMS ENGINEERING, YASAR UNIVERSITY, TÜRKİYE

Arif Hepbasli has dealt with energy-related issues for 41 years. Of these, he spent working in the Izmir industry for ten years and the remainder at different domestic and abroad universities. He has been working as a faculty member in the department of Energy Systems Engineering at Yaşar University for the last 11 years. He has served as a consultant for the industry in cases involving his research area and is also a member in the International Advisory Board of different prestigious energy-related journals.

Professor Cengız S. Ozkan

MECHANICAL ENGINEERING, MATERIALS SCIENCE AND ENGINEERING, AND CHEMISTRY, UNIVERSITY OF CALIFORNIA RIVERSIDE, USA

Prof. Cengiz Ozkan is a faculty member in the Department of Mechanical Engineering at the University of California, Riverside. He received his Ph.D. Degree in Materials Science and Engineering at Stanford University in 1997. Research in the Ozkan group involves the design and synthesis of nanoscale materials for energy storage, nanoelectronics and sensors applications; fundamental understanding and characterization of electrical and optical properties of nanoscale materials; and nanoscale structure–property relationships. Dr. Ozkan made pioneering contributions to manufacturing of sustainable high-performance materials for Li-ion batteries and supercapacitors for electric vehicles, smart grids, and mobile electronics; 2D materials for low-power electronics, and sustainable materials for mitigating environmental pollution. Dr. Ozkan has been a member of several prestigious National Centers including the SRC MARCO Center for Functional Engineered Nano Architectonics at UCLA; and the SRC STARnet Center for Spintronic Materials, Interfaces and Novel Architectures at UMN. He received a number of awards including the William Johnson International Founders Award, the John J. Guarrera Engineering Educator of the Year Award, and the TUBITAK Presidential Scientific Achievement Award. Dr. Ozkan co-organized and chaired over 40 scholarly conferences worldwide, and he had been elected a Meeting Chair for the Fall 2021 MRS Meeting in Boston, MA.

Professor Mihri Ozkan

ELECTRICAL AND COMPUTER ENGINEERING, UNIVERSITY OF CALIFORNIA RIVERSIDE, USA

Mihri Ozkan is a professor of the Electrical and Computer Engineering Department at UCR. Mihri is a Fellow of National Academy of Inventors and a Fellow of Frontier National Academy of Engineering. She is the Climate Action Champion and Changemaker Professor of the University of California and selected as the Remarkable Women of UCR. Mihri completed her graduate studies at Stanford University and at UC-San Diego. She integrated her concerns about climate justice and environmental improvement into her research. Over twenty years, her research group developed innovative solutions for Li-ion battery technologies using sustainable and waste materials with green solutions and low power processing to achieve low carbon footprint in manufacturing. Mihri's creative nature resulted in 47 granted and 10 active patents. She published more than 340 scientific publications and her Google scholar citations is 11400, h-Index is 56 and i10-Index is 143. She advised and graduated nearly 80 graduate students. She is very passionate and actively participating on the Climate Justice related actions. Lately, she was the lead organizer for the Climate Change Mitigation Technologies Symposium at the Fall MRS Boston Meeting. She guest edited a special issue of the MRS Bulletin titled "Materials for Carbon Capture Technologies". She led the CHEM Voices piece on direct air capture (DAC) of carbon dioxide together with presidents of National Academies and DAC company leaders. She has given numerous worldwide keynote presentations about climate change, decarbonization, carbon capture, electrification of transportation and renewable energy storage technologies.

Professor Donghai Wang

PENN STATE INTERCOLLEGE GRADUATE DEGREE PROGRAM (IGDP) IN MATERIALS SCIENCE AND ENGINEERING (MATSE)

This faculty member is associated with the Penn State Intercollege Graduate Degree Program (IGDP) in Materials Science and Engineering (MatSE) where a multitude of perspectives and cross-disciplinary collaboration within research is highly valued. Graduate students in the IGDP in MatSE may work with faculty members from across Penn State. Prof. Donghai Wang's Energy Nanostructure Laboratory (E-Nano) focuses on nanomaterial development for clean energy technologies, such as batteries, solar cells, fuel cells, and environmental remediation. The experimental research includes nanomaterial synthesis, characterization and device fabrication and evaluation. Nanomaterials are made by a variety of methods, including sol-gel method, high temperature synthesis, templating approach, and self-assembly.

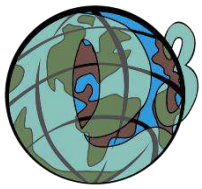

INVITED SPEAKERS

Professor Adnan Midilli

MECHANICAL ENGINEERING DEPARTMENT, FACULTY OF MECHANICAL ENGINEERING

Working places :Industrial Thermodynamics, Hydrogen Systems Management, Hydrogen Production and Storage, Hydrogen Station Design.

Educational Status : Karadeniz Technical University, Mechanical Engineering (dr) (Ph.D.)

Unit he works in : Energy Institute

Professor Birol Kılkış

MECHANICAL ENGINEERING DEPARTMENT OF MIDDLE EAST TECHNICAL UNIVERSITY

Dr. Kilkis received his Ph.D. in 1980 from the Mechanical Engineering Department of Middle East Technical University with high honors and received TUBITAK Encouragement Award in 1981. Dr. Kilkis has been working on heat transfer, unified heat transfer theory, high-performance buildings, quantum mechanics, fluid dynamics, heat pumps, cogeneration, decarbonization, green hydrogen 5th generation, nearly-zero-exergy cities and buildings, district energy systems, and sustainable aviation. He is a Fellow of ASHRAE, a Life Member, recipient of ASHRAE Distinguished Service and ASHRAE Exceptional Service Awards after acting as the Section 6 Head and founder-chair of TC 7.4, Committee Exergy Analysis for Sustainable Buildings. Dr. Kilkis was the first academician serving as a president of the Turkish Society of HVAC and Sanitary Engineers (TTMD), an affiliate society of ASHRAE, between 2017 and 2019. Currently, he is a distinguished lecturer at ASHRAE RAL. He is a professor at OSTIM Technical University, Ankara, Türkiye.

Professor Ali Cemal Benim

THE DUSSELDORF UNIVERSITY OF APPLIED SCIENCES, AT THE FACULTY OF MECHANICAL AND PROCESS ENGINEERING

Prof. Dr.-Ing. habil. Ali Cemal Benim received his B.Sc. and M.Sc. degrees in Mechanical Engineering at the Bosphorus University, Istanbul, Turkey. The subject of his Master Thesis was Finite Element Modeling of Navier-Stokes Equations. He earned his Ph.D. degree at the University of Stuttgart, Germany, at the Institute of Process Engineering and Power Plant Technology of the Faculty of Energy Technology. Subsequently, he joined ABB Turbo Systems Ltd. in Baden, Switzerland. In the Thermal Machinery Laboratory, which acted as an R&D department for the whole ABB enterprise, he gained experience on a broad range of industrial applications in the area of fluid flow, heat transfer and combustion, with emphasis on gas turbine combustion, gas and steam turbines. Since 1996, he is Professor for Energy Technology at the Düsseldorf University of Applied Sciences, at the Faculty of Mechanical and Process Engineering, currently leading the Center of Flow Simulation (CFS), and has been continuously active in mathematical modelling and computational simulation of fluid flow, heat and mass transfer in a broad range of engineering applications, quite often in cooperation with industrial companies.

Professor Derek Baker

MECHANICAL ENGINEERING AT MIDDLE EAST TECHNICAL UNIVERSITY (METU)

Derek Baker is a Full Professor in Mechanical Engineering at Middle East Technical University (METU). He is also the Co-Director of ODAK, The Concentrating Solar Thermal (CST) Research Laboratory, which is part of The Center for Solar Energy Research and Applications (GÜNAM) at METU. He received his BS from Virginia Tech in 1992, and his MS and PhD from The University of Texas-Austin in 1996 and 2000, respectively, all in Mechanical Engineering. Currently he is the METU Principal Investigator for the European Union (EU) Horizon 2020 project Integrating National Research Agendas on Solar Heat for Industrial Processes (INSHIP). From 2012-2016 he participated in the EU-SOLARIS Research Infrastructure project on CST. He regularly serves as an independent expert for the evaluation of EU research proposals and is active in the European Energy Research Alliance Joint Program on Concentrating Solar Power (EERA JP CSP). He received awards from the Turkish Council of Higher Education (YÖK) for his research performance in 2016 and 2017 and from METU for his overall academic performance (research, education, and service) in 2017.

Professor Levent Kurnaz

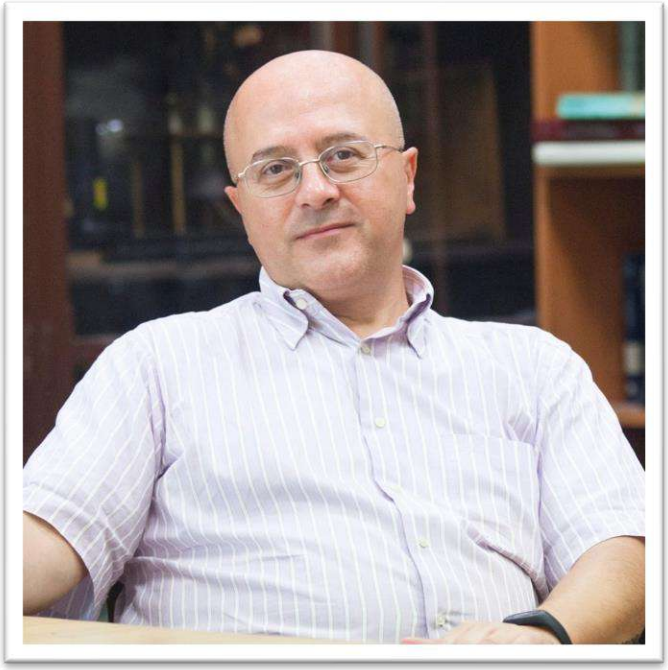

DIRECTOR OF BOGAZICI UNIVERSITY CLIMATE CHANGE AND POLICIES RESEARCH CENTER

Levent Kurnaz graduated from Austrian High School in 1984, Boğaziçi University Electrical and Electronics Engineering Department in 1988, and Physics Department in 1990, and also received a master's degree in Electrical and Electronics. He graduated from the Department of Physics of the University of Pittsburgh, USA, with a master's degree in 1991 and a doctorate in 1994. After completing his postdoctoral studies at the Department of Chemistry at Tulane University in New Orleans until 1997, he returned to Turkey and worked as a faculty member at Boğaziçi University. Prof. currently continues his studies at Boğaziçi University, Department of Physics. Dr. Levent Kurnaz has two books, one published abroad, and over thirty scientific articles. He is also the Director of Boğaziçi University Climate Change and Policies Research Center.

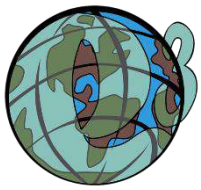

SCIENTIFIC PAPERS

IEEES-001

Sizing and Performance Evaluation of Photovoltaic System Coupled With Electrolyzer Hydrogen Production in Algeria

Malika Ouagued
Affiliation (e.g., University Hassiba Benbouali of Chlef, Faculty of Technology, Department of Process Engineering),
BP 151 02000., Chlef, Algeria
*E-mails: m.ouagued@univ-chlef.dz

Abstract
The aim of this study was to design a photovoltaic system to produce hydrogen by electrolysis of water. In the first part of this work, a study of the energetic aspect of solar radiation is characterized by modelling the incident global irradiation. Using this model, we estimated the global solar radiation for different sites covering the Algerian territory. Based on the results of the calculation model developed, we found that annual solar radiation is higher in the south, with 2175.320 kWh/m2/year in Béchar, 2178.708 kWh/m2/year in Ouargla, and 2202.082 kWh/m2/year in Tamanrasset, leading us to conclude that the southern region is more reliable when choosing a photovoltaic installation. In the second part, the sizing of the hydrogen production installation was carried out according to the production capacity of the electrolyzer on the one hand and according to the solar radiation incident on each site on the other. We determined the number of modules and surface area required to operate the electrolyzer. A comparative study of the sites showed that for the maximum surface area of photovoltaic generator, the annual production of hydrogen exceeds 500 tons in the south, rising to 545 tons in Tamanrasset, while in the north, it reaches 440 and 461 tons in Algiers and Chlef, respectively.

Keywords: Algerian climate, hydrogen production, photovoltaic solar energy, water electrolysis

I. Introduction

Water electrolysis is one of the most efficient hydrogen production methods because it uses renewable H_2O and produces only pure oxygen as a by-product. Moreover, electrolysis uses electricity from sustainable energy resources, such as solar power. In addition, water electrolysis offers major advantages such as high cell efficiency and a higher rate of hydrogen production with high purity (Cipriani et al., 2014, Mraoui et al.2018, Dunn, 2002). The studied system consists of a photovoltaic field and a hydrogen generator. The objective was to determine the surface area of photovoltaic panels required to meet the energy requirements of the electrolyser. Sizing the photovoltaic installation requires knowledge of the nature of the installation, the amount of solar energy received at the installation site, and the characteristics of the panels to be used. The sizing method first determines the peak power of the photovoltaic panel that supplies the electrical energy required during the day. Photovoltaic installation sizing involves determining the necessary surface area of the array to cover the energy requirements of the electrolyzer. This step consists of determining the power of the photovoltaic generator by calculating the quantity of photovoltaic modules that will be needed to cover the electricity requirements (surface area), based on the local solar irradiation data. The photovoltaic generator used was a 72-cell monocrystalline PV solar panel, model SIRAJ 5BB MONO-PERC, manufactured by MillTech (MillTech, 2023). The energy obtained from the solar panels is sent to the electrolyzer to produce hydrogen. In this study, we used a McLyzer 20-30 high-pressure alkaline electrolyzer from the Italian company McPhy, which has a hydrogen production capacity of 20 Nm^3/h and an electricity consumption of 4.5 kWh/Nm^3. It is perfectly suited for coupling renewable energy sources with high energy efficiency (McPhy, 2023).

II. Global solar radiation incident on pv panels

For this purpose, we have chosen approximate models that provide good results for estimating the irradiance on horizontal and inclined planes. A tilting panel is characterized by its inclination, β, (with respect to the horizontal) and its orientation or azimuth with respect to the south. The daily solar radiation on an inclined plane *Gin* is calculated as a function of the solar radiation on a horizontal plane using Liu Jordan's model (Capderou, 1986). Radiation is expressed as $Wh/m^2/d$.

$$G_{in} = (G_h - D_h) \cdot R_b + D_h \cdot \frac{(1+\cos\beta)}{2} + G_h \cdot \rho \cdot \frac{(1-\cos\beta)}{2} \quad (1)$$

Where *Rb* is Inclination factor, for an inclined location of latitude, *ρ is* Albedo at ground level, D_h is diffuse solar radiation in any sky incident on a horizontal plane, and *Gh is t*he solar radiation received on a horizontal plane. *Dh* can be related to the fraction of average insolation for σ > 0.2 by the following relationship (Capderou, 1986):

$$Dh = Gh \cdot (-0.35 \cdot \sigma + 0{,}53) \quad (2)$$

Gh is related to the solar radiation received on a horizontal plane for a clear day (*Gh*°) using the formula given by Angstrom (Capderou, 1986, Bernard et al., 1979).

$$Gh = Gh° \cdot (a \cdot \sigma + b) \quad (3)$$

The study carried out on solar radiation in Algeria in the book "Atlas solaire algérien" by Michel Capderou, 1986, shows that the coefficients *a* and *b* can be constant for all locations. Their values are: *a = 0.58; b = 0.41.*

To study the performance of a solar hydrogen production plant in Algeria, we selected six sites that are typical of the Algerian climate: Chlef and Algiers in the north, Ghardaïa, Ouargla, and Bechar in the north of the Sahara, and Tamanrasset in the extreme south. The locations of various sites and their geographical coordinates are shown Table 1.

Table 1. Geographical data for the sites studied (Mefti et al., 2008)

	Latitude (deg)	**Longitude (deg)**	**Altitude (m)**	**Albédo**
Algier	*36.76*	*3.05*	*25*	*0.2*
Chlef	*36.13*	*1.2*	*143*	*0.2*
Ghardaïa	*32.48*	*3.66*	*500*	*0.3*
Béchar	*31.38*	*-2.15*	*806*	*0.3*
Ouargla	*31*	*5.24*	*141*	*0.35*
Tamanrasset	*22.47*	*5.31*	*1378*	*0.35*

The evolution of solar irradiation over tilting panel with latitude angle of location as a function of the climatic conditions of the sites studied for typical days, are grouped together in Figure 1:

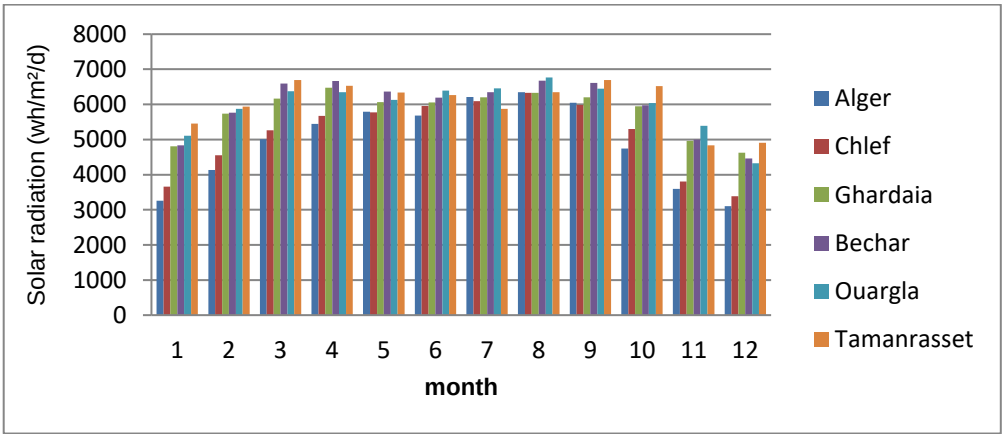

Fig. 1. Average monthly solar radiation incident on tilting panel with latitude angle.

The annual solar radiation for tilted panel *Gan (kWh/m²/year)* was calculated by integrating the daily radiation over the entire year:

Table 2. Incident annual solar radiation on tilting panel with latitude angle.

Sites	**Alger**	**Chlef**	**Ghardaïa**	**Bechar**	**Ouargla**	**Tamanrasset**
G_{in} (kWh/m²/an)	*1807.128*	*1879.977*	*2115.393*	*2175.320*	*2178.708*	*2202.082*

Clearly, annual irradiation is ideal in southern Algeria, with annual radiation around 2115 kWh/m^2 in Ghardaia, 2175 kWh/m^2 in Béchar, 2178 kWh/m^2 in Ouargla and over 2200 kWh/m^2 in Tamanrasset. In northern Algeria, Chlef has the highest level of radiation, with an annual radiation of approximately 1880 kWh/m^2.

III. Sizing photovoltaic generator

The electrolyzer energy requirement over the operating time $E_{H2}(W)$ is determined using the following equation (Chennouf et al., 2012, Labouret and. Villoz, 2006):

$$E_{H2} = E_H \cdot d_0 \quad (4)$$

Where E_H is electrolyzer electrical consumption (W/h) and d_0 is daily insolation duration (hr). The peak power, *Pc (Wc)*, of the panels to be installed depended on the irradiation at the installation site. It was calculated by applying the following formula (Labouret and. Villoz, 2006):

$$Pc = E_{H2}/(G_{in}.K) \quad (5)$$

Where *K* is Correction coefficient. Number of photovoltaic panels to be used (Chennouf et al., 2012):

$$N_m = \frac{P_c}{P_{mod}} \quad (6)$$

Where P_{mod} is unit power of the module, *W*. After determining the number of solar panels used each month for electrolyzer operation, it was necessary to determine the total area of the photovoltaic array. This can be determined using the following expression (Chennouf et al., 2012):

$$A_{ch} = A_{mod} \cdot N_m \quad (7)$$

Where A_{mod} is module surface area, m^2. The sizing results of PV array are as follows:

Table 3. Number of modules and area of photovoltaic field (m^2).

Month	Algier		Chlef		Ghardaïa		Bechar		Ouargla		Tamanrasset	
	N_m	$A(m^2)$	N_m	$A(m^2)$	N_m	$A(m^2)$	N_m	$A(m^2)$	N_m	$A(m^2)$	N_m	$A(m^2)$
Jan.	*525*	*1026*	*672*	*1117*	*634*	*1238*	*630*	*1229*	*641*	*1252*	*628*	*1226*
feb.	*507*	*990*	*576*	*1124*	*598*	*1166*	*595*	*1161*	*596*	*1164*	*577*	*1127*
mar.	*494*	*965*	*514*	*1002*	*556*	*1085*	*578*	*1128*	*561*	*1095*	*569*	*1111*
Apr.	*525*	*1024*	*544*	*1062*	*589*	*1149*	*600*	*1171*	*587*	*1146*	*584*	*1139*
May.	*625*	*1220*	*620*	*1211*	*628*	*1226*	*658*	*1284*	*612*	*1194*	*661*	*1290*
Jun.	*670*	*1309*	*704*	*1374*	*692*	*1350*	*707*	*1380*	*681*	*1330*	*729*	*1422*
Jul.	*705*	*1376*	*688*	*1343*	*676*	*1320*	*690*	*1347*	*696*	*1358*	*649*	*1266*
Aug.	*629*	*1229*	*625*	*1221*	*602*	*1175*	*628*	*1225*	*630*	*1230*	*560*	*1170*
Sep.	*567*	*1108*	*560*	*1093*	*553*	*1079*	*576*	*1124*	*561*	*1095*	*569*	*1111*
Oct.	*522*	*1018*	*561*	*1095*	*577*	*1126*	*574*	*1120*	*573*	*1120*	*584*	*1139*
Nov.	*530*	*1035*	*550*	*1074*	*614*	*1199*	*610*	*1191*	*629*	*1227*	*551*	*1076*
Dec.	*552*	*1078*	*585*	*1143*	*659*	*1286*	*640*	*1249*	*624*	*1217*	*621*	*1212*

IV. Hydrogen production potential

According to previous results, the number of solar panels varied over 12 months. To determine the performance of the system, we needed a working surface area throughout the year, so we considered the maximum surface area at each site. The assessment of potential is based on the use of photovoltaic electrical energy, which drives the operation of the electrolyzer.
The volume of hydrogen produced in Nm^3/d was calculated as follows (Chennouf et al., 2012):

$$P_{H_2} = E_{ch}.k.\frac{P_{hor}}{E_H} \quad (8)$$

Where P_{hor} Nominal H_2 flow rate, (Nm^3/h), k is electrical efficiency, and E_{ch} is the average monthly electrical energy delivered by the PV array *(Wh/d)*, calculated by (Tsoutsos et al. 2911, Yadav and Bajpai, 2018):

$$E_{ch} = \eta_{pv}.A_{ch}.G_{in} \quad (9)$$

Where η_{pv}The efficiency of a photovoltaic generator. To compare hydrogen production in different sites, we present in Fig. 2 and fig. 3 the mean monthly hydrogen production and annual hydrogen production respectively for the six Algerian locations.

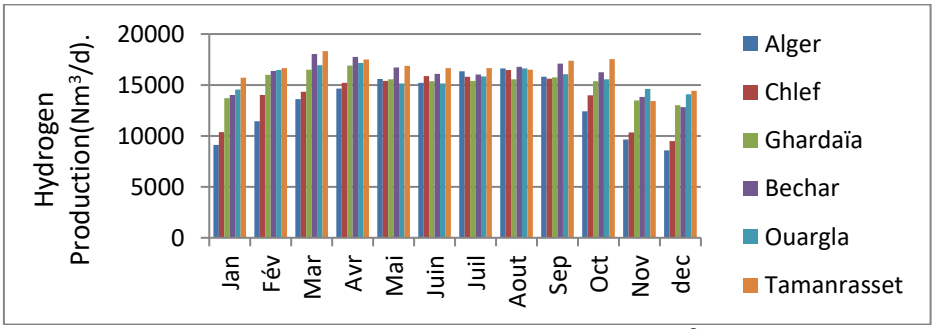

Fig.2. Average monthly hydrogen production (Nm^3/d).

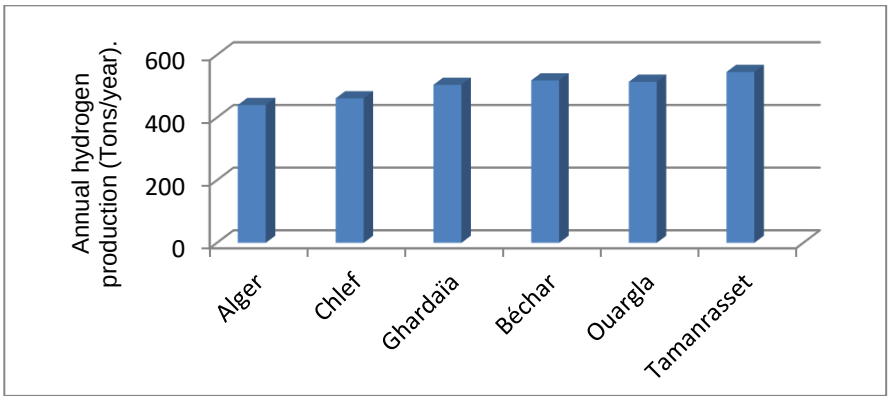

Fig. 3. Annual hydrogen production (Tons/year)

The results reveal that hydrogen production is not uniform throughout the year, peaking in March in the south and August in the north. Annual production exceeds 500 tons in the south, reaching 545 tons in Tamanrasset, while in the north it reaches 440 and 461 tons in Algiers and Chlef respectively.

V. Conclusion

In this work, the sizing of the hydrogen production installation was carried out according to the production capacity of the electrolyzer and the solar radiation incident on each site. We determined the number of modules and surface area required to operate the electrolyzer. We found that the number of panels varies from month to month for each site; therefore, working with a fixed number throughout the year is necessary to assess the hydrogen production potential of each region. A comparative study of the sites showed that for the maximum surface area of photovoltaic generator, the annual production of hydrogen exceeds 500 tons in the south, rising to 545 tons in Tamanrasset, while in the North, it reaches 440 and 461 tons in Algiers and Chlef, respectively.

References

Bernard, R., Menguy, G., Schwartz, M., 1979. Solar Radiation Thermal Conversion and Applications. Technique and Documentation, Paris, 256.

Capderou, M., 1986. Atlas Solaire de l'Algérie. Office des Publications Universitaire tome 1 et 2, Algérie.

Chennouf, N Settou, B Negrou, K Bouziane, B Dokkar. 2012. Experimental study of solar hydrogen production performance by water electrolysis in the south of Algeria N Energy procedia 18, 1280-1288.

Cipriani, G. Di Dio, V. Genduso, F. La Cascia, D. Liga, R. Miceli, R. et al. (2014). Perspective on hydrogen energy carrier and its automotive applications. Int. J. Hydrogen Energy 39, 8482–8494.

Dunn, S. (2002). Hydrogen futures: toward a sustainable energy system. Int. J.Hydrogen Energy 27, 235–264.

Labouret, A. Villoz, M.. (2006). Energie Solaire Photovoltaïque. 3ème Edition, DUNOD, Paris.

McPhy. (2022). https://cellar-c2.services.clever-cloud.com/commcphy/uploads/2022/02/22.01.McPhy_Portfolio_ELY_McLyzer_FR.pdf.

Mefti, A. Adane, A. Bouroubi, MY. (2008). Satellite approach based on cloud cover classification: Estimation of hourly global solar radiation from meteosat images. Energy Conversion and Management 49 (4), 652-659.

MillTech. (2022). https://www.milltechdz.com/Application/up/nouveau_dossier/siraj_mono_perc_72_module.pdf

Mraoui, A. Benyoucef, B. Hassaine, L. (2018). Experiment and simulation of electrolytic hydrogen production. Case study of photovoltaic-electrolyzer direct connection, Volume 43, Issue 6, Pages 3441-3450.

Tsoutsos, T. Savvakis, N. Kanakis, I. Papadakis, G. Kyriakarakos, G. Schwartz, B. (September 2011). Temperature Effect On PV Performance Experimental Results From A 2.18 Kwp Thin Film PV System. 26th Photovoltaic Solar Energy Conference and Exhibition.

Yadav, S.K. Bajpai, U. (2018). Performance evaluation of a rooftop solar photovoltaic power plant in Northern India. Energy for Sustainable Development 43, 130–138.

IEEES-002

Future Methanol Cost Projections in Specific Regions: A Comprehensive Study

[1*]Metin Gül, [2]Ersin Akyüz,
[1] Balıkesir University, Institue of Science, Mechanical Engineering, Balıkesir, Turkey, 10145, Turkey
[2] Balıkesir University, Dept of Electrical and Electronics Engineering, Balıkesir, Turkey, 10145, Turkey
*E-mails: metingul@balikesir.edu.tr, eakyuz@balikesir.edu.tr

Abstract

This study thoroughly explores the feasibility of green methanol production facilities strategically located in Bandirma, Mersin, and Çeşme, Turkey. The comprehensive feasibility study assesses various cost factors, including expenses related to PV systems, electrolyzers, methanol plants, compressors, and grid infrastructure. Projecting costs from 2023 to 2050, potential reductions in component and grid electricity prices were considered. Within the 2023-2050 projection, a regional examination of the Levelized Cost of Methanol (LCOM) highlights varying outcomes based on different electrolyzer efficiencies. In Çeşme, the LCOM is projected to decrease from $843/ton in 2023 to as low as $389 in the optimistic 2050 scenario. Similar decreasing trends are observed for Bandırma and Mersin. Çeşme notably emerges as the most favorable region, with potential technological advancements in electrolyzer efficiency contributing to cost reduction. In addition to forecasting methanol prices, this study conducted a comprehensive cost analysis for hydrogen (H_2). The Levelized Cost of H_2 (LCOH) in Çeşme, starting at $4.08/kg in 2023, demonstrates a decline to $1.78/kg in the optimistic 2050 projection. Similarly, for Mersin, the LCOH decreases from $4.17/kg to $1.85/kg, and for Bandırma, it undergoes a reduction from $4.19/kg to $1.87/kg. Additionally, assessments have been conducted based on the obtained results regarding when the prices of green H_2 and methanol are expected to reach levels comparable to conventional prices.

Keywords: Methanol synthesis, techno-economic evaluation, hydrogen, power-to-methanol

I. Introduction

Greenhouse gas emissions emerge as a pivotal environmental issue in the 21st century, with carbon dioxide (CO_2) standing out as the primary contributor. The substantial increase in its release over recent decades is primarily linked to the burning of fossil fuels for power generation and transportation. Additionally, global energy demand is expected to double by 2050, with fossil fuel dominance persisting despite the growing presence of renewable energy sources (Varone and Ferrari, 2015). Lately, many countries have mandated renewable energy targets, enforcing the use of renewables for electricity generation. To support this, they have introduced government initiatives like subsidies and tax credits. As renewable energy usage increases, surplus electricity is inevitable due to intermittent sources like fluctuating solar radiation and wind speed. Consequently, there is a growing requirement for storage. Moreover, water electrolysis (WE), a process that separates water (H_2O) into hydrogen (H_2) and oxygen (O_2), emerges as a viable method for energy storage. The resulting H_2 can be directly harnessed as an energy carrier, boasting an exceptionally high energy density per unit mass (142 MJ/kg). Nevertheless, H_2 exhibits a notably low density of 0.0813 g/L in its standard state (298 K and 1 bar), posing challenges in storage and transportation. Consequently, a thermochemical conversion process, such as CO_2 hydrogenation, is being explored as a promising industrial-scale method for CO_2 utilization (Chauvy et al., 2019). In this context, a promising technology for efficiently storing excess electricity is the proposed renewable methanol (MeOH) synthesis process, which relies on CO_2 hydrogenation. The produced MeOH can be further employed as a precursor for various chemicals such as dimethyl ether, formaldehyde, and acetic acid. Additionally, this MeOH holds the potential for use as a carrier for H_2 and as an alternative fuel (Olah, 2005).

In spite of the potential advantages it offers, the existing cost of producing green methanol is noted to be relatively high compared to conventional methanol, with costs reaching as much as 799-960 dollars per ton, according to the literature (Bellotti et al., 2021; Sollai et al., 2023). Hence, there is a critical necessity for thorough cost evaluations. These assessments are instrumental in ascertaining the current production costs of green methanol and investigating the timeframe for it to potentially attain cost parity with traditional methanol, which is approximately an average of €573 (Europe for the year 2022) (Methanex, 2023).

The fluctuation in the LCOM is a widespread occurrence. This variability is mainly influenced by factors specific to each location, such as the dynamic nature of power purchase agreement (PPA) prices, varying discount rates, and the diverse capacity factors commonly used in research studies (Bourne, 2012). Using the planned wind-supported hydrogen facility in Bandırma (The "Southern Marmara Hydrogen Coast Platform" project) (GMKA, 2023) as a reference, we conducted a comprehensive assessment and cost comparison with other regions. Economic parameters were dynamically analyzed, factoring in varying PPA prices and discount rates on an hourly basis throughout the year (8760 hours). Additionally, we explored the impact of varying electrolyzer efficiencies in the evolving technological landscape on LCOM.

II. Experimental Procedure/Methodology/System Description

System Description

Figure 1 depicts a simplified diagram of a power-to-methanol plant utilizing 2 MW photovoltaic (PV) system. H_2 production is facilitated by commercial 1 MW large-scale PEM electrolysers operating at 30 bars. CO_2 for the reaction is sourced from industrial producers at prevailing market prices. After compression and heating to achieve optimal thermodynamic conditions, the resulting gas mixtures are directed to methanol synthesis units.

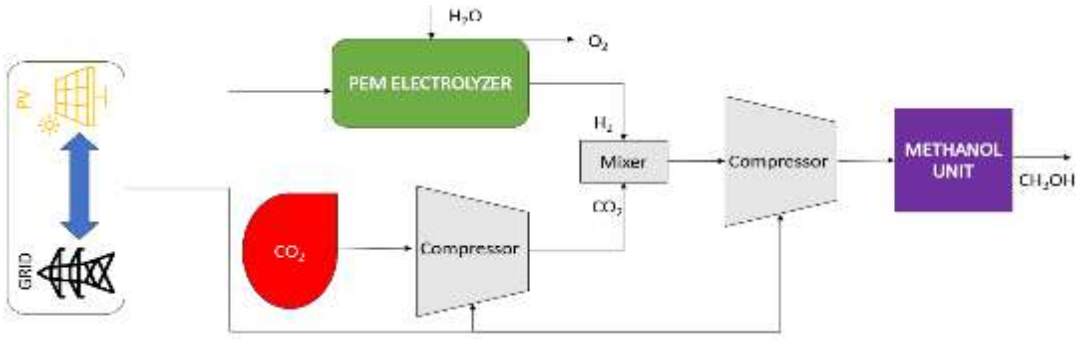

Fig. 1. Plant layout

With reference to the parameters in Table 1, a 1 MW electrolyser yields approximately 19 kg/h of H_2 and 152 kg/h of oxygen (H_2:O_2 ratio of 8). To meet the stoichiometric requirements of the methanol reaction, about 140 kg/h of CO_2 is needed for every 19 kg/h of H_2 produced. The CO_2 is then compressed to 30 bars. Following this, H_2 and CO_2 are blended and compressed to the reactor's 80-bar operational pressure. The tecno-economic analysis extends over an 8760-hour period, accounting for the time-dependent fluctuations in both the energy quantity and price, arising from variations in PV-based electricity and grid conditions.

Site Selection and Electrical Output Calculations

We employed a decision-making procedure to identify the most suitable regions for implementing the PV-based methanol production system. Based on insights derived from the referenced study (Shura, 2021), Mersin, Çeşme, and Bandırma provinces were determined for the analysis. We utilized a 22-year median dataset (1983-2005) with resolution of 60 minutes for analysis. This dataset includes validated ground data, specifically global horizontal irradiance values and air temperature, obtained from the NASA solar energy database. Mersin boasts a solar potential of 1700-1750 kWh/m^2/yr, while Bandırma exhibits 1531 kWh/m^2/yr, and Çeşme features 1800 kWh/m^2/yr. All three regions hold strategic importance in terms of energy-intensive industries, port availability, chemical production, water resources, among other factors. The single-diode model was employed on MATLAB Simulink to calculate the amount of produced electricity. The resulting hourly energy production data was then analyzed to evaluate the viability of H_2 production. The electrolyzer is operated at an approximate 90% capacity factor (22 hours a day) feeding with PV-grid system. PV-grid system powers the electrolyzer and other system components. Excess electricity is sold back to the grid, and during periods of insufficient production, the electrolyzer is supplied from the grid.

Economic Analysis

The LCOM model was employed for the economic analysis of methanol cost calculation by considering the Capital and Operational Expenditure (CAPEX-OPEX), and replacement costs of system components. This calculation was conducted using the following equation:

$$LCOM = \frac{\left(CAPEX_{pv,elc,comp,unitmethanol}\right).CRF_{plant} + OPEX_{pv,elc,comp,unitmethanol} + (Replace_{elc}).CRF_{replace} - Revenues}{MeOH_{produced}} \quad (1)$$

Table 1 illustrates the technical and economic considerations used in the analysis. It provides a comprehensive overview of crucial technical and economic parameters incorporated into the model, featuring projected costs for system components based on literature-derived data in 2023, 2035, and 2050. These projections encompass both upper and lower cost estimates, ensuring a comprehensive analysis of potential scenarios.

Table 1. Technical and economic assumptions for techno-economic analysis

Components or Economic Assumptions	2023	2035	2050	Unit	Reference	Cost Equation
PEM Electrolyzer (1MW) CAPEX Low	1.280	0.545	0.460	[M US$]	(Bertuccioli et al., 2015; Christensen, 2020)	-
PEM Electrolyzer (1MW) CAPEX High		1.031	0.820	[M US$]	(Bertuccioli et al., 2015; Christensen, 2020)	-
Electrolyzer (1 MW) OPEX	5	5	5	[%]		0,05 of CAPEX
PV (2 MW) CAPEX Low	1102	579	466	[(US$/kW]	(NREL, 2022)	-
PV (2 MW) CAPEX High		1046	751	[(US$/kW]	(NREL, 2022)	-
PV (2 MW) OPEX Low	19,65	12.63	10.86	[US$/kW-yr]	(NREL, 2022)	-

PV (2 MW) OPEX High		18.77	15.22	[US$/kW-yr]	(NREL,2022)	-
Methanol Unit (159 kg/h) CAPEX	-	High=0,95 of CAPEX Low =0,90 of CAPEX	High=0,85 of CAPEX Low =0,80 of CAPEX	[US$]	(Bellotti et al., 2017)	$14{,}2.10^6.(M_{out}/54000)^{0{,}65}$
Methanol Unit (159 kg/h) OPEX	-	High=0,95 of OPEX Low =0,90 of OPEX	High=0,85 of OPEX Low =0,80 of OPEX	[US$]	(Bellotti et al., 2017)	0,02 of CAPEX
Compressor 1 for H_2 (8,9 kW) CAPEX	-	High=0,95 of CAPEX Low =0,90 of CAPEX	High=0,85 of CAPEX Low =0,80 of CAPEX	[US$]	(Reddi et al., 2017)	$23907.(P_{kW})^{0{,}71}$
Compressor 1 for H_2 (8,9 kW) OPEX	-	High=0,95 of OPEX Low =0,90 of OPEX	High=0,85 of OPEX Low =0,80 of OPEX	[US$]	(Reddi et al., 2017)	0,03 of CAPEX
Compressor 2 for Syngas (13 kW) CAPEX	-	High=0,95 of CAPEX Low =0,90 of CAPEX	High=0,85 of CAPEX Low =0,80 of CAPEX	[US$]	(Bellotti et al., 2017)	$1490.(P_{kW})^{0{,}71}$
Compressor 2 for Syngas (13 kW) OPEX	-	High=0,95 of OPEX Low =0,90 of OPEX	High=0,85 of OPEX Low =0,80 of OPEX	[US$]	(Bellotti et al., 2017)	0,06 of CAPEX
Oxygen Price	0.15	0.15	0.15	[US$/kg]	(Bellotti et al., 2017)	
CO_2 Price	0,015	0,015	0,015	[US$/kg]	(Bellotti et al., 2019)	
Nominal Discount Rate	8	8	8	[%]		
Inflation Rate	2	2	2	[%]	(Gu et al., 2022)	
Project Lifetime	20	20	20	[yr]		
Tax Rate	20	20	20	[%]		
Replacement for Elc	-	-	-	Hour-[US$]		80000-0,05 of CAPEX

III. Results and discussion

The study assesses methanol production potential through PV systems in three Turkish locations. This involves estimating PV energy generation, analyzing H_2 and methanol production, and calculating LCOM to evaluate economic viability. Future price estimations are also considered for a comprehensive analysis. Considering of a 2 MW solar PV plant, the energy production in Çeşme leading at 3225.6 MWh annually, followed by Mersin at 3006 MWh and Bandırma at 2942.5 MWh. The calculated capacity factors for Çeşme, Mersin, and Bandırma stand at 18.9%, 17.7%, and 15.4%, respectively. The electricity drawn from the grid is 5149.7 MW, 5369.1 MW, and 5432 MW for each location. In the established methanol production system, the electrolyzer initially produces 1220.6 tons of O_2 and 152.6 tons of H_2. The resulting H_2, combined with 1124.2 tons of CO_2 from hydrogeneration, is utilized to produce 778.9 tons of methanol. The individual CAPEX and OPEX costs for each system component are depicted in Figure 2. The data also underscores the proportional percentage influence of these expenses on the total budget.

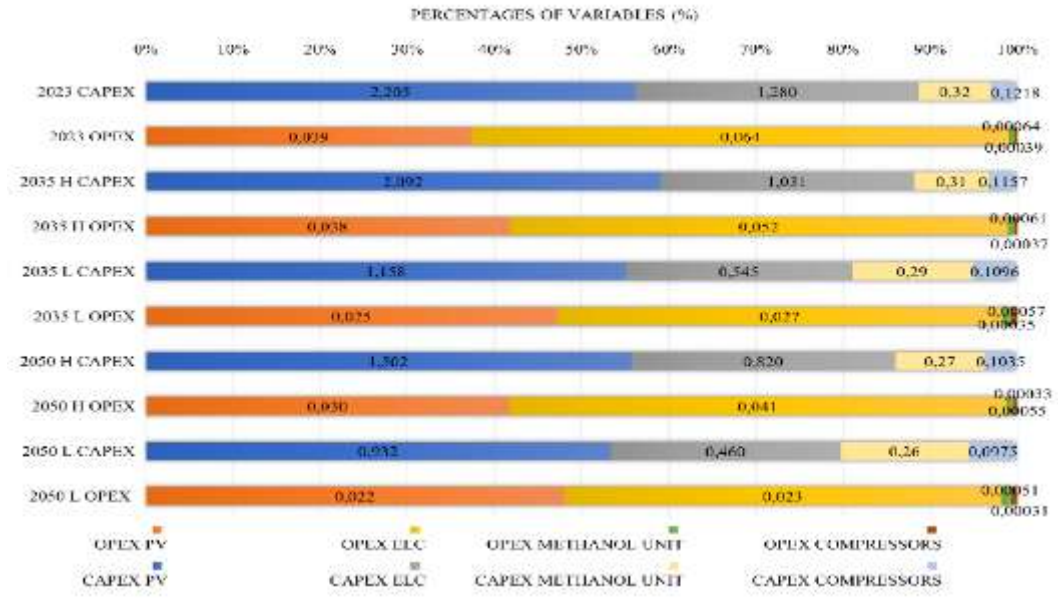

Fig. 2. Graphical representation of CAPEX and OPEX costs for each system component: a detailed breakdown

The PPA prices provided by EPIAS for the 8760 hours for the year of 2021 and revenues from electricity sales and purchases are presented in Figure 3.

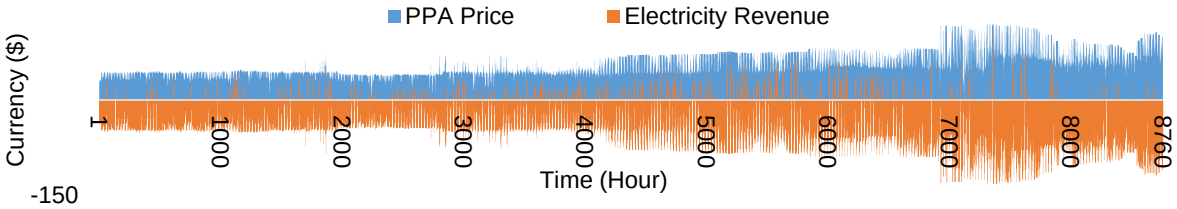

Fig. 3. Hourly PPA prices and electricity revenue variation

Within the 2023-2050 projection, an examination of LCOM prices on a regional basis reveals varying outcomes based on different electrolyzer efficiencies. For Çeşme, the value is projected to decrease from $843/ton in 2023 to as low as $389 in the optimistic scenario for 2050 (Figure 4). Similar decreasing trends are evident for Bandırma and Mersin. Notably, Çeşme emerges as the most favorable region. In addition, it appears that increases in electrolyzer efficiency, attributable to potential technological advancements, contribute to lowering costs.

Fig. 4. Cost analysis of green methanol a) Çeşme, b) Mersin, and c) Bandırma: Projections for 2023, 2035, and 2050

Beyond methanol price predictions, this study encompassed a cost analysis for H_2. The LCOH in Çeşme, initially at $4.08/kg in 2023, exhibits a decrease to $1.78/kg in the optimistic 2050 projection. Similarly, for Mersin, the LCOH drops from $4.17/kg to $1.85/kg, while for Bandırma, it decreases from $4.19/kg to $1.87/kg (Figure 5).

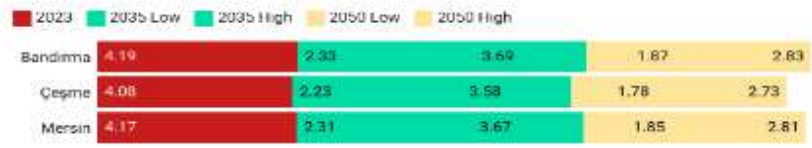

Fig. 5. Cost analysis of green hydrogen production for Bandırma, Çeşme, and Mersin: Projections for 2023, 2035, and 2050

IV. Conclusion

In conclusion, this study marks a groundbreaking endeavor in assessing the potential for H_2 production through photovoltaic technology. The key findings of this research include:

- The study revealed significant variations in energy production potential across the selected sites, with Çeşme leading at 3225 MWh/year, followed by Mersin at 3006 MWh/year and Bandırma at 2942 MWh/year.
- Enhancing electrolyzer efficiency from 70% to 80% resulted in significant cost reductions across locations, highlighting the crucial impact of technological advancements on system efficiency.
- Despite the current higher costs of green hydrogen and methanol compared to fossil-based alternatives, the upcoming implementation of carbon taxes is expected to render green hydrogen and methanol costs competitive.
- CAPEX and power purchase agreement price variations emerged as the most influential factors impacting LCOM.

References

Bellotti, D., Rivarolo, M., Magistri, L., 2021. Clean fuels synthesis from green hydrogen: A techno-economic comparative analysis, in: E3S Web of Conferences. EDP Sciences. https://doi.org/10.1051/e3sconf/202123803001

Bellotti, D., Rivarolo, M., Magistri, L., Massardo, A.F., 2017. Feasibility study of methanol production plant from hydrogen and captured carbon dioxide. Journal of CO2 Utilization 21, 132–138. https://doi.org/10.1016/j.jcou.2017.07.001

Bellotti, D., Sorce, A., Rivarolo, M., Magistri, L., 2019. Techno-economic analysis for the integration of a power to fuel system with a CCS coal power plant. Journal of CO2 Utilization 33, 262–272. https://doi.org/10.1016/J.JCOU.2019.05.019

Bertuccioli, L., Chan, A., Hart, D., Lehner, F., Madden, B., Standen, E., 2014. Study on development of water electrolysis in the EU Final Report E4tech Sàrl with Element Energy Ltd for the Fuel Cells and Hydrogen Joint Undertaking.

Bourne, S., 2012. The future of fuel: The future of hydrogen. Fuel Cells Bulletin 2012, 12–15. https://doi.org/10.1016/S1464-2859(12)70027-5

Chauvy, R., Meunier, N., Thomas, D., De Weireld, G., 2019. Selecting emerging CO2 utilization products for short- to mid-term deployment. Appl Energy 236, 662–680. https://doi.org/10.1016/J.APENERGY.2018.11.096

Christensen, A., 2020. Assessment of Hydrogen Production Costs from Electrolysis: United States and Europe. International Council on Clean Transportation 1.1 (2020): 1-64. https://theicct.org/wp-content/uploads/2021/06/final_icct2020_assessment_of-_hydrogen_production_costs-v2.pdf (accessed 20.11.2022).

GMKA, 2023. https://www.gmka.gov.tr/haber/guney-marmara-hidrojen-kiyisi-platformu-gudumlu-projesinde-imzalar-atildi.

Gu, Y., Wang, D., Chen, Q., Tang, Z., 2022. Techno-economic analysis of green methanol plant with optimal design of renewable hydrogen production: A case study in China. Int J Hydrogen Energy 47, 5085–5100. https://doi.org/10.1016/J.IJHYDENE.2021.11.148

Methanex, 2023. https://www.methanex.com/about-methanol/pricing/.

NREL, n.d. https://atb.nrel.gov/electricity/2022/about.

Olah, G.A., 2005. Beyond Oil and Gas: The Methanol Economy. Angewandte Chemie International Edition 44, 2636–2639. https://doi.org/10.1002/anie.200462121

Reddi, K., Elgowainy, A., Rustagi, N., Gupta, E., 2017. Impact of hydrogen refueling configurations and market parameters on the refueling cost of hydrogen. Int J Hydrogen Energy 42, 21855–21865. https://doi.org/10.1016/J.IJHYDENE.2017.05.122

Shura, 2021. Türkiye'nin yeşil hidrojen üretim ve ihracat potansiyelinin teknik ve ekonomik açıdan değerlendirilmesi.

Sollai, S., Porcu, A., Tola, V., Ferrara, F., Pettinau, A., 2023. Renewable methanol production from green hydrogen and captured CO2: A techno-economic assessment. Journal of CO2 Utilization 68, 102345. https://doi.org/10.1016/J.JCOU.2022.102345

Varone, A., Ferrari, M., 2015. Power to liquid and power to gas: An option for the German Energiewende. Renewable and Sustainable Energy Reviews 45, 207–218. https://doi.org/10.1016/J.RSER.2015.01.049

IEEES-003

Preliminary Study on a Transient Freezer Model with Phase Change Material (PCM)

[1]Mehmet Furkan Koparan,[2]Okan Gök, [2]Ersin Alptekin, [2,*]Mehmet Akif Ezan, [2]Aytunç Erek,
[1] ARCELIK Refrigerator Plant, Manisa, Türkiye
[2] Dokuz Eylül University, Faculty of Engineering, Department of Mechanical Engineering, Izmir, Türkiye
*Corresponding author e-mail: mehmet.ezan@deu.edu.tr

Abstract

In the current work, a numerical model of a freezer with multiple compartments is developed in the MATLAB-SIMULINK environment. The model geometry and thermal properties are based on a commercially available household freezer, and the unloaded scenario is studied under different ambient conditions. The cooling capacity of the freezer is evaluated from experimental measurements under various indoor conditions. The capacity is then defined as a function of indoor temperature variations. The model resolves the 1D heat conduction inside the insulation domain, and the rest of the components, i.e., the evaporator and air domains, are considered lumped domains. The temporal and spatial temperature variations are determined under various set temperatures, and the influence of PCM implementation is also observed.

Keywords: Deep freezer, Dynamic Simulation Model, Phase Change Material (PCM), MATLAB-Simulink

I. Introduction

Nowadays, humanity faces several problems associated with increasing the earth's temperature, which is associated with using fossil fuels to generate electricity, dramatically altering the CO_2 content in the atmosphere since the evolution of industrialization. Increasing the population also increases the consumption rates, and it is quite essential to improve the efficiencies of the existing systems to prolong the limited lifetime of energy resources. Apart from energy, another critical need of humanity is reaching healthy food. Cooling systems have a crucial role in providing a sustainable food supply chain. Various cooling systems in different scales are used, from food producers to end users. It is reported that the energy usage associated with household refrigerators is almost 6% of the global electricity consumption (Choi et al., 2018). Considering the ideal conditions, i.e., the Carnot efficiency, the currently available household refrigerators only reach 15% of the Carnot COPs (Christian et al., 2008). It looks like there is a huge space for improvement in the cooling systems, and the enhanced system efficiencies would ultimately reduce energy consumption on a global scale.

The producers mostly follow the pre-defined standard test routines to evaluate the system's performance. Such attempts provide rapid results in the short term, yet it is not feasible to work on large parameter matrices. Therefore, mathematical models are developed to study different scenarios more quickly and economically. The work of Davis and Scoot (1976) is one of the earliest studies in literature to simulate the refrigeration system components. This pioneering work develops sub-models for the compressor, air-cooled heat exchanger, thermostatic expansion valve, and receiver. Then, an iterative scheme is developed to obtain the system's working condition under the steady state. After this pioneering study, numerous mathematical models were developed to evaluate the system's thermal behavior in either steady or unsteady conditions. Borges et al. (2011) developed a transient model to predict the energy consumption of a household refrigerator. Empirical resistances and capacitances are used in the model, and the transient variations in compressor power and compartment temperatures are evaluated. Simulating the cooling system's dynamic characteristics with novel approaches is also important. Implementing phase change materials (PCMs) has recently been studied in various cooling systems to improve the thermal mass of the components. Azzouz et al. (2005) implemented PCM at the rear surface of the vertical evaporator of a static household refrigerator. It is concluded that the PCM reduces the compressor working time by 25% and yields an improvement of 72% in the system COP. Cheng and Yuan (2013) developed a numerical model for a household refrigerator that includes PCM around the condenser. Shape-stabilized PCM is wrapped around the condenser coils to improve heat transfer. The developed model involves a condenser, compressor, capillary, evaporator, and compartments with food and insulation domains. It is reported that implementing PCM around the condenser coils improves the COP by up to 20.5% and provides an energy saving of 16%.

This study aims to present the preliminary results of a mathematical model developed to simulate the household freezer with PCM. The model is developed in MATLAB-SIMULINK, and the predicted results are compared with the experimental measurements.

II. System Description & Methodology

A numerical model is developed to dynamically simulate the temperature distributions inside a household refrigerator. ARCELIK 2062 MB model household freezer is considered. The freezer has a storage volume of 196 liters with five compartments and six tube-on-sheet evaporators. In Fig. 1(a), a simplified schematic is presented. From top to bottom, the air and evaporator domains are labeled from 1 to 5 and 1 to 6, respectively. The bottom compartment is adjacent to the compressor indentation and has a vertical evaporator. R600a is used in the refrigeration cycle, and the cooling load of the freezer is determined with preliminary experiments as a function of the mean indoor air temperature, as depicted in Fig. 1(b).

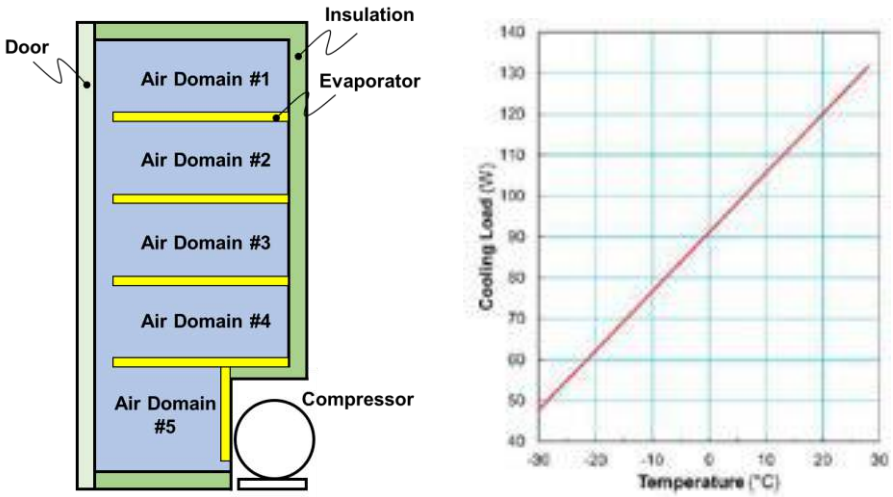

(a) (b)

Fig. 1: (a) Schematic of the freezer and (b) cooling load variation against indoor temperature

A lumped model is developed in MATLAB-SIMULINK. The model basically involves compartment and insulation sub-systems. The insulation interacts with air domains and evaporator plates with convective and radiative heat transfers, respectively. The insulation domain is spatially discretized to consider the temperature gradient within its thickness. For other domains, i.e., air, evaporator, and PCM, the lumped capacitance approach is assumed to be valid. The compartment sub-systems include the air domains and adjacent evaporators. A representative layout of the Simulink blocks is given in Fig. 2 for Air Domain #1.

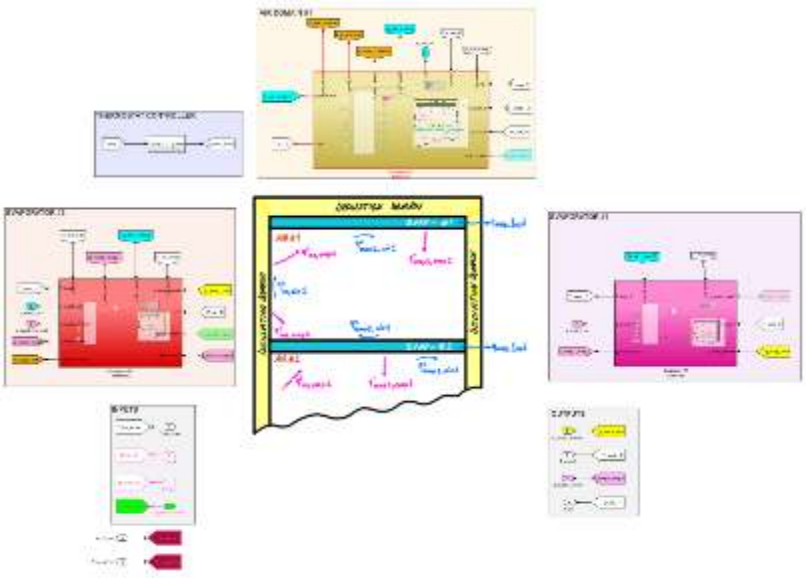

Fig. 2: The layout of the Simulink model for Air Domain #1.

The model resolves the radiative and convective heat exchange and determines the domain temperature from the energy balance equations. Due to the limited space, energy balance equations are given below for Air Domain #1 and Evaporator #1:

Air Domain #1

$$\left(mc\frac{dT}{dt}\right)_{air,1} = q^{c}_{air,1-evap,1} + q^{c}_{air,1-evap,2} + q^{c}_{air,1-ins} + (\dot{m}c)_{air}(T_{in} - T_{air,1}) \quad (1)$$

Evaporator Domain #1

$$\left(mc\frac{dT}{dt}\right)_{evap,1} = q^{r}_{ins-evap,1} + q^{r}_{evap,2-evap,1} + q^{c}_{air,1-evap,1} + q_{evap\ capacity} \quad (2)$$

The superscripts on the right-hand side of the equation define the heat transfer mechanism: "*c*" corresponds to convection, and "*r*" corresponds to radiation. In Eq. 1, the terms on the right-hand side correspond to heat transfer between air and Evaporator #1, air and Evaporator #2, and air and insulation inner wall, respectively. The last term is related to the bulk air motion from top to bottom due to natural convection. The convective heat transfer coefficients on the top and bottom surfaces of the horizontal cold plate, i.e., tube-on-sheet evaporator and the vertical walls, are determined using the correlations suggested by Cengel & Ghajar (2020). In Eq 2., the first two terms on the right-hand side correspond to the radiative heat transfers between the bottom surface of Evaporator #1, the inner wall of the insulation, and the upper surface of Evaporator #2, respectively. The last term is the cooling load of the

evaporator. Fig. 3(a) shows the time-wise variations in the convective heat transfer coefficients on the evaporator and insulation surfaces for the first compartment. The convective heat transfer coefficients on all surfaces increase during the pull-down period. Beyond the pull-down, the coefficients fluctuate within a specific range due to the compressor's on/off modes. Fig. 3(b) reveals the variations in the evaporator #1 temperature with the cooling load. For the given case, the pull-down period takes around 2.2 hours, and the evaporator temperature varies within the pre-defined upper and lower limits throughout the simulation.

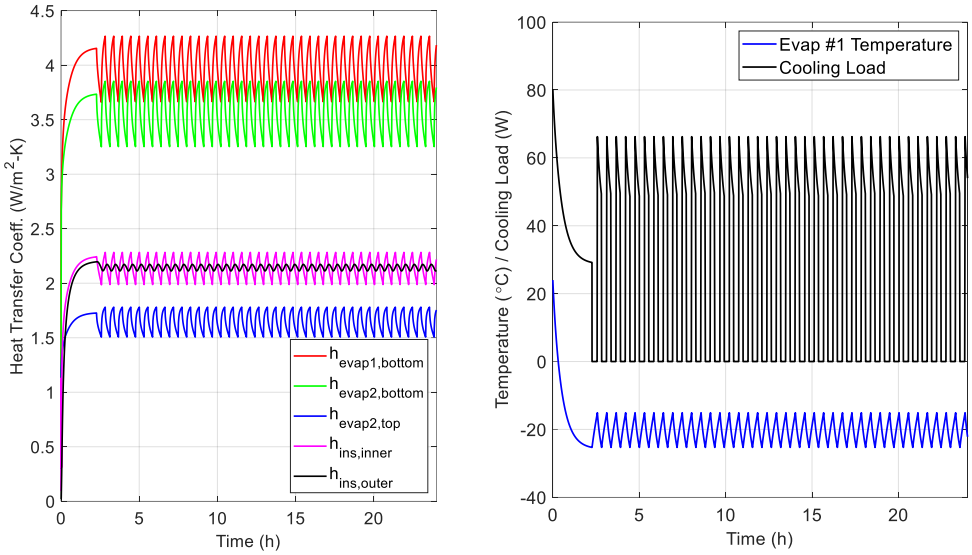

(a) (b)

Fig. 3: Time-wise variations of (a) convective heat transfer coefficients and (b) Evap #1 temperatures and cooling load

III. Results and Discussion

The success of the developed model is tested by comparing the predicted results against the measured data. Fig. 4(a) shows the evaporator temperature variations obtained from experiments and simulations. Considering the temperature gradients from the top (1st) to the bottom (5th) evaporator plates in the measured data, it is clear that the predicted mean temperature has the same trend as the experiments. Parametric simulations include different amounts of phase change materials (PCM) around the evaporator tubes. The selected PCM has a melting temperature of -15 °C, and the latent heat of fusion is 100 kJ/kg. In the base case, the freezer is empty. For the PCM cases, the PCM mass is varied in such a way that the ratio of the thermal mass of PCM to the sum of thermal masses of the evaporator and air are defined to be 2.31, 4.63, and 9.25. Fig. 4(b) and Table 1 reveal the influence of PCM mass on the evolution of temperature and the compressor's on/off durations. Increasing the PCM's mass significantly extends the initial pull-down period, and it takes longer to reach the set point when the mass of the PCM is larger. For an empty freezer, the pull-down duration is 1.42 hours, and wrapping the PCM around the evaporator tubes extends the pull-down duration by as much as 2.9 hours. The PCM mass also affects the compressor's on and off durations. The compressor-off duration increases from 12.58 minutes to 55 minutes when the thermal mass of the freezer is raised by 9.25 times. In parallel, the compressor on time also increased from 7.90 to 30. 17 minutes. The mass of PCM not only increases the thermal mass inside the freezer and limits the heat transfer between the cold evaporator walls and the indoor air.

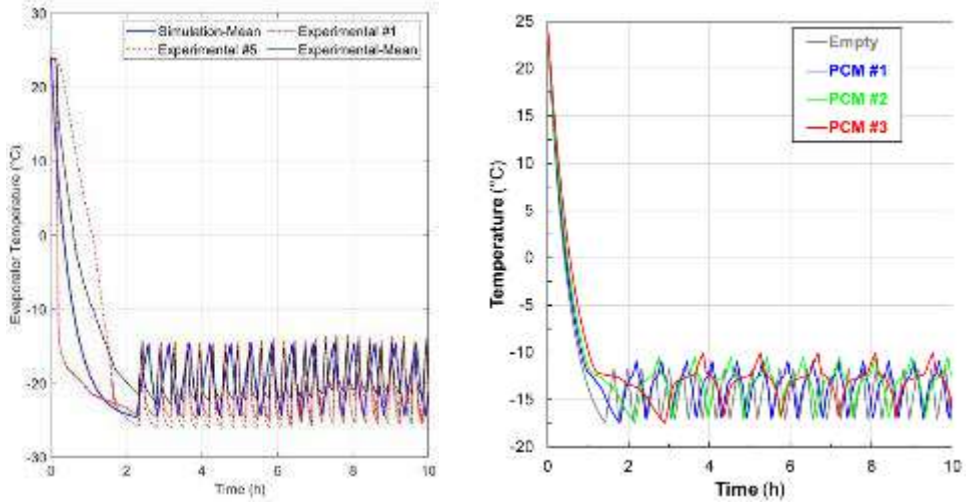

(a) (b)

Fig. 4: (a) Validation of the mathematical model (b) Influence of PCM mass on the mean air temperature of the freezer

Table 1: Effect of PCM's thermal mass on the cycle durations

Thermal Mass Ratio	**Pull-Down Duration** (h)	**Compressor ON Duration** (min)	**Compressor OFF Duration** (min)

Empty Freezer	1.42	7.90	12.58
PCM#1: 2.31	1.78	13.73	23.67
PCM#2: 4.63	2.15	19.30	34.29
PCM#3: 9.25	2.90	30.17	55.00

IV. Conclusion

A dynamic model is developed for a household freezer in MATLAB-SIMULINK, and preliminary results are represented. It is concluded that the thermal mass of the PCM significantly prolongs the pull-down duration of the freezer. In comparison to the empty freezer, the off time of the compressor is extended 4.35 times while the compressor working duration is increased by 3.82 times for the case in which the highest amount of PCM, i.e., PCM's thermal mass is 9.25 times larger than the empty freezer, is implemented. The current model will be improved by including the meat blocks inside the compartments and modeling the 1D heat transfer inside the PCM domains. Such improvements will lead to better predictions and an in-depth understanding of the PCM's cons and pros on the freezer's performance.

Acknowledgements
This research was supported by The Scientific and Technological Research Council of Turkey (TUBITAK) TEYDEB 1505 program with project number 5220120.

References

Azzouz, K., Leducq, D., Guilpart, J., & Gobin, D. (2005, June). Improving the energy efficiency of a vapor compression system using a phase change material. In Second conference on phase change material and slurry: scientific conference and business forum (pp. 15-17).

Borges, B. N., Hermes, C. J. L., Gonçalves, J. M., & Melo, C. (2011). Transient simulation of household refrigerators: A semi-empirical quasi-steady approach. Applied Energy, 88(3), 748–754.

Cengel, Y. A., & Ghajar, A.J. (2020). Heat and mass transfer: Fundamentals and Application. McGraw-Hill Education.

Cheng, W. L., & Yuan, X. D. (2013). Numerical analysis of a novel household refrigerator with shape-stabilized PCM (phase change material) heat storage condensers. Energy, 59, 265-276.

Choi, S., Han, U., Cho, H., & Lee, H. (2018). Recent advances in household refrigerator cycle technologies. *Applied Thermal Engineering*, *132*, 560-574.

Christian J.L. Hermes, Cláudio Melo (2008). A first-principles simulation model for the start-up and cycling transients of household refrigerators, *International Journal of Refrigeration*,31, 1341-1357.

Davis, G, L., Scott, T. C. 1976, Component Modeling Requirements for Refrigeration System Simulation, Proc. 1976 Purdue Compressor Technology Conference, 401-8.

IEEES-004

Sustainable Solar Energy: Repurposing Discarded Materials in Parabolic Concentrator Fabrication

[1]Emre Mandev, [1]Mehmet Akif Ceviz, [1]Ali Çelik, [1]Burak Muratçobanoğlu, [1*]Faraz Afshari
[1]Erzurum Technical University, Faculty of Engineering and Architecture, Department of Mechanical Engineering, Erzurum, 25100, Turkey
*E-mails: faraz.afshari@erzurum.edu.tr

Abstract

This study explores an alternative approach to fabricating parabolic solar concentrators (PSC) by incorporating discarded materials like dish antennas, recycled aluminum foil, and broken mirrors. The study evaluates the efficiency and practicality of utilizing these unconventional resources for PSC production. By adopting this innovative method, the researchers aim to contribute to sustainable and eco-friendly PSC manufacturing processes. This research investigates the technical aspects and potential benefits of using such materials, shedding light on their viability in solar energy usage and applications. Ultimately, this research presents a sustainable perspective on obtaining alternative materials to create efficient solar systems. By utilizing discarded materials and evaluating their performance within PSCs, we demonstrate a promising pathway toward achieving both environmental and energy efficiency goals.

Keywords: Parabolic solar concentrator, Waste material, Solar energy, Hot water production

I. Introduction

One of the most pressing challenges confronting humanity today is the quest for clean and renewable energy sources capable of meeting the ever-growing global demand. Solar energy emerges as a highly promising solution due to its abundant, sustainable, and environmentally friendly nature. Among the pivotal technologies at the forefront of harnessing solar energy is the Parabolic Solar Concentrator (PSC). These sophisticated systems are purpose-built to capture and convert solar radiation into valuable forms of energy, including heat, electricity, and even hot or distilled water, catering to a multitude of applications (Devanarayanan and Murugavel, 2014; Tian et al., 2018; Masood et al., 2022). Solar concentrators, at their core, are ingeniously engineered devices employing reflector or lenses to concentrate copious amounts of solar radiation into a confined area, thus significantly amplifying the intensity of sunlight. Through the concentrated solar energy they yield, these concentrators can achieve remarkably high temperatures, furnishing thermal energy for a diverse range of purposes such as electricity generation, heating, cooling, culinary applications, and industrial processes (Singh et al., 2017; Paul, 2019). Noteworthy among their advantages are their exceptional efficiency, robust power output, and the flexibility and scalability they offer. The topic of solar concentrators has borne witness to extensive research and development endeavors over recent decades. A plethora of studies, spanning an extensive array of investigations into their performance, optimization, enhancements, and practical applications, has fueled the continuous evolution of solar energy technologies (Hijazi et al., 2016; Patel et al., 2018). These cumulative efforts underscore the promising potential to address the global energy crisis, marking a significant stride towards a sustainable and secure energy future. On the other hand, the importance of recovering and reusing waste materials cannot be overstated for a multitude of compelling reasons. Firstly, it plays a pivotal role in curbing the alarming influx of waste into garbage dumps, thus mitigating the detrimental environmental repercussions, including pollution and the release of greenhouse gases into atmosphere. Secondly, this practice supports the conservation of our valuable natural resources, including water, minerals and timber, by reducing the need to extract fresh raw materials from our planet's limited reserves. Third, it supports energy savings by significantly reducing the energy demands associated with the extraction, processing and transportation of raw materials. Finally, it serves as a cost-effective solution by significantly reducing the costs associated with waste disposal, thus easing the burdens on recycling facilities and garbage dumps (Ravichandran et al., 2011; Onyelowe et al., 2019; Milad et al., 2020).

This research is founded on the principles of sustainable solar energy and the recovery of discarded materials. Within this study, a PSC was constructed utilizing recycled materials, including dish antennas, aluminum foil, and broken mirror pieces. The primary objective is to assess the effectiveness and viability of these materials in the fabrication of PSCs and to showcase their potential in sustainable and eco-friendly solar energy applications. Furthermore, the study encompasses an evaluation of the performance achieved by the constructed PSC.

II. System Description

This section provides a comprehensive overview of the testing procedure conducted for the PSC. Figure 1 offers a visual representation of the essential components comprising the integrated PSC. The PSC, boasting a 65 cm diameter, was manufactured at a laboratory scale with the primary aim of evaluating its capability to generate hot water. The chosen test element for the PSC consists of a repurposed dish antenna, as meticulously depicted in Figure 1(f) with a focal point at 17.2 cm, and the corresponding parabolic equation presented alongside. As delineated in Figures 1(d) and 1(e), recycled broken mirror pieces and aluminum foil were thoughtfully chosen as the reflective materials and meticulously affixed to the dish antenna's surface using appropriate adhesive techniques. Visual representations of the PSCs, crafted with these reflective elements, are showcased in Figures 1(b) and 1(c). The reservoir, situated at the focal point of the PSC, was employed for the heating of water and was tactfully coated in black to enhance its absorptive properties.

To monitor temperature, thermocouples were strategically positioned at four discrete points on the reservoir's surface within the test area's center. Furthermore, an internal thermocouple was immersed within the reservoir to diligently track the fluid's temperature. Simultaneously, atmospheric temperature was vigilantly monitored throughout the duration of the experiments. All

temperature measurements were executed employing Type T thermocouples, celebrated for their high precision with an accuracy level of ±0.2°C. The collected temperature data was seamlessly transferred to a computer through an Ordel Brand data card during the experiments. In an effort to replicate solar irradiance levels, an external light source, described in Figure 1(a), was carefully positioned in front of the PSC. The light source maintained a consistent irradiance level of approximately 0.35 kW/m^2. The experiments persisted for a duration of 1.5 hours, during which temperature data was unwaveringly monitored and systematically recorded.

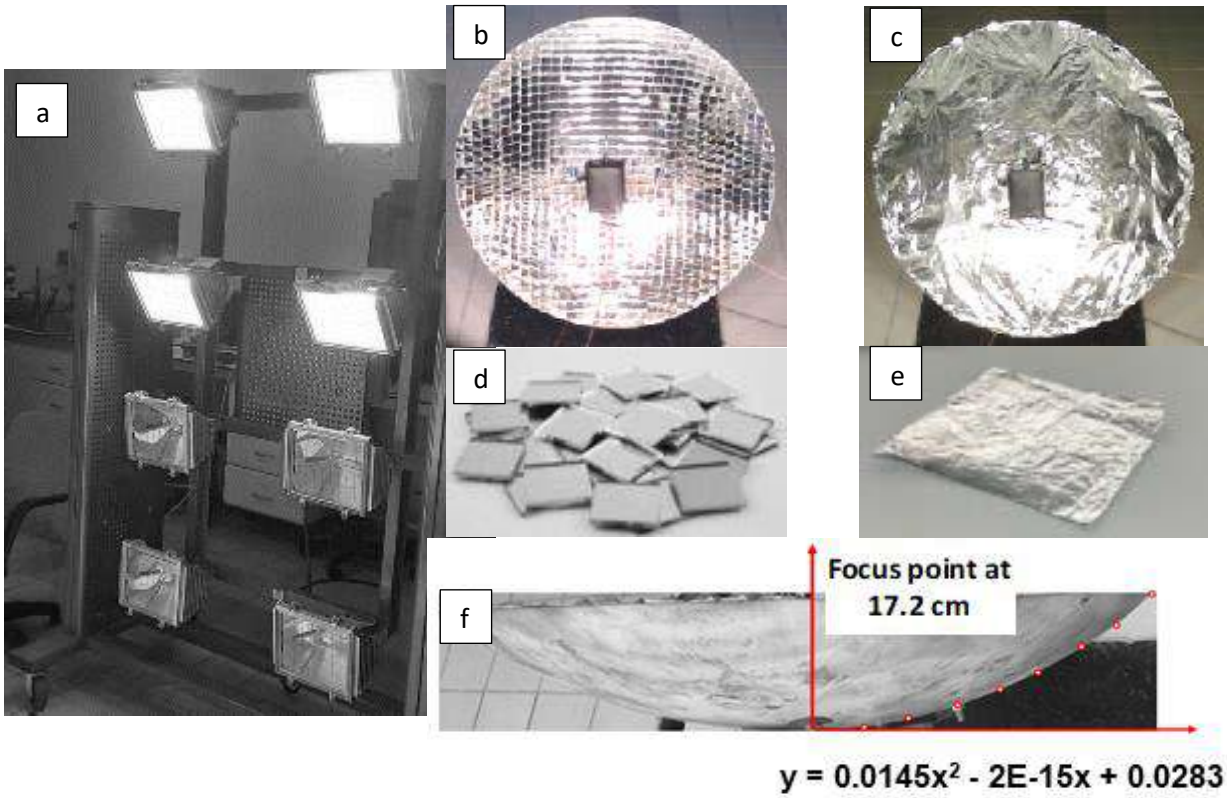

Fig. 1: Experimental setup and essential components comprising the integrated PSC

III. Analysis

In addition to collecting temperature data, thermal camera imaging was conducted over the test area. The Testo-885 thermal camera was utilized to capture these images. After acquiring the images, they were analyzed using the software provided by the device. Figure 2 presents the scales derived from these images and the analysis results. The images in Figure 2, labeled (a) and (b), were taken 10 minutes after the start of the experiment for recycled broken mirror pieces and aluminum foil, respectively. Similarly, images (c) and (d) correspond to approximately 10 minutes before the end of the experiment. The values of the regional surface temperatures obtained from this analysis are presented in Table 1.

Table 1. Regional surface temperatures at various test periods

Material	Point	Temperature (°C)	Time (min)
mirror pieces	*M1*	*26.1*	*10*
mirror pieces	*M1*	*60.3*	*80*
aluminum foil	*M1*	*27.2*	*10*
aluminum foil	*M1*	*64.2*	*80*

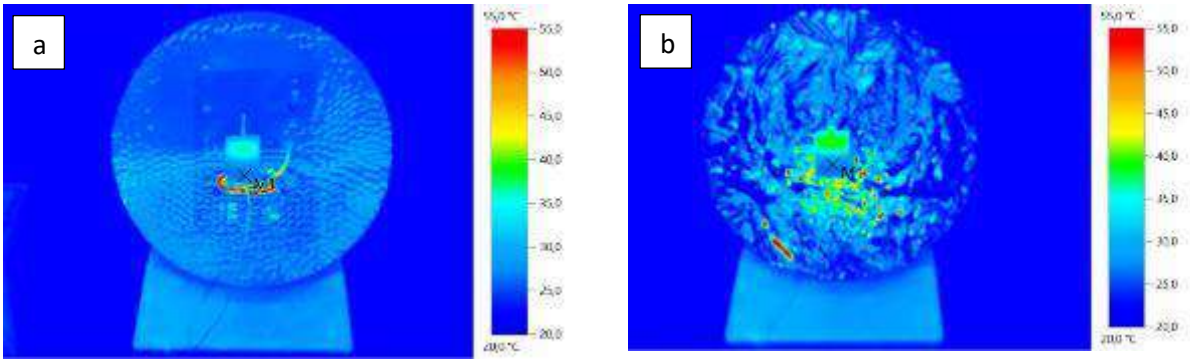

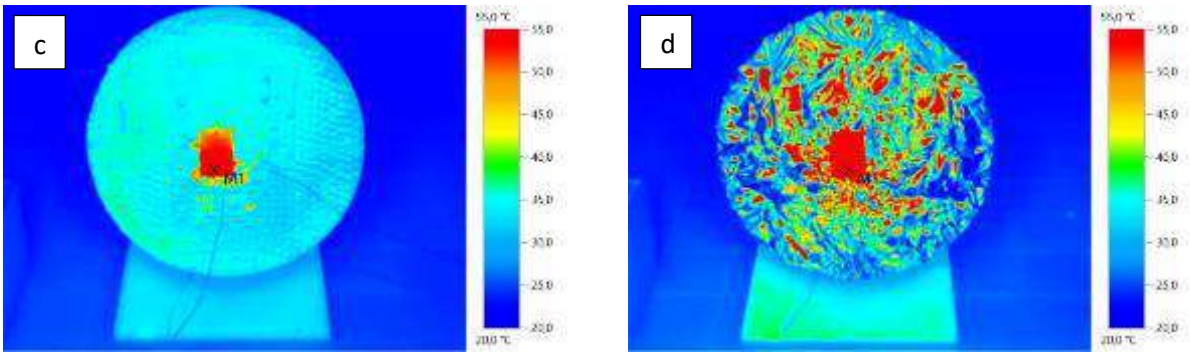

Fig. 2: Thermal camera images and results

IV. Results and discussion

Figure 3 illustrates time-dependent temperature measurements acquired from PSCs constructed using waste glass and aluminum foil materials, denoted as (a) and (b), respectively. These graphs depict temperature values of ambient, fluid, and temperature averages collected from various points on the fluid supply reservoir surface. Upon examining the figures, it becomes evident that the ambient temperature follows a similar trend in both cases. This consistency trend is pivotal for the thorough examination of diverse cases. Although the initial average surface temperature increase in both cases is rapid, a state of stability is reached over time. This phenomenon is expected when employing a highly conductive metal reservoir. Additionally, it is noteworthy that the average surface temperatures remain slightly below the fluid temperature, likely due to measurements taken from the relatively cooler upper surfaces of the reservoir.

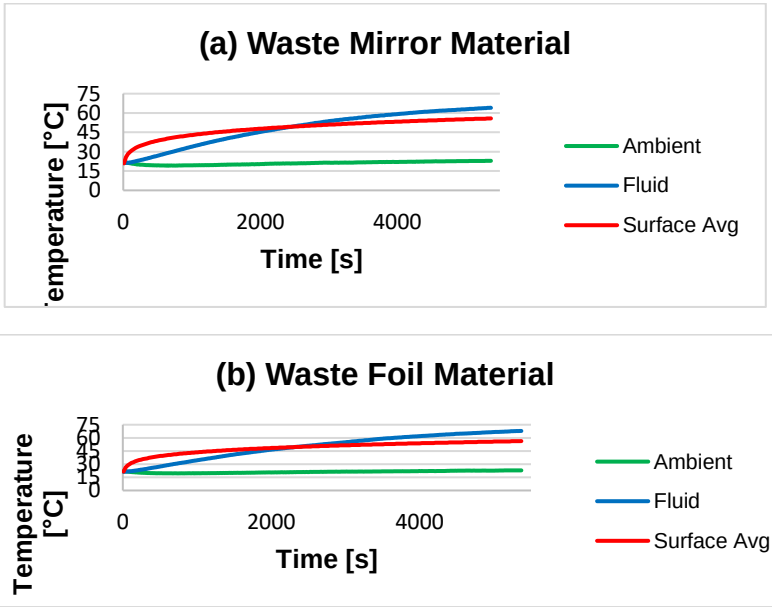

Fig. 3: Time-dependent temperature variations for (a) waste mirror (b) waste foil material

Following approximately 1.5 hours of experimentation, the PSC constructed with waste aluminum foil approaches water temperatures of approximately 70°C, whereas, in the PSC constructed with waste glass material, these temperatures slightly surpass 60°C. Theoretically, water temperatures within the range of 45-55°C are deemed suitable for domestic use (Lévesque et al., 2004). In both cases, fluid temperatures were observed to exceed this temperature range. Nonetheless, further studies of capacity are indispensable to satisfy the demand for domestic hot water. In the PSC constructed with waste mirror material, despite its high reflectivity, low fluid temperature rates are attributed to boundary regions formed between mirror pieces. These boundaries, situated at the junctions of waste mirror pieces, result in losses in the reflective area, consequently leading to a reduction in energy concentration performance. As a result, this has led to diminished outcomes in comparison to the alternative case.

V. Conclusion

This study represents a pioneering effort in exploring alternative approaches to fabricating Parabolic Solar Concentrators (PSC) using discarded and repurposed materials. By integrating elements like dish antennas, recycled aluminum foil, and broken mirrors, we have evaluated the viability and practicality of such unconventional resources in PSC production. This research contributes significantly to the discourse on sustainable and eco-friendly PSC manufacturing processes. Effective Utilization of Discarded Materials: We have demonstrated the potential to repurpose discarded materials effectively, such as dish antennas, recycled aluminum foil, and broken mirrors, in the construction of PSCs. These materials, when used thoughtfully, can contribute to the creation of efficient solar systems. Importance of Sustainable Practices: The practice of recovering and reusing waste

materials is crucial for environmental, economic, and energy conservation reasons. It mitigates environmental pollution, reduces the depletion of natural resources, conserves energy, and lowers costs associated with waste disposal. Performance and Viability: We found that PSCs constructed with waste aluminum foil reached water temperatures of approximately 70°C, while those using waste glass material surpassed 60°C. These temperatures are suitable for many domestic applications. However, the waste mirror material, despite its high reflectivity, faced challenges due to the formation of boundary regions, leading to reduced energy concentration performance.

References

Devanarayanan, K., & Murugavel, K. K., 2014. Integrated collector storage solar water heater with compound parabolic concentrator–development and progress. Renewable and Sustainable Energy Reviews, 39, 51-64. https://doi.org/10.1016/j.rser.2014.07.076

Hijazi, H., Mokhiamar, O., & Elsamni, O., 2016. Mechanical design of a low cost parabolic solar dish concentrator. Alexandria Engineering Journal, 55(1), 1-11. https://doi.org/10.1016/j.aej.2016.01.028

Lévesque, B., Lavoie, M., & Joly, J., 2004. Residential water heater temperature: 49 or 60 degrees Celsius?. Canadian Journal of Infectious Diseases, 15(1), 11-12. https://doi.org/10.1155/2004/109051

Masood, F., Nor, N. B. M., Nallagownden, P., Elamvazuthi, I., Saidur, R., Alam, M. A., ... & Ali, M., 2022. A review of recent developments and applications of compound parabolic concentrator-based hybrid solar photovoltaic/thermal collectors. Sustainability, 14(9), 5529. https://doi.org/10.3390/su14095529

Milad, A. A., Ali, A. S. B., & Yusoff, N. I. M., 2020. A review of the utilisation of recycled waste material as an alternative modifier in asphalt mixtures. Civil Engineering Journal, 6, 42-60. https://doi.org/10.28991/cej-2020-SP(EMCE)-05

Onyelowe, K. C., Bui Van, D., Ubachukwu, O., Ezugwu, C., Salahudeen, B., Nguyen Van, M., ... & Ugorji, B., 2019. Recycling and reuse of solid wastes; a hub for ecofriendly, ecoefficient and sustainable soil, concrete, wastewater and pavement reengineering. International Journal of Low-Carbon Technologies, 14(3), 440-451. https://doi.org/10.1093/ijlct/ctz028

Patel, D. K., Brahmbhatt, P. K., & Panchal, H., 2018. A review on compound parabolic solar concentrator for sustainable development. International Journal of Ambient Energy, 39(5), 533-546. https://doi.org/10.1080/01430750.2017.1318786

Paul, D. I., 2019. Application of compound parabolic concentrators to solar photovoltaic conversion: A comprehensive review. International journal of energy research, 43(9), 4003-4050. https://doi.org/10.1002/er.4428

Ravichandran, S., Bouldin, R. M., Kumar, J., & Nagarajan, R., 2011. A renewable waste material for the synthesis of a novel non-halogenated flame retardant polymer. Journal of Cleaner Production, 19(5), 454-458. https://doi.org/10.1016/j.jclepro.2010.09.010

Singh, D., Singh, A. K., Singh, S. P., & Poonia, S., 2017. Economic analysis of parabolic solar concentrator based distillation unit. https://doi.org/10.5958/2322-0430.2017.00218.9

Tian, M., Su, Y., Zheng, H., Pei, G., Li, G., & Riffat, S., 2018. A review on the recent research progress in the compound parabolic concentrator (CPC) for solar energy applications. Renewable and Sustainable Energy Reviews, 82, 1272-1296. https://doi.org/10.1016/j.rser.2017.09.050

IEEES-005

Assessment of the Effect of Lint Accumulation in the Heater Channel on the Performance of the Water Cooled Washing Drying Machines in Different Operating Conditions

[1*]Nazım TAŞ, [2]Ayşegül ABUŞOĞLU
[1] Istanbul Technical University, Faculty of Mechanical Engineering, Mechanical Engineering Department, Gümüşsuyu, Beyoğlu, İstanbul, 34437, Turkey
[2] Istanbul Technical University, Faculty of Mechanical Engineering, Mechanical Engineering Department, Gümüşsuyu, Beyoğlu, İstanbul, 34437, Turkey
*E-mails: tasna@itu.edu.tr, abusoglu@itu.edu.tr

Abstract

In this study, the specific moisture extraction rate (SMER) is determined by collecting and measuring the lint accumulated in the heating channel after each washing and drying cycle under different washing and drying conditions, and the effective washing and drying parameters on lint accumulation and SMER are investigated with the experimental design used for the statistical model. Experimental design and analysis of the data obtained as a result of the experiments are carried out in the MiniTab program. The parameters used to evaluate the drying performance are the energy consumed during the drying process, the amount of liquid evaporated from the textile, and the drying time. The amount of water evaporated on the textile is obtained by theoretical investigation of the conjugate heat and mass transfer between the textile and air in the drum. It is aimed to reveal the accuracy of the theoretical investigation of the dehumidification created by comparing the performance values obtained as a result of the theoretical studies with the experimental data. The experiments are conducted for the number of drum revolutions per minute of the second stage of drying at 40 RPM, 50 RPM, and 60 RPM conditions; for the final spin speed of rinsing and for the spin speed of the first stage of drying at 800 RPM, 1050 RPM, and 1300 RPM conditions; for the heating power in the heating channel at 600 W, 800 W, and 1000 W conditions; and finally for the volume flow rate of the fan at 22 Lt/s, 26 Lt/s, and 30 Lt/s conditions. In the scope of this study, the aim is to determine and optimize the optimal (improved) washing and drying parameters for water-cooled washing-drying machines. Consequently, the problem of lint accumulation can be reduced, and drying performance can be enhanced.

Keywords: Specific Moisture Extraction Rate (SMER), Conjugate Heat and Mass Transfer, Lint

I. Introduction

The advancements in the textile industry have consistently led to the adoption of new technologies to enhance the performance of household washer-dryer machines. In water-cooled washer-dryer systems used in these machines, air circulation and heat transfer play a crucial role in the drying process of textiles. Studies in the literature, particularly those focusing on the accumulation of lint in the heating channel and various parameters contributing to the moisture absorption process in household washer-dryer machines, have been conducted at this point.

The drum rotation speed, at high speeds (45-50 rpm), indicates optimal drying efficiency by reducing damage to the textile through the use of complex motion patterns. However, at low speeds (35-40 rpm), fabric movement and friction with the drum wall can increase fabric damage. (Wei, Zhang and Yuan, 2019). In studies conducted on polyester and cotton textiles, a statistically significant relationship was found between the amount of load and the amount of lint released into the atmosphere for polyester. However, this relationship could not be detected in cotton textiles (Zhang, 2022). Another study conducted under real-world conditions has shown that as the laundry load increases, the gradual reduction in lint emission occurs (Volgare, Falco, Avolio, Castaldo, Errico, Gentile, Ambrogi and Cocca, 2021). In studies conducted on acrylic textiles, approximately 1.4 times more lint emission was observed in textiles dried for 60 minutes compared to 30 minutes. However, a statistically significant result could not be obtained (Mahbub and Shams, 2022). In another study, it was determined that as the washing time increased, lint emission also increased, and mechanical stress affected the formation of lint (Kumar and Mariappan, 2022).

The decrease in the moisture content on textiles over time contributes to a reduction in drying times. It has been observed that with the increase in indoor air flow and heating power, the Specific Moisture Extraction Rate (SMER) value also increases (Wei, Hua and Ding, 2016) (Stawrebeg and Nilson, 2010). The variation in textile temperature at different heating power values indicates that situations with higher heating power lead to shorter drying times and higher Specific Moisture Extraction Rate (SMER) values. This allows for more water to be evaporated from the textile per unit of time with higher energy input (Wei, Hua and Ding, 2016) (Wei, Gong, Ning and Ning, 2017). When examining the effect of the initial moisture content on drying performance, it was determined that the initial moisture amount does not have a significant impact on the moisture absorption rate (Wei, Hua and Ding, 2016). The impact of spin speed values on drying performance was evaluated, and it was observed that high spin speeds negatively affect drying performance by making the moisture absorption process more difficult due to the textile approaching the drum wall. There is a relationship between drum speed, motor speed, and SMER; for example, the lowest SMER value was obtained at 1000 rpm, while the highest SMER value was observed at 1200 rpm (Wei, Hua and Ding, 2016) (Yu, Li and Ding, 2020).

A study modeling moisture absorption includes the mathematical modeling of heat and mass transfer in the drying process of porous cotton fabric. The experimental design involves parameters such as the initial moisture content of the textile, load amount, heating power, air flow rate, and drum speed. The created mathematical model defines the drying mechanism of the textile inside the drum, describes the heat and mass transfer occurring during the drying process, and determines the time-dependent moisture and temperature values of the textile by numerically solving under boundary conditions (Wei, Hua and Ding, 2016).

II. Experimental Procedure/Methodology/System Description

The experimental setup for the master's thesis was designed to investigate the drying performance and lint accumulation of washer-dryer machines for different values of drum revolutions per minute of the second stage of drying, final spin speed of rinsing, spin speed of the first stage of drying, heating power in the heating channel, and volume flow rate of the fan. In the experimental setup, parameters heating power in the heating channel and volume flow rate of the fan, respectively, were adjusted using a variac and a frequency converter. The values of other parameters could be directly modified through the software.

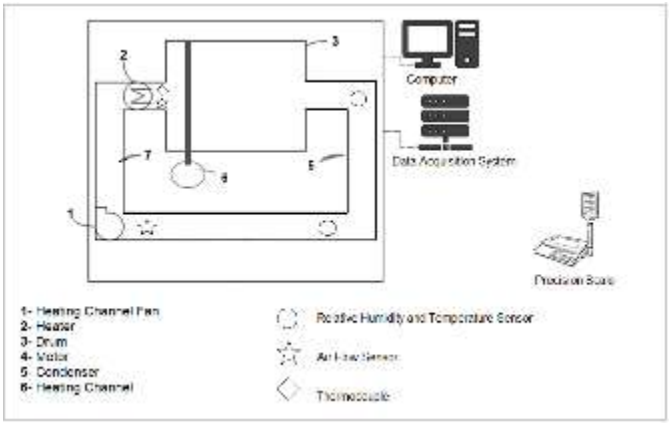

Fig. 1: Schematic representation of the experimental setup

The experiments were conducted with 1 kg of 100% cotton textile using the Beko B3D59644U machine. For the investigation of moisture absorption inside the drum, relative humidity and temperature sensors were placed at the condenser inlet and outlet, and a thermocouple was installed at the drum inlet. Flow sensors measuring differential pressure were placed at the entrance and exit of the heating channel to measure the circulating air flow in the system. To record the energy consumption and duration during the experiment, a data acquisition system (VTS) was utilized. To identify parameters affecting lint accumulation, lint collected on the fan in the heating channel was weighed using a precision scale with a sensitivity of 0.001 grams at the end of each wash-dry cycle, and the weight was recorded. For determining parameters affecting drying performance, the textile was weighed with a precision scale of 5 grams before washing and after drying, and the weight was recorded. Using the energy consumption data recorded through VTS throughout the experiment, Specific Moisture Extraction Rate (SMER) in kg/kWh, representing the drying performance for each experiment, was obtained. Finally, for the study of moisture absorption from the textile, data from temperature, relative humidity, and flow sensors were utilized.
The experiments are conducted for the number of drum revolutions per minute of the second stage of drying at 40 RPM, 50 RPM, and 60 RPM conditions; for the final spin speed of rinsing and for the spin speed of the first stage of drying at 800 RPM, 1050 RPM, and 1300 RPM conditions; for the heating power in the heating channel at 600 W, 800 W, and 1000 W conditions; and finally for the volume flow rate of the fan at 22 Lt/s, 26 Lt/s, and 30 Lt/s conditions.

III. Analysis

Using the Minitab program, the statistical results and effects of parameters influencing lint accumulation and drying performance within the heating channel were examined through ANOVA analysis. Parameters that were kept constant throughout the experiments were specified, and the uncontrollable parameter, which is the application time of the heater in the first phase of drying, examined as a covariance. The analysis results determined the degrees of influence of the examined parameters on lint accumulation and drying performance.
Within the scope of this thesis, the theoretical examination of the evaporation of water on textiles inside the drum of washer-dryers has been calculated using an approach similar to the drying process in vented dryers under specific assumptions stated in the literature.
The relationship between the moisture absorption rate from the laundry in the drum and mass transfer in vented tumble dryers operating on the open-loop principle is represented by Equation 1. (Yadav and Moon, 2008).

$$m_k = k * A * \frac{\rho_v}{0{,}622}\left[\alpha * \omega_o - \frac{\omega_{giriş} - \omega_{çıkış}}{2}\right] \quad (1)$$

Where k is the mass transfer coeffient (m/s), A is the effective surface area of the textile (m^2), ρ_v is the water density on the fabric surface, ω_o is the average specific humidity of the air along the textile surface (kg_w/kg_d), $\omega_{giriş}$ is the specific humidity of the air at the drum inlet (kg_w/kg_d), $\omega_{çıkış}$ is the specific humidity of the air at the drum outlet (kg_w/kg_d), and α is the activity coefficient.
With the study conducted in the literature, the activity coefficient, which depends on textile moisture content, process temperature, and direction, was calculated for cotton-type textiles and is presented in Equation 2, which is part of Equation 1. (Lambert, Spruit and Claus, 1991).

$$a = 1 - \frac{\beta + \delta}{1 + \delta^{\gamma * X}} \quad (2)$$

In Equation 2, the values for the activity coefficient (β) for cotton are determined to be 18, δ is 2, and γ is 30. Here, X represents the moisture content of cotton ($kg_w/kg_{textile}$).

IV. Results and discussion

In the scope of the study, five parameters were examined through Design of Experiments (DOE) based on the principles of 6 Sigma. Within the experimental design of the study, two replicated experiments were conducted to measure drying performance (SMER) and lint accumulation.

According to the results of statistical analysis, parameters drum revolutions per minute of the second stage of drying, volume flow rate of the fan, and spin speed of the first stage of drying have been identified as factors affecting lint accumulation in the heating channel. It has been determined that air flow has a higher impact on lint accumulation compared to mechanical effects. The amount of lint accumulation increases as volume flow rate of the fan and spin speed of the first stage of drying increase, but decreases as drum revolutions per minute of the second stage of drying increases.

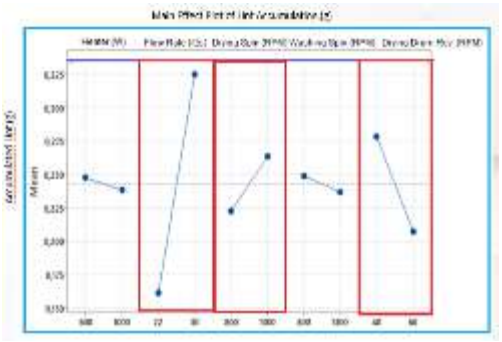

Fig. 2. Main Effect Plot of Lint Accumulation

According to the results of statistical analysis, parameters heating power in the heating channel, spin speed of the first stage of drying, final spin speed of rinsing, and covariance have been identified as factors affecting drying performance. As spin speed of the first stage of drying increases, drying performance improves, but as both final spin speed of rinsing and heating power in the heating channel increase, performance decreases. An increase in heating power in the heating channel leads to an increase in the temperature of circulating air, but due to heat losses, drying performance decreases. An increase in spin speed of the first stage of drying leads to an increase in moisture content on the surface, causing the textile to stretch more and expel more water.

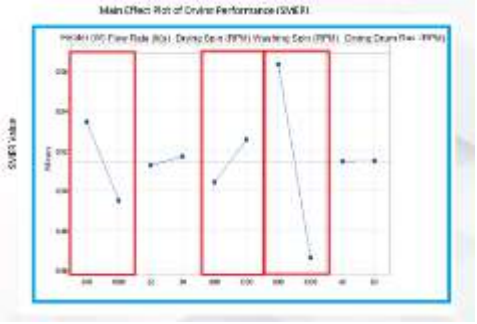

Fig. 3. Main Effect Plot of Drying Performance

According to the theoretically modeled studies on moisture absorption, the activity coefficient affects the rate of water evaporation; a higher activity coefficient implies faster evaporation of water. As the activity coefficient decreases, the rate of water evaporation decreases, making it more challenging to dry the textile.

V. Conclusion

According to the results of statistical analysis, the degree of influence of parameter volume flow rate of the fan on drying performance is the highest at 45%, followed by the interaction of spin speed of the first stage of drying, and drum revolutions per minute of the second stage of drying with a value of 28%. In lint accumulation, parameter final spin speed of rinsing has the highest degree of influence at a rate of 79%, followed by and heating power in the heating channel with a value of 7%.

In the study of theoretically examining moisture absorption, it was observed that when the activity coefficient is around 1, water is present on the surface, and the rate of water evaporation increases until all the surface water evaporates, reaching its maximum level.

A random condition was selected from the Design of Experiments (DOE) tests, and both the theoretical examination and experimental verification of moisture absorption were conducted. According to the comparison with experimental data, it was observed that the textile moisture content after drying could be predicted with a 6.3% error.

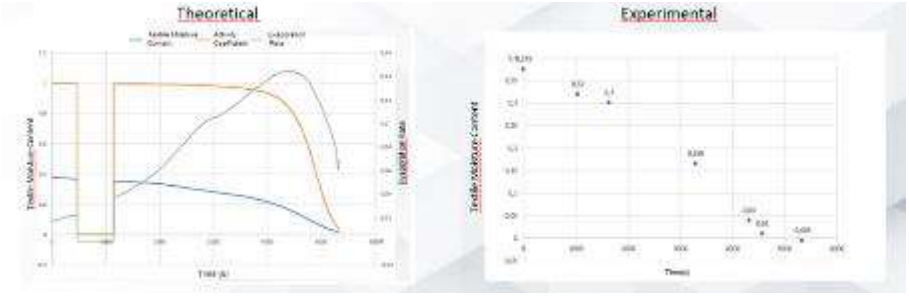

Fig. 4. Theoretical moisture absorption analysis of a randomly selected condition from DOE tests (left) and experimental validation test (right)

In the theoretical calculation studies of the moisture content of all conditions in the Design of Experiments (DOE) tests, it was observed that the textile moisture content after drying could be predicted with a maximum error of 6.5%.

Acknowledgements

I would like to express my gratitude to Arçelik A.Ş., one of the leading manufacturers in the white goods sector, for providing the opportunity to use the Central R&D laboratory facilities and measurement devices.

References

Kumar, A., & Mariappan, G. (2022). Effect of laundry parameters on micro fiber loss during washing and its correlation with carbon footprint. Journal of Natural Fibers, 1–11.

Lambert AJD, Spruit FPM, Claus J. Modelling as a tool for evaluating the effects of energy-saving measures. Case study: a tumble dryer. Appl Energy 1991;38:33–47.

Mahbub, S., ve Shams, M. (2022). Acrylic fabrics as a source of microplastics from portable washer and dryer: Impact of washing and drying parameters. Science of the Total Environment

Stawreberg, L. & Nilsson, N. (2010). Modelling of Specific Moisture Extraction Rate and Leakage Ratio in a Condensing Tumble Dryer, Applied Energy, 30(14-15), 2173-2179

Volgare, M., De Falco, F., Avolio, R., Castaldo, R., Errico, M. E., Gentile, G., Ambrogi, V., & Cocca, M. (2021). Washing load influences the microplastic release from polyester fabrics by affecting wettability and mechanical stress. Scientific Reports, 11(1).

Wei Y., Gong R.H., Ning L. ve Ding X. (2017). Enhancing the Energy Efficiency of Domestic Dryer by Drying Process Optimization, Drying Technology

Wei W., Hua J. ve Ding X. (2016). A mathematical model for simulating heat and moisture transfer within porous cotton fabric drying inside the domestic air-vented drum dryer, The Journal of The Textile Institute

Wei, Y., Su, Z., Zhang, Y., Li, P., ve Yuan, H. (2019). The effect of fabric movement on drying performance of the domestic drum dryer. Journal of the Textile Institute, 110(7), 1059–1071

Yadav, V., ve Moon, C. S. (2008). Fabric-drying process in domestic dryers. Applied Energy, 85(2–3), 143–158

Yu X., Li Y. ve Ding X. (2020). Relationship between drying parameters and drying performance in domestic tumble dryers, Textile Research Journal

Zhang, K. (2022). Microfibers Released into the Air from a Household Tumble Dryer. Environmental Science and Technology Letters, 9(2), 120–126

IEEES-006

Thermodynamic and Parametric Analysis of a Double Adsorptive Solar Cooling Cycle

*Wassila Chekirou, Nahman Boukheit, Ahcene Karaali
Laboratory of Thermodynamic and Treatment of Materials surface, Department of Physics, Faculty of Exact Sciences, Frères Mentouri University, Route Ain El Bey, Constantine 25000, Algeria.
*Corresponding author e-mail: chekirou.wassila@umc.edu.dz, chekirouw@yahoo.fr

Abstract

Since the Montreal Protocol called for a ban on the use of CFCs, research efforts focused on the development of refrigeration technologies, which address the environmental concerns of ozone layer depletion and global warming have increased over the past 20. Solar adsorption cooling machines constitute very attractive solutions. They are of significance to meet the needs for cooling requirements such as air conditioning, ice-making, and medical or food preservation in remote areas far from electric grids. Compared with electric driven vapor-compression refrigerator systems, these machines are advantageous because: They are noiseless; They usually employ environmentally friendly substances as refrigerants, which exert no harmful effects on the environment. However, the wide- spread application of adsorption systems is limited by its rather low coefficient of performance, low specific cooling power and long cycle time. In order to improve the performances of the solar adsorption cooling system, the continuous cycle which incorporated heat recovery cycles is one of the best advanced cycles proposed in this way. In this paper, we interest to use a double adsorptive cycle using a solar energy us a heat source of the system. A numerical analysis was carried out, for studying the influence of the main parameters on both of regeneration and performance coefficients of the machine. A detailed thermodynamic and parametric analysis of a proposed cycle is given, where the Dubinin-Astakhov equation is used to describe the isotherm of adsorption. The simulation technique takes into account the variation of ambient temperature and solar intensity for Constantine region, which is situated at the north- east of Algeria. The results of a base case as a reference, demonstrated that the performance coefficient of the double bed adsorption refrigeration cycle increase with respect to the single bed configuration. Several main factors affecting the performance of cycle and the heat recovery ratio are discussed according to simulation results.

Keywords: Adsorption solar cooling system, Heat recovery process, Performance coefficient, Thermodynamic and parametric analysis.

I. Introduction

Since the Montreal Protocol called for a ban on the use of CFCs, research efforts focused on the development of refrigeration technologies which address the environmental concerns of ozone layer depletion and global warming have increased over the past 20.

Solar adsorption cooling machines constitute very attractive solutions. They are of significance to meet the needs for cooling requirements such as air conditioning, ice-making, and medical or food preservation in remote areas far from electric grids. Compared with electric driven vapor-compression refrigerator systems, these machines are advantageous because: They are noiseless; They usually employ environmentally friendly substances as refrigerants, which exert no harmful effects on the environment (such as water, methanol and ammonia. With the development of its technologies and theories [1-4], the application of adsorption refrigeration is getting extensive, research indicates that adsorption is friendlier for environment than HFC vapor compression in several cases. Hover, the basic cycle of adsorption refrigerating machines presents two main draw backs: the production of cold is intermittent and the efficiency is low. To attain higher efficiencies and to achieve continuous production of cold, it is necessary to use advanced cycles. Several kinds of advanced cycles have been proposed and tested. Two main technologies have been developed: regenerative processes with uniform temperature adsorbers and regenerative processes with temperature fronts (or thermal waves). The basic idea is to use the heat discarded by one adsorber under cooling to pre-heat another adsorber under heating. In so doing, the COP is enhanced and the production of cold is continuous.

On the basis of our previous work done by Chekirou et al. [5], a mathematical model, which accounts for heat and mass transfer in a tubular adsorber as well as the effects of non-uniform temperature and uniform pressure distribution, another computer program has been developed in order to determine the influence of the type of the solar collector on the system's performance.

The thermal and solar performance coefficient, respectively) are used as an optimization criteria. The Activated carbon AC35/methanol is chosen as an adsorptive pair. It has proved to be the best pair among those studies so far, because it is reasonably stable chemically, has a high performance coefficient and it is less expensive than others [6]. All the basic parameters used in the model are also cited by Chekirou et al. [5]. In this paper, we interest to the uniform temperature adsorbers. A numerical analysis was carried out, studying the influence of the main parameters on both of regeneration and performance coefficients of the machine. A detailed thermodynamic and parametric analysis of a double adsorptive cycle is given, where the dubinin-astakhov equation is used to describe the isotherm of adsorption.

The discontinuity of the useful effect makes the system with single adsorber commercially unsuitable. The idealized thermodynamic cycle of a double bed adsorption machine. The adsorbent beds operate the same cycle but in counter phase, so that the heat recovery is obtained by transferring the heat from one bed to the other, until a fixed difference of temperature δT_r between two beds is reached. Adsorption refrigeration systems have been initially proposed of a single adsorbent bed alternately connected to a condenser and evaporator. However a double effect machine used two adsorbers as presented in Fig. 1.

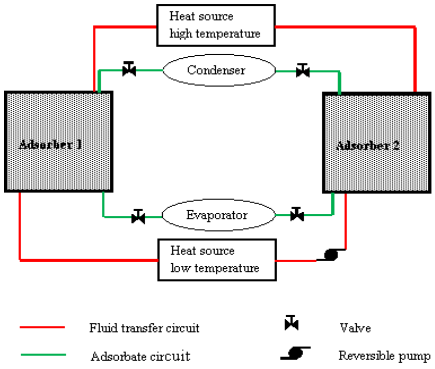

Fig. 1. Schematic diagram of simple heat recovery solar adsorption cooling machine

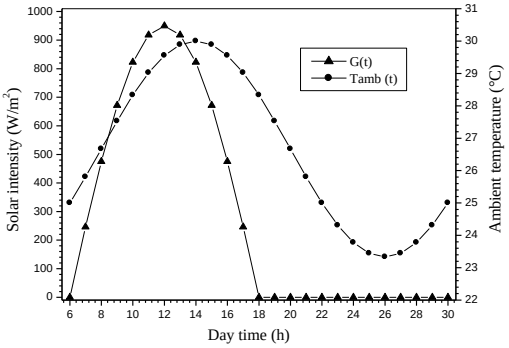

Fig 2. Variation of ambient temperature and solar intensity along a simulated day [2].

Both of two adsorbers are heated by solar energy and contain a porous medium constituted of activated carbon AC-35 reacting by adsorption with methanol. The simulation technique takes into account the variation of ambient temperature and solar intensity along a simulated day, which corresponds to a total daily insolation of 26,12 MJ/m^2 and an average ambient temperature of 27.7 °C. These meteorological conditions are taken for Constantine region, which is situated at the north- east of Algeria, at 6°,37' East (longitude) and 37°,17' North (latitude), with an average altitude of about 625 m [2]. Fig. 2. represent this simulated day.

II. Performance Analysis

In the regenerative cycle case, the performance of the machine can be calculated by the following formulae:

$$COP = \frac{COP_s}{1-r} \tag{1}$$

COP_s is the coefficient of performance of single adsorbent bed, can be calculated as the ratio of useful effect produced Qf and energy supplied to the machine Q_c:

$$COP_s = \frac{Q_f}{Q_c} \tag{2}$$

r is the coefficient of regeneration (or the heat recovery ratio), it can be calculated by:

$$r = \frac{Q_r}{Qc} \tag{3}$$

Q_r is the recovered heat during the heat recovery process. Q_c is the necessary heat for heating the full solar adsorbers to the maximum temperature of regeneration, taking into account the necessary heat for methanol desorption.

III. Results and Discussion

The pair activated carbon AC-35/methanol is chosen as an adsorptive pair, the copper is a material of construction of the adsorber; $m_g = 5kg$ its mass and $m_a = 1\ kg$ is an adsorbent mass.

We present in the flowing section, the effect of regeneration, condensation, evaporation temperatures and the two-adsorber temperature difference at end of heat recovery process, on both of performance's system coefficient and heat recovery coefficient. The influence of condensation and regenerating temperatures on performance coefficient, heat recovery coefficient is shown in Figs. 3 and 4, respectively.

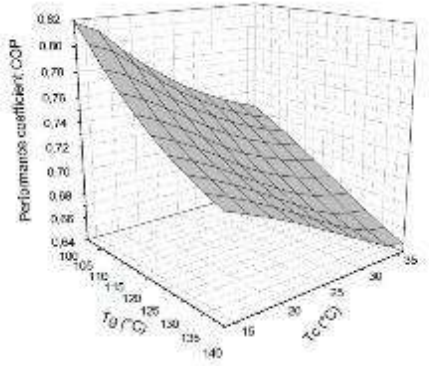

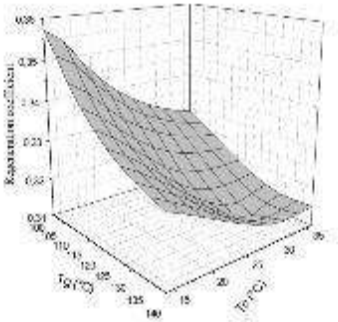

.

Fig. 3. Condensation and regenerating temperature effect on performance's system coefficient

Fig. 4. Condensation and regenerating temperature effect on heat recovery coefficient

An increase in condensation temperature makes the saturation pressure increases. Thus, the adsorbed mass of the methanol increases and consequently, there is a decreasing in the cycled mass of the methanol, the cooling power and the performance coefficient and heat recovery coefficient. The influence of evaporation and regenerating temperatures on performance coefficients, heat recovery coefficient is shown in Figs. 5 and 6, respectively.

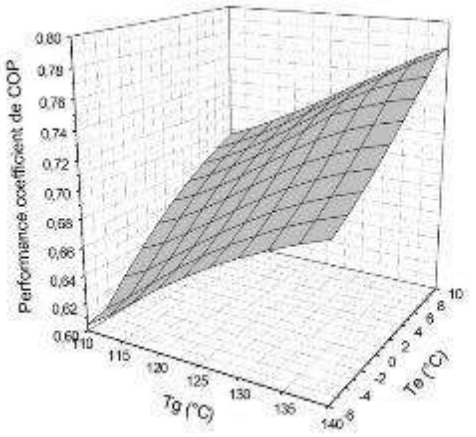

Fig. 5. Evaporation and regenerating temperature effect on performance's system coefficient

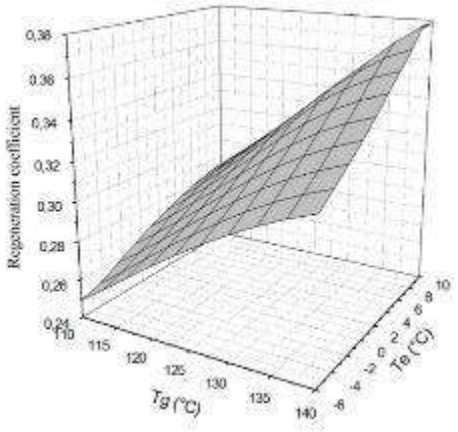

Fig. 6. Evaporation and regenerating temperature effect on heat recovery coefficient

The performance coefficient increases with the evaporation temperature. This increment in evaporation temperature implies that the saturation pressure increases together with the adsorbed mass of methanol. Therefore, it increases the cycled mass of the methanol. The cooling power increases and also, the performance coefficient and the heat recovery coefficient.

Figs. 7 and 8 show the effect of regenerating temperature and two-adsorber temperature difference at end of heat recovery process (varying between 0 and 8°C) on performance's system coefficient and heat recovery coefficient.

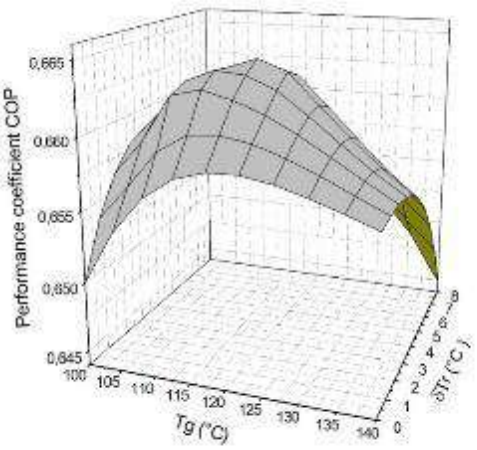

Fig. 7 . Effect of regenerating temperature and two-adsorber temperature difference at end of heat recovery process on performance's system coefficient

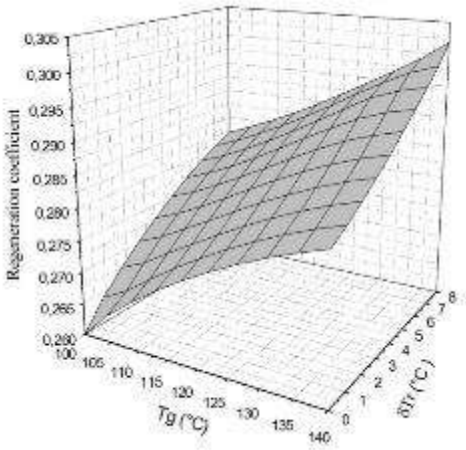

Fig. 8 Effect of regenerating temperature and two-adsorber temperature difference at end of heat recovery process on heat recovery coefficient

Fig.7 represents the logical decrease of performance's system coefficient with an increase of two-adsorber temperature difference at end of heat recovery process δT_r. Where the heat transfer between two adsorbers becomes largest when $\delta T_r = 0°C$ and decreases with the increase of δT_r. Thus, temperature at the end of the regeneration phase decreases and like the regeneration coefficient is defined as the fraction between the heat recovered between two adsorbers and the heat required in a process without heat regeneration, this coefficient decreases also (Fig.8).

IV. Conclusion

In this paper, an analytical thermodynamic model has been developed for the analysis of solar adsorption refrigeration system using heat recovery process. Tthe pair activated carbon AC-35/methanol as an adsorptive pair. This model was usually expressed in algebric or relatively simple equations based on the representation of Dubinin-Astakhov.

The developed model is described with reference to a single bed adsorption system and the main differences introduced in modelling of a two bed system are also presented. Coefficient of performance might be increased or decreased with different working condition (evaporation, condensation and regeneration temperatures). The influence of the two-adsorber temperature difference at the end of heat recovery is also presented.

References

[1] F. Meunier, Adsorption heat pump technology: possibilities and limits, Proceedings of the International Sorption Heat Pump Conference, Munich, 1999, p. 25.
[2]G. Cacciola, G. Restuccia, Progress on adsorption heat pump, Heat Recovery Syst. CHP 4 (1994) 409–420.
[3] H.T. Chua et al., Modeling the performance of two-bed silicagel–water adsorption chillers, Int. J. Refrigeration 22(1999) 194–204.
[4]R.E. Critoph, Forced convection adsorption cycle with packed bed heat regeneration, Int. J. Refrigeration 22 (1) (1999) 38–46.
[5] W. Chekirou, et al. 2014, "Dynamic modelling and simulation of the tubular adsorber of a solid adsorption machine powered by solar energy", Int. j. Refrig. 39, pp 137-151.
[6] Hu. Jing, R. H. B. Exell, 1994, "Simulation and sensitivity of an intermittent solar-powered charcoal/ methanol refrigerator", Renew. Energy, Vol. 4(1), pp 133-149.

IEEES-007

Effect of Adsorbent/Adsorbate Working Pairs on Solar Adsorption Cooling Performance's

*Wassila Chekirou, Nahman Boukheit, Ahcene Karaali
Laboratory of Thermodynamic and Treatment of Materials surface, Department of Physics, Faculty of Exact Sciences, Frères Mentouri University, Route Ain El Bey, Constantine 25000, Algeria.
*Corresponding author e-mail: chekirou.wassila@umc.edu.dz, chekirouw@yahoo.fr

Abstract

Many adsorbent-adsorbate pairs can be considered as working materials in solar adsorption refrigeration systems, and a careful selection of this pairs is essential, because, the thermal performance coefficient of these systems depends on it, however, its selection depends on certain desirable physical and chemical characteristics. This paper presents a detailed thermodynamic and parametric analysis of simple intermittent cycle of a solar adsorption refrigerator. The basic fundamentals of adsorption process and the criteria for choice of the adsorbent-adsorbate pairs are discussed. The Dubinin-Astakhov (D-A) equation is used to describe the isotherm of adsorption for a different activated carbon /methanol pairs. Factors mostly influencing the performance of the system and the cold quantity produced at evaporator level are discussed. The best pair used in this kind of machines is also investigated.

Keywords: Adsorption, adsorbent/adsorbate, solar refrigeration and simulation

I. Introduction

The use of solar energy for environmental control is receiving much attention as result of the projected world energy shortage. Refrigeration is particularly attractive as a solar energy application because of the near coincidence of peak cooling loads with the available solar power. Solar refrigeration, especially solar refrigeration with adsorption has the potential to improve the quality of life of people who live in areas with electricity shortage. It is usually used for storage of agricultural products, food and medicines (e.g. vaccines) in remote areas [1-4]. It is largely identifies that one of the most significant problems in the design of a refrigerating machine with adsorption is the choice of pair adsorbent / adsorbate. Many pairs can be regarded as pairs adsorptifs in this kind of systems. However the selection of them is essential because the effectiveness of the machine translated by the adimensional number, the thermal coefficient of performance depends on certain desirable physical and chemical characteristics. In this paper, we present the effect of the choice of pairs adsorbent / adsorbate on performance's of solar adsorption machine, using a an equilibrium thermodynamic model of de Dubinin Astakhov. We test our program to various pairs.

II. Choice of Adsorbent-Adsorbate Pair

Many adsorbent-adsorbate pairs can be considered as working materials in solar adsorption refrigeration systems, and a careful selection of this pairs is essential, because, the thermal performance coefficient of these systems depends on it, however, its selection depends on certain desirable physical and chemical characteristics:

III. Choice of Adsorbent

The suitable adsorbents are porous materials that should adsorb a range of refrigerants and the choice of these adsorbents depends mainly on the following factors:

- Must have high adsorption capacity at ambient temperatures and low pressures but less adsorptive capacity at high temperature and high pressures in order to attain high cooling effect;
- A large specific surface area in order to providing large adsorption capacity;
- Low cost and widely available;
- Good thermal conductivity , in order to shorter the cycle time;
- Low specific heat capacity;
- Chemically compatible with the chosen adsorbate;
- No deterioration with time or use;
- Non toxic and non corrosive.

IV. Choice of the Adsorbate

The refrigerant or the adsorbate is one of the most important elements of any refrigeration system, because the adsorbent-adsorbate pair conditions and compatibility with the environment principally depend on it.
The selected adsorbate must have the following desirable thermodynamic and heat transfer properties:

- High latent heat of evaporation;
- Good thermal stability with adsorbent at the cycle operating temperature range;
- High thermal conductivity;
- Low viscosity;
- Low specific heat;
- Molecular dimensions should be small enough to allow easy adsorption;

- The choice of the evaporation temperature according to the application;
- Chemically stable in the working temperature range;
- Non -toxic, non inflammable and non-corrosive;

Based on the above criteria, some of the appropriate adsorbent-adsorbate pairs are used in the solar adsorption systems of refrigeration such as: zeolite/ water, silicagel/ water, activated carbon/methanol and activated carbon/ammoniac. However, the choice of the good pair depends on the application object, the zeolite / water and silicagel / water pairs are usually used in the refrigeration , air conditioning [19] ,another benefit using them, that are can be reach high regenerating temperature T_g . More, the adsorbate water in the most thermally stable with the adsorbents, but it cannot be used for freezing purposes because its evaporation temperature 0°C, whereas, the activated carbon/methanol and the activated carbon/ammoniac pairs are used for ice production systems,

Another different pairs have been evaluated by various authors, and the pair activated carbon/ methanol was selected the best pair, but the choice between the methanol and ammoniac as adsorbates is not easy, several authors shown that the adsorptive properties of activated carbon with methanol gives the high COP_{th} than ammonia with some activated carbon adsorbents. However, the ammonia operates at supra-atmospheric pressure, whereas, systems with methanol or water at under –atmospheric pressure, more, the ammonia is toxic and corrosive, while water and methanol are not. Until now, there is not a refrigerant that satisfies all above conditions at the same time, it doesn't practically exist, nevertheless, we can consider that the methanol is the refrigerant that satisfies the maximum of these conditions, and this justifies our choice of the activated carbon/ methanol as an adsorbent-adsorbate pair in this study.

V. Thermodynamic Model

Thermal performance coefficient is defined by the ratio of cooling power produced at evaporator level Q_f to the heat Q_C necessary for heating the adsorber to the maximum temperature T_g taking into account the heat necessary for gas desorption.

$$COP_{th} = \frac{Q_f}{Q_c} \tag{1}$$

The adsorber receives the energy from the hot source, where a part will be used to heat the metal parts of the adsorber, a part is used to heat the adsorbent and the adsorbate and another being used for the desorption. The *Properties of pairs used in this paper is presented in table 1.*

Table 1*: Properties of pairs adsorbent/adsorbate used in the model.*

pair adsorbente /adsorbate	$q_{st}\,(MJ/Kg)$	$Cp\,(J/Kg\,K)$	$w_0\,(l/Kg)$	D	n
Activated carbon /methanol [5]	1.4	920	0.425	$5.02\ 10^{-7}$	2.15
Activated carbon -40/methanol [6]	1.4	920	0.611	$4.78\ 10^{-5}$	1.53
Gel de silice S-50 /water [7]	2.8	924	1.436	1.0339	0.24
Zeolithe 13-X/water [8]	3.2	836	0.269	$4.15\ 10^{-7}$	2
Activated carbon PX -21/ammoniac [9]	1.5	920	1.64	$5.42\ 10^{-4}$	1.235

VI. Results and discussion

This paragraph gives account of the sensitivity of performance of the cycle COP to the operating temperatures, regeneration temperature, evaporation temperature and condensation temperature, respectively in figures 1,2 and 3.

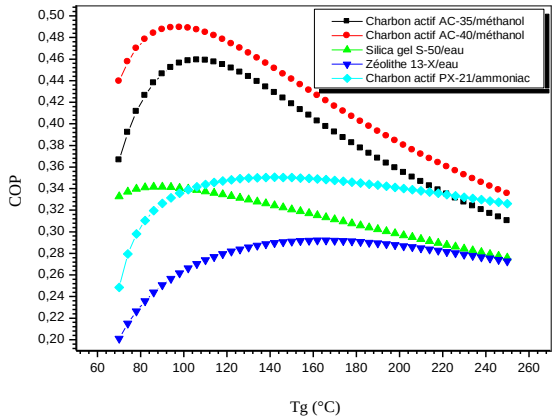

Fig. 1 Performance coefficient according to regeneration temperature for various pairs.

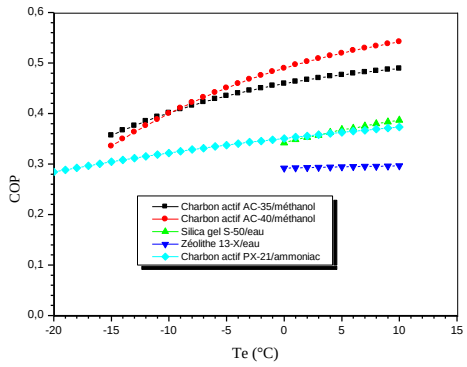

Fig2. Performance coefficient according to evaporation temperature for various pairs.

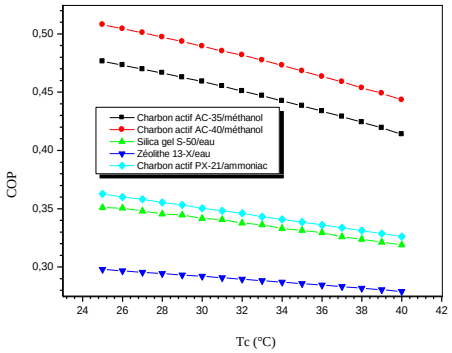

Fig3. Performance coefficient according to condensation temperature for various pairs.

The performance increases with regeneration temperature until a maximum reached for an optimal temperature noted $T_{g\,max}$. For the temperatures superior to this value the performance decreases. This behaviour can be justified by the fact that after certain regenerating temperature $T_{g\,max}$, the energy of heating only serves to increase the activated carbon temperature, the adsorber metal parts temperature and the methanol temperature, nevertheless the desorbed mass of methanol becomes more and more weak Where, the heat provided to the adsorber increases more than the quantity of cold produced at evaporator level Q_f. The values of maximum regeneration *temperature of each pair is present in table 2.*

Table 2 Maximum regeneration temperature of pairs

Pair adsorbent /adsorbate	$T_{g\,\max}\ (°C)$
Activated carbon AC-35/methanol	106
Activated carbon AC-40/methanol	97
Gel de silice S-50 /water	89
Zeolithe 13-X/water	164
Activated carbon PX -21/ammonia	132

The Fig. 2 shows the influence of evaporation temperature on the performance of the system. Indeed, The COP increases with the evaporation temperature . This increment in evaporation temperature implies that the saturation pressure increases together with the adsorbed mass of methanol. Therefore, it increases the cycled mass of the methanol. It is easy to verify the qualitative effect of the increase of evaporation temperature according to Clapeyron diagram. This notice for all pairs. The Fig.3 shows the influence of condensation temperature on the performance of the system. The COP of the system decreases with the increase of

condensation temperature, because of an increase in condensation temperature makes the saturation pressure increases. Thus, the adsorbed mass of the methanol increases. Consequently, there is a decreasing in the cycled mass of the methanol, in the cooling power and also in the COP. According to the Clapeyron diagram of the cycle; it is easy to notice that the minimum desorbed mass of methanol increases for the low values of condensation temperature and for a fixed value of regeneration temperature. This notice for all pairs.

VII. Conclusion

A thermodynamic model has been developed for the analysis of solid adsorption refrigerator using the activated carbon AC-35/ methanol as an adsorptive pair, based on the representation of Dubinin-Astakhov. Based on the previous results and the analysis discussed above, some conclusions are summarized in the following:

- This model is a good tool for optimizing the adsorption system;
- The performance and cooling power of adsorption systems depend strongly on the operating temperatures;
- There is an optimum regenerating temperature for the pairs at various condensation, adsorption and evaporation temperatures.

With a study such as this, it is possible to estimate the performance of an adsorption refrigerating cycle, which can be easily transported to any type of adsorbate and several types of adsorbent, especially activated carbons. This method can also be applied to all the different cycles (internal heat recovery system, cascading cycle …etc).

References

[1]. INTRODUCTION R E . Critoph. Performance limitations of adsorption cycles for solar cooling. Solar energy 1988; 41(1):21-31.
[2]. A. Mimet, Etude théorique et expérimentale d'une machine frigorifique à adsorption d'ammoniac sur charbon actif, thèse de Doctorat, 1991.
[3]. Lian Ming Sun. Francis Meunier. Adsorption :Aspects théorique. J 2730 ; 1-16
[4]. Leite A P F, Daguenet M . Performance of a new solid adsorption ice maker with solar energy regeneration. Eenrgy convers Manag 2000;41:1625-47.
[5]. E. Passos, F. Meunier and J. C. Gianola, "Thermodynamique performance improvement of an intermittent solar powered refrigeration cycle using adsorption of methanol on activated carbon", *Heat recovery systems*, Vol.6, N 3, pp. 259-264, 1986.
[6]. A. Boubakri, M. Arsalane, B. Yous, L. Alimoussa, M. Pons, F. Meunier, . J.J Guilleminot, "Experimental study of adsorptive solar powered ice makers in AGADIR (Morocco)-2", *Renewable energy*, Vol.2, N 01, pp. 15-21, 1992.
[7]. K. Daou, R. Z. Wang, Z. Z. Xia, "development of a new synthesized adsorbent for refrigeration and air conditioning application", *Applied thermal engineering* , Vol.26, pp. 56-65, 2006.
[8]. L. Krache, "Contribution à l'étude théorique d'un réfrigérateur solaire à adsorption utilisant le cycle Zéolithe 13-X/eau, thèse de Magister en physique énergétique, Constantine, 1996.
[9]. J. Llobet, V. Goetz, "rotary system for the continuous production of cold by solid-gas sorption,: modelling and analysis of energy performance", *International journal of refrigeration*, Vol.23, pp. 609-625, 2000.

IEEES-008

A Year-Round Dynamic Simulation of a Solar Trigeneration System in Hot and Humid Climate

[1*]Maryam Karami, [2]Seyedeh Somayeh Nasiri Gahraz
[1]Kharazmi University, Faculty of Engineering, Department of Mechanical Engineering, Tehran, 15719-14911, Iran
*E-mails: karami@khu.ac.ir

Abstract

In this study, the performance of a solar trigeneration system using a photovoltaic/thermal collector and a hybrid humidification-dehumidification/reverse osmosis desalination system in hot and humid climates (Bushehr, Iran) is investigated. Dynamic simulation of the solar trigeneration system is performed using TRNSYS software and since there is no model for the desalination system in TRNSYS, it is modeled separately by MATLAB software and coupled with TRNSYS model. The results show that electricity of 7,261.66 kWh is annually generated by the proposed system, of which 10% is used by system pumps, 55% for building electricity consumption, 4.2% for fresh water production by reverse osmosis, and 2.6% to supply domestic hot water. In addition, from January to November, 100% of the required fresh water can be supplied using the solar trigeneration system.

Keywords: Solar trigeneration system; Photovoltaic-thermal (PVT) solar collector; Humidification-dehumidification desalination unit; Reverse osmosis; Economic Analysis; Hot and humid climate

I. Introduction

The use of renewable energy as an alternative to fossil fuels due to their environmental and economic characteristics, is one of the concerns of energy policymakers in this century. Among the types of renewable energy, solar energy is the most unique source of renewable energy on Earth. With 300 sunny days a year, Iran is one of the best countries in the world in terms of solar energy potential (Karami et al., 2022). Today, thermal applications of solar energy in buildings are noticed by researchers. One of these applications is solar combisystems, which are the same as solar water heaters but use more collector area to supply both domestic hot water and space heating. Many studies have been conducted in the field of solar combisystems. Mehdaoui et al. (2016) used underfloor heating with one and two active layers. The two active layer solar combisystem is presented as the optimal system in this study and the solar fraction (SF) in supplying the required thermal load of the building is reported to be about 72% annually. Hazemi et al. (2017) simulated the performance of a solar combisystem to generate electricity and heat for Tunisian weather conditions. Their results showed that the solar combisystem provides 20% to 40% of the energy required for space heating (SH) and 40% to 70% of the energy required for domestic hot water (DHW). Katsaprakakis and Zidianakis (2019) optimized a solar combisystem to heat a school on the Greek island of Crete with biomass fuel. They found that solar energy provided more than 50% of the energy needed. Karami and Javanmardi (2020) investigated the effect of weather conditions on the performance of the solar combisystem using underfloor heating system. Their results showed that the annual SF in hot-dry, cold-dry, moderate-humid, hot-semi-humid and hot-humid climates are 74%, 61%, 47.8%, 87.9% and 92%, respectively.

Another application of solar energy is water desalination using solar thermal energy (Belessiotis et al., 2016). Despite the large resources of brine water, oceans, seas, and local resources in desert areas, water desalination systems are a reasonable solution to the problem of freshwater scarcity. In recent years, the production of fresh water by solar combisystem, which is also called solar trigeneration system, has been attractive to researchers. Zamen et al. (2014) experimentally evaluated the performance of a combined solar water heater/desalination system. They reported that the proposed system produces up to 20 l of fresh water and about 250 l of DHW per day using a Humidification-dehumidification (HDH) desalination system. Asim et al. (2016) analyzed a solar trigeneration system for simultaneous production of fresh water and DHW for a villa with a demand of 15 l to 25 l of drinking water per day and a demand of 250 l of DHW per day in Dubai. Calise et al. (2016) investigated a photovoltaic/thermal (PVT) system with a multi-effect distillation plant. The results showed that to reduce the payback period, the optimal ratio of collector area to absorption chiller capacity is 5.9 m2/kW and the number of optimal desalination steps is 14 steps. Kumar and Martin (2017a) studied the simultaneous production of fresh water and DHW in the United Arab Emirates using solar energy that is connected directly to the distillation loop, and the effect of DHW tank volume and collector area on desalination. The results showed that in the independent state, the desalination rate is 36% higher than the combined state and the maximum desalination rate in the independent state is 4.5 kg/h; while in the combined state is 1.3 kg/h. In another study, they evaluated and optimized a solar trigeneration system for the simultaneous production of DHW and fresh water by membrane distillation (Kumar and Martin, 2017b). Based on the results, this trigeneration system uses more than 80% of the available solar energy and the efficiency of the flat plate and evacuated tube collectors are 45% and 60%, respectively. In this paper, a solar trigeneration system is used to simultaneously generate electricity, heat and fresh water required for a villa. In this system, a PVT collector is used as a power supply and, if necessary, a gas-fired boiler is used as a backup source. Considering the urgent need of fresh water in the southern cities of Iran as well as the access of this region to saline water, the performance of the proposed system in the hot and humid climate zone (Bushehr, Iran) is examined. Finally, using the life cycle cost method, the combisystem is also economically analyzed.

II. Solar trigeneration system

The proposed system is a solar trigeneration system to provide electricity, DHW, SH, and fresh water demands for a one-story house with an area of 100 m2 with 4 occupants. Figure 1 shows the schematic of the proposed solar trigeneration system, in which water first enters the PVT collectors (No. 1). Due to the absorption of thermal energy from the absorber plate of the collector, the

water temperature increases and after leaving the collector, it enters the flow diverter (No. 2). Since in this system, the priority is to supply DHW, the hot water out of the collector first goes to the DHW tank (No. 3). If there is no need to DHW, hot water enters the flow diverter (No. 5) and in case of demand for SH, hot water enters the SH tank (No. 6) and leads to preheating of the water going to the boiler (No. 7). It is heated by the boiler and enters the radiator (No. 8) which is used to heat the space. In this study, the boiler turns on only in the cold months of the year, and in the warm months when SH is not required, the boiler is off. In summer, when there is no demand for SH, the hot water enters the fresh water tank (No. 9) using a flow diverter (No. 5) and leads to the heating of the saline water (No. 11). The heated water enters the humidifier (No. 12), in which the water temperature decreases and the air temperature increases because of the spray of saline water in the air, which leads to transfer of heat from water to air. As the air temperature increases, its moisture absorption capacity increases. Hot and humid air enters the dehumidifier and in contact with the inlet water to the dehumidifier causes the water vapor carried by the air to condense and produce fresh water. After transferring energy, the hot water temperature decreases and enters the mixing valve (No. 13). Then, it enters the mixing valve (No. 15) through the pump (No. 14) and mixes with the cold water leaving the DHW tank and then returns to the collector. It should be noted that the electricity generated by the PVT collectors, in addition to supplying the electricity demand of the building, enters the reverse osmosis unit (No. 20) to produce fresh water.

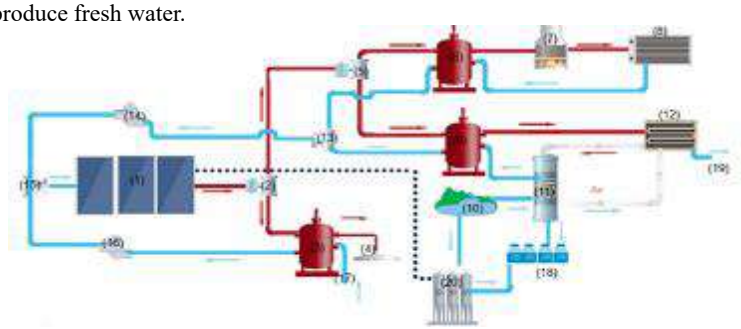

Fig. 1: Schematic of the proposed solar trigeneration system
(1: PVT collectors; 2,5: Flow diverter; 3: DHW tank; 4: DHW; 6: SH tank; 7: Auxiliary boiler; 8: Radiator; 9: Saline water tank; 10: Sea water; 11: Dehumidifier; 12: Humidifier;13,15: Mixing valve; 14,16: Pump; 17: Main water; 18: Fresh water; 19: Brine; 20: RO unit)

III. System modeling

The simulation of the solar trigeneration system is performed by TRNSYS software. Table 2 lists the TRNSYS types used in the simulation and their characteristics. It should be noted that Type 109 was used to read weather data from the Typical Meteorological Year (TMY) files and calculates the solar radiation in different directions. Psychometric properties such as dew point, relative humidity, etc. are calculated by Type 33. System controllers (Type 2b) were used to control the flow rate of the collectors and the storage tanks. For example, if the difference between the outlet and inlet temperature of the collector is less than 5℃, the collector loop pump will be turned off. Also, if the difference exceeds 10℃, the pump will turn on. Type 14b is used to simulate the daily DHW demand, which profile is obtained from Antoniadis and Martinopoulos, 2019.

Table 1. TRNSYS types for modeling the solar trigeneratioon system components

Component	TRNSYS typre
PVT collectors	50a
Pumps	3b
Storage tanks	4
Boiler	700
Radiator	689
Flow diverter	11

The main purpose of the system modeling is to determine the solar fraction in supplying the electrical and thermal loads required by the building. Solar fraction is the ratio of the energy supplied by the sun to the total energy required (Kalogirou, 2014):

$$SF = \frac{L - L_{Aux}}{L} \tag{1}$$

where L is the thermal energy required by the building and L_{Aux} is the thermal energy supplied by the auxiliary source.

Since there is no HDH desalination model in TRNSYS, the desalination system is modeled separately by MATLAB software and connected to the TRNSYS model. The details of the HDH modeling can be found in (Karami and Nasiri Gahraz, 2021 and 2022). In this study, the following relation is considered to calculate the amount of fresh water produced by the RO unit (Narayan et al., 2012):

$$\dot{m}_{DW,RO} = \frac{Electrical\ power\ (kWh)}{5} \tag{2}$$

where $\dot{m}_{w,RO}$ is the mass flow rate of fresh water produced by RO unit. The efficiency of the RO unit is considered 50%.

IV. Results and discussion

Figure 5 (a) shows the monthly variation of the DHW required and supplied energy by the thermal and electrical energy, as well as

the SF of DHW. In all months of the year, the amount of solar energy is more than the DHW required energy, and the use of electrical energy produced by the collector for DHW supply is due to the temperature decrease in the storage tank, as a result of the lack of solar radiation on cloudy days or nights. Figure 5 (b) shows the SH load of the building and the solar energy supplied using the PVT collector and auxiliary boiler. The SH load in January, February, and December is 7.94 MJ/m^2, 2.2 MJ/m^2, and 3.95 MJ/m^2, respectively. In February, the SH load is supplied by the electricity generated by the system. This is due to the need for heating at night and the lack of need during the day. In January, 0.5 MJ/m^2 of SH energy is supplied by the thermal energy supplied by the system.

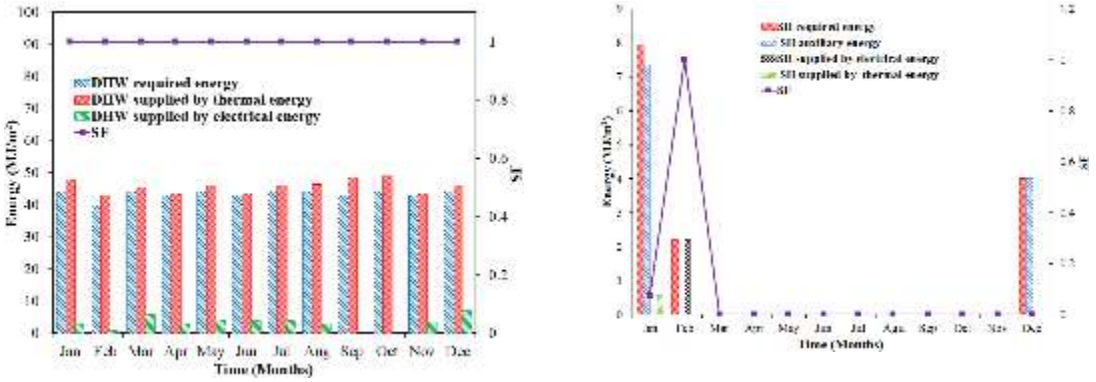

(a) (b)

Fig. 5. Monthly variation of (a) DHW and (b) SH required and supplied energy and SF

Figure 6(a) shows the electrical energy generation by the system and electrical load of the case study building. The results show that the highest and lowest electricity generations are respectively in October (632.9 kWh) and in December (503.44 kWh). As the air warms and the humidity increases, the incident radiation decreases and therefore the amount of electricity generation also decreases. Annually, 7261,600 kWh of electricity is generated by the trigeneration system. As shown, all the electrical building load is supplied. In addition, the surplus of generated electricity, about 10% is used to supply the electricity required by the system pumps, 4.2% to produce fresh water by reverse osmosis and 2.6% to supply DHW load. About 2,048.848 kWh of surplus electricity is sold to the electricity grid and is considered as the profit of the proposed system in economic analysis.

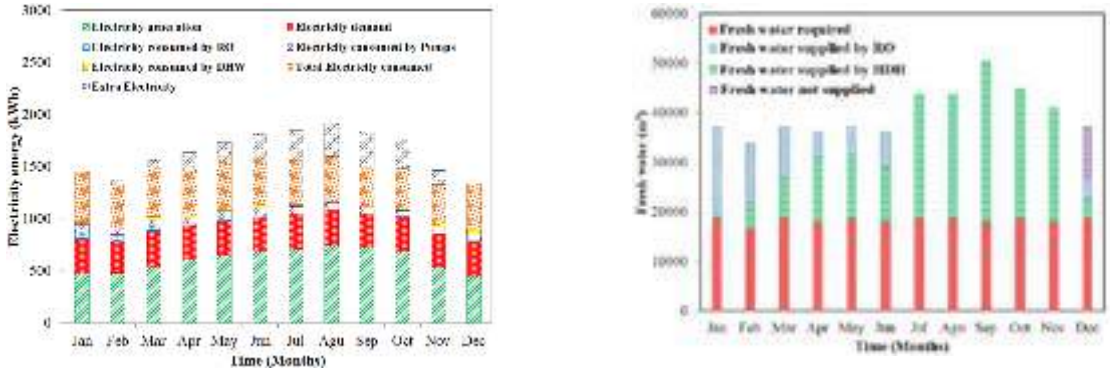

(a) (b)

Fig. 7: Monthly variation of (a) electricity and (b) fresh water generation and consumption

Figure 6 (b) shows the required fresh water and produced by the trigeneration system. As can be seen, in January only 6.5% of the required fresh water was supplied by the HDH unit and 93.5% by the RO unit, which consumed the electricity generated by the system. From February to July, 30% to 73% of the required fresh water is supplied by HDH, and 27% to 70% by RO. From July to November, all the required water is supplied by HDH. In December, 21.5% of fresh water is supplied by HDH and 21% by RO; therefore, 57.5% of the required fresh water must be purchased.

V. Conclusion

In this study, the solar trigeneration system including PVT collectors and HDH/RO desalination unit has been dynamically simulated using TRNSYS software. The following results have been obtained from the study of the performance of the proposed system in hot and humid climate zone (Bushehr):

- The annual electricity production of the system meets the electrical load of the building and also, 10% of it is used for electricity consumption of the system pumps, 4.2% is used for fresh water production by RO and 2.6% is used for DHW supply.
- Due to the use of thermal and electrical energy produced by the system to supply DHW, all this demand is met by the system.
- In the warm months, the fresh water demand is generated by the HDH unit using the thermal energy produced by the system, while in the cold months, the RO unit also should meet the fresh water demand. Only in December, the system did not meet the fresh water demand of the building and 57.5% of the demand had to be met by purchasing fresh water.

References

Antoniadis, C.N., Martinopoulos, G., 2019. Optimization of A Building Integrated Solar Thermal System with Seasonal Storage using TRNSYS. Renew. Energy 137: 56–66. https://doi.org/10.1016/j.renene.2018.03.074

Asim, M., Kumar, N.T.U., Martin, A.R., 2016. Feasibility Analysis of Solar Combi-system for Simultaneous Production of Pure Drinking Water via Membrane Distillation and Domestic Hot Water for Single-family Villa: Pilot Plant Setup in

Dubai. Desalin. Water Treat. 57 (46): 21674–21684. https://doi.org/10.1080/19443994.2015.1125806

Belessiotis, V., Kalogirou, S., Delyannis, E., 2016. Thermal Solar Desalination, Methods and Systems, Academic Press.

Calise, F., D'Accadia, M.D., MacAluso, A., Piacentino, A., Vanoli, L., 2016. Exergetic and Exergoeconomic Analysis of A Novel Hybrid Solar-geothermal Polygeneration System Producing Energy and Water. Energy Convers. Manag. 115: 200–220. https://doi.org/10.1016/j.enconman.2016.02.029

Hazami, M., Mehdaoui, F., Naili, N., Noro, M., Lazzarin, R., Guizani, A.A., 2017. Energetic, Exergetic and Economic Analysis of an Innovative Solar CombiSystem (SCS) Producing Thermal and Electric Energies: Application in Residential and Tertiary Households. Energy Convers. Manag. 140: 36–50. https://doi.org/10.1016/j.enconman.2017.02.040

Kalogirou. S.A., 2014. Solar Energy Engineering: Processes and Systems, 2014. Second Edition, Elsevier Inc.

Karami, M, Nasiri Gahraz, S.S., 2021. Transient simulation and life cycle cost analysis of a solar polygeneration system using photovoltaic-thermal collectors and hybrid desalination unit. Int. J. Heat and Mass Transfer Research 8 (2), 243-256. https://doi.org/10.22075/JHMTR.2021.23429.1343

Karami, M, Nasiri Gahraz, S.S., 2022. Improving thermal performance of a solar thermal/desalination combisystem using nano fluid-based direct absorption solar collector. Transactions on Mechanical Engineering (B) 29 (3), 1288-130. https://doi.org/10.24200/SCI.2021.58321.5666

Karami, M., Javanmardi, F., 2020. Performance Assessment of a Solar Thermal Combisystem in Different Climate Zones. Asian J. of Civil Eng. 21: 751–762. https://doi.org/10.1007/s42107-020-00236-0

Katsaprakakis, D. A., Zidianakis, G., 2019. Optimized Dimensioning and Operation Automation for a Solar-Combi System for Indoor Space Heating. A Case Study for a School Building in Crete. Energies, 12 (1). https://doi.org/10.3390/en12010177

Karami, M., Akbari, K., Jalalizadeh, M. 2022. Monte Carlo Optimization of a Solar Combisystem Using Photovoltaic-Thermal Systems in Hot and Dry Climatic Condition. Journal of Heat and Mass Transfer Research 9: 233 – 244. https://doi.org/10.22075/JHMTR.2023.28432.1394

Kumar, N.T.U., Martin, A., 2017. Techno-economic Optimization of Solar Thermal Integrated Membrane Distillation for Cogeneration of Heat and Pure Water. Desalin. Water Treat. 98: 16–30.

Kumar, N.T.U., Martin, A.R., 2017. Co-production Performance Evaluation of a Novel Solar Combi system for Simultaneous Pure Water and Hot Water Supply in Urban Households of UAE. Energies 10 (4):481. https://doi.org/10.3390/en10040481

Mehdaoui, F., Hazami, M., Noro, M., Lazzarin, R., Farhat, A., Guizeni, A.A., 2016. Performance Study of a Solar Combisystem for Tunisian Houses with TRNSYS Simulation, 2016 7th International Renewable Energy Congress (IREC), Hammamet, Tunisia: 1-6. https://doi.org/10.1109/IREC.2016.7478951

Narayan, G.P., McGovern, R.K., Zubair, SM, Lienhard, J.H., 2012. High-Temperature-Steam-Driven, Varied-Pressure, Humidification-Dehumidification System Coupled with Reverse Osmosis for Energy-Efficient Seawater Desalination, Energy 37 (1): 482–493. https://doi.org/10.1016/j.energy.2011.11.007

Zamen, M., Rezakhani, N., Rajabi, M., Zeinali, M., 2014. Performance evaluation of combined solar water heater/desalination system. Iranian Journal of Chemistry and Chemical Engineering (IJCCE) 34 (3): 91-102. (In Persian).

IEEES-009

Acetate Cellulose Modified Nanofiltration Membrane Efficiency and Performance

[1]*ABURIDEH Hanane , [1]ZIOUI Djamila , [1] TIGRINE Zahia, [1] HOUT Sarra, [1] BELGROUN Zoubir, [1]ABBAS Mohamed*
[1]Solar Equipment Development Unit, UDES/Renewable Energies Development Center,
CDER, 42004, Tipaza, Algeria
*E-mails : h_aburideh@yahoo.fr

Abstract

This work focuses on the performance study of cellulose acetate-polysulfone (CA- PSf) membrane in the presence of polyethylene glycol additive PEG, at different concentrations, using thermal annealing on the surface of the membrane. The membrane was prepared by the phase inversion process; its films obtained were subjected to thermal annealing at 90° C. for 15 minutes. The influence of the composition of the polymer blend, the concentration of the additive and the effect of annealing on the membrane performancewere studied. The membranes were characterized in terms of contact angle and mechanical strength, as well as a molecular weight cut-off threshold. The efficiency of the membranes was evaluated in terms of flux, retention of di-monovalent salts and fouling phenomenon. The molecular weight cut-off values were ranging between 300-600 Dalton for all treated membranes. This suggest that the thermal annealing treatment resulted in nanofiltration NF membranes; The membrane pores radius determination was carried out to confirm the nanometric character of these membranes. The incorporation of PEG within the mixture increases the hydrophilic character and improves the flow rate by going from a value of 14.3 L/m2h to 87.2 L/m2h by introducing 25% in PSf and 12% in PEG in the cellulose acetate membrane. The rejection of divalent ions indicates that the membrane with better flow, MC (PSf/PEG/AC): (25/12/63) showed satisfactory retention which is in agreement with the standards required by the WHO with the exception ofmonovalent salts which has a maximumrate elimination of 27%. An excellent antifouling capacity was achieved with values of the flux recovery rate of 94% confirming that the anti-clogging character of CA was well preserved despite the incorporation of PSf.

Keywords: Cellulose acetate, Heat treatment, Nanofiltration, PEG, Pore diameter,Eliminationof mono-divalent ions.

I. Introduction

Water makes up the majority of living tissue and is a basic requirement of life.Today, the depletion of fresh water resources in the world has created a difficult situation for man and ecosystems. As such, water crisis is a growing concern in many developing countries due to globalization and industrialization. Although 70% of the earth is covered with water,various government organizations report that approximately 1.2 billion people will not have access to fresh water and that 70% of the world's population will live in water-stressed countries by 2050 (Subramanian and al,2013). Some of the alternative sources that have been studied to address the scarcity of fresh water are the treatment of brackish water, sewage and seawater (Turhan and al 2012). One of the main challenges in sustaining society is ensuring adequate water resources of the quality required for many designated uses. To meet this challenge, many studies have been carried out for the purification of wastewater and the preservation of freshwater sources. Many techniques have been demonstrated to remove pollutants from wastewater including adsorption, chemical precipitation, ion exchange, conventional coagulation, electrodialysis, electrolysis and Reverse osmosis(Buruga and al, 2019). Among these techniques, the membrane separation technique should play an essential and leading role in arriving at definitive and reliable solutions. Membrane technology is emerging as a viable method for molecular separation offering many advantages over conventional methods(Aburideh and al, 2021). It consumes less energy, creates less space and can be used in amuch simplerway. It consumes up to a tenth of the energy currently used for conventional distillation (Marchetti and al, 2014). Its application has been extended to a wide range of fields including medicine, chemistry, chemical technology and engineering. Membrane technology has received particular attention for wastewater treatment, as micro/ultra/filtration can reject particles, colloids and macromolecules and aid in disinfection. After the significant commercial success of reverse osmosis (RO) and ultrafiltration (UF), membranes with separation characteristics between these two technologies are expected to be a promising market. Such membranes are callednanofiltration (NF) membranes. It is an essential technique in the industriesfood, chemical and pharmaceutical(Lakhotia and al 2018). Typically, NF membranes involve the separation of salts (monovalent and divalent) and/or organic solutes. The NF technique is one of the filtration techniques widely used, especially in desalination and in many industrial applications for the production of clean and safe water. NF is becoming a viable alternative to conventional water treatment technologies because it can operate at lower pressures, provide high flow, and be more energy efficient than RO systems. It has been shown that twice the permeate flow rate can be achieved with NF compared to RO and by thereplacement of RO by NF membranes about 20% electrical energy can be saved (Subramanian and al,2013). Although NF membranes have undergone several improvements, there are still challenges for their development, such as the trade-off relationship between permeability and selectivity, fouling and scaling are the main constraints of NF membranes today. In recent years, several types of work have been carried out to improve the membrane performance (Mansourpanah and al, 2011). Improving the flux and efficiency of membrane separation has been the subject of these investigations . Usually, the scheme that increases water flux decreases membrane selectivity and vice versa (Aburideh and al, 2021). Therefore, it is more advantageous to use such kind of process which can simultaneously increase flux efficiency and membrane separation(Homayoonfal and al, 2014). It is essential to produce membranes with sufficiently high flux and rejection, but it isat least as important to identify a simple and environmentally friendly manufacturing process.

Membrane annealing can be introduced as a beneficial and synergistic effect helping to improve the densification and compactness of the membrane skin layer.This modification process can help to provide a new approach for designing an NF membrane with good chemical stability and more preferable separation performance in large-scale applications(Jyothiand al,2017). n this perspective, the objective of the present work is to use thermal annealing to modify the morphology of the membrane by combining

two polymers with different physico-chemical properties. The latter have advantages and disadvantages which allows to take advantage of the strengths of each polymer and compensate for the disadvantage of one by the other. The membranes were prepared by the inversion phase method. This method consists of preparing filtration membranes from collodion solutions. These are made up of; polymers of cellulose acetate (CA) and polysulfone (PSF),using N,N-dimethylformamide (DMF) as solvent and Polyethylene glycol (PEG) as additive.The prepared membranes were characterized by several techniques, namely, mechanical strength, contact angle measurements and the MWCO cut-off threshold. Filtration tests were carried out on samples of synthetic waters of monovalent and divalent salts. Other parameters have been taken into consideration such as fouling which has an impact on th emembrane life and its performance.

II. Experimental

II.1. Polymer blend preparation

The membranes were prepared by the NIPS (nonsolventinduced phase separation) phase inversion method. The polymer blend solutions (17.5% byweight) were prepared by mixing polysulfonePSf withcellulose acetate CA with different compositions inDMF for 4 h at 90 °C, and in the presence of PEG asadditive, with constant stirring of 500 rpm (Aburideh and al, 2019). A homogeneous solution was obtained and then leftwithout stirring for 30 minutes to remove air bubbles.The homogeneous casting solutions were spread on aglass plate, using a casting knife with a thickness of250 µm. After evaporation for 30 seconds, the filmswere immersed in a coagulation bath at 4 °C, annealed in an oven at 75 °C for 30 seconds.30,44 Allthe membranes were stored in distilled water. The casting compositions of the membranes areshown in Table 2 and the structure of the mixturecomponents is illustrated in Figure 1. The castingsolution became cloudy and the mixture was nothomogeneous at a polysulfone concentration of 30%,which allowed concluding that the optimalcomposition of PSf is 25%.

II.2.Study of the wettability of the membrane Contact angle/Water absorption

The membranes wettability Studies were carried out taking into account parameters such as the contact angle and water absorption. They make it possible to identify the hydrophilic character, the roughness and the porosity of the surface. The measurement of the contact angle of water is the method which permits to specifically evaluate the hydrophobic/hydrophilic nature of the surface of a membrane. Usually the smaller the contact angleis, the more hydrophilic the membraneis. Cellulose acetate are respectively 88° and 59°, which confirms the hydrophobic and hydrophilic character of these two respective membranes (Pendergast, 2011).
fig.1 show that the contact angle depends on the incorporation of PEG and the concentration of polymer in the mixture. The lowest value is obtained for the MC membrane with 12% by weight of PEG. It is 60°, one degree less, the MA membrane also has a value close to that of pure acetate. On the other hand, the incorporation of 15% in PEG increased the contact angle to 69°, this is probably due to the delayed demixing during the coagulation of the membrane, thus causing the modification of the process of the phase separation reaction. . This confirms the roughness of its surface obtained by SEM. The highest value of the contact angle (74°) within the mixture is obtained for the MH membrane with 10% by weight of PSF and in the absence of PEG. We can conclude that for mixtures composed of PEG ≤ 12 and a highest ratio of PSf / PEG, the membranes have interesting contact angle values. Increasing the amount of PEG in the mixture preserves the hydrophilic character of the membrane because the CH2-OH groups present in the structure of the PEG, on the surface of the membrane, interact with water via Van der Waals forces and hydrogen bonds, so that the aspect of wettability increases (Aljumaily,2018).

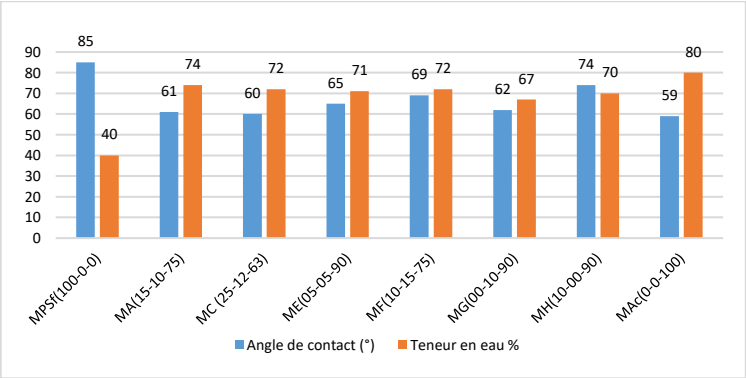

Fig.1 Variation of contact angle and water absorption of membranes

II.3. MWCO membrane cut-off threshold

The relationship between the PEG retention rate and the different PEG molecular weights is presented in fig.2 for all the PSf/AC membranes and at a pressure of 20 bar. The MWCO of the membranes was determined by interpolation of the values obtained for a rejection rate of 90% and are listed in Table 3.1. It is observed that the separation of the solute increases with the increase in the molecular weight of the solutes, a rejection is detected at around 83% of PEG 400 for the MC membrane. It varies from 85% and 88% respectively for the MA and MG membranes and exceeds 90% for the MAc membrane. The determination of the MCWO cut-off threshold for this range of membranes is located in an interval of 300-600 Da in PEG. The largest value is detected for the MC membrane at 579.12 Da and the smallest corresponds to the pure cellulose acetate membrane MAC at 308.03 Da. The elimination of PEG was almost total for all the membranes for a PEG solution equal to 1000 Da.
From these results and according to the literature, we can therefore conclude that the pores of the membrane are of nanometric size, which is in the range of NF membranes (Ganesh and al , 2012). It is clearly demonstrated that the membranes which contain the

PSf have a higher MWCO compared to the membrane without PSf, and that the membranes PSf/AC which contains the PEG as additive present a higher MWCO compared to those without additive.

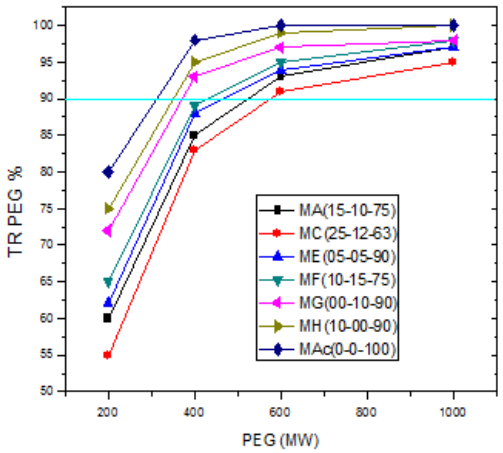

Fig.2 Rejection rate TR vs molecular weight of PEG for all membranes

Table.1. MWCO and pore diameter of each membrane.

Membrane	**MA**	**MC**	**ME**	**MF**	**MG**	**MH**	**MAc**
% **(PSf/PEG/AC)**	15-10-75	25-12-63	5-5-90	10-15-75	0-10-90	10-0-90	0-0-100
MWCO	528.33	579.12	380.22	471.02	370.32	352.5	308.03
µp(nm) **(TR=50%)**	0.54	0.57	0.36	0.41	0.45	0.30	0.16

II.4. Determination of the membranes pore radius

The solutes separation curves according to their diameter for the PSf/AC membranes with additives of different molecular weights are presented in fig.3. The regression curve was drawn with a high correlation coefficient (r^2 0.98). The Stokes diameter "ds" can be determined using Eq. (2 and1). The average pore size of the µp membranes corresponds to the value of the pore diameter obtained with a maximum of distribution and a rejection of 50%; it varies from 0.16 to 0.57, which is in the range of NF nanopores.

$$ds = 2a \quad (1)$$

$$\text{and} \quad a = 0.01673 \times M^{0.557} \quad (2)$$

Where a (nm) is the diameter of the solute and M is the molecular weight of PEG (Da).

MWCO serves as a guide for membrane pore sizes as MWCO increases, it implies a large membrane pore size (Singh and al , 1998). The largest membrane pore size is obtained for the MC membrane having a rate of 12% in PEG and 25% in PSf. It is equal to 0.57 nm followed by the MA membrane for a µp= 0.54 nm (see table 3.1). Then it decreases to reach lower values for ME and MH membranes around 0.3 nm. The pore size of MAc membranes is very small, close to 0.16 nm. These observations are in good agreement with the densification of the surface layer observed on the SEM micrographs. We also find that the average pore size of the MF membrane consisting of 15% PEG is lower than that of the MC membrane, thus confirming that the delayed demixing affected the number and size of the pores.These results also reveal that the membrane pore size depends on the PSf/PEG ratio in the mixture. This ratio plays a significant role in the formation of pores on the membrane surface. Nevertheless, the PEG alone in the mixture increases the pore size, on the other hand the presence of PSf alone in the mixture does not affect the pore size of the cellulose acetate membrane. In summary, the incorporation of PEG as well as PSF gave interesting results from the point of view of pore size and MWCO in order to improve the flux of the pure membrane in AC because the pore size increased from 0.16 to 0.57nm. We can still conclude that thermal annealing makes it possible to obtain pores of the nanometric order for PSf/AC membranes in the presence of DMF as solvent and PEG as additive.

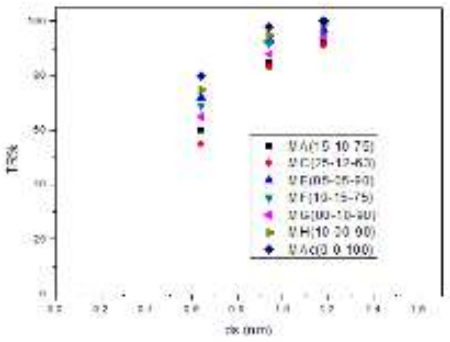

Fig .3 PEG retention rate as a function of Stokes diameter

II.5. Membrane Performance

II.5.1.Study of the thermal annealing effect

To better illustrate the effect of thermal annealing on membrane performance; we deemed it useful to make a quantitative comparison via table 3.3 which groups the values of different parameters of the two membranes MC and MC' of the same mixture composition (PSF/PEG/AC): (25/12/63) and which differs by thermal annealing. The membrane labeled MC is the membrane which underwent thermal annealing at 90°C for 15 min (Aburideh and al, 2019). During this comparison, a clear difference was observed for the studied parameters. We find that the size of the pores and its distribution decreased sharply after treatment, a significant change in MWCO occurs after treatment; it goes from 35KDa to 579.12 Da from the MC' membrane to the MC membrane. It is the same for the pore distribution, the pore size is almost 16 times smaller for the MC membrane. It is equal to 0.45 nm while that of the MC' membrane is 7.16 nm.

Table 2. Values of different parameters for the MC and MC' membrane

	MCWO (Da)	**µp (nm)**	**PWF Pure water flux (L/m^2 h à 20 bar)**	**Lp permeability (L/m^2 h bar)**	**Contact Angle (°)**	**Water uptake (%)**
MC	579.12	0,45	87.2	4.003	60±1	75
MC'	35000	7,16	6553.19	302.12	61±2	80

About the water permeability and pure water flux, it is obvious that the MC' membrane has a very high flux and water permeance since it is classified as a UF membrane. They are around 6553.6 L/m2 h and 302.12 L/m2 h bar at 20 bar, whereas with thermal annealing they have dropped to 87.2 L/m2 h and 4 L/m2 h bar at 20 bar. Their contact angles are almost identical while the percentage of water content is better for the MC' membrane because it has larger pores and therefore better absorbance. These results clearly indicate that the thermal annealing induces the packing of the polymer chain and the reduction of the free volume [31-34]. Therefore, the thermal annealing process is an efficient method to adapt the pore size from ultrafiltration (MWCO) to nanofiltration (MWCO between 200 and 1500 Da and a pore size between 0.2 and 2.0 nm). In summary, these results prove that thermal annealing is a powerful tool to regulate the state of polymer aggregates and the pore structure of membranes. The obtained pore sizes are suitable for the range of dense membranes, reverse osmosis membranes, nanofiltration membranes (Zhou and al , 2018). This treatment constitutes a simple and effective strategy for converting the ultrafiltration membrane to a nanofiltration one based on hydrophilic copolymers and additive polymers.

II.6.Study of MgSO4 and CaCO3 and NaCl salts retention

Water hardness is related toits dissolved minerals concentrationrate , more particularly of calcium (Ca^{2+}) and magnesium (Mg^{2+}) ions. The higher the concentration of these minerals is, the harder the wateris. Hard water has consequences on health because it brings a greater quantity of mineral salts to the body,it can cause certain cardiovascular diseases. The presence of limestone is also responsible for the deterioration of certain installations present in homes (piping, household appliances, water heaters, etc.). These calcium (Ca^{2+}) and magnesium (Mg^{2+}) ions are mainly present in the different types of 'water. Among other things, the great particularity of seawater is that the relative proportions of its constituents are substantially constant (ie independent of salinity). Dittmar's law thus makes it possible to determine the salinity of seawater by a single measurement: the concentration of one of these constituents (for example, Cl^-) or one of the physical properties of seawater at a given temperature such as relative density, refractive index or conductivity (Zhou and al , 2018). Based on these data, and in this context, we have considered in this part, the retention study of a single monovalent salt NaCl and the divalent salts Mg^{2+} and Ca^{2+}. To this end, synthetic solutions of salts consisting of 300 mg/l of $CaCO_3$, 200 mg/l $MgSO_4$ and 13.6 g/l of NaCl prepared in distilled water were used to study the ability of the membranes tested to eliminate them.

II.6.1.Study of the permeability to pure water PEP of salts

Fig.4 represents the permeability of pure water before and after each salt filtration test, the membranes are abundantly rinsed then a water permeability test is carried out at a pressure of 20 bars in order to check the state of the membrane. We observe that a decrease in the permeability to pure water PWF of the order of 2° after filtration of the NaCl solutions, regardless of the membrane used.

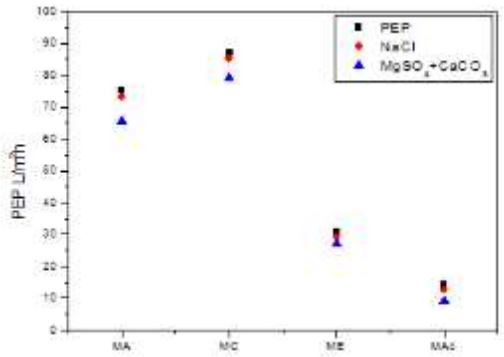

Fig.4. Evolution of the water permeability of the different membranes

after $MgSO_4$, $CaCO_3$ and NaCl salts filtration .Contrary to the case ofthe NaCl solutions, this quantity indicates a greater decrease for the filtration of the solution containing $MgSO_4$ and $CaCO_3$ for all the membranes, it is greater in the case of the MAc membrane, it drops by 14.3 L/m2h at 9.15 L/m2h. This is explained by the accumulation of limestone on the surface of the membrane which affects the permeation at a pressure equal to 20 bars which is considered low for this membrane.

II.6.2. Salt rejection rate

According to frig 5, which includes the dosage and the different salt concentrations, we note that for Magnesium (Mg^{++}), a strong elimination was observed for all the membranes, it goes from 70 to 98%. The hydrated radius of Mg^{2+} is larger than that of Ca^{++} (Table 3), so the membrane exhibits greater rejection of Mg^{2+}. For calcium, the rejection rate is estimated between 63% to 35%. We find that the rejection of divalent ions illustrated in table 3 respects the standards for fresh water according to the WHO. The low retention of the MAc membrane is probably due to the compaction effect which caused an increase in flux and a decrease in retention, since this membrane consists solely of cellulose acetate which is very sensitive to compaction (Ismail, 2020). These results are consistent with that of pure water flow. In addition, this phenomenon is accentuated in the absence of PEG because the pores do not form (Gohil and al, 2009). Among other things, the retention of the NaCl salt reaches the maximum peak of 50% for the MAc membrane and the minimum for the MC membrane. It is the lowest compared to that of the divalent salts $MgSO_4$ and $CaCO_3$. This reduction is justified by the increase in the level of PEG within the mixture; this is the sieving of the sizes pores of the membranes formed; that is, the larger the pore sizeis, On the other hand, the smaller the pore size, the greater the rejection of ions. We find that the highest retention rate is obtained for the membrane characterized by a low filtration flux. These two parameters vary inversely. This supports the previous results.

Table 3. WHO salt standards for fresh water [38].

Ions	**Mg^{2+}(mg/L)**	**Ca^{2+}(mg/L)**	**NaCl (g/L)**
Norme OMS	<50	<270	< 1

Due to the higher charge density of sulfate ions (SO_4^{2-}) compared to chloride ions (Cl_2), the rejection of sulfate salts is greater than that of chloride salts (Xu, 2019). The removal rate of NaCl and $MgSO_4$ is 27% and 98% respectively, i.e. there is a difference of 71% or a 3.62 times greater rejection ratio for the rejection of $MgSO_4$ compared to that of NaCl. The preferential rejection of sulfate salts over chlorides is evident because the bivalents are retained more than the monovalents. Indeed, such membranes will be useful for the elimination of water hardness as well as for the partial desalination of brackish water. These results affirm that the retention of monovalent salts is limited by the nanofiltration process (Cihanoğlu and al, 2018).

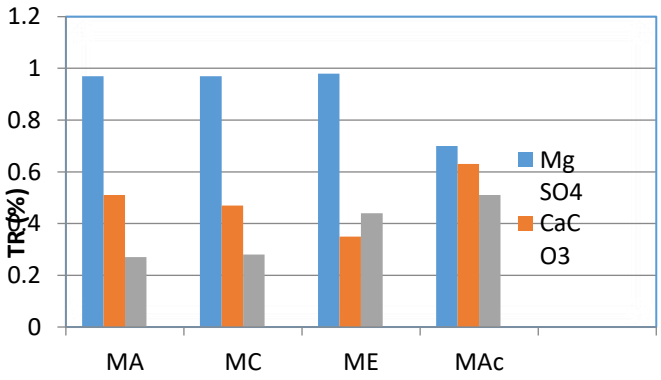

Fig.5 Salt retention rates for the different membranes.

In summary, the study ofsalts elimination for MA, MC, ME, Macmembranes , allowed us to say that in terms of selectivity; MC and MA membranes showed more or less similar results with maximum retention efficiency of Mg^{2+} and Ca^{2+} salts. Regarding the NaCl salt, the best retention rate is obtained for the MAc membrane but it remains insufficient to meet the salinity standards required by the WHO. In conclusion, the salt rejection rate for the studied membranes follows the following sequence: MgSO4>CaCO3>NaCl. The membranes MA (PSF/PEG/AC):(10/15/75) and MC (PSF/PEG/AC):(25/12/63), can be considered as the most reliable and the most effective for the elimination of divalent salts from a flux point of view. They present the optimal parameters; but it is the MC membrane which prevails for a flow of 87.2 l/h.m2 at 20 bars, retention rates of Mg^{2+} and Ca^{2+} salts of 98% and 35%, which is in line with WHO standards.

II.7. Anti-fouling membranesproperties

The permeation flux of the BSA solution is shown in Fig.6. It decreases rapidly compared to the flow of pure water in the first 30 minutes due to the fouling of proteins for the three membranes and the phenomenon of the concentration polarization of these membranes. However, it was explicit that the water flux from all membranes retained a slight decrease from the initial water flux. Therefore, the decrease in water flow was mainly a result of the ASB fouling.

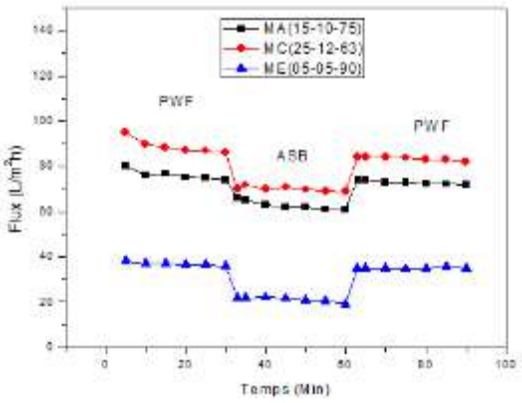

Fig.6 Flux of pure water and ASB as a function of time

for MA, MC and ME membranesMembrane fouling behavior was tested using bovine serum albumin (BSA) as a model(Kevin and al, 1993) [40]. The concentration of the SBA solution was set at 1.0 g/L. First, the pure water flux (JW) of the clean membrane was measured with deionized water at 20 bar for 30 min. Then, the flux of the SBA solution (JP) crossing the membrane for 30 h was measured. The fouled membrane was washed with deionized water under static conditions for 15 min and the pure water flux (JR) of the washed membrane was remeasured. The filtration and washing cycle was repeated 3 times. The recovery rates of flux (TRF), total fouling (Rt), reversible fouling (Rr) and irreversible fouling (Rir) have been shown in Fig.6.

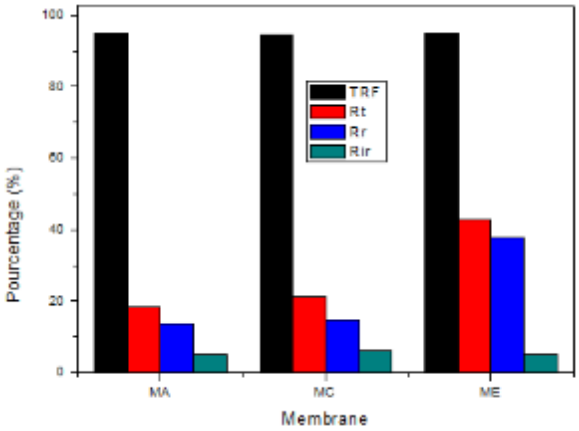

Fig.7 TRF water flux recovery rate and fouling resistance of MA, MC and ME membranes

Taking into account the level of cellulose acetate in the different MA MC and ME hybrid membranes, in particular the values of the contact angle and the hydrophilic nature; high values of 94% in TRF were obtained. This is explained by the fact that the surface layer of the PEG/AC membrane formed is hydrated by the adsorption of water molecules due to the hydroxyl groups present on the surface of the membrane. Therefore, the presence of PEG makes it difficult for fouling to adhere to the surface of the membrane (Jeon and al,1991) and explains this high TRF for the three membranes. In addition ; Since the interactions between PEGs and proteins are weak, very little adsorption of these on membrane films is observed (Zhang and al, 2021).
The reversible adsorption for membrane fouling, caused by proteins, is 13.5%, 14.8% and 37.8% for MA (15-10-75) MC 25-12-63) and ME membranes respectively. (05-05-90), it is more accentuated for the membrane rich in acetate and presenting a low level of PEG. This can be explained by a deposition of the material on the surface of the membrane due to its low permeability which correlates with a narrower pore diameter. This clogging problem could be eliminated by simple washing with water or backwashing. Nevertheless, a relatively low irreversible fouling Rirwas obtained for the three membranes at a pressure of 20 bars. The highest value of 6.27% is obtained for the membrane with the highest level of PSf. The latter contributes to the formation of

larger aggregative pores and has a hydrophobic character, it can be responsible at the base for the violent adsorption of protein molecules on the surface of the membrane or for the impaction of protein molecules in the membranes. As expected, the PEG groups present on the surface of the membranes help to fight against irreversible clogging by hydrophilizing the surfaces, especially since basically the membrane is itself hydrophilic (Aburideh and al, 2023).

IV. Conclusion

Several objectives have been targeted through this thesis work. The first being to prepare new, more efficient membrane materials with new or improved properties by combining two polymers which have different physico-chemical properties. The work consisted of combining polysulfone (PSf) and cellulose acetate (CA) to take advantage of the strengths of each polymer and to compensate for the disadvantage of one by the other. The second is the conversion of a UF ultrafiltration membrane to a NF nanofiltration membrane, using a new approach in the membrane design method. The last objective being to use such a type of process to produce membranes with a flux and a sufficiently high rejection. Most of the study involved validating the performance of nanofiltration membranes in terms of flux and rejection rate while simultaneously preserving the best flux, optimizing membrane selectivity and improving membrane lifetime.

The preparation of the membranes was based on two successive steps which are the elaboration of the PSf/AC organic polymer membranes using the phase inversion technique induced by coagulation in a NIPS water bath followed by heat treatment in an oven for 15 min at 90°C. PEG polyethylene glycol was used as an additive and DMF as a solvent. It has been shown that the parameters for developing the membranes such as the thermal annealing treatment , the PEG level, the PSf/PEG ratio in the casting solution, have considerably influenced their structure and consequently the efficiency and performance of the membranes. The essential results can be summarized as follows:

The membrane wettability studies were carried out taking into account parameters such as contact angle and water absorption, for mixtures composed of PEG ≤ 12 and the highest PSf/PEG ratio. The membranes present interesting contact angle values. Increasing the amount of PEG in the mixture increases the hydrophilic character of the membrane because the CH2-OH groups present in the PEG structure, on the surface of the membrane, interact with water via Van der Waals forces and hydrogen bonds, so the wettability aspect increases.

It has been shown that it is possible to control the enlargement or tightening of pore size while using heat treatment. In fact, NF membranes with MWCO in the range of 300-600 Da by tightening the pores of UF membranes with MWCO 35KDa could be fabricated. We can still conclude that the thermal annealing allows to obtain pores of the nanometric order for all the membranes.

The performance of the elaborated membranes was estimated in terms of flux and rejection rate. These two aspects require a good understanding of a membrane module at the laboratory scale. Thus, the preliminary laboratory tests carried out have shown a significant increase in flux and permeability. They go from 14.3 L/m2h and 0.74 L/m2 h bar for the pure acetate MAc membrane to 87.2 L/m2h and 4.003 L/m2hbar for the MC membrane: (PSF/PEG/AC), (25-12-63) or it is 6 times larger. The PEP of the membranes increases by incorporating the PEG within the mixture.The hydrophilic character of the PEG additive favors the formation of pores for less than 12%. The incorporation of additives in the solution increases the penetration rate of the water in the membrane. The water flux of the modified membranes is greater than that of the unmodified membranes regardless of the PEG levelin the mixture due to the improvement in the hydrophilicity of the membranes. The qualitative results concerning the rejection of salts studied for theMA, MC, ME membranes, revealed that the best retention rate of NaCl salt is obtained for the MAc membrane and remains insufficient to satisfy the standards of salinity, concerning the rejection of salts divalent Mg2+ and Ca2+. The MC membrane (PSF/PEG/AC), (25/12/63), can be considered the most reliable and efficient. It presents the optimal parameters; a flow of 87.2 l/h.m2 at 20 bars, retention rates for Mg2+ and Ca2+ salts of 98% and 35%, which is in line with WHO standards.

Surface hydrophilicity is a sought-after property for membranes because it makes it possible to increase the flow of aqueous solutions and to obtain materials resistant to clogging. In this context, we carried out a study using a clogging protein “bovine serum albumin (BSA)” with the most competent membranes MA, MC and ME. The values of the flux recovery rate of 94% confirm that the objective of achieving excellent antifouling capacity has been achieved despite the incorporation of PSf, the anti-clogging character of CA has been well preserved.

References

Aburideh, H., Kasbadji, N., Naceur, M.W. Tigrine, Z., Tassalit D and ABBAS, M.,2019. Thermal annealing effect on morphology and performance of polysulfone-cellulose acetate membranes: application for water defluoridation, Cellulose Chem. Technol. 53, 583-597 DOI: https://doi.org/10.35812/CelluloseChemTechnol.2019.53.58.

Aburideh,H., Tigrine,Z., Aoudjit, l., Belgroun, Z., Redjimi, K., and Tassalit, T., 2021. Development of acid modified cellulose acetate membranes for salt water treatment cellulose chemistry and technology 55, 9,. DOI: https://doi.org/10.35812/CelluloseChemTechnol.2021.55.99

Aburideh, H., Tigrine, Z., Tassalit, D., Zioui, D., Hout ,S., and Abbas, M., 2021. Wastewater treatment using a modified cellulose acetate membrane, cellulose chemistry and technology , 56,5. DOI:10.35812/Cellulose ChemTechnol .2021.55.59

Aburideh, H., Tigrine, Z., Tassalit, D., Zioui, D., Hout ,S., and Abbas, M., 2023. Performance Of Carboxymethyl Cellulose/Polysulphone Membranes Prepared Via Different Immersion Methods For Salt Rich Waters, Cellulose Chem. Technol. 57, 7, 911-921.

Aljumaily M., Alsaadi Hashim N.A., Alsalhy Q.F., Das R., Mjalli F.S. 2019. Embedded high-hydrophobic CNMs prepared by CVD technique with PVDF-co-HFP membrane for application in water desalination by DCMD, Desalination and Water Treatment, 142, 37–48.

Buruga, K., Song, H., Jin, S., Bolan, N., Jagannathan, T.K., Kim, K.-H.,2019. A review on functionnal polymer-clay based nanocomposite membranes for treatment of water”, Journal of Hazardous Materials, https://doi.org/10.1016/j.jhazmat. 2019.04. 067.

Cihanoğlu, A. , Altınkaya, A. S., 2018. A facile approach for preparation of positively charged nanofiltration membranes by in-situ crosslinking between polyamide-imide and polyethy-lenimine”, Separation and Purification Technology. 207, 353-362, doi: https://doi.org/ 10.1016/ j.seppur.2018.06.020

Ganesh, B.M., Isloor, A. M., Padaki, M., 2012. Preparation and characterization of polysulfone and modified poly isobutylene-alt-maleic anhydride blend NF membrane, Desalination. 287, 103–108. DOI:10.1016/j.desal.2011.09.047.

Gohil, J.M., Ray, P., 2009. Polyvinyl alcohol as the barrier layer in thin film composite nanofil -tration membranes: Preparation, characterization, and performance evaluation", Journal of Colloid and Interface Science. 338,121–127. https://doi.org/10.1016/j.jcis.2009.06.020.

Homayoonfal, M., Mehrnia, M.R., Niassar, S-M., Akbari, A., Ismail, A.F., Matsuura, T., 2014. A comparison between blending and surface deposition methods for the preparation of iron oxide/polysulfone nanocomposite membranes", Desalination. 354 (2014), 125-142. DOI:10.1016/j.desal.2014.09.031.

Ismail N. H.2020. Hydrophilic polymer-based membrane for oily wastewater treatment: A review. Sep. Purif. Technol., 233, 116007. DOI: 10.1016/j.seppur.2019.116007.

Jeon, S. I., Lee , J.H ., Andrade, J.D., Gennes, P.G., 1991. Protein-Surface Interactions in the Presence of Polyethy lene Oxide. II. Effect of Protein Size", Journal of Colloid and lnterface Science.142, 1, 149-158. https://doi.org/10.1016/0021-9797(91)90043-8

Jyothi, M.S., Soontarapa, K., Padaki, M., Balakrishna, R. G., Isloor, A. M., 2017. Favora-ble influence of mPIAM on PSf blend membranes for ion rejection, Journal of Membrane Science. 533, 229–240. http://dx.doi.org/10.1016/j.memsc i.2017 .03.039.

Kevin L. Prime and George M. Whitesides, 1993. Adsorption of Proteins onto Surfaces Containing End-Attached Oligo(ethylene oxide): A Model System Using Self-Assembled Monolayers", J. Am. Chem. Soc. 115, 23, 10714–10721. https://doi.org/10.1021/ja00076a032

Lakhotia, S. R., Mukhopadhyay, M., Kumari, P., 2018. Iron oxide (FeO) nanoparticles embedded thin-film nanocomposite nanofiltration (NF) membrane for water treatment", Separation and Purification Technology, (2018), https://doi.org/10.1016/ j.seppur. 2018. 09. 034.

Mansourpanah, Y., Madaeni, S.S., Rahimpour, A., Adeli, M.,Hashemi, M.Y., Moradian, M.R.,2011. Fabrication new PES-based mixed matrix nanocomposite membranes using polycaprolactone modified carbon nanotubes as the additive: property changes and morphological studies", Desalination. 1, 171-177.https://doi.org/10.1016/j.desal.2011.04.022

Marchetti, P., Solomon, G. M.F., Szekely, Livingston, A.G., 2014. Molecular separation with organic solvent nanofiltration: a critical review", Chem. Rev.114, 10735–10806.

Pendergast M.M., Hoek E.M.V. 2011. A review of water treatment membrane nanotechnologies. Energy Environ. Sci., 4(6), 1946–1971. DOI: 10.1039/c0ee00541j.

Singh, S., Khulbe, K.C., Matsuura, T. and Ramamurthy, P. (1998). Membrane Characterization by Solute Transport and Atomic Force Microscopy. Journal of Membrane Science.142,111-127.http://dx.doi.org/10.1016/S0376-7388(97)00329-3.

Subramanian, S., Seeram, R., 2013. New directions in nanofiltration applications are nano fibers the right materials as membranes in desalination", Desalination, 308, 198–208.

Turhan, K., Durukan, I., Ozturkcan, S.A., Turgut, Z.,2021. Decolorization of textile basic dye in aqueous solution by ozone", Dyes Pigments 92, 897–901.

Xu X. 2019.Nanofiltration membrane constructed by tuning the chain interactions of polymer complexation. J. Memb. Sci. 580, 289–295.DOI:10.1016/j.memsci.2019.02.055.

Zhang Y., Xu X., Yue C., Song L., Lv Y., Liu F., Li A. 2021. Insight into the efficient co-removal of Cr (VI) and Cr (III) by positively charged UiO-66-NH2 decorated ultrafiltration membrane. Chemical Engineering Journal, 404, 126546

Zhou,Y., Fang, M-Y., Fengsun, L., 2018. Pore size tailoring frpmultrafiltration to nano filtration with PVC-g-PDMA via rapid immersion thermal annealing", Journal of membrane science. 572, ISSN : 0376-7388. DOI:10.1016/j.memsci .2018 .10.060

IEEES-010

Fabrication and Photocatalytic Activity of Undoped and Mg doped ZnO

1BOUDINE Boubekeur, 1,2AMEUR Imene, 1HALIMI Ouahiba, 1SEBAIS Miloud
1 Constantine 1 University, Faculty of Exact Sciences, Physics Department, Crystallography Laboratory, Route Ain El Bey 25000 Constatine Algerie
2 Mila University Center, Physics Department, Mila 43000 Algerie.
*Email: boubekeur.boudine@umc.edu.dz

Abstract

Environmental pollution has recently become a major concern for humanity. More and more scientists are trying to find ways to overcome this problem. The increasing water pollution has motivated researchers to develop materials capable of degrading pollutants in the water. Among these materials are semi-conducting oxides, especially ZnO, which display high effectiveness in degrading dyes and organic species. Using semi-conducting oxides as photocatalysts is very effective in the degradation of organic pollutants and helps eliminate hazardous species in water. This work reports the chemical fabrication of pure and Mg doped ZnO thin films, their structural and optical characterization and the evaluation of their photocatalytic activity. Different concentrations of Mg (1, 3 and 5 wt. %) were added to the ZnO solution. The pure and Mg doped ZnO thin films have been fabricated using sol gel method. The XRD of samples have revealed that ZnO crystallizes in the Wurtzite structure and presents a preferential orientation. The size of crystallites of ZnO thin films is nanometric. The optical transmittance spectra of samples exhibited a high level average transparency in the visible range. A strong absorption in the UV region, this adsorption is owing to the electronic band-to-band transition. Photocatalytic degradation of the pure and Mg-doped ZnO films was carried out using the photo-degradation process of an aqueous MB solution under UV light irradiation with $\lambda = 365$ nm. It is clear that there is no degradation of MB in the absence of pure and Mg-doped ZnO under irradiation. The photocatalytic performance of Mg-doped ZnO is greatly improved.

Keywords: Mg doped ZnO, XRD, wurtzite, UV-visible.

I. Introduction

In recent years, humanity has suffered enormously from the pollution caused by uncontrolled industrialization. The efforts made by scientists constitute a great challenge. The degradation of pollutants in water has grown rapidly. The use of oxide semiconductors in the degradation of organic pollutants has emerged rapidly. ZnO is one of the oxide semiconductors which exhibit good dye degradation. It is interesting inorganic substance which has wurtzite type crystal packing, abundantly used raw material because of its high thermal stability, biodegradability and low toxicity. ZnO is a chosen material due it's potential application in chemical industry as it is used as air pollutant scrubber for gases, catalysis, optoelectronics, insulating material filler, refractory materials, antibacterial agent and as a catalyst support (Darabi, E. et al,). In photocatalytic application ZnO is seen one of the promising photocatalyst and have been successfully applied for methylene blue dye degradation. Doping of ZnO is an effective method to increase photocatalytic activity of ZnO catalyst (Boudine, B et al 2020). This work presents the results of the photodégradation of methylene blue dye by undoped and Mg doped ZnO NPs under UV radiation.

II. Experimental procedure

Undoped and Mg doped ZnO (Mg: 1, 3 and 5 wt%) NPs were fabricated by sol-gel method. The precursor species used in the preparation solution were: zinc acetate tetra-hydrate $Zn(CH3COO)2{\cdot}4H2O$ as a zinc source, magnesium acetate tetra hydrate as a dopant source, a 2-methoxyethanol as a solvent, and monoethanolamine as stabilizer agent. First, zinc acetate tetra-hydrate and magnesium acetate tetra hydrate were dissolved in 30 ml of 2- methoxyethanol under magnetic stirring at 60°C. When the solution turned milky, the monoethanolamine was added drop by drop. Finally, the solution becomes transparent and maintained during 1 hour. The undoped and Mg doped ZnO thin films were deposited by dip coating technique.

III. Photocatalytic procedure

A UV light source (VL -215.LC, 15W), with emission maximum at 365 nm was employed to check the photocatalytic activity of undoped and Mg doped ZnO. 10 ml MB solution with an initial concentration of 10-5 mg/ml was taken in a glass beaker. A thin glass strip (5×2.5 cm) containing the films of undoped ZnO(or Mg doped ZnO) was put in the beaker containing MB. The beaker was kept under UV light at a distance of 20 cm emitted by a 15 W iodine tungsten lamp (Philips and Co). The whole system was covered by cloth so that natural white light would have no role in catalysis. During irradiation the aliquots of solution was taken out after every 30 min from the reactor and checked by analyzed by a 723 UV–Vis spectrometer (UV-1800 Shimadzu LC 2010-HT).

IV. Results and discussion

Figure 1 shows the XRD pattern of undoped and Mg doped ZnO thin film. A small broadening of the diffraction peaks is observed, which is due to the nanometric size of the of undoped and Mg doped ZnO thin film. The nanocrystallites of of undoped and Mg doped ZnO thin film has a hexagonal (wurtzite) structure (JCPDS card No 00-001-1136).

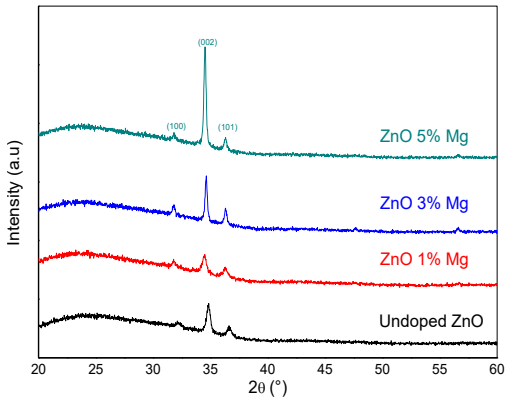

Figure 1 : X-ray diffraction of undoped and Mg-doped ZnO thin film (3, 5, 7 and 10 wt. %).

Table 1 shows the diffraction angles, half-height width (FWHM), diffraction planes and sizes of NC ZnO. The size was estimated using the Scherer formula [21]:

$$D = \frac{0.9\lambda}{\beta cos\theta} \quad (1)$$

Where

D is the size of the ZnO crystallites,. is the wavelength of the X-rays (1.5402 Å). represents the full half width at mi- height (FWHM). is the diffraction angle. The apparent sizes of undoped and Mg doped ZnO are nanometric (Table 1).

Table 1 : Structural parameters of the prepared films obtained by using High Score plus software.

Mg%	Phases	2θ (°)	β (°)	D (nm)	δ × 10-4 (lines/nm2)	a (Å)	c (Å)	V (Å3)
0	ZnO	34.79	0.18	51	17	3.22	5.15	53.27
1	ZnO	34.49	0.19	50	4.0	3.25	5.19	54.87
3	ZnO	34.49	0.22	43	4.0	3.25	5.20	54.88
5	ZnO	34.50	0.36	24	5.0	3.25	5.20	54.94

Figure 2 displays UV-visible spectra of undoped and Mg doped ZnO. It was observed that all nanoparticles are almost transparent in the visible region and show a strong absorption in the UV region. The UV-visible absorption spectra displayed with the absorption shoulder of undoped ZnO at about ~ 350 nm while doped ZnO samples donated the absorption shoulders at the range of (300–3300 nm). Therefore, owing to the Mg doping the absorption edge slight shifted towards the shorter wavelength (blue shifted) which proved that the Mg were successfully doped, this shifting results decreasing the band-gap of the fabricated nanoparticles which is a considerable factor that promoted the photocatalytic activity.

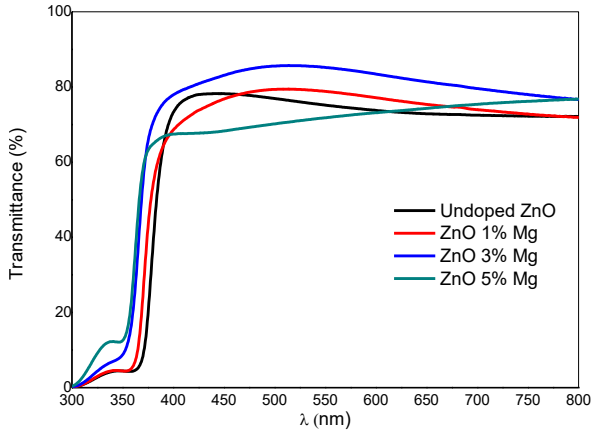

Figure 2 Absorbance spectra of undoped and Er-doped MgO NPs

The optical band-gap was estimated from the absorption spectrum using the relation between energy and wavelength.

$$Eg = \frac{1240}{\lambda_{edge}} \text{ eV} \quad (2)$$

Where λ edge indicates the absorption limit of the materials, λ edge can be determined using the absorption spectrum by estimated the derivative of absorption with keep the wavelength near the absorption edge and the maximum values of derivative spectrum represents λ edge of the samples. This maximum values is similar to that the reflection point values of the absorption curve, the tangent line of the absorption curve at the reflection point intersects with the x-axis on which absorbance reaches 0 and shows the λ edge [3]. The gap was found to be 3.28, 3.30, 3.34 and 3.37 eV respectively correspond to undoped and (1, 2, and 3% in wt) Mg doped ZnO. The photocatalytic activity of undoped and Mg doped ZnO (Mg:0, 1, 3, and 5 wt. %) thin films were evaluated through the degradation of methylene bleu (MB) dye under UV-light irradiation. The evolution of absorption spectra of MB aqueous solution in the presence of undoped and Mg doped ZnO (Mg:0, 1, 3, and 5 wt. %) NPs under UV-light irradiation are recorded. The dark adsorption the photolysis of MB and catalyst was done of during 30 min before achieving the photocatalytic. To monitor the temporal variation of MB dye concentration the maximum absorbance at 664 nm was selected, the intensity of the absorption peak gradually decreased with irradiation time on MB solution; the catalyst phenomena shows that less than 50% of MB was degraded for pure ZnO, and it was increased with increasing of Mg doping concentration in ZnO NP's. Also Mg doped ZnO NPs exhibited improvement photocatalytic activity compared to pure. After 90 min Mg doped ZnO enables us to completely degrade MB in water. Figure 3 shows the concentration ratio (C/C0) of MB dye versus the irradiation time of undoped and Mg doped ZnO (Mg:0, 1, 3, and 5 wt. %) thin films, there is no degradation of MB in the absence of NPs under UV-light irradiation. It is observed that the catalyst and the photocatalytic performance of Mg doped ZnO is greatly improved compared to undoped ZnO, 5 wt. % Mg doped ZnO thin films show faster catalyst and photocatalytic activity.

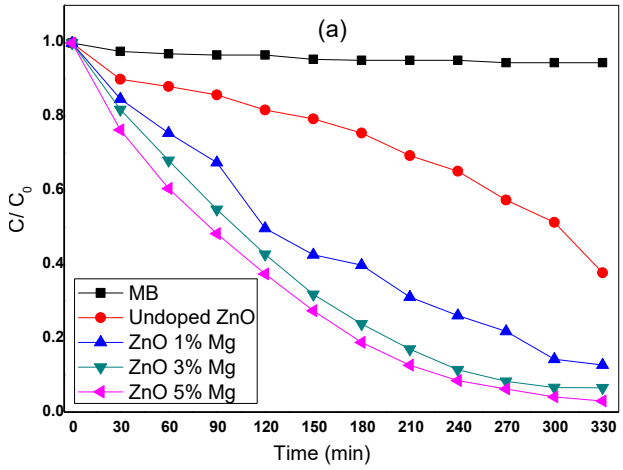

Figure 3 : The effect of the Mg dopant on the MB dye solution under irradiation of.

V. Conclusion

Undoped and Mg doped ZnO (Mg:0, 1,3 and 5 wt. %) thin films were prepared successfully by the sol-gel method. The crystalline structure of NPs was checked by XRD, which confirms the hexagonal (wurtzite) structure of ZnO, the crystallite size decreases when the Mg doping is incorporated in the ZnO lattice. UV-visible measurement shows that the optical gap decrease when the Mg concentration increases. Finally, ZnO and Mg doped ZnO thin films were used for the removal of MB dye from water and showed that the removal efficiency of dyes increases as the concentration of Mg increases, more particularly for short irradiation times. The maximum MB dye removal was 99 % for 5 wt. % Mg doped ZnO NPs.

References

Boudine, B., Guedri, A., Hafdallah, A., Zaabat, M. (2020). 30. 4884-4894 Synthesis, Characterization, Structural, and Optical Properties of Polyvinyl Chloride/Zinc Oxide Nanocomposite Films for Photocatalysis Application.
Journal of Inorganic and Organometallic Polymers and Materials, https://doi.org/10.1007/s10904-020-01604-8.

Darabi, E., Ghoranneviss, M., Hosseinnejad, M. T., Hantehzadeh, M. R., Shirazi, M., (2016). 26 405-412 Preparation of Nanostructured ZnO Thin Films Using Magnetron Sputtering for the Gas Sensors Applications. Journal of Inorganic and Organometallic Polymers and Materials. https://doi.org/10.1007/s10904-015-0324-0.

Challali, F. , Chelouche, A., Djouadi, D., Mendil, D., Mohamedi, M., Ouhenia, S., Souici, A.H., Touam, T. (2022) 244 : 118739-118750. Role of substrate and annealing on microstructural, optoelectronic and luminescence properties of RF magnetron sputtered AZO thin films in confocal configuration. Journal of Luminescence. https://doi.org/10.1016/j.jlumin.2022.118739.

Dhayal, S., S., Kaliramna, S., Kumar, N., (2022) 133: 112891-112-900. Structural and optical studies of ZnO doped PMMA thin film and its photocatalytic and antibacterial activities. Optical Materials.https://doi.org/10.1016/j.optmat.2022.112891

IEEES-011

Hydrogen as the Fuel of the Future and Hydrogen-Powered Aircraft

[1]Cengizhan Gok, [2]Selcuk Ekici, [3]Ozgur Balli, [4]T.Hikmet Karakoc
[1]1st Air Maintenance Factory Directorate (1.HBFM), General Directorate of Military Factories (AFGM), Ministry of National Defense (MND), Eskisehir, TR-26320, Turkey
[2]Department of Aviation, Iğdır University, TR-76000, Iğdır, Turkey
[3]Turkish Aerospace Industries Inc. (TAI), TR-06980, Kahramankazan/ Ankara, Turkey
[4]Department of Aircraft Airframe Powerplant Maintenance, Eskisehir Technical University, TR-26000, Eskisehir, Turkey
*E-mails: cengizhangok64@gmail.com ; selcukekici@gmail. com ; balli07balli@yahoo.com ; hikmetkarakoc@gmail.com

Abstract

The aim of this work is promotion hydrogen as the fuel of the future which is planned to be used in the aviation industry. While talked about fossil fuels, solar energy, wind energy, and electrical energy, also run into hydrogen energy. What is this hydrogen, Why is it used by aircraft, Are there any disadvantages or avantages? This paper will seek answers to these questions Initially, Hydrogen is a gas that is scentless , achromatic, non-metallic, tasteless, highly flammable, and appear as H2 under standard temperature and pressure. Then paper focused on can be alternative fuel for aviation because Hydrogen is the most ample element in the nature, making up three quarter of the mass of the universe. And hydrogen has the top energy ingredient per unit mass among.It is an mean of 1.33 times more efficient fuel than oil fuels. The volume of liquid hydrogen is only 1/700 of its gaseous volume. In section Use of hydrogen have a new practise for hydrogen aircraft. Considering its production in order to be used as energy, it must be separated from compounds in nature. It is not as lucrative as ready-made fuels for example oil. However, a significant difference of hydrogen from other fuels is that it can be produced from water with the help of solar or wind energy and can be converted back into water when used. In conclusion This characteristics makes hydrogen a fuel that can be produced and used by everyone if science, busines word and governments look for answer to use of hydrogen for aviation therefore hydrogen can be in an aircraft that uses as a power resource. Also hydrogen can either be burned in a jet engine or another kind of internal combustion engine or can be used to force a fuel cell to produce electricity to power an electric propulsor.

Keywords: Hydrogen, Airplane, Fuel cell, gas turbine

I. Introduction

In the future, hydrogen is one of the important fuel Technologies. The time of limitless energy effectualness is notorious finishing. The changing of fossil-based energy transition by emission-free convention will desperate be fairly costly and it will give rise to fatal difficulty. The world inpopulation from a level well beneath 1 billion for thousands of years to mounth from that level in at the beginning of 1800s to the today level of 8 billion (Platzer, 2023).

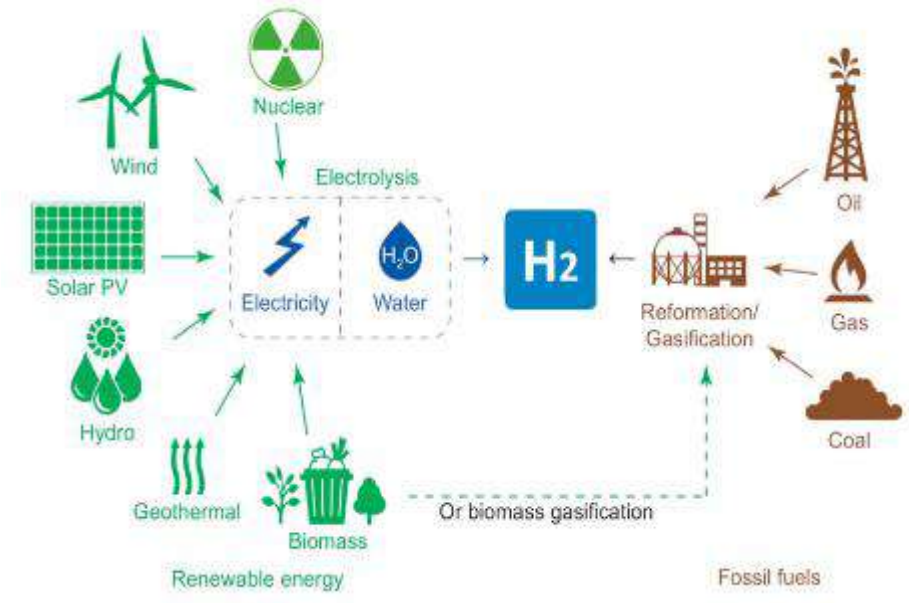

Fig 1 Generation path for hydrogen

Decarburizing is one of the greatest rigors for community and particularly in the hard-to-decrease industry of aeronautical. but hydrogen with airplane have the likely to fly present routes with carbon free emissions and decrease or rule out other emissions. Instruction for example the Green Deal of the European Council were promote to achive carbon neutrality by 2050 perfected all

sectors. Furthermore such as flying to rely upon economic backing from states who made their backing depending on to environmental sustainability aim. In France for such as, the state assistance the national aviation sector economically, there of EUR 1.5 Bn with the provision to enhance a carbon-neutral airplane by 2035 and hydrogen airplane seem to be the best compulsory choice to today's conventional powered airplane As a result of emissions and greenhouse gases , Industries seek solution. So hydrogen-powered transport for example train , car, ship, aircraft etc. Maybe can help our. (J. Hoelzen, 2022)

II. Fuel Hydrogen Production

Our nonstop thriving energy need is driven by large-scale increase in economic growing and population and places an ever-increasing load on fossil fuel usage that stand for a substantial percentage of this growing energy need but also creates difficulties connected with growing greenhouse gas (GHG) emissions and resource exhaustion. Research working should concentrate mitigating their heaviness with novice requisites, designs, and production techniques this investigate survey the hydrogen as a fuel in a powered-airplane, which has the capability to cut down NOx emissions, increase of productivity while importantly step down pollutants for instance carbon monoxide. Hydrogen can make use of traditional gas turbines for impulsion. Modern gas turbines turn fuel to mechanical work at effectivity of nearby 40%. Also Hydrogen fuel cells are an choice to combustion-based impulsion. They turn hydrogen into electricity at effectivity larger than 50%. Energy consumption for Hydrogen aircraft are expected to be at least approximately the same to kerosene powered aircraft. However alert consern of factors for instance both combustion, fuel storage, emissions and required shift to the engine system are essential. On the whole, hydrogen has the ability to be a feasible choice to classic fuels in airplane.

Hydrogen could be generated from divers foisons that makes it further several with regard to non-renewable foisons. Figure 1 demonstrate the hydrogen generation from various sources. Hydrogen can be generated from wind energy and solar energy. The hydrogen is clear heating rate is capability above than other traditional fuels but the energy safety is over measure to other fuels. Hydrogen is a synthetic fuel and its production resources are extremely abundant and diverse. Morever these include water, air, coal and natural gas. However, this is considered coal and natural gas are fossil fuels and have limited reserves. In 2022 aeronautics explain 2% of global energy-connected CO2 emissions, having grown up quicker in recent decades than rail, road or shipping. As international journey request improve pursuit the Covid-19 pandemic, emissions in 2022 for aeronautics attained almost 800 Millon ton CO2.

Beyond fuselage and impulsion, the feasibility of hydrogen airplane mainstay on affordable green hydrogen generation, which requires enormous enterprise in the energy substructure.

III. Use of hydrogen in aircraft

Studies on the use of hydrogen as fuel in aircraft Its beginning is at United States in 1956., a B57 Canberra He powered his plane using hydrogen fuel pressurized with helium in one of its engines. He managed to fly. The oil crisis that emerged in the 1970s Like all other industries dependent on oil, aviation has to find an alternative fuel.
put him in search. However, after the crisis was over, the studies on this issue Most of the work has been shelved.

Table 1 Current hydrogen aircraft developments.

Airplane	Year	Power	Explanation	Storage	Distance (km)/ time	Referance
NASA CHEETA	2019	Hydrogen Fuel Cells	Blended wing-body large commercial aircraft/under developmant	Liquid	n/a	(Chandel, Reband, Hall, & Greitzer, 2021)
ZeroAvia	2019	Hydrogen Fuel Cells	10–20 seats fixed-wing aircraft, two propellers	Gas	800	(Bris, ve diğerleri, 2022)
Airbus ZEROe	2020	Hydrogen Combustion	Large commercial aircraf	Liquid	n/a	
ZeroAvia Dornier 228 demonstrator	2023	Hydrogen Fuel cell	19-seat twin-engine aircraft	Gas	23 min	(Adler & Martins, 2023)
De Havilland Canada Dash 8	2023	Hybrit / Hydrogen Fuel Cells	Regional aircraft with turboprop engines	Gas	15 min	

Hydrogen can be used in aircraft in two ways. First, engines using traditional fuels can be redesigned and used, or by driving an electric motor thanks to hydrogen fuel cells to be placed in aircraft. Expectant that renewable energy generation will allow 'green' hydrogen to be generated at scale, thus abatement upstream carbon emissions and creating an excessive invitingenergy storage choosing. CFM International, GE and Safran, is launch out enhance the hydrogen burning engine and design it for experiment. Especially, the company will work on the combustor, fuel system and control system of a GE PassportTM turbofan to operate upon hydrogen. Hydrogen is a high-energy clean-burning fuel whose primary burning output is water vapour and traces of nitrogen oxides.

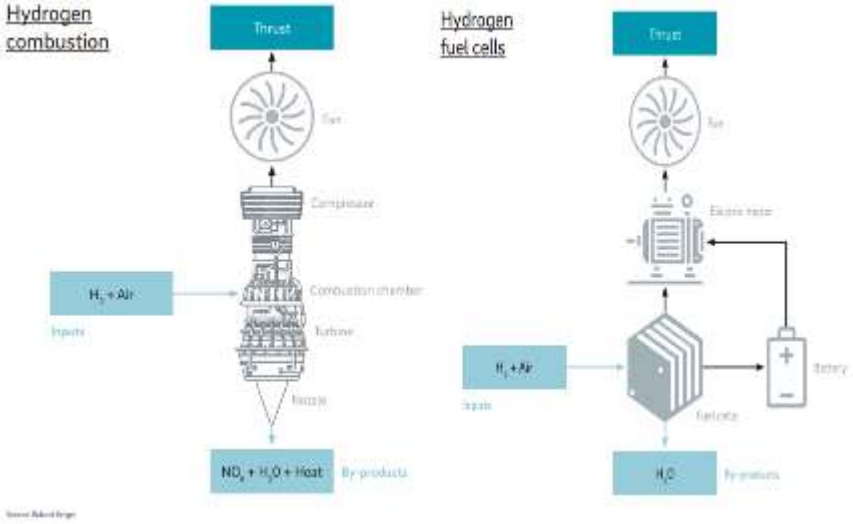

Fig 2 Implimentation of hydrogen two important use of by aircraft

Hydrogen technologies is one of the most probably technologies to decrease aviation's climate change. When produced from renewable energy sources, it emits zero CO2.Transportation and storage systems need to be developed for hydrogen energy to become widespread. The total length of hydrogen pipelines in America does not exceed 2000 miles. Besides have need for reduce charge, more safe, and more enduring hydrogen compression technics. Especially in the last 20 years, important studies have been carried out on alternative green sustainable fuels. It is predicted that they will become widespread in the coming years, especially in the 2040s. Although the expectations are optimistic, there is still a long way to go because special pressurized tanks are required for the storage and transportation of hydrogen. Excessive first costs, and not quick recharging performance of batteries are critical disadvantages. Also altering a traditional engine from kerosene burning to hydrogen burning without achieving large-scale hardware exchanges does not seem like a possible task.

V. Conclusion

There is importing difficulties fabrication process for hydrogen, storage, practise of hydrogen, shipping and delivery and in the trading expanse of aviation sector. Altough the difficulties, both for mitigation carbon emissions and finding alternative optimized way much better energy cost. New aircraft fuel tecnologies is crucial in the aviation sector and moving toward a further sustainable fortune.

Generally, remarked that hydrogen has the potential to be a applicable alternative to traditional fuels in airplane engines. In view of developing tecnologies and support and state subsidy by governments

The access fossil fuels should be decreased for aviation sector, and fossil-based technologies should be gradually transformed to hydrogen-based technics.

The significance of hydrogen and hydrogen technologies that possibly decrease the world problems and succeed a sustainable energy system therefore required emphasizing and taking into consideration the sustainable energy strategies. Furtermore, a conversion to the green energy-based economy need be promote, and developed countries, in especially should enhance enterprise in hydrogen and technics.

Engines which use hydrogen operate cooler than those using kerosene and this fact turn into a dramatically lengthier engine life.

Utilization in fuel cells permit for zero-emission impulse. When burned in a turbine engine, greatly little particle emissions can be anticipated, in addition deciresed NOx emissions, on condition that the combustion system is optimised

Acknowledgement

In the future, studies can be focused on gas turbine engines which the combustion of hydrogen and the current engine efficiencies can be compared with those obtained with hydrogen.

References

Adler, E. J., & Martins, J. R. (2023). Hydrogen-powered aircraft: Fundamental concepts, key technologies, and environmental impacts. *Aerospace Sciences*.

Berger, R. (2020). Hydrogen, A Future Fuel for Aviation.

Berger, R. (2020). *Preparing Your Airport for Electric Aircraft and Hydrogen Technologies.* https://www.rolandberger.com/en/Insights/Publications/Hydrogen-A-future-fuel-for-aviation.html adresinden alındı

Bris, G. L., Nguyen, L.-G., Tagoe, B., Jonat, P., Justin, C. Y., Reindel, E., . . . Ansell, P. J. (2022). *Preparing Your Airport for Electric Aircraft and Hydrogen Technologies.* Washington,DC: National Academies.

Carlo Cunanan, M.-K. T. (2021). A Review of Heavy-Duty Vehicle Powertrain Technologies Diesel Engine Vehicles, Battery Electric Vehicles, and Hydrogen. *Clean Technologies*.

Chandel, D., Reband, J. D., Hall, D. K., & Greitzer, E. M. (2021). Conceptual Design of Distributed Electrified Boundary Layer Ingesting Propulsors for the CHEETA Aircraft Concept. *AIAA Propulsion and Energy Forum*.

Corchero, G., & s, J. L. (2005). An approach to the use of hydrogen for commercial aircraft engines. *Sage journals*.

Eytan J. Adler, J. R. (2023). Hydrogen-powered aircraft: Fundamental concepts, key technologies, and environmental impacts. *Aerospace sciences*.

Finlay, M. (2022). *martin-b-57b-hydrogen-powered-flights-1950s*. Simpleflying: https://simpleflying.com/martin-b-57b-hydrogen-powered-flights-1950s/ adresinden alındı

Ishaq, H., Dincer, I., & Crawford, C. (2022). A review on hydrogen production and utilization Challenges and opportunities. *Hydrogen Energy*.

J. Hoelzen, D. S.-R. (2022). Hydrogen-powered aviation and its reliance on green hydrogen infrastructure Review and research gaps. *Hydrogen Energy*.

Manigandan, S., T.R.Praveenkumar, Ryu, J. I., Verma, T. N., & Pugazhendhi, A. (2023). Role of hydrogen on aviation sector: A review on hydrogen storage, fuel flexibility, flame stability,and emissions reduction on gas turbines engines. *Fuel Science Dİrect*.

Platzer, M. F. (2023). *Aerospace sciences*.

Safety Issues with Hydrogen as a Vehicle Fuel, . (1999). Idaho National Engineering and Environmental Laboratory (INEEL).

Şenel, K. (2007). Hidrojenin Yakıt Olarak Uçaklarda Kullanımı.

www.macrotrends.net. (2023, 09 25). https://www.macrotrends.net/1369/crude-oil-price-history-chart adresinden alındı

Xiumei Zhang, R. Y. (2022). Assessment of hydrogen and nanoparticles blended biodiesel on the diesel engine performance and emission characteristics . *Science Dİrect*.

Zhang, B., Zhang, S.-X., Yao, R., Wu, Y.-H., & Qiu, J.-S. (2021). Progress and prospects of hydrogen production Opportunities and challenges. *Electronic Science and Technology*.

Zixuan Luo, Y. H. (2020). Cost-Economic Analysis of Hydrogen for China's Fuel Cell Transportation Field. *MDPI*.

IEEES-012

Performance Improvement of PV Generator Using a Sun Tracking System

[1*]Sakina Atoui, [2]Fouad Aissaoui, [2]Amel Berkane, [1] Ayad Mohammed, [1]Djamila Ghribi, [1]Saïd Boudjana
[1]Unité de Développement des Équipements Solaires, Udes/Centre De Développement des Énergies Renouvelables, CDER, 42004, Tipaza, Algerie
[2]Tipaza University Center, Institute of Science, Department of Electronic, Oued Merzoug, 42000, Algeria
*E-mails: atouisakina@gmail.com

Abstract

This work is devoted to improve the performance of the photovoltaic generator. It is based on the use of a sun tracker to collect the maximum of solar radiation in order to obtain maximum efficiency from the panel. The goal of this study is to increase the power generated by the PV generator using a control card of two-axis solar tracker. The project aims to develop a control board for the tracking system and evaluating the energy performance of the photovoltaic generator with solar tracker. The design and construction of this tracker is based on light sensors, a microcontroller for controlling the circuit and a mechanical solar tracking system. The energy evaluation shows that the sun tracking system improves the production of the photovoltaic generator especially in the morning and in the evening when the production has been multiplied.

Keywords: Photovoltaic energy, tracking system, sensor light based tracking system.

I. Introduction

Much of the greenhouse gases that surround the Earth come from the production of energy by fossil fuels like oil, coal, natural gas. They are responsible for global climate change. To avoid the worst effects of climate change, emissions must be minimized. To achieve this, we must end our dependence on fossil fuels and invest in alternative sources of energy that are clean, accessible, affordable, sustainable and reliable. Solar energy is one of these sources and it is 100% green energy because its production does not directly emit CO2. Therefore, it is becoming more and more a solution among the promising energy options with advantages such as abundance, the absence of any pollution and the availability in greater or lesser quantities at any point on the earth. However, few countries are investing in these technologies (Aqachmar et al., 2021).

The installation of photovoltaic systems are growing year after year in the world. They reached at least 942GW at the end of 2021 (Report IEA-PVPS T1-42, 2022). Therefore, PV system technology is being developed to facilitate and spread the use of this energy in the world (Gutiérrez-Martín et al., 2023). One of the challenge of PV system is how to increase the performance of the system. There are several parameters that directly and indirectly influence the performance of the PV system like solar radiation, tilt angle, installation site, humidity, dust accumulation, wind, temperature, shading, etc., (Lei et al., 2021; Gupta et al., 2019; Gupta et al., 2022; Mani and Pillai, 2010). Many works are studied this issue in different aspects, some works studies the cleaning of the panels and other examine the inclination and the third study how to increase the efficiency of the cells. The contribution of this work search the best orientation of the panels to enhance the performance of the PV system.

Novel high efficient offline sensorless dual-axis solar tracker for using in photovoltaic systems and solar concentrators that tracks the sun direction with a very small tracking error of only 0.43º was studied in (Fathabadi, 2016). In addition, its fabrication is not expensive compared to sensor-based tracker. (Chong et al., 2017) analyzed the performance of off-grid residential solar photovoltaic power systems using five solar tracking modes in Kunming, China. They showed that the highest available solar energy (3081 kWh/y) and minimum missing energy (48.53 kWh/y, in October) are obtained for the dual axis tracking system.

Comparative study between the performance of the sensor-based and sensorless tracker was reported in (Fathabadi, 2016). Even though, the sensor based tracker give good score than sensor less, the latter is cheaper and its structure is very simple.

Novel online sensorless dual axis sun tracker regulated by the maximum power point tracking (MPPT) unit was proposed in (Fathabadi, 2017). The proposed sun tracker finds the sun direction with the tracking error of only 0.11°. Although tracking PV system produce energy more than fixed one, is not commonly used comparing to fixed systems. These are for several reasons like cost, maintenance and not widely known. The aims of this work is to show the effectiveness of tracking systems and to encourage the use of this technology in the future.

This study introduces the design, implementation, and characterization of a low cost, small-scale dual-axis solar tracking system. The paper is organized as follows. In section 2, the algorithm and the simulation of the electronic circuit is presented. In section 3, a PV sun tracking system is configured and implemented. In section 4, the results and relevant discussion are carried out. Conclusions are drawn in section 5.

II. Realization of two axis solar tracking system

The tracking system produced is made up of a mechanical structure that supports and orients the solar panel along two axes, horizontal and vertical, in the direction of solar radiation, as well as an electronic part: solar sensors with an "Arduino" microcontroller board followed actuators, in this case two electric servomotors.

The mechanical structure consists of two moving parts. A part on the horizontal axis for the variation of azimuth of the panel in relation to the sun and the other part on the vertical axis for the variation of elevation of the panel.

A panel tracks the sun using Light sensors. The simulation show the perfect operation of the program. The light sensors indicate the directions of the sun and then they push the servomotors to move the panels in the direction with increased light intensity.

The simulation of the proposed system was carried out using Proteus (figure 1) to ensure proper operation before practical implementation.

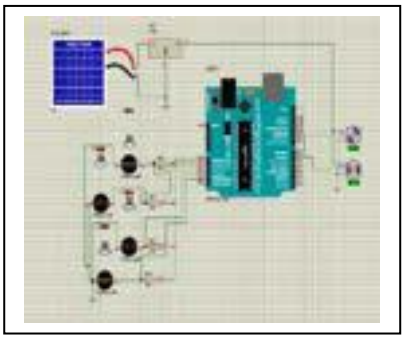

Fig. 1: Simulation of the different components of the tracking system using Proteus.

Fig. 2: Two-axis solar tracker system.

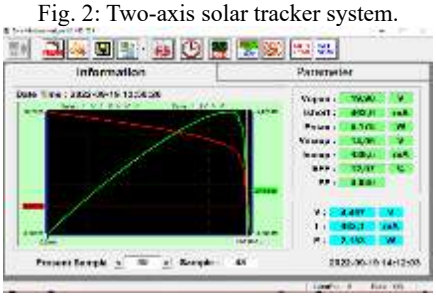

Fig.3: Measurement of I (V) characteristic of the panel used in our prototype using PROVA200A.

Figure 2 presents the operated Two-axis solar tracker system and the figure 3 shows I (V) characteristic of the panel used in our prototype using PROVA200A. The PV module is of the polycrystalline type with a power of 10W.

III. Results and discussion

The output power produced by photovoltaic panels strongly depends on the incident light radiation. The continuous modification of the relative sun-earth position determines a continuous change of the incident radiation on a fixed PV panel. The point of maximum energy received is reached when the direction of solar radiation is perpendicular to the surface of the panel. In order to maximize the power output of solar PV panels, it is necessary to keep the panels aligned with the sun, which means sun tracking is necessary.

The electrical production of the panel was calculated from the solar irradiation on a fixed plane and on a plane that follows the trajectory of the sun (tracking system). It is clear that the amount of radiation that follows the sun tracker is greater than that of the fixed system. According to practical tests, the difference in irradiation between the tracking system and the fixed system is significant in the morning and in the afternoon, but at noon, this difference in irradiation is reduced.

Fig. 4: Variations in panel current, voltage and wattage with a south tilted fixed system using a fixed load of 23Ohm.

Figure 4 represents the evolution of the intensity of the current, the tension and the power according to time during one hour of the evening of a fixed panel directed towards the south with an angle of 30 degrees. We noticed that the maximum voltage at 4:00 p.m. reached a value of 5.65 V and started to decrease with time until 2.16 V at 5:00 p.m., the same evolution for the current; it reaches a value of 0.24 A at 4 p.m. and drops to 0.098 A at 5 p.m. Therefore, the power at 4:00 p.m. has a value of 1.43 W and it started to decrease with time until the value of 0.21 W at 5:00 p.m.

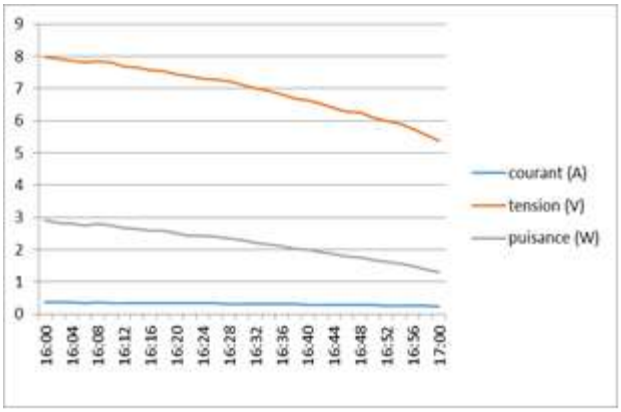

Fig. 5: Panel current, voltage and wattage variations with the sun tracking system using a fixed load.

Figure 5 represents the evolution of the intensity of the current, the voltage and the power as a function of time during one hour of the evening of our solar tracking system. We noticed that the maximum voltage at 4:00 p.m. reached a value of 7.97 V and it started to gradually decrease to a small value with time until it reached 5.37 V at 5:00 p.m. The current reaches a value of 0.364 A at 4 p.m. and gradually drops to 0.243 A at 5 p.m. Consequently, the power at 4:00 p.m. reached the value of 2.90 W and it started to decrease with time until it reached 1.3 W at 5:00 p.m.

From the figures, five and seven we notice that the photovoltaic panel placed on a solar tracking system produces better energy than the same panel placed on a fixed system.

Percentage increase in power is calculated using the energy production between 4:00 p.m. and 5:00 p.m. for both fixed and tracking system and the following formula:

Percentage = [E_tracking value – E_fixed value] / E_fixed value) x 100.

Percentage = [68.65208 – 20.85939] / 20.85939) x 100.

Percentage =229.11%.

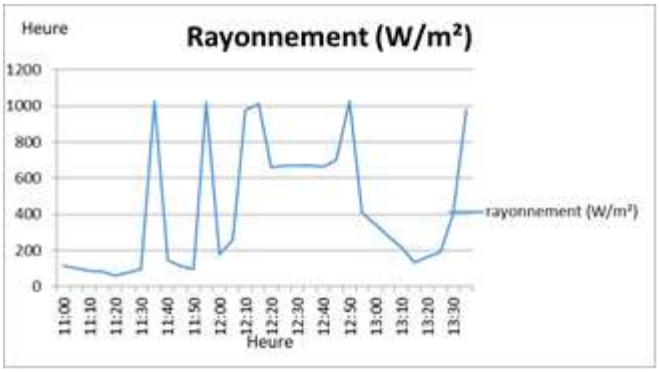

Fig. 6: solar irradiation for two and a half hours on a partly cloudy day.

Figure 6 gives the variation of solar irradiation for two and a half hours of a partly cloudy day.

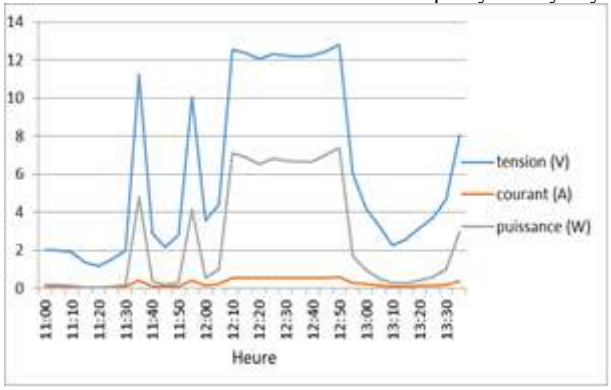

Fig. 7: Panel current, voltage and power variations with the tracking system using a fixed load.

Figure 7 represents the variations of current, voltage and power of the panel with the tracking system using a fixed load. We have seen that the current, voltage and power curves follow the solar irradiation curve. When the irradiation increases the current, the voltage and the power also increase in the same way and the reverse. Therefore, the use of a sun tracking system improves the performance of the photovoltaic generator.

IV. Conclusion

The realization and performance analysis of the two-axis solar tracker has been presented in this work. It has been shown that the solar tracking panel has a higher electricity production than the fixed panel especially in the morning and in the evening. Thus, it will be consider as an excellent option to maximize the production of the photovoltaic generator. This tracker is suitable for laboratory tests.

References

Aqachmar, Z., Ben Sassi, H., Lahrech, K., Barhdadi, A., 2021. Solar technologies for electricity production: An updated review. International Journal of Hydrogen Energy. 46, 30790-30817.

Chong, L., Dequn, Z., Weiyan, Y., Hui, W., Dasheng, Z., Menghui, S., Guo, L., 2017. Performance of off-grid residential solar photovoltaic power systems using five solar tracking modes in Kunming, China. International Journal of Hydrogen Energy. 42, 6502-6510.

IEEES-013

Numerical Investigation of The Effect of Forced Air/nanofluid Pairs on PV/T System Performance

[1*]Gökhan Sefer, [2]Süleyman Karsli
[1]Gebze Technical University, Engineering Faculty, Mechanical Engineering Department, Gebze Teknik Üniversitesi Rektörlüğü, Kocaeli, 41400, Türkiye
[2]Gebze Technical University, Engineering Faculty, Mechanical Engineering Department, Gebze Teknik Üniversitesi Rektörlüğü, Kocaeli, 41400, Türkiye
*E-mails: g.sefer2020@gtu.edu.tr, skarsli@gtu.edu.tr

Abstract

PV/T systems are systems that convert solar energy into electricity and heat energy. These systems have gained widespread popularity worldwide in recent years. While solar panels typically operate with low efficiency, the conversion efficiency of solar energy to electrical energy decreases as the panel temperature rises. PV/T systems have been analyzed in order to improve the thermal efficiency in addition to increasing the electrical efficiency in solar panels. The system was modelled using the ANSYS-Fluent program for numerical analysis. Cooling is necessary in PV/T systems to maintain conversion efficiency as the temperature increases, water is commonly used for this purpose. In this study, the impact of forced air, water, and nanofluid coolants on the performance of PV/T systems was numerically focused on and the results were compared. Changes in system performance have been observed by using various air velocities, nanofluid flow rates, and nanofluid compositions in the analysis. During this study, the temperature and pressure variations resulting from the analysis were taken into consideration. The study employed water as the base fluid and included multi-walled carbon nanotubes (MWCNT) and graphene-nano pellets with a weight concentration of 0.5% as nanofluids. Numerical analyzes were conducted for three various coolant compositions such as water, MWCNT-water and Graphene nanopellet-water, with three different velocities of 1, 3 and 5 m/s, as air and coolant nanofluid. Additionally, water and nanofluids were numerically analyzed for both finned and unfinned serpentine configurations under the same experimental conditions. According to the analysis results and calculations, it was observed that the MWCNT-water mixture provides better cooling performance than other coolants in all conditions.

Keywords: PV/T systems, Nanofluid, Forced Air, PV/T Efficiency, Exergy

I. Introduction

The importance of renewable energy is rapidly increasing in light of the limited nature of fossil fuel resources worldwide. Renewable energy sources, which are unlimited, are considered sustainable sources of energy. Their environmental impact is significantly lower compared to fossil fuel sources. Therefore, taking economic reasons into account, the utilization of renewable energy sources has been on a rapid upward trend in recent years.

One of the most significant renewable energy sources is solar energy. Energy derived from the sun is the largest and cleanest among renewable energies. Approximately 174,000 TW of solar radiation is continuously received from the upper layers of the Earth's atmosphere, and it is presented that the amount of solar energy reaching the Earth in one hour has the capacity to fulfill the world's annual energy needs. Factors such as location, weather, time variations, and available space, both natural and human-made, should be considered in designs to harness this abundant energy.

The use of efficient and cost-effective technologies to harness solar energy can reduce dependence on fossil fuels, meet the increasing energy demands, and minimize climate concerns for the near future. (Sachit and Rosli, 2018) PV/T (Photovoltaic/Thermal) systems involve numerous parameters that influence their thermal efficiency. Among the parameters affecting collector efficiency, we can list PV material type, glass cover thickness, coolant fluid type, coolant fluid flow rate, pipe diameter, pipe material, and insulation material.

Due to its cost-effectiveness, water is commonly used as a coolant fluid in solar collectors. However, water has lower thermal conductivity compared to nanofluids. Therefore, one of the important parameters affecting thermal efficiency is the composition of the working fluid. With advancements in nanotechnology, new working fluid compositions have been developed to enhance the thermal conductivity of the coolant fluid. These fluids, obtained by mixing metals in the range of 1 to 100 nm, are referred to as nanofluids. Various studies and research have been conducted regarding the thermal properties of nanofluids containing different metals, and different nanofluids have been used in PV/T systems. Experimental and numerical studies using nanofluids have shown varying levels of efficiency improvement for each type of nanofluid. (Fudholi and Razali, 2020)

II. Experimental Procedure/Methodology/System Description

In this study, graphene nano-pellet-water and multi-walled carbon nanotube (MWCNT)-water nanofluids were used as the working fluids, and their effects on the thermal efficiency of PV/T were investigated through numerical analysis. To achieve this, a PV/T system model was first created using the SOLIDWORKS modeling software. Two different serpentine configurations were designed in the model: one with fins and one without fins. The fins were mounted in a semi-circular shape on the outer surface of the working fluid serpentine. The created model was imported into ANSYS Workbench, and a model capable of performing the desired numerical analyses and comparisons using the FLUENT module was set up. Two different geometries were considered: one with fins and one without fins. Three different coolant flow rates were simulated at speeds of 1 m/s, 3 m/s, and 5 m/s, using three types of working fluids: tap water, a mixture of 0.5% mass fraction MWCNT-water, and a mixture of 0.5% mass fraction graphene nano-pellet-water. Additionally, five different solar radiation flux values representing different times of the day, 200 W/m^2, 400 W/m^2, 600 W/m^2, 800 W/m^2, and 1000 W/m^2, were used. In total, 100 different experiments were conducted, and the

results obtained from these experiments were analyzed and compared by examining the contours and graphical outputs.

Table 1. Summary of Heat Transfer Properties Obtained for Some Commonly Used Nanofluids in the Literature

Nanofluid/base fluid type	Concentration by Mass %	Heat transfer increase %	Flow type
Cu/Water	*2*	*60*	*Laminar*
Cu/Water	*2*	*60*	*Turbulent*
Al_2O_3 /Water	*1,6*	*41*	*Laminar*
Grafite/Water	*2*	*22*	*Laminer*
TNT/Water	*2,5*	*13,5*	*Laminar*
ZrO_2/Water	*1,32*	*3*	*Laminer*
Al_2O_3 /Water	*6*	*27*	*Laminar*
Al_2O_3 /Water	*0,3*	*8*	*Laminar*
CuO/EG-Water	*6*	*35*	*Turbulent*
MWCNT/Water	*0,12*	*25*	*Laminar*
TiO_2/Water	*2*	*26*	*Turbulent*
TiO_2/Water	*1*	*14*	*Turbulent*
Al_2O_3-Cu/Water	*0,1*	*13,56*	*Laminar*
MWCNT/Water	*0,45*	*159,3*	*Turbulent*
MWCNT/Water	*0,5*	*47*	*Turbulent*

In this study, the dimensions of the modelled PV/T system are as follows: the overall system measures 675 mm x 380 mm x 17.3 mm, the absorber plate has dimensions of 675 mm x 380 mm x 0.7 mm thickness, the serpentine is made of copper and is placed in a curved manner beneath the PV cells, and the pipe has an outer diameter of 10 mm, an inner diameter of 8 mm, and a total length of 280 cm.

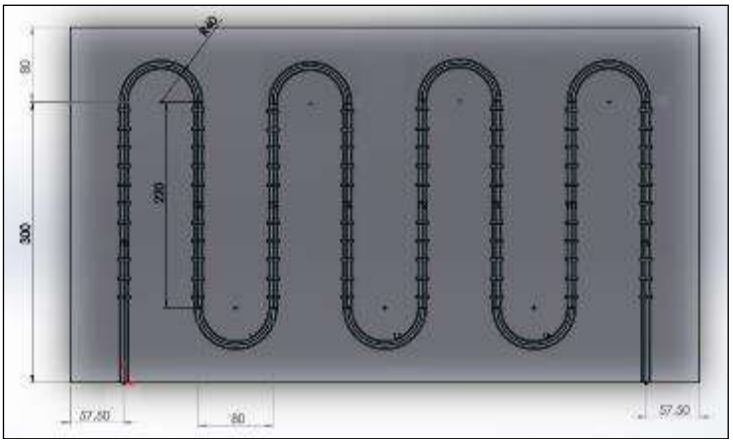

Fig. 1: Dimensions of the serpentine

In this study, different mesh types were employed for various layers. Tetrahedral mesh structures were used for the solid components, while hexahedral mesh structures were utilized for the confined air. For the mesh structure of the working fluid and the pipe, tetrahedral mesh was also employed.
Since this study includes two different serpentine geometries (straight and finned), there are two distinct mesh structures. In the straight geometry, there are 1507318 mesh elements, whereas in the finned geometry, there are 2194180 mesh elements.

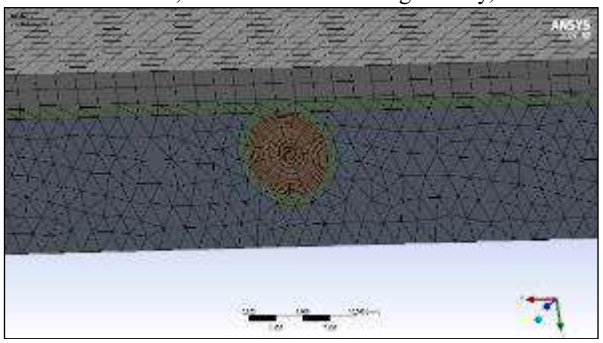

Fig. 2: Mesh

The computational fluid dynamics (CFD) analyses in the study were conducted using the ANSYS FLUENT module. To examine the thermal performance of PV/T systems, steady-state conditions, which are independent of time, were assumed. Temperature-dependent energy equations were activated, and the analysis was carried out considering incompressible flow (constant density). In the current study, the SST k-epsilon turbulence model was chosen. The concentration of nanofluids was set at 0.5% by mass, as

it is commonly regarded as the most effective concentration in the literature. (Sachit and Rosli, 2018)

III. Analysis

The efficiency of the first law of thermodynamics is a measure of the amount of energy that can be extracted from an energy source by a specific device. The overall efficiency (η_{pvt}) of a flat PV/T system is equal to the ratio of output energy to input energy over a specific period of time.

$$\eta_{pvt} = \frac{\dot{E}_{out}}{\dot{E}_{in}} = \frac{\dot{Q}_u + \dot{E}_{el}}{\dot{E}_{in}} \tag{1}$$

Therefore, the overall efficiency of a flat PV/T collector is the sum of its thermal and electrical efficiencies (η_{th} and η_{el}, respectively), and it can be expressed as follows:

$$\eta_{pvt} = \frac{\dot{Q}_u}{\dot{E}_{in}} + r * \frac{\dot{E}_{el}}{\dot{E}_{in}} = \eta_{th} + r * \eta_{el} \tag{2}$$

Here, r is the packing factor, defined as the ratio of the PV area (A_{pv}) to the collector area (A_c). When r = 0, it means there are no PV cells, and when r = 1, it means the entire collector area is covered by PV cells.

$$r = \frac{A_{pv}}{A_c} \tag{3}$$

Based on these equations, the thermal efficiency of the system can be expressed as follows:

$$\eta_{th} = \frac{\dot{Q}_u}{\dot{E}_{in}} = \frac{\left[\dot{m}_{liq} c_{p_{liq}} \left(T_{liq_{out}} - T_{liq_{in}}\right) + \dot{m}_{air} c_{p_{air}} \left(T_{air_{out}} - T_{air_{in}}\right)\right]}{I_{(t)} * A_C} \tag{4}$$

Exergetic efficiency is a parameter that measures the performance of a system under reversible conditions for the same final states. In other words, exergetic efficiency quantifies the quality of energy produced by the system. The overall exergetic efficiency of a flat PV/T panel represents the quality of energy obtained from the solar energy collected by the PV/T panel and can be expressed as follows (Alou, 2019):

$$\varepsilon_{pvt} = \frac{\dot{E}x_{out}}{\dot{E}x_{in}} \tag{5}$$

Here, $\dot{E}x_{in}$ represents the exergy output of the system, and $\dot{E}x_{in}$ represents the exergy input to the system. They can be expressed as follows:

$$\dot{E}x_{out} = I_o * V_o + \left\{ \begin{array}{l} \dot{m}_{liq} c_{p_{liq}} \left[\begin{array}{c} \left(T_{liq_{out}} - T_{liq_{in}}\right) - T_a \times \\ \ln\left(\frac{T_{liq_{out}}}{T_{liq_{in}}}\right) - R_{liq} \ln\left(\frac{P_{liq_{out}}}{P_{liq_{in}}}\right) \end{array} \right] \\ + \dot{m}_{air} c_{p_{air}} \left[\begin{array}{c} \left(T_{air_{out}} - T_{air_{in}}\right) - T_a \times \\ \ln\left(\frac{T_{air_{out}}}{T_{air_{in}}}\right) - R_{air} \ln\left(\frac{P_{air_{out}}}{P_{air_{in}}}\right) \end{array} \right] \end{array} \right\} \tag{6}$$

$$\dot{E}x_{in} = I_{(t)} * A_C \left[1 - \frac{4}{3}\left(\frac{T_a}{T_{sun}}\right) + \frac{1}{3}\left(\frac{T_a}{T_{sun}}\right)^4\right] \tag{7}$$

The equation (7) provides a way to calculate the exergy input to the system. Here, T_a represents the ambient temperature, and T_{sun} represents the surface temperature of the sun, both expressed in Kelvin units. The input exergy from solar radiation can be determined using Jeter's model (Jeter, 1981):

$$\dot{E}x_{sun} = \left[1 - \left(\frac{T_a}{T_{sun}}\right)\right] I_{(t)} \tag{8}$$

Here, T_{sun} is the surface temperature of the sun, which is 5777 K.

IV. Results and discussion

In the scope of this study, a design aimed at improving the efficiency of PV/T systems was developed and analyzed using the computational fluid dynamics approach. The analysis was conducted using the ANSYS FLUENT software on two different PV/T models.

Firstly, the selection of working fluids for this study was based on literature research, and the boundary conditions given in section 4 were applied to the analysis. In the PV/T models, forced air in parallel direction, at a constant speed, and at room conditions were applied as the working fluid, and this was incorporated into the analysis.

When the results were examined, the PV/T system using the finned serpentine achieved an average 10% increase in total thermal efficiency and an average 0.5% increase in total exergetic efficiency compared to the other design. Additionally, the MWCNT/water mixture outperformed both the graphene nanopelet/water mixture and water as the working fluid. The performance ranking of working fluids can be listed as follows from highest to lowest: MWCNT/water mixture, graphene nanopelet/water mixture, and water. Here, the MWCNT/water mixture showed an average 5% improvement in thermal efficiency and an average 0.4% improvement in exergetic efficiency compared to the graphene nanopelet/water mixture. This difference becomes more pronounced at higher working fluid velocities.

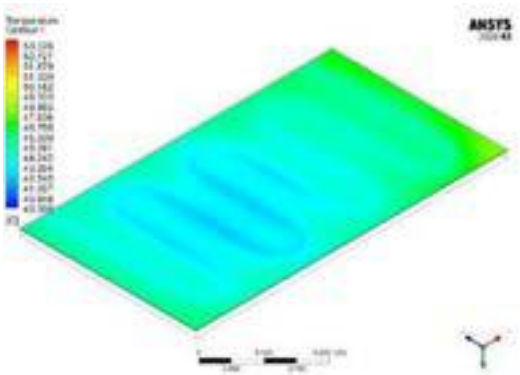

Fig. 3. The temperature distribution for the working fluid of MWCNT/water with a velocity of 5 m/s.

V. Conclusion

Studies in the literature primarily focus on comparing nanofluids used as working fluids in PV/T systems. In this study, a design difference was introduced, and its potential effects were analyzed using the computational fluid dynamics approach, and the results were compared. More complex designs can be created and analyzed in this regard, and these analyses can be validated experimentally. Additional working fluids for nanofluids can be explored. Within the scope of this study, experimental research can be conducted to validate the increase in efficiency.

Acknowledgements

I would like to express my deepest gratitude to my advisor, Prof. Dr. Süleyman KARSLİ, who has been a constant source of support and guidance throughout my master's education and academic journey, contributing significantly with his profound knowledge and expertise to the completion of this study.

References

Sachit F.A, Rosli M.A.M, Tamaldin N, Misha S, Abdullah A.L, 2018. “Nanofluids Used in Photovoltaic Thermal (PV/T) Systems: a Review” International Journal of Engineering and Technology 7(3.20):599-611

Fudholi A, Razali N.F.M, Ruslan M.H, Sopian K, 2020. “Application of Nanofluids for Photovoltaic Thermal (PVT) Collectors: A Review” Journal of Advanced Research in Fluid Mechanics and Thermal Sciences 74, Issue 1 (2020) 35-44 https://doi.org/10.37934/arfmts.74.1.3544

Alou S.A.M., (2019) “Experimental Investigation of Using MWCNT and Graphene Nanoplatelets Water-Based Nanofluids as Coolants in PVT Systems” Applied Thermal Engineering, https://doi.org/10.1016/j.applthermaleng.2019.114265

Jeter, S. M., 1981. "Maximum conversion efficiency for the utilization of direct solar radiation", Solar Energy, 26 (3): 231–236 https://doi.org/10.1016/0038-092X(81)90207-3

IEEES-014

Exergy-Based Performance Assessment of an Ejector-Enhanced Auto-Cascade Refrigeration Cycle

[1]İbrahim Karacayli, [2*]Lutfiye Altay, [3]Arif Hepbasli
[1]Ege University, Graduate School of Natural and Applied Sciences, 35100 Bornova, Izmir, Turkey
[2]Ege University, Faculty of Engineering, Department of Mechanical Engineering, 35100 Bornova, Izmir, Turkey
[3]Yasar University, Faculty of Engineering, Department of Energy Systems Engineering, 35100 Bornova, Izmir, Turkey
*E-mails: ibrahim.karacayli@ege.edu.tr, lutfiye.altay@ege.edu.tr, arif.hepbasli@yasar.edu.tr

Abstract

This study assesses the exergetic performance of a modified ejector-enhanced auto-cascade refrigeration (MEACR) cycle under various operating conditions and compares it with a conventional automatic cascade refrigeration (ACR) cycle. A parametric investigation is also conducted on the system basis for different vapor qualities at the condenser outlet and varying mass fractions of the low-boiling-component. The primary objective is to enhance exergy efficiency while simultaneously minimizing the total exergy destruction. To achieve these goals, the study employs strategies, such as reducing the vapor quality of the refrigerant at the evaporator inlet, maintaining a lowered condensing temperature of 20°C irrespective of high outdoor temperatures, and incorporating an ejector into the system. As a result of these measures, the exergy efficiency increases by 20.02% when the vapor quality at the condenser outlet is increased from 0.42 to 0.58. Additionally, a 5.5% improvement in the exergy efficiency is observed with raising the mass fraction of R170 from 42% to 58%. Moreover, the study records a notable enhancement, with an exergy destruction rate improvement of up to 88.94% compared to the ACR cycle. Moreover, the study records a remarkable improvement with an increase in exergy destruction rate up to 88.94% compared to the ACR cycle.

Keywords: Auto-cascade refrigeration, ejector, exergy destruction, exergy efficiency, sustainability index.

I. Introduction

Contrasted with cascade refrigeration systems employing multiple compressors, which are favored for low and ultra-low temperature applications, the ACR system operates with a single compressor (Llopis et al., 2023) and can achieve temperatures spanning from –40 °C to –160 °C (He et al., 2023). In recent years, theoretical and experimental research has been carried out to enhance the performance of the system by modifying the ARC cycle (Bai et al., 2021).

Tan et al. (2023a) proposed a component-based double-stage compression ACR cycle using R170/R600a to achieve an improved cooling performance at temperatures below –60 °C, at condensation temperatures of 26 °C and 40 °C. They compared this model with the performance of a conventional single-stage ACR cycle. Liu et al. (2022a) modified the ACR cycle with a self-recuperator and compared its performance with the conventional ACR cycle for R290/R170 and R600a/R1150 refrigerant mixtures, operating at condensing temperatures ranging from 28 °C to 36 °C and evaporation temperatures varying between –55 °C and –60 °C.

Li et al. (2023) modified the ACR cycle with vapor injection to achieve a better performance compared to conventional ACR cycles for condensing temperatures ranging from 25 °C to 45 °C and refrigeration applications below –80 °C. They compared various refrigerant mixtures, such as R1150/R290, R1150/R600a, and R1150/R600. In numerous studies, ejectors have been employed to minimize irreversibilities in expansion valves of ACR cycles. Liu et al. (2022b) developed an ejector-enhanced ACR cycle and compared its performance with both the conventional ACR and the previously developed ACR cycle with self-recuperator. Tan et al. (2023b) proposed a fractionated ACR cycle, utilizing R1150/R600a with a two-phase ejector for refrigerating processes at temperatures below –80 °C, with condensation temperatures of 30 °C and 45 °C.

In previous studies within the literature, reductions of condensing temperatures to 20°C in modeled ACR cycles were typically achieved either through lower ambient temperatures or by utilizing internal heat exchangers. However, a novel approach was adopted in this study. The modified ejector-assisted ACR cycle is retrofitted with a dual evaporator refrigerator (DER) which aims not only to reduce the condensing temperature but also to achieve the lowest possible vapor quality of the refrigerant at the evaporator inlet.

This study involves the calculation of exergy destruction rates and exergy efficiencies for the MEACR cycle, considering vapor quality at the condenser outlet ranging from 0.42 to 0.58 and R170 mass fractions varying from 42% to 58%. These results are then compared with the exergetic performance of the ACR cycle.

II. System description

The MEACR cycle illustrated in Fig. 1 is designed to operate with R170/R290 and consists of various components, namely a compressor (I), an air-cooled heat exchanger (AHE) (II), a condenser (III), a separator (IV), an ejector (V), a cascade heat exchanger (CHE) (VI), an internal heat exchanger (IHE) (VII), three expansion valves (EV1, EV2, and EV3), an evaporator (IX), an auxiliary condenser (X), and an auxiliary compressor (XI). During operation, the compressor significantly elevates the temperature by increasing the pressure of the refrigerant mixture. AHE (II) reduces the temperature of the refrigerant mixture, and condensation occurs in the condenser at temperatures lower than the ambient temperature. The condensed mixture is separated in the separator into high and low-boiling-point components. The temperature of the low-boiling-point component is further reduced by the CHE and IHE to reach the compressed liquid phase. The low-boiling-point component is then expanded through EV-1 and enters the evaporator to undergo the cooling process. The ejector draws in the high-boiling-point component from the separator and the low-boiling-point component from the evaporator, passing through the CHE to reach the superheated vapor phase before being drawn

into the compressor of the main cycle.

In the main cycle, heat is extracted from the condenser and CHE using the DER with R1234yf. The auxiliary condenser condenses the refrigerant after compression by the auxiliary compressor. EV-2 and 3 subsequently reduce the compressed liquid refrigerant to the required pressures for the condenser and CHE.

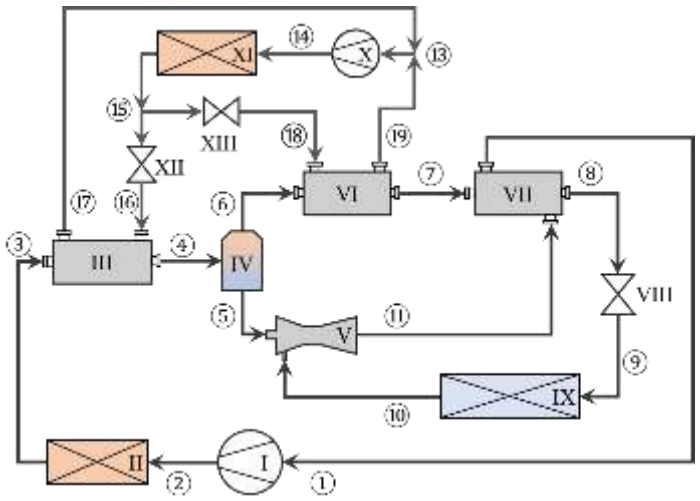

I	Compressor
II	AHE
III	Condenser
IV	Separator
V	Ejector
VI	CHE
VII	IHE
VIII	EV-1
IX	Evaporator

Fig. 1: Schematic diagram of the MEACR cycle

III. Exergy analysis

The energy and exergy balances under steady-state conditions are written as follows:

$$\dot{Q}_{net,in} + \sum(\dot{m}h)_{in} = \dot{W}_{net,out} + \sum(\dot{m}h)_{out} \quad (1)$$

$$\sum \dot{E}x_{in} = \sum \dot{E}x_{out} + \dot{E}x_D \quad (2)$$

where $\dot{Q}_{net}$ is the net heat transfer rate (kW), $\dot{W}_{net}$ is the net work transfer rate (kW), h is the specific enthalpy (kJ/kg), $\dot{m}$ is mass flow rate (kg/s) and $\dot{E}x$ is the exergy rate (kW) while the subscripts 'in', 'out', and 'D' stand for the into the system, from the system and destruction, respectively.

Total exergy destruction rate within the MEACR cycle is calculated as

$$\dot{E}x_D = \dot{Q}_{evp}\left(1 - \frac{T_o}{T_R}\right) + \dot{W}_{comp} + \dot{W}_{pump} \quad (3)$$

where T_o and T_R are ambient and refrigerated space temperatures (°C), respectively while the subscripts 'evp', 'comp', and 'pump' stand for evaporator, condenser, and pump, respectively. The exergy efficiency of the MEACR cycle can be expressed as (Dincer and Rosen, 2015)

$$\eta_{ex} = 1 - \frac{\dot{E}x_D}{\dot{W}_{comp} + \dot{W}_{pump}} \quad (4)$$

The sustainability index (SI) is utilized to assess the effectiveness of converting resources into valuable outputs (Canpolat Tosun et al., 2023) and is computed as follows:

$$SI = \frac{\eta_{ex}}{1 - \eta_{ex}} \quad (5)$$

IV. Results and discussion

The exergy destruction rates in the components of the MEACR and ACR cycles, both operating with a vapor quality of 0.58 and a mass fraction of 54% for the low-boiling-component, are shown in Fig. 2. Notably, the compressor, where the highest exergy destruction occurs, exhibits a substantial difference in exergy destruction rates between the MEACR and ACR cycles. Specifically, in the MEACR cycle, the exergy destruction rate in the compressor is 0.342 kW, representing an 89.4% reduction compared to the ACR cycle. Furthermore, when comparing the exergy destruction rate in the expansion valve, the ACR cycle registers an exergy destruction rate of 0.891 kW whereas the MEACR cycle, utilizing the ejector instead of the expansion valve, has resulted in a significantly lower exergy destruction rate of 0.091 kW. This change indicates a notable reduction in the total exergy destruction in the MEACR cycle, which decreases to 0.342 kW, representing an 88.94% reduction compared to the ACR cycle.

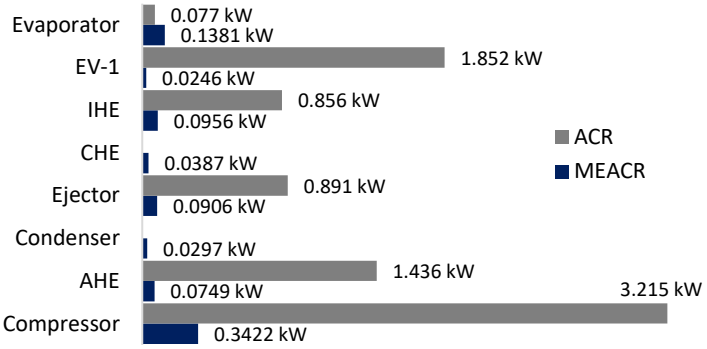

Fig. 2: Exergy destruction rates in the components of the MEACR and ACR cycles

Fig. 3 illustrates the variation of exergy efficiency, exergy destruction rate, and sustainability indices for the MEACR and ACR cycles in relation to the vapor quality at the condenser, specifically for a 54% mass fraction of R170. In the MEACR cycle, the exergy destruction rate exhibits a range of variability, spanning from 1.194 kW to 0.932 kW. This represents a substantial reduction ranging from 73.80% to 88.94% in comparison to the ACR cycle. Particularly, remarkable improvements were observed at the condenser outlet where the vapor quality was0.58, with a 570.7% increase in exergy efficiency and a sustainability index reaching 804.03%.

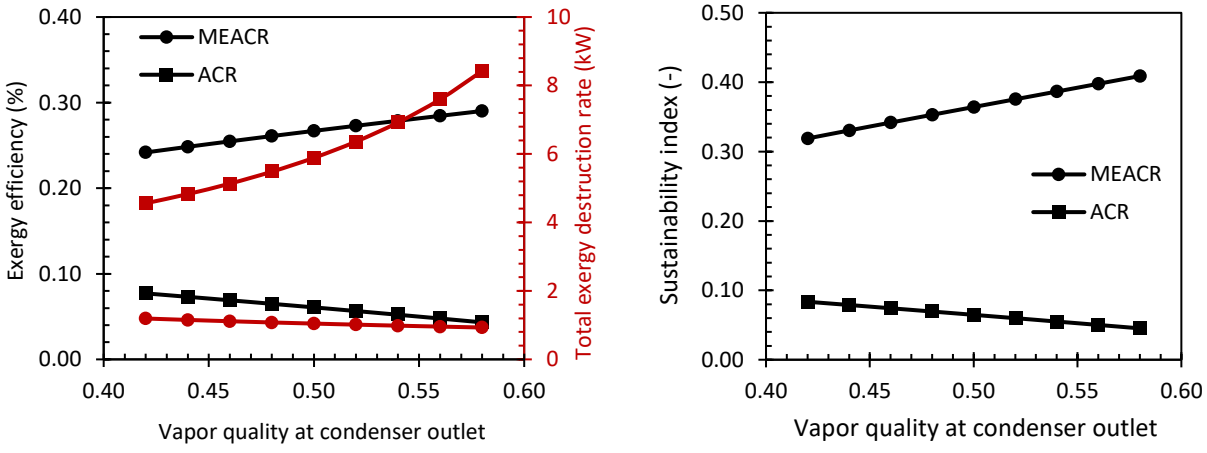

(a) (b)

Fig. 3: Effect of vapor quality at the condenser outlet on (a) exergy efficiency, total exergy destruction rate and (b) sustainability index

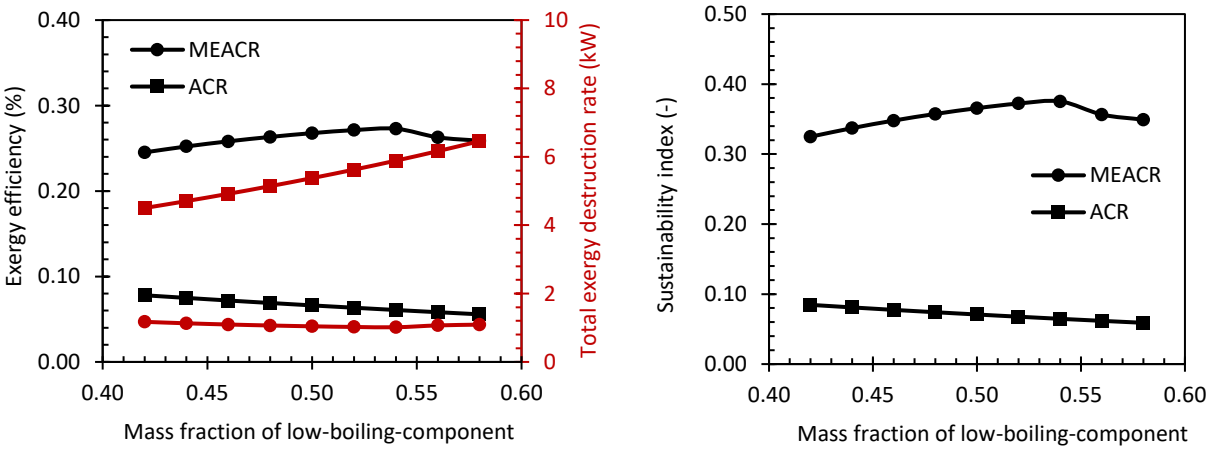

Fig. 4: Effect of mass fraction of low-boiling-component on (a) exergy efficiency, total exergy destruction rate and (b) sustainability index

(a)

(b)

Fig. 4 depicts the variation of exergy efficiency, exergy destruction rate, and sustainability indices for the MEACR and ACR cycles as a function of the mass fraction of the low-boiling-component, with a fixed vapor quality of 0.50 at the condenser outlet. When the mass fraction of R170 is increased from 42% to 58%, notable trends emerge in the ACR and MEACR cycles. In the ACR cycle, the exergy destruction rate increases by 43.5%. Conversely, in the MEACR cycle, there is a 7.0% decrease in the exergy destruction rate. Additionally, there is a 5.5% increase in the exergy efficiency.

V. Conclusion

At an outdoor ambient temperature of 35°C, the study conducted an exergy analysis of the MEACR cycle, considering vapor quality at the condenser outlet ranging from 0.42 to 0.58 and R170 mass fractions between 42% and 58%. These results were then compared to the exergetic performance of the ACR cycle, leading to the following findings:

1. As the vapor quality increased from 0.42 to 0.58 at 54% R170 mass fraction, a notable reduction of 22.0% in the total exergy destruction rate occurred. Simultaneously, there was a substantial increase in the exergy efficiency by 20.02% and a significant enhancement in the sustainability index by 28.21%.
2. When the vapor quality at the condenser outlet was maintained at 0.50, increasing the mass fraction of R170 from 42% to 58% resulted in a 6.96% reduction in the total exergy destruction rate. Furthermore, there was a 5.54% increase in the exergy efficiency and a 7.48% improvement in the sustainability index.
3. In comparison to the ACR cycle, the MEACR cycle exhibited remarkable benefits, reducing the exergy destruction by up to 88.94% and increasing the exergy efficiency by a factor of 4.65.

These results highlight the significant improvements achieved by the MEACR cycle in terms of exergetic performance and sustainability when compared to the conventional ACR cycle.

Acknowledgements
The authors would like to thank the Turkish Academy of Sciences (TUBA) for the financial support given.

References

Bai, T., Xie, H., Liu, S., Yan, G., Yu, J., 2021. Experimental investigation on the influence of ejector geometry on the pull-down performance of an ejector-enhanced auto-cascade low-temperature freezer. Int. J. Refrig. 131, 41–50. https://doi.org/10.1016/J.IJREFRIG.2021.08.021

Canpolat Tosun, D., Açıkkalp, E., Altuntas, O., Hepbasli, A., Palmero-Marrero, A.I., Borge-Diez, D., 2023. Dynamic performance and sustainability assessment of a PV driven Carnot battery. Energy 278, 127769. https://doi.org/10.1016/J.ENERGY.2023.127769

Dincer, I., Rosen, M.A., 2015. Exergy Analysis of Heating, Refrigerating and Air Conditioning: Methods and Applications. Exergy Anal. Heating, Refrig. Air Cond. Methods Appl. 1–387. https://doi.org/10.1016/C2013-0-06800-4

He, Y., Wu, H., Xu, K., Zhang, Y., Wang, T., Wu, X., Cheng, C., Jin, T., 2023. Theoretical performance comparison for a regenerator-enhanced three-stage auto-cascade refrigeration system using different zeotropic mixed refrigerants. Energy Build. 283, 112815. https://doi.org/10.1016/J.ENBUILD.2023.112815

Li, D., Bai, T., Yu, J., 2023. Thermodynamic performance optimization and analysis of an auto-cascade refrigeration cycle with vapor injection for ultra-low temperature freezer. Int. J. Refrig. 145, 425–435.

Liu, J., Liu, Y., Yan, G., Yu, J., 2022a. Thermodynamic analysis on a modified auto-cascade refrigeration cycle with a self-recuperator. Int. J. Refrig. 137, 117–128. https://doi.org/https://doi.org/10.1016/j.ijrefrig.2022.02.012

Liu, J., Liu, Y., Yu, J., Yan, G., 2022b. Thermodynamic analysis of a novel ejector-enhanced auto-cascade refrigeration cycle. Appl. Therm. Eng. 200, 1359–4311. https://doi.org/10.1016/J.APPLTHERMALENG.2021.117636

Llopis, R., Martínez-Ángeles, M., García-Valero, M., 2023. A novel method to measure the energy efficiency and performance of an auto-cascade refrigeration cycle. Appl. Therm. Eng. 233, 121146. https://doi.org/10.1016/J.APPLTHERMALENG.2023.121146

Tan, Y., Yuan, J., Wang, L., Li, X., Wang, Z., Liang, K., 2023a. Proposal and performance study on a component-based double-stage compression auto-cascade refrigeration cycle. Energy Convers. Manag. 276, 116566. https://doi.org/10.1016/J.ENCONMAN.2022.116566

Tan, Y., Li, X., Wang, L., Huang, L., Xiao, Y., Wang, Z., Li, S., 2023b. Thermodynamic performance of the fractionated auto-cascade refrigeration cycle coupled with two-phase ejector using R1150/R600a at −80 °C temperature level. Energy 281, 128328. https://doi.org/10.1016/J.ENERGY.2023.128328

IEEES-015

Effects of H_2 admixture on RCCI combustion dual-fuel marine engines: A model-based study

[1*]Aneesh Vasudev, [1]Maciej Mikulski, [3]Jari Hyvönen
[1]University of Vaasa, School of Technology and Innovations, Energy Technology, Wolffintie 32, Vaasa, FI-65200, Finland
[2]Wärtsilä Finland Oy, Teollisuuskatu 1, Vaasa, FI-65170, Finland
*E-mail: aneeshvasudev@uwasa.fi

Abstract

Besides favoring carbon dioxide (CO_2) reduction, Hydrogen (H_2) admixture in conventional combustion engines shows benefit of improved performance in terms of reduced specific energy consumption and lowered emissions. With combustion engines forecasted to play an integral role towards decarbonization, low-temperature combustion strategy of RCCI (reactivity-controlled compression ignition) has emerged as a proven technology for next generation clean and efficient combustion engines. Being a dual-fuel concept, demonstrators show RCCI achieving indicated efficiencies crossing 50% and emissions well below the stringent EURO VI norms without aftertreatment devices. As such, significant unexplored potential lies in H_2 blending within RCCI engines. To this end, the present work conducts a model-based exploration of the simultaneous and interactive combustion of 3 fuels, wherein H_2 and methane are admitted premixed with fresh air into the combustion chamber. Pilot injected diesel like fuel aids the auto-ignition of the charge mixture. A validated chemical-kinetics based multizone model (MZM) is used to perform the investigations to real world engine operating conditions. The in-house developed model is therefore, physics-based and performance-oriented, enabling predictive simulations within 5% error margin to equivalent CFD results, but at a fraction of the simulation time (3 minutes). The baseline platform is a single cylinder large-bore research engine operating on natural gas and diesel in RCCI combustion mode. Considering durability limits of peak cylinder pressure and pressure rise rate, the study demonstrates an improvement in combustion performance in terms of combustion phasing with peak indicated thermal efficiency reaching 55% for part and low-load operation. The decrease in unburnt hydrocarbon emissions is nearly twice the observed increase in nitrogen oxides , for H_2 blending limited to 25% on energy basis. Furthermore, a reduction in CO_2 emissions is observed by 2.22 g/kWh per percentage point energy-based blending of H_2.

Keywords: Low-temperature combustion, hydrogen, RCCI, multizone-model

I. Introduction

Hydrogen (H_2) is observing a growing need in the energy domain driven by its utilization in the hard-to-electrify sectors such as the maritime industry. Given that routes typically extend beyond 6000 nautical miles between fuelling stops, this sector is reliant on CI engines still powered ~65% (Aakko-Saksa *et al.*, 2023) by tar-like, heavy fuel oil. However, in search of cleaner alternatives, natural gas has gained momentum in recent decades. Against this backdrop, a clear potential exists in utilizing H_2, at least in admixed form, to reduce carbon intensity but also improve the uptake of this resource.

Studies show that H_2 addition in conventional CI and gasoline engines improves performance by enhancing burning rate, improving the range of lean burning ability. and decreasing cyclic combustion variations (Karagöz *et al.*, 2015; Yu *et al.*, 2017). Also, it enhances thermal efficiency and reduces the UHC/soot and CO_2 emissions. In low temperature combustion concepts, H_2 blending with low octane fuels retards combustion phasing, as in dimethyl ether (Guo & Neill, 2013; Shudo *et al.*, 2003) and for high octane fuels like natural gas, H_2 advances combustion phasing (Bastawissi *et al.*, 2010). Importantly, higher blending rates of H_2 is limited by the maximum pressure rise rate (PRR_{max}) and shortened operating window (Saxena & Maurya, 2023).

Among, natural gas (NG) engines, dual-fuel reactivity controlled compression ignition (RCCI) has emerged as proven technology to simultaneously achieve ultra-low emissions, well below the stringent EURO VI norms (Doosje *et al.*, 2014) (without aftertreatment devices), and improved thermal efficiency, over 4 percentage points (pp) above contemporary commercial technologies (Hanson *et al.*, 2016). With the focus of this research on the influence of H_2 blending on RCCI engines, the investigations are conducted by employing a recently developed (Vasudev *et al.*, 2022) physics-based, performance-oriented combustion model. Specifically, it is chemical-kinetics based multi-zone model, validated for natural-gas and diesel fuelled RCCI marine engine (Kakoee *et al.*, 2023).

Therefore, using H_2 admixtures with the NG as the low-reactivity fuel stream, and in combination with diesel as the high-reactivity fuel, this model-based study focuses on the influence on RCCI combustion performance under fixed (total) fuel energy, with respect to (1) heat release characteristics (2) Engine performance indicators (3) Durability limitations of peak pressure and PRR_{max} (4) emissions of unburnt hydrocarbons and NO_X

II. Methodology

The research is based on a single cylinder marine engine following the geometry of the commercial Wärtsilä W31 dual-fuel (DF) platform. The engine is operated in RCCI mode wherein the low reactivity fuel (LRF) is port-fuel injected, followed by direct injection of high reactivity fuel (HRF). Further details on the setup ca\n found in (Åstrand *et al.*, 2016; Jay, 2016). Two steady-state operating points (Cases A and B in Table 2) are considered as the RCCI representative baseline conditions. The test fuels used under the baseline operation is NG with methane number 80 as LRF, and ISO standard light fuel oil (LFO) as the HRF. The volume ratio of the two fuels is presented along with the total air to fuel ratio (AFR). The measurement data include crank angle resolved (0.2 ^{0}CA) cylinder pressure signal and pressure within the ducts upstream and downstream of the combustion chamber. The data is further postprocessed to obtain performance indicators such as indicated mean effective pressure, heat release trace and crank angle of X% mass burned (CAX).

Table 2. Simulation conditions

Test Engine	Wärtsilä 31DF | Displacement 34.45L | Bore/Stroke 1.39
Engine Speed	720 rpm
High reactivity fuel (HRF)	$nC_{12}H_{26}$ (ISO 8217 LFO) | Direct-injected
Low reactivity fuel (LRF)	Natural gas (MN=80) & H_2 | Port fuel injected
RCCI Reference Operating conditions	
Case A	25% load | $9.6x10^{-5}$ (v/v) HRF/LRF | 58 AFR
Case B	50% load | $2.1x10^{-4}$ (v/v) HRF/LRF | 58 AFR

Table 3 highlights the governing assumptions of the chemical-kinetics based combustion model referred to as University of Vaasa Advanced Thermo-kinetic multi-Zone (UVATZ) model. The reacting zones of the model are arranged in a fashion (

Fig. 1) to best capture the bulk in-cylinder thermal and fuel inhomogeneity, which dictate the heat release in RCCI engines. Furthermore, in-cylinder mixing by fluid motion is reflected by turbulence based interzonal exchange of heat and mass. Heat transfer at cylinder walls is modelled following the correlation of Chang et al (Chang *et al.*, 2004). The scheme by Yao et al. (Yao *et al.*, 2017) is used to represent the chemistry of diesel by $nC_{12}H_{26}$ and NG by CH_4 and C_2H_6. Modelling of (direct) diesel injection is simplified to imposing a predefined quantity of $nC_{12}H_{26}$ into each zone at the injection time, following a stratification profile processed from CFD results. Despite being fully physics-oriented, the model offers simulation speeds of less than 3minutes per cycle. The model has been validated against the NG-diesel RCCI operation (Vasudev *et al.*, 2022), wherein the pressure trace was predicted within an RMS error of 0.85bar and combustion performance indicators within 5% accuracy.

Table 3. Governing assumption of UVATZ model

Source code	C++ & Cantera (thermo-kinetic library)
Reaction mechanism	Yao et al. (Yao *et al.*, 2017)
Zonal configuration	12 zones (onion-skin, 2x boundary layer zone)
Interzonal mixing	turbulence-based, diffusive mixing
Wall heat loss	Chang et al. (Chang *et al.*, 2004); zone dependent
Simulation time	<3 min/cycle; desktop @Intel Core i5 8th gen
HRF stratification	generated from CFD simulations
Validation	Wärtsilä 31DF (NG-diesel) RCCI measurements; details in Vasudev et al. (Vasudev *et al.*, 2022)

Considering the chemical kinetics nature of the model, the widely validated scheme of Yao et al. (Yao *et al.*, 2017) includes the H_2/O_2 mechanism. Thus, with the research focused on trend-wise insights on the influence of H_2 admixture on RCCI performance, validity of UVATZ on baseline conditions is deemed sufficient for this study. To this end, H_2 is considered port-fuel injected, and along with NG forms the blended LRF. Based on cases A and B, H_2 is blended such that the total fuel energy input of the baseline operation is maintained. The parameter blend rate (BR) is used quantify, on energy basis, the amount of H_2 in the LRF mixture. Sweeps of BR: $0\% \leq BR \leq 25\%$ on cases A and B is performed, while fixing the other operating parameters at baseline. As such, for diesel injection, the HRF stratification profile from baseline is maintained. The simulations are performed over the closed part of the 4-stroke cycle. Accurate thermodynamic state at intake valve closing (IVC) including composition of residual burnt gas is obtained from a detailed 1-D air-path model (GT-Power) as elaborated in (Kakoee *et al.*, 2023).

At this point, it is worth noting that higher load points are excluded from the simulation cases in order to provide sufficient margin to conduct the research from the P_{max} and PRR_{max} limits of the engine. This is also the reason why BR is limited to 25%. Also worth noting that the model's validity on dual-fuel RCCI over a broader dataset, apart from cases A and B, has been demonstrated (Kakoee *et al.*, 2023).

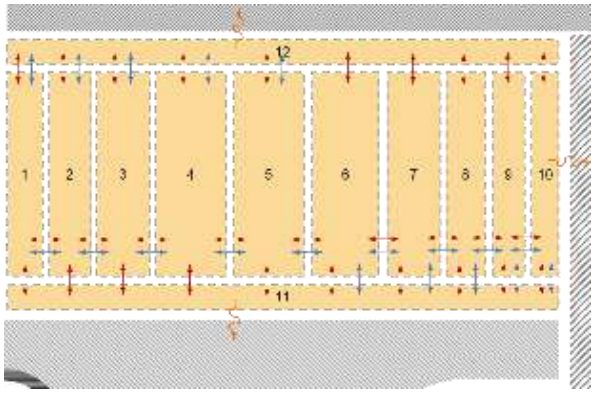

Fig. 1. Schematic of the UVATZ combustion model. Zones are represented by the orange boxes. Red arrows indicate heat flow and blue *arrows indicated mass transfer*

III. Results

Model validation on NG-diesel (baseline) RCCI measurements

Validity of UVATZ in predicting combustion performance of baseline NG-diesel fuelled RCCI operation is demonstrated first. This establishes the backdrop for the model's capability to predict H_2 blended RCCI performance.

Fig. 2a. shows the calibrated HRF distribution imposed across the zones at the moment of fuel injection. The resulting predictions by the model for cases A and B (

Fig. 2b) is synthesized by the performance parameters. Prediction of heat release rate is characterized by combustion phasing parameters (CA10 and CA50) and net heat released (NHR). Peak pressure (Pmax) and gross indicated mean effective pressure directly quantify the predicted pressure trace. Results show the relative error of model predictions against measurement data, which are within a 5% error margin, sufficient for most of practical applications. Although the validation discussion here is terse, a complete account is provided in the previous works by the authors (Kakoee *et al.*, 2023; Vasudev *et al.*, 2022).

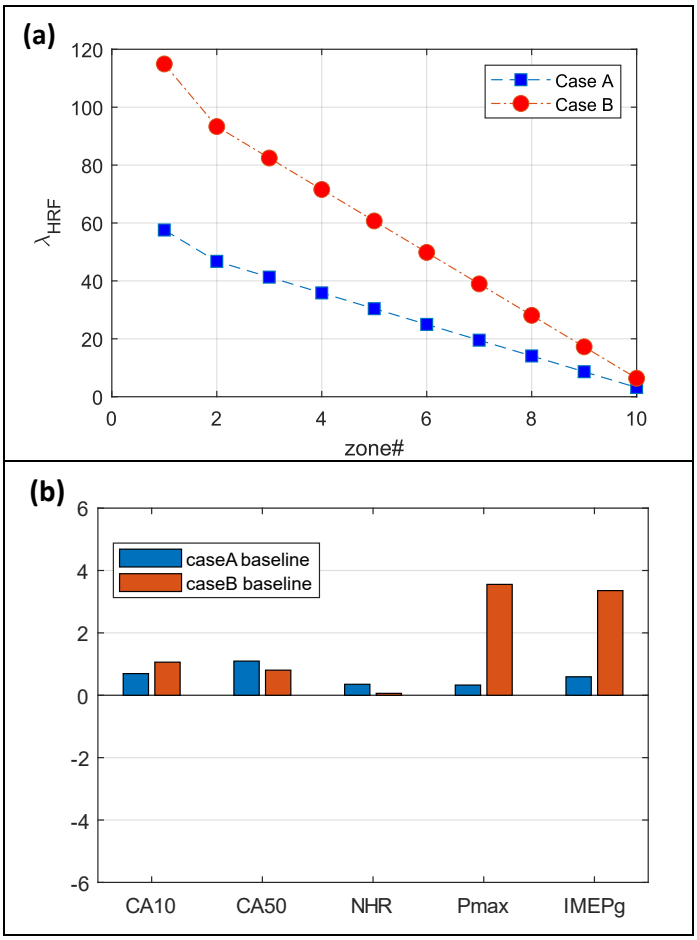

Fig. 2. (a) HRF stratification profile imposed across the zones. (b) Prediction results for baseline conditions for cases A and B

RCCI performance with H_2 blending

Compared to baseline operation of case A (0% BR), H_2 invigorates the combustion rate observed by the steeper rise in temperature and heat release, illustrated in Figure 6. The increase in peak temperature is an understandable behaviour since H_2 increases the high temperature combustion chain branching reaction rates. Further insight on heat release can be obtained from the top plot of Figure 7. The burn duration decreases with BR which is in line with the previous observations (Bastawissi *et al.*, 2010; Guo & Neill, 2013). Although CA10 and CA50 (not shown explicitly in the figures) display relatively minor sensitivity, CA50 advanced with BR, whereas CA10 retarded. Importantly, the retarding trend was stronger in case A where the share of HRF is larger. This is because H_2 influence on high octane fuels like NG advances combustion phasing (Bastawissi *et al.*, 2010; Guo & Neill, 2013).

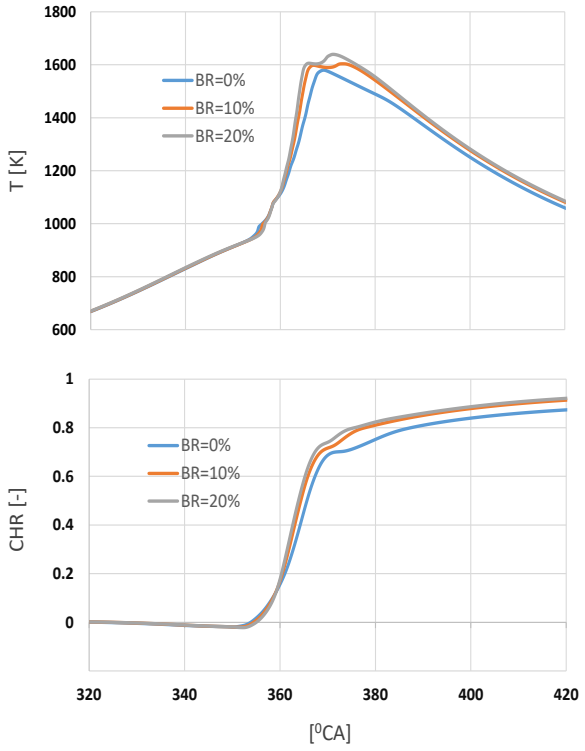

Figure 6. In-cylinder temperature and cumulative heat release (CHR) normalized to total fuel energy at different BR on case A conditions.

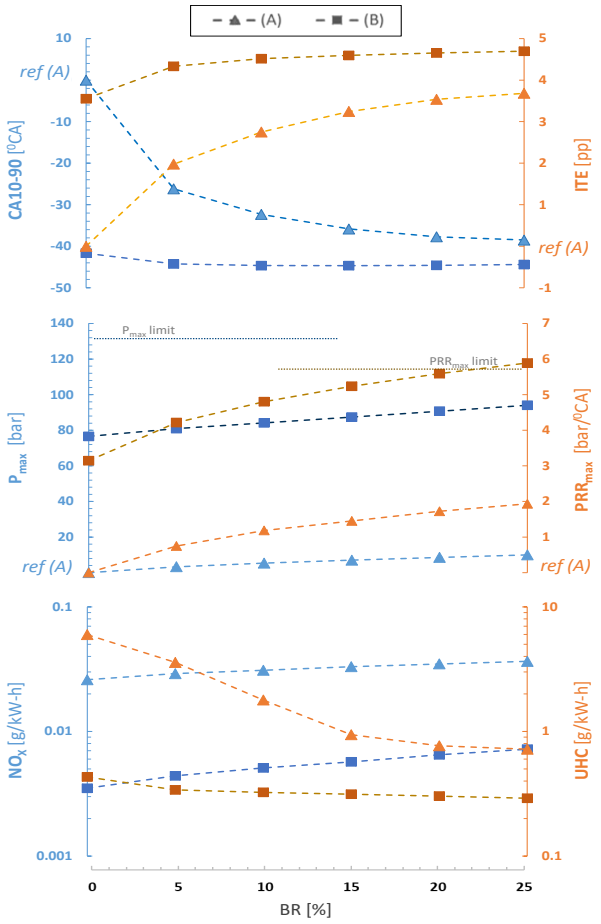

Figure 7. Burn duration and ITE (top), P_{max} and PRR_{max} (middle), NO_X and UHC emissions (bottom). Data, i.e., y-axis for top and middle plot is shown with respect to baseline condition of case A as ref(A)

Understandably, P_{max} and PRR_{max} increase with BR and the trend is approximately 0.4bar per pp BR change and 0.1bar/^{0}CA per pp BR change respectively. While P_{max} values are within the material limits in the explored BR range, the PRR_{max} for case B, reaches durability limit at BR=20%. However, it is worth exercising caution when interpreting results of P_{max} and PRR_{max}, since these quantities are typically overestimated by the MZM. This is a characteristic of the model since its sequentially autoigniting zones cause sharp, step-wise increase in thermodynamic state. This manifests itself, for instance, in the kink observed in the temperature trace (Figure 6) for 20% BR near peak value. This occurrence is coupled with the fact that combustion phasing advances with BR, where peak approaches TDC. Still, the trends observed in combustion performance is valid, as it matches with reported observations from literature (Bastawissi *et al.*, 2010; Guo & Neill, 2013; Kongsereeparp & Checkel, 2007).

Owing to improved combustion performance, indicated thermal efficiency (ITE) increases, shown in the top plot of Figure 7. The increase is nearly 0.3pp per pp increase in BR for case A, but levels off at high BR levels. This effect is more starkly observed for case B, where the ITE of baseline is already quite high, and eventually saturates near 55%. Correspondingly, it can be reported that the indicated specific fuel combustion (ISFC) decreases, at an average rate of 0.85 g/kWh per pp BR increase. Emissions of unburnt hydrocarbons (UHC) reduce, at a rate of 0.25g/kWh per pp increase in BR. While this is due to higher combustion temperatures, there is small penalty on NO_X emissions, which increases at a smaller rate of $4x10^{-4}$ g/kWh per pp BR change. Finally, due to the increasing substitution of hydrocarbon fuel with H_2 the CO_2 cylinder out emissions reduces nearly 2.22g/kWh per pp BR change.

IV. Conclusion and Outlook

This model-based study reveals the potential of hydrogen (H_2) enrichment in the context of natural gas-diesel marine engine working in Reactivity Controlled Compression Ignition (RCCI) mode. The findings are highlighted in the following conclusions:

- The indicated thermal efficiency is improved ≈5pp from baseline, approaching 55% for 20% blend rate (BR) of H_2. While similar improvements were observed for the mid-load case, it comes at the cost of operating near the knock-boundary. Furthermore, the difference in performance improvement over baseline operation decreases at higher loads
- The decrease in UHC emissions ≈0.5% with BR over baseline for low-load operation, while the increase in NO_X is ≈0.05%. However, for case B, the decrease in UHC is 0.03% on average, while the increase in NO_x is 0.13%.

Thus, the recommendation based on the current findings is that H_2 blending is beneficial for low- and part-load operation of the engine. The follow-up full-scope research based on this preliminary study, outlooks towards the following improvements:

- Regarding the model: the zone resolution will be reconsidered from 12 to 14 zones, to improve prediction (smoothness) of the pressure trace. This helps to determine P_{max} , PRR_{max} and emission prediction with greater degree of certainty. Furthermore, full cycle simulations will improve the IVC conditions especially in determining the composition of residual burnt gas (Yap *et al.*, 2004)
- Regarding methodology: the model predictions on H_2 admixtures will be validated with an experimental campaign on our research platform, where the already present NG pipeline allows for H_2 blending up to 9% on energy basis without risk of leakage.
- Regarding scope: H_2 blending in low temperature combustion concepts typically report lowered T_{IVC} requirement to achieve a target load. In combination with modulating combustion phasing (CA50) to a target value, the current investigation can be expanded to explore the resulting combustion performance
- Regarding insight: The full-scope research will include description on the fundamental reasons behind improved performance and emissions with H_2 blending

Acknowledgements

The work was conducted in the framework of the Clean Propulsion Technologies project ('Clean Propulsion Technology', 2021) with financial support in part from Business Finland (ref. 38485/31/2020). The authors would also like to acknowledge Ella and Georg Ehrnrooth foundation for graciously (17-12898-11) funding the research.

References

Aakko-Saksa P.T., Lehtoranta K., Kuittinen N., Järvinen A., Jalkanen J.-P., Johnson K., Jung H., Ntziachristos L., Gagné S., Takahashi C., Karjalainen P., Rönkkö T. & Timonen H. (2023). Reduction in greenhouse gas and other emissions from ship engines: Current trends and future options. Progress in Energy and Combustion Science 94: 101055. https://doi.org/10.1016/j.pecs.2022.101055.

Åstrand U., Aatola H. & Myllykoski J. (2016). Wärtsilä 31-world's most efficient fourstroke engine. In: 28th CIMAC world congress. Presented at the CIMAC Congress, Helsinki.

Bastawissi H., Yu-Sheng Z., Elkelawy M. & Bastawissi A. (2010). Detailed 3D-CFD/Chemistry of CNG-Hydrogen Blend in HCCI Engine. In: SAE Technical Paper. SAE. https://doi.org/10.4271/2010-01-0165.

Chang J., Güralp O., Filipi Z., Assanis D., Kuo T.-W., Najt P. & Rask R. (2004). New Heat Transfer Correlation for an HCCI Engine Derived from Measurements of Instantaneous Surface Heat Flux. SAE Transactions, Section 3: Journal of Engines 113: 1576–1593.

Clean Propulsion Technology (2021). In: Clean Propulsion. https://cleanpropulsion.org/ (accessed 12 August 2021).

Doosje E., Willems F. & Baert R. (2014). Experimental Demonstration of RCCI in Heavy-Duty Engines using Diesel and Natural Gas. https://doi.org/10.4271/2014-01-1318.

Guo H. & Neill W.S. (2013). The effect of hydrogen addition on combustion and emission characteristics of an n-heptane fuelled HCCI engine. International Journal of Hydrogen Energy 38 (26): 11429–11437. https://doi.org/10.1016/j.ijhydene.2013.06.084.

Hanson R., Ickes A. & Wallner T. (2016). Comparison of RCCI operation with and without EGR over the full operating map of a heavy-duty diesel engine. SAE, USA. https://doi.org/10.4271/2016-01-0794.

Jay D. (2016). CR development in the last decade in Wärtsilä. In: 28th CIMAC world congress. Presented at the CIMAC Congress, Helsinki.

Kakoee A., Vasudev A., Smulter B., Hyvönen J. & Mikulski M. (2023). A fully predictive 1-D modelling framework for reactivity-controlled compression ignition engine via chemistry based multi-zone model. In: SAE Technical Paper. Presented at the 16th International Conference on Engines & Vehicels, SAE. https://doi.org/10.4271/2023-24-0001.

Karagöz Y., Sandalcı T., Yüksek L. & Dalkılıç A.S. (2015). Engine performance and emission effects of diesel burns enriched by hydrogen on different engine loads. International Journal of Hydrogen Energy 40 (20): 6702–6713. https://doi.org/10.1016/j.ijhydene.2015.03.141.

Kongsereeparp P. & Checkel M.D. (2007). Investigating the Effects of Reformed Fuel Blending in a Methane- or n-Heptane-HCCI Engine Using a Multi-Zone Model. SAE International. https://doi.org/10.4271/2007-01-0205.

Saxena M.R. & Maurya R.K. (2023). Hydrogen Fueled Low-Temperature Combustion Engines. In: Tingas E.-Al. (ed.). Hydrogen for Future Thermal Engines. Springer International Publishing, Cham, p. 483–519. https://doi.org/10.1007/978-3-031-28412-0_13.

Shudo T., Ono Y. & Takahashi T. (2003). Ignition Control by DME-Reformed Gas in HCCI Combustion of DME. SAE Transactions 112: 1195–1202.

Vasudev A., Cafari A., Axelsson M., Mikulski M. & Hyvönen J. (2022). Towards Next Generation Control-Oriented Thermo-Kinetic Model for Reactivity Controlled Compression Ignition Marine Engines. Presented at the Powertrains, fuels & Lubricants, SAE, Cracow, Poland. https://doi.org/10.4271/2022-01-1033.

Yao T., Pei Y., Zhong B.-J., Som S., Lu T. & Luo K.H. (2017). A compact skeletal mechanism for n-dodecane with optimized semi-global low-temperature chemistry for diesel engine simulations. Fuel 191: 339–349. https://doi.org/10.1016/j.fuel.2016.11.083.

Yap D., Megaritis A., Peucheret S., Wyszynski M.L. & Xu H. (2004). Effect of Hydrogen Addition on Natural Gas HCCI Combustion. SAE Transactions 113: 1296–1305.

Yu X., Du Y., Sun P., Liu L., Wu H. & Zuo X. (2017). Effects of hydrogen direct injection strategy on characteristics of lean-burn hydrogen–gasoline engines. Fuel 208: 602–611. https://doi.org/10.1016/j.fuel.2017.07.059.

IEEES-016

The Management of Electrical and Thermal Energy in a House at Different Climates Algeria

[1*]Mezidi Ahmed, [1] Tassoult Houda, [1] Bendjebbas Hicham.
[1]Solar Equipements Development Unit, UDES/CDER, National road N°11, BP 386, Bou-Ismail, 42415, Tipaza, Algeria.
*E-mails: mazidiahmed@yahoo.fr
tassoulthouda@yahoo.fr
hbendjebbas@gmail.com

Abstract

This paper discusses the status of energy consumption in a house, in the four main energy consuming seasons: Autumn, winter, spring and summer. The aim of this study is to determine the energy needs of a house taking into account both the architectural aspect and the materials used in its construction, as well as the optimization of energy to meet the needs of the occupants of house. The selection of the site will focus on various Algerian climates, in the north, in the highlands and in the south. Optimizing thermal insulation is crucial to ensuring energy efficiency, rational consumption, and consideration of bioclimatic architecture parameters during its design. To address this issue, renewable energy sources are being consideredhort

Keywords: Energy efficiency; thermal insulation; rational consumption; energy consumption.

I. Introduction

Global increase in the number of population leads to greater energy consumption. As a result, there is a lack of resources, especially energy. It is estimated that the global energy consumption is likely to grow faster than the population growth in the next 15–20 years and 80% of the energy supply is provided by fossil fuels. These resources are not unlimited (Key World Energy Statistics, 2021). The growth in global energy demand increases the consumption of fossil fuels, as well as the negative effects of climate change caused by the emission of greenhouse gases (Ministry of Energy (Algeria), 2018). However, find other means of satisfying energy needs is a challenge. Indeed, reducing energy consumption is essential to reduce the environmental impact of our activities through the integration of rational energy consumption in houses. The energy needs of a house depend on several factors such as its geographical location, thermal insulation, electrical and thermal equipment, as well as the occupant's lifestyle. Reducing energy consumption have several benefits such as reducing GHG (Greenhouse gas) emissions, leading to savings on household energy factors which can improve their quality of life. Specialists recommend more advantages to turn to renewable energies (Boudiaf and Meddi, 2021). Therefore, an analytic study of the problem is required in order to minimize energy consumption. This paper is organized as follows: after this section, section 2 presents the geographical characteristics of Algeria and their effects on energy needs, of which we divided the Algerian territory into three zones, which are the North, the High Plateaus and the South. In section 3, the mathematical models applied were highlighted in order to size the seasonal energy needs relating to each region following by interpretation of all results obtained. Finally, as solution, we proposed the integration of renewable energies to meet energy needs.

II. Study of the geographical characteristics of Algeria

Text Geographically, Algeria represents: the northern region bordered by the Mediterranean Sea and the Atlas Mountains to the south. The climate in Northern Algeria is Mediterranean, with hot summers and mild, wet winters. The High Plateaus region is situated in the central part of the country, with an average elevation of 800 to 1200 meters. This region covers a large part of Algeria and includes the states of Médéa, Bouira, Tizi Ouzou, Béjaïa, Batna, Sétif, M'sila, Tiaret, Chlef and Tlemcen. For the southern part, a geographic zone includes the states of Tamanrasset, Illizi, Adrar, Tindouf, Bechar, El Bayadh, Naâma and El Oued. This region mainly consists of the Sahara desert, which is characterized by an arid climate with extreme temperatures, low rainfall, and a wide variation in daytime temperatures. Winds can be strong, particularly during sandstorms. The climatic data for Algeria in terms of the four seasons of the year are presented in the following table. 1 (J Ritterbush, 2006), (https://en.climate-data.org).

· Table 1 geographical characteristics of Algeria

Seasons	Mean temperatures, (°C)	Mean precipitation (mm/month)	Mean wind speed (km/h)
North Algeria			
Autumn	20-25	60-120	10-15
Winter	10-15	100-200	9-15
Spring	18-23	90-120	9-15
Summer	25 - 35	Very low, often less than 10	9-15
High plateaus Algeria			
Autumn	15-20	50-60	10-15
Winter	5-15	100-200	10-20
Spring	15-20	50-60	10-15
Summer	25-30	5-15	15-25

South Algeria			
Autumn	10-15 but reach 25 during the day	5-10	15-20
Winter	25-30	3-5	10-15
Spring	25-30	3-5	10-15
Summer	30-40 often exceeding 45.	Precipitation is very rare, but some thunderstorms can occur in the Saharan ATLAS Mountains between 3-5	Hot, dry winds from the Sahara often blow during this season; they can be strong, especially during sandstorms.

Energy of a house

The energy needs of a house depend on several factors such as the size, layout of the house, the climate, the orientation of the house in relation to the sun, the quality of the insulation and the quantity of energy required in order to ensure the proper functioning of the various equipment and systems. The rational energy sizing of a house makes it possible to determine the useful and necessary energy.

Type of energy in a house

- Electrical energy is a form of energy that is produced from different sources such as nuclear, thermal, hydraulic, and solar or wind power plants.
- Thermal energy is a form of energy that appears in the form of heat. It is mainly used to heat and cool houses or as hot water and the thermal insulation is a process that aims to control heat transfer between two surfaces that have a different temperature and reduce heat loss by using construction materials with low thermal conductivity. Thermal insulation is important for improving the energy efficiency of houses.

III. Mathematical Models

For the calculation of thermal energy, one of the most used formulas is the following (Guruprasad and all, 2017)

$$Q = m \cdot c_p \cdot \Delta T \quad (1)$$

Where Q is thermal energy (J), m is the mass of the substance (kg), and ΔT is change in temperature of the substance (°C).

For the calculation of electrical energy, one of the most used formulas is the following (Kondoh and all, 2000):

$$EC = P \times t \quad (2)$$

Where *EC* is Electrical, energy consumed (J), *P* is the Electrical power of the device (W) and *t* is the length of time the device (s).

For the energy produced EP, the law of the energy produced is equal to the energy consumed (EC) plus the energy consumed (EC) multiplied by the losses, in this case the losses are 25%. Mathematically, this can be expressed by the following formula:

$$EP = EC + 0.25(EC) \quad (3)$$

Where EP is Produced electrical energy (J), EC is electrical energy consumed [J] and 25% is percentage of losses.

IV. Results and discussions

A. Useful Energy of a Periodic (Seasons) House

The gross energy produce in Algeria depicted in figure .1. The chart characterized by strong consumption growth in summer. While, a notable consumption registered in spring, in autumn and winter, the gross consumption is is convergent. The most important factors influencing energy consumption trends are the economic growth, population, heating demand, household characteristics and energy prices.

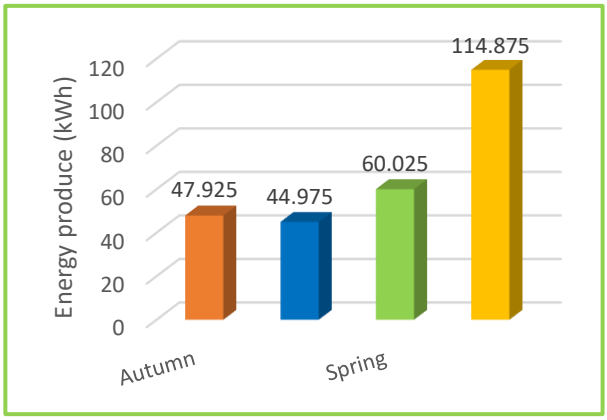

Fig. 1. Gross useful energy in Algeria

B. ***COMPARATIVE USEFUL ENERGY BETWEEN THE THREE AREAS OF THE COUNTRY***

Fig.2. shows a comparative useful energy between the three areas of the country. The gross energy produce accounted for more than 42%, 22%, 16% and 17% in summer, spring, winter and autumn respectively. The gross energy produce in summer has increased by 58.28% reaching 114.875 kWh compared to autumn and then by 60.84% and 47.74% respectively compared to previous seasons. In summer, southern zone registered the highest increase by 50.34 % more compared to others seasons. In contrast, a decrease of 17.20% registered in winter.

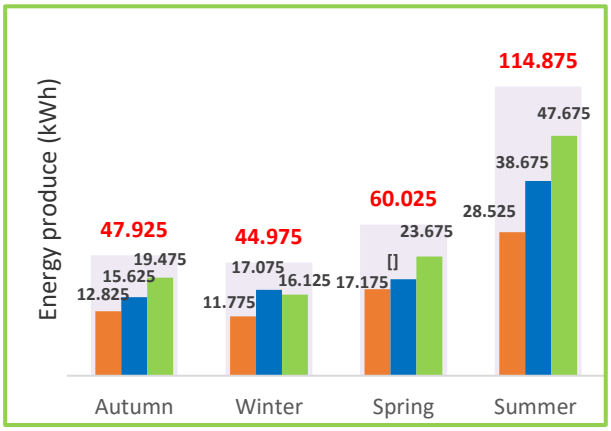

Fig. 2. Comparative useful energy between the three areas of the country

V. Renewable energy integrations in a building

The context of this part aims to improve energy efficiency in a house. Reduce in total energy consumption leads to improve energy efficiency. This decrease has been accompanied with a drop in energy intensity and energy consumption per capita. One way for this reduction is the integration of renewable energy. The integration of renewable energy in homes is becoming an imperative step to reduce its environmental footprint and its dependence on non-renewable energy sources

- **Renewable energy in a house by region**

A. In the north of Algeria:

The most commonly used renewable energy sources in this region are solar energy and wind energy.
For solar energy, solar panels are installed on the roof of the house; they capture solar radiation and convert it into electricity.
PV solar panels are usually connected to an inverter, which converts the electricity produced by the solar panels into alternating current (AC) to direct current (DC), which is compatible with the electrical appliances in the house.
For wind energy, installing a small urban wind turbine on the roof of the house or in the garden can also provide electricity.

B. **In the Algerian highlands*:***

In the high Plateaus area, the integration of renewable energy into a home can be done in different ways, in particular:

- For solar energy, this sunny region is ideal for the installation of photovoltaic solar panels on the roofs or facades of buildings. These panels convert sunlight directly into electricity. You can also install a solar water heater, which is a device that produces domestic hot water.
- For wind energy, this area is rich in wind (Nedjari and Guerri, 2018) the installation of small wind turbines can be considered to supplement the supply of renewable energy, especially in the windier areas.

C. In southern Algeria:

The most commonly used renewable energy sources in this region are solar energy and wind energy since the region is often sunny and windy (BENATIALLAH, 2019). For solar energy, the installation of photovoltaic solar panels on the roof of the house can make it possible to produce electricity. The south of Algeria enjoys significant sunshine throughout the year, which allows optimal solar energy production. It is also possible to use thermal solar panels to heat the water of the house like the solar water heater. For wind power, installing a small wind turbine in the garden or on the roof of the house can also provide electricity. Southern Algeria is also known for its windy conditions, which can allow for optimal wind power generation (**https://www.energyeducation).**

V. Conclusion

Algeria intends to be an important player in the production of electricity from the photovoltaic and wind sectors by emphasizes the importance given to the diversification of energy supply of the country through the implementation of a national renewable energy integrating the thermal solar, under its renewable energy program. With 86% of Saharan desert composing its territory and with its geographical position, Algeria considers the solar energy, which is widespread on the territory as a new opportunity and a lever for economic and social development. Moreover, Algeria has the most important solar field worldwide. This new energy model will enable Algeria to ensure its economic and social development through improving their energy efficiency.
In this context, this work concerns the dimensioning of the energy needs of the residential sector of Algeria, of which we have divided our analysis into three parts, taking into account the geographical characteristics and the climate by season.
These parameters are important to identify the needs in energy resources necessary in order to satisfy the demand of the occupants of a dwelling during the year in the North, the High Plateaus and the South of Algeria.
This is essential to design solutions adapted to each area. After studying the geographical characteristics of the studied region of a dwelling. Among the energy aspects to be evaluated in this study, the production of hot water, the heating of the spaces of a house, their air conditioning, (thermal energy), as well as the lighting and the supply of household appliances, (electrical energy) . For the

evaluation of the energy consumption of all these needs we used adequate mathematical models, with a temporal seasonal analysis of the northern regions, the highlands and the south of Algeria.

The results obtained show that the energy management in a house requires the rational sizing of the energy needs of a residence.

The analytic study carried out in the present work has driven to the following facts:

1. Evaluate the energy consumption
2. Reducing the energy needs ultimately improve the economy

References

Boudiaf, A., & Meddi, M. (2021). Impact of climate change on precipitation variability in the North-West of Algeria. Theoretical and Applied Climatology, 144(1-2), 297-310.

Climate Algiers: Temperature Algiers, climate diagram for Algiers - Climate-Data.org. (n.d.).

D Benatiallah, A Benatiallah - 2019 - Determination of the solar deposit by satellite imagery with integration, into a geographic information system for southern Algeria space. Univ-adrar.edu.dz

Guruprasad A, Lingkun L, Xiang H, Guiyin Fang 2017 February. Thermal energy storage materials and systems for solar energy applications for Renewable and Sustainable Energy Reviews

IEA. (n.d.). Key World Energy Statistics 2021 – Analysis.

Kondoh J, and all, 2000, November. Electrical energy storage systems for energy networks for Energy Conversion and Management

Ministry of Energy (Algeria). (2018). National Energy Report 2017 (2018 Edition)

Nedjari, H. D., S. K. Haddouche, A. Balehouane, and O. Guerri. 2018. Optimal windy sites in Algeria: potential and Perspectives. Energy 147:1240–55. (doi:10.1016/j.energy.2017.12.046).

W. (n.d.-c). World Weather Information Service. World Weather Information Service

https://www.energyeducation.ca/Encyclopedie_Energie/index.php/Installation_hydroélectrique

IEEES-017

Comparative Analysis of Energy Storage Methods for a Parabolic Through Collector Solar Power System

[1*]Ömer Faruk GÜLER
[1]AfyonKocatepe University, Technology Faculty, Mechanical Engineering Department, ANS Campus GazlıgölYolu, Afyonkarahisar, 03200, TÜRKİYE
*E-mails:ofguler@aku.edu.tr

Abstract

Solar energy is an important renewable energy source. However, the electricity produced by solar energy does not syncronize the time it is consumed. Storing energy obtained from the sun is a very important and costly process. There are studies on different storage systems in the literature. One of these is storing thermal energy. In these systems, hot fluid is stored in an isolated tank. Another method is to produce electricity and to produce Hydrogen from this electricity. Hydrogen has the potential to be stored in the tank and converted back into electricity. Another system is the storage of energy with the Vanadium Redox Battery. In this study, these three different systems were examined comparatively. When stored as heat energy, energy loss remains at 35%. Losses in the battery and fuel cell are 51% and 58%. A detailed thermo-economic analysis will be carried out in the continuation of the study. According to the first results, although it seems advantageous to store heat energy, the fact that hydrogen has other uses makes it stand out.

Keywords: PTC, Hydrogen, Thermal Storage, VRB

I. Introduction

Solar energy has an important place among renewable resources. Studies on solar energy are based on many and different methods. Concentrating systems and PV panels are generally used for electricity generation. In recent years, the number of concentrating systems has been increasing due to high power densities. Here, parabolic trough collectors are highly preferred due to their ease of installation and scalability. They serve as an important energy collector with temperatures reaching up to 400 °C(Kanoglu et.al., 2020). But the biggest problem of solar energy systems is storing energy. Because the energy collected during the day is used intensively in the evening. There are different solutions for these storage methods in the literature.

One of the first methods considered was to store energy in the form of hot fluid. For this method, large thermally insulated tank must be established. Hot fluid is drawn from this tank as needed and electricity is produced. These systems, developed for villages and towns far from the grid, are suitable for providing electricity day and night.

Another method of storing energy is to convert the electricity into Hydrogen by an electrolyzer. Hydrogen is preferred because it is a clean energy and it is also possible to transfer energy to different vehicles outside the grid. Stored hydrogen can be used in the iron and steel industry and hydrogen-powered electric vehicles with the development of Hydrogen transportation and infrastructure works. In addition, energy can be stored and used at any time through hydrogen fuel cells, thus providing energy to the grid (Guler et.al.,2022).

Another developing technology that is not included in the literature as much as other methods is large battery systems. Unlike conventional batteries, these have high power potential. They are suitable for stationary systems. In these systems, which work on the principle of ion transfer in fuel cells, electricity is produced by the reduction and oxidation of different ions. One of these is the Vanadium redox battery (Barclay, 2006). As the name suggests, Vanadium redox batteries produce electricity by oxidizing Vanadium ions. Just like in fuel cells, electrons complete the circuit from the outside and create electric current. Here, there are vanadium ions instead of hydrogen, and the system can be charged and discharged reciprocably. Integration into renewable energy systems has also gradually found its place in the literature recently(Ni et.al.,2022),(Yesilyurt et.al.,2023),(AlShafi and Bicer, 2021).

Within the scope of this study, these three different energy storage methods will be comparatively included for a solar energy system operating with PTC. In the first model, the fluid heated in the PTC will be stored in a thermal energy storage as hot water. In the second model, electricity will be produced directly and some of the energy will be stored as hydrogen. A fuel cell will also be integrated to convert hydrogen back into electricity. As the third method, the vanadium redox battery system, which has not been studied extensively in the literature but is increasingly studied, will be integrated. Thus, the advantages and disadvantages of these three methods can be seen more clearly.

II. System Description

Three different models have been created to store energy, these can be seen in Fig.1. The first of these is the system that stores the energy obtained from solar energy directly as hot fluid. This hot fluid will then be used to generate electricity. An Organic Rankine Cycle (ORC) is used to generate electricity. The energy stored in this system is sent directly to the grid after being converted into electricity. The second model produces electricity directly from the hot fluid obtained. This process is carried out with an ORC. The electricity obtained is then converted into Hydrogen by electrolyser. Hydrogen is stored in a tank and can be used as needed. A fuel cell is used to generate electricity. Electricity is supplied to the grid from here. In the third model, another storage system, Vanadium Redox Battery, is used. The battery has its own solution tanks. It can be charged or discharged from here. Again, electricity is produced according to need.

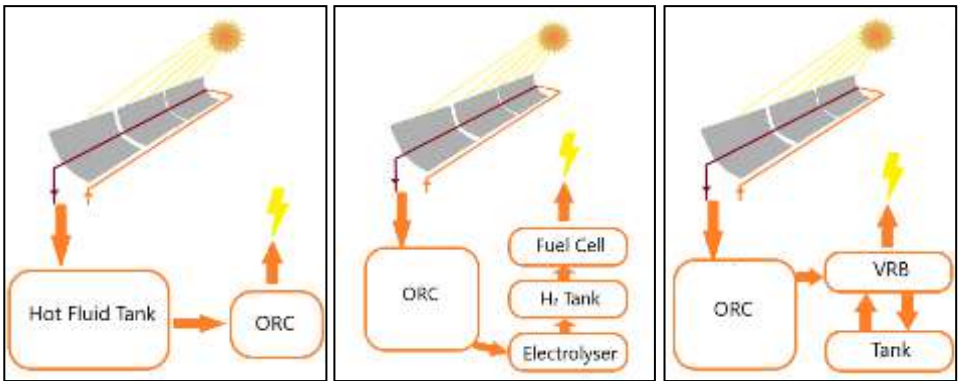

Fig. 1: Schematic of three models respectively left to right

III. Analysis

In the first model, there are some losses caused by storing heat energy. Thermal losses of the tank are the biggest source of loss. Even though the walls of the tank are insulated, there is heat loss from here. For this, first the heat loss coefficients inside and outside the tank must be determined. It is assumed that the tank is constructed as double walls with insulation. The inner wall was built in the form of a 20 cm thick concrete wall. The External Wall was similarly constructed as a 20 cm concrete wall, and the space between them was filled with 25 cm thick rock wool which has a thermal conduction coefficient of 0.035 W/m K. Thus, a tank that is both resistant to the lateral forces of water and has thermal insulation was created. To calculate heat loss from the tank the total heat transfer coefficients on its walls will be derived. U_t is the loss from the upper surface, U_e is the loss from the side walls, U_b is the loss from the bottom. According to all these U values and surface areas, the losses of the tank will be calculated with the help of equation (1).

$$\dot{Q}_{loss} = UA(T_i - T_o) \tag{1}$$

Where T_i and T_o are the internal and external temperatures, respectively. A is the surface area where heat loss occurs.ORC system consists of 4 parts: Turbine Pump, condenser and evaporator. The evaporator is a heat exchanger that evaporates the working fluid R-134a with the heat coming from the hot fluid. A water-cooled system was used for the condenser. In the first model, the energy from the turbine is directly given to the grid. A similar ORC was used for the other two models. Electricity is produced directly with the hot fluid coming from solar energy in second third models. Thermodynamic calculations for the turbine pump heat exchanger and condenser in the ORC will be made with the help of the following equations (2), (3), (4), (5).

Turbine energy:

$$\dot{W}_{act,T} = \dot{m}_i(h_i - h_o) \tag{2}$$

where $\dot{W}_{act,T}$ is the power production of the turbine, $\dot{m}_i$ is the mass flow rate of the working fluid, h values are the enthalpy values for the inlet and outlet.Transferred heat:

$$\dot{m}_h(h_{h,i} - h_{h,o}) = \dot{m}_c(h_{c,o} - h_{c,i}) \tag{3}$$

where $\dot{m}_h$ and $\dot{m}_c$ are the hot and cold fluid mass flow rate respectively, and the h values are the cold and hot fluid inlet-outlet enthalpy values according to their indices.Pump power:

$$W_{act,P} = \dot{m}_i(h_o - h_i) \tag{4}$$

where $\dot{W}_{act,P}$ pump energy consumption. $\dot{m}_i$ is the mass flow rate of the working fluid, h values are the enthalpy values for the inlet and outlet.Condenser heat:

$$\dot{m}_i(h_i - h_o) = \dot{m}_{cw}(h_{cw,o} - h_{ce,i}) \tag{5}$$

where $\dot{m}_i$ is the mass flow rate of the working fluid and $\dot{m}_{cw}$ is the mass flow rate of the cooling water. h values are the cold and hot fluid inlet-outlet enthalpy values according to their indices.

IV. Results and discussion

The net power output of the ORC system containing R-134a working fluid circulating at a flow rate of 25 kg/s can be seen in Fig. 2. The pump and turbine operate at 85% isentropic efficiency. Turbine inlet and outlet pressures are calculated as 3600 kPa and 700 kPa, respectively. EES software was used for these calculations.

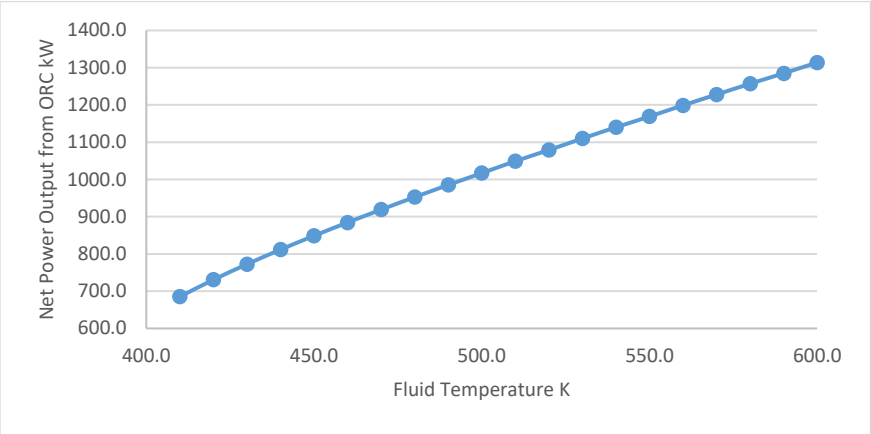

Fig. 2. Net power output from ORC with varius fluid temperatures.

It is calculated that the loss due to heat is around 35%, although it varies depending on the time of use. As long as water remains in the tank, it continues to lose energy. This causes a similar decrease in energy production.

PEM Electrolyser efficiency is generally around 60% in the literature (Nieminen et.al., 2010). Similarly, in the literature, fuel cell efficiency is around 70%. These vary depending on the amount of power drawn. For Vanadium redox batteries, it is around 70%. According to the first results, the energy loss as heat energy is in the 30-35% range. In the fuel cell electrolyser system, this loss is 58%, and in the Vanadium Redox system, this loss is 51%.

V. Conclusion

It is seen that the loss of heat energy is less than other storage system. Fuel cell - Electrolyser and Vanadium Redox battery systems have similar efficiencies (less than %50). At this point, the costs and energy exergy efficiencies of the construction of the tank and other fuel cell, electrolyzer and battery investments should be examined in more detail. The use of hydrogen in different areas should also be taken into consideration in this regard. Although the hydrogen system is low in terms of efficiency, the use of hydrogen in automobiles and for other purposes is the prominent aspect of hydrogen.

References

AlShafi, M., & Bicer, Y. (2021). Life cycle assessment of compressed air, vanadium redox flow battery, and molten salt systems for renewable energy storage. Energy Reports, 7, 7090-7105.

Barclay, F. J. (2006). Fuel cells, engines and hydrogen: an exergy approach. John Wiley & Sons.

Guler, O. F., Sen, O., Yilmaz, C., & Kanoglu, M. (2022). Performance evaluation of a geothermal and solar-based multigeneration system and comparison with alternative case studies: Energy, exergy, and exergoeconomic aspects. Renewable Energy, 200, 1517-1532.

Kanoğlu, M., Çengel, Y. A., & Cimbala, J. M. (2020). Fundamentals and applications of renewable energy. McGraw-Hill Education.

Nieminen, J., Dincer, I., & Naterer, G. (2010). Comparative performance analysis of PEM and solid oxide steam electrolysers. International Journal of Hydrogen Energy, 35(20), 10842-10850.

Ni, J. W., Li, M. J., Ma, T., Wei, W., & Li, Z. (2022). The configuration optimized design method based on real-time efficiency for the application of vanadium redox flow battery in microgrid. Energy Conversion and Management, 267, 115899.

Yesilyurt, M. S., Ozcan, H. G., & Yavasoglu, H. A. (2023). Co-simulation-based conventional exergy evaluation of a hybrid energy generation-vanadium redox flow battery-air source heat pump system. Energy, 281, 128301.

IEEES-018

Greenhouse Heating with Low Enthalpy Solar and Geothermal Energy

[1*]Ömer Faruk GÜLER
[1]AfyonKocatepe University, Technology Faculty, Mechanical Engineering Department, ANS Campus GazlıgölYolu, Afyonkarahisar, 03200, TÜRKİYE
*E-mails:ofguler@aku.edu.tr

Abstract

Within the scope of this study, a greenhouse heating system was designed with geothermal water at 60°C, which is left over after certain processes and contains a small amount of usable energy. This temperature alone is not sufficient for most applications. In order to increase the usability of energy, additional heating was done with solar energy and the storability of this hot water was examined. An underground tank will be built as a storage method. The outer surface of the tank will be isolated or a film layer will be created with increased geothermal water to reduce the temperature difference with the environment. Heat losses were calculated for both cases. As the first results of the study, the nightly heat loss of the greenhouse is 40100 MJ. When a heating system operating with a temperature difference of 30°C with 80°C water is used, a total of 319166 kg of water is required. This amount increases when the heat losses of the tank are included. Considering the heat losses of the tank, it turns out that it is more convenient to cover the tank wall with insulation material rather than covering it with a layer of water.

Keywords: Geothermal energy, Solar energy, Greenhouse heating.

I. Introduction

Greenhouses create a suitable environment for plants, minimizing the negative effects of the climate and allowing production throughout the year. Winter months are harsh in Turkey, especially in the central and eastern parts, and agricultural production is suspended. Although sunny days are frequent, temperatures drop significantly, especially at night, due to the influence of the continental climate. Greenhouse heating is carried out where possible. Different systems are being developed for this.

There are systems that use geothermal energy. There are also greenhouses heated with geothermal energy available in Afyon province. Greenhouse heating with geothermal energy is an application encountered in the literature (Kendirli, B., & Çakmak, B. 2010).

Solar energy is also used for greenhouse heating in studies such as geothermal energy. The use of solar energy occurs in different ways. Electricity generation with PV panels is one way of this. (Gorjian et al., 2021) This electricity is used in various systems from irrigation to heating. Heating is also done with the help of hot fluid with concentrator solar energy (Jafari et.al., 2017). There are also systems that use solar energy as an auxiliary source (Hepbasli, 2011).

As can be understood from the literature, many different systems are used for greenhouse heating in different ways. Especially systems powered by solar energy take up a lot of space. In this study, a 60°C geothermal spring water remaining from various processes with low heating effect or coming out of the ground at low temperature will be used in greenhouse heating with the help of additional heating. This additional heating process will be provided by solar energy. Thus, a thermal storage at 80°C will be established and this storage will be used for heating at night.

II. System Description

Geothermal resources come to the surface at various temperatures. Generally, sources of 100°C and above can be used in processes such as energy production. As a result of these processes, geothermal waters at 40-60°C are injected back into the soil on the grounds that they can no longer be used (Guler et.al., 2022). Although 60 °C seems suitable for heating, it cannot be used most of the time due to convection to the heating zone and other losses. Although greenhouse heating is possible with solar energy systems, it is necessary to cover very large areas with collectors. This study aims to use energy more efficiently by bringing these two sources together. System heating water will be heated with both geothermal and solar energy and a heating water pool with a temperature of 80°C will be obtained. The heat loss of the greenhouse and the heat loss of the tank are important for this study. There are two different scenarios for the tank. One of these is to create a thermal film layer around the tank with the last remaining warm geothermal water. Thus, the tank surface will contact a warm surface instead of a low temperature surface. The second scenario is to isolate the tank. Thus, heat loss will be minimized.

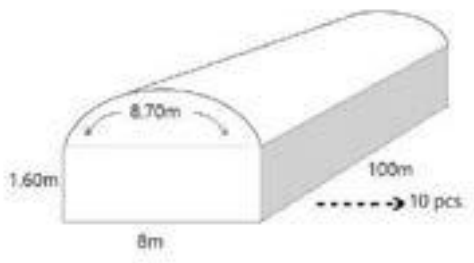

Fig. 1: Dimensions of the greenhouse planned to be built. The dimensions of the greenhouse planned to be established are given in Fig.1. This greenhouse will be built with 10 parabolic roofs adjacent to each other. An area of 80 meters wide and 100 meters deep will be covered. For this covering, polyethylene film, which is widely used and easily available in most greenhouse applications in the region, will be used. The average night temperature in the region's coldest season is around 0 degrees. The night temperature for greenhouse plants is stated as 14-18°C degrees. The aim is to keep the inside of the greenhouse at 16°C degrees. Heat loss calculation was made according to all these values. Heat loss coefficients for polyethylene film greenhouses are given in table 1. The heating period at night is planned to be 12 hours. Heat loss calculation for these values was made using equation (1).

$$Q_{loss,g} = UA_g(T_g - T_o)t_h \quad (1)$$

where A_g is the total greenhouse external surface area responsible for heat loss. T_g is greenhouse internal temparature T_o is the average outdoor temperature during the heating period on the coldest days. t_h is the time with total heat loss.

Table 1. Total heat loss and loss coefficient for varius greenhouse coatings

Coating of Greenhouse	**Loss Coefficient**	**$Q_{loss,g}$**
Polyethylene Film Single Layer	6.2 W/m^{2}K	40100 MJ
Polyethylene Film Double Layer	4.0 W/m^{2}K	25871 MJ
Polyethylene Film Double Layer with thermal insulation	2.5 W/m^{2}K	16169 MJ

The required heat for total greenhouse heating has been found, but since the water used for heating will be kept in a tank, this tank will also have heat losses. This tank will be constructed like a square pool for ease of manufacturing. To insulate the pool wall, either increased warm water (35° C) will be used or insulation material will be used instead. Heat loss calculations were made for both cases. Wall section is shown in Fig. 2. Hot water will be stored in the area shown in blue. The wall will be built from concrete. The part where the W_2 gap is located will either be filled with excess geothermal warm water or filled with insulation material to ensure heat preservation in the hot water tank. Since the upper surface of the greenhouse pool will form the floor of the greenhouse, heat loss from here has been neglected. Natural convection coefficient calculations were made for water-filled surfaces. For air and soil surfaces, the values used in standard heat loss calculations were taken.

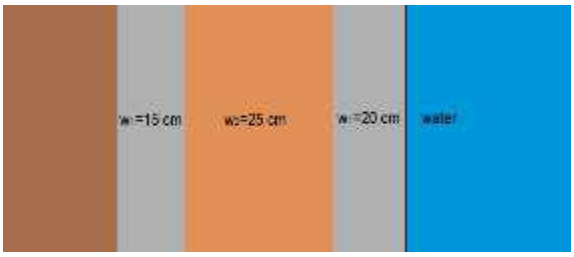

Fig. 2. Tank wall cross section

The inside of the tank is completely filled with water. When the walls are filled with warm water (35°C), the natural convection coefficient must be calculated for both surfaces. Since it is not possible to measure surface temperatures, surface temperatures are found by approximating with an iterative method and the total heat transfer through the wall can be calculated. Similarly, for the second case, the wall gap is filled with a suitable insulation material and the heat loss is calculated for this system as well.

III. Analysis

One of the most important points is to determine the natural convection coefficient inside and outside the tank. Therefore, it is necessary to first determine the fluid temperatures. And after, the Rayleigh number must be determined for the fluid. Öncelikle akışkan için Rayleigh number belirlenmelidir (2). Burada g yerçekimi ivmesi,

$$Ra = \frac{g\beta(T_s - T_f)}{\nu\alpha} \quad (2)$$

where g is gravity, T_s is surface temperature, T_f is fluid temperature at far enough from the wall ν is kinematic viscosity, β is volumetric coefficient of thermal expansion.α is thermal diffusivity coefficient.

Nusselt correlation suggested by (Churchill and Chu, 1975) gives positive results in most engineering applications. Although the expression (3) seems complicated, it produces results only depending on the Ra and Pr numbers.

$$Nu = \left(0.825 + \frac{0.387Ra^{1/6}}{(1+(0.492/Pr()^{9/16})()^{8/27})}()^2\right) \quad (3)$$

IV. Results and discussion

The heat loss of the greenhouse is 40100 MJ. The amount of hot water required for a heating system operating between 80-50°C to heat this greenhouse is 319166 kg. Hot water will be stored with solar energy during the day and used in the evening. It will be stored at approximately 10 °C in a tank placed underground. The size of this tank will be 400 m^3. The amount of heat loss from the tank according to the water temperature was calculated in two scenarios. If this is done by creating a 0.25 m film layer with the

remaining geothermal water at 35°C between the walls, the loss from each meter-long tank wall at a lenght of 4 meters is 20889 W. Having the loss throughout the day will carry this to a much greater energy value. In the second scenario, this gap is filled with insulation material with a thermal conduction coefficient of 0.040 W/mK instead of warm water. Heat loss decreased significantly and amounted to 10.24 W/m wall in this scenario.

V. Conclusion

Geothermal water at 50 °C is not hot enough for greenhouse heating. However, it is possible to raise this water to a working temperature with the support of solar energy. It is possible to reach 70-80°C levels with panel solar collectors. However, it would be more efficient to reach higher temperatures by using concentrating systems, such as parabolic trough solar collectors. One of the first methods to save energy may be to reduce the temperature difference by using warm water, but it seems to be quite ineffective on heat loss. Using an insulated wall instead significantly reduces heat loss. There will also be a cost to using extra insulation. This cost can be calculated by thermo-economic analysis.

References

Churchill, S. W., & Chu, H. H. (1975). Correlating equations for laminar and turbulent free convection from a vertical plate. International journal of heat and mass transfer, 18(11), 1323-1329.

Gorjian, S., Calise, F., Kant, K., Ahamed, M. S., Copertaro, B., Najafi, G., ... & Shamshiri, R. R. (2021). A review on opportunities for implementation of solar energy technologies in agricultural greenhouses. Journal of Cleaner Production, 285, 124807.

Guler, O. F., Sen, O., Yilmaz, C., & Kanoglu, M. (2022). Performance evaluation of a geothermal and solar-based multigeneration system and comparison with alternative case studies: Energy, exergy, and exergoeconomic aspects. Renewable Energy, 200, 1517-1532.

Hepbasli, A. (2011). A comparative investigation of various greenhouse heating options using exergy analysis method. Applied Energy, 88(12), 4411-4423.

Jafari, M., Mortezapour, H., Jafari Naeimi, K., & Maharlooei, M. (2017). Experimental Investigation of a Solar Greenhouse Heating System Equipped with a Parabolic Trough Solar Concentrator and a Double-Purpose Flat Plate Solar Collector. Journal of Agricultural Machinery, 7(2), 364-378.

Kendirli, B., & Çakmak, B. (2010). Yenilenebilir Enerji Kaynaklarının Sera Isıtmasında Kullanımı. Ankara Üniversitesi Çevrebilimleri Dergisi, 2(1), 95-103.

IEEES-019

Integrating Phase Change Materials (PCMs) Into Cotton Ring Spun Yarn Structure For Thermo-Regulating Function

[1*]Demet Yılmaz, [1]Sennur Alay Aksoy
[1]Süleyman Demirel University, Faculty of Engineering, Department of Textile Engineering, Isparta, 32260, Turkey
*E-mails: demetyilmaz@sdu.edu.tr

Abstract

Nowadays, limited and non-renewable fossil energy resources made energy savings and the efficient use of energy an important issue. Thermal energy storage systems in the form of latent heat via phase change materials (PCMs) can be an effective solution are for energy savings. PCMs can capable to store and release high amounts of heat during phase change processes. PCMs have been incorporated into textiles to realise thermoregulating and temperature buffering effects for human body. From this point, in this study, it was aimed to develop PCM incorporated the yarns for the production of textiles with thermo-regulation function. In the study, two types of nanocapsules (poly(methyl methacrylate-co-methacrylic acid) (PMMA-co-MAA) walled and 1-tetradecanol core, and gelatine-gum Arabic walled and n-octadecane core) were synthesized and applied to cotton textile fibres via an alternative application method, developed by the authors. Morphological and thermal properties and particle size of the produced capsules were characterized by Scanning Electron Microscope (SEM), Differential Scanning Calorimetry (DSC) and particle sizer, respectively. Morphological and thermal properties of PCM incorporated cotton ring spun yarns were analysed. The results indicated that PCM nanocapsules with ideal spherical morphology and enough energy storage capacity were successfully applied into the cotton fibers and produced PCM incorporated yarns exhibit thermo-regulation function more than 2 °C compared to unloaded virgin cotton yarns. With respect to the analysis results, obtained novel heat storage cotton yarn is a promising material for thermal energy storage and desirable thermal comfort applications.

Keywords: Phase change materials (PCMs), thermoregulating, cotton, ring spun yarn, fabric.

I. Introduction

Today, utilization of energy, sustainable and renewable energy resources becomes a major issue because limited and non-renewable fossil energy is becoming more and more intense and consumption of these resources causes serious environmental pollution and climate change. This case shifted the priority towards environmentally friendly alternative energy sources. Thermal energy storage (TES) is a promising solution for this issue and therefore they have received more and more attention on reducing energy consumption and protect the environment. The core and key of TES is energy storage materials.TES utilizes the change of the internal energy within the storage media. Latent heat storage, which is one of TES, provides a much higher energy density with a smaller temperature difference between storing and releasing heat and therefore it is a more efficient TES method. Phase change materials (PCMs) called as latent heat storage materials and they can store/release a large amount of energy (Zhao et al., 2021; Peng et al., 2020). In recent years, microencapsulation of PCMs has become popular in thermal energy storage field (Alva et al., 2017).

In the field of textiles, PCMs have been incorporated into textiles to realize thermoregulating and temperature buffering effects for human body. By absorbing or releasing thermal energy through the phase-change process of PCMs contributes to keeping thermal comfort of human body. Besides physical and psychological health, maintaining human body thermal comfort is important for efficient human body energy management. Furthermore, regulating human body thermal comfort shows a prominent impact on saving energy consumption of building heating, ventilation, and air conditioning (HVAC) systems. HVAC systems account for about 40% of total building energy consumption. For example, to maintain the thermal comfort of the human body within an extended heating and/or cooling range of 2 ºC, HVAC can realise about 20% of energy savings. Therefore, to develop new strategies and solutions for improved human body thermal comfort control is essential and promising.

In this study, from this point of view, it was aimed to develop the yarns for the production of textiles with thermo-regulation function. Different the studies in the literature, an environmental-friendly and innovative method, developed by the authors previously, was used in the production of yarns. Main principle of the developed method is based on the integration of PCM nanocapsule dispersion to the open fiber bundle prior to spun yarn formation and the application PCM microcapsules inner structure as well as the outer surface of the yarn. In contrast to widely used wet application methods in textile, the dispersion containing PCM nanocapsules which is sprayed on the open fiber bundle could be completely transferred to the material with the zero-waste principle. Additionally, in the method, there is no need for energy-intensive processes such as post-drying and usage of high volumes of water. It can be thought that the method could enable PCM-loaded yarn production in an environmentally friendly manner.

In literature, there are relatively few studies on PCM microcapsule integrated staple spun yarns. In these studies, various methods based on core-spun, wrap and friction yarn spinning were used and a core material was often coated with PCM capsules and wrapped with staple fibres (Yu et al., 2022; Lin et al., 2016; Marsal, 2012). Different from these studies, in this study, no core yarn was used and the focus was on the application of PCM capsules to all fibres in the yarn structure.

II. Experimental Procedure/Methodology/System Description

As known, polymerization method and core material is important to improve the heat storage performance of the encapsulated phase change materials. Therefore, nanocapsules produced by two different methods and core materials were used to get better thermo-regulating function and applied to cotton textile fibres during yarn production. The nanocapsules with PMMA-co-MAA walled and 1-tetradecanol core were produced by emulsion polymerization method in our previous study (Yılmaz and Alay Aksoy, 2022). In this study, nanocapsules with gelatine-gum Arabic walled and n-octadecane core were produced by complex coaservation method. In the

study, cotton textile fiber was selected due to its widely used in textile products. For the PCM nanocapsule incorporation, at first, nanocapsule dispersions were prepared at 6% concentration, as described in previous study (Yılmaz et al., 2023). Following to preparation process, PCM nanocapsule dispersion was applied to the cotton fiber rovings during the drafting process of the ring spinning by using 2 different feeding rates varying between 62.5 mL/h and 80 mL/h and Ne 24/1 cotton ring spun yarns with knitted twist (αe=3.4) were produced. Yarn production parameters such as draft and spindle speed were kept constant for both feeding rate values during the yarn production.

III. Analysis

Morphological and thermal properties of the produced capsules were characterized by LEO 440 Computer Controlled Digital Scanning Electron Microscope (SEM) and Differential Scanning Calorimetry (DSC). DSC analysis was carried out in nitrogen (N_2) atmosphere at a heating/cooling rate of 10 °C/min between -5 °C and +80 °C using the Perkin-Elmer Jade DSC device. Particle size of PCM capsules were determined by a particle size analyzer (Malvern Brand MS2000E model). Morphological properties of the produced cotton ring spun yarns were analysed by SEM images. Thermal properties of the PCM nanocapsule loaded yarns were measured by the Thermal-History (T-History) test method and the changes in surface temperatures of yarn samples were analysed (Yılmaz et al., 2023; Alay et al., 2017). Dynamic temperature regulation feature of the samples was evaluated resulting from absorbed latent heat by the nanoencapsulated PCMs in the yarn structure in variable temperature environments.

IV. Results and discussion

In this part, some of the properties of PCM nanocapsule and produced yarn samples are discussed.

PCM nanocapsule properties
As seen in Fig. 1C and 1F, PCM capsules with two different core materials ands wall materials had ideal spherical morphology. Uniform particle size ranged from 150 nm to 400 nm for 1-tetradecanol core nanocapsules (Yılmaz and Alay Aksoy, 2022). The particle sizes were about 200 nm for n-octadecane core nanocapsules. According to DSC thermal measurements, PMMA-co-MAA walled and 1-tetradecanol core nanocapsules had an energy storage capacity of 101.7 j/g at 34 °C (Yılmaz and Alay Aksoy, 2022). The heat storage capacity of nanoencapsulated n-octadecane with gelatin-gum Arabic wall was 63 j/g during solid-liquid phase transition at 25.9 °C. They released -67.97 j/g latent heat during at 25 C during crystallization.

Morphological properties of the PCM nanocapsule incorporated yarns
As seen in longiditual SEM images of the PCM incorporated cotton ring spun yarns, the surface of fibers treated with two types of nanocapsules was obviously covered with a number of particles (Fig. 1A-F). PCM nanocapsules could be clearly observed on the cotton fiber surfaces. They were filled up some of the interstices between fibers. In the SEM images, it was observed that the particle sizes of microcapsules were getting larger along the fiber length and this case might be resulted from particle agglomeration. Additionally, the cross-sectional image also indicated the presence of PCM nanocapsules on the surface of the fiber and they were seen the inner and outer structure of the yarn (Fig. 2). On the other hand, no significant differences in morphological structure were observed in terms of nanocapsule type. The above results indicated that both PCM nanocapsules were successfully applied to the surface of cotton fibers.

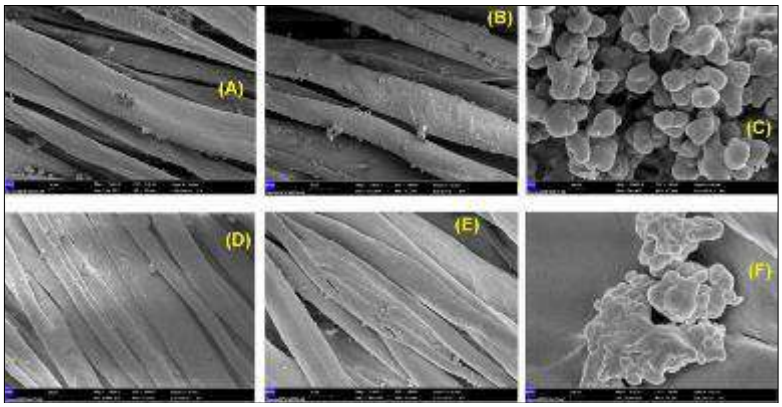

Fig. 1. SEM images of PCM nanocapsules and PCMs incorporated cotton yarns
(A:Yarn samples produced with nanocapsules with 1-tetradecanol core at 62.5 mL/h, B:Yarn samples produced with nanocapsules with 1-tetradecanol core at 80 mL/h, C: Nanocapsules with PMMA-co-MAA wall and 1-tetradecanol core, D:Yarn samples produced with n-octadecane core at 62.5 mL/h, E:Yarn samples produced with n-octadecane core at 80 mL/h, F: Nanocapsules with gelatin-gum Arabic wall and n-octadecane core)

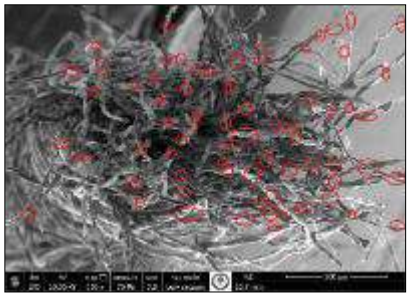

Fig. 2. Cross-sectional images of PMMA-co-MAA walled and 1-tetradecanol core nanocapsule incorporated cotton yarns

Thermal properties of the yarns

Thermal History (T-History) test method was used for the analysis of thermal properties of unloaded virgin and PCM nanocapsule incorporated cotton ring spun yarns. The changes in surface temperatures of the yarn samples in variable temperature environments were determined. According to the T-History test results, all capsule incorporated cotton yarns produced with two different nanocapsule types and feeding rate values had lower surface temperature values compared to virgin cotton yarns (Fig. 3).

Two different temperature change trends were observed from the curves. They were summarized as a rapid surface temperature increase and it was called as warming-up region. The other was a slower temperature increase and named as saturated temperature region. The temperature differences in virgin and PCMs incorporated yarns were significantly high during warming-up region while this difference showed decreasing trend during the saturated surface temperature region. During the warming up period, the surface temperature of the virgin cotton yarns increased rapidly to 25.6 °C in the first 10 minutes, and then warmed up slowly and reached a maximum of 37.6 °C at the end of the measurement period (1 hour 6 minutes). As to PCM nanocapsule incorporated cotton yarns, surface temperatures increased to 11.8-9.8 °C for 1-tetradecanol nanocapsules and 12.6-12.2°C for n-octadecane nanocapsules in the first 10 minutes. After this point, yarn samples warmed up similarly slowly and reached a maximum of 31.8-30 °C for 1-teradecanol nanocapsules and 31.6-31.7 °C for n-octadecane nanocapsules at the end of the measurement period. However, PCM nanocapsule incorporated cotton yarns provided lower surface temperatures compared with virgin yarn during all the measurement process.

The difference values between the surface temperatures of virgin and PCM nanocapsule incorporated yarns at different measurement times were investigated and the results were given in Table 1. Temperature difference value was about 1.3-2.3 °C for 1-tetradecanol nanocapsules while it was determined as 5.9-6.0°C for n-octadecane nanocapsules at the end of the measurement. Mean surface temperature differences at 62.5 mL feeding rate value were about 3.3 °C for 1-tetradecanol nanocapsules while it was 8.2 °C n-octadecane nanocapsules. The values determined at 80 mL feeding rate were about 4.2 °C for 1-tetradecanol nanocapsules while it was 9 °C n-octadecane nanocapsules. Based on these results, n-octadecane nanocapsules produced by complex coacervation polymerization method gave higher surface temperature difference values than 1-tetradecanol nanocapsules obtained by emulsion polymerisation method. Particularly, the difference reached up to 2-3 times during the warming-up region. However, it was found that the surface temperature difference values between virgin and PCM loaded yarns tended to decrease at a higher level in the saturated surface temperature region for n-octadecane nanocapsules in comparison to 1-tetradecanol capsules.

As a result, two different nanocapsule types incorporated into the cotton fibers provided lower surface temperature difference values during all measurement period compared to unloaded virgin cotton yarns. This case was considered as a cooling effect of PCM in yarn structure. High latent heat capacity for energy transfer feature of PCM nanocapsules doped into the yarn structure enhanced the temperature difference. The surface temperature difference values were higher than 2 °C and 2 °C is considered as sufficient for the thermoregulation effect. Therefore, produced PCM incorporated cotton ring spun yarns enhanced a significantly effective thermoregulation function.

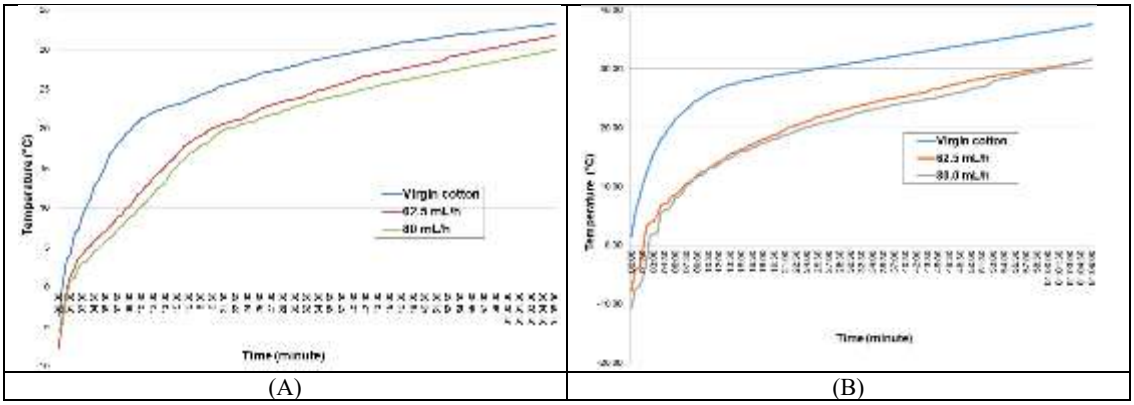

(A) (B)

Fig. 3. T-history curves of virgin and PCM nanocapsule incorporated cotton ring spun yarns for of PMMA-co-MAA walled and 1-tetradecanol core (A) and gelatin gum Arabic wall and n-octadecane core (B) nanocapsules

Table 1. Differences in surface temperatures (ºC) of virgin and PCM nanocapsule incorporated cotton yarns at different feeding rates for two different PCM nanocapsule types

Time (minute)	PMMA-co-MAA walled, 1-tetradecanol core nanocapsules		Gelatin-gum Arabic wall, n-octadecane core nanocapsules	
	62.5 mL/h	80 mL/h	62.5 mL/h	80.0 mL/h
05:00	*6.7*	*6.6*	*12.50*	*13.70*
30:00	*2.6*	*3.6*	*7.70*	*9.10*

01:00:00	*1.8*	*2.8*	*6.10*	*6.40*
01:06:00	*1.3*	*2.3*	*6.00*	*5.90*
Mean	***3.3***	***8.2***	***4.2***	***9.0***

V. Conclusion

In this study, poly(methyl methacrylate-co-methacrylic acid) (PMMA-co-MAA) walled, 1-tetradecanol core and gelatin-gum arabic wall, n-octadecane core nanocapsules were synthesized by emulsion and complex coaservation polymerization methods, respectively. Morphological and thermal analysis of nanocapsules indicated that capsules have ideal spherical morphology, nano sized diamensions and enough energy storage capacity. Nanocapsules were applied to cotton textile fibers via an alternative application method and PCM incorporated ring spun yarns were obtained. SEM images of the produced yarns showed that PCM nanocapsules were placed inner structure as well as the outer surface of the yarn. Due to the PCM nanocapsules contained in the yarn structure, thermal measurements indicated that PCM nanocapsule incorporated cotton yarns provided lower surface temperatures compared with virgin yarn during all the measurement process. Temperature difference between unloaded virgin and PCM-loaded yarns varied to a certain extent according to PCMs feeding rate values and the type of nanocapsules. However, compared to unloaded virgin cotton yarns, the temperature difference was determined about 3.3-4.2 °C for 1-tetradecanol nanocapsules while it was determined as 8.2-9 °C for n-octadecane nanocapsules. Regardless of feeding rate values and capsule types, the surface temperature difference values were higher than 2 °C and 2 °C is considered as sufficient for the thermoregulation effect. Therefore, produced PCM incorporated cotton ring spun yarns enhanced a significantly effective thermoregulation function. Integration of PCMs into the yarn structure will give an opportunity to fabricate textile based thermal energy storage and thermoregulating materials.

Acknowledgements
This study is funded by The Scientifc And Technological Research Council Of Turkey (TUBITAK), 1505 University-Industry Cooperation Support Program, Project No: 5200098. The authors also would like to thank ADIM Tekstil San. ve Tic. A.Ş. (ISPARTA) for its contribution to the project and study.

References

Alay Aksoy, S., Alkan, C., Tözüm, M. S., Demirbağ, S., Altun Anayurt, R., Ulcay, Y., 2017. Preparation and textile application of poly(methyl methacrylate-co-methacrylic acid)/n-octadecane and n-eicosane microcapsules. The Journal of The Textile Institute 108(1), 30-41. https://doi.org/10.1080/00405000.2015.1133128

Alva, G., Lin, Y., Liu, L., Fang, G., 2017. Synthesis, characterization and applications of microencapsulated phase change materials in thermal energy storage: A review. Energy and Buildings 144, 276-294. doi.org/10.1016/j.enbuild.2017.03.063

Lin, J. H., Huang, Y. T., Li, T. T., Lin, C. M., Lou C. W., 2016. Bamboo charcoal/ phase change material/stainless steel ring-spun complex yarn and its far-infrared/anion-releasing elastic warp-knitted fabric: Fabrication and functional evaluation. Journal of Industrial Textiles 46, 624-642. https://doi.org/10.1177/1528083715595007.

Marsal Amenós, F., 2012. New method for applying microcapsules in the spinning process. In International Scientific Conference, 98-102.

Peng, G., Dou, G., Hu, Y., Sun, Y., Chen, Z., 2020. Phase change material (PCM) microcapsules for thermal energy storage. Advances In Polymer Technology, 2020. https://doi.org/10.1155/2020/9490873

Yılmaz D, Alay Aksoy S., 2022. Temperature regulating polyester short staple ring spun yarns by PCM nanocapsule application, 8th International Technical Textiles Congress (ITTC 2022), 13-14 October, İzmir, Turkey.

Yılmaz, D., Özen, Ö., Özkayalar, S., Alay Aksoy, S., Söğüt, B., 2022. An Innovative Method for Microcapsule Based Functional Yarn Production. Journal of Natural Fibers 19(14), 8051-8064. https://doi.org/10.1080/15440478.2021.1958435

Yılmaz, D., Alay Aksoy, S., Maleki, H., Rahbar, R. S., Söğüt, B., Azimi, S. S., 2023. Fabrication of PCM-loaded polylactic acid (PLA)/cotton biocomposite yarn with thermoregulation function. Cellulose 30, 3995-4009. https://doi.org/10.1007/s10570-023-05101-2:3995–4009.

Yu, L., Ke, G., Wang, Y., Tang, J., 2022. Fabrication and characteristics of polyethylene glyco/cotton friction spun composite yarn. Journal of Energy Storage 48, 103978. https://doi.org/10.1016/j.est.2022.103978.

Zhao, Y., Zhang, X., Hua, W., 2021. Review of preparation technologies of organic composite phase change materials in energy storage. Journal of Molecular Liquids 336, 115923. doi.org/10.1016/j.molliq.2021.115923

IEEES-020

Shading Strategies as Energy Efficient Retrofit Measures in Residential Buildings: Implementations for Adaptation to Future Climate Change

[1*]Mümine Gerçek Şen
[1]Izmir Institute of Technology, Department of Architecture, IYTE Gülbahçe Kampüsü, Urla, İzmir, 35430, Turkey
*E-mails: muminegercek@iyte.edu.tr

Abstract

With climate change projected warming temperatures, ensuring that buildings designed and built today will be adapted to future extreme heat is essential. For this purpose, the use of shading elements as retrofit measures is applicable to adapt residential buildings in both present and future climate. This study aims to identify the energy efficient shading strategies that could be employed on the existing multi-storey residential buildings in İzmir to minimize the annual heating and cooling loads as well as operational CO_2 emissions. In order to achieve this aim, the study is based on an analytical method by using energy simulation tools EnergyPlus and OpenStudio 2.9.1. The application of blinds, overhangs, the combinations of overhangs and side fins, and louvers are the selected parameters. In this sense, considering the most recent meteorological data as the baseline, future weather data for 2080s is used to perform building energy modeling. The results indicate that overhang with projection factor of 0.75 combined with side fins shows the lowest energy and environmental effects. Besides, the projection factor of 0.5 for the overhangs provided the second least energy consumption and CO_2 emission results. Accordingly, when compared with the base case, the outcomes indicated energy efficiency tendencies regarding the application of overhangs with 29% lower total energy consumption and 31% lower emission values in 2080s. The study can provide shading guidelines for architects to support the efforts of employing energy efficient strategies to improve the thermal behavior of stock buildings, using local and prevailing methods of construction. The importance of considering climate change scenarios can also provide information on the long-term design decisions for professionals.

Keywords: Energy-efficiency, shading strategies, building energy performance, residential buildings, climate change

I. Introduction

As the impacts of climate change increases, the priority to decrease its impacts on the built environment has been given by universal authorities. Residential buildings, as integral components of urban landscapes, play a critical role in the overall ecological footprint (UNEP, 2019). Accordingly, retrofitting emerges as a proactive and strategic approach to enhance the climate resilience of residential structures (Gouldson et al., 2018). Therefore, the significance of retrofitting is critical, specifically focusing on the integration of shading strategies adapted to endure the dynamic challenges caused by climate change.

The built environment is not only a significant contributor to greenhouse gas emissions but is also vulnerable to the harmful effects of changing climatic conditions (IPCC, 2018). Increasing temperatures, severe weather incidents, and altering precipitation patterns require additional solutions to strengthen existing residential structures against potential risks. Retrofitting, defined as the process of converting existing buildings to improve performance, energy efficiency, and overall sustainability, is one of the essential actions toward climate-resilient housing (Perez-Lombard et al., 2008).

By making use of the envelope elements of the buildings, the chance is possible to reduce energy consumption and greenhouse gases emissions that result from air conditioning processes (Samuel et al, 2017; Sayigh, 2013). One of the parameters to reduce these effects is the integration of shading strategies. Shading, when strategically implemented, functions as an instrument to reduce the impacts of climate change on residential buildings, especially in hot climates (Nguyen et al., 2021). Efficient shading also reduces the need for energy-intensive cooling systems. Furthermore, shading strategies can contribute to improving natural lighting, thereby lowering dependence on artificial lighting systems, and increasing energy efficiency (Touma and Ouahrani, 2017).

At that point, energy performance simulations provide insight into assessing and optimizing energy usage, by analyzing potential retrofitting strategies that can enhance the energy efficiency of existing structures. The simulations provide a quantitative base for understanding dynamic interactions between shading elements, local climate conditions, and the overall energy performance of a structure. By modeling the impact of shading configurations on heating and cooling loads as well as operational emissions, simulations enable a thorough analysis of the potential benefits in terms of energy efficiency.

Consequently, a synergistic approach that combines accurate energy simulations, climate change awareness, strategic retrofitting, and innovative facade shading can contribute significantly to the sustainability of residential buildings by evolving environmental challenges. This study focuses on systematic computational analyses supporting the adoption of shading strategies in retrofitting residential buildings. By examining the potentials on decreasing energy consumption as well as environmental performance, in terms of operational CO_2 emissions, associated with shading retrofit interventions, the study aims to contribute insights to the sustainable retrofitting interventions against climate change. Finally, the integration of various shading strategies in residential buildings can contribute to the correlation between environmental sustainability, energy efficiency, and climate resilience.

II. Experimental Procedure/Methodology/System Description

Climate data of İzmir

İzmir is the third largest city of Turkey. It is in the west part which is also surrounded by the Aegean Sea. It has a hot and humid climate. It is demonstrated in the Köppen environment characterization as a portrayal of Mediterranean environment, named with Csa (Cs - for dry summer, a - for warm summer). The site chose to play out the reenactments has environment conditions which is illustrative

of this framework. Consequently, it lets a consistent estimation of the effect of the weather variability on the energy efficiency of the building envelope.
Weather information used in simulations is based on International Weather Files for Energy Calculations (IWEC). Besides, future climate data is retained from HadCM3 climate model in this study to evaluate the impacts of climate change on building energy consumption (Johns et al., 2004). Future weather file is delivered for 2080s from HadCM3 climate model.

Building case-study and modelling setup
A reference residential building model has been generated to investigate the impacts of blinds, louvres, overhangs, and overhangs combined with side fins on annual energy consumption and operational CO_2 emissions. The building is in the west part of Turkey, in İzmir. Izmir is the third largest city in Turkey; accordingly, it is one of the cities that has the density of representational traditionally constructed residential apartments.

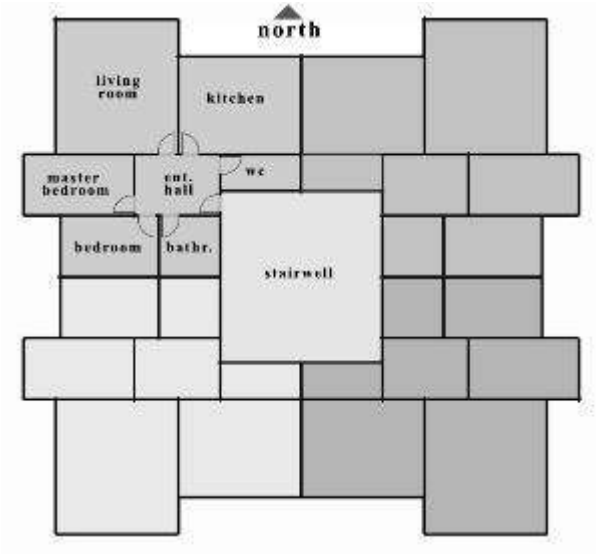

Figure 1: Building plan, space arrangements.

The building has one ground floor and five repeated floors. There are four residential units on each floor, and they are symmetrically located in north-east, north-west, south-east and south-west directions. Each unit has approximately 90 m^2 floor area. The residential building has an orthogonal plan, and the dimensions of floors are (21.0 L x 20.0 W x 3.0 m H) as shown in Figure 1. The units are comprised of an entrance hall, living room, kitchen, master bedroom, second bedroom, a bathroom, and a toilet. The floor height is 3.00 m.
Concrete framework structure as well as brickwork fillings for walls are selected for envelope of the building. The exterior walls have 0.45 $W/m^2.K$ U values with EPS insulation layer, and the windows are double-glazed with an air gap of 12mm. The glazing ratio is around 25% of the total area of the external walls. Thermophysical properties of the building components are defined in consistency with Thermal Insulation Regulations in Buildings (TS 825).
EnergyPlus 8.2 simulation engine with SketchUp 2017 and OpenStudio 2.9.1 software are used to calculate required cooling and heating capacity and energy consumption for the residential building described above. Furthermore, annual operational CO_2 emission properties of the building are calculated based on the annual heating and cooling consumption values. Lastly, obtained results are evaluated for assessing the efficiencies of different shading strategies for a residential building located in İzmir.

Generating the shading strategies
The base version of the building has no shading units installed on the envelope. Accordingly, ten other building energy models are generated. The scenarios included different shading element applications scenarios, such as blinds, louvres, overhangs, and overhangs combined with side fins. In each scenario only the shading elements are modified, and all the other building characteristics and thermal properties are kept constant.

Table 1. Scenarios including shading configurations.

Scenarios										
1	2	3	4	5	6	7	8	9	10	11
Base case	Blinds	Louvres (Incident angle)			Overhangs (Projection factors)			Overhangs with side fins (Projection factors)		
No shading	All facades	South facade			All facades			Side fins on east and west facades		
		30°	45°	60°	0.25	0.5	0.75	0.25	0.5	0.75

The initial case is the base case with no shading elements applied. Secondly, interior blinds are applied on each facade and glazing unit. The scenarios are followed by the application of blinds on glazing elements located on the south facade of the building. Three incident angle variations are generated in terms of louvre usage. Therefore, the louvres are applied with angles of 30°, 45° and 60°. Furthermore, usage of overhangs is generated as different models. Overhangs are also applied on each glazing element on all facades of the building. To provide variations in overhang configurations, projection factors are modified. Projection factor (PF) is the ratio

between the distance the overhang projects from the window surface and its height above the sill of the window it shades. Accordingly, 0.25, 0.5 and 0.75 are used for PF modifications. Lastly, combination of the side fins with already applied overhangs are created as part of different scenarios. However, side fins are applied only on the glazing elements on east and west facades. The overall information is shown in Table 1.

III. Results

In this section, the simulation results for recent and 2080s weather data are explained. The application of blinds, overhangs, the combinations of overhangs and side fins, and louvers are simulated and analyzed. In this sense, considering the most recent meteorological data as the baseline, future weather data for 2080s is used for building performance analyses.

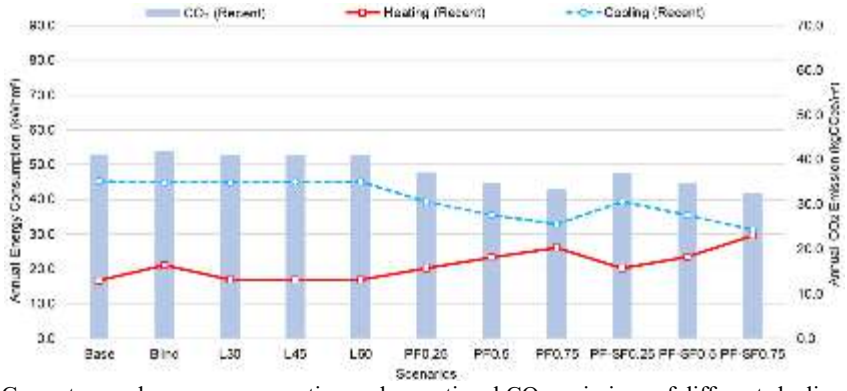

Figure 2. Current annual energy consumption and operational CO_2 emissions of different shading strategies

The outcomes of the recent climatic analyses are depicted in Figure 2. Owing to the warm and humid climatic conditions prevailing in İzmir, the annual cooling loads surpass the heating loads across all examined scenarios. The base case and scenarios incorporating louvres exhibit the highest annual cooling consumption and operational CO_2 emission values. The blind application scenario reveals the highest annual total energy loads. Optimal mitigation of annual cooling demands is achieved with overhangs featuring a 0.5 projection factor. Within these scenarios, the highest annual total energy consumption stands at 66 kWh/m^2, while the lowest is approximately 59 kWh/m^2. Regarding operational CO_2 emissions, the blind application scenario manifests the highest emissions at 42 kgCO_2e/m^2. In contrast, the combination of overhangs with a 0.75 projection factor and side fins yields the lowest emission levels, measuring at 33 kgCO_2e/m^2.

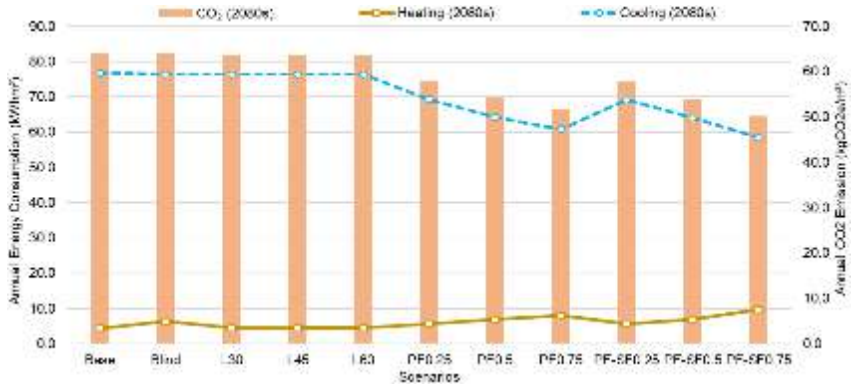

Figure 3. Annual energy consumption and operational CO_2 emissions of different shading strategies in 2080s

The results of the future 2080s climatic analyses are depicted in Figure 3. Owing to the results of global warming, the annual cooling loads increase drastically across all examined scenarios. The base case and scenarios including louvres exhibit the highest annual cooling consumption and operational CO_2 emission values similarly to the recent simulation results. The highest annual total energy loads are again generated by the application of blinds on glazing units. The lowest annual cooling consumption is achieved with overhangs featuring a 0.75 projection factor combined with side fins. The highest annual total energy consumption stands at 83 kWh/m^2, while the lowest is approximately 68 kWh/m^2. In relation to operational CO_2 emissions, the blind application scenario manifests the highest emissions at 64 kgCO_2e/m^2. The combination of overhangs with a 0.75 projection factor and side fins yields the lowest emission levels, measuring at 50 kgCO_2e/m^2.

Overall, the outcomes show that overhang with projection factor of 0.75 combined with side fins has the lowest energy and environmental effects. Besides, the projection factor of 0.5 for the overhangs provided the second least energy consumption and CO_2 emission results. When compared with the base case, the outcomes indicated energy efficiency tendencies regarding the application of overhangs with 28.7% lower total energy consumption and 30.5% lower emission values in 2080s.

IV. Conclusion and Discussion

This comprehensive study evaluates the impact of various configurations in shading strategies such as blinds, overhangs, side fins and louvres as well as future climatic conditions regarding a residential building. It can be outlined from the point of energy and environmental efficiency, the retrofits in building envelope by offering shading elements provide lower amounts of energy consumption

and CO_2 emissions. Besides, it shows better performance when future weather conditions are considered rather than current situation in terms of annual energy consumption and operational CO_2 emission characteristics of the building. Though, energy and environmental impacts increase over the years, as expected. However, the highest impact of climate change conditions is observed on the energy and environmental performance characteristics of the buildings with blind and louvre applications. Besides, buildings with overhangs combined with side fins are the most energy and environmentally efficient options with the conditioning demands. Such a multilayered approach underlines the interdisciplinary nature of sustainable building research and emphasizes the importance of integrating diverse methodologies for the relations between design strategies, climatic conditions, and building performance.

The geographical specificity of the study, focused on İzmir, prompts consideration of broader applications in different regions with comparable climatic profiles. A cross-cultural analysis of countries sharing similar climatic conditions has the potential for collecting more detailed perceptions about energy performance and environmental demands. Furthermore, the study calls for a complementary field study involving an existing residential building to strengthen the reliability of results. On-site measurements would supply validated data and enhance the viability of the conclusions drawn from this research.

References

Al Touma, A., & Ouahrani, D. (2017). Shading and daylighting controls energy savings in offices with fully glazed facades in hot climates. Energy and Buildings, 151, 263-274.

Gouldson, A., Sudmant, A., Khreis, H., & Papargyropoulou, E. (2018). The economic and social benefits of low-carbon cities: A systematic review of the evidence. Coalition for Urban Transitions.

IPCC (2018) Global warming of 1.5°C: An IPCC special report on the impacts of global warming of 1.5°C above pre-industrial levels and related global greenhouse gas emission pathways, in the context of strengthening the global response to the threat of climate change, World Meteorological Organization, Geneva, Switzerland

Johns, T., Durman, C., Banks, H., Roberts, M., McLaren, A., Ridley, J. and Rickard, G. (2004) HadGEM1 – Model Description and Analysis of Preliminary Experiments for the IPCC Fourth Assessment Report, Hadley Centre Technical Note 55.

Nguyen, A. T., Rockwood, D., Doan, M. K., & Le, T. K. D. (2021). Performance assessment of contemporary energy-optimized office buildings under the impact of climate change. Journal of Building Engineering, 35, 102089.

Pérez-Lombard, L., Ortiz, J., & Pout, C. (2008). A review on buildings energy consumption information. Energy and buildings, 40(3), 394-398.

Samuel, E.I., E. Joseph-Akwara, and A. Richard, (2017). Assessment of energy utilization and leakages in buildings with building information model energy. Frontiers of Architectural Research. 6(1): p. 29-41.

Sayigh, A., (2013). Sustainability, energy and architecture: Case studies in realizing green buildings. Academic Press.

United Nations Environment Programme (UNEP), (2019). Guidance on the global monitoring plan for persistent organic pollutants. Conference of the Parties to the Stockholm Convention on Persistent Organic Pollutants, Ninth meeting, Geneva, 29 April–10 May 2019.

IEEES-021

Photovoltaic-Phase Change Materials-Thermoelectric System Coated With Radiative Cooling

[1*]Aminu Yusuf, [1] Sedat Ballıkaya
[1]İstanbul University-Cerrahpaşa, Faculty of Engineering, Department of Engineering Sciences, Avcılar, İstanbul, 34320, Türkiye
*E-mails: aminu.yusuf@iuc.edu.tr

Abstract

A passive cooling system, such as the photovoltaic-phase change material-thermoelectric (PV-PCM-TE) setup, often faces challenges in providing continuous power output around the clock, making it less suitable for remote applications. The incorporation of radiative cooling technology on the cold side of the thermoelectric generator (TEG) can guarantee uninterrupted power supply by the PV-PCM-TE system. In this study, a 3D numerical analysis of the PV-PCM-TE system (with a surface area of 40 × 40 mm^2) integrated with a radiative cooler (RC) is presented. This innovative system can operate continuously over extended periods with minimal or zero maintenance requirements, as it lacks moving components and does not rely on an active cooling system. The performance of this integrated system is assessed in Cairo (Egypt), Istanbul (Türkiye), and Helsinki (Finland) on both summer and winter days, thereby examining its suitability across various geographical locations. The results demonstrate that, on a summer day, the PV systems in Cairo, Istanbul, and Helsinki generated maximum output powers of 192 mW, 171 mW, and 118 mW, respectively. During the night, the TEGs produced a consistent output power of 17 µW and 15.2 µW in Cairo and Istanbul, respectively. On a winter day, the PV systems in Cairo, Istanbul, and Helsinki generated peak output powers of 147 mW, 57 mW, and 13 mW, respectively. Likewise, the maximum output powers produced by the TEGs on a winter day in these cities are 23 µW, 20.5 µW, and 15.5 µW, respectively.

Keywords: 24-hour operation, Carbon footprint reduction, Energy storage, Passive thermal management, Power generation, Solar energy

I. Introduction

In spite of attempts to decrease energy consumption and enhance energy efficiency, the demand for electricity is swiftly on the rise (Kang et al., 2023). This upsurge is primarily fueled by the widespread utilization of both household and industrial electrical appliances, along with electronic gadgets. Particularly, Internet of Things (IoT) sensors have gained significant popularity due to their versatile applications. These sensors often require continuous remote operation. Traditionally, IoT sensors are powered by batteries, which necessitate frequent recharging and have a shorter lifespan compared to energy harvesters like photovoltaic (PV) and thermoelectric generators (TEGs). Ensuring the uninterrupted operation of these IoT sensors is of paramount importance, and it serves as the driving force behind this research. One of the most sustainable solutions involves the integration of PV technology with IoT sensors. This configuration enables a PV module to capture solar radiation and supply the required electrical energy for the sensors. However, in hot and arid regions characterized by harsh temperatures and minimal precipitation, standalone PV modules require substantial cooling to avert performance degradation and extend their lifespan (Rahmanian et al., 2021). The incorporation of a phase change material (PCM) into the PV system can effectively tackle this challenge. PCM has the capacity to absorb and store latent energy during phase transitions, releasing it when the surrounding temperature drops below the PCM's melting point. Integrating a PCM on the backside of a PV panel serves to regulate and diminish the panel's temperature.

In addition, a thermoelectric generator (TEG) can harness thermal energy and convert it into electrical energy (Yusuf and Garcia, 2023). The energy stored by the PCM can be harnessed by the TEG to generate electricity. Furthermore, the integration of radiative cooling technology on the cold side of the TEG can further enhance the performance of the TEG when operating within the PV-PCM-TE system. A radiative cooling material applied to the TEG's cold side reflects solar energy during the daytime in the wavelength range of 0.3–2.5 µm and releases thermal energy to outer space during the nighttime via a wavelength range of 8–13 µm (Omair et al., 2022). Although this technology is not novel, its application to TEGs for passive cooling is relatively recent (Fan et al., 2020; Liao et al., 2022). Effective radiative cooling material properties encompass high diurnal solar reflectivity and nocturnal thermal emissivity.

This study is conducted with the aim of evaluating the viability of employing the PV-PCM-TE-RC system to power IoT sensors during remote operation on summer and winter days in different cities with varying levels of solar insolation.

II. System Description

The proposed system, depicted in Figure 1, comprises several components: a photovoltaic (PV) panel, a phase change material (PCM) housed within an insulated container, an aluminum plate, and a thermoelectric generator (TEG) integrated with radiative cooling (RC). The PV panel captures solar energy and converts it into electrical energy, while the PCM container, attached to the rear of the PV panel, effectively regulates the panel's temperature. An insulated aluminum plate serves as a conduit for transferring heat from the bottom of the PCM container to the hot side of the TEG, and the RC system passively cools the cold side of the TEG. To enhance heat transfer between these components, thermal paste is applied at the interfaces. Subsequent sections will delve into the mathematical modeling of the PV-PCM-TE-RC system.

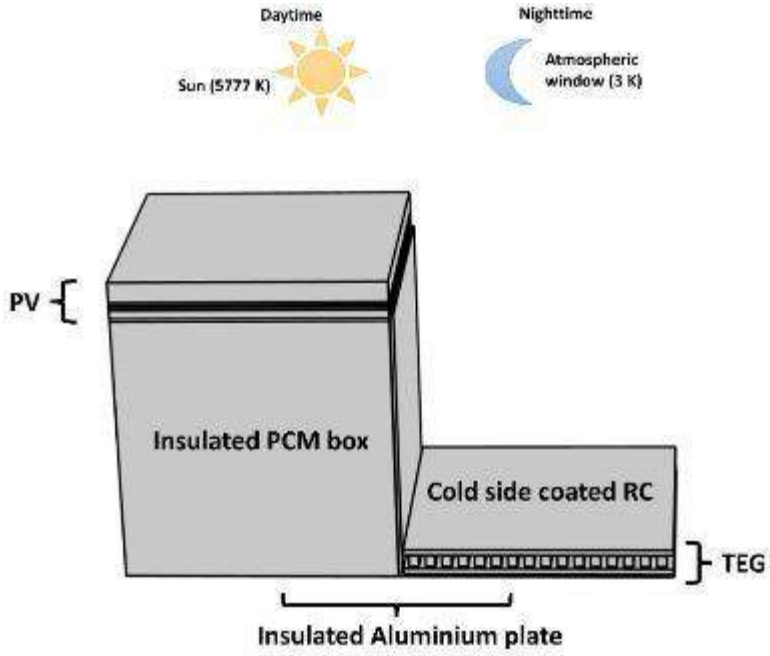

Fig. 1: Proposed PV-PCM-TE-RC system

III. Analysis

The three-dimensional geometry of the model under consideration is developed in COMSOL Multiphysics version 6.1. Following this, material properties are allocated, and physics nodes are established. To assess the system's performance, built-in heat energy equations are employed. A standard solar energy system is comprised of multiple layers, encompassing a glass cover, EVA, silicon, Tedlar, and a back sheet. The heat energy within each layer can be calculated as follows:

$$\rho_i C_{p,i} \frac{\partial T_i}{\partial t} - \nabla \cdot (k_i \nabla T_i) = Q_i - P_{gen,i} \qquad i = 1, 2, 3, \ldots, n \tag{1}$$

where i represent a particular layer, k is the thermal conductivity (W/(m K)), C_p is the specific heat capacity (J/(kg K)), p is the density (kg/m^3), T is the temperature (K), Q is the energy absorption per volume of the PV (W/m^3), P_{gen} is the output power generated per volume (W/m^3) given as:

$$P_{geni} = \eta_r \left[1 - \beta\left(T_{pv} - 298\right)\right] Q_i \tag{2}$$

where η_r is the reference efficiency, T_{pv} is the surface temperature of the PV cell, β is the efficiency temperature coefficient.

The behaviour of the PCM is also modelled by modifying the heat energy equation such that convective term u (m/s), which takes care of the velocity of the PCM in liquid form is added:

$$\rho C_p \frac{\partial T}{\partial t} + \rho C_p u \cdot \nabla \mathrm{T} = \nabla \cdot (\mathrm{k} \nabla \mathrm{T}) \tag{3}$$

The apparent heat capacity method is utilized to simulate the behavior of the phase change material (PCM). In this approach, the properties of the PCM in its liquid and solid states are interpolated to ascertain its properties during the phase transformation, where both solid and liquid phases coexist. The heat absorbed or released during this phase transition is denoted by the final term on the right side of Equation 4.

$$C_p = \frac{1}{\rho}\left(\theta \rho_1 C_{p1} + (1 - \theta)\rho_2 C_{p2}\right) + L \frac{d\varphi}{dT} \tag{4}$$

where L is the latent heat (kJ/kg), φ is the mass fraction, θ is the liquid fraction (1 for solid and 0 for liquid).

The heat energy equation is also modified to fully model the TEG. Herein, Joule and Seebeck terms are included as shown below (Yusuf and Ballikaya, 2022):

$$\rho C_p \frac{\partial \mathrm{T}}{\partial \mathrm{t}} + \nabla(-\mathrm{k} \nabla \mathrm{T}) - \frac{J^2}{\sigma} + TJ \cdot \nabla \mathrm{S} = Q_a \tag{5}$$

where Q_a is the additional internal heat source. The output power generated by the TEG is computed as:

$$P_{te} = \left[\frac{NS(T_h - T_c)}{R_i + R_L}\right]^2 R_L \tag{6}$$

where N = 127 is the number of TE couples, S (μV/K) is the averge Seebeck coefficient, T_h (K) and T_c (K) are the temperatures of the

hot and cold sides of the TEG, R_i (Ω) and R_L (Ω) are the internal and load resistances. The cooling on the cold side of the TEG can be achievd when the following equation is positive:

$$P_{net} = P_{rad} - P_{sun} - P_{atm} \quad (7)$$

where P_{net} (W/m^2) is the net radiative cooling, P_{rad} (W/m^2) is the radiative power density, P_{sun} (W/m^2) and P_{atm} (W/m^2) are the solar and atmospheric power absorbed by the RC. Each of the PV and the TEG has a surface area of 40 x 40 mm^2, while the volume of the PCM box is 40 × 40 × 40 mm^3, other properties of the PV, TEG, and the RT28HC PCM are the same as reported by Yusuf and Ballikaya(Yusuf and Ballikaya, 2023), while the thermoelectric materials are obrtained from the work of Gürkan et al.(Gürkan et al., 2023). The radiative cooler is assumed to have reflectivity of 90% in the solar spectrum and emissivity of 90% in the atmospheric window.

IV. Results and discussion

In Fig. 2, variations in PV and TE output power throughout the simulation period can be observed. In the initial 4 hours, the system operating in CAI exhibits the highest PV output power, while the system in HKI displays the lowest output. However, as time progresses, the PV output power in HKI surpasses the other systems. During the night, all systems cease to generate PV output power. Around 9 am, the PV output power reaches its peak at 192 mW, 171 mW, and 118 mW for the systems operating in CAI, IST, and HKI, respectively. Similarly, when analyzing the TEG performance, it's evident that the TEG operating in HKI generates the highest output power in the first 4 hours of the simulation. Subsequently, the TEGs operating in the other two cities produce higher output power than the TEG in HKI. During the night, the TEGs in IST and CAI consistently generate output powers of 17 µW and 15.2 µW, respectively, whereas the TEG in HKI exhibits fluctuating output power. The consistent nighttime power output is attributed to the PCM's continual release of heat energy, underscoring the essential role of the PCM in the TEG's nighttime operation. With the PCM supplying heat energy to the TEG's hot side and the RC providing cooling on the cold side, this arrangement ensures the 24-hour operation of the TEG.

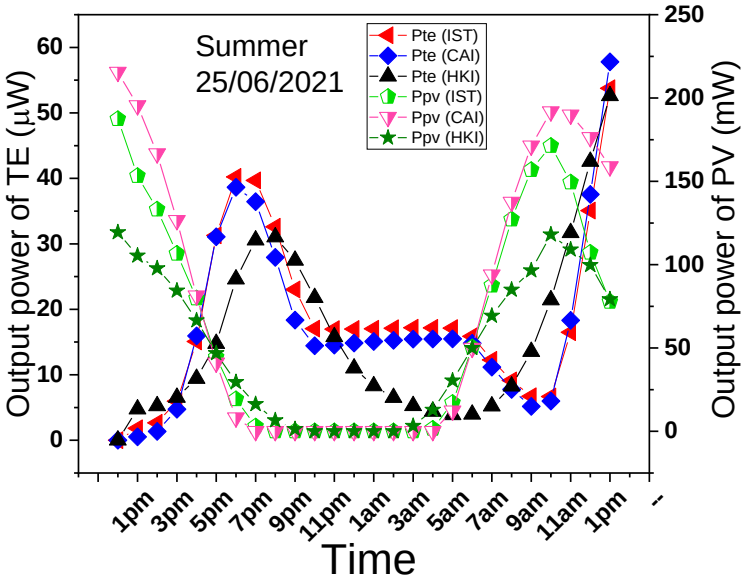

Fig. 2. Output performance of the PV-PCM-TE-RC system on a summer day

In Fig. 3, the fluctuations in TEG and PV output powers during the simulation period can be observed. The PV system operating in CAI stands out, delivering the highest output power over an extended duration, thanks to the city's abundant sunshine hours and elevated ambient temperatures. Over the 24-hour simulation, the PV systems in CAI, IST, and HKI reach their peak output powers at 147 mW, 57 mW, and 13 mW, respectively. Likewise, the TEG systems in CAI, IST, and HKI achieve their highest output powers throughout the simulation period, measuring 23 µW, 20.5 µW, and 15.5 µW, respectively, although they reach these peaks at different times. It's worth noting that the TEGs in these cities consistently generate output power even during nighttime, highlighting the advantages of utilizing radiative cooling technology.

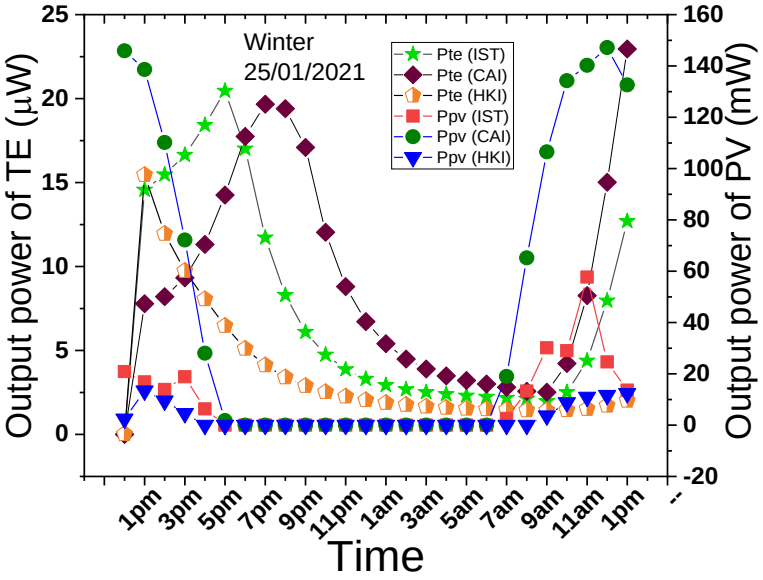

Fig. 3. Output performance of the PV-PCM-TE-RC system on a winter day

V. Conclusion

An analysis was conducted on a PV-PCM-TE system integrated with radiative cooling technology to assess its continuous 24-hour operation in various locations worldwide. Specifically, three cities with distinct solar insolation levels were considered: Cairo (CAI), Istanbul (IST), and Helsinki (HKI). On a summer day, the PV systems in CAI, IST, and HKI achieved their peak output powers, recording values of 192 mW, 171 mW, and 118 mW, respectively. During the night, the TEGs in CAI and IST consistently maintained output powers of 17 μW and 15.2 μW, respectively. Conversely, on a winter day in CAI, IST, and HKI, the PV systems reached their maximum output powers at 147 mW, 57 mW, and 13 mW, respectively. Even during the night, the TEGs in these cities were able to generate output powers. This ability for nighttime operation is attributed to the radiative cooling technology, which emits thermal energy into the sky. These findings indicate that the system can consistently generate power both day and night, making it a feasible option for real-world applications. Moreover, the system's size can be easily scaled up to meet practical demands.

Acknowledgements
This work is supported by the Scientific and Technological Research Council of Türkiye (TÜBİTAK) with grant number 123E144.

References

Fan, L., Li, W., Jin, W., Orenstein, M., Fan, S., 2020. Maximal nighttime electrical power generation via optimal radiative cooling. Opt. Express 28, 25460. https://doi.org/10.1364/OE.397714

Gürkan, K., Karaman, H., Ballikaya, S., 2023. Optimization of high-performance flexible thermoelectric generator from material synthesis to simulation and device application. Energy Conversion and Management 291, 117335. https://doi.org/10.1016/j.enconman.2023.117335

Kang, Y.-K., Joung, J., Kim, M., Jeong, J.-W., 2023. Energy impact of heat pipe-assisted microencapsulated phase change material heat sink for photovoltaic and thermoelectric generator hybrid panel. Renewable Energy 207, 298–308. https://doi.org/10.1016/j.renene.2023.03.042

Liao, T., Xu, Q., Dai, Y., Cheng, C., He, Q., Ni, M., 2022. Radiative cooling-assisted thermoelectric refrigeration and power systems: Coupling properties and parametric optimization. Energy 242, 122546. https://doi.org/10.1016/j.energy.2021.122546

Omair, Z., Assawaworrarit, S., Fan, L., Jin, W., Fan, S., 2022. Radiative-cooling-based nighttime electricity generation with power density exceeding 100 mW/m2. iScience 25, 104858. https://doi.org/10.1016/j.isci.2022.104858

Rahmanian, S., Rahmanian-Koushkaki, H., Omidvar, P., Shahsavar, A., 2021. Nanofluid-PCM heat sink for building integrated concentrated photovoltaic with thermal energy storage and recovery capability. Sustainable Energy Technologies and Assessments 46, 101223. https://doi.org/10.1016/j.seta.2021.101223

Yusuf, A., Ballikaya, S., 2023. Performance analysis of concentrated photovoltaic systems using thermoelectric module with phase change material. Journal of Energy Storage 59, 106544. https://doi.org/10.1016/j.est.2022.106544

Yusuf, A., Ballikaya, S., 2022. Electrical, thermomechanical and cost analyses of a low-cost thermoelectric generator. Energy 241, 122934. https://doi.org/10.1016/j.energy.2021.122934

Yusuf, A., Garcia, D.A., 2023. Energy, exergy, economic, and environmental (4E) analyses of bifacial concentrated thermoelectric-photovoltaic systems. Energy 128921. https://doi.org/10.1016/j.energy.2023.128921

IEEES-022

The improvement of the Mebeverine Hydrochloride photocatalytic degradation by using combined Activated Carbon/ZnO under sunlight

[1]Assia Djebri, [1]Ouiza Allalou, [2]Noreddine Boudechiche, [1]Zahra Sadaoui
Laboratory of Reaction Engineering, Faculty of Mechanical and Processes Engineering,
[1]University of Sciences and Technology Houari - Boumediene,
BP n°32, El alia, bab ezzouar, 16111 Algiers, Algeria.
[2]Khemis Miliana University, Algeria.
*E-mail : sadaouizahra@yahoo.fr

Abstract

The photocatalytic degradation of the Mebeverine hydrochloride (MEB) by the combined ZnO-Activated Carbon (ZnO-AC) under solar light has been investigated in batch system. The AC was prepared from dates stems using $ZnCl_2$ as chemical activation agent. The effect of some operating parameters on the MEB degradation efficiency such as: mass ratio (ZnO/AC) and initial MEB concentration, has been examined. The photocatalytic efficiency of the mixture (ZnO-AC) is dependent on the mass ratio (ZnO/AC), which was optimized for a value of 15 wt%. Besides, the obtained results show that the combined system (adsorption/photocatalysis) is effective for the MEB degradation than the photocatalysis process alone. A comparative study with the literature indicated the benefits of coupling (ZnO-AC) under the solar light (93 $mW.cm^{-2}$).

Keywords : Activated Carbon, Dates Stems, Mebeverine Hydrochloride, Photocatalysis, ZnO.

I. Introduction

The extensive use of the pharmaceutical drugs resulted in frequent detection of their residues in water through many ways. They have been detected in surface water, wastewaters and even in drinking water at levels up to a few µg/L. A lot of unused, expired and residual drugs have been discharged into the aquatic environment during and after treatment (Kühne et al, 2000 ; Xu Zhang et al., 2008).The photocatalysis can be improved by exploiting the physical properties of activated carbons, because of their large specific surface area, which is usually attributed to the increased contact AC/MEB which is favored by the porous nature of the activated carbons (Haro et al., 2012 ; Velasco et al., 2013 ; Matos et al, 2001 ; Herrmann et al., 1999). However, some carbons play more than just a supporting role, as shown by recent studies (Matos et al., 2001; Matos et al., 2009) where 80 % of the phenol mineralization was achieved by photooxidation under UV radiation in the presence of the activated carbon. The specific objective of this section was to study the MEB degradation by the photo-system (solar light/ZnO-AC) and to elucidate the role of the AC physical and chemical properties. Indeed, the current research provides new data of the adsorption/photocatalytic process of the MEB elimination from water**.**

II. Experimental procedure

II.1. Preparation of the activated carbon (AC)

Dates stems were provided from the southern Algeria; the raw material was thoroughly washed with distilled water to remove dirt; it was cut into 1-2 mm particle size, dried at 60 °C, milled and then screen-sieved. The chemical activation of the precursor was performed by using $ZnCl_2$ as chemical agent. The procedure of the AC preparation was illustrated in our previous paper (Djebri et al., 2021).

II.2. Reagents and analysis

The Mebeverine Hydrochloride (MEB) was provided by SAIDAL Company (Algiers). A commercially available ZnO (100% Zincite form, specific surface area (BET) of 9 m^2/g and an average size of 1.5 µm), was supplied by Aldrich Chemical Company. The pH of the solutions was adjusted by addition of NaOH or HCl.All the chemicals were of an analytical grade quality. The MEB concentration was determined with an UV-Visible spectrophotometer (model Specord 200) at the maximum absorption (λ_{max}= 265 nm), using 1 cm quartz cell. The MEB concentrations from aqueous solutions were determined by linear interpolation of the calibration curve.

II.3. Hybrid process (adsorption/photocatalysis) experimental

The activity of the combined processes (adsorption/photocatalysis) was assessed by varying the proportion of ZnO from the ratio (ZnO/AC) referred by x = 15, 35, 50 and 70 wt%). A mass of 1 g of the mixture (ZnO-AC) at different ratio values was magnetically dispersed in MEB solutions at different initial concentrations. The photocatalytic reactions were carried out in batch mode under solar light; this allowed us to establish the experimental protocol and to realize both processes (adsorption/photocatalysis) in the same time within 30 min of irradiation. For the kinetic study, the samples (5 mL) were carried out at regular times and then filtered through the syringe filter (pore size 0.45 µm) for analysis.

III. Results and discussion

III.1. Effect of the (ZnO/AC) ratio

In order to determine whether the AC truly maintains the photoactive properties, we studied its capacity for the MEB oxidation. For this purpose, the experiments were performed by varying the mass ratio (m_{AC}/m_{ZnO}) = x, with x = 15, 35, 50 and 70 wt % for MEB initial concentration of 30 mg/L and free pH of 6.5. The experiments focus on the combined adsorption/photocatalysis and the results

from Fig.1, showed an enhancement of the MEB removal efficiency with decreasing the (ZnO/AC) mass ratio suggesting the activated carbon contribution to the overall MEB removal. These results are consistent with the ability of the activated carbon to promote photocatalysis in which the AC itself acts as a porous support (Galindo et al., 2000 ; Sohrabi et al, 2008) The optimal value of the ZnO/AC mass ratio is found to be 15 % for a MEB initial concentration of 30 mg/L under solar light irradiation of 93 mW cm^{-2}.

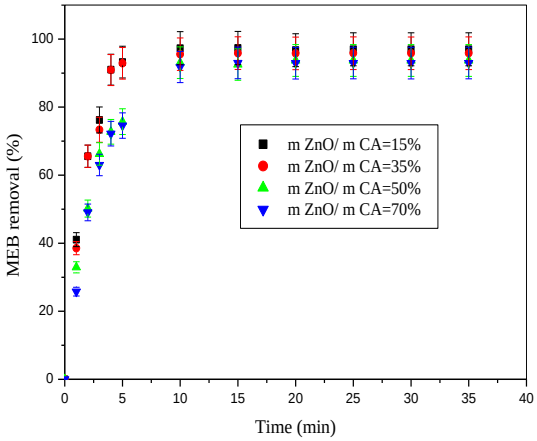

Fig. 1 The influence of (ZnO-AC) ratio on the MEB photo-degradation efficiency ($[MEB]_0$ = 29,6 mg/L, T = 25°C, pH = 6.5).

III.1. Effect of the initial MEB concentration

The Fig.2 shows clearly that the MEB photo-oxidation by the (ZnO-AC) system is higher than by ZnO only. Indeed, high degradation rates of MEB were observed during the first 5 min of irradiation. This is due to the free surface of the AC at early stage, which led to a higher adsorption capacity of the catalyst and the abundance of •OH radicals near the surface. This shows that ZnO-AC system does not only attain a higher MEB degradation efficiency but also accelerates the photocatalytic process.

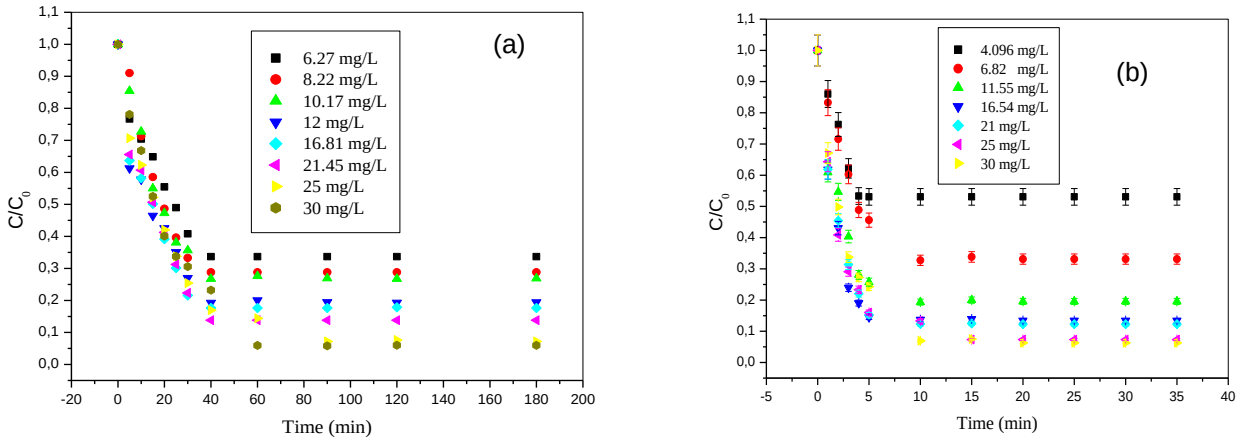

Fig. 2 The Photocatalytic MEB degradation at different initial concentrations for (a) ZnO (b) (ZnO/AC) systems ((a) ZnO dose = 0,4g/L, (b) (ZnO-AC) ratio = 50 %, pH ~ 6.6, T = 25°C).

Apparently, the combined process enhances the reaction between •OH and MEB molecules because of the MEB molecules attraction to the active sites on the catalyst surface at pH 6.5. Moreover, the degradation efficiency is attributed to the affinity to the binding sites for the ZnO-AC system. The MEB degradation increases with initial concentration and no inhibition of the catalyst is observed.

In addition, ZnO is able to absorb more light without provoking great light scattering effect (Anandan et al., 2007), which can be proved by the enhanced removal efficiency with raising MEB initial concentration. After only 5min, the degradation reached 97% for MEB initial concentration of 30 mg/L, showing the performance and synergy of the activated carbon.

The modification of the surface was highlighted by FTIR spectroscopy, a powerful tool to identify the presence of certain functional groups as well as coordination between active functional groups and ZnO. Fig. 3 displays the spectra of ZnO and ZnO-AC systems. The peaks between 500 and 700 cm^{-1} gave ZnO information on the FTIR spectra (Kleinwechter et al., 2002) ; Waseem et al., 2014). For pure ZnO, no significant peaks were observed between the bands range (1200-3390 cm^{-1}). However, in the spectra of ZnO-AC system, some peaks were observed in these regions. The broad bands in the bands range (3000-3390 cm^{-1}) are assigned to–OH group (Kleinwechter et al., 2002) ; Anandan et al., 2007). They provide indirect evidence for the presence of AC as it can absorb water unlike pure ZnO and this clearly shows a good interaction between AC and ZnO.

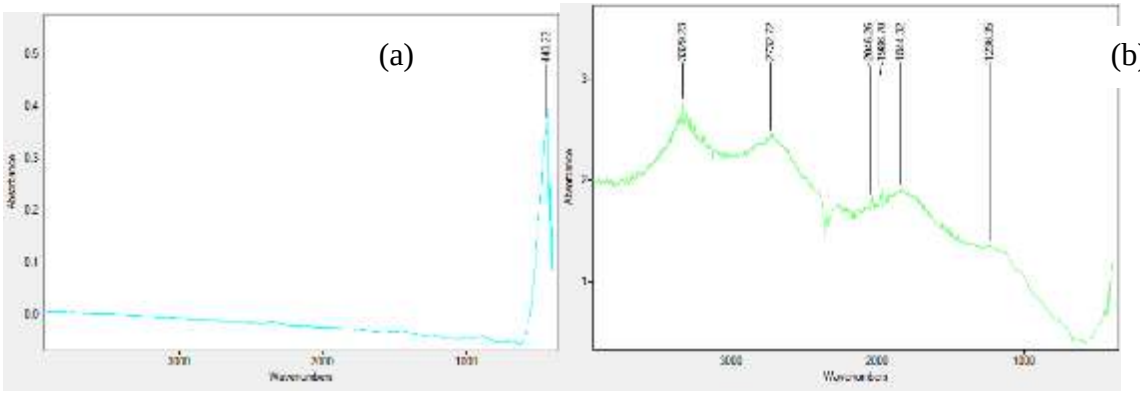

Fig. 3 FTIR spectra of (a) ZnO and (b) (ZnO/AC) systems

IV. Conclusion

The photocatalytic MEB degradation has been studied on ZnO/AC system under solar light. The results indicate that the coupled system ZnO-AC may be a viable alternative and a new way to increase the MEB photodegradation. The effect of the mass ratio (ZnO/AC) and initial MEB concentration on the MEB degradation has been investigated. The experimental results showed an optimal value of the ZnO/AC mass ratio of 15 % for a MEB initial concentration of 30 mg/L. 97 % of MEB removal has been achieved in a relatively short solar light irradiation time than for ZnO system (5 min and 40 min respectively).
The FTIR spectra revealed successful interaction between the activated carbon surface and ZnO. The presence of the activated carbon during the MEB photodegradation process markedly increases the removal rate. The results indicate that activated carbon exerts a greatest synergic effect on MEB removal by the ZnO-AC system.

Acknowledgments
The authors are gratefully acknowledged the General Direction of Scientific Research and Technological Development (DGRSDT) of Algeria for the encouragement. We would like to thank all people have contributed, from far or near, to the best running and carrying out of this research work.

References

Anandan A.V.S., Sheeja Lovely K.L.P., Gokulakrishnan N., Srinivasu P., Mori T., Murugesan V., Sivamurugan V., Ariga K., (2007), Photocatalytic activity of La-doped ZnO for the degradation of monocrotophos in aqueous suspension. Journal of Molecular Catalysis A: Chemical, (266) 149–157.

Djebri A., Sadaoui Z., Belmedani M., Domergue L., Trari M., (2021), Removal efficiency of pharmaceutical drugs Mebeverine hydrochloride (MEB) by an activated carbon prepared from dates stems. Journal of Environmental Health Science and Engineering, 19 (1) 917-931.

Galindo C., Jacques P., Kalt A., (2000), Photodegradation of the aminoazobenzene acid orange 52 by three advanced oxidation processes: UV/H_2O_2, UV/TiO_2 and Vis/TiO_2 : comparative mechanistic and kinetic investigations. J. Photochem Photobiol A Chem 130:35–47.

Haro M., Velasco L.F., Ania C.O., (2012), Carbon-mediated photo-induced reactions as a key factor in the photocatalytic performance of C/TiO_2. Catalysis Science & Technology 2, 2264–2272.

Kühne D.I.M., Moller G., Agthe O., (2000), Stability of tetracycline in water and liquid manure. Journal of Veterinary Medicine Series A, 47 (379-384.

Herrmann J. M., Matos J., Disdier J., Guillard C., Laine J., Malato S., and Blanco J., (1999), Solar photocatalytic degradation of 4-chlorophenol using the synergistic effect between titania and activated carbon in aqueous suspension. Catal. Today 54, pp. 255–265.

Kleinwechter C.J.H., Knipping J., Wiggers H., Roth P., (2002), Formation and properties of ZnO nanoparticles from gas phase synthesis processes. Journal of material sciences, 37 4349–4360.

Matos J., Chovelon J.-M., Cordero T., and Ferronato C., (2009), Influence of surface properties of activated carbon on photocatalytic activity of TiO_2 in 4-chlorophenol degradation. The Open Environmental Engineering Journal 2, pp. 21–29.

Matos J., Laine J., and Herrmann J.-M., (2001), Effect of the type of activated carbons on the photocatalytic degradation of aqueous organic pollutants by UV-irradiated titania. J. Catal. 200, pp. 10–20.

Sohrabi M.R., Ghavami M., (2008), Photocatalytic degradation of direct red 23 dye using UV/TiO2: effect of operational parameters. J Hazard Mater 153:1235–1239

Velasco L.F., Maurino V., Laurenti E., Fonseca I.M., Lima J.C., Ania C.O., (2013), Photoinduced reactions occurring on activated carbons. A combined photooxidation and ESR study. Applied Catalysis A (452)1–8.

Waseem Raza M.M.H., Muneer M., (2014), Synthesis of visible light driven ZnO : Characterization and photocatalytic performance, Applied Surface Science (322) 215-224.

Xu Zhang F., Xu W., Pengyu C., Nansheng D., (2008), Photodegradation of acetaminophen in TiO_2 suspended solution. Journal of Hazardous Materials, (157) 200-207.

IEEES-023

Production of Microencapsulated Thermochromic Systems in Poly(methyl methacrylate-co-methacryl amide) Shell and Application to Polyester Fabric for Thermal Management

[1*]Sennur Alay Aksoy, [2]Simge Özkayalar, [3]Cemil Alkan
[1] Suleyman Demirel Üniversity, Faculty of Engineering, Department of Textile Engineering, West Campus Çünür, Isparta, 32260, Türkiye
[2] Dokuz Eylül University, Faculty of Engineering, Department of Textile Engineering, Tınaztepe Campus-Buca, İzmir, 35390, Türkiye
[3] Tokat Gaziosmanpaşa University, Faculty of Science and Literature, Department of Chemistry, Taşlıçiftlik Campus, Tokat, 60250, Türkiye
*E-mail: sennuralay@sdu.edu.tr

Abstract

In this study, it was aimed to produce microencapsulated thermochromic system with thermal energy storage property which could be used in thermal comfort and sensory applications. For this reason, fluoran dye based thermochromic systems (TSs) were prepared and microencapsulated into poly(methyl methacrylate-co-methacryl amide) shell by emulsion polymerization method. The systems include a fluoran dye as leuco dye, phenolphatelein (PP) as color developer, and 1-tetradecanol (TD) as solvent. The solvent component of the system performs the function of thermal energy storage/releasing and its melting temperature corresponds to the activation temperature of the system. According to SEM images, microcapsules were spherical and had homogenous sizes. The PSD analysis results showed that the mean particle sizes of microcapsules were in an extensive range (12-15 µm) but suitable for textile applications. DSC analysis results indicated that microcapsules had good latent heat energy storage capacity and their melting enthalpy values were in a range of 139.3-176.1 J/g. According to TG analysis results, microcapsules degraded in two distinguishable. The thermochromicity of the microcapsules was proven using UV-Vis spectrophotometer analysis and photographic images taken with a camera. Based on the photographs, it was also proven that microcapsules exhibited reversible color changing behavior with thermal stimuli. In the study, microcapsules were applied to 100% polyester fabric by the impregnation method. Causticizing and anionizing pre-treatments were applied to the fabric before application. From the SEM images of the fabric, the presence of clustered, dense microcapsules in the fabric structures was observed. The sample fabric was darker in colour and the colour homogeneity was relatively better there. The total colour difference value (ΔE) calculated using hot-cold colour measurement values were between the 19.08 and 23.97. Thermal energy storage capacity of the microcapsule applied sample fabric was determined as 31.9 j/g during heating at 34.2°C.

Keywords: Thermochromic system, phase change material, thermal energy storage, thermal stimuli

I. Introduction

Thermochromism is the mechanism of reversible color change that exhibited by the material in response to temperature change (Ibrahim, 2012; Chowdhury et al. 2014). There are different types and structures of organic or inorganic thermochromic materials, and one of them is leuco dye based three-component thermochromic systems. The leuco dye based thermochromic systems consist of three components: a leuco dye as color former, a weak acid developer and co-solvent (Kulcar et al. 2010; Zhang et al. 2017). Color formers are colorless in closed ring form while they are colored in open ring form. The closed ring is open by protonation, using a weakly acidic developer such as a phenolic component (Ibrahim, 2012). At below the melting temperature of the solvent (when system is solid), the reaction of color former and developer forms the colored form, while their separation in the molten form creates the colorless form (Zhang et al. 2017). In summary, three-component thermochromic systems exhibit reversible color change based on the temperature sensitive solid-liquid phase change process of the solvent component. They are encapsulated in a solid shell structure for most end-use areas due to the risk of leakage of the solvent carrying dye and color developer. There are many studies in the literature on the encapsulation of three-component thermochromic systems into different wall structures using different methods (Guan et al. 2018; Zhu et al. 2018; Kim et al. 2018; Ma et al., 2019; Tözüm et al., 2020; Özkayalar et al. 2020; Pu and Fang, 2022; Li et al., 2023). However, it is noteworthy that in these studies, Bisphenol A, which is known to have toxic effects, was generally used as a color developer. In this study, we focused on the development of alternative non-toxic thermochromic systems against the toxic effect of Bisphenol A and their encapsulation to provide application possibility. For this purpose, a three-component system containing fluorane type leuco dye was prepared and encapsulated into the poly(methyl methacrylate-co-methacryl amide) (P(MMA-co-MAA)) shell by the emulsion polymerization method. In the study, the potential of producing textile-based thermal energy storage and thermochromic functional fabrics was evaluated by applying the prepared thermochromic microcapsular polyester fabric. In this context, the selected microcapsule sample was applied by the impregnation method to the fabric that was subjected to two pre-treatments: causticizing and anionicization. Temperature sensitive color change, morphological analysis and thermal energy storage properties of the fabrics were examined.

II. Experimental Procedure/Methodology/System Description

In the preparation of TSs, 2'-(Dibenzylamino)-6'-(diethylamino) fluoran dye supplied from TCI Chemicals Company was used as color former. The weight ratio of dye/phenolphthalein/1-tetradecanol in TSs was 0.055/0.09/6.42, respectively. The dye and phenolphthalein (PP, Carlo Erba) were added to the 1-tetradecanol (TD, Alfa Aesar, 97% +) solvent at 90 °C and mixed until dissolution was completed. In order to improve the UV resistance of TSs, UV absorber (2,4-Dihydroxybenzophenone, Alfa Aesar, 99%) was added to ternary mixture (Özkayalar et al. 2020). The amount of UV absorber was four and six times of the amount of dyestuff in TSs (Table 1). The

production of poly(methyl methacrylate-co-methacryl amide) (P(MMA-co-MAA)) walled microcapsules containing TSs was carried out by oil in water emulsion polymerization method. The shell/core ratio was chosen as 0.5:1. A 6.5 g of TS was added into 100 ml of deionized water at 50 °C and emulsified by adding 2 g of PEG1000 surfactant stirring for half an hour at a mixing speed of 2000-3000 rpm. Then, 3.25 g of MMA (Sigma Aldrich, 99%), 0.32 g of MAA (Acros Organics, 98%), 1.35 g of EGDM (Sigma Aldrich, 98%) crosslinker and 1 gram of 2-Azobis(2-methyl-propionamidine) dihydrochloride (Aldrich, 97%) initiator were added to the prepared emulsion. The temperature was increased to 80 °C and stirring speed was decreased to 1000-2000 rpm to initiate polymerization reaction. The microcapsules produced after stirring for about three hours were washed several times using hot water at around 70 °C and filtered. The prepared TSs and microcapsules were given in Table 1.

Table 1. The abbreviations and features of the TSs and microcapsules

Microcapsule code	Core material	UV Absorber	Dye	Color developer	Solvent
P(MMA-co-MAA)/ TSUVA1	TSUVA1	0.22 g-UVA	0.055 g	0.09 g	6.42 g
P(MMA-co-MAA)/ TSUVA2	TSUVA2	0.33 g-UVA			

In the study, microcapsules coded P(MMA-co-MAA)/TSUVA2 were applied by the impregnation method to a woven fabric made of 100% polyester and having a weight of 220 g/m^2. Causticizing and anionizing pre-treatments were applied to the fabric one after the other before application. In order to increase the uptake of microcapsules into the fabrics, causticizing was carried out by the exhaustion method as a pre-treatment. With the alkalization process, the chains are not completely broken down by the saponification reaction in the ester bonds of the polyester fibers, but the chains break, resulting in the release of alcohol and carboxylic acid groups at the chain ends. Thus, the number of functional groups in the fiber increases. In the causticizing process, an aqueous solution containing sodium hydroxide (NaOH) at a concentration of 40 g/L was applied to the fabrics at a liquor ratio of 1:50 at 98 °C for 30 minutes. Then, the fabrics were washed with distilled water at 40 °C for 30 minutes and left to dry at room temperature. P(MMA-co-MAA) walled microcapsules are positively charged under application conditions due to the presence of methacrylamide monomer in their wall structures. In order to increase the affinity of positively charged microcapsules towards polyester fiber, polyester fabrics were pre-treated with tannic acid and gained anionic character before microcapsule application. The fabric/tanic acid (wt) ratio was selected as 1/0.15 and the flotte ratio was adjusted as 1:40. The prepared flotte was absorbed into the fabric at a temperature of 50 °C for 60 minutes. The remaining solution was impregnated into the fabric at a speed of 2 m/d and a pressure of 2 bar in a foulard and the ratio of the extracted flotte was calculated as approximately 90%. The prepared fabrics were dried at room temperature. In the application of capsules to pre-treated fabrics, an aqueous dispersion with 300 g/L microcapsules and dispersant (5% of the capsule amount) was impregnated to the sample fabris. To preparation of the reference fabric, microcapsule aqueous dispersion without dispersant (Permulsin FF) was also prepared and applied to the fabrics. After application, the fabrics were left to dry at room temperature.

III. Analysis

The color changes behaviors of TSs and microcapsules by a change of temperature were investigated with photograph images taken by using a digital camera at different temperatures. To examine the morphology of the produced microcapsules, scanning electron microscopy (SEM, LEO 440 Computer Controlled Digital) analysis was carried. Particle sizes and particle size distribution of microcapsules were determined by particle size analyzer (Malvern Brand MS2000E model). FTIR spectroscopy analysis was performed with KBr pellet technique at 4 cm^{-1} resolution, in the 4000-400 cm^{-1} middle infrared region with 2 cm^{-1} intervals to determine chemical structures of the produced microcapsules using Perkin Elmer Spektrum BX instrument.The phase transition points and heat storage/release capacities of the microcapsules were determined by a differential scanning calorimetry (DSC, Perkin-Elmer Jade) at a heating rate of 1 °C/min, between the temperature of -5 °C and 65 °C under nitrogen gas.

TG analysis was carried out to examine the thermal stability of microcapsules using a Perkin Elmer TGA7 instrument in the range of 0-500 °C, at a heating rate of 10 °C/d under air atmosphere. The changes in temperature-dependent UV absorption values of TSs and microcapsules were examined by using Shimadzu-UV3800 spectrophotometer in the wavelength range of 400-800 nm. The visible region absorption values of the samples in hot and cold states were measured. The fabrics were characterized morphological by SEM and thermally by DSC. Additionally, visual inspection and color measurements of the fabrics in hot and cold conditions were also performed. To determine the temperature-dependent reversible color change resulting from the presence of thermochromic microcapsules in the structures of the fabrics, the color values of fabric samples cooled below the transition temperature and heated above the transition temperature (40°C) were measured with a spectrophotometer. Measurements were made using the Datacolor CHECK 3 spectrophotometer device. Colorimetric parameters were calculated using CIELAB color space under D65 light and 10° standard observers. In the study, the cold-warm total color difference value (ΔE) is calculated with the following formula (Equation 1):

$$\Delta E = \sqrt{[(Lx^* - L0^*)2 + (ax^* - a0^*)2 + (bx^* - b0^*)2]}, \text{ (Equation 1)}$$

Here: L0*, a0*, and b0* represent the L*, a*, and b* values of the colored fabric samples.

ΔE value expresses the total color difference, and an increase in this value indicates that the color difference is large. Commercially, a ΔE value of less than 1 indicates that the color difference is nonsignificant. A negative (-) ΔL value indicates that the color of the compared sample is darker than the reference, and a positive (+) value indicates that it is lighter.

IV. Results and discussion

The prepared TSs worked reversibly, and colored and colorless photo images of them and their microcapsulated forms were presented in Figure 1. According to the images, TSs were dark green in cold as they were colorless when heated. Similarly, microencapsulated TSs were green in color when cold, but became colorless when heated. However, the color darkness of TSs decreased after microencapsulation as expected due to the white wall material of the microcapsules. In the UV-vis spectra of the capsules taken in the cold, the absorbance values at the wavelength of 400-800 nm were around 2.5-3 A, while the values decreased to 0.5 and below when

the capsules were heated. According to the SEM images, microcapsules were homogeneously distributed and spherical shaped. The average particle size of the microcapsules (d50) was measured as 14,750 µm and 12,474 µm for P(MMA-co-MAA)/ TSUVA1 and P(MMA-co-MAA)/ TSUVA2, respectively (Figure 1).

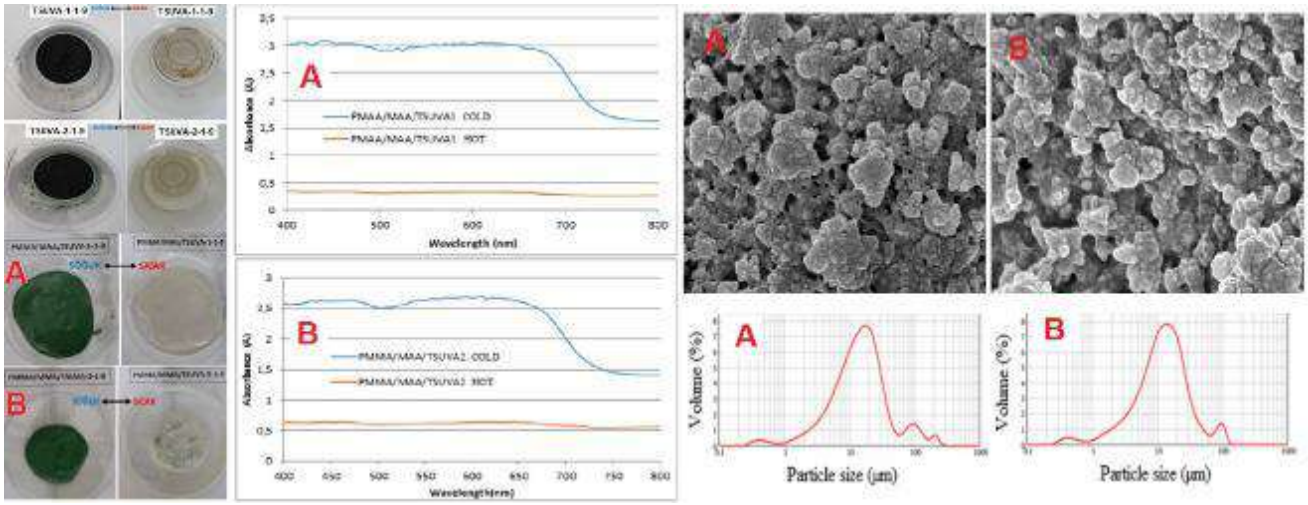

Figure 1. Temperature responsive reversible color change of TSs and microcapsules, UV-Vis spectrums of microcapsules, SEM images of the microcapsules, particle size distribution curves of microcapsules (A: P(MMA-co-MAA)/TSUVA1, B: P(MMA-co-MAA)/ TSUVA2)

Chemical structure examination by FT-IR spectroscopy confirmed that the copolymer shell structure produced by reacting the monomers with each other and the TSs were incorporated into the structure. According to the DSC analysis results, P(MMA-co-MAA)/TSUVA1 and P(MMA-co-MAA)/TSUVA2 microcapsules absorbed the latent heat of 144.2 J/g and 176.1 J/g at 33.6 °C, respectively. According to TGA curves, microcapsules showed two distinguished steps for degradation. While the weight loss in the first step was assigned to the solvent of the TS diverging from the microcapsule shell structure, the weight loss in the second step was due to the complete degradation of the shell structure. The microcapsules began to decompose over 200 °C.

In the study, P(MMA-co-MAA)/TSUVA2 microcapsules were impregnated to the pre-treated polyester fabric. The SEM images and photos of the fabrics were given in Figure 2. From the SEM images, the presence of clustered, dense microcapsules in the fabric structures was observed. According to the photographs of the fabrics in cold and coloured condition, it was determined that the sample fabric was darker in colour and the colour homogeneity was relatively better there. The total colour difference value (ΔE) calculated using hot-cold colour measurement values were 19.08 for the reference fabric and 23.97 for the sample fabric. When evaluated together with the colour measurement results, it was observed that the sample fabric was darker green in the coloured state compared to colorless hot sample fabric and the colour homogeneity was more pronounced. This difference was thought to be due to the use of Permulsin FF dispersing agent (anionic character, Bozzetto Group) in the microcapsule application to the fabric in question. The dispersant reduces the tendency of the capsules to cluster and ensures their homogeneous distribution on the fabric surface. Thermal energy storage capacity of the microcapsule applied sample fabric was determined as 31.9 j/g during heating at 34.2°C and 28.6 j/g during cooling at 35.5°C. There was also a solid-solid phase change at 29.1°C.

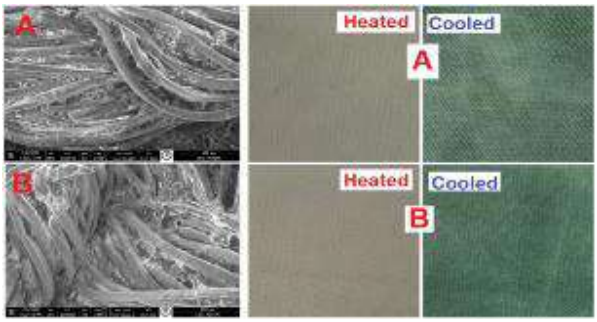

Figure 2. SEM images and colored and colorless images of the fabrics (A: reference, B:sample)

V. Conclusion

In this study, three-component thermochromic systems consisting of a fluorane dye, phenolphthalein colour developer and 1-tetradecanol solvent, with considerable enthalpy were prepared and encapsulated in a P(MMA-co-MAA) shell succesfully. In addition to thermal storage capacity, the working temperatures of the capsules are close to body temperature which is suitable to be exploited for sensory property. Copolymer structure of the shell resulted in homogeneously distributed application possibility onto a polyester fabric. The thermochromic property of the microparticles persisted in the polyester woven fabric, i.e. fabric form of sensory material with thermal energy storage property was obtained.

Acknowledgements

This work was supported by the scientific and technological council of Turkiye (TUBITAK, Project Number 118M012). Therefore authors would like to express their appreciation to TUBITAK.

References

Chowdhury, M.A., Joshi, M., Butola, B.S., 2014. Photochromic and thermochromic colorants in textile applications, J. Eng. Fibers Fabr. 9(1), 107-123. https://doi.org/10.1177/155892501400900111

Guan Y, Zhang L, Wang D, West JL, Fu S., 2018. Preparation of thermochromic liquid crystal microcapsules for intelligent functional fiber. Mater. Design. 147, 28-34. https://doi.org/10.1016/j.matdes.2018.03.030

Ibrahim, W., 2012. An Investigation into textile applications of thermochromic pigments. Heriot-Watt University, School of Textiles and Design, PhD Thesis, 280p, Edinburgh.

Kim, I.J., Ramalingam, M., Son, Y.A. 2018. Investigation of reversible self-thermochromism in microencapsulated fluoran-based materials, Dyes Pigm. 151, 64-74. https://doi.org/10.1016/j.dyepig.2017.12.047

Kulcar, R., Friskovec, M., Hauptman, N., Vesel, A., Klanjsek Gunde, M., 2010. Colorimetric properties of reversible thermochromic printing inks, Dyes Pigm. 86(3), 271-277. https://doi.org/10.1016/j.dyepig.2010.01.014

Li, Y., Jiang, Z., He, F., Chen, Z., Li, X., Wang, P., ... & Yang, W. 2023. Reversible thermochromic microcapsules with SiO2 shell for indicating temperature and thermoregulation. J. Energy Storage, 72, 108674. https://doi.org/10.1016/j.est.2023.108674

Ma, X., Wang, L., Li, L., Bian, L., Yang, W., & Meng, Q. 2019. The novel thermochromic and energy-storage microcapsules with significant extension of color change range to different tones. J. Macromol. Sci. A, 56(6), 588-596. https://doi.org/10.1080/10601325.2019.1590125

Özkayalar, S., Adıgüzel, E., Alay Aksoy, S., Alkan, C. 2020. Reversible color-changing and thermal-energy storing nanocapsules of three-component thermochromic dyes, Mater. Chem. Phys. 252, 123162. https://doi.org/10.1016/j.matchemphys.2020.123162

Pu, Y., & Fang, J. 2022. Preparation and thermochromic behavior of low-temperature thermochromic microcapsule temperature indicators. Colloids Surf. A Physicochem. Eng. Asp., 653, 129889. https://doi.org/10.1016/j.colsurfa.2022.129889

Raditoiu, A., Raditoiu, V., Nicolae, C.A., Raduly, M.F., Amariutei, V., Wagner, L.E., 2016. Optical and structural dynamical behavior of crystal violet lactone-phenolphthalein binary thermochromic systems. Dyes Pigm., 134, 69-76. https://doi.org/10.1016/j.dyepig.2016.06.046

Tözüm MS, Alkan C, Alay Aksoy S. 2020. Preparation of poly(methyl methacrylate-co-ethylene glycol dimethacrylate-co-glycidyl methacrylate) walled thermochromic microcapsules and their application to cotton fabrics. J. Appl. Polym. Sci. 137(24), 1-13. https://doi.org/10.1002/app.48815

Zhang, W., Ji, X., Zeng, C., Chen, K., Yin, Y., Wang, C. 2017. A new approach for the preparation of durable and reversible color changing polyester fabrics using thermochromic leuco dye-loaded silica nanocapsules, J. Mater. Chem. C, 32, 5, 8169-8178. https://doi.org/10.1039/C7TC02077E

Zhu, X., Liu, Y., Li, Z., Wang, W. 2018. Thermochromic microcapsules with highly transparent shells obtained through in-situ polymerization of urea formaldehyde around thermochromic cores for smart wood coatings, Sci. Rep., 8,4015. DOI:10.1038/s41598-018-22445-z

IEEES-024

A Study On The Comparıson Of Battery Parameters Of An Electrıc Bus Accordıng To Passenger Occupancy

[1*]Muhammet Sefa ODABAŞI, [2]Berkay TAHİRAĞAOĞLU, [3]Gökhan SEVİLGEN
[1] Ulaşım İç ve Dış Ticaret A.Ş, R&D Center, Hamzabey OSB, İnegöl, Bursa, 16400, Turkey
[2] Bursa Uludağ University, Graduate School Of Natural and App. Science, Department of Automotive Engineering, Nilüfer, Bursa, 16059, Turkey
[3] Bursa Uludağ University, Engineering Faculty, Department of Automotive Engineering, Nilüfer, Bursa, 16059, Turkey
*E-mail: mailto: sefa. odabasi@ulasim – as. comsefa.odabasi@ulasim-as.com,
mailto: tahiragaogluberkay@gmail. comtahiragaogluberkay@gmail.com, gsevilgen@uludag.edu.tr

Abstract

The rate of electrification in public transportation is increasing day by day as a result of growing environmental awareness, decreasing fossil fuel resources and the emergence of strict regulations worldwide. The batteries used in electric buses are the main constraint that directly affects many specific parameters of the vehicle. Real data from the batteries is of great importance in improving these parameters. In this study, the real driving data of an electric bus is obtained from the CAN Bus of the vehicle. Battery parameters of the vehicle in loaded and unloaded conditions were analyzed based on the vehicle test scenario. The test data obtained for both cases are compared and the effect on the vehicle driving parameters is investigated. Based on the results obtained in the study, some determinations were made to improve both vehicle and battery thermal management system performance. This study is expected to contribute to the literature since there are limited studies in the literature on data collected from batteries under real driving conditions.

Keywords: Electric Bus, Battery, Loaded-Unloaded Tests, Battery SoC, Energy Consumption, Power, Heat

I. Introduction

Public transportation buses are the most widely used vehicles in urban transportation. However, city buses driven by conventional internal combustion engines have a significant share in terms of carbon dioxide emissions (Xu et al., 2023). Especially in recent years, increasing environmental awareness and tightening emission standards, a significant increase in the electrification rates of public transportation buses is expected in the coming years as a precautionary method against rising environmental pollution (Bashjaweesh et al., 2021). The conversion rate in electrification is increasing in parallel with the development in battery technologies and thus the improvement in vehicle range.

Lithium ion batteries are the most open to development and the most studied battery technology in recent years. The performance of lithium ion batteries is affected by many parameters. The temperature factor is the most important of these (Liu et al., 2022). It is stated that the ideal operating temperature for batteries is between 15°- 35°C (Bamrah et al., 2022). (Önçağ et al., 2021) compared electric buses and diesel buses on the same line in various aspects. At the end of the study, they revealed the advantages of electric buses over diesel buses in terms of cost and energy consumption. (İnce and Başlamışlı, 2021) conducted a study on the initial investment cost and operating costs of diesel, hybrid electric and battery electric buses by considering their energy consumption. (Tong and Ng, 2023) revealed the importance of route topography in terms of seeing the effect of energy consumption and developed a driving cycle for Hong Kong. (Basma et al, 2020) investigated the energy consumption of electric buses by building a single model including subsystems (air conditioning, propulsion, auxiliary systems, etc.). (Xu et al., 2023) collected real-time data on electric buses and calculated energy consumption using two metrics. (Szilassy and Földes, 2022) developed a model for the energy consumption of an electric bus that takes into account the auxiliary systems. As a result, they pointed out that the reasons for high energy consumption are the low ambient temperature and the high distance between stops. (Tahiragaoglu et al., 2022) calculated the recyclable waste heat of an electric vehicle during the driving cycle and used it as an additional source in a heat pump system. (Alarrouqi et al., 2022) investigated the energy consumption of electric buses used in Qatar under different operating conditions by collecting real data. They found that the energy consumption of the air conditioning system corresponds to 30% of the energy requirement of the entire vehicle. It is also stated that the effect of driver behavior on energy consumption is very limited.

In this study, real-time data was collected from the CAN Bus of an Ulaşım 12 meter LF12 battery electric bus ("Ulasim A.S.," n.d.) traveling on a specific test route. The collected data is analyzed and battery parameters such as SOC, heat generated in the battery, energy consumed are compared for loaded and unloaded conditions.

II. Material and Method

This section provides information about the methodology of the study. Our work can be considered in two phases: collecting real-time data from the bus CAN Bus line and analyzing the data. In this study, real-time driving data was obtained using a 12-meter long Ulaşım LF12 vehicle. Technical specifications of the tested vehicle and its battery are given in Table 1.

Table 1. Technical specifications of the test vehicle and battery pack

- Vehicle Specs		- Battery Specs	
Model	Ulaşım LF12 Electric Bus	Capacity	88 Ah
Dimensions(LxHxW)	12.000x3.350x2540 mm	Cell Configuration	168S2P
Un/Loaded Weight	12.500 kg / 19.500 kg	Installed Energy	215 kWh
Passenger Capacity	92	BTMS	8kW, liquid coolant

In order to determine the heat generated in the battery and energy consumption values of the vehicle, tests were carried out within certain scenarios. For this purpose, two different test scenarios were designed as unloaded and fully loaded. In both scenarios, the test route was 50 km long. Acceleration was carried out with a non-aggressive profile throughout the entire drive. The braking procedure was done in a way not to disturb passenger comfort. The air conditioning system was kept off throughout the test drive. In the scenario where the fully loaded condition was examined, passenger boarding and alighting was represented by stopping the vehicle at certain intervals and opening the doors for 15 seconds to better simulate urban public transportation conditions. Sandbags and dummies were used to represent passenger occupancy. The driving was then continued in exact accordance with the acceleration and braking procedures followed in the unloaded state. In order to see the effect of the air conditioning system, which is one of the parameters that most affect energy consumption and battery temperature in electric buses, it was tested with the air conditioning system active in this scenario. Thus, the test was carried out to represent the worst case scenario. The tests were run on a route between Dushanbe and Qurghonteppa region of Tajikistan. During the tests, real-time data was recorded by connecting to the vehicle's CAN Bus line with interface devices.

$$Q = I_L(E_0 - U_L) - I_L T \frac{dE_0}{dT} \quad (1)$$

In the above equation, Q represents the total heat generated by the cell (W), I_L is the current (A), E_0 is the open circuit voltage (V), U_L is the voltage (V), T is the temperature (K) (Li, n.d.). Only ohmic heat is considered in this study. The ohmic heat generated in the battery is as follows:

$$Q = R_{eq} I^2 \quad (2)$$

Here; R_{eq} is the equivalent cell resistance (Ohm) calculated according to the open circuit voltage method, I is the cell current (A). The expression giving the electrical power (W) drawn from the battery is as follows:

$$P = UI \quad (3)$$

The LF12 electric bus was driven in two different test scenarios and the data received from the CAN Bus line were analyzed in the CANalyzer program and the heat generated in the battery and energy consumption were investigated. In the analytical studies, the relations given above were used.

III. Results and discussion

When the data obtained from the loaded and unloaded weighted tests of the LF12 electric bus on the 50 km test route were analyzed with the CANalyzer program, energy consumption and battery parameters were obtained. Accordingly, energy consumption for loaded and unloaded conditions is presented in Figure 1.

Although the vehicle covered the same distance in the loaded and unloaded tests, the driving time is longer in the loaded condition as shown in Fig.1. This is due to the higher number of stops and starts in order to better represent the loaded conditions, the varying traffic conditions between the tests, and the effect of driver behavior. In addition, the fact that the HVAC systems turned on and the total mass was higher in the loaded condition led to an increase in the total energy consumed. The total energy consumption in the loaded state was 62 kWh, while the total energy consumption in the unloaded state was 52.9 kWh. Due to the energy consumption of 1.24 kWh/km in the loaded state and 1.05 kWh/km in the unloaded state of the electric bus, it brings an extra cost of 0.05 USD/km.

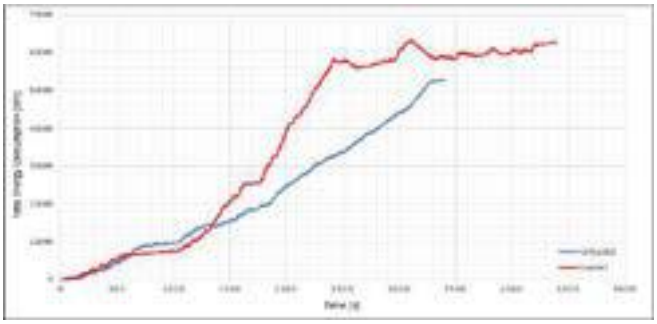

Fig.1) Comparison of Total Energy Consumption based on Load Conditions.

When Fig.2 is examined, it is seen that the heat generated in the loaded state is higher than the unloaded state. This is due to the fact that the air conditioning system is on in the loaded test and the current drawn and the internal resistance of the cell increase due to the high total mass. In the graph, the heat generation near the horizontal axis is different from zero and has relatively small values. When a comparison is made in terms of average heat generation, the average heat generated in the loaded state is 188.35 W and the average heat generated in the unloaded state is 123.6 W.

The maximum temperature in the battery was 30°C under load and 29°C under no load. According to these results, the battery cooling system of the electric bus offers the required performance for optimum operating temperature even under extreme conditions.

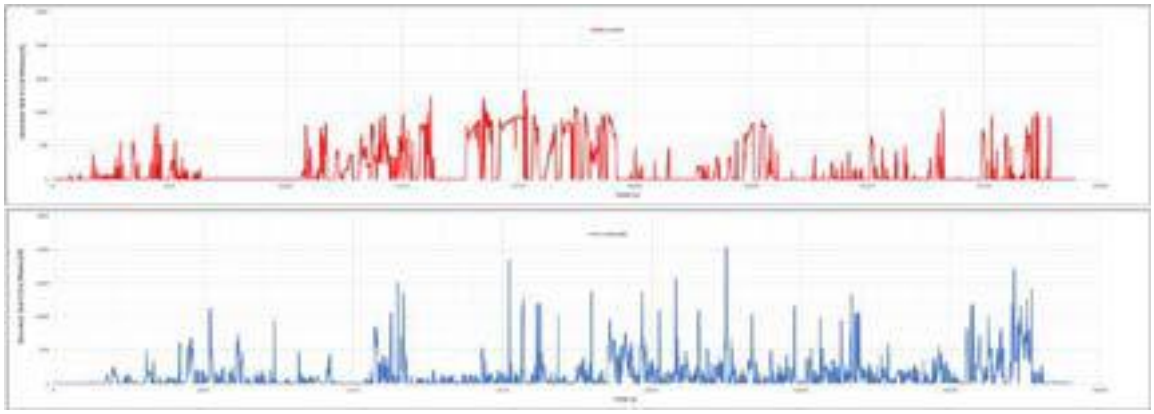

- **Fig.2)** Generated Heat per Module based on Load Conditions.

The change in the battery charge state of the electric bus after loaded and unloaded tests on the 50 km test route is shown in fig.3. After 10 km of driving, the SoC value decreases much faster in the loaded state than in the unloaded state due to parameters such as stop and go operations to represent passenger circulation, the air conditioning system being on and the slope of the road. Stop and go operations were more frequent between kilometers 10 and 20 than the rest of the route. Between km 20 and 25, power demand was low and the vehicle maintained a certain speed. Between km 30 and 35 there is an increase in SoC due to deceleration in regenerative braking mode when going downhill. After 35 km, the SoC value showed small changes depending on the speed profile. The SoC value of the electric bus in the loaded state is much more sensitively affected by the road topology, driver behavior and environmental factors than in the unloaded state.

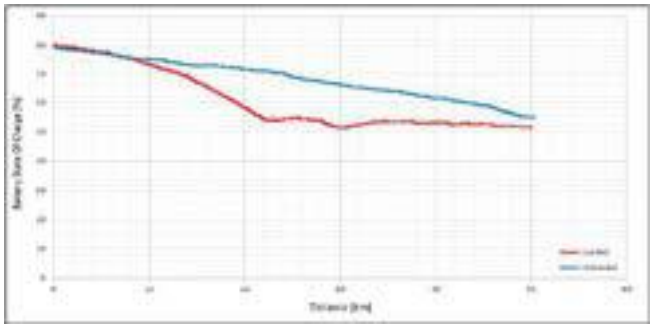

- **Fig.3)** Comparison Of Battery State of Charge According to Passenger Occupancy

IV. Conclusion

In this study, real-time data of the LF12 electric bus under loaded and unloaded operating conditions were collected from the CAN Bus line and analyzed to determine the battery parameters and energy consumption values for the two conditions. The results show that the energy consumption and driving cost are higher in loaded conditions than in unloaded conditions. Since the power demanded from the vehicle battery is higher in loaded conditions, it is seen that more heat is generated in the battery due to the current drawn from the battery and increased internal resistance. When the battery temperatures are analyzed, it is understood that the battery cooling system of the LF12 vehicle performs to keep the cells at optimum operating temperature. In the study, auxiliary systems such as HVAC systems were also included in order to apply the worst-case scenario and it was understood that the loaded vehicle is much more affected by factors such as road topology, environmental factors and driver behavior when driving at full passenger capacity compared to the unloaded state. In this study, a comparison was made between the ideal case and the worst case. Future studies should be conducted to examine the separate effects of auxiliary systems such as air conditioning, topological factors, driver behavior, traffic density and other environmental factors.

Acknowledgements

The authors would like to thank Ulaşım İç ve Dış Tic. A.Ş. for their support.

References

Alarrouqi, R.A., Bayhan, S., Al-Fagih, L., 2022. Battery Electric Buses Operating in Qatar: A Comprehensive Energy Consumption Analysis, in: 2022 IEEE Transportation Electrification Conference and Expo, ITEC 2022. Institute of Electrical and Electronics Engineers Inc., pp. 1236–1241. https://doi.org/10.1109/ITEC53557.2022.9813924

Bamrah, P., Chauhan, M.K., Sikarwar, B.S., 2022. CFD Analysis of Battery Thermal Management System, in: Journal of Physics: Conference Series. IOP Publishing Ltd. https://doi.org/10.1088/1742-6596/2178/1/012035

BASHJAWEESH, M., MANSOUR, O., GEDİZ İLİŞ, G., 2021. An Investigation on the Cooling System of Synchronous Motor for Electric Buses. Deu Muhendislik Fakultesi Fen ve Muhendislik 23, 567–573. https://doi.org/10.21205/deufmd.2021236819

Basma, H., Mansour, C., Haddad, M., Nemer, M., Stabat, P., 2020. Comprehensive energy modeling methodology for battery electric buses. Energy 207. https://doi.org/10.1016/j.energy.2020.118241

İnce, B., Başlamışlı, S.Ç., 2021. Design of energy management system algorithms for the improvement of fuel economy of intracity hybrid buses and development of an adaptive hybrid algorithm. Journal of the Faculty of Engineering and Architecture of Gazi University 36, 559–575. https://doi.org/10.17341/gazimmfd.626431

Li, J., n.d. Modeling and Simulation of Lithium-ion Power Battery Thermal Management Key Technologies on New Energy Vehicles.

Liu, Z., Guo, X., Meng, N., Yu, Z., Yang, H., 2022. Study of thermal runaway and the combustion behavior of lithium-ion batteries overcharged with high current rates. Thermochim Acta 715. https://doi.org/10.1016/j.tca.2022.179276

Önçağ, A.Ç., Üzkat, H., Yeşil, Z.C., Eliiyi, U., 2021. A comparative evaluation on electric buses: Izmir city field analysis. Pamukkale University Journal of Engineering Sciences 27, 43–51. https://doi.org/10.5505/pajes.2020.99582

Szilassy, P.Á., Földes, D., 2022. Consumption estimation method for battery-electric buses using general line characteristics and temperature. Energy 261. https://doi.org/10.1016/j.energy.2022.125080

Tahiragaoglu, B., Basak, E., Bayram, H., Sevilgen, G., 2022. The Investigation on the Heating Performance of the Heat Pump System with Waste Heat Recovery for the Electric Vehicle, in: ISMSIT 2022 - 6th International Symposium on Multidisciplinary Studies and Innovative Technologies, Proceedings. Institute of Electrical and Electronics Engineers Inc., pp. 947–951. doi:10.1109/ISMSIT56059.2022.9932859

Tong, H.Y., Ng, K.W., 2023. Developing electric bus driving cycles with significant road gradient changes: A case study in Hong Kong. Sustain Cities Soc 98. https://doi.org/10.1016/j.scs.2023.104819

Ulasim A.S. [WWW Document], n.d. URL https://www.ulasim-as.com/LF12EV (accessed 11.16.23).

Xu, Z., Wang, J., Lund, P.D., Zhang, Y., 2023. Analysis of energy consumption for electric buses based on low-frequency real-world data. Transp Res D Transp Environ 122. https://doi.org/10.1016/j.trd.2023.103857

IEEES-025

Sustainable Efficiency based Development of A Painting Robot Machine Simulating Operator Movements for Wind Turbine Tower Painting Process

[1]Sakıp Tüzköz, [1]Salih Aksu, [1]Can Tuncer, [1,2]Ali Oral, [1,2,*]Enver Yalçın
[1]Gesbey Enerji Türbini Kule Üretim San. ve Tic. A.Ş., Ar&Ge Merkezi, Bandırma Organize Sanayi Bölgesi, 10900-Bandırma-Balıkesir-Turkey
[2]Balıkesir University, Engineering Faculty, Mechanical Eng. Dept.,10145- Balıkesir-Turkey
*E-mails: sakip.turkoz@gri.com.es; salih.aksu@gri.com.es; can.tuncer@gri.com.es; alioral@balikesir.edu.tr; [*]eyalcin@balikesir.edu.tr

Abstract

The production of wind turbine tower consists of design, shaping and assembly stages. The painting process, which can be considered an indispensable part of the shaping phase, is one of the most important applications in terms of system life in wind turbine tower manufacturing. In the study, instead of the manual painting process with the operator, a paint robot, which is driven by servo motors displaced on axes and can simulate human movements during the painting process, has been developed. Thanks to the control system of the developed machine, the approach distance of the paint gun to the surface to be painted and its tracking are performed automatically. In this way, a good surface quality and a reduction in the amount of paint used are achieved.

Keywords: Painting robot, surface treatment, painting booth

I. Introduction

The painting process is done for cathodic protection of the metal material surface against corrosion and rust. Air jet painting, which is a typical example of surface protection, is widely used in many fields such as vehicles, furniture, aviation and so on. Wind turbine tower parts are painted with two types of paint which are epoxy and polyurethane, in a paint booth. Before painting, there is a surface sandblasting process. Steel grits are thrown on the surface under pressure with air and sandblasted and surface roughness is obtained, then the painting surface is cleaned with a spatula and compressed air. The paint mixture is prepared at the desired temperature, the pump air pressure is adjusted, and the preparation process is completed by reaching the spraying position with the spray gun. While the wind turbine tower part is rotated on the rotating equipment in the cabin, the paint is sprayed onto the surface by the painting operator with the paint pump and compressed air paint gun, which is mixed in the painting pump reservoir, simultaneously. With the paint robot, there is an expectation of obtaining a good surface quality thanks to the constant speed of the shot, a homogeneous paint distribution as much as possible, and a reduced paint consumption. In general, wind turbine tower manufacturers have been studying on this issue in which paint is sprayed with robots working with this type of servo motor motion technology in paint booths.

Nowadays, robotic spray-painting technology is increasingly preferred because it improves the painting quality and sustainable stability of spray paint, reduces paint waste, prevents operator damage from manual spray painting, and prevents operator-induced painting errors. Off-line programming is the key technology that uses spray painting robots to automate production to ensure continuity. The main issue here is how to set up an efficient and practical painting motion line pattern that does not overlap for robotic air spray painting (Xia et al., 2010). By performing the painting process in the shortest distance without overlap the painted line again, it will provide a considerable saving in paint consumption as well as obtaining the desired result in painting quality.

Three different models can be seen in the literature, including Beta, Gaussian and dual-beta distribution models related the paint thickness distribution model to a specific function by referring to the measurement results of the paint thickness on flat surfaces (Balkan and Arikan,1999; Hyotyniemi, 1994; Zhang et al., 2006). However, these models are not successful on free surfaces.

Off-line programming technology includes two modules, model reconstruction by using computer aided design (CAD) and trajectory planning stage. CAD model reconstruction basically includes creating a freeform surface model thanks to CAD, dividing the model into a finite element mesh, obtaining its document in stereolithography format, and modifying the model in a spray-painting system. The purpose of dividing into a finite number of elements is to obtain a finite number of surface normals and to plan the trajectory accordingly. The main problem of trajectory planning in the robotic air-jet painting system is to accurately determine the paint deposition pattern, which determines the paint thickness distribution on the free-form surface. The basic approach here is to determine the radius of curvature of each of the free surfaces divided into a finite number of elements and to reference them.

II. Painting mechanism and design specification

In the paint shop sections of the wind turbine tower production facilities, the tower painting processes are usually carried out manually by the operator. While the operator is working, the painting progress speed and the spray distance to the painting surface vary from person to person due to differences in hand movements. These unstable variables affect the amount of paint applied to the surface, cause a fluctuating thickness distribution, paint thickness close to the upper tolerance limits can be observed, and for these reasons, paint consumption increases. To reduce the paint consumption by making the surface paint thickness homogeneous, the need for a machine design that can control the above-mentioned parameters has arisen. In addition, operators work in special clothes in the cabin and are exposed to solvents. When evaluated in terms of operator health, the benefit of the output of the design issue cannot be ignored in this sense. Considering that the wind turbine tower consists of large parts, the part dimensions of which vary between 15-36 meters

in length and 2.5-6 meters in diameter, it is inevitable that the paint booths will be large in parallel with these dimensions. The machines designed to be used here are likewise machines that require large-scale construction. There are applications such as a profile construction system projected in this study, which moves on a rail, and a coupled rack-and-pinion movement system. It is aimed to develop a painting robot that applies paint to the outer surface of the wind turbine tower that simulates operator movements.

In evaluating the application quality, compliance with the ISO 12944 standard is required. Dry film thickness (DFT) distribution must be within the limit values specified in the standard on the entire surface. Otherwise, it is considered defective during the quality control phase. Since different limit values are defined for different paint types, they are not given here. In the developed system, it is aimed to build a robot that will paint the outer surface of the tower part with a length of 15-36 meters and a diameter of 3-4.7 meters and simulate operator movements. The design visual of the paint shop cabin and robot is given in Figure 1. The process time is almost the same as the time taken with the operator.

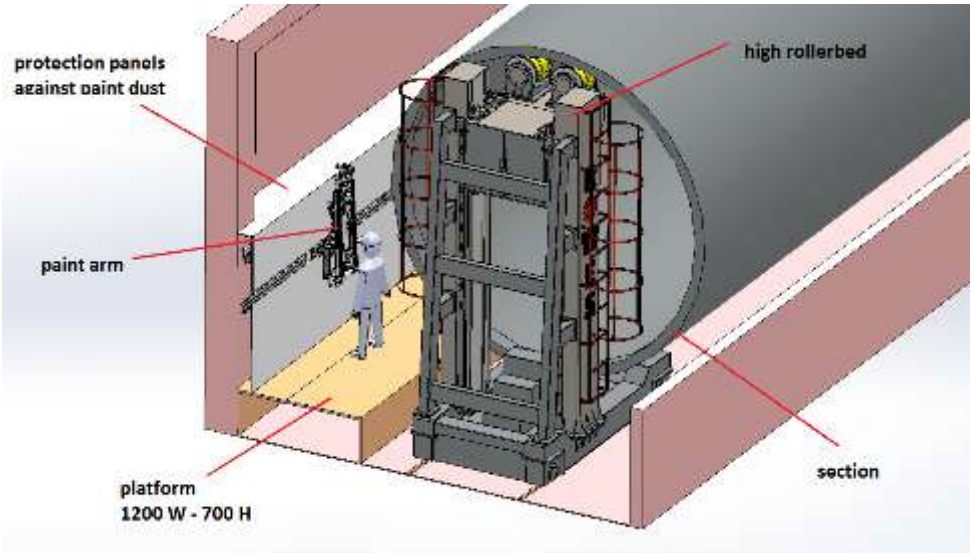

(a)

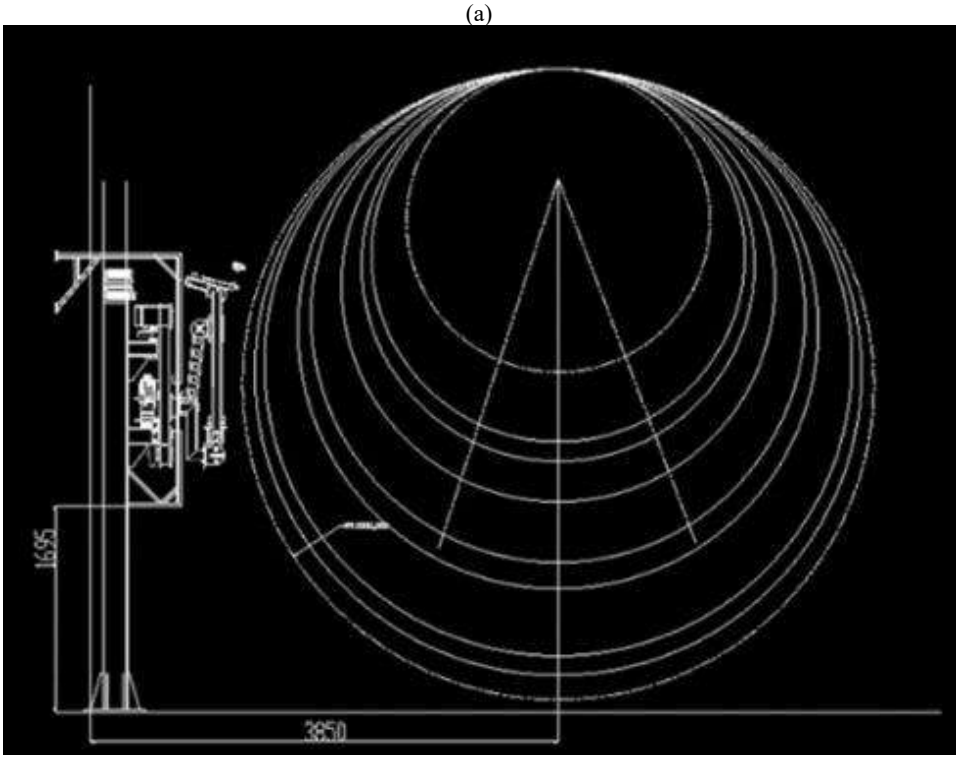

(b)

Fig. 1: (a) Paint booth equipment layout plan (b) Robot arm and tower diameters

The paint spraying process is applied simultaneously by dividing the product length into determined distances (for example, 3 meters) while the workpiece rotates with a controllable rotator speed setting. The robot will continuously move back and forth within the specified distance, painting the product while it rotates. In these movements, overlapping zones are formed. In these overlap areas, the operator makes a wrist movement to ensure that the paint thickness (DFT measurement) is at the desired tolerance values. For this reason, this wrist movement was predicted for the robot as well. In the parameters, the distance in millimeters before this wrist movement starts from the stopping point of the main axis (X axis) and the maximum and minimum wrist angle positions are determined. Figure 2 shows the determined parameters.

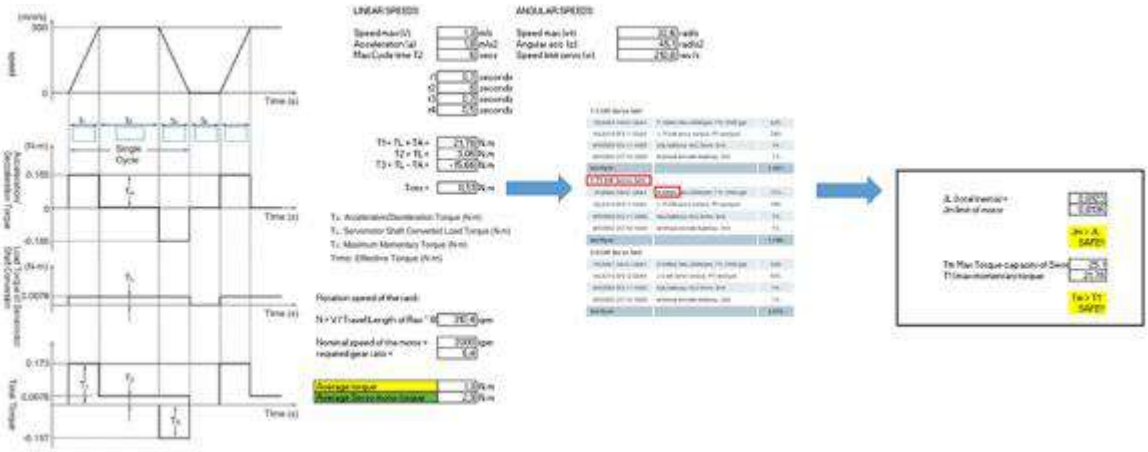

Fig. 2 Speed and torque calculations for servo motor selections

For the design, movement distances were determined, starting with the design of the robot arm that could reach variable diameters on the outer surface of the tower. Figure 3 shows the robot arms and main axes.

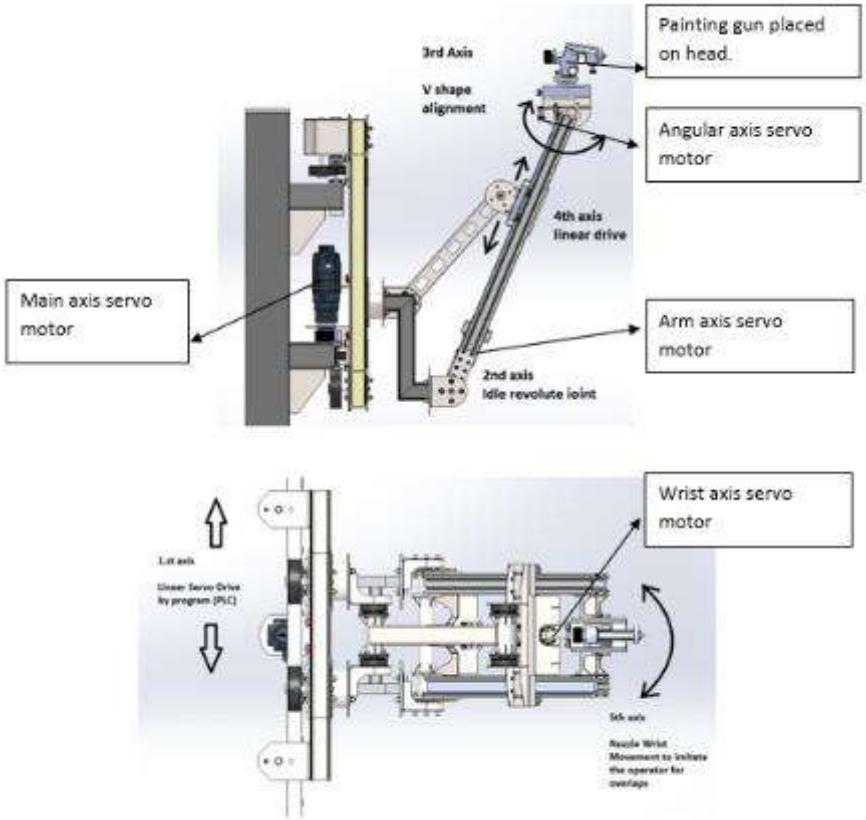

Fig. 3 The robot arms and main axes.

By calculating the powers and speeds required for the operation of the robot arm, the information needed for servo motor selection was prepared. The robot arm is designed to move on the structure with a pinion gear on a rack. Calculations were made regarding rack and pinion selections. Figure 6 shows the speed, angular velocity and torque calculations. Module 4 pinion is used. There are a total of 4 axes on the robot. As can be seen from the calculations and the parameters that the process must reach, there are accelerations for high speeds and fast rotations in the system. For this reason, servo motors were selected for all axes. The main axis (X) provides movement of the robot along its construction. It is designed to reach speeds of 1 meter/second. It is an engine with a power of 2.1 KW

and a torque of 12 Nm. In axes that can reach these speeds, the selection of the cable channel in which the cables will run is also important. The arm axis is the axis that adjusts the approach distance of the paint gun to the tower surface. A 1.5 kW and 6 Nm servo motor was selected. It is designed to work with ball screw movement. Movement at slow speeds is envisaged (10 mm/s). The approach distance is determined as 50 cm and is followed. The angle axis is the axis that allows the paint gun to be positioned so that it faces perpendicular to the center of the tower. A servo motor with a power of 0.57 kW was selected. Movement at slow speeds is envisaged (10 mm/s). The wrist movement axis is the axis that gives the right-left movement of the paint gun. It is designed to mimic operator wrist movement. A servo motor with a power of 0.57 kW was chosen. Wrist movement is designed to operate within the ±90° degree range.

III. Experimental procedure

Many tests were carried out during the parameter determination phase during the production testing phases. In the painting process, it is important to adjust parameters such as the paint mixing ratio, the air pressure of the paint pump, the paint temperature, the diameter of the paint nozzle used and the distance to the surface to be painted. In addition, in order to adjust the parameters such as speed, acceleration and axis positions in the robot, these values must be kept at a constant setting. At the same time, the speed of the turning machine that turns the product is adjusted. As the robot main axis (X axis) speed is set to a constant value as a result of the trials, the rotator speed is also adjusted according to the changing product diameter. Since the paint pumps used in painting work according to the set pressure, the eroded paint does not give a constant flow rate according to the gun nozzle, so there is a constantly changing flow rate in the system. However, when we compare paint spraying with a robot compared to manual processing with an operator, it is predicted that better thickness tolerance results will emerge since many parameters are constant.

IV. Results and discussion

Prototype production and testing of the designed painting robot has been completed and it has started to be used in the painting process. As a result of the trials carried out in production, the most appropriate parameter settings were determined, and the parameters were fixed. After the tower part is positioned in the cabin, following the painting preparation stage, the robot is operated after defining the properties of the workpiece to be painted on the HMI control screen. As a result of the designed movements and trials, it was observed that all movements worked as planned and the measured paint thicknesses were determined to be within the tolerance limits defined in the standard on the entire surface. It can be seen that aimed paint DFT values and paint saving values have been achieved. Experimental measurement values are given in Table 1.

Table 1. Experimentaly measured DFT values and consumptions

Section number	**OPERATOR APPLICATION**			**ROBOT APPLICATION**		
	DFT	*Nominal DFT*	**Paint consumption (liter)**	*DFT*	*Nominal DFT*	*Paint consumption (liter)*
1	235	215	185	213	215	140
2	269	200	170	301	200	180
3	329	215	140	304	215	160
4	249	215	160	222	215	160
5	282	215	140	317	215	155
6	248	215	130	282	215	140
7	252	215	110	283	215	100
8	265	215	140	249	215	110
9	253	200	170	287	200	180
10	276	200	180	277	200	190
11	232	200	160	245	200	170
12	288	215	170	223	215	140
13	242	200	150	221	200	130
14	324	200	170	221,8	200	140
15	284	200	180	265	200	170
16	265	215	140	271	215	120
17	241	200	160	275	200	170

As seen in Table 1, there are large fluctuations in both DFT values and paint consumption in the applications made by the operator. In the use of robots, compliance with the standard in both parameters and homogeneous DFT thicknesses, as well as a considerable paint efficiency, have been achieved.

V. Conclusion

First of all, it should be stated that with the implementation, great gains have been achieved in terms of worker health and environmental impact. Depending on the section diameters, a paint saving of 10-15% is achieved. In parallel with the decrease in volatile solvent consumption, a great step has been taken towards the transition to a greener production.

References

Balkan, T. and Arikan, M.A.S. (1999), "Modeling of paint flow rate flux for circular paint sprays by using experimental paint thickness distribution", Mechanics Res. Commun., Vol. 26 No. 5, pp. 609-17

Hyotyniemi, H. (1994), "Minor moves-global results: robot trajectory planning", Proceedings of the IEEE International Conference on Robotics & Automation, San Diego, CA, USA, May, Vol. 3, CAP: IEEE, New York, NY, pp. 2570-7

Xia Wei, Sheng-Rui Yu, Xiao-Ping Liao, (2010),"Paint deposition pattern modeling and estimation for robotic air spray painting on free-form surface using the curvature circle method", Industrial Robot: An International Journal, Vol. 37 Iss 2 pp. 202 – 213

Zhang, Y., Huang, Y., Gao, F. and Wang, W. (2006), "New model for air spray gun of robotic spray painting", Chinese Journal of Mechanical Engineerig, Vol. 42 No. 11, pp. 226-33

IEEES-026

Parameters of Renewable Energy Use in Rail Systems

Mine Sertsöz
[2] Eskisehir Technical University, Railway Systems Department, Eskisehir/Turkiye
*E-mail: msertsoz@eskisehir.edu.tr

Abstract

The idea of using renewable energy sources in rail systems; is a result of increasing energy demand, global warming, and the exponential increase of the rail system network in recent years. Currently, two types of renewable energy sources are generally used in rail systems. The first of these is solar energy and the other is hydrogen energy, although it is relatively less than the sun.
This study focuses on which parameters should be taken into consideration when using these two resources in rail systems. Some parameters are independent of rail systems, the area where the system will be installed, cost, etc. However, some parameters are dependent on the rail system such as frequency of trips, an increase of weight of the vehicle, etc.
The effects of all these were investigated and then, by trying different scenarios in the study, a rail system vehicle using both solar and hydrogen energy was designed, and the results were interpreted. While the use of hydrogen energy brings restrictions due to cost in the short term, however, it is easier to use solar energy although solar energy has some limitations in rail systems. A study is made for three cities in Turkey to meet a tram's energy requirement from solar panels.

Keywords: Renewable Energy, Energy Efficiency, Rail Systems, Energy Storage.

I. Introduction

Utilizing renewable energy sources in rail systems is one of the topics on which many studies have been carried out in recent years.

In this regard, an innovative microgrid has been designed for an electric railway with PV/wind/hybrid storage. A fast-charging EV system is also integrated into this system. The applicability of the design can be evaluated in MATLAB/Simulink with and without a grid connection. Thus, it was found that the energy drawn from the main grid decreased (Ahmadi et al., 2021). There is a need for the use of microgrids integrated with solar and wind in railways due to the hidden dangers of electricity supply. However, there may be problems in the use of microgrids due to some problems such as harmonics (Xie et al., 2020). In this study, an energy flow of the rail system microgrid is presented and optimized by linear programming. Electricity costs, energy storage efficiencies, train power consumption, and time concepts are taken into consideration for this purpose. In this way, it has been found to reduce operating costs (Ahmadi et al., 2021). Another study has also shown that renewable energy sources can be used along the way for trains for both DC and AC supply systems. Thus, it is possible to prevent trains from losing energy when the network is interrupted in situations such as outages, malfunctions, or natural disasters. Also, the microgrid created in this way would prevent voltage fluctuations (Cheng et al., 2021).
Apart from this, the energy control of a train operating system hybridized with renewable energy sources is also discussed in the literature. In this study, this time a multi-agent system is used for energy control. It has been observed that the continuity and stability of the system increase with this control method (Boudoudouh & Maaroufi, 2019). Hydrogen energy is a solution to rail system energy requirements such as iLint (Alstom).

In this case study, solar energy, which is the most used area of rail systems, was used. The utilization rates of solar energy for tram lines in three different cities in Turkey have been determined.

II. System Description

There are some principles of renewable energy usage in railway systems. These topics are listed below:

- **Electrification of Railways:** Diesel trains are still used in the world, although they are few. In such a system, before talking about renewable energy, a transition to electrical systems must be made. In Turkey, in the data for 2023, there are 431 Diesel-Electric locomotives (77.5%), while there are 125 Electric locomotives (22.5%). While the rate of electrified lines in the TCDD network in 2023 is 47.6% (6,244 km), the fact that the number of Electric locomotives remains at a low rate of 22.5% causes more diesel operation in electric lines, therefore less efficient diesel fuel is consumed, and exhaust emissions are reduced and inevitably increases (TCDD).

-

- **Solar Energy Integration:** The use of solar panels as a renewable energy source in rail systems is the most common application type. By using solar panels, many issues such as investment costs, labor, maintenance, and climate compared with other sources can be solved much more easily. Studies on this have been implemented in Hungary (Jo, 2013), Switzerland (Reuters), China (Jia et. al.,) and India (Nazir, 2019).

-

- **Wind Energy Integration:** There is the potential for wind turbines along railway corridors and on railway land. A portable wind energy harvesting system is designed for self-powered applications in a high-speed railway tunnel (Pan et al., 2019). However, this energy type is not as common as solar energy.

- **Energy Storage Solution:** In railway systems, two different energy storage types generally (Li-ion batteries and ultra-capacitors) are used. There is technical comparative (Energy Density, Energy Efficiency, Charge/Discharge Cycle, Total Project Cost, and Life) points are given in Table 1:

-

Table 1: Some Parameter Values for Different Storage Devices (Sertsöz, 2022)

	Energy Density (kWh/m3)	Char./Disc. Cycle	Energy Efficiency (%)	Total Project Cost in 2025 ($/kWh)	Average Calendar Life (years)
Li-ion Batteries	94.00-500.00	900	70-100	362	10
Ultra-cap.	1.00-35.00	1 million	65-99	66,640	16

- **Challenges in Implementing Renewable Energy in Railway Systems:**
  - Infrastructure Adaptation
  - Energy Demand Variability
  - Economic Considerations

III. Analysis

In the analysis part, it is assumed that solar energy will be used in the tram lines of Istanbul, Izmir, and Samsun cities in Turkey. Interfaces of simulation programs used in this study are given below:

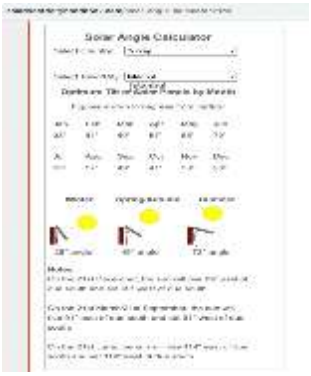

Fig. 1. Interface of Solar City Handbook

Solar City Handbook is used for finding the optimum tilt angle of solar panels. The interface of the program can be seen in Fig.1. The Panel can be placed according to different seasons to get maximum solar energy.

Fig. 2. Interface of Global Solar Atlas

Global Solar Atlas is used for finding the solar energy rate according to different locations in the World. The interface of the program can be seen in Fig.2. The Angle of solar placement, and capacity of solar panels can be changed in Global Solar Atlas.

IV. Results and discussion

The solar energy system characteristics are shared in Figure 3 below. In this study, the system size is chosen as 100kWp.

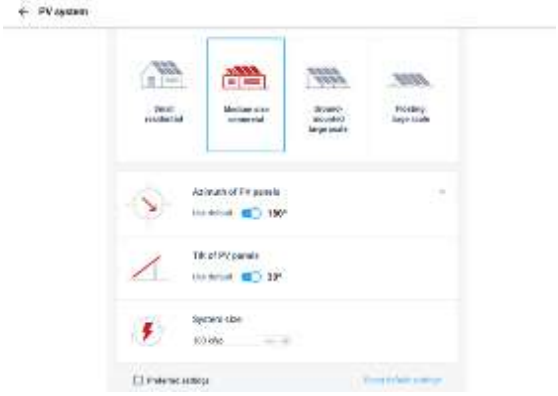

Fig. 3. Solar Panel System in Rail Systems

Table 2. Daily Electricity Production Amounts According to Annual Optimum Panel Placement Angles

İstanbul	30°/4384 kWh
İzmir	30°/5054 kWh
Samsun	32°/4122 kWh

Table 3. Energy Production by Solar Energy

İstanbul	30°/4384 kWh
İzmir	30°/5054 kWh
Samsun	32°/4122 kWh

It is assumed that there is a set of 3 wagons, where one wagon will consume an average of 3.3 kWh. Trams are operated at 24 hours and there is a trip in average of 5 minutes (288 trips in a day). Energy production rates for the tram system according to 3 different cities are given in Table 4:

Table 4. Energy Production by Solar Energy

İstanbul	153,7%
İzmir	177,2%
Samsun	144,5%

V. Conclusion

Renewable energy integration in railway systems for sustainability and reduced emissions is very important. However, some issues should be considered as the electrification of railways, renewable energy integration, energy storage, and challanges in implementing.

In this study, three different cities from Turkey are chosen to meet tram energies from solar energy. 100 kWp solar panel system can meet the 244 trips of tram's energy 153,7%,177,2%, and 144,5% rates respectively for Istanbul, Izmir, and Samsun.

Accelerating these types of Projects can be only Grid Connectivity and Net Metering, Public-Private Partnerships, and Sustainability Certifications and Standards. In future studies there will be more city examples and different renewable energy sources will be considered.

References

Ahmadi, M., Kaleybar, H. Brenna, J. M., Castelli-Dezza F. and Carmeli, M. S. (2021). DC Railway Micro Grid Adopting Renewable Energy and EV Fast Charging Station. 2021 IEEE International Conference on Environment and Electrical Engineering and 2021 IEEE Industrial and Commercial Power Systems Europe (EEEIC / I&CPS Europe), 1-6, doi: 10.1109/EEEIC/ICPSEurope51590.2021.9584729

Boudoudouh, S. and Maaroufi, M., (2019). Renewable Energy Sources Integration and Control in Railway Microgrid. IEEE Transactions on Industry Applications, 55(2), 2045-2052. doi: 10.1109/TIA.2018.2878143

Cheng, P., Kong, H., Ma, J. and Jia, L. (2020). Overview of resilient traction power supply systems in railways with interconnected microgrid. CSEE Journal of Power and Energy Systems, 7(5), 1122-1132. doi: 10.17775/CSEEJPES.2020.02110.

Jia, L., Ma, J., Cheng P., and Liu, Y., (2020) A perspective on solar energy-powered road and rail transportation in China. CSEE Journal of Power and Energy Systems. 6(4), 760-771. doi: 10.17775/CSEEJPES.2020.02040.

Joo, F., (2013) Solar-powered rail vehicle ready for service. International Railway Journal. Simmons-Boardman Publishing Inc.

Nazir, C.P., (2019). Solar energy for traction of high speed rail transportation: a techno-economic analysis. Civil Eng. J. 5, 1566 1576. https://doi.org/10.28991/cej-2019-03091353

Pan, H., Li, H., Zhang, T., Laghari, A.A., Zhang, Z., Yuan, Y., Qian, B., (2019) A portable renewable wind energy harvesting system integrated S-rotor and H-rotor for self-powered applications in high-speed railway tunnels. Energy Convers. Manag. 196, 56-68. https://doi.org/10.1016/j.enconman.2019.05.115.

Sertsöz, M. (2022). Energy Storage for High Speed Trains: Economical and Energy Saving Evaluation. International Journal of Innovation in Engineering. 2(4), 66–77. https://doi.org/10.59615/ijie.2.4.66

Xie, S., Gao, Y., Tian M. and Jia, Z. (2020). A novel power supply method for railway stations in Western China based on microgrid. 2020 5th Asia Conference on Power and Electrical Engineering (ACPEE), 2020, pp. 1085-1089, http://doi:10.1109/ACPEE48638.2020.9136476.

https://www.alstom.com/solutions/rolling-stock/alstom-coradia-ilint-worlds-1st-hydrogen-powered-passenger-train [visited: 18.11.2023].

Solar power for trains dawns in rainy Belgium, http://www.reuters.com/article/ usbelgium-solar trainsidUSTRE77B2KD20110812 [visited: 08.08.2023].

IEEES-027

Hydrogen Energy In Transportatıon

Ali Burak Gögebakan[1] Mine Sertsöz[2*]
[1] Eskisehir Technical University, Railway Systems Department (Postgraduate), Eskisehir/Turkiye
aliburakgogebakan@ogr.eskisehir.edu.tr
[2] Eskisehir Technical University, Railway Systems Department, Eskisehir/Turkiye
*E-mail:msertsoz@eskisehir.edu.tr

Abstract

The use of hydrogen energy in vehicles has been seen as a solution for alternative energy-based vehicles in recent years. However, the limiting factor here is the cost of hydrogen. For this reason, using hydrogen energy in vehicles not to provide all the energy the vehicle demands, but as a range extender; this method is a solution until the cost of hydrogen comes down. In this study, the use of hydrogen energy is mentioned in rail systems, especially for use in tunnels where rail system vehicles cannot be fed from catenary, in historical areas where catenary is not available for a certain period, and in situations such as short-term power cuts. The amount of energy that can be supplied from hydrogen is calculated by trying different scenarios in Matlab Simulink, and then the costs depending on these scenarios amount are calculated.

Keywords: Hydrogen Energy, Transportation Vehicles, Green Energy, Rail System, Energy Efficiency

I. Introduction

What makes this study unique is that the amount of energy that can be provided from hydrogen by trying different fuel types scenarios, the costs related to the amount, and the energy consumption caused by the additional load created by hydrogen energy in the vehicle are included in the calculations. The simulation outputs and modeling performed in the study were performed in the Matlab Simulink program.

Why Hydrogen Energy?

From research to usage, hydrogen energy is a renowned clean energy source that may be produced with zero emissions or pollutants. Concurrently, hydrogen energy is seen to be one of the most promising energy sources due to its high energy density and high conversion efficiency. (Guerra, C. F., Reyes-Bozo, L., Vyhmeister, E., Salazar, J. L., Caparrós, M. J., & Clemente-Jul, C. 2021). Hydrogen and oxygen react to produce energy and water as byproducts. As such, it is a clean and environmentally friendly fuel in addition to being an effective energy carrier (Herwartz, S., Pagenkopf, J., & Sterling, C. 2021).

The Use of Hydrogen Energy in Transportation Vehicles

Hydrogen energy is widely used on many platforms today. Vehicles are at the forefront of this platform. Hydrogen energy is preferred as an innovative energy source in vehicles because it is clean, renewable, and efficient. Nowadays, the transportation sector encounters a globally serious challenge. Excessive fossil fuel consumption pathways, belonging to the transportation sector, have become the main concern for those global warming environmentalists, who believe in a relationship between the carbon footprint and global warming. (Akhoundzadeh, M. H., Panchal, S., Samadani, E., Raahemifar, K., Fowler, M., & Fraser, R. 2021). Public transit is a key to maintaining a clean environment in the future. Extensive research has been performed into the use of hydrogen as a fuel source for transportation applications. Due to climate change impact and energy security issues, hydrogen can be utilized as a promising energy carrier for fueling rail and other vehicles. (Haseli, Y., Naterer, G. F., & Dincer, I. 2008). The transportation industry faces a significant worldwide challenge today. To preserve a clean environment going forward, public transportation is essential. Hydrogen transportation and infrastructure in Germany is currently expanding. In Germany, there were 89 hydrogen refueling stations (HRS) operating for road vehicles as of June 2020. By 2023, the government wants to have 400 HRSs established. Several experimental programs run bus routes on hydrogen (Norouzi, N. 2021).

The Use of Hydrogen Energy in Railways

There are numerous advantages to rail transit. When compared to alternative modes of transportation (road or marine freight), the usage of trains decreases traffic congestion, is safer, and has lower emissions per passenger or freight. (Rashid, M. D., Al Mesfer, M. K., Naseem, H., & Danish, M. 2015). Railroads are a suitable zone for devoted hydrogen product installations for a couple of reasons. Firstly, trains consume considerable quantities of energy which is second, well predictable, and constant over several times (Norouzi, N. 2021). The train named Coradia iLint is a train produced by Alstom company. It has a range of 1000 km and can reach 140 km/h. It is claimed to be the world's first hydrogen-fueled FC-powered passenger train. (Sun, Y., Anwar, M., Hassan, N.M.S., Spiryagin, M., & Cole, C. 2021). This zero-emission train emits low noise and only brume and condensed water as exhaust. This is a significant train because it combines colorful innovative rudiments clean energy conversion, flexible battery energy storehouse in batteries, and smart operation of traction power
(Salvi,B.L., & Subramanian,K.A. 2015). In recent times, several exploration sweats have been carried out to develop locomotives and tramways powered by the PEMFC to encourage hydrogen frugality development and reduce dependence on fossil energies. (Li, Q., Yang, H., Han, Y., Li, M., & Chen, W. 2016).

II. System Description

The system includes 3 different hydrogen energy storage scenarios with real tram data based on modeling made in the Matlab Simulink program. The general system view is shown in Figure 1:

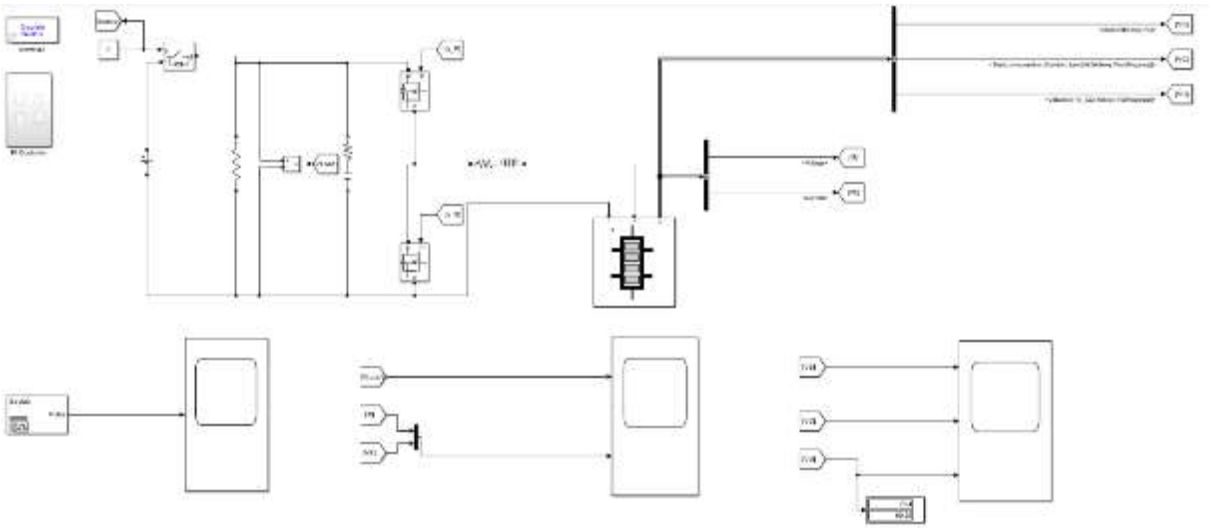

Figure 1: Hydrogen Storage System in Matlab SIMULINK

III. Analysis

$$H_2O(\text{Liquid}) + \text{Energy} = H_2(g) + \frac{1}{2}O_2(g) \quad (1)$$

Eq.1. This technique produces clean energy without emission of pollution by utilizing electricity (Sun, Y., Anwar, M., Hassan, N. M. S., Spiryagin, M., & Cole, C. 2021).

Another important parameter of an electrolyzer is its efficiency η_E. It shows the ratio between the energy of hydrogen during production and the energy needed to electrolyze the consumed water. Consequently, η_E can be easily calculated as the ratio between the HHV of hydrogen (3.54 kWh/Nm^3) and the energy consumption CE in kWh/Nm^3 (Ursua, A., Gandia, L. M., & Sanchis, P. 2011). Eq. 2 declares this relation:

$$\eta_{E=} \frac{\text{HHV of } H_2}{C_E} \cdot 100 \quad (2)$$

IV. Result and Discussion

In this study, the PEMFC (Proton Exchange Membrane Fuel Cell) fuel type was used and three different fuel cell scenarios were focused on. Figures 2, 3, and 4 are the simulation results for the changes in stack efficiency, stack consumption, and utilization values according to the time of PEMFC Fuel Cells. Also, Figure 5 shows the amount of energy consumed by the Bombardier tram. These figures are built by Matlab SIMULINK.

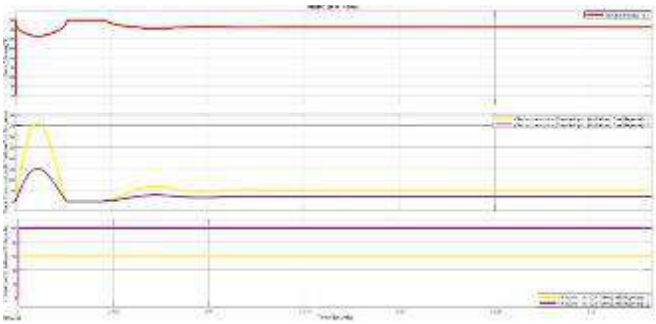

Figure 2: PEMFC Fuel Cell (1.26kW – 24Vdc)

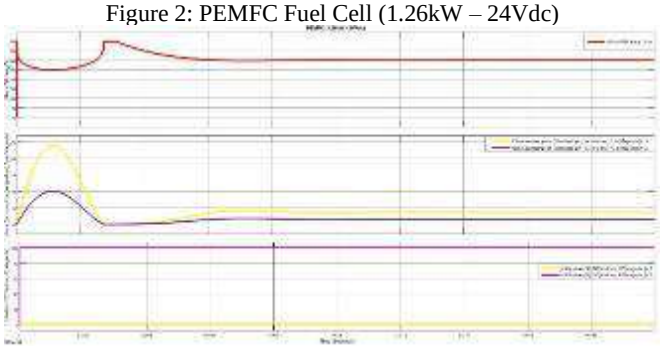

Figure 3: PEMFC Fuel Cell (6kW – 45Vdc)

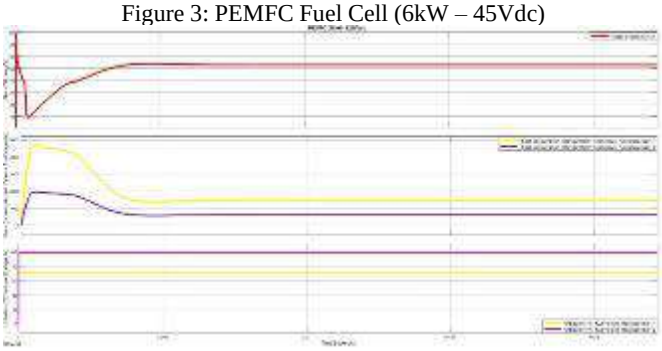

Figure 4: PEMFC Fuel Cell (50kW – 625Vdc)

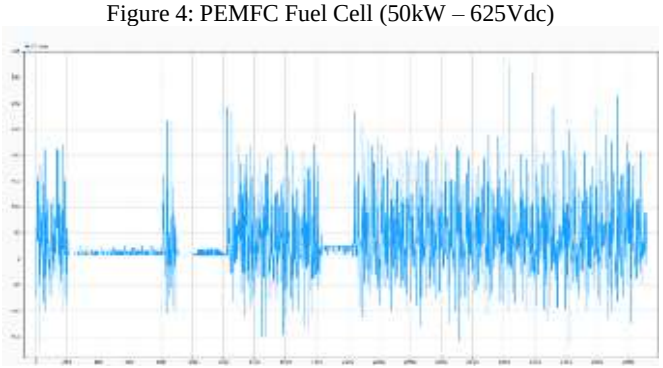

Figure 5: Energy Consumption of Bombardier Tram

The engine power of the Bombardier brand tram of the T1 line, which is taken as reference in this study, is 440 kW and the average energy consumption for a vehicle is 6 kWh. In addition, the vehicle travels 2080 km with an average of 10 trips per day. By using hydrogen energy, I provided 150% of the Bombardier vehicle based on PEMFC fuel type.

Table 1. Utilization, Efficiency, and Cost Analysis According to PEMFC

Value of Cell (kW-Vdc)	Amount of Hydrogen Used (kg/min)	Amount of Hydrogen Energy (kWh/kg)	Efficiency (%)	Cost Analysis ($/kg)
1.26 kW-24 Vdc	Min:9 kg/min Max:17.34 kg/min	Min: 5.07 Mwh Max: 9.77 Mwh	59.9	Min: 15.22 ($/kg) Max: 29.33 ($/kg)
6 kW- 45 Vdc	Min: 37 kg/min Max: 62.5 kg/min	Min: 17.35 Mwh Max: 29.31 MWH	71.8	Min: 52.05 ($/kg) Max: 87.93 ($/kg)
50 kW-625 Vdc	Min: 308kg/min Max:1079 kg/min	Min: 9.57 Mwh Max: 45.40 Mwh	52.9	Min: 591 ($/kg) Max: 2804 ($/kg)

V. Conclusion

This study is about hydrogen energy usage in transportation, especially in trams. The novelty part of the study is using hydrogen energy in three different hydrogen scenarios in the tram and also calculating the cost of these scenarios. An average of 60% of the 12.5 MWh energy consumption of the Bombardier brand vehicle of the T1 line (an Istanbul Line) was supplied in the 1st scenario, an average of 180% in the 2nd scenario, and an average of 220% in the 3rd scenario by hydrogen energy. These coverage costs per kg for 1st scenario vary between 15.22-29.33 $/kg; 52.05-87.93 $/kg for 2nd Scenario and 591-2804 $/kg for 3rd Scenario.

In this study, 3 different scenarios were used. In future studies, different types of fuel cells will be tested by increasing the number of scenarios, and the most suitable options will be investigated by optimizing the energy consumption values associated with these cells and the weight they bring to the vehicle.

References

Akhoundzadeh, M. H., Panchal, S., Samadani, E., Raahemifar, K., Fowler, M., & Fraser, R. (2021).
Investigation and simulation of electric train utilizing hydrogen fuel cell and lithium-ion battery. 101234. https://doi.org/10.1016/j.seta.2021.101234

Guerra, C. F., Reyes-Bozo, L., Vyhmeister, E., Salazar, J. L., Caparrós, M. J., & Clemente-Jul, C. (2021). 13748-13759. https://doi.org/10.1016/j.ijhydene.2020.10.044

Haseli, Y., Naterer, G. F., & Dincer, I. (2008). Comparative assessment of greenhouse gas mitigation of hydrogen passenger train. 1788-1796. https://doi.org/10.1016/j.ijhydene.2008.02.005

Herwartz, S., Pagenkopf, J., & Streuling, C. (2021). Sector coupling potential of wind-based hydrogen production and fuel cell train operation in regional rail transport in Berlin and Brandenburg, 29597-29615. https://doi.org/10.1016/j.ijhydene.2020.11.242

Li, Q., Yang, H., Han, Y., Li, M., & Chen, W. (2016). A state machine strategy based on droop control for
an energy management system of PEMFC-battery-supercapacitor hybrid tramway. 16148-16159. https://doi.org/10.1016/j.ijhydene.2016.04.254

Norouzi, N. (2021). Assessment of technological path of hydrogen energy industry development: a review. 273-284. https://doi.org/10.5829/ijee.2021.12.04.01

Rashid, M. D., Al Mesfer, M. K., Naseem, H., & Danish, M. (2015). Hydrogen production by water electrolysis: a review of alkaline water electrolysis, PEM water electrolysis, and high-temperature water electrolysis.

Salvi, B. L., & Subramanian, K. A. (2015). Sustainable development of road transportation sector using hydrogen energy system. 1132-1155. https://doi.org/10.1016/j.rser.2015.07.030

Sun, Y., Anwar, M., Hassan, N. M. S., Spiryagin, M., & Cole, C. (2021). A review of hydrogen technologies and engineering solutions for railway vehicle design and operations. 212-232. https://doi.org/10.1007/s40534-021-00257-8

Ursua, A., Gandia, L. M., & Sanchis, P. (2011). Hydrogen production from water electrolysis: current status and future trends. 410-426. https://doi.org/10.1109/JPROC.2011.2156750

IEEES-028

Investigation of Optimal PV Panel Angle for Güney/Denizli

[1,2*]Muhammed Rıza Bozelli, [1,2]Berk Kurt
[1]Hidropar Hareket Kontrol Teknolojileri Merkezi (HKTM) Inc., Kocaeli, , Türkiye
[2]Izmir Institute of Technology, Engineering, Mechanical Eng., Gülbahçe/Urla/İzmir, 35433, Türkiye
*E-mails: muhammedbozelli@iyte.edu.tr

Abstract

In this study, the potential of solar energy in Güney province of Denizli, Türkiye is calculated using temperature data. In addition, Photovoltaic (PV) panel orientation is optimized using the direct normal irradiance (GNI) data. The azimuth and latitude positions of solar are calculated over the year. Then, the optimal orientation of the PV panel is calculated for fixed panels and 1-axis tracker systems using the GNI data. The results show that annual total solar irradiation is maximum in 2-axis tracker while minimum in fixed panels. 1-axis azimuth tracker systems is close to performance of 2-axis tracker and 1-axis altitude tracker systems is closed to fix panels.

Keywords: Solar Panel, Angle, Optimum, Solar Irradition, Irradiance

I. Introduction

Global warming and climate change is becoming the biggest problem of humankind. The released harmful greenhouse gases coat the world hence the surface temperature of the world increases. Although the world's surface temperature has increased by 0.9 degrees Celcius since 1906 (“Global Warming”,2010), there were 12 thousand extreme weather events between 1970-2021 years that caused more than 2 million people to die. And also as a result of global warming, 420 billion ice floes melt every year in Greenland and Antarctica.

One of the biggest causes of the global warming is the fossile fuels for electricity demand. In 2010, 57.9% of electricity demand provided by fossil fuels such as coal and oil while less than 3% came from solar panels (IEA,2022). In order to prevent the disasters, governments are starting to take action against global warming and also reduce their external dependence on energy. As a result, government policies changed and investment in renewable energy sources increased. As a result, the production cost of a photovoltaic (PV) panel fell by 82% and its efficiency also increased (NREL,2021). Low cost and low carbon emissions increased the demand for solar energy and 16% of electricity demand provided by solar energy in 2023. According to studies and projections, solar energy will supply more than 22% of the world's total electricity demand after 2027 (IEA,2022). As a consequence, solar energy will become the most widely used method of energy generation instead of fossile fuels. In 2020, Turkey had 95.9 GW of power plants, of which 57.6% were thermal power plants and 6.7% were solar power plants. This is a low ratio for a country that has annual sun exposure 2741 hour and annual 1527 kWh/m^2 solar irradiance. According to the Ministry of Energy and Natural Resources' targets, 52.9% of the 189.7 GW of annual installed capacity should be solar (Türkiye National Energy Plan, 2022).

In today's world, one of the most important things is to get the highest price with the least effort, which means achieving the highest efficiency. In solar energy, high efficiency means balancing the electricity demand with fewer PVs. This saves space, initial investment and maintenance costs. Reduced costs and increased electricity generation will result in a reduction in the levelized cost of electricity, which is an important measure of the feasibility of the electricity generation method. The efficiency of solar panel is related to 5 topics as follows; (1) panel and sun position, (2) surface cleanliness, (3) solar panel type and quality, (4) surface temperature and (5) shadowing effect on solar panel.

In this study, the elevation and azimuth angles of the sun were calculated for every hour of 365 days for the city of Güney, Denizli province, for which vertical solar radiation data are known. Using the hourly position information of the sun relative to Güney/Denizli, the vertical solar radiation information obtained from the Global Solar Atlas was used to calculate the solar radiation falling on a solar panel at different inclination and azimuth angles (Solargis). Then, if the solar panel is used with tracking systems, the solar radiation value falling on it on an annual basis is calculated and a comparison is made between fixed and tracking mechanisms. Last but not least, the potential of solar energy has been calculated by considering environmental parameters for Denizli/Güney province in Turkey.

II. Experimental Procedure/Methodology/System Description

The angle of solar panels must be carefully adjusted to achieve maximum efficiency. As the sun's rays reach the earth, their angle can change due to diffraction by the atmosphere. In addition, the sun's rays can be reflected around the panel and fall on the panel. Depending on the reflectance of the reflecting surface, these values can be very low compared to the normal direct normal irradiance value. In this study, calculations were made using only direct normal irradiance data, neglecting other parameters. The method used in this work is to theoretically calculate the amount of irradiation harvested in relation to the position of the sun. The position of the sun is described in terms of altitude and azimuth. Altitude is the relative angle between the horizon and the sun. Azimuth describes the relative direction of the sun in relation to the north. Although there is an absolute position of the sun, the position of the sun is relative to the position of the observer because of the observer. Previous work on calculating the sun's position gives a fairly good result when the declination angle of the world is taken into account. By combining sun position with direct normal irradiance data, the amount of solar radiation on a solar panel can be calculated for a known panel tilt and azimuth angle. The total annual solar irradiance is then examined for each panel tilt and azimuth angle to determine the maximum potential for optimum panel angles.

III. Analysis

The relative position of the Sun with respect to a known observer can be calculated by performing the following calculations. Equation 1 gives the declination angle (δ) of the world with respect to the day.

$$\delta = -23.45° \sin\left(360\left(\frac{10+N}{365}\right)\right)$$
(1)

where (δ) is the declination angle and (N) is the number of days with starting from 1st day of January.The declination angle is a global parameter for the world in other words, it is does not change with respect to the local position. However, the hour angle (ω) is location dependent. In order to schedule our days each government uses different time zones. For accurate calculation of the sun's position, the hour angle has been calculated with respect to time zones (Zhang, 2021).

$$\omega = -15(h - GMTx - 12)$$
(2)

where (ω) is the hour angle, (h) is the hour and $(GMTx)$ is the time zone. In equation 2, the hour of 13 hours 30 minuntes should be written as 13.5.The time zone for the Türkiye is $GMTx = 3$. The position of the observer in Denizli/Güney, the latitude ($\phi_s = 38.18°$) and longitude ($\gamma_s = 29.04°$) the position of the Sun in cartesian coordinates can be calculated as follows (Zhang, 2021).

$$S_x = \cos(\delta) * \sin(\omega - \gamma_s)$$
(3)
$$S_y = \cos(\phi_s)\sin(\delta) - \sin(\phi_s)\cos(\delta)\cos(\omega - \gamma_s)$$
(4)
$$S_z = \sin(\phi_s)\sin(\delta) + \cos(\phi_s)\cos(\delta)\cos(\omega - \gamma_s)$$
(5)

Then using trigonometric functions the altitude (θ) and azimuth (α) can be calculated using the north-clockwise convention as follows (Zhang, 2021).

$$\alpha = atan2(Sx, Sy)$$
(6)
$$\theta = \sin^{-1}(Sz)$$
(7)

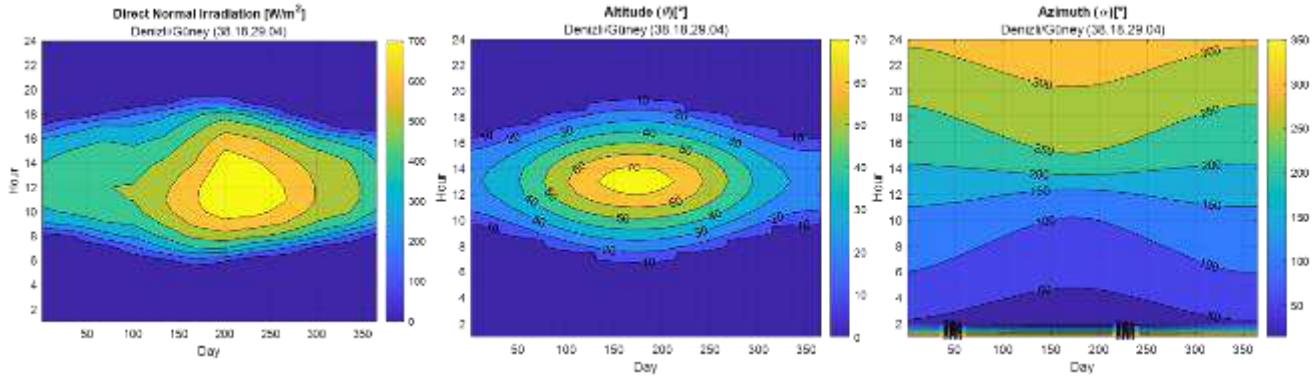

Fig. 1: Direct Normal Irradiation distribution, Sun Altitude and Azimuth angles for Denizli/Güney

When examining Fig.1, it can be seen that the peak sunrise (altitude) reaches 70° between the months of May and July. Negative angles in the altitude graph are set to 0 for simplicity. Negative angles represent that the sun is below the horizon, in other words it means that it is night. After calculating the position of the sun using the direct normal irradiance data, the amount of irradiance on the solar panel can be calculated using the following equation (Kelly, 2009).

$$PVI = (I_s)\cos\left(\frac{\pi}{2} - \theta - \beta\right)\cos(\gamma - \alpha)$$
(8)

where (PVI) is the irradiance on the solar panel, (I_s) is direct normal irradiance, θ is the altitude of sun, β is the solar panel tilt angle, γ is the azimuth angle of solar panel and α is the azimuth angle of the sun. There are different ways of mounting the solar panels such as (1) fixed system β and γ is constant, (2) two axis trackers $\beta = \frac{\pi}{2} - \theta$ and $\gamma = \alpha$, (3) single axis azimuth trackers β is constant, $\gamma = \alpha$ and (4) single axis altitude trackers γ is constant, $\beta = \frac{\pi}{2} - \theta$.

Solar radiation exergy is a theoretical calculation that shows the amount of energy potential available for a given location. Solar radiation exergy is calculated using Petela's theorem as follows (Pour Rahmati, 2021),

$$\frac{E\dot{x}_{in}}{\mathrm{A}} = I_s\left[\left[1 - \frac{4}{3}\left(\frac{T_a}{T_s}\right)\right] + \frac{1}{3}\left(\frac{T_a}{T_s}\right)^4\right]$$
(9)

where, $E\dot{x}_{in}$ is the input exergy [W], T_a ambient temperature [K], T_s surface temperature of sun, which is accepted as 5800 [K], A is

the surface area [m^2].

IV. Results and discussion

Solar panel efficiency is directly related to panel orientation. In order to achieve the highest efficiency, optimisation studies need to be carried out. The total solar irradiance can be seen in Fig.2 for a fixed solar panel, a single-axis altitude tracker and a single-axis azimuth tracker.

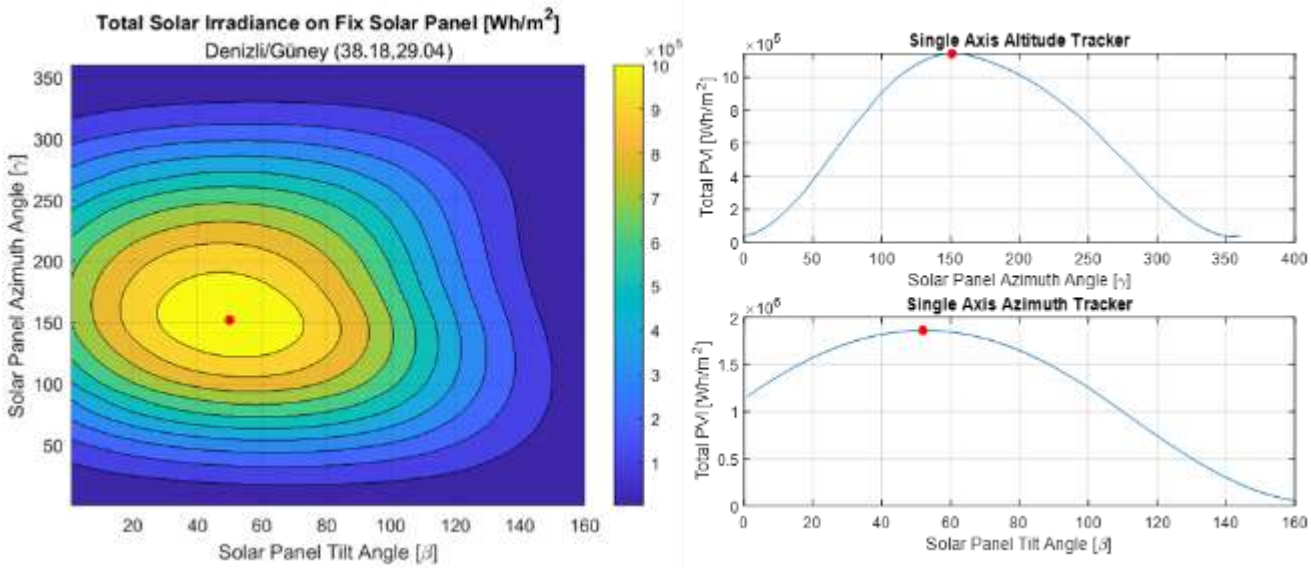

Fig. 2: Total Solar Irradiance on a (a) fixed solar panel (b) single axis altitude tracker and (c) single axis azimuth tracker systems in Denizli/Güney

When the Fig.2 investigated it is seen that, there is a global maximum exist where the solar panel azimuth angle is $\gamma = 151°$ and the solar panel tilt angle $\beta = 52°$. As expected after certain tilt angles the amount of solar irradiance on a solar panel decreases as does the solar panel azimuth angle. This study shows that, the annual total irradiation on solar panel is 1081.5 kWh/m^2. For two axis tracker systems, annual total irradiation value is equal to 1996.3 kWh/m^2. There is a global maximum point for each tracker systems similarly fixed types. For single axis altitude tracker systems optimum panel azimuth angle is $\gamma = 151°$ while single axis azimuth tracker systems these value equals to $\beta = 52°$. Annual total irradiation value for single axis altitude tracker systems 1145.9 kWh/m^2 while 1860.5 kWh/m^2 for single axis azimuth tracker systems.

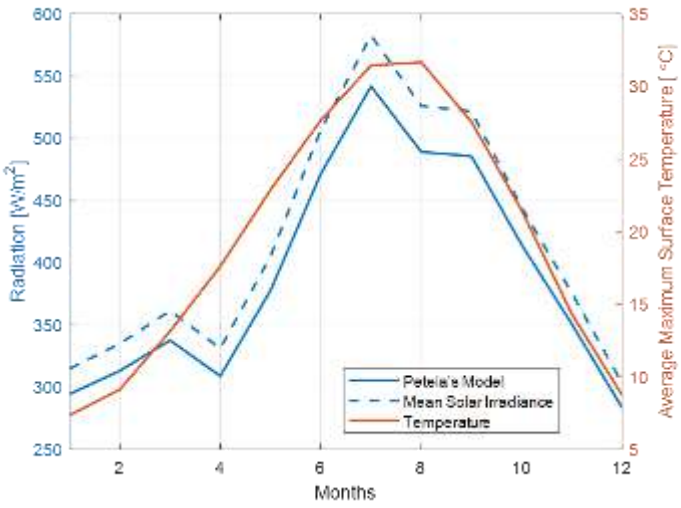

Fig. 3: Effect of ambient temperature on Radiation.

Fig.3 compares the radiation on a surface by Peleta's Model and the data obtained from Global Solar Atlas. The average maximum surface temperature for Denizli/Güney is also shown.

Table 1. Comparision of fixed and axis tracker systems

	Fixed	**Two Axis Tracker**	**Single Axis Azimuth Tracker**	**Single Axis Altitude Tracker**
Tilt Angle [β]	*52*	$\frac{\pi}{2} - \theta$	*52*	$\frac{\pi}{2} - \theta$
Azimuth Angle [γ]	*152*	α	α	*151*
Annual Total Irradiation [kWh/m^2]	*1081.5*	*1996.3*	*1860.5*	*1145.9*

V. Conclusion

Finally, using the solar irradiance data for Denizli/Güney, the optimum panel mounting angles for different types of solar panel systems were investigated. The required relative position of the sun is calculated using given equations for each hour of each day of a year. The results show that two-axis tracker systems can absorb the highest solar radiation. However, a single-axis azimuth tracker system is also capable of absorbing high levels of total irradiance, as is a two-axis tracker system. In such a system, a single-axis azimuth tracker system may be more efficient than a two-axis tracker system, taking into account the initial investment cost and the tracking energy of the panels. On the other hand, fixed systems have the lowest total irradiance and single axis altitude tracker systems have slightly higher total irradiance than fixed systems.

Acknowledgements

We would like to thank Mr. Hamed Pour Rahmati, Mr. Evren Samur, Mr. Tolga Cankurt and all the R&D staff of Hidropar Motion Control Center Inc. who assisted us in our study.

References

"Documenting a Decade of Cost Declines for PV Systems." NREL.Gov, 20 Feb. 2021, www.nrel.gov/news/program/2021/documenting-a-decade-of-cost-declines-for-pv-systems.html.

"Global Warming." NASA, NASA, 3 June 2010, earthobservatory.nasa.gov/features/GlobalWarming/page2.php.

IEA, "Share of cumulative power capacity by technology, 2010-2027", IEA, Paris https://www.iea.org/data-and-statistics/charts/share-of-cumulative-power-capacity-by-technology-2010-2027, IEA. Licence: CC BY 4.0

Kelly, Nelson A., and Thomas L. Gibson. "Improved photovoltaic energy output for cloudy conditions with a solar tracking system." Solar Energy, vol. 83, no. 11, 2009, pp. 2092–2102, https://doi.org/10.1016/j.solener.2009.08.009.

Pour Rahmati Khalejan, Seyed Hamed, and Vedat Keskin. "Effects of shading on Thermal Exergy, power conversion and exergy efficiency of a grid connected PV plant in Samsun-Turkey." SSRN Electronic Journal, 1 Oct. 2021, https://doi.org/10.2139/ssrn.3977765.

Solargis. Global Solar Atlas, globalsolaratlas.info/map?c=38.205814%2C29.002876%2C11&s=38.206352%2C29.036904&m=site. Accessed 1 Nov. 2023.

Türkiye National Energy Plan - Enerji.Gov.Tr, 2022, enerji.gov.tr/Media/Dizin/EIGM/tr/Raporlar/TUEP/T%C3%BCrkiye_National_Energy_Plan.pdf.

Zhang, Taiping, et al. "A solar azimuth formula that renders circumstantial treatment unnecessary without compromising mathematical rigor: Mathematical Setup, application and extension of a formula based on the subsolar point and ATAN2 function." Renewable Energy, vol. 172, 2021, pp. 1333–1340, https://doi.org/10.1016/j.renene.2021.03.047.

IEEES-029

Dissociation of Methane for Hydrogen Production in a Solar Reactor

[1*]Rabah GOMRI, [1] Cheima HADEF, [1]Belkcem NEZZARI,
[1] University Constantine 1, Faculty of Science and Technology, Department of Genie Climatique, Constantine, 25000, Algeria
*E-mails:rabahgomri@yahoo.fr

Abstract

Hydrogen has been proven to be the best fuel solution for greenhouse gases. In order not to contradict this concept, hydrogen must be produced by exploiting renewable energies. We are studying here the cracking of methane in a solar reactor. The cracking reaction leads to a two-phase mixture composed of hydrogen and methane, which is not cracked and a heterogeneous powder of black carbon. To take this reality into consideration, we studied the case of a homogeneous powder with a single diameter and then two other cases with heterogeneous powders. The particles of the powder form an important radiative medium and thus allow a heat transfer by significant radiation which constitutes the dominant factor of the dissociation of methane. The particles of the carbon powder constitute a catalyst for cracking.

Keywords: Concentrated Solar Energy, Hydrogen Production, Radiative Heat Transfer.

I. Introduction

The global warming caused by greenhouse gases is the challenge facing humanity and to which it must find an answer to ensure sustainable development with little impact on the biosphere. The solution sought by the entire international community is the use of renewable energies with their diversity. According to the United Nations Brundtland Report (International Energy Agency, 2015), sustainable development is a process of development of land, cities, businesses, communities, etc., "it is a development that meets the needs of the present without compromising the ability of future generations to meet their own needs." The ideas agree and are directed towards the hydrogen sector as energy and energy vector considering these multiple advantages provided that it is obtained from clean sources based on the exploitation of solar energy (Immonen and Powell, 2023, Ahmedet al., 2022, Dawood et al., 2020, Dincer and Zamfirescu, 2017). However, much must be invested in producing, distributing and using hydrogen which can provide energy for transport, industry, agriculture and domestic use; its distribution will become a major issue in the context of a true "hydrogen economy" (Veziroglu and Muradov, 2005). The methods and techniques for thermochemical production of hydrogen using solar energy are diverse. So far, researchers and scientists have used different pathways like solar thermolysis, solar thermochemical cycles, solar reforming, solar cracking, solar gasification, solar biomass pyrolysis, and other solar techniques. Water is the source of hydrogen for thermolysis and solar thermochemical cycles; fossil materials (natural gas, oil, coal) are the source of hydrogen by solar reforming, cracking and gasification processes while biomass is used as a source of hydrogen for solar pyrolysis.
The reasons cited above encourage us to present this study of the dissociation of methane by introducing new chemical reactions and by concentrating the study on the effect of heat transfer by thermal radiation on the conversion of methane into hydrogen and black carbon.

II. System Description

The phenomenon of methane cracking into hydrogen and carbon black takes place in a cylindrical cavity of a 16cm in diameter and 40cm in length under the heat of concentrated solar radiation without any catalyst (Figure 1).
The reactor is formed by a cylindrical cavity in which is placed a core containing a tubular vacuum allowing the injection of methane. The side wall opposite the methane inlet is subjected to solar radiation.

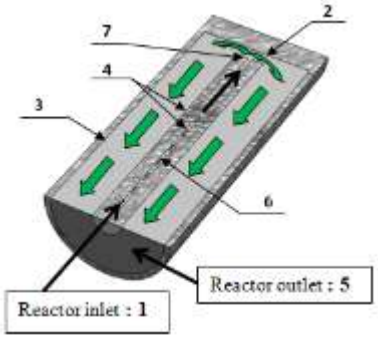

1. Orifice (Methane inlet)
2. Wall subjected to solar radiation
3. External longitudinal wall (adiabatic)
4. Interior longitudinal walls (adiabatic)
5. Reactor exit (outlet)
6. Axis of the reactor (Symmetry)
7. Side wall (adiabatic)

Fig. 1: Half-section of the reactor shape filled with a mixture

III. Analysis

The cracking is governed by the chemical reaction given by the equation (1):

$$CH_4(g) \rightarrow C(s) + 2H_2(g) \quad (1)$$

The constant rate of progress of the chemical reaction is calculated by applying the modified Arrhenius law equation (equation 2). Assuming that the reaction (1) is of order 1, from (Abanades and Flamant, 2008) and (Flamant, 2004), the activation energy is 147kJ.mol^{-1} and the pre-exponential factor is equal to 1×e + 6s^{-1}.

$$K(T) = k_0 \cdot \exp\left(-\frac{E_a}{RT}\right) \quad (2)$$

Boundary conditions

1. Orifice (methane inlet): methane injection orifice
2. Wall subjected to solar radiation
3. Longitudinal external wall (adiabatic): $\left(\frac{\partial T}{\partial y}\Big|_{y=80mm}\right) = 0.$
4. Longitudinal interior walls (adiabatic): $\left(\frac{\partial T}{\partial y}\Big|_{y=3 \text{ and } 20 \text{ mm}}\right) = 0.$
5. Outlet: we consider that the quantity of material introduced into the reactor is equal to the quantity which leaves.
6. Symmetry: the flow is considered independent of the angle of rotation around the axis of symmetry.
7. Internal lateral wall (adiabatic): $\left(\frac{\partial T}{\partial x}\Big|_{x=380mm}\right) = 0$

Choice of black carbon powder diameters

Abanades and Flamant (Abanades and Flamant, 2008) obtained a carbon black powder formed by particles from 20 to 100 nm and Dahl et al. (Dahl et al., 2004) also obtained particles from 20 to 40 nm. In this simulation we chose diameters included in the intervals found by these researchers. Three cases have been chosen; in all cases the primary phase contains methane and hydrogen gases. In the first case, we consider two phases; its main phase is formed of CH_4 and H_2 gases; the secondary phase is a homogeneous carbon black powder with 50 nm of diameter. For the second case we have a mixture with a heterogeneous nanopowder of two diameters (d=20 and 80nm) in addition to CH_4 and H_2. And finally, a third case of five phases with a powder of four different diameters 20, 40, 60 and 80nm in addition to CH_4 and H_2.

Solar radiation profiles

According to works (Hernandez et al, 2003, Flamant, 2004 and Z'Graggen and Steinfeld, 2008), the profiles of the solar radiation applied to the reactor wall is illustrated by the two Figures 2 and 3.

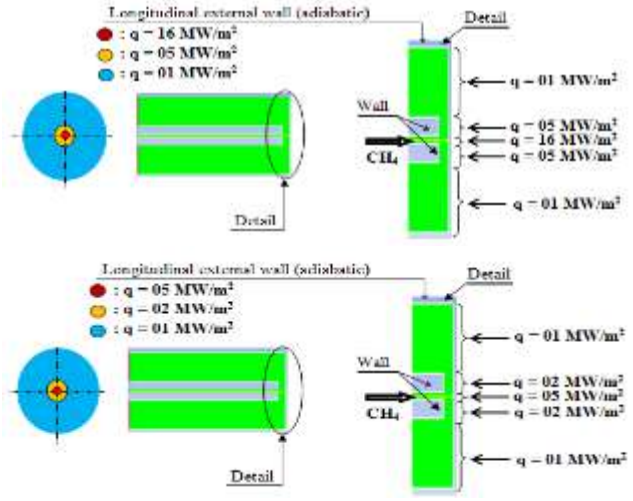

Fig. 2: Flux of solar radiation incident on the reactor wall (wall subjected to solar radiation) under a solar concentration of 16000 suns

Fig.3: Flux of solar radiation incident on the reactor wall (wall subjected to solar radiation) under a solar concentration of 5000 suns

IV. Results and discussion

The low Reynolds k–ε turbulence model was applied. A calculation code "ANSYS FLUENT" is used to simulate the cracking phenomena by choosing the Eulerian - Eulerian model. The mesh is produced by "Gambit" mesh software.

Heat transmitted by radiation as a function of the number of phases

This section deals with the balances of the incident radiation passing through the main cracking zone. For this, we have chosen three sections C1 - C1, C2 - C2 and C3 - C3 located at 5, 10 and 15 mm from the wall subjected to solar radiation. Table 1 and Figure 4 show the effect of the number of phases constituting the mixture on the heat transfer by radiation through the reactor during the cracking process. The results of the simulation show that this flux is directly proportional to the number of phases. It may be that the existence of several phases promotes the intensification of the heat transfer through the mixture and the reactor by the absorption, emission, diffraction and diffusion of the different particles of the carbon black powder and the gases obtained by thermal dissociation of methane.

Table 1: Average thermal radiation flux (W/m^2) as a function of the number of phases at 5, 10 and 15 mm from the wall heated by the concentrator

Average thermal radiation flux in W/m^2						
	Section C1 – C1		Section C2 – C2		Section C3 – C3	
	16000 Suns	5000 Suns	16000 Suns	5000 Suns	16000 Suns	5000 Suns
2 phases	1,8300 e+6	1,6400 e+6	1,780 e+6	1,610 e+6	1,730 e+6	1,58366 e+6
3 phases	2,0620 e+6	1,63373e+6	2,000 e+6	1,6030 e+6	1,9510 e+6	1,57259 e+6
5 phases	2,1813 e+6	1,6897 e+6	2,12621 e+6	1,6602 e+6	2,0745 e+6	1,63149 e+6

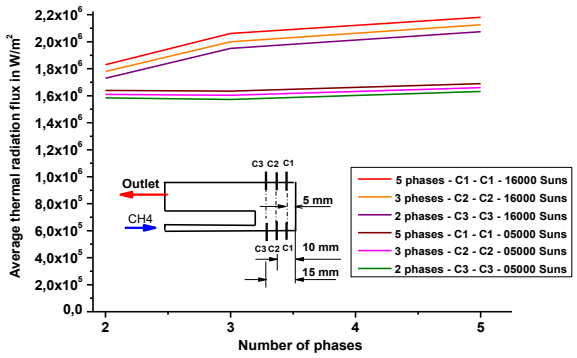

Fig. 4: Average thermal radiation flux as a function of the number of phases at 5, 10 and 15 mm from the wall heated by the solar concentrator

Temperatures at 5 mm from the heated wall by the concentrated solar energy

The temperature is a principal parameter for cracking; we compare the results of temperature for the phases studied at 5 mm from the wall subjected to solar concentrated radiation (x = 0.395 mm). Figure 5 represents the temperature on the section C1 - C1 at 5 mm from the heated wall for different phases studied previously as a function of solar concentration. This Figure shows that the temperature for the 5-phase case is higher than the other two cases. This difference is due to the number of particles diameters. In practice, the carbon black powder is heterogeneous. The increase in the number of diameters is getting closer to reality. Increasing the number of phases allows more efficient heat transfer.

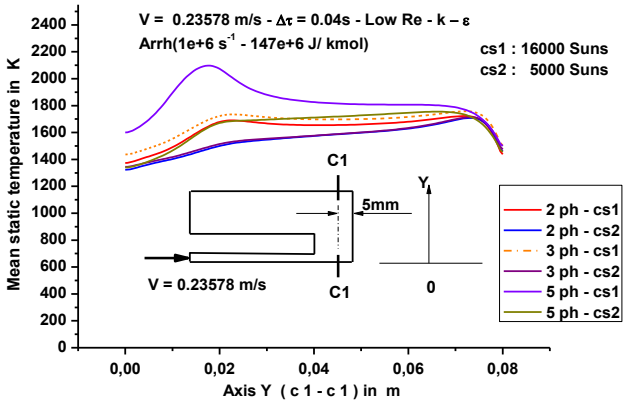

Fig. 5: Temperature at 5 mm from the heated wall as a function of the number of phases and the solar concentration for a flow rate of 0.4 L / min.

Rate conversion to Hydrogen and mass fractions produced

Figure 6 illustrates the hydrogen conversion rates for the cases studied. This Figure shows that the case of the mixture of five phases gives the highest rate for the two solar concentrations. In practice, the carbon black powder obtained is heterogeneous with particles diameters varying from 20 to 100 nm and any simulation taking into account the largest number of these diameters approaches the reality of cracking.

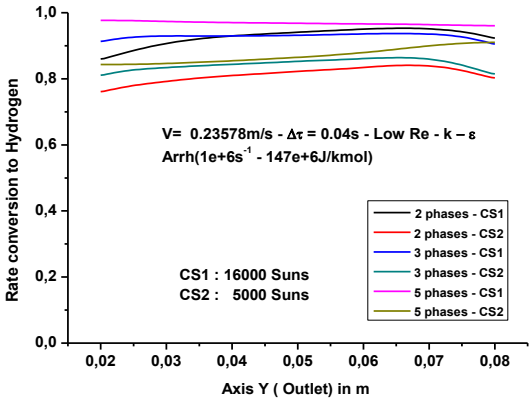

Fig. 6: Rate conversion to hydrogen as function of the number of phases and of the concentrated solar energy

-

V. Conclusion

The analysis of the dissociation of methane in a solar reactor is carried out as a function of the solar concentration supplied to the reactor. The effect of the resulting reactor powder is approved. The simulation results show that the methane cracking rate increases with the consideration of more diameters of the particles constituting the carbon black powder. It has been approved that the presence of a heterogeneous powder formed by various particles of different diameters constitutes an important radiative medium. As soon as these particles are created, they become a catalyst favouring the increase of the internal energy of the cracking components and the transport of heat by the thermal radiation transfer through the reactor.

References

Abanades, S., Flamant, G. (2008). Hydrogen production from solar thermal dissociation of methane in a high- temperature fluid wall chemical reactor". Chemical engineering and processing: Process Intensification, 2008, 47, 490-498. https://doi.org/10.1016/j.cep.2007.01.006

Ahmed, S.F, Mofijur, M., Nuzhat, S., Rafa, N., Musharrat, A., Lam, S.S., Boretti, A. (2022). Sustainable hydrogen production: Technological advancements and economic analysis, International Journal of Hydrogen Energy, 47(88), 37227-3725. https://doi.org/10.1016/j.ijhydene.2021.12.029

Dahl, J.D., Buechler, K.J., Alan W., (2004). Weimer, Allan Lewandowski, Bingham, Solar-thermal dissociation of methane in a fluid-wall aerosol flow reactor - International Journal of Hydrogen Energy ,2004, 29 ,725 – 736, https://doi.org/10.1016/j.ijhydene.2003.08.009

Dawood, F., Anda, M., Shafiullah, G.M. (2020). Hydrogen production for energy: An overview. International Journal of hydrogen energy 45 (2020) 3845-3869. http://dx.doi.org/10.1016/j.ijhydene.2019.12.059

Flamant, G., (2004). Production d'hydrogène par énergie solaire –Programme énergie CNRS-MRNT - DGA–Rapport final du projet intégré HYSOL. (2002-2004).

- http://www.gedeon.prd.fr/ATELIERS/27-28/11/2003/presentations/H2-SolaireIMP-CNRS%20flamant.pdf

Hernandez E.D., Olalde G., Bonnier G., LeFrious F., Sadli M., (2003). Evaluation of the application of a solar furnace to study the suitability of metal oxides to be used as secondary reference points in the range 2000-3000°C. Measurement 34:101-109. https://doi.org/10.1016/S0263-2241(03)00027-7

Ibrahim Dincer, Calin Zamfirescu, Sustainable Hydrogen Production. ISBN 978-0-12-801563-6, Published by Elsevier, 2017.

Immonen, J., Powell K.M., (2023). Hydrogen from solar? A rigorous analysis of solar energy integration concepts for a high temperature steam electrolysis plant. Energy Conversion and Management, 298(15). https://doi.org/10.1016/j.enconman.2023.117759

International Energy Agency (IEA). Technology roadmap: hydrogen and fuel cells. Paris; 2015. https://www.aeh2.org/images/stories/PDF/DOCS_SECTOR/technologyroadmaphydrogenandfuelcells.pdf (2013). PEM

Veziroglu, T.N., Muradov N.Z. (2005). From hydrocarbon to hydrogen-carbon to hydrogen economy. International Journal of Hydrogen Energy, 2005, 30, 225-237. https://doi.org/10.1016/j.ijhydene.2004.03.033

Z'Graggen A., Steinfeld A., (2008). A two-phase reactor model for the steam-gasification of carbonaceous materials under concentrated thermal radiation. Chem Eng Process: Proces Intensification 47(4):655-662. https://doi.org/10.1016/j.cep.2006.12.003

IEEES-030

Examination of the Impact of Electric Vehicles on Line Losses in the IEEE 14-Bus System

[1*]Ozan Gül,
[1] Electrical-Electronics Engineering, Bingol University, Engineering Faculty, 12000, Bingol, TURKEY
*E-mails: ogul@ bingol.edu.tr

Abstract

Electric vehicles (EVs) have gained significant attention as a sustainable mode of transportation in recent years. As their popularity continues to grow, it is crucial to evaluate their impact on various aspects of the energy infrastructure. One critical area of study is the examination of the impact of electric vehicles on the 14-bus system's line losses. The 14-bus system is a fundamental component of the electrical grid, responsible for distributing electricity across a network. Line losses, or energy losses that occur during transmission and distribution, are a significant concern in power systems. When EVs are introduced into this system, their charging and discharging processes can have implications for line losses. EVs draw power from the grid during charging and return energy during regenerative braking or vehicle-to-grid (V2G) applications. These interactions can introduce fluctuations in power demand and alter the load profile of the 14-bus system. Consequently, this can affect line losses by increasing or decreasing energy losses at various points in the grid. Understanding these effects is vital for grid operators and policymakers as they work to optimize grid performance and minimize energy waste. It also has implications for grid capacity planning and the integration of renewable energy sources. Therefore, thorough research into the impact of EVs on the 14-bus system's line losses is essential to ensure the efficient and sustainable operation of the electrical grid in an increasingly electrified transportation landscape.

Keywords: Electric vehicles, load flow analysis based on daily hours, distributed sources, IEEE 14-Bus system, line losses.

I. Introduction

Electric vehicles (EVs) have emerged as a transformative technology in the realm of transportation, promising a sustainable and eco-friendly alternative to conventional combustion engine vehicles. The integration of EVs into existing power systems has garnered significant attention due to its potential implications on grid operations and performance (W. Yin, J. Ji, and X. Qin, 2023). This study delves into the intricate dynamics between electric vehicles and the IEEE 14-Bus System, specifically focusing on the consequential impact on line losses within this power network.

The IEEE 14-Bus System serves as a widely acknowledged benchmark in power systems research, offering a standardized platform for evaluating various grid scenarios and assessing the performance of different components (X. Zhong, G. xin Li, and C. Zhng, 2021). Understanding the implications of introducing EVs into this system is pivotal, considering the ever-growing adoption of these vehicles and their direct link to the power grid through charging infrastructure.

One of the paramount concerns in power systems management is line losses, representing the energy dissipated as heat during transmission and distribution of electrical power (V. S. Tabar, S. Ghassemzadeh, and S. Tohidi, 2022). The introduction of EVs, characterized by their charging requirements and subsequent power consumption, poses a new dimension to this challenge. The charging patterns, locations, and density of EVs within the IEEE 14-Bus System can significantly impact line losses, thereby necessitating a comprehensive examination to comprehend these effects thoroughly.

This examination embarks on a multifaceted analysis, commencing with an in-depth exploration of the behavior of electric vehicles within the power system. The charging profiles, ranging from slow overnight charging to fast charging during peak periods, create varying demands on the grid, leading to fluctuations in power flow and, consequently, affecting line losses (T. Theodoropoulos, P. Pantazopoulos, E. Karfopoulos, P. Lytrivis, G. Karaseitanidis and A. Amditis, 2022). By simulating diverse scenarios of EV integration, this study aims to capture the nuances of these impacts under different load conditions and EV penetration levels.

Moreover, the study delves into the intricacies of grid infrastructure, considering the existing capacities, conductor sizes, and network configurations within the IEEE 14-Bus System. Understanding the limitations and capabilities of the system is indispensable in evaluating its resilience to the added stress imposed by the integration of electric vehicles. This involves simulating scenarios where the system operates close to its maximum capacity, thereby illuminating potential vulnerabilities and areas necessitating reinforcement to mitigate increased line losses.

Furthermore, this examination extends beyond quantitative analysis, delving into potential mitigation strategies and technological interventions aimed at curbing line losses induced by EV integration. Innovative solutions encompassing demand-side management, smart grid technologies, and optimized charging algorithms are explored to minimize the adverse impacts on line losses while ensuring efficient and reliable operation of the power system.

In conclusion, the integration of electric vehicles into the IEEE 14-Bus System introduces a complex interplay between transportation and power networks, necessitating a meticulous examination of its impact on line losses. Through comprehensive analysis and exploration of mitigation strategies, this study endeavors to provide insights crucial for the sustainable and efficient coexistence of electric vehicles within power systems.

II. Load Flow Analysis Using the Newton-Raphson Method

Load flow analysis using the Newton-Raphson method is a widely employed technique in power systems engineering to determine the steady-state operating conditions of an electrical network. This method is particularly effective for solving nonlinear equations that model the power flow within complex systems.

The voltage magnitude, phase angle, and active and reactive power passing via each transmission line in each bus may all be found

using the load flow issue solution. It is assumed that the system is represented by a single-line diagram and runs under typical, well-balanced conditions for addressing the load flow problem. Voltage magnitude (|V|), voltage phase angle (δ), active power (P), and reactive power (Q) are the key factors at each bus. Production buses are buses that are powered by generators; in these buses, the voltage and active power are constant. Load buses are additional buses that are not connected to the generator. It is believed that each bus's complicated load power is known. To summarize, there are three groups of buses in a power system(W. F. Tinney and C. E. Hart, 1967) :

i. The oscillation bus, also called the reference bus, is where the active power (P) and reactive power (Q) are calculated, as well as the voltage magnitude (|V|) and phase angle (δ). This bus evaluates the discrepancy resulting from power system losses between the generated power and the expected load.

ii. Load buses, sometimes referred to as P-Q buses, are those in which the phase angle (δ) and voltage magnitude (|V|) of the bus are sought after, along with the active (P) and reactive power (Q). The active and reactive power numbers in these buses become negative when power is used up.

iii. Generation buses, sometimes referred to as P-V buses or voltage-controlled buses, are where the reactive power (Q), voltage phase angle (δ), and active power (P) are calculated.

The Newton-Raphson method is an iterative technique used for load flow analysis in power systems to find the steady-state operating conditions. Here's a concise summary with the key equations:

Objective: Find the voltage magnitudes (V) and phase angles (θ) at all buses in the power system.

Steps:

1) Nodal Power Equations:

Real Power Equation: $P_i = \sum_{J=1}^{n} |Y_{ij}||V_i||V_j|\cos(\Theta_{ij} - \delta_i + \delta_j)$ (1)

Reactive Power Equation $Q_i = \sum_{J=1}^{n} -|Y_{ij}||V_i||V_j|\cos(\Theta_{ij} - \delta_i + \delta_j)$ (2)

2) Jacobian Matrix: Construct the Jacobian matrix (J) that contains partial derivatives of the power equations with respect to voltage magnitudes and phase angles.

3) Update Equations: The update equations are derived from the Newton-Raphson method, aiming to find corrections to the initial voltage estimates

$\Delta P = Pcalculated - Pmeausered$ (3)

$\Delta Q = Qcalculated - Qmeausered$ (4)

$\Delta X = J^{-1}\left(\begin{bmatrix}\Delta P \\ \Delta Q\end{bmatrix}\right)$ (5)

$Xnew = Xold - \Delta X$ (6)

4) Convergence Check: Assess convergence by evaluating changes in voltage magnitudes and phase angles (ΔV and Δθ) against a predefined tolerance.

5) Iteration: Iterate until convergence:

Update voltage magnitudes and phase angles using the update equations.

Recalculate power injections and build the Jacobian matrix for the updated estimates.

Check for convergence criteria. If not met, continue iterating.

III. 24-Hour Dynamic Load Flow Analysis Based on the Newton-Raphson Method

Twenty-four-hour dynamic load flow assessments were performed using the Newton-Raphson load flow analysis method, which was briefly reviewed in the previous section. The steps in computation are: 1) Models for the power system, load, and resources are defined. 2) The Newton-Raphson approach is used to analyze hourly load flow. 3) The calculation of line losses. 4) The 24-hour period ends when the calculations are completed.

Low-variable and variable power demand profiles were the two types of load profiles at buses that were modeled to correspond with their power demand characteristics. Load models with small changes during 24 hours were applied to low-variable loads, e.g., industrial districts with night shifts. Conversely, load models that saw notable variations over a 24-hour period—such as EVs—were fitted with variable power demand profiles. Using P_L and Q_L vectors with 24 components, variable loads were defined. The relevant source and load values for each hour of the day (from 1 to 24) were retrieved using pre-defined G_P, G_Q, P_L and Q_L vectors, and the Newton-Raphson method was used to conduct daily hourly load flow assessments.

IV. 24-Hour Dynamic Load Flow Analyses on the IEEE 14-Bus Test System

Hourly load flow analysis tests were conducted on a frequently used IEEE 14-bus test system for energy market problems in an exemplary application. Different test scenarios were constructed by adding electric cars to this test system, as seen in Fig. 1. To this end, two types of dynamic load profiles were defined. The first, representing load demand profiles with relatively low power consumption variability, such as factory or business center, was represented by vectors P_{L1} and Q_{L1} as shown in Fig. 2(a). The other load model, which exhibits high variability in power consumption, such as the charging status of electric cars, is represented by vectors P_{L2} and Q_{L2}, as shown in Fig. 2(b).

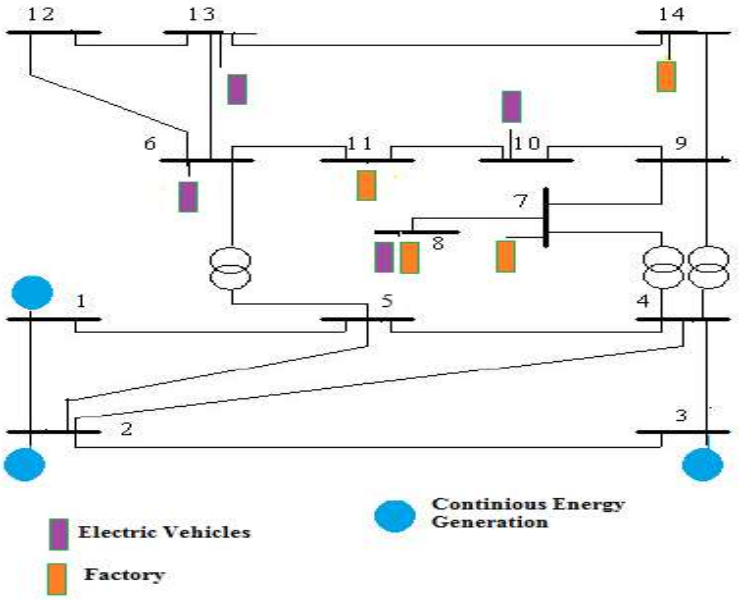

Fig 1. a) IEEE 14-bus test system for example application

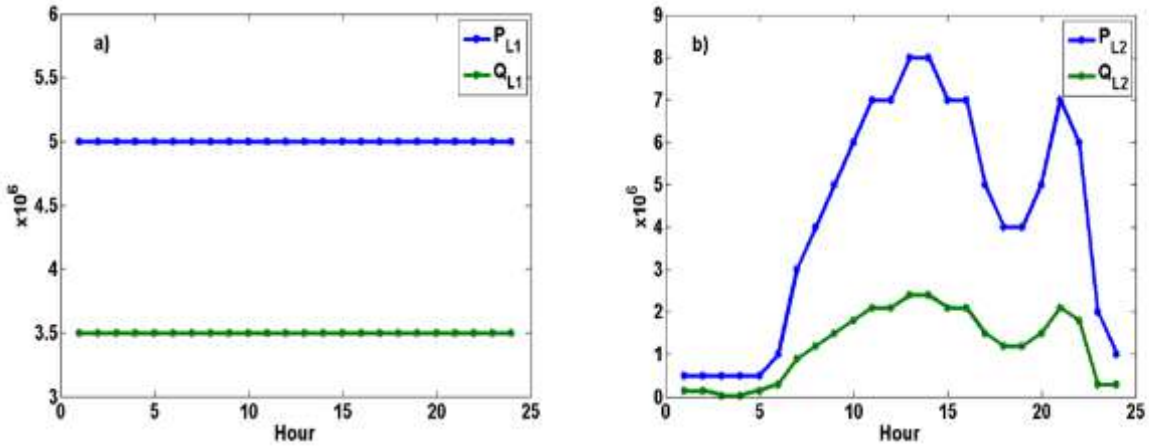

Fig 2. a) Low-variation load demand profile (P_{L1}, Q_{L1}) that models Low-variation load demand profile modeling the power consumption of industrial zones. (b) High variability load demand profile (P_{L2}, Q_{L2}), modeling EV power consumption.

To better examine the impact of EVs on the network; two different load demand scenarios (LDx3and LDx7) were compared LD scenario, with the load power demand increased by tree and seven times than LD scenario, respectively. In Table 1, 24-hour line loss results are given for LD, LDx3 and LDx7 scenarios in the test system only when there is a load structure with relatively low power consumption variability, such as industrial zones. In Table 2, 24-hour line loss results are given for LD, LD x3 and LDx7 scenarios in the case where there is only an EVs load structure with high power consumption variability in the test system.

Table 1. Line Losses for IEEE 14-Bus Test System contain Factorys Load

Total Loss	P (MW)	Q (MVar)
LD scenario	77.904	456.000
LDx3 scenario	82.968	325.800
LDx7 scenario	405.624	2.116.032

Table 2. Line Losses for IEEE 14-Bus Test System contain EVs Load

Total Loss	P (MW)	Q (MVar)
LD scenario	75.600	448.104
LDx3 scenario	76.800	273.768
LDx7 scenario	240.728	816.212

When analyzing Table 1 and Table 2, an increase in active power values resulting in line losses was observed with higher load values in both scenarios. A comparison between the LDx3 and LD scenarios reveals a 6% increase in line losses attributed to active power values (MW) in the industrial load-containing system, whereas the increase in the system containing EV load measured at 1%. Conversely, a substantial increase in reactive power values causing line losses was notable in the LDx7 scenario (high-power demand

situation) for both load types. These results indicate that while the power consumption structure of the added load to the network has a limited effect on line losses, an increase in the overall load value significantly impacts line losses within the network. As Electric Vehicles (EVs) become more integrated into the grid, there arises a pressing need for extensive technological research and development focused on reducing line losses.

V. Conclusion

In conclusion, this study has delved into the intricate relationship between Electric Vehicles (EVs) and line losses within the IEEE 14-Bus System. The analysis showcased distinct patterns of impact stemming from EV integration, shedding light on crucial facets of power distribution network efficiency.

The findings underscore the significance of load scenarios in influencing line losses, elucidating that EV incorporation affects these losses differently across varying load conditions. Specifically, while the increase in EV adoption marginally impacts line losses in certain scenarios, the effect amplifies substantially under higher power demand situations. This nuanced understanding highlights the intricate nature of EV-induced line losses and their sensitivity to network conditions.

Moreover, the research underscores the need for tailored strategies in managing EV integration within distribution networks. Addressing the observed fluctuations in line losses due to EVs demands a holistic approach, considering both load diversity and network resilience.

Ultimately, this study contributes essential insights to power system planners, enabling them to devise optimized strategies for accommodating EVs while mitigating the impact on line losses in the evolving landscape of electric mobility.

References

T. Theodoropoulos, P. Pantazopoulos, E. Karfopoulos, P. Lytrivis, G. Karaseitanidis and A. Amditis, (2022) Proportionally fair and scalable EV charging under distribution line voltage constraints, Electric Power Systems Research, 208, https://doi.org/10.1016/j.epsr.2022.107797. htps://doi.org/10.1016/j.epsr.2022.107797.

V. S. Tabar, S. Ghassemzadeh, and S. Tohidi, (2022) Risk-based day-ahead planning of a renewable multi-carrier system integrated with multi-level electric vehicle charging station, cryptocurrency mining farm and flexible loads. Journal of Cleaner Production. 380:1. https://doi.org/10.1016/j.jclepro.2022.134898.

W. F. Tinney and C. E. Hart, (1967) Power Flow Solution by Newton's Method, IEEE Trans. Power App. Syst., 86, 1449-1460.

W. Yin, J. Ji, and X. Qin, (2023) Study on optimal configuration of EV charging stations based on second-order cone. Energy. 284. https://doi.org/10.1016/j.energy.2023.128494.

X. Zhong, G. Xin Li, and C. Zhng, (2021) False data injection in power smart grid and identification of the most vulnerable bus; a case study 14 IEEE bus network. Energy Reports. 7, 8476-8484. https://doi.org /10.1016/j.egyr.2021.08.029.

IEEES-031

Examination of the Impact of Electric Vehicles and Cryptocurrency Mining Operations on Line Losses in the IEEE 14-Bus System with Renewable Energy Sources

[1*]Ozan Gül,
[1] Electrical-Electronics Engineering, Bingol University, Engineering Faculty, 12000, Bingol, TURKEY
*E-mail: ogul@ bingol.edu.tr

Abstract

Electric vehicles (EVs) and cryptocurrency mining operations are two rapidly growing technological advancements that have the potential to reshape our energy landscape. As we transition towards more sustainable energy sources, it becomes essential to examine their combined impact on the efficiency of the power grid, particularly in systems integrating renewable energy sources.

The 14-bus system is a crucial component of the electrical grid responsible for the distribution of electricity. Line losses, or energy losses that occur during the transmission and distribution of electricity, are of significant concern in power systems. The introduction of electric vehicles and cryptocurrency mining operations can create dynamic changes in energy consumption patterns, which, in turn, affect line losses.

Electric vehicles draw power from the grid for charging and, in some cases, return excess energy to the grid during regenerative braking or vehicle-to-grid (V2G) applications. Cryptocurrency mining operations, on the other hand, demand substantial electricity for computing power. When these activities coincide with periods of high renewable energy generation, there is an opportunity to reduce the environmental impact and cost of energy production. However, the intermittent nature of renewable energy sources can lead to fluctuations in the grid's supply and demand balance, potentially increasing line losses. Therefore, it is crucial to conduct a comprehensive examination of the interplay between electric vehicles, cryptocurrency mining, and renewable energy sources within a 14-bus system to assess their collective impact on line losses.

Keywords: Electric vehicles, cryptocurrency mining operations, renewable energy sources, load flow analysis based on daily hours, distributed sources, IEEE 14-Bus system, line losses.

I. Introduction

The confluence of evolving technologies, such as electric vehicles (EVs) and cryptocurrency mining operations, alongside the integration of renewable energy sources (RES) into power systems, marks a transformative juncture in the landscape of energy consumption and distribution (V. S. Tabar, S. Ghassemzadeh, and S. Tohidi, 2022). This study embarks on a comprehensive examination of their collective impact on line losses within the IEEE 14-Bus System, aiming to elucidate the intricate dynamics arising from the intersection of these innovative domains.

The IEEE 14-Bus System, a standard benchmark in power systems analysis, provides a foundational framework for evaluating the complex interplay between these emerging technologies and their implications on network performance (X. Zhong, G. xin Li, and C. Zhng, 2021). Understanding how the integration of electric vehicles, cryptocurrency mining, and renewable energy sources influences line losses is pivotal for ensuring the stability and efficiency of modern power grids.Electric vehicles, representing a paradigm shift in transportation, are increasingly becoming an integral part of the energy ecosystem. Their connection to the power grid for charging introduces new load dynamics, varying charging profiles, and localized demand surges that can significantly impact power flow and distribution, subsequently affecting line losses.

In parallel, the emergence of cryptocurrency mining operations (CMO) presents a unique set of challenges and opportunities in the energy sector (H. Treiblmaier, 2023). These operations involve high computational intensity, often requiring substantial electricity consumption. When integrated into the grid, cryptocurrency mining activities can cause load spikes and alter demand patterns, potentially influencing line losses within the system.

Simultaneously, the growing integration of renewable energy sources further complicates the dynamics within the power system. The intermittency and variability of RES, such as solar and wind, introduce fluctuations in generation patterns that can alter power flow and impact line losses, adding another layer of complexity to the network dynamics.

This examination initiates with a comprehensive analysis of the behavior and characteristics of electric vehicles, cryptocurrency mining operations, and renewable energy sources within the IEEE 14-Bus System. Understanding the charging behaviors of EVs, power demands of mining operations, and generation profiles of RES is foundational in assessing their collective influence on power flow and line losses (R. Lotfi, S. G. Zare, A. Gharehbaghi, S. Nazari, and G-W. Weber, 2023).

Moreover, the study delves into the intricacies of power system operations, considering the network's topology, transmission capacities, and load characteristics in the presence of these evolving technologies. Simulating scenarios of EV integration, cryptocurrency mining activities, and RES penetration at varying levels enables a detailed assessment of their combined impact on line losses and power flow dynamics.

Furthermore, the research explores mitigation strategies and technological interventions aimed at optimizing the integration of these technologies while minimizing adverse effects on line losses. Innovative solutions encompassing demand-side management, grid optimization techniques, smart charging algorithms for EVs, and adaptive control mechanisms for mining operations are investigated to mitigate increased line losses while maximizing the utilization of renewable resources.

In conclusion, this study endeavors to unravel the intricate nexus between electric vehicles, cryptocurrency mining operations, renewable energy sources, and line losses within the IEEE 14-Bus System. By dissecting the multifaceted interactions among these transformative technologies, this examination aims to provide insights crucial for fostering a harmonious integration of these domains within power systems while ensuring grid stability, reliability, and efficiency.

II. Load Flow Analysis Using the Newton-Raphson Method

Load flow analysis using the Newton-Raphson method is a widely employed technique in power systems engineering to determine the steady-state operating conditions of an electrical network. This method is particularly effective for solving nonlinear equations that model the power flow within complex systems.

The voltage magnitude, phase angle, and active and reactive power passing via each transmission line in each bus may all be found using the load flow issue solution. It is assumed that the system is represented by a single-line diagram and runs under typical, well-balanced conditions for addressing the load flow problem. Voltage magnitude (|V|), voltage phase angle (δ), active power (P), and reactive power (Q) are the key factors at each bus. Production buses are buses that are powered by generators; in these buses, the voltage and active power are constant. Load buses are additional buses that are not connected to the generator. It is believed that each bus's complicated load power is known. To summarize, there are three groups of buses in a power system (W. F. Tinney and C. E. Hart, 1967):

i. The oscillation bus, also called the reference bus, is where the active power (P) and reactive power (Q) are calculated, as well as the voltage magnitude (|V|) and phase angle (δ). This bus evaluates the discrepancy resulting from power system losses between the generated power and the expected load.

ii. Load buses, sometimes referred to as P-Q buses, are those in which the phase angle (δ) and voltage magnitude (|V|) of the bus are sought after, along with the active (P) and reactive power (Q). The active and reactive power numbers in these buses become negative when power is used up.

iii. Generation buses, sometimes referred to as P-V buses or voltage-controlled buses, are where the reactive power (Q), voltage phase angle (δ), and active power (P) are calculated.

The Newton-Raphson method is an iterative technique used for load flow analysis in power systems to find the steady-state operating conditions. Here's a concise summary with the key equations:

Objective: Find the voltage magnitudes (V) and phase angles (θ) at all buses in the power system.

Steps:

1) Nodal Power Equations:

Real Power Equation: $$P_i = \sum_{J=1}^{n} |Y_{ij}||V_i||V_j| \cos(\Theta_{ij} - \delta_i + \delta_j) \quad (1)$$

Reactive Power Equation $$Q_i = \sum_{J=1}^{n} -|Y_{ij}||V_i||V_j| \cos(\Theta_{ij} - \delta_i + \delta_j) \quad (2)$$

2) Jacobian Matrix: Construct the Jacobian matrix (J) that contains partial derivatives of the power equations with respect to voltage magnitudes and phase angles.

3) Update Equations: The update equations are derived from the Newton-Raphson method, aiming to find corrections to the initial voltage estimates

$$\Delta P = Pcalculated - Pmeausered \quad (3)$$

$$\Delta Q = Qcalculated - Qmeausered \quad (4)$$

$$\Delta X = J^{-1}\left(\begin{bmatrix}\Delta P \\ \Delta Q\end{bmatrix}\right) \quad (5)$$

$$Xnew = Xold - \Delta X \quad (6)$$

4) Convergence Check: Assess convergence by evaluating changes in voltage magnitudes and phase angles (ΔV and Δθ) against a predefined tolerance.

5) Iteration: Iterate until convergence:

Update voltage magnitudes and phase angles using the update equations.

Recalculate power injections and build the Jacobian matrix for the updated estimates.

Check for convergence criteria. If not met, continue iterating.

III. 24-Hour Dynamic Load Flow Analysis Based on the Newton-Raphson Method

Twenty-four-hour dynamic load flow assessments were performed using the Newton-Raphson load flow analysis method, which was briefly reviewed in the previous section. The steps in computation are: 1) Models for the power system, load, and resources are defined. 2) The Newton-Raphson approach is used to analyze hourly load flow. 3) The calculation of line losses. 4) The 24-hour period ends when the calculations are completed.

Two distinct types of distributed resources were modeled in this study: intermittent and continuous. It was believed that the active and reactive power values of continuous resources would stay roughly constant during a 24-hour period at an average value. Thermal and hydroelectric power facilities, for example, have output power. On the other hand, 24-component G_P and G_Q vectors, which show the active and reactive power generation profiles for various resource types (such solar and wind) over a 24-hour period, were used to depict intermittent resources. It was anticipated that these resources' active and reactive power outputs would fluctuate over the course of a 24-hour period.

Similar to this, two distinct types of load profiles—low-variable and variable power demand profiles—were developed for buses in order to correspond with their power demand characteristics. For load models with small changes at 24 hours, low-variable loads were used, such cryptocurrency mining operations. Conversely, load models that saw notable variations over a 24-hour period—such as electric vehicles—were fitted with variable power demand profiles. Using P_L and Q_L vectors with 24 components, variable loads were defined. The relevant source and load values for each hour of the day (from 1 to 24) were retrieved using pre-defined G_P, G_Q, P_L and Q_L vectors, and the Newton-Raphson method was used to conduct daily hourly load flow assessments.

IV. 24-Hour Dynamic Load Flow Analyses on the IEEE 14-Bus Test System

Hourly load flow analysis tests were conducted on a frequently used IEEE 14-bus test system for energy market problems in an exemplary application. Different test scenarios were designed by adding loads of different structures and renewable distributed resources to this test system, as seen in Fig. 1.

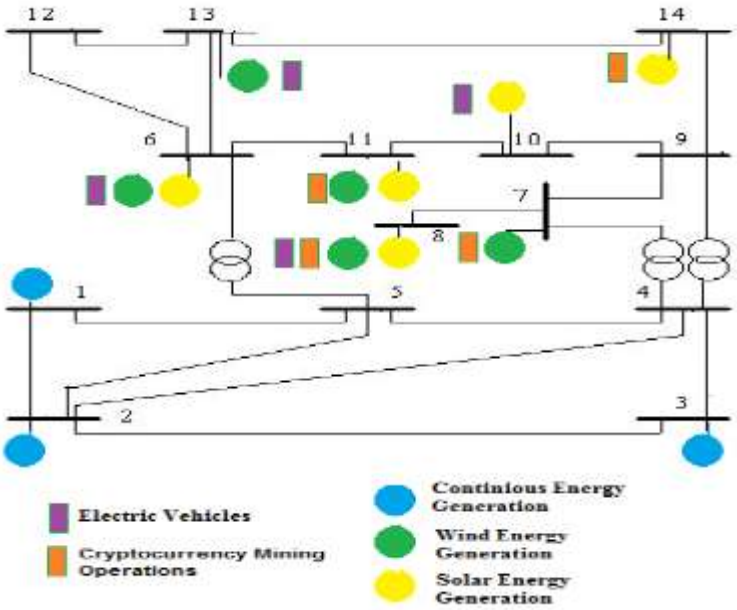

Fig 1. a) IEEE 14-bus test system for example application

To comprehensively examine the impact of load systems on the network, two distinct load demand scenarios (DLDx3 and DLDx5) were implemented within the renewable energy-integrated test system, elevating the load power demand by three and seven times, respectively. Another scenario investigated the effects of expandable distributed resources on line losses within the test system on an hourly basis, employing two test scenarios. In these scenarios, while maintaining a constant load, renewable energy production (DU) in the grid was augmented by 5 (DUx5) and 8 (DUx8) times. Table 1 presents the measured line losses in the test network for these specified test scenarios in the system.

Table 1. Line Losses for IEEE 14-Bus Test System with Renewable Energy Sources contain EVs and CMO

Total Loss	P (MW)	Q (MVar)
DU scenario	74.440	460.800
DLDx3 scenario	79.200	290.400
DLDx5 scenario	220.800	1.195.200
DUx5 scenario	75.600	453.600
DUx8 scenario	78.000	432.000

These results depict the impact of increased load power demand and augmented renewable energy production on line losses (both active and reactive) within the renewable energy-integrated IEEE 14-Bus test system. When the load power demand increases three times, the active losses rise from 74.400 MW to 79.200 MW, while the reactive losses decrease notably from 460.800 MVar to 290.400 Mvar. A fivefold increase in the load power demand causes a substantial surge in both active losses, escalating to 220.800 MW, and reactive losses, reaching 1,195.200 Mvar. With a fivefold increase in renewable energy production, there's a minor elevation in active losses from 74.400 MW to 75.600 MW, while reactive losses remain relatively stable at 453.600 Mvar. An eightfold increase in renewable energy production leads to a moderate rise in active losses to 78.000 MW, while reactive losses decrease slightly to 432.000 Mvar.

Increased load power demand significantly impacts line losses, especially when it reaches five times the initial demand. This elevation leads to a substantial increase in both active and reactive losses, signifying higher stress and inefficiencies within the system. Conversely, when renewable energy production increases, the impact on line losses is relatively moderate. Although there are slight fluctuations, especially in active losses, the effect is not as pronounced as the load power demand escalation.

These findings underscore the critical influence of load demand variations on line losses within the renewable energy-integrated system. Managing load demand becomes crucial to mitigate substantial increases in line losses, highlighting the need for efficient load management strategies in power systems. Additionally, the impact of increased renewable energy production on line losses remains comparatively less significant than that of load demand.

V. Conclusion

In this study, we explored the intricate interplay of Electric Vehicles (EVs), cryptocurrency mining operations, and renewable energy sources on line losses within the IEEE 14-Bus System. The investigation revealed compelling insights into the impacts of these components on the system's efficiency.

The findings underscored the substantial influence of load variations from EVs and cryptocurrency mining on line losses. Particularly, significant load increases resulted in escalated line losses, emphasizing the pressing need for load management strategies to mitigate system inefficiencies.

Additionally, while renewable energy integration exhibited a mitigating effect on line losses, the study highlighted the importance of balancing renewable energy production increments against escalating loads for optimal system performance.

These results signify the complexity of managing multiple dynamic components within a renewable energy-integrated grid. Addressing the challenges posed by EVs, cryptocurrency mining, and load fluctuations necessitates adaptive strategies to ensure the reliability and efficiency of power distribution networks in the evolving energy landscape.

References

H. Treiblmaier, (2023) A comprehensive research framework for Bitcoin's energy use: Fundamentals, economic rationale, and a pinch of thermodynamics, Blockchain:Research and Applications, 4(3). https://doi.org /10.1016/j.bcra.2023.100149.

R. Lotfi, S. G. Zare, A. Gharehbaghi, S. Nazari, and G-W. Weber, (2023) Robust optimization for energy-aware cryptocurrency farm location with renewable energy, Computers & Industrial Engineering, 177, https://doi.org /10.1016/j.cie.2023.109009

V. S. Tabar, S. Ghassemzadeh, and S. Tohidi, (2022) Risk-based day-ahead planning of a renewable multi-carrier system integrated with multi-level electric vehicle charging station, cryptocurrency mining farm and flexible loads. Journal of Cleaner Production. 380:1. https://doi.org/10.1016/j.jclepro.2022.134898.

W. F. Tinney and C. E. Hart, (1967) Power Flow Solution by Newton's Method, IEEE Trans. Power App. Syst., 86, 1449-1460.

X. Zhong, G. Xin Li, and C. Zhng, (2021) False data injection in power smart grid and identification of the most vulnerable bus; a case study 14 IEEE bus network. Energy Reports. 7, 8476-8484. https://doi.org /10.1016/j.egyr.2021.08.029.

IEEES-032

Examination of the Impact of Renewable Energy Sources on Line Losses in the IEEE 14-Bus System

[1*]Ozan Gül,
[1] Electrical-Electronics Engineering, Bingol University, Engineering Faculty, 12000, Bingol, TURKEY
*E-mails: ogul@ bingol.edu.tr

Abstract

The adoption of renewable energy sources, such as solar and wind power, has gained significant momentum in recent years due to their environmental benefits and potential to reduce reliance on fossil fuels. However, the integration of these sources into existing power grids is not without challenges. One important area of study is the examination of the impact of renewable energy sources on line losses within a 14-bus electrical system. The 14-bus system serves as a fundamental component of the electrical grid, responsible for transmitting and distributing electricity to end-users. Line losses, which occur during the transmission and distribution of electricity, represent a significant concern in power systems. When renewable energy sources are introduced into this system, their intermittent nature and variable power output can lead to fluctuations in the grid's supply and demand balance.

These fluctuations can have a direct impact on line losses, potentially increasing or decreasing them depending on the circumstances. Understanding how renewable energy sources influence line losses is crucial for grid operators, as it helps them optimize grid performance, reduce energy waste, and enhance the overall efficiency and sustainability of the electrical grid. Furthermore, this research is essential for effective grid capacity planning and the integration of renewable energy sources into the energy mix. By studying the impact of renewable energy sources on line losses within a 14-bus system, we can make informed decisions to ensure a reliable, resilient and eco-friendly electrical grid for the future.

Keywords: Wind energy**,** solar energy, load flow analysis based on daily hours, distributed sources, IEEE 14-Bus system, line losses

I. Introduction

The integration of renewable energy sources (RES) into power systems represents a pivotal transition towards sustainable and cleaner energy generation. Understanding the impact of this transition on the operational dynamics of power networks is essential for ensuring efficient and reliable electricity transmission (J.A. Peças Lopes, N. Hatziargyriou, J. Mutale, P. Djapic, and N. Jenkins, 2006). This study delves into the intricate interplay between the incorporation of renewable energy sources and their influence on line losses within the IEEE 14-Bus System, aiming to elucidate the implications of RES integration on the network's performance.

The IEEE 14-Bus System, a standard test system widely used in power system analysis, provides a representative platform for evaluating different scenarios and assessing the behavior of various components within a network (X. Zhong, G. xin Li, and C. Zhng, 2021). Investigating the effects of renewable energy integration within this system serves as a crucial step in comprehending the broader implications of transitioning towards sustainable energy sources. Renewable energy sources encompass a diverse range of technologies such as solar photovoltaics, wind turbines, hydroelectric power, and others. These sources exhibit distinct characteristics, including intermittent generation patterns, variability, and location-specific generation capacities. Such attributes present both opportunities and challenges in power system operation, particularly concerning their impact on line losses.

One of the primary concerns when integrating RES into power systems is the potential alteration of power flow patterns and, consequently, line losses. The variability and intermittency of renewable sources can lead to fluctuations in power injections and alter the network's operating conditions (M. N. Absar, M. F. Islam, and A. Ahmed, 2023). This, in turn, affects the flow of electricity across transmission lines, potentially influencing line losses within the system.

This examination initiates with a comprehensive analysis of the behavior and characteristics of renewable energy sources within the IEEE 14-Bus System. Understanding the generation profiles, capacities, and temporal variability of these sources is crucial in assessing their influence on power flow and line losses.

Moreover, the study delves into the intricacies of power system operations, including the network's topology, transmission capacities, and load characteristics. This involves simulating scenarios of RES integration at varying penetration levels, considering different locations and generation capacities (V. S. Tabar, S. Ghassemzadeh, and S. Tohidi, 2022). Evaluating these scenarios allows for a detailed assessment of how changes in renewable energy penetration impact the overall line losses and power flow dynamics within the system.

Furthermore, the research explores potential mitigation strategies and technological interventions aimed at minimizing the impact of RES integration on line losses. Innovative solutions encompassing advanced grid management techniques, energy storage systems, optimal resource allocation, and smart grid technologies are investigated to mitigate increased line losses while ensuring the efficient utilization of renewable resources.

In conclusion, this study endeavors to unravel the complex relationship between the integration of renewable energy sources and line losses within the IEEE 14-Bus System. By dissecting the multifaceted aspects of RES integration and their implications on power flow dynamics, this examination seeks to provide insights crucial for ensuring the seamless and efficient integration of sustainable energy sources while maintaining grid stability and reliability.

II. Load Flow Analysis Using the Newton-Raphson Method

Load flow analysis using the Newton-Raphson method is a widely employed technique in power systems engineering to determine the steady-state operating conditions of an electrical network. This method is particularly effective for solving nonlinear equations that model the power flow within complex systems.

The voltage magnitude, phase angle, and active and reactive power passing via each transmission line in each bus may all be

found using the load flow issue solution. It is assumed that the system is represented by a single-line diagram and runs under typical, well-balanced conditions for addressing the load flow problem. Voltage magnitude (|V|), voltage phase angle (δ), active power (P), and reactive power (Q) are the key factors at each bus. Production buses are buses that are powered by generators; in these buses, the voltage and active power are constant. Load buses are additional buses that are not connected to the generator. It is believed that each bus's complicated load power is known. To summarize, there are three groups of buses in a power system (W. F. Tinney and C. E. Hart, 1967):

i. The oscillation bus, also called the reference bus, is where the active power (P) and reactive power (Q) are calculated, as well as the voltage magnitude (|V|) and phase angle (δ). This bus evaluates the discrepancy resulting from power system losses between the generated power and the expected load.

ii. Load buses, sometimes referred to as P-Q buses, are those in which the phase angle (δ) and voltage magnitude (|V|) of the bus are sought after, along with the active (P) and reactive power (Q). The active and reactive power numbers in these buses become negative when power is used up.

iii. Generation buses, sometimes referred to as P-V buses or voltage-controlled buses are where the reactive power (Q), voltage phase angle (δ), and active power (P) are calculated.

The Newton-Raphson method is an iterative technique used for load flow analysis in power systems to find the steady-state operating conditions. Here's a concise summary with the key equations:

Objective: Find the voltage magnitudes (V) and phase angles (θ) at all buses in the power system.

Steps:

1) Nodal Power Equations:

Real Power Equation: $$P_i = \sum_{J=1}^{n} |Y_{ij}||V_i||V_j|\cos(\Theta_{ij} - \delta_i + \delta_j) \quad (1)$$

Reactive Power Equation $$Q_i = \sum_{J=1}^{n} -|Y_{ij}||V_i||V_j|\cos(\Theta_{ij} - \delta_i + \delta_j) \quad (2)$$

2) Jacobian Matrix: Construct the Jacobian matrix (J) that contains partial derivatives of the power equations with respect to voltage magnitudes and phase angles.

3) Update Equations: The update equations are derived from the Newton-Raphson method, aiming to find corrections to the initial voltage estimates

$$\Delta P = Pcalculated - Pmeausered \quad (3)$$

$$\Delta Q = Qcalculated - Qmeausered \quad (4)$$

$$\Delta X = J^{-1}\left(\begin{bmatrix}\Delta P \\ \Delta Q\end{bmatrix}\right) \quad (5)$$

$$Xnew = Xold - \Delta X \quad (6)$$

4) Convergence Check: Assess convergence by evaluating changes in voltage magnitudes and phase angles (ΔV and Δθ) against a predefined tolerance.

5) Iteration: Iterate until convergence:
Update voltage magnitudes and phase angles using the update equations.
Recalculate power injections and build the Jacobian matrix for the updated estimates.

III. 24-Hour Dynamic Load Flow Analysis Based on the Newton-Raphson Method

Twenty-four-hour dynamic load flow assessments were performed using the Newton-Raphson load flow analysis method, which was briefly reviewed in the previous section. The steps in computation are: 1) Models for the power system, load, and resources are defined. 2) The Newton-Raphson approach is used to analyze hourly load flow. 3) The calculation of line losses. 4) The 24-hour period ends when the calculations are completed.

In this study, distributed resources are modeled in two different types: continuous and discontinuous resources. It is assumed that the active and reactive power values of continuous sources can remain almost constant around an average value for 24 hours. For example, the output power of dams and thermal power plants. As for discontinuous sources, 24-hour active and reactive power production profiles are represented by 24-component P G and Q G vectors according to the source type (Wind, solar, etc.). It is assumed that the active and reactive power values of these sources vary for 24 hours. With a similar approach, busbar loads are modeled in two different types, suitable for less variable and variable power demand profiles. Less variable loads were used for load patterns that did not fluctuate highly over 24 hours due to night shifts, such as in industrial areas. Variable power demand profiles are used for load models that show significant oscillations within a 24-hour period, such as household consumers.

IV. 24-Hour Dynamic Load Flow Analyses on the IEEE 14-Bus Test System

Hourly load flow analysis tests were conducted on a frequently used IEEE 14-bus test system for energy market problems in an exemplary application. Analyses of situations arising from the integration of renewable distributed resources into the system, as depicted in Fig. 1, were conducted across various test scenarios. The first scenario employed solar energy (SG scenario), the second involved wind energy (WG scenario), and the third combined both wind and solar energy (HG scenario) in a hybrid system. Fig. 2 illustrates the production profiles utilized in the analysis for wind and solar energy sources.

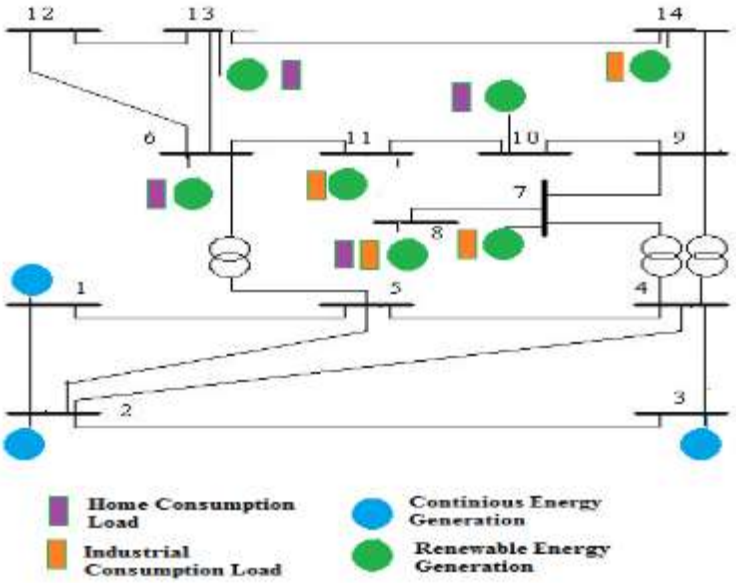

Fig 1. a) IEEE 14-bus test system for example application

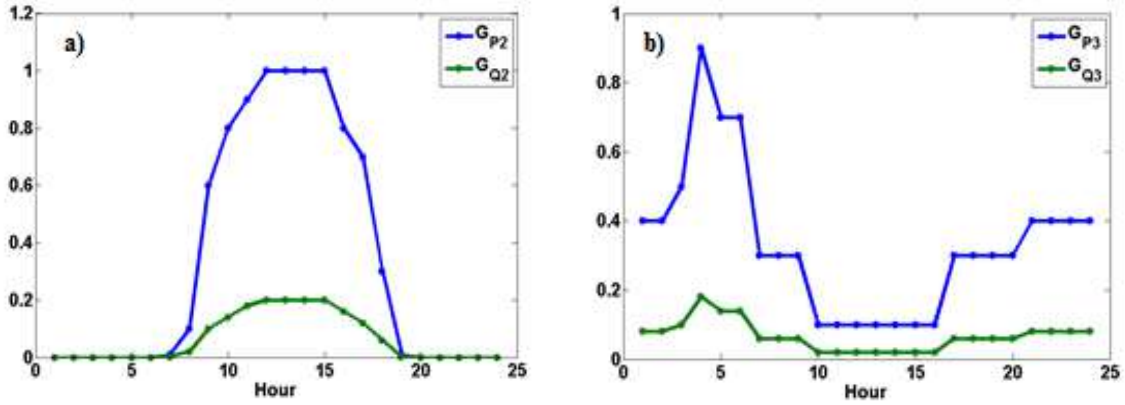

Fig 2. a) Solar energy resources production profile b) Wind energy resources production profile

To assess the influence of renewable energy resources on the grid, the present scenarios (SG, WG, HG) and their distributed generation variants (SG, WG, HGx5, SG, WG, HGx8) were compared across all three scenarios. In the x5 and x8 scenarios, the renewable distributed resources' energy production levels were increased to five and eight times the normal production, respectively. Table 1 shows the line losses measured in the test network for these suggested test scenarios in the test system.

Table 1. Line Losses for IEEE 14-Bus Test System contain Rewable Energy Sources

Total Loss	P (MW)	Q (MVar)
SG scenario	69.600	446.400
SGx5 scenario	76.800	451.200
SGx8 scenario	88.800	420.200
WG scenario	69.600	439.200
WGx5 scenario	70.080	444.000
WGx8 scenario	70.560	448.800
HG scenario	70.800	453.600
HGx5 scenario	78.000	458.400
HGx8 scenario	91.200	432.000

Table 1 show the impact of increased solar, wind, and hybrid (combined solar and wind) energy production on line losses (both active and reactive) within the IEEE 14-Bus test system. When solar energy production increases 5 times, there's an increase in active losses (P) from 69.600 MW to 76.804 MW. With an 8 times increase in solar energy production, active losses further rise to 88.800 MW. Reactive losses (Q) vary slightly with the increase in solar production. Increasing wind energy production 5 times leads to a minor increase in active losses from 69.600 MW to 70.800 MW. An 8 times increase in wind energy production results in a slight decrease in active losses to 70.560 MW. Reactive losses show marginal fluctuations with the rise in wind production. In the hybrid scenario (combining solar and wind), an increase of 5 times in energy production leads to a rise in active losses from 70.800 MW to 78.000 MW. When the hybrid energy production increases 8 times, active losses further increase to 91.200 MW. Reactive losses also demonstrate variations with the increased hybrid energy production.

Higher increments in energy production (8 times compared to 5 times) generally result in more pronounced increases in active losses for all scenarios. Reactive losses also fluctuate but not consistently, showing variations with different levels of increased energy production.

These findings suggest that higher levels of renewable energy production lead to increased line losses, particularly in active power, within the test system. Managing these losses effectively becomes crucial as renewable energy penetration rises, indicating a need for strategies to optimize grid efficiency amidst increased renewable generation.

V. Conclusion

In conclusion, this study delved into the complex relationship between renewable energy sources and line losses within the IEEE 14-Bus System. The investigation revealed distinct patterns of impact associated with increased solar, wind, and hybrid (solar-wind) energy production on line losses.

The findings underscore that heightened increments in renewable energy production lead to notable escalations in active losses across all scenarios. However, the impact on reactive losses demonstrated variable trends, showing sensitivity to the type and level of increased energy generation.

These results emphasize the necessity for vigilant management strategies in power systems as renewable energy penetration rises. While renewable sources offer sustainable energy solutions, their integration poses challenges to grid efficiency, especially concerning line losses. Addressing these challenges demands a tailored approach considering both active and reactive loss components. Optimizing grid infrastructure, employing advanced technologies, and devising adaptive control mechanisms emerge as essential strategies in mitigating the escalating impact of renewable energy sources on line losses within power distribution networks.

References

J.A. Peças Lopes, N. Hatziargyriou, J. Mutale, P. Djapic, and N. Jenkins, (2006) Integrating distributed generation into electric power systems: A review of drivers, challenges and opportunities," Electric Power Systems Research, 77, 1189-1203, https://doi.org/10.1016/j.epsr.2006.08.016.

M. N. Absar, M. F. Islam, and A. Ahmed, (2023) Power quality improvement of a proposed grid-connected hybrid system by load flow analysis using static var compensator, Heliyon, 9, https://doi.org/10.1016/j.heliyon.2023.e17915.

V. S. Tabar, S. Ghassemzadeh, and S. Tohidi, (2022) Risk-based day-ahead planning of a renewable multi-carrier system integrated with multi-level electric vehicle charging station, cryptocurrency mining farm and flexible loads. Journal of Cleaner Production. 380:1. https://doi.org/10.1016/j.jclepro.2022.134898.

W. F. Tinney and C. E. Hart, (1967) Power Flow Solution by Newton's Method, IEEE Trans. Power App. Syst., 86, 1449-1460.

X. Zhong, G. Xin Li, and C. Zhng, (2021) False data injection in power smart grid and identification of the most vulnerable bus; a case study 14 IEEE bus network. Energy Reports. 7, 8476-8484. https://doi.org /10.1016/j.egyr.2021.08.029.

IEEES-033

Development of Metal Loaded Minerals as Heterogeneous Catalysts in the Degradation of Dye Solutions

*Zafer Metin ATAŞ, Gizem BAŞARAN DİNDAŞ, Hüseyin Cengiz YATMAZ
Gebze Technical University, Environmental Engineering Department, Gebze, 41400, Kocaeli, Turkey
*E-mails: z.atas2022@gtu.edu.tr

Abstract

Heterogeneous catalysis is a novel area of advanced oxidation processes (AOP) for degradation of organic pollutants. In this study, transition metal embedded minerals were developed as heterogeneous catalysts and utilized for the degradation of dye chemicals used in the textile industry. Zeolite and beidellite minerals from local natural sites of Türkiye were acquired and modified by using $FeSO_4$ and $CoSO_4$ solutions. Fe^{2+} and Co^{2+} exchanged minerals were developed as Fe-Zeolite (Fe-Z), Fe-Beidellite (Fe-B), Co-Zeolite (Co-Z), Co-Beidellite (Co-B) and used as Fenton and Fenton like heterogeneous catalysts, respectively. Fe-Z and Fe-B were tested for heterogeneous Fenton oxidation of Remazol Red 180 (RR180) textile dye solutions in the presence of H_2O_2. On the other hand, Co-Z and Co-B were also tested as heterogeneous Fenton like oxidation but using peroxymonosulfate (PMS). 100mL of 50 mg/L RR180 dye solutions with 1g/L catalyst loading amount were utilized with different concentration of H_2O_2 and PMS at ambient temperature and solution pH in 120min final time. Results with both Fe-Z and Fe-B have given lower than 20% color removal efficiency. However, over 90% color removal efficiency was obtained in 30min with both Co-Z and Co-B catalysts. High removal efficiency, negligible Co leaching into the solution, operation in a wide pH range have given novel heterogeneous competence to the Co-Z catalyst with PMS.

Keywords: heterogeneous catalysis, zeolite, beidellite, cobalt, iron.

I. Introduction

The surge in the demand for textile products has led to a proportional rise in the production and use of synthetic dyes, making wastewater from the textile industry a significant contributor to environmental pollution (Balapure et al., 2015). During the washing process, loss of reactive dyes is about 50% in their hydrolyzed and unfixed form (Benkhaya et al., 2020). Dyes also play important role in contributing as a breakdown product producing toxic amines and benzene with a period of increasing cancer cases (Manogaran et al., 2021). Therefore, the treatment of textile wastewater is unavoidable, and it is of utmost importance to decrease the levels of organic matter, suspended solids, and toxic substances in wastewater to meet the desired standards.

Researchers have used many techniques to treat textile wastewater, such as segregation into streams, adsorption, filtration, coagulation/flocculation, biological treatments, and advanced oxidation processes (AOPs) (Paździor et al., 2019; Saleh et al., 2021; Zhang et al., 2021). The limitations and disadvantages of the other mentioned conventional methods have instructed for researchers to further develop AOPs.

AOPs utilizing radicals represent simple and sustainable approaches for efficiently treating industrial wastewater and mitigating environmental degradation (Ceylan et al., 2022; Gupta et al., 2023). Fenton's reagent ($Fe^{2+}/Fe^{3+}/H_2O_2$) has been one of the most common homogeneous systems mentioned in AOPs. However, HO• based homogeneous Fenton systems have notable deficits, including requirement of low pH, the generation of iron-containing sludge for disposal, limited total organic carbon removal, quenching of hydroxyl radical by the carbonate species, and catalyst deactivation due to iron complexing agents (Gallard et al., 1999; Shukla et al., 2010; Tekbaş et al., 2008).

Various clay minerals including clinoptilolite from zeolite group and beidellite from smectite group have been used as heterogeneous catalysts in photo-Fenton reactions (Basaran Dindas et al., 2022; Yatmaz and Keris Sen, 2018).

On the other hand, Fenton-like oxidation with heterogeneous catalysts of reactive dyebath effluents are novel area that offers advantages worth researching. Heterogeneous catalysts with more efficient, sustainable and commercial advantages are possible by combining the metal, the surface for ion exchange/modification and the appropriate oxidizer under the most optimum conditions and processes.

Transitions metal ions such as Co^{2+} based on peroxymonosulfate (PMS) can also activate and generate SO_4•- at ambient temperature, which have the advantages of a wide range of pH, a high oxidation potential, a long half-life time, and biodegradability (Chen and Ma, 2011; Ling et al., 2010; Yan et al., 2022). SO_4•- also has a higher oxidation potential [2.5–3.1 eV] as compared to the hydroxyl HO• [1.7 eV], thereby promising to be an efficient oxidant. However, the oxidation reaction using Co^{2+} and PMS under homogeneous system has extensive disadvantage in terms of cobalt leaching (Yu et al., 2016). The cobalt leaching in discharged renders its toxic as cobalt is recognised as a considerabl metal pollutant.

Preventing the cobalt leaching is essential to make this technology commercially viable. In addition, (i) the aggregation of the small porous materials particles and covers up the active sites; (ii) difficulty to recycle and reducing their recyclability cause of fine powder form of porous material, have been reported as other problems that need to be solved (Chen et al., 2022).

In this study, zeolite and beidellite minerals from local natural sites of Türkiye were acquired and modified by using $FeSO_4$ and $CoSO_4$ solutions. Fe^{2+} and Co^{2+} exchanged minerals were developed as heterogeneous catalysts and utilized for the degradation of dye chemicals used in the textile industry. Transition metal embedded minerals were developed as Fenton and Fenton like heterogeneous catalysts.

II. Materials and Methods

2.1. Chemicals and Reagents

The Remazol Red 180 (RR180, Remazol Brilliant Red F3B), the peroxymonosulfate (PMS) as triple salt $KHSO_4 \cdot ½KHSO_4 \cdot ½K_2SO_4$ (Trade name OXONE, monopersulfate compound) and H_2O_2 (35% w/w) were obtained from Sigma-Aldrich. $FeSO_4 \cdot 7H_2O$ (Merck) and $CoSO_4 \cdot 7H2O$ (Fluka) were used for production of heterogenous catalysts. Natural zeolite minerals used in this work were obtained from Bigadiç, and the beidellite obtained from clay deposits in the Black Sea region, Türkiye. Deionised water was used throughout the experiments.

2.2. Preparing Catalysts

Pre-washed and dried zeolite minerals were obtained in the range of 1.2-2 mm diameter and beidellit clays was taken in powder form. Per 100 mL solution, 2.38 g $FeSO_4$ salts for iron loadings and 2.48 g $CoSO_4$ salts for cobalt loadings were taken for the ratio between metals and minerals 1:6 by weight. Then, 3 g of minerals were added to the solutions and 100 mL mixtures containing $FeSO_4$/Zeolite, $FeSO_4$/Beidellite, $CoSO_4$/Zeolite and $CoSO_4$/Beidellite were continuously agitated at 65 °C for 24 h. The obtained catalysts were washed several times with deionized water, dried at 100 °C for an hour and then calcined at 550 °C for 5 h.

2.3. Characterization of Catalysts

The morphology and elemental distribution characteristic of catalysts was obtained using Scanning Electron Microscopy (SEM, Philips XL30SFEG) and energy dispersive X-ray spectrometry (EDS). EDS analysis results and SEM images of Fe-Z, Fe-B, Co-Z and Co-B catalysts were presented in Fig. 1, respectively.

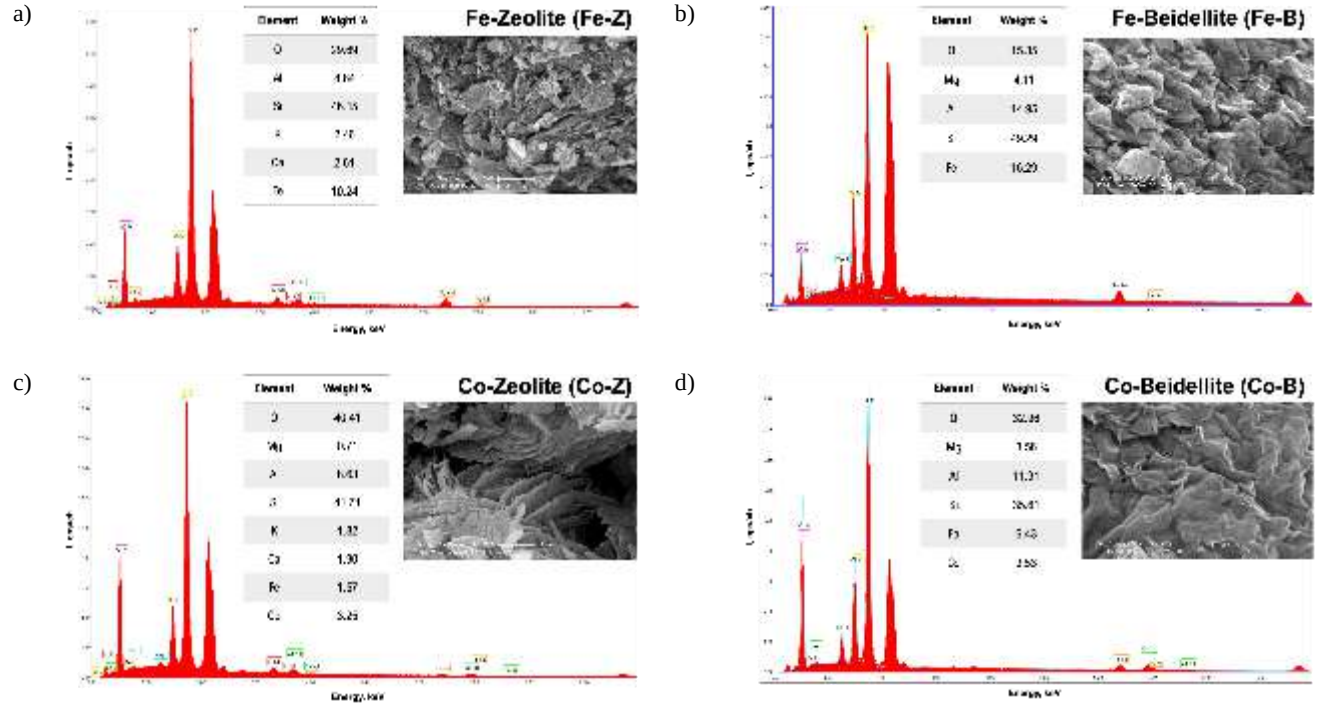

Fig. 1: EDS analysis results and SEM images of a) Fe-Zeolite (Fe-Z), b) Fe-Beidellite (Fe-B), c) Co-Zeolite (Co-Z) and d) Co-Beidellite (Co-B)

2.4. Experimental Procedure

The experiments were conducted at ambient temperature (25±3 ºC) in batch reactors. 100 mL, 50 mg/L RR180 dye solutions were treated with 1g/L catalyst load by presence of various amount of oxidizes. 1 mM, 2 mM, 5 mM and 10 mM H_2O_2 were studied for iron-based Fenton's reagent; and 0.5 mM, 1 mM, 2.5 mM and 5 mM PMS for cobalt-based Fenton-like reactions. pH of the dye solutions with Co-based solutions measured as 5.7; and Fe-based solutions measured as 5 and reduced to 2.6 with 6N H_2SO_4 for Fenton's reagent's needs.

The samples were continuously agitated on the shaker at 320 rpm under visible light. The dye solution samples were taken out for analysis at pre-defined time intervals such as 0, 15, 30, 60, 90 and 120 min for degradation analysis.

2.5. Analytical Method

Degradation of RR180 dyestuff was determined by colorimetric determination. The absorbance of each solution was determined using a 520 nm wavelength against blank using a Hach DR 3800 VIS Spectrophotometer.

III. Results and discussion

In the degradation processes carried out with heterogenous-Fenton reaction, the effect of the Fe-Z catalyst on decoloration could not be observed. The highest color removal of Fe-B catalyst was observed 25.8% with 5 mM H_2O_2; and the lowest color removal was observed 3.1% with 10 mM H_2O_2, at the end of 120 minutes. Changes depending on the amount of oxidant were not considered to be significant.

In heterogenous-Fenton-like reactions performed with Co-B catalyst, over 99% efficiency at the end of the 15th minute suggested Co leaching into the solution. It has been noted that the homogeneous reaction of Co^{2+} ions with PMS was more efficient (Shukla et al., 2010). However, it was mentioned in the introduction that Co^{2+} leaching itself was a serious pollutant. Apart from this, the slime form of beidellite catalyst formed after the process made its recovery and reuse difficult.

The results obtained for the Fe-Z catalyst were significant. Removal efficiency increased proportionally depending on the amount

of PMS oxidant usage. However, at the end of the 30th minute, 92.4% color removal efficiency was obtained with 0.5 mM PMS, while the efficiency obtained with 5 mM PMS was 97.7% at final time. Even when Co and PMS were used in very low amounts, highly efficient color removal could be achieved.

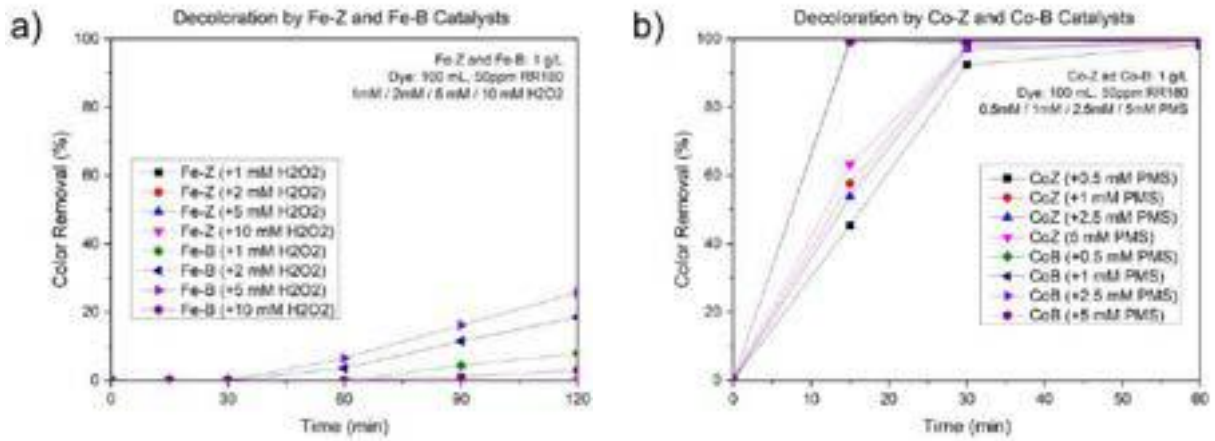

Fig. 2: Color removal efficiencies a) Fenton (pH = 2.6, oxidizer: 1, 2, 5 and 10 mM H_2O_2, catalyst: Fe loaded zeolite and beidellite) **and b) Fenton-like (pH = 5.7, oxidizer:** 0.5, 1, 2.5 and 5 mM PMS, catalyst: Co loaded zeolite and beidellite**) systems. Dye concentration: 50 mg/L, catalyst loading: 1g/L, solution volume: 100 mL, under visible light and ambient temperature.**

IV. Conclusion

Co loaded zeolites were found effective heterogeneous catalysts for RR180 dye degradation using PMS. Co-Z catalysts indicated stable performance in heterogeneous dye oxidation. Although powdered beidellite resulted in a very effective reaction rate for homogeneous activation of PMS, it was not evaluated as an efficient heterogenous catalyst due to the leaching of Co ions into the solution and the slime form of beidellite precipitate was difficult to recover.

The fact that the highest efficiency color removal (25.8%) was observed after 120 minutes in Fenton reactions by iron-loaded heterogenous catalysts in the presence of H_2O_2 with Fe-B catalyst, and no efficient removal could be observed with the Fe-Z catalyst, indicated that they were less efficient under similar conditions when compared to Fenton-like systems by Cobalt-loaded catalysts in the presence of PMS. The results also showed that zeolite minerals as a cobalt holder were worth investigating as a heterogeneous catalyst that produced very effective radicals in the presence of PMS.

References

Balapure, K., Bhatt, N., Madamwar, D., 2015. Mineralization of reactive azo dyes present in simulated textile waste water using down flow microaerophilic fixed film bioreactor. Bioresour Technol 175, 1–7. https://doi.org/10.1016/J.BIORTECH.2014.10.040

Basaran Dindas, G., Koseoglu-Imer, D.Y., Yatmaz, H.C., 2022. A novel Fe/HNT visible light-driven heterogeneous photocatalyst: Development as a semiconductor and photocatalytic application. Progress in Natural Science: Materials International 32, 273–281. https://doi.org/10.1016/J.PNSC.2022.03.003

Benkhaya, S., M' rabet, S., El Harfi, A., 2020. A review on classifications, recent synthesis and applications of textile dyes. Inorg Chem Commun 115, 107891. https://doi.org/10.1016/J.INOCHE.2020.107891

Ceylan, E., Dindaş, G.B., Bektaş, N., Yatmaz, H.C., 2022. Modification of natural chitosan with Fe and Ce cations as photocatalyst beads: Degradation of dye chemicals and textile wastewater under UVA light. J Environ Manage 310, 114790. https://doi.org/10.1016/J.JENVMAN.2022.114790

Chen, D., Bai, Q., Ma, T., Jing, X., Tian, Y., Zhao, R., Zhu, G., 2022. Stable metal–organic framework fixing within zeolite beads for effectively static and continuous flow degradation of tetracycline by peroxymonosulfate activation. Chemical Engineering Journal 435, 134916. https://doi.org/10.1016/J.CEJ.2022.134916

Chen, L., Ma, J., 2011. A Fenton-like system combined by Co2+ and potassium Monopersulfate for the treatment of benzoic acid. 2011 International Conference on Consumer Electronics, Communications and Networks (CECNet) 2861–2864. https://doi.org/10.1109/CECNET.2011.5769359

Gallard, H., De Laat, J., Legube, B., 1999. Spectrophotometric study of the formation of iron(III)-hydroperoxy complexes in homogeneous aqueous solutions. Water Res 33, 2929–2936. https://doi.org/10.1016/S0043-1354(99)00007-X

Gupta, S., Fernandes, R., Patel, R., Spreitzer, M., Patel, N., 2023. A Review of Cobalt-based Catalysts for Sustainable Energy and Environmental Applications. Appl Catal A Gen 119254. https://doi.org/10.1016/J.APCATA.2023.119254

Ling, S.K., Wang, S., Peng, Y., 2010. Oxidative degradation of dyes in water using Co2+/H2O2 and Co2+/peroxymonosulfate. J Hazard Mater 178, 385–389. https://doi.org/10.1016/J.JHAZMAT.2010.01.091

Manogaran, M., Yasid, N.A., Othman, A.R., Gunasekaran, B., Izuan, M., Halmi, E., Yunus, M., Shukor, A., Proença, N., Maria, P., Morais, V., Tischler, D., 2021. Biodecolourisation of Reactive Red 120 as a Sole Carbon Source by a Bacterial Consortium—Toxicity Assessment and Statistical Optimisation. International Journal of Environmental Research and Public Health 2021, Vol. 18, Page 2424 18, 2424. https://doi.org/10.3390/IJERPH18052424

Paździor, K., Bilińska, L., Ledakowicz, S., 2019. A review of the existing and emerging technologies in the combination of AOPs and biological processes in industrial textile wastewater treatment. Chemical Engineering Journal 376, 120597. https://doi.org/10.1016/J.CEJ.2018.12.057

Saleh, M., Bilici, Z., Kaya, M., Yalvac, M., Arslan, H., Yatmaz, H.C., Dizge, N., 2021. The use of basalt powder as a natural heterogeneous catalyst in the Fenton and Photo-Fenton oxidation of cationic dyes. Advanced Powder Technology 32, 1264–1275. https://doi.org/10.1016/J.APT.2021.02.025

Shukla, P., Wang, S., Singh, K., Ang, H.M., Tadé, M.O., 2010. Cobalt exchanged zeolites for heterogeneous catalytic oxidation of phenol in the presence of peroxymonosulphate. Appl Catal B 99, 163–169. https://doi.org/10.1016/J.APCATB.2010.06.013

Tekbaş, M., Yatmaz, H.C., Bektaş, N., 2008. Heterogeneous photo-Fenton oxidation of reactive azo dye solutions using iron exchanged zeolite as a catalyst. Microporous and Mesoporous Materials 115, 594–602. https://doi.org/10.1016/J.MICROMESO.2008.03.001

Yan, Y., Zhang, X., Wei, J., Chen, M., Bi, J., Bao, Y., 2022. Understanding the Iron-Cobalt Synergies in ZSM-5: Enhanced Peroxymonosulfate Activation and Organic Pollutant Degradation. ACS Omega 7, 17811–17821. https://doi.org/10.1021/acsomega.2c01031

Yatmaz, H.C., Keris Sen, U.D., 2018. Photocatalytic Efficiencies of Alternate Heterogeneous Catalysts: Iron Modified Minerals and Semiconductors for Removal of an Azo Dye in Solutions. Environment Protection Engineering 44, 5–17. https://doi.org/10.37190/epe180101

Yu, L., Chen, J., Liang, Z., Xu, W., Chen, L., Ye, D., 2016. Degradation of phenol using Fe3O4-GO nanocomposite as a heterogeneous photo-Fenton catalyst. Sep Purif Technol 171, 80–87. https://doi.org/10.1016/j.seppur.2016.07.020

Zhang, Y., Shaad, K., Vollmer, D., Ma, C., 2021. Treatment of Textile Wastewater Using Advanced Oxidation Processes - A Critical Review. Water (Basel) 13. https://doi.org/10.3390/w13243515

IEEES-034

CO_2 Removal by Calcined Eggshell

Sena Erkent[1], Barış Gürel[2], Karani Kurtuluş[2], Savaş Özün[3], Murat Varol[4], Kamil Ekinci[5], Sema Yurdakul[1*]
[1]Department of Environmental Engineering, Suleyman Demirel University, 3200, Isparta, Türkiye;
[2]Department of Mechanical Engineering, Suleyman Demirel University, 3200, Isparta, Türkiye;
[3]Department of Mining Engineering, Suleyman Demirel University, 3200, Isparta, Türkiye;
[4]Department of Environmental Engineering, Akdeniz University, 07070, Antalya, Türkiye;
[5]Agricultural Machinery and Technology Engineering Department, Isparta University of Applied Sciences, Isparta 3200, Türkiye
*E-mail: semayurdakul@sdu.edu.tr

Abstract

Turkey ranks ninth in the world with a share of 1.5% in egg production. In 2020, 19 297 591 000 chicken eggs were produced in Turkey, and approximately 93 000 to 111 600 tons of waste eggshell (ES) were produced as a result of this production. Among the eggshell disposal methods, the most basic ones are to send to landfills, mix with soil, or use as an additive to poultry feed. Among these alternatives, landfills seem to be the most suitable option as operating costs are considered. However, during the disposal of the eggshells in the landfills, some problems, such as odor, flies, etc., arising from microbiological deterioration are observed. Therefore, alternative disposal methods of waste eggshells are important in terms of both disposing of waste in a more environmentally friendly manner and obtaining a product with economic value.

Although eggshells can be used to remove various pollutants as an adsorbent, there are limited studies for gas removal. In this study, after determining the optimum calcination parameters of raw eggshells for three different temperatures and five different holding times to produce CaO, the CO_2 adsorption capacity of the calcined eggshells was determined for nine different particle sizes for CO_2 removal. The adsorption capacity of the calcined eggshells was between 0.15 g CO_2/g ES (+2.8-1.7 mm) and 0.33 g CO_2/g ES (-75+45 µm). The analysis also revealed that the CO_2 adsorption was increased with the decreasing particle size.

Keywords: Eggshell, Waste valorization, CO_2, Adsorption

I. Introduction

The combustion of fossil fuels results in the release of large amounts of CO_2 emissions into the atmosphere. Therefore, an inexpensive process is required to remove CO_2 from flue gas before it is compressed, cooled, liquefied, transported, and finally separated. High-temperature sorbents such as CaO offer significant advantages over existing CO2 separation techniques (adsorption, absorption, membrane separation, etc.) due to their high sorption capacity (5-10 times higher than adsorbents/absorbents).

One of the most critical problems faced by food producers is the disposal of eggshells. The amount of eggs consumed in the domestic market in Türkiye in 2020 was 930 thousand tons (Chicken Egg, 2021). Furthermore, the eggshell fractures can reach up to 10% of the production. Eggshell constitutes approximately 10-12% of the egg by mass. Therefore, approximately 93,000 to 111,600 tons of eggshells were generated as waste in Türkiye in 2020. In Türkiye, waste eggshells are generated in large quantities and collectively in pasteurized egg and industrial egg powder production facilities. However, waste eggshells can be utilized as CO_2 and SO_2 sequestering material. Thus, during the energy generation, by burning the waste eggshell together with lignite, both CO_2/SO_2 emissions will be reduced, and the waste will be disposed of in a controlled manner.

Although the density of $CaCO_3$ extracted from eggshells (0.4236 g cm-3) is relatively lower than the mineral density of $CaCO_3$ (0.467 g cm-3) (Hassen et al., 2015), it is reported to have the same effect as commercial calcium carbonate in removing sulfur dioxide (Hoo, 2018). Although it is reported in the literature that CaO derived from eggshells has a larger macropore volume than commercially available $CaCO_3$ (Cree and Rutter, 2015), the studies systematically investigating the pretreatment and regeneration of eggshells for CO_2 capture are very limited. Therefore, in this study, after determining the optimum calcination parameters of raw eggshells for three different temperatures (850, 900, and 1000 ^oC) and five different holding times to produce CaO, the CO_2 adsorption capacity of the calcined eggshells was determined for nine different particle sizes for the determination of CO_2 adsorption capacity.

II. Materials and Methods

In the study, the eggshells were first washed in tap water, and then the shells were cleaned from the membranes and rinsed in deionized water. They were then left to dry at room temperature (20±5^oC). After drying, the samples were crushed and sieved into nine different particle sizes, namely -2,8+1,7 mm, -600+425 µm, -212+150 µm, -150+106 µm, -106+90 µm, -90+75 µm, and -75+45 µm to investigate the effect of particle size on the CO_2 adsorption. For this purpose, the eggshells were calcined at three different temperatures (850, 900, and 950 ^oC) and for five different holding times (30-60-90-120-180 minutes). The calcination was performed in a muffle furnace (Nüve 500). On the other hand, the carbonation experiments were performed in a Thermogravimetric Analyzer (TG) under the CO_2 atmosphere at nonisothermal conditions. Analyses were carried out by heating up to 1000 ^oC at a heating rate of 15 ^oC per minute at a 40 ml/min flow rate in a CO_2 atmosphere.

III. Results and Discussion

At 850 ºC, as the eggshells could not be calcinated completely (i.e., black color was observed), the experiment was not performed at this temperature (Figure 1a). In their study, Stanmore and Gilot (2005) reported that powdered eggshells were sintered at 950 ºC and beyond. Therefore, a decreasing adsorption capacity was observed in the literature>950 ºC. Accordingly, calcination experiments were performed at two temperatures (900 and 950 ºC) (Figure 1b). In the study, the adsorption capacity was calculated from the mass losses. Calcination of the ESs was performed in a muffle furnace for 30, 60, 90, 120, and 180 minutes, and mass losses were found to be 47%, 46%, 44%, 44%, and 43%, respectively. Therefore, desorption was observed as the holding time increased. Thus, the calcination time was selected as 30 minutes.

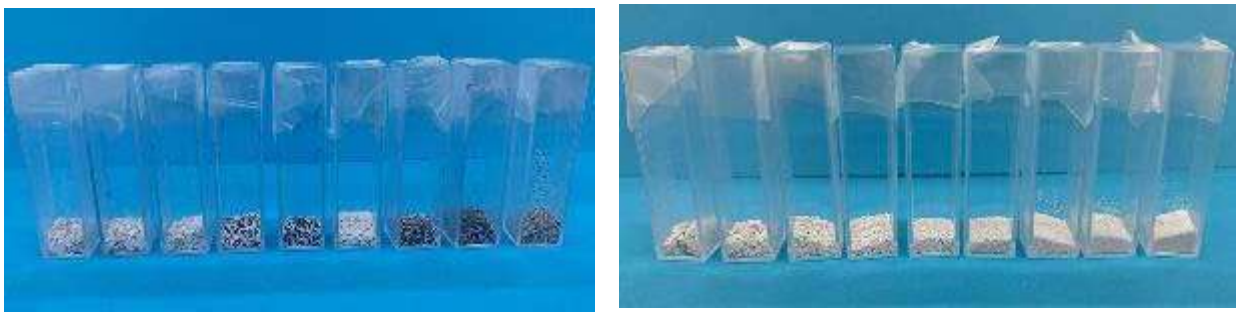

Fig 1. The calcinated eggshells at 850 ºC (on the left side) and calcinated eggshells at 900 ºC (on the right side) (Erkent, 2024)

After the calcination, carbonation experiments were performed in a Thermogravimetric Analyzer (TG) under the CO_2 atmosphere for nine different particle sizes, and the optimum temperature was obtained based on the mass increments in CO_2 adsorption for two calcination temperatures. On the other hand, the CO_2 adsorption amounts were found to be close to each other; therefore, the calcination temperature was selected as 900 ºC to save energy. At 900 ºC, the carbonation experiments were performed at TG under a carbon dioxide atmosphere to obtain the optimum particle size yielding the highest CO_2 adsorption amount (Figure 2).

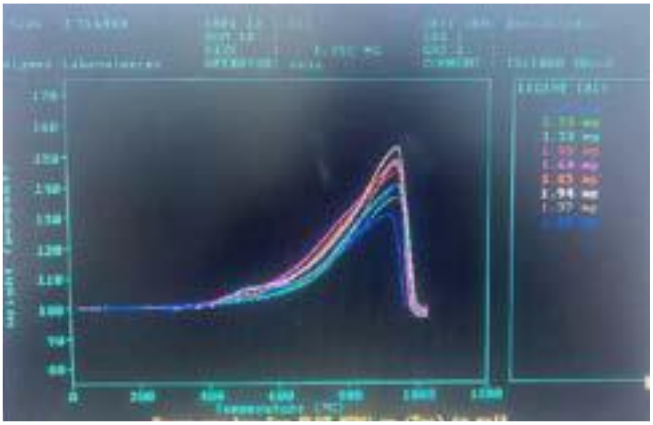

Fig 2. TG curves of the nine different particle sizes during the carbonation at 15 ºC/min ramp (Erkent, 2024)

The CO_2 adsorption capacities of the calcined eggshells were 0.152 g CO_2/g, 0.188 g CO_2/g, 0.204 g CO_2/g, 0.201 g CO_2/g, 0.329 g CO_2/g, 0.324 g CO_2/g, 0.329 g CO_2/g, 0.331 g CO_2/g and 0.328 g CO_2/g for -2,8+1,7 mm, -600+425 µm, -212+150 µm, -150+106 µm, -106+90 µm, -90+75 µm, and -75+45 µm particle sizes, respectively. Therefore, it can be said that particle size affects the carbon dioxide adsorption capacity of the calcined eggshells.

IV. Conclusion

The eggshells underwent the calcination and carbonation processes in the study. Accordingly, weight loss and weight gain were observed on TG curves. The study observed that the calcination temperature, holding time, and particle size of the eggshells significantly affect the produced CaO's ability to adsorb CO_2. As a result, the CO_2 adsorption capacities of the eggshells were found to be between 0.15 g CO_2/g (+2.8-1.7 mm) and 0.33 g CO_2/g (-75+45 µm).

Acknowledgments

This study was funded by the Scientific and Technological Research Council of Turkey (TUBITAK) ARDEB 1001 Grant No 123M067.

References

Cree, D. and Rutter, A., (2015). Sustainable bio-inspired limestone eggshell powder for potential industrialized applications. ACS Sustain. Chem. Eng, 3(5), 941-949.

Erkent, S. (2024). Investıgatıon Of Combustıon Kınetıcs Of Waste Eggshells Wıth Lıgnıte and CO2 Sequestratıon Potentıal Of Waste Eggshells, Unpublished MSc thesis, SDU, Isparta, Türkiye.

Hassen, A.A., Dizbay-Onat, M., Bansal, D., Bayush, T. and Vaidya, U., 2015. "Utilization of Chicken Eggshell Waste as a Bio-Filler for Thermoplastic Polymers: Thermal and Mechanical Characterization of Polypropylene Filled With Naturally Derived CaCO3". Polym. Polym. Compos., 23(9), 653-662.

Hoo, S.K., (2018). Sulphur dioxide removal using dried eggshell, Unpublished Ph.D. thesis, Universiti Tunku Abdul Rahman (UTAR), Malesia.

Stanmore, B.R. and Gilot, P., (2005). Calcination and carbonation of limestone during thermal cycling for CO2 sequestration. Fuel Process. Technol. 86(16),1707-1743.

Chicken Egg, (2021). https://arastirma.tarimorman.gov.tr/tepge/Belgeler/PDF%20Tar%C4%B1m%20%C3%9Cr%C3%BCnleri%20Piyasalar%C4%B1/2021-Ocak%20Tar%C4%B1m%20%C3%9Cr%C3%BCnleri%20Raporu/Tavuk%20Yumurtas%C4%B1,Ocak-2021,%20Tar%C4%B1m%20%C3%9Cr%C3%BCnleri%20Piyasalar%C4%B1%20Raporlar%C4%B1%20--.pdf

IEEES-035

Numerical Investigation of the Effect of Different Boundary Conditions and Geometrical Properties on CO_2 Removal Efficiency in the Retention of CO_2 from Flue Gas in a CO_2 Capture Column With Calcined Eggshell By Carbonation Reaction

Barış Gürel[2], Karani Kurtuluş[2], Savaş Özün[3], Murat Varol[4], Kamil Ekinci[5], Sena Erkent[1], Sema Yurdakul[1*]
[1]Department of Environmental Engineering, Suleyman Demirel University, 3200, Isparta, Türkiye;
[2]Department of Mechanical Engineering, Suleyman Demirel University, 3200, Isparta, Türkiye;
[3]Department of Mining Engineering, Suleyman Demirel University, 3200, Isparta, Türkiye;
[4]Department of Environmental Engineering, Akdeniz University, 07070, Antalya, Türkiye;
[5]Agricultural Machinery and Technology Engineering Department, Isparta University of Applied Sciences, Isparta 3200, Türkiye
*E-mail: semayurdakul@sdu.edu.tr

Abstract

Sequestration of CO_2 gas is significant for reducing the impact of greenhouse gases. One of the most important sources of CO_2 is the release of flue gas from combustion boilers. In this study, the flue gas produced by the co-combustion of lignite and biomass in a Circulating Fluidized Bed Boiler was sent to a cylindrical column (i.e., CO_2 retention column, with an inner diameter of 0.4 m with a total length of 5 m with 3 m downward vertical direction and 4 m horizontal direction) whose inlet temperature was about 750 ^oC, and the conversion of CO_2 to $CaCO_3$ in the column with calcined eggshells was investigated. The effect of column diameter, flue gas velocity, air flow rate to be sent to avoid excess heat generated as a result of the reaction, column length, column slope, calcined eggshell flow rate, and particle diameter of calcined eggshell on the CO_2 retention efficiency in the column was numerically analyzed. Baracuda VR Particle Fluid Dynamics Software was used for the numerical analysis. Lagrange multiphase flow and LES turbulence methods were also used, and time-dependent analyses were performed during the study. The A and E_a values of the carbonation and calcination reactions between calcined eggshell and CO_2 were determined by a Thermogravimetric Analysis instrument and introduced to the software. As a result of the analyses, it was determined that approximately 99.9% of the CO_2 was captured in the flue gas containing 0.13 mol of CO_2 at an inlet temperature of 800 ^oC at a flow rate of 112.5 kg/hr using eggshell with a particle size of 90 µm at a flow rate of 400 kg/hr in the column. As a result of the analysis, it was interpreted that the amount of calcined eggshell to be used can be reduced by developing different designs and process parameters. In addition, it was concluded that the developed process successfully achieved the desired targets due to the use of waste eggshells and the efficient capture of CO_2.

Keywords: CO_2 Capture, Calcined Eggshell, Computational Particle Fluid Dynamics, Carbonation.

I.Introduction

Carbon capture, utilization, and storage (CCUS) technologies are garnering attention due to their ability to eliminate CO_2, the primary contributor to global warming, as the issue of global warming has spread worldwide. The most promising method, carbon capture and storage, has been the subject of numerous studies (Kim et al., 2018). Nevertheless, there are several drawbacks, such as the high expense of CO_2 separation, high transportation expenses, and a dearth of appropriate places to store the captured CO_2 (Li et al., 2016). In this study, the flue gas produced by the co-combustion of lignite and biomass in a Circulating Fluidized Bed Boiler was sent to a cylindrical column, and the conversion of CO_2 to $CaCO_3$ in the column with calcined eggshells was investigated. The effect of column diameter, flue gas velocity, air flow rate to be sent to avoid excess heat generated as a result of the reaction, column length, column slope, calcined eggshell flow rate, and particle diameter of calcined eggshell on the CO_2 retention efficiency in the column was numerically analyzed.

II. Methodology

Baracuda VR Particle Fluid Dynamics Software was used for the numerical analysis. Lagrange multiphase flow and LES turbulence methods were also used, and time-dependent analyses were performed during the study. The A and E_a values of the carbonation and calcination reactions between calcined eggshell and CO_2 were determined by a Thermogravimetric Analysis instrument and introduced to the software. The shape of the Compact Circulating Fluidized Bed Boiler and CO_2 Capture System is given in Figure 1. As shown in Figure 1, the system consists of a fluidized bed boiler and an inclined cylinder-shaped CO_2 capture system.

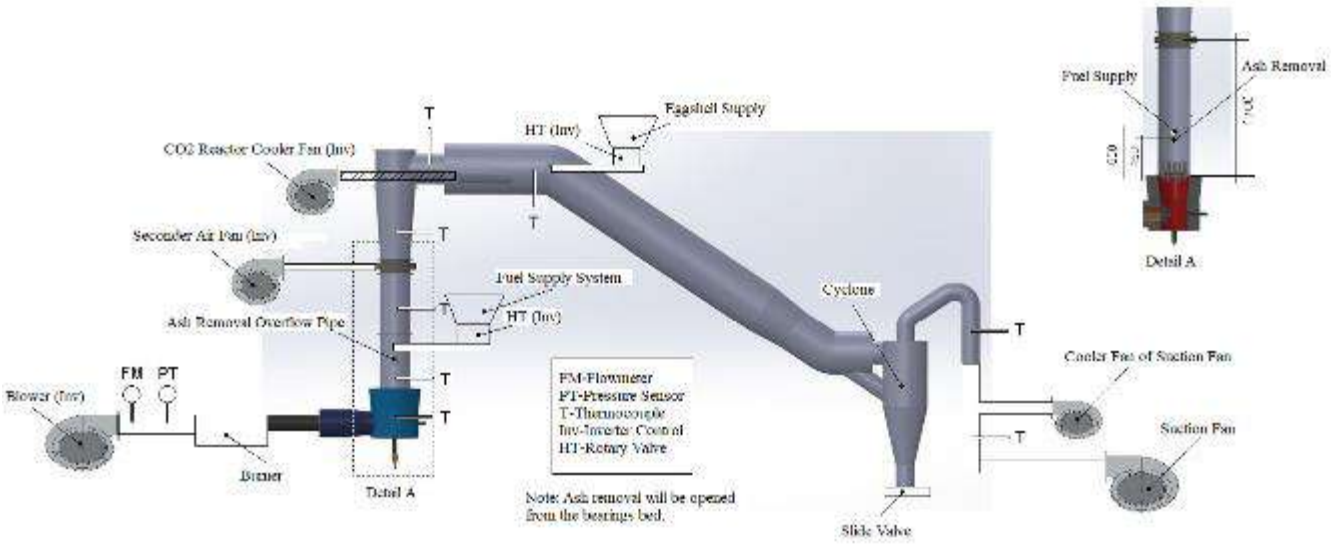

Fig. 1: Compact Circulating Fluidized Bed Boiler and CO_2 Capture System

The carbonation and calcination reactions used in the analyses are given in Equations 1 and 2 below.

$CaO(s) + CO_2 => CaCO_3(s)$ (1)
$CaCO_3(s) => CaO(s) + CO_2$ (2)

The kinetics of the carbonation reaction for the calcined eggshell calculated from the thermograms obtained from Thermogravimetric Analysis (TGA) is given in Equation 3. Calcination reaction kinetics, also calculated as a result of TGA, is shown in Equation 4.

$$k1 = 1.1e + 06\ e^{-6134.23/T} \quad (3)$$
$$k2 = 1.1e + 08\ e^{-15016.8/T} \quad (4)$$

III. Analysis

Two different cases were modeled in the analyses. In the first case, flue gas containing 0.13 mol of CO_2 at an inlet temperature of 800 ^oC at a flow rate of 112.5 kg/hr using calcined eggshell with a particle size of 90 µm at a flow rate of 400 kg/hr in the column. The flow rate of the column cooling air is 86.4 kg/hr, and the temperature is 300 K. The diameter of the CO_2 capture column is 0.4 m, the length of the inclined zone is 3 m, the height is 2 m, the size of the column is 3.6 m.

In the second case, flue gas containing 0.13 mol of CO_2 at an inlet temperature of 800 ^oC at a flow rate of 112.5 kg/hr using calcined eggshell with a particle size of 90 µm at a flow rate of 400 kg/hr in the column. The flow rate of the column cooling air is 54 kg/hr, and the temperature is 300 K. The diameter of the CO_2 capture column is 0.4 m, the length of the inclined zone is 4 m, the height is 3 m, and the size of the column is 5 m.

IV. Results and discussion

As a result of the analyses, the CO_2 mole fraction distributions in the CO_2 capture column for the first and second cases are given in Figures 3 and 4, respectively.

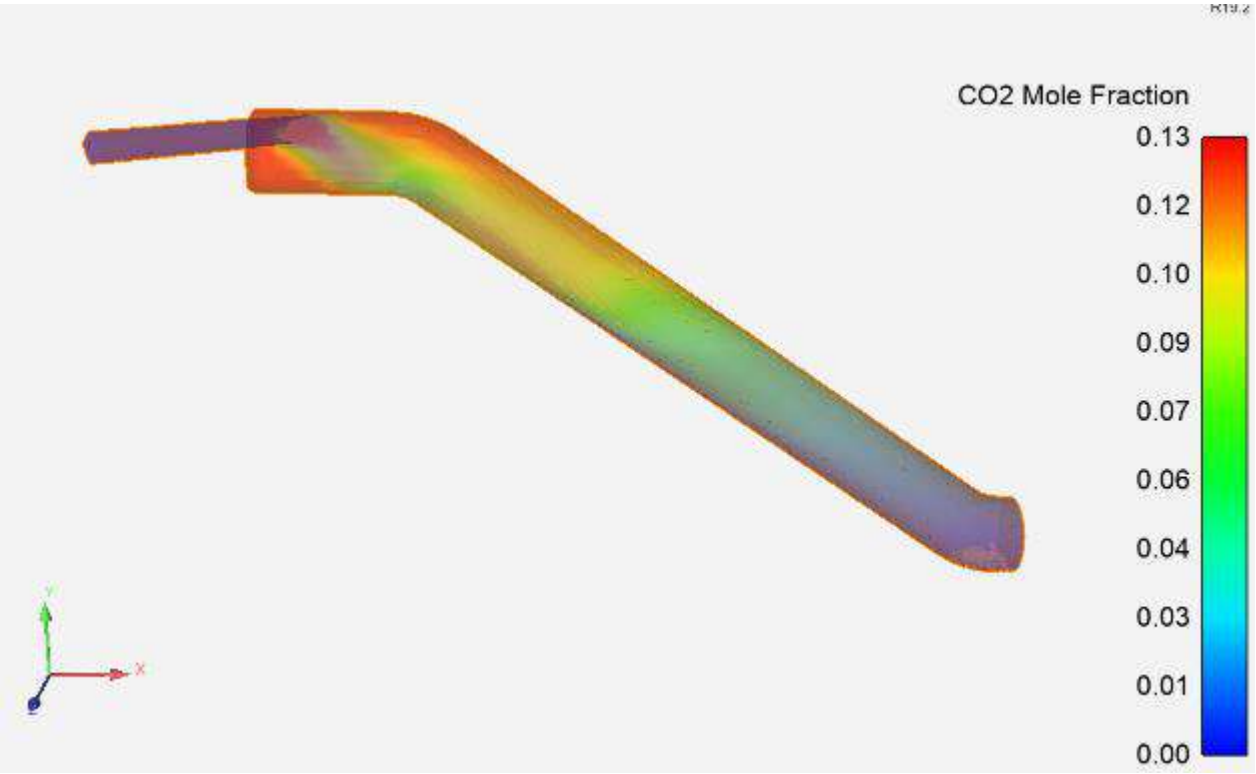

Fig 3: CO_2 mole fraction in the CO_2 Capture Column for the first case

As seen in Figure 3, while the CO_2 mole ratio is 0.13 at the entrance to the inclined zone in the column, it decreases in the inclined zone along the column. At the exit of the column, the average CO_2 mole ratio is 0.01. In the first case, the CO_2 adsorbtion in the column is 92.3%.

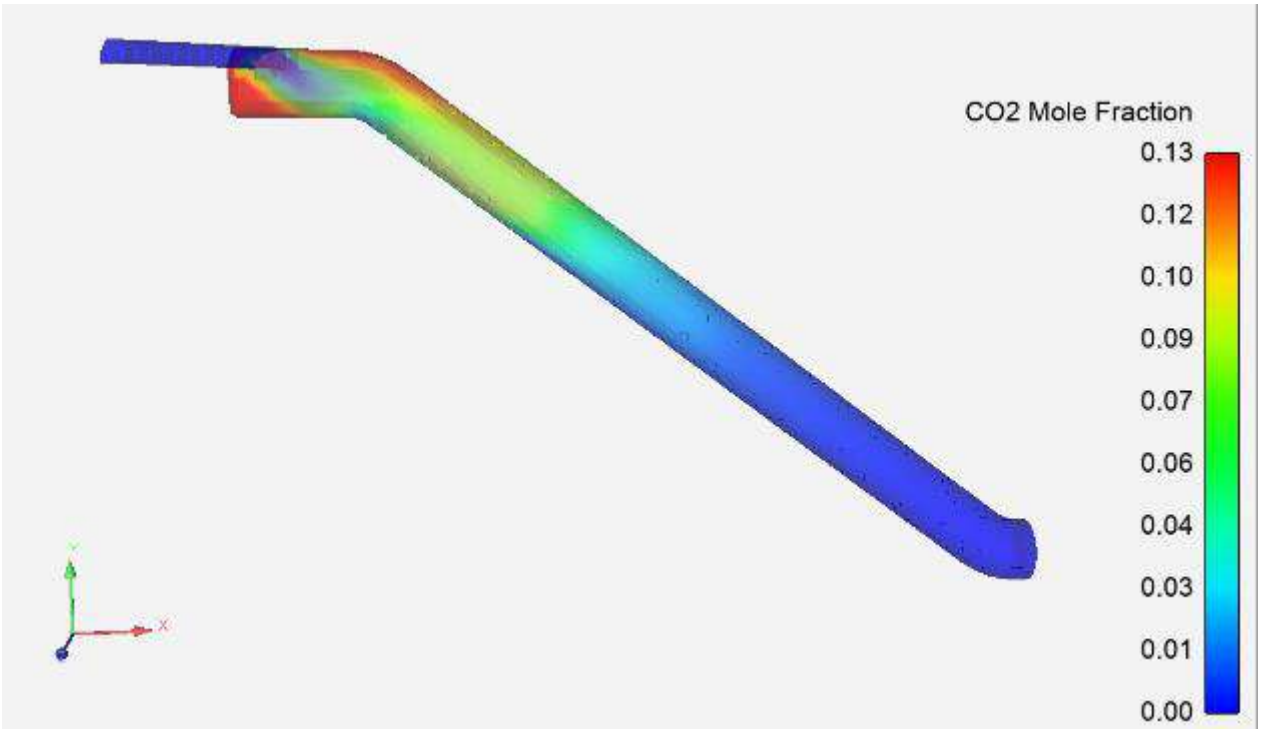

Fig 4: CO_2 mole fraction in the CO_2 Capture Column for the second case

As seen in Figure 4, while the CO_2 mole ratio was 0.13 at the entrance to the declining zone in the column, it decreased rapidly in the declining zone along the column. After about 3.5 m along the column, the CO_2 mole fraction decreased to 0.00001. From this length to the column outlet, the CO_2 mole fraction becomes almost zero. In the second case, the CO_2 adsorption in the column is 99.9%.

V. Conclusion

As a result of the analyses, it was determined that approximately 99.5% of the CO_2 was captured in the flue gas containing 0.13 mol of CO_2 at an inlet temperature of 800 ºC at a flow rate of 112.5 kg/hr using calcined eggshell with a particle size of 90 µm at a flow rate of 400 kg/hr in the column. Under optimum CO_2 holding conditions, the flow rate of the column cooling air is 54 kg/hr, the temperature is 300 K, the diameter of the CO_2 capture column is 0.4 m, the length of the inclined zone is 4 m, the height is 3 m, and the size of the column is 5 m. It was concluded that the developed process successfully achieved the desired targets in terms of the use of waste eggshells and the efficient capture of CO_2.

Acknowledgments
This research was supported by the TUBITAK 123M067 grant number.

References

Kim, M., Na, J., Park, S., Park, J.H. and Han, C. (2018). Modeling and validating a pilot-scale aqueous mineral carbonation reactor for carbon capture using computational fluid dynamics. Chem Eng. Sci. 177, 301-312.

Li, K., Leigh, W., Feron, P., Yu, H. and Tade, M. (2016). Systematic study of aqueous monoethanolamine (MEA)-based CO_2 capture process: Techno-economic assessment of the MEA process and its improvements. Appl. Energy. 165, 648-659.

IEEES-036

A Computational Investigation Into the Leakage and Dispersion of Hydrogen in Enclosed Areas

[1, 2]Lekshmipriya J, [1*]Abhilash Suryan, [3]Prasanth P Nair
[1] Department of Mechanical Engineering, College of Engineering Trivandrum, Kerala, India, 695016
[2] APJ Abdul Kalam Technological University, Kerala, India, 695016
[3] Mechanical Engineering Discipline, IIT Gandhinagar, Gujarat, India, 382355
*E-mail: suryan@cet.ac.in

Abstract

The utilization of hydrogen, as an energy source brings forth possibilities along with significant safety concerns especially in partially enclosed areas. Hydrogen has a wide range of flammability, which makes it crucial to assess potential ignition hazards. In this study, a computational analysis is performed to examine the behavior of hydrogen leakage in confined spaces. Comprehensive three-dimensional models of hydrogen leak scenarios are built using Ansys Fluent, modeling various situations such as pressure differentials, pipe geometries, and environmental factors. Parameters such as leak location, velocity, temperature, and ventilation rates are considered to predict hydrogen's spatial distribution and concentration. Moreover, the effectiveness of forced ventilation systems in mitigating risks is assessed. The study considers factors such as the shape, the ventilation system design and the rate at which hydrogen is released. The insights gained from this research will be utilized for designing and operating forced ventilation systems, in enclosed spaces where hydrogen is stored, transported, or used. The effects of hydrogen leaks on temperature can be evaluated using ANSYS thermal analysis. In a semi-closed area, the hydrogen mole fraction is analysed at several points to ascertain concentration levels at various times. Based on the results of the simulation, suggestions for the architecture and design of semi-closed regions handling hydrogen are made. These recommendations are intended to increase safety and prevent the buildup of significant hydrogen mole fractions.

Keywords: Hydrogen leak, Hydrogen safety, Semi closed space, Forced ventilation

I.Introduction

Development of compact, reliable, leak proof and safe storage technology is an important barrier to be overcome for hydrogen to gain acceptance as a major source of energy (Suryan et al., 2012). Recognizing Hydrogen leaks and associated possible risks is of paramount significance for environment protection and safety. Hydrogen has several perilous qualities. It is prone to leaks and diffusion, has a low threshold for ignition, a diverse range of fuel explosions, and intense explosion powers. Hydrogen is extremely combustible and light, which can cause leakage issues (Najjar, 2013). Burning volume proportion of hydrogen fluctuates from 4% to 75%, (Hao et al., 2020) whereas the explosion volume fraction ranges from 18.3% to 59%. Plus, the lowest energy needed to kick start ignition is just 0.02mJ (Phanichphant, 2014). Any hydrogen leakage in a small area used by cars, such a parking garage or a tunnel, is extremely dangerous (Hajji et al., 2015). Hydrogen leakage and diffusion process in open space include three stages: leakage and diffusion, concentration dilution and stable balance. At the beginning of the leakage, when the air can dilute hydrogen, the distribution range is reduced. After the hydrogen leakage, diffusion and dilution, the hydrogen distribution range does not change. When the distribution is stable, the hydrogen concentration is characterized by a conical stratified distribution structure, the hydrogen concentration and concentrated gradient near the leakage port. The width increases with the diffusion distance and with the inclined straight-line characteristics (Jiao et al., 2021). The potential effects of interior hydrogen leaks differ from those of outdoor emissions in that they may affect individuals, structures, and the environment. There are two phases to the unintentional hydrogen leak: the high-speed leakage stage and the ventilation disposal stage. Hydrogen has a far higher flammability than other fuels and that is dependent on concentration level. In addition, the flame is hotter and faster. The conditions of release, including the hydrogen pressure, leak size, direction of release, and enclosure parameters like volume and vent sizes, determine the hydrogen dispersion in a semi-closed space with one open boundary and the uniform or nonuniform concentration distribution of the hydrogen. The hydrogen is released and rises quickly to a point above the leakage point. This results from the significant discrepancy in hydrogen and air densities (Malakhov et al., 2020). In the event of a hydrogen leak, the primary objective of compressed air is to reduce the hydrogen concentration in the air to a safe level, with low risk of explosion or fire. If air volume is required based on the desired initial and final hydrogen concentrations. Airflow, usually measured in cubic feet per minute (CFM) or cubic meters per hour (m3/h), is key. It is calculated based on the volume of the space, initial air volume and desired final volume. Higher ventilation levels can reduce the time to achieve safe conditions. The composition and size of the hydrogen leak will affect the critical gas velocity. Generally speaking, forced ventilation is anticipated to occur more quickly than natural ventilation, however, the real-time sensing based approach was only suggested for natural ventilation. The feasibility of utilizing forced or natural ventilation varies based on the geometrical arrangement of a vented space. However, creating forced ventilation plans based on on-the-spot hydrogen detection will also be crucial for areas belonging to a certain class (Matsuura et al., 2010).

II.Experimental System Description

This experimental facility is a standard-sized container measuring 12.11 m in length, 2.39 m in height, 2.34 m in width (Malakhov et al., 2020). The pure hydrogen source is situated in the container's front wall, away from both the side wall and the floor. The enclosure is having open boundary as shown in the figure. Employed a matrix of sensors to measure the hydrogen concentration inside the ventilation facility. The sensors have been calibrated as closely as feasible to the working circumstances in order to minimize errors and eliminate any errors in hydrogen concentration measurements. The hydrogen sensors have a maximum error of 0.138% and a

typical sensing accuracy of 3% of the recorded value.

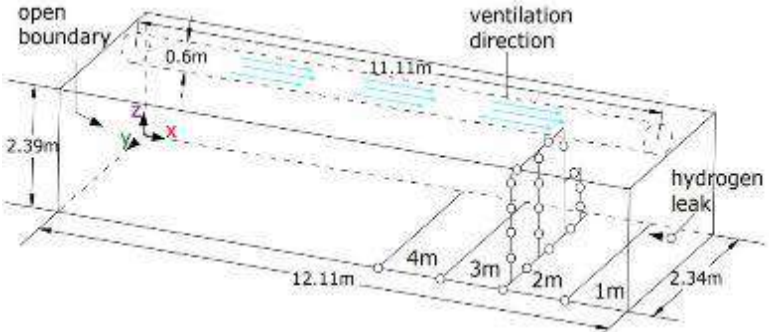

Fig. 1: Schematic diagram of facility with ventilation tube

III. Numerical Analysis

A three-dimensional model of the semi-closed area and ventilation systems is made with walls, apertures, obstructions, and ventilation elements appropriately represented. The computational grid is made is almost uniform throughout the whole calculation domain with the exception of a correction made to the hydrogen leak position to improve simulation accuracy. Simulation included the forced ventilation system. The ventilation flow rate and direction are specified. Reynolds-averaged Navier - Stokes (RANS) approach is used to simulate Hydrogen leakage. Boundary conditions included air velocity of inlet 3m/s for ventilation, Hydrogen leak with orifice size of 0.8mm, 20 bar absolute is the inlet pressure of H_2 and outlet pressure of H_2 is 1 bar absolute. Turbulence modeling for compressed hydrogen gas has been studied by Suryan et al (2013). The k-epsilon ($k-\epsilon$) model for turbulence is used in this study (Johansson, 2012). In order to model the air hydrogen combination as an incompressible ideal gas, the gravitational constant was adjusted to 9.8 m/s2. The second-order upwind approach in Fluent was used to discretize the flow and turbulence equations. The species transport with the diffusion energy source was used to represent the diffusion.

Any possible danger areas where, depending on the ventilation circumstances, hydrogen concentrations might above safety limits are to be identified. Information on maximum hydrogen concentrations, the amount of time needed to reach particular concentration levels and velocity profiles with ventilation effects using quantitative data extraction have to be determined. Concentration measurements can be carried out by moving the frame with the sensors to different distances from the point of hydrogen leakage in the simulation.

IV. Results and discussion

The fluctuating levels of hydrogen concentration throughout the semi-enclosed area are visualized through contour plots shedding light on the movement of hydrogen from its origin point and its subsequent dispersion in the surrounding environment. Figure 2 shows the behavior of Hydrogen from leak point throughout the enclosure and variation of mass fraction of H_2 from area of injection to the entire facility.

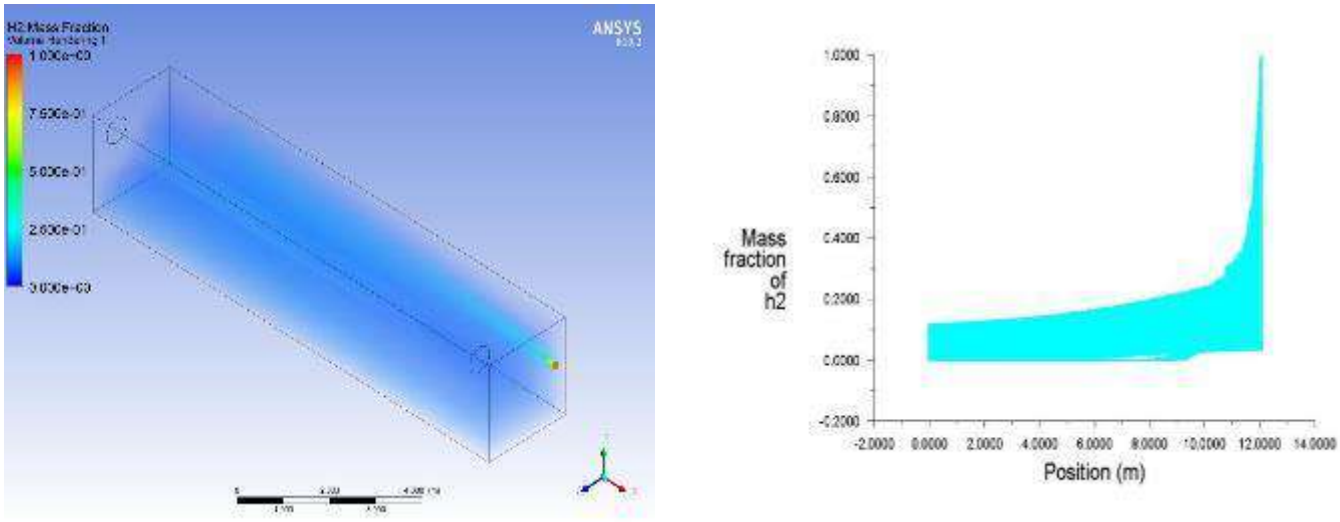

Fig. 2: Distribution of hydrogen at ventilation rate 3 m/s

The movement of hydrogen within the ventilation system, which has a low air velocity, causes it to rise and form layers, resulting in a higher concentration in the area of the leak. However, as the gas travels 6m from the leak, the concentration decreases and becomes more even. This is evident by the lowest measured level of 0.1 mass fraction after 4m, indicating a reduced risk of explosion. It is important to note that the Lower Explosive Limit (LEL) for hydrogen is typically 4% by mass. Therefore, if the hydrogen concentration falls below this level, it is too lean to cause an explosion. Result from computational study clearly shows the efficiency of forced ventilation. Maximum concentration is at leak point

V. Conclusion

The behavior and effects of a hydrogen leak are significantly influenced by the rate of ventilation in a space. The space at which hydrogen diffuses and dilutes in the ambient air impacts safety, the environment, and the likelihood of an ignition. This is determined by the ventilation rate. The concentration of hydrogen leakage is diluted when the ventilation rate is increased because more fresh air is brought into the room. Because of this diluting effect, hydrogen is less likely to accumulate and reach explosive amounts. In the case of a hydrogen leak, adequate ventilation is essential for everyone's safety. A high enough ventilation rate can stop dangerous hydrogen pockets from forming, which could cause an explosion or fire. Maintaining hydrogen concentrations is aided by ventilation. Hydrogen can spread quickly, lowering the possibility of localized environmental harm or problems with air quality brought on by high hydrogen concentrations. The chance of hydrogen ignition is influenced by ventilation rate. The probability of reaching the concentrations at which hydrogen can ignite, known as the lower and higher flammability limits, is decreased by high ventilation rates. This lessens the possibility that unintentional sources of ignition will start flames or explode. The amount of time it takes to find a leak can be affected by how quickly hydrogen evaporates as a result of ventilation. Traditional hydrogen sensors may have a harder time detecting leaks due to faster dissipation because the concentration may drop below detectable levels more quickly. When constructing hydrogen-related systems or facilities, ventilation rate needs to be taken into consideration. To keep things safe, engineers and safety experts need to make sure the ventilation system can efficiently remove hydrogen that has leaked. To minimize safety concerns and control the spread of hydrogen in the case of a leak, emergency reaction methods may include lowering the ventilation rate. It's crucial to remember that the necessary ventilation rate is dependent on a number of variables, such as the space's size, the rate at which hydrogen leaks, the characteristics of hydrogen (such as its temperature and pressure), and safety laws and standards.

References

Hajji, Y., Bouteraa, M., Elcafsi, A., Belghith, A., Bournot, P., Kallel, F., 2015. Natural ventilation of hydrogen during a leak in a residential garage. Renew. Sustain. Energy Rev. 50, 810–818. https://doi.org/10.1016/j.rser.2015.05.060

Hao, D., Wang, X., Zhang, Y., Wang, R., Chen, G., Li, J., 2020. Experimental Study on Hydrogen Leakage and Emission of Fuel Cell Vehicles in Confined Spaces. Automot. Innov. 3, 111–122. https://doi.org/10.1007/s42154-020-00096-z

Jiao, M., Zhu, H., Huang, J., Zhang, X., 2021. Numerical Simulation of Hydrogen Leakage and Diffusion Process of Fuel Cell Vehicle. World Electr. Veh. J. 2021, 12(4), 193; https://doi.org/10.3390/wevj12040193

Johansson, M., 2012. Evaluation of RANS turbulence models for the hydrodynamic analysis of an axisymmetric streamlined body with special consideration of the velocity distribution in the stern region.

Malakhov, A.A., Avdeenkov, A. V., du Toit, M.H., Bessarabov, D.G., 2020. CFD simulation and experimental study of a hydrogen leak in a semi-closed space with the purpose of risk mitigation. Int. J. Hydrogen Energy 45, 9231–9240. https://doi.org/10.1016/j.ijhydene.2020.01.035

Matsuura, K., Nakano, M., Ishimoto, J., 2010. Forced ventilation for sensing-based risk mitigation of leaking hydrogen in a partially open space. Int. J. Hydrogen Energy 35, 4776–4786. https://doi.org/10.1016/j.ijhydene.2010.02.068

Najjar, Y.S.H., 2013. Hydrogen safety: The road toward green technology. Int. J. Hydrogen Energy 38, 10716–10728. https://doi.org/10.1016/j.ijhydene.2013.05.126

Phanichphant, S., 2014. Semiconductor Metal Oxides as Hydrogen Gas Sensors. Procedia Eng. 87, 795–802. https://doi.org/10.1016/j.proeng.2014.11.677

Suryan, A., Kim, H.D., Setoguchi, T., 2012. Three dimensional numerical computations on the fast filling of a hydrogen tank under different conditions, Int. J. Hydrogen Energy 37(9), 7600-7611, https://doi.org/10.1016/j.ijhydene.2012.02.019

Suryan, A., Kim, H.D., Setoguchi, T., 2013. Comparative study of turbulence models performance for refueling of compressed hydrogen tanks, Int. J. Hydrogen Energy 38(22), 9562-9569, https://doi.org/10.1016/j.ijhydene.2012.07.055

IEEES-037

Evaporative Coolıng of Solar Photovoltaıc Panels: A Computatıonal Study

[1, 2]Fathima Ancy M, [1*]Abhilash Suryan, [3]Prasanth P Nair, [4]Sriram Chandran R
[1]Department of Mechanical Engineering, College of Engineering Trivandrum, Kerala, India, 695016
[2]APJ Abdul Kalam Technological University, Kerala, India, 695016
[3]Mechanical Engineering Discipline, IIT Gandhinagar, Gujarat, India, 382355
[4]Indian Institute of Science, Bangalore, India, 560012
*E-mail: suryan@cet.ac.in

Abstract

The demand for energy is ever increasing and dealing with climate change is imperative in the coming years. Hence it is very important to identify sustainable methods of electricity production. Photovoltaic (PV) panels have emerged as a promising solution for converting sunlight into electricity. However, a persistent challenge lies in the adverse effects of excessive heat on these panels, leading to reduced energy output and a shorter operational lifespan. Numerous studies have focused on proposing and evaluating cooling methods to address the challenge and improve the electrical efficiency of photovoltaic panels. The main objective of this study is to develop a method to improve the efficiency of solar panels through evaporative cooling, similar to how human sweat cools the skin on a hot day. This requires creating a computer model to simulate how evaporative cooling affects solar panel performance, helping to understand and optimize the cooling process. Validation of the computer model is done by comparing its predictions with real-life experiments, which ensures the practical applicability of the results. In addition, this research project aims to find out the effect of various factors such as solar panel shape, air flow, temperature, amount of water and humidity on the efficiency of evaporative cooling.

Keywords: Solar Energy, Solar Photovoltaic, PV Panel, Evaporative cooling

I. Introduction

Photovoltaic (PV) panels, often simply called solar panels, are advanced technical devices designed to convert sunlight into electricity. This conversion process takes place in the panels through the interaction of photons of sunlight with semiconductors, creating a flow of electrons and thus an electric current. Solar panels have gained immense importance in the search for sustainable energy solutions due to their ability to produce clean and renewable energy. Maintaining an optimal operating temperature is critical to the efficiency and effectiveness of PV panels. Their efficiency is often reduced due to various factors, such as dust accumulation and heat losses, which cause the surface temperature to rise. This increase in temperature negatively affects the electrical output of the panels and ultimately affects their efficiency (Haidar et al.) [1]. To alleviate these problems, several cooling methods have been investigated in previous studies. One notable approach involves evaporative cooling with water, which has gained attention for its ability to lower PV panel temperatures (Haidar et al.). This technology uses latent heat of evaporation to absorb the heat generated by the solar panels, lowering their temperature. Ghadikol et al. [2] provides a comprehensive overview of cooling methods for solar cells, emphasizing the importance of improving electrical efficiency and extending the life of solar panels. Their analysis emphasizes the importance of previous studies and technical optimization details and provides valuable information for future research. The use of phase change materials (PCM) has proven to be an effective method to maintain the temperature of PV panels in an optimal range, regardless of local temperature variations. PCM-based cooling is particularly useful in both hot and cold environmental conditions, making it a versatile solution (Ghadikol aei et al.). In a practical experimental study, Haidar et al. [3] demonstrated the effectiveness of evaporative cooling of solar panels. In their experimental setup, the back surface of the PV panel was wetted and allowed to interact with the surrounding environment. The results of this study showed a significant decrease in the temperature of the PV panels, more than 20 °C, as a result of which the efficiency of electricity production significantly increased by 14%. Aljubury et al. [4] launched an innovative hybrid PV/EC system designed to generate electricity while cooling the solar panel and providing cooled and humidified air. They investigated two cooling techniques: back-side evaporative cooling and a combination of back-side evaporative cooling with front-side water jet. The study found that both techniques effectively reduced PV panel temperatures, with the latter approach achieving more significant temperature reductions. These cooling methods improved the efficiency and energy production of solar panels. High temperatures can cause a number of negative effects, including a reduction in the conversion efficiency of the panel's semiconductor materials. This reduction in efficiency can reduce electrical output and overall system performance. Thus, the need to regulate and lower the operating temperature of solar panels to maximize their potential and efficiently use solar energy becomes paramount. Computational studies of fuel vapor cooling are motivated by its potential to mitigate the negative effects of elevated temperatures on solar panel performance. Evaporative cooling is a technique that involves the controlled evaporation of a liquid, usually water, to lower the surface temperature. Applying this cooling method to solar panels involves investigating its feasibility and effectiveness in lowering their operating temperature to increase their electrical output. Such research can significantly improve the overall performance of photovoltaic systems and promote their wider adoption as a sustainable energy source.

II. Computational Methodology

In this study, a three-dimensional computational model is developed to simulate the cooling process of a photovoltaic (PV) panel integrated into an inclined duct. The duct has dimensions measuring 3 cm in height, 140 cm in length, and 67 cm in width. The airflow is directed inside the duct in the same direction as the water flow, following a co-current configuration, and is facilitated by a fan. Water is injected into the duct through the inlet.

To simulate this cooling process, a numerical model based on Computational Fluid Dynamics (CFD) is employed. The model focuses on resolving the complex fluid flow and heat transfer interactions within the system. Specifically, the discrete phase model (DPM) is utilized to track the behaviour of water droplets within the airflow.

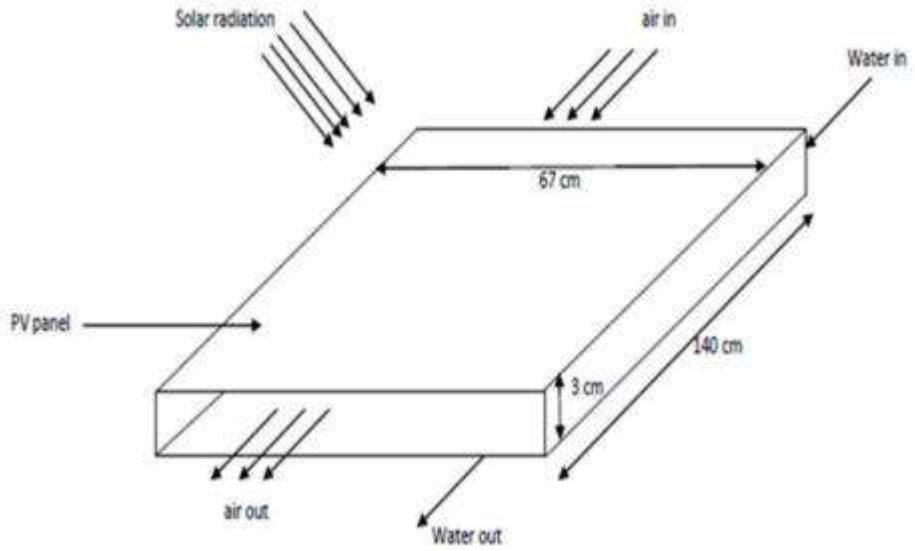

Fig. 1: Schematic model

III. Analysis

The boundary conditions are lower part of the duct is adiabatic therefore no heat exchange with the surroundings. The PV panel is subjected to uniform solar radiation with an intensity of 800 W/m². Water droplets are injected from three locations within the duct. It is assumed that the velocities of both the air and the injected water droplets are equal. The velocity of both air and water droplets entering the duct is set at 3 m/s. The diameter of the injected water droplets is specified as 100 microns. Both air and water vapor are considered ideal gases, and their specific heat capacities are assumed to be independent of temperature. The side walls of the duct are considered adiabatic, implying no heat exchange with the environment. Relative humidity is assumed to vary spatially within the duct and is taken as 60%. The outlet boundary is set as a pressure outlet at atmospheric pressure. The model considers heat exchange between air, water droplets, and the PV panel.

IV. Results and discussion

The simulation results show a significant decrease in the surface temperature of the solar panels when evaporative cooling is used. The cooling effect is stronger during peak hours of sunlight. The rate of heat transfer is analyzed to determine the efficiency of the evaporative cooling process. In addition, the efficiency of the solar panels improved, showing the potential of evaporative cooling to improve the overall efficiency of the system. The drop in surface temperature observed in the simulations indicates that evaporative cooling effectively reduces the thermal stress on the solar panels. Better heat removal helps improve electrical performance and increase power. The study suggests that adding evaporative cooling systems to solar energy systems may be a viable strategy to maximize energy production in regions with high ambient temperatures.

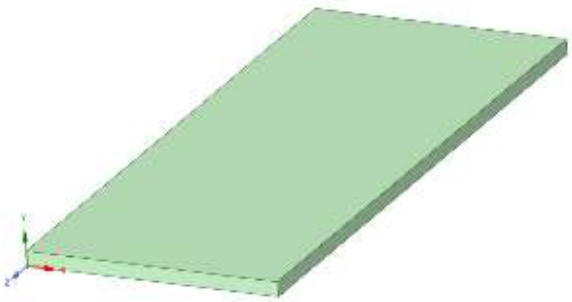

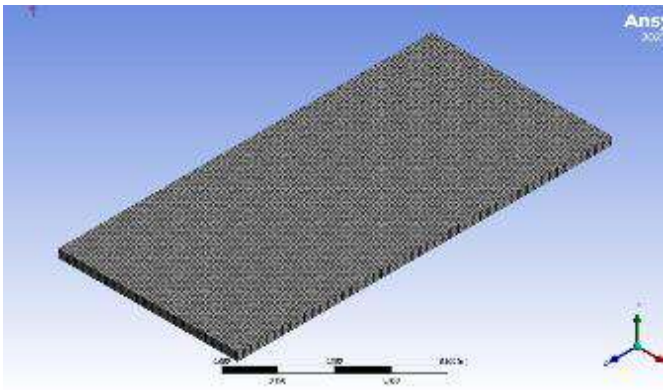

Fig. 2. 3D Geometry developed using ANSYS Fluent

Fig.3. Mesh developed using ANSYS Fluent

The computational approach used in this study allows a detailed analysis of the fluid dynamics and heat transfer processes associated with evaporative cooling. Although the results are promising, further experimental validation is recommended to confirm the results and optimize the design parameters for practical application.

V. Conclusion

In this comprehensive computational study of the application of evaporative cooling to solar panels (PV), we discovered key insights that have profound implications for the field of renewable energy. The research has shown that the use of evaporative cooling strategies leads to significant reductions in the operating temperature of PV panels. This result is an important factor in improving the electrical efficiency of the panels, which is critical to optimize solar energy production. The core of the results points to a paradigm shifts in the field of renewable energy, highlighting the potential of evaporative cooling as a game-changing solution. This technology not only increases short-term energy production, but also promises to significantly extend the lifetime of PV panels, ensuring consistent and reliable performance in the long term. The impact of this research is particularly profound given the ever-increasing need to accelerate the transition to sustainable energy sources and reduce our dependence on non-renewable fossil fuels. However, it is important to acknowledge the limitations inherent in the study. The accuracy and validity of the results depends on the accuracy of the input parameters, such as material properties and weather conditions, as well as the assumptions made in our computer model. Furthermore, although the model provides a solid basis for analysis, it oversimplifies some real-world complexities and may not account for all factors affecting solar panel performance. Therefore, it is necessary to emphasize the need to validate the model through real experiments and the need to consider environmental conditions, water availability and the practical application of evaporative cooling in different contexts. In conclusion, the study not only underlines the enormous potential of evaporative cooling to increase the efficiency of solar panels, but also emphasizes the importance of further investigation, refinement and validation of these findings. Continuing to advance sustainable energy solutions, the research is a critical step in realizing the full potential of solar energy through innovative cooling strategies.

References

Attia, Hussain, Khaled Hossin, and Muataz Al Hazza. "Experimental investigation of photovoltaic systems for performance improvement using water cooling." Clean Energy 7.4 (2023): 721-733.

Cuong, Ngo Xuan, Nguyen Duc Minh, and Y. Do Nhu. "Effect of Control Temperature on The Performance of PV Modules Using Active Water-Spray Cooler." IOP Conference Series: Earth and Environmental Science. Vol. 1111. No. 1. IOP Publishing, 2022.

Dwivedi, P., Sudhakar, K., Soni, A., Solomin, E., & Kirpichnikova, I. (2020). Advanced cooling techniques of P.V. modules: A state of art. Case Studies in Thermal Engineering, 21. https://doi.org/10.1016/j.csite.2020.100674

Elminshawy, Nabil AS, Ahmed Elminshawy, and Amr Osama. "An Innovative Cooling Technique for Floating Photovoltaic module: Adoption of partially submerged angle Fins." Energy Conversion and Management: X (2023): 100408

Gharzi, M., Arabhosseini, A., Gholami, Z., & Rahmati, M. H. (2020). Progressive cooling technologies of photovoltaic and concentrated photovoltaic modules: A review of fundamentals, thermal aspects, nanotechnology utilization and enhancing performance. In Solar Energy (Vol. 211, pp. 117–146). https://doi.org/10.1016/j.solener.2020.09.048

Haidar, Z. A., Orfi, J., & Kaneesamkandi, Z. (2018). Experimental investigation of evaporative cooling for enhancing photovoltaic panels efficiency. Results in Physics, 11, 690–697. https://doi.org/10.1016/j.rinp.2018.10.016

Haidar, Z.A., Orfi, J., Oztop, H.F. and Kaneesamkandi, Z., (2016). Cooling of solar PV panels using evaporative cooling. Journal of Thermal Engineering, 2(5), pp.928-933.

Mahmood, D. M. N., & Aljubury, I. M. A., (2023). Experimental Evaluation of PV Panel Efficiency Using Evaporative Cooling Integrated with Water Spraying. Journal of Engineering, 29(5), 29–48. https://doi.org/10.31026/j.eng.2023.05.03

Raju, M., Sarma, R. N., Suryan, A., Nair, P. P., Nižetić, S., (2022). Investigation of optimal water utilization for water spray cooled photovoltaic panel: A three-dimensional computational study, Sustainable Energy Technologies and Assessments, Volume 51,101975, https://doi.org/10.1016/j.seta.2022.101975.

Sornek, Krzysztof, et al. "Development and tests of the water cooling system dedicated to photovoltaic panels." Energies 15.16 (2022): 5884.

IEEES-038

Analysis of Wind Flow around Major Buildings in the Campus of College of Engineering Trivandrum

[1, 2]Yorken Chrisha C, [1*]Abhilash Suryan, [3]Prasanth P Nair, [1]Suresh Lal S R
[1]Department of Mechanical Engineering, College of Engineering Trivandrum, Kerala, India, 695016
[2]APJ Abdul Kalam Technological University, Kerala, India, 695016
[3]Mechanical Engineering Discipline, IIT Gandhinagar, Gujarat, India, 382355
*E-mail: suryan@cet.ac.in

Abstract

Ever increasing demand for energy has necessitated the search for maximizing the power generation from renewable energy sources in developing nations. Wind energy potential can be significantly augmented with the use of mini and micro wind turbines. This study involves an investigation of wind flow patterns around tall buildings within the campus of an academic institution using numerical simulations. A three dimensional computational model is made and the simulations are performed with the stated inlet velocity set to 6 m/s, which is the average wind velocity for the region. The numerical results obtained are in close agreement with the experimentally measured data for the locations considered. The results are utilized for optimum positioning of mini and micro wind turbines to maximize power generation.

Keywords: Wind Analysis, ANSYS Fluent, CFD Simulation, Tall Building.

I. Introduction

Architecture and engineering have long been fascinated by and concerned with the wind flow patterns surrounding tall buildings. Understanding these complex dynamics is essential for improving energy efficiency, building design, occupant comfort and safety, as well as all other aspects of building construction. Yousef Abu-Zidan et al., investigatd the effect of computational domain size in CFD simulations of wind loading on tall buildings with sensitivity studies examining domain dimensions, blockage ratio, wind speed, and geometric scale.[1] Yu-Hsuan Juan et al., conducted a detailed evaluation of the impacts of the building arrangement and height for a 2 × 2 array with a building height-to-street width ratio of 30 on the mean wind velocity and the wind energy potential along the passages between both upstream and downstream buildings as well as on their roofs.[3] Shu Zheng et al., explored appropriate surrounding building regions that can ensure an accurate prediction of wind flow characteristics around the target building.[4] Nourhan Sayed Fouad et al., research aims to facilitate the necessary wind parameters for the structural design such as pressure distribution, drag coefficient for some building adopting the Computational Fluid Dynamics (CFD) techniques.[5] Bert Blocken et al., conducted a study using code Fluent 6.1.22 was conducted on wind speed in passages between parallel buildings for various widths.[2] K.C.S. Kwok et al., presents a review of current developments of wind energy systems in the built environments, factors affecting urban wind flow and resulting consequences, examples of recent designs of urban/building-based wind energy systems, including building integrated vertical axis wind turbine, power window, wind-induced vibration-based wind energy harvesters, double skin and other innovative building façade systems, and wind source exploration.[6] Jang-Woon Wang et al., studies the method determined the rate of change in wind speed associated with the morphological parameters in the urban or suburban districts by conducting multiple regression analyses.[7] Sumei Liu et al., investigates wind information from a meteorological station to conduct a CFD study of wind distribution in an urban configuration. The resulting mean wind velocity was 5.5% higher than that computed with the use of detailed building structures between the meteorological station and the urban configuration, which is acceptable for most applications. This investigation then explored the influence of surrounding buildings on the wind flow around the target building with different geometrical models.[8] We explore the field of wind flow analysis using ANSYS software in this era of sophisticated computational tools and simulations in an effort to explain an unexpected and fascinating event. Urban settings, which are distinguished by their dense assemblages of tall structures, provide particular difficulties for wind flow dynamics. High-rise building wind behaviour affects a wide range of factors, including architectural beauty, energy use, and tenant well-being. Our research focuses on a particular high-rise building where computer simulations using the potent computational fluid dynamics (CFD) tool ANSYS Fluent reveal an unexpected result that defies expectations. We use a 3D model that carefully takes into account the architectural details of the high-rise structure, the surrounding topography, and the current climatic conditions in order to comprehend wind flow patterns. The chosen input velocity is initially set at the standard 6 meters per second (m/s). An unexpected twist occurs in our ANSYS models, though: the outlet velocity downstream of the building often exceeds the desired inlet velocity. This surprising occurrence not only piques our curiosity but also highlights the crucial role that precise computer modelling plays in foretelling wind dynamics near tall buildings. It provides as evidence of the intricate interaction of elements that affect wind flow in urban environments and serves as a reminder of the possible shocks that lie in store for those who attempt to unlock the mysteries of the wind. We explore the methods, findings, and ramifications of this work in more detail in the sections that follow, providing helpful insights into the intriguing state of wind flow around high-rise structures.

II. Procedure

1. Study Area Selection
2. Data Collection
3. Computational Modeling
4. Data Analysis
5. Interpretation and Visualization

5.1. Study Area Selection:

- Identify Major Buildings: Begin by selecting the major buildings within the College of Engineering Trivandrum campus that will be the focus of the analysis. Consider factors such as building height, architectural significance, and potential impact on wind flow.

5.2. Data Collection:

Architectural Plans:

Acquire architectural plans and drawings for the selected buildings, including dimensions, orientations, and any unique architectural features that may influence wind flow.

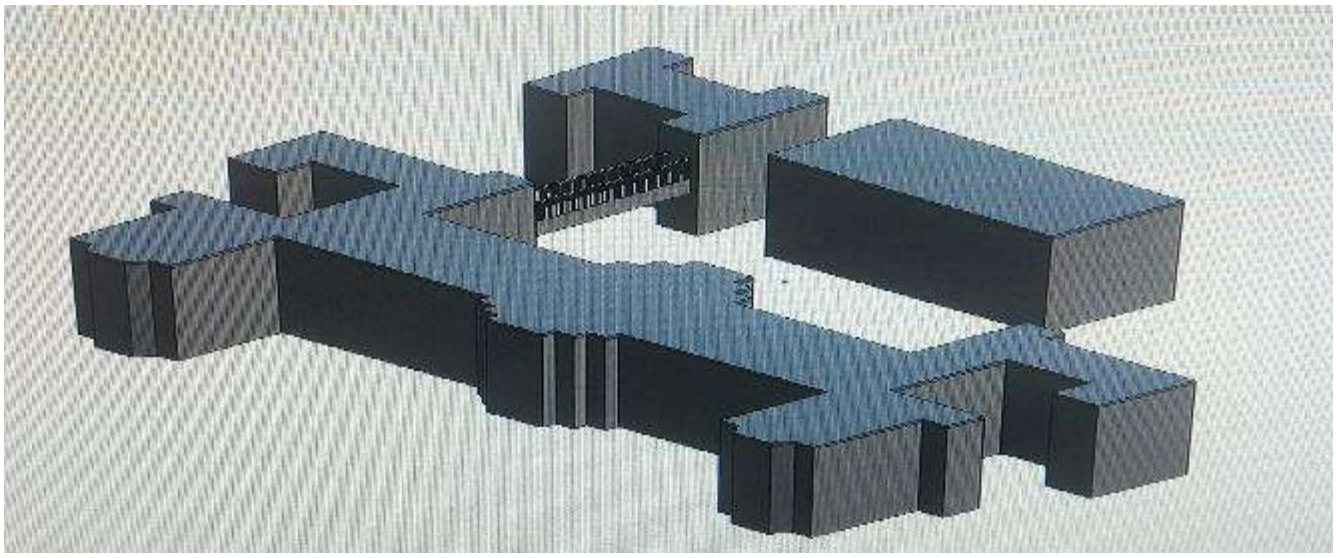

Fig. 1: 3D View of the Buildings

Where A – Main Building
B – Library Building
C- Mechanical Building

Dimensions of the building:-

Main Building - Length = 158.17m and Width = 59.62m and Height = 19m

Library Building - Length = 49.50m and Width = 21.75m and Height =10m

Mechanical Building - Length = 34.75m and Width = 27.23m and Height = 10m

- Maximum length = 158.17m
- Maximum width = 81.87m
- Maximum Height = 19m

For computation,

If max. length is L, then computational domain is taken as 2L.

Likewise, if max. width is B, then computational domain is taken as 2B.

Likewise, if max. height is H, then computational domain is taken as 2H.

Meteorological Data:

Collect historical meteorological data for the region, including wind speed, wind direction, temperature, and atmospheric stability. This data will provide insight into prevailing wind conditions.

- North-west is the direction of the wind.
- The wind speed is assumed as 6 m/s.

5.3. Computational Modeling:

- ANSYS Fluent Setup: Utilize ANSYS Fluent, computational fluid dynamics (CFD) software, to create a 3D numerical model of the study area. Set up the model to incorporate the buildings, terrain, and meteorological conditions.
- Mesh Generation: Generate a high-quality mesh to discretize the computational domain, ensuring accuracy in capturing flow patterns near the buildings and terrain.
- Boundary Conditions: Define boundary conditions, including the inlet velocity, temperature, and turbulence parameters, based on the meteorological data collected.
- Numerical Simulations: Run steady-state or time-dependent CFD simulations to analyze wind flow around the selected buildings. Conduct simulations for various wind directions and speeds to capture different scenarios.

5.4. Data Analysis:

- Velocity and Pressure Fields: Analyze the CFD results to obtain velocity and pressure fields around the buildings. Identify areas of high wind speed, turbulence, and pressure gradients.
- Comparative Analysis: Compare the simulated wind flow patterns with observed wind flow patterns in the campus, if available, to validate the accuracy of the model.
- Identification of Flow Characteristics: Identify key flow characteristics, such as separation zones, vortices, and flow accelerations, that may impact the buildings and their surroundings.

5.5. Interpretation and Visualization:

- Visualization Tools: Use visualization tools to create graphical representations of wind flow patterns, including contour plots, streamline visualizations, and vector plots. These visuals aid in conveying the findings.

III. Analysis

The study focuses on wind flow around major buildings on the College of Engineering Trivandrum campus. It uses theoretical Atmospheric Boundary Layer (ABL) profiles and the RNG k-ϵ turbulence model to analyze the complex interactions between buildings and wind flow. The ABL profiles, specified by Richards and Norris (2011)[9], serve as the foundation for the simulation, ensuring the model reflects realistic atmospheric conditions. The RNG k-ϵ turbulence model, incorporating Renormalization Group (RNG) theory, is used to capture turbulent wind flow behavior around buildings, particularly in complex geometries. The study also incorporates user-defined functions within FLUENT to implement inlet profiles and modified wall functions, ensuring the accuracy and reliability of the simulation results. The modified wall function accurately captures interactions between wind flow and building surfaces, addressing complexities introduced by buildings. The analysis provides a comprehensive understanding of the complex aerodynamic interactions between the built environment and surrounding atmospheric conditions.

IV. Results and discussion

The study focused on evaluating wind flow patterns around significant structures on the College of Engineering Trivandrum campus. The data show a significant difference in wind speeds across the campus. Interestingly, wind speeds were consistently higher near the back side of the main building when compared to other places. This phenomenon indicates the presence of a distinct wind channel or pathway that leads to enhanced wind flow in this area.Several variables contribute to the observed increase in wind speed along the back side of the main building. The arrangement of the campus, with its many buildings and structures, can have a considerable impact on wind patterns. Tall buildings serve as wind barriers, forcing wind to accelerate as it is channeled into narrower areas between structures.

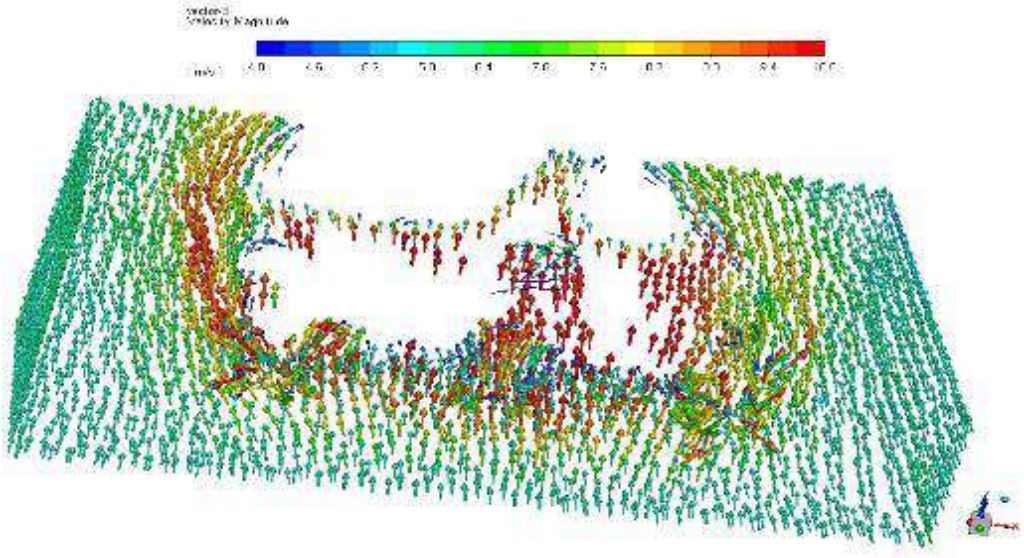

Fig. 2 – Vector image of Velocity Magnitude

Wind speeds at the back of the main building at the College of Engineering Trivandrum have increased due to a variety of variables. The campus layout, which includes a variety of buildings and structures, has a considerable impact on wind patterns. Tall buildings operate as wind barriers, increasing wind speeds as they funnel through the tighter spaces between these structures. This phenomenon can result in concentrated areas of high wind speeds, such as the back side of the main building. Topographical considerations, such as the College's location atop a tiny hill, can also influence wind flow patterns. Wind flow dynamics in this area are improved by the relationship between the construction plan and the natural landscape. Understanding these issues is critical for making educated campus decisions.

V. Conclusion

Finally, the study of the wind flow patterns surrounding the larger buildings on the College of Engineering Trivandrum campus has provided important new understandings of the intricate dynamics of wind behavior in urban environments. The findings highlight the crucial role that precise computer modeling plays in forecasting wind dynamics, particularly when it comes to the thoughtful installation of mini and micro wind turbines atop tall buildings. The results of this study lay the groundwork for choosing turbine locations that would optimize power output, which is a key step toward capturing wind energy inside the urban environment. Further research must be done in order to optimize the turbine placement options, taking into consideration the complex interactions between structures and wind flow. These initiatives have the potential to make a substantial impact on the development of environmentally friendly building techniques both on the campus and off it.

References

Yousef Abu-Zidan, Priyan Mendis, Tharaka Gunawardena, (2021) “Optimising the computational domain size in CFD simulations

of tall buildings", Heliyon, Volume. 9 Issue. 7, https://doi.org/10.1016/j.heliyon.2021.e06723.

Bert. B et al., (2007) "CFD evaluation of wind speed conditions in passages between parallel buildings—effect of wall-function roughness modifications for the atmospheric boundary layer flow", Journal of Wind Engineering and Industrial Aerodynamics, pg. 941-972, doi:10.1016/j.jweia.2007.01.013.

Yu-Hsuan Juan (2022) "CFD assessment of wind energy potential for generic high-rise buildings in close proximity: Impact of building arrangement and height", Applied Energy, https://doi.org/10.1016/j.apenergy.2022.119328.

Shu Zheng (2021) "Characteristics of wind flow around a target building with different surrounding building layers predicted by CFD simulation", Building and Environment, https://doi.org/10.1016/j.buildenv.2021.107962.

Nourhan Sayed Fouad (2018) "Comparative study of international codes wind loads and CFD results for low rise buildings", Alexandria Engineering Journal, Volume 57, Issue 4, Pages 3623-3639, https://doi.org/10.1016/j.aej.2017.11.023

Kwok, K. C. S., & Hu, G. (2023). Wind energy system for buildings in an urban environment. Journal of Wind Engineering and Industrial Aerodynamics, 234, 105349.

Rakesh Narayana Sarma, Vineeth Kumar, Suresh Lal S R, Minu Reghunath, Arya Jayan & Abhilash Suryan (2022) Wind power resource assessment and wind-hydrogen generation potential: a case study, Energy Sources, Part A: Recovery, Utilization, and Environmental Effects, DOI: 10.1080/15567036.2022.2026537

Wang, J. W., Yang, H. J., & Kim, J. J. (2020). Wind speed estimation in urban areas based on the relationships between background wind speeds and morphological parameters. Journal of Wind Engineering and Industrial Aerodynamics, 205, 104324.

Liu, S., Pan, W., Zhao, X., Zhang, H., Cheng, X., Long, Z., & Chen, Q. (2018). Influence of surrounding buildings on wind flow around a building predicted by CFD simulations. Building and Environment, 140, 1-10.

Richards, P., & Norris, S. (2011, April 1). Appropriate boundary conditions for computational wind engineering models revisited. Journal of Wind Engineering and Industrial Aerodynamics; Elsevier BV. https://doi.org/10.1016/j.jweia.2010.12.008

IEEES-039

Investigation on combustion, performance and emission characteristics of Waste Cooking oil – diesel blends with hydrogen in CI engine – A dual fuel approach

[1]Kiran Suresh [2]Leenus Jesu Martin and [3]Edwin Geo Varuvel*
[1,2] Green Vehicle Technology Research Centre, Department of Automobile Engineering,
Faculty of Engineering and Technology, SRM Institute of Science and Technology,
Kattankulathur, Tamil Nadu, 603203, India
[3] Department of Mechanical Engineering, Faculty of Engineering and Natural Sciences,
Istinye University, Istanbul, Turkey

Email: vedwingeo@gmail.com

Abstract

The primary objective of this paper is to study the influence of hydrogen induction on combustion, performance and exhaust emissions of a compression ignition engine fueled with waste cooking oil biodiesel. Waste cooking oil biodiesel was produced by trans-esterification process and mixed with diesel fuel by a volume fraction of 80% (WCO B80). In addition to this 99.9% pure hydrogen was inducted into the intake manifold along with air at the volume flow rate of 3, 6, 9 and 12 lpm. The test was conducted in a single cylinder DI diesel engine at various load conditions. At first, test results were compared with neat diesel fuel and WCO B80 fuel at all loads. WCO B80 fuel indicates an insignificant reduction in BTE when compared to neat diesel fuel. Emission study revealed that WCO B80 usage depreciates CO, HC and smoke opacity and slightly increases NO_x emission. However, hydrogen enrichment significantly decreased exhaust emissions such as smoke opacity, HC and CO except for NO_x emission and improves BTE. Among various liquid fuels tested, WCO B80 + 12 LPM H_2 resulted in improvement in BTE with the increasing volume flow rate of 12 lpm hydrogen in the intake manifold. At maximum power output in cylinder pressure and heat release rate were found to be higher for WCO B80 + 12 lpm H_2 blend which concludes it as a suitable fuel for diesel engine compared to other test fuels without any major engine modifications.

Keywords: Waste cooking oil, Hydrogen fuel, Biodiesel, Dual fuel engine, Exhaust Emissions.

I Introduction:

In the current scenario, managing emissions from petroleum-based engines poses a significant challenge for the automotive industry. Internal combustion engines generate major pollutants including carbon monoxide, nitric oxide, hydrocarbons, and smoke emissions (Jamrozik, Arkadiusz, 2019). To mitigate these pollutants, researchers have employed various methodologies over the past decades. Waste cooking oil (WCO) derived from used palm oil or sunflower oil can be employed as an alternative fuel for diesel engines, offering reductions in fossil fuel consumption, cost, and global energy demand (Karthic. S, 2019). However, using pure waste oil directly in an internal combustion engine, without modification, results in subpar performance due to its significantly higher viscosity compared to petroleum fuels (Rekhate, 2019). To overcome this limitation, a transesterification process is undertaken to reduce the viscosity of the vegetable oil, transforming it into biodiesel for use in the engine.

II Materials and methods:

Initially around five litres of WCO were collected from nearby restaurants in and around our university. Consequently, in this study, transesterification was selected as the preferred technique for biodiesel production. This method entails a chemical reaction between the triglycerides in waste cooking oil (WCO) and alcohol. This study employed the widely utilized catalyst, potassium hydroxide (KOH), owing to its accessibility and affordability. Finally, the prepared WCO methyl ester was blended with ND fuel over volume fraction of 80%. The selective properties of prepared blend were estimated using appropriate measuring instruments using ASTM standards.

III Experimental Setup:

This configuration primarily consists of a four-stroke single-cylinder, direct-injection, constant-speed, water-cooled diesel engine equipped with an eddy current dynamometer. The mass flow rate of air was determined using a U-Tube manometer and an orifice flow meter. An EGT measurement was obtained using a k-type thermocouple positioned on the exhaust manifold. The exhaust emission parameters such as NOx, HC and CO were measured using AVL 444 Di-gas analyzer. The smoke intensity from the exhaust was measured in opacity using AVL 437C smoke meter. The flow of hydrogen gas from the cylinder to the engine intake was measured and regulated using a hydrogen flow meter equipped with a control valve.

IV Results and Discussion:

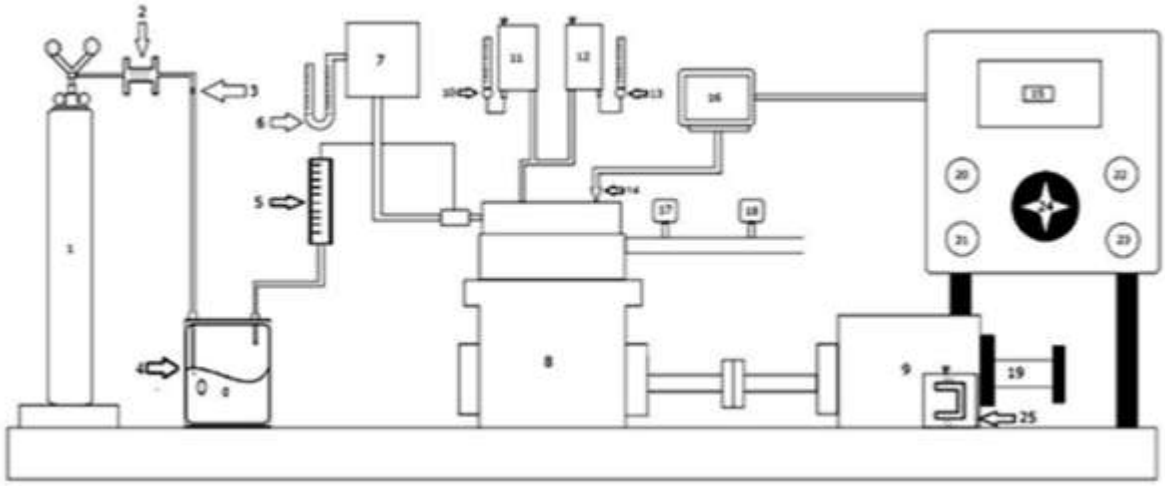

1.Hydrogen cylinder 2. Dry flame arrester 3. Safety valve 4. Wet flame arrester 5. Volume flow meter 6. U-tube manometer 7. Air tank 8. Diesel engine 9. Eddy current dynamometer 10. Burette 11. Waste oil tank 12. Diesel tank 13. Burette 14. Pressure sensor 15. Data logger 16. Computer 17. Di gas analyser 18. Smoke meter 19. Crank angle encoder 20. RPM indicator 21. Exhaust temperature indicator 22. Coolant temperature indicator 23. Load indicator 24. Load control 25. Load cell

Performance characteristics:

Brake Thermal Efficiency:

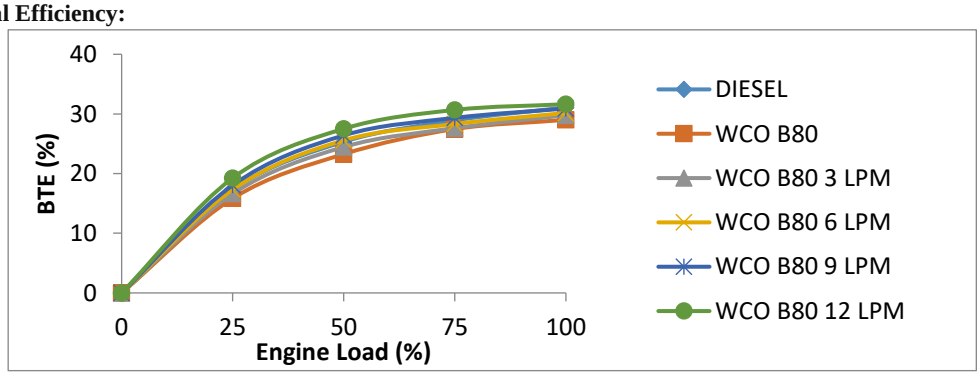

Fig. 1. Brake thermal Efficiency Vs Engine load

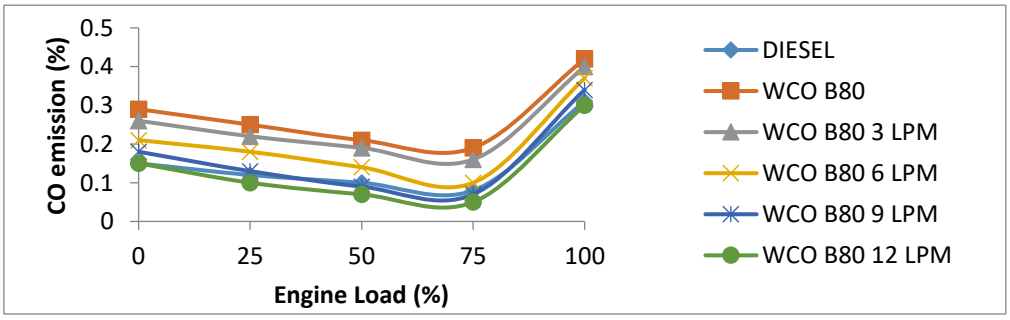

Fig. 2. CO emission Vs Engine load

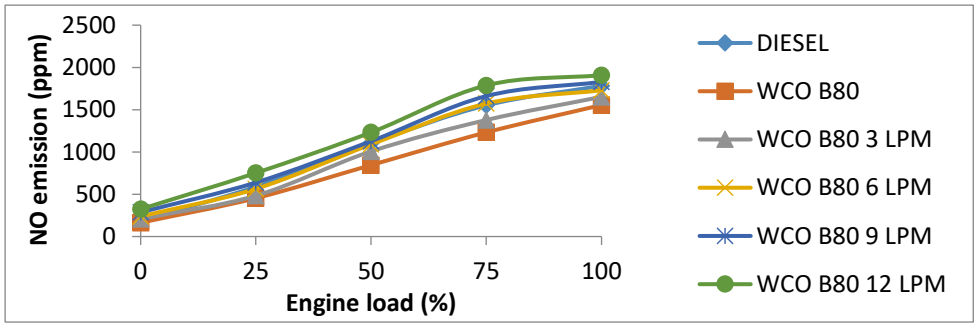

Fig. 3. NO emission Vs Engine load

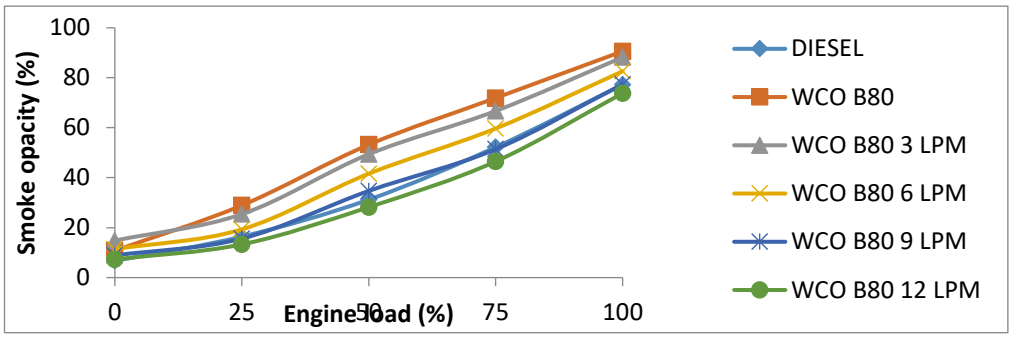

Fig. 4. Smoke emission Vs Engine load

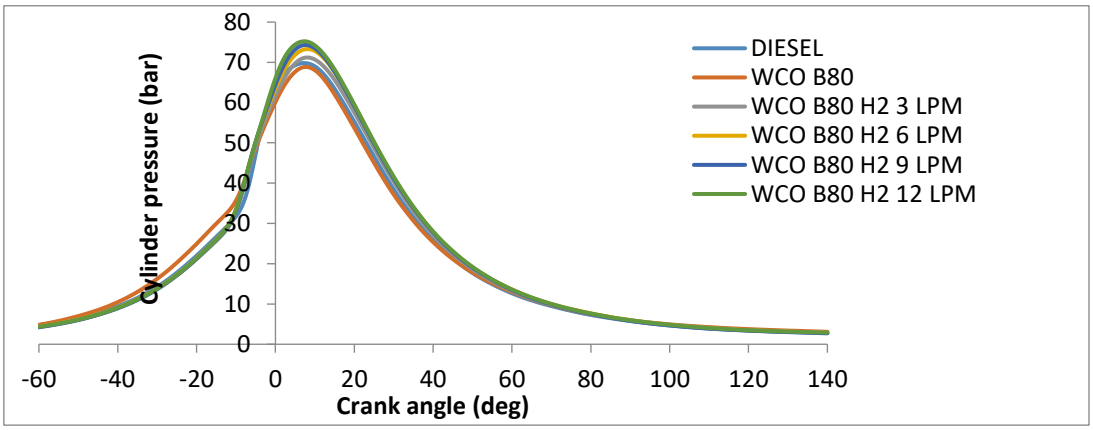

Fig. 5. Cylinder pressure Vs Crank angle

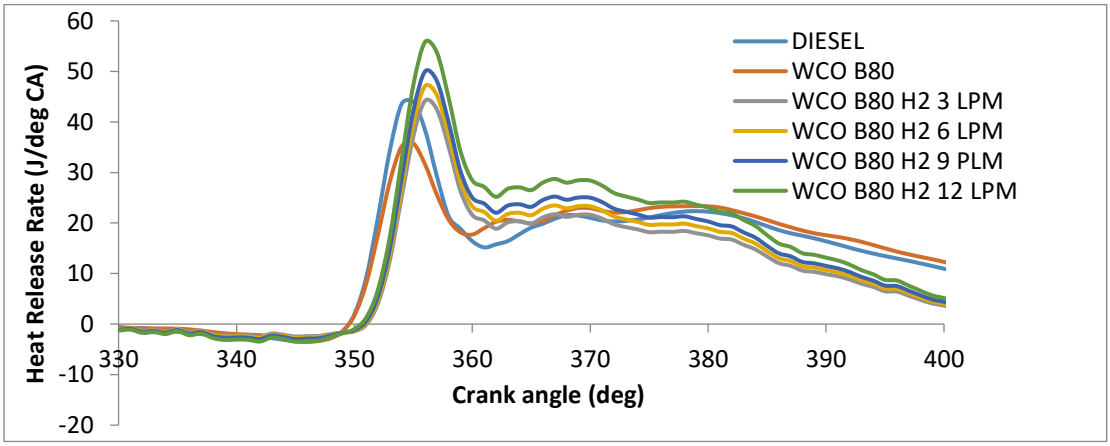

Fig. 6. Heat release rate Vs Crank angle

V. Conclusion:

1. The dual fuel mode of operation significantly enhances both the performance and emission characteristics of the test engine.
2. At all load conditions, WCO B80 fuel exhibited a decrease in BTE compared to diesel fuel.
3. Hydrogen enrichment improved the BTE of the engine when operated with WCO B80 fuel, while ND fuel demonstrated the highest BTE at peak power output.
4. With WCO B80 fuel, there was a slight reduction in exhaust emissions such as smoke opacity, HC, and CO, but NOx emissions increased across all load conditions.
5. The addition of hydrogen resulted in a substantial reduction in HC, CO, and smoke opacity. However, there was a significant increase in NOx emissions with higher hydrogen fuel levels in conjunction with intake air.
6. The cylinder pressure and HRR were found to be increased with increase in hydrogen flow rates.

Finally, it is concluded that WCO B80 with 12 lpm hydrogen induction gives better results in terms of engine performance, combustion and emission parameters compared to ND without much engine modification.

References:

Jamrozik, Arkadiusz, Wojciech Tutak, and Karol Grab-Rogaliński (2019) "An Experimental Study on the Performance and Emission of the diesel/CNG Dual-Fuel Combustion Mode in a Stationary CI Engine.", Energies, 12(20), 3857; https://doi.org/10.3390/en12203857.

Karthic. S. V, Senthil Kumar.M, Nataraj.G & Pradeep.P. (2019) “Experimental investigations on the influence of hydrogen and LPG mixtures on performance behavior of a mahua bio oil-powered dual fuel engine”, International Journal of Green Energy, 16:12, 878- 889, DOI: 10.1080/15435075.2019.1641713.

Rekhate, Chhaya, and Abhinesh Kumar Prajapati (2019) "Production, engine performance, combustion, emission characteristics and economic feasibility of biodiesel from waste cooking oil: A review." Environmental Quality Management. https://doi.org/10.1002/tqem.21645.

Yesilyurt, Murat Kadir (2019). "The effects of the fuel injection pressure on the performance and emission characteristics of a diesel engine fuelled with waste cooking oil biodiesel-diesel blends." Renewable energy 132 (2019): 649-666. https://doi.org/10.1016/j.renene.2018.08.024.

Patel, Chetankumar, Joonsik Hwang, Krishn Chandra, Rashmi A. Agarwal, Choongsik Bae, Tarun Gupta, and Avinash Kumar Agarwal (2019). "In-Cylinder Spray and Combustion Investigations in a Heavy- Duty Optical Engine Fueled With Waste Cooking Oil, Jatropha, and Karanja Biodiesels." Journal of Energy Resources Technology 141, no. 1 : 012201. https://doi.org/10.1115/1.4040579.

IEEES-040

Thermodynamic Analysis of Desalination System on Combined Cycle Power Plants Through Throttling Process Method by Using a Vapor Compressor

[1*]Ahmad Zikri, [2]Muhsin Kilic, [3]Fatih Ozcan
[1,2]Bursa Uludag University, Faculty of Engineering, Department of Mechanical Engineering, Gorukle Campus, Bursa, 16059, Turkiye
[3] Bursa Uludağ University, Orhangazi Yeniköy Asil Çelik Vocational School, Mechanical and Metal Technologies Department, Orhangazi/BURSA, 16810, Türkiye
*E-mails: 512110013@ogr.uludag.edu.tr, mkilic@uludag.edu.tr, fatihozcan@uludag.edu.tr

Abstract

Innovative strategies are being developed to concurrently address the urgent needs for freshwater resources and power due to the ever-increasing worldwide demand for both resources. One method offers a sustainable response to the rising demand for clean water and electricity by integrating desalination systems with combined cycle power plants (CCPP). As a result, this study aims to provide the thermodynamic analysis of desalination systems in CCPP, emphasizing the throttling process method in conjunction with a vapor compressor. The entire understanding of the energy interactions and efficiency gains possible in these interconnected systems is provided by this novel technique. Desalination integrated with CCPP presents a promising synergy in which waste heat from power generation is used to fuel the desalination process, resulting in higher overall system efficiency. When combined with a vapor compressor, the throttling process approach improves desalination efficiency and assures optimal utilization of available energy resources. Briefly, the method employed in this research is a thermodynamic simulation that uses the throttle valve temperature and the percentage of water discharged into the sea to determine the amount of aquadest generation and the Specific Energy Consumption (SEC) in this combined system. In this study, lowering the condenser pressure from 10.89 to 8.43 kPa increases the power of the steam turbine to 2.18%, allowing the temperature of water discharged to seawater to drop to 32.5°C eco-friendly with a Pinch Point Temperature Difference (PPTD) of 10. It generated vapor that could be condensed into aquadest with an SEC (Specific Energy Consumption) of -1423.36 kJ/kg of distilled water at best conditions, a mass flow rate of 3.63 kg/s at a pressure on the throttle valve of 2.65 kPa, and a mass of water discharged to the sea of 99.5%.

Keywords: Combined Cycle Power Plants, Desalination System, Energy Consumption, Freshwater, Waste Heat.

I. Introduction

The ever-increasing worldwide demand for freshwater resources and power has driven novel techniques to meet both essential demands simultaneously (Di Martino et al. 2021; Zikri et al. 2020; Zikri et al. 2021). One option combines desalination systems with combined cycle power plants (CCPP), providing a long-term solution to freshwater scarcity and energy efficiency concerns. In this context, thermodynamic analysis is critical in optimizing the performance of such integrated desalination systems inside CCPP, particularly in applying the throttling process approach in conjunction with a vapor compressor. This novel technique thoroughly explains the energy interactions and efficiency gains possible in these integrated systems (Shokri and Fard 2022).

Desalination removes salts and other contaminants from seawater or brackish water to generate freshwater suitable for drinking, agriculture, and industrial uses (Kosasih et al. 2021; Zikri et al. 2020; Dzaky et al. 2020). Desalination operations have traditionally been energy-intensive, relying on multi-effect distillation (Farsi and Rosen 2022; Liponi, Wieland, and Baccioli 2020) & reverse osmosis technologies (Di Martino et al. 2021). However, these systems frequently require large amounts of electricity, resulting in significant running costs and carbon emissions.

Several other studies on the thermodynamic analysis of desalination systems have been conducted, including Dzaky et al.'s research, which resulted in distilled water production with a mass flow rate of 0.996 kg/s and SEC (Specific Energy Consumption) of -1194.02 kJ/kg when using heat from a steam power plant's condenser (Dzaky, Kosasih, and Zikri 2022). Another study examined how cyclone separation pressure and the amount of water extracted affected energy use. The lower the temperature in the cyclone separator, the greater the aquadest output. Conversely, the bigger the volume of water dumped into the sea; the less SEC will receive. The mass flow rate achieved for producing 0.86 kg/s distilled water with SEC at the same water discharged at 99% is -1137.62 kJ/kg (Dzaky, Kosasih, and Zikri 2020).

Integrating desalination systems with CCPP provides a one-of-a-kind chance to address the main dual concerns of water scarcity and power-generating efficiency. In addition, this study also emphasizes the environmental and economic benefits of combining desalination with CCPP. These integrated systems can minimize greenhouse gas emissions and operational costs by efficiently utilizing waste heat and decreasing energy losses. The CCPP are very efficient and use waste heat from the power generation process to improve total energy efficiency, often via a steam cycle. When combined with a vapor compressor, the throttling process method improves the efficiency of the desalination process and ensures the optimal utilization of available energy resources.

II. Methodology

This study explores the thermodynamic analysis of a desalination system integrated into CCPP through the throttling method with a vapor compressor, as shown in Figure 1 below. In a CCPP, power generation typically involves both gas and steam cycles. The gas turbine cycle operates at a higher temperature, generating electricity by expanding high-pressure gas, as shown in process lines D and E in Figure 1. The exhaust heat from the gas turbine to HRSG 1 and 2 is then used to produce steam, which drives a steam turbine for additional power generation in process lines C combined with a desalination system on process lines A and B. This combination enhances the overall efficiency of power production.

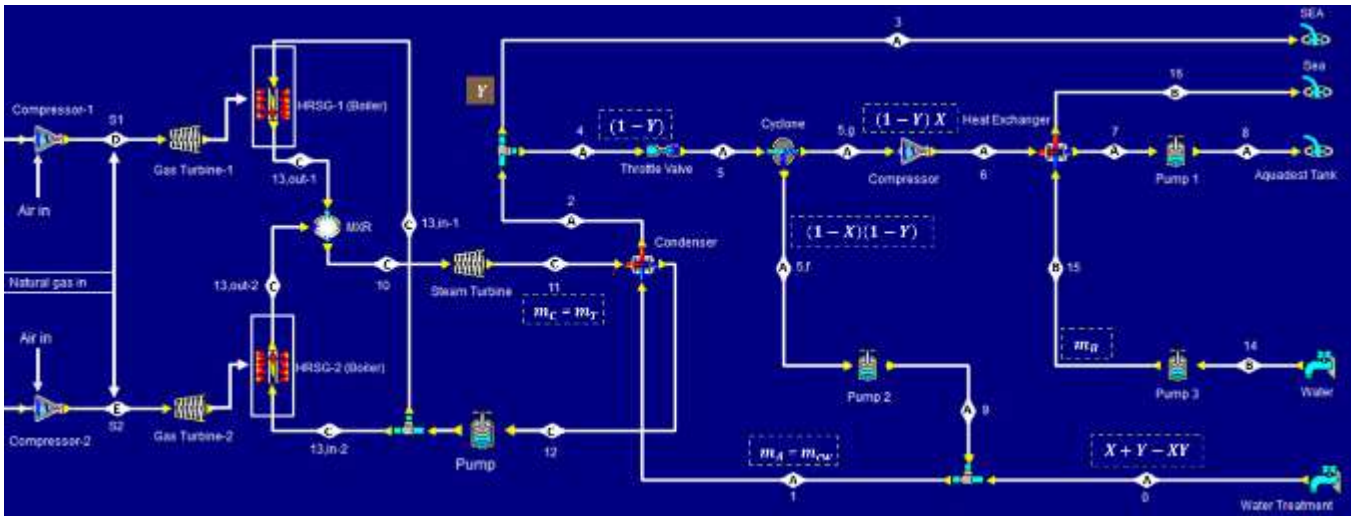

Fig. 1. Schematic diagram of a combined desalination system with a CCPP

Integrating the thermodynamic simulation method, which relies on theoretical calculations, into a power plant, specifically the CCPP in Bursa City, Turkiye (Unver and Kilic 2007). This study consistently applies the analysis parameters outlined in Table 1 below.

Table 1. Constant parameters used during integration of the thermodynamic simulation

	Parameter	Value		Parameter	Value
Power Plant Side	**Gas Power Plant capacity**	*239 MW*	**Desalination Side**	$\boldsymbol{T_0 = T_{14}}$	*30 ℃*
	Steam Power Plant capacity	*237,5 MW*		$\boldsymbol{p_0 = p_{atm}}$	*101.325 kPa*
	$\boldsymbol{T_{10}}$	*535 ℃*		$\Delta\mathbf{T}_{\boldsymbol{condenser}}$	*10 ℃*
	$\boldsymbol{p_{10}}$	*11960 kPa*		$\boldsymbol{T_7}$	*44 ℃*
	$\boldsymbol{\eta_{i,Turbine}}$	*0.85*		$\boldsymbol{\eta_{i,\mathrm{Pump}}}$	*0.85*
	$\boldsymbol{\dot{m}_T}$	*1*		$\boldsymbol{T_5}$	*2-22 ℃*
	$\boldsymbol{T_{11,\mathrm{old}}}$	*47.5 ℃*		$\boldsymbol{Y}$	*90-99.5%*
	$\boldsymbol{T_{11,\mathrm{new}}}$	*42.5 ℃*		$\boldsymbol{p_{14} = p_{atm}}$	*101.325 kPa*

III. Analysis

In this exploration, we delve into the principles of thermodynamics, analyzing how energy is transferred and transformed within the integrated system. We investigate the fundamental components, such as the vapor compressor, heat exchangers, and turbines, that facilitate the conversion of thermal energy into both electricity and fresh water. To calculate energy consumption in systems integrating desalination systems with CCPP, we must calculate the increase in turbine power. The increase in steam turbine power is the effect of decreasing the temperature in the condenser in a steam power plant, which can be calculated using the following formulation.

$$\Delta W_T = \left(h_{10} - h_{11,new}\right)\dot{} - \left(h_{10} - h_{11,old}\right) \quad (1)$$

where ΔW_T is the increasing of turbine power, h is the specific enthalpy (kJ/kg) for the given state point.

Then, the power of pump 1 ($W_{P,1}$), pump 2 ($W_{P,2}$), pump 3 ($W_{P,3}$), and the vapor compressor (W_C) can be calculated by the equation below.

$$W_{P,1} = \dot{m}_{Aq}\, v_f (p_{atm} - p_7) \quad (2)$$
$$W_{P,2} = \dot{m}_{cw}\,(1-X)(1-Y)(h_9 - h_{5,f}) \quad (3)$$
$$W_{P,3} = \dot{m}_B\, v_f (p_{atm} - p_{15}) \quad (4)$$

where $\dot{m}_{Aq}$ is the mass flow rate (kg/s) of aquadest production, $\dot{m}_{cw}$ is the mass flow rate (kg/s) of cooling water, $\dot{m}_B$ is the mass flow rate (kg/s) of cooling water to the pump 3. Before calculating each pump power, we should calculate the heat capacity on the heat exchanger ($Q_{HE,Aq}$) using the equation below.

$$Q_{HE,Aq} = \dot{m}_{Aq}\, c_p\, \Delta T \quad (5)$$

where c_p is the specific heat (kJ/kgK), and ΔT is the different temperature (°C) in the heat exchanger. Furthermore, the vapor compressor power (W_C) can be calculated by the equation below.

$$W_C = X(1-Y)\dot{m}_{cw}\left(h_6 - h_{5,g}\right) \quad (6)$$

where X is the essential vapor fraction, and Y is the mass discharged to the sea.

On the other hand, water that enters the condenser absorbs latent heat from the fluid that works in the CCPP. The following equation, the heat capacity on the condenser (Q_c) can express this heat release from a CCPP can be calculated by the equation below.

$$Q_c = \dot{m}_{cw}\,(h_2 - h_1) \quad (7)$$

$$Q_c = \dot{m}_T\,(h_{11} - h_{12}) \quad (8)$$

where $\dot{m}_T$ is the turbine mass flow which is assumed of 1 kg/s. By substituting method, we can obtain the mass flow of cooling water ($\dot{m}_{cw}$). Then it can calculate the water mass ($\dot{m}_{Aq}$) using the equation below.

$$\dot{m}_{Aq} = \dot{m}_{cw}\,[X(1-Y)] \quad (9)$$

Thus, we can obtain energy consumption which is all of the power requirements used in integrating desalination systems with CCPP. Besides that, the SEC can be determined by the following equation below.

$$EC = W_{P,1} + W_{P,2} + W_{P,3} + W_c \quad (10)$$

$$SEC = \frac{EC - \Delta W_T}{\dot{m}_{Aq}} \quad (11)$$

where EC is energy consumption (kW), and SEC is specific energy consumption (kW/kg).

IV. Results and discussion

The thermodynamic analysis of a desalination system integrated into CCPP through the throttling method with a vapor compressor, which in this research has looked at the impact of aquadest production on water discharged and throttle valve temperature, as well as analyzing how much energy is transferred and transformed (in this case SEC) on the desalination system integrated into CCPP.

Based on Figure 2.a, increasing the percentage of water discharged and throttle valve temperature impacts decreasing aquadest production. Suppose the rate of water discharged is 90%, and the throttle valve temperature is 2°C. In that case, the aquadest production is 101.71 kg/s, while the same percentage of water discharged and the throttle valve temperature is enlarged to 11 times, the aquadest production becomes 9.97 kg/s. This case is because the ratio of water discharged is constant, but the temperature at the throttle valve is increased; this causes $h_{5,g}$ (in saturated vapor) to decrease while h_5 remains constant because it uses the throttle valve principle. Therefore, the greater the temperature of the throttle valve with a consistent percentage of water discharged, the smaller the aquadest produced.

On the other hand, if we look at the relationship between SEC with the percentage of water discharged and throttle valve temperature, we can see Figure 2.b below. The ratio increased of water discharged at a constant throttle valve temperature result in lower SEC and aquadest production. This case is because less water flows into the cyclone separator. Similarly, the temperature of the throttle valve increases at a constant percentage of water discharged. If the ratio of water discharged is 99.5% and the throttle valve temperature is 22°C then the SEC is -1423.36 kJ/kg, while the same rate of water discharged at the throttle valve temperature is reduced to 11 times, then the SEC becomes 125.05 kJ/kg.

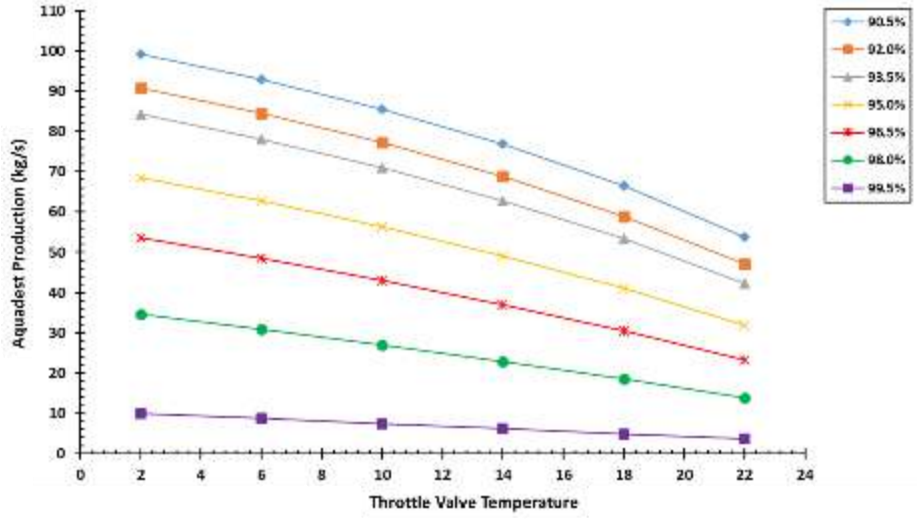

(a)

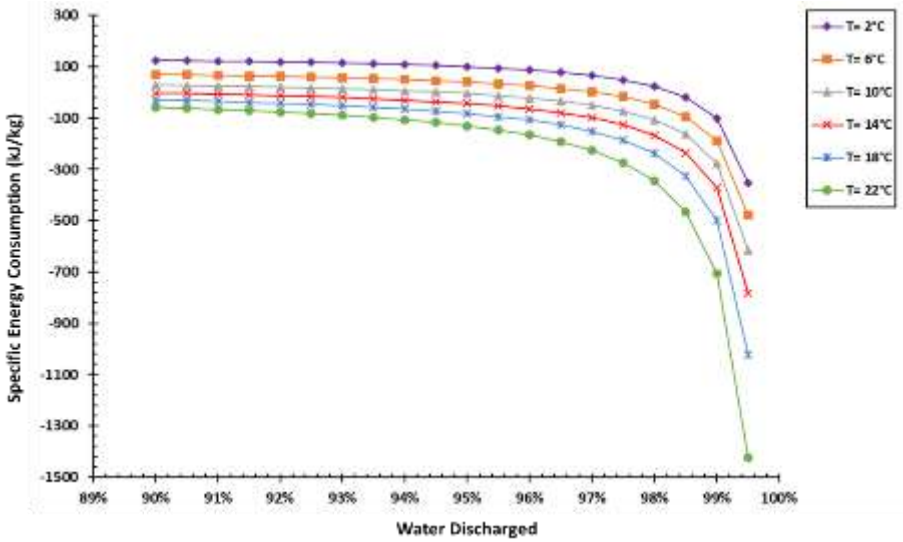

(b)

Fig. 2. Water discharged and throttle valve temperature versus (a) aquadest production and (b) SEC

This case is because SEC is inversely proportional to the mass flow rate of aquadest. In addition, lowering the condenser pressure from 10.89 to 8.43 kPa increases the power of the steam turbine to 2.18%, allowing the temperature of water discharged to seawater to drop to 32.5°C eco-friendly with a PPTD of 10°C.

V. Conclusion

Based on the results of the thermodynamic simulation of the integration of the desalination system with CCPP, it can be concluded that the effect of reducing condenser pressure will increase the steam turbine power by approximately 2.18% and cause the temperature of the water discharged into the sea to be eco-friendly, namely 32.5°C. In addition, decreasing the percentage of water discharged and throttle valve temperature impacts increasing aquadest production. On the other hand, the relationship between SEC with the rate of water discharged and throttle valve temperature, in which the ratio increased of water discharged at a constant throttle valve temperature, results in lower SEC and aquadest production. Therefore, it can provide a more energy-efficient (ensuring optimal utilization of available energy resources) and cost-effective approach to desalination within CCPP.

Acknowledgements

We gratefully acknowledge the support of Türkiye Scholarships, administered by the Presidency for Turks Abroad and Related Communities (YTB), which contributed to the completion of this scientific publication.

References

Di Martino, Marcello, Styliani Avraamidou, Julie Cook, and Efstratios N Pistikopoulos. 2021. "An optimization framework for the design of reverse osmosis desalination plants under food-energy-water nexus considerations." *Desalination* 503: 114937.

Dzaky, Muhammad Irfan, Engkos Achmad Kosasih, and Ahmad Zikri. 2020. "Aquadest Production with Compression System: Influence Cyclone Separator Pressure and Percentage of Water Discharged on Specific Energy Consumption." *Journal of Advanced Research in Fluid Mechanics and Thermal Sciences* 75 (2): 79-93.

Dzaky, Muhammad Irfan, Engkos Achmad Kosasih, and Ahmad Zikri. 2022. "Thermodynamic Simulation in Eco-Friendly Aquadest Production Through Compression System Method Combined with Steam Power Plant as Heat Source." *Journal of Advanced Research in Fluid Mechanics and Thermal Sciences* 100 (1): 63-76.

Dzaky, Muhammad Irfan, Engkos Achmad Kosasih, Ahmad Zikri, Salsabil Dwikusuma Prasetyo, Muhammad Badra Shidqi, and Fakhri Rabbani Putranto. 2020. "The effect of water mass flow rate and pressure on specific energy consumption and aquades production using throttling process method." AIP Conference Proceedings.

Farsi, Aida, and Marc A Rosen. 2022. "Assessment of a geothermal combined system with an organic Rankine cycle and multi-effect distillation desalination." *Earth Systems and Environment* 6 (1): 15-27.

Kosasih, Engkos Achmad, Muhammad Irfan Dzaky, Ahmad Zikri, and Ahmad Fadhil Nugraha. 2021. "Simulation Influence of Compressor 3 Pressure and Cyclone Pressure on Specific Energy Consumption And Cooling Heat In Renewable Desalination." *Journal of Advanced Research in Fluid Mechanics and Thermal Sciences* 81 (2): 59-66.

Liponi, Angelica, Christoph Wieland, and Andrea Baccioli. 2020. "Multi-effect distillation plants for small-scale seawater desalination: thermodynamic and economic improvement." *Energy conversion and management* 205: 112337.

Shokri, Aref, and Mahdi Sanavi Fard. 2022. "Techno-economic assessment of water desalination: Future outlooks and challenges." *Process Safety and Environmental Protection*.

Unver, Umit, and Muhsin Kilic. 2007. "Second law based thermoeconomic analysis of combined cycle power plants considering the effects of environmental temperature and load variations." *International journal of energy research* 31 (2): 148-157.

Zikri, Ahmad, Engkos Achmad Kosasih, Muhammad Irfan Dzaky, and Muhammad Badra Shidqi. 2020. "Influence of water mass flow rate and water salinity on specific energy consumption and aquadest production using throttling process method." AIP Conference Proceedings.

Zikri, Ahmad, Engkos Achmad Kosasih, Muhammad Irfan Dzaky, and Muhammad Pasha Wibisono. 2021. "Investigation of outlet temperature on heat exchanger 1 and cyclone pressure of specific energy consumption and cooling heat in renewable desalination systems." AIP Conference Proceedings.

IEEES-041

Dynamic Modeling of a Compressed Natural Gas Refueling Station

[1]Fatih Ozcan, [2]Muhsin Kiliç,
[1]Bursa Uludağ University, Orhangazi Yeniköy Asil Çelik Vocational School, Mechanical and Metal Technologies Department, Orhangazi/BURSA, 16810, Türkiye
[2]Bursa Uludağ University, Faculty of Engineering, Department of Mechanical Engineering, Nilüfer/BURSA, 16059, Türkiye
*E-mails: fatihozcan@uludag.edu.tr ; mkilic@uludag.edu.tr

Abstract

Compressed Natural Gas (CNG) is one of the alternative vehicle fuels. Benefits of CNG include cost savings, reduced emissions, ease of vehicle maintenance, and increased energy security. CNG is stored in high pressure cylinder on the vehicle which calls natural gas vehicle or tank (NGV). There are two types of CNG infrastructure; time-filling and fast-filling process. At the fast-filling process, desired filling time is less than 300 s. At the CNG refueling stations, natural gas compressed by compressors and storage in the high-pressure reservoir tanks. During refueling, natural gas vehicles (NGV) are connected to the high-pressure reservoir tanks by a dispenser. While dispensing the fuel, the temperature and pressure changings must be controlled. To understand these changes, in this study a CNG Refueling station is modelled in Matlab/Simulink/Simscape. Model is used with ideal gas and real gas assumptions.

Keywords: Compressed Natural Gas, Matlab/Simulink/Simscape Modelling.

I. Introduction

Compressed Natural Gas (CNG) is a clean alternative fuel rather than gasoline and diesel. Natural gas vehicles (NGV) receive CNG from high-pressure storage tanks to their fuel cylinder at refueling stations. During filling NGV cylinder temperature rises. This temperature rise reduces the density of the gas in the cylinder, resulting in an under-filled cylinder. If this temperature rise is not compensated in the fuelling station, the vehicle driving range will reduce. To control the temperature rises, time-filling process can bu used. The NGV industry tries to provide a system to refuel a NGV comparable to a gasoline dispenser. To be comparable to the fill time is taken to fill a gasoline powered automobile. This fill time can be referred to as a fast fill or rapid charge which is under 300 seconds.

At CNG refueling stations one of the most important equipment for producing high pressure gas is reciprocating compressors. In order to reduce electricity consumption in CNG stations, (Yong-Liang et all., 2021) regulated the frequency of activation of the compressor (which consumes the most electricity) using genetic algorithm models. Flow chart of CNG base station: filtration, dehydration, compressor, storage. They modeled: prefilter, dehydration device, compressor, expansion tank, storage tanks, dispenser. Genetic algorithm models were solved with the help of matlab. Gas masses for the tank are considered as 250, 350, 450 kg. The buffer tank is designed to hold 200 kg of gas.

Ideal and real gas assumption models are important to see the difference. (Farzaneh-Gord et al., 2015) The models are solved with the AGA8 equation of state (EOS). The piston compressor is the most important element of the system and the affecting factors are; angular velocity, cut-in, pressure ratio. The temperature in the control volume is higher in the ideal gas, the mass flow rate and work are higher in the real gas, and the work done for the compressor is higher in the ideal gas. With a 3 or 4 stage piston compressor, 20 and 25 MPa pressure can be reached. The biggest expense in CNG stations is the energy supplied to the compressor. Therefore, optimizing the compressor parameters, achieving high efficiency and low work input is the main goal. To achieve this, volumetric effectiveness, work done per mass and reduced efficiency are calculated by making changes in 5 main and 4 second dimensionless parameters.

There are three objectives for the development of CNG stations. (Farzaneh-Gord et al., 2016) Filling time minimization, filling of storage tanks and maximization of usability rate. Two types of storage systems are used in CNG stations. single and multiple storage system CNG flow is modeled as one-dimensional and isothermal flow for both the vehicle interior and storage tanks. The system can be thought of as storage tanks, connection pipes, dispenser, and vehicle tank. The multiple storage system is divided into low, medium and high-pressure tanks. Filling is done first with low storage tanks. The vehicle tank is increased to 200 bars. Then medium and high-pressure tanks can come into play. AGA8 EOS general form as long as the mass flow rate is above 0.02 kg/s, vehicle tank filling will take less than 5 minutes. High pressure 500 liters, medium pressure 1000 liters, low pressure 1500 liters are suitable. Starting reservoir tank pressures are 230 bar.

According to the results of the study, (Deymi-Dashtebayaz et al., 2012) the initial pressure of the storage tank has a great impact on increasing the vehicle tank to the targeted pressure (20 MPa). The results showed that the effect of ambient temperature on filling is very large. Especially to the final condition of the vehicle tank and storage tank. Mass transfer is thought to be direct from the storage tank to the vehicle tank. The control volume is considered for both the storage tank and the vehicle tank. The continuity equation, that is, the conservation of mass, the first law of thermodynamics, was solved by considering two control volumes and was concluded with the assumption of an adiabatic cylinder surface. The second law of thermodynamics for entropy was derived with the same assumptions. Storage tank drops from 234 to 226 bar. Vehicle tank increases from 0 to 8 kg.

According to the results of the study, (Farzaneh-Gord et al., 2014) the components that make up natural gas have a significant impact on the filling process and the final state of the fuel tank. Moreover, compounds with less methane gas are more suitable for filling. Standard usage for CNG vehicles is to fill the fuel tank at 20 or 24.5 MPa pressure. Due to overheating during filling, the filling test is performed at higher pressure and the value allowed by ISO 11439 is 26 MPa, regardless of the external temperature. Maximum values are determined so that the tank cylinder can be filled 1000 times a year and can be used for 20 years. The operating temperature is expected to be between -40 and 65^0 C and rises to a maximum of 82^0 C. In previous studies, natural gas was assumed to be pure methane or a fixed mixture, and the effects of different natural gas mixtures on the filling process and the

values of the final cylinder tank were not examined. The aim of this study is to examine this effect for buffer storage systems.

In this study, a dynamic model is constructed for the designed CNG refueling station and simulated by MATLAB/Simulink/Simscape program. Pressure and temperature changes are investigated.

II. System Description

The schematic view of the designed system is shown in Fig. 1. The model consists of pipeline, 3 stages compressor, buffer reservoir tanks, a dispenser and a vehicle cylinder. Those 5 subsystems are controlled by control logic state flow. This state flow decides the timing of the natural gas flow from pipeline to vehicle.

The pipeline subsystem contains solver configuration and natural gas properties for begining, entering and custody metering of the gas to the station. The ideal and real gas assumptions are made here.

Multistage compressor subsystem contains 3-stage reciprocating compressor and cooling system. All stages of the compressor pressure ratio are 3. There are 2 intercooler and 1 aftercooler. Cooling fluid is water and it cools with fan air.

Buffer tanks subsystem contains reservoir tanks. For this model tanks total volume is chosen 960 liters.

Dispenser subsystem contains reduce valf to dispatch the CNG to the cylinder. There is a hose between dispenser and cylinder to add impact the friction of the pipes.

Vehicle tank subsystem contains a cylinder tank. There are mass, pressure and temperature sensors. Tank volume is 70 liters.

For this study natural gas assumed pure methane.The models aim is basicly to reach the buffer and vehicle tanks pressure to 250 and 200 bar respectively.

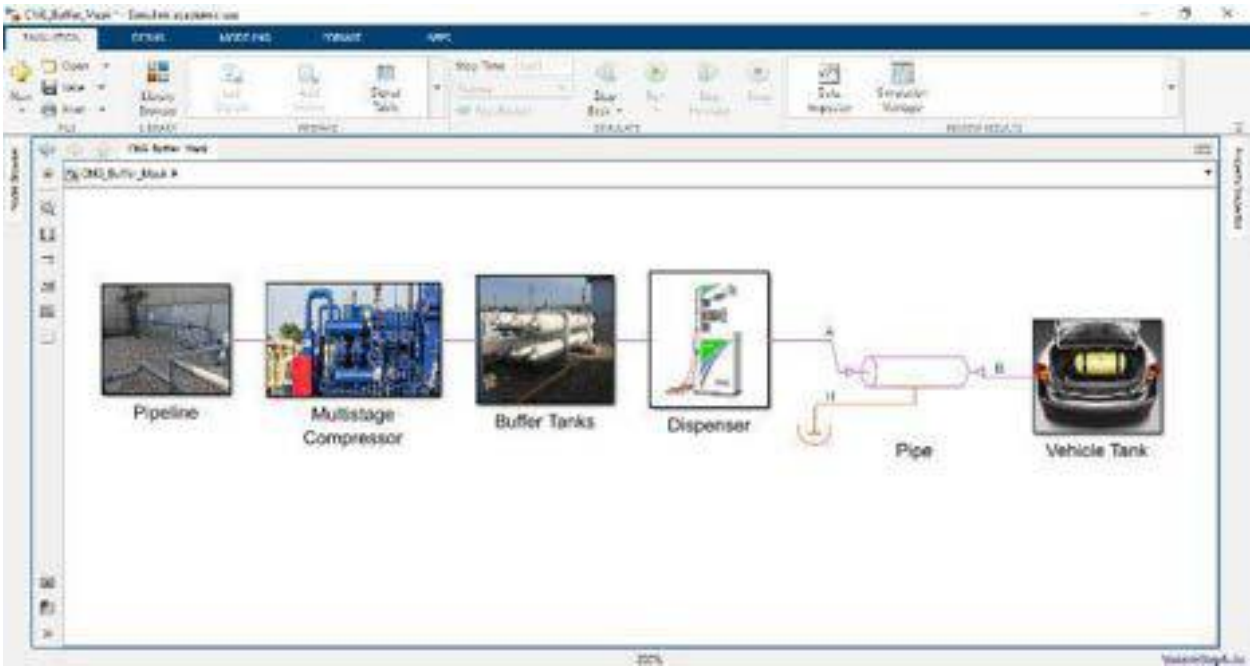

Fig. 1. Designed Model

III. Analysis

To model the fast filling process, vehicle cylinder is considered as a simple thermodynamic control volume. Applying the mass conservation principle to the control volume, the conservation of mass equation may be written as follow:

$$\dot{m}_i = \frac{dm_c}{\mathrm{dt}} \tag{1}$$

where m_i is inlet mass flow rate. The general form of the first law of thermodynamics for an open system yields:

$$\dot{Q_{cv}} + \sum \dot{m}_i \left(h_i + \frac{{V_i}^2}{2} + gz_i\right) = \sum \dot{m}_e \left(h_e + \frac{{V_e}^2}{2} + gz_e\right) + \frac{d}{dt}\left[m(u + \frac{V^2}{2} + gz)\right]_{cv} + \dot{W_{cv}} \tag{2}$$

The change in kinetic and potential energy and the work term could be neglected. Above equation could be simplified:

$$\frac{dU_c}{dt} = \dot{Q_{cv}} + \dot{m}_i \left(h_i + \frac{{V_i}^2}{2}\right) \tag{3}$$

IV. Results and discussion

In CNG station model results are shown in Figure 2.The results is determined for real gas assumption.The NGV cylinder initial pressure is 10 bar when the filling process is completed the final pressure of the NGV cylinder increases to 193 bar. The temperature of NGV

cylinder rises 82^0 C from 25^0 C. The mass flow into the NGV cylinder is between 0.044 – 0.03 kg/s. The buffer tank initial pressure is 20 bar and the compressor shut down when the final pressure of the buffer tank increases to 255 bar at nearly 17 minutes. The temperature of buffer tank rises $41{,}5^0$ C from 25^0 C. Total mass of the CNG in cylinder is 7,4 kg in nearly 4 minutes.

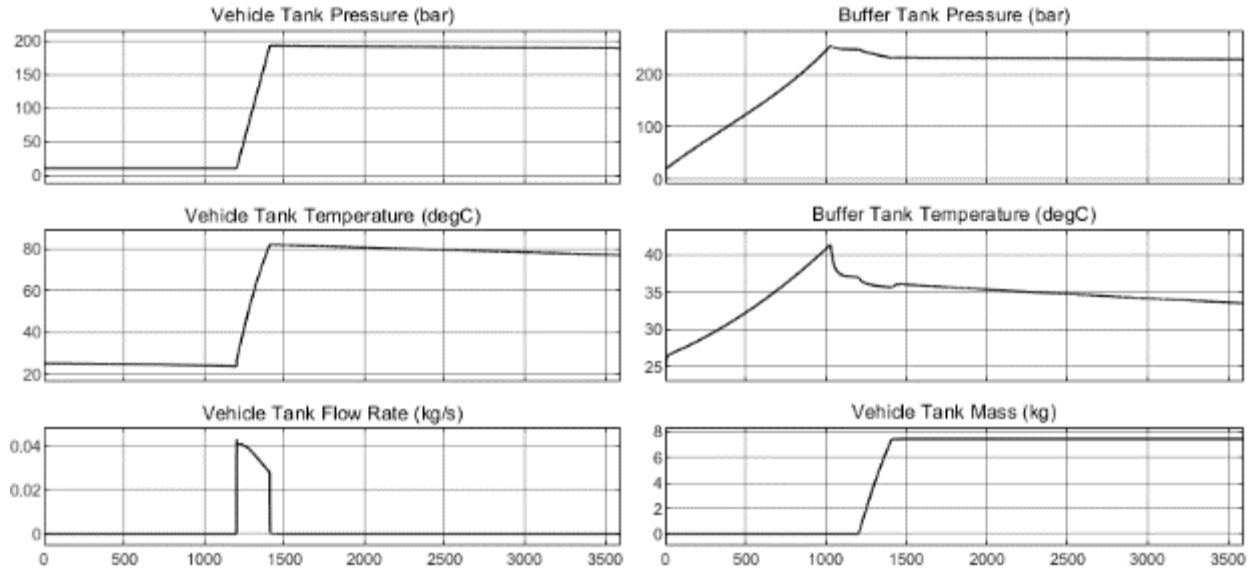

Fig. 2. Simulation Results for Real Gas Assumptions

Fig. 3. Compare the Simulation Results for Ideal and Real Gas Assumptions

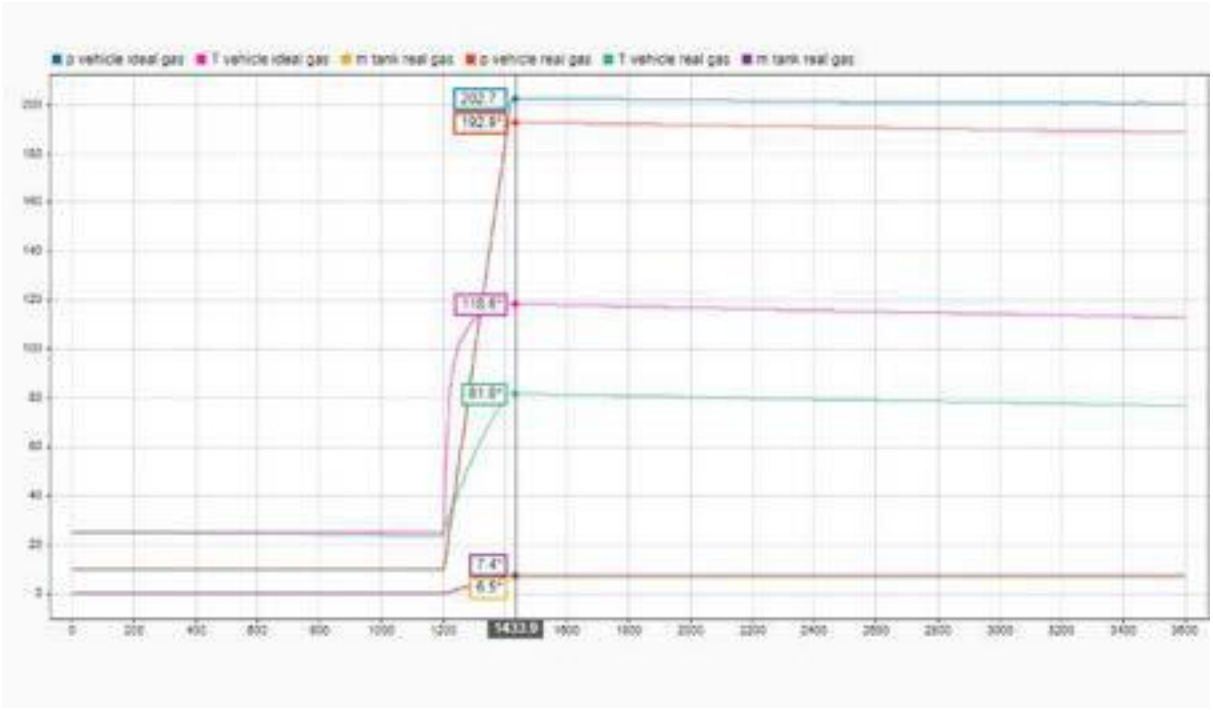

The compare of the simulation results for ideal gas and the real gas assumptions are shown in Figure 3. The NGV cylinder final pressure is 202.7 bar for ideal gas and 192,9 bar for real gas. The temperature of NGV cylinder rises 118.6^0 C for ideal gas and 81.8^0 C for real gas. Total mass of the CNG in NGV cylinder is 6.5 kg for ideal gas and 7.4 kg for real gas.

V. Conclusion

The Compressed Natural Gas (CNG) station model was created by using the Matlab/Simulink/Simscape media. Since, CNG is stored in high pressure cylinder on the vehicles, natural gas must be pressurized then charge on the vehicles tanks in a required very short time interval. It is generally required to make fast filling process under 300s. For fast filling process, buffer tanks are used. In the simulations, both ideal gas approach and real gas properties are employed. Comparing both gases approach, it is observed that Natural Gas Vehicle (NGV) cylinder's temperature increases in an acceptable range for real gas properties, however, higher temperature increases observed for ideal gas. Meanwhile, it is also observed that the temperature rises caused to less mass filling in CNG cylinder.

To prevent this and to get more mass in cylinder, the buffer tanks can changed with multi line storage system (cascade system).

References

Deymi-Dashtebayaz M, Farzaneh-Gord M, Rahbari HR., (2012) Studying transmission of fuel storage bank to NGV cylinder in CNG fast filling station. J Braz Soc Mech Sci Eng 2012;34(2):429e35.

Farzaneh-Gord M, Rahbari HR, Deymi-Dashtebayaz M., (2014) Effects of natural gas compositions on CNG fast filling process for buffer storage system. Oil Gas Sci Technol e Rev 2014;69(2):319e30. IFP Energies nouvelles.

Farzaneh Gord M, Niazmand A, Deymi-Dashtebayaz M, Rahbari HR., (2015) Thermodynamic analysis of natural gas reciprocating compressors based on real and ideal gas models. Int J Refrig 2015; 56:186e97. http://dx.doi.org/10.1016/j.energy.2015.06.056

Farzaneh-Gord M, Saadat-Targhi M., Khadem J., (2016) Selecting optimal volume ratio of reservoir tanks in CNG refueling station with multi-line storage system. International Journal of Hydrogen Energy, vol. 48, no. 41, pp. 23109-23119. http://dx.doi.org/10.1016/j.ijhydene.2016.10.050

Yong-Liang L., Chen-Xian G., Ke-Jun L., Ming-Yang L., (2021) Economic scheduling of compressed natural gas main station considering critical peak pricing. Applied Energy 292 116937. https://doi.org/10.1016/j.apenergy.2021.116937

IEEES-042

Green Synthesis of Encapsulated Nano Silver Biochar Composite for Malachite Green Removal from Aqueous Solution: *Novel Synthesis and Optimization*

[1*]Erol Pehlivan, [2] Elif Gezginci, [3] Busra Ozkok,
[1,2,3]Konya Technical University, Faculty of Engineering and Natural Sciences, Department of Chemical Engineering, Selçuklu-Konya, 42250,
Türkiye
*E-mails: [1]erolpehlivan@gmail.com, [2]elfgezginci@gmail.com, [3]busraozkok93@gmail.com

Abstract

In order to remove the malachite green dye (MG) from the aqueous solution, a functional adsorbent with biological origins was synthesized in this research. Grapefruit albedo (GA), waste biomass, was progressively pyrolyzed in a nitrogen (N_2) atmosphere to produce grapefruit albedo-biochar (GA-BC), which underwent a thermochemical transition. About 500 °C ultimate temperature and a 10 °C/min heating rate were used to successfully synthesize GA-BC. Encapsulated silver nanoparticles (eAgNPs) were produced on GA-BC via green synthesis, increasing the efficiency of the adsorbent. Myrtle leaf (*Myrtus communis*) extract (MCE) was used in experiments on green synthesis as the reducing agent and $AgNO_3$ solution as the metal ion (Ag^+) source. The pH, $AgNO_3$ solution concentration, and plant extract to $AgNO_3$ solution ratio were among the variables that were optimized for green synthesis. These variables were found to be pH 7, a 1:1 MCE-$AgNO_3$ solution ratio, and a concentration of 0.01 M $AgNO_3$ solution. By using the best feasible conditions, the synthesis of eAgNPs with MCE on GA-BC in the slurry phase was accomplished in 24 hours. The presence of eAgNPs was proven using a UV-visible spectrophotometer. Strong peaks were observed around 420 nm, which is an eAgNP characteristic wavelength. The structural, morphological, and optical characteristics of the environmentally friendly encapsulated nano silver biochar composite (eAg^o@BC) were investigated utilizing XRD, FT-IR, and FE-SEM investigations. The produced eAg^o@BC was used in adsorption processes to remove the MG from the aqueous environment. Batch studies were employed to investigate the factors impacting adsorption, such as pH, contact time and the amount of eAg^o@BC. The biochar-based nanocomposite successfully removed MG, with a dye adsorption efficiency of 99.41% after 90 minutes of contact.

Keywords: Green synthesis; Grapefruit albedo; Silver nanoparticle; Biochar; Composite; Adsorption; Malachite green.

I. Introduction

Large amounts of dyes released into the environment by the paper, leather, textile, cosmetic, and clothing sectors are the primary contributors to pollution in waterways. Although dyes are extensively utilized in industry, the contamination they cause results in the production of harmful industrial effluent. Due to the synthetic origins and intricate aromatic structures of dyes, their removal is difficult, and wastewater treatment is costly (Srinivasan & Viraraghavan, 2010). There are many benefits to adsorbing dyes, which is why researchers are employing various techniques to do so more efficiently. Traditional physical, chemical, and biological techniques have been used in these techniques, including flotation, chemical precipitation, adsorption, membrane processes, photocatalytic degradation, coagulation, chemical purification, liquid-liquid extraction, ion exchange, biological purification, and electrolyte recovery (Bayram et al., 2022); (Shi et al., 2007); (Low et al., 2013); (Anwer et al., 2019); (Jalilvand et al., 2020); (Patra, Gupta, et al., 2020); (Patra, Shahnaz, et al., 2020). Adsorption is the process of removing ions or molecules from a liquid phase and retaining them in a solid phase. This can be accomplished by using materials like activated carbon, biochar, zeolites, metal oxides etc. (Altintas Yildirim & Pehlivan, 2022). These adsorbents are often more effective and less expensive than traditional methods like precipitation, flocculation, or electrostatic attraction.

One significant treatment approach is the use of biochar in adsorption procedures (Parlayıcı & Pehlivan, 2023). As an alternative, these carbon-containing structures can be combined with other nanoparticles to form new adsorbent composites. Different techniques are used to manufacture metal nanoparticles for this purpose. Numerous chemical and physical techniques can be used to produce metal nanoparticles, but they are expensive and produce hazardous byproducts. Because of this, composites made by incorporating metal nanoparticles produced by green synthesis into the biochar domain have started to be applied in wastewater treatment. In summary, adsorbing dyes by nanocomposite is a useful, affordable, and versatile replacement for conventional methods. Researchers are always thinking of new methods to improve this technology so that it can be used more broadly in the future.

In this work, biochar was loaded with green synthesis-produced Ag^o-nanoparticles and employed as a novel nanoscale adsorbent for the removal of dyes. The adsorption process is complex and is affected by many parameters. To optimize the adsorption process, it is important to understand how each parameter affects the process. In this study, we examined the effect of some parameters on the adsorption process: contact time, composite quantity, and solution pH. These parameters provide valuable information about the adsorption process and allow for the optimization of the adsorption procedure.

II. Experimental Procedure

2.1. Materials

All chemicals were of analytical grade, and they were used as received with no further purification. Grapefruit Albedo (GA) was obtained by cutting waste grapefruit peels. Silver nitrate ($AgNO_3$), hydrogen chloride (HCl), sodium hydroxide (NaOH) and ethanol (EtOH) were purchased from Sigma Aldrich/Germany. Malachite green dye (MG) was obtained from Merck Sigma Aldrich/Germany. *Myrtus communis* leaf (MC) was collected in Antalya/Turkiye.

2.2. Green Synthesis of Encapsulated Silver Nanoparticles-*Optimization Study*

MC was ground, washed with deionized water (DI) and dried in an oven at 70°C. MCE was prepared by addition of 10 grams of

MC to 1000 ml DI at room temperature. The mixture was mixed with a magnetic stirrer for 24 hours. The extract was filtered using filter paper to obtain a clear solution with a light-green color. A series of experiments were organized to control green synthesis conditions such as $AgNO_3$ solution concentration (0.001 M to 0.1 M), MCE-$AgNO_3$ solution ratio (1:5, 2:5, 3:5, 4:5, 5:1, 5:2, 5:3, 5:4 and 1:1) and pH (pH 3 to 10). The formation of encapsulated silver nanoparticles (eAgNPs) was monitored by UV-visible spectrophotometer at the end of the 24-hour mixing period.

2.4. Synthesis of Encapsulated Silver Nanoparticles-Biochar Composite

The synthesis of eAgNPs on GA-BC matrix process was carried out by reacting 0.01 M aqueous $AgNO_3$ solution (500 ml) with MCE (500 ml) in 5 grams of GA-BC containing beaker. After the arrangement of the mixture to pH 7, the mixture was stirred with a magnetic stirrer for the reduction of Ag^+ ions into Ag^0 nanoparticles on GA-BC matrix. During the reaction, the colour of the solution changed from light green to dark brownish black, indicating completion of the formation of eAgNPs. After a 24-hour mixing period, the synthesized eAg^0@BC was separated by centrifugation at 4000 rpm, washed several times with DI, dried in an oven at 80°C and then stored in the desiccator for adsorption study.

2.5. Batch Adsorption Experiments for MG Removal from Aqueous Solution

The adsorption parameters were investigated in batch experiments. MG stock solution (400 ppm) was prepared by dissolving the solid dye in DI. The effect of various pH (3.0 to 10.0), contact time (1 min to 240 min) and dosages of eAg^0@BC (0.1 g/L to 4.0 g/L) were tested. At the end of the experiments, dye solutions were filtered, and the remaining dye concentration was measured by using UV-visible spectrophotometer. In the UV-visible spectrum, the peak value was observed at 617 nm for MG. Equilibrium adsorption capacity (q_e), which expresses the MG adsorption on eAg^0@BC, was calculated using the following equations (Eq. 1):

$$q_e = \frac{(C_0 - C_e)V}{m} \quad (1)$$

In the equation, C_0 and C_e (in ppm) are the initial and the equilibrium concentration of MG, respectively. V (in L) is the volume of the dye solution, and m (in g) is the amount of the adsorbent. The percent sorption was calculated using the formula below (Eq. 2):

$$\%Sorption = \frac{100(C_0 - C_e)}{C_0} \quad (2)$$

III. Analysis

A UV-Visible spectrophotometer (Shimadzu UV-1700) was used to measure the MG concentration during the experiments. A Thermo Scientific-Nicolet IS20 Model Fourier Transform Infrared (FT-IR) spectrometer was used to identify functional groups on the FT-IR peaks. A ZEISS Gemini SEM 500 Model Field Emission Scanning Electron Microscope (FE-SEM) was used to analyze the surface morphology of the eAg^0@BC. X-ray diffractometry (XRD) was used to determine the crystalline structures of the nano composite. XRD analyses were performed at Konya Technical University Merlab Laboratories in EUROPE Model device with a Cu-K α radiation at the $10° \leq 2\theta \leq 80°$ boundary values.

IV. Results and discussion

4.1. Structural and Morphological Analyses

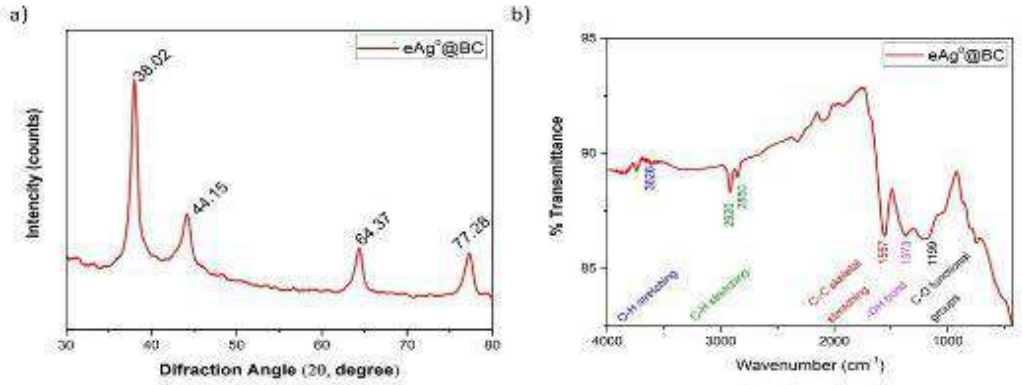

Figure 1 a) XRD and b) FTIR pattern of eAg^0@BC

The determination of the phases of nanostructure was investigated using XRD analyses. Figure 1-a) shows the XRD pattern of eAg^0@BC. Strong peaks appeared at 2θ = 38.02, 44.15, 64.37, 77.73, which are characteristic of Ag^0 formation (Hatipoglu, 2022). The FT-IR analysis was performed to investigate the chemical natures of the eAg^0@BC. As seen in Figure 1-b), the peak of 1373 cm^{-1} indicates the -OH bond (Nowrouzi et al., 2022). The double peaks at 2920 cm^{-1} and 2850 cm^{-1} correspond to -CH stretch (Abuderman et al., 2019). The characteristic peak at around 1557 cm^{-1} can be caused by C=C skeletal stretching (Tripathy et al., 2022). Exploring morphological details was done using FE-SEM micrographs of the eAg^0@BC. In Figure 2-a), the image shows the regular structure of the pores and eAgNPs positioned on the surface. As shown in Figure 2-b) Ag^0 distribution and compositional analysis of the eAg^0@BC were investigated using energy dispersive X-ray spectroscopy (EDX). Elemental mapping images of nanocomposite were proved that Ag nanoparticles were uniformly distributed on the biochar surface (Figure 2-c to f).

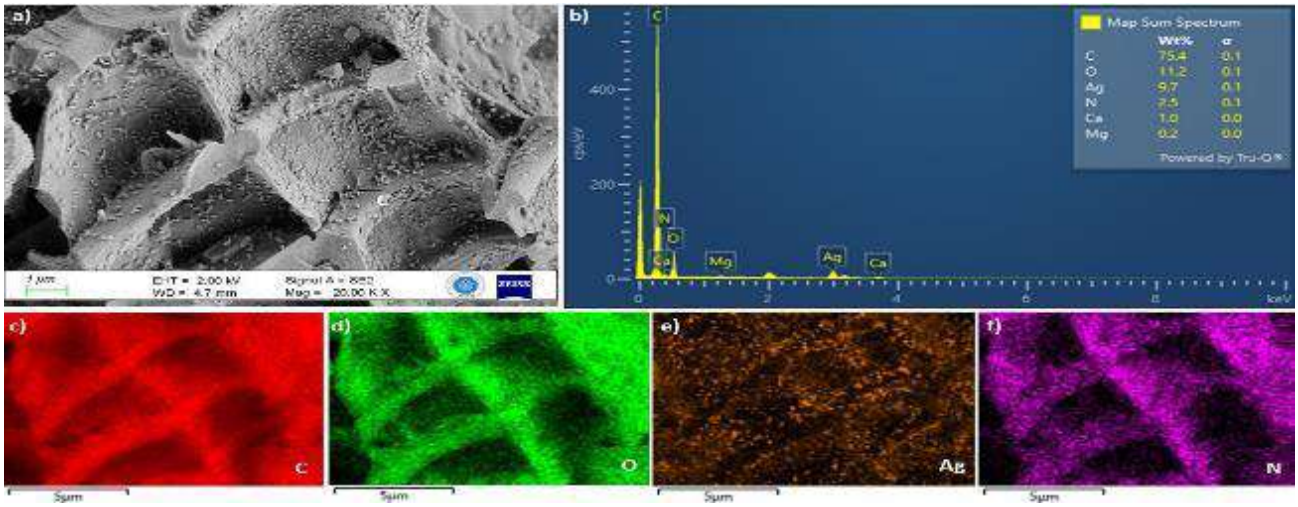

Figure 2-a) FESEM image; and b) EDX profile; and (c-f) elemental EDX mapping images of the C, O, Ag, and N of eAg0@BC nanocomposite.

4.2. Optimization of Green Synthesis Conditions

Figure 3-a). shows the eAgNPs formation as a function of absorbance at different MCE/$AgNO_3$ solution ratios by volume. Figure 3-b) shows the concentration dependence of absorbance at 420 nm. It is observed that silver nanoparticle formation increases with an increase in $AgNO_3$ concentration up to 10 mM. The decrease in eAgNPs formation after this point can be explained by the particles agglomerating and remaining in the precipitate. Figure 3-c) shows the pH effect on the green synthesis process. The optimal conditions of green synthesis were found to be 0.01M $AgNO_3$ solution concentration, 1:1 of MCE/$AgNO_3$ solution ratio by volume, and pH 7. Figure 3-c) also shows the appearance of I) MCE II) $AgNO_3$ solution, and III) color change by eAgNPs formation.

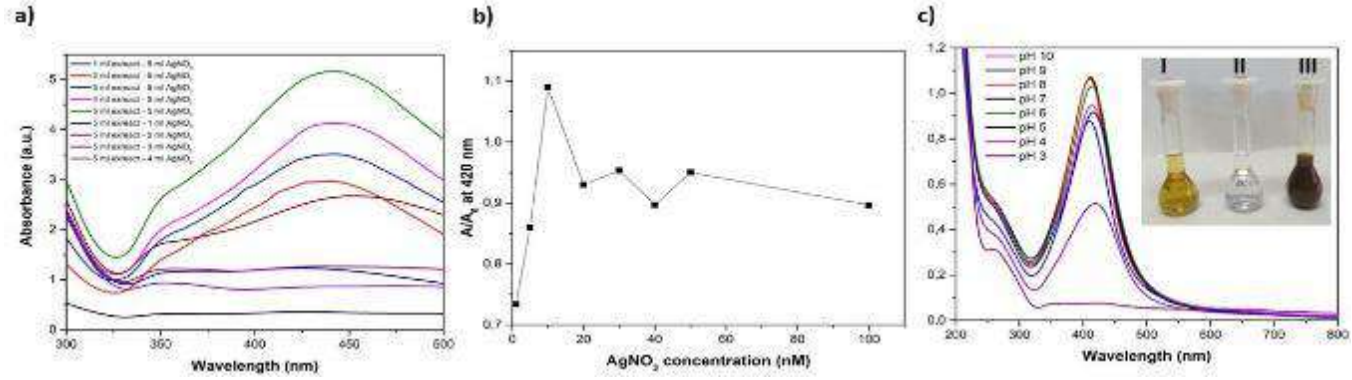

Figure 3. a) MCE/$AgNO_3$ volume ratio optimization; b) appearance of MCE (I), $AgNO_3$ solution (II) and color change of green synthesis after 24 hours incubation; c) pH and $AgNO_3$ solution concentration optimization study.

4.3. Effect Operational Parameters on MG Adsorption

The results of the batch experiments are shown in Figure 4. According to these experiments, optimum conditions for MG removal using Ag^0@BC were pH 10, 1 g/L dosage. The dye removal process using Ag^0@BC showed 99.41% sorption efficiency after 90 minutes of contact time.

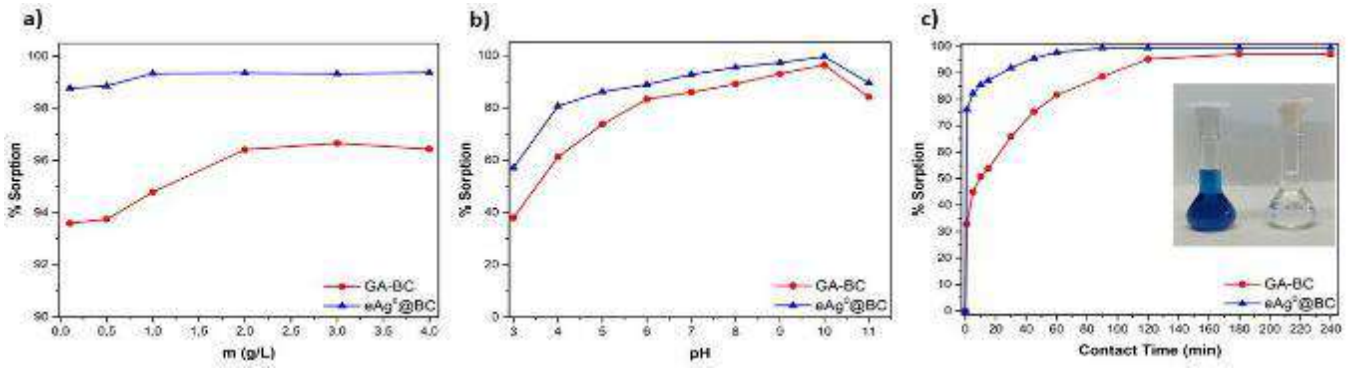

Figure 4. Parameters affecting adsorption process a) dosage of adsorbent; b) pH; and c) contact time.

V. Conclusion

The initial green synthesis of Ag^0@BC was targeted by this investigation and was used for the removal of MG dye from aqueous solutions. Both green synthesis and adsorption process conditions were optimized through batch experiments. Using plant extract during synthesis of eAgNPs instead of toxic chemical-reducing agents is a positive aspect of this method. The composite synthesized in this study proved to be suitable for aqueous medium with a sorption efficiency of 99.41%. 90 minutes of contact time and pH 10.0 for the adsorption of the MG were determined as optimum conditions. MG removal from aqueous solutions with nanocomposites is a highly effective method for the advanced treatment of wastewater.

References

Abuderman, A. A., Syed, R., Alyousef, A. A., Alqahtani, M. S., Ola, M. S., & Malik, A. (2019). Green synthesized silver nanoparticles of Myrtus communis L (AgMC) extract inhibits cancer hallmarks via targeting aldose reductase (AR) and associated signaling network. *Processes*, *7*(11). https://doi.org/10.3390/pr7110860

Altintas Yildirim, O., & Pehlivan, E. (2022). Removal of methylene blue using a novel generation photocatalyst based on nano-SnO2/wild plumb kernel shell biochar composite. *Journal of Dispersion Science and Technology*, *0*(0), 1–12. https://doi.org/10.1080/01932691.2022.2144878

Anwer, H., Mahmood, A., Lee, J., Kim, K. H., Park, J. W., & Yip, A. C. K. (2019). Photocatalysts for degradation of dyes in industrial effluents: Opportunities and challenges. *Nano Research*, *12*(5), 955–972. https://doi.org/10.1007/s12274-019-2287-0

Bayram, O., Köksal, E., Göde, F., & Pehlivan, E. (2022). Decolorization of water through removal of methylene blue and malachite green on biodegradable magnetic Bauhinia variagata fruits. *International Journal of Phytoremediation*, *24*(3), 311–323. https://doi.org/10.1080/15226514.2021.1937931

Hatipoglu, A. (2022). Gümüş Nanopartiküllerin Yeşil Sentezi ve Bazı Gıda Patojenleri Üzerindeki Antimikrobiyal Etkileri. *Süleyman Demirel Üniversitesi Fen Bilimleri Enstitüsü Dergisi*, *26*(1), 106–114. https://doi.org/10.19113/sdufenbed.970654

Jalilvand, P., Rahbar-Kelishami, A., Mohammadi, T., & Shayesteh, H. (2020). Optimizing of malachite green extraction from aqueous solutions using hydrophilic and hydrophobic nanoparticles. *Journal of Molecular Liquids*, *308*, 113014. https://doi.org/10.1016/j.molliq.2020.113014

Low, L. W., Teng, T. T., Rafatullah, M., Morad, N., & Azahari, B. (2013). Adsorption Studies of Methylene Blue and Malachite Green From Aqueous Solutions by Pretreated Lignocellulosic Materials. *Separation Science and Technology (Philadelphia)*, *48*(11), 1688–1698. https://doi.org/10.1080/01496395.2012.756912

Nowrouzi, I., Mohammadi, A. H., & Manshad, A. K. (2022). Preliminary evaluation of a natural surfactant extracted from Myrtus communis plant for enhancing oil recovery from carbonate oil reservoirs. *Journal of Petroleum Exploration and Production Technology*, *12*(3), 783–792. https://doi.org/10.1007/s13202-021-01336-6

Parlayıcı, Ş., & Pehlivan, E. (2023). An ecologically sustainable specific method using new magnetic alginate-biochar from acorn cups (Quercus coccifera L.) for decolorization of dyes. *Polymer Bulletin*, *80*(10), 11167–11191. https://doi.org/10.1007/s00289-022-04609-0

Patra, C., Gupta, R., Bedadeep, D., & Narayanasamy, S. (2020). Surface treated acid-activated carbon for adsorption of anionic azo dyes from single and binary adsorptive systems: A detail insight. *Environmental Pollution*, *266*, 115102. https://doi.org/10.1016/j.envpol.2020.115102

Patra, C., Shahnaz, T., Subbiah, S., & Narayanasamy, S. (2020). Comparative assessment of raw and acid-activated preparations of novel Pongamia pinnata shells for adsorption of hexavalent chromium from simulated wastewater. *Environmental Science and Pollution Research*, *27*(13), 14836–14851. https://doi.org/10.1007/s11356-020-07979-y

Shi, B., Li, G., Wang, D., Feng, C., & Tang, H. (2007). Removal of direct dyes by coagulation: The performance of preformed polymeric aluminum species. *Journal of Hazardous Materials*, *143*(1–2), 567–574. https://doi.org/10.1016/j.jhazmat.2006.09.076

Srinivasan, A., & Viraraghavan, T. (2010). Decolorization of dye wastewaters by biosorbents: A review. *Journal of Environmental Management*, *91*(10), 1915–1929. https://doi.org/10.1016/j.jenvman.2010.05.003

Tripathy, S., Sahu, S., Patel, R. K., Panda, R. B., & Kar, P. K. (2022). Novel Fe3O4-Modified Biochar Derived from Citrus Bergamia Peel: A Green Synthesis Approach for Adsorptive Removal of Methylene Blue. *ChemistrySelect*, *7*(10). https://doi.org/10.1002/slct.202103595

IEEES-043

Co-Pyrolysis of Walnut Shell and Waste Rubber Blend to Produce Sustainable Bio-based Materials

[1]Burcu KİREN, [2*]Esin APAYDIN VAROL
[1,2] Eskişehir Technical University, Faculty of Engineering, Chemical Engineering Department, İki Eylül Campus, Eskişehir, 26555, Turkey
*E-mails: eapaydin@eskisehir.edu.tr
burcukiren@eskisehir.edu.tr

Abstract

Fossil fuel depletion and increasing demand for energy and sustainable materials have created new opportunities to explore sustainable materials. Bio-based materials offer an environmentally friendly and cost-effective solution as they are derived from biomass and waste recycling. In addition, waste elastic polymers are becoming an environmental problem since they do not deteriorate in nature for many years resulting in toxic gas formation. A saturated non-polar rubber, ethylene propylene diene (EPDM) has a growing potential as a waste due to industrialization. Sustainable bio-based materials derived from various types of biomass-polymer blends include carbonaceous materials with superior physical and chemical properties. Torrefaction, gasification, pyrolysis, and hydrothermal carbonization are the main thermochemical conversion methods to produce bio-based carbons to be used in different technological areas, such as supercapacitors, polymer composites, energy storage, and soil amendment. In this study, a blend of walnut shells, a biomass source, and EPDM, a waste rubber, was used as the feedstock. The goal was to produce solid carbonaceous materials through the co-pyrolysis of different blending ratios. The co-pyrolysis process was performed at 500 °C at a heating rate of 10 °C/min in an N_2 atmosphere with a flow rate of 100 mL/min. Various characterization techniques have been employed to evaluate the physicochemical, morphological, and crystallinity properties of the carbonaceous products. The highest solid product yield (47%) was achieved with a blend of 25% walnut shell and 75% EPDM. The increase in the biomass ratio resulted in a decrease in the content of the inorganics and BET surface area from 19.29 to 9.83 m^2/g. As a result, it was determined that co-pyrolysis of biomass/EPDM to carbonaceous materials seems to be a promising method for the disposal of waste elastomers.

Keywords: Co-pyrolysis, biomass, EPDM, bio-based materials, characterization.

I. Introduction

Waste generation has been driven by worldwide urbanisation, economic development, and population growth. Waste elastomers (rubbers-elastic polymers) are becoming an important environmental problem all over the world (Da Silva and Wiebeck, 2020). The automobile industry heavily depends on the usage of rubbers, specifically EPDM, to manufacture parts resulting in the generation of significant waste. EPDM is a co-polymer of ethylene and propylene that incorporates a diene monomer, creating unsaturated sites or double bonds in the macromolecule. EPDM is currently the fastest-growing general-purpose rubber due to its exceptional properties, particularly its resistance to ozone and oxygen, and ability to tolerate high filler loadings (Mohaved et al., 2015). These elastomeric materials exhibit remarkable resistance to heat and steam and are widely employed for their resilient properties (Bravaya et al., 2022). Polymeric materials do not readily decompose, making their waste disposal a major environmental concern. For this reason, rubber recycling is becoming increasingly important globally due to rising raw material costs, limited resources and growing awareness of environmental issues and sustainability (Mohaved et al., 2015). Waste elastomers are used in cement factories to obtain energy by burning or in floor coverings by reducing particle size and compressing (Fazli and Rodrigue, 2020). With the increasing industrialisation in the world and in our country, the conversion of waste elastomers into valuable products is one of the most important issues of recent years. Toxic gases are released when waste elastomers are intended to be disposed of in landfill sites. These toxic gases threaten the environment as they carry the risk of explosion when they remain under a certain pressure. In addition, waste elastomers in scrap tyre collection areas threaten the balance in the ecosystem by creating an ideal environment for the reproduction of disease-carrying insects (Kordoghli et al., 2016). Since they do not degrade in nature for many years, they are mixed into different ecosystems and harm the lives of many living things and the environment they live in. To minimise the negative effects of these wastes, it is becoming gradually important to increase the added value of environmentally harmful waste elastomers by using recycling/upcycling processes and to carry out studies to reduce environmental pollution.

Apart from this, it is known that fossil-based energy reserves are gradually decreasing in the face of significantly increasing energy consumption needs due to the increase in the competitive environment of countries that want to take part in the global economy. In addition to the decrease in fossil energy reserves, their use in energy production has started to be replaced by renewable energy sources due to the damage they cause to the environment and the expensive technologies they require in terms of cost. Sustainable biomass, one of the renewable energy sources, is preferred because it is abundant in nature and environmentally friendly. In the pyrolysis process, which is one of the thermochemical methods, solid, liquid and gas products obtained as a result of thermal degradation of biomass. The materials produced by obtaining solid products after pyrolysis are called biochar or bio-based carbon. Although bio-based materials are used as energy storage, supercapacitor and catalytic activity materials, it is mostly used in increasing soil fertility in agriculture, soil amendment and wastewater treatment, which is one of the most important parts of environmental problems (Jeyasubramanian et al., 2021).

In this study, it is aimed to convert waste elastomer (EPDM) into high value-added products by pyrolysis process together with biomass, which is an environmentally friendly renewable resource. The recycling/upcycling of waste EPDM was studied previously, and the thermal degradation behaviour, kinetics, and pyrolysis of EPDM was reported (Eren et al., 2023; Perejón et al., 2013). However, co-pyrolysis of this waste rubber with biomass has not been studied so far. Therefore, in this study, biomass and elastomer blends prepared at different ratios were pyrolzed to determine the blend ratio that has the most suitable solid product yield and bio-based materials properties. Accordingly, it is aimed to solve an environmental problem by evaluating waste elastomers that cause

environmental pollution, and in addition, this study is a preliminary report to provide sustainable renewable energy production against fossil resources.

II. Experimental Procedure Walnut shell (WS) as biomass was obtained from the fields of Mihalıççık, Eskişehir, Turkey. EPDM raw material, supplied from ICarbon Chemistry R&D and Engineering in Bursa, Turkey. Prior to experiments, the raw materials were ground to a particle size of 1.25< Dp< 1.8 mm. Proximate analysis were conducted using American Society for Testing and Materials (ASTM) procedures to establish the properties of the raw materials.

Slow pyrolysis experiments were carried out in a fixed bed reactor at a temperature of 500 °C with a heating rate of 10 °C/min in a 100 mL/min N_2 flow environment in a fixed bed reactor for the blends of walnut shell and EPDM waste elastomer prepared separately and at different ratios (wt. 0, 25, 75, 100%). Repeated pyrolysis experiments were carried out for samples prepared at five different mixture ratios. 20 g of feedstock was put inside the reactor for each run. The details of the pyrolysis setup used in this study was given previously (Eren et al., 2023).

III. Characterization

Density, moisture content, surface functional groups, crystal structure, surface and morphology of bio-based materials were determined using conventional characterization techniques.

Density measurement analyzes were performed using a helium pycnometer device (Quantachrome, Ultrapyc 1200E). The analysis was repeated 5 times for each sample and the average result was taken from the device.

Moisture content analyzes were conducted using the Precisa brand moisture analyzer. Each sample analysis was repeated 3 times, and the average result was calculated.

Thermo Scientific Nicolet iS10 device was used to determine the surface functional groups of bio-based materials. Samples prepared with the KBr pellet method were analyzed with 32 scans in the wavenumber range of 500-4000 cm^{-1}.

To determine crystal structures of the samples, X-ray diffraction patterns using Cu Kα (λ = 1.54056 Å) radiation were collected using a Rigaku Rint 2200 diffractometer (Tokyo, Japan). The diffractometer operated at 40 kV and 40 mA, recording XRD patterns within a 2θ range of 3-80°, with a step size of 0.02° and a scan speed of 2°/min.

The surface areas were assessed via the Brunauer-Emmett-Teller (BET) equation utilizing the 77 K N_2 adsorption data. Quantachrome Autosorb-1 equipment was employed in conducting 11-point BET experiments. All samples were degassed at 120°C prior to undergoing adsorption.

Morphological analysis of bio-based materials was conducted using a high-resolution Scanning Electron Microscope (SEM), operating at 20 kV (ZEISS-SUPRA 50 VP), to obtain SEM images. Before analysis, the samples were covered with thin layers of Au/Pd by sputtering for 30 seconds to enhance electron mobility. To determine the quantity of specific elements, Energy-dispersive Spectrometer (EDS) spectrum results were obtained.

IV. Results and discussion

Table 1 displays the moisture, ash, volatile matter, and fixed carbon contents of the raw materials based on the approximate analysis results. The results indicate that the fixed carbon content of the walnut shell, which has a lignocellulosic structure, is 6%, while the fixed carbon content of the EPDM raw material is 33.5%.

The moisture, density (true and bulk) and surface area analyses for the carbonaceous bio-based materials, which was produced by pyrolysis of WS and EPDM blends, are presented in Table 2. According to densities presented in Table 2, true density values exhibit a declining trend with an increase in the walnut shell ratio. The effective removal of volatile components in the biomass source along with the residual carbon content was observed. Nevertheless, upon analysing the bulk density values, it can be inferred that bulk density values escalate with an increase in the walnut shell ratio, which runs contrary to the true density. This is due to the reduction in biomass volume as the carbon content increases during the pyrolysis process. The rise in biomass ratio led to a reduction in inorganic content and surface area from 19.29 to 9.83 m^2/g.

Table 1. Approximate analysis of raw materials

Sample	Moisture (%)	Ash (%)	Volatile Matter (%)	Fixed Carbon (%)
EPDM	*1.1*	*14.7*	*50.7*	*33.5*
WS	*10.5*	*0.4*	*83.1*	*6.0*

Table 2. Density, moisture, and surface area properties of bio-based carbonaceous materials

Sample	Moisture (wt. %)	True Density (g/cm^3)	Bulk Density (g/cm^3)	BET Surface Area (m^2/g)
100 % EPDM	*2.2*	*2.087*	*0.381*	*17.94*
75 % EPDM-25 % WS	*2.4*	*1.888*	*0.220*	*19.29*
50% EPDM-50 %WS	*3.2*	*1.739*	*0.245*	*14.00*
25 % EPDM-75 % WS	*3.8*	*1.566*	*0.350*	*9.83*
100 % WS	*5.3*	*1.405*	*0.626*	*13.90*

Figure 1.a. displays the XRD patterns gathered to ascertain the crystal structures and phases existing within the bio-based materials. The XRD analysis of the walnut shell sample shows a broad peak at 22.0° between 2θ=20-27°, indicating the presence of an amorphous carbon phase in the walnut shell. The peak, which is unique to the walnut shell, is composed primarily of cellulose, hemicelluloses, and lignin (Yang et al., 2016). Figure 1.a. shows the appearance of strong and weak diffraction peaks at 2θ = 26° and 2θ = 45°

respectively. These diffractions demonstrate the existence of graphite crystallites due to the carbon properties (Xie et al., 2014). It is observable that a rise in the proportion of EPDM in the blend leads to an increase in diffraction intensity.

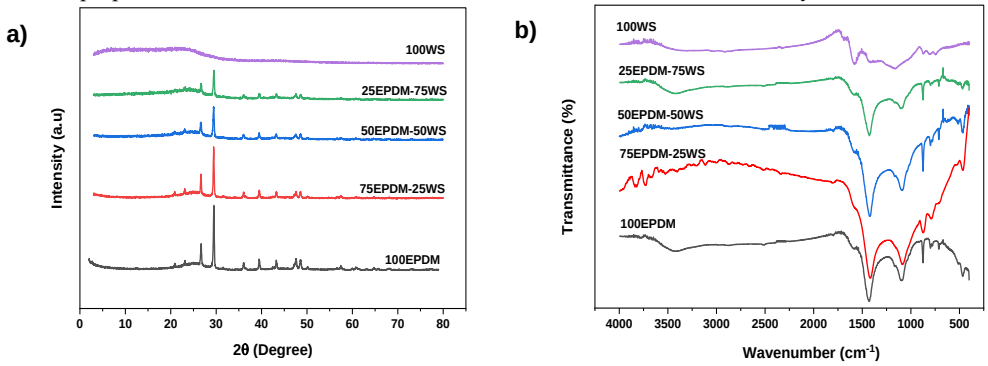

Fig. 1: (a) XRD patterns and (b) FT-IR spectra of bio-based carbonaceous materials

The surface functional groups of bio-based materials were analyzed, and the results are depicted in Figure 1.b. The peaks observed at the wavenumbers 1500 cm^{-1} and 1350 cm^{-1} are attributed to the CH_2 asymmetric vibrations and C-H symmetric stretching vibrations respectively for the EPDM based carbonaceous material (Tang et al., 2013). The vibration band that occurs between 1423 and 1450 cm^{-1} displays C-H bending vibrations and is representative of the alkanes existincy. The vibration peaks within the range of 1092 and 1000 cm^{-1} are caused by sulfurous compound vibration bands resulting from the carbonyl groups in the additives. The presence of alkenes arising from C=C bands is confirmed by the peaks observed at 875 cm^{-1}.

Figure 2 illustrates the SEM image and EDS spectrum of the bio-based carbonaceous material obtained from 75 % EPDM-25 % WS which gave the highest solid product yield after pyrolysis. In the SEM image it is seen that the surface of solid particulates includes agglomerations of organic and inorganic layers resulting in a flat morphology which is far from the lignocellulosic structure of WS char. It was determined that the bio-based product contains approximately 75 % carbon by weight.

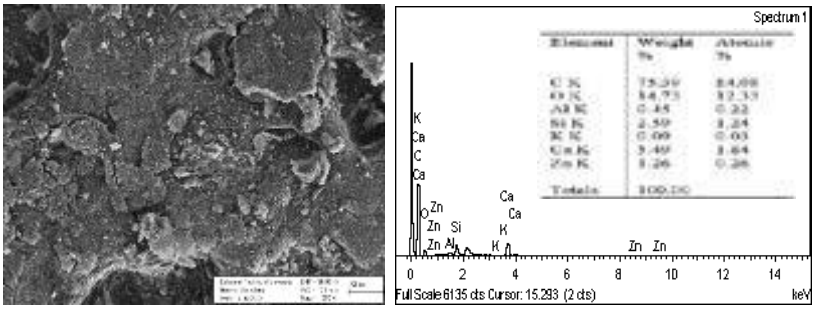

Fig. 2: SEM image and EDS spectrum of 75 % EPDM-25 % WS bio-based carbonaceous material

V. Conclusion

The bio-based carbonaceous materials characteristics are given in this study. Bio-based carbonaceous material was obtained from waste materials through a one step pyrolysis process at 500 °C. Waste EPDM contributed to the improvement of the pyrolytic solid product properties through its high fixed carbon content. The highest solid product yield (47%) was achieved with a blend of 25% walnut shell and 75% EPDM. As a result, it was proposed that this alternative technology offers a simple solution that can produce sustainable bio-based materials for their utilization in different application areas to solve environmental problems.

Acknowledgements
Authors would like to acknowledgement Eskişehir Technical University Scientific Research Projects Commission through the research project 22ADP376. The authors would also like to thank Eskişehir Technical University Materials Science Engineering Department and Ceramics Research Center for allowing them to use their device infrastructure in XRD and SEM analysis, and Erdem Mutlu from ICARBON Chemistry R&D to provide waste EPDM.

References

Bravaya, N.M., Faingol'd, E.E., Sanginov, E.A., Badamshina, E.R., 2022. Homogeneous Group IVB Catalysts of New Generations for Synthesis of Ethylene-Propylene-Diene Rubbers: A Mini-Review. Catalysts 12, 704. https://doi.org/10.3390/catal12070704

Da Silva, D.J., Wiebeck, H., 2020. Current options for characterizing, sorting, and recycling polymeric waste. Progress in Rubber, Plastics and Recycling Technology 36, 284–303. https://doi.org/10.1177/1477760620918603

Eren, M.R., Güneş, I., Varol, E., 2023. The effect of carbonization temperature on the properties of carbonaceous material obtained from ethylene-propylene-diene-monomer (EPDM) wastes. Inter J Ener Clean Env. https://doi.org/10.1615/InterJEnerCleanEnv.2023047205

Fazli, A., Rodrigue, D., 2020. Waste Rubber Recycling: A Review on the Evolution and Properties of Thermoplastic Elastomers. Materials (Basel) 13, 782. https://doi.org/10.3390/ma13030782

Jeyasubramanian, K., Thangagiri, B., Sakthivel, A., Dhaveethu Raja, J., Seenivasan, S., Vallinayagam, P., Madhavan, D., Malathi Devi, S., Rathika, B., 2021. A complete review on biochar: Production, property, multifaceted applications, interaction mechanism and computational approach. Fuel 292, 120243. https://doi.org/10.1016/j.fuel.2021.120243

Kordoghli, S., Paraschiv, M., Kuncser, R., Tazerout, M., Prisecaru, M., Zagrouba, F., Georgescu, I., 2016. Managing The Environmental Hazards of Waste Tires. JESR 20. https://doi.org/10.29081/jesr.v20i4.52

Mohaved, S.O., Ansarifar, A., Nezhad, S.K., Atharyfar, S., 2015. A novel industrial technique for recycling ethylene-propylene-diene waste rubber. Polymer Degradation and Stability 111, 114–123. https://doi.org/10.1016/j.polymdegradstab.2014.11.00

Perejón, A., Sánchez-Jiménez, P.E., Gil-González, E., Pérez-Maqueda, L.A., Criado, J.M., 2013. Pyrolysis kinetics of ethylene–propylene (EPM) and ethylene–propylene–diene (EPDM). Polymer Degradation and Stability 98, 1571–1577. https://doi.org/10.1016/j.polymdegradstab.2013.06.029

Tang, G., Hu, Y., Song, L., 2013. Study on the Flammability and Thermal Degradation of a Novel Intumescent Flame Retardant EPDM Composite. Procedia Engineering, 9th Asia-Oceania Symposium on Fire Science and Technology 62, 371–376. https://doi.org/10.1016/j.proeng.2013.08.078

Xie, Z., Guan, W., Ji, F., Song, Z., Zhao, Y., 2014. Production of Biologically Activated Carbon from Orange Peel and Landfill Leachate Subsequent Treatment Technology. Journal of Chemistry 2014, 1–9. https://doi.org/10.1155/2014/491912

Yang, F., He, Y., Sun, S., Chang, Y., Zha, F., Lei, Z., 2016. Walnut shell supported nanoscale Fe0 for the removal of Cu(II) and Ni(II) ions from water. Journal of Applied Polymer Science 133. https://doi.org/10.1002/app.43304

IEEES-044

Experimental Studies on Energy and Exergy-based Assessments of a Freezer

[1]Burak Vardar, [1]Fazli Ozan Bovatekin,[2]Yunus Mert Becermen, [1]Okan Gök, [1]Ersin Alptekin, [1,*]Mehmet Akif Ezan, [1]Aytunç Erek
[1] Dokuz Eylül University, Faculty of Engineering, Department of Mechanical Engineering, Izmir, Türkiye
[2]ARCELIK Refrigerator Plant, Manisa, Türkiye
*Corresponding author e-mail: mehmet.ezan@deu.edu.tr

Abstract

This work focuses on experimental studies of a freezer under various evaporation temperatures. Temperature and pressure measurements are conducted to evaluate the variations in energetic and energetic performance indicators. Time-wise temperature variations within the freezer compartments and evaporator surfaces are measured to do so. Also, pressure and temperature probes are placed at the inlet/outlet ports of the cycle components to end up with thermodynamic assessments of the cycle components. An in-house MATLAB script is coded to conduct detailed 1st-law and 2nd-law-based analyses using the Cool Prop add-in. Consequently, transient variations in the system's first-law and second-law COPs, isentropic compressor efficiency, and entropy generations in each component of the refrigeration cycle are obtained for four different evaporation set-points of the freezer.

Keywords: Freezer, exergy and energy analyses, exergy destruction.

I. Introduction

Energy consumption in the cooling sector worldwide has increased significantly in the last two decades. According to statistics from the International Refrigeration Institute, refrigeration systems, air conditioning systems, and heat pumps are responsible for approximately 20% of global electricity consumption worldwide (Dupont, 2019). Refrigerators and freezers are among the most used appliances that are classified as essential needs in the modern era. Domestic refrigerators account for 6% of global electricity consumption (Choi et al., 2018), and optimizing the performance of household refrigerators and freezers is essential to fulfilling the short and long-term targets that aim to reduce energy consumption globally. In the existing literature studies, many studies have been conducted to evaluate the refrigeration and/or freezer performance at either component or system level. In the following paragraphs, a short literature review on exergy-based research on refrigeration systems is first provided, and then the main objectives of the work are highlighted.

Ahamed et al. (2011) classified the exergy-based investigations on vapor compression systems. It is shown that exergy-based studies evaluate the influences of *(i)* the type of refrigerant, *(ii)* the evaporation and condensation temperatures, *(iii)* the dead state temperature, *(iv)* the lubrication, and *(v)* the types of additives such as nanofluids in refrigerants or lubricants. It is concluded that R600a, R410a, and R1270 performed better in the energetic and exergetic aspects. It is also stated that the degree of subcooling improves exergy efficiency. Exergy efficiency is also enhanced by reducing the temperature difference between the condensation and evaporation temperatures. Joybari et al. (2013) considered a household refrigerator and analyzed the influence of the type of refrigerant on the required amount of refrigerant and the component-based exergy destructions transiently. The results showed that the highest exergy destruction occurred in the compressor, followed by the condenser, capillary tube, evaporator, and superheat coil. At the optimum design condition, the amount of refrigerant charged into the system is reduced from 145 g to 50 g with the replacement from R134a to R600a. Such a significant reduction in refrigerant mass provides an economic value and reduces the environmental effects and flammability risk associated with the refrigerant. Alhamid et al. (2019) performed parametric experiments for a household refrigerator with R600a under various loading scenarios of M-packages to optimize the system performance regarding the exergetic indicators, such as exergy destruction rate and relative irreversibility. It is concluded that the optimum amount of refrigerant is 43-gram and the relative irreversibilities of the system components are achieved as 77.52% for the compressor, 1.836% for the condenser, 19.8% for the capillary tube, and 0.8473% for the evaporator under the optimum design configuration. Kabul et al. (2008) conducted theoretical calculations based on 2nd law aspects to determine the performance of a refrigerator with an internal heat exchanger performance by varying the degree of superheating, the evaporation and condensation temperatures, and the isentropic efficiency of the compressor. Results highlighted that increasing the evaporation temperature enhances the COP and exergy efficiency of the cycle. In contrast, an increment in the condensation temperature adversely affects the system COP and exergetic efficiency. Babarinde et al. (2018) developed an experimental facility to compare the performances of household refrigerators that use R600a and LPG as refrigerant. Detailed exergy analyses are performed based on the experimental measurements to evaluate the system's first-law and second-law efficiencies. Results show that the pull-down durations for R600a and LPG-based refrigerators are 240 min and 210 min, respectively. The fridge's evaporation temperature and exergy efficiency with LPG are determined as -14°C and 45%. Besides, the evaporation temperature and exergy efficiency are -12°C and 42% for the refrigerator with R600a. It is concluded that the system performance increased by replacing R600a with LPG, considering the exergetic performance indicators, such as irreversibility and exergy efficiency. Sun et al. (2020) studied a new refrigerant, R513a, a mixer of R1234yf and R134a. The proposed refrigerant performance is studied experimentally, and the results are discussed considering the first-law and second-law aspects. It is concluded that the mass of R513a is 12% less than R134a with a higher performance. The exergy efficiency of the system with R513a is 14% higher than that of the system with R134a.

The current study aims to present the experimental results for an empty freezer with four different set temperatures. A MATLAB script is coded to evaluate the transient and time-average 1st-law and 2nd-law performance indicators from the long-term measured data.

II. System Description

In this study, the dynamic behavior of a freezer is experimentally evaluated, and the energy/exergy analyses are carried out. Some technical features of the freezer are provided in Table 1. The freezer has a storage capacity of 196 L and involves five separate compartments (Fig. 1a). 42 gr of isobutane (R600a) is charged in the refrigeration cycle. Six tube-on-sheet evaporators are inside the freezer, and buoyancy forces drive the air circulation. The components of the refrigeration cycle and sensor locations are illustrated in Fig. 1(b). Six thermocouples (T-type) and three pressure transducers (Emerson PT5-07M & PT5-18M) are used to monitor the temperature and pressure variations of the refrigerant, respectively. Indoor temperature, outdoor temperature, evaporator surface temperature, and inner and outer surface temperatures are also measured in different positions, and 36 thermocouples are placed inside and outside the freezer. Temperature and pressure data are collected at a 10-second interval with the Keysight DAQ970A data acquisition system. The controller monitors the thermostat temperature placed on the evaporator coil surface in the topmost compartment. Experiments are conducted for five different set-points of -18°C, -20°C, -23°C, -24°C and -27°C. In Fig. 2, the time-wise variations in inlet/outlet ports of each component of the refrigeration cycle and the *p-h* diagram are represented for a sample experiment. 1st-law and 2nd-law data reduction analyses are conducted for the collected data to quantify the system performance metrics. The following section outlines the data reduction techniques from the transient measurements.

Table 1. Technical specifications of the freezer

Cooling system	Static	**Width**	54 cm
Refrigerant	R600a	**Height**	145.7 cm
Capacity	196 L	**Depth**	57.5 cm
Daily energy consumption	0.613 kWh/day	**Number of compartments**	5

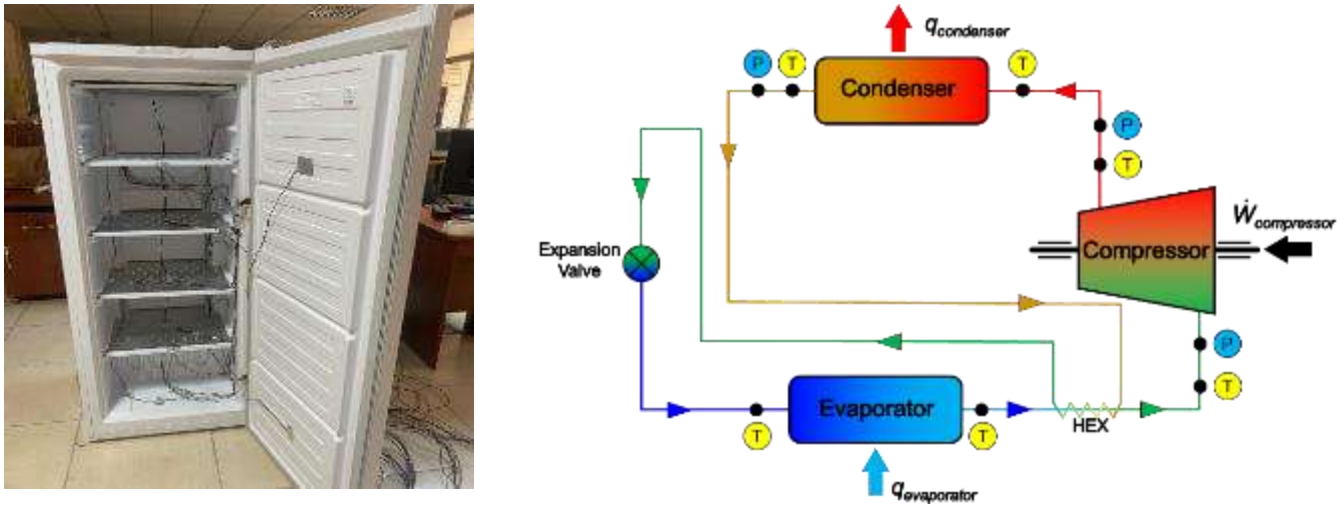

(a) (b)

Fig. 1: (a) Freezer with sensors (b) Refrigeration cycle with measurement sensor locations

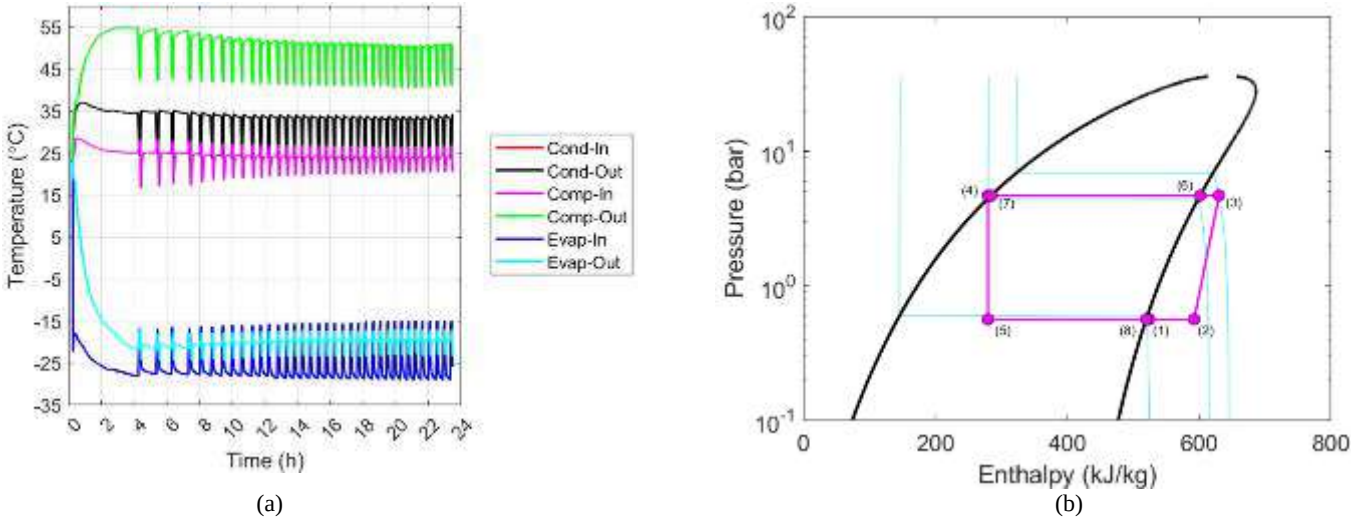

(a) (b)

Fig. 2: (a) Time-wise variations in cycle temperatures, (b) *p-h* diagram @ t = 20 h

III. Analysis & Data Reduction

A MATLAB script is coded to determine the system's performance indicators based on 1st and 2nd law aspects. The balance equations for each system component are summarized in Table 2. Energy balance equations are implemented to determine the capacities of the system components and COP of the cycle. Entropy balance equations are resolved to determine the entropy generations associated with each of the system's components. The second-law COP, i.e., exergetic efficiency, is evaluated from the following well-known equation:

$$\mathrm{COP_{II}} = \frac{\mathrm{COP}}{\mathrm{COP_{carnot}}} \tag{1}$$

where COP stands for the 1st-law COP, i.e., $\mathrm{COP} = q_{evaporator}/\dot{W}_{compressor}$, and $\mathrm{COP_{carnot}}$ is the Carnot efficiency, which is defined in terms of the freezer and ambient temperatures as $\mathrm{COP_{carnot}} = T_{freezer}/(T_{ambient} - T_{freezer})$. The mass flow rate of the refrigerant is predicted from the equation suggested by Li (2012):

$$\dot{m}_2 = \left(\frac{\rho_{suction}}{P_{suction}}\right)(\dot{W}_{elec} \times \eta_{isen})\left(\frac{k-1}{k}\right) / \left[\left(\frac{P_{discharge}}{P_{suction}}\right)^{\frac{k-1}{k}} - 1\right] \tag{2}$$

Table 2. Balance Equations

System Component	Energy Balance	Entropy Balance
Condenser	$q_{condenser} = \dot{m}(h_{in} - h_{out})_{condenser}$	$\dot{S}_{gen,cond} = \dot{m}(s_{out} - s_{in})_{cond} + q_{condenser}/T_{ambient}$
Evaporator	$q_{evaporator} = \dot{m}(h_{out} - h_{in})_{evaporator}$	$\dot{S}_{gen,evap} = \dot{m}(h_{out} - s_{in})_{evap} - q_{evaporator}/T_{freezer}$
Compressor	$\dot{W}_{compressor} = \dot{m}(h_{out} - h_{in})_{compressor}$	$\dot{S}_{gen,comp} = \dot{m}(s_{out} - s_{in})_{comp} + q_{loss}/T_{ambient}$

The freezer thermostat has five predefined evaporator set points of -18°C, -20°C, -23°C, -24°C and -27°C and corresponding experiments are labeled from 1 to 5 in the figures. Experiments are conducted for at least 10 hours for each set point to achieve a periodic steady-state condition (PSSC). Fig. 3 shows the long-term time-average temperatures and pressures after the system reaches the PSSC. The condensation and evaporation pressures significantly reduce to maintain the lower set temperatures. Reducing the evaporation pressure from 0.61 bar to 0.43 bar drops the evaporator inlet temperature from -22.5°C to -30°C. As a result, refrigerator mean temperatures decrease from -12.8°C to -22.6°C. Even though the condensation pressure reduces from 5.04 bar to 4.39 bar, no significant change is observed regarding the condenser inlet temperature. Besides, the reduction in the outlet temperature of the condenser is almost 5°C.

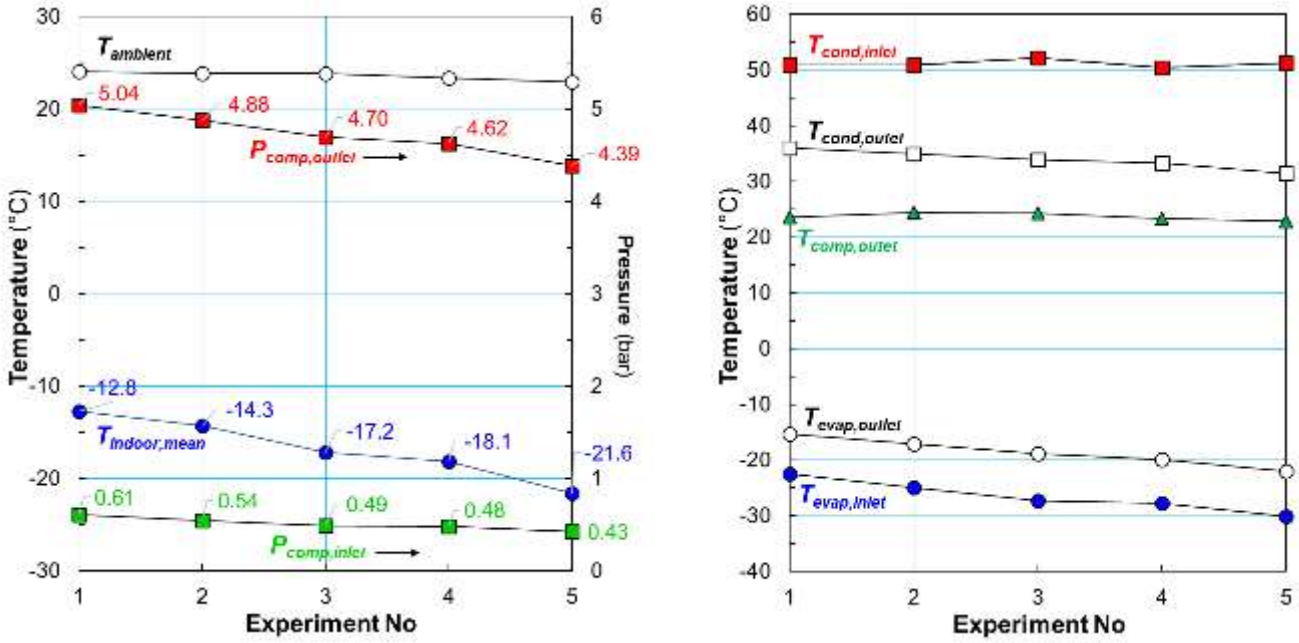

Fig. 3: Time-average temperatures and pressures after the system reaches the PSSC

IV. Results and discussion

Some major results are outlined in Fig. 4. In Fig. 4(a), the mass flow rate of the refrigerant, condenser, and evaporator capacities and 1st-law and 2nd-law COPs are given. Reducing the set-point of the freezer drops the condenser and evaporator capacities. Decreasing the indoor temperature of the freezer from -12.8°C to -21.6°C reduces the cooling capacity from 61.9 W to 48.9 W. The 1st-law COP of the system is also adversely affected by the indoor temperature reduction. Lowering the indoor temperature from -12.8°C to -21.6°C reduces the COP by almost 20%. Besides, no significant change is observed for 2nd-law COP, which varies around 27%. Fig. 4(b) represents the normalized entropy generations associated with the system components. The compressor is responsible for almost half of the irreversibility inside the refrigeration cycle. The entropy generation associated with the compressor increases as the freezer set point is reduced. Besides, the normalized entropy generation rates are similar for the evaporator and the condenser. The entropy generation associated with the expansion valve seems independent of the system's set point variations. The lowest share in entropy generation is related to the superheater HEX, which is almost 5%.

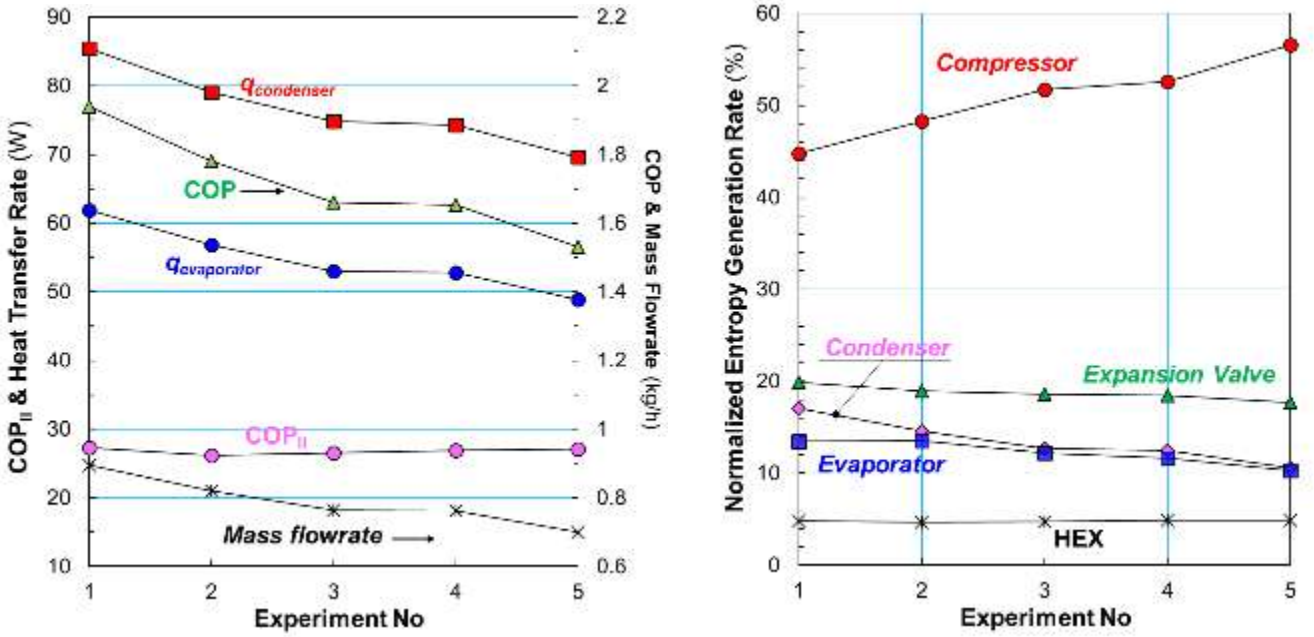

Fig. 4: Effect of freezer temperature on the system capacities and performance indicators

V. Conclusion

Current work aims to represent the preliminary findings that are obtained from lab-scale experiments on a freezer. A MATLAB script is developed to evaluate a freezer's 1st law and 2nd law performance indicators from the long-term transient measured data. The results show that achieving periodic steady-state conditions takes 10-24 hours, depending on the freezer's set point. Lowering the set-point significantly reduces the COP and evaporator capacity, yet there is no significant change in the 2nd law COP. Moreover, the irreversibility associated with the compressor is almost half of the total irreversibility of the refrigeration cycle.

Acknowledgements

This research was supported by The Scientific and Technological Research Council of Turkey (TUBITAK) TEYDEB 1505 program with project number 5220120.

References

Ahamed, J. U., Saidur, R., & Masjuki, H. H. (2011). A review on exergy analysis of vapor compression refrigeration system. *Renewable and Sustainable Energy Reviews*, *15*(3), 1593-1600.

Alhamid, M. I., Nasruddin, N., Susanto, E., Vickary, T. F., & Budiyanto, M. A. (2019). Refrigeration cycle exergy-based analysis of hydrocarbon (r600a) refrigerant for optimization of household refrigerator.

Babarinde, T. O., Akinlabi, S. A., & Madyira, D. M. (2018, September). Exergetic performance of household refrigerator using R600a and LPG. *In IOP Conference Series: Materials Science and Engineering* (Vol. 413, No. 1, p. 012069). IOP Publishing.

Choi, S., Han, U., Cho, H., & Lee, H. (2018). Recent advances in household refrigerator cycle technologies. *Applied Thermal Engineering*, *132*, 560-574.

Dupont, J. L., Domanski, P., Lebrun, P., & Ziegler, F. (2019). The role of refrigeration in the global economy. *38th Informatory Note on Refrigeration Technologies*.

Joybari, M. M., Hatamipour, M. S., Rahimi, A., & Modarres, F. G. (2013). Exergy analysis and optimization of R600a as a replacement of R134a in a domestic refrigerator system. *International Journal of Refrigeration*, *36*(4), 1233-1242.

Kabul, A., Kizilkan, Ö., & Yakut, A. K. (2008). Performance and exergetic analysis of vapor compression refrigeration system with an internal heat exchanger using a hydrocarbon, isobutane (R600a). *International Journal of Energy Research*, 32(9), 824-836.

Li, W. (2012). Simplified steady-state modeling for hermetic compressors with focus on extrapolation. International journal of refrigeration, 35(6), 1722-1733.

Sun, J., Li, W., & Cui, B. (2020). Energy and exergy analyses of R513a as a R134a drop-in replacement in a vapor compression refrigeration system. *International Journal of Refrigeration*, 112, 348-356.

IEEES-045

3D Steady-State Numerical Modeling of a Static Freezer

[1]Salih Bilgiç, [1]Eren Cankılıç, [2]Alper Gülmez, [1]Okan Gök, [1]Ersin Alptekin, [1*]Mehmet Akif Ezan, [1]Aytunç Erek
[1]Dokuz Eylül University, Faculty of Engineering, Department of Mechanical Engineering, Izmir, Türkiye
[2]ARCELIK Refrigerator Plant, Manisa, Türkiye
*Corresponding author e-mail: mehmet.ezan@deu.edu.tr

Abstract

Specific storage conditions should be maintained for food products to prevent spoilage. Depending on the structure and duration, food products require different temperature ranges during storage. Inappropriate preservation methods can lead to severe health problems and cause food to be wasted. Current work deals with numerical modeling of a commercially available and widely used freezer geometry. A 3D steady model is developed in ANSYS-FLUENT, and parametric analyses are conducted with different evaporator cooling rates. The freezer consists of five compartments with six evaporator plates. The static freezer is considered so that the natural convection-driven heat transfer is simulated. In order to determine the influence of surface-to-surface radiation within the freezer, the simulations are conducted with and without considering the radiation effects. Comparative results are assessed in terms of the mean air and evaporator temperatures, temperature distributions, and velocity fields. Results would help provide an in-depth understanding of the thermal stratification within the freezer compartments and the influence of radiation in modeling static freezers.

Keywords: Freezer, steady-state analyses, computational fluid dynamics (CFD).

I. Introduction

Early humans initially preserved their food by drying, salting, or burying, and with technological advancements, humankind has discovered more practical ways to store food. Today, refrigerators and freezers are widely used in developed and developing countries worldwide. According to recent statistics (GfK Marketing, 2017), over 100 million refrigerators are produced annually. Research estimates suggest that approximately 1.6 billion households use cooling systems (Harrington et al., 2018). The presence of cooling systems in 1.6 billion households and the increasing global population impact energy consumption worldwide. About 20% of global electricity consumption is associated with cooling, ventilation, and heat pump systems; it will be doubled by 2050 (Dupont, 2019). Enhancing the efficiency of refrigerators and freezers through engineering applications significantly impacts mitigating and preventing climate change in the future. In the literature, various numerical works investigate the steady and transient behaviors of cooling systems. Laguerre et al. (2007) developed numerical models in FLUENT for household refrigerators without shelves, with shelves, and with test products. Comparative results reveal that radiative heat transfer significantly affects the temperature variations along the vertical direction for a static refrigerator working in steady-state conditions. Predicted results fit well with the experimental measurements when the radiative heat transfer is included in the model. Ezan et al. (2017) numerically investigated the effect of phase change material implementation inside the empty beverage cooler. The results show that the PCM implementation prolongs the pull-down periods and extends the compressor-off duration. Ghodrati et al. (2022) considered a single cabinet of a freezer in COMSOL software and conducted transient simulations to assess the influence of phase change material on the dynamic temperature variations. Cheng et al. (2022) developed a steady 3D model for a chest freezer cooled with forced convection. For the loaded freezer, temperature and velocity variations are evaluated by changing the inlet and outlet port positions. The studies in the literature mainly focus on household refrigerators, and there is a limited study on freezers. The current work aims to develop a numerical model for a commercially available household freezer and study the influence of radiative heat exchange on thermal stratification within the freezer compartments. To do so, a numerical model is developed in ANSYS-FLUENT, and steady-state analyses are conducted by varying the cooling load.

II. Problem Definition & Analysis

The current work considers a static household freezer. A numerical model is developed in ANSYS-FLUENT software to evaluate the natural convection-driven temperature and velocity fields. In the cooling cycle of the freezer, R600A (Isobutane) is used as the refrigerant. The outer dimensions of the freezer are 54 cm in width, 145.7 cm in height, and 57.5 cm in depth. The freezer has an internal storage capacity of 196 liters. The freezer has five compartments with six tube-on-sheet evaporators (Fig. 1). Thanks to the geometrical and thermal symmetry along the width of the freezer, half of the geometry is considered in the CFD model. The full and half freezer geometries are given in Fig. 1(a-b). As a further simplification, the sliders of drawers and thicknesses of the tubes and shelves are disregarded to reduce the total number of mesh and achieve improved convergence in the numerical solver. The reduced freezer geometry used in the CFD simulations is provided in Fig. 1(c). The evaporator tubes with circular cross-sections are simplified into square pipes with the same equivalent hydraulic diameter. The compressor is adjacent to the bottom-most compartment, and there is an indentation for the container labeled “Air Domain #1”. The bottom-most container has horizontal and vertical evaporators.

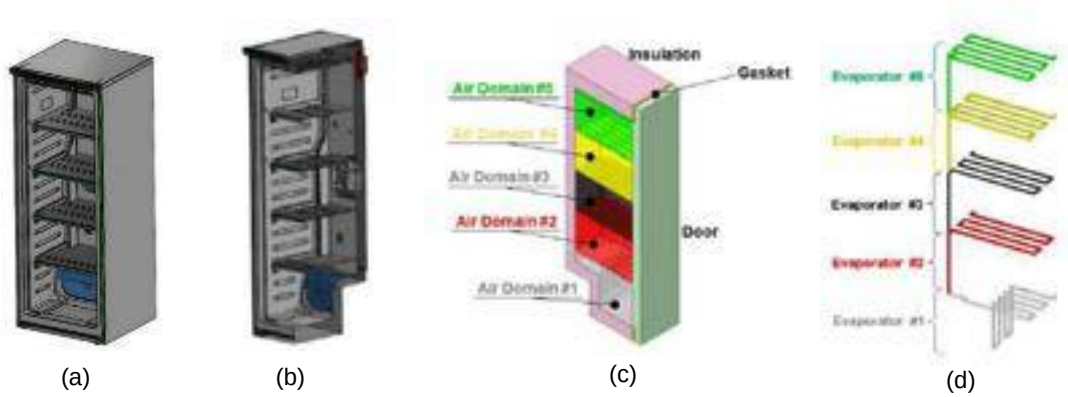

Fig. 1: (a) Full freezer geometry, (b) Half freezer geometry, (c) Simplified CFD model, and (d) Evaporator tubes

Balance equations for resolving natural convection-driven heat transfer and fluid-fluid occurring within the refrigerated space can be expressed as follows:

Mass balance equation:

$$\frac{\partial}{\partial x}(\bar{u}) + \frac{\partial}{\partial y}(\bar{v}) + \frac{\partial}{\partial z}(\bar{w}) = 0 \tag{1}$$

Momentum balance equations:
x-direction:

$$\frac{\partial}{\partial x}(\rho\bar{u}\bar{u}) + \frac{\partial}{\partial y}(\rho\bar{v}\bar{u}) + \frac{\partial}{\partial z}(\rho\bar{w}\bar{u}) = -\frac{\partial\bar{p}}{\partial x} + (\mu+\mu_t)\left[\frac{\partial^2\bar{u}}{\partial x^2} + \frac{\partial^2\bar{u}}{\partial y^2} + \frac{\partial^2\bar{u}}{\partial z^2}\right] \tag{2}$$

y-direction:

$$\frac{\partial}{\partial x}(\rho\bar{u}\bar{v}) + \frac{\partial}{\partial y}(\rho\bar{v}\bar{v}) + \frac{\partial}{\partial z}(\rho\bar{w}\bar{v}) = -\frac{\partial\bar{p}}{\partial y} + (\mu+\mu_t)\left[\frac{\partial^2\bar{v}}{\partial x^2} + \frac{\partial^2\bar{v}}{\partial y^2} + \frac{\partial^2\bar{v}}{\partial z^2}\right] + \rho g \tag{3}$$

z-direction:

$$\frac{\partial}{\partial x}(\rho\bar{u}\bar{w}) + \frac{\partial}{\partial y}(\rho\bar{v}\bar{w}) + \frac{\partial}{\partial z}(\rho\bar{w}\bar{w}) = -\frac{\partial\bar{p}}{\partial z} + (\mu+\mu_t)\left[\frac{\partial^2\bar{w}}{\partial x^2} + \frac{\partial^2\bar{w}}{\partial y^2} + \frac{\partial^2\bar{w}}{\partial z^2}\right] \tag{4}$$

Energy balance equation:

$$\frac{\partial}{\partial x}(\bar{u}\bar{T}) + \frac{\partial}{\partial y}(\bar{v}\bar{T}) + \frac{\partial}{\partial z}(\bar{w}\bar{T}) = \frac{1}{\alpha}\left[\frac{\partial^2\bar{T}}{\partial x^2} + \frac{\partial^2\bar{T}}{\partial y^2} + \frac{\partial^2\bar{T}}{\partial z^2}\right] - \frac{1}{\rho c}\frac{\partial}{\partial x_i}\left(\frac{\partial\overline{T}}{\partial x_i}\frac{c_p\mu_t}{\sigma_t}\right) \tag{5}$$

The FLUENT-Meshing program is used to discretize the simplified model into a finite number of control volumes. The mesh structure significantly influences the predicted results; that is, a preliminary mesh independency survey is conducted to be sure that the predicted results are free from spatial discretization errors. Four different numerical models are developed with different mesh intensities. Table 1 summarizes the features of the meshes. The total number of control volumes is varied from 648800 (Case #4) to 1.9 million (Case #1). Fig. 2 compares the results from models with different mesh intensities. It is clear that mesh size slightly changes the mean air and evaporator temperatures, and the optimum mesh is determined as 960359 to reduce the computational time in the parametric simulations. Results also show that thermal stratification occurs inside the freezer. The air temperature varies from 3°C to -6°C and the evaporator temperature varies within a range of -8°C to -19°C. This is mainly due to disregarding the radiative heat transfer inside the freezer. Surface-to-surface (S2S) model is employed for inter-surface radiation heat transfer calculations. Emissivities for aluminum and plastic surfaces are 0.05 and 0.85, respectively. The influence of radiative heat transfer on the temperature field is discussed in the next section.

Table 1: Details of the mesh structures

Parameter	Case #1	Case #2	Case #3	Case #4
Total number of Control Volumes	1,903,277	1,629,746	960,359	648,800
Air Domain Control Volume	1,714,964	1,488,674	862,120	585,869
Isolation Domain Control Volume	70255	59118	48508	39061
Orthogonal Quality	0.27	0.30	0.29	0.26
Skewness	0.72	0.70	0.70	0.74
Evaporator Volume (mm^3)	470,788.57	470,788.57	470,788.57	470,788.57

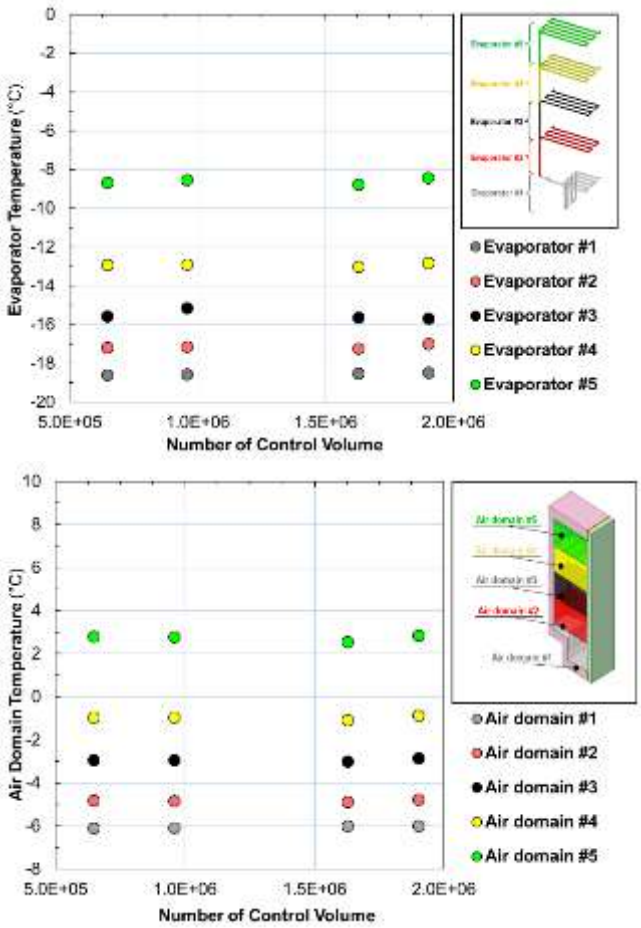

(a) (b)

Fig. 2: The impact of the number of control volumes on the average temperatures of (a) the evaporators and (b) air domains

III. Results and discussion

Comparative results are evaluated for cooling loads of 40 W, 50 W, and 60 W to assess the influence of radiative heat transfer on the temperature and velocity fields inside the freezer. Temperature distributions given in Fig. 3 show that including the radiative heat transfer inside the freezer suppresses the thermal stratification, and the temperature variations become more homogenous. Besides, the streamlines look almost identical, with slight discrepancies. Fig. 4 presents the variations in average air domain temperatures and evaporator temperatures as a function of cooling load and also reveals the influence of radiative heat transfer inside the freezer. It is interesting to note that radiation's impact on mean evaporator temperature looks weak at lower cooling loads, i.e., 40 W. In contrast, the influence of radiation on average air domain temperature looks negligible when the cooling load is higher, i.e., 60 W. Considering only the average values would not give a clear outlook, so the model outputs are compared in terms of the compartment-base average values.

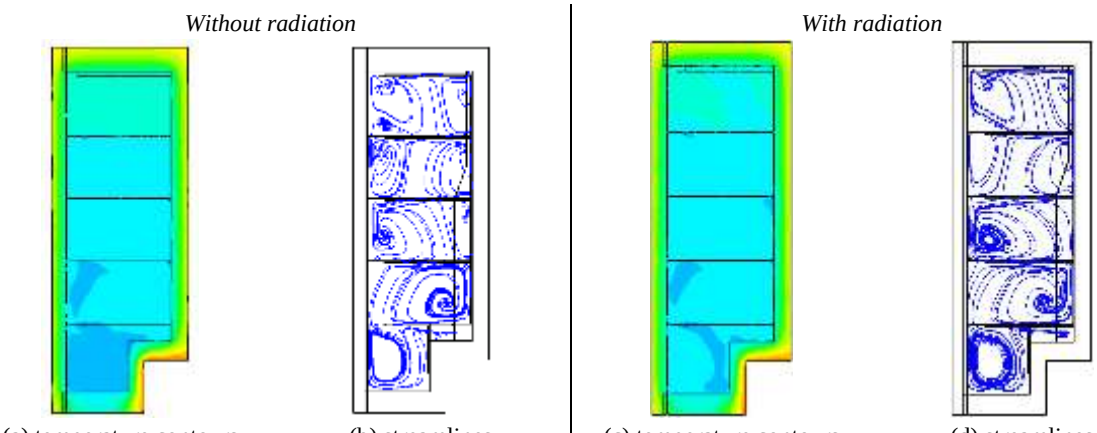

(a) temperature contours (b) streamlines (c) temperature contours (d) streamlines

Fig. 3: Temperature distributions and streamlines – Cooling Load: 50 W

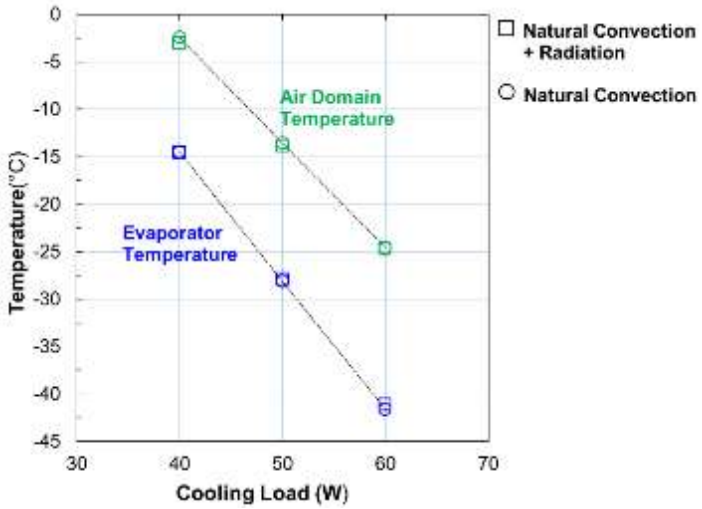

Fig. 4: The effects of the solution method and the cooling load on the mean evaporator and air domain temperatures

Fig. 5 provides a detailed look at the influence of radiation on the temperature distribution inside the freezer. Fig 5. (a) shows that from the top to the bottom of the freezer, the mean temperature of the evaporators varies by almost 12.5°C when the heat transfer mode is only natural convection. At the top of the freezer, the evaporator temperatures reduce when the radiative heat transfer is activated. In contrast, the evaporator temperatures at the bottom of the freezer increase when the radiative heat transfer is included in the solver. As a result, the difference between the top-most and bottom-most evaporator temperatures reduces to 8.3°C. The influence of radiative heat transfer on the mean compartment temperatures has a similar fashion. The difference between the top and bottom mean air temperatures is reduced from 11°C to 7.3°C. Results show that the surface-to-surface radiative heat transfer disturbs the thermal stratification and provides more homogenous temperature distribution within the freezer.

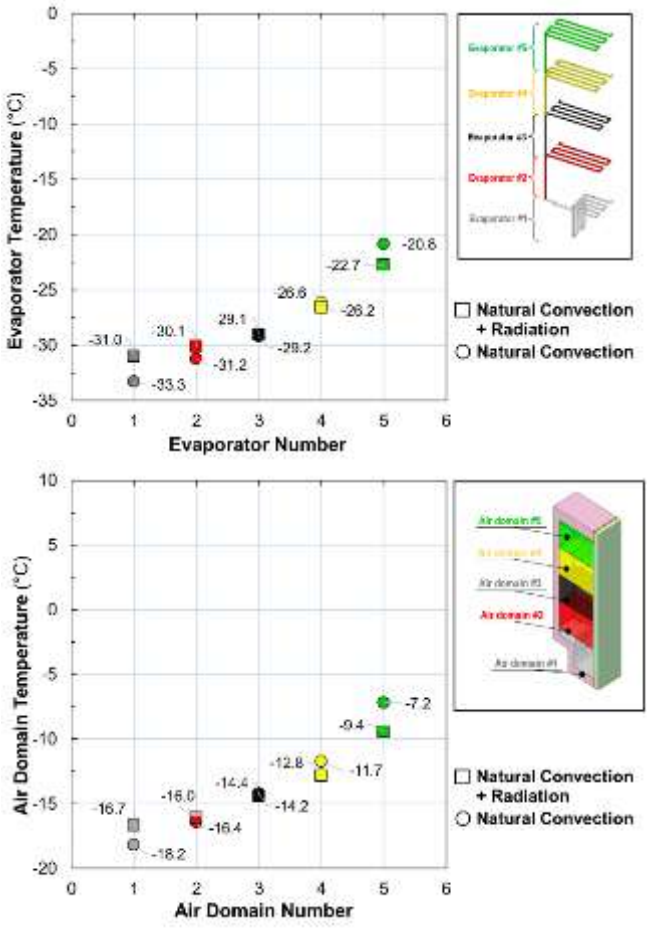

(a) (b)

Fig. 5: The variations in average (a) evaporator and (b) air domain temperatures – Cooling load: 50 W.

V. Conclusion

The current study aims to develop a steady-state 3D model for a commercially available household freezer. Comparative results with different cooling loads clearly show that radiative heat transfer dominates the temperature field inside the freezer and cannot be disregarded. Further studies will be conducted for a freezer with M-packages under cyclic transient conditions to assess the thermal stratification inside the air domain and the blockage effect of the packages.

Acknowledgements
This research was supported by The Scientific and Technological Research Council of Turkey (TUBITAK) TEYDEB 1505 program with project number 5220120.

References

Cheng, Y., Yu, J., Yan, G., & Qian, S. (2022). Improving temperature uniformity in a large frost-free chest freezer. *International Journal of Refrigeration*, *141*, 12-20.

Dupont, J. L., (2019). The role of refrigeration in the global economy. 38th IIR-informatory note. https://inis.iaea.org/search/51010281 (Accessed on November 19, 2023).

Ezan, M. A., Doganay, E. O., Yavuz, F. E., & Tavman, I. H. (2017). A numerical study on the usage of phase change material (PCM) to prolong compressor off period in a beverage cooler. Energy conversion and management, 142, 95-106.

GfK Marketing., (2017) Major domestic appliances – world market estimation. Nuremberg (Germany): GfK Retail and Technology GmbH. https://www.gfk.com/blog/2017/07/strong-momentum-built-major-domestic-appliances-opportunity-brands (Accessed on November 19, 2023).

Ghodrati, A., Zahedi, R., & Ahmadi, A. (2022). Analysis of cold thermal energy storage using phase change materials in freezers. Journal of Energy Storage, 51, 104433.

Harrington, L., Aye, L., & Fuller, B. (2018). Impact of room temperature on energy consumption of household refrigerators: Lessons from analysis of field and laboratory data. *Applied energy*, *211*, 346-357. https://doi.org/10.1016/j.apenergy.2017.11.060

Laguerre, O., Amara, S. B., Moureh, J., & Flick, D. (2007). Numerical simulation of air flow and heat transfer in domestic refrigerators. Journal of food engineering, 81(1), 144-156.

IEEES-046

Analyzing the Lean Burn Combustion Stability by Hydrogen Induction in Gasoline Direct Injection Engine

[1]Jerome Stanley M, [1]Leenus Jesu Martin M, [1,2*]Edwin Geo Varuvel
[1]Green Vehicle Technology Research Centre, Department of Automobile Engineering,
SRM Institute of Science and Technology, Kattankulathur, Tamilnadu, 603203, India.
[2]Department of Mechanical Engineering, Faculty of Engineering and Natural Sciences,
Istinye University, Istanbul 34460, Turkey
*E-mails: vedwingeo@gmail.com

Abstract

The combustion stability of the small-bore Gasoline Direct Injection (GDI) engine at extended lean burn combustion is investigated experimentally. The intake manifold is slightly modified to accommodate the hydrogen induction of about 6 to 12 lpm, where mixture of hydrogen and air is formed in the intake manifold, attaining the excess air ratio of 1.29 to 1.56. With the increment of hydrogen fraction the fuel leaning (Gasoline) is attained and achieving economical fuel consumption rate. The hydrogen fraction decreases the coefficient of variance, and it was found to be within the limit of 5%. For the lean limits it was found that the peak pressure of the lean air fuel ratio was reduced consistently. The spark timing was optimized for the lean limit with hydrogen addition to attain the maximum brake torque and CA 50 location of the mass fraction burn. Hydrogen induction improves the combustion rate and mean effective pressure; shortens the flame propagation, maximize the heat release rate and peak pressure attainment. On the emission side there is a consistent decrease in CO and HC emission; and increase of NOx emission since the mean gas temperature has increased. The cycle-to-cycle variation during the lean operating condition at 1.56 shows combustion stability and effective flame propagation.

Keywords: Hydrogen Induction, Small Bore, Gasoline Direct Injection, Coefficient of Variance, Lean Combustion.

I.Introduction

The reputation of Internal Combustion Engine in recent days with fossil fuel as the working fuel has been has been in the downfall as the intense promotion of electric vehicle technology. The transportation sector contributes to 10% of the greenhouse gas (GHG) emission which makes it meager when compared to the energy sector [1]. The 100 years of scientific improvement in engine technology makes it more mature than other recent alternative technologies. It is clear those alternatives to compete with IC engine do not cover the vast range of application. A lot of times the blame of the IC engine is about the source of the working fuel and not on the IC engine technology. Compared with conventional fossil fuels hydrogen pose superior characteristic and more suitable for SI engine, where it offers wider flammability range with high diffusivity and low ignition energy. With the safety precaution and advancement towards the storage of hydrogen makes it viable option for alternate for fossil fuels. From the prior arts it is found that adding little quantity of hydrogen with the conventional fuels offers better heat release rate, stable lean mixture formation and improved combustion efficiency. Further it shortens the delay period and offers peak pressure attainment close to top dead center (TDC). The cycle-to-cycle variation of the engine operating behavior was also reduced with the addition of hydrogen with gasoline. On the emission side significant reduction in CO and HC emission was noticed; with some penalty on NO_x emission, but particulate emission in the direct injection gasoline has consistent reduction with addition of hydrogen. The implementation of direct fuel injection technology in SI engine is one of the advancements that pushes the limits of SI engine in terms of its thermal efficiency, power performance, emission, and lean operating limits [2]. The gasoline direct injection (GDI) engines are getting more robust since the research advancement was towards various combustion modes, alternate fuels, dual spark ignitions, plasma ignition, dilution techniques to treat emission, in-cylinder water injection, fuel injector study, dual fuel injection, combustion diagnosis and furthermore [3]. The Gasoline Direct Injection (GDI) Engine is known for its economical fuel consumption, improved thermal efficiency and better torque characteristic. Application of GDI technology for small bore engine increases the operating limits of the engine for the light commercial vehicles (LCV) and two-wheeler segment; where this percentage of vehicles in Indian roads are higher in meeting the daily commutation. The GDI technology and the usage of Hydrogen as the primary/secondary fuel paves the path towards the lean combustion technology, wherein the real problems associated with the driving condition will be addressed [4]. On roads most of the engines are operated only at the partial load conditions, wherein the actual efficiency of the engine is poor due to the poor load characteristic, throttling effect and traffic conditions (start and stop). Leaning the gasoline by operating the engine under lean conditions leads to other technical issues like overheating engine misfire and unstable combustion [5]. Addition of hydrogen for the lean operating condition of GDI engine provides more stable combustion and significant reduction in the cycle-to-cycle variations will be attained. After accessing the prior literature, the author aims for hydrogen-gasoline lean burn combustion for small bore GDI engine, with the performance, emission evaluation. The effect of lean burn combustion with addition of hydrogen in gasoline and the lean limit estimation with stable combustion is also investigated.

II. Experimental Apparatus And Methods

Experimental Apparatus

The engine used for the present investigation is the 390 cm^3 small bore single cylinder air cooled GDI engine. The layout of the experimental setup is shown in Fig. 1. The engine was originally available as the carburetor engine, Honda make; it was later modified to direct injection gasoline engine. The engine head was modified to support the GDI injector, throttle control was replaced with the electronic actuator and to control the spark and injection timing, an Electronic Control Unit (ECU) was fitted. To make the close-loop system CAM and crankshaft position (CKP) sensors were additionally fitted with fuel rail pressure control. The modification details of the engine were

not included since it is beyond the scope of the article. The engine details are listed in the Table 1. The spark plug location in the engine is at the sides with hemispherical type combustion chamber. The piston head was not modified, production type flat piston head was maintained throughout the investigation. The spray guided fuel injector was used and it was fitted near the spark plug. The details of the fuel injector and pump are listed in the Table 2. The water cooled eddy current type dynamometer was used to load engine for operating conditions. To measure the inlet air HFM (Hot Film) Type T-MAF Sensor was employed and the gravimetric type fuel flow measuring system was used to calculate the fuel consumption by the engine. Contact type encoder was coupled with the crankshaft, this was utilized to trigger the data acquisition system to record the various sensor data. Piezoelectric pressure transducer with the resolution of 0.1 crank angle degree (CAD) was employed to record the in-cylinder pressure data. Wideband Lambda sensor (from Bosch) LSU 4.9 was used to monitor the air fuel ratio and the exhaust gas temperature was monitored by K-type thermocouple. Di-gas analyser 444 (from AVL) was used to record the engine out emission.

Experimental Methods

The test condition for the investigation is 3000 rpm with 100% throttle opening, where the maximum brake torque was obtained for the given spark timing. The engine operating conditions are listed in Table 3. The hydrogen flow rates are estimated with the energy balance of not exceeding 50% by hydrogen and the maximum limit was set to 8 LPM. For the equivalence ratio of 1, the hydrogen flow rate was varied from 8 to 1 LPM and similarly the equivalence ratio was increased to 1.02 and 1.08. For the consistent increment in the equivalence ratio the subsequent gasoline leaning will be carried out.

Table 1. Engine Details

Particulars	**Details**
Make	M/s. Honda
No. of Cylinders	1
No. of Valves	2
Type of CAM	Single Overhead
Ignition	Spark
Bore*Stroke (mm)	88*64
Displacement (cm^3)	390
Compression Ratio	8.2:1
Induction	Naturally Aspirated
Rated Torque	24 Nm @3000 rpm
Rated Power	8 hp @3600 rpm
Cooling system	Air

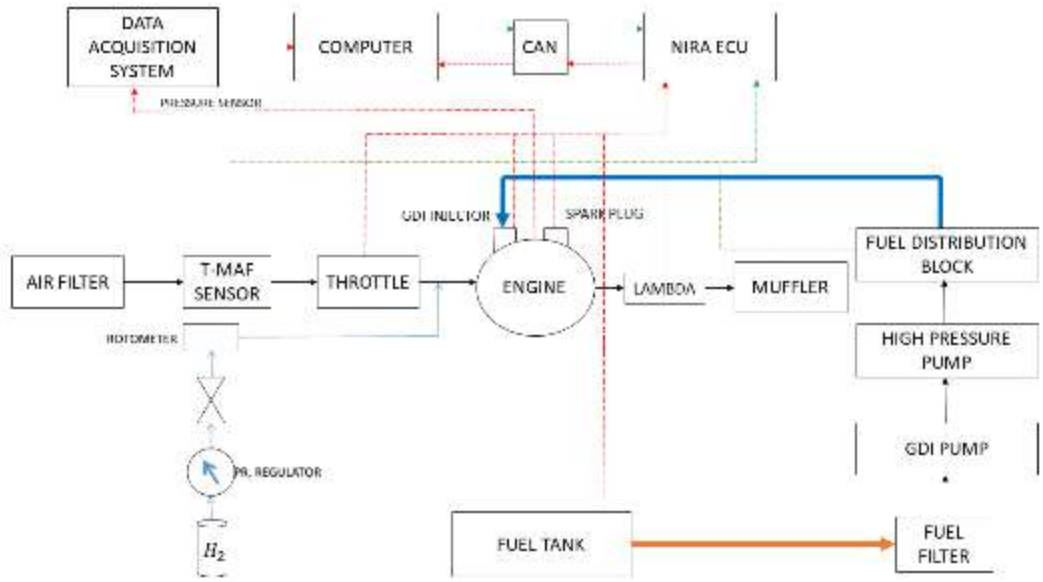

Fig. 1. Experimental Layout

III. Result And Discussion

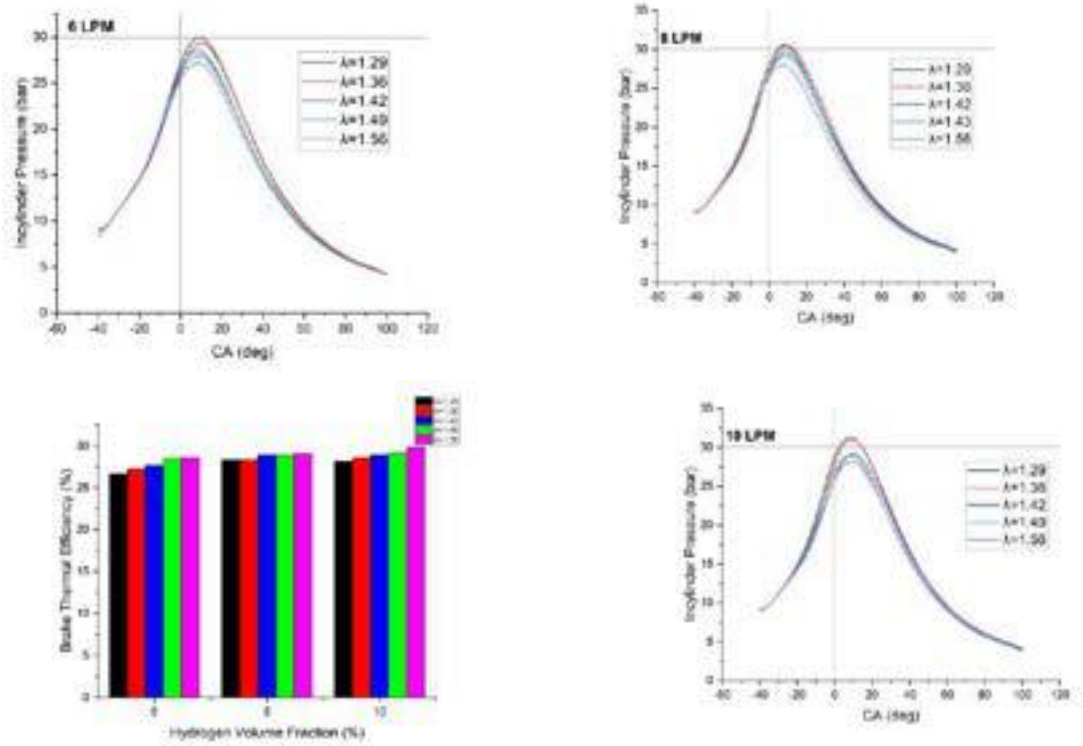

IV. Conclusion

1. The spark timing for the equivalence ratio for the given equivalence ratio was set as location of CA50, the peak pressure improved by 12%. Spark advancement beyond 37°CAD causes misfire in the engine.
2. The lean limit was engine was further increased to 1.56 with the air fuel ratio of 23 for the spark timing of 30°CAD bTDC as the hydrogen addition favour the combustion stability.
3. Engine operation with 100% wide open throttle, equivalence ratio of 1.29, 1.36, 1.42, 1.49 & 1.56 and the varied hydrogen fraction of 6 to 10 LPM has the significant effect on the engine performance, combustion, and emission characteristic. As the hydrogen fraction increases for the equivalence ratio significant increment in thermal efficiency and indicated mean effective pressure.
4. Engine operation with 100% wide open throttle, equivalence ratio of 1, 1.02 & 1.08 and with the increase in hydrogen fraction the combustion duration was shortened leading to peak pressure attained after TDC. Keeping the hydrogen fraction constant and increasing the equivalence ratio improves the heat release rate and consistent reduction in the delay period.
5. Engine operation with 100% wide open throttle, equivalence ratio of 1.29, 1.36 & 1.42 and with the increase in hydrogen fraction CO and HC emissions decreases and increment in NO_x emissions.. Keeping the hydrogen fraction constant and increasing the equivalence ratio, CO emission significantly reduces and HC emission reduces initially and increases in the later part. The NO_x emission has the adverse effect with the higher amount of hydrogen fractions.

References

1. Du Y, Yu X, Wang J, Wu H, Dong W, Gu J. (2016) Research on combustion and emission characteristics of a lean burn gasoline engine with hydrogen direct-injection. *International Journal of Hydrogen Energy*, 41(4):3240-8.
2. Eichhorn A, Lejsek D, Hettinger A, and Kufferath, A., (2013) From Challenge Determining a Combustion System Concept for Downsized SI-Engines - Comparison and Evaluation of Several Options for a Boosted 2-Cylinder SI-Engine, *SAE Technical Paper*. 2013-01-1730.
3. Gong C, Huang K, Jia J, Gao Q, Liu X., (2011) From Improvement of fuel economy of a direct-injection spark-ignition methanol engine under light loads, *Fuel*. 90:1826 to 1832.
4. Liu Y, Pei Y, Peng Z, Qin J., From Spray Development and Droplet Characteristics of High Temperature Single Hole Gasoline Spray, (2017) *Fuel*. 191:97-105.
5. Reitz R.D, Ogawa H, Payri R and Fansler T., (2019) From IJER Editorial: The Future of the Internal Combustion Engine, *International Journal of Engine Research*. 21:3-10.
6. Wang J, Huang Z, Tang C, Zheng J.,(2010) From Effect of hydrogen addition on early flame growth of lean burn natural gas-air mixtures, International Journal of Hydrogen Energy. 35:7246 to7252.

IEEES-047

Energy and Exergy Analysis of CLC Based Biomass Fired Power Plant With Different Oxygen Carriers

Shailesh Singh Sikarwar, *Ramsagar Vooradi, Venkata Suresh Patnaikuni, Manohar Kakunuri Surname
Chemical Engineering Department, National Institute of Technology Warangal, Warangal, 506004, India
*E-mails: ramsagar@nitw.ac.in

Abstract

The use of fossil fuels has led to the depletion of these non-renewable resources and a decline in environmental quality. This has encouraged a surge of interest in generating electricity from renewable sources. In recent years, the chemical looping combustion of biomass is gaining significant attention as this technology: operates as a carbon-negative solution, efficiently capturing CO_2 with minimal energy input, offers a promising alternative to traditional processes. In this work, a CLC based biomass fired power plant integrated with ORC cycle is analysed for electricity generation using Fe_2O_3, CuO, NiO, Co_3O_4 and mixed oxygen carriers. To increase process energy efficiency, a sensitivity analysis is performed to optimize important design parameters such as oxygen carrier flow rate, operating pressure and operating temperature of air, fuel and steam reactors. The performance of the different oxygen carriers is compared in terms of energy and exergy. The analysis reveals that the oxygen carrier in the form of blends could improve process economics, carbon conversion, redox characteristics and overall performance of the plant.

Keywords: Chemical looping combustion, biomass, oxygen carriers, CO_2 capture, ORC cycle.

I. Introduction

As per the International Energy Agency (IEA) 2010 recommendation, by the 2050th year, the CO_2 emissions from the power plants need to be reduced to 20% of the 2009 emissions. At present in most of the countries, coal is the primary fossil fuel source for power generation. The coal-fired power plants cause enormous greenhouse gas (GHG) emissions, hence the power sector has major share in anthropogenic CO_2 emissions. As fossil-based fuels still remain as our primary source of energy in this century, the emission of CO_2 into the atmosphere leading to climate change and global warming has become a global colossal issue, which requires immediate attention (Jain, 2019). India stands as the fourth largest emitter of CO_2 in the world after China, the US and the EU as per the EC, Emissions database for global atmospheric research, 2019. To curtail the CO_2 emissions and to limit the global temperature rise to 2 °C by end of this century as per the Paris agreement in CoP-21, 2015, countries should adopt multi-pronged strategies including use of alternative energy sources (e.g., solar, wind and geothermal) and renewable (e.g., biomass and biofuel); integration of CO2 capture, storage and utilization (CCS&U) and improving process efficiencies to reduce energy consumption (Razi and Dincer, 2022).

To effectively limit the global temperature, rise to the critical threshold of 2°C by the close of this century, the imperative is clear: a substantial shift towards renewable energy sources is paramount. This transition necessitates not only a reduction in the unrestrained consumption of fossil fuels but also a robust embrace of diverse renewable sources (Sharif et al. 2021). However, the prevailing strategy of centralized energy generation, particularly in the realm of electricity, proves to be an unsuitable avenue for the efficient harnessing of renewables, and this is attributed to a combination of compelling factors: (i) The requirement for ample space to accommodate high-capacity power plants stands as a significant limitation in the current context. The substantial land footprint needed for such installations raises concerns about the utilization of valuable areas and the environmental impact of such large-scale facilities (Rahman et al. 2022). (ii) Critical efficiency consideration revolves around heating applications. In this context, the direct utilization of renewable energy sources exhibits a clear advantage over the more intricate route of converting renewable energy to electricity and then further converting it to heat. This direct application approach is not only more straightforward but also ensures minimal energy losses in the transformation process. (iii) The intermittent nature of renewable energy, largely determined by geographical location and seasonal variations, creates a formidable challenge. The inconsistency in energy production from a single renewable source renders it inadequate to meet the continuous, centralized demand characteristic of the current energy consumption model. The reliance on a singular renewable source becomes impractical, necessitating a more diverse and adaptable approach. Though, the abundant availability of solar and wind energy serves as exemplary cases of these environmentally friendly resources, boasting zero carbon emissions. However, their inherent seasonality introduces challenges in maintaining a consistent power supply to meet continuous demand, particularly during periods of reduced sunlight or wind. To bridge this gap and ensure a dependable energy supply throughout the year, the utilization of biomass emerges as a compelling alternative (Hossen et al. 2022). Various forms of biomass, such as agricultural waste, forest waste, municipal solid waste, and sewage waste, can be harnessed for power production. This approach not only reduces dependence on fossil fuels but also serves as a reliable complement to solar and wind energy during off-seasons, thus addressing both energy requirements and waste management challenges simultaneously.

In the realm of advanced combustion technologies, Chemical Looping Combustion (CLC) has emerged as a standout contender, drawing significant attention as a highly promising option for thermal power plants. The distinctive feature of CLC lies in its impressive capability to simultaneously achieve minimal energy penalties and inherent 100% CO_2 capture, achieved through the utilization of efficient metal oxides as oxygen carriers. The fundamental concept of the CLC process is combining the oxy-combustion and pre-combustion capture techniques. Instead of direct air supply, CLC employs metal oxide/oxygen carrier particles to facilitate the conversion/oxidation of fuel into CO_2 and steam within the fuel reactor. This innovative approach has sparked heightened research interest in the combustion of gaseous, liquid, and solid fuels using CLC technology over the past few decades. In the CLC scheme, the sold/gaseous fuel and oxygen carrier are introduced directly into the fuel reactor. Within this reactor, fuel undergoes combustion, and the oxygen carrier is simultaneously reduced. The reduced oxygen carrier is subsequently re-oxidized in the air reactor in the presence of air. The resulting exit streams from the fuel and air reactors exhibit a CO_2 rich composition and a N_2 rich composition, respectively.

The block diagram for this two reactor configuration is shown in Figure 1. A wide range of oxygen-carrying metal oxides, including copper oxides, iron oxides, manganese oxides, and magnesium oxides, can be effectively employed within the two-reactor CLC system. Importantly, the CLC technology has not only found its place in conventional power generation but is also being actively explored for cogeneration applications (li et al. 2023).

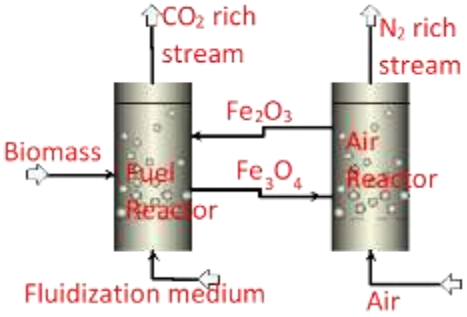

Figure 1: Schematic of CLC configuration

In summary, the imperative to restrict global temperature rise necessitates a multifaceted approach that leverages the immense potential of renewables. The development of adaptable and resource-aware smart energy systems, coupled with the strategic utilization of environmentally friendly resources and the integration of waste-to-energy principles, provides a comprehensive framework to achieve this critical goal. By embracing renewable diversity, optimizing energy usage, and mitigating environmental impacts, we can chart a course toward a more sustainable energy future, effectively combating climate change while ensuring reliable energy access for generations to come.

II. Modelling and simulation methodology

Figure 2 illustrates a comprehensive block diagram showcasing the operational architecture of a CLC-based BFPP. The core constituents driving this innovative system encompass several integral units, each playing a pivotal role in the overall process efficiency. The fundamental components within this advanced setup encompass a sizing and drying unit, a dual-reactor configuration utilizing Chemical Looping Combustion, intricate thermal oil and organic fluid loops, an Organic Rankine Cycle unit, gas turbine assembly, and a designated CO_2 compressor and storage unit. A noteworthy deference from conventional BFPP is the substitution of the standard combustor with distinct air and fuel reactors within the CLC-based framework. This alteration forms the foundation for enhanced efficiency and reduced emissions. The synergy of Chemical Looping Combustion, Organic Rankine Cycle, and gas turbine systems within the CLC-based BFPP configuration not only ensures sustainable energy production but also significantly reduces carbon emissions.

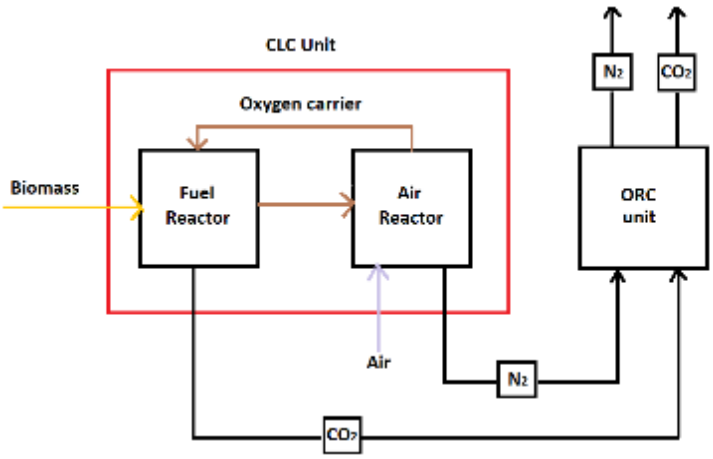

Figure 2. Block diagram of CLC integrated BFPP

The above presented configuration is simulated in Aspen Plus software using the appropriate models and necessary reference data from the literature. To enable the direct comparison between the conventional and CLC integrated BFPP configurations, similar unit models and common operating assumptions have been considered. In this analysis, the stream class MIXED defines the conventional fluids and the stream class CIPSD and NCPSD defines the conventional and non-conventional solids, respectively. The HCOALGEN and DCOALIGT are used as enthalpy models to define non-conventional components (coal and ash). Peng Robinson and Boston Mathias (PR-BM), Soave Redlich Kwong (RKS), Electrolyte NRTL, Ideal gas, and STEAMNBS were used for the estimation of properties of solid, electrolytes components in the CO2 capture process, air, flue gases, steam and water.

The performance of the proposed configurations are systematically analysed by evaluating different energy and exergy parameters. For steady flow processes, the mass and energy balances are shown in equations 1 and 2.

$$(\sum \dot{m}_n)_{in} = (\sum \dot{m}_n)_{out} \quad (1)$$

$$(\sum \dot{E}_n)_{in} = (\sum \dot{E}_n)_{out} \quad (2)$$

The plant net power ($\dot{W}_{net}$) is calculated by using equation 3, where, $\dot{W}_{gross}$ is the gross power output of turbine, $\dot{W}_{SOFC}$ is the AC power output of SOFC, $\dot{W}_{comp}$ is the energy consumption by air compressor, $\dot{W}_{pump}$ is the energy consumption by centrifugal pump and $\dot{W}_{aux}$ is the sum of all other auxiliary power consumptions.

$$\dot{W}_{net} = \dot{W}_{gross} + \dot{W}_{SOFC} - \dot{W}_{comp} - \dot{W}_{pump} - \dot{W}_{aux} \quad (3)$$

The net energy efficiency (η_{bp}) of biomass fired power plant is determined by using equation 4. The chemical energy of biomass ($\dot{E}_b$) is calculated by using the Higher Heating Value of biomass (HHV_b) in kJ/kg. In the HHV_b calculation as shown in equation 5, the carbon, H_2, oxygen and sulphur components weight percent are represented as C, H_2, O_2 and S, whereas m_b denotes the mass flow rate (kg/sec) of biomass in biomass fired power plants.

$$\eta_{bp} = \frac{(\dot{W}_{net.bp})}{(\dot{E}_b)} \quad (4)$$

$$\dot{E}_b = \dot{m}_b \times 338.3 \times C + 1443 \times \left(H_2 - \frac{O_2}{8}\right) - 94.2 \times S \quad (5)$$

The individual unit exergy efficiency and destruction are calculated in terms of kW using the equations 6 and 7, respectively.

$$Ex_d = (\sum Ex_{in} - \sum Ex_{out}) \quad (6)$$

$$Ex_{eff,unit} = \left(1 - \frac{Ex_d}{\sum Ex_{in}}\right) \times 100 \quad (7)$$

The net exergy efficiency of the biomass fired power plants (ψ_{bp}) is calculated by using Equation 8.

$$\psi_{bp} = \frac{Gross/Net\ power\ output}{\dot{m}_{coal} \times Specific\ exergy\ of\ the\ fuel} \quad (8)$$

III. Results and discusion

The proposed BFPP configuration is analysed by changing the oxygen carrier to biomass ratio, the operational pressure, and the operational temperature. This analytical endeavor inherently seeks to unravel the nuanced interplay between these variables and the overall system performance. The step by step improvement in process efficiency by the above sensitivity analyses has been presented for different oxygen carriers in Table 1.

Table 1: Optimal conditions for operating CLC integrated BFPP

Oxygen Carrier	OC-to-biomass ratio	Operating Pressure (Bar)	Air Reactor Operating Temperature (°C)
Fe_2O_3	54.43	11	1050
CuO	19.66	12	900
NiO	9.07	12	1100
Co3O4	27.22	7	750
CuO + Fe2O3	45.36	11	1050

Table 2 displays the energy and exergy efficiencies of CLC-based BFPP using various oxygen carriers. Among these, nickel-based oxygen carriers demonstrated the highest efficiencies, followed by copper-based and cobalt-based OCs. While Ni-based OCs exhibit greater reactivity, they have a lower oxidation rate in the air reactor. Additionally, these metal oxides are both toxic and expensive, making them less favourable as oxygen carriers. Cu-based metal oxides possess a high oxygen transfer capacity and reaction rates, without any thermodynamic limitations in achieving complete fuel conversion to H_2O and CO_2. However, these oxygen carriers are more expensive compared to iron-based, bauxite, perovskite, and pyrite cinder options. Therefore, in order to enhance the economic viability and energetic efficiency of the process, blends of metal oxides are being investigated. The inclusion of a fraction of Cu-based oxygen carrier in Fe-based oxygen carrier, enhanced the carbon conversion, redox characteristics, and overall performance of the plant.

Table 2: Efficiency of CLC integrated BFPP with different oxygen carriers

Oxygen carrier	Gross energy efficiency (%)	Net energy efficiency (%)	Gross exergy efficiency (%)	Net exergy efficiency (%)
Fe_2O_3	21.74	19.45	18.94	16.29
CuO	23.63	21.42	20.32	18.42
NiO	25.93	23.77	22.30	20.44
Co_3O_4	20.64	17.88	17.75	15.37
10% CuO + 90% Fe_2O_3	22.41	20.19	19.28	17.46

IV. Conclusion

This study is intended to demonstrate the feasibility of a chemical looping combustion of biomass based power plants for zero CO_2 emissions. The performance of CLC-integrated BFPP is compared using different oxygen carriers to find out the most suitable one. Nickel-based oxygen carriers exhibit higher reactivity but they exhibit a low oxidation rate in the air reactor, and furthermore, these metal oxides are toxic and expensive. Cu-based metal oxides have high oxygen transfer capacity and reaction rates with no thermodynamic restrictions to achieve 100% fuel conversion to H_2O and CO_2. These oxygen carriers are costlier than iron-based, bauxite, perovskite and pyrite cinder but, they are cheaper than cobalt and nickel based oxygen carrier. This makes Cu-based oxygen carriers more suitable for CLC applications than Fe-based oxygen carriers. Hence, addition of some fraction of Cu-based oxygen carrier in Fe-based oxygen carrier improves process economics, carbon conversion, redox characteristics and overall performance of the plant.

Acknowledgements
Financial support for this study was provided by a grant from the Scheme for Promotion of Academic and Research Collaboration (SPARC), Ministry of Education.

References

Hossen, M. D., Islam, M. F., Ishraque, M. F., Shezan, S. A., & Arifuzzaman, S. M. (2022). Design and implementation of a hybrid solar-wind-biomass renewable energy system considering meteorological conditions with the power system performances. International journal of photoenergy, 2022.

Jain, V. (2019). Fossil fuels, GHG emissions and clean energy development: Asian giants in a comparative perspective. Millennial Asia, 10(1), 1-24.

Li, G., Li, K., Ma, S., & Zhang, Y. (2023). Techno-economic analysis of a glycerol to methanol, ethylene glycol and 1, 2-propanediol cogeneration process integrated with biomass chemical looping hydrogen generation. Journal of Cleaner Production, 416, 137988.

Rahman, A., Farrok, O., & Haque, M. M. (2022). Environmental impact of renewable energy source based electrical power plants: Solar, wind, hydroelectric, biomass, geothermal, tidal, ocean, and osmotic. Renewable and Sustainable Energy Reviews, 161, 112279.

Razi, F., & Dincer, I. (2022). Renewable energy development and hydrogen economy in MENA region: A review. Renewable and Sustainable Energy Reviews, 168, 112763.

Sharif, A., Bhattacharya, M., Afshan, S., & Shahbaz, M. (2021). Disaggregated renewable energy sources in mitigating CO2 emissions: new evidence from the USA using quantile regressions. Environmental Science and Pollution Research, 28(41), 57582-57601.

IEEES-048

Impact of Biofuels on Maritime Decarbonization and Vessel Performance

[1*]Emir Ejder, [2]Hasan Göler, [3]Ergün Demirel
[1] Istanbul Technical University, Maritime Faculty, Tuzla, Istanbul, 34940, Turkey
[2,3] Piri Reis University, Faculty, Maritime Faculty, Tuzla, Istanbul, 34940, Turkey
*E-mails: ejder18@itu.edu.tr

Abstract

The marine industry tends to transition from traditional marine fuels to more sustainable and environmentally friendly fuels. The transition is particularly critical in line with Greenhouse Gas Emissions (GHG) reduction targets. The GHG Strategy established by the International Maritime Organization (IMO) aims to accelerate this transformation by promoting low-emission fuels. To evaluate the potential and impacts of biofuels in the maritime sector, data from an RO-RO vessel using B100 biofuel during three months of sea voyages are analysed. The study also examines the possible effects of the energy density of biofuel on fuel consumption. According to the well-to-wake (WtW) approach, the use of biofuels has the potential to reduce carbon dioxide (CO_2) emissions by up to 82%. The findings demonstrate that biofuels can be a technically and operationally effective alternative for the transition to alternative fuels in the maritime sector.

Keywords: Decarbonization, Alternative Marine Fuels, Emission Reduction, Biofuels.

I.Introduction

The maritime transport sector, which is at the center of global trade, constitutes the backbone of the world economy. More than 80 percent of the merchandise volume of international trade is transported by sea, even higher for developing countries (UNCTAD, 2023). The increase in carbon emissions from this sector is of concern in the context of environmental sustainability and combating climate change. GHG emissions from the maritime sector account for 3 percent of the global total and have increased by 20 percent over the last decade (IMO, 2020). This has fuelled interest in alternative energy sources, necessitating the development of innovative strategies aimed at reducing the sector's carbon footprint.

In particular, the research and development of sustainable energy sources that can replace fossil fuels form the basis of these new strategies. Hydrogen, ammonia, methanol, and liquefied natural gas (LNG) are among the alternative fuel types (Ejder & Arslanoğlu, 2022; Harahap et al., 2023). The International Maritime Organization's (IMO) goal of achieving net zero greenhouse gas emissions from international shipping by 2050 further increases the importance of such innovative solutions (IMO, 2023). Alongside these efforts, biofuels also stand out with their potential to reduce environmental impacts. Biofuels produced from vegetable oils, animal fats, and biological wastes can contribute positively to the carbon cycle in the atmosphere. Biofuels such as biodiesel and bioethanol are presented as sustainable alternatives to fossil fuels and attract attention with their potential for use especially in the transport sector. The sustainability of biofuels varies according to the nature of the source material, production processes, and application areas. Second and third-generation biofuels have the potential to further reduce environmental impacts by being produced from more sustainable sources such as waste materials and microalgae.

The use of biofuels in the maritime sector can have a significant impact on global carbon emissions. Biofuels derived from plant sources absorb carbon dioxide (CO_2) from the atmosphere in the process of photosynthesis and this carbon is released again in the combustion process of the fuel. This balanced carbon cycle can significantly reduce the net carbon emissions of biofuels. Biofuels such as biodiesel and bioethanol can replace or blend with fossil fuels, thus helping to reduce greenhouse gas emissions in the maritime sector. However, factors such as the energy density of biofuels, and storage and transport costs affect the applicability and cost-effectiveness of this technology in the maritime sector (Neupane, 2023).
Difficulties in the production and application processes of biofuels are important factors limiting the widespread use of the technology. The type of feedstock directly affects the properties and efficiency of biofuels. While second and third-generation biofuels reduce environmental impacts when produced from sustainable sources, production processes need to be optimized in terms of cost and efficiency (Singh et al., 2020a). The complexity and cost of production processes are among the factors limiting the commercial viability of biofuels.
To promote the widespread use of biofuels in the maritime sector, policymakers and industry leaders need to take an active role. Regulations to reduce the environmental impacts of biofuel production and utilization processes will support the sector in achieving its carbon footprint reduction targets. Economic incentives and research and development programs can encourage wider adoption and effective use of these innovative fuel solutions This will accelerate the evolution of the maritime sector towards a carbon-neutral future and will be an important step in the fight against global climate change (Segovia Hernández et al., 2022).
In the decarbonization process, the transition of the maritime sector to sustainable and environmentally friendly fuels plays a critical role in achieving global climate targets. B100 biofuel, one of the options for this transformation, stands out as an important alternative with both advantages and disadvantages. Experiments using B100 biofuel during a three-month sea voyage comprehensively address the effects of this fuel on energy density and CO_2 emissions. This research aims to provide valuable information to shipping companies in the decarbonization process about the use of biofuels and their environmental impacts.

This analysis is important for the energy efficiency, emission reduction potential, and operational viability of biofuels. Furthermore,

the potential of this approach to reduce the carbon footprint of the maritime industry and promote environmentally friendly practices is an important guide for policymakers and businesses in the industry. This study provides a basis for both academic and applied research and has the potential to contribute to the maritime industry to achieve its sustainability goals.
The rest of this article is organized as follows: Information on biofuels is given in Section II. Analyses of biofuels are discussed in Section III. Section IV contains a detailed discussion and presentation of the findings.

II. Research Method

The aim of the study is to investigate the effectiveness of gas emissions and competency of energy efficiency for the use of biofuel on board merchant ships.
This study is based on a life experiment conducted on board a selected ship and findings will be analysed in terms of both reduction of gas emissions and negative impact of energy efficiency. The research questions are;

- Investigate reductions of gas emissions.
- Evaluation of energy losses as use of biofuels

III. Research

III.I Literature Review

Recent studies have comprehensively assessed the environmental impacts, performance, and viability of biofuels in reducing carbon emissions in the transportation and maritime sectors. (Watanabe et al., 2022) assesses the potential of drop-in and hydrogen-based biofuels to decarbonize European maritime transport. Using a multi-metric approach and life cycle assessment, the study finds that both biofuel options have the potential to reduce greenhouse gas emissions. It also notes that drop-in biofuels have the potential for more widespread use and hydrogen-based biofuels have a higher potential for deeper decarbonization through carbon capture and storage. (Kim & Choi, 2023) investigate the feasibility of using bio-heavy fuel (BH20) as an alternative to conventional marine fuels. The research evaluates engine performance and emissions tests and environmental impacts and shows that BH20 can reduce NO_X and CO_2 emissions, improve engine performance and durability, and is compatible with existing ship facilities. (Kalavathy et al., 2022) present a techno-economic analysis of biofuel production from seaweeds. The study includes an analysis of production costs and provides examples of bioethanol production from seaweed biomass, noting that the production cost for biodiesel accounts for a large proportion of the total cost. (Stathatou et al., 2022) examine the emission impacts of biofuel blends used on dry cargo ships. The study finds that the biofuel blend has lower particulate matter, carbon monoxide (CO), and hydrocarbon (HC) emissions than conventional fossil fuels and shows that the ship's performance and efficiency are similar when using low-sulphur Marine Gas Oil (MGO). (Yang et al., 2022) investigate the effects of different biodiesel fuels on the combustion performance and emissions of marine diesel engines. Bench tests show that the use of biodiesel can reduce NO_X, carbon monoxide (CO), and particulate matter (PM) emissions but increase HC and CO_2 emissions. This study demonstrates the potential of biodiesel as a more sustainable fuel option for the maritime industry. (Rudko et al., 2023) discuss the impacts of biofuel use in marine diesel engines on their environmental and economic performance. The study shows that the use of biofuels in marine diesel engines can lead to a reduction in emissions and an improvement in economic performance, with the optimal blend being around 20-30% biofuels mixed with diesel fuel. These wide-ranging studies demonstrate the potential of biofuels as a sustainable and environmentally friendly fuel alternative in the marine sector. It also highlights challenges to their widespread adoption.

III.II. Use of Biofuels

The production of biofuels is based on biomass, in particular biological components derived from plant and animal sources. In this context, biodiesel, bioethanol, and bio-oils are analysed as four distinct generations with different characteristics. The development of these generations is based on the main drivers such as improving the energy and production efficiency of fuels (Saha et al., 2018).
First-generation biofuels are made from crops such as corn, wheat, and sugar cane, which are usually produced for human consumption. In this generation, sugar cane, sugar beet, or starch-containing crops and grains are preferred for bioethanol production. With this generation, bioethanol has become a substitute for gasoline worldwide.
Second-generation biofuels are produced from non-food crops that have the least impact on farmland. This generation uses materials such as wood chips, straw, and forestry waste. These feedstocks offer alternatives that are lower cost and less affected by market fluctuations (Lin, 2022).
The third generation of biofuel production takes place with alternative sources such as waste oils and especially algae. Algae is characterized by its high lipid and carbohydrate content and provides high-quality energy while creating less environmental pollution than other generations. The fourth generation of biofuel production aims to extract biofuels from microorganisms and plants using genetic engineering and systems biology techniques.
Energy from biomass is stored as biofuels. They are based on by-products of biomass resources used for energy production. Biodiesel is derived from vegetable oils such as sunflower, soybean, rapeseed, palm, and castor oils among first-generation bioenergy sources, while second-generation sources are feedstock sources (Singh et al., 2020b).

IV. Application and Results

This study evaluates the effectiveness of the use of sustainable energy sources in the maritime sector, specifically analysing biofuel trials carried out on a commercial RO-RO vessel. Test performed from Oct 2022 to Jan 2023 on an RO-RO vessel with 209 meters length, 11978 DWT, built in 2017 and uses Ultra Low Sulphur Content Fuel Oil (ULSFO). During the three-month period, the vessel's main engines were fuelled with biofuel, while the auxiliary engines and boiler were fuelled with Marine Gas Oil (MGO). The aim of the trial was to evaluate the energy efficiency, emission profile, and overall operational effectiveness of the biofuel.
Figure 1 shows the speed-consumption trend during the use of biofuel B100 compared to the pre-trial period. The trend lines show that there is about 14% higher consumption during biofuel use, which supports the energy content difference.

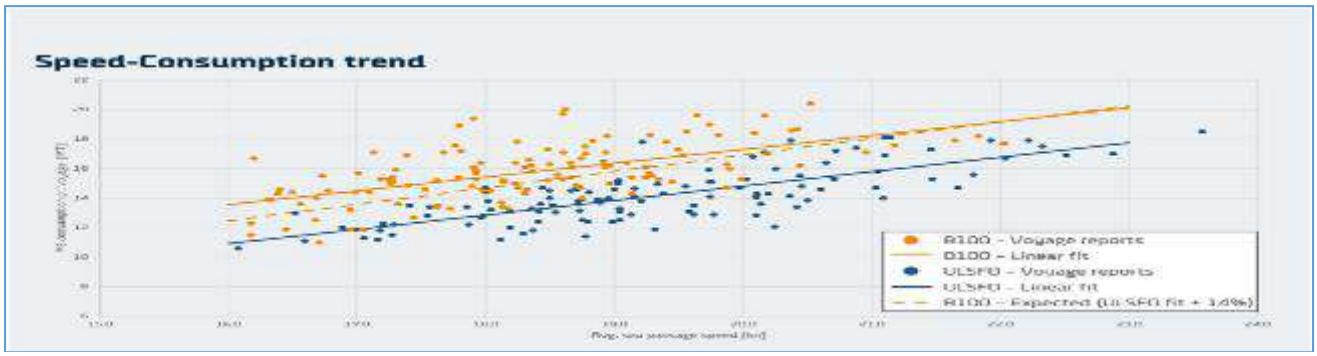

Fig.1: Speed-consumption trend for biofuel B100 trial and the pre-trial period on ULSFO.

During the trial, the vessel traveled at an average speed of 5% lower compared to the three-month period prior to the trial. This reduction in speed affected the fuel consumption and the main engine consumption caused only an 11% increase in the average fuel consumption per voyage. Figure 2 shows the consumption and speed per voyage, where it can be seen how the consumption increases and how the decrease in speed is observed, but it is not as pronounced as the difference in consumption.

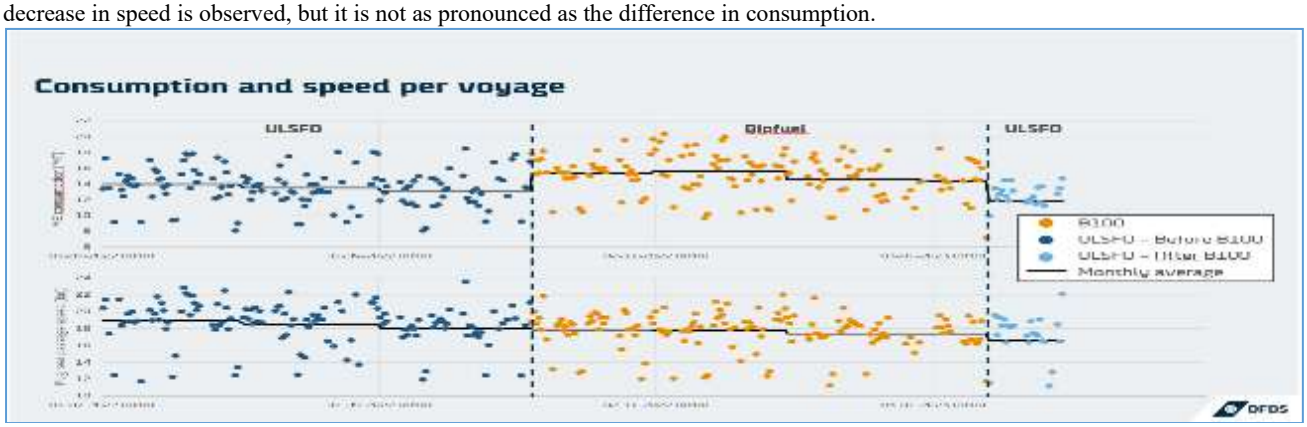

Fig.2: Consumption and speed per voyage over time during the biofuel B100 trial, pre-trial and post-trial period.

Well-to-Wake (WtW) and Tank-to-Wake (TtW) calculation methods were applied to assess changes in CO_2 emissions. The analyses revealed that the biofuel achieved a reduction of 5,297 metric tonnes of CO_2 equivalent over its life cycle on a Well-to-Wake basis, which corresponds to a WtW CO2e reduction of 82%. Calculations on a tank-to-Wake basis showed that the biofuel trial contributed to a total of 5,918 metric tonnes of CO_2 emission reductions. In the Tank-to-Wake calculations, the B100 biofuel was considered zero-emission, resulting in a TtW CO_2 reduction of 100%. This explains the higher Tank-to-Wake savings than Well-to-Wake savings.
In terms of energy efficiency, it was observed that biofuel consumed approximately 14% more to achieve the equivalent energy level compared to ULSFO. This result was based on pre-trial ULSFO tests and biofuel samples taken during the trial. The average energy content of ULSFO was 42.5 MJ/kg, while the energy content of biofuel was 37.2 MJ/kg. This shows that, despite the advantage of the reduced carbon footprint of biofuel, it needs to be consumed in higher volumes to achieve energy balance. Therefore, a 14% higher fuel requirement when replacing ULSFO with B100 biofuel was included in the Well-to-Wake analysis. The energy content of different fuel types is an important parameter when assessing the environmental impacts of fuel switching.

V. Conclusion

The aim of the trial was to evaluate the energy efficiency, emission profile, and overall operational effectiveness of the biofuel. The findings obtained within the scope of the study show the potential of Biofuels, which are considered as one of the sustainable energy sources in the maritime sector. Biofuels and/or Biofuel blends with fossil fuels can be considered as a reliable and efficient energy source and the capacity of second-generation sustainable biofuels to significantly reduce CO_2 emissions emphasizes the importance of sustainable energy solutions during the green transition period of the shipping industry. However, further research and development in energy efficiency, storage, and management are required for the large-scale adoption of biofuels.

References

Ejder, E., & Arslanoğlu, Y. (2022). Evaluation of ammonia-fueled engine for a bulk carrier in marine decarbonization pathways. *Journal of Cleaner Production*, *379*, 134688. https://doi.org/https://doi.org/10.1016/j.jclepro.2022.134688

Harahap, F., Nurdiawati, A., Conti, D., Leduc, S., & Urban, F. (2023). Renewable marine fuel production for decarbonized maritime shipping: Pathways, policy measures and transition dynamics. *Journal of Cleaner Production*, *415*, 137906. https://doi.org/https://doi.org/10.1016/j.jclepro.2023.137906

IMO. (2020). *Fourth IMO GHG Study 2020*.

IMO. (2023). *MEPC.377(80), 2023 IMO Strategy on Reduction of GHG Emissions From Ships*.

Kalavathy, G., Pandey, A., Gnansounou, E., & Gurunathan, B. (2022). Technoeconomic analysis of biofuel production from marine algae. In *Biofuels and Bioenergy: A Techno-Economic Approach* (pp. 627–652). Elsevier. https://doi.org/10.1016/B978-0-323-90040-9.00012-6

Kim, J. S., & Choi, J. H. (2023). Feasibility study on bio-heavy fuel as an alternative for marine fuel. *Renewable Energy*, *219*. https://doi.org/10.1016/j.renene.2023.119543

Lin, C. Y. (2022). The Influences of Promising Feedstock Variability on Advanced Biofuel Production: A Review. In *Journal of Marine Science and Technology (Taiwan)* (Vol. 29, Issue 6, pp. 714–730). National Taiwan Ocean University. https://doi.org/10.51400/2709-6998.2552

Neupane, D. (2023). Biofuels from Renewable Sources, a Potential Option for Biodiesel Production. *Bioengineering*, *10*(1). https://doi.org/10.3390/bioengineering10010029

Rudko, A., Sagin, S., Karianskyi, S., Madey, V., Sagin, A., Stoliaryk, T., & Tkachenko, I. (2023). Marine Science and Engineering Impact of Biofuel on the Environmental and Economic Performance of Marine Diesel Engines. *J. Mar. Sci. Eng*, 11. https://doi.org/10.3390/jmse

Saha, S., Sharma, A., Purkayastha, S., Pandey, K., & Dhingra, S. (2018). Bio-plastics and biofuel: Is it the way in future development for end users? In *Plastics to Energy: Fuel, Chemicals, and Sustainability Implications* (pp. 365–376). Elsevier. https://doi.org/10.1016/B978-0-12-813140-4.00014-5

Segovia Hernández, J. G., Gómez-Castro, F. I., Romero-Izquierdo, A. G., Conde-Mejía, C., & López-Molina, A. (2022). Partial energy integration between biofuels production processes: Effect on costs, CO2 emissions and process safety. *Process Safety and Environmental Protection*, *159*, 918–930. https://doi.org/10.1016/j.psep.2022.01.069

Singh, D., Sharma, D., Soni, S. L., Sharma, S., Kumar Sharma, P., & Jhalani, A. (2020a). A review on feedstocks, production processes, and yield for different generations of biodiesel. In *Fuel* (Vol. 262). Elsevier Ltd. https://doi.org/10.1016/j.fuel.2019.116553

Singh, D., Sharma, D., Soni, S. L., Sharma, S., Kumar Sharma, P., & Jhalani, A. (2020b). A review on feedstocks, production processes, and yield for different generations of biodiesel. In *Fuel* (Vol. 262). Elsevier Ltd. https://doi.org/10.1016/j.fuel.2019.116553

Stathatou, P. M., Bergeron, S., Fee, C., Jeffrey, P., Triantafyllou, M., & Gershenfeld, N. (2022). Towards decarbonization of shipping: direct emissions & life cycle impacts from a biofuel trial aboard an ocean-going dry bulk vessel. *Sustainable Energy and Fuels*, *6*(7), 1687–1697. https://doi.org/10.1039/d1se01495a

UNCTAD. (2023). *Review of Maritime Transport 2023*. https://shop.un.org/

Watanabe, M. D. B., Cherubini, F., Tisserant, A., & Cavalett, O. (2022). Drop-in and hydrogen-based biofuels for maritime transport: Country-based assessment of climate change impacts in Europe up to 2050. *Energy Conversion and Management*, *273*. https://doi.org/10.1016/j.enconman.2022.116403

Yang, N., Deng, X., Liu, B., Li, L., Li, Y., Li, P., Tang, M., & Wu, L. (2022). Combustion Performance and Emission Characteristics of Marine Engine Burning with Different Biodiesel. *Energies*, *15*(14). https://doi.org/10.3390/en15145177

IEEES-049

A Effective Moisture Diffusivity of a Hybrid Double Pass Collector-Solar Dryer For Tomato Slices Drying

[1*]Korti A.N., [1]Guellil H.
[1]ETAP Laboratory, University of Tlemcen, Faculty of Technology, Department of Mechanics BP 230,13000, Algeria
*E-mails: korti72@yahoo.fr

Abstract

In present study, a hybrid drying system incorporating a double passes solar collector and an electric auxiliary heater was developed to make advances in tomato drying. The dryer was made to operate in a combined mode with solar energy as the main energy source, and the auxiliary heater was used during the absence of solar radiation or limitation in generated solar power. It was found that in hybrid indirect solar dryer, tomatoes slices reaches to equilibrium moisture content of 8.9% (wet basis) from 94% (wet basis) of initial moisture content in just 7h of drying time. Whereas in the same time it reaches to 8.4 % (wet basis) for open sun drying, respectively. It was also observed that the highest temperature was achieved by upper tray. During strong sunshine, the drying ratio is the highest in the case of open drying with 2.67 g/min. During low sunlight, the hybrid drying become most efficient way of drying when compared to open sun drying.

Keywords: hybrid solar Drying, Reneweble energy, experimental data analysis, solar collector, environment.

I. Introduction

"Noting that about 1/3 of food produced is wasted or lost in post-harvest processing. Drying is widely accepted as an important preservation technique for agricultural products. It is one of the most attractive and cost-effective application of solar energy. In natural sun drying, the products are exposed directly to sunlight. It is widely used because it is cheap, easy and convenient. Nevertheless, the products are subject to degradation of quality due to the intermittence of climatic conditions and to the action of insects and animals. Drying under controlled conditions of temperature and humidity helps the agricultural products to dry reasonably rapidly to safe moisture content and to ensure superior quality of the product. The solar dryers are subdivided in mixed-mode, hybrid, direct, and indirect solar dryer types. In the hybrid dryer type, the solar dryer may be supplied by an auxiliary heat from other energy sources to decrease the dehydrating period and advance the moisture removal process
A hybrid drying system incorporating a compound parabolic concentrator solar collector was developed by Ebadi [1] and the quality of dried tomatoes was determined. They reported that the minimum drying time was achieved as 83 min for samples of 4 mm thickness with 0.04 m3/s airflow rate and 75 °C drying temperature. The hybrid system showed excellent responses to changes in solar radiation. The minimum fraction of CPC solar collector was achieved in the highest load operation with nearly 30%. An energy and exergy analysis of the drying process of corn was developed by Silva [2] for a hybrid dryer coupled with a PV system. It was found that the hybrid dryer was able to successfully dry the corn in 8.5 h, while natural sun drying failed to achieve the final desired moisture content in 24 h. The PV system significantly increased the air temperature at the inlet of the solar collector and can reaches a maximum increase of 19°C. A Parabolic hybrid active greenhouse solar dryer embraced with a solar air heater has been designed and fabricated by Koli [3]. They concluded that the average drying room temperature by using the solar air heater is 40.1 °C, which is 4 °C and 11.8 °C higher than without solar air heater and ambient air temperature. The drying time of green chilli in the case of with solar air heater is 31 h, while without solar air heater and open sun drying take 40 h and 48 h, correspondingly. Krabich [4] carried out on drying kinetics and quality of dried orange slices in three indirect solar dryers with natural convection, to compare the thermal performance of solar dryers. With the conventional configuration of solar dryer it was possible to dry the oranges with an evaporation rate of 72.7% after 15 days of drying. However, due to the presence of the air collector, its cost is relatively high. Composed by a lower floor with double glazing to heat the air and an upper floor constituting the drying place, the drying of the oranges took 18 days to reach an evaporation rate of 72.3% with the second solar dryer. The third solar dryer, consisting of a single compartment and absorber walls, appears to be more efficient and the drying of the oranges took 6 days to reach an evaporation rate of 72.77%. An experimental analysis of hybrid dryer combined with spiral solar air heater is investigated by Heydari [5]. It concluded that the approximate time of drying process is 12.5 h for apple slices, 23.5 h for kiwi and banana slices and 24 h for quince strips. The maximum and the minimum drying rate are related to apple crop which is 0.3224 kg/h and kiwi slice which is 0.188 kg/h respectively.

II. Materials and methods

In this work, tomatoes were experimentally dried and tested inside a forced-ventilation solar-indirect cabin hybrid dryer. This system employs a double passes solar collector using an absorbing wavy plate which is completely painted in black for maximum absorption of solar energy. An electrical heating element that acts as a complementary section aids the drying process during the deficit of sun energy. After supplying the lack of heat by the heating element, air flows into the dryer cabin and passes through the crops in separate trays. Finally, it is driven out of the system by the output fan located at the top of the drying cabinet. In order to minimize the amount of thermal loss, all walls of dryer chamber, and the entire collector were insulated using Rockwool insulation sheets. Temperature measurement was achieved using K type sensors installed in several positions to record air inlet temperature of collector ($T_{in,c}$), air outlet temperature of collector ($T_{out,c}$), glass cover temperature (T_g), absorber temperature (T_{abs}), ambient temperature (T_{amb}), air temperature inside the drying chamber (T_d), air inlet temperature of dryer chamber ($T_{in,d}$), and air outlet temperature of dryer chamber ($T_{out,d}$). The mean initial moisture was estimated as a 94% wet basis, and the final moisture of dried material was found as a 15% wet basis.

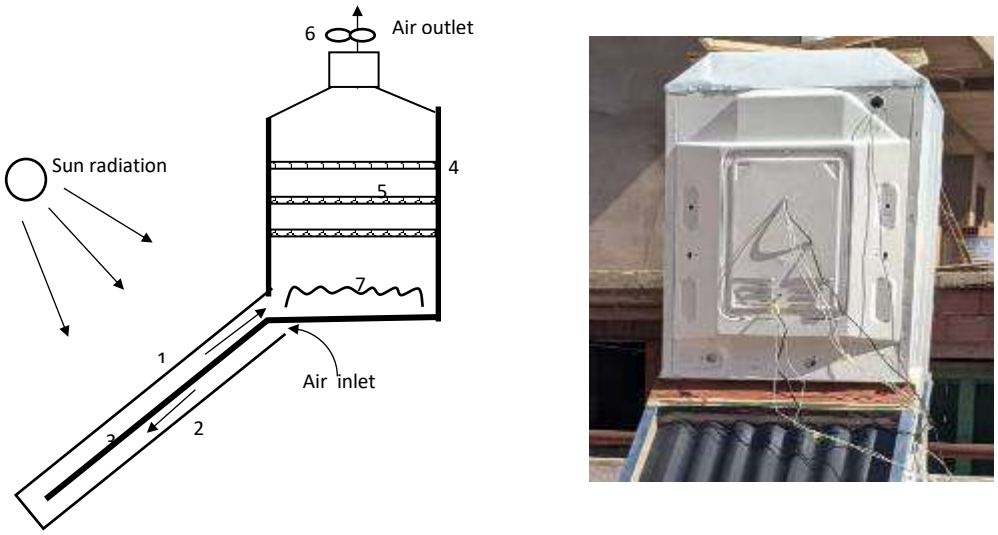

Fig. 1. Photo and Schematic view of the solar dryer: 1 glass cover, 2 solar collector, 3 absorber, 4 drying chamber, 5 crop trays, 6 air fan, 7 auxiliary heater.

Moisture content on a wet basis (M_w) can be determined by the ratio of the remained water inside the sample to the total weight of the initial sample. Therefore, the drying rate (DR) was obtained using the following expression

$$M_w = \frac{w_i - w_d}{w_i} \times 100 \quad (1)$$

where w_i is the wet matter or initial mass of the sample before drying and w_d indicates the mass of dry matter.

$$DR = \frac{M_{w+dt} - M_w}{dt} \quad (2)$$

III. Results and discussion

Fig. 2 shows the temperatures of various elements of the solar collector. The absorber records the higher temperature in the solar collector since it directly absorbs the solar irradiation transmitted by the glass cover. Thus, it represents the main natural thermal source of the collector and of the dryer system. The absorber temperature increases during the morning to reach maximum temperatures around 81°C between 13:00 and 13:30, it decreases quickly after 15:00 to reach 27°C at 19:30. The outlet air temperature exceeds 45°C during the period between 11:30 and 17:00. During this period, the solar collector provides the necessary thermal conditions to drying tomatoes without need the auxiliary thermal energy. Out this period, using the auxiliary thermal energy (hybrid system) becomes the solution to this deficit.

Fig. 3. Sows the air temperature trough the auxiliary heater. When the heater is off, the outlet air outlet temperature of the collector is higher than the inlet cabinet one due to the thermal losses. Thus, the solar collector is the only natural source supplying the dryer chamber between 12:00 and 17:00. The inlet chamber temperature remains higher than 45°C to ensure the drying of the product. Before 12:00 and after 17:00, the temperature at the inlet of the chamber is higher than that at the outlet of collector thanks to the thermal input from the electrical heater. The temperature fluctuations at the chamber inlet are due to heater on/off times.

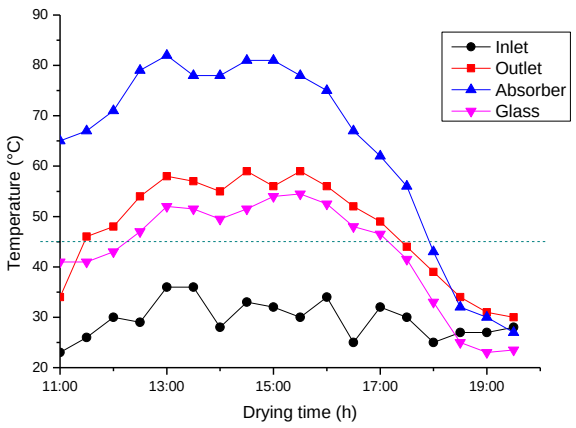

Fig. 2. Temperatures of various elements of the solar collector.

Fig. 4 shows the variation of moisture ratio of drying for hybrid indirect dryer and open sun drying. It can be seen that the moisture ratio shows remarkable changes with respect to time. Initially, fast evaporation of moisture from top surface of the product leads to high moisture removal means high moisture ratio, afterwards moisture removal or moisture ratio is low, as low moisture content available in the product decreases with time.
The initial moisture ratio of 94% (wet basis) for tomatoes samples were reduced to 0.2, 0.28 and 0.17 for bottom and top trays hybrid dryer and open sun drying, respectively in 5 h of drying. Thus, the measured moisture ratio for hybrid drying is higher than the open sun drying,

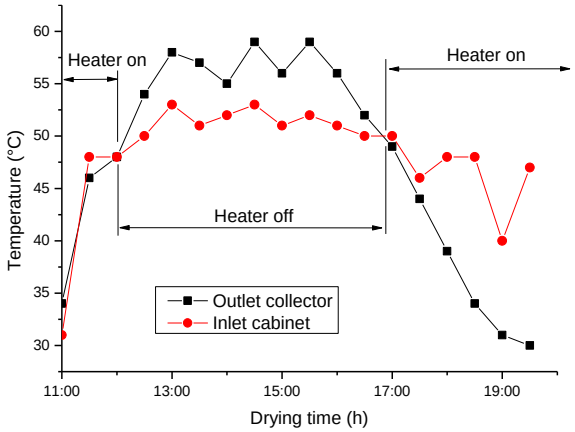

Fig. 3. Air temperature trough the auxiliary heater

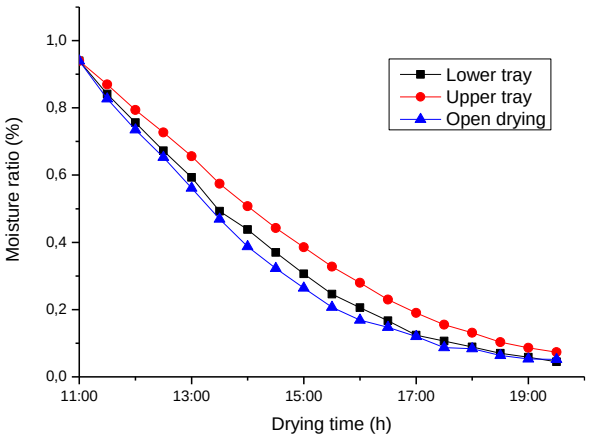

Fig. 4. Comparison of moisture ratio with time for hybrid dryer open sun drying.

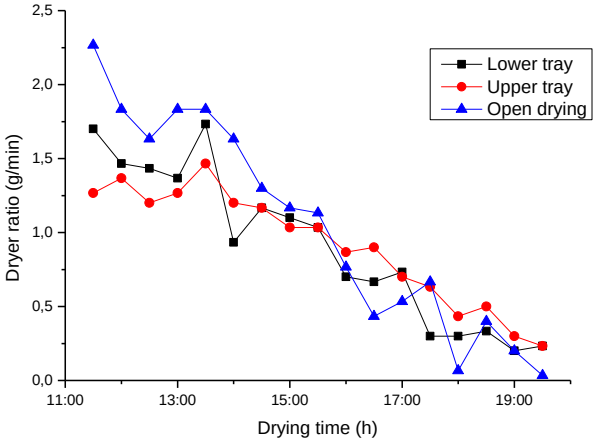

Fig. 5. Comparison of dryer ratio with time for hybrid dryer open sun drying.

Fig. 5 represents the plot of drying rate verses drying time. It has been found that the drying rate of open sun drying is faster than the hybrid dryer. It has been also observed that the graph is fluctuating in nature. This is due to its dependency on ambient temperature and solar radiation. It is noted that the drying ratio is higher in the case of open drying which starts with 2.67 g/min and ends by 0.033 g/min with a moisture ration of 5.18%. For the bottom tray-hybrid dryer, the drying ratio starts with 1.7 g/min and ends by 0.023 g/min and moisture ration of 4.46%. For the bottom tray, the drying ratio starts with 1.26 g/min and ends by 0.023 g/min and moisture ratio of 7.35%. Thus, open drying is faster than hybrid dryer. After 17:00, the drying ratio of the hybrid dryer increases and becomes higher the open sun drying thanks to the heat amount generated by the auxiliary heater. Hybrid solar drying is therefore a very effective solution to prolong operation time of indirect solar drying.

IV. Conclusion

A novel designed hybrid cabinet solar dryer using double passes solar collector integrating wavy absorber. The experiments were conducted from 11:00– 19:30 in month of April. The following conclusions have been observed from the present study:

1. The highest temperature of trays obtained as 51 °C for lower tray. It has been also noticed that 7 °C temperature difference has found in between lower and upper trays.
2. The initial moisture ratio of 94% (wet basis) for tomatoes samples were reduced to 0.2, 0.28 and 0.17 for bottom and top trays hybrid dryer and open sun drying, respectively in 5 h of drying.
3. At beginning, the drying ratio is the highest in the case of open drying with 2.67 g/min followed by lower and upper trays by 2.67 g/min and 1.26 g/min, respectively.
4. After 17:00, the drying ratio of the hybrid dryer increases and becomes higher the open sun drying thanks to the heat amount generated by the auxiliary heater. Hybrid solar drying is therefore a very effective solution to prolong operation time of indirect solar drying.

References

Hossein, E., Dariush, Z., Masoud A., Guangnan, C. (2021) Performance of a hybrid compound parabolic concentrator solar dryer for tomato slices drying, Solar Energy 215, 44–63

Gisele, M. S., Andre, G.F., Rogerio, M. C., Cristiana, B. M. (2020) Thermodynamic analysis of a sustainable hybrid dryer, Solar Energy 208 388–398

Chandra, S.K., Gaur, M.K., Pushpendra, S. (2022) Energy and exergy assessment of a novel parabolic hybrid active greenhouse solar dryer, Solar Energy 245 211–223

Krabch, H., Tadili, R., Idrissi, A. (2022) Design, realization and comparison of three passive solar dryers. Orange drying application for the Rabat site (Morocco), Results in Engineering 15 100532

Heydari, A. (2022) Experimental analysis of hybrid dryer combined with spiral solar air heater and auxiliary heating system: Energy, exergy and economic analysis, Renewable Energy 198 1162–1175

Amira, T., Saber, C., Fethi, Z., (2014) Moisture Diffusivity and Shrinkage of Fruit and Cladode of *Opuntia ficus-indica* during Infrared Drying, Hindawi Publishing Corporation, Journal of Food Processing, http://dx.doi.org/10.1155/2014/175402

IEEES-050

Production of Microencapsulated Thermochromic Systems Based on Fluoran Dye and Investigation of Their Thermal Properties

[1]Cemil Alkan, [2]Simge Özkayalar, [3]Sennur Alay Aksoy
[1] Tokat Gaziosmanpaşa University, Faculty of Science and Literature, Department of Chemistry, Taşlıçiftlik Campus, Tokat, 60250, Türkiye
[2] Dokuz Eylül University, Faculty of Engineering, Department of Textile Engineering, Tınaztepe Campus-Buca, İzmir, 35390, Türkiye
[3] Suleyman Demirel Üniversity, Faculty of Engineering, Department of Textile Engineering, West Campus Çünür, Isparta, 32260, Türkiye
*E-mail: cemil.alkan@gop.edu.tr

Abstract

Thermochromic materials change their color reversibly depending on change in temperature. Because of their temperature sensing property, thermochromic materials have attracted considerable interest in the production of chameleon-type building coatings, thermographic recording materials, strip thermometers, military, engineering science, thermal mapping and cosmetic industry. When thermochromic materials for different fields are examined, two groups of materials stand out in particular. These are ternary systems and liquid crystals. Ternary systems or thermochromic systems (TSs) compose of a color former (a leuco dye), a developer and a solvent. Their color change from colorless to colored at a given temperature depends on interaction of the color former and developer in an environment formed by a solvent. The solvent is a phase change material and it's melting and crystallization points determine color change temperatures of the system. Furthermore, the solvent provides the TS with a thermal energy storage function by storing and releasing latent heat during phase change processes. In this study, ternary systems composed of a fluoran dye (2'-(Dibenzylamino)-6'-(diethylamino) fluoran or 2-Anilino-6-dibutylamino-3-methylfluoran, phenolphthalein (PP) as a color developer, and 1-tetradecanol (TD) as a solvent were prepared. In order to increase UV light stability of the thermochromic system, a UV absorber (2,4-Dihydroxybenzophenone) was added in the system. Prepared thermochromic systems were microencapsulated in poly(methyl methacrylate) wall using emulsion polymerization method. The study focused on investigating the temperature regulation functions of microencapsulated TSs. In addition, the effect of increasing the amount of solvent in the system on the thermal energy storage temperature and capacity of microcapsules was investigated. The morphology of the microcapsules produced were investigated by SEM, thermal energy storage properties by DSC, thermal stability by TGA and temperature regulation functions by T-History test method. The temperature-sensitive reversible colour change properties of the capsules were demonstrated by photographs taken above and below the activation temperatures of TSs. SEM images revealed spherical morphology and homogeneous particle size of the capsules. According to the results of DSC analysis, the capsules have energy storage capacity ranging from 127 to 170 j/g at 34.2 ℃ and 35 ℃. Increasing the amount of 1-tetradecanol in TS significantly increased the melting point of the systems. According to the results of TG analysis, the thermal stability of the capsules is above 220 ℃. According to the T-history test results, encapsulated systems provided a cooling effect of more than 10 ℃ during heating.

Keywords: Thermochromic system, energy storage, phase change material, thermal property.

I. Introduction

Energy is essential for the survival and development of the human society. Excessive consumption of non-renewable fossil energy resources due to technological advances has led to increasingly serious environmental pollution (Liu et al., 2021). One of the possible methods to solve the problem of environmental pollution caused by the burning of fossil fuels is the use of renewable energy sources (Sipponen et al., 2020). Solar energy is an inexhaustible clean energy with the advantages of easy availability, abundant reserves and cleanliness, and the efficient use of solar energy can be an effective renewable energy source (Wang et al., 2017; Yuan et al., 2020). However, various problems such as low energy density, discontinuity and instability of solar energy due to factors such as day and night variations, weather changes and seasonal changes severely limit the application of solar energy (Wang et al., 2017). One of the possible methods to overcome these problems and utilize solar energy efficiently is to use phase change materials (PCMs) to store solar energy directly and release it simultaneously (Zhang et al., 2021; Zhang et al., 2021). By storing and releasing energy, PCMs can perfectly solve the contradiction between solar energy supply and demand mismatch and improve the efficiency of solar energy utilization. On the other hand, termochromic phase change materials can change their color reversibly before and after the phase transition, providing tunable photothermal conversion efficiency (Yuan et al., 2022).

Thermochromic materials are a class of temperature-sensitive materials and their color can vary with a variation of temperature in a certain range. It is noted in the literature that the use of thermochromic dyes can greatly enrich the functionality and intelligence of a material. For example, a reversible thermochromic and phase change microcapsule system can indicate the phase change state of the PCM core inside the microcapsule by color change. Such a combination can significantly improve the efficiency of thermal energy storage and ease of operation. Moreover, the application of thermochromic materials can contribute to improving energy efficiency by controlling the energy balance in energy-saving buildings. The study of reversible thermochromic phase-change microcapsules (TCMs) for thermal energy storage and temperature display has attracted great interest from many scientists in the past three years (Zhang et al., 2020).

In our previous study, we have successfully nanoencapsulated fluoran dye-based three-component thermochromic systems by emulsion polymerization method into poly(methyl methacrylate) (PMMA) wall. In the study, we used 1-tetradecanol as solvent and phenolphthalein as color developer. Thermochromic systems and their nanocapsules exhibited reversible color change with thermal stimuli. While TSs nanocapsules under phase change temperature were colored solids, they turned into colorless transparent liquids above phase change temperature. This change was reversible depending on the change in temperature. Similiarly, nanocapsules were

green color at room temperature and lost their color at temperatures upon melting point of the thermochromic systems. While thermochromic systems had a heat storage capacity of over 200 J/g, the heat storage capacity of their nanocapsulated derivatives had reached up to 180 J/g (Özkayalar et al., 2020). In this study, we prepared and encapsulated thermochromic systems containing different types of fluoran dyes and a larger amount of solvent (phase change material) by the same process. Our aim was to investigate the thermoregulation properties of the developed microcapsules as well as to determine the effect of the larger amount of solvent added to the thermochromic system on the thermal properties of the capsules.

II. Experimental Procedure/Methodology

Material

2′-Dibenzylamino-6′-diethylaminofluoran or 2-Anilino-6-dibutylamino-3-methylfluoran was used as color former in the TSs. Phenolphthalein (PP, Carlo Elba) and 1-tetradecanol (TD, Alfa Aesar, %97+) were used as color developer and solvent in the system. Methylmethacrylate (MMA, Sigma Aldrich, %99) and ethylene glycol dimethacrylate (EGDM, Sigma Aldrich, %98) were used as monomer and crosslinker, respectively, in the microcapsule synthesis. 2,2′-Azobis(2-methylpropionamidine) dihydrochloride (Aldrich, % 97) used as an initiator and polyethylene glycol 1000 (PEG 1000) was used as an emulsifier. 2,4-Dihydroxybenzophenone (Alfa Aesar, 99%) was used as UV absorber to increase UV stability of the thermochromic systems.

Table 1. The abbreviations and features of the TSs and microcapsules

Microcapsule	Microcapsule core dye and solvent content/quantity (g)	Microcapsule core color developer and UV absorber/quantity (g)
PMMA/TS-UVA-2-9-1-Reference*	2'-(Dibenzylamino)-6'-(diethylamino)fluoran (0.055)/ 1-tetradecanol (6.42)	Phenolphthalein (0.09)/ UVA (0.33)/
PMMA/YTS-UVA-2-9-1	2'-(Dibenzylamino)-6'-(diethylamino) fluoran (0.055)/ 1-tetradecanol (9,63)	Phenolphthalein (0.09)/ UVA (0.33)
PMMA/YTS-UVA-2-9-2	2'-(Dibenzylamino)-6'-(diethylamino)fluoran (0.055)/ 1-tetradecanol (12.84)	Phenolphthalein (0.09)/ UVA (0.33)
PMMA/YTS-UVA-2-11	2-Anilino-6-dibutylamino-3-methylfluoran (0.055)/ 1-tetradecanol (12.84)	Phenolphthalein (0.09)/ UVA (0.33)

*: produced in our previous study, used as reference in this study (Özkayalar, et al., 2020)

The dye and phenolphthalein were added into the 1-tetradecanol solvent at 90 °C and mixed until dissolution was completed. In order to improve the UV resistance of TSs, UV absorber was added to ternary mixture (Özkayalar et al. 2020). The amounts of components of TSs were given in Table 1. The production of poly(methyl methacrylate) walled microcapsules containing TSs was carried out by oil in water emulsion polymerization method. The shell/core ratio was chosen as 0.5:1. A 7.75 g of TS and a 2.38 g of PEG1000 were added into 100 mL of distilled water and the emulsion was prepared by stirring at 1500 rpm for 30 minutes. A 3.77 g MMA monomer was added to the emulsion medium and mixing was continued for 10 minutes. Then, a 3.09 g EGDM crosslinker was added and mixing was continued for another 10 minutes. A 0.4 g initiator was added and after 10 minutes of stirring, the temperature was increased to 80 °C and the polymerization reaction was started. The stirring speed was reduced to 500 rpm, the reaction was stopped after 2.5 hours of stirring and the microcapsules produced were filtered and stored after rinsing with hot water several times in succession.

III. Analysis

The thermochromic behavior of microcapsules were investigated using photograph images taken by using a digital camera at different temperatures. The photographs of the microcapsules at melting temperature of the TS were taken. Then, photographs of the same samples were taken when they cooled back to room temperature. To examine the morphology of the microcapsules, scanning electron microscopy (SEM, LEO 440 Computer Controlled Digital) analysis was performed on sample coated with gold. TG analysis was performed to investigate their thermal stability using a Perkin Elmer TGA7 instrument. Measurements were realized in the range of 0-500 °C, at a heating rate of 10 °C/d under air atmosphere. The phase transition characteristics of the microcapsules were determined by differential scanning calorimetry (DSC, Perkin-Elmer Jade). The measurements were carried out at a heating rate of 1 °C/min, between the temperature of -5 °C and 65 °C under nitrogen gas.

T-history measurement was carried out to determine the thermo-regulation property of PMMA/YTS-UVA2-9-2 microcapsule during heating. In the test, microcapsule samples placed in locked bags were used. Reference microcapsules represented microcapsules without TS (empty capsules). Before test, microcapsule sample and reference capsule were cooled in the refrigerator (+4 °C) until the surface temperatures were constant. The measurements were carried out on a hot plate heater with a temperature fixed at 55 °C for sample microcapsules and reference empty microcapsules using thermocupl placed inside microcapsules, and temperature values were recorded by a datalogger (AHLBORN).

IV. Results and discussion

At below and above the phase transition temperature of TSs, colored and colorless photos of microcapsules were presented in Figure 1. The capsules exhibited a markedly thermochromic color change. Their color changed significantly from green or black to colorless (capsule wall polymer color) depending on the color of the color former.

PMMA/YTS-UVA-2-9-1	PMMA/YTS-UVA-2-9-2	PMMA/YTS-UVA-2-11

Fig. 1: Colorless (hot) and Colored (cold) photos of the microcapsules

SEM images were used to study the morphology of the microcapsules. According to the SEM images of the microcapsules given in Fig.2, capsules with spherical morphology were produced. In addition, the images showed that the particles were homogeneous in size. According to the size scales given on the images, their particle sizes were below 200 nm.

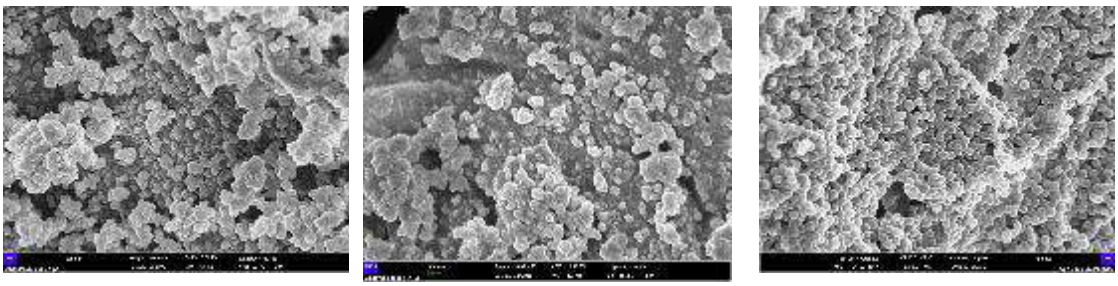

Fig. 2: SEM images of the microcapsules

According to the DSC analysis results of microcapsules (Table 2), they had a high energy storage capacity with a melting enthalpy of above the 120 j/g. Their energy storage temperatures were suitable for the human body temperature. On the other hand, it was determined that increasing the amount of solvent component in the TS, the core material, did not increase the enthalpy as expected, but increased the melting temperature of the encapsulated system by a few degrees.

According to the TG analysis results, microcapsules were subjected to a two-stage thermal degradation. The first degradation was due to the evaporation of the solvent component of the capsule core material and its leakage from the shell structure. The second stage degradation was caused by the degradation of the nanocapsule wall structure. The degradation initiation temperatures of the nanocapsules were above 220 ℃ and the encapsulated TSs exhibited sufficient thermal resistance for low temperaure thermal energy storage application fields such as textile, building.

Table 2. DSC analysis results of microcapsules

Microcapsules	Melting Temp. (°C)	Melting Enthalpy (j/g)	Crystallization Temp.(°C)	Crystallization Enthalpy (j/g)
PMMA/TS-UVA-2-9-1-Reference*	32.5	191.1	34.8	192.2
PMMA/YTS-UVA2-9-1	35,6	156,8	34,5	173,5
PMMA/YTS-UVA2-9-2	34,2	170,9	34,9	172,7
PMMA/YTS-UVA2-11	34,2	127,0	34,0	123,8

Table 3. TG analysis results of microcapsules

	First step			**Second step**		
Microcapsules	**Start (ºC)**	**End (ºC)**	**weight loss, %**	**Start (ºC)**	**End (ºC)**	**weight loss,%**
PMMA/TS-UVA-2-9-1-Reference*	226.7	273.3	77.4	378.1	440.2	10.5
PMMA/YTS-UVA-2-9- 2	231,9	278,4	83,8	359,0	440,2	16,3
PMMA/YTS-UVA-2-9-1	222,7	268,0	87,1	365,8	441,5	11,5

The commonly applied T-history test method is used to determine the thermo-regulation performance resulting from latent heat absorption or releasing of PCMs. During measurement of the cooling effect, the encapsulated TS absorbed the latent heat and caused to decrease in temperature of the microcapsule surfaces. Fig. 3 shows the temperatures of the reference and sample microcapsules during heating. As seen, the difference between the sample and reference microcapsule surface temperatures was determined above 10°C. During the whole measurement period, TS microcapsules heated to lower temperatures than empty microcapsules without TS. The lower surface temperature of TS-containing capsules is related to the latent heat absorbed during the melting of 1-tetradecanol in their structure. This result reveals the cooling effect of TS-containing capsules due to their latent heat absorption.

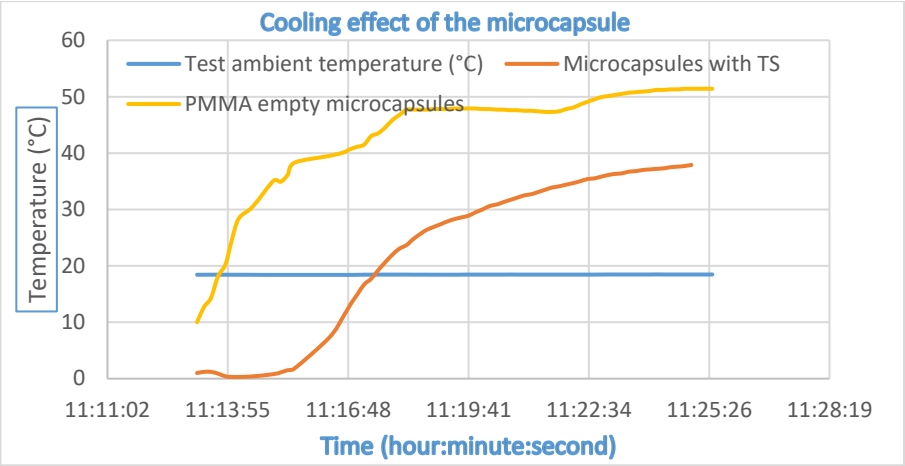

Fig. 3: T-history measurement result of PMMA/YTS-UVA-2-9-2 during heating process

V. Conclusion

In the study, different TSs containing fluoran dye with two different colours were microencapsulated by emulsion polymerization method. The capsules were colourless above the melting temperature of the solvent, while they became green or black at temperatures below the solidification temperature of the solvent. SEM analysis showed capsules had nano-sized. Their particle sizes were less than 200 nm. According to the DSC analysis, the energy storage/releasing temperatures were suitable for human body temperature. The capsules had high energy storage capacity, ranging from about 127 to 191 j/g. Larger amount of solvent (PCM) component added to the TS did not increase the thermal energy storage capacity of the microcapsules as expected, but it did bring the temperature of melting closer to human body temperature. The degradation initiation temperatures of the microcapsules were above 220°C. They exhibited cooling effect of more than 10 °C during their heating. The microcapsules exhibit sufficient thermal resistance and high thermal energy storage capacities for applications in thermal energy storage materials.

Acknowledgements
This work was supported by the scientific and technological council of Turkiye (TUBITAK, Project Number 118M012). Therefore, authors would like to express their appreciation to TUBITAK.

References

Liu, Y., Yang, H., Wang, Y., Ma, C., Luo, S., Wu, Z., Zhang, W., & Liu, S. (2021). Fluorescent thermochromic wood-based composite phase change materials based on aggregation-induced emission carbon dots for visual solar-thermal energy conversion and storage. Chem. Eng. J. *424*, 130426.

Özkayalar, S., Adıgüzel, E., Aksoy, S. A., & Alkan, C. (2020). Reversible color-changing and thermal-energy storing nanocapsules of three-component thermochromic dyes. *Mater. Chem. Phys. 252*, 123162.

Sipponen, M. H., Henn, A., Penttilä, P., & Österberg, M. (2020). Lignin-fatty acid hybrid nanocapsules for scalable thermal energy storage in phase-change materials. *Chem. Eng.J. 393*, 124711.

Wang, Z., Tong, Z., Ye, Q., Hu, H., Nie, X., Yan, C., Shang, W., Song, C., Wu, J., Wang, J., Bao, H., Tao, P., Deng, T. (2017). Dynamic tuning of optical absorbers for accelerated solar-thermal energy storage. Nat. Commun, 8(1), 1478.

Yuan, A., Wu, B., Wang, Y., Zhao, Y., Liu, Q., & Lei, J. (2020). Recyclable solid-solid phase-change materials cross-linked by reversible oxime carbamate bonds for solar energy storage. Int. J. Energy Res. 44(11), 9185-9193.

Yuan, A., Zhao, S., Liu, T., Zhao, Y., Jiang, L., & Lei, J. (2022). Temperature-responsive Thermochromic Phase Change Materials with Tunable Photothermal Conversion Efficiency Toward Solar Energy Storage. Adv. Mater. Technol., 7(11), 2200226.

Zhang, S., Feng, D., Shi, L., Wang, L., Jin, Y., Tian, L., ... & Yan, Y. (2021). A review of phase change heat transfer in shape-stabilized phase change materials (ss-PCMs) based on porous supports for thermal energy storage. *Renewable and Sustainable Energy Rev. 135*, 110127.

Zhang, H., Liu, Z., Mai, J., Wang, N., Zhong, J., Mai, X., & Zhang, N. (2021). Super-elastic smart phase change material (SPCM) for thermal energy storage. *Chem. Eng.J. 411*, 128482.

Zhang, Y., Liu, H., Niu, J., Wang, X., & Wu, D. (2020). Development of reversible and durable thermochromic phase-change microcapsules for real-time indication of thermal energy storage and management. *Appl. Energy*, *264*, 114729.

IEEES-051

Biogas Renewable Energy: Conversion of Solid Waste To Energy In The Marmara Region

[1*]Muhammed Ömer BUDAK, [2]Canan AĞLAN GÖKLER
[1] Marmara University, Industrial Engineering, Institute of Science, Istanbul, 34722, Turkey
[2] Marmara University, Industrial Engineering, Institute of Science, Istanbul, 34722, Turkey
*E-mails: m.omerbudak@gmail.com, canan.aglan@marmara.edu.tr

Abstract

In today's world, the demand for environmentally friendly energy sources is steadily growing. Responding to this demand, biogas energy has emerged as a noteworthy alternative. Biogas, derived from diverse sources like domestic and agricultural waste, organic materials, and animal byproducts, serves as a viable substitute for natural gas. The resulting biogas energy is widely embraced in both residential and industrial sectors as a sustainable energy source. Moreover, the capacity to generate electrical energy through biogas combustion underscores the significance of this energy source. In this study delves into the production of biogas energy from domestic and agricultural waste, as well as the establishment of facilities for electricity generation using this resource. The study proposes the utilization of anaerobic fermentation techniques to harness energy from domestic solid waste in the provinces of the Marmara Region. This approach aims to yield a methane gas concentration of 60-75%. The obtained methane gas is effectively employed in electricity production within cogeneration facilities. The ultimate goal is to generate electricity at these facilities in the Marmara Region, feed it into the regional power grid, and thereby meet the region's electricity demands. The study also addresses various factors pertinent to facility installation, such as industrial engineering methods, along with an analysis of the advantages, disadvantages, and cost considerations.

Keywords: anaerobic fermentation, biogas, municipal solid waste, smart grid, electricity generation facilities.

I. Introduction

One of the most important reasons for the increasing demand for new sustainable energy sources is the decrease in energy resources due to the rapid increase in the human population (M. Khalil et al, 2019). Fossil fuels, which have 84% global energy supply of the world and 81.88% primary energy sources of Turkey, cause environmental problems, especially air pollution and global warming. Through renewable energy sources, dependence on fossil fuels such as coal, oil, and natural gas can be reduced (O. Ellabban et al, 2014).

Biogas is a renewable energy source that is easy to produce in contrast to other sources and can be used in various ways for transportation, heat, electricity generation, or mechanical energy for transportation (R. Hakawati et al, 2017). Animal wastes, municipal wastes, agricultural wastes, and forest wastes are the most common sources used in biogas production (B. Özer, 2017). The implementation of full-recycling systems and the conversion of waste to energy is the best solution for a sustainable world [(B. Baran et al, 2016).

Biogas is a type of renewable energy that is produced by the breakdown of organic matter through a process called anaerobic digestion. It is composed mainly of methane and carbon dioxide, along with small amounts of other gases such as hydrogen, nitrogen, and oxygen (Arshad et al, 2018).

Biogas can be produced from a variety of organic materials, such as agricultural waste, food waste, sewage sludge, and even energy crops. The organic material is placed in an airtight container called a digester, where microorganisms break down the material in the absence of oxygen, producing biogas as a byproduct (M., Bano, et al, 2018). Biogas can be used as a source of fuel for heating, cooking, and electricity generation. It is considered a sustainable energy source because it is produced from renewable organic materials, reduces greenhouse gas emissions by capturing methane that would otherwise be released into the atmosphere, and can help to reduce dependence on fossil fuels (I., Khan, et al, 2018).

II. Experimental Procedure/Methodology/System Description

In 2022, 34.6% of our electricity production will come from coal, 22.9% from natural gas, 20.3% from hydraulic energy, 10.6% from wind, 5.1% from solar, 3% from solar energy. 4% from geothermal energy and 3% from other sources. As of the end of September 2023, our country's installed power has reached 105,668 MW. Turkey's electrical energy consumption decreased by 0.5% compared to the previous year, reaching 331.1 TWh in 2022, and electricity production decreased by 1.9% compared to the previous year, reaching 328.3 TWh.

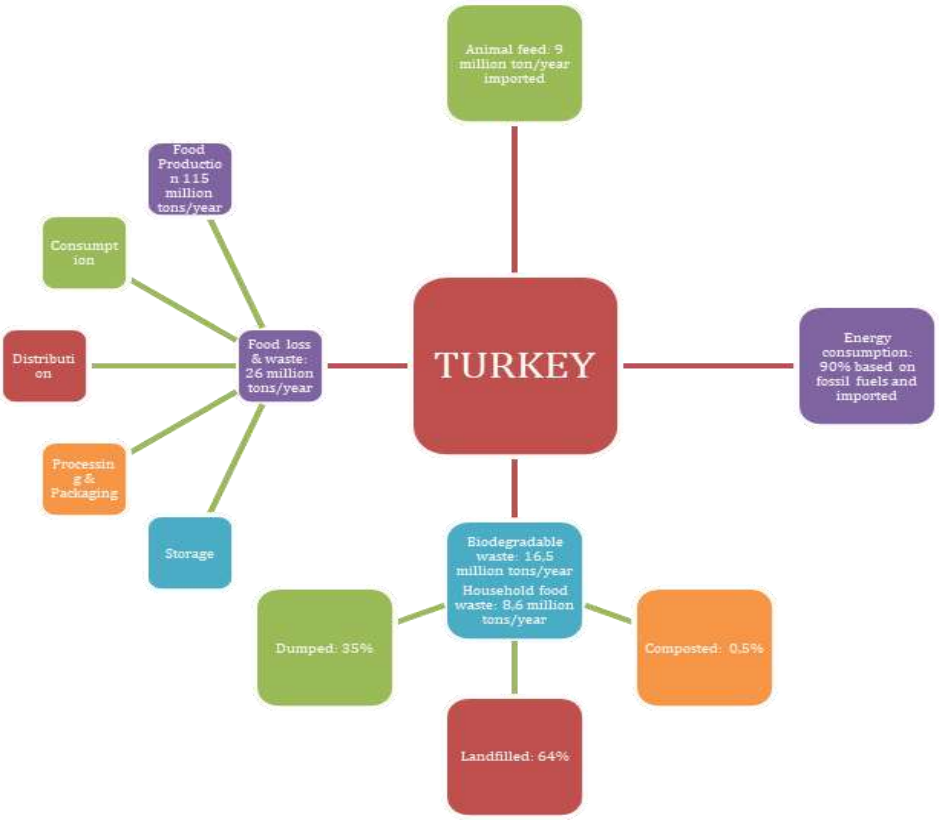

Figure 8. Agricultural food production and losses in Turkey [11]

Fossil fuel consumption, the conventional means to meet energy demands, has led to detrimental consequences such as air pollution and global warming. In response to these ecological challenges, the focus on biogas production from waste emerges as a significant and sustainable alternative energy solution. This approach, rooted in the utilization of organic waste, offers a method of energy production that is both economically efficient and environmentally conscientious (M. Khalil et al,2019).

Embedded within the broader spectrum of renewable energy sources, biomass emerges as a cornerstone. This encompasses diverse inputs like animal wastes, forest residues, agricultural byproducts, and municipal refuse, which can be channeled into biogas production. This innovative process yields a dual benefit – a reduction in greenhouse gas emissions alongside the attainment of a pristine energy source. Through anaerobic fermentation, biogas emerges, characterized by a composition of 60-75% methane, 25-50% carbon dioxide, as well as trace amounts of hydrogen sulfide, nitrogen, and carbon monoxide, as outlined in Table 3 [4]. Noteworthy for its odorless and colorless nature, biogas boasts a high heat content and an impressive methane (CH4) concentration, rendering it a potent and eco-friendly energy reservoir. Not only is it clean and efficient, but biogas also emerges as a cost-effective and versatile energy source (A. YILMAZ, 2019).

III. Analysis

The calculations involved assessing the feasibility of constructing biogas plants within the Marmara region, utilizing gathered data. Referencing Table 8, a breakdown of requirements and costs for establishing a 1 MWh electricity-generating biogas plant is provided. Provides a comprehensive overview of the annual costs associated with the potential generated electricity in different cities, quantified in billions of USDs. This detailed breakdown encompasses the economic implications of harnessing the available energy resources to meet the electricity demands of these cities, offering a valuable perspective on the financial considerations involved in sustainable energy production and utilization.

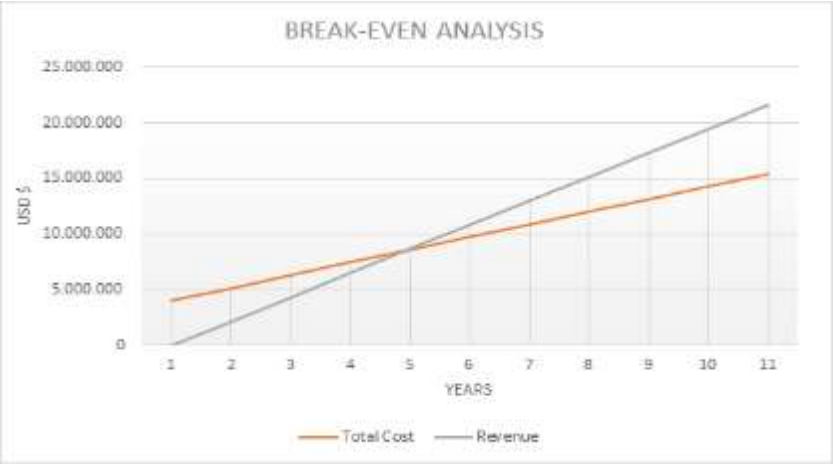

Figure 2. Break-Even Analysis of Biogas Plant

Figure 2 presents a comprehensive visual comparison between the total costs and revenues associated with the Biogas Plant over a span of ten years, quantified in USD. The graphical representation not only highlights the financial trajectory of the project but also reveals a critical milestone: the investment reaches full amortization within a span of five years. This milestone underscores the swift return on investment, signifying the point at which the project's operational revenue covers the incurred costs. Notably, it's imperative to underscore that the depicted accounts were meticulously crafted without the inclusion of any external grants, underscoring the project's self-sufficiency and financial sustainability. This illustration stands as a testament to the efficacy and feasibility of the Biogas Plant endeavor, shedding light on its capacity to stand on its own merits within a government-regulated context.

IV. Results and discussion

The escalating global energy demand, in tandem with advancements in industrialization and progress, has spurred a pronounced inclination towards renewable energy sources. Among the diverse array of renewable energy options explored in this article, biogas energy emerges as a notable contender. This energy form is harnessed through the cogeneration method, wherein the fermentation of organic waste yields biogas, from which both heat and electrical energy can be derived. This approach brings forth a dual benefit: not only does it furnish a sustainable energy supply, but it also yields a valuable byproduct—a nutrient-rich fertilizer—that can enrich agricultural lands.

Despite its global and domestic success stories, the widespread adoption of this biogas energy system in our country is yet to reach optimal efficiency. Bolstering this system and proliferating its implementation would not only bolster our energy security but also invigorate our economic landscape. This initiative holds the potential to mitigate environmental harm by curbing the release of methane gas—a natural byproduct of waste decomposition—into the environment.

The Marmara region, with its substantial organic waste reserves evidenced in environmental status reports of various cities, stands poised to play a pivotal role in this transformation. The outcomes of meticulous studies and simulations unveil a compelling picture: The Marmara region's electrical energy demand, towering at 8.32 GW, can find substantial support from 10 proposed biogas plants. These facilities are projected to yield a staggering 1,198 GW of electricity, translating to a remarkable 14.40% contribution to the region's electricity needs.

In essence, the fusion of biogas energy with cogeneration presents a symbiotic solution, satiating energy demands while concurrently diminishing waste and environmental harm. With careful cultivation, this approach holds the potential to energize both our nation's power grid and its sustainable future.

Table 1. Efficiency of Biogas Plants

Plant	***Efficiency (%)***
Istanbul (Asia)	*14.97*
Istanbul (Europa)	*12.95*
Kocaeli & Sakarya	*4.1*
Bursa 1	*28.15*
Bursa 2 (Bursa & Bilecik & Yalova)	*56.5*
Balıkesir	*9.4*
Çanakkale	*2.35*
Tekirdağ	*13.67*
Edirne	*4.9*
Kırklareli	*5.13*

V. Conclusion

Considering these efficiencies, 2 large facilities including Bursa, Yalova & Bilecik should be imp Our long-term proposal for raising this rate is to raise awareness of the society. In this context, we are expecting to increase the efficiency of organic waste collection and thus the energy production efficiency. This will be achieved by increasing the awareness about renewable energy through trainings provided to the younger generations of our country. As a result of the studies carried out in our article, it is evident that all our facilities work with high efficiency.

The fixed and annual variable costs of the biogas plants are calculated based on available data. As the capacity of the facility increases, its costs and revenues also increase. Moreover, the investments to be undertaken are proving to be highly efficient. By the 5th year, these investments are successfully passing through all our facilities across the land.

In this 5th year, the plants amortize, and a balance is achieved. This rate of return is notably higher compared to other energy plants, reflecting the success of our approach in raising awareness and optimizing efficiency.

Acknowledgements

References

A. Yılmaz, Türkiye'de Biyogaz Üretimi Ve Kurulu Santrallerin Ürettiği Elektrik Enerjisi, Ecological Life Sciences 14(1) 12-28.

B. Baran, M.S. Mamis, B.B. Alagoz, Utilization of energy from waste potential in Turkey as distributed secondary renewable energy source, Renewable energy 90 (2016) 493-500.

B. Özer, Biogas energy opportunity of Ardahan city of Turkey, Energy 139 (2017) 1144-1152.

M. Khalil, M.A. Berawi, R. Heryanto, A. Rizalie, Waste to energy technology: The potential of sustainable biogas production from animal waste in Indonesia, Renewable and Sustainable Energy Reviews 105 (2019) 323-331.

O. Ellabban, H. Abu-Rub, F. Blaabjerg, Renewable energy resources: Current status, future prospects and their enabling technology, Renewable and Sustainable Energy Reviews 39 (2014) 748-764.

R. Hakawati, B.M. Smyth, G. McCullough, F. De Rosa, D. Rooney, what is the most energy efficient route for biogas utilization: Heat, electricity or transport?, Applied energy 206 (2017) 1076-1087.

https://energypedia.info/wiki/Electricity_Generation_from_Biogas (Accessed November 2023)

https://ourworldindata.org/grapher/share-electricity-coal (Accessed November 2023)

https://ourworldindata.org/grapher/share-electricity-gas (Accessed November 2023)

https://ourworldindata.org/grapher/share-electricity-renewables (Accessed November 2023)

https://ourworldindata.org/energy/country/turkey (Accessed November 2023)

https://enerji.gov.tr/bilgi-merkezi-enerji-elektrik#:~:text=2023%20y%C4%B1l%C4%B1%20Eyl%C3%BCl%20ay%C4%B1%20sonu%20itibar%C4%B1yla%20kurulu%20g%C3%BCc%C3%BCm%C3%BCz%C3%BCn%20kaynaklara%20g%C3%B6re,s%C4%B1%20ise%20di%C4%9Fer%20kaynaklar%20%C5%9Feklindedir. (Accessed November 2023)

IEEES-052

Applications of Fresnel Concentrated Solar Power System and their Impact Towards Environment

[1*]Houda Tassoult, [1]Ahmed Mezidi
[1]Unité de Développement des Equipements Solaires, UDES/ Centre de Développement des Energies Renouvelables, CDER, Bou-Ismail, 42415, Tipaza, Algeria
*E-mails: tassoulthouda@yahoofr

Abstract

The non renewable energy resources is depleting with alarming rate in near future and their usage ensues the emission of CO_2 that exerts negative influence on the environment (Ministry of Energy (Algeria), 2018). Hence, it is necessary to find an alternative source that are ecofriendly and easily available on the earth. In this context, renewable energy technologies, notably solar power, are increasingly gaining interest . To meet the Algerian energy demand in rural areas, the government has set out a set of strategies including the integration of CSP system for consumptive and productive purposes. To bring these plans to reality, we, reasercher at solar equipment development unit UDES, established the first Linear Fresnel (LFR) CSP prototype that producing a heat reaching 450°C intended for building and industrial applications to preserve the environment by avoiding releasing the CO_2. This technology leads to produce electricity during off- peak hours and the cloudy day or night time. Finally, this system will strengthened by storage system.

Keywords: Renewable energy, Thermal, solar energy, Concentrated solar.

I. Introduction

The use of non-renewable energy resources ensues the emission of CO_2 that exerts negative influence on the environment. Hence, it is necessary to find an alternative source that are ecofriendly and available on the earth to dramatically reducing the global warming and looking out for a technology that representing a powerful, clean, endless, and reliable source. In this context, renewable energy technologies, notably solar power, are increasingly gaining interest. One of the promising solar energy technologies is the Concentrated Solar Power (CSP) system (Boudiaf and Meddi, 2021). This technology has received a special interest worldwide since it produces no air pollutants or greenhouse gas. CSP have been accepted as sustainable energy sources. To meet the energy demand in Algerian rural areas, the government has set out a set of strategies including the integration of CSP system for consumptive and productive purposes. To bring these plans to reality, we, researchers at solar equipment development unit UDES, established the first Linear Fresnel (LFR) CSP prototype that producing a heat reaching 450°C intended for industrial applications to preserve the environment by avoiding releasing of CO_2.

II. Methodology, System Description and Experimental Procedure

Fresnel technology uses a succession of plane mirrors forming the parabolic shape of the collector. These mirrors are equipped with a motorization system which makes it possible to follow the sun on a single EAST-WEST axis to permanently redirect and concentrate the solar rays towards a tube or a set of fixed linear receiver tubes located on the focal length. The working temperature of this technology ranges from 270°C to 550°C, with a concentration factor ranging from 25 to 100. The working heat transfer fluid in this technology is either water or oil.
The receiver has strong absorption and will absorb the reflected rays and consequently transform them into thermal energy. This thermal energy obtained is either directly used in a thermodynamic cycle to produce electricity, or for cogeneration. This energy is generally stored for later use. During this process, losses can be observed at several levels namely the Concentrator, Receiver, Transport and Storage (K. lovegrove, 2012) (F. RAMADJI, 2015) (see Fig.1)

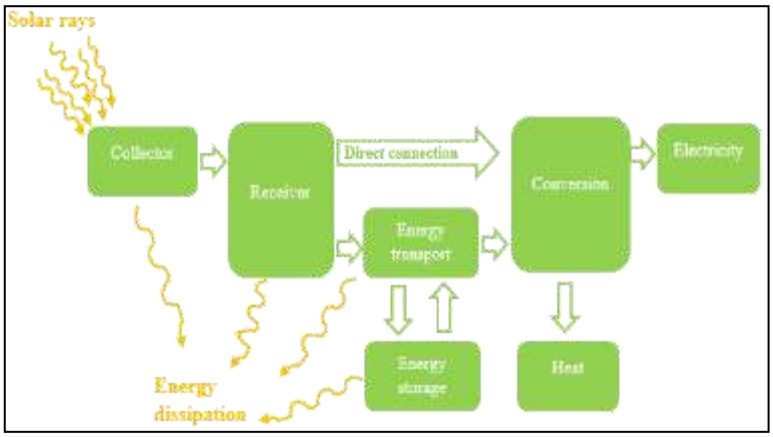

Fig. 1: The energy transfer process

$$\eta_{system} = \eta_{concentrator} * \eta_{receiver} * \eta_{storage} * \eta_{conversion} \quad (1)$$

To have a preliminary assessment of concentrated solar power production practices as compared to a conventional option, studies have bee carried out (I.A.S. Ehtiwesh, M.C. Coelho, A.C.M. Sousa, 2016) it was conducted an environmental impact comparison of the three different plants CSP power plant, Fossil plants-natural gas combined cycle (NGCC) and oil thermal power plants.

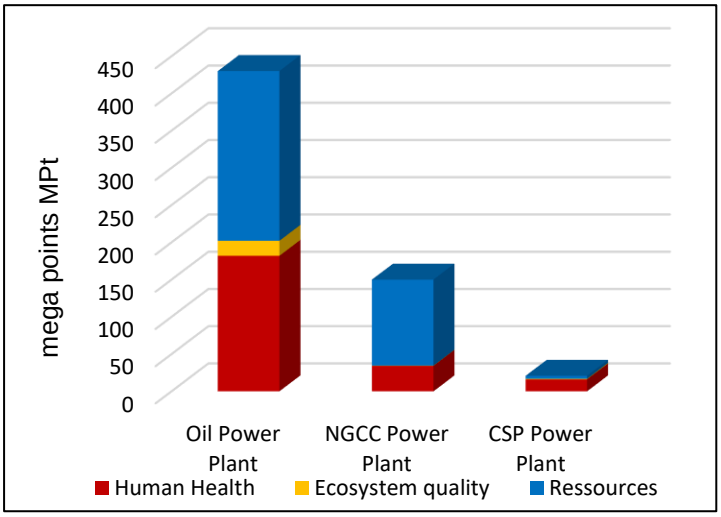

Fig. 2: Total damage impact of the three different plants

The results indicate that the CSP plant has the lowest environmental impact as compared to the two other plants; while the oil power plant presents the worst environmental performance.The CSP parabolic power plant has the advantage over oil plant in all damage categories and over NGCC power plant in the Resources and Human Health damage categories. However, the Ecosystem Quality damage category has very small impact for the NGCC power plant.

Taking this study as environmental reference, The unit's researchers decided to develop and built a thermal system, see Figure 4, and try to generalize its uses to all sectors in order to preserve the environment. The Fresnel linear concentrating solar system is composed of three elements: The reflector (Mirrors), the receiver, and the sun tracking system. The receiver placed at a height of 3 m from the surface of the reflectors which are placed parallel and continuously oriented such that the reflection of the solar rays is always on the focal line (receiver). Each of these elements has a particular role and the combination of their action which makes it possible to convert solar radiation into heat. This heat is subsequently designated for specific applications. Each plane reflector must be mobile so as to follow the path of the sun. The distance separating the reflectors is calculated to avoid optical losses and mechanical stresses due to wind thrust. On the other hand, the same goes for the height separating the receiver. This invention is a thermodynamic solar equipment producing heat with temperatures ranging from 100°C up to 250°C (O. Achkari, a. El fadar , 2020) (A. Luque, S. Hegedus). Several applications can be associated with this heat production technique such as water heating, seawater desalination, electricity production, pasteurization for the food industry, etc.

Fig. 3: Fresnel solar concentrator built at UDES

a. Description of the reflector

The reflector is a linear type collector where the mirrors are segmented by adopting the Fresnel segmentation principle. The challenge of this project is to approximate the parabolic shape of the collector by a succession of plane mirrors in order to be permanently facing the sun, to redirect and concentrate the solar rays towards a fixed linear absorber tube. Each reflector must be mobile to follow the path of the sun. To avoid optical losses, the distance separating the reflectors (mirrors) is calculated.The inclination of each mirror was calculated so that the solar radiation was incident on the aperture plane. On the other hand, an appropriate distance was maintained between two consecutive mirrors so that each mirror does not cast a shadow compared to the adjacent mirror.

b. Description of the receiver

The receiver is a parallelepiped shape of 3m in length, 50cm in width and 20cm in height, perfectly insulated on all sides except the lower face or a 5mm thick double-glazed glass window placed at the focal point of the reflector. It is an arrangement of different elements: composed of 06 copper tubes and two collectors at the inlet and outlet with a double-jacketed aluminum absorber which is specially designed to increase the heat exchange surface for better performance. This receiver uses a double-envelope absorber fixed by original methods. The purpose of the receiver is to absorb concentrated solar radiation, convert it into heat and subsequently transmit it to the heat transfer fluid which circulates in the absorber. Its temperature can reach 250°C measured via thermocouples placed in different locations, namely: 2 thermocouples one at the entrance and the other at the exit of the absorber and 3 others distributed on different points of its surface.

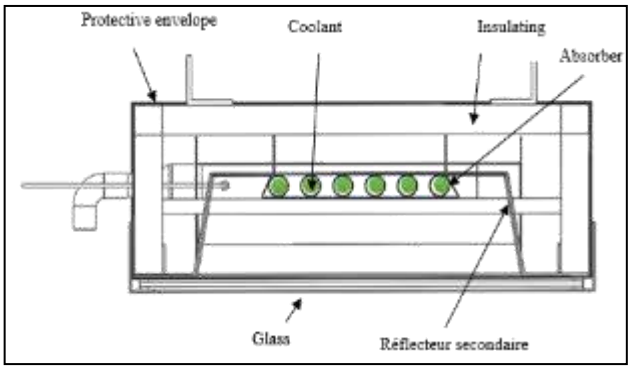

Fig.4: Receiver section (double-shelled absorber shape)

c. Description of the sun tracking system

Solar tracking can be done using two methods: optical tracking using photosensitive sensors and tracking by an algorithm used to calculate the position of the sun. The first monitoring is less precise and is strongly disturbed during cloudy periods while the second is more precise where it requires the intervention of a programming tool.

In our study we adopted a third tracking which is blind tracking using a stepper motor although the tracking is done by an Arduino card.

The solar tracking system must be adjusted so that it is always aimed precisely at the sun. During a specular reflection, the angle of reflection and the nail of incidence are symmetrical with respect to the reflecting surface. Knowing the angle of incidence of the sun and the position of the receiver, it is possible to determine the appropriate angle of the reflectors so that all of the incident rays are reflected towards the receiver. The angle of reflection is imposed by the position of the reflector relative to the receiver while the angle of incidence of the sun is varied depending on the path of the sun. The angle of reflection is estimated again in relation to the new angle of incidence of the sun in order to always reflect the incident rays towards the receiver. Solar monitoring of linear Fresnel type collectors is done at a single angle.

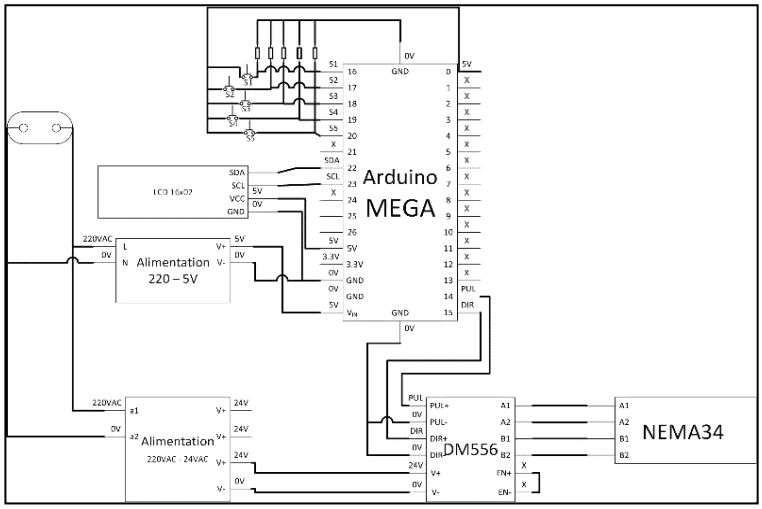

Fig.5: Presentation of the assembly of the electronic circuit of a single motor associated with a control system

III. Results and discussion

The systematization of the experimental tests made it possible to present the evolution of the different temperatures as a function of time which is represented in the form of curves.
The tests are scheduled to take place during a period one week with different sunshine, three (3) days before glazing the receiver and three (3) days after glazing. Each day, tests are taken between 9:30 a.m. and 3:00 p.m. with intervals of five (5) minutes.
It was recorded that the days were sunny and not windy. These days were characterized by clear skies throughout the day, also overcast and not very windy towards the end of the day, with a maximum temperature of Ta =36°C.
The thermocouples are placed on the different constituent parts of the five sensors following the objective of our study (three sensors to measure the temperature at the receiver and two others to ensure the inlet and outlet temperatures.
Fig.6(a) relates to the temperature evolution for different points as a function of time before glazing of the receiver and Fig.6(b) that of the temperature evolution for different points as a function of time after glazing of the receiver.

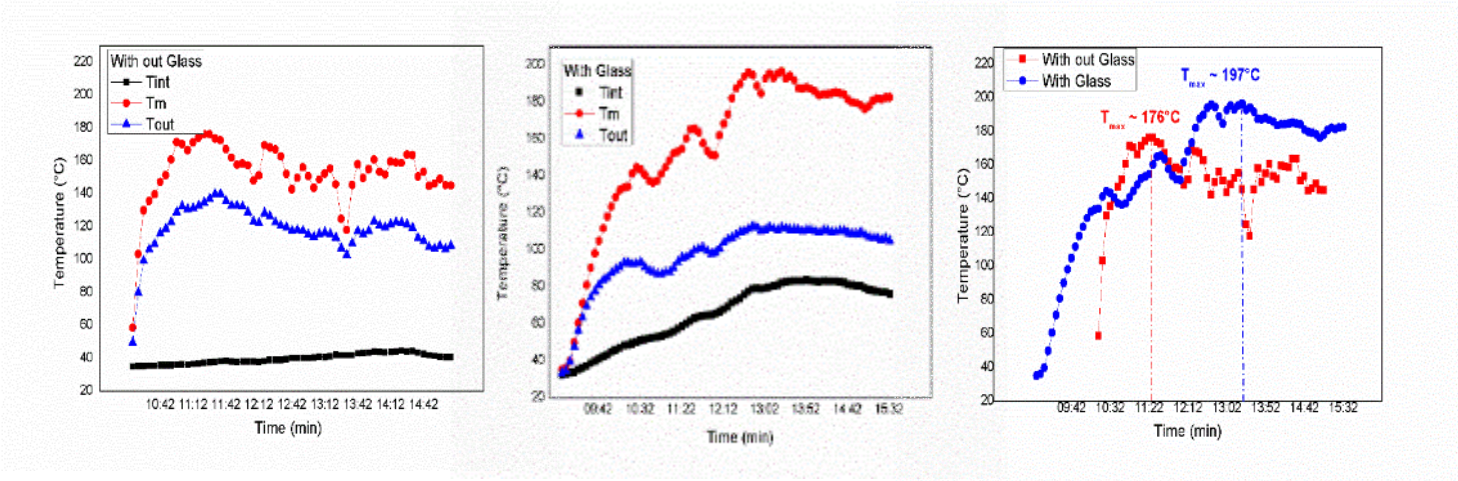

Fig. 5. Evolution of temperature as a function of time
(Left before glazing of the receiver, middle after glazing of the receiver, right comparative evolution)

These figures show conformity and logic in the distribution of temperatures on the receiver. In fact, the temperature of the receiver measurement points after the glazing is higher than that before the glazing. This difference is explained by the greenhouse effect, which promotes heat transfer between the absorber and the air.
It is clear from the graphs that the addition of the glass plays an important role in the evolution of the temperature profile. This higt temprerature used directly or later to produce electricity during off- peak hours (a shortage of electricity demand) and the cloudy day or night time or intended for building and industrial applications to preserve the environment by avoiding releasing the CO_2 (M. T. Islam et al 2018)..

IV. Conclusion

It is expected that solar energy plays an important role in the energy expected electricity production. It has been assumed that CSP plants could meet up 7% of world's electricity production rate by 2030 and 25% by 2050. This green technology and renewable energy dramatically reducing the greenhouse gas (GHG) emissions typically associated with conventional electricity production result from coal or natural gas burning and have been a severe factor in global pollution in climate change. This technology represents a powerful, clean, endless, and reliable source of energy with the intention of preventing the unwanted threats to the planet.
Besides that, with advanced industry development and high levels of energy efficiency, it predicted that CSP contribute about 6% of the world's power demand by 2030 and 12% by 2050.

References

Achkari.O, El fadar.A, (2020). Latest developments on TES and CSP technologies – energy and environmental issues, applications and research trends. applied thermal engineering 167, 114806.
Boudiaf, A., & Meddi, M. (2021). Impact of climate change on precipitation variability in the North-West of Algeria Theoretical and Applied Climatology, 144(1-2), 297-310.
Islam. M. T, Huda. N, Abdullah. A. B, and Saidur. R; (2018), A comprehensive review of state-of-the-art concentrating solar power (CSP) technologies: Current status and research trends, *Renew. Sustain. Energy Rev.*, vol. 91, no. November 2017, pp. 987–1018, 2018, doi: 10.1016/j.rser.2018.04.097.
Ismael A.S. Ehtiwesh, Margarida C. Coelho, Antonio C.M. Sousa; (2016), Exergetic and environmental life cycle assessment analysis of concentrated solar power plants, *Renew. Sustain. Energy Rev.*, vol. 56, pp. 145–155, 2016, doi.org/10.1016/j.rser.2015.11.066
Lovergove .K, Stein. W., (2013). Woodhead Publishing Limited, Concentrating solar power technology: Principles, developments and applications.
Luque. A., Handbook of Photovoltaic Science and Engineering
RAMADJI. F (2015), Master memory, Contribution à la conception et dimensionnement d'un recepteur lineaire pour un concentrateur solaire de type lineaire fresnel.

IEEES-053

Impact of Natural Gas Composition on the Energy-Exergy-Environmental Performance of a Combined Cycle Power Plant

[1*]Tayfun Tanbay, [2]Ahmet Durmayaz
[1] Bursa Technical University, Faculty of Engineering and Natural Sciences, Department of Mechanical Engineering, Mimar Sinan Campus, Bursa, 16310, Türkiye
[2] Istanbul Technical University, Energy Institute, Maslak, Istanbul, 34469, Türkiye
*E-mail: tayfun.tanbay@btu.edu.tr

Abstract

The aim of this study is to investigate the impact of natural gas composition on the energetic, exergetic and environmental performance of a natural gas-fired combined cycle power plant. A thermodynamic model based on a 1220 MW power plant of Türkiye is built and actual plant operational data is used for the analysis. Natural gas is assumed as a mixture of methane, ethane, propane and nitrogen and the effect of constituents' fraction on the thermal efficiency, net power output, exergy efficiency and CO_2 emission rate of the plant is examined. The results reveal that the thermal and exergy efficiencies of the plant improve with a decrease in methane and an increase in ethane and propane fractions. On the other hand, these variations have a negative impact on the net power output and environmental performance of the plant. Thermal and exergy efficiencies increase by 0.4% and 0.3%, respectively, whereas the power output decreases by 1.8 MW and the CO_2 emission rate increases by 1 kg/s with a 15% decrease in methane fraction. The results of this study provide useful insight for policy makers. A comparative analysis for a combined cycle plant fueled with natural gas imported from Russia, Iran and Azerbaijan shows that the maximum and minimum thermal efficiency and CO_2 emission rate differ by 1.0% and 1.2 kg/s, respectively.

Keywords: Natural gas, Combined cycle, Energy analysis, Exergy analysis, CO_2 emission.

I. Introduction

Combined cycle power plants (CCPP) are highly efficient energy systems and are widely utilized for electricity production. These plants integrate a gas turbine to steam turbines through a heat recovery steam generator (HRSG) to exploit the thermal energy of high-temperature combustion products leaving the gas turbine. CCPPs are fired by natural gas or coal. Natural gas is a mixture of methane (CH_4), ethane (C_2H_6), propane (C_3H_8), butane (C_4H_{10}), pentane (C_5H_{12}), hexane (C_6H_{14}), nitrogen (N_2) and carbon dioxide (CO_2). The chemical composition of natural gas depends on the source and varies regionally. For instance, the mean methane fraction in Michigan and Colorado are 93.4% and 82.5%, respectively (Liss et al., 1992). Natural gas is advantageous to coal in terms of both energy efficiency (Reddy et al., 2014) and environmental impact (de Gouw et al., 2014), and therefore it is the preferred fuel for CCPPs.

There exists several studies on the energy, exergy, economic and environmental analysis, optimization and performance improvement of CCPPs. Garcia et al., (2017) reviewed different plant configurations within the energy efficiency perspective, while a review study by Ibrahim et al., (2018) focused on the exergy analysis of CCPPs. A recent work by Pattanayak and Padhi, (2022) studied the impacts of fuel preheating and compressor precooling on the performance of a CCPP, and revealed that the thermal efficiency of the plant could be increased by 0.58-2.20% with a 15^0C decrease in the air temperature. In another work, Shireef and Ibrahim, (2022) analyzed the effects of operating conditions on the performance of a CCPP, and found that plant's thermal efficiency improve with an increase in compressor pressure ratio and turbine inlet temperature.

Regarding the performance analysis of CCPPs, none of the studies in the literature focus on the effect of fuel composition on the characteristics of a natural gas-fired CCPP. In order to fill this research gap, this study aims to investigate the impact of natural gas composition on the energy-exergy-environmental performance of a CCPP. The modelling is based on a currently operational natural gas-fired CCPP in Türkiye and actual plant data is used to carry out the performance analysis. The fuel is assumed to be a mixture of CH_4-C_2H_6-C_3H_8-N_2, and the effect of the constituents' fractions on the thermal efficiency, net power output, exergy efficiency and CO_2 emissions of the CCPP are examined.

II. System Description

Figure 1 shows the schematic representation of the natural gas-fired Hamitabat CCPP. The plant is located in Kırklareli, and it is the first CCPP of Türkiye. Hamitabat CCPP consists of two combined cycle blocks and has a nominal net power output of 1220 MW. Fuel is supplied to the plant from the Turusgaz natural gas pipeline which imports the gas from Russia. Natural gas enters the plant through a preheater (NGPH) and combusts in the combustion chamber (CC) by reacting with compressed air coming from a compressor (C). The combustion products expand in the gas turbine (GT) to produce power and then enter the triple pressure HRSG to transfer heat to a Rankine cycle. Steam leaving the HRSG is expanded in high-, intermediate- and low-pressure steam turbines (HPST, IPST, LPST) to produce additional power. Expanded steam is condensed in a Heller system which consists of a condenser (COND), hydraulic turbine (HT), cooling cycle circulation pump (CCCP) and cooling tower (CT). Liquid water is pumped to HRSG inlet by the condenser pump (CP) and feedwater pump (FWP). Gland condenser (GC) is utilized for steam sealing of steam turbines, while the polishing unit (PU) removes harmful substances from the Rankine cycle.

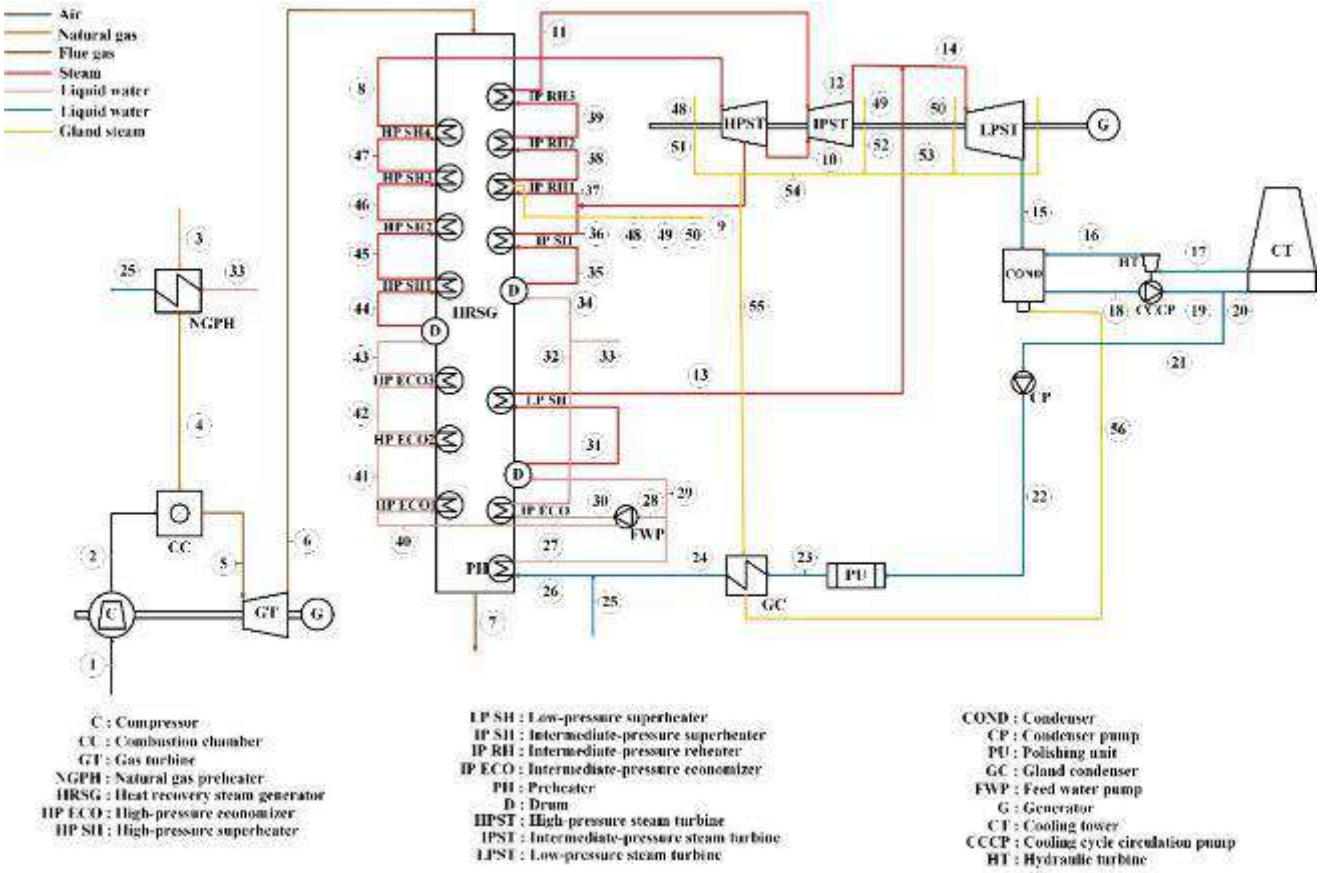

Fig. 1: Schematic illustration of the Hamitabat CCPP (Topal and Tanbay, 2023).

III. Analysis

The CCPP is modeled by applying the mass and energy conservation equations to the components of the plant:

$$\sum \dot{m}_{in} = \sum \dot{m}_{out} \tag{1}$$

$$\dot{Q}_{in} + \dot{W}_{in} + \sum(\dot{m}h)_{in} = \dot{Q}_{out} + \dot{W}_{out} + \sum(\dot{m}h)_{out} \tag{2}$$

where $\dot{m}$ is the mass flow rate (kg/s), $\dot{Q}$ and $\dot{W}$ are the energy transfer rates by heat transfer and work done (kW), respectively, and h is the specific enthalpy (kJ/kg). By using the actual plant data (Topal and Tanbay, 2023), the thermodynamic properties of all states are determined and the exergy destruction rates of all components can be calculated with the exergy balance equation:

$$\dot{X}_{dest} = \sum_{i\in in} \dot{X}_i - \sum_{i\in out} \dot{X}_i + \left(1 - \frac{T_0}{T_b}\right)\dot{Q}_{in} - \left(1 - \frac{T_0}{T_b}\right)\dot{Q}_{out} + \dot{W}_{in} - \dot{W}_{out} \tag{3}$$

where T_0 and T_b are the dead state and average boundary temperature respectively, and the exergy flow rate is defined as

$$\dot{X}_i = \dot{m}_i[h_i - h_0 - T_0(s_i - s_0)] \tag{4}$$

In Eq. (4), s is the specific entropy (kJ/kgK).

Combustion of natural gas with air in the CC is governed by

$$aCH_4 + bC_2H_6 + cC_3H_8 + dN_2 + eO_2 \rightarrow fCO_2 + gH_2O + dN_2 + hO_2 \tag{5}$$

The molar flow rates of the molecules in Eq. (5), a, b, c, d, e, f, g, h, depend on the composition of the natural gas and are determined by equivalence of chemical species and mass flow rates of air and natural gas.

The energetic and exergetic performance of the CCPP are evaluated by the thermal efficiency, net power output and exergy efficiency defined respectively by

$$\eta_{th} = \frac{\dot{W}_{net}}{\dot{Q}_{in}} \tag{6}$$

$$\dot{W}_{net} = \dot{W}_{GT} + \dot{W}_{HPST} + \dot{W}_{IPST} + \dot{W}_{LPST} + \dot{W}_{HT} - \left(\dot{W}_C + \dot{W}_{CP} + \dot{W}_{FWP} + \dot{W}_{CCCP}\right) \tag{7}$$

$$\eta_{ex} = \frac{W_{net}}{\dot{X}_{fuel}} \quad (8)$$

where $\dot{Q}_{in} = \dot{m}_{fuel} LHV$ is the rate of thermal energy transfer from CC as a result of combustion, $\dot{W}_{net}$ is net power output of the plant while $\dot{m}_{fuel}$ is the mass flow rate and LHV is the lower heating value (in kJ/kg) of the natural gas that is calculated based on the fuel composition and $\dot{X}_{fuel}$ is the exergy transfer rate of the fuel.

IV. Results and discussion

The results of the analysis are presented in this section. Figure 2 shows the variation of energy, exergy and environmental performance indicators with the CH_4 fraction for three different values of C_3H_8 fractions where an increase in CH_4 percentage corresponds to a decrease in C_2H_6 percentage and the share of N_2 in the fuel composition is 1%. The results reveal that an increase in CH_4 fraction (decrease in C_2H_6 fraction) decreases the thermal and exergy efficiencies, however it improves the net power output and environmental impact of the plant. The cause for the decrement in thermal efficiency despite the increase in power output is that the lower heating value of the fuel increases faster with the CH_4 fraction than increment rate of power output. With a 15% decrement in methane fraction, the thermal and exergy efficiencies of the CCPP increase by 0.4% and 0.3%, respectively, and correspondingly the power output decreases by 1.8 MW and the CO_2 emission rate increases by 1 kg/s. C_3H_8 fraction also affects the performance of the plant. A higher C_3H_8 fraction leads to a better thermal and exergy efficiency, and it decreases the power output and environmental performance of the CCPP.

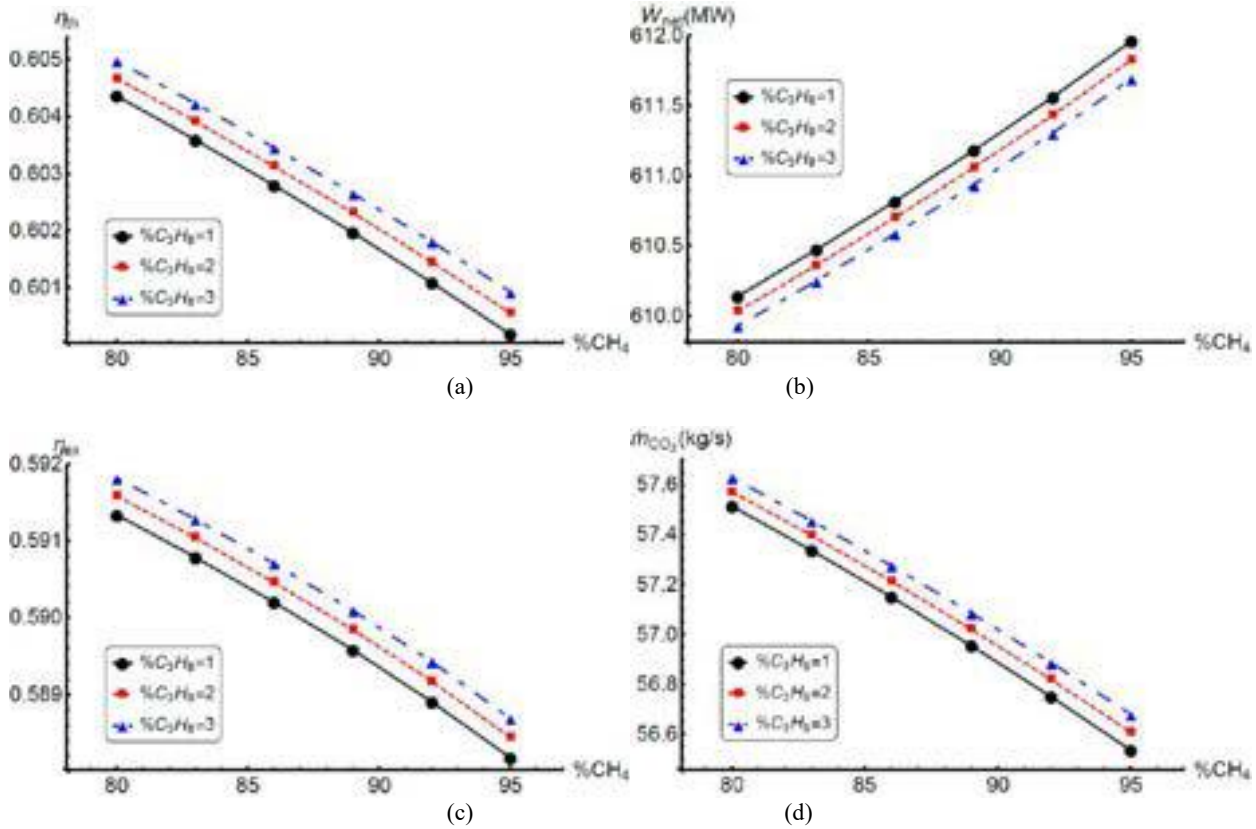

Fig. 2. Effect of natural gas composition on (a) η_{th}, (b) $\dot{W}_{net}$, (c) η_{ex} and (d) $\dot{m}_{CO_2}$ of a CCPP.

The analysis carried out in this research has practical implications. For instance, Türkiye imports natural gas from Russia, Iran and Azerbaijan. As shown in Table 1, these fuels have different compositions (Topal and Tanbay, 2023, Nazari and Maleki, 2016, GGTC, 2023) and therefore result with different performance for certain operating conditions. The natural gas compositions are adjusted to be compatible with the four constituent assumption of this study by incorporating the fractions of butane, pentane, hexane and carbon dioxide into the fraction of C_3H_8. The results for the objective functions presented in Table 1 show that the choice of fuel has a noticeable impact on the performance of the plant. The maximum and minimum thermal efficiencies and CO_2 emission rates differ by 0.5% and 1.2 kg/s, respectively.

Table 1. Performance comparison of a CCPP fueled with natural gas imported from Russia, Iran and Azerbaijan.

Country	Natural gas composition				η_{th}	$\dot{W}_{net}(MW)$	η_{ex}	$\dot{m}_{CO_2}(kg/s)$
	CH_4	C_2H_6	C_3H_8	N_2				
Russia	97.1874	1.5719	0.4939	0.7468	0.597	612.5	0.585	56.6
Iran	84.81	11.08	3.61	0.50	0.600	610.7	0.587	57.8
Azerbaijan	92.3809	3.5107	3.9032	0.2052	0.595	611.7	0.583	57.7

Table 1 shows that although a CCPP fueled by natural gas imported from Iran has maximum thermal and exergetic efficiencies, it also has maximum CO_2 emission rate and minimum power output. On the other hand, this analysis also shows that a CCPP fueled

by natural gas imported from Russia has maximum power output and minimum CO_2 emission rate.

V. Conclusion

This study investigates the impact of natural gas composition on the energetic, exergetic and CO_2 emission performance of a CCPP. A plant in Türkiye with its actual operating conditions serves as a basis for the analysis. Natural gas is assumed to be a mixture of methane, ethane, propane and nitrogen. Thermal efficiency and net power output are chosen as energetic performance indicators, exergy efficiency is used to assess the exergetic performance and carbon dioxide emission rate is considered as the environmental performance indicator. It is found that a decrease in methane fraction and an increase in ethane and propane fractions tend to improve the thermal and exergy efficiencies, however these variations have a negative impact on the power output and environmental performance of the CCPP. This study has practical implications since the results give useful information to decision makers in energy industry. The economic value of the results obtained in this analysis should be taken into account in deciding the best alternative for natural gas import.

References

de Gouw, J.A., Parrish, D.D., Frost, G.J., Trainer, M., (2014) Reduced emissions of CO_2, NO_x, and SO_2 from U.S. power plants owing to switch from coal to natural gas with combined cycle technology. Earth's Future 2, 75-82. https://doi.org/10.1002/2013EF000196

Garcia, S.I., Garcia, R.F., Carril, J.C., Garcia, D.I., (2017) Critical review of the first-law efficiency in different power combined cycle architectures. Energy Conversion and Management 148, 844-859. https://doi.org/10.1016/j.enconman.2017.06.037

GGTC, (2023) Analysis of natural gas done by "Georgian Gas Transportation Company" LLC. https://e-platform.ggtc.ge/gasanalisisen.aspx

Ibrahim, T.K., Mohammed, M.K., Awad, O.I., Abdalla, A.N., Basrawi, F., Mohammed, M.N., Najafi, G., Mamat, R., (2018) A comprehensive review on the exergy analysis of combined cycle power plants. Renewable and Sustainable Energy Reviews 90, 835-850. https://doi.org/10.1016/j.rser.2018.03.072

Liss, W.E., Thrasher, W.H., Steinmetz, G.F., Chowdiah, P., Attari, A, (1992) Variability of natural gas composition in select major metropolitan areas of the United States. Report No: GRI-92/0123, American Gas Association Laboratories.

Nazari, R., Maleki, G., (2016) Chemical and combustion analysis of Iran natural gas with emission level. The Second Iranian Combustion Conference, Islamic Azad University of Mashhad, Mashhad.

Pattanayak, L., Padhi, B.N., (2022) Thermodynamic simulation and economic analysis of combined cycle with inlet air cooling and fuel pre-heating: Performance enhancement and emission reduction. Energy Conversion and Management 267, 115884. https://doi.org/10.1016/j.enconman.2022.115884

Reddy, V.S., Kaushik, S.C., Tyagi, S.K., (2014) Exergetic analysis and evaluation of coal-fired supercritical thermal power plant and natural gas-fired combined cycle power plant. Clean Technologies and Environmental Policy 16, 489-499. https://doi.org/10.1007/s10098-013-0647-x

Shireef, L.T., Ibrahim, T.K., (2022) Influence of operating parameters on the performance of combined cycle based on exergy analysis. Case Studies in Thermal Engineering 40, 102506. https://doi.org/10.1016/j.csite.2022.102506

Topal, G., Tanbay, T., (2023) Energy and exergy analysis of the 1220MW natural gas-fired Hamitabat combined cycle power plant. International Journal of Energy Studies, Submitted to journal.

IEEES-054

Development of a VIV System for Hydrokinetic Energy Harvesting and Pumped Hydro Storage

[1]Alkın Erdal Demirhan [1]Murat Emre Demir, [1]Ömer Kemal Kınacı
[1] Faculty of Naval Architecture and Ocean Engineering, Istanbul Technical University, Maslak-Sariyer, Istanbul, Turkey
*E-mails: demirhana@itu.edu.tr, medemir@itu.edu.tr, kinacio@itu.edu.tr

Abstract

In this study, a novel vortex-induced vibration (VIV) energy conversion and storage system is proposed and analyzed. The proposed system consists of a VIV cylinder array, a water reservoir, and hydro turbines. In the present scenario, a 100 VIV cylinder array with 0.8m and 14.23m of diameter and length, serves as a pump for elevating current to the water reservoir located 30 m above the cylinders. The novel-designed VIV cylinders divert the flow through the piping system. The water storage has a capacity of 170,000 m^3 and ensures stable and continuous electricity production. It provides over 8 hours of constant electricity production in the discharge period. Therefore, it aims to address problems in VIV energy conversion systems related to intermittency and production flexibility. The production capacity of the proposed system is 1.3 MW, with an energy efficiency of 7.6%. Furthermore, a parametric study is conducted to evaluate system performance with varying design and operating condition parameters. The study shows promising electricity production rates even for relatively slow water currents below 2 m/s.

Keywords: Efficiency, energy, pumped hydro energy storage, flow-induced oscillations, vortex-induced vibrations.

I. Introduction

Reducing dependence on fossil fuels and transitioning to renewable energy sources is essential for mitigating climate change and attaining sustainable development objectives. One of the promising aspects of renewable energy is harnessing marine hydrokinetic power available in oceans and rivers. Vortex – Induced vibrations (VIV) are one of the fundamental sub-branches of flow-induced motions (FIM). VIV is a phenomenon about vorticities that are shed from a bluff body. Vortices arise at the aft as the flow encounters the cylinder in a suitable Reynolds number. These vortices apply bi-directional forces on the cylinder. While the first streamline forms a vortex in the wake, a part of the second streamline passes through the cylinder and the vortex and eventually breaks the formed vortex.

The vortex shedding causes the cylinder to be pushed downward. The streamlines pass under the cylinder, which causes vortex shedding. Finally, the lifting force appears under the cylinder. That force lifts the cylinder in an upward way. Then, this process repeats itself as bi-directional and periodically continues. Some studies focused on the vortex-induced vibration aquatic clean energy VIVACE converter introduced by (Bernitsas et al., 2008), which converts ocean/river current energy to electricity. A harmonic, bidirectional motion is generated perpendicular to the flow direction. Due to the flow and vortex shedding of the VIVACE converter system, the cylinder moves in both an upward and downward direction, which causes the bearing to rise. Consequently, the power is transmitted to the generator via connections, and the gear belt is rotated.

However, the hydrokinetic energy of oceans is intermittent by nature. Therefore, for reliable energy production, they should be assisted by conventional energy production systems in hybrid systems or outfitted with large-scale storage systems. Pumped hydro storage is regarded as a straightforward method of energy storage. This technique entails pumping water into a reservoir during periods of low energy demand. With a typical storage cycle efficiency of 65–75%, when energy demand is high, stored water is discharged and flows downwards, driving the turbines and generating electricity. In order to meet energy demands during periods of high demand, this system is extensively utilized in the energy sector to store excess energy during periods of low capacity. In most cases, the guiding principle consists of two dams of varying heights or a dam with an ample water supply, and it is the only well-established method for storing energy on a large scale (Dincer and Rosen, 2021). This study aims to propose and analyze a large-scale system for hydrokinetic energy conversion via VIV cylinders combined with pumped hydro energy storage for the first time in the open literature.

II. System Description

The proposed system includes a collection of VIV cylinders, a water reservoir, and hydroelectric generators. Design parameters of experimental setup and scaled up system is tabulated in Table 1. In the current scenario, a set of one hundred VIV cylinders with diameters and lengths measuring 0.8 meters and 14.23 meters, respectively, acts as a pump to transport current to a water reservoir positioned thirty meters above the cylinders. The flow is redirected through the pipe system thanks to the innovative design of the VIV cylinders. Aperture to the flow, the cylinder experiences motion in a direction perpendicular to the flow due to the vortices it generates. Additionally, the roller elevates the pumps located within the struts on both sides. The water accumulated in the pipes is propelled upwards by the pistons via the water outlet holes.

Table 1. Design parameters of the experimental setup and scaled-up system

Parameters	**Value**
Length of the VIV cylinder used in experiments, $L_{VIV,exp}$	1.423 (m)
Diameter of the VIV cylinder used in experiments, $D_{VIV,exp}$	0.08 (m)
Spring constant of VIV setup used in experiments, k_{exp}	766 (N/m)
Length of a VIV cylinder in the scaled-up system, L_{VIV}	14.23 (m)
Number of VIV cylinders in the scaled-up system, N	100
Diameter of a VIV cylinder in the scaled-up system D_{VIV}	0.8 (m)
The depth at which the cylinders are located under water d_{VIV}	5 (m)
VIV pipe diameter, $d_{Penstock}$	0.2 (m)
VIV pipe length, $l_{Penstock}$	30 (m)
Water reservoir capacity, V_{dam}	170,000 (m^3)
Depth of water reservoir d_{dam}	5 (m)
Penstock diameter at water reservoir $d_{Penstock}$	3 (m)
Penstock length at water reservoir $l_{Penstock}$	30 (m)
Water turbine efficiency	90%

Consequently, the water stored in the system's lower reservoirs is collected as it is pressed upwards via the pipes. Kinaci, an author of this study, established the patent for the pump system design (Kinaci, 2020). The proposed water storage facility has a volume of 170,000 m^3 and assures that the power generation will be at the desired rate and stable. During the discharge phase, it maintains a production rate of nearly 8 hours' worth of continuous energy. As a result, this project aims to address issues in VIV energy conversion systems associated with intermittent production and flexibility. Based on the experimental configuration in the FIMLab at Istanbul Technical University Faculty of Naval Architecture and Ocean Engineering, the design characteristics of the scaled-up system are determined. The experimental apparatus can be seen in Fig. 1.

Fig. 1: ITU Naval Architecture and Ocean Engineering Building Ata Nutku Ship Model Testing Laboratory the circulation channel

III. Analysis

A cylinder with a definite degree of freedom (DOF) provides a way to extract power from the fluid. Here, a cylinder moves only in 1 direction, which is in the transverse direction of incoming flow. The power available in the fluid relies on the force that is created by the flow on the cylinder. The incoming flow pressures the cylinder which drives a radial force. The power is defined as force times the velocity as follows:

$$P_{fluid,D} = \frac{1}{2}\rho U^3 DL \quad (1)$$

When the cylinder moves in 1DOF, which is perpendicular to the incoming flow, the swept area by the cylinder can be calculated as the summation of diameter of the cylinder and two amplitudes times the length of the cylinder ((D+2A)L) (Duranay et al., 2022). Thus, the formula of the fluid power exerted on an oscillating cylinder can be defined as follows:

$$P_{fluid} = \frac{1}{2}\rho U^3 (D + 2A)L \quad (2)$$

(Duranay et al., 2022) states that the formula of the power capture of a cylinder in a VIV system is indicated in equation as follows:

$$P_{CAP} = \frac{W_{cyl}}{T_{osc}} \quad (3)$$

Here, while W_{cyl} is the work done by the fluid force that acts on the cylinder, T_{osc} is the oscillation period. The work done through a cycle of cylinder can be calculated as follows:

$$W_{cyl} = \int_0^{T_{osc}} F_{y,(tot)}\dot{y}dt \quad (4)$$

The following equation is derived from a series of algebraic operations in order to represent the fluid power captured by the cylinder: (Duranay et al., 2022):

$$P_{cap} = \frac{1}{2}\rho C_{y,tot} U^2 f_{osc} ADLsin\phi_{tot} \quad (5)$$

The energy converter systems cannot wholly capture the fluid power acting on the cylinder. By considering the Betz limit for turbines theoretical maximum efficiency, which Albert Betz defined in 1919, the efficiency of VIVACE can be defined by the power conversion of oscillator efficiency (Kim & Bernitsas, 2016) as follows:

$$\eta_{cap} = \frac{P_{cap}}{P_{fluid}\, x\, Betz\ limit} \quad (6)$$

Here, the Betz limit is a theoretical limit for turbines. Betz limit corresponds to 59.26% (16/27) in open flows. In cases where no losses occur within the pipe, the volumetric flow that the captured energy can theoretically transport to the upper reservoir can be expressed as follows:

$$\dot{V}_{water} = \frac{U^3 L(D+2A)\cdot Betz\ limit\cdot \eta_{cap}}{2\, g\, h} \quad (7)$$

Where h represents the maximum height (m) that water can be pumped.. The mathematical model in this study considered the piping loss through upwards and penstock loss in discharging processes. Furthermore, the hydro-turbine conversion efficiency is assumed to be 90% in calculations. By taking into account all the system inputs, the overall energy efficiency of the system is defined as follows:

$$\eta_{ov} = \frac{P_{fluid}}{\dot{W}_{turbine}} \quad (8)$$

The flow and VIV motion characteristics used in the mathematical model of the scaled-up system are based on experiments. The VIV phenomenon is directly related to a fluid. Therefore, some dimensionless numbers, such as Reynolds's number (Re) and Strouhal's number (St), are used in VIV. Similar to VIV studies in literature, some parameters are nondimensionalized in this study to assess the results independent from sizes. Some dimensionless parameters are used in VIV amplitude ratio (A*), velocity ratio (U*), mass ratio (m*), and frequency ratio (f*). The dimensionless numbers determined from the experimental study are implemented in the scaled-up system.

IV. Results

The results show that the VIV array that operates under 1.74 m/s of current can produce 1.1 MW of electricity. VIV cylinders capture the flow energy with an efficiency of η_{cap}=25.04%. The power production is calculated based on the same charging and discharging rate of the energy storage system. It should also be noted that not all the captured power is stored. 12.4 kW of hydrokinetic power is lost during charging due to piping loss, and 0.1 kW of power is lost during downflow current to the turbine through penstock. Also, 10% is lost in the water turbine. Considering all the inputs and outputs, overall energy efficiency is determined as η_{ov}=11.03%.

Furthermore, it takes 10 hours to charge the hydro-pump energy storage reservoir with the VIV pump force corresponding to 4.757 m^3/s charging rate. A parametric study assesses the impact of system performance with changing working conditions. Fig. 2(a) presents the variation of the captured power of the VIV cylinder array and its efficiency with the flow speed. While the efficiency reaches a maximum value of around 1.8 m/s, the maximum output is calculated as 2.1 m/s by around 1.77 MW. At that rate, the overall system efficiency is obtained as 7.6%. Charging and discharging periods are other parameters that must be considered. As presented in Fig 2.(b), the proposed system offers promising charging rates between 1.6 m/s and 2.8 m/s flow speeds. It reaches a maximum charging rate at 2.1 m/s of flow speed with 8.2 hours of fill time and 5.783 m^3/s flow rate.

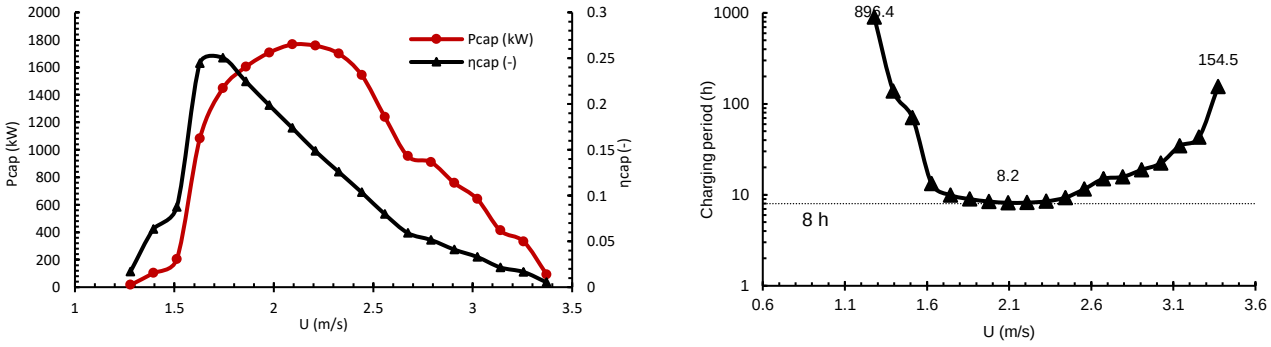

(a) (b)

Fig. 2: Variation of system performance with current spend. (a) Captured power by VIV cylinder and efficiency, (b) Charging period of pumped hydro storage water reservoir

V. Conclusions

In this study, a VIV cylinder array assisted with a pumped energy storage system for electricity generation is designed and analyzed. The performance of the scaled-up system is assessed based on the experimental results of the prototype VIV system at Istanbul Technical University. The main findings of this study can be listed as follows:

- At 1.74 m/s of current speed, the VIV array operates with a maximum capture efficiency of 25.04%.
- At 1.74 m/s of current speed, the proposed system produces 1.1 MW of electricity with an overall energy efficiency of 11.03% after accounting for losses during capture, storage, and conversion.
- At 2.1 m/s of current speed, the VIV cylinder array yielded a maximum captured power output of 1.8 MW.
- At 2.1 m/s of current speed, the proposed system yielded a maximum electricity generation of 1.3 MW and an overall efficiency of 7.6%.
- The proposed system has promising charging rates ranging from 1.6 m/s to 2.8 m/s of current speed, with a maximum charging rate of 2.1 m/s, an 8.2-hour fill time, and a pumping flow rate of 5.783 m^3/s.

References

Bernitsas, M.M., Raghavan, K., Ben-Simon, Y., Garcia, E.M.H., 2008. VIVACE (Vortex Induced Vibration Aquatic Clean Energy): A new concept in generation of clean and renewable energy from fluid flow. J. Offshore Mech. Arct. Eng. 130, 1–15. https://doi.org/10.1115/1.2957913

Dincer, I., Rosen, M.A., 2021. Thermal Energy Storage Systems and Applications, 3rd ed, Wiley. Wiley.

Kinaci, O.K., 2020. Akımla kendini tahrik eden pompa. Turkish Patent and Trademark Office 2015 17104.

IEEES-055

Harnessing Wind Energy: Solid Sails in Maritime Transport for Sustainable Energy Utilization

[1]Cihan Emre Şahin, [1]Murat Emre Demir
[1] Faculty of Naval Architecture and Ocean Engineering, Istanbul Technical University, Maslak-Sariyer, Istanbul, Türkiye
*E-mails: sahinci20@itu.edu.tr, medemir@itu.edu.tr

Abstract

Using solid sails powered by wind energy in maritime transport represents a significant strategy supporting renewable energy resource utilization and environmental sustainability. To evaluate the impact of wind sails on ships, it is essential to calculate the aerodynamics of the sails accurately. However, most of the research on sails is based on stable wind conditions rather than natural wind, which varies horizontally and vertically. This study investigates the thrust force provided by a 130-square meter NACA0012 foil wing to a ship traveling from Türkiye to Norway, covering a route from Istanbul's Kalamış to Norway's Herdla-Utsiden, which includes a total of 46 waypoints. Annual average wind data has been collected at each waypoint. The lift and drag forces generated by the wing result in the force. This force's x-direction (heading) component directly provides thrust to the ship, serving as the efficient force for our calculations. Based on natural annual average wind data, the findings reveal that, compared to natural average wind conditions, the maximum thrust energy occurs in February and December, reaching 31,836 kWh, while the minimum is recorded in September at 22,250 kWh.

Keywords: Wind Energy, Green Technology, Wing Sail, Carbon Reduction.

I. Introduction

An annual transportation of millions of commodities constitutes a substantial sector of international commerce known as shipping. Unfortunately, the predominant environmental consequence of this enormous scale pertains to elevated carbon emissions. The primary contributor to greenhouse gas emissions in the transport industry is the substantial consumption of fossil fuels. This presents a substantial obstacle in the effort to mitigate the effects of global warming and climate change. Regarding this, the use of solid wing sails in maritime transportation not only increases environmental sustainability but also enables efficient use of energy resources. Solid wing sails were one of the main sources of energy from the early days of shipping until the development of the industrial revolution and enabled the formation of maritime trade. However, with the increase in fossil fuel use after the industrial revolution, sails were replaced by internal combustion engines in maritime over time, causing carbon emissions to increase.

The International Maritime Organization (IMO) has set a goal of reducing carbon emissions from shipping to zero by 2050. There is an urgent need for the maritime sector to intervene in emissions in line with IMO's targets. Solid wing sails can play a crucial role in achieving this goal. Sails can reduce fuel consumption and the environmental impacts of this consumption by providing some of the propulsion power needed by the ship by using wind, which is a renewable energy source. Solid wing sails can be defined as an additional system that assists the ship's own propulsion system. "Shin Aitoku Maru", the world's first advanced wing-assisted sailboat, has two wing sails with a total sail area of 194.4 m². In Chen Li's research, which started in 1980 and lasted for four years, it was determined that energy savings of up to 8.5% were achieved compared to other ship types (Chen Li, 2020).

The purpose of this research is to demonstrate the value of substantial wing sails for ships and to serve as a guide for expanding their use in the maritime industry. The investigation also encompasses the potential contribution of these sails to the International Maritime Organization's 2050 objectives and the utilization of renewable energy sources in maritime transportation. Furthermore, the research investigates the implications of the most recent technological advancements on environmental sustainability.

As a result, using wing sails on ships contributes to environmental sustainability and significantly reduces the carbon emissions created by the shipping industry. This study aims to contribute to the build of a cleaner and greener future for maritime transportation.

II. System Description

Foil wings are designed for create lift force according to the Lift equation created by Bernoulli's principle. Sailing systems are used to control the wind on ships, but traditional sails can only control the wind coming from the stern of the ship. However, instead of traditional sails, it is possible to create lift and drag forces can use with wing sail, and it can use these two forces as a thrust for the ship. To use lift force for ship propulsion, we can use a system that takes advantage of the horizontal and vertical lift generation of the aircraft when it is in a vertical position. Additionally, efficiency can be increased by the lift coefficient of the wing through suction from the upper surface of the wing. However, there is a limitation in this situation, because the power required for suction will eventually pass over its contribution to power and efficiency will decrease. The optimum point can be obtained the right method. In this way, we can use wind energy as propulsion energy. In addition, the air absorbed here can be used as an air cover on the ship and reduce friction. This serves to both reduce the resistance of the ship and increase wing efficiency. If this process is not efficient at the specified routes and speeds, this air can be used for ventilation and air conditioning purposes, as well as for electricity generation with a turbine.

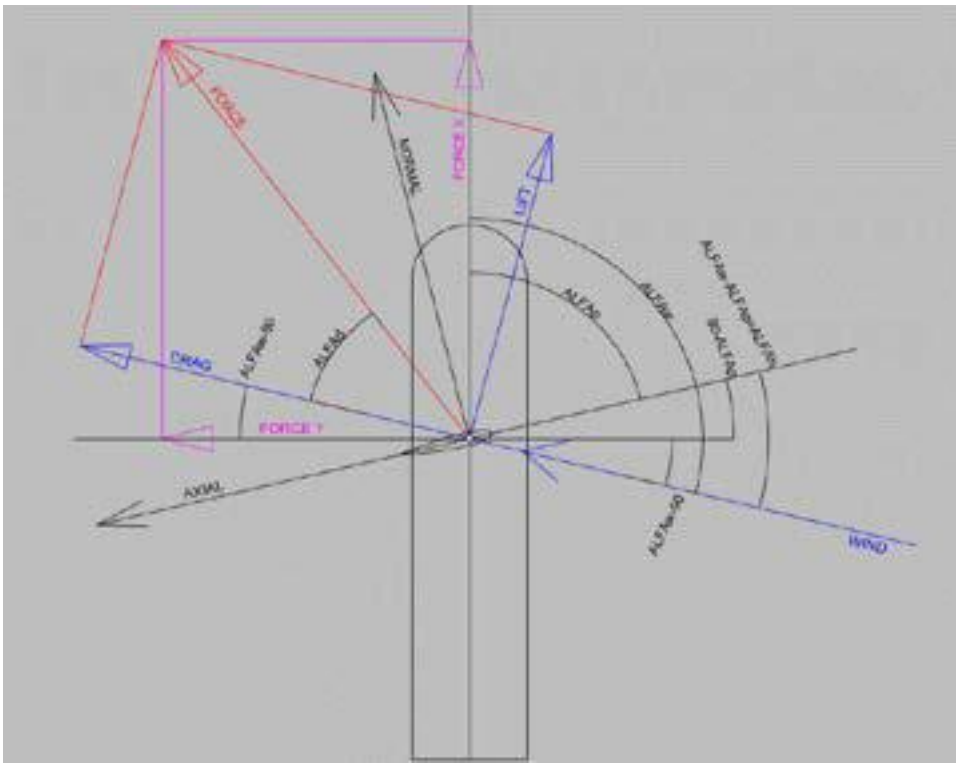

Fig. 1: Wing foil force schema"

III. Analysis

In this study, the wing values of the NACA 0012 airfoil have been used (A. Michos, 1983). The calculations were based on a route covering a total of 46 intermediate points, starting from Istanbul Kalamis to Norway Herdla+Utsiden. Annual average wind data was collected at each transition point. The lift and drag forces created by the wing created the resultant force called Force, as seen in Figure 1. The x-direction (direction) component of this Force provides thrust directly to the ship, being the effective force used in the calculations. The y-direction component of the Force is neglected in this study, but it will also create some drag on the ship. To eliminate this drift, the captain must adjust the rudder. This will lead to a slight increase in total resistance.

$$F = \frac{Cl \times \rho \times A \times V^2}{2} \quad (1)$$

where F: Lifting Force, Cl: Wing lift coefficient, ρ: Air Density, A: Profile Area, V: Velocity

The other data used in addition to wing data and wind data are as follows:

ρ= 1.29 (kg/m^3)
A= 130 (m^2)
V= 6.1733 (m/s)

IV. Results and discussion

These results show that the use of a NACA0012 type 130 m^2 airfoil can reduce the ship's energy needs by a total of 31,836 kWh, especially when a ship maintains a constant speed of 6.1733 m/s on a given route for a total of 306 hours. Looking at the table, it can be seen that December and February are the months with the highest potential for generating propulsion energy. This is attributed to the fact that the chosen route was in winter and in strong wind conditions.

It should be noted that these results do not depend only on wind speed, but the angle of approach of the wind also plays an important role. The angle at which the wind hits the ship relative to its direction of travel is a critical factor affecting the power produced by the wing. Therefore, in order to analyze the route, a system that can calculate wing angles in real time must be used.

Table 1. Monthly Solid-Wing Thrust Energy

Month	Total Navigation Time (hours)	Total Thrust Energy (kWh)
January	306	31815
February	306	31836
March	306	29975
April	306	25805
May	306	25026
June	306	22992
July	306	22993
August	306	22260
September	306	22250
October	306	24206
November	306	28595
December	306	31836

This feature facilitates the ship's perpetual pursuit of the most optimal course.
Another striking finding on this route is that the energy production in September was 22,250 kWh. The most important reason for this is that in the summer months, the wind's approach angle is more parallel to the ship's direction of travel, resulting in lower energy production in September. For instance, in June and July, wind angles are more perpendicular to the ship's direction of travel, these results are showing to more produce energy compare to September.

All these findings highlight the potential for increasing energy efficiency in the use of wing sails in maritime transport. Optimization of sail design and the use of wind energy make significant contributions to a sustainable future. This research emphasizes the environmental impact of wing sails on the marine sector, both reducing carbon emissions and their potential to increase environmental sustainability.

V. Conclusions

Solid sails are crucial for a sustainable future in the maritime industry because they substantially reduce carbon emissions. The present investigation demonstrates the capacity of substantial sails to convert wind energy. This results in increased interest in renewable energy sources and decreased reliance on nonrenewable energy sources. An estimation suggests that a NACA0012 type 130 m^2 wing, operating at a consistent speed of 6.1733 m/s for 306 hours along the route connecting Istanbul and Norway, is capable of generating a maximum of 31,836 kWh of energy and simultaneously meeting the energy requirements of the vessel.

The findings underscore the viability of implementing rigid-wing sails as a supplementary propulsion mechanism within the realm of maritime transportation. It is a successful measure in the pursuit of establishing environmental sustainability within the maritime industry, thereby contributing to the fulfillment of the International Maritime Organization's (IMO) 2050 objectives. Sails with solid wings can significantly contribute to the attainment of these sustainability objectives.

Furthermore, the implementation of solid wing sail technology advancements results in improved efficiency of these systems, thereby expanding their practical applications and rendering them more economically viable and environmentally sustainable. It has a distinct significance that the maritime voyage that began with the wind continues with the wind.

Thus, solid-wing sails are a system that contributes to the achievement of the International Maritime Organization's 2050 objectives for environmental sustainability and emission reduction in the maritime sector. It is a system that, through the use of wind energy and more efficient sail design, can contribute to a greener and more sustainable future in the maritime industry. The primary objective of this study is to contribute to and facilitate a more comprehensive comprehension of the manner in which solid wing sails mitigate carbon emissions within the maritime sector, as well as to identify potential avenues for environmental sustainability.
assistance.

References

A. Michos, (1983). Aerodynamic Characteristics of NACA 0012 Airfoil in Relation to Wind Generators,, Wind Engineering, cilt No. 4 (1983), no. pp. 247-262, p. Vol. 7,

Chen Li, (2020). Numerical Investigation of a Two-Element Wingsail for Ship Auxiliary Propulsion,» Journal of Marine Science and Engineering DOI: 10.3390/jmse8050333

IEEES-056

Effects of Distance and Absorber Shape on the Energetic and Exergetic Performance of a Solar Collector

[1*] Hocine Guellil, [2] AbdelIllah Nabil Korti
[12] ETAP Laboratory, University of Tlemcen, 230, 13000, Algeria
E-mails: *guellil10@yahoo.fr
korti72@yahoo.fr

Abstract

The objective of this work is to develop an air-based solar collector using three distinct absorbers: flat (as a reference), corrugated, and trapezoidal, under constant radiation from an artificial thermal source. The study focuses on comparing the energetic and exergetic performances of the collector. Tests are conducted under constant radiation and airflow, while varying the distance between the absorbers and the glazing, namely 3, 6, 9, and 12 cm.
The results obtained highlighted the superiority of the trapezoidal absorber compared to the flat and corrugated absorbers in terms of thermal and exergetic efficiency. However, the trapezoidal absorber located at 12 cm from the glazing recorded a maximum thermal efficiency of 85%, while the flat and corrugated absorbers located at 6 cm from the glazing recorded maximum efficiencies of 78% and 82% respectively. The exergetic efficiency of the trapezoidal absorber was significantly higher than that of the flat and corrugated absorbers, reaching 47% compared to only 27% and 32% respectively for the flat and corrugated absorbers at the previously mentioned distances.
The results allowed for the determination of the most efficient absorber type and the optimization of the design of air-based solar panels.

Keywords: "Double Pass Collector, flat, corrugated and trapezoidal absorber, thermal efficiency, exergetic efficiency, energetic efficiency".

I. Introduction

The concern over severe environmental pollution resulting from the use of fossil fuels has created an urgent need to explore energy sources with lower environmental impact. Among these sources, solar energy stands out as one of the most significant and environmentally friendly options. Solar energy has been utilized for a long time for lighting, heating, and crop drying purposes [1]. The interest in solar energy gained momentum after the events of 1973, when fossil fuel prices surged. This prompted research efforts to focus on inventing and developing both simple and complex solar-powered systems (for water and air). Among the latter, air-based solar collectors are frequently employed for heating [2], industrial drying [3,4], and agricultural crop drying [5]. These air-based solar collectors vary in form, characteristics, and application domain [6]. Systems range from single-pass to multi-pass [6], with the latter allowing for a longer air exchange distance, consequently improving efficiency.

Furthermore, the concept of exergy has also played a significant role, as many researchers are currently focusing their studies on the performance of solar collectors based on the second law of thermodynamics and its entropy [7]. This is because the latter provides a more precise assessment of the efficiency of energy conversion systems [8]. The thermal exchange between the circulating air and the absorbers represents the most crucial challenge driving researchers to enhance it. They do so by proposing and testing various models and forms of the absorber. Among these, we can mention fins, flaps, obstacles, porous media, and so on [9]. These obstacles create a slowing down of the airflow and improve heat exchange. Mohammed S et al [10] studied a solar collector system with triangular longitudinal fins attached to the surface of the absorber in four collector models made of aluminum and for three flow rate values. The results demonstrated that the temperature difference gradually increased until midday. The findings proved that the presence of fins was an effective technique for enhancing the thermal performance of the double-pass solar collector with a non-significant increase in pressure drop. Omojaro and Aldabbagh [11] conducted an experimental study on the performance of a single-pass and double-pass solar collector with attached fins, using a wire mesh as an absorber plate. The study examines the influence of varying airflow rates on the outlet temperature and thermal efficiency for bed heights of 7 cm and 3 cm respectively for the lower and upper channels. The results demonstrated that efficiency increases with higher mass flow rates of air. Additionally, the double-pass collector's efficiency proved 7 to 19.4% higher compared to the single-pass collector.

The addition of layered wire mesh showed a much more significant improvement in thermal efficiency. Another experimental study of a double-channel air-based solar collector with a perforated "V"-shaped corrugated absorber plate aimed to evaluate the thermal and exergetic performance of the collector and compare it to a flat-plate collector [12]. The experiments were conducted over a range of mass flow rates and levels of solar radiation. The results indicated that the double-channel collector with the perforated "V"-shaped corrugated absorber plate exhibited higher thermal efficiency compared to the flat-plate collector.

II. Experimental Procedure

The prototype of our solar collector choice involves the use of two air passages. The first air passage occurs by drawing in air at the base of the collector, while the second air passage flows across the collection surface of 0.714, 0.768, and 0.92352 m² respectively for the flat, corrugated, and trapezoïdal absorbers. The aim of this work is to vary the gap used between the absorbers and the glazing by 3, 6, 9, and 12 cm. A variable artificial thermal source is used at 750 W/m², which approximates the maximum sunlight in the month of April in the city of Tlemcen (Algeria).

IV. Results and discussion"Arial, 10 points, bold"

Fig. 1 illustrates the comparison of the best recorded temperature differences among the three sensors. At the 12 cm position between the trapezoïdal-shaped absorber and the glazing, there is a higher temperature difference (35 °C) compared to the corrugated (28 °C) and the flat shape (25 °C) spaced 6 cm apart.

The trapezoïdal shape at the 12 cm position records 35% more than the corrugated shape and 45% more than the flat shape, respectively, at the 6 cm position.

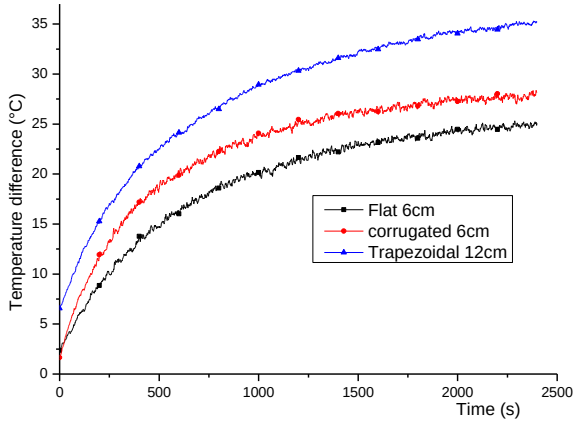

Fig. 1. Temporel evolution of temperature difference for flat, trapezoïdal and corrugated absorbers

The previous temperature difference results are represented by the different energy levels in Fig. 2. The temporal evolution of the energy quantity at the 12 cm position between the trapezoidal-shaped absorber and the glazing records a maximum energy (1300 kW) higher than that of the corrugated shape (1000 kW) and the flat shape (850 kW) spaced 6 cm apart, representing energy gains of 30% and 53%, respectively. These values confirm that the recovered energy varies significantly depending on the shape and gap used between the absorber and the glazing.

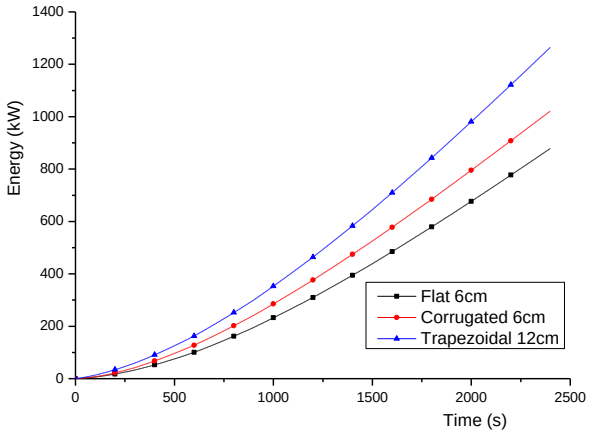

Fig. 2. Temporel evolution of energy for flat, trapezoïdal and corrugated absorbers

Fig. 3 represents a comparison of the temporal evolution of efficiencies between the trapezoidal-shaped absorber spaced 12 cm from the glazing and the flat and corrugated shaped absorbers with a 6 cm gap. It is evident that the trapezoidal shaped absorber displays a higher efficiency compared to both the flat and corrugated absorbers for all tested gap variations. This improvement can be attributed to a better distribution of airflow and a larger absorption surface. However, the efficiency of the flat absorber for the optimal 6 cm gap remains lower than that of the trapezoidal and corrugated absorbers.

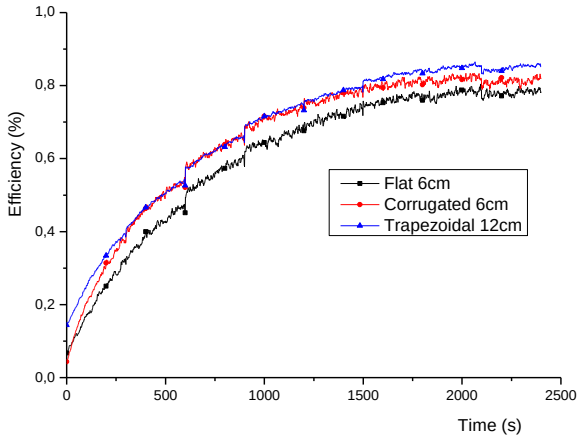

Fig. 3. Temporel evolution of efficiency for flat, trapezoïdal and corrugated absorbers

The effect of different spacings relative to the glazing in the experiment on exergy loss and second-law efficiency is shown in Fig. 4 for the three types of absorbers. It is evident from Fig. 4 that exergy loss decreases with the shape and spacing that record the highest useful energy. The minimum loss for the trapezoidal-shaped absorber is approximately 40 kW, while the highest exergy loss approaches 55 kW for the flat and corrugated absorbers.

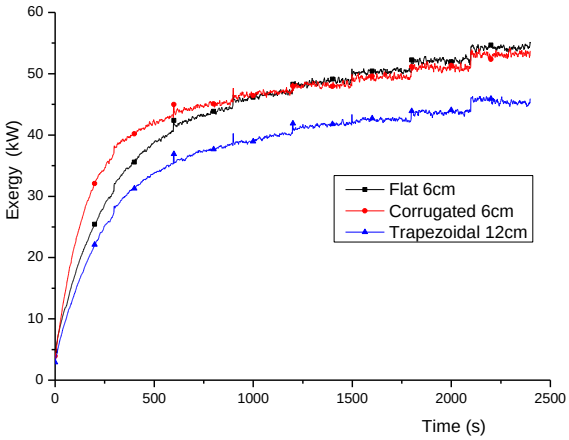

Fig. 4. Temporel evolution of exergy for flat, trapezoïdal and corrugated absorbers

Fig. 5 represents the effect of the gap between the absorber and the glazing on the exergetic efficiency of the collector for different absorber shapes. The figure clearly demonstrates that the trapezoidal shape spaced 12 cm records a higher exergetic efficiency than the other two shapes. For a 6 cm gap, the flat shape records the lowest exergetic efficiency at around 22%, whereas the most substantial exergetic efficiency is approximately 45% for the trapezoïdal shape positioned at 12 cm due to the considerable amount of useful energy absorbed by the collectors. This leads to a significant enhancement in heat transfer

.

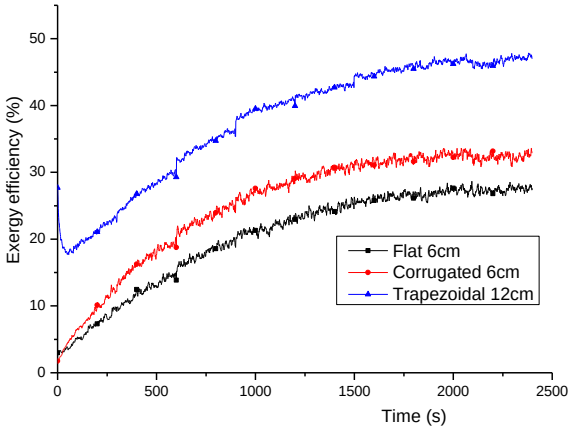

Fig. 5. Temporel evolution of exergy efficiency for flat, trapezoïdal and corrugated absorbers

V. Conclusion

This work focuses on the performance and efficiency of different absorber designs, specifically flat, corrugated, and trapezoïdal absorbers with varying gaps from the glazing.

An important aspect of our experimental setup was the inclusion of a thermal source to provide a consistent input of radiation. This allowed us to control and standardize the thermal source, ensuring consistent conditions throughout the experiments. Additionally, a constant air flow rate was maintained to simulate realistic operating conditions and facilitate accurate temperature measurements.

The experimental analysis of exergy losses and exergetic efficiency for different absorber plates was investigated in this study. The exergy losses and exergetic efficiency of three types of absorber plate configurations with different shapes and gaps were compared to those of the traditional flat absorber plate. Well-chosen gaps between the glazing and the absorber as well as their shapes increase the surface area and promote good mixing of fluid layers, resulting in an enhancement of the efficiency of solar collectors. The main conclusions are as follows:

1. A 6 cm gap between the flat and corrugated absorbers and the glazing resulted in a significant temperature difference, reaching 22 and 26 °C respectively by the end of the experiment. The 12 cm gap also recorded a higher temperature difference for the trapezoïdal absorber.
2. The maximum recorded energy quantity is 1300 kW for the trapezoidal-shaped absorber positioned 12 cm from the glazing. The undulating and flat shapes (both at 6 cm from the glazing) record energy gains of 1000 and 850 kW respectively, which are 30% and 53% lower. These values confirm that the recovered energy varies significantly depending on the shape and gap used between the absorber and the glazing.
3. The trapezoidal absorber positioned 12 cm from the glazing exhibits a maximum efficiency of approximately 89%, while the minimum efficiency is around 70% for the flat absorber positioned 6 cm from the glazing.
4. The highest exergy loss occurred with the conventional flat absorber, approximating 45 kW. This can be explained by the fact that, for this type, only a small amount of solar energy absorbed by the absorber plate is utilized in the exergetic analysis.
5. The optimal value of exergetic efficiency is achieved for the solar collector equipped with the trapezoidal-shaped absorber spaced 12 cm from the glazing, and it is 45% higher than that of the conventional flat absorber, which is 19%, and that of the corrugated absorber, which is 22%, both spaced 6 cm from the glazing.
6. This study suggests that the absorber shape and the careful consideration of the gap from the glazing are effective procedures that can be employed in an air exchange system according to user requirements.
7. Exergetic analysis is a valuable tool for the design, development, and optimization of air-based solar collectors.

Acknowledgements
The study is carried out at the ETAP applied energy and thermal laboratory at the University of Tlemcen, Algeria..

References

[1] Om Prakash. 2017. Solar drying technology. Concept, design, testing, modelling, economics and environment, Springer.
[2] D. Yogi Goswani. 2015. Principles of solar engineering. Third edition. Taylor and Francis.
[3] John A. Duffie and William A. Beckman. 2013. Solair engineering of thermal processes. Gear team. Mechanical engineers. Fourth edition. J. Wiley.
[4] Shringi V, Kothari S, Panwar NL (2014) Experimental investigation of drying of garlic clove in solar dryer using phase change material as energy storage. J Therm Anal Calorim 118 (1):533–53
[5] Sharma VK, Colangelo A, Spagna G (1995) Experimental investigation of different solar dryers suitable for fruit and vegetable drying. Renew Energy 6(4):413–424
[6] Khartchenko NV (1997) Advanced energy systems. Institute of Energy Engineering & Technology University, Berlin.
[7] Erbay Z, Hepbasli A (2013) Advanced exergy analysis of a heat pump drying system used in food drying. Dry Technol 31:802–810.
[8] Kuzgunkaya EH, Hepbasli A (2007) Exergetic performance assessment of a ground-source heat pump drying system. Int J Energy Res 31(8):760–777.
[9] Sopian K, Supranto, Othman MY, Daud WRW, Yatim B (2007) Double-pass solar collectors with porous media suitable for higher-temperature solar-assisted drying systems. J Energy Eng 133 (1):1–18
[10]. Mohammed S. Fahmi, Wissam H. Khalil, Amer J. Shareef. Energy and Exergy Analysis of a Finned-Plate Double Pass Solar Air Heater with Different Arrangement. Journal of Power and Energy Engineering, Vol.8 No.10, October 19, 2020.
[11]. A.P. Omojaro, L.B.Y. Aldabbagh. Experimental performance of single and double pass solar air heater with fins and steel wire mesh as absorber. Applied Energy. Volume 87, Issue 12, December 2010, Pages 3759-3765.
[12] Suhaib J. Shbailat et al. 2019. Energy and Exergy Analysis of Solar Air Collector with Perforating Corrugated Absorber Plate. https://www.researchgate.net/publication/324991806.

IEEES-057

Thin Films in Solar Cell Applications

Büşra Osma [1*], Gülşen Akın Evingür[1*]
[1] Pîrî Reis University, Postane Maahallesi Eflatun Sk. No:8 Tuzla, İstanbul, 34940, Turkey
*E-mails: gulsen.evingur@pirireis.edu.tr , busra.osma@pirireis.edu.tr

Abstract

Thin films of the ethylene vinyl acetate (EVA) has different vinyl acetate percents (12%, 28% and 40%) and has been produced in toluene by solution processing technique. In this study, EVA polymers, which have various vinyl acetate percent were examined for their optical characteristics to use solar cell applications. The optical parameters, refractive index (n), optical conductivity ($\boldsymbol{\sigma}$), extinction coefficient(k), real ($\boldsymbol{\varepsilon_r}$) and imaginary ($\boldsymbol{\varepsilon_i}$) parts of dielectric constant were calculated in the range of between 200 and 800 nm by analyzing the UV-vis spectroscopy. Furthermore, refractive index(n), extinction coefficient(k), real($\boldsymbol{\varepsilon_r}$) and imaginary($\boldsymbol{\varepsilon_i}$) dielectric constants,which behave similarly as a function of wavelength were observed. Results suggest that 12% of EVA, 28% of EVA, and 40% of EVA polymers were compared among them and show promising to use solar cell.

Keywords: Ethylene vinyl acetate, solar cell, optical properties, optical conductivity, dielectric constant

I. Introduction

Nowadays, industry and academia have faced the need to examine more efficient technologies that have renewable energy systems and are clean to decrease global warming and environmental pollution effects. To develop novel photovoltaic technologies (PVs) that efficiently convert solar irradiation into electrical power, it is necessary to undertake research and innovation. Developing novel materials for efficient solar cells has increased the need for renewable and sustainable energy sources. Thus, sunlight energy, which is environmental, available, and cheap, is a possible solution in the long term. Polymers that can perform conversion energy effectively have the potential for quick charging, an easy manufacturing process, and lightweight properties. Thus, polymer materials have started to utilize photovoltaic technologies for solar cells (Alhamada, T.F., et al.).

In this research, the optical qualities of EVA polymers, which exhibit varying percentages of vinyl acetate, were investigated in relation to their potential usage in solar cells. The findings indicate that when comparing different types of EVA polymers, 12%, 28%, and 40% shown promising potential for use in solar cell applications.

II.Materials and Methods

II.I. Preparation of EVA Polymers

Ethylene-vinyl acetate copolymer (EVA), which occurs in ethylene and vinyl acetate (VA) with free radical polymerization between in 1 wt % and 50 wt %. VA (Sadiku, E. R., et al). EVA copolymers, which have 12 wt %, 28 wt % , and 40 wt % VA weight percents were put in 60 ml, 100 ml, and 100 ml xylene solvent, respectively. EVA was prepared by solution-processing technique. These commercial chemical materials were measured using ACJ 220-4M model sensitive scales.EVA and xylene were mixed in a beaker by IKA C-MAG HS7 model magnetic stirrer device with 70 ◦C as. They were spilt into 100mm x 15mm petri plates to dry samples.

II.I. Characterization of EVA Polymers

After drying in air, the optical properties (absorbance and wavelength values) of EVA polymers with various amounts of VA were measured using a Shimadzu 1800 UV-vis Spectrophotometer as seen in Figure 1.

Fig. 1: Shimadzu 1800 UV-vis Spectrophotometer

III. Analysis

The calculation of photon energy may be achieved by using the Planck-Einstein equation, which establishes a relationship between photon energy (E) and wavelength (λ):

$$E = hc/\lambda \tag{1}$$

Where h is the Planck constant, and c is the speed of light.

The calculation of absorption coefficient, (α) can be calculated by Eq 2 and 3 as a function of photon energy, E (Wypych, G.):

$$I = I_0 e^{-\alpha t} \tag{2}$$

$$\alpha(E) = (log_e 10/t)\, A(E) \tag{3}$$

The reflectance (R) in terms of the absorption coefficient can calculate from the following relation (Kalainathan, S. et. al):

$$R = \frac{exp\,(-\alpha t) \pm \sqrt{exp(-\alpha t)\,T - exp(-3\alpha t)\,T + exp\,(-2\alpha t)T^2}}{exp(-\alpha t) + exp(-2\alpha t)\,T} \tag{4}$$

The refractive index (n) of the polymer was calculated in terms of reflectance (R) using the following relation Kalainathan, S. et. al):

$$n_0 = -(R+1) \pm 2\frac{\sqrt{R}}{(R-1)} \tag{5}$$

The determination of the real and imaginary components of the dielectric constant was achieved by using the obtained relationships based on the complex refractive index (P Sharma and S C Katyal):

$$\varepsilon_r = n^2 - r^2 \tag{6}$$

$$\varepsilon_i = 2nk \tag{7}$$

The optical conductivity (σ) has been found from the relation (P Sharma and S C Katyal):

$$\sigma = \frac{\alpha n c}{4\pi} \tag{8}$$

where c is the velocity of light, α is the absorption coefficient and n is the refractive index.

IV. Results and discussion

The transmission spectrum of EVA thin film has been analysed in the range 200–800 nm for the calculation of the optical parameters. The refractive index and the extinction coefficient increase with the increase VA content between in 300 and 350 nm wavelength. The real and the imaginary parts of the dielectric constant increase with the increase between 3,56 eV and 4 eV photon energy related to increase VA content. The optical conductivity increases sharply for higher energy values and its maximum value is found to be 4,53 × 10^{11} s^{-1} at 6,2 eV

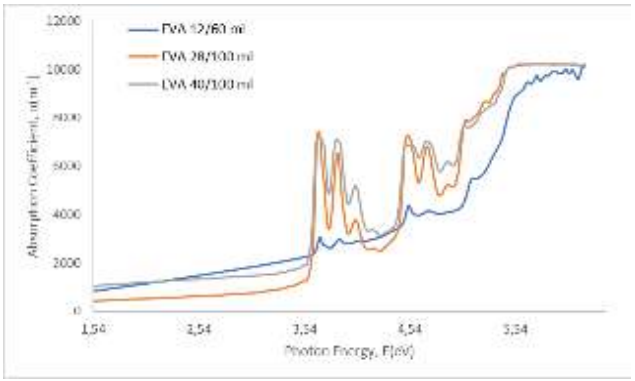

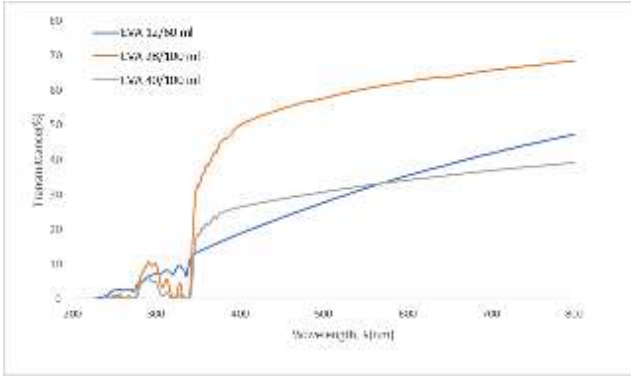

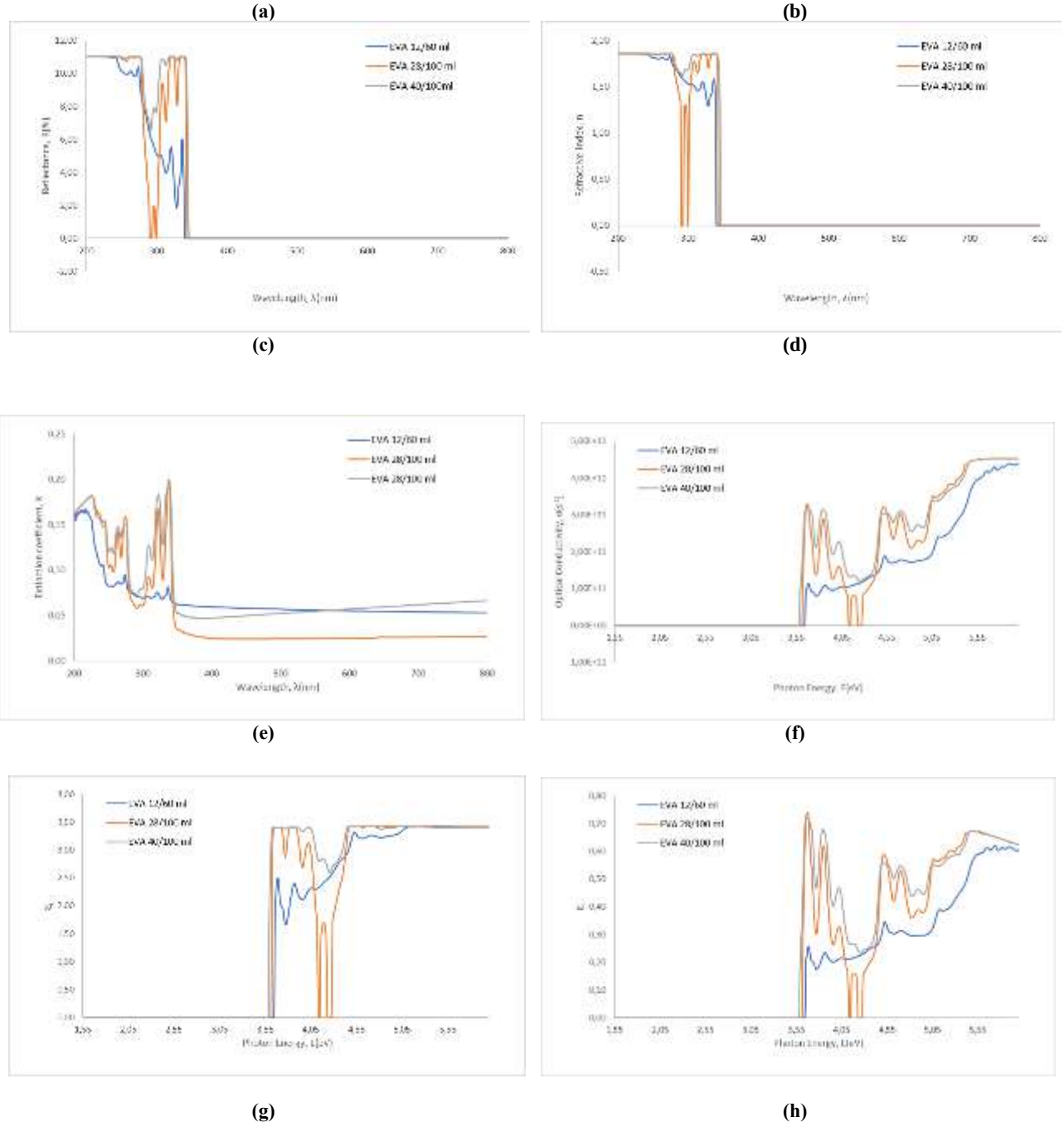

Fig. 2: (a) Absorption Coefficient, α and photon energy graph, (b) Transmittance (%) and wavelength, λ graph ,(c) Reflectance, R (%) and wavelength, λ graph,(d) Refractive index, n and wavelength, λ graph,(e) Extinction coefficient,k and wavelength, λ graph,(f) Optical conductivity, σ and photon energy graph,(g) real,$\varepsilon_r$dielectric constants and photon energy graph (h) imaginary(ε_i) dielectric constants and photon energy graph

V. Conclusion

The refractive index (n), extinction coefficient (k), real dielectric constant (ε_r), and imaginary dielectric constant (ε_i), which exhibit comparable behavior with respect to wavelength. Various types of EVA polymers, 12%, 28%, and 40% are compared. The optical conductivity increases with increase energy values and its maximum value is found to be 4,53 × 1011 s−1 at 6,2 eV. These results show that EVA polymers are promising potential material for use in solar cell applications.

Acknowledgements
The author Prof. Dr. Gülşen Akın Evingür and Büşra Osma thank Pîrî Reis University for Optical measurements.

References

Alhamada, T. F., Hanim, M. A., Saidur, R., Nuraini, A., Hasan, W. W., & Jung, D. W. (2022). Recent advances in polymer and perovskite based third-generation solar cell devices. Materials Today: Proceedings.

Sadiku, E. R., Reddy, A. B., Gnanasekarana, D., Oboirien, B., Aderibigbe, B. A., Varaprasad, K., & Goddeti, S. M. R. (2016). Nanostructured polymer blends for gas/vapor barrier and dielectric applications. In Design and Applications of Nanostructured Polymer Blends and Nanocomposite Systems (pp. 239-259). William Andrew Publishing.

Wypych, G. (Ed.). (2020). Handbook of UV degradation and stabilization. Elsevier.

Senthil, K., Kalainathan, S., Kumar, A. R., & Aravindan, P. G. (2014). Investigation of synthesis, crystal structure and third-order NLO properties of a new stilbazolium derivative crystal: a promising material for nonlinear optical devices. Rsc Advances, 4(99), 56112-56127.

Sharma, P., & Katyal, S. C. (2007). Determination of optical parameters of a-(As2Se3) 90Ge10 thin film. Journal of Physics D: Applied Physics, 40(7), 2115.

IEEES-058

Waste Management on Oil Spill Emergency Response in Turkish Coastal Waters

[1*]Duygu Ülker
[1] Istanbul University, Institute of Marine Sciences and Management, Department of Marine Environment, Vefa-Fatih, İstanbul, 34134, Türkiye
*E-mail: duygu.ulker@istanbul.edu.tr

Abstract

Türkiye is located on major sea routes and significant ports that facilitate maritime trade due to its strategic location. However, the high volume of maritime activities has resulted in numerous marine accidents, leading to oil pollution in Turkish coastal waters. Therefore, efficient and prompt oil spill emergency response is crucial in minimizing the environmental impact of such accidents. Oil spill management comprises of various components, such as detection, characterization, and monitoring, modeling and risk assessment, response methods and optimization, and waste management. Effective waste management is the final step in oil spill management activities. This paper aims to examine efficient waste management strategies for oil spill accidents in Turkish coastal waters by evaluating existing studies in the literature.

Keywords: waste management, oil spill, ship accidents, coastal waters, environmental management, reuse.

I. Introduction

Turkish Straits Sea Area (TSSA) is in the significant shipping routes of oil trade between the Middle East/Russia and Western Europe/USA (Cokacar, 2008; Ulker and Baltaoglu, 2018). According to statistics from the General Directorate of Merchant Marine approximately 35146 ships passed from the İstanbul Strait, and 42340 ships from Çanakkale Strait in 2022 where the number of ships decreased yearly total gross tonnage increased (Ministry of Transport Maritime Affairs and Communications Directorate General of Merchant Marine, 2022)

Turkish coastal waters suffered from accidents which caused oil spills since the 1970s. For instance, Independenta -Evriyali accident in Istanbul Strait in 1979, Nassia-Shipborker accident in Istanbul Strait in 1994, MT TPAO in Tuzla Shipyard in 1997, Volganeft-139 in the SoM in 1999, Volganeft-248 in the Istanbul Strait in 1999, Gotia in Istanbul Strait in 2002, Svyatov Panteleymo in the Istanbul Strait in 2003, Poliport in Izmit Bay in 2017, M/V Harrier in Foça coast in 2018.

Oil spill in a marine area has destructive effects on living and non-living environments due to the impact of the oil spill weathering process which are evaporation, emulsification, dispersion, dissolution, sedimentation, biodegradation and photooxidation (Ülker et al. 2022). Approximately 70% of oil diffuses to the atmosphere within 8 hours after a spill due to evaporation. Emulsification is one of the significant processes causing an increase in the volume of oily wastes. For instance, the M/T Prestige accident caused approximately 63.000 heavy oil spills in Spain but resulted in 128,000 tonnes of emulsion that had to be addressed (IPIECA-IOGP, 2014). For this reason, efficient oil spill contingency planning is necessary in the coastal waters.

Reducing the environmental impacts is the main target of the oil spill contingency planning. Efficient oil spill contingency planning depends on the efficiency of each operation. Components of oil spill contingency planning are monitoring; modeling and risk analysis; response methods and optimization; and waste management. The efficiency of the operational activity can be defined considering the removed oily waste amount from the marine area and the minimum contaminated surface and vertical area in the marine environment.

The techniques to remove oil from the marine area are mechanical, chemical and in-situ burning which are chosen depending on the location of the spill, oil type and environmental conditions.(Hu et al., 2020b, Mohammadiun et al., 2021). Mechanical techniques are the most commonly used for their capability of recovering spilt oil for reuse and minimizing the impacts on marine ecosystems. Oily waste removed by mechanical techniques consists of liquid waste and oils solid waste therefore waste management is a significant issue in oil spill management (Chen et al., 2021). However as stated by the study by Metcalf (2014), detailed planning for waste management appears to have not been considered after a release of waste has occurred. This is due to the inherent complexity, cost and lack of perceived benefit of pre-incident waste management planning.

Components of oil spill waste management include collection, segregation and sorting, initial treatment, safe transportation, resource recovery to final disposal which are complex and expensive (Saleem et al. 2022; IPIECA-IOGP, 2014). This study aims to evaluate the approaches to oil spill waste management to apply in Turkish Coastal Waters considering the environmental and economic benefits of the waste management strategies.

II. Methodologic approach

Components of oil spill management (Fig 1) should be studied in detail before defining waste management strategies. Although prediction of an accident is difficult regions at risk can be defined with modelling studies. This provides to define waste management strategies to provide optimum options for transportation, temporary landfill area and sanitary landfill area for different scenarios of accidents. Additionally, the estimation of an efficient oil spill response method contributes to waste elimination which is at the top of the waste hierarchy (see Fig 2).

The waste types produced because of oil spill and oil spill response; are oily liquid waste and solid waste. Oily liquid waste includes wastewater and emulsified oil; solid waste includes entrained debris, personnel protective equipment (PPE), and spent sorbents.

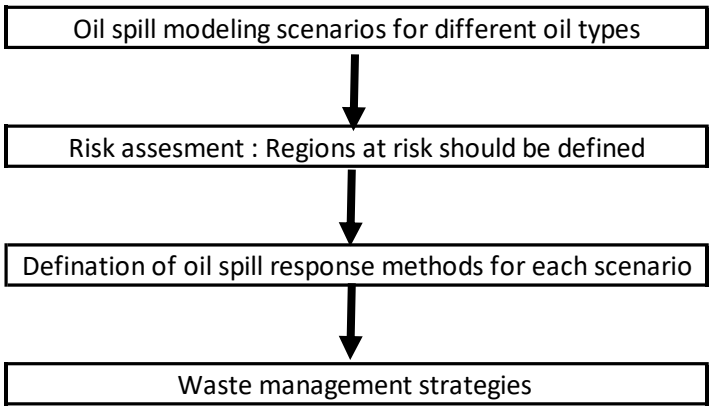

Fig 1. Oil spill management components

Oil spill waste management strategy should be considered the waste hierarchy (IPECA-IOGP, 2014).

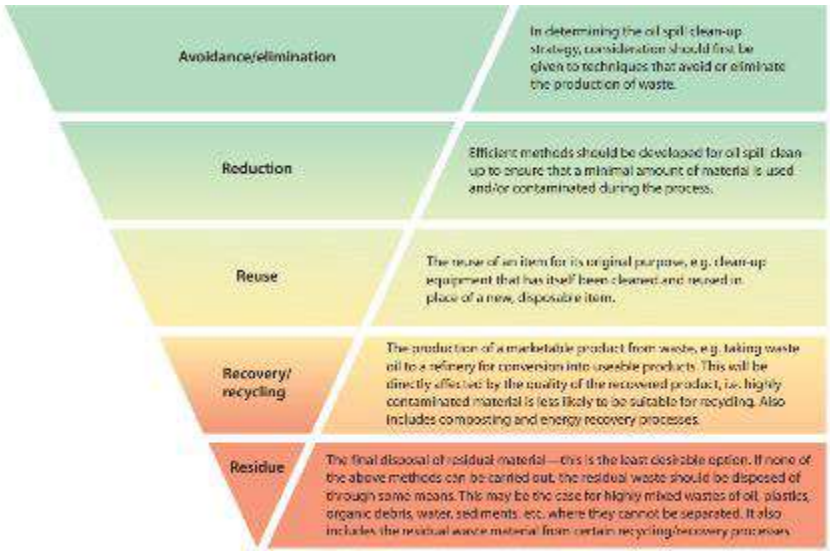

Fig 2. Waste hierarchy (received from IPECA-IOGP,2014)

III. Result and Discussion

The study by Saleem et al. (2022) used a life cycle assessment methodology to select low-impact strategies for oil spill waste management. The defined components of waste management by Saleem et al., (2022) are incineration, landfilling, oil-water separation by centrifugation, oil-water separation by chemicals, wastewater treatment and transportation. Impacts of each component were evaluated in terms of climate change, marine eutrophication, human toxicity, and marine ecotoxicity which are the highest impacts among the other environmental impacts. The impact assessment of 48 scenarios shows that the impact of each different oily waste is different. Chemical demulsification has the highest impact. Impacts of landfilling are high in climate change (> 80%) and marine eutrophication (12%) due to the release of gases from aerobic and anaerobic biodegradation of polycyclic aromatic hydrocarbons present in the oil and oil-contaminated waste are the main contributors to high climate change impacts (Liu et al., 2017). Centrifugation has the lowest impact on the environment especially if the energy source of electricity is from renewable resources. Consequently, they offer the waste management strategy which has the lowest impact centrifugation and landfilling or centrifugation and incineration. Chemical demulsification causes an extreme impact on marine ecotoxicity.

The study by Ulker et al. (2022) and Ulker (2022) modelled the oil spill weathering process in Izmit Bay with 36 scenarios. Water content in oil fractions shows that small and medium spill scenarios show over 50% of water content in oil in the 8th hours because of the emulsification process which impacts the increasing of water content in oil causing high contamination. Consequently, oily waste collection for these spills will have with high water content.

To provide a pre-waste management strategy for oil spills, previous steps of oil spill management should be clearly defined. The definition of areas at risk via modelling studies is important to the successful organization of oil spill management. In this way, decision-makers can see the options/alternatives to apply the optimal waste management plan.

Fig 3. Waste management strategy (derived from Saleem et. al. 2022)

Consequently, after the definition of the regions at risk by comprehensive modelling studies, waste management plans should be done for Turkish coastal waters. As a result, to provide efficient waste management, firstly temporary landfill areas should be defined especially for the regions at risk in TSSA. The waste management process derived from Saleem et al (2022) as seen in Fig 3 is offered for use in TSSA. Additionally, due to the partly low impact of incineration the oily solid waste can be applied before a sanitary landfill with Izaydaş (Izaydas, 2023). Reuse of the oily liquid waste should be provided to the various sectors as a raw material which is important share to reduce of environmental impacts of oil spills.

References

Cokacar, T., (2008). The Eastern Mediterranean-Black Sea system with high oil spill risk. In Oil Spill Response: A Global Perspective (pp. 327-340): Springer

Chen Z., An C., Chen X., Taylor E., Bagchi A., Tian X., (2021). Inexact inventory-theory-based optimization of oily waste management system in shoreline spill response. Sci. Total Environ., 777 (2021), 146078. https://doi.org/10.1016/j.scitotenv.2021.146078

Hu G., Mohammadium S., Gharahbagh A.A., Li, J.,Hewage K, Sadiq R., (2020). Selection of oil spill response method in arctic offshore waters: A fuzzy decision tree based framework. Mar. Pollut. Bull., 16. 111705. https://doi.org/10.1016/j.marpolbul.2020.111705

IPIECA-IOGP, (2014). Oil spill waste minimization and management. IPIECA-OGP good practice guide, London, UK. Retrieved from: https://www.ipieca.org/resources/good-practice/oil-spill-waste-minimization-and-management/

Izaydas (2023). Retrieved from: https://www.izaydas.com.tr/

Metcalf S., (2014). Developing location-based oil spill waste management plans. In *International Oil Spill Conference Proceedings* (Vol. 2014, No. 1, pp. 1633-1646). American Petroleum Institute.

Ministry of Transport Maritime Affairs and Communications Directorate General of Merchant Marine, (2022). Ship Passage Statistics of Turkish Straits. Retrieved from: https://denizcilikistatistikleri.uab.gov.tr/turk-bogazlari-gemi-gecis-istatistikleri

Mohammadiun S., Hu G., Gharahbagh A.A., Mirshahi R., Li J., Hewage K., Sadiq R., (2021). Optimization of integrated fuzzy decision tree and regression models for selection of oil spill response method in the Arctic. Knowl. Based Syst., 213 (2021),106676. https://doi.org/10.1016/j.knosys.2020.106676

Saleem, S., Hu, G., Li, J., Hewage, K., Sadiq, R. (2022). Evaluation of offshore oil spill response waste management strategies: A lifecycle assessment-based framework. *Journal of Hazardous Materials*, *432*, 128659.

Ülker D., Baltaoğlu S., (2018). Ship born oil pollution in Turkish straits sea area and MARPOL 73/78. *Oil Spill along the Turkish Straits* 363 (2018).

Ülker D., (2022). GIS-based modelling for advection and diffusion of oil pollution in coastal waters. PhD Thesis. Istanbul University, Institute of Marine Sciences and Management.

Ülker, D., Burak, S., Balas, L.,Çağlar, N. (2022). Mathematical modelling of oil spill weathering processes for contingency planning in Izmit Bay. *Regional Studies in Marine Science*, *50*, 102155.

IEEES-059

Thermodynamic Analyses Of A Organic Rankine Cycle (ORC) With Working Fluids R245FA, R245CA And R1233ZD In A Multigenerational Hybrid System

[1*]Özlem BOYDAK, [2]İsmail EKMEKÇİ, [3]Mustafa YILMAZ
[1]Istanbul Medeniyet University, Faculty of Eng. and Natural Sciences, Mechanical Eng. Dept., 34700, Istanbul, Türkiye
[2] İstanbul Ticaret Üniversitesi, Mühendislik Fakültesi, Endüstri Mühendisliği, İstanbul, 34840, Türkiye
[3]Marmara University, Faculty of Eng., Mechanical Eng. Dept., 34840, Istanbul, 34840, Türkiye
*E-mails: ozlem.boydak@medeniyet.edu.tr

Abstract

In this study, a multigenerational hybrid system, which is consisting solar, geotermal and Organic Rankine Cycle (ORC) with working fluids R245fa, R245ca and the new generation fluid R1233zd, was simulated via a simulation software. After simulations, the results were analyzed and compared. According to these results, the highest system thermal efficiency value as 0,158 was gained with the R245fa working fluid. Then, the system thermal efficiency with R1233zd is 0,15, and lastly the lowest thermal efficiency is 0,14 with R245ca, respectively, under similar working conditions of the multigenerational system. However, the biggest generator work is supplied with R1233zd as 99,403 kW, then with R245ca as 68,958 kW, then with R245fa the lowest generator work value as 27,526 kW. Accordingly, as a result, R1233zd, and then R245fa supplied the best performance values for this ORC system, respectively. Further future studies on this subject area is on spot and continuing.

Keywords: ORC, Organic working fluids, energy efficiency, energy recovery system, working fluid selection, thermodynamic analysis.

I. Introduction

Multigenerational hybrid systems are rather beneficial for optimum energy recovery [1]. This study also comprises a multigenerational system consisting solar, geotermal and ORC. Accordingly, ORC system utilization in multigenerational energy systems is rather significant for environment as it recovers low waste heat and produces electrical energy back. ORC system consists of condenser, pump, evaporator and generator parts which supply the cycle for the system. Additionally, organic fluid selection is important for the efficiency, availability and safety of the ORC as being organic fluid utilized system. Mainly, a fine working fluid should reveal not only low toxicity, good material compatibility and fluid stability limits, low flammability, corrosion, and fouling characteristics but also high system performance ([2],[3]). Working fluids can generally be classified as dry, wet and isentropic fluids based on their slope of saturated vapour phase in T-s curves as seen in Figure 1 ([4],[5]).

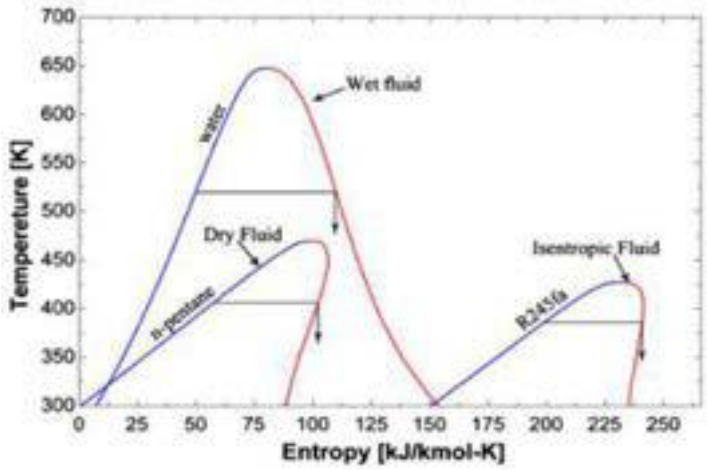

Fig. 1: Three types of ORC working fluids: dry, isentropic and wet

II. Experimental Procedure/Methodology/System Description

Within this study, a thermodynamic analysis of a multigenerational system which has a ORC working with three different organic fluids was performed with a simulation software and then performances of the multigenerational system was compared. These three different working fluids were isentropic organic fluids R245fa, R245ca and R1233zd. Each simulation was performed on the similar ORC system the schematic of which is demonstrated in Figure 2.

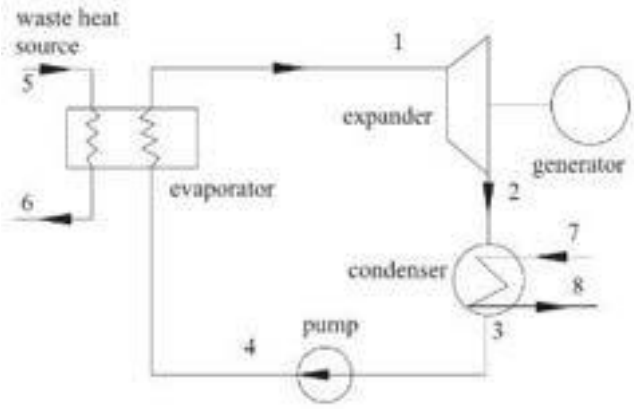

Fig. 2. Schematic diagram of the ORC

As shown in Figure 2, between points 1-2 expansion, between points 2-3 condensing, between points 3-4 pumping and between points 4-1 evaporating are the elements of this ORC. Accordingly, the related T-s diagram schematic of this ORC system can be observed from Figure 3 ([6],[7]).

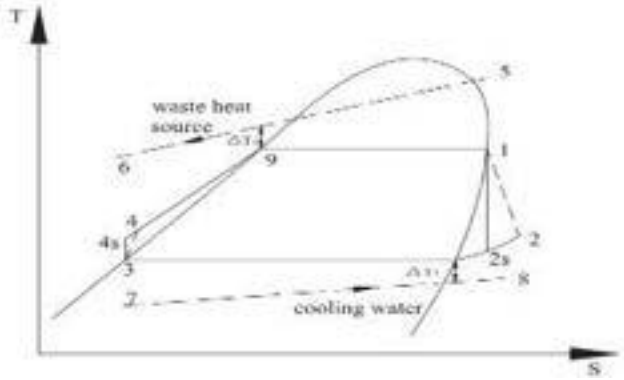

Fig. 3. T-s diagram of the ORC

With the help of this T-s diagram, the ORC temperature and entropy values related points were observed. In order to conduct the thermodynamic analysis, the basic energy and exergy equations are applied to the system in terms of three different working fluids R245fa, R245ca and R1233zd ([8],[9]).

II.I. Working Fluid Selection

Working fluid selection is one of the most significant phenomena for designing ORC system, and accordingly Table 1 demonstrates main organic working fluids utilized in ORCs ([10],[11]).

Table1: Main working fluids for ORCs and their properties [11]

	Substance	Physical data				Safety data	Environmental data			Type
		Molecular Mass(kg/kmol)	T_{fp} (°C)	T_{crit} (°C)	P_{crit} (MPa)	ASHRAE 34 safety group	ALT(yr)	ODP	GWP (100yr)	
1	R717	17.03	-33.33	132.25	11.333	B2	0.01	0	<1	wet
2	R600	58.12	-0.55	151.98	3.796	A3	0.02	0	~20	dry
3	R600a	58.12	-11.67	134.67	3.640	A3	0.02	0	~20	dry
4	R290	44.10	-42.09	96.68	4.247	A3	0.04	0	~20	wet
5	R1270	42.08	-47.69	92.42	4.665	A3	~0	0	~20	wet
6	R11	137.37	23.71	197.96	4.408	A1	45	1	4750	i
7	R12	120.91	-29.75	111.97	4.136	A1	100	1	10890	wet, i
8	R22	86.47	-40.81	96.15	4.990	A1	12	0.05	1810	wet
9	R32	52.02	-51.65	78.11	5.782	A2	4.9	0	675	wet
10	R113	187.38	47.59	214.06	3.392	A1	85	1	6130	dry
11	R114	170.92	3.59	145.68	3.257	A1	300	1	10040	dry
12	R123	152.93	27.82	183.68	3.662	B1	1.3	0.02	77	dry, i
13	R124	136.48	-11.96	122.28	3.624	A1	5.8	0.02	609	i
14	R134a	102.03	-26.07	101.06	4.059	A1	14	0	1430	i
15	R141b	116.95	32.05	206.81	4.460	n.a.	9.3	0.12	725	dry, i
16	R142b	100.50	-9.15	137.11	4.070	A2	17.9	0.07	2310	i
17	R143a	84.04	-47.24	72.71	3.761	A2	52	0	4470	wet
18	R152a	66.05	24.02	113.26	4.517	A2	1.4	0	124	wet
19	R218	188.02	-36.83	71.95	2.671	A1	2600	0	8830	dry
20	R227ea	170.03	16.45	101.65	2.926	A1	42	0	3220	dry
21	R236fa	152.04	-1.44	124.92	3.200	A1	240	0	9810	dry
22	R236ea	152.04	6.19	139.29	3.502	n.a.	8	0	710	dry
23	R245fa	134.05	14.90	154.05	3.640	B1	7.6	0	1030	dry
24	R245ca	134.05	25.13	174.42	3.925	n.a.	62	0	693	dry
25	RC318	200.03	-5.98	115.23	2.778	A1	3200	0	10250	dry
26	R718	18.02	99.97	373.95	22.064	A1	n.a.	0	<1	wet

Optimum working fluid is chosen for related ORC system according to the properties of the working fluid such as critical temperature, critical pressure, global warming potential (GWP), ozone depletion potential (ODP) and safety data values. These values base the thermodynamic structure of the ORC system. Some of the properties of the organic fluids used in this study are seen in Table 1 ([11],[12]).

III. Thermodynamic Analysis

The thermodynamic analysis of this studied ORC system was based on the main energy equations. Accordingly, the system of equations for the thermodynamic analysis are below ([12],[13]):

Pump work input: $\dot{W}_P = \frac{\dot{m}(h_{4s} - h_3)}{\eta_P}$

Expander (Turbine) work output: $\dot{W}_E = \frac{\dot{m}(h_1 - h_{2s})}{\eta_E}$

Evaporator heat input: $\dot{Q}_{evap} = \dot{m}(h_1 - h_{4s})$

Condenser heat output: $\dot{Q}_{cond} = \dot{m}(h_{2s} - h_3)$

Efficiency: $\eta_{th} = \frac{\dot{W}_E - \dot{W}_P}{\dot{Q}_{evap}}$

In order to explain some system variables to simulate and find outputs of the system, the mechanical efficiency of the pump and turbine was assumed to be 0.998, which is a reasonable efficiency value. The condensation temperature was varied in the range of 25 to 138 °C around, according to the thermodynamic properties of the fluids. Additionally, the evaporation pressure was varied in the range of approximately 12 to 13 bar according to the thermodynamic properties of the each fluid. And, the evaporation temperature was varied in the range of 30 to 200 °C around accordingly. Thus, the thermodynamic analysis calculations of the ORC system simulations were done according to these energy equations and values ([13],[14]).

IV. Results and discussion

As a result, three different working fluids R245fa, R245ca, R1233zd were analysed via a simulation software, within the ORC side of this multigenerational system explained, respectively. The thermodynamic outputs of the system were investigated and compared according to each working fluid.

Within the system parameters explained above, when this ORC simulated with R245fa working fluid, thermal efficiency of the multigenerational system was calculated as 0,158. Then, it was calculated as 0.15 with R1233zd, and 0.14 with R245ca under similar working conditions. In terms of generator works results, R1233zd working fluid resulted 99,403 kW generator work output, R245ca resulted as 68,958 kW generator output, and then R245fa working gave the lowest generator work value as 27,526 kW.

V. Conclusion

For the ORC of this multigenerational system studied, the best suited working fluids were founded as both R245fa and R1233zd according to the simulation results analysed. Thus, R245fa is the most efficient working fluid for this ORC in terms of multigenerational system thermal efficiency. Moreover, R1233zd is the best organic fluid in terms of ORC generator work output. The safety of R1233zd is also reasonable to utilize since the commonly used working fluid R245fa will be phased out in the near future because of the significant impact to climate change. In that case, the new refrigerant R1233zd with extremely low GWP is proposed as an environmental friendly substitute [15]. The future work is on topic for the application of other working fluids.

Acknowledgement

We would like to thank to the organizers of this conference for giving the chance to publish this study.

References

1. A. Mahmoudan, F. Esmaeilion, S. Hoseinzadeh, M. Soltani, P. Ahmadi, M. Rosen, "A geothermal and solar-based multigeneration system integrated with a TEG unit: Development, 3E analyses, and multi-objective optimization," Applied Energy, vol. 308, 118399, 15 February 2022.
2. S. Hu, Z. Yang, J. Li and Y. Duan, "A Review of Multi-Objective Optimization in Organic Rankine Cycle (ORC) System Design," Energies, vol. 14, 6492, 2021.
3. R. Loni, G. Najafi, E. Bellos, F. Rajaee, Z. Said, M. Mazlan, "A review of industrial waste heat recovery system for power generation with Organic Rankine Cycle: Recent challenges and future outlook," Journal of Cleaner Production, vol. 287, 125070, 2021.
4. Ö. Boydak, İ. Ekmekçi, M. Yılmaz, "A Thermodynamic Analysis and Comparison of an Organic Rankine Cycled (ORC) System with Six Different Wet, Dry and Isentropic Working Fluids," Journal of New Results in Engineering and Natural Science, no:17, pp. 1-8, August 2022.
5. X. Zhang, Y. Zhang, J. Wang, "Evaluation and selection of dry and isentropic working fluids based on their pump performance in small-scale organic Rankine cycle," Applied Thermal Engineering, vol. 191, 116919, 5 June 2021.
6. M. Bahrami, A. A. Hamidi and S. Porkhial, "Investigation of the effect of organic working fluids on thermodynamic performance of combined cycle Stirling-ORC," International Journal of Energy and Environmental Engineering, pp. 4-12, 2013.

7. C. Liu, C. He, H. Gao, X. Xu and J. Xu, "The Optimal Evaporation Temperature of Subcritical ORC Based on Second Law Efficiency for Waste Heat Recovery," Entropy, vol. 14, pp. 491-504, 2012.
8. T. Guo, H. Wang, S. Zhang, "Fluid Selection for a Low-Temperature Geothermal Organic Rankine Cycle by Energy and Exergy," 2010 Asia-Pacific Power and Energy Engineering Conference, March 28, 2010.
9. H. Zhang, M. Li, Y. Feng, H. Xi, T. Hung, "Assessment and working fluid comparison of steam Rankine cycle -Organic Rankine cycle combined system for severe cold territories," Case Studies in Thermal Engineering, vol. 28, 101601, December 2021.
10. H. Feng, Z. Wu, L. Chen, Y. Ge, "Constructal thermodynamic optimization for dual-pressure organic Rankine cycle in waste heat utilization system," Energy Conversion and Management, vol. 227, 113585, 2021, 1 January 2021.
11. O. Boydak, I. Ekmekci, M. Yılmaz, and H. Koten, "Thermodynamic investigation of organic rankine cycle energy recovery system and recent studies," Thermal Science, vol. 22, no. 6A, pp. 2679-2690, 2018.
12. A. Toffolo, A. Lazzaretto, G. Manente, M. Paci, "A multi-criteria approach for the optimal selection of working fluid and design parameters in Organic Rankine Cycle systems," Applied Energy vol. 121, pp. 219-232, 15 May 2014.
13. S. Thangavel, V. Verma, Rahul Tarodiya, P. Kaliyaperumal, "Comparative analysis and evaluation of different working fluids for the organic rankine cycle performance, " materialstoday:Proceedings, vol. 47, Part 10, pp. 2580-2584, 2021.
14. P. Malwe, B. Gawali , J. Shaikh, M. Deshpande, R. Dhalait, S. Kulkarni, V. Shindagi, H. Panchal, and K. K. Sadasivuni, "Exergy assessment of an Organic Rankine Cycle for waste heat recovery from a refrigeration system: a review," Chemical Engineering Communications, pp. 1-29, 2021.
J. Yang, Z. Sun, B. Yu, J. Chen, "Experimental comparison and optimization guidance of R1233zd(E) as a drop-in replacement to R245fa for organic Rankine cycle application," Applied Thermal Engineering, vol. 141, pp. 10-19, August 2018.

IEEES-060

Need of a Policy and Strategy on Intelligence versus Artificial Intelligence in Engineering Education?

Melda OZDINC CARPINLIOGLU
Gaziantep University, Engineering Faculty, Department of Mechanical Engineering , Şehitkamil , Gaziantep, 27310, Türkiye
*E-mail: melda@gantep.edu.tr

Abstract

A comment on learning/teaching/education with a somewhat philopsophical point of view from the site of engineering is the topic of discussion. The fact is obviously in relevance to knowledge. In case of no emphasis on the possibility of knowledge and its limits" learning/teaching /education "can simply be defined as the primary act of intelligence , I with a clear specification of who is ? A well known who is usually followed by a question stock of What /When / Why / For What and/or Whom/ and How can be … ? The appearance of artificial intelligence , AI particularly in science –engineering – technology introduces a new paradigm . Since the basic intention is towards an advancement of futuristic technologies engineering education E can be used as a discussion domain for I versus AI. The state of art is described with possible questions on past, now and future for the purpose.

Keywords: Intelligence , education, philosophy , science-engineering-technology**.**

I. Introduction

Artificial Intelligence, AI was introduced by the early historical proposal of (John McCarthy et al , 1955) which focused the attention to the so-called machine learning , ML in turn. We all realize the great steps taken in the 68 year-time period via natural language processing , neural networks ,abstraction and creativity , internet of things and e.t.c over simply computer –based abilities and achievements of the scientific and technological state of art.

As is detailed by (Parry, 2021) the accepted translations of the Greek words of "episteme" and "techne" are "knowledge" and "craft/art" respectively. As a further reasoning our well known assumptions are such that "theory" and "practice" are in relevance to" the domain of knowledge "and "concern of craft / art " correspondingly. The current status is well defined by his commitment by considering the theory as of pure mathematics having no obvious application to practical problems of engineering . Thus philosophically knowledge is simply the content of learning,L which can not be considered without teaching,T . The words of L ,T are conceptually two sides of education ,E which is referred as engineering education in this presentation .

Covid 19 pandemic shifted our attitudes from face to face to on line in our everyday lifes and of course in all levels of E globally. In post-covid times still online –hybrid web- based digital platforms including production/ transportation /communication layouts , seminars, conferences , workshops , undergraduate/ graduate levels of E are persisting in industry and academia.

It can be said that the governing power and dominancy of internet-web-digital platforms has a start after 1990's due to the so –called globalization. Therefore it is better to describe evolution of E from ancient times to 1990's as a cornerstone and from 1990's to 2019 - now for the questions to think on the vitality of a policy and strategy of I /AI in the coming times of days/ years /decades.

The presentation is founded on a conceptual description of the selected/restricted representative literature and analysis *written in Italics* to reach a sample list of questions for further discussion.

II. Conceptual Description and Analysis

The developments in AI prior to the start of globalization were detailed by (Solomonoff, 1985) concerning its application in the field of social studies. It can be summarized as a general theory of AI on human problem solving - cognitive psychology, the introduction of creative/insightful expert systems with learning , devising and testing new concepts , implementation /design of computers for gathering and storing information . The problem of self-improvement is the critical point in AI development. It is said that an enormous amount of information available in electronic data bases causes an increased ML ability in problem solution and even understanding. A machine has a general problem solving capacity near or over that of a human, in the areas of mathematics, science and industrial applications. However in dealing with conditions of uncertainty mankind will continue to make decisions. He estimates that very intelligent machines can also help mankind in prediction of the results of social facts .

Therefore in Solomonoff's time ; machine-computer- AI treated as modern era's slave who is under the control of mankind, I who is the authority to select/ formulate/ devise / analyse /understand the searching topic and to understand/predict/shape future.

AI only does its assigned duty by handling (collecting ,storing ,operating)enormous data .

In spite of the success of ML in prediction schemes of natural sciences and engineering the pure ML predicton models in social sciences are still found unsuccesful by (Buchholz Grate ,2023). They evaluated the strength of ML in prediction . ML is excellent in interpolation but fail in extrapolations particularly in reference to novel events of social sciences . They referred to the sample cases of 2008 financial crisis and Arab Spring . As a conclusion they introduced an integrative modelling approach combining explanatory-agent based and predictive ML models . Agent decision-making entities based models are called as theory driven ones.

Therefore it seems that AI/ ML by itself is not compatible in social sciences in spite of the time passed from 1985 to 2023. The next step seems to be the discussion in Engineering- Technology .

A current case study of the United Arab Emirates (UAE) by(Lachmi et al , 2023) describes the details for implementing an AI-based online education system in line with collaborative technical education partnerships. Their discussed extensive range of digital technologies , DT are mainly categorized as i)Management Systems(serving hubs for digital instructional materials of course management, content production - distribution, student monitoring -evaluation, online forums and group work tools as Moodle, Blackboard, and Canvas e.t.c) ii) e-Learning Content – Multimedia(Interactive - multimedia-rich instructional content through digital

learning technology - gamified learning modules, virtual reality (VR) experiences, online textbooks, video lectures, interactive simulations – evaluations e.t.c) iii) Adaptive Learning Systems(fitted to personalized requirements using AI and ML algorithms with mobile learning and social learning -collaboration means). They proposed that as a manner of deep learning and longer term recall ; augmented reality (AR) and virtual reality (VR) with flexible, interactive education should be under self control of the individuals . The problem they declared is the designing of the methodology providing a smooth passage to digital learning structure .

It is apparent that DT are in use with a direct link with AI /ML . What is the vitality of passage from so-called old version technology in E ? More truly old version should be of no sense. E should be in line with current technology . Their approach is an overall and inclusive treatment of E considering collaboration of industry. However specification of the sides of E and the medium of E are the critical points in their approach .It seems that they consider human being , I implicitly by individuals who uses AI. Do not we need a natural face to face interaction between the sides of E as I's or AI's ? Do we as human being intelligence I leave the stage to AI completely ? Is AI/ML / DT going to force a drastical change for the specification of the sides ? Is it possible to have the sides as: AI/ I , I/ AI and AI/ AI or AI+I / I+AI ? However the major point of discussion is related to the self-determination in Theory and Practice ? Who makes the selection of the topics- content-cases ? Who is the master ? Do we need a policy and a strategy for the future for which purpose?

As an overall experience during COVID 19 period (Shaikh et al , 2022) remote learning has emerged as a viable option, depending on AI/ML/DT to accomplish its goals. Learning is becoming more automated assisting individuals, I to be more concentrated on their learning opportunities. (Mahajan and Patil ,2021) analysed the COVID-19 pandemic situation for Indian engineering institutions which struggled to return to their normal track in a drastically changed students' behavior . They found that pandemic influence was positively affected by institutional influence with a change in institutional characteristics .

Does it mean a complete change in attitudes and use of AI /ML/DT under control ?

As a matter of fact for state of art and available policies /strategies we can refer to a discussion of (Chiu et al,2023). A question of "How AI technologies have been integrated into each of the four key educational domains of learning, teaching, assessment, and administration?" is answered by(Chiu et al,2023). Starting from a pre-Covid 19 time period (between 2012-2021) their review study is to understand the opportunities / challenges of AI education ; AIEd . In their model AI refers to the ability of a digital machine to perform tasks commonly associated with I. Computer vision, speech, ML , big data, and natural language processing are the technologies. The explosive growth is the cause of the life transformation (people interact, communicate, live, learn, and work) . The current strategic policies of AIEd in China , the United States, Finland, the Netherlands are summarized. Meanwhile according to the report from the Organization for Economic Cooperation and Development (Holmes et al ,2021) there is a need of research to determine the influence of outputs and educational practice and training of the educators in using of big data and learning analytics for an increased efficiency of education. The continuous advancement of AI technologies and implementation of relevant policies, AIEd serve fertile research site for educational researchers, policymakers, and practitioners. Prseumably research focused on scientific-engineering-technological aspects, such as developing new algorithms and enhancing ML /deep learning techniques are going on.

However the impact of AI on education in terms of offered benefits remains unclear (Holmes et al., 2021), A lack of familiarity with the technologies makes it challenging to introduce or integrate them into available education systems (Hussin, 2018). Therefore more review studies are needed to organize the literature, to provide an overview of the opportunities and challenges of AIEd in terms of future research.

It simply means that it is engineering handling/ having to do with AI/ML/DT for education and application- technology. Therefore it is better to have a general description of AI/ML/DT as a matter of realization of scientific knowledge from theory to practice. As described by (Olesiak ,2011) definition of scientific knowledge and its comparison with true opinion are given with the satisfaction of various criteria . It is said that smply for scientific knowledge ; the object must be (objectively) true and necessary; the object must be (subjectively) thought of being necessary; the true cause has to be known (subjectively); and the necessity of the causal connection of the known entity has to be perceived (subjectively) The most important one is the objective necessity. If any of these are not satisfied, it can be true opinion. Therefore treatment should be done in terms of scientific knowledge not in opinions.

At this step is it possible to compare I having always opinions/ true opinions and AI who does not ?

The introduction of AI/ML/DT can be extended to the history of science executed by intelligence I who had all the progress starting from the ancient times but being always as a human being . Cultural and historical background and all life- realizations have their severe impact . So leaving the stage to AI may be not the real future will and responsibility , cause of being of the intelligence ,I.

Scientific knowledge is simply transferred into technology by engineering . The generation of scientific knowledge and technology and use are by E. The sides and medium of E should be defined. Eventually do we need a policy and strategy to predict future of AI/ML/DT with us for a shaped world by us ? The strategy necessitates not only dealing with the pure engineering content –inputs -outputs but also an overall philosophical treatment .

III Results and discussion

Engineering education ,E is much more and beyond education in academia but it describes both in industry –applications – all the life. Engineering shapes the life through continuing lifetime education personally and/or professionally. Therefore first in terms of AI/ML we have to define the sides . Are we in and /or looking at from producers or users side? AI /ML in terms of well defined research – development – realization problems seem to be dealt with producers who are also users. However specification of relevant problems have to be be deduced from the users side. In the present state of art producers and users who are responsible /self determined with authority are I : Mankind . AI is taking part under the governence of I with defined duties both in production and application side . Philosophically AI is following the orders of I in a defined-ordered commonly cyclic paths without any opinion . In fact true / opinions and scientific knowledge seems to be a matter considered for comparison of AI/I. Does it ? Acting with /without reasoning is the task of AI . Is not ? . Making/ transforming/expecting AI with a complete self –determination similar to I is the next step ? Does I :mankind really want to leave the stage? Is it possible to have a conflict between I and AI ? So do we need a policy? What are the critical points of the policy? Are these reasonable and how are they activated ? What are the sample cases pilot projects ? ….?

IV. Conclusion

In dealing with all kinds of futuristic technologies we need to consider the current status of E we have with AI /ML /DT without disregarding philosophy. The listed questions are only the sample ones from the point of view of the author. It seems that need of a policy and a strategy founded on the policy is vital for the mankind, I who is/should be the only one ? having the free will.

Acknowledgements
The author would like to express her thanks to Philosophy Program offered by Open and Distance Education Faculty of Istanbul University for the inspiration given .

References

Buchholz, O., Grote, T. ,(2023) Predicting and explaining with machine learning models: Social science as a touchstone.
Studies in History and Philosophy of Science 102,60-69
Chiu ,K.F.T., (2023) Systematic literature review on opportunities, challenges, and future research recommendations of artificial intelligence in education
Computers and Education: Artificial Intelligence,4, 100118
Holmes, et al., (2021) AI and Education: Guidance for policy makers.
Hussin, A. A., (2018) Education 4.0 made simple: Ideas for teaching.
International Journal of Education and Literacy Studies, 6(3), 92–98.
https://doi.org/10.7575/aiac.ijels. v.6n.3p.92
Mahajan ,P., Patil,V.,(2021) Making it normal for 'new' enrollments: effect of institutional and pandemic influence on selecting engineering institutions under the COVID-19 pandemic situation
Heliyon 7,e08217
Lakshmi,A.J. et al., (2023) Artificial intelligence in steering the digital transformation of collaborative technical education.
Journal of High Technological Management Research ,34,100467
Mc Carthy, J., Minsky, M., Rochester, N., Shannon, C.E.,(1955) A proposal for the Dartmouth summer research project on artificial intelligence. http://raysolomonoff.com/dartmouth/boxa/dart564props.pdf
Parry, R., (2021) Episteme and Techne.
The Stanford Encyclopedia of Philosophy E.N. Zalta (Ed.)
URL = https://plato.stanford.edu/archives/win2021/entries/episteme-techne/>.
Shaikh , A.A. et al., (2022) The role of machine learning and artificial intelligence for making a digital classroom and its sustainable impact on education during Covid-19.
Materials Today Procedings 56,3211-3215
Solomonoff, R.J.(1985) The time scale of artificial intelligence; Reflections on social effects.
Human Systems Management, 5, 149-153
Olesiak, J., (2011) Knowledge and Opinion in Aristotle (2011) .
Diametros, 27 ,170-84
https://doi.org/10.13153/diam.27.2011.432

IEEES-061

Efficiency Increasing Coatings on Photovoltaic Panels (PV)

[1,2,4*] Merve Yılmaz, [2*] Erkan Dursun, [1,2*] Zehra Karagöz, [2,4*] Nazmi Ekren, [3,4*] Oğuzhan Gündüz
[1] National Defense University, Naval Academy, Electrical and Electronics Engineering, Tuzla, Istanbul, 34942, Turkey
[2] Marmara University, Faculty of Technology, Electrical and Electronics Engineering, Maltepe, Istanbul, 34854, Turkey
[3] Marmara University, Faculty of Technology, Metallurgical and Materials Engineering, Maltepe, Istanbul, 34854, Turkey
[4] Marmara University, Nanotechnology and Biomaterials Application and Research Centre (NBUAM), Kadikoy, İstanbul, 34730, Turkey
*E-mails: merveyilmz00@gmail.com

Abstract

Nowadays, self-cleaning and anti-reflective coatings are needed to improve the performance of photovoltaic panels and provide energy efficiency. In the literature, some solutions have been presented to reduce the impact of environmental factors that have negative effects on the efficiency and energy production of photovoltaic panels. These solutions include self-cleaning and anti-reflective coatings. Self-cleaning coatings prevent environmental pollution, dust accumulation and other pollutants from accumulating on the panels, allowing the panel to absorb sunlight more efficiently. Anti-reflective coatings help the panel to absorb more light by reducing the reflection of sunlight. In this way, the energy efficiency of the panels is increased. This study investigates the importance and potential of self-cleaning and anti-reflective coatings developed to improve the performance of photovoltaic panels. Different self-cleaning and anti-reflective coating materials and methods are reviewed. It is envisaged that the development and widespread use of these methods will contribute to a more sustainable and efficient adoption of solar energy technologies.

Keywords: Photovoltaic panels, Anti-fouling coatings, Anti-reflective coatings.

I. Introduction

Renewable energy sources are gaining increasing attention day by day due to their environmentally friendly nature and their lack of contribution to environmental pollution, unlike fossil fuels. (Ashok, 2007; Sun et al., 2010). In this context, solar energy stands out as a clean, safe, and limitless ideal renewable energy source (Ling et al., 2010; Yasa et al., 2017). The Sun sends a considerable amount of energy to Earth every day, equivalent to 4,000 trillion kWh of electromagnetic radiation power. When solar rays enter the atmosphere, a portion of these rays is reflected, refracted, and scattered in the atmosphere (Goetzberger et al., 1998).
Discovered by Becquerel in 1839, certain materials with photovoltaic (PV) properties led to the development of a method to convert solar energy into electricity through the photovoltaic effect of the P-N junction in 1940. The photovoltaic effect is based on the principle of electrons within a material gaining energy upon being struck by sunlight, becoming free and generating an electric current. Photovoltaic cells or solar panels are devices that utilize this effect to convert solar energy into electricity. These cells are typically structured with various layers on a thin silicon layer. When sunlight hits the cell, electrons are released through the photovoltaic effect, creating an electric current. This current can work on a load connected to external circuits or supply energy to a battery (Palit & Hussain, 2020).

There are various factors that affect the efficiency of photovoltaic modules. Among these factors are sunlight intensity, air temperature, cleanliness of the module surface, dust accumulation, module tilt, angle of incidence of sunlight rays, air pollution, material quality and characteristics, as well as connections and cable losses. Sunlight intensity and air temperature are fundamental factors that influence the electricity generation of the module. The cleanliness of the module surface, dust accumulation, and the angle of incidence of sunlight rays affect the efficiency of sunlight reaching the module surface. Air pollution can reduce efficiency by decreasing the amount of sunlight reaching the module. Material quality is critically important for ensuring high efficiency and a long lifespan of the module. Connections and cable losses can lead to energy losses during electrical transmission. Considering all these factors is a crucial step in enhancing the efficiency of PV modules.

Another factor is reflection. Surface contamination also leads to a significant decrease in output power by increasing the reflection of concentrated solar power (CSP) systems (Mazumder, Horenstein, Heiling, et al., 2015; Mazumder, Horenstein, & Joglekar, 2015) Sunlight arrives at the panel surface at a specific angle and reaches the cells by passing through the protective glass. However, not all light reaching the glass surface is transmitted to the cells; approximately 8-10% is reflected back from a clean glass surface. A pure silicon cell reflects about 35-36% of sunlight. Light reflections lead to optical power losses and result in losses in electricity generation. Therefore, reducing optical losses is a significant factor in increasing panel efficiency. To minimize optical losses, both an anti-reflection coating and an anti-soiling coating are applied to the cover glass to prevent both reflection and contamination (Yamada et al., 2001).

II. Anti-Soiling and Anti-Reflection Coatings

There are two types of self-cleaning coatings: hydrophobic and hydrophilic surfaces. Hydrophobic surfaces differentiate based on the movement of droplets, which can also be classified as hydrophobic and superhydrophobic surfaces. Self-cleaning is demonstrated by the ability of hydrophobic surfaces to remove dust particles through the movement of water droplets. (Gong & He, 2020; Maharjan et al., 2020; Nosonovsky & Bhushan, 2009). For instance, on superhydrophobic surfaces, spherical droplets remove dust and dirt through a rolling motion, while on hydrophobic surfaces, semi-spherical droplets remove dust and dirt through a sliding motion. In a study conducted by Parkin and Palgrave, it was found that the rolling motion of droplets is more effective than the sliding motion for surface cleaning (Fig. 1) (Parkin & Palgrave, 2005). Therefore, to achieve an effective self-cleaning mechanism, a hydrophobic surface needs

to have a very high static water contact angle (WCA) and a very low rolling angle.

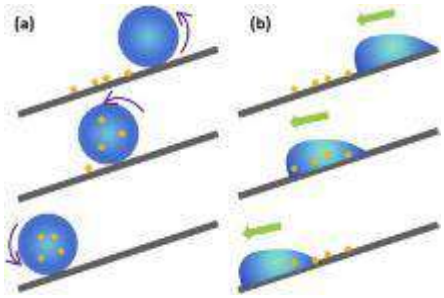

Fig. 1. The (a) rolling and (b) sliding motion of a water droplet (Zhang et al., 2016).

Nanostructured coatings can be applied to both the cell surface and the glass of photovoltaic panels. Currently, over 70% of photovoltaic panels have anti-reflective coatings. Some of the main materials commonly used for anti-reflective coatings include SiO_2, MgF_2, TiO_2, Si_3N_4 and ZrO_2. Detailed information about these materials is provided in Table 1.

Table 1. Comparison of Main Materials Used in PV Panel Coating

Material	Refractive Index (n)	Thickness (ı	Efficiency Gain (%)	Cost (USD/m^2)
SiO_2	1.46	100	2 - 3	0.1 - 0.2
MgF_2	1.38	100	3 - 5	0.2 - 0.3
TiO_2	2.55	50	5 - 7	0.3 - 0.4
Si_3N_4	2.02	100	4 - 6	0.4 - 0.5
ZrO_2	2.20	100	5 - 7	0.5 - 0.6

III. Coating Methods

a. Coating with Sol-Gel Method

The principle of the sol-gel process is the formation of an oxide network through molecular poly-condensation reactions in a liquid. Sol-gel methods are widely used in the production of superhydrophobic and superhydrophilic coatings with transparency and self-cleaning properties (Power et al., 2016; Wu et al., 2016). The widespread use of the sol-gel method in thin film production is attributed to its relatively simple and cost-effective nature. As it is commonly employed, the sol-gel technique offers a flexible process where parameters can be adjusted to achieve the desired product (Wu et al., 2016).

b. Spin Coating

During the spin coating process, the solution is spread and evenly distributed on the surface, and adhesion is achieved through the effect of the spin. The coating thickness during the process is controlled by the solution's viscosity, spinning speed, and rotation time. As shown in Fig. 2, the sol-gel deposition process consists of four stages: deposition, spin-up, spin-off, and evaporation. Applying sol-gel with high viscosity and low density can be challenging. A significant amount of sol-gel is consumed because excess sol-gel is thrown off the surface during the coating process. Spin coating and dip coating are inexpensive and fast methods in terms of application. (Bernsmeier et al., 2014).

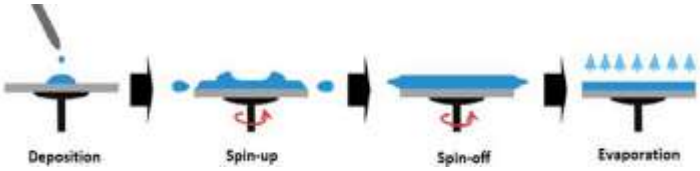

Fig. 2. Spin coating method stages (Shanmugam et al., 2020).

c. Electrospinning Method

Electrospinning is a simple and flexible technique for the continuous production of micro/nanofibers from polymers. It is a relatively straightforward method, as seen in Fig. 3, that can be adapted to develop superhydrophobic coatings from both natural and synthetic polymers. The electrospinning process involves the use of a high electric field between a syringe containing a viscous polymer solution and a conductive substrate. To create uniform fibres, the molecular weight of the polymer and the concentration of the solution must be taken into account. Regular superhydrophobic fibres can be obtained by electrospinning a mixture of polymer and hydrophobic material or by introducing secondary structures. (Suepueren et al., 2007).

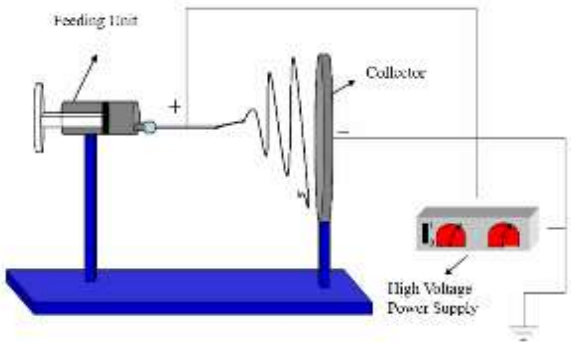

Fig. 3. Schematic representation of the electrospinning method (Selda et al., 2015).

d. Dip Coating Method

Dip coating is defined as the controlled immersion and withdrawal of a polymer into and from a precursor solution at a controlled speed (feeding rate). It offers advantages such as simplicity, controllability, reliability, and repeatability (Fig. 4). The process steps can be summarized as immersion, start-up, deposition, evaporation, and drainage. This method is commonly preferred for the preparation of nanostructured coatings due to its simplicity and speed, especially for the creation of dual-functional or multi-functional films. (Ma et al., 2005).

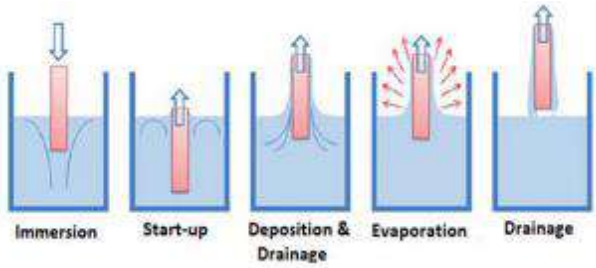

Fig. 4. Dip coating method stages (Shanmugam et al., 2020)

e. Spraying (Electrospray) Coating Method

The spraying technique involves applying a solution to a preheated surface by spraying. Factors determining the coating quality include spraying time, spraying distance, surface temperature, and solution content. In this technique, surface temperature stands out as the most crucial parameter. It can be applied to large surfaces and is fast and practical. The main challenge of the application is the droplets formed during spraying. After application, a reheating process can be carried out for the solidification of the liquid solution adhering to the surface (Perednis & Gauckler, 2005).

f. Chemical Vapor Deposition (CVD) Coating Method

Chemical Vapor Deposition (CVD) is a versatile deposition technique utilized in various applications, ranging from thin films to coatings, encompassing semiconductors, dielectrics, and metallic coatings. CVD modifies the properties of a substrate surface by depositing a thin film layer through chemical reactions at elevated temperatures. The CVD process involves the transportation of reactive gases and/or a carrier gas into a reaction chamber, followed by the deposition process to form a film. Film deposition can occur through dissolution, oxidation, hydrolysis, or compound formation. These reactions typically take place in the gas phase, with intermediate gases being absorbed onto the substrate, entering subsequent surface reactions. However, CVD is a costly process due to the requirement for expensive vacuum furnaces and the enlargement of anti-reflective (AR) thin film coatings on silicon substrates. Moreover, the utilization of highly toxic and flammable silane gas complicates the process. (Ebert & Bhushan, 2016).

IV. Conclusion

This study reveals the significant potential of coatings applied to enhance the efficiency of photovoltaic panels. Research in the literature indicates that the use of various coating materials increases sunlight absorption, leading to higher electricity generation. Particularly, anti-reflective coatings and the reduction of surfaces reflecting sunlight can substantially improve the performance of photovoltaic panels. However, the selection and application of efficiency-enhancing coatings have a complex impact on the efficiency of photovoltaic panels. Factors such as optical properties, durability, cost, and environmental effects should be considered when choosing coatings. Studies emphasize that different coating materials have varying environmental impacts, highlighting the importance of considering sustainability in the selection process.

In conclusion, the use of efficiency-enhancing coatings in photovoltaic panels presents the potential to improve the efficiency of solar energy conversion. This review study evaluates different coating materials and methods based on existing research in the literature. It emphasizes the need for future studies to focus on developing more efficient coating materials, optimizing application methods, and conducting more careful assessments from an environmental sustainability perspective. The development of efficiency-enhancing coatings in photovoltaic panels can contribute to the broader utilization of solar energy and reduce dependence on sustainable energy sources. Furthermore, there is a need for further research and improvement in the commercial applicability and cost-effectiveness of these coatings on a larger scale.

References

Ashok, S. (2007). Optimised model for community-based hybrid energy system. *Renewable energy, 32*(7), 1155-1164.

Bernsmeier, D., Polte, J. r., Ortel, E., Krahl, T., Kemnitz, E., & Kraehnert, R. (2014). Antireflective coatings with adjustable refractive index and porosity synthesized by micelle-templated deposition of MgF2 sol particles. *ACS applied materials & interfaces, 6*(22), 19559-19565.

Goetzberger, A., Knobloch, J., & Voss, B. (1998). *Crystalline silicon solar cells* (Vol. 1). Wiley Online Library.

Gong, X., & He, S. (2020). Highly durable superhydrophobic polydimethylsiloxane/silica nanocomposite surfaces with good self-cleaning ability. *ACS omega, 5*(8), 4100-4108.

Ling, X., Fan, D., & Yang, F. (2010). A study of the organization and performance of thermally evaporated aluminum reflector for solar energy system. 2010 The 2nd Conference on Environmental Science and Information Application Technology,

Ma, M., Hill, R. M., Lowery, J. L., Fridrikh, S. V., & Rutledge, G. C. (2005). Electrospun poly (styrene-block-dimethylsiloxane) block copolymer fibers exhibiting superhydrophobicity. *Langmuir, 21*(12), 5549-5554.

Maharjan, S., Liao, K.-S., Wang, A. J., Barton, K., Haldar, A., Alley, N. J., Byrne, H. J., & Curran, S. A. (2020). Self-cleaning hydrophobic nanocoating on glass: A scalable manufacturing process. *Materials Chemistry and Physics, 239*, 122000.

Mazumder, M. K., Horenstein, M. N., Heiling, C., Stark, J. W., Sayyah, A., Yellowhair, J., & Raychowdhury, A. (2015). Environmental degradation of the optical surface of PV modules and solar mirrors by soiling and high RH and mitigation methods for minimizing energy yield losses. 2015 IEEE 42nd Photovoltaic Specialist Conference (PVSC),

Mazumder, M. K., Horenstein, M. N., & Joglekar, N. R. (2015). *Prototype Development and Evaluation of Self-Cleaning Concentrated Solar Power Collectors*.

Nosonovsky, M., & Bhushan, B. (2009). Superhydrophobic surfaces and emerging applications: Non-adhesion, energy, green engineering. *Current Opinion in Colloid & Interface Science, 14*(4), 270-280.

Palit, S., & Hussain, C. M. (2020). Nanomaterials for environmental engineering and energy applications. *Handbook of Nanomaterials and Nanocomposites for Energy and Environmental Applications*, 1-24.

Parkin, I. P., & Palgrave, R. G. (2005). Self-cleaning coatings. *Journal of Materials Chemistry, 15*(17), 1689-1695.

Perednis, D., & Gauckler, L. J. (2005). Thin film deposition using spray pyrolysis. *Journal of electroceramics, 14*, 103-111.

Power, A., Barrett, A., Abubakar, J., Suarez, L., Ryan, L., Wencel, D., Sullivan, T., & Regan, F. (2016). Versatile Self-Cleaning Coating Production Through Sol–Gel Chemistry. *Advanced Engineering Materials, 18*(1), 76-82.

Selda, Ö., Çiftci, Ş., Fethiye, G., Aksoy, K., & Aksoy, S. A. (2015). Nanokil Katkılı PAN Nanolif Sentezi ve Karakterizasyonu. *Süleyman Demirel Üniversitesi Fen Edebiyat Fakültesi Fen Dergisi, 10*(1), 107-117.

Shanmugam, N., Pugazhendhi, R., Madurai Elavarasan, R., Pitchandi, K., & Das, N. (2020, 05/21). Anti-Reflective Coating Materials: A Holistic Review from PV Perspective. *Energies, 13*, 2631.

Suepueren, G., KANAT, Z. E., Ahmet, Ç., Kirci, T., Gueluemser, T., & TARAKÇIOĞLU, I. (2007). Nano fibres (Part 2). *Textile and Apparel, 17*(2), 83-89.

Sun, Z., Yan, Z., Yao, J., Beitler, E., Zhu, Y., & Tour, J. M. (2010). Growth of graphene from solid carbon sources. *Nature, 468*(7323), 549-552.

Wu, X., Fu, Q., Kumar, D., Ho, J. W. C., Kanhere, P., Zhou, H., & Chen, Z. (2016). Mechanically robust superhydrophobic and superoleophobic coatings derived by sol–gel method. *Materials & Design, 89*, 1302-1309.

Yamada, T., Nakamura, H., Sugiura, T., Sakuta, K., & Kurokawa, K. (2001). Reflection loss analysis by optical modeling of PV module. *Solar Energy Materials and Solar Cells, 67*(1-4), 405-413.

Yasa, U. G., Erim, M., Erim, N., Girgin, M., & Kurt, H. (2017). Design of anti-reflective graded height nanogratings for photovoltaic applications. 2017 International Conference on Numerical Simulation of Optoelectronic Devices (NUSOD),

Zhang, M., Feng, S., Wang, L., & Zheng, Y. (2016). Lotus effect in wetting and self-cleaning. *Biotribology, 5*, 31-43.

IEEES-062

Techno-Economic Analysis of the Distribution Network for the European Market of Green Ammonia Produced From Offshore Wind Farms to be Installed Off the Coast of Northern Europe

[1]Mikail Rıza Onat, [1]Murat Emre DEMİR
[1] Istanbul Technical University, Faculty of Naval Architecture and Ocean Engineering, Naval Architecture and Marine Engineering, Ayazaga Campus, Maslak, Istanbul, 34469, Turkey
*E-mails: onatm@itu.edu.tr, medemir@itu.edu.tr

Abstract

Green ammonia, a hydrogen derivative, is a promising chemical for storing and transporting renewable energy. In this study, the green ammonia production project with energy produced from offshore wind farms (OWF) is focused on. It is aimed to develop a model network to deliver green ammonia, which can be produced in Northern European countries with great potential for OWF, to European ports and end consumers. The ever-increasing ammonia demand of European countries is now met by its production from fuels such as natural gas and coal from places such as the Far East and Russia. Current conflicts in international arenas cause disruptions in ammonia shipments for the European market. The use of ammonia as ship fuel in the future and its increasing need in the agricultural industry reveal that there is a tendency for Europe to move away from global supply centers and towards environmentally friendly green ammonia production centers where regional production is encouraged. The infrastructure and economic feasibility of delivering the green ammonia to be produced to the ports of Rotterdam, Antwerp, Hamburg, Amsterdam and Le Havre were examined. In the transportation of ammonia to ports, emphasis has been placed on ship transportation and especially on pipelines in land transportation. The focus is on the feasibility of building new pipelines or converting existing natural gas pipelines. The effect of land distance and sea distance on transportation costs was examined.

Keywords: Energy, green ammonia, offshore wind farms, pipeline, shipping, transportation.

I. Introduction

Many developed countries have determined their future programs to meet their energy needs in an environmentally friendly way. Concrete steps are being taken for the goal of zero greenhouse gas emissions throughout the European Union (EU). Energy production from renewable energy sources is very important in the development of energy sustainability in the future. Contrary to the fossil fuels used in energy production today, renewable energy sources are unlimited in energy production and greenhouse gas emissions are very low in energy production. Although the use of energy produced especially from wind and solar energy is increasing with unlimited resources, decreasing costs and sustainable nature, it also has limitations due to the intermittent nature of its availability (Ziegler et al., 2019). Cost-effective and efficient technologies for renewable energy storage and utilization are critical to reduce disruptions to solar and wind resources and maintain the stability of the electricity grid (Pan et al., 2022). In this study, the efficiency of converting the energy produced from renewable energy sources to ammonia fuel, which will be used as ship fuel in the future, was investigated.
The volatility of wind power generation puts supply-demand grid balance at risk, and offshore installations require billions of euros in grid reinforcement. Water electrolysis, which uses green electricity to produce hydrogen, is a potential solution to these challenges. Hydrogen, which can be stored for longer periods and in larger quantities than electricity, can support the grid's supply-demand balance, help prevent grid back-ups, and form the basis for green fuels (e.g. methane, ammonia and methanol) (Egerer et al., 2023).

II. Methodology

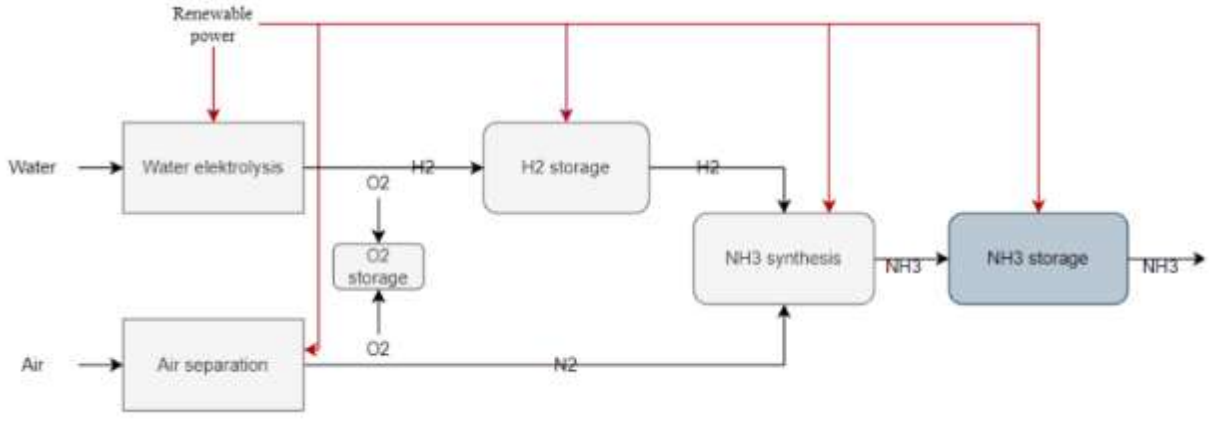

Fig. 1: The process of green ammonia production.

The dispersed structure of the places with high renewable energy potential in the world and the distance between the industrial and dense population regions with high energy needs will lead to an increase in the global trade of sustainable energy carriers. In the medium term, hydrogen-based fuels with high energy densities and relatively low transportation costs will be considered, which can

replace the trading of fossil resources (Egerer et al., 2023). Ammonia is one of the chemicals that is traded on an international scale and produced the most and can be used as a carrier system. Although today ammonia is produced from fossil fuels and coal, green ammonia production is possible for countries with renewable energy potential such as PV, wind or geothermal energy. Many projects aim to produce green ammonia for future export as an intercontinental energy vector (Dolan et al., 2021). The proliferation of ammonia-fueled ships in the future will increase the interest in the production of ammonia fuel on a global scale. After the ammonia is cooled to a temperature of about -33 ◦C, it can be transported by vessels equipped with pumps and cooling systems, and by pipelines (Aziz et al., 2020). Therefore, the difficulties in the storage and transportation of hydrogen are less with ammonia.

III. Analysis

Ammonia can be transported by different road and sea routes such as trucks, trains, ships and pipelines. Road transport, such as road and rail transport, is limited in weight and the cost balance of the amount of fuel that can be transported is negative. In road and rail transport, mostly ammonia is pressurized, while ships can transport by pressurized or low-temperature storage.

One of the cost-effective and safe transportation methods of land transportation is pipelines. Pipelines can transport ammonia in liquid phase from central production areas to terminals and ports serving distributors and end users (Yang & Ogden, 2007). There are some disadvantages of transportation by pipelines, some of which are high initial investment costs and lack of flexibility compared to other transportation routes. However, the increasing demand of the European market shows that these disadvantages will turn into an advantageous point.

It is quite difficult to determine the pipeline investment costs because it includes many parameters. The main capital costs of ammonia distribution through pipelines; It includes initial construction and investment costs, operating costs such as booster stations, costs according to the diameter size and transport pressure for the flow to be transported, and maintenance costs. Costs also vary with the mileage of the pipeline passing through rural and urban areas. We will focus on an average value in our study. The rural and urban capital expenditure for a 10 inch diameter X42 steel ammonia pipeline is approximately 857,000 $/km and 1,469,000 $/km, respectively (Nayak-Luke et al., 2020). Construction of a pipeline that will only be used to transport hydrogen will cost 1.5-1.8 times more than existing natural gas pipeline projects, depending on the length and diameter of the line. A 12 inch hydrogen pipeline costs about 310,000 $/km in rural Texas, compared to 1,250,000 $/km in urban California (Cheng & Cheng, 2023). The cost of transporting ammonia in the Kaneb pipeline is approximately 0.01616 $/ton/km (Department of Energy, 2006). It is estimated that transporting ammonia in pipelines will be cheaper than transporting hydrogen in pipelines due to lower pumping costs (Leighty & Holbrook, 2012).

IV. Results and discussion

Average pipeline cost for distribution network (5 USD/t); The cost of transporting ammonia via pipeline is higher than the cost of transporting it by ship over long distances. The cost of transporting ammonia by pipeline is approximately 5 USD/t/100 km, while ocean transportation costs an average of 1.25 USD/t/100 km. In the land distribution model, pipelines carry large amounts of ammonia over long distances, being very safe, planned as long as there is no malfunction, and have many economical and environmentally friendly advantages. It is thought that converting existing natural gas pipelines to be suitable for the transportation of hydrogen and ammonia will reduce the construction cost of new pipelines by 20% to 60%. The impact of initial investment costs can be reduced by increasing the pipeline carrying capacity with compressor stations. One of the most important advantages of transporting ammonia via pipelines is that harmful emissions are very low, as in other land transportation.

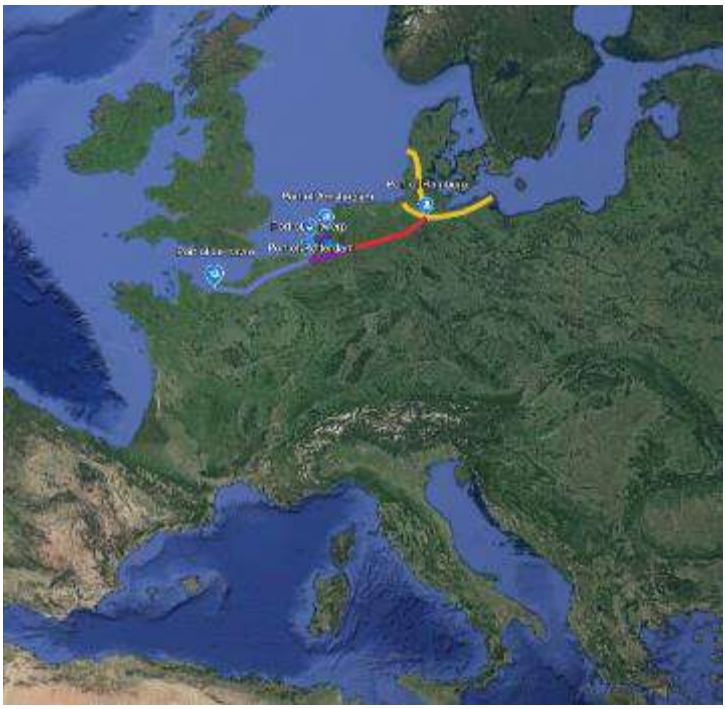

Fig. 2: Ammonia pipeline distribution scheme of Europe's large trade volume ports.

It is more cost-effective to use ship tankers to transport ammonia over distances longer than 1800 km. For this reason, maritime transportation will be very advantageous in intercontinental import-export. Since pipelines at long distances from the coast will be quite costly, it will be more profitable to produce offshore hydrogen and transport it by tankers to long distances.

Table 1. Costs of booster stations used in designed pipelines.

Pipelines	Length	Number of Booster Stations	The CAPEX of Booster Stations	Operating Cost of Booster stations
P1	257.79 km	2	4,50 MM USD	1,020,000 USD/year
P2	101.42 km	1	2,25 MM USD	510,000 USD/year
P3	276.48 km	2	4,50 MM USD	1,020,000 USD/year
P4	317.95 km	3	6,75 MM USD	1,530,000 USD/year
P5	86.09 km	1	2,25 MM USD	510,000 USD/year
P6-P7	96.22 km	1	2,25 MM USD	510,000 USD/year
P8-P9	521.34 km	4	9,00 MM USD	2,040,000 USD/year

V. Conclusion

The global trade of ammonia, one of the most produced chemicals in the world, is increasing day by day. It is also possible to produce green ammonia using offshore wind as power from ammonia, which today is mostly produced from fossil fuels and coal. This study focuses on the techno-economic model of the green ammonia supply chain for the European market as a result of comprehensive calculations. As a result, green ammonia can be produced economically in many regions where demand is increasing in Europe and globally. Distribution of green ammonia in the supply chain over short distances rather than long distances across continents can be made more efficient.

References

Aziz, M., TriWijayanta, A., & Nandiyanto, A. B. D. (2020). Ammonia as Effective Hydrogen Storage: A Review on Production, Storage and Utilization. *Energies 2020, Vol. 13, Page 3062*, *13*(12), 3062. https://doi.org/10.3390/EN13123062

Cheng, W., & Cheng, Y. F. (2023). A techno-economic study of the strategy for hydrogen transport by pipelines in Canada. *Journal of Pipeline Science and Engineering*. https://doi.org/10.1016/j.jpse.2023.100112

Department of Energy, U. (2006). *Potential Roles of Ammonia in a Hydrogen Economy A Study of Issues Related to the Use Ammonia for On-Board Vehicular Hydrogen Storage*.

Dolan, R. H., Anderson, J. E., & Wallington, T. J. (2021). Outlook for ammonia as a sustainable transportation fuel. *Sustainable Energy & Fuels*, *5*(19), 4830–4841. https://doi.org/10.1039/D1SE00979F

Egerer, J., Grimm, V., Niazmand, K., & Runge, P. (2023). The economics of global green ammonia trade – "Shipping Australian wind and sunshine to Germany." *Applied Energy*, *334*. https://doi.org/10.1016/j.apenergy.2023.120662

Leighty, W. C., & Holbrook, J. H. (2012). Alternatives to electricity for transmission, firming storage, and supply integration for diverse, stranded, renewable energy resources: Gaseous hydrogen and anhydrous ammonia fuels via underground pipelines. *Energy Procedia*, *29*, 332–346. https://doi.org/10.1016/j.egypro.2012.09.040

Nayak-Luke, R. M., Forbes, C., Cesaro, Z., & Bănares-Alcántara, R. (2020). Techno-Economic Aspects of Production, Storage and Distribution of Ammonia. In *Techno-Economic Challenges of Green Ammonia as an Energy Vector*. https://doi.org/10.1016/B978-0-12-820560-0.00008-4

Pan, Z., Liu, Y., Tahir, A., Christopher Esan, O., Zhu, J., Chen, R., & An, L. (2022). A discrete regenerative fuel cell mediated by ammonia for renewable energy conversion and storage. *Applied Energy*, *322*. https://doi.org/10.1016/j.apenergy.2022.119463

Yang, C., & Ogden, J. (2007). Determining the lowest-cost hydrogen delivery mode. *International Journal of Hydrogen Energy*, *32*(2). https://doi.org/10.1016/j.ijhydene.2006.05.009

Ziegler, M. S., Mueller, J. M., Pereira, G. D., Song, J., Ferrara, M., Chiang, Y. M., & Trancik, J. E. (2019). Erratum: Storage Requirements and Costs of Shaping Renewable Energy Toward Grid Decarbonization (Joule (2019) 3(9) (2134–2153), (S2542435119303009), (10.1016/j.joule.2019.06.012)). *Joule*, *3*(11), 2867–2869. https://doi.org/10.1016/J.JOULE.2019.10.014

IEEES-063

Assessing the Bilateral Impacts in a Changing Climate in terms of Shipping Sector

[1*]Duygu Ülker [2]Serap Goksu
[1]Istanbul University, Institute of Marine Sciences and Management, Department of Marine Environment, Vefa-Fatih, İstanbul, 34134, Türkiye
[2]Recep Tayyip Erdogan University, Turgut Kiran Maritime Faculty, Department of Maritime Transportation & Management Engineering, Rize, Turkiye.
*Corresponding author: duygu.ulker@istanbul.edu.tr

Abstract

By carrying out 80% of global trade, the shipping industry is an important indicator of globalization. The impact of climate change (CC) on the shipping sector, as well as the impact of shipping on CC, have been widely discussed in the literature. Ships produce exhaust gases like carbon dioxide (CO2), methane (CH4), and nitrous oxide (N2O), which contribute significantly to global greenhouse gas emissions. If no measures are taken, the future emission scenarios of the IPCC predict that ship-generated CO2 emissions will be more than double the current levels by 2050 (IPCC, 2014). To reduce the impact of shipping on CC, the International Maritime Organization (IMO) is regulating the maritime sector and setting 2050 emissions reduction targets to improve its environmental efficiency. However, the shipping industry is also affected by CC, particularly in terms of changing shipping routes and rising sea levels. This paper reviews the bilateral impacts of global CC on the shipping sector, taking into account scenarios from the IPCC and energy efficiency measures implemented by IMO.

Keywords: Climate change, GHG emissions, maritime, shipping routes, sea level rise, arctic shipping.

I. Introduction

The location of the Earth relative to the sun and the natural greenhouse effect of the atmosphere make the Earth habitable (Karl and Trenberth, 2003). Various atmospheric gases contribute to the greenhouse effect, whose impact in clear skies is —60% from water vapour, —25% from carbon dioxide (CO_2), —8% from ozone, and the rest from trace gases including methane (CH_4) and nitrous oxide (N_2O) (Karl and Trenberth, 2003). Human influences strongly impacted global climate change (CC) in the last decades especially because of using fossil fuels. The rates of anthropogenic greenhouse gas (GHG) are CO_2 at 74,4%, CH_4 at 17,3%, N_20 at 6,2%, and F Gases at 2,1%. Although CO_2 is the highest emitted anthropogenic GHG emissions, the impact of CH_4 and N_2O on CC is higher than CO_2.

The IPCC finalized the Synthesis Report for the Sixth Assessment Report in Switzerland from 13 - 19 March 2023 (IPCC, 2023a). IPCC AR6 Policy Makers report stated the estimation of global net anthropogenic GHG emissions in 2019 which is 59 ± 6.6 $GtCO_2$-eq. "*It is about 12% (6.5 $GtCO_2$-eq) higher than in 2010 and 54% (21 $GtCO_2$-eq) higher than in 1990 (IPCC,2023b). Sectoral share of net global GHG emissions in 2019 are stated in longer report of IPCC AR6 which are 34% (20 $GtCO_2$-eq) from energy sector, 24% (14 $GtCO_2$-eq) from industry, 22% (13 $GtCO_2$-eq) from AFOLU, 15% (8.7 $GtCO_2$-eq) from transport and 6% (3.3 $GtCO_2$-eq) from buildings*".

IPCC (2022) Transport report states that "*70% of direct transport emissions came from road vehicles while 1%, 11%, and 12% came from rail, shipping, and aviation respectively"*. Also, related emissions in developing countries have increased more rapidly than in Europe or North America" (IPCC, 2022). In 2010s IPCC (IPCC, 2014) stated that ship-generated CO_2 emissions will be higher than twice the value of the present emissions by 2050 if no measures are taken as stated also in (UN, 2018). However, the maritime sector was excluded from the COP21 (21st Paris Climate Conference) negotiations regarding greenhouse gas emissions in 2015 (Bullock et al., 2022). Also, the Kyoto Protocol (1997) argued that greenhouse gas emissions stemming from maritime activities could not be associated with any national economy because of their transboundary nature (Gritsenko, 2017).

IMO is a pioneer in establishing policies to decrease the carbon budget in the maritime sector (Van Leeuwen and Monios, 2022). IMO has been regulating the shipping industry to improve its environmental efficiency; however, increased efficiency has not been adequate so far in limiting the emissions coming from shipping. IPCC 2022 offers improvement in Research and Development (Jaramillo et al., 2022). The Environment Committee of the European Parliament decided that transport emissions should be included in the European Union Emission Trading System (EU-ETS) as of 2023 for the integration into the EU greenhouse gas reduction policies (Gritsenko, 2017). In response to this, IMO Secretary-General Kitack Lim argued to senior EU officials that unilateral or regional practices in maritime transport would undermine the global status of IMO (IMO, 2017). However, regional (i.e., PSC, port incentives, etc.) and sectoral (i.e., audit, certification, etc.) implementations provide the advantage of including maritime stakeholders (e.g., cargo owners or port administrations, who have a direct share in reducing greenhouse gas emissions) in the management (Gritsenko, 2017). Maritime activities have a complex and polycentric management system that is guided by international conventions (Van Leeuwen and Monios, 2022).

The 2023 IMO strategy for reducing GHG Emissions from ships was approved in 2017 as the 2017-2023 Roadmap (Gritsenko, 2017). IMO Member States met at MEPC80 on 3-7 July 2023. It adopted the revised IMO GHG strategy, which included a common target to achieve net-zero GHG emissions from international shipping until the year 2050 and indicative control points for 2030 and 2040, as well as a commitment to ensure the uptake of alternative zero and near-zero GHG fuels until 2030. To do this, decreasing the carbon intensity of ships by strengthening energy efficiency design requirements for new ships, and reducing CO_2 emissions per transportation job by at least 40% on average compared to 2008 by 2030 in international transportation were determined as the target levels that guided the 2023 IMO GHG strategy. Indicative control points that intended to achieve net-zero GHG emissions from international shipping included reducing total annual greenhouse gas emissions from international shipping at a rate of at least 20% until the year

2030 when compared to 2008 and reducing total annual greenhouse gas emissions from international shipping by 70% until 2040 when compared to 2008 (IMO, 2023).
The average commercial life of ships is over 25 years in the maritime industry, which is also an important limitation because Heavy Fuel Oil (HFO) is used as the fuel in maritime transportation with a rate of 79%, followed by Marine Diesel Oil, Marine Gas Oil, and Liquefied Natural Gas (LNG) (IMO, 2020). Considering the transition of ships to the new fuel system, the production of alternative fuels, transporting refuelling points and storage, and the delayed years in the transition process will make the already-difficult Paris Agreement targets for maritime transportation become even more difficult (Bullock et al., 2022; Van Leeuwen and Monios, 2022). The maritime industry often reflects such investments as additional costs to their customers. For this reason, IMO preferred Market-Based Mechanisms (MBM) (e.g., carbon tax or ETS) (Lagouvardou, 2018). In this framework, this study aims to evaluate the bilateral impacts of global CC in terms of the shipping sector considering scenarios of IPCC and energy efficiency measures by IMO.

IPCC scenarios

Intergovernmental Panel on CC (IPCC) evaluates/models CC with four scenarios of 'Representative Concentration Pathway' (RCP) which are (RCP 2.6, RCP4.5, RCP6, and RCP8.5) considered a possible range of radiative forcing values in the year 2100 (2.6, 4.5, 6, and 8.5 W/m^{-2}, respectively). These scenarios are considered according to effort level to keep down GHG emissions. The scenarios define modelling results with global temperature increase and sea level rise in 2100 according to GHG mitigation efforts.
RCP 2.6 represents the highest effort. Radiative forcing peaks at approximately 3 W m^{-2} before 2100 and temperature and sea level rise increase average of 1^0C and 0,4 m respectively. RCP 4.5 represents medium-high effort. Radiative forcing stabilized at approximately 4,5 W m^{-2} before 2100 and temperature and sea level rise increases average 1,8 ^{o}C and 0,47 m respectively. RCP 6 is a medium effort. Radiative forcing stabilized at approximately 6 W m^{-2} after 2100 and temperature increase, and sea level rise is average 2,2 ^{o}C and 0,48 m respectively. RCP 8.5 is a low effort. Radiative forcing reaches greater than 8,5 W m^{-2} by 2100 and continues to rise. Temperature increase and sea level rises are average of 3-7 ^{o}C and 0,63 m respectively.

II. **Methodology**

Bilateral evaluation
The framework of the bilateral evaluation of climate change in terms of the shipping sector is given in Fig 1.

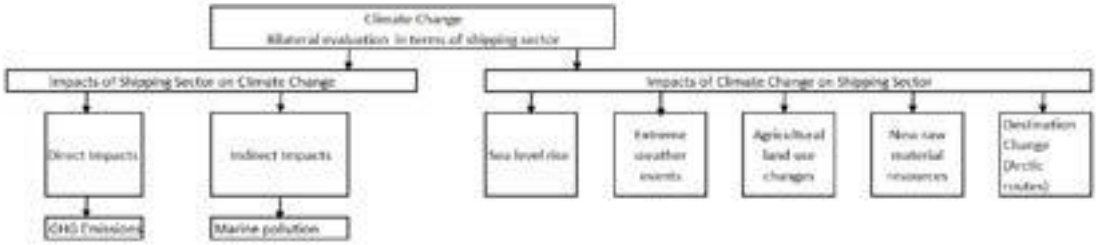

Fig 1. Bilateral evaluation of CC.

Impacts of the Shipping Sector:

GHG emissions produced by the shipping sector are evaluated in direct impacts. Ship/port-generated marine pollution causes indirect CC destroying marine habitat and impacting the ecosystem balance of the oceans.
GHG emissions due to usage of fossil fuels: It is necessary to separate economic growth from environmental pollution to achieve sustainable development, which will have various difficulties in maritime. For example, the growth in maritime trade is described as having a positive effect on the flag state, but the environmental damage caused by this growth in the marine and terrestrial ecosystem has a negative impact (DeSombre, 2006). Alternative fossil fuels (e.g., LNG or methanol) used in shipping are similar to traditional petroleum fuels in terms of their life cycles. However, biofuels are not available at a certain scale (Winnes et al., 2015). The supply of fossil fuels must be stopped to achieve the decarbonization target by 2050, instead of focusing on improving the supply of alternative fuels and propulsion systems or influencing demand through efficiency targets and taxes (Monios and Wilmsmeier, 2022). Planned extraction and production of fossil fuels (future finds excluded), already exceed the amount we need if the world is to be decarbonized before 2050 (The Production Gap, 2020). Unless this supply is discontinued, the industry will continue to use it regardless of advances in other fuels.
Marine pollution by ships and activities of natural resource discovery: Marine pollution impacts the Oceans' carbon storage budget which indirectly causes CC impacts. The potential for shipping, exploring natural resources, and production is huge in the Arctic (Afenyo et al., 2019). For this reason, the socio-economic livelihoods of local people might be affected negatively by increased ship traffic and ship accidents in the region. For this reason, any preparations to be made in the region are important regarding the proper management of the Arctic Seas.

Impacts of CC on shipping:

Sea level rise: IPCC RCP scenarios show that the sea level rise impacts CC with each scenario. Ports are structures which are in interaction with the coast and ocean. Consequently, the climate-related vulnerability of this sector is extremely high.
Extreme weather events: Many ports will be affected by extreme weather events due to CC. IPCC states that an increase in the frequency and intensity of "extreme" atmospheric events—shocks such as storms, heavy precipitation, and heat waves (IPCC, 2012);

as well as long-term changes to climatic variables resulting in "slow onset" changes like sea level rise, wave climatology, and sea-surface salinity.

Agricultural land use change: CC results such as increases in temperature, extreme temperatures, heat waves, droughts, and rainfall intensity are expected to substantially impact agricultural production and crop pattern change in the regions (IPCC 2007; Attavanich and McCarl, 2011).

Raw material resources: It is estimated that the Arctic contains large oil deposits, a significant percentage of the world's natural gas reserves along with other minerals (Lee et al., 2015). This makes the area attractive from a commercial and industrial viewpoint. The activities performed by the United States Royal Dutch Shell in Alaska, ENI S.p.A.'s work on Spy Island, and Russian Rosneft and Exxon Mobil finding oil in the Black Sea and starting production can be given as examples of the activities in the Arctic (Afenyo et al., 2019; BOEM, 2017). China, which is not one of the Arctic Countries, has also joined the Arctic Shipping Route and the Belt and Road Initiative (BRI) in the form of 2.0 BRI (Schach and Madlener, 2018). It is considered that China will become more active in the area with the Polar Silk Road Policy, which will cause increased shipping traffic on routes that pass through Korea, Japan, the North East, and North America (Afenyo et al., 2019).

Destination change: The rate of ice that melts in the North Pole is increasing with the effect of CC, and for this reason, the duration of the ice-free season is extending, which means that Arctic Waterways become more accessible for commercial shipping (Afenyo et al., 2019). There are currently three main trans-Arctic navigation options: the Northern Sea Route (NSR), the Northwest Passage (NWP), and the Trans-Polar Sea Route (TSR) (Ng et al., 2018). The feasibility and economic viability of these Arctic routes are still under intense debate. Arctic shipping is under-examined. Literature has the studies which addressed the potential cost savings of using Arctic routes compared to existing trans-continental shipping networks. For example, the Northern Sea Route (NSR) would have approximately 40% and 3-5% reductions in distance and fuel costs when compared to using the Suez Canal, respectively (Under Normal Circumstances) (Schøyen and Bråthen, 2011; Østreng et al., 2013; Zhu et al. al., 2018) and is envisaged to carry approximately 5% of the global maritime transport (Afenyo et al., 2019). Although the Arctic routes as serious alternatives, opening these routes with a lack of infrastructural support will cause environmental and social impacts due to the risk of maritime accidents (Ng et al., 2018).

Data of maritime statistics and global CO_2 emissions

Figure 2 a) gives the maritime trade statistics in the world given by the review report of Maritime trade by UNCTAD (2022) in terms of loaded tons which shows an increased trend since the 1970s. A significant increase has been shown since the year 1990. Although a decrease in loaded tons has been shown due to the global crisis in 2008-2009 and the COVID-19 pandemic in 2020, the system recovered and continued to increase trend in the next years as seen from loaded tons in 2021 which is slightly below pre-pandemic amount—consequently, significant increases in maritime trade point out an increasing share of GHG emissions emitted. The increasing trend of global anthropogenic CO_2 emissions is given in Fig 2b with data represented by (Friedlingstein et al., 2022). There is a high correlation between the number of tons loaded in the maritime sector and global CO_2 emissions amount which is 0,977629.

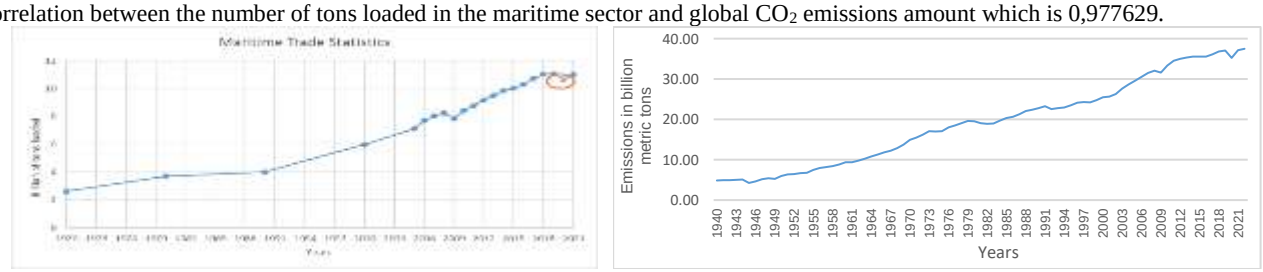

Fig 2. a)Maritime trade statistics between 1970 and 2021 (Data received from UNCTAD (2022)), b)Yearly global CO_2 emissions (Friedlingstein et al., 2022).

III. Results and Discussion

A "*One-Size-Fits-All*" approach is not suitable for the maritime industry because the factors affecting greenhouse gas emissions are diverse. For example, ship design and operational processes are not similar in shipping, and greenhouse gas emissions differ in this context (Jalkanen, et al., 2016; Tichavska et al., 2017). In other words, the environmental footprint of ships' navigation in the Arctic Area and the Mediterranean are different (Gritsenko, 2017). However, the Maritime Sector is dynamic economically and when we evaluate their actions on the environment their targets and regulations are also dynamic although they need improvement. Also, this sector has significant vulnerability in terms of the CC impacts considering the outcomes of IPCC scenarios. Limiting the GHG emissions is one of the most significant issues in the world. Each country, each sector, and each person should be aware of the circumstances of CC and act accordingly because if the world does not act as soon as possible, action taken in the next can be insufficient in terms of adaptation and mitigation to CC. In this context, global emission reduction strategies should be improved by all the sectors (especially energy and industry sectors) and countries to provide more habitable earth to future generations.

References

ACEA, (2020). Joint Statement: The Transition to Zero-Emission Road Freight Transport. https://www.acea.auto/files/acea-pik-joint-statement-the-transition-to-zero-emission-road-freight-trans.pdf (accessed on October, 04, 2023)

Afenyo, M., Jiang, C., Ng, A. K., (2019). Climate change and Arctic shipping: A method for assessing the impacts of oil spills in the Arctic. Transportation Research Part D: Transport and Environment, 77, 476-490. https://doi.org/10.1016/j.trd.2019.05.009

Attavanich, W., McCarl, B.A., 2011. The effect of climate change, CO_2 fertilization, and crop production technology on crop yields and its economic implications on market outcomes and welfare distribution.

Bureau of Ocean Energy Management (BOEM), 2017 December, 7. BOEM Approves Eni Beaufort Sea Exploration Plan. Retrieved: https://www.boem.gov/newsroom/press-releases/boem-approves-eni-beaufort-sea-exploration-plan (accessed on October, 04, 2023)

Bullock, S., Mason, J.,Larkin, A., (2022). The urgent case for stronger climate targets for international shipping. Climate Policy, 22(3), 301-309. https://doi.org/10.1080/14693062.2021.1991876

DeSombre, E.R, (2006). "Flagging Standards: Globalization and Environmental, Safety, and Labor Regulations at Sea," MIT Press Books, The MIT Press, edition 1, volume 1, number 0262541904, February.

Friedlingstein, P., O'Sullivan, M., Jones, M.W,…., Zheng, B., (2022). Global Carbon Budget 2022. Earth Syst. Sci. Data 14, 4811–4900. https://doi.org/10.5194/essd-14-4811-2022

Gritsenko, D., (2017). Regulating GHG Emissions from shipping: Local, global, or polycentric approach?. Marine Policy, 84, 130-133.

IMO, (2017). IMO, the Secretary-General speaks out against regional emission trading system. IMO Briefing 03, Retrieved from: https://www.imo.org/en/MediaCentre/PressBriefings/Pages/3-SG-emissions.aspx (accessed on November, 04, 2023).

IMO, (2020). Fourth IMO GHG study, International Maritime Organization (IMO), London, UK, Retrieved from: https://www.imo.org/en/ourwork/Environment/Pages/Fourth-IMO-Greenhouse-Gas-Study-2020.aspx

IMO, (2023). Retrieved from: https://www.imo.org/en/MediaCentre/PressBriefings/pages/Revised-GHG-reduction-strategy-for-global-shipping-adopted-.aspx (accessed on November, 04, 2023).

IPCC, (2007). Climate Change 2007: Impacts, adaptation and vulnerability. Contribution of Working Group II to the Fourth Assessment Report of the Intergovernmental Panel on Climate Change., eds. M. L. Parry, O. F. Canziani, P. J. Palutikof, P. J. van der Linden and C. E. Hanson. Cambridge, UK: Cambridge University Press.

IPCC (2014). Prather, M., Flato, G., Friedlingstein, P., Jones, C., Lamarque, J.F., Liao, H., Rasch, P. Annex II: Climate System Scenario Tables. page 1395-1445 available at: https://www.ipcc.ch/site/assets/uploads/2017/09/WG1AR5_AnnexII_FINAL.pdf

IPCC, (2023a). https://www.ipcc.ch/report/sixth-assessment-report-cycle/

IPCC, (2023b). Summary for Policymakers. In: Climate Change 2023: Synthesis Report. Contribution of Working Groups I, II and III to the Sixth Assessment Report of the Intergovernmental Panel on Climate Change [Core Writing Team, H. Lee and J. Romero (eds.)]. IPCC, Geneva, Switzerland, pp. 1-34, doi: 10.59327/IPCC/AR6-9789291691647.001

Jalkanen, J. P., Johansson, L., Kukkonen, J., (2016). A comprehensive inventory of ship traffic exhaust emissions in the European sea areas in 2011. *Atmospheric Chemistry and Physics*, *16*(1), 71-84. https://doi.org/10.5194/acp-16-71-2016

Jaramillo, P., S. Kahn Ribeiro, P. Newman, S. Dhar, O.E. Diemuodeke, T. Kajino, D.S. Lee, S.B. Nugroho, X. Ou, A. Hammer Strømman, J. Whitehead, (2022). Transport. In IPCC, 2022: Climate Change 2022: Mitigation of Climate Change. Contribution of Working Group III to the Sixth Assessment Report of the Intergovernmental Panel on Climate Change [P.R. Shukla, J. Skea, R. Slade, A. Al Khourdajie, R. van Diemen, D. McCollum, M. Pathak, S. Some, P. Vyas, R. Fradera, M. Belkacemi, A. Hasija, G. Lisboa, S. Luz, J. Malley, (eds.)]. Cambridge University Press, Cambridge, UK and New York, NY, USA. doi: 10.1017/9781009157926.012.

Lagouvardou, S., Psaraftis, H. N., Zis, T., (2020). A literature survey on market-based measures for the decarbonization of shipping. *Sustainability*, *12*(10), 3953. https://doi.org/10.3390/su12103953

Lee, K., Chen, B., Boufadel, M., Swanson, S. M., Hodson, P. V., Foght, J., & Venosa, A. D. (2016). Behaviour and environmental impacts of crude oil released into aqueous environments. ISBN: 978-1-928140-02-3

Karl, T.R., Trenberth, K.E., 2003. Modern global climate change. Science (80-.). 302, 1719–1723.

Monios, J., Wilmsmeier, G., (2022). Maritime governance after COVID-19: how responses to market developments and environmental challenges lead towards degrowth. *Maritime Economics & Logistics*, *24*(4), 699-722.

Ng, A.K.Y., Andrews, J., Babb, D., Lin, Y., Becker, A., (2018). Implications of climate change for shipping: Opening the Arctic seas. Wiley Interdiscip. Rev. Clim. Chang. 9, e507.

Ostreng, W., Eger, K. M., Fløistad, B., Jørgensen-Dahl, A., Lothe, L., Mejlænder-Larsen, M., Wergeland, T., (2013). *Shipping in Arctic waters: a comparison of the Northeast, Northwest and trans polar passages*. Springer Science & Business Media.

Schach, M., Madlener, R., (2018). Impacts of an ice-free Northeast Passage on LNG markets and geopolitics. Energy Policy 122, 438–448. https://doi.org/10.1016/j.enpol.2018.07.009

Schøyen, H., Bråthen, S. (2011). The Northern Sea Route versus the Suez Canal: cases from bulk shipping. *Journal of Transport Geography*, *19*(4), 977-983.https://doi.org/10.1016/j.jtrangeo.2011.03.003

Shi, Y., Gullett, W., (2018). International regulation on low-carbon shipping for climate change mitigation: development, challenges, and prospects. *Ocean Development & International Law*, *49*(2), 134-156. https://doi.org/10.1080/00908320.2018.1442178

Winnes, H., Styhre, L.,Fridell, E., (2015). Reducing GHG emissions from ships in port areas. *Research in Transportation Business & Management*, *17*, 73-82. https://doi.org/10.1016/j.rtbm.2015.10.008

van Leeuwen, J., Monios, J., (2022). Decarbonisation of the shipping sector–Time to ban fossil fuels?. *Marine Policy*, *146*, 105310. https://doi.org/10.1016/j.marpol.2022.105310

The Production Gap, (2020). Special Report 2020. The Production Gap.

Tichavska, M., Tovar, B., Gritsenko, D., Johansson, L.,Jalkanen, J. P., (2019). Air emissions from ships in port: Does regulation make a difference?. *Transport Policy*, *75*, 128-140. https://doi.org/10.1016/j.tranpol.2017.03.003

UNCTAD (2022). https://unctad.org/system/files/official-document/rmt2022_en.pdf

Zhu, S., Fu, X., Ng, A. K., Luo, M., Ge, Y. E. (2018). The environmental costs and economic implications of container shipping on the Northern Sea Route. *Maritime Policy & Management*, *45*(4), 456-477.

IEEES-064

Numerical Investigation in a Dishwasher Hub: Reducing Pressure Difference and Pump Power

[1*]Fazıl Erinç Yavuz, [1*]Vasıf Can Yıldıran, [2*]Sebastian George Colleoni
[1] Haier Europe – Renta Elektrikli Ev Aletleri San. Ve Dış Tic. Ltd. Şti, Eskişehir, 26110, Türkiye
[2] Haier Europe - Via Privata Eden Fumagalli, Brugherio, 20861, Italy
*E-mails:
erinc.yavuz@haier-europe.com, vasifcan.yildiran@haier-europe.com, sebastian.colleoni@haier-europe.com

Abstract

Energy and water consumption usage are increasing day by day due to the human population and the tools we have, and engineers are studying to reduce this consumption. In dishwashers, after the resistance to heat the water, one of the most electric-consuming devices is a pump. When the pressure difference in the hydraulic line is reduced, engineers can reduce the pump rotational speed during the machine operation, and this eventually reduces the energy consumption of the dishwasher.
In this study, the pressure difference caused in the hub were investigated and some improved designs were suggested. Throughout the investigation, the exclusive consideration of pressure differentials was avoided, as focusing solely on pressure differences between the lower and upper spray arms might result in undesirable flow imbalances. Consequently, equal attention was dedicated to the volumetric flow distribution of water, striving to achieve optimal outcomes without necessitating alterations in the fluid allocation percentages to the lower and upper spray arms.

Keywords: Dishwasher, Hub, CFD, Pump, Pressure Difference Reduction.

I. Introduction

Dishwashers one of the most used products for household and industrial appliances. The first concept design of modern dishwashers with water spraying system was introduced in 1924 (Livens,1924). Since then, engineers have been working on a creation of more efficient systems.
When engineers or researchers investigate the system performance of dishwasher one of the most essential part is heating the water. To heat the water there is several solutions in literature such as, using resistance or implementing the heat pump system in machines. The machine that was investigated in this study is heating the water with resistance. Beside of the performance of the resistance and heating system the second crucial system is the hydraulic systems due to the pressure drop and pump power. If the pressure drops in the sub-hydraulic system is high, the pump should be worked higher rpm's, and this will eventually increase the energy consumption of the machine to feed the spray-arms. In our study, part of the hydraulic system was investigated. Other areas such as inlet of the circulation pump and diverter cover were investigated and published in different papers (Yıldıran et al.,2023, Yıldıran et al., 2023).
To create computational fluid dynamic (CFD) domain first researchers must understand that if the flow of the water is laminar or turbulent. According to study, if the pump has the 1800 rpm rotation speed than the Reynolds Number (Re) of the system can change between 8000 and 30000 (Munson et al.,2012). For the machine that investigated in the scope of this study pump speed is changing its value between 2400 and 2800. Therefore, flow can be considered as turbulent.
For energy consideration in pipe flow if the researcher considers basic piping without bends, valves etc. Bernoulli equation can be used. However, in a complex system such as hydraulic system of dishwasher researchers this equation is not sufficient. Therefore, energy equation for incrompressible, steady flow between two points can be written as Eq.1 which is shared in below (Pritchard & Mitchell, 2016).

$$\frac{p_1}{\rho g} + \alpha_1 \frac{V_1^2}{2g} + z_1 = \frac{p_2}{\rho g} + \alpha_2 \frac{V_2^2}{2g} + z_2 + h_{l_T} \quad (1)$$

II. Method

In a dishwasher there are several of components for controlling and routing the water flow such as, pump, delivery tube, sump, spray arms, hub, etc. the visual of hydraulic line of dishwasher is shared in Figure 1a.
The system works like as follows. Firstly, water is pressurized with the help of circulation pump, and sent to the diverter. Diverter works as a three-way valve, according to washing programme, diverter arrange its position and send the water in lower and/or upper spray arm. Diverter sends water to the hub, which is investigated in this study, then these parts allow water to reach different spray arms.
Topology study has been conducted for both connection (lower spray arm and delivery tube of upper spray arm) for both cases, the aim were reaching the minimum pressure difference and minimum water volume in the component. While pressure difference is essential for reducing pump power, keeping the water volume as minimum is essential for reducing the water usage in one cycle to reach more efficient system in the hydraulic system.
In Figure 1b close view of hub is shared. In this paper, topology studies were conducted with the help of CFD for upper spray arm water inlet and lower spray arm water inlet.

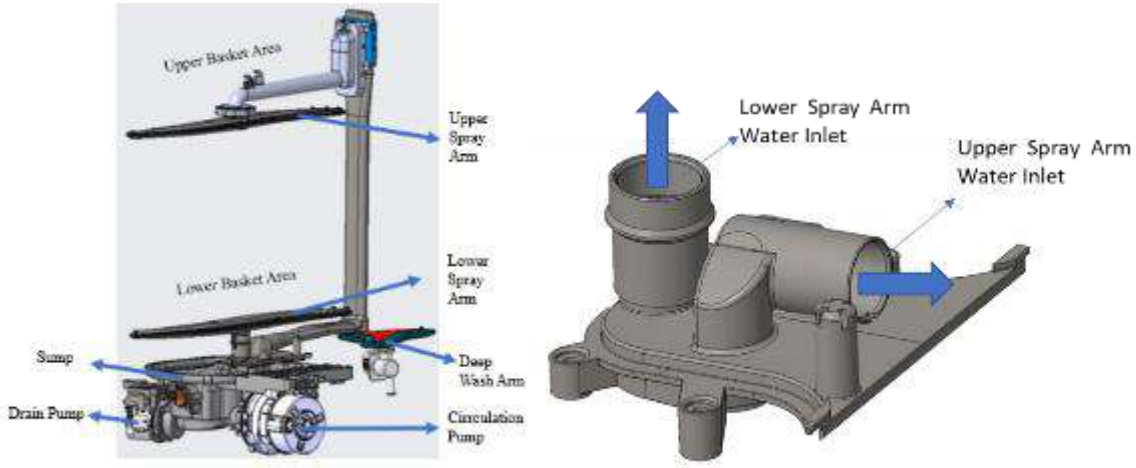

(a) (b)

Figure 1. a) CAD visual of hydraulic system on a dishwasher b) CAD visual of hub

As explained in the section of Introduction turbulent flow has been considered in both cases. To modelling of turbulence effect k-ω SST model (Menter,1994) were used. For each case almost 3.4 million elements have been used for mesh and for all study mesh independency has been investigated. The control surface or point created for each case and the behaviour of the outcomes (pressure, velocity) has investigated for mesh independency when the results is not changed with the increased mesh number, minimum mesh number which is given the appropiete result were used in the final solutions.

For upper and lower spray arm connection points three different geometry were investigated under some geometrical constrains and moldability of the plastic part were also taken into consideration. Figure 2 shows the considered designs for upper spray arm connection, and for the lower spray arm the investigation just considers the section diameter on that region. Because, on that region other components such as sump or sheet metals were in contact with that region and due to that only diameter of the area can be investigated. Also, the diameter values are restricted due to the other connections.

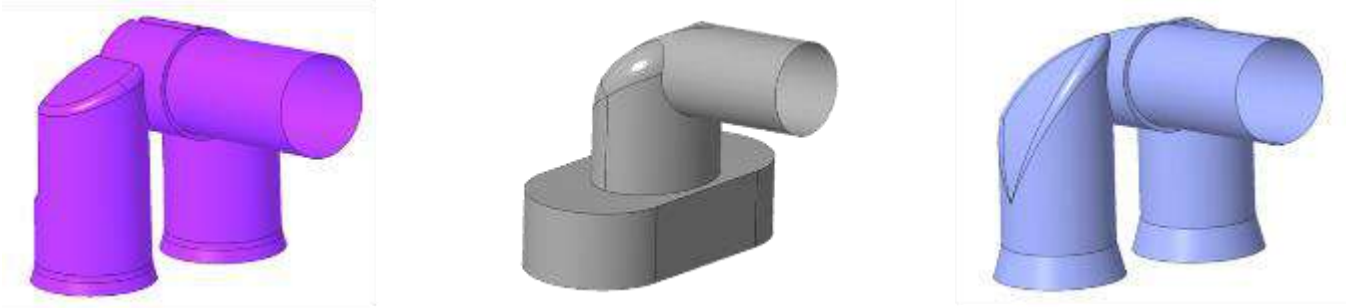

(a) (b) (c)

Figure 2. Investigated designs for upper spray arm (a) Current, (b) Version 1, (c) Version 2

As a boundary condition, exit of the circulation pump is taken as a pressure inlet with the value of 101.325 kPa, exit of the upper and lower spray arms are modelled as flow outlet with the volumetric flow rates of 24.7 and 25.3 l/min, respectively. These results were obtained from the preliminary laboratory studies.

III. Results and Discussion

Firstly, the investigation on current product were conducted. Pressure lose from the inlets and control surfaces is shared in Table 1. Also, velocity profiles of the studies are shared in Figure 3.

It can be clearly said that, especially in lower spray arm has very high-pressure differences in current system and possible modifications on that area is restricted due to geometrical constrains as mentioned above.

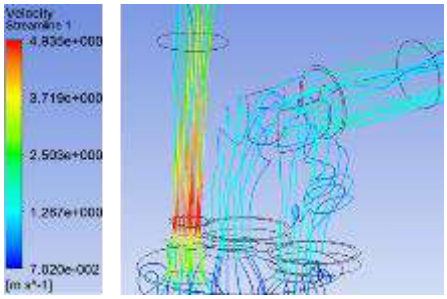

Figure 3. Streamlines of Current Product

Table 1. Pressure Results of Current Product

Location	Unit	Inlet Pressure	Outlet Pressure	Difference
Lower Spray Arm	mbar	1013.25	997.7	53.7
Upper Spray Arm	mbar	1013.25	959.3	15.3

Without changing the lower spray arm geometry all tests were conducted for Version 1 and Version 2 of upper spray arm and the results of pressure values has shared in Table 2 and velocity profile is shared in Figure 4.

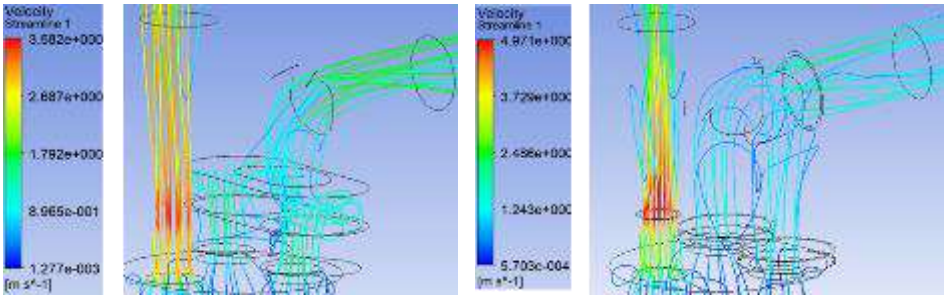

(a) (b)

Figure 4. Streamlines of (a) Version 1 (b) Version 2

Table 2. Pressure Results Comparison on Upper Spray Arm

Design	ΔP (mbar)
Current	15.3
Version 1	15.7
Version 2	11.5

For lower spray arm inlet five different section diameter were investigated and this diameter is restricted between Ø9.5 and Ø12 mm due to the connection with spray arm and the other geometric considerations.

In Figure 5 pressure distribution of the current model and the best result are shared. It can be clearly seen that narrowing the pipe has a big impact on pressure reduction. However, to see the effect of section narrowing even narrower case were carried along with the other studies. The lowest pressure reduction is obtained at the section diameter of Ø12mm.

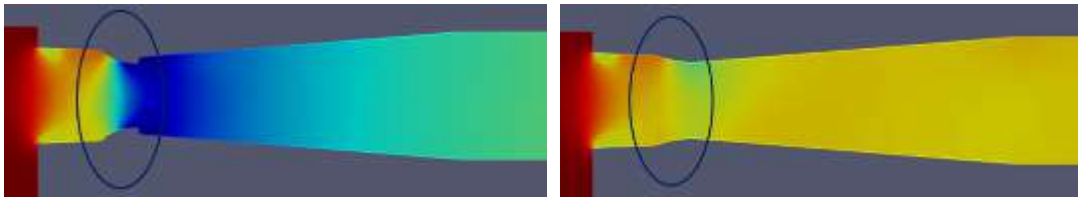

(a) (b)

Figure 5. Pressure Distribution on a Lower Spray Arm Connection (a) Current (b) Ø12mm

Results of the conducted analysis are shared in Table 3. The results show that by increase of section pressure drop on the lower spray arm is reduced more than 50%.

Table 3. Pressure Results Comparison on Lower Spray Arm

Section Diameter	Ø10 mm (Current)	Ø9.5 mm	Ø10.5 mm	Ø11 mm	Ø12 mm
ΔP (mbar)	53.7	76.5	40.9	36.1	21.1

IV. Conclusion

According to the study, the foundings can be listed in below.

1. According to the upper spray arm study, one can clearly say that sharp corners has increasing the pressure drop. With the curved profiles, pressure drop is reduced, and hydraulic advantage is created.
2. Section narrowing has very high effect on pressure drop according to lower spray arm study. This founding can be express from the Bernoulli Equation or for more complicated problems Eq. 1 can be used to calculate the pressure drop.

With these modifications on the machine almost 40 Pa of pressure reduction is achieved. The modification not just reducing the pressure but also, after implementing these changes to the machine, pump motor rpm values can be reduced either. This reduction will eventually cause an energy consumption reduction in our machine which is the goal of this study.

The summary of this study can be found at Table 4. After the modifications on lower spray arm inlet and upper spray arm inlet pressure loss inside the machine is reduced as 60.71%, 24.8%, respectively and the total ratio can be found as 52.8%.

Table 4. Summary of The Study

Location	ΔP Baseline (mbar)	ΔP Revised (mbar)	Δ%
Lower Spray Arm	53.7	21.1	-60.71
Upper Spray Arm	15.3	11.5	-24.84

Acknowledgements
We extend our gratitude to Renta Electric Home Appliances Industry and Foreign Trade Ltd. and our affiliated company, Haier Europe, for their contributions to our work.

References

B. R. Munson, A. P. Rothmayer, T. H. Okiishi and W. W. Huebsch, Fundamentals of Fluid Mechanics, 7th ed., Wiley, 2012.
Livens, W. H. (1924). Improvements in apparatus for washing household crockery and the like. FR579765. UK Intellectual Property Office. Url-2 , Energy and environment, son erişim tarihi 11.05.2010.
Menter, F. R. (1994). Two-equation eddy-viscosity turbulence models for engineering applications. AIAA journal,32(8), 1598-1605
Pritchard, P. J., & Mitchell, J. W. (2016). Fox and McDonald's introduction to fluid mechanics. John Wiley & Sons.
Yıldıran, V.C. & Yavuz, F.E. & Colleoni, S.G. (2023). INVESTIGATION OF DISHWASHER CIRCULATON PUMP INLET CHANNEL. The Eurasia Proceedings of Science, Technology, Engineering & Mathematics (EPSTEM), 26, Page X-Page Y.
Yıldıran, V.C. & Yavuz, F.E. & Colleoni, S.G. (2023). Investigation Of The Flow Performance Of The Diverter Cover In The Dishwasher. The Eurasia Proceedings of Science, Technology, Engineering & Mathematics (EPSTEM), 26, Page X-Page Y.

IEEES-065

Energy Footprint of Gypsum Plasterboard Production Plant

[1,2*]Zehra Sakınç, [3]Abdullah Muratoğlu, Mehmet İshak Yüce[1]
[1] Gaziantep University, Civil Engineering Department, Gaziantep, 27310, Türkiye
[2] Fernas Alçı San.ve Tic. A.Ş Ar-Ge Merkezi, Batman,72202, Türkiye
[3] Batman University, Civil Engineering Department, Batman, 72100, Türkiye
*E-mails: zhrsakinc@gmail.com

Abstract

The rising energy demand, driven by technology, per capita energy usage, and environmental concerns, has prompted scientists and engineers to explore the technical feasibility and efficiency of energy conversion systems. This growing demand presents challenges in sustainability and resource management, emphasizing the need to optimize energy utilization for future generations. Gypsum plasterboard, a versatile material extensively used in the energy-intensive construction industry, serves various functions in different types of buildings. This study focuses on assessing the energy consumption during the production of gypsum plasterboard, a widely utilized material in multiple industries. The objective is to optimize the production process by analyzing energy-intensive processes and identifying opportunities for energy reduction. Specifically, the research evaluates the energy footprint of a gypsum plasterboard factory's production line. Through data collection and analysis, the energy-consuming processes are examined, system boundaries are identified, and the inputs (raw materials, paper, water, energy) and outputs for gypsum plasterboard production are quantified. The findings indicate that manufacturing one square meter of standard gypsum plasterboard requires an average consumption of 0.4623 kWh of electrical energy and 0.4097 m^3 of natural gas, with the drying process identified as the most energy-intensive phase. The results are analyzed considering their implications for sustainable production.

Keywords: Energy, Footprint, Gypsum, Plasterboard, Sustainability.

I. Introduction

Energy is a crucial resource for meeting human needs. With the growth of the global population, industrialization, and technological advancements, the demand for energy has correspondingly increased. It is projected that the world's primary energy demand will increase by approximately 40% from 2013 to 2030 (Kaygusuz et al., 2015). Renewable energy sources have desirable characteristics such as being clean, environmentally friendly and sustainable, but the use of non-renewable energy sources is still high in the world and in Türkiye. According to the International Energy Agency (IEA), Türkiye's energy consumption is divided as follows: 38% from oil, 24% from natural gas, 10% from coal, and 21% from electricity (IEA, 2021). The increasing energy demands, and depletion of primarily utilised fossil fuels raise concerns regarding accessibility of future energy. Therefore, it has become increasingly crucial for both state authorities and private companies to conduct research on alternative renewable energy sources, efficient energy use, and energy measurement and quantification.

Calculating the Energy Footprint is a field of study that aim the sustainability of energy resources. The term "energy footprint" (EF) has been defined in a number of ways. According to the Global Footprint Network, EF is defined as the sum of all land used to provide non-food and non-fodder energy (GFN, 2009). The World Wide Fund for Nature has defined the energy footprint as the land needed to maintain energy consumption and is calculated as the amount of forest needed to offset the resulting CO2 emissions (Loh et al., 2002). Another definition to determining the energy footprint is to calculate the energy consumption for the boundary conditions set by the Life Cycle Analysis method. The energy footprint (EF) indicator attributes the direct and indirect energy resources used to produce goods and services to the final consumer (Tian et al., 2019). In this study, we concentrated on the type of the energy used in the production processs based on the last definition. We did not relate the energy and land use.

To promote a more sustainable environment, it is crucial to conduct energy footprint analysis in energy-intensive sectors. The building and construction materials manufacturing sector is among the industries that consume energy extensively. Gypsum and gypsum plasterboard is an extensively used material in the construction industry.
The initial usage of gypsum in building construction goes back to the Neolithic era, as evidenced by its use in Çatalhöyük, Türkiye, approximately 6,000 BC (de Brito & Flores-Colen, 2015). Gypsum plaster, also known as 'Plaster of Paris', has been used as a coarse mortar and plaster for over 5000 years, dating back to the pyramid of Khufu (Karni & Karni, 1995). It has continued to be widely used as a mineral-based hydraulic binder in the global construction sector due to its low cost per unit volume of finished product (Gartner, 2009). The application areas of gypsum have expanded, resulting in increased usage of gypsum plasterboard, a type of gypsum product.

Plasterboard is composed of a layer of gypsum plaster, sandwiched between two layers of speciapaper. This composition allows them properties that makes gypsum plasterboards particularly suitable for use in situations where fireprotection, sound, and thermal insulation are required (Revuelta, 2021). Gypsum plasterboard is a versatile material and is employed in various types of buildings for multiple purposes, including wall cladding, partitioning, sound insulation and fire prevention.

This study calculated the energy footprint of a gypsum plasterboard production facility located in Batman, Türkiye. The life cycle analysis approach was utilised in this study and the 'gate to gate' approach was adopted as the system boundary. The main objective of this study is to calculate the energy consumed in the production of plasterboard from the entrance to the exit. Another objective is to analyse the energy-intensive stages of the production process and investigate the factors that contribute to energy consumption. It is essential to conduct energy analyses of this extensively used material in the construction industry for sustainable and energy-efficient

production.

II. Materials and Method

The gypsum plasterboard manufacturing plant has been established on a 20 000 m^2 area in the province of Batman, Türkiye. It has an annual production capacity of 8 812 800 m^2. At this production facility, four types of plasterboard are manufactured according to the demands of the market: standard gypsum plasterboard, water-resistant gypsum plasterboard, fire-resistant gypsum plasterboard, and both of fire- and water-resistant plasterboard.

The manufacture of plasterboard follows a set of stages, beginning with the production of gypsum in the same company's gypsum production facility. Gypsum is conveyed to the silo at the plasterboard plant for further processing using a blower-assisted conveying system. Initially, the lower paper is introduced into the system. Subsequently, a blend of gypsum, water, foam agent and chemical additives, better known as 'stucco', is poured onto the lower paper. After this stage, air bubbles are reduced through the use of air spraying and vibration techniques. The bottom sheet is folded, and adhesive is applied where the top sheet will be positioned. Afterwards, the top layer is placed, and the gypsum mixture is compressed between the two sheets thus determining the fineness of the product. The product is then conveyed through an 80-meter-long freezing conveyor and subjected to its initial freezing stage. Subsequently, it is cut to the desired dimensions at the shearing stage. Typically, the produced dimensions are a thickness of 11.5 mm, a width of 1.2 m and a length of 2.5 m. After cutting, the product is turned upside down to avoid damaging the application surface in the oven, and then placed in the dryer. The dryer consists of 8 floors, each 66 m long, and each floor holds 2 gypsum boards. The speed of the board in the dryer is 1.0625 m/s and the board remains in the dryer for approximately 70 minutes. The dryer is composed of two parts having air flows in opposite directions. The first part has an average temperature of 115 degrees and the second part has an average temperature of 130 degrees. After drying process, one product is flipped with flipper while the other remains untouched. This process shields the product from external factors by packaging the two inner surfaces together. The burnt portions of the product are then shaved away to achieve smooth edges. After trimming, the product is packaged and then the wallboard is stored.

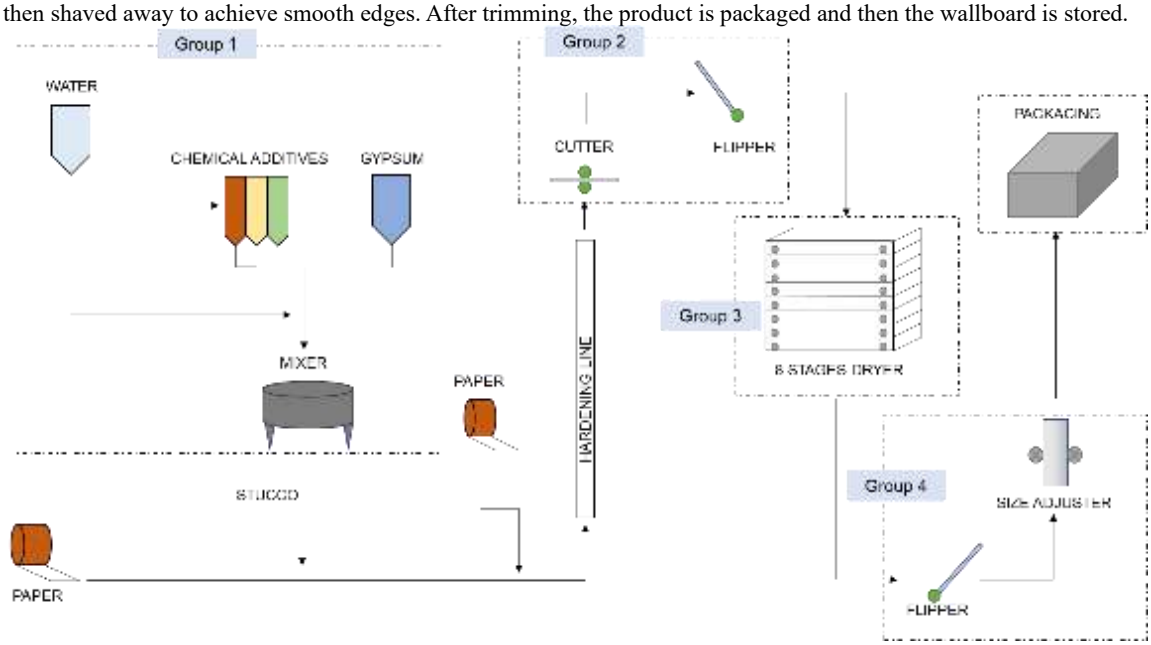

Fig. 1. Manufacturing process of gypsum plasterboard

The primary inputs for gypsum plasterboard production are gypsum, paper, water, chemical additives such as setting accelerator additive, foaming agent, plasticising fibre, paper glue, natural gas for the kiln and electricity for the whole plant. The main product of this process is gypsum plasterboard, with the waste from gypsum board production due to the interruptions that occur in various parts of the board production process. Several controls are carried out during production to ensure the quality of the final product. These controls include checking the density and even spreading of the plaster, freezing prior to shearing, and assessing the weight, flexibility, and humidty of the plate upon exiting the oven. Additionally, the paper adhesion and strength are checked at the end of production.

III. Results

The production amount, electricity and natural gas used for this study were taken directly from the production plant. The study considers the gate-to-gate approach of plasterboard, excluding production stages such as gypsum crushing, transportation and calcination, as well as off-site energy consumption such as the amount of energy required to produce paper. The analysis focused on the first nine months of the year 2023. The facility produces an average of 570,000 m^2 of gypsum board per month, with an average monthly electricity consumption of 260 MWh and an average monthly natural gas consumption of 230,700 m^3. The amount of energy footprint per square meter of plaster board is obtained by dividing the energy of overall monthly natural gas and electricity consumption to the total quantity of product produced. Figure 2 illustrates the monthly consumption of electricity and natural gas per square metre.

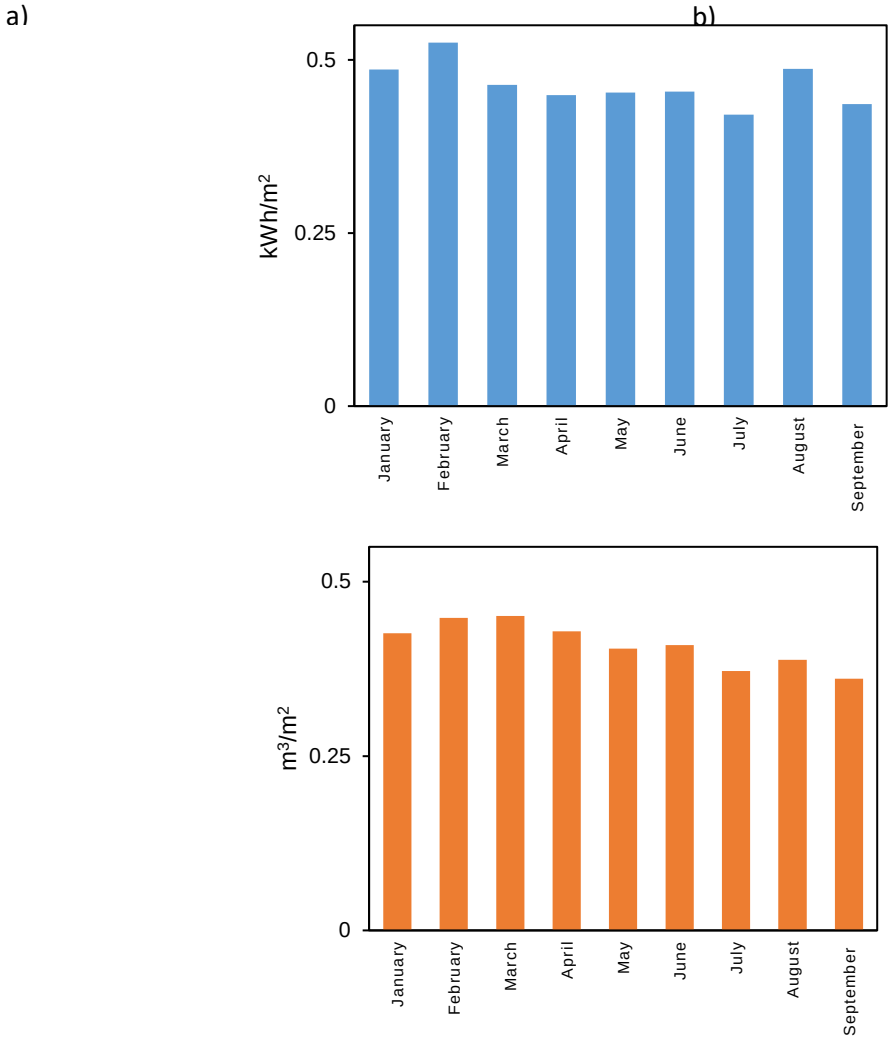

Fig. 2. a) Monthly electric (kWh/m^2) and b) Natural gas (m^3/m^2) consumption of one square metre of plasterboard

To analyze the electricity usage of plasterboard production, the machines involved in the process were categorized into five groups and their energy consumption was measured. These groups are shown in Figure 1. The production line comprises five groups of machinery. The first group is combination of the mixer, raw material transmission screws and conveyor belt. The second group consists of the cutter and flipper, the third group features the elevator that carries the product to different floors of the dryer and the transport rolls inside the dryer. The fourth group consists of the flipper and size adjuster machine for product exiting the dryer, while the fifth group handles stacking and packaging machine. The plasterboard roll transport system is responsible for the remaining electricity usage, as it conveys the plate through the system to enable its progress.

Figure 4 presents the electricity consumption across the examined groups. The highest electricity consumption in group 3 is in the drying system, while the lowest electricity consumption is in the packaging process, in group 5.

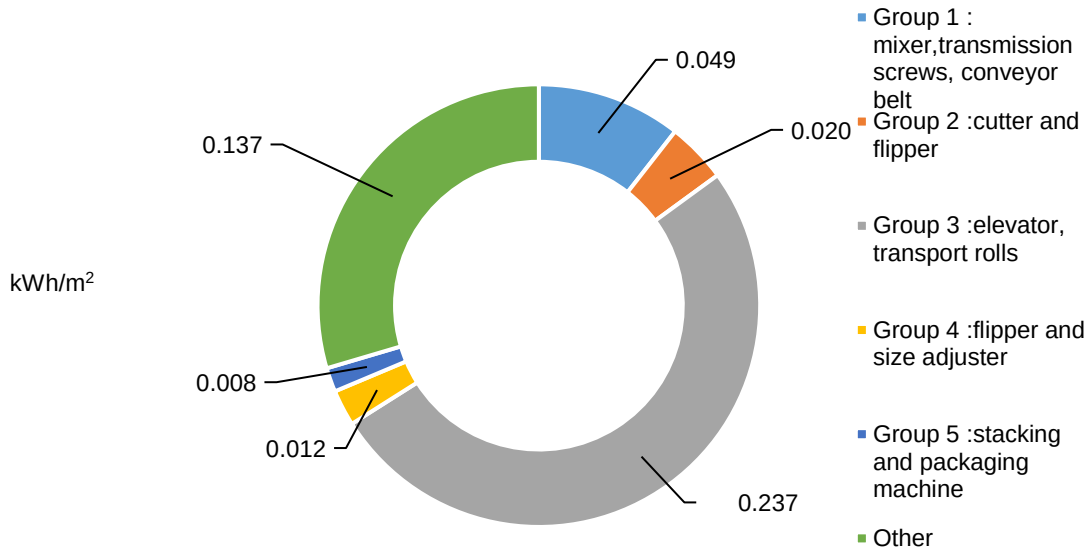

Fig. 3. Average electric consumption of group process (kWh/m^2)

According to results, the unit EF of plasterboard is found to be 17.36 MJ/m^2. This means that, to manufacture 1 m^2 of plaster board, 17.36 MJ or 4.82 kWh of energy is used in the specific study area. It was observed that the drying process has the largest EF among all processes. Natural gas and electricity consumption during the drying process surpassed that of other processes. Monthly EF of 1 m^2 of gypsum plasterboard shown in Fig.3.

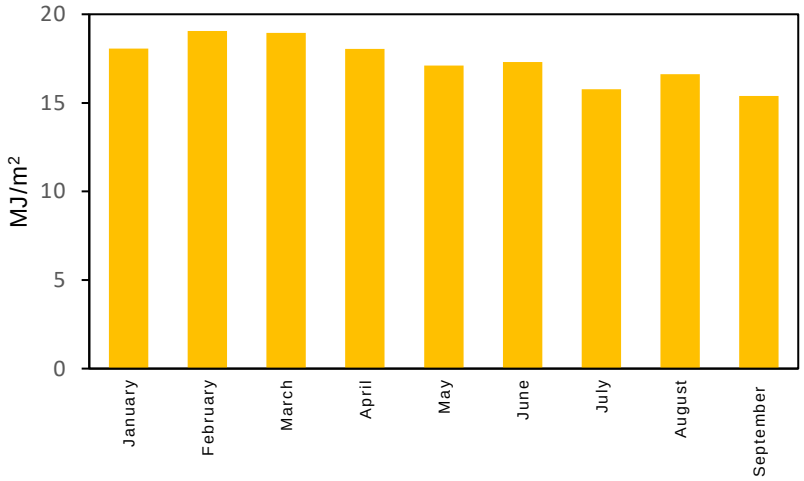

Fig. 4. Energy Footprint (MJ/m^2) of gypsum plasterboard obtained in this study

V. Conclusion

In this study, the energy footprint of plasterboard manufactured at a production facility located in Batman is calculated using a gate-to-gate approach. The energy footprint calculation of plasterboard, a widely-used construction material, makes a significant contribution to sustainable production. The production processes of gypsum plasterboards are presented, and energy utilization data have been gathered from the factory. There are two main energy uses: the oven that is powered by natural gas and the electricity that is required to run the system. The study shows that 1 m^2 of plasterboard has an EF of 17.36 MJ and 4,82 kWh. The drying process was identified as the process with the highest EF with the EF of 4,597 kWh. To decrease the EF of plasterboard, the primary attention should be on the drying process. Factors that influence the consumption of natural gas in the dryer are seasonal fluctuations, raw material impurities and raw materials grain size, as well as the amount of water used in the stucco. Efforts must be made to diminish the usage of natural gas in the furnace by addressing these factors. Improving the dryer's insulation could reduce energy usage by minimizing energy losses.

Acknowledgements
This study is carried out as a parto of the M.Sc. thesis in Civil Engineering by Z. Sakınç under the supervision of Dr. A. Muratoglu and Dr. MI Yuce.

References

de Brito, J., & Flores-Colen, I. (2015). Gypsum Plasters. In *Materials for Construction and Civil Engineering: Science, Processing, and Design* (pp. 123–184).

Gartner, E. M. (2009). Cohesion and expansion in polycrystalline solids formed by hydration reactions — The case of gypsum plasters. *Cement and Concrete Research*, *39*(4), 289–295. https://doi.org/10.1016/J.CEMCONRES.2009.01.008

Global Footprint Network. (2009). *www.footprintnetwork.org*.

IEA. (2021). *Türkiye 2021 - Energy Policy Review*. www.iea.org/t&c/

Karni, J., & Karni, Y. (1995). Gypsum in construction: origin and properties. In *Materials and Structures* (Vol. 28).

Kaygusuz, K., Toklu, E., & Avci, A. C. (2015). *Energy security in a developing world: a case of Türkiye*. www.journaleras.com

Loh, Jonathan., World Wildlife Fund., United Nations Environment Programme., & World Conservation Monitoring Centre. (2002). *Living planet report: 2002*. WWF International.

Revuelta, M. B. (2021). Gypsum Products. In *Construction Materials: Geology, Production and Applications* (pp. 195–215). Springer International Publishing. https://doi.org/10.1007/978-3-030-65207-4_8

Tian, X., Chen, B., Geng, Y., Zhong, S., Gao, C., Wilson, J., Cui, X., & Dou, Y. (2019). Energy footprint pathways of China. *Energy*, *180*, 330–340. https://doi.org/10.1016/j.energy.2019.05.103

IEEES-066

An Assessment of A Novel Hybrid Photoelectrochemical-Conventional Hydrogen Generator

[1*] Mehmet Gursoy, [2]Ibrahim Dincer.
[1,2]Clean Energy Research Laboratory (CERL), FEAS, Ontario Tech University, Oshawa, Ontario, L1H 7K4, Canada
*E-mails: mehmet.gursoy@ontariotechu.net, Ibrahim.Dincer@ontariotechu.ca

Abstract

The increasing worldwide need for environmentally friendly and renewable energy sources has prompted much scholarly investigation in the realm of hydrogen generation. Hydrogen, renowned for its multifunctionality and ecological compatibility, has the potential to emerge as a pivotal participant in the paradigm shift towards a more sustainable energy landscape. The hybrid photoelectrochemical (PEC)-conventional hydrogen generator has emerged as a promising technology that has garnered significant interest in recent years. This novel methodology integrates the advantages of PEC water splitting with traditional hydrogen production techniques, offering potential solutions to the obstacles encountered by both technologies. The thermodynamic assessment is utilized to evaluate the efficiency of the generator being studied. Furthermore, the research explores the influence of crucial process indicators on the energetic and exergetic performance of the hybrid reactor. The initial test inquiries produced results suggesting that increasing the applied voltage from 2.5 V to 3.5 V increased the total hydrogen production rate by 32%.

Keywords: Solar energy, hybrid hydrogen generator, energy, exergy, efficiency.

1. Introduction

Hydrogen has the potential to play a crucial role in enabling the transition towards an era defined by the absence of carbon emissions. The projected ramifications of climate change stemming from the substantial dependence on fossil fuels for energy production are expected to escalate soon.

The hybrid PEC-conventional hydrogen generator integrates the benefits of PEC water splitting with conventional electrolysis, therefore offering a cutting-edge approach to hydrogen production. The photovoltaic process in the PEC water splitting facilitates the conversion of water into hydrogen and oxygen by an electrochemical mechanism, which is driven by solar radiation. However, it is prone to corrosion and has a low-efficiency rate. In contrast, conventional electrolysis is efficacious, but it relies on grid electricity, often derived from nonrenewable sources. The limitations are effectively addressed by the synergistic integration of PEC cells with conventional electrolysis, resulting in a novel hybrid technology. This enables the efficient production of hydrogen only from renewable energy sources. The internal mechanisms of this hybrid system are mentioned in this study. The main aim of the research conducted by (Acar and Dincer, 2018) is to carry out a thorough examination of a continuous-type hybrid photoelectrochemical system for the generation of hydrogen. The primary objective of this hybrid system is to enhance the efficiency of solar spectrum utilization via integrating photocatalysis with a photovoltaic/thermal (PV/T) system. By combining a PEC and a photo fuel cell (PFC) in a hybrid system, (Liu et al. 2017) investigated the practicability and efficiency of producing hydrogen from solar light and the decomposition of organic substances. This was accomplished by linking the two technologies together in the research. The photoanode of the PEC cell was made of TiO_2 nanorod arrays, while the cathode was made of platinum.

2. System Description

Figure 1 illustrates the hybrid PEC-conventional reactor. Two distinct kinds of electrolysis cells, namely the PEC and conventional cells, are present inside the reactor. The three main components of the PEC consist of an anode, a cation exchange membrane (CEM), and a photocathode. The anode garners significant attention because of its common presence in both cells. Sodium chloride (NaCl), distilled water, and potassium hydroxide (KOH) are the three distinct electrolytes used.

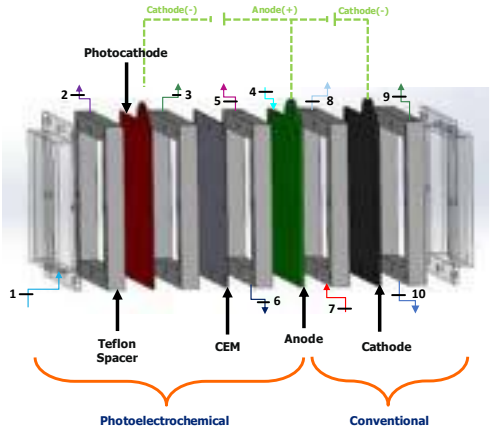

Fig. 1: The newly developed hybrid PEC-conventional reactor

Furthermore, the primary role of the membrane is to minimize the occurrence of hydroxide ions (OH^-) in the cathode compartment by the selective promotion of sodium ions (Na^+) migration from the anode to the cathode partition. The reactor is equipped with transparent windows to facilitate the irradiation of the photocathode.

3. Analysis

The EES (Engineering Equation Solver) was used to calculate the projected system's energy and exergy requirements. High-efficiency hydrogen generation is the primary emphasis of this study, which takes a design-centric approach. The following equations are used to describe the chemical reactions occurring during hydrogen production in a hybrid electrolyzer:

For the PEC cell:

$$\text{Overall reaction} = 2H_2O + 2NaCl \rightarrow H_2 + Cl_2 + 2NaOH \quad (1)$$

$$\text{Anode} = 2Cl^- \rightarrow Cl_2 + 2e^- \quad (2)$$

$$\text{cathode} = 2H_2O + 2e^- \rightarrow H_2 + 2OH^- \quad (3)$$

e conventional cell:

$$\text{ll reaction} = 2H_2O \rightarrow 2H_2 + O_2 \quad (4)$$

$$\text{Anode} = 2H_2O \rightarrow O_2 + 4OH^-_{aq} + 4e^- \quad (5)$$

$$\text{de} = 4OH^-_{aq} + 4e^- \rightarrow 2H_2 + 2H_2O \quad (6)$$

Each state point within the reactor is accompanied by a fluid description and mass flow rate, both of which are detailed in Table 1.

Table 1. Fluids descriptions and mass flow rates of each state point in the reactor.

Point	n	flow rate (kg/s)
	water inlet	$\dot{m}_1$
	l solution	$\dot{m}_2$
	s	$\dot{m}_3$
	ated NaCl solution	$\dot{m}_4$
	s	$\dot{m}_5$
	ished NaCl solution	$\dot{m}_6$
	solution	$\dot{m}_7$
	s	$\dot{m}_8$
	s	$\dot{m}_9$
	ished KOH solution	$\dot{m}_{10}$

To determine how efficient the proposed system is in terms of energy and exergy, the mass, energy, entropy, and exergy balance equations (BE) are expressed as follows:

BE: $\dot{m}_1 + \dot{m}_4 + \dot{m}_7 = \dot{m}_2 + \dot{m}_3 + \dot{m}_5 + \dot{m}_6 + \dot{m}_8 + \dot{m}_9 + \dot{m}_{10}$

y BE: $\dot{m}_1 h_1 + \dot{m}_4 h_4 + \dot{m}_7 h_7 + \dot{W}_{in} = \dot{m}_2 h_2 + \dot{m}_3 h_3 + \dot{m}_5 h_5 + \dot{m}_6 h_6 + \dot{m}_8 h_8 + \dot{m}_9 h_9 + \dot{m}_{10} h_{10}$

y BE: $\dot{S}_{gen} + \dot{m}_1 s_1 + \dot{m}_4 s_4 + \dot{m}_7 s_7 = \dot{m}_2 s_2 + \dot{m}_3 s_3 + \dot{m}_5 s_5 + \dot{m}_6 s_6 + \dot{m}_8 s_8 + \dot{m}_9 s_9 + \dot{m}_{10} s_{10}$

y BE: $\dot{W}_{in} + \dot{m}_1\, ex_1 + \dot{m}_4\, ex_4 + \dot{m}_7\, ex_7 = \dot{m}_2 ex_2 + \dot{m}_3 ex_3 + \dot{m}_5\, ex_5 + \dot{m}_6\, ex_6 + \dot{m}_8\, ex_8 + \dot{m}_9\, ex_9 + \dot{m}_{10}\, ex_{10} + \dot{E}x_D$

In the given state points, the mass flow rates (kg/s), specific enthalpies (kJ/kg), entropies (kJ/kg.K), and exergies (kJ/kg) of the corresponding fluids are denoted by the variables $\dot{m}_{1\text{-}10}$, $h_{1\text{-}10}$, $s_{1\text{-}10}$, and $ex_{1\text{-}10}$, respectively. $\dot{W}_{in}$ is the total amount of input work performed by the reactor. $\dot{S}_{gen}$ represents the entropy generated by the system. The following equations may be employed to calculate the system's energy and exergy efficiency.

$$\eta_{overall} = \frac{\dot{m}_3 LHV_{H_2} + \dot{m}_9 LHV_{H_2}}{\dot{W}_{in} + \dot{m}_1 h_1 + \dot{m}_4 h_4 + \dot{m}_7 h_7}$$

$$_I = \frac{\dot{m}_3 LHV_{H_2} + \dot{m}_9 LHV_{H_2}}{\dot{W}_{in} + ex_1 h_1 + ex_4 h_4 + ex_7 h_7}$$

4. Results and discussion

The first stages of the tests were conducted using the devised experimental configuration shown in Figure 1. The investigation included monitoring the hydrogen production rate of individual electrolysis cells and the overall reactor while the applied voltage was varied. The length of the testing session for each participant was established at one hour. The first experiments were conducted without both sun illumination and applying a photocathode coating. The objective of these experiments was to examine the impact of various potentials on the hydrogen generation rate. The rate of hydrogen synthesis is exclusively determined by the electrical energy input into the cell in the absence of solar radiation. Figure 2 depicts the impact of different potentials on the rate of hydrogen production in the absence of solar light. Upon observing Figure 2, a discernible association between the applied voltage and the overall hydrogen generation rates becomes apparent. In particular, the increase of the applied voltage from 2.5 V to 3.5 V is accompanied by a proportional enhancement in the cumulative hydrogen generation rates, up to a 32% rise. The main factor influencing these phenomena is the rising conductivities of the components.

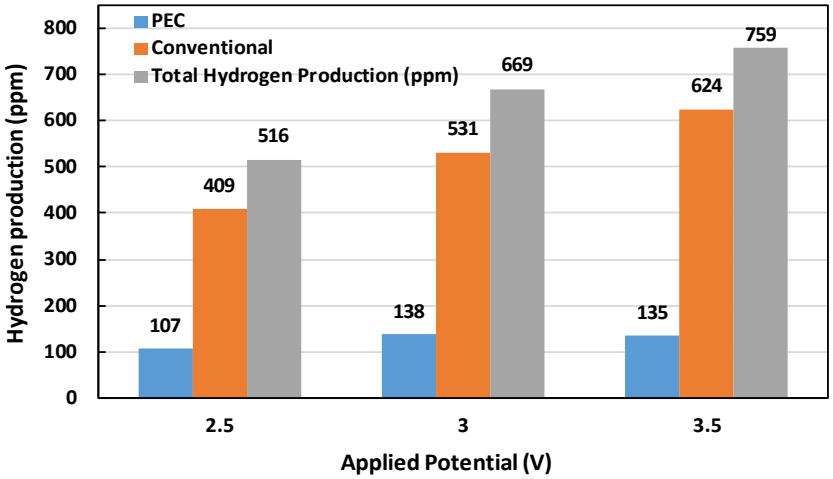

Fig. 2. How the rate at which hydrogen is produced by both cells in the absence of solar radiation changes as a function of the applied voltage.

5. Conclusions

The examination of Figure 2 demonstrates a distinct and significant correlation between the applied voltage and the collective hydrogen production rates. Significantly, an increase in the applied voltage from 2.5 V to 3.5 V results in a proportional augmentation in the cumulative hydrogen production rates, exhibiting a rise of up to 32%. The observed behaviour may primarily be ascribed to the increasing conductivities of the components within the system. The findings given in this study underscore the significant influence of voltage on the efficiency of hydrogen production. The increased applied voltage results in heightened conductivity of the components, facilitating more efficient hydrogen synthesis. This has notable implications for various applications, including fuel cells and electrolysis processes. The results highlight the significance of controlling the applied voltage to get the necessary hydrogen production rates. Additionally, these findings provide useful insights that may inform the design and operation of hydrogen-generating systems.

Acknowledgements

We would like to extend our deepest gratitude to all individuals and organizations, including the Clean Energy Research Laboratory (CERL) and Clean Energy Research Institute (TEMEN), as well as the Turkish Energy, Nuclear and Mineral Research Agency (TENMAK), for their valuable contributions that greatly facilitated the successful culmination of this research endeavor.

References

Acar, Canan, and Ibrahim Dincer., (2018). "Energetic and Exergetic Investigations of an Innovative Light-Based Hydrogen Production Reactor." *International Journal of Hydrogen Energy* 43 (22): 10249–57. https://doi.org/10.1016/j.ijhydene.2017.08.117.

Liu, Xiao-He, Fan Du, Qing-Yun Chen, and Yun-Hai Wang., (2017). "An Effective Self-Driven PFC-PEC Hybrid System for Hydrogen Generation from Organic Substance." *Electrochimica Acta* 245 (August): 379–85. https://doi.org/10.1016/j.electacta.2017.05.163.

IEEES-067

Design and Implementation of Lighting and Household Loads Monitoring System based on Power Line Carrier Communication

[1]Fathia Chekired, [1]Ali Laldji, [2]Imed Eddine Drioueche, [2]Younes Nezzari, [1]Fethi. Akel, [1]Aissa Meflah, [2]Slimane Kerrouchi, [3]Laurent Canale
[*1]Unité de Développement des équipements Solaires UDES/EPST CDER, Tipaza 42415, Algeria
[2]Département du Génie Industriel et Maintenance Ecole Nationale Supérieure des Technologies Avancées, Alger.
[3]CNRS, LAPLACE UMR 5213, 31000 Toulouse, France
*E-mails : f.chekired@udes.dz

Abstract

Based on proven and robust technology (Power Line Communication system), we have developed and tested in a real demonstrator a home automation control solution applied to smart lighting and appliances remote control. This technological solution is robust, reliable, economical and perfectly suited to developing countries. The design of power Line carrier communication system based on FSK-KQ330 module has two main advantages: a simple hardware circuit, which makes the module easy to design, manufacture, and maintain. In addition, a low cost, which makes the module affordable for a wide range of applications. The results obtained in real conditions made it possible to prove the feasibility and effectiveness of this remote control device for lighting and household appliances.

Keywords: Power Line Communication, Home automation, FSK-KQ330.

I.Introduction

Home automation is an active field that aims to improve comfort, security and energy efficiency. Among the many communication technologies used in home automation, power line communication (PLC) wich has become a popular solution due to its ease of installation and ability to use existing power lines as a communication medium (Wenhui Xiao et al, 2020), (QUN Yin and Zhang Jianbo, 2014). This technology can use the household electrical power wiring as a transmission medium. It is emplyed in home automation for lighting remote control, household appliances control, alarm systems… etc without any additional wiring installation (Yousuf and El-Shafei,2007), (Jean Paul et Al, 2020) . It is deployed also for various tasks including monitoring, telemetry, tele-protection and speech (Ambasta and Gupta, 2019), (Abdulsalam, 2023). Power line communication is the exchange of information over power lines. This method reduces deployment time and operating costs by avoiding the need for new cables or additional equipment has been preferred to provide low-cost and reliable communication links as power-lines have been deployed widely (Angie et Al, 2021),
This work presents the design and implementation of a domestic appliance control system (including lighting) based on PLC technology. The ultimate objective is to validate the viability and evaluate the effectiveness of the low-cost PLC system developed in data transfer using power lines, as the only communication link, for smart homes intended for developing countries.
The rest of the paper is organized as follows: Section II presents experimental system description. The case study is described in Section III. The results found are discussed in Section 4. Section 5 presents somes conclusions and recommandations.

II. Experimental System Description

The proposed system remotely controls different types of household loads as presented in Figure 01. The design of power line communication system can be divided into data transmission and data reception according to the data flow (Gowsalya et al, 2015). In the transmitter, the control device sends control data via Bluetooth to the microcontroller (Arduino), which transmits the data to the transmitter (PLC modem). The PLC module is based on an FSK-KQ330 (Carrier Modulation and Demodulation Module) (Ambasta and y Gupta, 2019), which will convert digital data into an analog form so that it can be sent over a power line. In the receiver, the FSK-KQ330 module receives and demodulates the transmitted signal and sends it back to the microcontroller via serial ports. Depending on the received commands, the microcontroller activates or deactivates the relays to monitor the connected household loads.

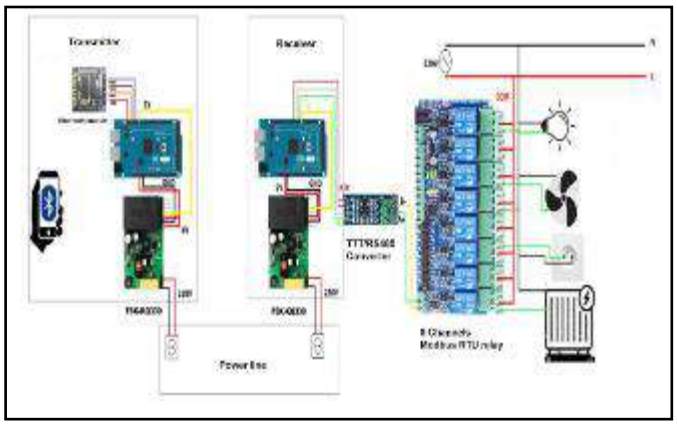

Fig. 1 Overview of the designed PLC system

III Case study

The installed dwelling of this case study is located in Solar Equipment Development Unit (UDES) in the town of Bou–Ismaïl (Latitude: 36°38′33.43″ North; Longitude: 2°41′24.25″ East), Algeria, and its area is 57 m^2. [19,20]. Figure 1 describes the UDES' solar house (Chekired et al 2022), (Meflah et al 2023) .

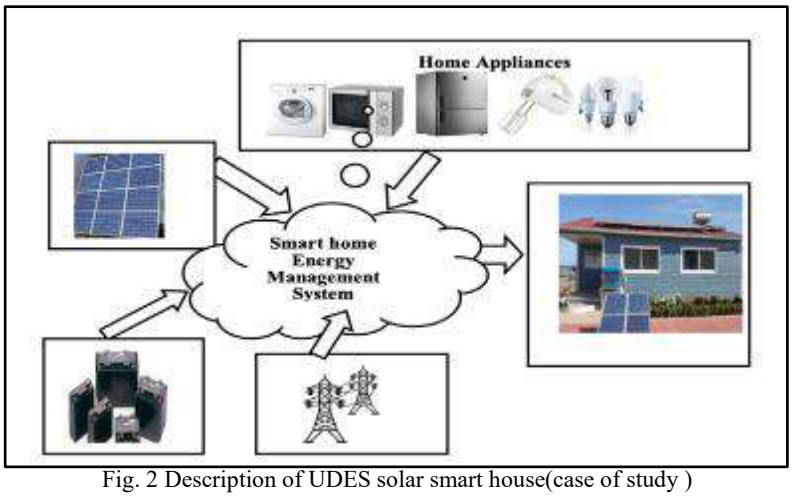

Fig. 2 Description of UDES solar smart house(case of study)

IV. Results and discussion

Simulations and experimental tests are carried out to evaluate the feasibility and effectiveness of the designed PLC system for data transfer across power lines. Fig. 3 shows the experimental setup of data transmission through the PLC system.

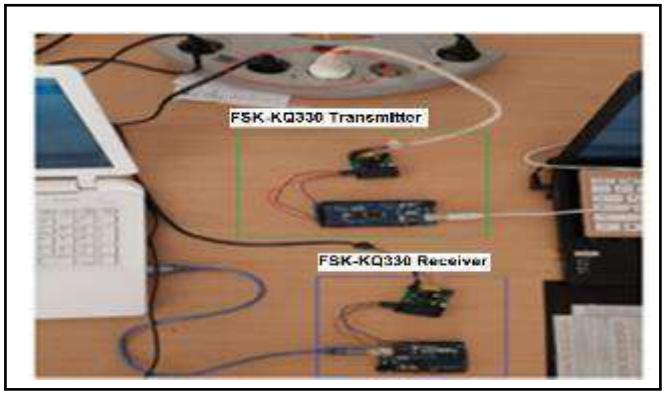

Fig. 3. Data transmission through PLC

TTL (Transistor-Transistor Logic) Digital signal coming out of the microcontroller square wave has a frequency of 4.807 KHZ and an amplitude of 5v) is modulated by the FSK modulator (Transmitter) to an analog signal (frequency of 131 kHz, amplitude of 5V (Figure 4) which will subsequently be coupled with the power line. At the other end, the FSK demodulator ((Receiver) picks up a sinusoidal signal (234 V, 50 Hz) and feeds it to the signal decoder, there the decoding takes place and data issent to the Micro controller (Figure 5). Finally, according to the received commands, the Microcontroller turns-on or off the relays the relays to manage the connected household loads.

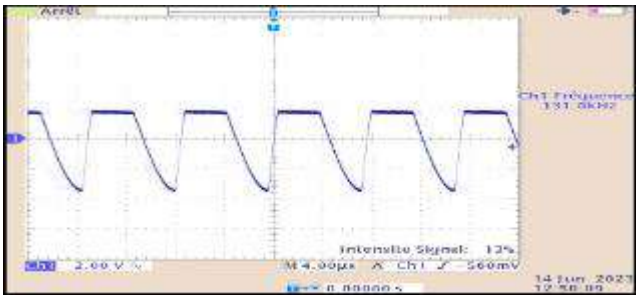

Fig. 4. Modulated Signal by the FSK-KQ330 -PLC Modulator (Transmitter)

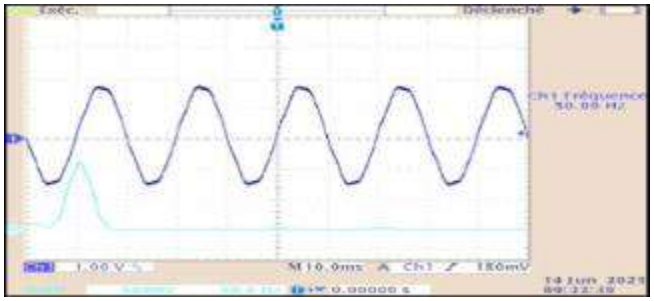

Fig. 5. Demodulated Signal by the FSK-KQ330 PLC Modem (Receiver)

To evaluate the effectiveness and viability of the developed PLC system, real-time tests are carried out by integrating it in a prototype of a low consumption smart hom. Figure 6 shows the control of lighting and some household appliances using the PLC system. The home automation system based on PLC technology is implemented in the smart home (the case study). The system consists of two parts: a transmitter and a receiver.The transmitter consists of a master microcontroller, which is connected to a mobile application via Bluetooth. It is located inside the house and is plugged into the power line. Its main role is to send commands to the "receiver" part using the power line that connects the two parts. The "receiver" part of the system is made up of a slave microcontroller, depending on the commands it receives, it activates or deactivates the relays in order to control the household appliances according to specific needs. The system is installed in the control room where the electrical cabinet containing all the household appliances is located. This receiving part is also connected to power line of the house. Its role is to receive commands and information from the transmitter, then transmit them to the corresponding household appliances.

Fig. 6. Lighting and loads monitoring based on PLC system

Acknowledgements
This research was funded by Directorate General for Scientific Research and Technological Development DGRST / Ministry of Higher Education & Scientific Research, Algeria.

V. Conclusion

The present study highlights the importance of communication technologies in the smart home operation, promoting connectivity and the information exchange between household appliances in the home network. Among these technologies, power line communication (PLC) system is proposed and realised, revealing its distinct advantages over other communication methods. The feasibility and reliability of this technology is verified through simulations and experimental tests in the laboratory and then the implementation of the realised PLC system into a real house. The PLC system remotely controls various household appliances, including peripheral lighting in the studied house. This integration opens new perspectives for remote control and centralized management of connected devices.

The design of power Line carrier communication system based on FSK-KQ330 module has two main advantages: a simple hardware circuit, which makes the module easy to design, manufacture, and maintain. In addition, a low cost, which makes the module affordable for a wide range of applications. The design can provide reliable guarantee for data communication based on chip microcontroller. For a better and effective applications, it is recommended to install PLC-based control systems in locations where the distance between the transmitter and the receivers is large.

References

Abdulsalam K. A., John Adebisi, Michael Emezirinwune, Olubayo Babatunde, An overview and multicriteria analysis of communication technologies for smart grid applications, e-Prime - Advances in Electrical Engineering, Electronics and Energy, Volume 3,2023, 100121, ISSN 2772-6711, https://doi.org/10.1016/j.prime.2023.100121.

Ambasta, A., Gupta, V. (2019). Load Monitoring using Power Line Carrier Communication (PLCC) Systems, IJSRD International Journal for Scientific Research & Development| Volume 7(5).

Angie A.G. Liong, Filbert H. Juwono, Lenin Gopal, Choo W.R. Chiong, Yue Rong, Multiple blanking preprocessors for impulsive noise mitigation in OFDM-based power-line communication systems, International Journal of Electrical Power & Energy Systems, Volume 130,2021, 106911, ISSN 0142-0615, https://doi.org/10.1016/j.ijepes.2021.106911.

Chekired, F., Oussama,T., Khellili, Z., Tilmatine, A., T. de Almeida, A., Canale, L . (2022). NearZero-Energy Building Management Based on Arduino Microcontroller—On-Site Lighting Management Application" Energies 15, no. 23:9064. https://doi.org/10.3390/en1523906.

Gowsalya, M., Barathi , Selvaraj M., Murthy2 S. E,Yadhiri, K.(2015).Design and Analysis of a PLCC Based Home Automation System. International Journal of Science, Technology and Society; Volume 3(2), pp. 36-39.

Jean Paul A. Yaacoub, Javier Hernandez Fernandez, Hassan N. Noura, Ali Chehab, Security of Power Line Communication systems: Issues, limitations and existing solutions, Computer Science Review, Volume 39, 2021, 100331, ISSN 1574-0137, https://doi.org/10.1016/j.cosrev.2020.100331.

Meflah A .,. Chekired F.,. Akel F., and Bouhouche Y., "Indoor Lighting Study: case of UDES' Solar Smart House Bou-Ismail-Algeria", *J. Ren. Energies*, vol. 1, no. 1, pp. 103 -, Sep. 2023.

Xiao,W Bo,L and Kaur. R(2020). Design of led lighting system based on power line communication. 5th International Conference on Computer and Communication Systems (ICCCS), pages 835–839. IEEE.

Yin, Q, . Zhang, Z. (2014). Design of power line carrier communication system based on fsk-kq330 module. Electrotehnica, Electronica, Automatica, 62(3).

Yousuf M. S. and El-Shafei M., "Power Line Communications: An Overview - Part I," *2007 Innovations in Information Technologies (IIT)*, Dubai, United Arab Emirates, 2007, pp. 218-222, doi10.1109/IIT.2007.4430363

IEEES-068

A Novel Approach for Estimating Chemical Exergy Values of Biomass Mixtures Using Artificial Neural Networks

*Dogan Erdemir and Ibrahim Dincer
Ontario Tech University, Clean Energy Research Laboratory, Oshawa, Ontario, Canada
Yildiz Technical University, Department of Mechanical Engineering, Istanbul, Turkey
*E-mails: dogan.erdemir@ontariotechu.net

Abstract

This study presents a new technique based on the artificial neural network (ANN) for predicting thermodynamic properties of biomass sources such as higher heating value and chemical exergy content. An ANN model has been developed based on 86 different biomass sources. The elemental content of the biomasses is used as the inputs and the higher heating value, lower heating value and chemical exergy are considered as the output. Different training algorithms are tested for better modelling. Along with input and output layers, one hidden layer is used with the rectified linear unit transfer function. The model developed has reached a higher accuracy in estimating the output values with R^2=0. 99586. For the overall evaluation of biomass sources, the exergy factor for biomass sources is found to be 1.047. In other words, multiplying the higher heating value of any biomass sources or mixtures by 1.047 will give the chemical exergy content of the source.

Keywords: Biomass, biomass mixture, energy, chemical exergy, lower heating value, higher heating value, gross calorific value, net calorific value.

I. Introduction

Biomass is a renewable and abundant source of energy that can be converted into various forms of useful products, such as fuels, chemicals, and electricity. The importance of biomass lies in its sustainability and versatility. Unlike fossil fuels, which are finite and contribute to climate change, biomass is renewable and has a lower carbon footprint. It can be continuously grown and harvested in a sustainable way, making it a reliable and environmentally friendly energy source. Moreover, biomass can be converted into different forms of energy to meet various needs, making it a versatile solution for our growing energy demands. Therefore, biomass plays a significant role in promoting sustainable development and combating climate change.

Among the different conversion pathways, direct combustion of biomass for power generation is one of the common methods. Gasification is a promising thermochemical process that involves the partial oxidation of biomass at high temperatures to produce a mixture of gases, mainly hydrogen, carbon monoxide, carbon dioxide, methane, and other hydrocarbons. This gas mixture, also known as syngas, can be further processed to obtain hydrogen or synthetic fuels via catalytic reactions.

Any applications of the biomass-based energy systems require thermodynamic analyses based on the first and second laws of thermodynamics like in all energy systems. Thermodynamics analysis based on the energy and exergy efficiencies is essential to assess the system performance and optimize it. The main issue in thermodynamic analysis of biomass sources energy is the variable elemental structure of biomass sources, which really affect thermodynamic properties. They vary depending on many conditions such as climatic conditions, storage technique, location, etc.

Higher heating value (HHV), lower heating value (LHW), chemical exergy are critical parameters for the biomasses. Therefore, many attempts have been made to determine them for biomasses with different input parameters and methods. One of the common techniques is the use elemental analysis of the biomass sources as input parameters and use some correlations to find the HHV, LHW and chemical exergy. This study develops an ANN model to predict the HHV and chemical exergy content of any biomasses by using elemental analysis of the biomasses as input parameter.

II. Methodology

In this work project, an Artificial Neural Network (ANN) model is developed by using MATLAB 2023a. The architecture of our ANN model is defined with three layers: an input layer, a hidden layer, and an output layer. Fig. 1 shows the illustration of the ANN model. The input layer consisted of 5 neurons, representing the 5 different elements in the biomass, which are C, H, O, N, and S. The hidden layer has 20 neurons and uses the ReLU (Rectified Linear Unit) activation function. The output layer has two neurons, as the HHV and chemical exergy of biomasses and their mixture are predicted. 86 different biomass sources which are listed by Song et al. (2011) are used for training, test and validation of the ANN model. While 70% of the total data is used for the training, the rest is equally shared for test and validation.

After defining the architecture, we initialized our network. MATLAB automatically initialized the weights and biases when we created the network using the back propagation algorithm. The train algorithm in MATLAB was used to adjust the weights and biases of our network based on our training data. After training, the model is validated by using a separate validation dataset to check its performance and ensure that the model developed is not overfitting. Also, the model is tested by using a test dataset to evaluate its performance on unseen data. Once the network is trained, validated, and tested, it can be used to make predictions on new data.

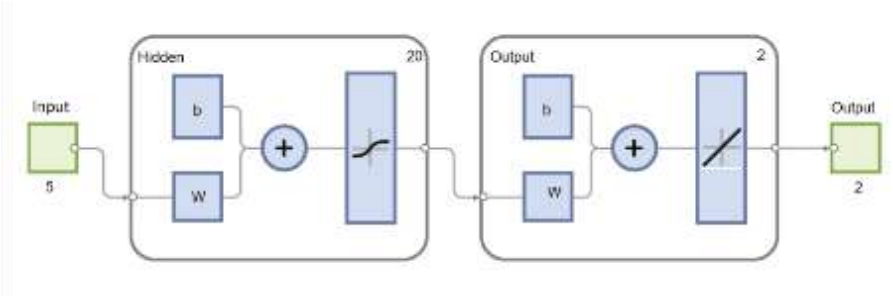

Fig. 1: Illustration of ANN model used.

III. Results and discussion

In this study, we implemented an Artificial Neural Network (ANN) model to predict the HHV and the chemical exergy content of the biomass sources and their mixture. The ANN is trained on a dataset of 86 different biomass sources. After rigorous training and validation, the model achieved an impressive accuracy of 96.4% on the test dataset. This result demonstrates the effectiveness of our ANN in capturing complex patterns in the thermochemical properties of biomass sources. Fig. 2 shows the performance of the ANN model developed. The training performance graph generated by MATLAB provides valuable insights into the performance of the model. The R^2 value, which represents the coefficient of determination, stands at approximately 0.99586. This value suggests that the ANN explains about 0.004% of the variance in the observed data, signifying a strong correlation between the model's predictions and the actual biomass properties. Table 1 also compares the actual and predicted HHV and chemical exergy values for five different biomass sources. It is clear from Table 1 that there is a good match between the actual and predicted values. Moreover, a sensitivity analysis has been conducted by perturbing the input features to assess the robustness of model. The ANN has demonstrated a resilient behavior, maintaining its accuracy within a 1% deviation even with significant input variations. This robustness is a crucial aspect, ensuring the reliability of the model in practical applications where input data may have some degree of uncertainty.

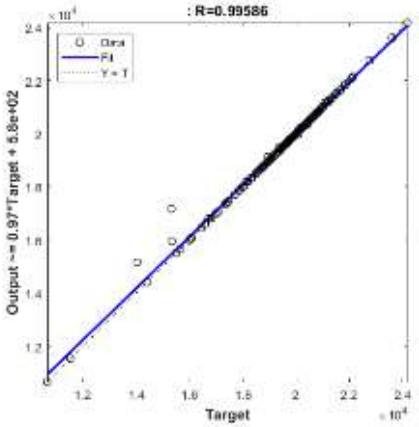

Fig. 2. The performance of the ANN model developed.

Table 1. Comparison of actual and predicted values for biomass sources

Biomass	Actual		Predicted	
	HV (kJ/kg)	Chemical exergy (kJ/kg)	HV (kJ/kg)	Chemical exergy (kJ/kg)
Alder-fir sawdust	19949	20891	19939	20885
Balsam bark	20597	21549	20600	21558
Wood yard waste	16073	16992	16073	16992
Sewage sludge	10665	11540	10665	11540
Pepper plant	14405	15659	14405	15659

IV. Conclusion

In this study, we have successfully developed an Artificial Neural Network (ANN) model to predict the Higher Heating Values (HHVs) and chemical exergy contents of various biomass sources and their mixtures, utilizing the elemental composition of the biomass as input parameters. Overall, our study has presented a robust ANN model that excels in predicting the HHV and chemical exergy content of biomass sources. The high accuracy, as evidenced by the R^2 value and the close alignment between predicted and actual values, emphasizes the model's effectiveness and its potential as a valuable tool in the field of biomass energy analysis and utilization. This work not only contributes to a better understanding of biomass properties but also underscores the significance of ANN-based approaches in addressing challenges related to renewable and sustainable energy sources.

References

Song, G., Shen, L., Xiao, J., (2011). Estimating Specific Chemical Exergy of Biomass from Basic Analysis Data, Industrial & Engineering Chemistry Research, 50(16), 9758-9766. https://doi.org/10.1021/ie200534n

IEEES-069

Capacity Potential and Cost Assessment for Hydrogen Production from Marine Sources

*G. Kubilay Karayel and Ibrahim Dincer
Clean Energy Research Laboratory, Faculty of Engineering and Applied Science, Ontario Tech. University, Ontario, Canada
*Corresponding author: gorkem.karayel@ontariotechu.net

Abstract

The present study comprehensively examines the application of wave, tidal, and undersea current energy sources of Turkiye for green hydrogen fuel production and cost analysis. The estimated potential capacity of each city is derived from official data and acceptable assumptions and is subject to discussion and evaluation in the context of a viable hydrogen economy. According to the findings, the potential for green hydrogen generation in Turkiye is projected to be 7.33 million tons. Cities with the highest hydrogen production capacities from marine applications are Mugla, Izmir, Antalya, and Canakkale with 998.10 kt, 840.31 kt, 605.46 kt, and 550.42 kt, respectively. From the calculations, surplus hydrogen production can be converted to an equivalent of 3.01 billion US $. The primary objective is to provide comprehensive hydrogen maps for each city in Turkiye, which will be based on the identified renewable energy potential and the utilization of electrolysers.

Keywords: Green hydrogen, wave energy, undersea current energy, cost analysis, electrolyser.

1. Introduction

Climate change mitigation and the execution of appropriate laws and regulations are badly needed to cope with international commitments and fulfill the targeted carbon-neutral future. On the closely connected energy front, the market has struggled and will continue to struggle to finance the shift away from fossil fuels and into the era of decarbonization. Human health and well-being have been impacted by the substantial rise in atmospheric quantities of anthropogenic carbon dioxide (CO_2) since the Industrial Revolution. These anthropological effects are inevitable, despite governmental denials and conventional fossil fuel lobbying attempts. This legislation will lead to the adoption of carbon-free fuels in several energy market segments, and hydrogen, which can be used as a feedstock, fuel, and energy carrier, is a crucial component for such a sustainable fuel. Sustainable energy has become a crucial topic for international competitiveness as well as a huge possibility for economic growth and employment creation.
The primary objective of this study is to propose an innovative approach for mapping hydrogen resources in Turkiye, specifically focusing on wave, tidal, and current sources. These sources will be thoroughly examined and assessed for their potential to produce green hydrogen and cost analysis will be done.

2. Methodology

The utilization of electrolysis as a prominent technology for the production of pure hydrogen through the process of water molecule splitting is rapidly gaining popularity. The process of water electrolysis relies on the transfer of electrons through an external circuit, which remains intact during the whole process. The electrolysers now offered for sale in the market encompass three main types: alkaline, solid oxide electrolysers (SOEL), and proton exchange membrane electrolysers (PEMEL). To facilitate the process of water splitting, it is necessary to apply a certain magnitude of direct current across two electrodes that are physically isolated from each other by an aqueous electrolyte exhibiting superior ionic conductivity. This assertion holds for all three electrolyser systems examined in the present investigation, as evidenced by the overall reaction as

$$H_2O(l)+\text{electrical energy} \rightarrow H_2(g)+1/2O_2(g) \quad (1)$$

Regarding produced and consumed electricity, there are a few assumptions considered in the calculations. First, the total electricity production of a renewable source is equal to the total sum of already existing power plants of that type and the theoretical potential of it. The second factor is the energy consumption of households, utilities, enterprises, and any other auxiliary consumers. Energy consumption data of the 81 cities in Turkiye are taken from the Energy Market Regulatory Authority (EPDK, 2022).
Turkiye is bordered by three seas, however, these seas lack the swift currents often found in oceans. Therefore, the velocity of submarine currents is exceedingly slow. The average velocity of underwater currents in cities ranges from 0.1 to 2.35 m/s. When it comes to offshore applications, the coastline of every city is taken into consideration. The coastal statistics for the relevant cities are considered, assuming a net width of 2 km. This strip, which comprises over 30% of the offshore area in most places, is designated as the transit corridors and private zones. The assumption is subject to modifications in accordance with international agreements and the available provisions. The Ministry of National Defence (MSB, 2022) supplies the data. The present study focuses on selecting selected strategic areas in Turkiye to calculate the underwater currents. Consequently, distinct areas have been selected from the Black Sea (Yılmaz, 2018), Hellespont (Yucel and Tarhan, 2019), the Mediterranean Sea, and the Bosporus (MGM, 2022). The calculations take into account two distinct types of subsea turbines, namely Forster and Atlantis, which are chosen for their significant variances in low cut-in speed.
The mechanical energy of a flowing fluid can be described as:

$$\dot{E}_{mech} = \dot{m}\left(\frac{P}{\rho}+\frac{V^2}{2}+gz\right) \quad (2)$$

If the current is flowing at a location at the velocity of V, with water density ρ, and A is the disk area of rotating blades of the turbine, power potential can be expressed as:

$$\dot{W}_{available} = \frac{1}{2}\rho A V^3 \quad (3)$$

Some main assumptions are made in the study as follows:

- The assumed sea depth for wave energy is 75 m, and the wave height is calculated from sea level.
- Typical wave energy harvesting Pelamis turbines have a capacity of 2.62 GWh/year (750 kW power output), a capacity factor of 0.40, and a length of approximately 150 m considered for wave energy applications.
- For tidal energy, tidal barrages are considered. Total tidal energy potential is the combination of currently installed tidal energy generators and theoretical potential.
- The average tidal range is chosen as 8.2 m. The Basin area for the tidal generator is considered 22 km².
- In the calculations for the undersea current, commercial undersea turbines were used. In order to circumvent the wake regions of subsequent turbines, they are separated by 20 m.

The electricity generated from maritime applications is initially utilized to meet the power requirements of the provinces. Subsequently, it is directed towards a PEM electrolyser in order to make green hydrogen.

3. Results and discussion

The potential for the production of green hydrogen in a Turkish city is estimated by taking into account a variety of different resources. These include wave, tidal, and underwater current resources. It is assumed that the city's whole need for electricity is satisfied by the power that is generated from renewable energy sources. After that, the electricity is fed through electrolysers and produces green hydrogen. Green hydrogen production of Turkiye from wave, tidal, and undersea current energies are tabulated in Table 1 with 7,323.11 kt, and 6.65 kt, respectively. Total green hydrogen production potential comes to 7,329.76 kt. Turkiye's 2022 electric consumption was 331.1 TWh (ETKB, 2023). The hydrogen equivalent of this value is 6.68 Mt. Not every city in Turkiye has access to marine or offshore applications however cities with access can produce enough hydrogen to cover whole countries' power demand from properly installed wave, tidal, and current power generators.

		gen from wave and tidal energies (kt)	gen from undersea current (kt)			gen from wave and tidal energies (kt)	gen from undersea current (kt)
	ı	4			a		
	man				ya		
	ı				ya		
					a		
	ya				raş		
	a				n		
	ya	1			ı	9	
	ı						
		5			hir		
	esir	7					
	k					4	
	l					3	
					ya		
					ın	5	
	r						
		5				0	
	kale	2					
	rı				dağ	4	
	n						
	li				on	1	
	bakır				li		
	e	5			rfa		
	can						
	ım				t		
	ehir				ldak	4	
	ntep				ay		
	ın	3			rt		
	şhane				han		
	ari				cale		
		0			ın		
	a						
	n	3				5	
	ul	6			an		
		5					
					a	5	
	monu	7			ük		
	ri						
	areli				niye		
	hir						

	li	3				11	

The unit energy gain (UEG) is determined by evaluating the possible excess hydroelectric energy generation. Once the power requirement is supplied, any surplus hydrogen generated is directed towards a fuel cell to generate electricity. In this scenario, a fuel cell with an efficiency of 65% that operates on a mixture of hydrogen and air is considered. Regarding the electricity load for consumers, the peak load for both industry and homes is selected at the highest possible rate to ensure a more accurate and practical approach. One kilogram of hydrogen necessitates 44 kWh of energy. The energy charge per unit is 0.173 $/kWh, as specified by the EPDK in 2023. According to the Central Bank of Turkiye (TCMB, 2023), the exchange rate between the US dollar and the Turkish lira is projected to be 1 to 28 for the purpose of this computation. The energy gain per unit kg of hydrogen is calculated by multiplying the energy consumption per unit kg of hydrogen by the per-unit energy charge rate (UECR):

$$\mathrm{UEG} = 44*\mathrm{UECR}[\frac{\mathrm{US\$}}{\mathrm{kgH_2}}] \quad (4)$$

From the calculations, surplus hydrogen production from marine applications in available cities can be converted to an equivalent of 3.01 billion US$.

4. Conclusion

Turkiye possesses a diverse array of renewable energy sources that may be used to mitigate its reliance on carbon-based fuels. The country's capacity for marine energy presents a significant opportunity for facilitating this transition. The findings of the current study indicate that the potential of wave, tidal, and underwater current energy sources hold promise for the generation of hydrogen and the development of a hydrogen-based economy in various regions of Turkiye. The statistics and data used in the calculations are taken from official Turkish Government resources. The main findings of the study are as follows:

- The potential for green hydrogen generation in Turkiye is projected to be 7.33 mt.
- Cities with the highest hydrogen production capacities from marine applications are Mugla, Izmir, Antalya, and Canakkale with 998.10 kt, 840.31 kt, 605.46 kt, and 550.42 kt, respectively.
- From the calculations, surplus hydrogen production can be converted to an equivalent of 3.01 billion US$.

References

Atlantis-AR1500 Undersea Turbine specification brochure, Accessed 28.10, 2023, from https://simecatlantis.com/wp-content/uploads/2016/08/AR1500-Brochure-Final-1.pdf

Central Bank of the Republic of Turkiye, Accessed 28.10, 2023, from https://www.tcmb.gov.tr/wps/wcm/connect/tr/tcmb+tr/main+page+site+area/bugun

Energy and Natural Resources Ministry, Accessed 28.10, 2023, from https://enerji.gov.tr/bilgi-merkezi-enerji-elektrik#:~:text=T%C3%BCrkiye%20elektrik%20enerjisi%20t%C3%BCketimi%202022,328%2C3%20TWh%20olarak%20ger%C3%A7ekle%C5%9Fmi%C5%9Ftir.

Forster GL-P-502-25 Undersea Turbine specification brochure, Accessed 28.10, 2023, from https://turkish.alibaba.com/product-detail/1-30m-water-head-tubular-turbine-generator-applied-for-tidal-power-station-60219023725.html?spm=a2700.galleryofferlist.normal_offer.d_title.36e43cd6g9bl8q

General Directorate of Meteorology, Accessed 28.10, 2023, from https://pirireis.mgm.gov.tr/swan/3

Ministry of National Defence, General Directorate of Mapping, Accessed 28.10, 2023, https://www.harita.gov.tr/urun/il-ve-ilce-yuzolcumleri/176

Republic of Turkiye Energy Market Regulatory Authority, Accessed 28.10, 2023, from https://www.epdk.gov.tr/Detay/Icerik/3-0-23/elektrikaylik-sektor-raporlar

Yılmaz, N. (2018). Samsun Körfezi kıyı sularında rüzgar iklimi, dalga iklimi ve akıntı düzeni modellemesi. Gazi Üniversitesi Mühendislik Mimarlık Fakültesi Dergisi, 33(1).

Yucel, M., Tarhan, I. (2019). Çanakkale Boğazi Akinti Türbin Modellenmesi. Uludağ University Journal of The Faculty of Engineering, 24(3), 59-74.

IEEES-070

Performance Study of a Desiccant Dehumidification Wheel

[1*]Fatih Bouzeffour, [1]Walid Taane, [2]Mouna Kassim, [1]Zahra Neffah, [1]Djelloul Belkacemi
[1]Unité de Développement des Equipements Solaires, UDES, Centre de Développement des Energies Renouvelables, CDER, 42415, Tipaza, Algeria
[2]Université de SAAD DAHLEB, Blida, Algeria.
*E-mails:bofateh@gmail.com

Abstract

The objective of the present work was to test a rotary solid desiccant dehumidifier system in order to verify the feasibility and the progress of the dehumidification process. The system proposed in this study consisted of a solid desiccant wheel, an electric air heater, and a fan. The desiccant wheel is divided into two parts, namely an adsorption section and a regeneration section. The temperatures (T) and relative humidity (RH) were measured by the sensors that were connected to the data logger. Test results revealed that the relative air humidity at the outlet of the rotary desiccant wheel decreases from 70% to 15% and the process air temperature at the outlet can reach 50°C. Moreover, the relationship between the working parameters were also presented and discussed.

Keywords: Solid desiccant, Adsorption, Regeneration, Dehumidification effectiveness.

I. Introduction

The desiccant cooling system compared to the conventional vapor compression is an environmentally friendly system, zero CFC and HCFC within the system or produced. The solide desiccant air conditioning offers a tool for controlling the humidity and temperature in hot and humid climate (Jia et al. 2006).
In the field of a desiccant cooling system, several studies have been conducted to build and test a desiccant wheel system with different experimentally conditions of hot dry and hot humid climate, regeneration temperature and desiccant wheel speed (Ali Mandegari and Pahlavanzadeh 2009); to construct, test and evaluate the performance of desiccant wheel system with a two stage rotary desiccant cooling system (Ge et al. 2009); fabricate, test and evaluate the performance of a solid vapor compression hybrid air-conditioning system with typical hot and humid weather conditions (Jani, Mishra, and Sahoo 2016); to test experimentally and evaluate the performance of the desiccant wheel cycle with a new composite of zeolite adsorbent as a desiccant material (Al-Alili, Hwang, and Radermacher 2015); to build and test a desiccant wheel system with a silica gel as adsorbent material and to estimate the moisture removal capacity, and the sensible heat ratio for low temperatures of the process airflow rate and air regeneration temperature (Comino and Ruiz de Adana 2016); to develop an analytical model in order to predict the temperature and the humidity ration of the outlet air in the desiccant wheel with various parameters such as inlet temperature and humidity ration of the regeneration air, rotational cycle period and split ration of the desiccant wheel (Kang, Choi, and Lee 2018); to establish a novel dehumidification and thermal performance correlation of a desiccant wheel system as a function of the inlet air temperature and humidity ration, the air flow rate, the regeneration air temperature and the rotational speed (Angrisani, Roselli, and Sasso 2018) and to develop a CFD (Computational Flow Dynamic) in order to examine and analysis the performance of the dehumidification process with the different desiccant wheel channel (Bhabhor and Jani 2021).
The present study was to test a rotary solid desiccant dehumidifier system in order to verify the feasibility and the progress of the dehumidification process. The system proposed in this study consisted of a solid desiccant wheel, an electric air heater, and a fan. The desiccant wheel is divided into two parts, namely an adsorption section and a regeneration section. The temperatures (T) and relative humidity (RH) were measured by the sensors that were connected to the data logger.

II. Experimental Procedure

The experimental system was a solid desiccant dehumidification system. It consisted of two sections, namely an adsorption part and a regeneration part. Figure 1.A shows a photograph of the experimental apparatus. The system was equipped with two fans, one connected with the adsorption section and the other one was used to connect with the regeneration section. A detailed schematic representation of the component system is shown in Figure 1.B.The system proposed in this study consisted of a solid desiccant wheel, an electric air heater, and a fan. The desiccant wheel is divided into two parts, namely an adsorption section and a regeneration section. The temperatures (T) and relative humidity (RH) were measured by the sensors that were connected to the data logger. The airflow rate was measured by a digital anemometer.

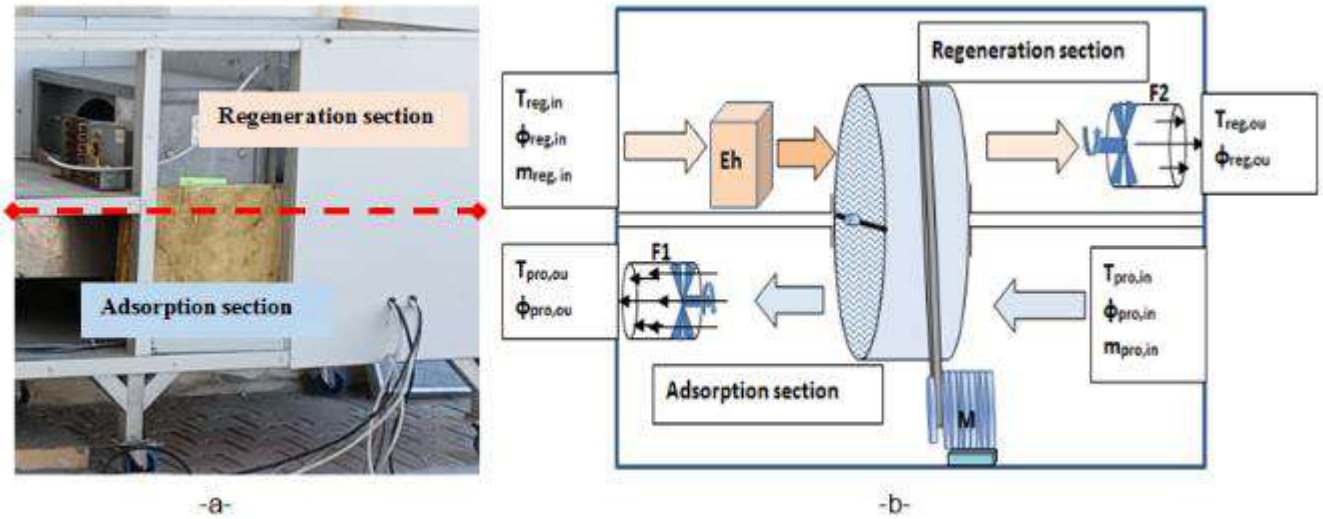

Fig. 1: a) Photograph of the experimental apparatus, b) A detailed schematic representation of the component system

III. Results and discussion

A. Process air temperature change in desiccant wheel

For the rotary desiccant wheel, the experimental result of air temperature during the dehumidification process is shown in figure 2. The measured temperatures were taken at intervals of ten second. The process air temperature at the outlet of the desiccant wheel started to increase. It can be seen that the maximum temperature varied from 47 to 53 °C during the dehumidification process. The highest temperatures achieved by the dehumidification can be explained by the adsorption procedure; wheach means that the adsorption is an exothermic process.

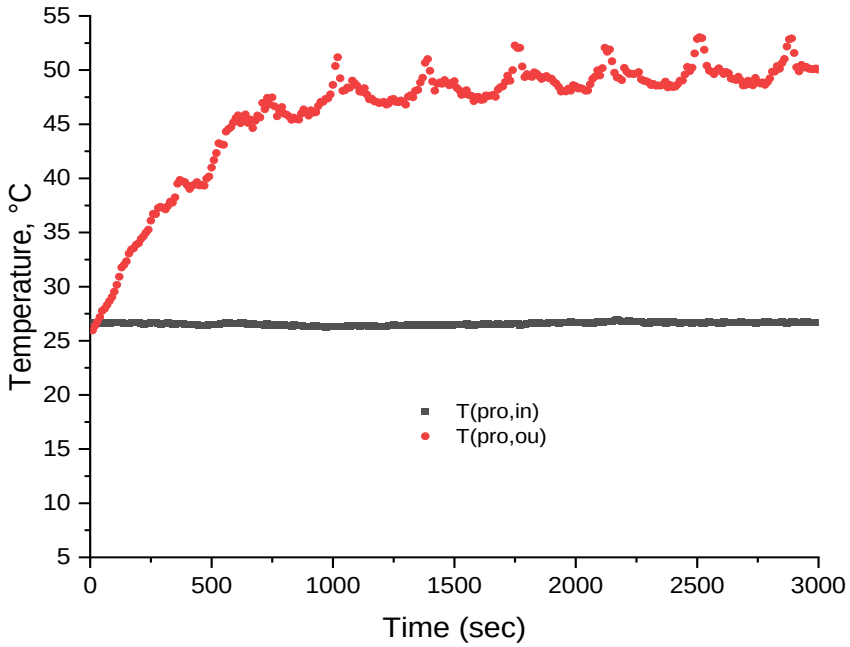

Fig. 2. Evolution air temperature with time in desiccant wheelduring the dehumidification process

B. Process air humidity change in desiccant wheel

Figure 3 shows the time variation of the air humidity at the outlet of rotary desiccant whell. The air humidity decreased from the maximum value ($\phi_{pro,in}$= 70, 80%) mbar to the minimum value corresponding to ($\phi_{pro,ou}$= 15%) mbar. As shown in figure 3, the air humidity started to decrease from 250 second and follow the minimum value due to an adsorption of the water vapor in air.

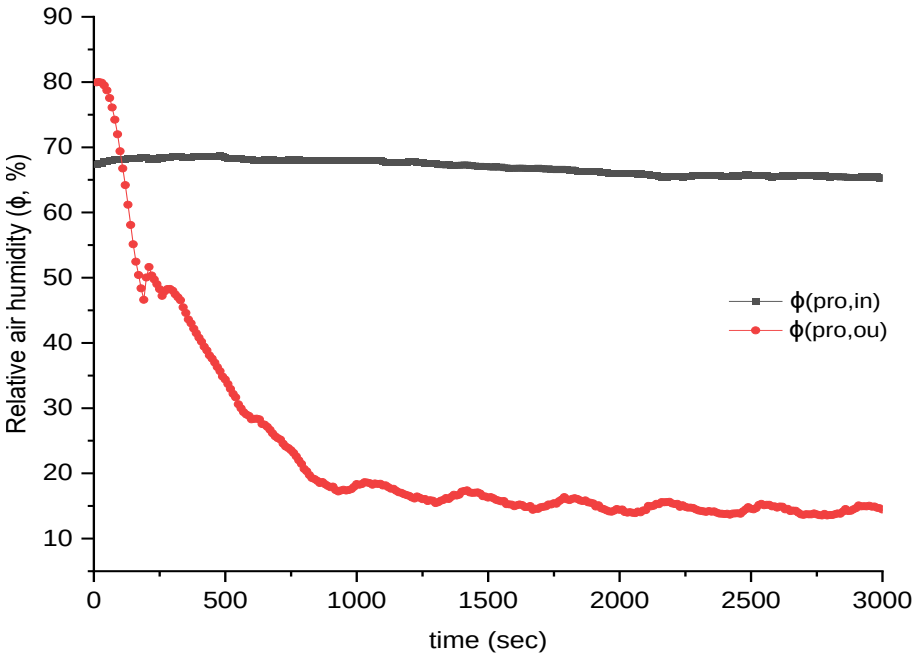

Fig. 3: Evolution of air humidity in desiccant wheel

C. Analysis of the correlations among, and intensity of the relationship of variables

In statistics and probability theory, correlation indicates the strength of a linear relationship between two variables (Samani, Gohari-Moghadam, and Safavi 2007). Therefore, the correlation is a dimensionless quantity that can be used to compare linear relationships between pairs of variables in different units (Montgomery and Runger 2010). The aim of the "Pearson product-moment" technique is to find the best line between the two operating variables. If the two variables are perfectly linearly related with a positive or negative slope, then this coefficient "r" is equal to +1 or -1 respectively. If "r" is equal to zero, there is no association between the pairs of selected variables. This "r" coefficient is described for two variables, Y and X according to the following relation (Nabipour 2018):

$$r = \frac{\sum_{i=1}^{n}\left(X_i - \overline{X}\right)\left(Y_i - \overline{Y}\right)}{\sqrt{\sum_{i=1}^{n}\left(X_i - \overline{X}\right)^2 \sum_{i=1}^{n}\left(Y_i - \overline{Y}\right)^2}}$$

Where;
Xi and Yi : represents the measured values.
$\overline{X}$ and $\overline{Y}$: represents the mean measured values.

Table 1. Correlation coefficient analysis

	$T_{pro,in}$	$\varphi_{pro,in}$	$T_{reg,in}$	$\varphi_{reg,in}$	$T_{pro,out}$	$\varphi_{pro,out}$	$T_{reg,out}$	$\varphi_{reg,out}$
$T_{pro,in}$	1	-0,657	-0.059	0.074	0.062	-0.001	0.460	-0.620
$\varphi_{pro,in}$	-0,657	1	-0.554	0.423	-0.645	0.600	-0.935	0.973
$T_{reg,in}$	-0.059	-0.554	1	-0.941	0.961	-0.983	0.740	-0.522
$\varphi_{reg,in}$	0.074	0.423	-0.941	1	-0.914	0.945	-0.661	0.420
$T_{pro,out}$	0.062	-0.645	0.961	-0.914	1	-0.972	0.807	-0.625
$\varphi_{pro,out}$	-0.001	0.600	-0.983	0.945	-0.972	1	-0.789	0.585
$T_{reg,out}$	0.460	-0.935	0.740	-0.661	0.807	-0.789	1	-0.935
$\varphi_{reg,out}$	-0.620	0.973	-0.522	0.420	-0.625	0.585	-0.935	1

The results of the correlation coefficient analysis of the air temperature, and the relative air humidity at the outlet of rotary desiccant wheel according to the working parameters of the process air temperature (Tpro,in), the process relative air humudity (ϕpro,in), the regeneration air temperature (Treg,in), the regeneration relative air humidity (ϕreg,in) are listed in Table 2. For a multivariate system, the elements of the correlation matrix indicate the relationship between each of the two variables. It is clear from Table 1 that, there is a strong relationship between the regeneration air temperature at the inlet and the process air temperature at the inlet of the desiccant wheel (r = 0,961) and also a strong linear relationship between the air humidity at the inlet and the regeneration air humidity at the outledt of the desiccant wheel (r=0.973). Moreover, a considerable linear relationship between the process air humidity at the inlet and the regeneration air humidity at the outlet of the desiccant wheel (r = 0,945).

V. Conclusion

Solid desiccant dehumidification system is considered as an environmentally friendly procedure to a conventional air-conditioning system. The air temperature and the relative air humidity are the main parameter that should be studied in order to characterize the solid desiccation dehumidification technology. Based on the experimental results obtained, the main conclusions are:

- Experimental results of a rotary desiccant wheel reveals that the system can achieve better air dehumidification in a humid climate.
- Strong relationship between the regeneration air temperature at the inlet and the process air temperaturat the inlet of the desiccant wheel.
- Considerable relationship between the process air humidity at the inlet and the regeneration air humidity at the outlet of the desiccant wheel.

References

Al-Alili, Ali, Yunho Hwang, and Reinhard Radermacher. 2015. "Performance of a desiccant wheel cycle utilizing new zeolite material: Experimental investigation." Energy no. 81:137-145. doi: https://doi.org/10.1016/j.energy.2014.11.084.

Ali Mandegari, M., and H. Pahlavanzadeh. 2009. "Introduction of a new definition for effectiveness of desiccant wheels." Energy no. 34 (6):797-803. doi: https://doi.org/10.1016/j.energy.2009.03.001.

Angrisani, Giovanni, Carlo Roselli, and Maurizio Sasso. 2018. "Dehumidification and Thermal Behavior of Desiccant Wheels: Correlations Based on Experimental and Manufacturer Data." Heat Transfer Engineering no. 39 (3):293-303. doi: 10.1080/01457632.2017.1295743.

Bhabhor, K. K., and D. B. Jani. 2021. "Performance analysis of desiccant dehumidifier with different channel geometry using CFD." Journal of Building Engineering no. 44:103021. doi: https://doi.org/10.1016/j.jobe.2021.103021.

Comino, F., and M. Ruiz de Adana. 2016. "Experimental and numerical analysis of desiccant wheels activated at low temperatures." Energy and Buildings no. 133:529-540. doi: https://doi.org/10.1016/j.enbuild.2016.10.021.

Ge, T. S., Y. Li, R. Z. Wang, and Y. J. Dai. 2009. "Experimental study on a two-stage rotary desiccant cooling system." International Journal of Refrigeration no. 32 (3):498-508. doi: https://doi.org/10.1016/j.ijrefrig.2008.07.001.

Jani, D. B., Manish Mishra, and P. K. Sahoo. 2016. "Experimental investigation on solid desiccant–vapor compression hybrid air-conditioning system in hot and humid weather." Applied Thermal Engineering no. 104:556-564. doi: https://doi.org/10.1016/j.applthermaleng.2016.05.104.

Jia, C. X., Y. J. Dai, J. Y. Wu, and R. Z. Wang. 2006. "Experimental comparison of two honeycombed desiccant wheels fabricated with silica gel and composite desiccant material." Energy Conversion and Management no. 47 (15):2523-2534. doi: https://doi.org/10.1016/j.enconman.2005.10.034.

Kang, Hyungmook, Sun Choi, and Dae-Young Lee. 2018. "Analytic solution to predict the outlet air states of a desiccant wheel with an arbitrary split ratio." Energy no. 153:301-310. doi: https://doi.org/10.1016/j.energy.2018.03.177.

Montgomery, D.C., and G.C. Runger. 2010. Applied Statistics and Probability for Engineers: John Wiley & Sons.

Nabipour, Milad. 2018. "Prediction of surface tension of binary refrigerant mixtures using artificial neural networks." Fluid Phase Equilibria no. 456:151-160. doi: https://doi.org/10.1016/j.fluid.2017.10.020.

Samani, N., M. Gohari-Moghadam, and A. A. Safavi. 2007. "A simple neural network model for the determination of aquifer parameters." Journal of Hydrology no. 340 (1):1-11. doi: https://doi.org/10.1016/j.jhydrol.2007.03.017.

IEEES-071

Development of Electrolytic Cation Exchange Reactor Module for Generation of Hydrogen Gas Using Ocean Water

*Hilal Sayhan Akci Turgut and Ibrahim Dincer.
Clean Energy Research Laboratory (CERL), FEAS, Ontario Tech University, Oshawa, Ontario, L1H 7K4, Canada
*E-mail: Hilal.Akci@ontariotechu.ca

Abstract

Significant volumes of carbon dioxide (CO2) are extracted from naturally existing seawater, where it primarily occurs as bicarbonate and carbonate, using a developed electrolytic cation exchange technique, which also produces hydrogen gas (H2). Two different configurations of the electrolytic cation exchange reactor were examined and assessed to understand the impact of voltage variation. The energy efficiency of the present system is determined as 7.82%.

Keywords: Hydrogen, Ocean water, Electrolysis, Carbon capture.

1. Introduction

The advancement of carbon capture and storage (CCS) technology has been greatly aided by research aimed at addressing the worldwide rise in anthropogenic CO_2 levels in Earth's atmosphere. The total carbon dioxide CO_2 in the oceans is estimated to be 100 mgL1, of which 2–3% is dissolved CO_2. (Takahashi et al., 1981). Willauer et al. (2017) developed a novel E-CEM module with three configurations. Through testing, they were able to quickly lower the pH of seawater by 65%. This allowed the carbonate and bicarbonate in the saltwater to re-absorb and convert back into CO_2 gas, which helped the water recover. Xu et al. (2022) employed electrodeionization to extract ammonia from wastewater for use as fuel. This investigation included NH_3 recovery, NH_4^+ penetration, and the interaction of NH_4^+ and Na^+ with the functional groups inside a cation exchange membrane (CEM) by both theoretical computations and experimental testing. Na_2SO_4 was employed in this investigation as the supporting electrolyte.In this study, this method involves utilising protons produced at the anode through electrolysis to acidify seawater. At the cathode, protons are devoured simultaneously by electrons generated, producing hydrogen gas.

2.System Description

Continuous electrodeionization (CEDI)-based electrochemical techniques are being developed to take advantage of pH changes in the oceanwater to produce hydrogen (H_2) from the ocean water. The E-CEMs are composed of up of two cation-permeable membranes that act as partitions between the three compartments, a central compartment, and electrode compartments with cathode and anode capable of polarity reversal. The acidic characteristics allow cations to go through the polymer matrix in different ways while blocking anions from doing so. The electrode chambers inside the module are defined and contoured in detail in Figure 1. These electrode compartments were housed within the acrylic end plates of the modules and comprised both mesh and solid steel anode and cathode electrodes. Gasket material was used in the compartments of these arrangements to provide the membranes with a supporting framework. The cation-exchange membrane nearest to the cathode transports sodium ions (Na^+) from the seawater in the centre compartment. At the cathode, water splits in the meanwhile, producing hydroxide ions (OH^-) and hydrogen gas (H_2).

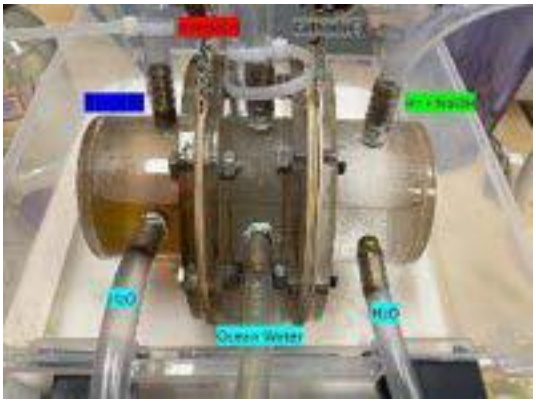

Fig. 1: The present E-CEM Reactor

According to equation 1, a mole of hydroxide ions (OH^-) is chemically replaced for every mole of bicarbonate ions ($HCO3^-$) in oceanwater, as per the complete reaction. Overall chemical reaction:

$$2H_2O + 2HCO_3^- \rightarrow 2OH^- + O_2 + 2H_2 + 2CO_2 \quad (1)$$

3. Results and discussion

The E-CEM utilizes the advantages of the continuous electrodeionization (CEDI) principles, which involves the use of an electrical potential to change the ionic transport properties of liquids in order to eliminate ionizable compounds. According to Faraday's rule, the amount of H^+ ions the anode produces is directly correlated with the electrical current that is delivered. Figure 2 illustrates that the recorded hydrogen production ratio increases as the voltage increases, but the E-CEM's functionality is unaffected. The maximum produced

IEEES-072

Integrating Ultrasound Technology for Wastewater Treatment and Hydrogen Production into an Energy System: Analysis and Assessment

Moslem Sharifishourabi*, Ibrahim Dincer and Atef Mohany
Clean Energy Research Laboratory, Faculty of Engineering and Applied Science, Ontario Tech. University, 2000 Simcoe Street North, Oshawa, Ontario, L1H 7K4, Canada
*Corresponding author e-mail: moslem.sharifishourabi@ontariotechu.ca

Abstract

This is study of an integrated energy system designed to achieve sustainable wastewater treatment and hydrogen production. It utilizes various subsystems; Solar Power System, Biomass Energy System, Steam Rankine Cycle (SRC), Brayton Cycle (BC), Absorption System, Reverse Osmosis, Water Treatment, and sonohydrogen production, the system aims to optimize both energy and exergy efficiencies. The energy, exergy, and environmental analyses are carried out to evaluate the system's performance and sustainability. The engineering equation solver is used for the analysis. The energy and exergy efficiencies of the steam Rankine cycle are found to be 24.46 % and 45.47 % respectively. Additionally, various parametric studies are conducted to understand the impacts of different operating conditions and configurations. The results demonstrate the capability of the system for significantly enhancing wastewater treatment efficiency and hydrogen production, while minimizing environmental impacts.

Keywords: Sonic hydrogen production, Ultrasound-assist wastewater treatment, Energy, exergy, efficiency.

1. Introduction

In today's rapidly evolving industrial landscape, the need for sustainable water treatment methods and alternative energy sources is more crucial than ever. The treatment of wastewater generated from industrial processes is not just an environmental imperative but also an economic necessity. The urgency to manage wastewater effectively is further intensified by global water scarcity and the rising costs associated with conventional treatment methods. Concurrently, the quest for clean and renewable energy has led to a renewed focus on hydrogen production as a viable and sustainable alternative to fossil fuels. One innovative solution that has been gaining traction in recent years is the use of ultrasound technology for both wastewater treatment and hydrogen production. It often termed as "sonohydrogen" production (Rashwan et al., 2020). Ultrasound technology offers a range of advantages including low energy consumption, reduced chemical usage, and high efficiency, thereby making it a strong candidate for large-scale implementation. More intriguingly, this technology can be seamlessly integrated into a comprehensive energy system. This integration creates a symbiotic relationship between wastewater treatment and hydrogen production processes.

The flexibility of such an integrated energy system allows for the incorporation of various renewable energy sources like solar power and biomass energy. In this context, heliostats could be employed to focus sunlight onto a receiver to produce thermal energy. Biomass energy could be harnessed through the use of digesters that convert organic waste, including municipal waste, into biogas. This biogas can then be used to produce either electricity or heat. One of the key components in this integrated system is the role of reverse osmosis in water treatment. Reverse osmosis serves as a critical step. It is responsible for the removal of ions, unwanted molecules, and larger particles from wastewater. This subsystem improves both the quality of treated water and enhances the overall efficiency of the system. Thermal energy storage (TES) systems can be incorporated into this integrated framework to store excess energy produced, thereby ensuring a stable and continuous energy supply (Dinçer, 2020). The stored thermal energy can be employed in various thermodynamic cycles, such as the Rankine and Brayton cycles, for electricity generation. Furthermore, absorption systems can be integrated to optimize the overall energy and exergy efficiencies of the system.

The integration of ultrasound technology for wastewater treatment and hydrogen production into an energy system offers a technical advancement. It also marks a standard shift in the approach to sustainability. By coupling these processes, it is possible to harness synergies that enhance both energy and exergy efficiencies, while simultaneously mitigating environmental impacts. This article aims to provide energy, exergy, and environmental analyses of such an integrated system.

2. System and Analysis

The system depicted in Fig.1 presents a comprehensive, integrated energy system that leverages various technologies to achieve synergistic wastewater treatment and hydrogen production. Overall, the system is divided into nine major subsystems: Solar Power System, Biomass Energy System, Steam Rankine Cycles (SRC1 and SRC2) Brayton Cycle (BC), Absorption System, Reverse Osmosis, Water Treatment, and Sonohydrogen Production Process. The Solar Power System employs heliostats to focus sunlight onto a receiver, generating thermal energy. This thermal energy can either be used directly in various subsystems or stored for later use. On the other hand, the Biomass Energy System uses digesters to convert organic and municipal waste into biogas, which can also be converted into thermal energy or electricity. The TES subsystem acts as the central hub for energy storage, storing the excess thermal energy generated by the Solar and Biomass systems. This stored energy can be dispatched when required, providing flexibility and ensuring a constant energy supply to other subsystems. The SRC serves as one of the primary energy conversion subsystems, taking thermal energy from both TES and the Brayton Cycle. The SRC is responsible for generating electricity and heat, which in turn drives the SRC2 and the Single Effect Absorption System (SEAS). The SRC2 and BC are thermodynamic cycles employed to optimize the system's energy and exergy efficiencies. The SRC2 is driven by the SRC1, while the Brayton Cycle can operate independently to produce work and to run the SRC1. The SEAS is a versatile subsystem that provides both heating and cooling services. It is operated using the waste heat generated by the SRC. The Reverse Osmosis subsystem is pivotal for water treatment, taking wastewater from

the treatment vessel and purifying it to produce fresh water. This fresh water serves dual purposes: it is used for community supply and also as a feedstock for the sonohydrogen production process. Ultrasound technology is utilized to split water into hydrogen and oxygen. The process harnesses the high-frequency sound waves to induce cavitation in water, facilitating the breaking of the molecular bonds and leading to the production of hydrogen gas.By intertwining these subsystems, the integrated system capitalizes on their individual efficiencies and functionalities to create a holistic solution for wastewater treatment and hydrogen production. The design ingeniously allows for the coupling of various energy sources and technologies, thereby optimizing energy and exergy efficiencies while minimizing environmental impacts.

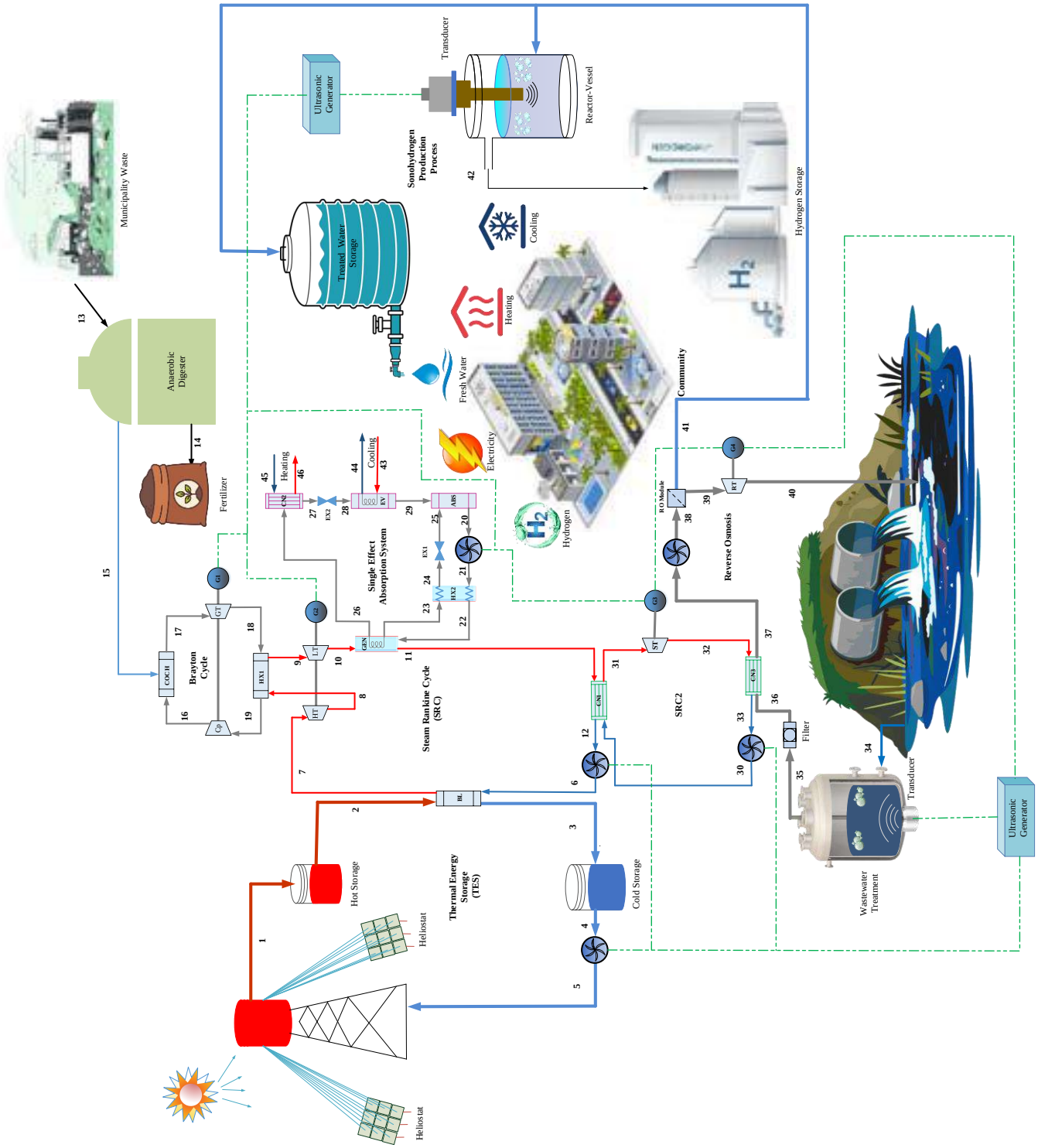

Fig. 1: Schematic of the developed system

3. Results and discussion

Fig.2 provides an insightful depiction of how the energy and exergy efficiencies of the Steam Rankine Cycle (SRC2) vary with changes in ambient temperature. It is evident that the energy efficiency remains constant at 24.46 % across the range of ambient temperatures considered (280K to 320K). This suggests that the SRC2's energy efficiency is not significantly impacted by fluctuations in ambient temperature. Contrastingly, the exergy efficiency shows a noticeable increase as the ambient temperature rises. Starting at 43.21% at 280 K, it reaches 48.53% at 320K. This ascending trend indicates that the exergy efficiency of the SRC2 improves with an increase in ambient temperature.

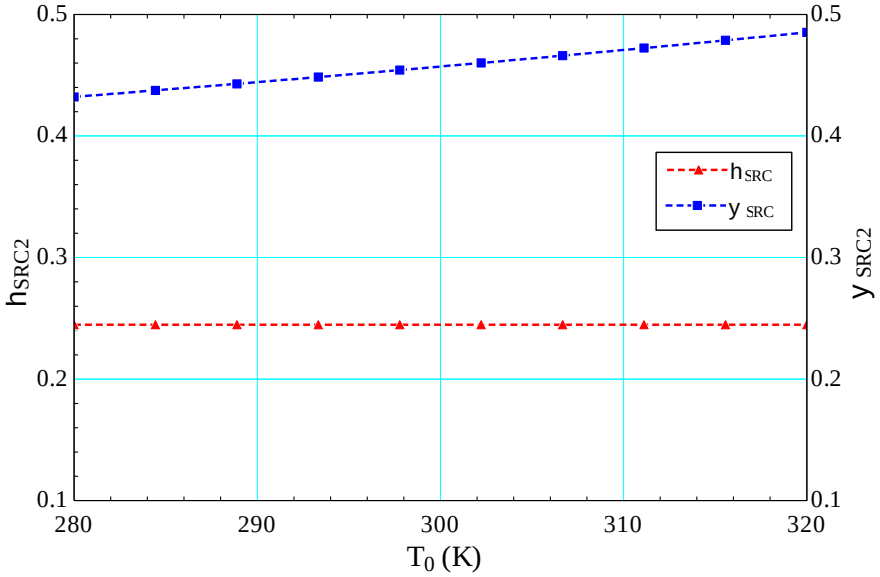

Fig. 2. Variation of energy and exergy efficiencies of the steam Rankine cycle (SRC2) with ambient temperature

The inlet temperature in the steam Rankine cycle (SRC) is a critical parameter that significantly impacts the cycle's performance metrics, including the net work output and the heat supply to the Reverse Osmosis subsystem. A higher inlet temperature generally results in increased thermodynamic efficiency, enabling the SRC to produce more work and deliver more heat, thereby optimizing the performance of the entire integrated system. Fig.3 explains the relationship between the inlet temperature of the SRC2 (in K) and two key performance indicators: the net work output of the SRC (in kW) and the heat inlet supplied to the Reverse Osmosis subsystem (in kW).

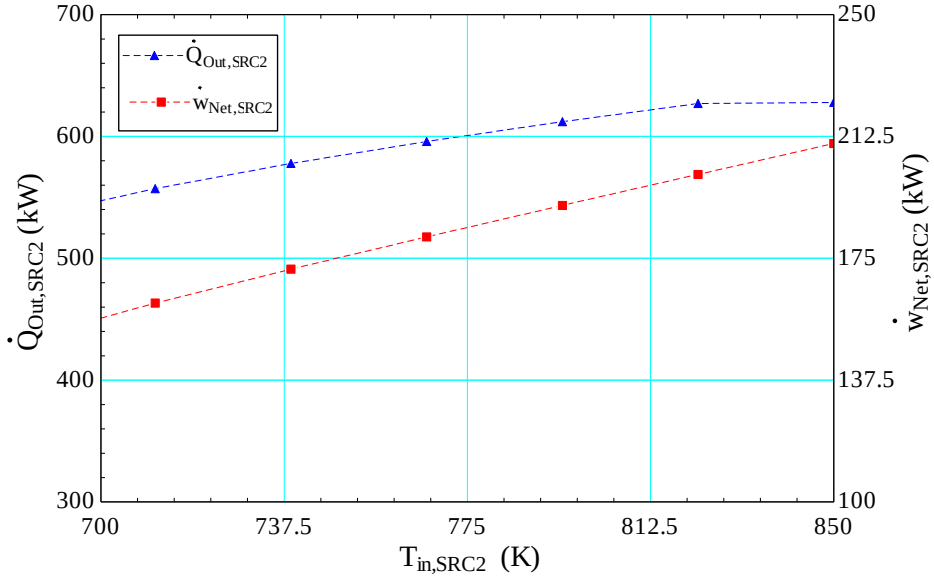

Fig. 3. Influence of Inlet Temperature on the output of the SRC2

As the figure indicates, an increase in the inlet temperature of the SRC2 results in corresponding increases in both the net work output and the heat inlet to the Reverse Osmosis subsystem. Specifically, the net work output shows a substantial rise, starting from 36.15 kW at a lower inlet temperature of 600K, and reaching up to 210.3 kW at a higher inlet temperature of 850K. This enhancement underscores the system's improved capability to generate more work and heat, which is crucial for effectively driving other subsystems like Reverse Osmosis and Sonohydrogen Production. Similarly, the heat inlet to the Reverse Osmosis subsystem also increases, beginning at 215.5 kW with an inlet temperature of 600K and escalating to 627.9 kW at 850K. This additional heat supply significantly impacts the efficiency of the Reverse Osmosis process, which in turn has positive implications for the overall performance of the integrated system.

4. Conclusion

The integrated energy system explored in this article offers a new approach to wastewater treatment and hydrogen production. Through the symbiotic arrangement of various subsystems, the system not only ensures high energy and exergy efficiencies but also mitigates environmental concerns. The energy, exergy, and environmental analyses have substantiated the system's effectiveness and sustainability. The energy and exergy efficiencies of the steam Rankine cycle are found to be 24.46% and 45.47%, respectively. Furthermore, the parametric studies provide valuable insights into optimizing the system under varying conditions, thereby making it adaptable for real-world applications. One of the significant aspects of the system is its ability to harness renewable energy sources, such as solar and biomass, efficiently. The thermal energy storage (TES) ensures a stable energy supply, thereby enhancing the reliability of the system. Additionally, the incorporation of various thermodynamic cycles like SRC, SRC2, and BC, along with an absorption system, contributes to the overall efficiency of the system. Reverse osmosis plays a pivotal role in improving the quality of treated water, which is then used both for community supply and as a feedstock in the sonohydrogen production process. The latter, utilizing ultrasound technology, presents an innovative method for hydrogen production with minimal environmental impact.

References

Dincer, İ., 2020. Thermodynamics: a smart approach. John Wiley & Sons.

Rashwan, S.S., Dincer, I., Mohany, A., 2020. A unique study on the effect of dissolved gases and bubble temperatures on the ultrasonic hydrogen (sonohydrogen) production. International Journal of Hydrogen Energy 45, 20808–20819. https://doi.org/10.1016/j.ijhydene.2020.05.022

IEEES-073

Theoretical Investigation of Solar Energy Assisted Cooling in Refrigerated Trailers

[1*]Yusuf Taha İsmailoğlu, [1]Deniz Ulusarslan
[1] Yıldız Technical University, Faculty of Machinery, Mechanical Engineering Department, Barbaros Avenue A Block Floor:2 Room No:203, Istanbul, 34349, Türkiye
*E-mail: taha.ismailoglu@std.yildiz.edu.tr

Abstract

According to TUIK's (Turkish Statistical Institute) 2020 greenhouse gas emission inventory data, 94.9% of CO2 emissions from transportation are caused by road transportation. The leading sector in road transportation is refrigerated product transportation. The reason for the importance of refrigerated product transportation is that additional fuel is consumed for the cooling of the product and the emission emission increases accordingly. In this study, a theoretical analysis of the cooling of a certain product in a refrigerated trailer with solar energy support was made and its effects on energy, cost, fuel consumption and CO2 emissions were investigated. For this purpose, a trailer whose technical specifications and dimensions are known from the company catalogs and used in commercial applications has been selected and it is thought that mono-crystalline solar panels are placed on the top and side surfaces. The energy obtained from the panels will be used in the cooling unit. The trailer with solar panels is assumed to move in the city of Istanbul. In the selection of the cooler and evaporator, one of the brands with the highest sales rate in the market was chosen. The cases of cooling the trailer when it is empty and cooling the trailer when the product inside is frozen fish are analyzed. In July, the month of the year with the highest radiation intensity, 29% of the electrical energy consumed by the cooling system was provided with the energy obtained from the panels. In this case, 30% of the fuel consumed by the cooling unit can be saved with the energy provided by solar panels. This will reduce emissions, contribute to the protection of nature and reduce the cost of product transportation.

Keywords: Solar energy, refrigerated trailer, cold chain, food transportation.

I. Introduction

In a 2021 study, a solar-assisted cooling system was designed for milk tankers. In milk cooling, the tanker has to work continuously. To solve this problem, a solar-powered smart cooling system was developed. It is also designed to operate this thermoelectric cooler intelligently. The system is designed to display the volume of milk in the tanker and the system power consumption (Komako, 2021). In a 2022 study, an electrically powered refrigeration unit integrated with photovoltaic generators was designed for a flatbed truck to travel around Athens. The system prototype was tested under stable conditions and demonstrated the capacity of the solar system to significantly impact the net energy balance. The results show that in Athens climatic conditions, depending on the time the truck spends in direct sunlight, the energy consumed by the cooling unit can instantaneously provide 65% to 112% of the solar panels (Rosetti, 2022). Another study in 2022 examined the current state of experimental research and numerical simulations on refrigerated trucks. Several solutions and recommendations were presented to improve the quality and safety of food during transportation. Important issues related to temperature-controlled transportation of these products and performance improvements of pre-cooling units and truck design described in the literature were examined (Taher, 2022). When these studies are examined, it is determined that there is a gap in solar energy applications especially for the transportation sector. In this sector, which ranks high in emission emissions in freight transportation, fuel consumption and emissions should be reduced. In order to achieve this, it is aimed to utilize solar energy and it is proposed to place solar panels on trailer surfaces. In this study, it is aimed both to bring a new research to the literature and to apply solar energy systems to freight transportation.

II. Methodology

In the conventional system, the cooler on the trailer is usually driven by a diesel engine or an externally attached electric motor. All components of the refrigeration system are in a unit mounted on the front wall of a trailer. The system usually has the motor, condenser and other accessories mounted outside the front wall, only the evaporator and fan are placed inside the trailer.
The power of the cooler selected for this study from the market is 17.9 kW, the air flow rate is 9.5 m/s and the evaporator return air is -20°C. AGM batteries is used in the cooler. AGM means absorbent glass mat and refers to the fine glass fiber separator between the positive and negative plates that helps absorb all the battery acid. AGM batteries are advanced lead-acid batteries.
Thermostats are used to regulate the air temperature inside the trailer. Modern refrigeration units measure both supply and return air temperatures and are used to keep the temperature very close to the set point.
For the solar energy assisted cooling system, it is assumed that the top and side surfaces of the trailer shown in Figure 1 are covered with solar panels. The solar panels generate electricity from solar radiation during the daily sunshine period. The generated electricity will power the cooling unit. Thus, the refrigeration unit will consume less fuel and refrigerated road transportation will become more efficient. Fuel costs will also decrease due to reduced fuel consumption and refrigerated transportation will be a more environmentally friendly sector with reduced emissions.

Fig. 1: Solar energy assisted cooling system on refrigerated trailer

III. Analysis

The trailer selected from the market for this study is 13,6 meters long, 2,650 meters high and 2,450 meters wide. With this data, the internal volume of the trailer is calculated, and the product layout is determined.
For the cooling of the product, the product placement literature in the trailer was examined. After determining the appropriate layout model for the selected product, calculations for convection cooling of the product by exposure to the evaporator air were made. Frozen fish is selected as the product to be cooled in this section. Both the cooling of the selected product and the cooling of the trailer when it is empty are calculated. In addition, the fuel consumption and CO2 emissions of the cooler during this cooling were also calculated. The selected air distribution system is shown in Figure 2. The heat that the trailer will gain from the external environment is calculated depending on the conditions of the external environment.

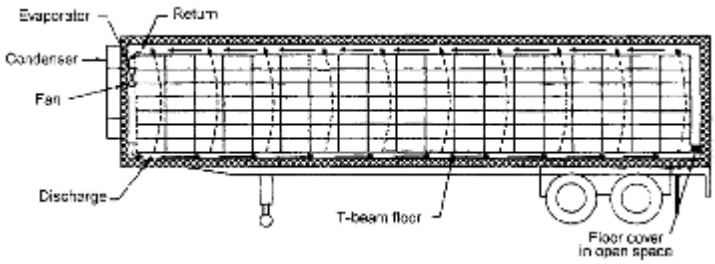

Fig. 2: Airflow pattern in the bottom-air delivery system (Hui, 2001)

After the cooling load calculations, solar radiation calculations are made. The solar radiation intensity is calculated for a situation where the vehicle in which the solar panels will be placed will travel around Istanbul. Solar angles for the city of Istanbul are given in Table 1 (Yiğit, 2018).

Table 1. Solar angles for Istanbul

Angle	**Symbol**	**Value**
Latitude Angle	*φ*	*41,14°*
Altitude	*z*	*33m*
Average Number of Days (July)	*n*	*162*
Relative Insolation Duration	*n/N*	*0,73*

Using these values, the declination angle according to (Yiğit, 2018) is calculated by Equation 1.

$$\delta = 23{,}45^{*}\sin\left(360^{*}\,{}^{(284+n)}/_{365}\right) \quad (1)$$

According to (Yiğit, 2018), the hour angle is used in the calculation of instantaneous solar radiation and the hour angle is calculated according to Equation 2.

$$\cos(w_s) = -\tan\delta^{*}\tan\varphi \quad (2)$$

The daily solar radiation falling on a surface outside the atmosphere is calculated by Equation 3 according to (Yiğit, 2018).

$$H_0 = \frac{24^{*}3600}{\pi}{}^{*}G_{sc}{}^{*}\left[1+0{,}033^{*}\cos\left(\frac{360^{*}n}{365}\right)\right]^{*}\left[\cos\delta^{*}\sin w_s + \frac{2^{*}\pi^{*}w_s}{360}{}^{*}\sin\delta^{*}\sin\varphi\right] \quad (3)$$

The solar radiation falling on a surface in the atmosphere is calculated by Equation 4 according to (Yiğit, 2018).

$$H = H_0{}^{*}\left(a + b^{*}\,{}^{n}/_{N}\right) \quad (4)$$

Calculations were made for all main directions. Thus, the contribution of solar panels placed on the side surfaces of the trailer to energy savings was also determined. In the calculation of the daily irradiance to the side surfaces of the trailer, the sum of the instantaneous irradiances falling during the day depending on the daily sunshine duration was used. In addition, since the calculations are made for

all months of the year, the performance of the proposed system can be compared according to the months. In addition to the fuel savings data obtained depending on the selected cooler, the reduced CO2 emissions are also shown in graphs. The amount of energy and fuel to be saved when using a solar cooling system can be determined according to the direction in which the vehicle is traveling, and its location on the globe.
Daily and instantaneous irradiance values for the city of Istanbul were calculated for both a flat surface and surfaces inclined 90 degrees in the cardinal directions. The daily radiation falling on the roof surface of a trailer conforming to the selected standards and the total daily solar radiation falling on the side surfaces of this trailer are given in Figure 3.

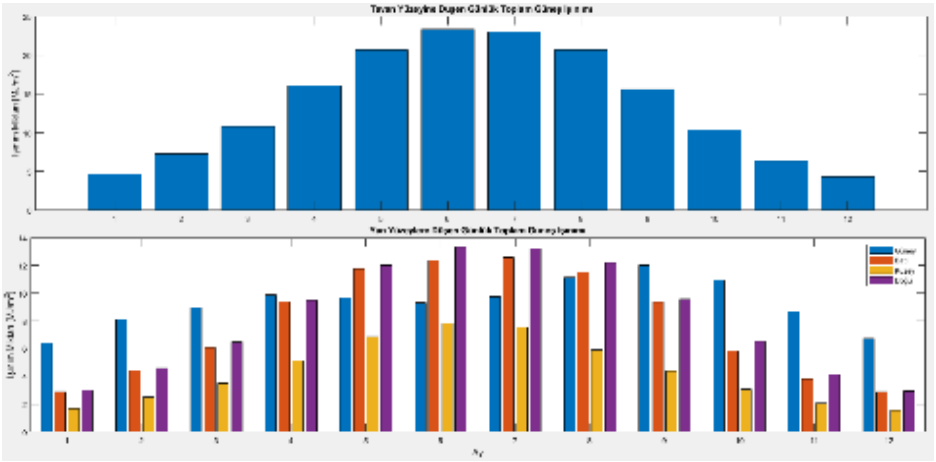

Fig. 3: Daily solar radiation on trailer roof and surfaces by month

IV. Results and discussion

The main purpose of this study is to provide an environmentally friendly solution for the refrigerated product transportation sector, which has a very important share in emission emissions. In this direction, it is aimed to generate electricity by placing solar panels on the top and side surfaces of the refrigerated trailer and to feed the cooler with this electricity. Thus, the emission emission of refrigeration engines during the transportation of products can be reduced and a more environmentally friendly refrigerated transportation network can be created.
In this study, one of the brands with the highest sales rate in the market was chosen for the selection of the chiller and evaporator for cooling the trailer. With the conventional system using this chiller, the emission emission when the trailer is empty is 13,83 grams. In order to understand the performance of the solar-assisted cooling system, the case where the trailer benefits from instantaneous solar radiation between 14:00-16:00 hours is considered. In this case, the avoided CO2 emission from solar-assisted cooling is 4,08 grams in July. Thus, the amount of CO2 emission in case of solar cooling of the trailer will be 9,79 grams. According to these results, CO2 emissions can be reduced by 30% compared to the conventional system. The emissions that will be emitted and the emissions that will be reduced with the conventional system and the solar energy assisted system are given in Figure 4.

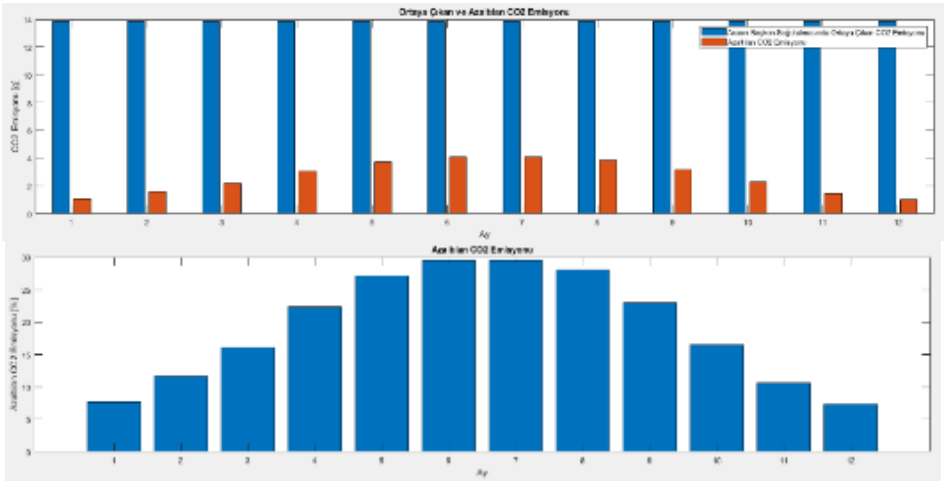

Fig. 4: Emissions reduced by cooling the vehicle when empty (north-south movement) by month

In conventional refrigeration, the amount of fuel consumed to cool the frozen fish from the maximum allowable transport temperature to the return air temperature is 28 liters. The CO2 emission during this period is 85 grams. The amount of fuel that can be saved in July is 0,5 liters if the solar energy assisted cooling system is used. Depending on this saving amount, the CO2 emission that can be reduced with the solar energy assisted cooling system is 1,45 grams. According to these results, as seen in Figure 5, the solar energy assisted cooling system can save 1,7% of fuel and reduce CO2 emissions by 1,7% compared to the conventional system.

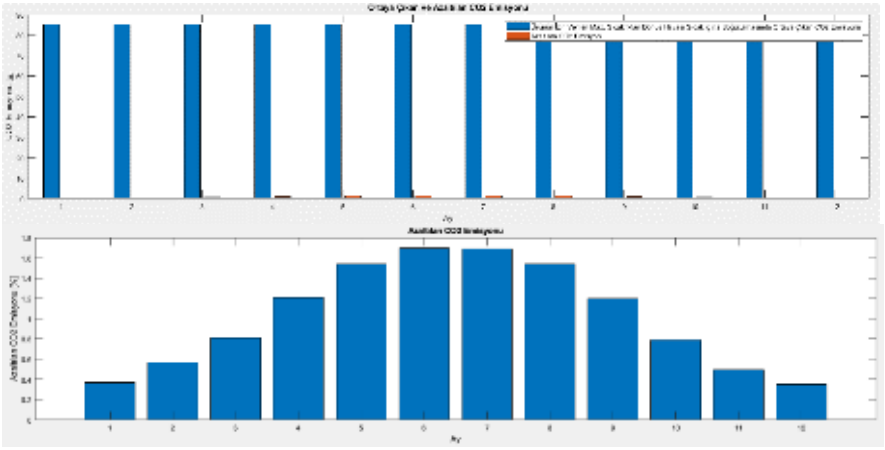

Fig. 5: Reduced CO2 emission when the trailer is full of Rand in cooling state

V. Conclusions

For this study, a trailer with known technical specifications and dimensions from company catalogs and used in commercial applications was selected. It is assumed that mono-crystalline solar panels will be placed on the top and side surfaces of the trailer. It is assumed that the trailer with solar panels will move within the city of Istanbul. For the selection of the trailer, market sales data was analyzed and one of the trailers with a high sales rate was selected. Product placement is determined depending on the dimensions of the selected trailer. The external insulation of the trailer was also included in the calculations. In the selection of cooler and evaporator, one of the brands with the highest sales rate in the market was selected. Solar radiation calculations were made both daily and instantaneously. Thus, the results are shown in graphs both daily and for certain hours of the day. In these results, the cooling of the trailer when it is empty is analyzed. Also, the cooling situation is analyzed when the product inside the trailer is frozen fish.
When the trailer is loaded with product, the cooling time of the product is longer than the daily sunshine time. Therefore, the energy required to cool the product is considerably higher than the total daily solar radiation. In the study, it is assumed that the vehicle moves only in the North-South and East-West axes. Radiation calculation can give better results if the exact location of the vehicle is determined. The amount of radiation to be calculated in these products should be higher than the daily average radiation value.

References

Güler, T., & KILIÇ, M. (2019). Klimatik Kontrollü Treyler İçerisindeki Hava Akışının Optimizasyonu. Mühendis ve Makina, 60(697), 289-302.

Hui, K. P. C. (2001). Air circulation inside refrigerated semi-trailers transporting fresh produce.

Komako, T. A., Townsend, A. K., Jiya, I. N., & Gouws, R. (2021, April). Smart Cooling System for Milk Transportation in Rural Areas. In 2021 IEEE International IoT, Electronics and Mechatronics Conference (IEMTRONICS) (pp. 1-6). IEEE.

Rossetti, A., Marinetti, S., Artuso, P., Fabris, F., & Minetto, S. (2022). Implementation of a solar aided refrigration unit for refrigerated trucks employing photovoltaic generators. Energy Reports, 8, 7789-7799.

Sono Motors and CHEREAU to codevelop solar refrigerated trailer to be unveiled at IAA 2022 (2022). Electrek. (https://electrek.co/2022/05/31/sono-motors-and-chereau-to-co-develop-solar-refrigerated-trailer-to-be-unveiled-at-iaa-2022/) Accessed 15 July. 2023.

Taher, M. B., Ahachad, M., Mahdaoui, M., Zeraouli, Y., & Kousksou, T. (2022). A survey of computational and experimental studies on refrigerated trucks. Journal of Energy Storage, 47, 103575.

Ulaştırma Türüne Göre Seragazı Emisyonu (2022). Türkiye Cumhuriyeti Çevre Şehircilik ve İklim Değişikliği Bakanlığı Çevresel Göstergeler. (https://cevreselgostergeler.csb.gov.tr/ulastirma-turune-gore-seragazi-emisyonu-i-85790) Accessed 15 July. 2023.

Yiğit, A., & Atmaca, İ. (2018). Güneş enerjisi mühendislik uygulamaları. Baskı, Bursa: Dora Yayınları.

IEEES-074

Study of boiling heat transfer coefficient during evaporation of CO_2

[1*]Rabah GOMRI, [1] Nadim KAROUNE
[1] University Constantine 1, Faculty of Science and Technology, Department of Genie Climatique, Constantine, 25000, Algeria
*E-mail:rabahgomri@yahoo.fr

Abstract

In this work, a comparative study of the flow boiling heat transfer coefficient of CO_2 in evaporation is presented. The main objective of the this work is to analyze and evaluate 1886 experimental points of the CO_2 heat transfer coefficient with the help of two evaporation correlations (Fang et al., 2013 and Fang et al., 2017. Some mathematical indicators were used to evaluate the prediction models: The mean relative deviation (MRD) and the mean absolute deviation (MAD). The results obtained show that the correlation of Fang et al., 2017 gives the best results with an average absolute deviation (MAD) of 6.04%.

Keywords: CO_2; Heat transfer; Evaporation; Correlations.

I. Introduction

Carbon dioxide (CO_2) is an ancient natural inorganic refrigerant that is heavier than air, non-toxic, non-flammable, widely available in air, and has many industrial applications. CO_2 offers a high refrigeration capacity of 22,600 kJ/kg at 0°C, which is 5 to 22 times higher than other synthetic and natural fluids (Abas et al., 2018). At the same time, CO_2's low viscosity results in lower pressure losses than other refrigerants. Liquid viscosity and surface tension make CO_2 an attractive refrigerant for two-phase boiling applications (Bansal, 2012).

In order to tstudy the boiling heat transfer coefficient of CO_2, we extracted all the experimental data (1886 points) from the existung literature studies (Table 1) for comparison with the heat transfer coefficient prediction correlations.

Table 1: Experimental studies of flow boiling heat transfer coefficient

Authors	D [mm]	G [kg/m²s]	$\dot{q}$ [kW/m²]	T_{sat} [°C]	Number of points
Zhao and Bansal, 2012	7.94	100 /250	10/25	-30	68
Grauso et al., 2013	6	150 /500	5/20	7 /12	194
Hrnjak and Kim, 2013	11.2	40 /200	0.5/10	-15	38
Dang et al., 2013	2-6	360 /1440	4.5 / 36	15	135
Choi et al., 2014	1.5-3	50 /600	5 / 60	0 / 10	85
Hassan and Shedid, 2015	10	90 /750	5 / 40	-35 / -10	23
Zhu et al. 2015	2	400	15	0 / 10	67
Yoon et al., 2016	8-9.52	100 /300	10	-30 / -20	89
Jiang et al., 2017	1.5	300/600	7.5/30	0 / -40	225
Chien et al., 2017	1.5	150 /500	5 / 20	10	52
Linlin et al., 2017	1-2	50/1350	2 / 35	-10 /15	232
Liang et al., 2019	1.5	300 /600	7.5 / 30	-40 / 0	216
Keniar et al., 2020	1.55	100/500	15/72	15/22	128
Hellenschmidt et al., 2021	2.15/0.5	100/1800	5/35	15/-25	313
Dai et al., 2023	2	200/400	12/36	5/15	21

II. Analysis

In order to choose the correlation that gives the closest results to reality, we examine two correlations available the available in the literature:

The first correlation (Fang et al., 2013):

$$h_{tp=}\ Nu\lambda_l/D_h \quad (1)$$

$$Nu = \frac{0.00061(S+F)ReIFa^{0.11}Prl^{0.4}}{[\ln(1.024\mu_{lf}/\mu_{lw})]} \quad (2)$$

$$Bo = \frac{q}{G\,h_{lg}} \quad (3)$$

$$S = 41000Bo^{1.13}\text{-}0.275 \quad (4)$$

$$F = [x/(1\text{-}x)]^a \left(\frac{\rho_l}{\rho_g}\right)^{0.4} \quad (5)$$

$$a = \begin{cases} 0.48 + 0.00542(Re_l\,Fa^{0.11})^{0.85}\text{-}5.9\times10^{-6}(Re_l\,Fa^{0.11})^{1.85} & Re_l\,Fa^{0.11} < 600 \\ 0.87 & 600 \le Re_l\,Fa^{0.11} \le 6000 \\ 160.8/(Re_l Fa^{0.11})^{0.6} & Re_l\,Fa^{0.11} > 6000 \end{cases} \quad (6)$$

$$Rel = \frac{(1\text{-}x)GD_h}{\mu_l} \quad (7)$$

$$Fa = \frac{(\rho_l\text{-}\rho_g)\sigma}{G^2D_h} \quad (8)$$

The second correlation (Fang et al., 2017):

$$h = F_f M^{-0.18} Bo^{0.98} Fr_l^{0.48} Bd^{0.72} \left(\frac{\rho_l}{\rho_g}\right)^{0.29} \left[\ln\left(\frac{\mu_l}{\mu_{l,w}}\right)\right]^{-1} Y\left(\frac{\lambda_l}{d}\right) \quad (9)$$

$$Fr_l = \frac{G^2}{gd\rho_l^2} \quad (10)$$

$$Bd = \frac{g(\rho_l - \rho_g)D^2}{\sigma} \quad (11)$$

$$Y = 1 \quad \text{for} \quad P_r \leq 0.43 \quad (12)$$

$$Y = 1.38 - P_r^{1.15} \quad \text{for} \quad P_r > 0.43 \quad (13)$$

$$Pr = \frac{P}{P_{crit}} \quad (14)$$

All thermo-physical properties of the fluid are obtained using the NIST REFPROP 9.1.

III. Results and discussion

To validate the computational programs of all the models considered, a comparison of the results generated by the computational programs with the results found in the literature was made. In all the calculation programs, the input variables from the literature are evaporation temperature, vapor quality, heat flux density, mass flow rate and inner diameter, and while the only output variable is the heat transfer coefficient.

Figure 1 shows the distribution of the vapor quality data with the heat transfer coefficient (h_{exp}); we can see that the h_{exp} concentration is between 2 and 20 kW/m^2 °C.

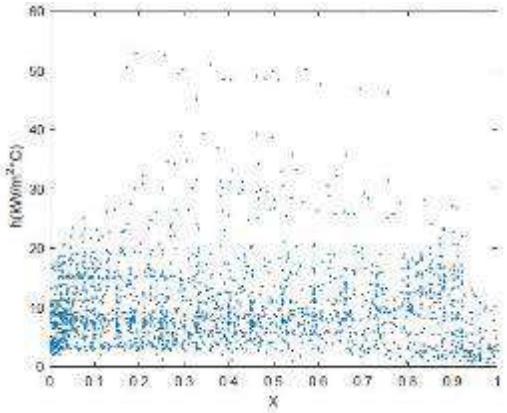

Fig. 1: Experimental flow boiling heat transfer coefficient as a function of vapour quality.

Figure 2 shows the distribution of the CO_2 heat transfer coefficient as a function of heat flux density, mass flux density and diameter. For the heat flux density, there is a point density between 0.5 and 35 kW/m^2°C where the heat transfer coefficient reaches the maximum values at q = 55 kW/m^2 °C and q= 73 kW/m^2°C. For mass flux density, the point density ranges from 100 to 800 kg/m^2, with a maximum value of 350 kg/m^2. For diameter, the boiling heat transfer coefficient CO_2 has a maximum value for D< 2mm.

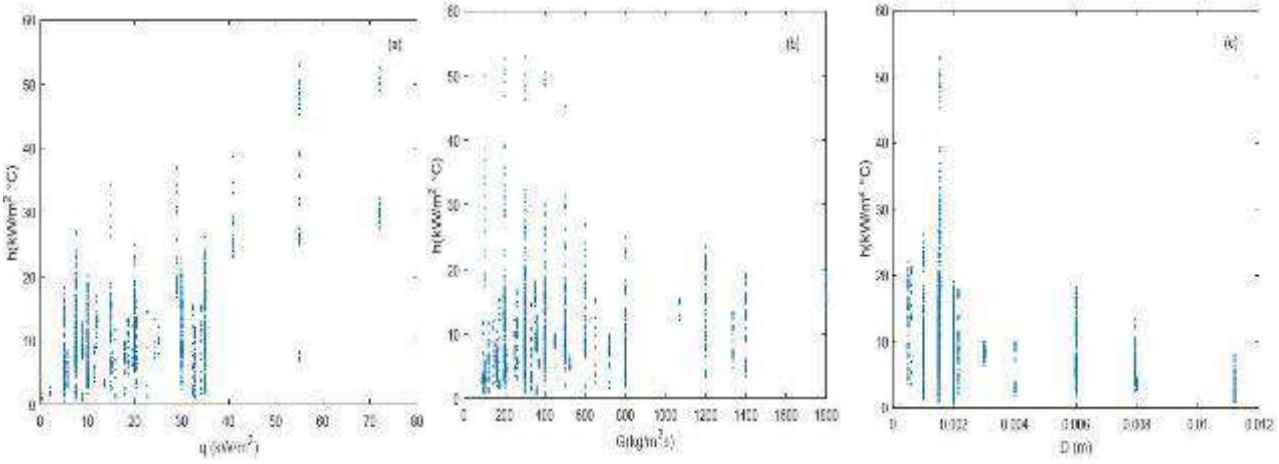

Fig.2: Experimental boiling heat transfer coefficient as a function of heat flux (a), heat flux density (b) and diameter (c).

Some mathematical indicators were used to evaluate the prediction models: The mean relative deviation (MRD) and the mean absolute deviation (MAD), N is the number of measurements.

$$MAD = \frac{1}{N}\sum_{i=1}^{N}\left|\frac{h_{(i)pred}-h_{(i)exp}}{h_{(i)exp}}\right| * 100 \quad (15)$$

$$MRD = \frac{1}{N}\sum_{i=1}^{N}\frac{h_{(i)pred}-h_{(i)exp}}{h_{(i)exp}} * 100 \quad (16)$$

The mean absolute deviation provides overall information about the accuracy of the predictive method. A low value of MAD corresponds to a high accuracy of the model. A positive value of MRD indicates an overestimation of the experimental data, while a negative value indicates an underestimation of the measurement.
Table 2 summarizes all values of the mean deviations and absolute mean deviations of the experimental data set.
Two existing CO_2 evaporation heat transfer coefficient correlations are evaluated using 1886 CO_2 evaporation heat transfer coefficient data points.

Table 2: Mean relative and absolute deviations for several studies

	Zhao and Bansal, 2012		**Grauso et al., 2013**		**Hrnjak and Kim,2013**	
	MAD (%)	MRD (%)	MAD (%)	MRD (%)	MAD (%)	MRD (%)
Fang et al., 2013	17.59	-14.24	63.91	-63.63	38.83	22.38
Fang et al., 2017	14.65	-14.65	3.87	-3.87	7.56	-7.65
	Dang et al., 2013		**Choi et al., 2014**		**Hassan and Shedid, 2015**	
	MAD (%)	MRD (%)	MAD (%)	MRD (%)	MAD (%)	MRD (%)
Fang et al., 2013	10.11	2.7	18.45	7.91	24.92	20.41
Fang et al., 2017	6.43	-6.43	3.98	-3.98	3.24	-3.23
	Zhu et al., 2015		**Yoon et al., 2016**		**Chien et al., 2017**	
	MAD (%)	MRD (%)	MAD (%)	MRD (%)	MAD (%)	MRD (%)
Fang et al., 2013	29.04	-23.79	12.07	8.98	18.81	6.39
Fang et al., 2017	1.57	0.98	12.57	-12.57	4.66	0.33
	Linlin et al., 2017		**Jiang et al., 2017**		**Liang et al., 2019**	
	MAD (%)	MRD (%)	MAD (%)	MRD (%)	MAD (%)	MRD (%)
Fang et al., 2013	22.95	19.30	30.03	9.74	18.36	-5.14
Fang et al., 2017	1.86	-1.79	16.25	-5.76	3.44	2.58
	Keniar et al., 2020		**Hellenschmidt et al., 2021**		**Dai et al., 2023**	
	MAD (%)	MRD (%)	MAD (%)	MRD (%)	MAD (%)	MRD (%)
Fang et al., 2013	22.15	3.83	32.78	-25.03	20.78	-18.66
Fang et al., 2017	3.91	-3.81	6.34	3.87	0.33	-0.14
	MAD (%) **(Total mean value)**			MRD (%) **(Total mean value)**		
Fang et al., 2013	25.59	7.03	25.59	7.03	25.59	7.03
Fang et al., 2017	7.74	-5.35	7.74	-5.35	7.74	-5.35

With the comparison of the heat exchange coefficient correlation considered (Fang et al., 2013) and the experimental data, it is noticed that the correlation overestimates the heat exchange coefficient of the experimental data of the Hrnjak and Kim, 2013 study with an average deviation of more than 60% and more than 30% for the study of Dang et al., 2013 and Linlin et al., 2017. The correlation of Fang et al., 2013 gives better results for the study of Dang et al. 2013 and Yoon et al., 2016 with MAD of 10.11% and 12.07% respectively.
With the comparison of the heat exchange coefficient correlation (Fang et al. 2017) with the experimental data, we notice that the study of Zhu et al., 2015 has the best result followed by Chien et al., 2017 with MAD of 1.57% and 1.86%. The obtained data confirm that the correlation of Fang et al., 2017 gives the best results with a MAD of 6.04%

IV. Conclusion

The boiling heat transfer coefficient of CO_2 depends considerably on the vapour quality and the heat flux density. There is a dominance of nucleate boiling in the CO_2 heat transfer mechanism as the heat transfer coefficient strongly depends on the heat flux density. Decreasing the inner diameter of the tubes increases the boiling heat transfer coefficient of CO_2. The obtained results confirm that the correlation of Fang et al., 2017 gives the best results.

References

Abas N., Kalairb A. R., Khan N., Haider A., Saleem Z. and Saleem M. S., (2018). Natural and synthetic refrigerants, global warming: A review. *Renewable and Sustainable Energy Reviews*, 90(C):557–569. doi: 10.1016/j.rser.2018.03.099

Bansal P., (2012). A review - Status of CO_2 as a low temperature refrigerant: Fundamentals and R&D opportunities. Applied Thermal Engineering, 41:18–29. doi: 10.1016/j.applthermaleng.2011.12.006

Cheng L., Ribatski G. and Thome J., (2008). New prediction methods for CO2 evaporation inside tubes: Part II – An updated general flow boiling heat transfer model based on flow patterns *International Journal of Heat and Mass Transfer*, 51(1-2):125–135. doi.org/10.1016/j.ijheatmasstransfer.2007.04.001.

Chien N.B., Vu P.Q., Choi K.I. and Oh J.T, (2017). Boiling Heat Transfer of R32, CO_2 and R290 inside Horizontal Minichannel. *Energy Procedia*, 105(5):4822–4827. doi: 10.1016/j.egypro.2017.03.955.

Choi K. I., Oha J.T., Saito K. and Jeong J. S., (2014). Comparison of heat transfer coefficient during evaporation of natural refrigerants and R-1234yf in horizontal small tube. *International Journal of Refrigeration*, 41(5):210–218. doi: 10.1016/j.ijrefrig.2013.06.017.

Dai B., Wu T., Liu S., Qi H., Zhang P., Wang D., Wang X., (2023). Flow boiling heat transfer characteristics of zeotropic mixture CO2/R152a with large temperature glide in a 2 mm horizontal tube. *International Journal of Heat and Mass Transfer*. 218, 124779. doi.org/10.1016/j.ijheatmasstransfer.2023.124779

Dang, N. Haraguchi, T. Yamada, M. Li and Hihara E., (2013). Effect of lubricating oil on flow boiling heat transfer of carbon dioxide. *International Journal of Refrigeration*, 36(1):136–144. doi: 10.1016/j.ijrefrig.2012.09.020.

Fang X., Zhou Z. and Li D., (2013). Review of correlations of flow boiling heat transfer coefficients for carbon dioxide. *International Journal of Refrigeration*, 36(8):2017–2039. doi: 10.1016/j.ijrefrig.2013.05.015.

Fang X., Wu Q. and Yuan Y., (2017). A general correlation for saturated flow boiling heat transfer in channels of various sizes and flow directions. *International Journal of Heat and Mass Transfer*, 107(4):972–981. doi.org/10.1016/j.ijheatmasstransfer.2016.10.125.

Grauso S., Mastrullo R., Mauro A.W. and Vanoli G.P., (2013). Flow boiling of R410A and CO_2 from low to medium reduced pressures in macro channels: Experiments and assessment of prediction methods. *International Journal of Heat and Mass Transfer*, 56(1-2):107–118, 2013. doi.org/10.1016/j.ijheatmasstransfer.2012.09.015.

Hassan M.A.M. and Shedid M. H. Experimental investigation of two phases evaporative heat transfer coefficient of carbon dioxide as a pure refrigerant and oil contaminated under forced flow conditions in small and large tube. *International Journal of Refrigeration*, 56(8):28–36, 2015. doi: 10.1016/j.ijrefrig.2015.03.027.

Hellenschmidt, D., Petagna, P., (2021). Effects of saturation temperature on the boiling properties of carbon dioxide in small diameter pipes at low vapour quality: Heat transfer coefficient. *International Journal of Heat and Mass Transfer*, 172, 121094. doi:10.1016/j.ijheatmasstransfer.2021.121094

Hrnjak P. and Kim S., (2013). Oil effects on in-tube evaporation of co2 by altering flow regime and properties. *In ASME 2013 Heat Transfer Summer Conference collocated with the ASME 2013 7th International Conference on Energy Sustainability and the ASME 2013 11th International Conference on Fuel Cell Science, Engineering and Technology, ISBN: 978-0-7918-5548-5, Minneapolis, Minnesota, USA, 14–19, July, 2013*. doi.org/10.1115/HT2013-17838. doi.org/10.1016/j.ijheatmasstransfer.2012.09.015.

Keniar, K., Mazzelli, F., Garimella, S., (2020). Experimental investigation of carbon dioxide flow boiling in a single microchannel. *International Journal of Heat and Mass* Transfer,159,120100. doi:10.1016/j.ijheatmasstransfer.2020.120100

Liang X. Z., Linlin J., Jianhua L. and Yue Z., (2019) Investigation of flow boiling heat transfer characteristics of CO_2 in horizontal mini-tube. *International Journal of Thermal Sciences*, 128(4):109–115. doi: 10.1016/j.ijthermalsci.2018.11.032.

Linlin J., Jianhua L., Liang Z., Qi L. and Xiaojin X., (2017). Characteristics of heat transfer for CO_2 flow boiling at low temperature in mini-channel. *International Journal of Heat and Mass Transfer*, 108(B):2120–2129. doi.org/10.1016/j.ijheatmasstransfer.2016.12.113.

Linlin J., Jianhua L., Liang Z., and Xiaojin X., (2017). A research on the dryout characteristics of CO_2's flow boiling heat transfer process in mini-channels. *International Journal of Refrigeration*, 83(11):131–142. doi: 10.1016/j.ijrefrig.2017.07.017.

Yoon J. I., Son C. H., · Jung S. H., Jeon M. J. and Yang D.I., (2017). Evaporation heat transfer of carbon dioxide at low temperature inside a horizontal smooth tube. *Heat and Mass Transfer*, 53:1631–1642. doi.org/10.1007/s00231-016-1922-2.

Zhao X. and Bansal P., (2009). Flow boiling heat transfer analysis of new experimental data of CO_2 in a micro-fintube at -30°C. *Journal of Mechanical Science and Technology*, 23(3):698–706. doi: 10.107/s1226-009-0202-1.

Zhu Y., Wu X. and Wei Z., (2015). Heat transfer characteristics and correlation for CO_2/propane mixtures. Applied Thermal Engineering, 81(4):253–261. doi: 10.1016/j.applthermaleng.2015.02.009.

IEEES-075

Microalgae Derived Biostimulants for Sustainable Agriculture Exergoeconomic Analysis

[1,2*]N. Melenek , [2,3*]M. Gasparin, [2,3*]G. Conor, [1,2*]A. C. D. Oliveira, [2*]K. Melenek, [1,2,3,4*]A. B. Mariano, [2,5*]V. M. Kava, [1,2,3,6*]J. V. C. Vargas.
[1] Graduate Program in Materials Science Engineering (PIPE), Federal University of Parana (UFPR), Curitiba, 81531-980, Brazil
[2] Sustainable Energy Research and Development Center (NPDEAS), Federal University of Parana (UFPR), Curitiba, 81531-980, Brazil
[3] Graduate Program in Mechanical Engineering (PGMEC), and Department of Mechanical Engineering, Federal University of Parana (UFPR), Curitiba, 81531-980, Brazil
[4] Department of Electrical Engineering, Federal University of Parana (UFPR), Curitiba, 81531-980, Brazil
[5] Department of Genetics, Federal University of Parana (UFPR), Curitiba, 81531-980, Brazil
[6] Department of Mechanical Engineering, Federal University of Parana (UFPR), Curitiba, 81531-980, Brazil
*E-mails: nicholassjp15@gmail.com, murilorampi@gmail.com, gabiconor@gmail.com, annewcaroline@yahoo.com.br, kauemelenek@ufpr.br, andrebmariano@gmail.com, vanessagenetica@gmail.com, vargasjvcv3@gmail.com

Abstract

The use of microalgae-based biostimulants is a promising avenue for boosting sustainability in contemporary agriculture. This research explores the thermoeconomic feasibility of an all-encompassing system designed to produce microalgae derived biostimulants, including an incinerator, heat exchanger, fixation column, photobioreactor, flocculator, centrifuge, dryer, and the application of the produced biomass as biostimulant. The system technical and economic feasibility is examined through an exergoeconomic analysis, which combines principles of thermodynamics and economics to evaluate the system's performance considering energy consumption, exergy losses, and economic aspects associated with each stage. The results show that the microalgae derived biostimulant system can provide a meaningful return on investment, which also means economic viability. The obtained energetic and environmentally friendly plant growth promoters in cogeneration are the key aspects of the study: i) Electricity is generated efficiently using an incinerator to convert municipal solid waste (MSW) into heat to supply a steam Rankine cycle (SRC) power plant, and ii) The photosynthetic process in a large scale microalgae cultivation photobioreactor captures and converts carbon dioxide and other greenhouse gas emissions from the incineration process into biomass, thus allowing for carbon and harmful substances sequestration (e.g., NO_x, dioxins, furans), so that only non-harmful gases are eventually released to the atmosphere. The final product, i.e., the microalgae derived natural biostimulant, enhances soil quality, reduces the need for artificial chemical fertilizers, minimizes nutrient runoff, and improves crops health thereby promoting sustainable agricultural practices. In sum, the system exergoeconomic analysis demonstrates the system potential to provide substantial economic gains while simultaneously offering significant environmental benefits. By generating "clean" electricity, adequately disposing MSW, reducing greenhouse gas emissions, sequestering carbon, and promoting sustainable agriculture, this innovative approach stands as a promising solution for addressing the growing demand for eco-friendly agricultural practices and sustainable energy and food production.

Keywords: mathematical model, sustainability, cogeneration, exergy analysis.

I. Introduction

In the face of mounting challenges to essential resources such as land and water due to population growth, economic development, and climate change, industries are pivoting toward sustainable practices. This paradigm shift is underscored by a pressing need to reevaluate the environmental impact of various sectors, including agriculture (Retallack, 2020; Rask, 2011; Lang, 2014). Modern agricultural practices, driven by increased demand and evolving climate conditions, heavily rely on fertilizers and chemicals to boost crop yield and resilience. However, stringent regulations on synthetic fertilizers have prompted a quest for eco-friendly alternatives, leading to the emergence of microalgae biomass as a promising biostimulants (Ronga, 2019).

Microalgae, as single-celled, rapidly reproducing microorganisms, have shown remarkable potential in positively influencing crop growth and environmental remediation (Furlan et al., 2020). Their significance in global photosynthesis and bioremediation, particularly in cleaning atmospheric air through photosynthesis, positions them as valuable contributors to sustainable agriculture (Navarro, 2021; Mazepa, 2021; Corbellini, 2020). Yet, despite extensive research on the techno-economic aspects of microalgal biomass production, a crucial gap exists in the literature concerning the exergy and exergoeconomic analysis of processes involving CO_2 fixation by microalgae and the subsequent use of biomass as biostimulants. This study aims to bridge this gap by developing a mathematical model for the thermodynamic analysis of a photobioreactor plant incorporating a CO_2 fixation column and a municipal solid waste (MSW) incinerator with energy recovery. By evaluating exergoeconomic feasibility, the study seeks to provide valuable insights into the potential of utilizing microalgae biomass as biofertilizers in the pursuit of sustainable agriculture.

To be able to evaluate and maximize the performance of the system, methods of entropy generation minimization (EGM), exergy analysis (EA), and exergoeconomics (EE) have been used. These three methods are established aspects of the evolution of thermodynamics in recent decades (Vargas et al., 2000; Ordonez, 2003).

II. System Description

All the facilities and equipment utilized for the growth of microalgae, production of dry biomass, and the incinerator system utilizing

MSW are installed at the NPDEAS (Sustainable Energy Research and Development Center) situated in the Federal University of Paraná (UFPR), located in Curitiba, Brazil.

In the incinerator system, electricity is generated efficiently using municipal solid waste (MSW) and methane as hybrid fuel, converting into heat to supply a steam Rankine cycle (SRC) power plant. The gas emissions from this system go through a heat exchange system to cool the gas temperature, ensuring it remains below 35°C to avoid harming the microalgae cultivation. Water is utilized in this system and can be recycled at higher temperatures.

The next step involves the gas fixation column, where the gases pass through and interact with the microalgae cultivation. This interaction primarily focuses on absorbing necessary components, especially CO_2 gas, which is essential for microalgae photosynthesis. A 12m³ closed-type tubular photobioreactor is utilized to maintain greater control over gas flow and cultivation temperature, this system allows high photosynthetic rates due to its optimized design that allows a maximized sunlight exposure in a small area. An electric pump facilitates the cultivation flow within the system and enables interaction with the gas fixation column, allowing for the capture of CO_2. Throughout the day, photosynthesis occurs, multiplying the microalgae biomass with the absorption of sunlight.

To prepare the biomass for various applications, including its use as an organic biostimulant, it needs to be in a dry form. Several steps are involved in achieving this dry biomass state. The first step is flocculation, where a specific amount of flocculating agent is added to the cultivation volume. The volume is stirred to ensure even distribution of the flocculant. After stirring, the material settles to facilitate decantation, enabling the removal of a volume of water without the biomass. Following flocculation, the biomass still retains a significant amount of water. Therefore, centrifugation is employed to further concentrate the biomass, removing 80% of the remaining water in the system.

The final step in producing dry biomass involves the use of heat-generating equipment, such as an oven or drying chamber. This equipment ensures the complete removal of remaining water from the biomass. To prevent damage to the biomass, a temperature of 60°C is used over an extended period.

Once the dry biomass is obtained, it can be directly applied as an organic biostimulant without requiring any additional steps. By assessing the increase in material and examining potential changes in internal energy resulting from the use of biomass as a fertilizer, we can evaluate the benefits and costs associated with this method, this stage is called Plant Growth Promoter (PGP) production process.

A schematic diagram of the system with the mass and energy flow are presented in Fig. 1.

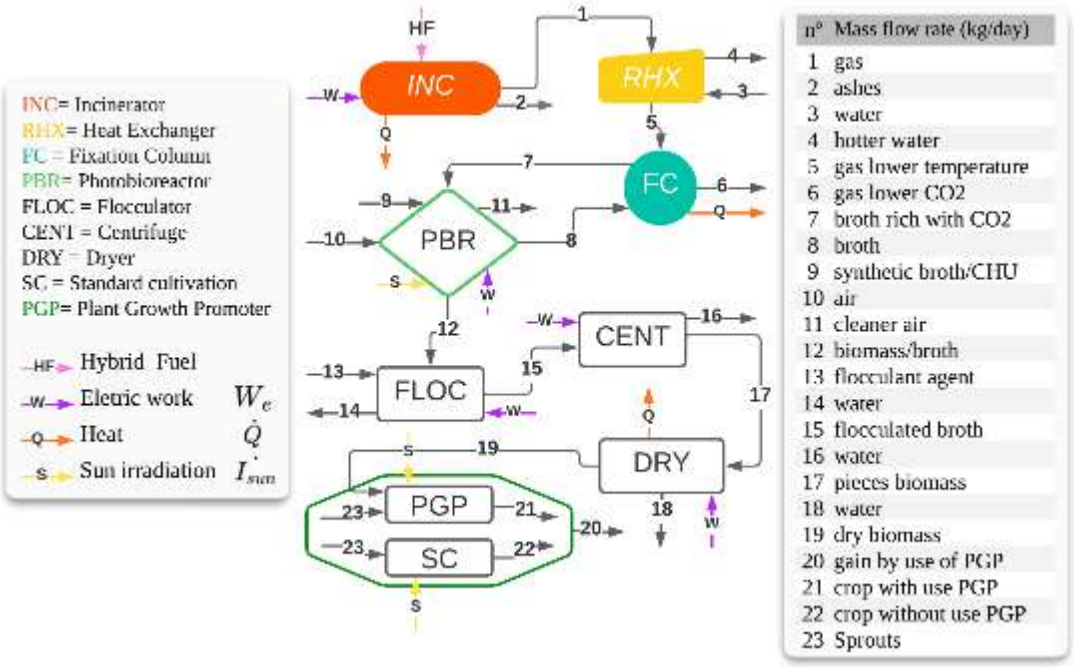

Fig. 1: Schematic diagram of the system under analysis.

III. Exergy and Thermoeconomic Analysis

In addition to the mass and energy balance, this paper will leverage exergy equations for a thorough exergoeconomic analysis. The exergy balance equation (Eq. 1) directs attention to the exergy rate (E), representing the system's maximum work potential, and the rate of exergy destruction (E_D). This equation encompasses the exergy associated with both incoming and outgoing mass within the system, along with the work executed (Bejan, 2006).

$$E_q + \Sigma E_{in} = W + \Sigma E_{out} - E_D \quad (1)$$

To determine the exergy rate (Eq. 2), the product of specific exergy (e_x) and the mass flow rate (m_x) is calculated.

$$E_x = m_x e_x \quad (2)$$

The determination of specific exergy (e) relies on Equation 3, incorporating diverse properties such as specific internal energy (u), volume (v), entropy (s), kinetic energy ($V^2/2$), and potential energy (gz). The subscripts "0" are indicative of the reference or initial state for these properties (Bejan, 2006).

$$e = (u-u_0) + p_0(v-v_0) - T_0(s-s_0) + \frac{V^2}{2} + gz \quad (3)$$

Equation 4 delineates the correlation between exergoeconomics and energy systems, elucidating the intricate connection between costs

and exergy flows within the system. Each component's costs are multiplied by their corresponding exergy rates, encompassing the investment, maintenance, and operational capital costs of the system denoted by the term Z (Bejan, 2006).

$$\Sigma c_{out} E_{out} + c_w W = c_q E_q + \Sigma c_{in} E_{in} + Z \quad (4)$$

Where c represents the costs of each component (BRL/kg), w is the work performed, Eq is the exergy in the form of heat, and Z is the sum of cost rates associated with the investment (Z_{CI}), maintenance, and operation capital of the system (Z_{OM}) (BRL/kg) (Bejan, 2006).

IV. Results and discussion

The 12 m^3 PBR system geometric and operating parameters utilized to produce results for this study could be found in the work of Ribeiro et al. (2017). The exergoeconomic analysis was used to determinate the final cost of each stream presented in Fig. 1. The result of the exergy, specific exergy and cost of each component are shown in Table 1.

Table 1. Exergoeconomic results for each component.

nº	Mass flow rate	m (kg/day)	E (kJ/day)	e (kJ/kg)	c (BRL/kJ)	C (BRL/day)
1	Gas	1.27E+04	4.16E+06	3.28E+02	1.26E-04	1.60E+00
2	Ashes	2.40E+01	1.80E+04	7.49E+02	1.26E-04	3.02E-03
3	Water	6.54E+09	0.00E+00	0.00E+00	4.25E-06	2.78E+04
4	Hotter water	1.51E+05	3.27E+06	2.16E+01	4.25E-06	6.43E-01
5	Gas lower temperature	1.27E+04	1.90E+04	1.50E+00	2.77E-02	3.51E+02
6	Gas lower CO2	1.14E+04	1.90E+04	1.67E+00	2.82E-02	3.21E+02
7	Broth rich with CO2	3.60E+04	1.71E+03	4.74E-02	4.25E-06	1.53E-01
8	Broth	3.60E+04	1.71E+03	4.75E-02	4.25E-06	1.53E-01
9	Synthetic broth/CHU	8.57E+02	0.00E+00	0.00E+00	4.25E-06	3.64E-03
10	Air	1.62E+05	0.00E+00	0.00E+00	0.00E+00	0.00E+00
11	Cleaner air	1.62E+05	0.00E+00	0.00E+00	0.00E+00	0.00E+00
12	Biomass/broth	8.57E+02	1.97E+03	1.61E+04	2.71E+03	2.32E+06
13	Flocculant agent	8.57E-01	-	-	-	-
14	Water	7.29E+02	0.00E+00	0.00E+00	4.25E-06	3.09E-03
15	Flocculated broth	1.30E+02	1.97E+03	1.61E+04	2.77E+03	3.59E+05
16	Water	1.29E+02	0.00E+00	0.00E+00	4.25E-06	5.48E-04
17	Pieces biomass	6.12E-01	1.97E+03	1.61E+04	2.77E+03	1.70E+03
18	Water	4.90E-01	4.84E+00	9.88E+00	4.25E-06	2.08E-06
19	Dry biomass	1.22E-01	1.97E+03	1.61E+04	2.77E+03	3.39E+02
20	Gain by use of PGP	3.00E+00	1.88E+03	6.28E+02	2.90E+03	8.71E+03
21	Crop with use PGP	1.30E+01	8.16E+03	6.28E+02	-	-
22	Crop without use PGP	1.00E+01	6.28E+03	6.28E+02	-	-
23	Sprouts	-	-	-	-	-

It is important to note the exergetic gain of the cultivation mass when we compare the addition or non-addition of the biostimulant, as highlighted in stream 20. This mass and exergetic gain implies a better product with higher added value compared to the common treatment. The analysis was extended to consider the initial investment, maintenance, and operation capital of the system. The results are shown in Table 2.

Table 2. Sum of costs for each stage.

Stage	Abbreviation	Z_{OM} (annual, BRL)	Z_{CI} (annual, BRL)	E_D(kJ/day)
Centrifuge	CENT	5.00E+02	6.00E+03	1.14E-03
Dryer	DRY	2.41E+04	1.00E+03	2.17E+02
Fixation Column	FC	0.00E+00	5.00E+03	1.29E+04
Flocculator	FLOC	0.00E+00	1.00E+02	4.29E-05
Incinerator	INC	9.60E+04	1.50E+04	2.21E+06
Photobioreactor	PBR	2.55E+04	2.00E+04	9.00E+01
Plant Growth Promoter	PGP	2.40E+04	5.00E+02	1.85E+03
Heat Exchanger	RHX	1.00E+03	5.00E+03	8.71E+05

In Table 2, it is evident that the PBR incurs the highest operational cost, attributed to its substantial installation, operational, and maintenance expenses. The exergy destruction in this stage remains notably elevated, indicating significant process losses. This highlights the potential for improvements to mitigate the exergy destruction and enhance the overall efficiency of the system. In the incinerator, we also observe a high level of exergy destruction due to the combustion process. Heat losses and incomplete combustion of fuels contribute to the elevated rate of exergy destruction in this procedure.

V. Conclusion

In conclusion, the exergoeconomic analysis revealed that the exergetic cost of using biomass as a promoter of plant growth is 2,902 BRL/kJ. Despite the implementation of a Rankine cycle, which reduces electricity expenses, the construction and maintenance costs

of the system remain prohibitively high. Each PBR can sequester 1363 kg of carbon per year, a value that, while offering a reward for carbon capture, is relatively low when considering the overall system costs, including operation and maintenance.
Given that the primary expense is associated with biomass production in the PBR, exploring alternatives such as using swine manure as a nutrient source for cultivation could be viable. Additionally, further exploration of the potential of bio-stimulants is warranted, as plants benefiting from the Plant Growth Promotion effect tend to have greater mass, leading to increased photosynthesis and carbon capture. Therefore, evaluating carbon capture through planting as a holistic gain for the entire system is worth consideration.

Acknowledgements
This research was carried out thanks to the technical support of the Sustainable Energy Research and Development Center - NPDEAS, from UFPR. To the Brazilian National Council of Scientific and Technological Development - (CNPq). To the ANP Human Resources Program - PRH 12.1, FINEP management. And finally, we also thank to the Brazilian Higher Education Personnel Improvement Coordination - (CAPES).

References

Bejan, A., (2006). Advanced engineering thermodynamics, 3rd Edition. Wiley, New York, NY. https://doi.org/10.1109/TNSRE.2003.814453

Corbellini, Joana Rosar; Ribas, Luciana Lopes Fortes; de Maia, Fabiano Rodrigo; Corrêa, Diego de Oliveira; Noseda, Miguel Daniel; Suzuki, Rogério Mamoru; Amano, Érika. Effect of Messastrum gracile and Chlorella vulgaris on the in vitro propagation of orchid Cattleya labiate. Journal of Applied Phycology, v. 32, p. 4013-4027, 2020. DOI: 10.1007/s10811-020-02251-9

Furlan, Beatriz Jacob; Zatta, Pedro Henrique Siqueira; Antenaza, Valeria Cristina Pereira; Martins, Lauber de Souza; Mariano, André Bellin., 2021. Estudo do crescimento de microalgas em meio de cultivo CHU e dejetos suínos. Meio Ambiente, Sustentabilidade e Tecnologia, Volume 6. 1ed. Belo Horizonte, Minas Gerais.: Editora Poisson, v. 6, p. 204-211. http://dx.doi.org/10.36229/978-65-5866-094-1.CAP.24.

Lang, T I M. "Sustainable Diets: Hairshirts or a Better Food Future?" Development (Society for International Development)57.2 (2014): 240-56. Web. DOI:10.1057/dev.2014.73

Mazepa, Ester, et al. "Plant growth biostimulant activity of the green microalga Desmodesmus subspicatus." Algal Research 59 (2021): 102434. DOI:10.1016/j.algal.2021.102434

Navarro, Quezia Rocha, et al. "Efficient use of biomass and extract of the microalga Desmodesmus subspicatus (Scenedesmaceae) in asymbiotic seed germination and seedling development of the orchid Cattleya warneri." Journal of Applied Phycology 33.4 (2021): 2189-2207. DOI:10.1007/s10811-021-02442-y

Ordonez, J.C., Integrative Energy-Systems Design: System Structure from Thermodynamic Optimization, PhD Dissertation, Duke University, 2003.

Rask, Kolleen J., and Norman Rask. "Economic development and food production–consumption balance: a growing global challenge." Food Policy 36.2 (2011): 186-196. DOI:10.1016/j.foodpol.2010.11.015

Retallack, Gregory J., and Giselle D. Conde. "Deep Time Perspective on Rising Atmospheric CO2." Global and Planetary Change 189 (2020): 103177. Web. DOI:10.1016/j.gloplacha.2020.103177

Ribeiro, R. L. L.; Vargas, J. V. C. ; MARIANO, A. B. ; ORDONEZ, J. C. . The experimental validation of a large-scale compact tubular microalgae photobioreactor model. INTERNATIONAL JOURNAL OF ENERGY RESEARCH, v. 41, p. 2221-2235, 2017. http://dx.doi.org/10.1002/er.3784

Ronga, Domenico, et al. "Microalgal biostimulants and biofertilisers in crop productions." Agronomy 9.4 (2019): 192. DOI:10.3390/agronomy9080469

Vargas, J., Ordonez, J., and Bejan, A., Power Extraction from a Hot Stream in the Presence of Phase Change, Int. J. Heat Mass Transf., vol. 43, no. 2, pp. 191–201, 2000. DOI:10.1016/S0017-9310(99)00146-5

IEEES-076

Design of an Electro Bio-membrane Reactor for Simultaneous Biohydrogen Production, Desalination, and Bacterial Energy Generation

[1,2*]A. Yagmur Goren, [1]Ibrahim Dincer, [3]Ali Khalvati
[1]Clean Energy Research Laboratory (CERL), Faculty of Engineering and Applied Science, Ontario Tech. University, 2000 Simcoe Street North, Oshawa, Ontario L1G 0C5, Canada
[2]Izmir Institute of Technology, Faculty of Engineering, Department of Environmental Engineering, Urla, Izmir 35430, Turkey
[3]Viona Consulting INC., Agro-Environmental Innovation and Technology, Research and Development Company, Thornhill, Ontario L3T 0C6, Canada
*E-mails: yagmurgoren@iyte.edu.tr

Abstract

Clean energy source biohydrogen ($bioH_2$) can be utilized as an alternative fuel. Abundant biomass from a variety of categories might be used to produce $bioH_2$, where it would be advantageous to combine waste treatment with the production of energy. Hence, utilizing energetic poplar biomass for $bioH_2$ production using a dark fermentation (DF) process is one of the critical objectives of this study. On the other hand, the key novelty of this study lies in developing a unique electro-bio-membrane reactor for concurrent $bioH_2$ production, desalination, and energy production by microorganisms in a single reactor. In this regard, the effect of biomass amount (5-50 g) on $bioH_2$ production efficiency was also considered. The lowest cumulative $bioH_2$ yield of 24.2 mL/g-biomass was obtained using a biomass amount of 5 g, while it was 44.7 mL/g-biomass at a biomass amount of 50 g. The highest H_2 production from water electrolysis was 0.719 mL/min at improved conditions. Moreover, the highest power and current density values were 2794.5 mW/m^2 and 2786.1 mA/m^2 at 1500 mL-inoculum, biomass amount of 30 g, initial pH of 5.5, and temperature of 37 °C in the DF cell. Overall, this study proved that the electro-bio-membrane reactor is a sustainable process thanks to simultaneous H_2 production, desalination, and bacterial energy production.

Keywords: Dark fermentation, poplar leaves, biohydrogen production, bio-membrane, desalination.

I. Introduction

Clean energy resources have become increasingly crucial to addressing the worldwide problems of energy scarcity and environmental degradation (H. Chen et al., 2022). Hydrogen (H_2) is the most promising green fuel among various alternative renewable and clean energy resources because of its high energy potential, efficiency in conversion, and environmental sustainability. Numerous techniques, including the thermochemical conversion of natural gas or coal, greener chemical procedures, and electrolysis, can be used to produce H_2 (Goren et al., 2023). However, providing sustainable H_2 production involves guaranteeing low energy utilization, commercial applicability, economic feasibility, and carbon neutrality (Anto et al., 2020). In this regard, biohydrogen ($bioH_2$) production pathways have received a lot of attention because, although the majority of commercial H_2 production technologies are based on thermochemical processes, they typically involve significant consumption of fossil fuels and necessitate combining H_2 production with carbon capture and storage to achieve the goal of carbon neutrality. The $bioH_2$ production is a carbon-neutral process that may benefit from thermochemical and electrochemical methods, including the lowest energy requirements due to its low temperature and pressure operation (Ananthi et al., 2022). On the other hand, inadequate $bioH_2$ production rate and insufficient substrate conversion present serious practical problems for $bioH_2$ technology (Chen et al., 2022). Therefore, various methods have been presented for designing bioreactors, optimizing fermentation media, and creating effective $bioH_2$-producing bacteria (Ramu et al., 2021).
In this context, most of the research in the literature focuses on the production of $bioH_2$. However, there is a significant knowledge gap in the concurrent $bioH_2$ production, energy production, and desalination in a single system. Therefore, this study aimed to develop a novel there-chambered electro bio-membrane reactor for mainly $bioH_2$ production based on the dark fermentation (DF) process from energetic poplar with anaerobic sludge. Furthermore, the effect of biomass and inoculum amount in the DF cell was studied considering $bioH_2$ production, bacterial energy production, and desalination. Consequently, it should be noted that this is the first comprehensive study investigating simultaneous $bioH_2$ production with DF process, H_2 production with water electrolysis, water desalination with membrane separation, and energy production by microorganisms.

II. Experimental Procedure/Methodology/System Description

The three-chambered electro-biomembrane reactor comprises three cells made of plexiglass: DF, desalination, and electrolysis cells with an operational volume of 2 L (Fig. 1). To guarantee airtightness, cells were clamped together. Anode and desalination cells were separated by an anion exchange membrane (AEM), and desalination and cathode cells were separated by a cation exchange membrane (CEM). The flexible carbon graphite plates are used as an anode and cathode electrodes. DF cell feed with anaerobic sludge from a wastewater treatment facility, and acid-treated energetic poplar as a biomass source. 1 M potassium hydroxide (KOH) solution was used as the electrolyte in the electrolysis cell. In the desalination cell, 10 g/L of sodium chloride (NaCl) solution was used, and the desalination performance was measured considering its conductivity.

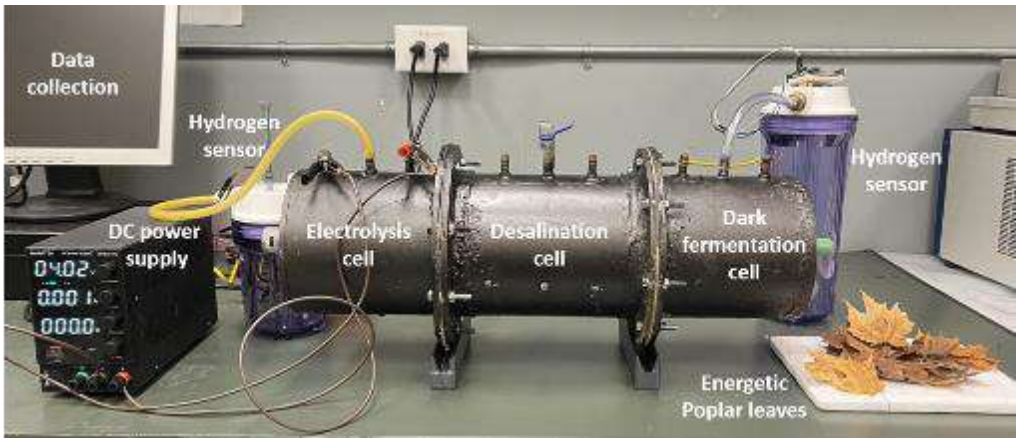

Fig. 1: Experimental set-up of the three-chambered electro-biomembrane reactor.

III. Analysis

The pH in the DF cell and electrical conductivity in the desalination cell to determine desalination performance were measured using a pH and conductivity meter, respectively. Moreover, to evaluate the organic matter removal, the chemical oxygen demand (COD) was measured using a spectrophotometer. The produced H_2 gas from the DF and electrolysis cells was analyzed with an MQ8-H_2 sensor. Furthermore, a multimeter was utilized to record voltage in the open circuit, which is produced by microorganisms with organic matter degradation in the DF cell. Total amount of H_2 produced for each time period was used to calculate the cumulative H_2 production as follows:

$$V_{H_{2,t}} = C_{H_{2,t}} \times V_{BG,t} + V_{HS} \times \left(C_{H_{2,t}} - C_{H_{2,t-1}}\right) \quad (1)$$

where $V_{H_{2,t}}$ is the volume of H_2 produced between t and t-1; $C_{H_{2,t}}$ and $C_{H_{2,t-1}}$ is the concentrations of H_2 measured at periods t and t-1, respectively; and $V_{BG,t}$ and V_{HS} is the volume of biogas produced from time t until time t-1 and headspace volume of the reactor, respectively. Then, the cumulative H_2 ($V_{H_{2,cum}}$) production was determined as a sum of H_2 productions between each measurement ($V_{H_{2,t}}$) during fermentation. In addition, H_2 yield is defined as mL H_2/g biomass and calculated using $V_{H_{2,cum}}$ and weight of added biomass ($W_{biomass}$) as follows:

$$H_2\ yield\ (mL\ H_2/g\ biomass) = \frac{V_{H2,cum}}{W_{biomass}} \quad (2)$$

Moreover, the cell voltage (V) in the DF, which is produced by microorganisms with organic matter degradation, was measured with a data aquation device at specified time intervals. The current (I, mA) was determined with $I=V/R_{ex}$. Power density (P_{An}, mW/m^2) normalized by surface area was calculated with the cross-sectional area of the carbon electrode (Ael, m^2) due to the microbial reactions occurring in the DF cell.

4. Results and discussion

The biomass amount is a critical operational parameter in the DF process, as it is utilized as a nutrient source for microorganisms. In this paper, the effect of biomass amount was studied at a temperature of 37 °C, initial pH of 5.5, and inoculum amount of 1000 mL during the retention time of 24 h. The effect of the biomass amount on the bioH_2 production in the DF cell is presented in Fig. 2. The lowest cumulative bioH_2 production of 120.8 mL and yield of 24.2 mL/g-biomass was achieved using a biomass amount of 5 g (Fig. 2a) since low biomass concentrations may cause long lag-phase time and slow fermentation rates. On the other hand, the bioH_2 production increased with the increment in retention time. For example, the bioH_2 production yield increased from 5.26 to 24.2 mL/g-biomass with increasing operating time from 2 to 24 h at a biomass amount of 5 g. Furthermore, the highest bioH_2 production yields were 28.5, 40.2, and 44.7 mL/g-biomass for biomass amounts of 10, 30, and 50 g, respectively (Fig. 1b).

In addition, during the H_2 production processes, the desalination efficiency of the system was investigated by considering the conductivity of the 10 g-NaCl/L solution at different biomass amounts. The highest desalination efficiencies were 57.2% for biomass amount of 5 g and 49.3% for biomass amount of 50 g. The reason for the relatively low desalination efficiencies observed in high biomass amounts is related to the small difference in concentration gradient between the desalination and DF cells. The bacterial energy production performance of the system was also evaluated at various biomass amounts. The maximum voltage values produced in the DF cell, for biomass amounts of 5, 10, 30, and 50 g were 842, 968, 1015, and 1012 mV, respectively. Based on the electrode surface area of 36 cm^2, the highest power and current density values were 2844.8 mW/m^2 and 2811.1 mA/m^2 using 50 g-biomass. These results proved that bacterial energy production enhanced with the increasing biomass amount.

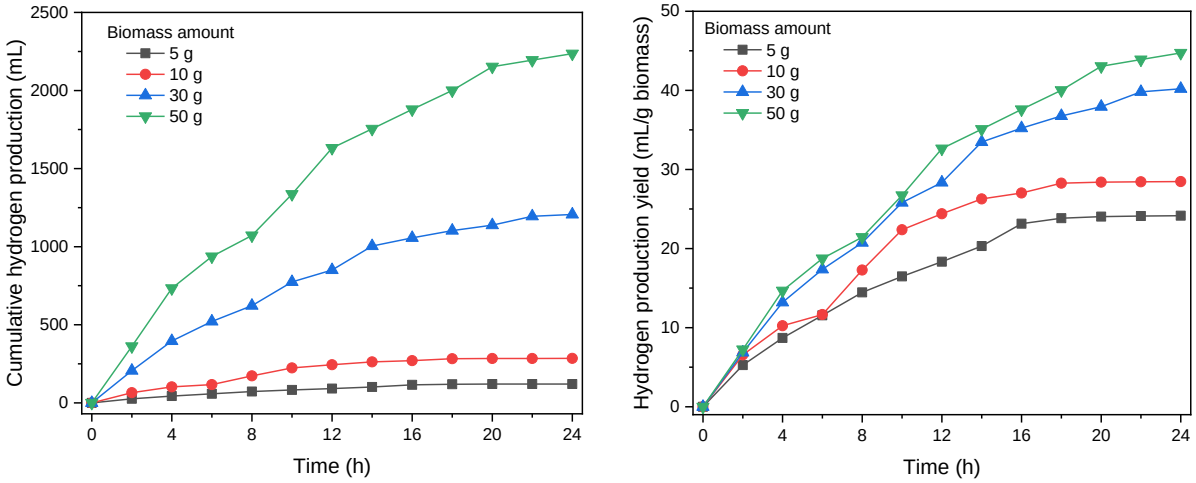

Fig. 2. Cumulative H_2 production (a) and H_2 production yield (b) in the DF cell at different biomass amounts.

5. Conclusions

Generally, novel electro bio-membrane reactor provided concurrent and effective bioH_2 production from energetic poplar, H_2 production from water electrolysis, desalination, and energy production by microorganisms. Specifically, it was observed that the biomass and inoculum amount have improving effects on the bioH_2 production and bacterial energy during the start-up of the DF process of the energetic poplar and through the retention time to the end of the experimental runs. At improved operating conditions (initial pH of 5.5, temperature of 37 °C, and inoculum amount of 1000 mL), as the biomass amount was increased from 5 to 50 g, the bioH_2 yield was increased from 24.2 to 44.7 mL/g-biomass. On the other hand, the increasing biomass presented a negative effect on the desalination performance of the system. In addition, the power and current density values were 2861.7 mW/m^2 and 2819.4 mA/m^2, respectively. Consequently, this study demonstrated effective, sustainable, and promising bioH_2 production using energetic poplar biomass with concurrent water desalination and bacterial energy production in electro bio-membrane reactor.

References

Ananthi, V., Ramesh, U., Balaji, P., Kumar, P., Govarthanan, M., Arun, A., 2022. A review on the impact of various factors on biohydrogen production. Int. J. Hydrogen Energy.

Anto, S., Mukherjee, S.S., Muthappa, R., Mathimani, T., Deviram, G., Kumar, S.S., Verma, T.N., Pugazhendhi, A., 2020. Algae as green energy reserve: Technological outlook on biofuel production. Chemosphere 242, 125079.

Chen, H., Wu, J., Huang, R., Zhang, W., He, W., Deng, Z., Han, Y., Xiao, B., Luo, H., Qu, W., 2022. Effects of temperature and total solid content on biohydrogen production from dark fermentation of rice straw: Performance and microbial community characteristics. Chemosphere 286, 131655.

Chen, W., Li, T., Ren, Y., Wang, J., Chen, H., Wang, Q., 2022. Biological hydrogen with industrial potential: Improvement and prospection in biohydrogen production. J. Clean. Prod. 135777.

Goren, A.Y., Dincer, I., Khalvati, A., 2023. A Comprehensive Review on Environmental and Economic Impacts of Hydrogen Production from Traditional and Cleaner Resources. J. Environ. Chem. Eng. 111187.

Ramu, S.M., Dinesh, G.H., Thulasinathan, B., Thondi Rajan, A.S., Ponnuchamy, K., Pugazhendhi, A., Alagarsamy, A., 2021. Dark fermentative biohydrogen production from rice mill wastewater. Int. J. Energy Res. 45, 17233–17243.

IEEES-077

Analysis of PEM Fuel Cell System Efficiency Using Machine Learning Algorithms

[1*]Emre KACMAZ, [1]Burcu YILMAZEL
[1] Eskişehir Technical University, Faculty of Engineering, Department of Computer Engineering, Eskişehir, 26100, Türkiye
*E-mails: emrekacmaz@eskisehir.edu.tr, byurekli@eskisehir.edu.tr

Abstract

Proton exchange membrane (PEM) fuel cells are one of the preferred fuel cell types, especially in vehicles and portable devices, due to their high-power density and energy conversion efficiency, small footprint, lightness and low operating temperature. The performance of a PEM fuel cell depends strongly on various structural (catalyst layer components, membrane material and thickness, GDL composition, flow channels, bipolar plate material, etc.) and operational parameters (operating temperature, reactant inlet/outlet relative humidity, pressurization state, reactant flow rates etc.) and studies have focused on improving PEM fuel cell performance with different approaches. In order for PEM fuel cell technology to perform better than existing technologies, machine learning and artificial intelligence-based methods are used to take into account various factors simultaneously and facilitate the design and applications of the PEM fuel cell. Within the scope of this study, it is aimed to run different PEM fuel cell inputs with machine learning algorithms. For this purpose, Linear Regression and *k*-Nearest Neighbors (*k*-NN) algorithms were used and the results were compared.

Keywords: PEM Fuel Cell, Machine Learning, Linear Regression, K-Nearest Neighbors.

I. Introduction

The rapid increase in climate change and environmental problems caused by fossil fuels, along with the gradual decrease in traditional energy sources, has attracted the attention of academic researchers, investors and policy makers around the world to hydrogen as one of the potential alternatives in the transition from fossil sources to renewable resources. Hydrogen is currently used for power generation in many systems such as hydrogen gas turbines and micro hydrogen fuel combustors (Alizadeh and Torabi, 2021). One of the technologies and applications where hydrogen is used is fuel cells. Fuel cells are clean, environmentally friendly and highly efficient energy conversion technologies. The fuel cell works on the principle of converting the chemical energy of the fuel into electrical energy, heat energy and water through electrochemical reactions (Saco et al., 2022). Proton exchange membrane (PEM) fuel cells have become the most preferred fuel cell type, especially in vehicles and mobile devices, due to their superior features such as high-power density (350 mW/cm^2), high energy conversion efficiency (45%-60%), low operating temperatures (50°C-80°C), compact system and light weight. PEM fuel cell consists of a polymer electrolyte membrane (specifically Nafion), a platinum (Pt)-based catalyst, a gas diffusion layer with electrical and thermal conductivity, and a bipolar plate. Although attempts to commercialize PEM fuel cells are rapidly expanding, the cost of fuel cells remains high. The high cost of PEM fuel cells is primarily due to expensive electrode materials and proton exchange membranes. Other significant contributions to fuel cell stack costs come mainly from stainless steel and coating for bipolar plates, perfluorosulfonic acid (PFSA) ionomer for the membrane, and similar materials. Obtaining cheaper alternatives to these materials, reducing the need for these materials, and achieving the highest power efficiency from the available material combination is a priority to make fuel cell applications more economically viable. In addition, it is also important to determine the appropriate cell operating conditions (cell pressure, flow rates of gases, relative humidity of gases, operating temperature, etc.) in order to reduce PEM fuel cell costs and increase performance (Karanfil, 2020). Analyzing and optimizing the performance of PEM fuel cells according to operating conditions and structural parameters is a meaningful field to meet the need for commercialization, especially considering that PEM fuel cell has attracted worldwide attention in recent years for transportation and stationary power systems applications (Li et al., 2021). In order for PEM fuel cell technology to perform better than existing technologies, machine learning algorithms are used to facilitate the design and applications of PEM fuel cells that are flexible enough to take into account various factors simultaneously. Machine learning algorithms show great potential in advanced PEM fuel cell technology by facilitating the development of fundamental knowledge and correlations, material selection and advancement, fuel cell design and optimization, system control, power management and operational status monitoring (Wang et al., 2020).
Within the scope of this study, it was aimed to run PEM fuel cell parameters with two different machine learning algorithms, namely Linear Regression and *k*-Nearest Neighbors, and determine the most consistent form of the results. In accordance with this purpose; Nafion membrane percentage, cathode relative humidity, pressure and membrane compression ratio and cell voltage were accepted as input, and the current density value obtained according to different input values was accepted as output. Factors affecting PEM fuel cell performance were predicted with machine learning models, and the adequacy of two different machine learning algorithms on PEM fuel cell efficiency was investigated.

II. Methodology

In this study, two different machine learning algorithms were applied to a PEM fuel cell dataset comprising 651 rows of experimental data, with the primary objective of optimizing PEM fuel cell performance. The assessment of model efficacy was conducted through the computation of key performance metrics for models derived from the application of the Linear Regression and *k*-Nearest Neighbors algorithms.

Machine learning algorithms

Machine learning, a subfield of artificial intelligence, involves the creation of computer systems that autonomously enhance performance through experience, implementing a learning process. This paradigm is particularly advantageous for automatically extracting valuable information from extensive datasets, constructing robust probability models, and addressing scenarios where

abundant data exists without a well-established general theory (Ayodele, 2010). The design and development of algorithms, facilitating computers to learn, constitute the core of machine learning. Machine learning algorithms enable the automatic creation of mathematical models grounded in training data, extending their utility to practical domains like web search, spam filters, and stock trading (Tian, 2020). Notably, this technique, allowing systems to adapt and glean insights from vast and varied datasets based on prior experiences, has found application in optimizing PEM fuel cells.

Linear Regression

Regression (Wu et al., 2019) is a technique generally used for two different purposes, the first being value estimation and the second being determining the relationship between dependent and independent variables. The technique used especially for estimation is frequently encountered in machine learning algorithms (Maulud et al., 2020). Considered the simplest supervised machine learning, linear regression is frequently used to analyze data such as real estate price prediction, estimated sales, prediction of students' exam scores, and movements in stock prices in the stock market. In linear regression, the assumption that the data is linearly distributed is used. Its ease of use makes the use of linear regression widespread. On the other hand, using this model will give incorrect results when working with a data set that is not linearly distributed. In this case, it is necessary to change the model (Ray, 2019). It is possible to divide linear regression models into two: simple linear regression and multiple linear regression, depending on the data set. In this application, multiple linear regression model was used. This model can be expressed as follows:

$$y_i = \beta_0 + \beta_1 x_{i1} + \beta_2 x_{i2} + \cdots + \beta_p x_{ip} + \epsilon \quad (1)$$

where, y_i = dependent variable, x_i = explanatory variables, β_0= y-intercept (constant term), β_p= slope coefficients for each explanatory variable, ϵ = the model's error term (also known as the residuals).

k-Nearest Neighbors

k-Nearest Neighbors (*k*-NN) is the most widely used classification algorithm. It is non-parametric as it does not assume any data distribution. It is an easily applied technique and the model is cheap to implement. It is well suited to flexible classification scheme and multi-modal applications, but its error rate is high. The size of the training set may cause the algorithm to be computationally intensive. *k*-NN algorithm has many areas of use, such as similar symptoms shown in the medical diagnosis of multiple diseases, similar features in person credit scores, handwriting detection, analysis by financial institutions before approving loans, and video recognitions.

III. Analysis

Figure 1 provides a visual representation of the experimental analysis conducted in this study. It outlines key stages starting with dataset analysis, followed by rigorous data preprocessing. Subsequently, machine learning algorithms were applied systematically, and the results underwent comprehensive evaluation.

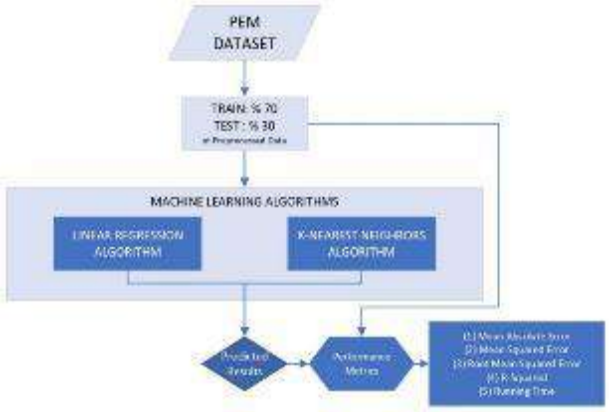

Figure 1. Demonstration of the experimental analysis

Dataset

PEM Fuel Cell Dataset was introduced to the literature within the scope of the study titled "Data set of Nafion 112 membrane standard tests and Membrane Electrode Assembly (MEA) activation tests of Proton Exchange Membrane (PEM) fuel cell" conducted by Hamidi et al. (Hamidi et al., 2020). In this data set, the effect of Nafion membrane percentage and cathode relative humidity on cell performance at different pressures and different compression ratios of the membrane was analyzed with polarization curves. Potential (V) changes as a result of changing the Nafion membrane percentage between 20% and 25%, the cathode relative humidity between 30%, 50%, 80% and 100%, the pressure between 5 psig, 15 psig and 25 psig, and the membrane compression ratio between 5% and 12%. The corresponding current density (mA/cm^2) and power density (mW/cm^2) values were recorded. The dataset comprises 651 rows of experimental data, with each row containing values corresponding to current density, cell voltage, power density, pressure, relative humidity, membrane compression ratio, and Nafion percentage.

Data preprocessing

Before model construction, all the data were normalized in the dataset. In utilizing the dataset curated by Hamidi et al., cell voltage, pressure, relative humidity, membrane compression ratio, and Nafion percentage values were employed as inputs for the machine learning model. The corresponding current density value within the dataset was identified as the model output, while the power density value was disregarded, given that the product of cell voltages (an input) and current density values yields the power density.

Model Training

For model training, a randomly selected 70% of the dataset was employed, leaving the remaining 30% for rigorous testing. The machine learning models underwent training on the designated partition, utilizing the Linear Regression and k-Nearest Neighbors algorithms. Input parameters for training included cell voltage, pressure, relative humidity, membrane compression ratio, and Nafion percentage, while the models predicted the current density as the output. This process ensured a robust evaluation of the models' predictive capabilities, leveraging a well-distributed dataset for both training and testing phases.

Performance metrics

After training, the models were applied to the test dataset to predict current density values. The subsequent analysis compared the obtained results with the expected outcomes, offering insights into the effectiveness of the models. To evaluate the performance of different machine learning techniques used in this study, five different performance indices were employed: Mean Square Error (MSE), Root Mean Square Error (RMSE), Mean Absolute Error (MAE), Coefficient of Determination (R2) and Runtime (T). It is noteworthy that a shorter runtime signifies the algorithm's computational speed, while lower error rates signify its success. The Coefficient of Determination, ranging from 0 to 1, provides a metric of the goodness of fit for the model, with a value approaching 1 denoting a higher degree of fit (Hu et al., 2019).

$$\mathrm{MSE} = \frac{1}{n}\sum_{i=1}^{n}(y_i - \hat{y}_i)^2 \quad (2)$$

$$\mathrm{RMSE} = \sqrt{\frac{1}{n}\sum_{i=1}^{n}(y_i - \hat{y}_i)^2} \quad (3)$$

$$\mathrm{MAE} = \frac{1}{n}\sum_{i=1}^{n}|y_i - \hat{y}_i| \quad (4)$$

$$R^2 = 1 - \frac{\sum_{i=1}^{n}(y_i - \hat{y}_i)^2}{\sum_{i=1}^{n}(\bar{y}_i - \hat{y}_i)^2} \quad (5)$$

IV. Results and discussion

In the experimental phase of this investigation, machine learning techniques were applied to the PEM fuel cell dataset, and the performance of two distinct models was systematically evaluated. The k-Nearest Neighbors algorithm was implemented with varying values of neighbors (k = 3, 5, and 7). For a comprehensive comparison of the algorithms, five fundamental evaluation metrics—Mean Square Error (MSE), Root Mean Square Error (RMSE), Mean Absolute Error (MAE), Coefficient of Determination (R^2), and Runtime (T)—were computed independently for each model. The obtained results, presented in Table 1, delineate the performance metrics derived from the application of Linear Regression and k-Nearest Neighbors.

Table 1. Performance of the machine learning algorithms

Algorithm Name		MSE	RMSE	MAE	R^2	Total Time (*seconds*)
Linear Regression		0.00590	0.07687	0.06120	0.90742	0.00418
k-Nearest Neighbors	*k* = 3	**0.00340**	**0.05833**	0.04493	**0.94667**	0.00502
	k = 5	0.00533	0.07307	0.05313	0.91635	**0.00348**
	k = 7	0.00727	0.08525	**0.03085**	0.88614	0.00388

Upon examining the values presented in Table 1, it becomes apparent that predictions generated using the Linear Regression algorithm closely align with those produced by the *k*-NN algorithm across various k values. Notably, the *k*-NN algorithm yields its most favorable outcome when k is set to 3. Conversely, the results for k=7 in the *k*-NN algorithm exhibit the least favorable performance, as evidenced by the respective metrics. Specifically, the R^2 value of 0.94 for k=3 in the *k*-NN algorithm signifies a substantial overlap between predictions and test data. It is noteworthy, however, that the *k*-NN algorithm with k=3 incurs a longer total processing time in seconds compared to the other algorithm. For comprehensive visualization the concordance between predicted and actual values for both Linear Regression and *k*-NN with k=3 is graphically illustrated in Figure 2.

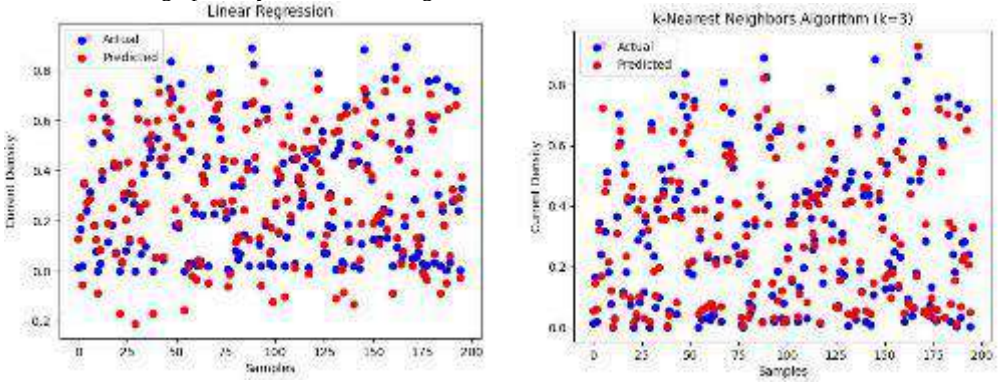

Figure 2. The overlap between the calculated values produced from predictions and the actual values.

V. Conclusion

The investigation undertaken in this study, focusing on the analysis and prediction of the system efficiency of PEM fuel cells through machine learning algorithms, addresses a timely and significant area of research. Notably, the comprehensive analysis of both the structural components and operational conditions of PEM fuel cells within a singular study represents a novel contribution to the existing literature. In the context of this research, two distinct supervised machine-learning algorithms, namely the linear regression algorithm and *k*-Nearest Neighbors algorithms, were employed on the normalized PEM Fuel Cell Dataset. The ensuing performance evaluation involved the computation and tabulation of five different performance metrics. The findings of this initial phase prompt further exploration, where additional traditional machine learning models, including Support Vector Machines, Decision Trees, Random Forest, and Naive Bayes, along with deep learning models, will be tested. Augmentation of the dataset through the inclusion of supplementary data is planned to enhance result accuracy. To evaluate the robustness of machine learning algorithms, cross-

validation will be implemented. This planned expansion of the study aims to provide a comparative analysis of the efficacy of traditional machine learning techniques against emerging machine learning approaches concerning PEM fuel cell efficiency. The anticipated outcomes hold promise for advancing our understanding and refining the predictive capabilities in this critical domain.

Acknowledgements

In this study, Assoc. Prof. Dr. Gamze KARANFIL KACMAZ and GMZ Enerji Sistemleri Sanayi ve Ticaret Limited Sirketi supported the analysis and interpretation of PEM fuel cell data sets.

References

Alizadeh, M., Torabi, F. (2021). Precise PEM fuel cell parameter extraction based on a self-consistent model and SCCSA optimization algorithm, Energy Conversion and Management 229,113777.

Ayodele, T. O. (2010). Machine Learning Overview, Intech Open Access Publisher.

Hamidi, S., Haghighi, S. and Askari, K., (2020). Dataset of Standard Tests of Nafion 112 Membrane and Membrane Electrode Assembly (MEA) Activation Tests of Proton Exchange Membrane (PEM) Fuel Cell, ChemRxiv. https://doi.org/10.26434/chemrxiv.11902023.v1

Hu, Z., Jin, Y., Hu, Q., Sen, S., Zhou, T., Osman, M. T., (2019). "Prediction of Fuel Consumption for Enroute Ship Based on Machine Learning", IEEE Access Digital Object Identifier. https://doi.org/10.1109/ACCESS.2019.2933630

Karanfil, G. (2020). Importance and applications of DOE/optimization methods in PEM fuel cells: A review, International Journal of Energy Research 44, 4-25. https://doi.org/10.1002/er.4815

Li, H., Xu, b., Lu, G., Du, C., Huang, N. (2021). Multi-objective optimization of PEM fuel cell by coupled significant variables recognition, surrogate models and a multi-objective genetic algorithm, Energy Conversion and Management 236, 114063. https://doi.org/10.1016/j.enconman.2021.114063

Maulud, D.H, Abdulazeez, A.M., (2020), "A Review on Linear Regression Comprehensive in Machine Learning", Journal of Applied Science and Technology Trends Vol. 01, No. 04, pp. 140 –147. https://doi.org/10.38094/jastt1457

Ray, S., (2019). "A Quick Review of Machine Learning Algorithms", 2019 International Conference on Machine Learning, Big Data, Cloud and Parallel Computing (Com-IT-Con), India. https://doi.org/10.1109/COMITCon.2019.8862451

Saco, A. Sundari, P.S., Karthikeyan, J., Anand, P. (2022). An Optimized Data Analysis on a Real-Time Application of PEM Fuel Cell Design by Using Machine Learning Algorithms, Algorithms 15, 346. https://doi.org/10.3390/a15100346

Tian, P. (2020). "Performance prediction of PEM fuel cell using artificial neural network machine learning", Master of Science in Mechanical and Aerospace Engineering, University Of California.

Wang, Y., Seo, B., Wang, B., Zamel, N., Jiao, K., Adroher, X.C. (2020). Fundamentals, materials, and machine learning of polymer electrolyte membrane fuel cell technology , Energy and AI, 1, 100014. https://doi.org/10.1016/j.egyai.2020.100014

Wu, J., Liu, C., Cui, W. and Zhang, Y. (2019) "Personalized Collaborative Filtering Recommendation Algorithm based on Linear Regression," in 2019 IEEE International Conference on Power Data Science (ICPDS), pp. 139-142.

IEEES-078

Implementation of Salp Swarm algorithm for optimal energy dispatching in microgrids

, [1*]Boulouma Sabri, [1]Seddaoui Naoual, [1]Belmili Hocine, [1]Bendib Boualem
[1] Unité de Développement des Equipements Solaires, UDES/Centre de Développement des Energies Renouvelables, CDER, Bou-Ismail, 42415, W. Tipaza, Algeria
*E-mail: sab_blm@yahoo.fr

Abstract

Efficient energy planning in microgrids is critical for optimizing resource allocation, scheduling, and ensuring reliable energy demand at least cost and environmental impacts. This paper focuses on the microgrid optimal energy planning problem using a newly proposed salp swarm algorithm (SSA) that addresses the simultaneous minimization of operation and emission treatment costs while satisfying many constraints related mainly to distributed generators (DG) power limits and load satisfaction. The simulation results and the statistical analysis show that the proposed SSA-based optimization strategy exhibits significantly better performance and robustness compared to commonly used metaheuristic algorithms from the research literature.

Keywords: Microgrid optimization, energy planning, metaheuristics, slap swarm algorithm.

I. Introduction

Microgrids are small-scale, localized energy systems that can operate independently or in conjunction with the grid (Parhizi et al., 2015) They aim to optimize energy generation, and consumption, often incorporating renewable sources and storage, as well as conventional sources such as fuel cells, gas turbines, or diesel generators (Dey et al., 2023).
Hourly energy planning plays a pivotal role in optimizing the operation of MGs, as it enables seamless integration of renewable energy sources, efficient energy management, and the provision of reliable power to communities. With the growing adoption of renewables like solar and wind, microgrid operators are faced with the challenge of balancing the intermittent nature of these sources with the continuous and often unpredictable energy needs of their users. Therefore, the development of advanced hourly energy planning strategies has become imperative to ensure the economic viability and sustainability of microgrid operations (Dey et al., 2023; Raghav et al., 2021).
Many optimization techniques were proposed to address the challenges of microgrid optimization. Optimization techniques fall into two main categories, classical or mathematical techniques and metaheuristics-based techniques. Some of the classical methods include Linear Programming (LP) and Mixed-Integer Linear Programming (MILP) (Sukumar et al., 2017), Quadratic Programming (QP) (Satya and Bhanu, 2022) Dynamic Programming (DP(Luu Ngoc An and Tran Quoc-Tuan, 2015). While the mentioned techniques are common and well-established, their use can be complemented by more specialized or newly developed techniques such as Metaheuristic techniques. metaheuristic algorithms have emerged as powerful tools for solving complex optimization problems. These algorithms offer a practical and efficient means of optimizing microgrid operations by considering factors such as renewable energy availability, load forecasting, and energy storage management. Metaheuristics, including genetic algorithms (GA), particle swarm optimization (PSO), simulated annealing (SA), differential evolution (DE), teaching learning-based optimization (TLBO), and many other algorithms, have been successfully applied to a range of optimization problems related to microgrids sizing and planning. A Comprehensive Review of Optimization Techniques and their application in microgrid optimization is given in (Zheng et al., 2023)
This paper presents the application of the Salp Swarm optimizer for hourly energy planning in a microgrid. Taking into account the storage state of charge and different DG power limits. In section 2, the system is described with the optimization objective, section 3 presents the SSA in brief, section 4 provides simulation results and discussion, and section 5 concludes the paper and provides guidelines for future developments and improvements.

II. System description and problem formulation

In this work, a small Low voltage microgrid is considered. It consists of distributed generators (DGs) (PV, Wind, MT, FC, Dgen), a battery storage system (BSS), and the main grid. The objective is to minimize the generation and emission costs by issuing optimal one-hour-ahead reference powers to local controllers from/to different DGs and storage systems. The inputs to the problem are the predictions of utility price, hourly load profile, PV, and Wind generations. Fig. 1 illustrates the overall outline of the MG EMS. The range of the hour index t is 1 to 24. Mathematically, this can be expressed as follows

$$P_{ref}^{t} = \arg\min_{P} \left\{ F\left(P\right) \right\},\ \text{t=1,...,24} \tag{1}$$

$P^{t} = \left[P_{1}^{t},...,P_{NG}^{t} \right]^{T}$ is a vector of hourly powers of DGs. $F\left(P\right)$ is the operating costs of the MG, it includes generation costs, emission treatment costs, etc. Therefore, the MG optimization problem can be formulated either as a single or multi-objective optimization problem. In this work, it is brought into a single objective optimization problem where the objective function is a scalar combining generation and emission costs. Mathematically (Dey et al., 2023):

$$F^{t}\left(P\right) = F_{g}^{t}\left(P\right) + F_{e}^{t}\left(P\right),\ \text{t=1,...,24}. \tag{2}$$

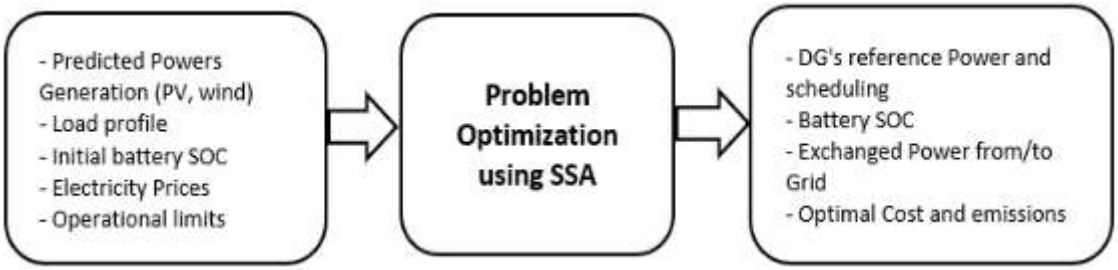

Fig. 1: Information flow in a typical energy planning strategy

The generation cost function $F_g^t\left(P\right)$ includes the fuel cost, operation and maintenance cost, depreciation cost, and electricity cost sold or bought to/from the utility grid and can be expressed as follows

$$F_g^t\left(P^t\right)=F_{fc}^t\left(P^t\right)+F_{om}^t\left(P^t\right)+F_{dc}^t\left(P^t\right)+F_{grid}^t\left(P^t\right) \quad (3)$$

where $F_{fc}^t\left(P^t\right), F_{om}^t\left(P^t\right), F_{dc}^t\left(P^t\right), F_{grid}^t\left(P^t\right)$ the fuel, operation and maintenance, depreciation, and grid costs are defined respectively by: $F_{fc}\left(P^t\right)=B_{fc}^tP^t$, $F_{om}\left(P^t\right)=B_{om}^tP^t$, $F_{dc}\left(P^t\right)=B_{dc}^tP^t$, and $F_{grid}\left(P^t\right)=B_{grid}^tP^t$.

where B_{fc}^t, B_{om}^t, B_{dc}^t, B_{grid}^t are the vectorized bid costs refereeing fule, om, dc, and grid respectively.

The generation cost function $F_e\left(P^t\right)$ can be expressed as a function of the pollutant's quantity vector T_j, the treatment cost Y_j, for all DG units, and can be written as follows:

$$F_e\left(P^t\right)=\sum_j\left(T_jY_j\right)P^t \quad (4)$$

The optimization problem is subject to many constraints related mainly to power limits from/to DGs, and the total energy balance. Grid and BSS.

The hourly energy balance (load satisfaction) constraint is expressed as follows

$$\sum_{i=1}^{n}P_i^t=P_{load}^t,\ \text{t=1,...,24} \quad (5)$$

The DGs, the grid and the battery must provide/receive powers within their capacity limits. Mathematically we have:

$$P_{\min}^t\le P\le P_{\max}^t \quad (6)$$

The battery state of charge must be maintained at assigned levels to increase battery lifetime,

$$SOC_{\min}\le SOC^t\le SOC_{\max} \quad (7)$$

The power boundaries from/to the battery generally depend on the battery capacity and battery SOC.

$$P_{b,\min}^t\le P_b^t\le P_{b,\min}^t \quad (8)$$

The aim is to minimize to cost function (2) along with the different constraints using the Salp Swarm Algorithm (SSA) as an emerging metaheuristic optimization technique. The next section provides a brief overview of this technique.

II. Overview of the Salp Swarm Algorithm (SSA)

The Salp Swarm Algorithm (SSA) is a nature-inspired optimizer (Mirjalili et al., 2017) that mimics the behavior of a salp chain inside the deep ocean. The salp chain has two levels of hierarchy: leader and followers. See Fig. 2.

The iterative nature of SSA involves the continual generation and evolution of random individuals (salps) within the defined problem space. During each iteration, all salps update their location vectors, with a designated leader salp advancing towards a food source (F), while the followers align their movements with the rest of the salps (both the leader directly or indirectly). Fig. 2 shows an illustration of the salp chain:

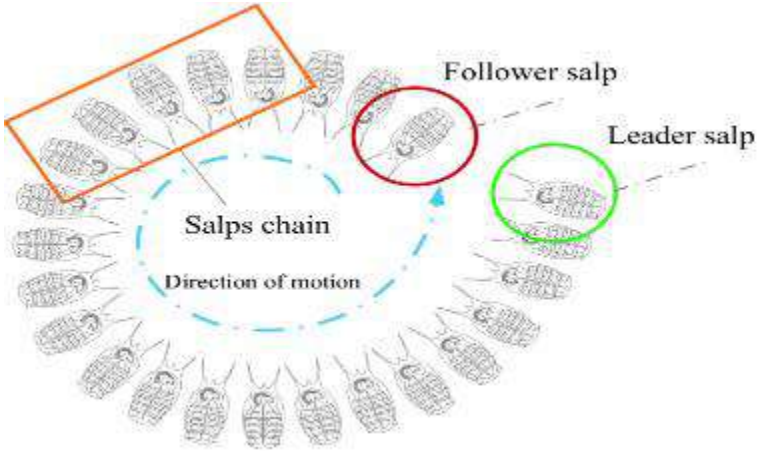

Fig.2: The leader and followers' mechanism in a salp chain (Mirjalili et al., 2017)

A. The Salp Swarm foraging strategy

In SSA, the population of salps consists of N agents with d-dimensions, the leader position is updated as follows:

$$x_1^j = \begin{cases} F_j + c_1\left(\left(ub_j - lb_j\right)c_2 + lb_j\right) & c_3 \geq 0.5 \\ F_j - c_1\left(\left(ub_j - lb_j\right)c_2 + lb_j\right) & c_3 < 0.5 \end{cases} \quad (9)$$

where x_j^1 denotes the leaders´ location and F_j is the position vector of food source in the j^{th} dimension, lb_j represents the upper limit of j^{th} dimension, and ub_j represents the lower limit of j^{th} dimension, c2 and c3 are random values in [0, 1], c1 is the main parameter of algorithm expressed as:

$$c_1 = 2e^{-(4l/L)^2} \quad (10)$$

where *I* denotes the current number of iterations whereas, L shows the maximum number of iterations that can be made. where t is the iteration, while T max. By increasing the iteration count, this parameter decreases. As a result, it can manage to put more emphasis on the diversification inclination in the initial stages and put more emphasis on the intensification tendency in the last steps of optimization. The position of the followers is updated as follows:

$$x_j^i = \frac{x_j^i + x_j^{i-1}}{2} \quad (11)$$

In summary, the pseudo-code of the proposed SSA is presented in Fig. 3

```
Initialize the salp swarm (population) xi (i = 1, 2, . . . n) considering ub and lb;
while end condition is not met do
        Calculate the fitness of each search agent (all salps);
        Set F as the leader salp (F=the best search agent)
        Update c1 by Eq. (15)
   for each salp xi do
      if (i == 1) then
           Update the position of the leader given by Eq. (14)
      else
Update the position of the follower salps given by Eq. (16)
      end
   end
Amend the salps based on the upper and lower bounds of variables;
   end.
Return F.
```

Fig. 3: Pseudo code of the SSA optimizer

III. Simulation results and discussion

In this section, the SSA is used to minimize the total operating cost of a typical micro-grid, for a one-hour time interval. The allowable power limits from/to each DG are tabulated in Table 1.

Table 1: power limits of different components of the microgrid

DGS	**PV**	**WT**	**GT**	**D_{Gen}**	**FC**	**Battery**	**Grid**
Min power	0	0	0	0	0	-30	-30
Max power	30	30	30	100	30	30	80

The hourly predicted values for PV, Wind generation, and load power and the hourly grid price over a day is shown in Fig. 4. All the generation and emission costs (economic data) related to different distributed generators (DGs) are taken from those in (Dey et al., 2023) and converted to the commonly used euro currency. The simulation is done using a population size of 100 individuals fo 1000 iterations.

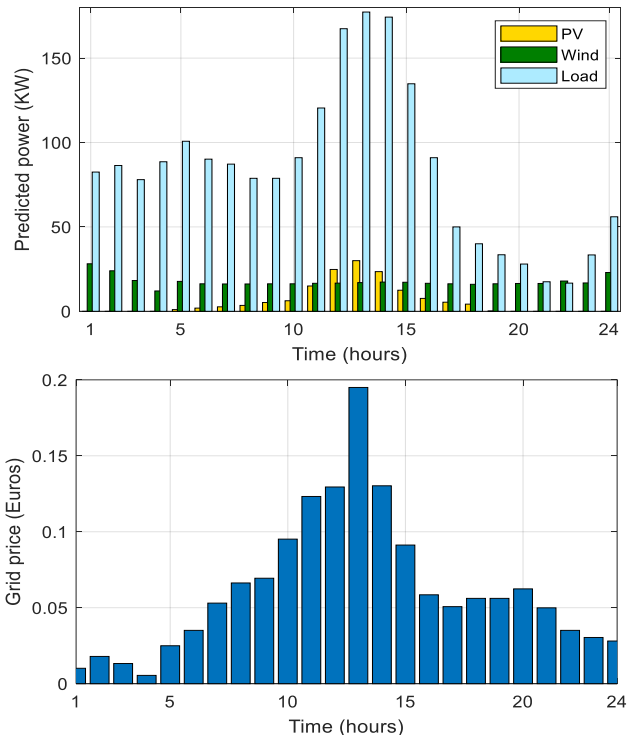

Fig. 4: PV, Wind, and load power predictions (left), Daily grid electricity price (right)

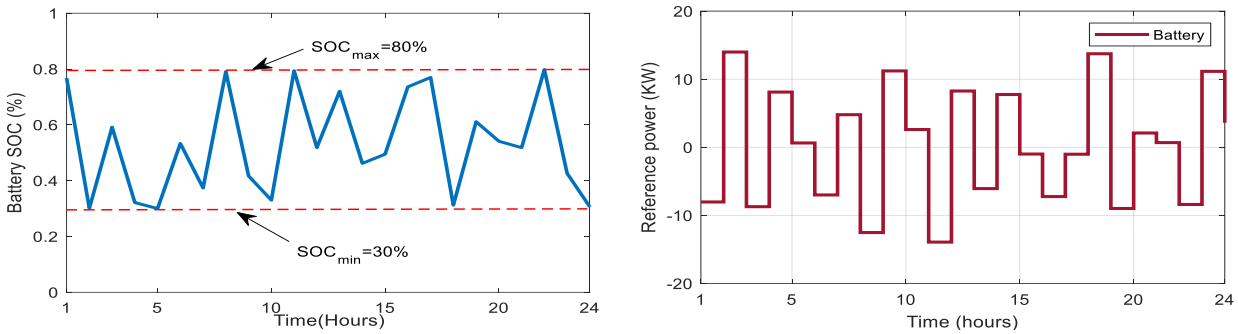

Fig.5: Battery SOC (left), battery charge/discharge powers (right)

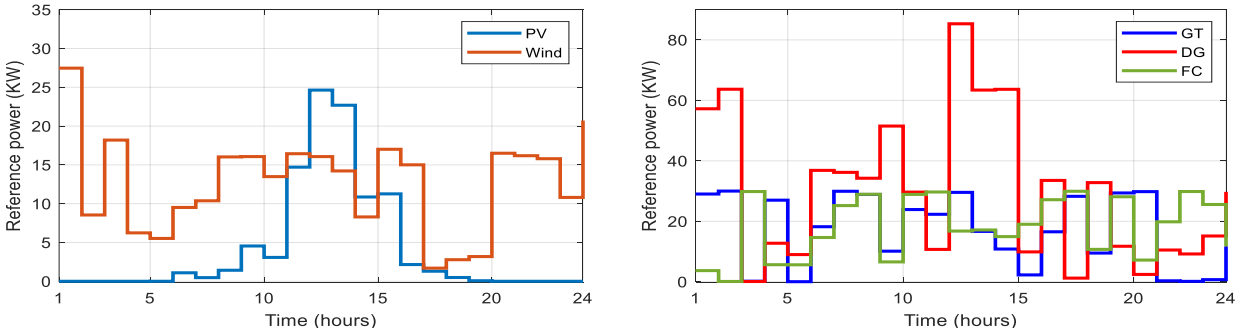

Fig.6: Daily PV and Wind powers (left), daily conventional sources powers (right)

The battery SOC and power are depicted in Fig. 5, we see that the SSA was able to maintain it within the allowable range.The power references for the DGs are depicted in Fig. 6 (left), Compared with the available renewable generation capacities (Fig. 2 left), notice that most the the renewable power was utilized to satisfy the load demands.
The conventional generators and grid powers are shown in Fig.6 (right), we see that the hourly load demand was satisfied within a tolerance of 1%. The algorithm was run for 25 runs, the statistical metrics are computed as: Mean cost = 517.1710, Median cost = 516.1256, Min cost = 423.6719, Max cost = 581.5825, Standard deviation = 40.1321.

IV. Conclusion

The SSA is proposed for optimal energy planning in a MG. The aim is to ensure reliable operation and load satisfaction via optimal utilization of all ressources at the lowest cost and emissions. The simulation results show the effectiveness of the proposed technique in ensuring load satisfaction, battery storage safety, and optimal resource utilization. The statistical analysis allows the assessment of the robustness of the SSA. As a future perspective, the SSA can be combined with other methods for better performance, besides, the

renewable generation and load prediction can be carried out along with the optimization using machine learning tools.

Acknowledgement

LEAP-RE MG-FARM project is part of the LEAP RE programme. LEAP RE has received funding from the European Union's Horizon 2020 Research and Innovation Program under Grant Agreement 963530.

References

Dey, B., Misra, S., Garcia Marquez, F.P., 2023. Microgrid system energy management with demand response program for clean and economical operation. Appl Energy 334, 120717. https://doi.org/10.1016/j.apenergy.2023.120717

Luu Ngoc An, Tran Quoc-Tuan, 2015. Optimal energy management for grid connected microgrid by using dynamic programming method, in: 2015 IEEE Power & Energy Society General Meeting. IEEE, pp. 1–5. https://doi.org/10.1109/PESGM.2015.7286094

Mirjalili, S., Gandomi, A.H., Mirjalili, S.Z., Saremi, S., Faris, H., Mirjalili, S.M., 2017. Salp Swarm Algorithm: A bio-inspired optimizer for engineering design problems. Advances in Engineering Software 114, 163–191. https://doi.org/10.1016/j.advengsoft.2017.07.002

Parhizi, S., Lotfi, H., Khodaei, A., Bahramirad, S., 2015. State of the Art in Research on Microgrids: A Review. IEEE Access 3, 890–925. https://doi.org/10.1109/ACCESS.2015.2443119

Raghav, L.P., Kumar, R.S., Raju, D.K., Singh, A.R., 2021. Optimal Energy Management of Microgrids Using Quantum Teaching Learning Based Algorithm. IEEE Trans Smart Grid 12, 4834–4842. https://doi.org/10.1109/TSG.2021.3092283

Satya, G.T.V., Bhanu, C.V.K., 2022. Economic dispatch of an islanded microgrid. International Journal of Applied Power Engineering (IJAPE) 11, 199. https://doi.org/10.11591/ijape.v11.i3.pp199-208

Sukumar, S., Mokhlis, H., Mekhilef, S., Naidu, K., Karimi, M., 2017. Mix-mode energy management strategy and battery sizing for economic operation of grid-tied microgrid. Energy 118, 1322–1333. https://doi.org/10.1016/j.energy.2016.11.018

Zheng, Z., Yang, S., Guo, Y., Jin, X., Wang, R., 2023. Meta-heuristic Techniques in Microgrid Management: A Survey. Swarm Evol Comput 78, 101256. https://doi.org/10.1016/j.swevo.2023.101256

IEEES-079

Projections for Türkiye's Net Zero Carbon Target by 2053

[1*]Ceren Şengül, [2]Mustafa Zeki Yılmazoğlu,
[1] Gazi University, Graduate School of Natural and Applied Sciences, Enviromental Sciences, Gazi University Central Campus Emniyet Mahallesi Faculty of Technology B Blok Annex Building 2nd Floor, Ankara, 06500, Türkiye
[2] Gazi University, Graduate School of Natural and Applied Sciences, Enviromental Sciences, Gazi University Central Campus Emniyet Mahallesi Faculty of Technology B Blok Annex Building 2nd Floor, Ankara, 06500, Türkiye
*E-mails: ceren.sengul@gazi.edu.tr
zekiyilmazoglu@gazi.edu.tr

Abstract

Global warming and climate change are closely linked to the increasing emissions of greenhouse gases. Therefore, the control of greenhouse gases in the atmosphere holds significant scientific and environmental importance in the fight against climate change. One of the primary sources of greenhouse gases is the use of energy resources. This study examines the necessary energy system projections to achieve Türkiye's net zero carbon target by the year 2053. The reference for this study is based on 2021 EUROSTAT data, and it utilizes the EnergyPLAN model for analysis. Türkiye's goal to reduce carbon emissions to zero is a vital step in addressing climate change. The focus of this study is to demonstrate how Türkiye can undergo an energy transformation by 2053. To achieve this goal, carbon reduction strategies have been examined with a focus on the years 2030 and 2053. Scenarios were developed with the use of renewable energy and smart energy system approaches. The 2030 reference model is based on the installed power values in National Energy Plan of the Ministry of Energy and Natural Resources. Analyses conducted with the EnergyPLAN model are done on an hourly basis, providing flexibility in electricity grids to work with a smart energy system approach throughout the year. The results emphasize that the existing energy infrastructure is insufficient for sustainability and that renewable energy resources need to be used more effectively. Enhancing energy efficiency, investing in renewable energy sources, and adopting an integrated approach to reduce carbon emissions are of vital importance for Türkiye to achieve its net zero carbon goal. In conclusion, this study provides an important guide for planning Türkiye's necessary energy system transformation to achieve the net zero carbon target by 2053. It also aims to contribute to fulfilling international commitments and help Türkiye reach a sustainable energy future.

Keywords: Climate Change, Net Zero Carbon, EnergyPLAN, Smart Energy Systems, Renewable Energy, Zero Emission Energy.

I. Introduction

The Paris Agreement, established in 2015 in Paris, defines the framework for the post-2020 climate change regime. It aims to limit global warming to well below 2°C, preferably to 1.5°C, compared to pre-industrial levels (Su et al, 2022) During COP 21, all countries committed to greenhouse gas emission reduction on a global scale for the first time post-2020. The National Determined Contributions (NDCs), including the climate change mitigation goals of countries, constitute a crucial pillar in the implementation of these targets (Paris Anlaşması / T.C. Dışişleri Bakanlığı, 2023).
Türkiye, through its initial National Determined Contribution (and Intended Nationally Determined Contribution), has confirmed its commitment to reducing greenhouse gas emissions by 41% by 2030 (695 Mt CO_2 equivalent) compared to the reference scenario, with the base year being accepted as 2012 (Paris Anlaşması / T.C. Dışişleri Bakanlığı, n.d.). Türkiye's updated first National Determined Contribution covers the entire economy, encompassing comprehensive assessments of reduction and adaptation actions, as well as evaluations of implementation tools. Türkiye aims to peak its emissions no later than 2038 and achieve a net-zero carbon target by 2053. (Türkiye Cumhuriyeti Güncellenmiş Birinci Ulusal Katkı Beyanı, n.d.)
To achieve these goals, significant investments in the energy sector are required. The fundamental objective for Türkiye is to attain a competitive structure that maximizes self-sufficiency in energy by evaluating domestic and renewable energy sources, prioritizing nuclear technology in electricity generation, enhancing energy efficiency, emphasizing localization in energy technologies, integrating new technologies, and strengthening our strategic position in international energy trade (On İkinci Kalkınma Planı, 2023).

II. Experimental Procedure/Methodology/System Description

The general term for the methodology employed to consider units at various scales, such as buildings, neighborhoods, cities, and countries, as a system and to model their energy demands and/or supplies is referred to as "energy system modeling." In the process of this modeling, simulation programs enable the representation of diverse energy scenarios, facilitating comparisons among parameters such as costs, greenhouse gas emissions, and utilized energy sources to make informed decisions (Akgün, 2021; 42-43)
In this study, energy data specific to Türkiye has been utilized, taking the reference year as 2021. An energy system modeling simulation has been designed using the EnergyPLAN model. The EnergyPLAN model serves as a computational tool for Energy Systems Analysis, and its interface is given in Figure 1 (EnergyPLAN, 2022).

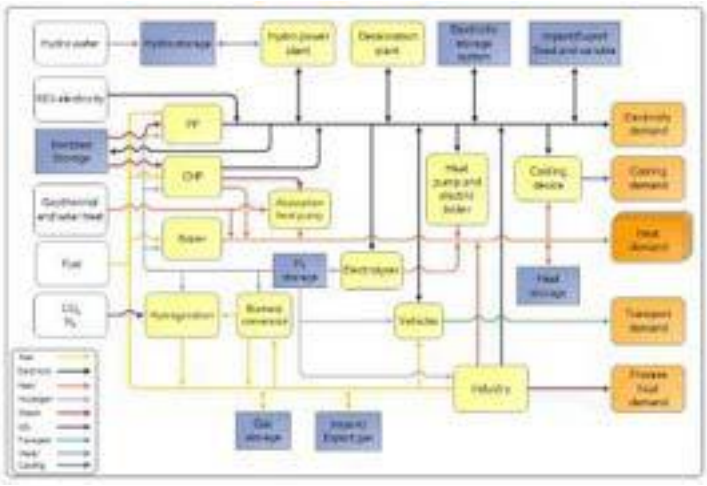

Fig. 1: EnergyPLAN diagram

The main purpose of the model is to assist the design of national energy planning strategies based on technical and economic analyses of the consequences of different national energy systems and investments. The model is an input/output model. General inputs are demands, renewable energy sources, energy plant capacities, costs and a few optional different simulation strategies emphasising import/export and excess electricity production. Outputs are energy balances and resulting annual productions, fuel consumption, import/exports and total costs including income from the exchange of electricity (EnergyPLAN, 2022).

III. Analysis

The consumption data defined as inputs in the system are extracted from the EUROSTAT "Energy Balance" table, specifically from the 2021 data pertaining to Türkiye. (Eurostat, n.d.)
An energy system analysis with EnergyPLAN tool requires data in the "**Demand"** and **"Supply"** sections. Demands data involves given headings:

1. Electricity (Demand): The electricity demand is defined by an annual value, D_E (TWh per year) and the name of an hourly distribution data set.
Electricity demand data consists of "available for final consumption + distribution losses + energy sector -energy use (electricity)" datas taken from EUROSTAT (28621 Thousand ton of oil equivalent = 332.57 Twh)

2. Heating (Demand): In Türkiye, heating is primarily provided in homes and other buildings through boilers. The quantity of fuels expended for heating in buildings is presented in the table below, in accordance with the classification from the Türkiye 2021 energy balance table obtained from EUROSTAT, categorized under "Residential" and "Commercial and Services." Simulation values are employed for efficiency measurements.

Table 1: Fuel Consumption Table in Household and Commercial and Public Services of Türkiye in 2021

Fuel Type	**Fuel Consumption**						**Efficiency**
	Household		**Commercial and public services**		**Total (fuel input verisi)**		
	Thousand TOE	**TWh**	**TTOE**	**TWh**	**TTOE**	**TWh**	
Coal	3571	41.53	774	9	4345	50.53	0.7
Oil	432	5.02	456	5.3	888	10.32	0.8
Ngas	13718	159.54	3926	45.66	17644	205.2	0.9
Biomass	1528	17.77	0	0	1528	17.77	0.7

In Türkiye, apart from fossil fuels and biomass, electric heating is utilized to meet heating demand. According to TURKSTAT (Turkish Statistical Institute) datas, electricity accounts for a 6.2% share in heating, considering the primary fuel type (TUIK, 2022). When considering the total fuel consumption, it is inferred that 14.776 TWh of electricity is used for heating households. Assuming proportional electricity usage for heating in commercial establishments, it can be estimated that 17.4 TWh of electricity is expended for heating in commercial spaces.
The overall electric heating data is calculated as follows: 17.4 TWh (commercial and public services) + 14.78 TWh (household) = 32.19 TWh. Other source used for heating in buildings include solar thermalheat. Solar thermal energy, combining industrial and residential usage, amounts to 860 ktoe, equivalent to 10 TWh according to EUROSTAT.

3. Industry and other Fuel Consumption (Demand): The quantities of fuels used for energy demand in the industrial sector and for agriculture and fisheries, as obtained from the energy balance table, are provided in the table 2 below. Additionally, the consumption of manufactured gases in the industrial sector has been added to the coal category.

Table 2: Fuel Consumption Table in Industry and other services of Türkiye in 2021

Fuel Type:	**Industry**		**Other services (agriculture+fishing)**	
	TTOE	**TWh**	**TTOE**	**TWh**
Coal	8511	98.98	0	0
Petrol	3362	39.1	3161	36.76
Ngas	11005	127.99	125	1.45

Biomass	0	0	0	0

4. Transport (Demand): The transport input tab sheet is designed to describe potential changes in the transport sector. The fuel inputs at the top comprise fuel for cars and other transport units divided into jet petrol, diesel, petrol, natural gas, and LPG. Addition to this electricity consumption due to car is 135 TTOE (1.57 TWh). The usage of fossil fuels and renewable biofuels in the transportation sector is provided in the table 3 below:

Table 3: Fuel Consumption Table in Transportation of Türkiye in 2021

Fuel Type:	Fossil Fuel		Biofuel	
	Thousand TTOE	TWh	TTOE	TWh
Jet Fuel	941	10.94	0	0
Diesel	22164	257.77	59	0.69
Petrol/methanol	3042	35.37	61	0.7
Ngas	258	3	-	
LPG	3485	40.53	-	

Once the demands have been defined, the user must design the supply side of the energy system. Here the user constructs different types of electricity, heat, cooling, and fuel production plants. Technical characteristics such as the capacities and efficiencies are typically required for each plant, while in some cases, a predefined hourly distribution is also necessary. [6] In EnergyPLAN, a single value needs to be entered for the modeled year concerning installed capacities. Below, the values for power plant capacities at the end of the year 2021 are entered in the table 4 below:

Table 4: Installed Capacity of Energy Sources of Türkiye in 2021

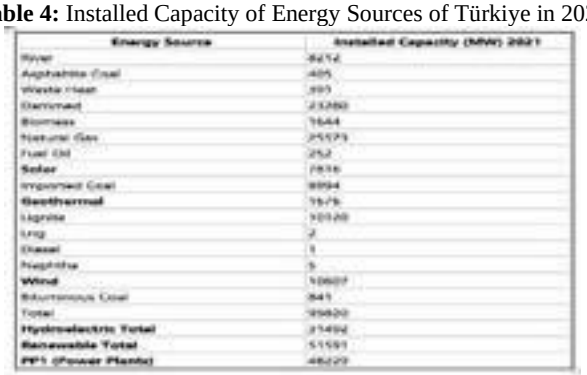

1. Heat and Electricity (Supply): Capacities and operation efficiencies of CHP units, power stations, boilers and heat pumps are defined as part of the input data. PP1 electricity production data is 2211 TWh and Fuel consumption is 503 Twh while electricity efficiency is 0.45.

2. Central Power Production (Supply): In this section only geothermal energy datas is used. Electricity production data is 10.8 TWh and fuel consumption is 108 TWh (electricity efficiency is 0.1)

3. Variable Renewable Electricity (Supply): In Türkiye, the installed capacities of hydroelectric power plants at the end of 2021 are 23,280 MW for dammed (reservoir) power plants and 8,212 MW for river power plants. EnergyPLAN acknowledges that river hydroelectric power plants do not participate in energy balancing, while dammed power plants, similar to central power plants like PP1, can adjust their capacity according to demand and contribute to balancing. The objective of establishing the 2021 reference energy system is to accurately simulate the actual energy demand and production on the EnergyPLAN software and calibrate EnergyPLAN with correction factors. Therefore, the installed capacities and hourly production quantities of both dammed and river hydroelectric power plants have been aggregated to model them as river hydroelectric power plants in EnergyPLAN.

4. Heat Only (Supply): Regional heating systems in Türkiye are exclusively utilized for the direct distribution of geothermal energy to end-users for space and water heating purposes. [5] The energy balance table indicates an annual total demand of 1327 TTOE energy for geothermal heat used in residences, with the distribution of the generated geothermal heat demand used as the distribution of heat production.

5. Fuel Distribution (Supply): Fuel distribution is used to determine the proportion of fuels consumed in the energy production section for electricity and heat generation. The data presented in the table below has been adjusted based on the quantities of fuels used for electricity and heat production in the energy balance table. Derived gas consumption has been aggregated under the "Coal" category.

6.

Table 5: Fuel Consumption of Türkiye in 2021

Fuel Type	Fuel Consumption TTOE	Fuel Consumption TWh
Coal	24687	287.1
Petrol	81	0.94
Ngas	16850	195.96
Biomass	1683	19.57

IV. Results and discussion

After entering the data provided in the analysis section, the model was executed, and the obtained results are presented in the table below:

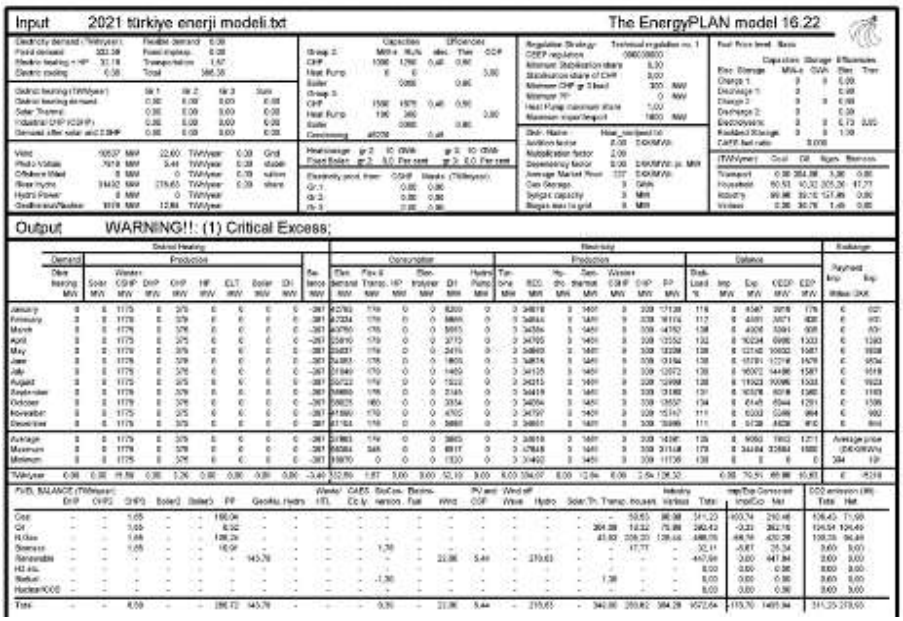

In the reference model, for now, only technical simulation has been conducted, and in addition to this, market simulation will also be implemented. Under the technical simulation sub-category, a demand balancing strategy for heat and electricity has been selected. Scenarios will be created for the years 2030 and 2053, each having subcategories, for Türkiye, with a focus on both technical and market simulations. The system will be modeled, and projections will be generated. When devising new scenarios, official existing plans covering Türkiye, such as the National Energy Plan, will be used as a reference for installed capacity values. Modeling efforts will be undertaken to enhance the representation of potential sources of the future and clean energy, such as offshore wind turbines, nuclear energy, electric vehicles, hydrogen energy, electrolyzers, etc. Percentages of these emerging and clean energy sources will be increased, and modeling studies will be conducted. In addition to these, methods that enhance energy efficiency, such as regional heating and heat pumps, will also be modeled.

V. Conclusion

Upon executing our referance model (2021), it becomes apparent that our carbon emissions remain at a substantial level. The findings underscore the inadequacy of the current energy infrastructure for sustainable practices, highlighting the imperative to enhance the effective utilization of renewable energy resources. Prioritizing energy efficiency, directing investments towards renewable sources, and adopting a comprehensive strategy to curtail carbon emissions are pivotal for Türkiye to attain its net-zero carbon objective. In conclusion, this research serves as a critical guide for orchestrating the requisite transformation of Türkiye's energy system, steering it towards the net-zero carbon target by 2053. Additionally, it aspires to contribute substantively to fulfilling international commitments, propelling Türkiye towards a future anchored in sustainable energy practices.

References

Akgün, Atakan. *Türkiye için %100 yenilenebilir enerji sisteminin tekno-ekonomik analizi*, Hacettepe Üniversitesi, 2021; 42-43
Bina ve Konut Nitelikleri Araştırması. TÜİK (2022). https://data.tuik.gov.tr/ Accessed 20 Nov. 2023.
EnergyPLAN | Advanced Energy Systems Analysis Computer Model. (2022). https://energyplan.eu/. Accessed 20 Nov. 2023.
Eurostat. (n.d.). *Energy balances*. Energy balance visualisation tool. https://ec.europa.eu/eurostat/ Accessed 20 Nov. 2023.
Su, Y., Hiltunen, P., Syri, S., & Khatiwada, D. (2022). Decarbonization strategies of Helsinki metropolitan area district heat companies. Renewable and Sustainable Energy Reviews, 160, Article 112274. https://doi.org/10.1016/j.rser.2022.112274
On İkinci Kalkınma Planı (2024-2028), (2023) http://www.sbb.gov.tr/. Accessed 20 Nov. 2023.
Paris Anlaşması / T.C. Dışişleri Bakanlığı, (n.d.) www.mfa.gov.tr/paris-anlasmasi.tr.mfa. Accessed 20 Nov. 2023.
Türkiye Cumhuriyeti Güncellenmiş Birinci Ulusal Katkı Beyanı, (n.d.) http://iklim.gov.tr/. Accessed 20 Nov. 2023.

IEEES-080

Investigation of the Effects of Heat Pump Applications on Cultural Heritage Buildings: A Case Study on Gazi University Rectorate Building

[1*]Nazlı Deniz Ünal,[2] Mustafa Zeki Yılmazoğlu,
[1] Gazi University, Graduate School of Natural and Applied Sciences, Environmental Science, Gazi University Central Campus Emniyet Mahallesi Faculty of Technology B Blok Annex Building 2nd Floor, Ankara, 06500, Turkey
[2] Gazi University, Faculty of Engineering, Mechanical Engineering, Gazi University Central Campus Emniyet Mahallesi Faculty of Technology B Blok Annex Building 2nd Floor, Ankara, 06500, Turkey
*E-mails: ndeniz.unal@gazi.edu.tr
zekiyilmazoglu@gazi.edu.tr

Abstract

With energy efficient system solutions in buildings with cultural values, both cultural heritage should be protected and carbon footprint should be reduced. With the Paris Climate Change Agreement, it has become a necessity to reduce energy consumption and greenhouse gas emissions with the measures to be taken on global warming, to which we are a party and have obligations. Renovations to buildings with cultural heritage value often damage the historical texture of the buildings. For this purpose, it is aimed to change heating/cooling systems of Gazi University Rectorate Building with the heat pump system selection, which is foreseen not to disturb the cultural heritage value. The effects of heat pump selection on energy consumption and global warming in Gazi University Rectorate Building are examined. The digital twin of the building is created and modeled. The building is modeled in Autodesk Revit software. With the creation of the model, the building current system solutions and heat pump alternatives are considered. The data obtained is analyzed with Energy+ software. Heat pump is an electrically powered system based on the principle of transferring heat energy from one medium to another. Due to the location and resources of Gazi University Rectorate Building, the study examines the air, ground (horizontal), and ground (vertical) source types of heat pumps. It is aimed to examine the energy efficiency of the system alternatives, operational energy costs, and potential reduction of green house gases. The main outcomes of the study can guide the policymakers to save the cultural heritage in buildings and reducing their carbon footprint.

Keywords: Historic buildings, heat pump, energy efficiency, global warming, carbon footprint, cultural heritage.

I. Introduction

The building, which is used as the Rectorate Building of Gazi University and whose foundation was laid on 8 August 1927 at 17:00 as "Gazi Mustafa Kemal Pasha Muallim Mektebi", is the last work of Architect Kemaleddin.

Fig. 1: Gazi University Rectorate Building

The building is located on the back of the 20 TL paper banknote currently used by the Republic of Turkey. For this reason, the building is a very important cultural heritage indicator for Turkey. Gazi University Rectorate Building is a building that has been actively used and kept alive from past to present. For this reason, it was tried to ensure minimum energy consumption by using today's technology while preserving the cultural heritage value of the building.

II. Experimental Procedure/Methodology/System Description

In the study, the current existing first state and current technical drawing files of Gazi University Rectorate Building were obtained from the Department of Construction Works and Technical Department. By using these technical drawings, the building has become ready for system selection by creating digital twins of the building. Many issues such as building usage parameters, lighting loads of the building, analysis of the structures around the building will be evaluated before the simulation and heat pump system alternatives will be evaluated. The green areas around and in front of the building will constitute alternative source areas for ground source (vertical and horizontal) heat pump use. The current situation and heat pump alternatives will be analysed with Energy+ software to determine the reduction values in energy consumption and greenhouse gas emissions. With current cost calculations, normalised payback periods of the applications according to future values will be calculated.

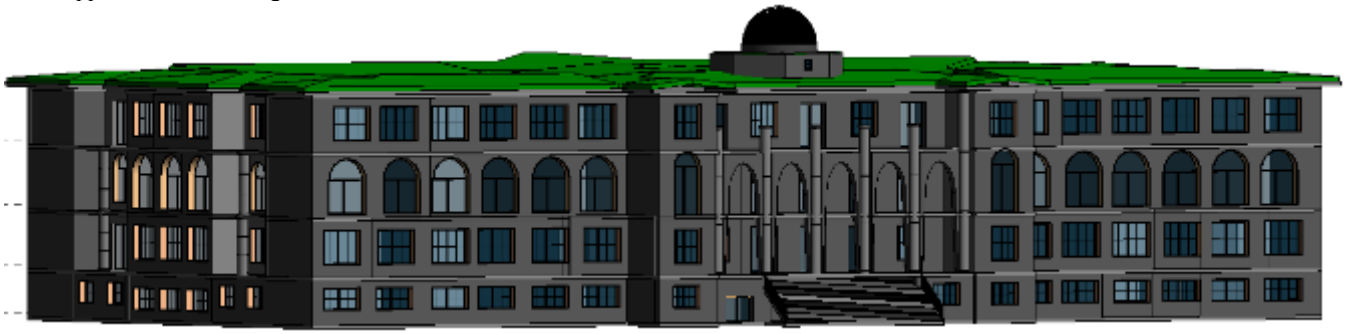

Fig. 2: Gazi University Rectorate Building Model

III. Analysis

Firstly, the model created was analysed with Energy+ software and the energy load and consumption of the building were found. The building is currently heated by 3 boilers with a capacity of 1.000.000 kcal/h and 1 boiler with a capacity of 400.000 kcal/h. Cooling is provided by 3 VRF outdoor units with a capacity of 28 kW and 1 VRF outdoor unit with a capacity of 22.5 kW. The consistency of the data obtained was compared with the invoices received from Gazi University Administrative Financial Affairs unit. After this stage, new heating and cooling systems were integrated into Gazi University Rectorate Building. In line with the results obtained, it will be tried to minimise the energy consumption of the building with air, ground (horizontal and vertical) source heat pump, and also the effect on global warming and carbon emissions will be reduced to the maximum level. The most efficient, economical and optimised system will be selected by considering the initial cost and operating costs of the studies.

IV. Results and discussion

When we examined the Gazi University Rectorate Building model in Energy + software, the following results were obtained.

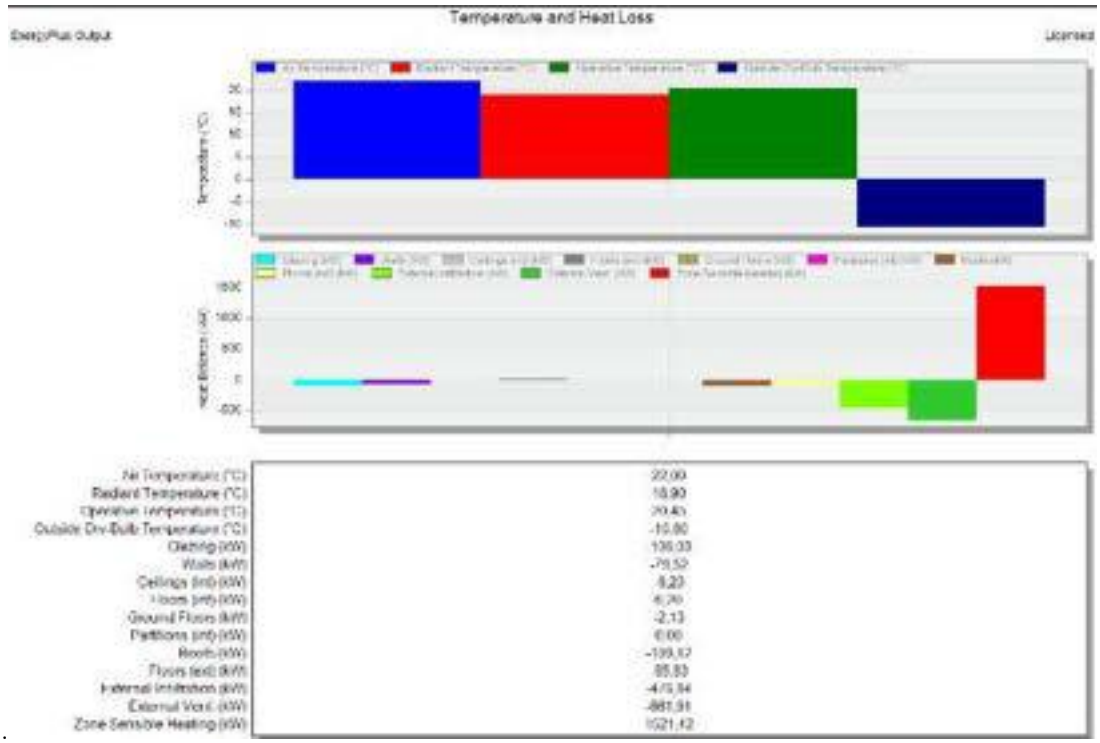

Fig. 3: Gazi University Rectorate Building Heating Load

Structure Costs	Floor Area (m2)	Cost (GBP)
Sub Total	16528,8	3.471.054,32

HVAC Costs	Floor Area (m2)	Cost (GBP)
Sub Total	16528,8	2.479.324,51

Lighting Costs	Floor Area (m2)	Cost (GBP)
Sub Total	16528,8	991.729,81

Sub-Structure Costs	Floor Area (m2)	Cost (GBP)
Sub Total	3846,0	423.058,68

Fig. 4: Gazi University Rectorate Building Cost

V. Conclusion

As a result, it has been observed that the heat pump consumes less energy if the heat pump is used with the existing heating and cooling system of Gazi University Rectorate Building. In this way, the carbon footprint of the building has been reduced.

References

https://gazi.edu.tr/view/page/219/binamizin-tarihi

https://www.iea-shc.org/Data/Sites/1/publications/2021-12-INTERVIEW-Task59-Renovating-Historic-Buildings-Towards-Zero-Energy.pdf

https://task59.iea-shc.org/Data/Sites/1/publications/D.B1e--Fact-Sheet-BES-Final.pdf

IEEES-081

Integration of Hydrogen Technologies into Buildings in Historic Urban Areas

[1] Emine Sacha Nokay, [1]Zeynep Durmuş Arsan,
[1] Izmir Institute of Technology, Faculty of Architecture, Architecture Department, IZTECH Architecture Faculty Gülbahçe Urla, İzmir, 35430, Türkiye
*E-mails: eminenokay@iyte.edu.tr , zeynepdurmus@iyte.edu.tr

Abstract

In view of the net zero carbon target for 2053, Turkey needs to switch 56% of its fossil fuels to sustainable energy sources and move towards solar energy technologies, which currently account for 4%. Thus how does hydrogen fit into this equation? The construction sector in Turkey, which includes residential, commercial and public buildings, accounts for more than 35% of the country's total final energy consumption and there are 16 million existing buildings in Turkey. Integrating renewable technologies that balance sustainability and heritage conservation offers a greener and more energy-efficient future for historic urban areas. While investigating the integration of solar panels into historic buildings in response to the question of how we can integrate sustainable energy technologies into these structures with approaches to the conservation, rehabilitation, restoration and reconstruction of historically significant areas and buildings, the increasing trend towards solar panels highlights the problems of energy storage and increases the importance of hydrogen technology to store the energy generated. With the help of PV panels, the electricity generated is converted into green hydrogen by electrolysis of water and used as storage for energy use. During peak times, when electricity is needed much more, the stored hydrogen gas is used to generate heat, electricity and water as co-generation in buildings. Energy retrofitting of historic buildings will reduce energy consumption and climate change impacts, improve human health, and preserve the aesthetic and cultural value of the historic district. The paper explores the potential of hydrogen energy systems integrated with solar panels to generate, store and reuse energy in historic urban areas that are difficult to integrate due to building and regulatory constraints.

Keywords: Historical Buildings, Historic Urban Areas, Solar PVs, Energy Storage, Hydrogen.

I. Introduction

Buildings account for 40% of global energy consumption, with residential buildings accounting for 22% and commercial buildings for 18%, with cooling and heating accounting for 27% of energy consumption in commercial buildings and lighting accounting for 26% (De Simone & Fajilla, 2019).

Turkiye was responsible for 1% of global carbon emissions 530 million tons in 2020, and the building sector, which includes residential, commercial and public buildings, is responsible for 35% of the country's total final energy consumption (GIZ, 2018). There are 130 million buildings in Europe, while Turkiye has 16 million existing buildings. Looking at Turkiye's electricity generation sources, fossil fuels, hydropower, wind power, solar power and geothermal power rank first with an installed capacity of 56.2%, 26.3%, 8.4%, 3.8% and 3.4% respectively, with biomass and waste being the lowest technologies at 1.5% and tides and waves at 0.4% (CIA, 2020). We should focus on existing buildings that use fossil fuels to find new solutions to decarbonize energy consumption and reduce global warming.

The aim of this work is to consider the sustainability concepts of existing historic buildings in heritage areas with renewable energy technologies without reducing carbon emissions and circumventing heritage protection regulations and to assess the potential of green hydrogen technology in historic buildings. In this context, the study of Kızlarağası Han in the historic Kemeraltı area in Izmir was examined.

a. Literature Review

i. Hydrogen production in Turkey

To maintain a carbon-free fuel option, green hydrogen is produced from renewable electricity generated using photovoltaic (PV) panels, solar thermal collectors, solar heliostats, etc. (Dincer & Ishaq, 2021), with water flowing through a proton exchange membrane (PEM) electrolyser to produce and safely store green hydrogen. Currently, these generation technologies have efficiency issues and the current infrastructure for hydrogen transport is not sufficient to be utilised on a large scale (Laezman, 2022). Therefore, we should consider how hydrogen can be produced in cities and small urban areas. Istanbul, where 16 million people currently live and consume 38.49 TWh of electricity, which is 16% of Turkey's energy consumption, has a high potential to reduce at least 13.719 million tonnes of CO2 emissions per year through the production of green hydrogen that can be used in various sectors (Dincer, Javani, & Karayel, 2022).

ii. Hydrogen use in buildings

There are a whole series of hydrogen houses that are pioneering projects demonstrating how hydrogen can be used as a fuel. Lochem, a Dutch town with 12 listed historic homes that are too drafty to be heated with electric heat pump systems, is heated with a hydrogen boiler using grey hydrogen produced at a nearby industrial plant piped through an existing natural gas pipeline to bypass heritage restrictions, preserve the 1900s architecture, and eliminate poor insulation that doesn't work with heat pumps in cold climates (Parkes, 2022). Hans-Olof Nilsson lives a completely carbon-neutral life with his 500 m2 Nilsson House, which has a green hydrogen system

generated by a 20 kW photovoltaic system that uses a battery when needed and stores the excess energy in hydrogen to bridge seasonal peaks such as cold winters in Gothenburg, Sweden (Evers, 2018). Last but not least, Mike Strizki's hydrogen house in New Jersey has been off-grid since 2006 and survived power outages during hurricanes thanks to its own solar panels and hydrogen storage systems. These power outages highlighted the importance of having a backup plan, which helped to develop a commercially used hydrogen module called the Joule Box that functions as a portable energy station (Loggins, 2023).

Despite the high cost and inefficiency of the overall systems due to pipelines and boiler systems in the current sector (Collins, 2022), hydrogen is a way to decarbonize the emissions caused by energy demand in buildings through heating and cooling. In addition, renewable technologies compatible with historic buildings are being explored to support the building stock and reduce carbon emissions. In this case, solar installations that are consistent with historic neighbourhoods to preserve appearance, infrastructure, and human health through emissions are becoming increasingly popular (LeSher, Rosenbloom, & Duerksen, 2019). Overall, the integration of renewable technologies to reduce energy consumption to the point of self-sufficiency is only possible with storage capacity that takes hydrogen a step forward.

II. Methodology

Kızlarağası Inn was built in 1744 by Hacı Beşir Ağa, who was the Dâruessaade Agha of Sultan Ahmet III and Sultan Mahmut I. 300 stores and workshops are located in the Kızlarağası Inn. It has 5 entrances with a large circulation through the courtyard. Kızlarağası Inn, one of the examples of Ottoman Bazaar architecture showing the pattern of its period was restored between 1988 and 1993 and put into operation as a tourist bazaar. There is a cafeteria in the courtyard and stores selling various handicrafts, clothes, souvenirs and decorative items around it. In Çuha and Cevahir Bazaar, there are mainly stores selling silver and other jewellery and accessories. There are also souvenir stores, antique stores and stores selling musical instruments. On the second floor of the Kızlarağası Inn, there are workshops for jewellery design, marbling, calligraphy, miniature art, antique stores, record stores and a cafeteria.

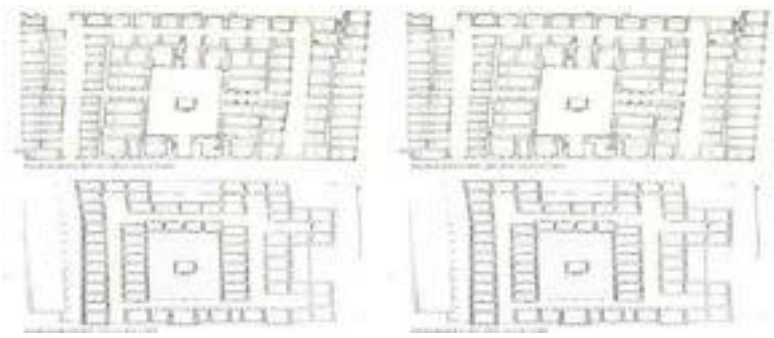

Fig. 1: Kızlarağası Inn Ground Floor Plan (left) and First Floor Plan (right)
(Asadollahi Asl Zarkhah, Tuna Ultav, & Ballice, 2022)

The methodology of the article is quantitative and qualitative chosen to understand the historical building and its users in terms of electricity consumption by asking questions through questionnaires that lasted 5 minutes.

Questionnaires were used to ask shopkeepers about their electricity bills and the heating/cooling systems they used. 35 surveys were conducted to determine the historic electricity consumption of 300 stores. The data was collected over two days in November 2023, with three questions asked in the surveys;

1. Which heating and cooling technologies are used in the store?
2. How often were these technologies used?
3. What is the difference between the summer and winter electricity bills with approximate values in Turkish lira (if possible in kWh electricity consumption)

Based on the surveys, the 33 stores were analysed to determine the total energy consumption of Kızlarağası Inn. The analysis showed that the inn consumed more electricity to cool the building on hot summer days.

III. Analysis

The on-site surveys show that the working hours at the Inn are between 09:00 and 20:00. The peak times depend on the outside temperature for the cooling and heating devices used in the individual stores. Due to the Inn's infrastructural problems, there are no radiators or heating pipes in the historic building. Most of the stores have air conditioning units that are used both in winter and summer, and some have both air conditioning and electric heaters for winter. Izmir is a city with similar heating and cooling degree days, where the heating and cooling degree days are 126 ($T \leq 15$ °C) and 133 ($T > 22$ °C) respectively (MGM, 2022), which means that more cooling is required than heating. Kızlarağası Inn studies have shown that the peak energy demand for cooling is higher than for heating. According to the surveys, the energy consumption in this listed building is 1812 MWh all year round. The question arises as to how we can improve the condition of this listed building in terms of energy consumption when decarbonizing the platform if the piping and water system are not introduced The roof of the listed building is vaulted and not flat, so the structure is needed to protect the monument without weighing down the roof.

The average sunshine duration in Turkiye is 7.2 hours per day (Oyman Serteller, 2018) and based on an average photovoltaic panel considered as 400W electricity production where efficiencies are considered around 22% (Aggarwal, 2023) with an area of 1 meter x 1.7 meters, daily production of 2.88 kWh with an annual production of 1051.2kWh (=1.051MWh) is expected. The total area of the

PV systems required is estimated at 1724 panels to generate electricity over an area of 2930 m2. The roof with domes of Kızlarağası is calculated as 2780m2, (-380 for the courtyard) +820 roof in total with a total area of 3220m2.

Furthermore, the roof is more than sufficient to install the required amount of PV systems, but peak loads during hot and cold days should be taken into account to achieve thermal comfort in the stores. The PV systems are required to store the energy generated, which is accessible through hydrogen to create a carbon-free cycle. Hydrogen enables storage between seasons and eliminates fluctuations during peak periods.The photovoltaic panels equipped with hydrogen fuel cells will not only decarbonize the system but also create a grid independent of the electricity grid for peak demand and cover cooling needs with hydrogen when needed. Hydrogen is used to store the energy generated by an electrolysis process with renewable electricity from solar energy and stored as H2 gas until it is necessary for peak loads to add O2 through fuel cells that work in reverse like electrolysis, giving us electricity, heat and water in a closed cycle at the end of the cycle.

IV. Results and discussion

In Izmir, an inclination angle of 32% is required on the south façade in order to receive the highest amount of sunlight and generate the highest amount of energy through photovoltaic systems. With this in mind, the Kızlarağası Inn offers enough space for the installation of photovoltaic systems to form a closed micro-grid that efficiently generates energy via hydrogen storage. As these discussions continue, further research should consider the efficiency of the system and the shortcomings in storage to demonstrate to policy makers that it is possible to move forward despite the financial criticisms and to test feasibility to commercialization. In addition, further research should be conducted on the efficiencies of photovoltaic systems that are above 39.5% (Glickson, Hicks, & Stottler, 2022) to stimulate interest in photovoltaic systems even in countries where solar radiation is not as high.

V. Conclusion

Due to the lack of infrastructure in historic buildings, the decarbonization of energy consumption in these cultural heritage sites is a topic of discussion. As mentioned earlier, Kızlarağası is a unique Ottoman architectural style bazaar that shows its period details. However, no water infrastructure and pipelines were designed for this Inn, which meant that the owners of the store did not have easy holes for air conditioning systems due to the lack of decision-making power to enter a comprehensive heating and cooling system considering the heritage protection for the historical ruins. Photovoltaic systems are one of the renewable technologies that help to preserve historic urban areas while generating energy to reduce carbon emissions in the future. Unfortunately, photovoltaic systems are not sufficient to meet peak energy demand during the seasonal transition period or during the day when the sky is cloudy. In this case, the hydrogen systems via electrolysis and fuel cells come into play. Hydrogen is on the list of fuels to be used to decarbonize the three most important sectors: Buildings, transportation and industry. Why don't we start with our heritage sites to bring back the values that were given to us in our past?

References

Aggarwal, V. (2023). *Retrieved from https://www.energysage.com/solar/solar-panel-output/*

Asadollahi Asl Zarkhah, S., Tuna Ultav, Z., & Ballice, G. (2022). Kamusal/Kentsel İç Mekânda Yer Kimliğinin Bir Bileşeni Olarak 'Anlam'ın önemi: Kızlarağası Hanı, izmir. Kent Akademisi, 15(4), 2025–2048. doi:10.35674/kent.1022581 Aggarwal, V. (2023). *Retrieved from https://www.energysage.com/solar/solar-panel-output/*

CIA. (2020). *Retrieved from https://www.cia.gov/the-world-factbook/countries/turkey-turkiye/#energy*

Collins, L. (2022). *Retrieved from https://www.rechargenews.com/energy-transition/revealed-what-18-independent-studies-all-concluded-about-the-use-of-hydrogen-for-heating/2-1-1240962*

De Simone, M., & Fajilla, G. (2019). Occupant Behavior: A "New" Factor in Energy Performance of Buildings -Methods for Its Detection in Houses and in Offices. *Journal of World Architecture, 2*(2). doi:10.26689/jwa.v2i2.544

Dincer, I., & Ishaq, H. (2021). Renewable Hydrogen Production. doi:10.1016/c2020-0-02435-7

Dincer, I., Javani, N., & Karayel, G. K. (2022). Sustainable City concept based on Green Hydrogen Energy. *Sustainable Cities and Society, 87*, 104154. doi:10.1016/j.scs.2022.104154

Evers, A. A. (2018). *Hans-Olof Nilsson's Off-The-Grid Hydrogen House near Goteborg, Sweden. Retrieved from https://www.hydrogenambassadors.com/aae/off-the-grid-hydrogen-house-sweden.html*

GIZ. (2018). *Ecofys, Istanbul Aydin University, & IZODER. Turkish Building Sector Executive Summary and Roadmap. https://c2e2.unepccc.org/kms_object/turkish-building-sector-executive-summary-and-roadmap/*

Glickson, D., Hicks, W., & Stottler, K. (2022). *Retrieved from https://www.nrel.gov/news/press/2022/nrel-creates-highest-efficiency-1-sun-solar-cell.html*

Laezman, R. (2022). Living Off the Grid: Meet the 'Hydrogen Houses.' Retrieved from https://www.theearthandi.org/amp/living-off-the-grid-hydrogen-houses

LeSher, A. (2019). Renewable Energy for Historic Buildings. Retrieved from https://sustainablecitycode.org/brief/renewable-energy-for-historic-buildings/

Loggins, S. (2023). Is Water the New Oil? Retrieved from https://www.savvysumer.com/post/is-water-the-new-oil

MGM. (2022). Isıtma ve Soğutma Gün Dereceleri. Retrieved from https://www.mgm.gov.tr/veridegerlendirme/gun-derece.aspx?g=yillik&m=06-00&y=2022&a=10#sfB

Parkes, R. (2022). Boiler Maker launches "first of its kind" 100% hydrogen heating trial in Draughty Historic Houses. Retrieved from https://www.hydrogeninsight.com/innovation/boiler-maker-launches-first-of-its-kind-100-hydrogen-heating-trial-in-draughty-historic-houses/2-1-1366946

Oyman Serteller, N. F. (2018). Examination and comparison of nuclear energy with other available energy sources for electricity production in Turkey. *International Journal of Humanities and Social Science Research, 3*, 38–42. doi:10.6000/2371-1655.2017.03.04

IEEES-082

PV Parameter Estimation Using Remora Optimization Algorithm

*Gamze Nalçacı
Necmettin Erbakan University, Engineering Faculty, Electrical and Electronics Department, Konya, 42005, Turkey
*E-mail: gnalcaci@erbakan.edu.tr

Abstract

Before installing a photovoltaic (PV) system, it is imperative to develop an accurate modeling methodology. The utilization of modeling approaches is crucial for ensuring the efficient operation of photovoltaic (PV) systems. In order to get the parameters of the PV model, it is important to utilize a more accurate and effective optimization methodology. The Remora Optimization Algorithm (ROA) is capable of determining the optimal configurations for both single and double-diode models. In order to assess the efficacy of the extraction methodology, two datasets comprising solar modules are utilized. In contrast to prior research, the results obtained from the ROA method demonstrate the smallest disparity between the data collected and the actual measurements. The statement holds true for all configurations and across the whole range of the irradiance spectrum. Upon comparing the ROA method with the PSO and GWO algorithms, it becomes evident that the ROA algorithm demonstrates superior convergence speed and a reduced convergence time. The Remora Optimization Algorithm is widely recognized as a highly efficient and precise method for parameter selection.

Keywords: Remora optimization algorithm, pv parameter estimation, particle swarm optimization, grey wolf optimizer.

I. Introduction

Currently, renewable energy, along with other alternative energy sources, is widely recognized as a feasible solution to address the challenge presented by the finite supply of fossil fuels. The utilization of solar energy has been suggested as a potential solution to address this problem, owing to its abundant accessibility and absence of detrimental environmental repercussions. The primary difficulty in the field of photovoltaic systems is the optimization of solar energy absorption to boost efficiency, mostly due to the high initial investment required (Alam et al., 2015; Ishaque et al., 2016). The optimization of system architecture plays a pivotal role in augmenting the overall performance of these systems. In order to enhance the effectiveness of system design, it is crucial to conduct accurate and dependable photovoltaic (PV) modeling prior to installation (Alam et al., 2015). The simulation can be categorized into two discrete time periods. The initial phase involves the formulation of a mathematical framework for the photovoltaic (PV) system, which is then proceeded by the implementation of parameter extraction techniques. Theoretical feasibility exists for simulating the linear and nonlinear characteristics of photovoltaic (PV) systems (Rekiouna and Matagne, 2012). The single-diode and double-diode variants are universally acknowledged as the most favored and reliable models in the field.

Several techniques are utilized to obtain the parameters of a photovoltaic (PV) system. The deterministic algorithm can be classified as a specific form of algorithm, whilst the stochastic algorithm serves as a separate alternative. Most algorithms employed in modern applications are deterministic in nature. Stochastic algorithms involve a variety of strategies, which include heuristic and meta-heuristic approaches. Deterministic algorithms are also referred to as gradient-based algorithms. Based on the reference provided (Yang, 2014), the aforementioned strategies exhibit notable efficacy in scenarios involving unilateral decision-making and situations requiring adaptability. Nevertheless, their performance is significantly subpar when the objective functions incorporate discontinuities. Additionally, the algorithms demonstrate a certain level of inertia. The deterministic approach is demonstrated by employing a nonlinear least squares optimization method, which utilizes a Newton model with Levenberg parameters (Elbaset et al, 2014). This phenomenon functions as a visual representation of a deterministic procedure. The utilization of the single-diode model allows for the acquisition of parameters, thereby presenting this approach as a feasible alternative. The Newton-Raphson method serves as an exemplification of a deterministic algorithm (Yuan et al., 2014). Upon the implementation of this methodology to the dual-diode model, a significant discrepancy between the observed and anticipated features (I-V) was detected.

However, there are other approaches to treatment plans that prioritize deterministically efficient processes. Stochastic algorithms, encompassing heuristic and meta-heuristic methodologies, present feasible options for implementation. The ability of individuals to express and understand complex associations is facilitated by initially establishing foundational connections. The subsequent instances exemplify stochastic methodologies that have been published in scholarly literature for the purpose of estimating parameters of photovoltaic (PV) models.

Numerous algorithms have been put up in scholarly publications as potential solutions for optimization problems. The algorithms under consideration encompass the Flower Pollination Algorithm (FPA) (Ishaque et al., 2012), the Whale Optimization Algorithm (WOA) (Nalcaci and Ermis, 2018), the Whippy Harris Hawks Optimization Algorithm (WHHOA) (Oliva et. al., 2017), and the Gray Wolf Optimizer (GWO) (Naeijian et al., 2021). The Cuckoo Search algorithm (CS) was proposed by Yang and Deb in their paper (Long et al., 2020). The parameters of a single-diode or two-diode model are obtained by applying the model to the test data presented in reference (Elbaset et al., 2014). However, the majority of these algorithms demonstrate notable inaccuracies and are unable to get the ideal solution until at least 2000 iterations have elapsed since the initial problem formulation.

Additionally, there is actual evidence indicating that evolutionary algorithms (EAs) have the capability to effectively recover the parameters of the dual diode model under normal conditions. However, the algorithms in question were not subjected to testing in order to assess their ability to accurately identify the highest attainable quantity, regardless of factors such as temperature or light intensity. The enhancement of photovoltaic (PV) module features requires the application of progressively sophisticated algorithms to determine the most advantageous outcomes.This article introduces a suggestion and conducts a comparative analysis of the Remora Optimization Algorithm (ROA) in relation to two commonly employed optimization algorithms, namely Particle Swarm Optimization (PSO) and Gray Wolf Optimizer (GWO). The application of this technique exhibits significant potential and efficacy in extracting

characteristics from both single- and dual-diode models of diverse photovoltaic (PV) modules. The aforementioned algorithm is utilized for the purpose of parameter extraction.
The following section of this survey will discuss the subject of model photovoltaic (PV) systems. The following part will present a comprehensive description of the process of problem generation. Section 4 of the document provides a thorough examination of ROA, deconstructing it into its core elements and delivering an in-depth explanation of each constituent. The following section will be devoted to the examination of simulations, while the subsequent segment will present the results. The subsequent portion will be dedicated to the conclusion.

II. PV Models

The operational and dynamic characteristics of the solar generator can be elucidated by several mathematical models. Presented below are multiple explanations of the prevailing models that are extensively utilized.

A. Single and double diode models

The utilization of the single diode model (SDM) is a prevalent approach in representing the steady-state characteristics of solar cells. The circuit illustrated in Figure 1(a) exhibits the precise arrangement of the SDM. Figure 1(b) depicts the almost identical electrical circuitry of the DDM. In this model, two diodes are interconnected in parallel with the current source to accurately depict the physical phenomena occurring at the PN junction. Diode D_1 functions by reflecting the diffusion current at the junction, specifically by employing the dispersion mechanism to transport minority carriers to the depletion region. In this context, diode D_2 takes into account the recombination effects, specifically addressing the recombination of charge carriers within the space charge region.

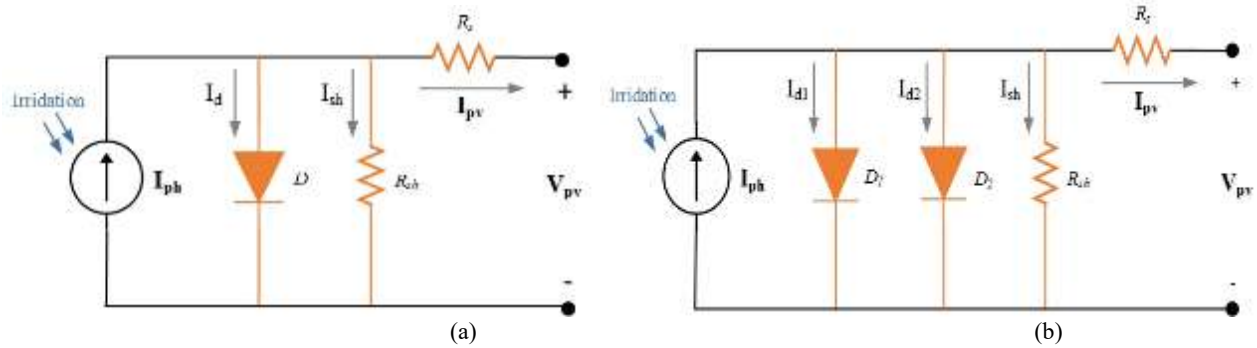

(a) (b)

Fig. 1. (a) Single diode model circuit scheme and (b) the circuit of double diode model

B. PV panels

A photovoltaic panel presented in Fig. 2 is comprised of a series of M cells organized in a specific configuration. The utilization of the SDM in the PV panel is anticipated for every constituent.

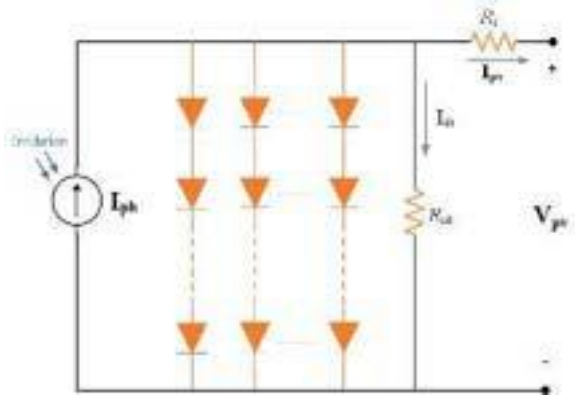

Fig. 2. The circuit scheme of PV model

III. Problem Formulation

The primary objective of the solar cell modeling technique is to determine the ideal values for the unknown parameters of the equivalent circuits for a single diode, a double diode, and a photovoltaic (PV) panel. The primary significance is in mitigating the gap between experimental and extraction data obtained under diverse environmental circumstances. The main objective of this work is to obtain accurate estimates of the dark components for both models. The flowchart presented in Figure 4 illustrates the streamlining system, which has been developed with the objective of enhancing the root mean square error (RMSE) by eliminating the impact of the perceived aspects of the model from the test data. Consequently, every model incorporates the characteristics of case clouds. In a similar vein, it can be observed that every model demonstrates a predetermined threshold in terms of pricing. The operational criterion utilized in our analysis is formally characterized as the error threshold, as outlined in condition equation 1. Consequently, the intentional modification of preexisting data and the subsequent reconfiguration of data (as denoted by equation 2 or equation 3 may also lead to inaccuracies.

$$\mathrm{RMSE} = \sqrt{\frac{1}{k}\sum_{i=1}^{k} f(I_{pv,} V_{pv,} X)} \quad (1)$$

I_{pv} and V_{pv} are the deliberate current and voltage separately, *k* is the umber of tests contained in the deliberate informational collection. *X* for single diode model can be characterized as *X*=[I_{ph}, I_d, a, R_s, R_{sh}] likewise *X* for double diode model can be characterized as

X=[I_{ph}, I_{d1}, I_{d2}, a_1, a_2, R_s, R_{sh}] in conditions equation 2 and 3.

$$f(I_{pv},V_{pv},X)=I_{ph}-I_{sd}\cdot[\exp(\frac{V_{pv}+I_{pv}*R_s}{a*V_t})-1]-(\frac{V_{pv}+I_{pv}*R_s}{R_{sh}}) \quad (2)$$

$$f(I_{pv},V_{pv},X) = I_{ph}-I_{sd1}\cdot[\exp(\frac{V_{pv}+I_{pv}*R_s}{a_1*V_t})-1]-I_{sd2}\cdot[\exp(\frac{V_{pv}+I_{pv}*R_s}{a_2*V_t})-1]-(\frac{V_{pv}+I_{pv}*R_s}{R_{sh}}) \quad (3)$$

IV. Remora Optimization

The Remora Optimization Algorithm, which was developed in 2021, attempts to imitate the occurrence of remora parasitism by employing metaheuristic approaches. Remoras exhibit a commensal relationship with sailfish, whales, and other creatures, whereby they establish a symbiotic association by attaching themselves to their hosts to acquire sustenance and mitigate the risk of predation. The updated positions of Return on Assets (ROA) are determined by utilizing the formulas for Sailfish Optimizer (SFO) and Whale Optimization Algorithm (WOA). Remoras demonstrate antagonistic behavior towards their host within a limited space as a method of assessing the viability of changing hosts. If the host is not replaced, they will provide sustenance to it. The visual depiction depicted in Figure 4 provides a comprehensive illustration of remora predation, as observed and documented in the study referenced as a citation (Jia et al., 2021).

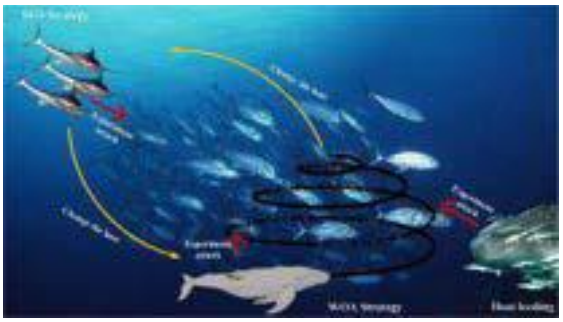

Fig. 3. ROA's varying intensity levels

V. Results and Discussion

Fig. 4(a) shows the single diode model fitness values according to iterations. Similarly, Fig. 4(b) is presented the double diode model fitness values of ROA, GWO, and PSO algorithms. For SDM and DDM model tests, 1000 iterations are made for accuracy and stability. Among all of the algorithms that were evaluated, the ROA algorithm was found to have the highest rank. This was followed by the GWO algorithm, which came in second place, and the PSO algorithm, which came in third place, respectively. Consequently, it is possible to draw the conclusion that the ROA algorithm is the method that is the most effective and trustworthy when it comes to the estimate of parameters for double diode poly-crystalline PV cells in comparison to other ways.

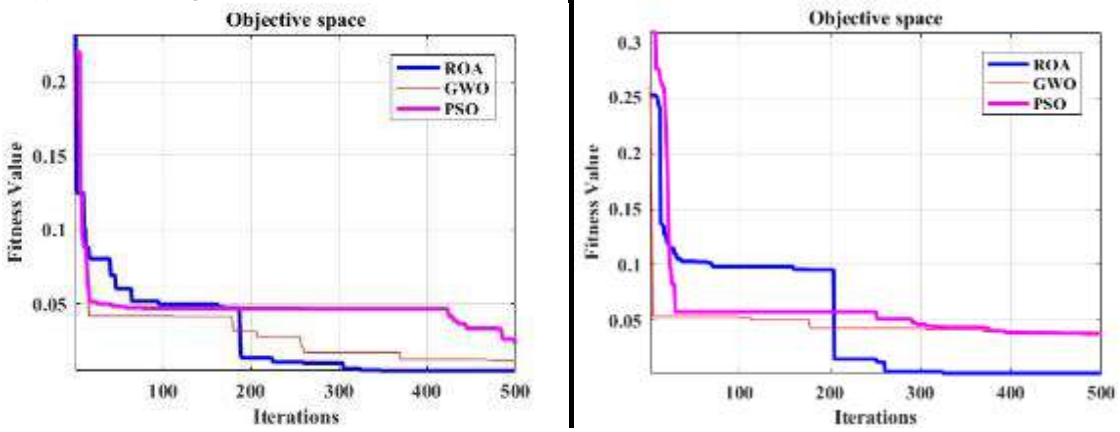

(a) (b)

Fig. 4(a) and (b) Fitness values-iterations graph for ROA, GWO and PSO algorithms

VI. Conclusion

The construction of an accurate depiction of a photovoltaic (PV) system is of utmost importance. The process of obtaining the most suitable parameters for the photovoltaic (PV) model requires the application of a tailored optimization methodology. The investigation of several solar module models can be undertaken through the utilization of a novel optimization technique referred to as the Remora Optimization Algorithm (ROA). The suggested approach for implementation (ROA) has the simultaneous impact of accelerating the achievement of optimal solutions and diminishing the root mean square error (RMSE) between estimated and experimental data. The use of ROA correction involves a reduced number of variables that require adjustment. The parameters established by the Return on Assets (ROA) framework for evaluating the characteristics of I-V exhibit a notable resemblance to the parameters obtained from empirical data. In scenarios characterized by diminished irradiance levels, such as instances of partial shading, the ROA exhibits the capability to ascertain the optimal module configurations spanning a diverse spectrum of irradiance and temperature situations. The Remora Optimization Algorithm stands out for its remarkable precision and efficacy. The precise simulation of PV modules is necessary in order to guarantee the optimal performance of the complete PV system. As a result, the PV system demonstrates improved

overall efficiency, leading to anticipated cost reductions in operational expenses.

References

Alam, D. F., Yousri, D. A., & Eteiba, M. B. (2015). Flower pollination algorithm based solar PV parameter estimation. Energy Conversion and Management, 101, 410-422.

Elbaset, A. A., Ali, H., & Abd-El Sattar, M. (2014). Novel seven-parameter model for photovoltaic modules. *Solar energy materials and Solar cells*, *130*, 442-455.

Ishaque, K., Salam, Z., Mekhilef, S., & Shamsudin, A. (2012). Parameter extraction of solar photovoltaic modules using penalty-based differential evolution. *Applied Energy*, *99*, 297-308.

Ishaque, K., & Salam, Z. (2011). An improved modeling method to determine the model parameters of photovoltaic (PV) modules using differential evolution (DE). *Solar energy*, *85*(9), 2349-2359.

Jia, H., Peng, X., & Lang, C. (2021). Remora optimization algorithm. *Expert Systems with Applications*, *185*, 115665.

Long, W., Cai, S., Jiao, J., Xu, M., & Wu, T. (2020). A new hybrid algorithm based on grey wolf optimizer and cuckoo search for parameter extraction of solar photovoltaic models. *Energy Conversion and Management*, *203*, 112243.

Naeijian, M., Rahimnejad, A., Ebrahimi, S. M., Pourmousa, N., & Gadsden, S. A. (2021). Parameter estimation of PV solar cells and modules using Whippy Harris Hawks Optimization Algorithm. *Energy Reports*, *7*, 4047-4063.

Nalcaci, G., & Ermis, M. (2018, May). Selective harmonic elimination for three-phase voltage source inverters using whale optimizer algorithm. In 2018 5th International Conference on Electrical and Electronic Engineering (ICEEE) (pp. 1-6). IEEE.

Oliva, D., Abd El Aziz, M., & Hassanien, A. E. (2017). Parameter estimation of photovoltaic cells using an improved chaotic whale optimization algorithm. *Applied energy*, *200*, 141-154.

Rekioua, D., & Matagne, E. (2012). *Optimization of photovoltaic power systems: modelization, simulation and control*. Springer Science & Business Media.

Yang, X. S. (2020). *Nature-inspired optimization algorithms*. Academic Press.

Yuan, X., Xiang, Y., & He, Y. (2014). Parameter extraction of solar cell models using mutative-scale parallel chaos optimization algorithm. *Solar Energy*, *108*, 238-251.

IEEES-083

Retrofitting Office Buildings on Global Warming Case Study: Turkey

[1]Gözde Nalçacı, [2*]Gamze Nalçacı
[1] Gazi University, Architecture Faculty, Architecture Department, Ankara, 06570, Turkey
[2] Necmettin Erbakan University, Engineering Faculty, Electrical and Electronics Department, Konya, 42005, Turkey
*E-mails: gmz.nlc@gmail.com

Abstract

The demand for energy and resources is steadily increasing on a daily basis. The construction sector significantly contributes to the utilization of energy and resources. Buildings constructed prior to the widespread adoption of energy-efficient and sustainable methods exhibit a higher energy consumption rate in comparison to more recently constructed buildings. Consequently, the construction sector places significant emphasis on improving energy efficiency by upgrading existing buildings. In contemporary urban landscapes, an abundance of technological advancements exists within the market that serve to improve the energy efficiency of constructed environments. This paper presents a review of the research and development initiatives for Turkey, as well as the practical implementation, of retrofit technologies in the context of existing office buildings. The objective of this study is to enhance the knowledge of building researchers and practitioners on the efficient implementation of building retrofits for the purpose of promoting energy saving and sustainability.

Keywords: Retrofitting, office buildings, global warming, energy efficiency.

I. Introduction

The global consumption of energy is experiencing a significant daily increase. The increasing need for energy leads to the exhaustion of resources, environmental pollution, and worldwide calamities such as climate change and global warming, which are already manifesting their impacts in contemporary times. The construction industry is responsible for a considerable amount of energy consumption, a factor that cannot be overlooked. Therefore, it is imperative to perform an energy efficiency assessment of the current structures and develop retrofitting strategies as a means of proactively addressing excessive energy use. The topic at hand has had an impact on both national protocols and law. The European Union (EU) has implemented several legislative measures in alignment with the Kyoto Protocol to fulfill its goals, encompassing the reduction of energy use, enhancement of energy efficiency, and eradication of waste. The Energy Performance of Buildings Directive, commonly referred to as EPBD (2002/91/EC), was implemented in the year 2002 (Kızıldağ et al., 2022). One of the stipulations necessitates the implementation of minimal standards in newly erected structures, as well as certain renovated edifices. Within the building business, a pivotal approach to mitigate excessive energy use involves the diligent monitoring of the energy efficiency of existing structures.

The topic at hand holds significant importance in the context of shifting towards sustainable structures. The strategy of demolishing existing structures in order to facilitate the construction of new ones is deemed impractical due to the substantial financial, labor-intensive, and environmentally detrimental implications associated with this approach (Moazzen et al., 2020). Additionally, this technique necessitates a heightened level of energy consumption. The initial alternative that can be taken to ensure proper performance is to begin with the implementation of passive solutions aimed at reducing the energy demand of buildings, followed by the retrofitting of building envelope layers. The primary objective of sustainable buildings is to optimize energy efficiency. A crucial measure in accomplishing this objective involves mitigating heat transfer between the interior and outdoor environments. The demarcation between the internal and external areas of a building is referred to as the envelope, which can be likened to the epidermis of a human body. The envelope plays a crucial role in regulating the heat transfer processes, namely in terms of heat acquisition and loss. In order to ensure optimal occupant comfort and minimize energy consumption, it is imperative to implement effective strategies for heat loss prevention. This can be achieved through the utilization of various envelope alternative solutions, coupled with the integration of efficient heating, ventilation, and air conditioning (HVAC) systems. In the first phases of the design process, it is imperative to ascertain the material and insulation thickness requirements that have the utmost significance.

Currently, the computation of building thermal parameters' efficiency is predominantly conducted by the utilization of uncomplicated energy models that capture the dynamics of the building envelope (Trgala et al., 2019). When assessing the thermal efficiency of educational building envelopes designed for thermal insulation, the key parameter in these calculations is thermal permeability. This is due to the fact that it enables the evaluation and comparison of the thermal performance parameters as outlined in the Turkish national standards. Several studies have examined various building factors in the context of refurbishment design for retrofitting office buildings towards nearly zero-energy buildings (NZEB) while ensuring cost efficiency (O'Donovan et al., 2019; Ascione et al., 2017; Kwiatkowski et al., 2017). Research examining the energy efficiency of buildings typically investigates various factors, including the attributes of the building envelope, insulation thickness, the effectiveness of the heating, ventilation, and air conditioning (HVAC) system, as well as the influence of sun shading mechanisms (Fathalian and Kargarsharifabad, 2018; Karjenic and Bednar, 2012; Çetin et al., 2019). Pereira et al. (2021) have established a correlation between occupancy schedules, characteristics associated with occupant behaviors inputted into computer systems, and the outcomes of energy efficiency tests.

Turkey exhibits a notable level of urbanization, with an annual growth rate of 2%. This phenomenon results in a rapidly expanding inventory of buildings, characterized by a growth rate in new constructions above 4%. The construction industry holds significant importance as a key catalyst for the Turkish economy, making a substantial contribution of 6.6% to the growth of the real gross domestic product (GDP). The building industry in Turkey, encompassing residential, commercial, and public structures, accounts for almost 35% of the nation's overall final energy consumption. As a result of substantial ongoing construction endeavors, it is anticipated that this proportion will continue to rise in the coming years. It is projected that the total area of residential buildings will reach about 4.0

billion square meters by the year 2050, in contrast to the approximately 2.4 billion square meters recorded in 2015. It is of utmost importance to ensure that these newly constructed buildings are outfitted with state-of-the-art energy efficiency technologies, while also expediting the rate of refurbishment for the current building stock. Recognizing this development would present significant prospects for the manufacturing sector of Turkey's energy efficiency technologies. This research investigates the retrofit technologies that enhance the energy efficiency of office buildings. Its purpose is to provide information to decision makers and private sector entities regarding the products, services, actors, and factors that drive the energy efficiency and retrofit for office buildings in Turkey. Hence, this study serves as a crucial resource for identifying areas that necessitate further efforts to expedite the accessibility and cost-efficient implementation of these technologies, as well as to enhance the construction markets.

II Retrofit Technologies for Office Buildings

The possible increase in technical investment is allocated as follows: the original investment of 0.55 billion exhibits a potential increase of 73% for ventilation. In the context of windows, there is a potential for an additional 69% investment above the existing market value of 1.34 billion. Similarly, in the insulation sector, the current investment of 1.24 billion has the potential to be raised by up to 62%. There is potential for a further investment of 48% in air conditioning, which now stands at 1.81 billion, as well as an extra 23% for space heating systems, which currently has an investment of 0.9 billion. The field of lighting has nearly reached its maximum technical capacity, as the initial investment of 0.33 billion only offers a limited growth potential of 18%.

A. Insulation

Even if we were to increase the current rehabilitation rate in existing buildings by double, reaching 1%, the majority of the increased investments, approximately 85%, would still be allocated to new construction projects. The Turkish market encompasses a diverse array of both domestic and foreign producers, who provide a broad selection of thermal insulation goods such as EPS, XPS, stone wool, glass wool, and others. Companies operating in the Turkish market possess the capability to effectively meet an escalated demand for thermal insulation. This is primarily attributed to their existing production facilities, which are already of a substantial size, as well as their ability to promptly respond to the requirements of newly constructed facilities. One primary policy difficulty that must be addressed to enable the successful implementation of the Energy Efficiency Targets (EETs) is the need to update the U-values in the TS 825. Additionally, it is crucial to consider the inclusion of cooling measures in the implementation process.

B. Windows

In addition to the existing EUR 1.3 billion in investments allocated towards windows, there exists a potential shortfall of EUR 0.9 billion in investment funds. More than half (53%) of the total amount is attributed to the replacement of windows in pre-existing structures. The non-residential sector accounts for only 25% of the overall investment shortfall. In order to enhance the energy efficiency of windows, it is necessary to enhance two key components: the glass and the frames. The expansion of the sector will be necessary in response to the increasing demand for additional dwellings. The NEEAP includes provisions for providing incentives, support, and tax advantages to the sector in order to encourage the implementation of renovation operations that involve the use of thermal insulation and high efficiency windows. This is particularly significant as the use of policy tools aimed at renovating buildings to incorporate more efficient windows would result in a substantial increase in the market for existing buildings. For example, if the necessary measures were implemented to prioritize retrofitting initiatives, the rate of window renovations might potentially increase twofold, from 1% to 2%.

C. Heating and cooling

The investment gap for energy efficient space heating systems has been determined to be EUR 0.2 billion, in contrast to the existing investments of EUR 0.9 billion. Focusing solely on promoting investments in pre-existing residential structures has the potential to generate around two-thirds of the aforementioned supplementary investments. The investment shortfall is attributed to 20% of new development. A significant portion of the potential investment (EUR 0.9 billion) for energy efficient cooling systems can be derived from existing buildings. This is primarily due to the extended lifespan of air-conditioning units, which is theoretically 15 years, and the substantial number of buildings that are affected. The replacement rate for the building stock is 7.5% annually, while the construction rate for new buildings is 4%. The majority of these buildings are in the residential sector, indicating a prevalence of older structures that consume high amounts of energy. There are no anticipated plans for further investments in cooling infrastructure in the region characterized by the coldest temperature. In recent years, Turkey has emerged as a prominent production hub for HVAC systems in both Europe and Africa. Natural gas is widely used as the primary source for heating purposes, and the market provides a variety of boilers with varying capacities and efficiencies. With the expansion of Turkey's gas infrastructure, there is an anticipated increase in market share for gas boilers. However, it is imperative to prioritize the manufacturing of highly efficient gas boilers and eliminate substandard products from the market. Regarding heat pumps, their current market share is very limited, and it is anticipated that without enough financial assistance, their growth potential may be hindered due to the substantial associated expenses. The achievement of efficient cooling technologies adoption necessitates improved integration of cooling within building energy policies and regulations.

D. Ventilation

The projected increase in investments in ventilation is expected to reach 74%, resulting in a total value of EUR 0.9 billion, up from the current value of EUR 0.5 billion. Approximately 66% of the supplementary expenditure can be allocated towards the maintenance and improvement of pre-existing structures. Due to the limited prevalence of integrated ventilation systems in residential buildings, the whole budget allocation is designated for the non-residential sector. Nevertheless, at now, there exists a lack of obligatory laws pertaining to the utilization of ventilation systems, and there is a notable absence of oversight over such systems. One potential strategy for addressing the investment gap associated with ventilation is to enhance public knowledge regarding its advantages, such as its positive impact on human health and indoor air quality. Additionally, implementing mandatory ventilation concepts that ensure specific air exchange rates and a minimum heat recovery rate of 80% could also help bridge this gap.

E. Lightning

The estimated investment shortfall for lighting amounts to EUR 0.1 billion. All supplementary investments are allocated towards Light Emitting Diodes (LEDs). The majority of supplementary investments are allocated towards pre-existing structures, mostly due to the substantial floor space that needs to be outfitted, as well as the relatively brief lifespan of the currently installed lighting equipment, leading to frequent replacements. The lighting industry has experienced significant expansion over the last 15 years in terms of its ability to produce, the quality of its products, the variety of its offerings, and its commitment to research and innovation. This growth has also led to an increase in the production capabilities of energy-efficient lighting systems, with a particular emphasis on LED technologies. In Turkey, the compound annual growth rate (CAGR) for LED technologies is projected to be 15.6% between 2016 and 2022. Continuous advancements have been made in the field of production technologies. There is a need for enhanced promotion of energy efficient lighting products, as well as the adoption of sensor-based automation for optimizing lighting consumption efficiency.

Advantages of Retrofitting

The results of this study demonstrate the significant impact that restoration plays in Turkey's pursuit of its energy efficiency and retrofitting objectives. In order to achieve these potentials, it is imperative to expedite the rates of refurbishment. An exemplary illustration in this context is the KfW Energy-Efficient renovation project in Germany, which provides low-interest loans along with redemption grants for residential buildings that are privately or publicly owned and already exist. Furthermore, it is crucial to optimize the energy savings potential of retrofits by prioritizing thorough renovation strategies that effectively mitigate any carbon lock-in consequences. Regardless, numerous buildings experience natural maintenance procedures. During these procedures, it is crucial to prioritize energy efficiency enhancements through deliberate policy choices aimed at implementing appropriate and, whenever feasible, the most advanced technology for insulation, lighting, windows, and heating/cooling systems. The facilitation of this endeavor necessitates the establishment of renovation schedules and compulsory renovation rates for various categories of structures, alongside the enforcement of more ambitious energy efficiency criteria and construction regulations that encompass both pre-existing and newly constructed edifices. In order to ensure effective implementation, policy initiatives should be accompanied by the provision of financial support mechanisms and the implementation of awareness activities. The acceleration of rehabilitation efforts and the achievement of planned retrofitting rates pose challenges for numerous countries, including Turkey. For example, both the European Union (EU) and the United States (US) want to achieve renovation rates of up to 3% each year. However, they encounter challenges in implementing sufficient measures to surpass a 1% annual renovation rate. To bridge the gap in achieving these aims, nations are formulating long-term strategies pertaining to the selection and implementation of technology for renovations. The December 2017 revision of the Energy Performance of Buildings Directive (EPBD) imposes a requirement on all European Union (EU) member states to develop and report comprehensive long-term strategy for their retrofitting endeavors. In Turkey, it is recommended to adopt a strategic approach to promote and encourage renovation activities in suitable contexts. Many nations are implementing additional incentives, such as targeted payments for renovations. There are several advantages associated with retrofitting buildings. Firstly, retrofitted buildings offer increased adaptability and suitability for both current and future activities. This flexibility allows for adjustments to be made as needed, ensuring optimal functionality. Additionally, retrofitted buildings tend to provide enhanced comfort for occupants. Another significant benefit of retrofitting is improved energy efficiency, resulting in reduced carbon emissions from building operations. This is particularly important in the context of environmental sustainability and efforts to mitigate climate change. By implementing retrofit measures, buildings can minimize their carbon footprint and contribute to a more sustainable future. Furthermore, retrofitting enables a more sustainable utilization of the embodied-carbon investment, also known as capital carbon. This means that the initial carbon emissions associated with the construction and materials used in the building are effectively utilized and optimized through retrofitting, reducing waste and maximizing the environmental benefits of the building.

III. Conclusion

Retrofitting existing office buildings is widely recognized as an environmentally sustainable, cost-effective, and efficient approach to enhancing energy performance. Moreover, it has been demonstrated to be particularly beneficial for historical structures, since it can contribute to their longevity. Therefore, it is imperative to advocate for the widespread implementation of retrofitting practices within the building and conservation sectors. Further research is required to obtain comprehensive and detailed data regarding the direct and indirect effects of retrofitting on the environment. Additionally, it is necessary to investigate the cost disparities between retrofitting and the standard construction of a building, as well as the expenses associated with maintenance. Furthermore, it is important to examine the impacts of retrofitted buildings on end users and the surrounding area.

Reference

Ascione, F., De Masi, R. F., De Rossi, F., Ruggiero, S., & Vanoli, G. P. (2017). NZEB target for existing buildings: Case study of historical educational building in Mediterranean climate. Energy Procedia, 140, 194-206.

Cetin, K. S., Fathollahzadeh, M. H., Kunwar, N., Do, H., & Tabares-Velasco, P. C. (2019). Development and validation of an HVAC on/off controller in EnergyPlus for energy simulation of residential and small commercial buildings. Energy and Buildings, 183, 467-483.

Fathalian, A., & Kargarsharifabad, H. (2018). Actual validation of energy simulation and investigation of energy management strategies (Case Study: An office building in Semnan, Iran). Case studies in thermal engineering, 12, 510-516.

Kızıldağ, H., Tomrukçu, G., Avgan, G., Dal, A. Ö., Ashrafian, T., Sağlam, N. G., & Özdemir, E. (2022). Energy performance retrofits targeting national strategy development for typical Turkish school building.

Korjenic, A., & Bednar, T. (2012). Validation and evaluation of total energy use in office buildings: A case study. Automation in construction, 23, 64-70.

Kwiatkowski, J., Mijakowski, M., & Trząski, A. (2017). The measures for achieving nZEB standard of retrofitted educational building for specific polish location–case study. In E3S Web of Conferences (Vol. 22, p. 00098). EDP Sciences.

Moazzen, N., Ashrafian, T., Yilmaz, Z., & Karagüler, M. E. (2020). A multi-criteria approach to affordable energy-efficient retrofit of primary school buildings. Applied Energy, 268, 115046.

O'Donovan, A., O'Sullivan, P. D., & Murphy, M. D. (2019). Predicting air temperatures in a naturally ventilated nearly zero energy building: Calibration, validation, analysis and approaches. Applied Energy, 250, 991-1010.

Pereira, V., Santos, J., Leite, F., & Escórcio, P. (2021). Using BIM to improve building energy efficiency–A scientometric and systematic review. Energy and Buildings, 250, 111292.

Trgala, K., Pavelek, M., & Wimmer, R. (2019). Energy performance of five different building envelope structures using a modified Guarded Hot Box apparatus—Comparative analysis. Energy and Buildings, 195, 116-125.

IEEES-084

LBM simulation of thermal comfort in a room cooled by displacement ventilation: effect of Inlet-outlet layouts

[1*] NASSERI Lyes, [1] HIRECHE Zouhira, [1] Ameziani Djamel Eddine
[1] Laboratory of Multiphase Transport and Porous Media (LTPMP), Faculty of Mechanical and Proceeding Engineering, University of Sciences and Technology Houari Boumediene, Algiers, 16111, Algeria
*E-mails: lyes.nasseri@usthb.edu.dz"

Abstract

This article examines thermal comfort in a square cavity with displacement ventilation. Two configurations have been compared: in the first case, the air diffuser is located in the heated wall, while in the second case it is placed in the opposite adiabatic wall. The conservation equations for mass, momentum and energy are solved using the LBM-MRT method. In addition, the values of the control parameters within the laminar regime, namely: Reynolds and Rayleigh numbers in the range [20-500] and [10-106] respectively, and the Prandtl number is fixed at 0.7. In the forced convection regime, results obtained as a function of control parameters (Re, Ra) relating to: flow structure, isotherms, and average Nusselt number, showed situations that guarantee thermal comfort against energy savings. Another important result is the average chamber temperature for two heights, H=0.3 and 0.6, corresponding to the sitting and standing positions respectively. All these results were compared with the two configurations, and correlations were established as well as mapping according to the Re-Ra pair.

Keywords: Forced convection, Displacement ventilation, Lattice Boltzmann Method.

I. Introduction

Displacement ventilation has been the subject of several numerical and experimental scientific papers. The scientists have chosen this type of ventilation for its efficacy and high efficiency. (Xamán et al., 2009) have carried out a numerical study of heat transfer in a displacement-ventilated cavity to analyze temperature distribution and determine the most efficient configuration of ventilation inside the cavity. The authors concluded that the optimum wall thickness (0.3 m) is the most appropriate to minimize heat load gains inside the room, and that it helps reduce ventilation efforts. In the case of an office, (Ahmed et al., 2016) analyzed the essential parameters of displacement ventilation : indoor thermal comfort, vertical temperature difference, average contaminant concentration, air quality and energy savings. The most significant improvements in IAQ in the breathing zone and in inhaled air quality were achieved when the exhaust was separated from the supply opening, and combined with heat sources. Overall, a better indoor thermal environment was achieved by associating indoor heat sources with the evacuation vent at ceiling floor level. Subsequently, (Yuce et al., 2023) chose a smaller room modeled separately with: a seated mannequin, a table and a computer. Overall, these results provide an effective optimization of ventilation parameters, particularly in the application of ventilation studies related to airborne transmission in rooms of different dimensions. ventilation studies related to airborne transmission in rooms of different dimensions.(Feng et al., 2021) used the method of temperature stratification stability (TSS) and temperature stratification recovery time (TSRT) to analyze the effects of dynamic factors on temperature stratification. The authors have detailed the influence of the study's control parameters on the temperature field and its stratification. (Khan et al., 2022) have carried out a comparative numerical study of the performance of mixing and displacement ventilation systems (MV and DV) in a room. the authors compared the room's thermal comfort and the distribution of temperature and veocity for the two ventilation modes.

Following an in-depth analysis of the literature on ventilated cavities, it was noted that very few studies have analyzed the position of openings (air inlet/outlet) in the case of displacement ventilation. In our analysis, we opted to use Lattice Boltzmann method with multi-relaxation-time (LBM-MRT) to solve the problem.

II. Mathematical formulation

The model comprises two ventilated square cavities shown in Fig. 1 (A) and (B). All walls are adiabatic with the exception of the left wall in the first cavity, and the right wall for the second cavity, which are maintained at a fixed temperature. The generalized model was used to solve the governing equations. The cavity is traversed by a jet of air assumed to be incompressible. All properties are assumed to be constant except density, where the Boussinesq approximation is applied.

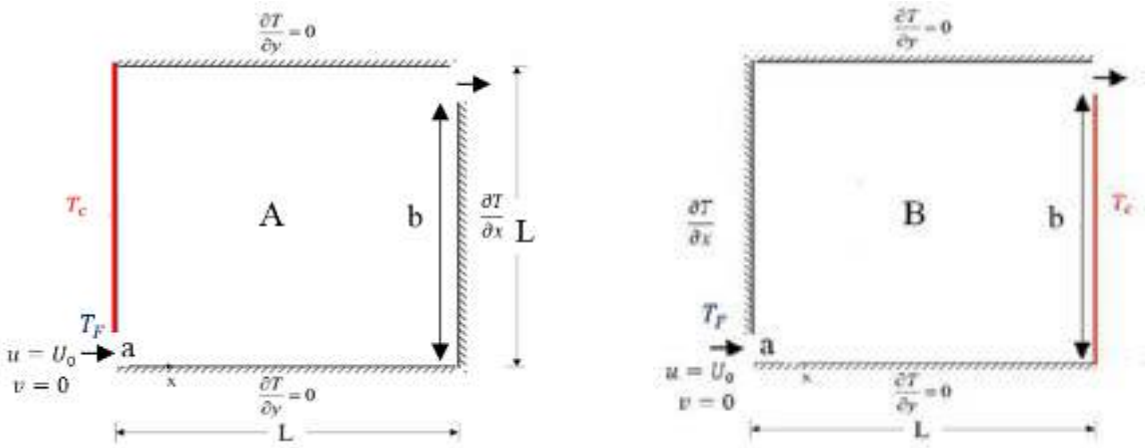

Fig. 1: Physical model and boundary conditions

The Conservation Equations in dimensionless form are :

$$\frac{\partial \rho}{\partial t}+\frac{\partial U}{\partial X}+\frac{\partial V}{\partial Y}=0 \quad (1)$$

$$\frac{\partial U}{\partial t}+\frac{\partial (UU)}{\partial X}+\frac{\partial (UV)}{\partial Y}=-\frac{\partial P}{\partial X}+\frac{1}{Re}\left[\frac{\partial^2 U}{\partial X^2}+\frac{\partial^2 U}{\partial Y^2}\right] \quad (2)$$

$$\frac{\partial V}{\partial t}+\frac{\partial (UV)}{\partial X}+\frac{\partial (VV)}{\partial Y}=-\frac{\partial P}{\partial Y}+\frac{1}{Re}\left[\frac{\partial^2 V}{\partial X^2}+\frac{\partial^2 V}{\partial Y^2}\right]+\frac{1}{Pr}\cdot\frac{1}{Re^2}\cdot R_a.\theta \quad (3)$$

$$\frac{\partial \theta}{\partial t}+\frac{\partial (U\theta)}{\partial X}+\frac{\partial (V\theta)}{\partial Y}=\frac{1}{RePr}\left[\frac{\partial}{\partial X}\left(\frac{\partial \theta}{\partial X}\right)+\frac{\partial}{\partial Y}\left(\frac{\partial \theta}{\partial Y}\right)\right] \quad (4)$$

The rate of heat transfer to the wall is defined as follows :

$$Nu=\frac{L\text{-}a}{L}\int_{a/L}^{1} Nu_x \, dy \quad (5)$$

III. Results and discussion

The computational code was validated by comparing our average Nusselt number results with those of Rahman et al [9]. The comparison was made for the limiting case of an unobstructed cavity, for different Richardson numbers : $Ri = Ra/Pr \cdot Re^2$ (see Figure. 2.)

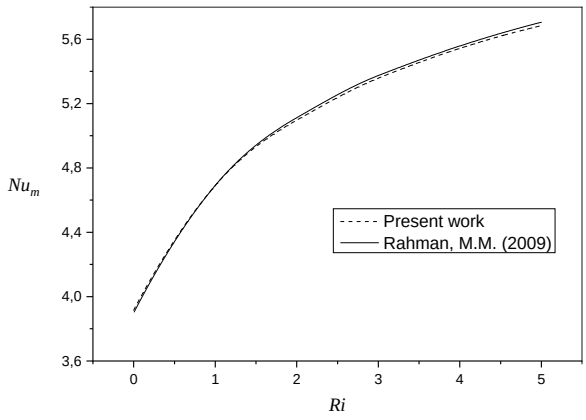

Fig. 2. Comparison of the evolution of Nu_m as a function of Ri of Ri with M. Rahman M.M. (2009)

Figure 3 shows the evolution of mean temperature at two heights (0.3 and 0.6), depending on the Reynolds number for Ra=10 (forced convection regime). For both configurations, the mean temperature decreases as Re increases. This result is more apparent in configuration B, where temperatures are lower. Also, we note that the deminution is more pronounced for this configuration (greater slope).

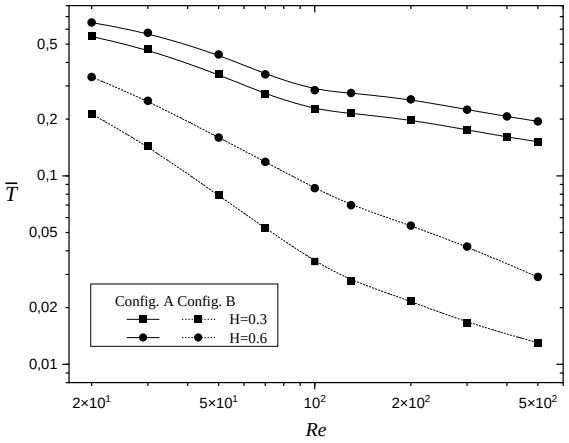

Fig. 3. Variation of mean temperature as a function of Re in forced convection (*i.e.* Ra=10)

Figure 4 shows the evolution of the Rayleigh critical number as a function of Reynolds number for both configurations. The curve separates the comfort zones in the cavity. Below the curve, the average temperature depends on the Reynolds number (controlled comfort temperature). But above the curve, it depends on both parameters (Reynolds and Rayleigh).
For configuration (A), the critical Rayleigh number values decrease for low Reynolds number values (i.e. Re<100). As Re increases, the curve passes through an optimum (minimum) from which it changes trend. On the other hand, for configuration (B), the value of the critical Rayleigh number is directly proportional to the value of the Reynolds number, according to two linear laws

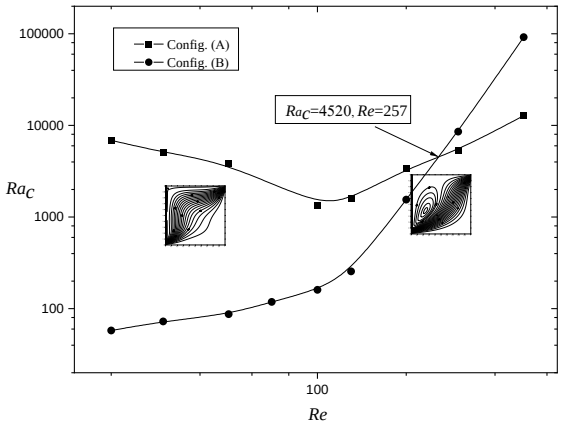

Fig. 4. Couples (Re-Ra$_c$) bounding the comfort zone curves.

Figure 5 shows that increasing Re intensifies transfer in both cases. For configuration (A), the evolution of Nusselt shows three distinct zones: the first has higher values than configuration (B), while for the other two the transfer rate is significantly lower. This decrease is due to the appearance of the recirculation cell as soon as the ventilation jet becomes more or less important.

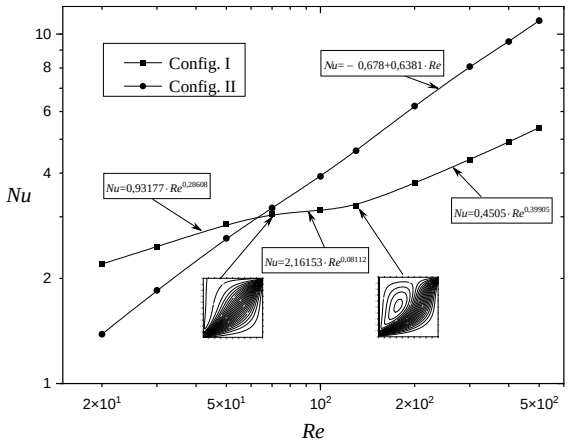

Fig. 5. Variation of the average Nusselt number as a function of Reynolds under forced convection (*i.e.,* Ra=10).

IV. Conclusion

This paper studies heat transfer in a square cavity with displacement ventilation. One of the vertical walls is assumed to be hot, while the other walls are adiabatic. The Lattice Boltzmann method (LBM) with multi-relaxation-time (MRT) was used to solve numerically the problem. Heat transfers are expressed as a function of the various parameters characterizing heat transfer by forced, natural or mixed convection, including the Rayleigh number, Ra, and the Reynolds number, Re. The influence of Re and Ra, as well as the position of the active wall, on heat transfer was discussed. At low Reynolds numbers, the effect of natural convection is present, but remains relatively weak. As the Reynolds number increases, the flow accelerates; the effect of natural convection becomes negligible compared with forced convection. By comparing the results of this configurations, we deduce that the configuration B offers the best comfort conditions, as the lowest mean temperatures relative to the two clean zone heights (Y=0.3 and 0.6) are obtained in this configuration. The variation in mean temperature and mean Nusselt number were correlated as a function of Reynolds number. Maps summarizing the transfer regime as a function of Nu_m, Ra_c and Re have also been drawn up.

References

Ahmed, A. Q., Gao, S., & Kareem, A. K. (2016). A numerical study on the effects of exhaust locations on energy consumption and thermal environment in an office room served by displacement ventilation. *Energy Conversion and Management*, *117*, 74-85.

Feng, L., Zeng, F., Li, R., Ju, R., & Gao, N. (2021). Influence of manikin movement on temperature stratification in a displacement ventilated room. *Energy and Buildings*, *234*, 110700.

Khan, M. A. H., Bennia, A., Lateb, M., & Fellouah, H. (2022). Numerical investigation of thermal comfort using the mixing and displacement ventilation systems within a fitting room. *International Journal of Heat and Mass Transfer*, *198*, 123379.

Xamán, J., Tun, J., Álvarez, G., Chavez, Y., & Noh, F. (2009). Optimum ventilation based on the overall ventilation effectiveness for temperature distribution in ventilated cavities. *International journal of thermal sciences*, *48*(8), 1574-1585.

Yuce, B. E., Aganovic, A., Nielsen, P. V., & Wargocki, P. (2023). Analysis of parameters influencing pathogen concentration in a room with displacement ventilation using computational fluid dynamics and Taguchi methods. *Journal of Building Engineering*, *80*, 108002.

IEEES-085

An Uninterrupted Hydrogen and Wind-Solar Renewable Energy System Design and Multi-Objective and Multi-Constrained Optimization Approach for Hybrid Renewable Energy Systems

[1*]Tuba TEZER
[1] 1 Balıkesir University, Balıkesir Vocational School, Çağış Campus,
Balıkesir, 10145, Turkey
*E-mail: tuba.tezer@balikesir.edu.tr

Abstract

The use of hydrogen for energy storage is increasing due to its clean energy and long-term use opportunity. However, it is rare for hydrogen to be used as an uninterruptible energy source in hybrid renewable energy systems and taken into account in size optimization. In this study, an off-grid energy system with a biomass-based reformer for uninterrupted hydrogen production, as well as photovoltaic panels and wind turbines, was discussed. Furthermore, a completely renewable hybrid system has been designed by using hydrogen not only as an energy source but also as an energy storage tool. A three-objective Pareto-based optimization approach has been developed to optimize the economy, reliability, and energy use of these systems. This includes minimizing the system cost, the loss of power supply probability (LPSP), and the percentage of waste energy (PEW). The three-objective optimization algorithm integrated with the system design optimization, developed in the MATLAB environment based on NSGA-II, is also a multi-constrained optimization algorithm that takes LPSP and PEW values into account as constraints. The system configurations that optimize the number and the power values (types) of the system elements were found for two different locations. In addition, the effect of different values of the PEW on the results as a constraint was examined. While LPSP and cost values increase for less waste energy (PEW value), it has been observed that lower cost and LPSP values can be obtained for acceptable waste energy values. It is envisaged that this will facilitate the decision maker's selection of a realistic system configuration that can be implemented among Pareto results.

Keywords: Multi-objective optimization, renewable energy systems, hydrogen energy, Pareto optimum.

I. Introduction

HRES have become increasingly prevalent as an alternative for electrifying remote areas, primarily due to the depleting trend of fossil fuels and growing environmental concerns. Studies have revealed that, for these systems to be economically viable, optimization is required not only in terms of size but also concerning the reliability of the system, CO2 emissions, and energy usage efficiency. The Pareto optimal solution approach for multi-objective optimization is considered a more suitable method for real-life problems, as it allows decision-makers to make preferences based on their priorities within the multiple solution spaces (Tezer et al., 2017; Cheraghi and Jahangir 2023). In this approach, a collection of solutions known as the Pareto front is obtained, a concept introduced by Vilfredo Pareto (Machairas et al., 2014). The Pareto front comprises solutions that cannot be enhanced for any objective without simultaneously deteriorating at least one other objective, so that have not been dominated by any other member in the population (Tezer and Yaman, 2021).

In most previous studies, the focus within economic optimization has been on the system cost, neglecting the consideration of the cost of wasted energy. This study aims to address this gap by incorporating the minimization of the percentage of wasted energy (PEW) alongside system cost as the objective function. This approach also includes the minimization of the loss of power supply probability (LPSP) as a measure of system reliability. The developed approach, integrated with a power management strategy, seeks to simultaneously optimize system cost, wasted energy percentage, and LPSP. To solve the three-objective and multi-constrained optimization problem, a Pareto optimal solution approach based on NSGA-II has been developed.

Another innovation in this developed approach is its capability to perform system design optimization. This is in addition to the determination of system configuration for the minimization of these three objectives.

II. System Description and Methodology

The designed algorithm can generate alternative solutions for HRES consisting entirely of renewable sources. However, in this study, to evaluate the results, a system comprising PV panels, wind turbines (WTs), electrolyzer, hydrogen tank, fuel cell, and reformer has been considered (see Figure 1). Mathematical models and formulations of the system components can be examined from (Tezer and Yaman, 2021).

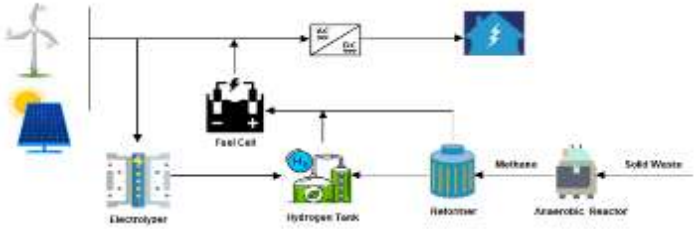

Fig. 1. Schematic diagram of components of the designed off-grid HRES

Multi Objective Optimization:

In this study, to solve the multi-objective and multi-constrained optimization problem i-NSGA-II (integrated size and design

optimization based NSGA-II) proposed. The objective functions aim to minimize ACS, LPSP, and PEW. The tri-objective optimization model can be expressed as follows.

$$\min\ F_{x,y} = \{F_{AC}, F_{LPSP}, F_{PEW}\} \quad (1)$$
$$x = (i_{PV}, i_{WT}, i_{FC}\ i_{ELC}, i_{HT}, i_{RFR})$$
$$y = (n_{PV}, n_{WT}, n_{FC}, n_{ELC}, n_{HT})$$
$$\text{subject to}$$
$$0 \le i_{PV}, i_{wt}, i_{FC}, i_{ELC}, i_{HT}, i_{RFR} \le I_{max}$$
$$1 \le n_{PV}, n_{WT}, n_{FC}, n_{ELC}, n_{HT} \le N_{max}$$
$$LPSP \le LPSP_{max}$$
$$PEW \le PEW_{max}$$

Here, N_{max} represents the maximum number that each system component can have in the system, and I_{max} represents the largest size value defined for each system component.

$$AC(\$) = \sum_{i=1}^{n} N_i \times [(CC_i + RC_i \times F_i(ir, L_i, y_i)) \times CRF(ir, R) + OMC_i] \quad (2)$$

where; n is the number of system elements, such as PV panels, reformers, vs; N is the number of component i, CC_i represents the capital cost ($/kW) of component I; RC_i is the difference between the total replacement costs of component i during the system lifetime and the remaining component cost at the end of the system life; F_i is the single payment present worth of component I; CRF is the capital recovery factor; OMC_i is the annual operation and maintenance cost of component i.

$$LPSP\ (\%) = \frac{\sum_{t=1}^{8760} LPS(t)}{\sum_{t=1}^{8760} P_{load}(t)} \quad (3)$$
$$LPS(t) = P_{load}(t) - P_{sist}(t) - P_{fc}(t) \quad (4)$$
$$PEW = \frac{\sum_{t=1}^{8760} P_{exc\_pvwt} - P_{load}(t) - P_{elc}(t)]}{\sum_{t=1}^{8760} P_{sist}(t)} \quad (5)$$

System design optimization: This optimization approach is different from the size optimization approach found in the literature, as it decides whether a component will be present in the system and, if so, its size (power). Thus, the presence of an element is represented by two separate structures representing its size and quantity, and the total size is equal to the product of these two. In addition, this approach includes the necessary steps to design a system where hydrogen can be present not only for energy storage but also as a direct energy source. Specifically, to ensure uninterrupted hydrogen production, if the system includes a fuel cell, there is a structure in place to have a reformer of a size that can meet the minimum and maximum hydrogen consumption of the fuel cell. Additionally, the presence of a hydrogen tank, along with the fuel cell, is ensured to store excess hydrogen in this case. Similarly, if an electrolyzer is present in the randomly generated initial population, it is arranged to include the fuel cell-HT pair with which it will work together is also included in the system.

In brief, the system is designed to regulate in a way that ensures the integrity of FC-ELC-HT or Reformer-FC-HT energy systems in a randomly generated initial population (system structure).

Finally, in the generated initial population, check whether there are at least two renewable energy sources in the system.

Here, it's important to note that the type (size) of a system component doesn't only refer to its nominal output power but also encompasses various characteristics such as the wind turbine's installation height, cut-in speed; PV temperature coefficient, efficiency; fuel cell hydrogen consumption, and so on. These values are read from the relevant table for each component within the PMS and are included in the calculations.

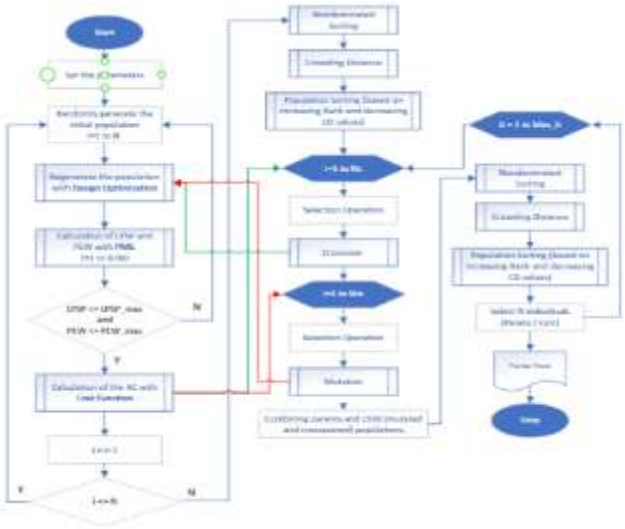

Fig.2 Flowchart of i-NSGA-II

Power Management Strategy (PMS)

The flow diagram and details of the PMS used in conjunction with NSGA-II can be thoroughly examined in detail in the author's previous work (Tezer and Yaman, 2021).

III. Analysis

In this study, an off-grid HRES consisting of PV-wind-hydrogen-reformer was evaluated as a case study for a typical house without access to a power distribution system in Balıkesir and Çanakkale, Turkey. The hourly load data from the IEEE (Institute of Electrical and Electronics Engineers) RTS (Reliability Test System) were employed to represent typical household electricity usage. The peak

load value was set at 4.5 kW. The hourly data for load, wind speed, solar radiation, and ambient temperature throughout the year are presented in Figure 3, Figure 4, and Figure 5, respectively.

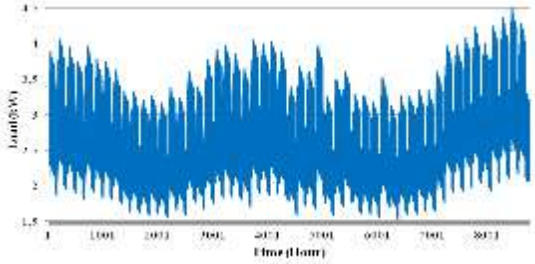

Fig. 3. Annual hourly load data of a typical house

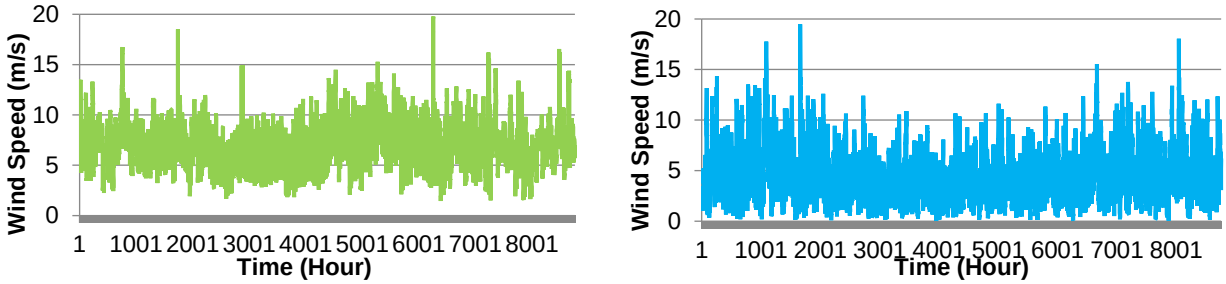

(a) (b)

Fig. 4. Annual wind speed data (a) Balıkesir (b) Çanakkale

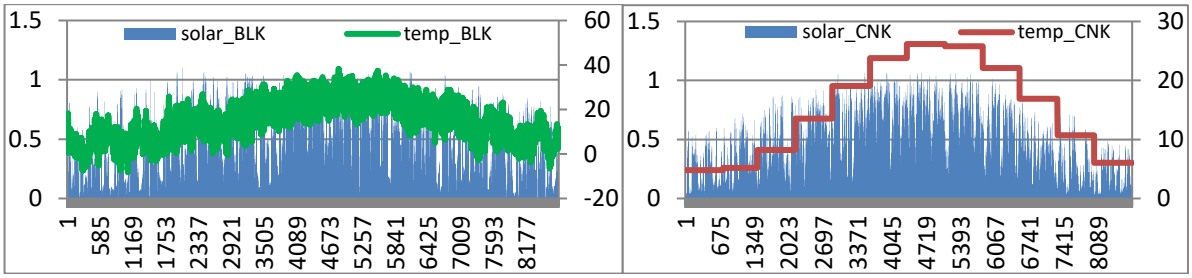

Fig. 5. Annual solar radiation and ambient temperature data (a) Balıkesir (b) Çanakkale

The total, average, minimum, maximum, and standard deviation values of the resources of both locations are given in Table 1.

Table 1. Comparison of data of wind, solar and temperature belonging to Balıkesir and Çanakkale**Hata! Bağlantı geçersiz.**

IV. Results and discussion

"Arial, 10 points, max 350 words" Usage and optimization studies of HRES for remote areas have been increasing in Turkey over the last decade. In this study, Balıkesir and Çanakkale provinces located in the west of Turkey were selected for simulations and their results were compared. Although the climate conditions of these two neighboring cities are similar, differences in wind energy potential have been identified. Annual average wind speeds are calculated as 4.41 m/s for Çanakkale and 6.98 m/s for Balıkesir. While the data for Balıkesir are based on hourly measurements from real data, the data for Çanakkale are obtained from the HOMERPro software. Despite the total solar radiation and temperature averages being relatively similar for both locations when examining Figure 5 and Table 1, significant differences in min, max, and standard deviation values for temperature data are observed. This difference is attributed to hourly variations in the real data. When examining the optimization results, regardless of the PEW constraint (see tables 2, 3, 4, 5), it is observed that PV panels are more prominent in the solutions for Çanakkale. This is because the Power Management System (PMS) tends to select less intermittent energy sources. Similarly, the inclusion of the reformer in the solutions is also attributed to this tendency. In the solutions for Balıkesir, wind turbines are preferred more, which is consistent with the higher average wind speed at this location, in addition to the same underlying reason.

Figures 6, 7, and 8 illustrate the Pareto solutions of the multi-objective optimization problem, taking into account the minimization of ACS, LPSP, and PEW values. In all scenarios, in addition to the objective functions, the constraint LPSP <= 5% has been considered. In Figures 7 and 8, additionally, constraints PEW <= 10% and PEW <= 5% have been evaluated, respectively.

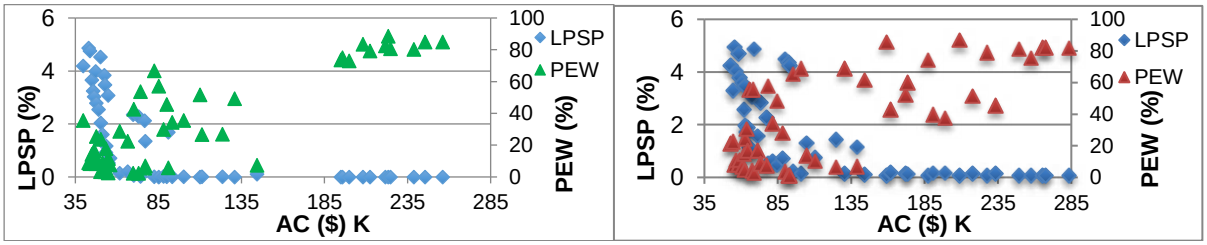

(a) (b)

Fig. 6. The Pareto front 5% LPSP and without PEW constraints (a) Balıkesir (b) Çanakkale

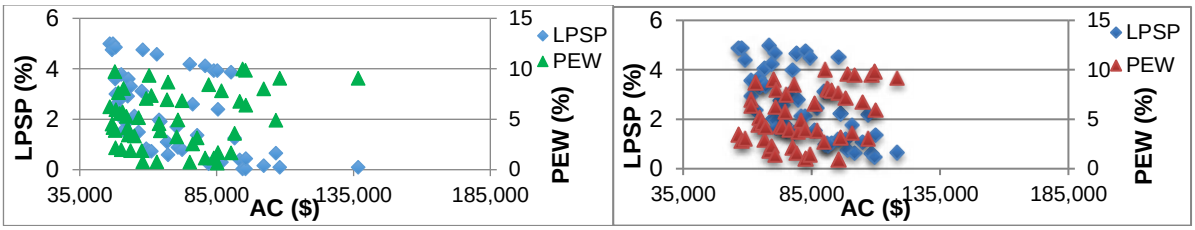

(a) (b)

Fig. 7. The Pareto front with 5% LPSP and 10% PEW constraints (a) Balıkesir (b) Çanakkale

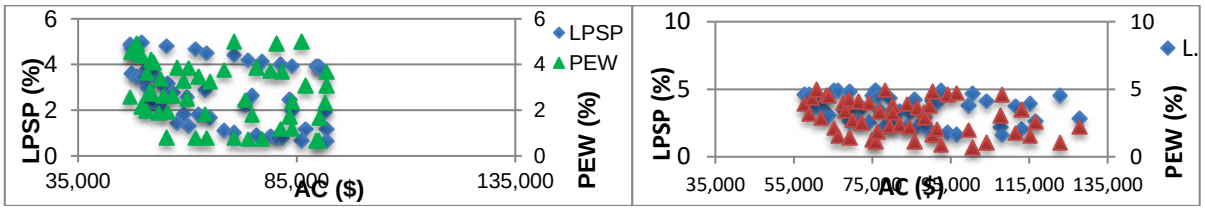

(a) (b)

Fig. 8 The Pareto front with 5% LPSP and 5% PEW constraints (a) Balıkesir (b) Çanakkale

Tables 2, 3, 4 and 5, include the lowest AC, LPSP, and PEW values from the Pareto results of Figure 6 (a), 6 (b), 8 (a) and (b), respectively.

Table 2. Solutions of the Pareto Front (with LPSP<=5% and no PEW constraint) for Balıkesir

		i_{PV} (kW)	n_{PV}	i_{WT} (kW)	n_{WT}	i_{FC} (kW)	n_{FC}	i_{ELC} (kW)	n_{ELC}	i_{HT} (kg)	n_{HT}	i_{RFR} (kg)	*ACS (25 yrs) ($)*	*LPSP (%)*	*PEW (%)*
1	Lowest AC Solution	1	4	1	8	1	2	0	-	2.5	1	0.6	39718	4.19	35.6
2	Lowest LPSP Solution	0	-	8	13	1	5	5	7	3.5	14	0.2	256092	0.00	84.8
3	Lowest PEW Solution	0	-	1	4	2	2	2	3	4	9	0.6	72926	2.3	2.4

Table 3. Solutions of the Pareto Front (with LPSP<=5% and no PEW constraint) for Çanakkale

		i_{PV} (kW)	n_{PV}	i_{WT} (kW)	n_{WT}	i_{FC} (kW)	n_{FC}	i_{ELC} (kW)	n_{ELC}	i_{HT} (kg)	n_{HT}	i_{RFR} (kg)	*ACS (25 yrs) ($)*	*LPSP (%)*	*PEW (%)*
1	Lowest AC Solution	6	2	1	3	2	2	0	-	3.5	2	0.6	52773	4.23	21.3
2	Lowest LPSP Solution	10	15	3	15	2	9	4	15	3.5	13	0.6	267558	0.06	81.9
3	Lowest PEW Solution	4	1	2	3	2	2	3	2	4	15	0.6	92955	4.23	1.05

Table4. Solutions of the Pareto Front (with LPSP <= 5% and PEW <= 5% constraints) for Balıkesir

		i_{PV} (kW)	n_{PV}	i_{WT} (kW)	n_{WT}	i_{FC} (kW)	n_{FC}	i_{ELC} (kW)	n_{ELC}	i_{HT} (kg)	n_{HT}	i_{RFR} (kg)	*ACS (25 yrs) ($)*	*LPSP (%)*	*PEW (%)*
1	Lowest AC Solution	2	1	1	3	2	2	0	-	4	1	0.6	46884	4.86	2.56
2	Lowest LPSP Solution	1	1	1	4	2	3	2	1	4	15	0.6	91830	0.64	3.65
3	Lowest PEW Solution	1	1	1	3	2	3	2	1	4	15	0.6	89976	3.92	0.66

Table 5. Solutions of the Pareto Front (with LPSP <= 5% and PEW <= 5% constraints) for Çanakkale

		i_{PV} (kW)	n_{PV}	i_{WT} (kW)	n_{WT}	i_{FC} (kW)	n_{FC}	i_{ELC} (kW)	n_{ELC}	i_{HT} (kg)	n_{HT}	i_{RFR} (kg)	*ACS (25 yrs) ($)*	*LPSP (%)*	*PEW (%)*
1	Lowest AC Solution	5	1	1	5	2	2	2	1	3.5	3	0.6	57807	4.60	3.86

2	Lowest LPSP Solution	5	1	2	4	2	4	3	3	4	15	0.6	108085	1.61	4.61
3	Lowest PEW Solution	6	1	1	6	3	2	4	2	4	15	0.6	100579	4.68	0.66

Upon reviewing the tables, it is observed that the systems with the presence of an electrolyzer have lower LPSP values. This indicates the importance of energy storage for system reliability. In Tables 4 and 5, the presence of the PEW constraint increases the system cost and decreases system reliability, as evident from the increasing AC and decreasing LPSP values, respectively. The reduction of waste energy, or in other words, an increase in the energy usage ratio, is achievable with less power and more storage. Considering LPSP and PEW values as constraints helps maintain a balance among all three objective functions.

V. Conclusion

This study introduced the i-NSGA-II approach including the system design optimization and the PMS, as a novel method for minimizing ACS, LPSP and PEW values. This approach stands out for its flexibility in designing power sources and hydrogen storage systems with different characteristics and quantities for both small and large-scale independent HRES. With an effective PMS, it enables the more efficient utilization of power. The addition of constraints that facilitate decision-makers in selecting the most suitable solution for the current situation also maintains a balance in the system between cost, reliability, and efficiency. This capability allows for the customization of solutions tailored to the specific needs of independent energy systems, offering a more effective and adaptable approach in HRES design.

Despite the geographical proximity and similar climate conditions of these two regions, notable differences in wind energy potential were identified. Furthermore, the difference between measured hourly data and the converted hourly data from average data has emerged in the results for these two distinct locations. Accordingly, the measured real data showing hourly variations leads to a longer calculation time due to greater fluctuations. This also indicates a shift in system design towards the utilization of more uninterrupted energy sources to increase the performance of the system.

References

Cheraghi R., Jahangir M.H., (2023) Multi-objective optimization of a hybrid renewable energy system supplying a residential building using NSGA-II and MOPSO algorithms, En. Con. and Manag. 294. https://doi.org/10.1016/j.enconman.2023.117515.

Koholé Y.W., Wankouo Ngouleu C.A., Fohagui F.C.V., Tchuen G., (2023) An effective sizing and sensitivity analysis of a hybrid renewable energy system for household, multi-media and rural healthcare centres power supply: A case study of Kaele, Cameroon, Int. Journal of Hydrogen Energy, In Press, Corrected Proof. https://doi.org/10.1016/j.ijhydene.2023.09.093.

Kilic M., Altun A.F., (2023) Dynamic modelling and multi-objective optimization of off-grid hybrid energy systems by using battery or hydrogen storage for different climates, Int. Journal of Hydrogen Energy 48 (60), 22834-22854. https://doi.org/10.1016/j.ijhydene.2022.12.103.

Machairas V., Tsangrassoulis A., Axarli K., (2014) Algorithms for optimization of building design: A review, Renew Sustain Energy Rev, 31 , 101-112. https://doi.org/10.1016/j.rser.2013.11.036.

Medghalchi Z., Taylan O., (2023) A novel hybrid optimization framework for sizing renewable energy systems integrated with energy storage systems with solar photovoltaics, wind, battery and electrolyzer-fuel cell, Energy Convers. Manag. 294. https://doi.org/10.1016/j.enconman.2023.117594.

Tezer T., Yaman R., Yaman G., (2017) Evaluation of approaches used for optimization of stand-alone hybrid renewable energy systems, Ren. and Sust. Energy Reviews 73, 840–853. https://doi.org/10.1016/j.rser.2017.01.118.

Tezer T., Yaman R., (2022) A Pareto Optimum Approach and a Power Management Strategy for a Stand-Alone Wind Turbine-PV-Hydrogen with Reformer Hybrid Renewable Energy System, Env. Prog. & Sust. En.41(4). **https://doi.org/10.1002/ep.13772**

IEEES-086

Comparison of Lithium-sulfur and Lithium Iron Phosphate Batteries for Present and Prospective Battery Management System of Electric Vehicles

*Gamze Nalçacı
Necmettin Erbakan University, Engineering Faculty,Electrical and Electronics Department, Konya, 42005, Turkey
*E-mail: gnalcaci@erbakan.edu.tr

Abstract

In order to be deemed suitable for use in portable devices, electric cars, and grid storage, advanced energy-storage systems must satisfy a range of requirements. These include but are not limited to affordability, durability, safety compliance, high energy density, high power output, and ecological compatibility. The implementation of a battery management system (BMS) is crucial in guaranteeing the safety and enhancing the longevity of lithium-ion battery packs. Lithium-sulfur (Li-S) batteries exhibit significant potential as a forthcoming high-energy system, given their particular characteristics. The innovation of this scientific work lies in the utilization of Li-S and lithium-iron phosphate batteries in a BMS for evaluating the vehicle's autonomy and the efficiency of various battery types during real-time driving cycles, which are digitized through computer simulation.

Keywords: Lithium-sulfur battery, lithium iron battery, electric vehicles, battery management system.

I. Introduction

The energy storage system (ESS) has gained significant popularity across various areas, including electric vehicles (EV), renewable energy storage, and micro/smart-grid applications, among others. Contemporary generations of electric vehicles (EVs) have emerged as a dependable alternative to internal combustion engines (ICEs) (Habib et al., 2023). Vehicles and boats that rely on internal combustion engines (ICE), including trucks, ships, cargo carriers, and aircraft, account for approximately one-third of global fossil fuel consumption. The emission of carbon dioxide (CO2), sulfur dioxide (SO2), carbon monoxide (CO), and nitrogen oxides (NO) is mostly attributed to the activities of ICE (Internal Combustion Engines) and other industries. These sources are widely recognized as the main contributors to the emissions above (Hasan et al., 2021). These gaseous substances contribute to atmospheric pollution, which in turn is accountable for the phenomenon known as the greenhouse effect. In the domain of electric vehicles (EVs), the Electric Energy System (EES) is responsible for powering the EV motor as well as several auxiliary components such as the air conditioner and navigation lighting. The electric vehicle (EV) is widely recognized for its ability to operate without emitting carbon, resulting in negligible levels of SO2, CO2, NO, and CO emissions when driving. It is important to acknowledge the environmental obstacles and the implications of fossil fuel consumption when evaluating the EV's impact (Gholami et al., 2022). EVs have emerged as a viable and promising option for diesel-based vehicles due to their advantages in emissions reduction, as well as their simplicity, reliability, comfort, and energy efficiency (Zheng et al., 2020). Nevertheless, the widespread implementation of electric vehicles (EVs) necessitates the establishment of effective functionalities and diagnostic procedures for the battery storage system (BSS). These functionalities include battery cell monitoring, discharge and charge control, cell balancing, heat management, and power management control (Kumar and Alok, 2020).

Currently, lithium-ion batteries (200-250 Wh/kg) have become the most popular option in the electric vehicle (EV) battery industry. This is due to the fact that these batteries possess a number of notable characteristics, including increased power and energy density, high voltage, extended life cycles, and minimal self-discharge rates (Nikolian et al., 2016). On the other hand, it is essential to keep in mind that lithium batteries are subject to the effects of temperature and the effects of aged batteries. As a result, it is of the utmost importance to pay strict attention to the conditions in which they function in order to avoid any potential physical damage, aging, or thermal runaways (Lipu et al., 2021). One of the most important aspects of the operation of electric vehicles (EVs) is the battery management system (BMS), which is responsible for monitoring a variety of factors, including the temperature, voltage, and current of the battery. Furthermore, it is accountable for evaluating the charge, energy, and overall health of the battery, in addition to regulating the temperature, ensuring that the voltage is uniform across all of the individual cells, and identifying any potential malfunctions that may occur (Lin et al., 2019). The fundamental responsibilities of an efficient Battery Management System (BMS) include the accurate calculation and evaluation of a number of different battery states. These states include the state of charge (SOC), the state of energy (SOE), the state of health (SOH), and the remaining useful life (RUL). Furthermore, it is the responsibility of the BMS to regulate the temperatures of the batteries in order to guarantee that they remain within the acceptable range. In addition, the BMS is responsible for fault diagnosis, fault prognosis, and fault handling activities. The battery management system (BMS) is responsible for ensuring that the voltage, charge, and capacity of the battery cells are distributed in an equitable manner (Ali et al., 2019).

Lithium-sulfur batteries (Li-S) have considerable potential as a viable option for future energy storage systems due to their notable theoretical energy density and the abundant availability of sulfur (Zhao et al., 2023). Currently, lithium-sulfur (Li-S) technology is regarded as highly promising due to its superior theoretical energy density of approximately 2600 Wh/kg. Additionally, Li-S batteries are manufactured using comparatively cheap and nonpoisonous materials, which is anticipated to result in reduced battery costs and negative environmental effects (Benveniste et al., 2018). Lithium iron phosphate has been the subject of substantial research due to its abundant supplies, minimal toxicity, exceptional stability, and cost-effectiveness.

In this study, next-generation Li-S and Lithium iron phosphate batteries are compared in detail. Especially Li-S batteries have superior performance in terms of energy density and cost than LFP batteries.

II. Li-S Batteries

The lithium-sulfur battery presented in Fig.1, often known as the Li-S battery, is classified as a rechargeable battery. The great particular energy of the subject is worthy of attention. The comparatively low atomic weight of lithium and the moderate atomic weight of sulfur contributes to the lightweight nature of Li-S batteries, which possess a density comparable to that of water. In August 2008, the Zephyr 6 aircraft utilized these devices during its unmanned solar-powered flight, which held the record for the longest duration and greatest altitude at that time.

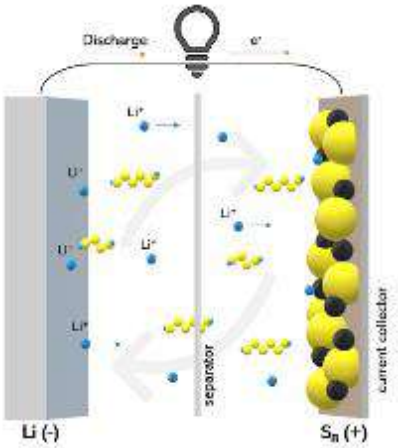

Fig. 1: Structure of Li-S battery

Lithium-sulfur batteries have the potential to replace lithium-ion cells due to their superior energy density and cost-effectiveness. The reason for this phenomenon can be attributed to the utilization of sulfur as an alternative to cobalt, which is a prevalent constituent in lithium-ion batteries. The user has not provided any text to rewrite. Li-S batteries exhibit specific energies approximately around 550 Wh/kg, as reported by a study [1]. In comparison, lithium-ion batteries possess specific energies ranging from 150 to 260 Wh/kg. In 2017, Li-S batteries were successfully proven to have a maximum of 1,500 charge and discharge cycles. However, it is important to note that comprehensive cycle life studies at a commercial scale and with a reduced amount of electrolyte have not yet been conducted. As of the beginning of 2021, there were no commercially available options.

There are some factors that have impeded the acceptance of this technology, one of which is the polysulfide "shuttle" effect. This phenomenon is accountable for the gradual loss of active material from the cathode, leading to a limited number of recharge cycles. The user's text is already academic and does not need to be rewritten. Moreover, sulfur cathodes exhibit a diminished level of conductivity, necessitating the inclusion of additional mass to serve as a conducting agent. This is done to effectively harness the contribution of the active mass towards enhancing the capacity. The expansion of the sulfur cathode volume during the conversion from sulfur to Li2S, as well as the substantial quantity of electrolyte required, are additional concerns. During the early 2000s, researchers initiated advancements in the development of sulfurized-carbon cathodes with enhanced stability [9]. Subsequently, in 2020, experts from Rice University successfully showcased batteries utilizing sulfurized carbon cathodes, which exhibited a remarkable capacity retention of over 70% after undergoing 1000 cycles (Gupta et al., 2022). The user's text is already academic and does not require any rewriting. Zeta Energy, a startup headquartered in Texas, has recently declared that its lithium-sulfur batteries, which utilize sulfurized-carbon cathodes, have been validated as polysulfide shuttle free by various national laboratories. This verification was conducted independently. It is projected that this achievement will be realized by the year 2023.

III. LFP Batteries

The battery seen in Figure 2 is commonly referred to as the lithium iron phosphate (LiFePO4 or LFP) battery. It is a distinct type of lithium-ion battery that employs lithium iron phosphate (LiFePO4) as its cathode material. Furthermore, it utilizes a graphitic carbon electrode that is supported by a metallic framework, serving as the anode. Lithium iron phosphate (LFP) batteries are gaining popularity in a range of applications, such as vehicular usage, utility-scale stationary systems, and backup power solutions, due to their cost-effectiveness, improved safety features, reduced toxicity, longer cycle life, and other factors. Lithium-iron phosphate (LFP) batteries do not contain cobalt. Based on the most recent data accessible as of September 2022, the market penetration of Lithium Iron Phosphate (LFP) batteries within the electric vehicle (EV) sector has attained a share of 31%. It is worth noting that a substantial proportion of the market share, precisely 68%, may be attributable only to the output of Tesla and the Chinese electric vehicle producer BYD. The user's text does not provide any information to rework in an academic manner. At present, Chinese manufacturers hold a substantial majority stake in the manufacturing of LFP batteries. It is expected that the expiration of patents in 2022, along with the increasing demand for cost-effective electric vehicle (EV) batteries, would lead to a significant rise in the manufacturing of Lithium Iron Phosphate (LFP) batteries. According to Mackenzie (2022), it is anticipated that by the year 2028, Lithium Iron Phosphate (LFP) batteries will surpass Lithium Nickel Manganese Cobalt Oxide (NMC) batteries in terms of production.

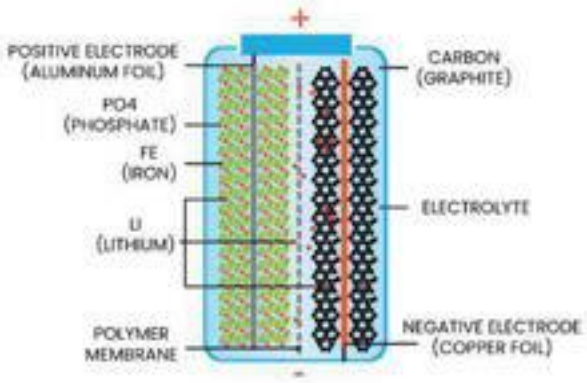

Fig. 2: Schematic diagram of LFP battery

The energy density of lithium iron phosphate (LFP) batteries is, in comparison to the energy density of other regularly used varieties of lithium-ion batteries, such as nickel manganese cobalt (NMC) and nickel cobalt aluminum (NCA), a figure that is somewhat lower. At the moment, the energy density of CATL's LFP battery is reported at 125 Watts-hours per kilogram (Wh/kg). However, with advancements in packaging technology, it is possible to achieve a higher value of up to 160 Wh/kg from this battery. The LFP battery manufactured by BYD is said to have an energy density of 150 Wh/kg, as mentioned in the publications that are currently available. In addition to having energy densities that are greater than 300 Wh/kg, NMC batteries have remarkable performance. The energy density of Panasonic's "2170" NCA batteries, which are used in Tesla's 2020 Model 3, is roughly 260 Wh/kg. This is something that should be mentioned because it is important. In the event that only the "pure chemicals" involved are taken into consideration, this figure represents seventy percent of the energy density of the batteries. In comparison to other types of lithium-ion batteries, lithium iron phosphate (LFP) batteries have a voltage that is significantly lower when they are in operation.

IV. Results and Comparison

Over the past three decades, the market for energy storage has been predominantly controlled by lithium-ion batteries. The attention of numerous researchers has been drawn to the need for increased energy density in Li-ion batteries, as a result of the significant expansion of electric vehicles (EVs) and hybrid electric vehicles. Consequently, there is a demand for electrode materials that possess high charge/discharge capacity or higher cell operating voltage. However, it is worth noting that the present cathodic materials used in Li-ion batteries, such as LiFePO4, mostly operate through an insertion mechanism. This mechanism imposes a constraint on the capacity, limiting it to below 200 mAh g^{-1}, and thus hinders the potential for enhancing the energy density of Li-ion batteries. Hence, the utilization of sulfur cathode materials in Li-S batteries, which exhibit a substantial specific theoretical capacity of 1675 mAh g^{-1} and a commendable energy density, renders them highly desirable for energy storage applications. Furthermore, the comparatively lower cost of sulfur and the environmentally friendly nature of LieS batteries position them as a more favorable option when compared to sophisticated Li-ion batteries. Table 1 presents a comprehensive comparison of the parameters of Li-S and LFP batteries in terms of physical properties.

Table 1. Comparison of Li-S and LFP batteries

Battery	Anode	Cathode	Capacity	Cycle life	Thermal properties	Voltage
Li-S	*Li metal*	*Sulfur*	*550*	*Approximately 200*	-	*2-2.5 V*
LFP	*Graphite*	*Lithium phosphate*	*90-120*	*>2000*	*270 °C*	*2.5-3.6*

V. Conclusion

Batteries provide distinctive attributes such as low cost, nontoxicity, availability, and notably, enhanced discharge capacity (1675 mAh g^{-1}) and energy density (2600 Wh kg^{-1}), which contribute to their potential for retaining value in the future. The resolution of the prevailing obstacles, namely, inadequate conductivity, limited lithium diffusivity, and abbreviated life cycle, will augment their feasibility in a commercial context. Nevertheless, several approaches have been documented in the literature to improve conductivity and reduce the shuttle effect through modifications of battery components such as the cathode, anode, and electrolyte. However, it is important to note that further investigation is needed in this area to fully explore the potential for future advancements. There is a requirement to enhance the performance of cells through modifications, while simultaneously ensuring that the associated costs remain acceptable. For instance, one potential approach is the incorporation of metal oxide in the cathode. One crucial aspect in the advancement of mass commercialization is the substantial improvement of the cycle life of Lithium-Sulfur (Li-S) cells. In order to be considered a viable product for the market, cells must demonstrate consistent performance across a minimum of 200 cycles, with a maximum capacity drop of 60%. Expanding the deployment possibilities for LieS cells would be significantly enhanced by achieving a goal cycle life of 500 cycles. The implementation of cathodes with high sulfur loading and increased thickness, along with the aforementioned reductions in electrolyte content and excess lithium, will lead to an augmented volumetric energy density. The facilitation of widespread deployment of LieS batteries has been recognized as a significant goal. In order to fully harness the capabilities of LieS cells, it is important to do comprehensive research including several aspects of the cell, such as the electrolyte and shielding anode. Additionally, attention must be given to control and technological variables that facilitate the operation of larger-scale batteries. Furthermore, it is important to consider novel fundamental understandings pertaining to the procedure of the reaction.

References

Ali, M. U., Zafar, A., Nengroo, S. H., Hussain, S., Junaid Alvi, M., & Kim, H. J. (2019). Towards a smarter battery management system for electric vehicle applications: A critical review of lithium-ion battery state of charge estimation. Energies, 12(3), 446.

Benveniste, G., Rallo, H., Casals, L. C., Merino, A., & Amante, B. (2018). Comparison of the state of Lithium-Sulphur and lithium-ion batteries applied to electromobility. Journal of Environmental Management, 226, 1-12.

Gholami, K., Azizivahed, A., & Arefi, A. (2022). Risk-oriented energy management strategy for electric vehicle fleets in hybrid AC-DC microgrids. Journal of Energy Storage, 50, 104258.

Gupta, R., Nguyen, T. A., Song, H., & Yasin, G. (Eds.). (2022). Lithium-Sulfur Batteries: Materials, Challenges and Applications.

Habib, A. A., Hasan, M. K., Issa, G. F., Singh, D., Islam, S., & Ghazal, T. M. (2023). Lithium-Ion Battery Management System for Electric Vehicles: Constraints, Challenges, and Recommendations. Batteries, 9(3), 152.

Hasan, M. K., Mahmud, M., Habib, A. A., Motakabber, S. M. A., & Islam, S. (2021). Review of electric vehicle energy storage and management system: Standards, issues, and challenges. Journal of energy storage, 41, 102940.

Kumar, R. R., & Alok, K. (2020). Adoption of electric vehicle: A literature review and prospects for sustainability. Journal of Cleaner Production, 253, 119911.

Lin, Q., Wang, J., Xiong, R., Shen, W., & He, H. (2019). Towards a smarter battery management system: A critical review on optimal charging methods of lithium ion batteries. Energy, 183, 220-234.

Lipu, M. H., Hannan, M. A., Karim, T. F., Hussain, A., Saad, M. H. M., Ayob, A., Mahlia, T. I. (2021). Intelligent algorithms and control strategies for battery management system in electric vehicles: Progress, challenges and future outlook. Journal of Cleaner Production, 292, 126044.

Mackenzie, W. (2022). Global lithium-ion battery capacity to rise five-fold by 2030.

Nikolian, A., Firouz, Y., Gopalakrishnan, R., Timmermans, J. M., Omar, N., Van den Bossche, P., & Van Mierlo, J. (2016). Lithium ion batteries—Development of advanced electrical equivalent circuit models for nickel manganese cobalt lithium-ion. Energies, 9(5), 360.

Zhao, F., Xue, J., Shao, W., Yu, H., Huang, W., & Xiao, J. (2023). Toward high-sulfur-content, high-performance lithium–sulfur batteries: Review of materials and technologies. Journal of Energy Chemistry.

Zheng, J., Sun, X., Jia, L., & Zhou, Y. (2020). Electric passenger vehicles sales and carbon dioxide emission reduction potential in China's leading markets. Journal of Cleaner Production, 243, 118607.

IEEES-087

Design and Analysis of a Floating Photovoltaic Based Ammonia Production System

*Sibel Uygun Batgi and Ibrahim Dincer
Clean Energy Research Laboratory (CERL), FEAS, Ontario Tech University, Oshawa, Ontario, L1H 7K4, Canada
*E-mails: sibel.uygun@ontariotechu.ca

Abstract

This proposed study introduces an analysis and assessment study of an ammonia production system. The system which is selected for a case study application in Adana, Turkey includes proton exchange membrane electrolyzer, cryogenic air separation, and ammonia synthesis reactor, with a floating PV system offsetting electricity demand. A proton exchange membrane electrolyzer produces H_2, which is used as a raw material in ammonia manufacturing, while cryogenic air separation produces N_2. The electricity needed for these systems is generated by floating photovoltaic panels placed on the dam. As a system analysis method, various software is used. The thermodynamic analysis of the entire system is performed using Engineering Equation Solver (EES), floating photovoltaic modelling is performed using System Advisor Model (SAM), and the ammonia production system is simulated using Aspen Plus software. A parametric study of the effect of hydrogen and ammonia flow rates on ammonia production was conducted using the Aspen Plus software program. The optimum values for the H_2 and N_2 flow rates into the system were 126.20 kg/h and 586.24 kg/h, respectively, and the ammonia production rate was 674.93 kg/h.

Keywords: Solar energy, hydrogen, ammonia, floating photovoltaic.

1. Introduction

The growing human population has raised energy demand and, consequently, energy consumption. Since fossil-based energy sources have mostly satisfied energy demand from the past to the present, our globe is confronting a climate crisis (Soares et al., 2018). Today, fossil-based power plants are still in the majority. To reduce greenhouse gas emissions, fossil fuels should be substituted by renewable energy. Some initiatives done to address the global warming crisis include increasing the number of hydroelectric power plants and producing energy from renewable sources (Ozbilen et al., 2012). Among renewable energy systems, solar photovoltaic (PV) offers one of the smallest levelized electricity costs. The key obstacles of solar PV systems, on the other hand, are the land-use needs of solar power plants and the fluctuating nature of solar energy (Martín-Chivelet, 2016). The intermittent nature of solar energy can be effectively addressed by implementing strategies such as integrating energy storage systems or grid within solar-based energy production facilities and incorporating a secondary energy source into the system. Solar PV systems could be constructed on underutilised surfaces such as rooftops or bodies of natural water to meet land-use requirements (Poulek et al., 2018). Floating PV systems use underutilised water resources such as the sea, lake, ocean, or river, freeing up land for uses like as agriculture, tourism, and housing (Temiz and Dincer, 2022). Green ammonia manufacturing plants are constructed with the integration of clean energy sources to produce ammonia, one of the most widely utilised compounds in the industrial sector, in an environmentally responsible manner. The raw materials utilised to manufacture sustainable ammonia must be manufactured using ecologically friendly technology. H_2, used as raw material, can be obtained by using electricity obtained from renewable energy sources in the electrolyzer. Another raw material is nitrogen, and nitrogen can be obtained by cryogenic air separation technique (Frattini et al., 2016). Ozturk and Dincer (2021) proposed an integrated system for ammonia production from renewable hydrogen. They found that the highest energy and exergy efficiencies for the total system are 26.08% and 30.17%, respectively, at the lowest solar radiation intensity. Hasan and Dincer (2019) developed an integrated wind and PV system for ammonia and power production for a sustainable community. They calculated the energy, exergy values as 75.8% and 73.6% respectively. The goal of this research is to design an integrated system for ammonia synthesis from renewable hydrogen and air for the city of Adana, Turkey, analyse it thermodynamically using energy and exergy techniques, and evaluate its performance using total energy and exergy efficiencies. The impact of modifying some features and operating circumstances on the performance of the proposed system were investigated through parametric studies.

2. System Description

In this proposed system layout, Figure 1 depicts an ammonia manufacturing plant including a PEM (polymer electrolyte membrane) electrolyzer, a cryogenic air separation unit, and an ammonia synthesis reactor. The ammonia manufacturing unit includes a PSA (pressure swing adsorption) unit. In the air separation unit, the compressor first compresses the air, which is then removed through a heat exchanger. This heat can be used for district heating or to provide hot water. Heat from exchangers will also be used to cool and heat greenhouses and food drying factories. The nitrogen required for ammonia production comes from the cryogenic air separation unit, while the hydrogen comes from the PEM electrolyzer. The floating photovoltaic (PV) panels mostly offset the electricity demand for electrolyzers and compressors. When sunlight is insufficient, the dam can serve as another energy source. If the electricity demand and network capacity are exceeded, using the excess electricity for hydrogen synthesis is a solution to store excess energy. The intended location for the floating PV panel is Adana, Turkiye. Fig. 2 depicts an annual direct normal irradiation (DNI)-months graph. Synthesized ammonia can be used in agriculture, transportation, industrial, commercial, utility, and residential sectors.

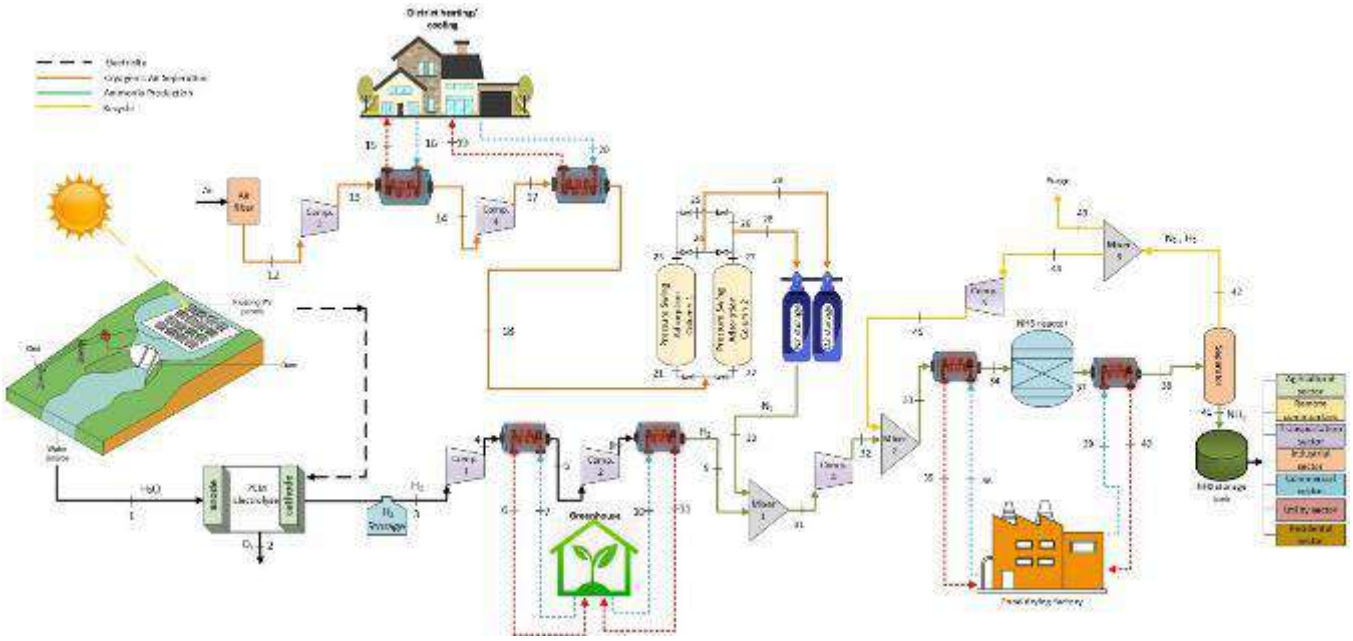

Fig. 1: A schematic layout of the renewable energy-based ammonia production system.

3. Analysis

The performance of the entire system was evaluated using both the first and second thermodynamic principles. The system is thermodynamically analysed using both energy and exergy examinations. The EES and Aspen Plus simulation software are utilised as analysis methods. The floating PV system is analyzed using SAM. For the thermodynamic analysis of the systems, the EES software is used. In this research, the ammonia production subsystem is simulated using the Aspen Plus.

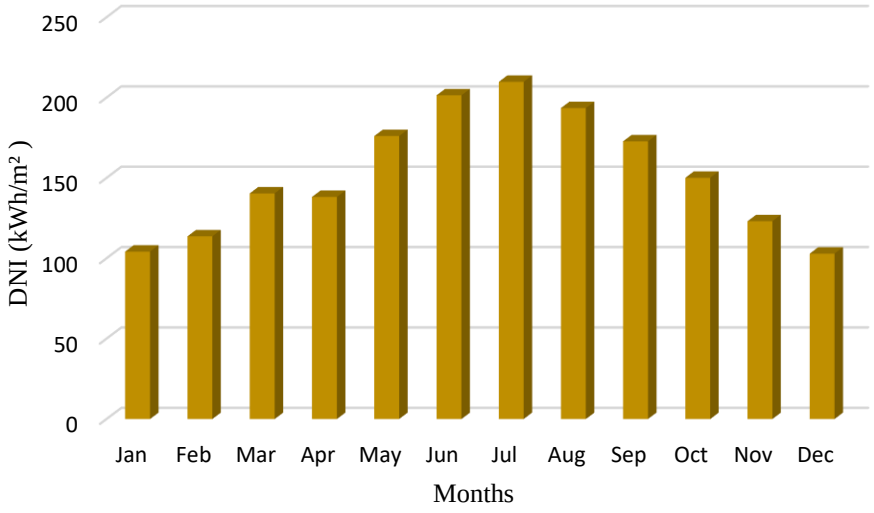

Fig. 2: Monthly DNI of Adana, Turkiye.

4. Results and discussion

Aspen Plus simulations of the Ammonia production system cycle have been performed in this study. Aspen Plus predicts the behavior of process reactions and steps using standard engineering relationships, mass, and energy. A parametric study looking at the molar flow rates of the raw materials (N_2 and H_2) fed into the system and the resulting ammonia production was carried out within the scope of this research. A parametric study was conducted for flow rates of 75, 80, 85, 90, 95, 100 kmol/h, respectively. Fig. 3 demonstrates the change of mass flow rate for different molar flow rate values of the streams. When the molar flow rates of the input streams are 75, 80, 85, 90, 95, and 100 kmol/h, ammonia production mass flow rates are 595.53 kg/h, 635.23 kg/h, 674.93 kg/h, 714.62 kg/h, 754.34 kg/h, and 794.04 kg/h, respectively.

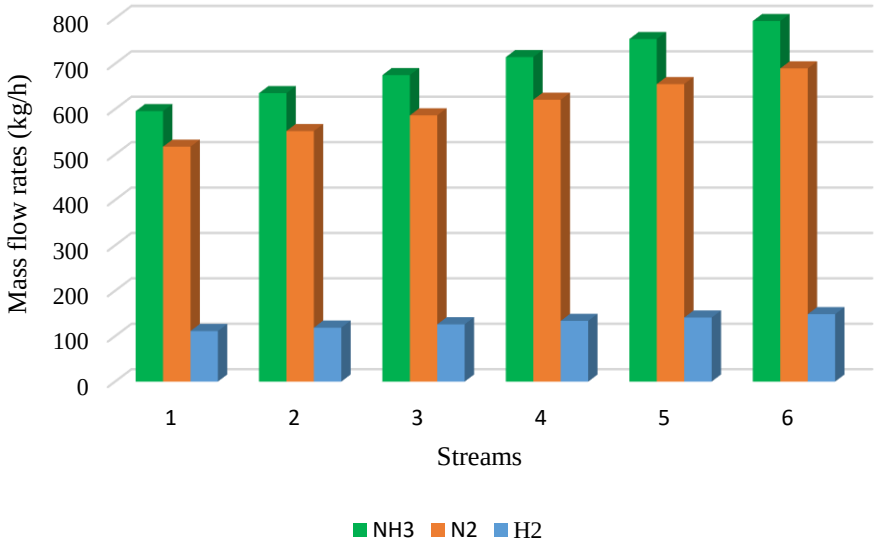

Fig. 3. The change of mass flow rate for different molar flow rate values of the streams

5. Conclusions

Working with various input molar flow rates for the ammonia production system in the Aspen Plus software programme, the optimum value for ammonia production has been determined to be 85 kmol/h. For this value, the mass flow rates of H_2 and N_2 input values are 126.20 kg/h and 586.24 kg/h, respectively, while the produced NH_3 value is 674.93 kg/h.

References

Frattini, D., Cinti, G., Bidini, G., Desideri, U., Cioffi, R., Jannelli, E., 2016. A system approach in energy evaluation of different renewable energies sources integration in ammonia production plants. Renew Energy 99, 472–482. https://doi.org/10.1016/j.renene.2016.07.040

Hasan, A., Dincer, I., 2019. Development of an integrated wind and PV system for ammonia and power production for a sustainable community. J Clean Prod 231, 1515–1525. https://doi.org/10.1016/j.jclepro.2019.05.110

Martín-Chivelet, N., 2016. Photovoltaic potential and land-use estimation methodology. Energy 94, 233–242. https://doi.org/10.1016/j.energy.2015.10.108

Ozbilen, A., Dincer, I., Naterer, G.F., Aydin, M., 2012. Role of hydrogen storage in renewable energy management for Ontario. Int J Hydrogen Energy 37, 7343–7354. https://doi.org/10.1016/j.ijhydene.2012.01.073

Ozturk, M., Dincer, I., 2021. An integrated system for ammonia production from renewable hydrogen: A case study. Int J Hydrogen Energy 46, 5918–5925. https://doi.org/10.1016/j.ijhydene.2019.12.127

Poulek, V., Matuška, T., Libra, M., Kachalouski, E., Sedláček, J., 2018. Influence of increased temperature on energy production of roof integrated PV panels. Energy Build 166, 418–425. https://doi.org/10.1016/j.enbuild.2018.01.063

Soares, W.M., Athayde, D.D., Nunes, E.H.M., 2018. LCA study of photovoltaic systems based on different technologies. Int J Green Energy 15, 577–583. https://doi.org/10.1080/15435075.2018.1510408

Temiz, M., Dincer, I., 2022. Design and analysis of a floating photovoltaic based energy system with underground energy storage options for remote communities. J Energy Storage 55. https://doi.org/10.1016/j.est.2022.105733

IEEES-088

Impact of Reaction Parameters on Biodiesel Yield and Fuel Characteristics: A Case Study on Algal Oil

[1*]Cemil Koyunoğlu, [2]Fevzi Yaşar
[1] Yalova University, Engineering Faculty, Energy Systems Engineering Department, Çinarcik Road 5th km, Yalova University, Yalova, 77200, Turkey
1. [2]Department of Refinery and Petro-Chemistry Batman University, 72100 Batman, Turkey
*E-mails: cemil.koyunoglu@yalova.edu.tr

Abstract

In the pursuit of sustainable energy sources, biodiesel production from algal oil has gained significant attention. This study delves into the optimization of key reaction parameters to enhance biodiesel yield and fuel properties. The investigation begins with the determination of the suitable catalyst amount, followed by assessing the effects of reaction temperature and time. The physical and chemical properties of the produced biodiesel are then compared with EN14214 and ASTM D6751 biodiesel standards, along with petroleum-derived diesel fuel.

Keywords: Biodiesel, algal oil, transesterification, catalyst, reaction parameters, fuel properties, optimization, sustainability.

I. Introduction

The conversion of algal oil into biodiesel via transesterification is a promising route to environmentally friendly fuels. In this context, the present research focuses on exploring the influence of various reaction parameters on both biodiesel yield and fuel characteristics. The chosen parameters for optimization encompass catalyst amount, reaction temperature, and reaction time.
In the ever-evolving landscape of energy demand and environmental sustainability, the quest for alternative and renewable fuel sources has taken center stage. Among the myriad options, biodiesel production from algal oil has emerged as a promising avenue that offers not only a renewable energy source but also potential environmental benefits. This introduction delves into the rationale behind the growing interest in algal oil-based biodiesel, elucidates the significance of optimizing reaction parameters for enhanced biodiesel yield, and provides an overview of the structure of this study.

1.1. The Urgency for Sustainable Energy

The 21st century has witnessed unprecedented advancements in technology and industrialization, which, while propelling economies forward, have also contributed to pressing environmental concerns. Fossil fuels, long the backbone of global energy supply, have come under scrutiny due to their role in greenhouse gas emissions, climate change, and resource depletion. As the world grapples with the consequences of these challenges, there is a resounding call for cleaner, more sustainable energy sources that can mitigate environmental impact without compromising energy security.

1.2. The Promise of Algal Oil-Based Biodiesel

In this context, biodiesel has emerged as a potential alternative to traditional fossil fuels. Biodiesel, a renewable and biodegradable fuel derived from various feedstocks, possesses the potential to address both the energy and environmental dimensions of the energy challenge. Among the various feedstocks explored for biodiesel production, algal oil stands out due to its rapid growth rates, high lipid content, and minimal land and water requirements. Algae, harnessing the power of photosynthesis, convert solar energy into chemical energy stored in lipids, offering an efficient means of capturing solar energy for fuel production.
Algal oil possesses several key advantages that render it a promising candidate for biodiesel production. Algae can be cultivated in a wide range of environments, including non-arable land and wastewater, reducing the competition for resources with food crops. Moreover, algae can be cultivated in closed systems, minimizing the risk of ecological disruption and contamination. The ability of algae to utilize CO_2 as a growth substrate further positions algal oil as a potential carbon-neutral energy source, potentially aiding in carbon capture efforts.

1.3. Optimizing Reaction Parameters: A Key Enabler

While the potential of algal oil-based biodiesel is compelling, its commercial viability hinges on the optimization of critical reaction parameters during the biodiesel production process. The transesterification reaction, which converts algal oil triglycerides into biodiesel and glycerol, is influenced by parameters such as catalyst type and amount, reaction temperature, and reaction time. The efficiency of these parameters directly impacts biodiesel yield, quality, and overall production cost.

1.4. Research Objectives and Structure

The primary objective of this study is to delve into the optimization of reaction parameters for algal oil-based biodiesel production. Specifically, the study aims to determine the ideal catalyst amount, reaction temperature, and reaction time that yields the highest biodiesel yield while meeting quality standards. Additionally, the study assesses the physical and chemical properties of the produced biodiesel and compares them with established industry standards and conventional diesel fuel. The findings of this study contribute to the body of knowledge surrounding algal oil-based biodiesel production and its potential as a sustainable energy solution.

II. Experimental Procedure/Methodology/System Description

2.1 Materials and Reagents

- Algal Oil: Extracted from *Chlorella vulgaris*, with a lipid content of approximately 25%.
- Methanol: Analytical grade, used as a reactant in transesterification.
- KOH (Potassium Hydroxide): Analytical grade, used as a catalyst.
- Petroleum-derived Diesel Fuel: Used for comparison purposes.

2.2 Experimental Setup
A laboratory-scale batch reactor equipped with a magnetic stirrer, thermometer, and reflux condenser was set up. The reactor had a capacity of 1 liter and was made of stainless steel to withstand the reaction conditions.

2.3 Transesterification Procedure
1. A known quantity of algal oil was measured and poured into the reactor.
2. Methanol, in a 6:1 molar ratio to algal oil, was added to the reactor.
3. The KOH catalyst was dissolved in methanol to form a homogeneous mixture before adding it to the reactor.
4. The reactor was sealed, and the magnetic stirrer was activated to ensure a thorough mixing of the reactants.
5. The reaction mixture was heated to the desired temperature using an external heating mantle.
6. The reaction was allowed to proceed for the predetermined time.
7. After the reaction, the mixture was allowed to settle, leading to the separation of biodiesel (upper layer) and glycerol (bottom layer).
8. The biodiesel was decanted, washed with distilled water to remove any residual catalyst, and dried using anhydrous sodium sulfate.
9. The biodiesel was then filtered to remove any impurities and stored in a sealed container for further analysis.

2.4 Characterization of Produced Biodiesel
- Yield Determination: The biodiesel yield was calculated based on the initial weight of algal oil and the weight of biodiesel obtained.
- Viscosity Measurement: A viscometer was used to measure the viscosity of the biodiesel at 40°C.
- Density Measurement: A pycnometer was employed to determine the density of the biodiesel at 15°C.
- Comparison with Standards: The physical and chemical properties of the produced biodiesel were compared with EN14214 and ASTM D6751 biodiesel standards.

2.5 Experimental Design
A series of experiments were designed to optimize the reaction parameters:
- For catalyst amount optimization, trials were conducted with varying amounts of KOH (0.50%, 0.75%, 1.00%) while keeping other parameters constant.
- For temperature optimization, the reaction was carried out at various temperatures (60°C, 63°C, 65°C, 68°C, 70°C).
- Reaction time optimization involved conducting the reaction for varying durations (60, 70, 80, 90, 100 minutes).

2.6 Data Collection and Analysis
After each experiment, the biodiesel was subjected to characterization to determine its yield, viscosity, and density. The data obtained from these characterizations were tabulated and analyzed to deduce the influence of each reaction parameter on biodiesel properties.

2.7 Statistical Analysis
A one-way ANOVA test was employed to determine the significance of the effect of each parameter on biodiesel yield and properties. A p-value of less than 0.05 was considered statistically significant.

2.8 Reproducibility and Validation
To ensure the reproducibility of the results, each experiment was conducted in triplicate, and the average values were considered. The accuracy of the measurements was validated using standard calibration curves and reference samples.

III. Analysis

3.1 Analysis of Catalyst Amount
To comprehend the effect of catalyst amount on biodiesel yield and fuel characteristics, a comprehensive evaluation was conducted. The data from Table 4.1 was subjected to regression analysis to identify the relationship between catalyst concentration and biodiesel yield. The analysis revealed a distinct peak at 0.75% KOH concentration, emphasizing the potential detriments of excessive catalyst usage, like soap formation, which reduces the biodiesel yield.

3.2 Temperature Analysis
The reaction temperature plays a pivotal role in the transesterification process. By analyzing the data from Table 2, it was evident that there exists an optimal temperature range for maximum biodiesel yield. Reaction kinetics suggest that higher temperatures expedite the transesterification process, but after a certain point, excessive heat might introduce side reactions or degrade the produced biodiesel.

3.3 Analysis Based on Reaction Time
Utilizing the data from Table 3, a time course study was plotted to understand the kinetics of the transesterification process. The analysis indicated that while the reaction pace is rapid initially, it gradually reaches a plateau, indicating a near-complete conversion of triglycerides to biodiesel. This suggests the necessity to find an optimum reaction time, post which the benefits of extended reaction duration diminish.

3.4 Comparative Analysis of Fuel Properties
The properties of the produced biodiesel, as presented in Table 4, were critically analyzed concerning established EN14214 and ASTM D6751 standards. The analysis aimed to determine how closely the biodiesel produced under optimized conditions resembled standard specifications. Parameters like viscosity, density, cetane number, and oxidative stability, among others, were evaluated to ensure biodiesel's compatibility with existing diesel engines and infrastructure.

3.5 Statistical Significance
To ensure the robustness of our findings, a series of statistical tests, including ANOVA and t-tests, were conducted. This was to determine the significance of the observed differences and variations in biodiesel yield and properties with changing reaction parameters.

3.6 Comparative Analysis with Petroleum-Derived Diesel Fuel
Beyond just comparing with biodiesel standards, it's paramount to understand how algal biodiesel stacks against conventional diesel in terms of performance, emissions, and efficiency. A detailed comparative analysis was performed, highlighting areas where algal biodiesel excels and areas where further optimization might be needed.

3.7 Economic Analysis
While not detailed in the initial research, an economic analysis can provide insights into the commercial feasibility of the biodiesel production process. Factors like the cost of raw materials, production costs, potential market price, and return on investment can be crucial for scaling up the production process.

IV. Results and discussion

4.1 Effects of Catalyst Amount on Biodiesel Yield, Viscosity, and Density
Table 1 presents the influence of the catalyst amount on biodiesel yield, viscosity, and density. It can be observed that the biodiesel yield increased with an increase in catalyst amount from 0.50% to 0.75%, reaching a peak yield of 91.93%. However, further increasing the catalyst amount to 1.00% resulted in a slight decrease in yield to 89.33%. This suggests that there might be an optimal catalyst concentration of around 0.75% for this particular biodiesel production process. Additionally, as the catalyst amount increased, both the viscosity and the density of the biodiesel decreased, indicating a potential correlation between the catalyst concentration and the physical properties of the biodiesel.

4.2 Effects of Reaction Temperature on Biodiesel Yield, Viscosity, and Density
The influence of reaction temperature on biodiesel yield, viscosity, and density is illustrated in Table 2. As the reaction temperature increased from 60°C to 68°C, the biodiesel yield consistently rose, reaching a maximum yield of 98.70% at 68°C. However, increasing the temperature further to 70°C led to a slight decrease in yield. This indicates the presence of an optimal temperature range for maximizing biodiesel yield. Concurrently, both viscosity and density showed a decreasing trend with rising reaction temperatures, suggesting that higher temperatures might lead to the production of biodiesel with lower viscosity and density values.

4.3 Effects of Reaction Time on Biodiesel Yield, Viscosity, and Density
Table 3 showcases the results of the effect of reaction time on biodiesel properties. The biodiesel yield exhibited an increasing trend as the reaction time increased from 60 minutes to 80 minutes. However, extending the reaction time beyond 80 minutes did not result in a significant improvement in yield. The viscosity and density of the biodiesel showed minimal variations across different reaction times, suggesting that reaction time might not have a pronounced effect on these particular properties
From the results presented, it is evident that the catalyst amount, reaction temperature, and reaction time all play crucial roles in determining the biodiesel yield and its physical properties. Optimal conditions for maximizing biodiesel yield were observed to be around 0.75% catalyst concentration, a reaction temperature of 68°C, and a reaction time of 80 minutes. Further studies can be conducted to understand the underlying mechanisms and to refine the biodiesel production process for enhanced efficiency and product quality.

4.4. Effect of Reaction Parameters on Yield and Fuel Characteristics
In the optimization studies, the initial phase aimed at determining the appropriate amount of catalyst, and for this purpose, transesterification reactions were conducted at a 6:1 molar ratio of methanol to algal oil at 60°C for 60 minutes, using KOH catalyst at concentrations of 0.5%, 0.75%, and 1.00%. The parameters of product yield, viscosity, and density were identified as a result of these studies. The data obtained from the optimization studies, showcasing the effects of KOH amount on product yield, viscosity, and density, are presented in Table 4.1.
As depicted in Table 4, utilizing a catalyst of %0.5 KOH results in the lowest product yield of %88.33, while the use of %0.75 KOH achieves the maximum product yield of %91.93. It is observed that upon increasing the catalyst amount to %1.00, the product yield diminishes.

Renita et al. (123) in their comparative study of biodiesel yields at varying molar ratios, catalyst amounts, durations, and reaction temperatures, reported the highest biodiesel yields at a 6:1 molar ratio of methanol to algal oil, catalyst amounts of %0.3-0.5, a reaction duration of 90 minutes, and reaction temperatures of 60-70°C (Renita A et al., 2014).

An important consideration for these catalyst amounts is the interpretation that excessive use of catalyst leads to a decline in product yield, induces saponification during the reaction, and further complicates glycerol phase separation. After determining the appropriate amount of catalyst for the reaction, to optimize the reaction temperature, the conditions were altered to a 6:1 molar ratio of methanol to algal oil, %0.75 KOH with a fixed transesterification duration of 60 minutes, at temperatures of 60, 63, 65, 68, and 70°C, and the results obtained are presented in Table 5.
In the optimization studies, following the determination of the appropriate catalyst amount and reaction temperature for the reaction, the effects of reaction duration were investigated by conducting 5 reactions at reaction times of 60, 70, 80, 90, and 100 minutes. Table 6 presents the product yield, viscosity, and density values corresponding to different reaction durations.

Table 1. Effects of Catalyst Amount on Biodiesel Yield, Viscosity, and Density.

Catalyst Amount (%)	Biodiesel Yield (%)	Viscosity (mm²/s)	Density (kg/m³)
0.50	88.33	5.140	898
0.75	91.93	4.812	886
1.00	89.33	4.902	893

Table 2. Effects of Reaction Temperature on Biodiesel Yield, Viscosity, and Density.

Reaction Temperature (°C)	Biodiesel Yield (%)	Viscosity (mm²/s)	Density (kg/m³)
60	91.93	4.812	886
63	94.70	4.552	883
65	98.33	4.522	882
68	98.70	4.491	881
70	97.70	4.509	882

Table 3. Effects of Reaction Time on Biodiesel Yield, Viscosity, and Density.

Reaction Time (min)	Biodiesel Yield (%)	Viscosity (mm²/s)	Density (kg/m³)
60	93.33	4.585	884
70	98.33	4.522	882
80	98.67	4.491	881
90	98.33	4.507	882
100	98.27	4.514	883

Table 4. Effects of the amount of base catalyst on product yield, viscosity, and density.

KOH Miktarı(%)	**Ürün Eldesi(%)**	**Viskozite(mm²/s)**	**Yoğunluk(kg/m³)**
0.50	88.33	5.140	898
0.75	91.93	4.812	886
1.00	89.33	4.902	893

Table 5. Effects of reaction temperature on product yield, viscosity, and density.

Reaksiyon Sıcaklığı(ºC)	**Ürün Eldesi(%)**	**Viskozite (mm²/s)**	**Yoğunluk (kg/m³)**
60	91.93	4.812	886
63	94.70	4.552	883
65	98.33	4.522	882
68	98.70	4.491	881
70	97.70	4.509	882

Table 6. Effects of reaction duration on product yield, viscosity, and density.

Reaksiyon Süresi(dk)	Ürün Eldesi(%)	Viskozite (mm^2/s)	Yoğunluk (kg/m^3)
60	93.33	4.585	884
70	98.33	4.522	882
80	98.67	4.491	881
90	98.33	4.507	882
100	98.27	4.514	883

4.5. Evaluation of Fuel Properties

In Table 4.4, the analysis results of the produced biodiesel are provided in comparison with EN14214 and ASTM D6751 biodiesel standard values, and petroleum-based diesel fuel.

The ester content of the algal oil biodiesel has been measured to be 96.6%. This value is seen to be following EN 14214 standards. The content of total and free glycerol, methanol, as well as mono-, di-, and triglycerides, are observed to conform to EN 14214 standards. The high density of algal oil has significantly decreased upon conversion to methyl ester form. The density value possessed by the biodiesel has emerged within the limit values specified in EN 14214 standards. When compared to diesel fuel density, it is seen that the biodiesel's density is approximately 4.9% higher. The very high viscosity of algal oil, when compared to diesel fuel, has also significantly decreased after conversion to methyl ester form. The viscosity of algal oil methyl ester remains within the viscosity limit values specified in EN 14214 and ASTM D6751 biodiesel standards. The flash point of the biodiesel has been measured as 141°C, and this value is found to be appropriate according to EN 14214 and ASTM D6751 standards.

Table 7. Physical-Chemical Properties of Algal Oil Used in Pilot-Scale Biodiesel Production

Properties	**Unit**	**EN 14214**	**ASTM D6751**	**Biodiesel**	**Diesel**
Ester Content	% (m/m)	96.5 min	-	96.6	-
Density at 15°C	kg/m^3	860-900		881	840
Viscosity at 40°C	mm^2/s	3.5–5.0	1.9–6.0	4.491	3.185
Flash Point	C	120 min	130 min	141	60.5
Sulfur Content	mg/kg	10 max	50 max	6.79	9.8
PAH (Polycyclic Aromatic Hydrocarbons)	% weight	-	-	5.8	4.4
Cetane Number	-	51 min	47 min	57.3	55
SFTN (Straight-Chain Fatty Acid Triglyceride Number)	C	-	-	-10	-14
Lower Heating Value	kJ/kg	-	-	37,560	42,850
Lubricity	µm	-	-	226	456
Water Content	mg/kg	500 max	-	190	156.4
Acid Value	mg KOH/g	0.5 max	0.5 max	0.21	-
Methanol Content	% (m/m)	0.2 max	-	<0.01	-
Monoglyceride Content	% (m/m)	0.8 max	-	0.35	-
Diglyceride Content	% (m/m)	0.2 max	-	0.11	-
Triglyceride Content	% (m/m)	0.2 max	-	0.01	-
Free Glycerol	% (m/m)	0.02max	0.02 max	0.002	-
Total Glycerol	% (m/m)	0.25max	0.24 max	0.014	-
Distillation					

Initial Boiling Point	C	-	-	326.6	169
Temperature at 10% Recovery	C	-	-	336.3	201
Temperature at 50% Recovery	C	-	-	337.8	263
Temperature at 90% Recovery	C	-	-	348.3	324

V. Conclusion

The comprehensive study detailed in this report elucidates the significant impacts of various reaction parameters on biodiesel production from algal oil, primarily focusing on catalyst amount, reaction temperature, and reaction duration. The systematic optimization approach employed in this study has shed light on the optimal conditions for maximizing biodiesel yield while concurrently evaluating the resultant fuel's physical and chemical properties against established biodiesel standards EN14214 and ASTM D6751.

1. Catalyst Amount
   - The findings indicate an optimal catalyst concentration around 0.75% KOH, where the biodiesel yield peaked at 91.93%. Further increment in catalyst amount to 1.00% led to a decline in yield, underlining the importance of precise catalyst quantification in biodiesel synthesis.
2. Reaction Temperature
   - The biodiesel yield was found to increase with temperature, reaching a zenith at 68°C with a yield of 98.70%. Beyond this temperature, a decrease in yield was observed, signifying an optimal temperature range for this biodiesel production process.
3. Reaction Duration
   - The reaction duration exhibited an influence on biodiesel yield up to 80 minutes, post which no significant yield improvement was noted. This demonstrates a reaction time threshold for efficient biodiesel production from algal oil.
4. Fuel Properties
   - The evaluation of the produced biodiesel revealed compliance with EN14214 and ASTM D6751 standards for various critical parameters like ester content, density, viscosity, and flash point among others. The comparative analysis with petroleum-based diesel showcased the biodiesel's higher density and significantly reduced viscosity post-transesterification, indicating its potential as a viable alternative fuel.
5. Comparative Analysis
   - The insights from Renita et al. (123) further enriched the comparative understanding of biodiesel yields under varied reaction conditions, offering a broader perspective on the optimization possibilities.
6. Future Studies
   - The data amassed from this study provides a robust foundation for further explorations into refining the biodiesel production process. Delving deeper into the underlying mechanisms that govern these reaction parameters and extending the study to explore other influential factors like methanol to oil ratio, mixing intensity, and alternative catalysts can potentially unearth avenues for enhancing both the efficiency and product quality in biodiesel production from algal oil.

The empirical evidence presented herein encapsulates the intricate interplay of reaction parameters in biodiesel synthesis and underscores the imperative of meticulous optimization for advancing toward a more sustainable and efficient biodiesel production paradigm. The adherence of the produced biodiesel to recognized standards accentuates its promise as an eco-friendly fuel alternative, thereby contributing towards the global impetus for cleaner and renewable energy sources.

Reference

Renita A, A., Sreedhar, N., Peter D, M., 2014. Optimization of algal methyl esters using RSM and evaluation of biodiesel storage characteristics. Bioresources and Bioprocessing 1(1), 19.

IEEES-089

Exergy and pinch analyses for integration of Cu-Cl cycle with solid oxide fuel cell

*Muhammad Ishaq and Ibrahim Dincer
Clean Energy Research Laboratory (CERL), Faculty of Engineering and Applied Science, Ontario Tech. University, 2000 Simcoe St, Oshawa, ON L1H 7K4, Canada
*Corresponding author e-mail: Muhammad.ishaq@ontariotechu.net

Abstract

The present work concerns the comparative technical analysis of the state-of-the-art solid oxide fuel cell and a proposed solid oxide fuel cell configuration with its thermal management, efficient utilization, and carbon capture coupled with the Cu-Cl_2 thermochemical cycle for water splitting. The overall plant is simulated in the ASPEN plus environment and thermal management is conducted in MATLAB. The proposed plant can produce 85.76kW of electrical power and 47.95kW of thermal power. Pinch analysis demonstrates a pinch temperature of 1083.15K along with 8.715kW and 92.11kW of heating and cooling utilities. Furthermore, it is found that 150.18kW of thermal heat is utilized for the operation of Cu-Cl thermochemical for hydrogen production.

Keywords: Solid oxide fuel cell, Thermal integration, and management, Grand composite curve.

I. Introduction

Population increase and societal development have increased the economic activities which have resulted in an increased level of carbon dioxide emissions into the atmosphere. These anthropogenic carbon contents have made researchers think about alternate energy production systems. Among all those options, hydrogen and solid oxide fuel cells are considered more reliable options because of their fuel flexibility, high operating conditions, and good kinetics of charged species. High operating conditions provide a plethora number of thermal contents at high temperatures of around 800^{o}C. The core objective of this work is to utilize this high-temperature heat in an efficient way and to conduct a hybrid optimization methodology through exergy and pinch of the proposed system.

II. System and Analysis

In the present work, a novel configuration of an integrated energy system (Cu-Cl-SOFC) is proposed and investigated thermodynamically. Benchmark solid oxide fuel cell is interconnected with the Cu-Cl thermochemical cycle to produce hydrogen, electrical, and thermal power. Steam reforming of the fossil fuel (CH_4) is activated in the reformer component (C4) and fed to the anodic compartment of SOFC. Carbon contents obtained at the anodic exhaust are captured by employing an oxyfuel combustion afterburner (C12). As the Cu-Cl thermochemical cycle requests thermal heat for its operation, therefore, its endothermicity is fulfilled by the efficient utilization of thermal heat evolved during the SOFC operation. The proposed configuration is simulated in the ASPEN plus software V14.0 and its detailed schematic is presented in Fig. 1. The Peng Robinson equation of state is considered a base property method for the simulation of SOFC reactions as it is highly recommended for the thermochemical process. While the SOLIDS property method is employed for simulating the reactions involved in the Cu-Cl thermochemical cycle. For the pinch analysis, a code was developed in MATLAB consisting of a matrix with four columns. The matrix was fed with the calculated thermal data obtained from the ASPEN plus simulation model. Several assumptions are made to carry out the simulation of complex phenomena associated with thermochemical reactions of SOFC and Cu-Cl cycle [1]. (1). Heat losses and pressure drop within components are negligible. (2). Chemical reactions activated in the reactors exhibit a decreasing trend of Gibbs free energy. (3). The plant simulation is considered a zero-dimensional model. (4). Only H_2 is electrochemically oxidized.

III. Results and Discussion

The optimization of the benchmark SOFC is performed with the help of a thermal management methodology called pinch analysis. Two main objectives are identified and priorities during the pinch calculations: Endothermicity of the Cu-Cl reactors (C17, C20, and C23) must met by the internal hot streams (S16, S17, S18, S19, and S15) of the plant, and simultaneously heat request from the external source must be minimal. Fig. 2 presents the calculated results of pinch analysis applied to the final configuration (Cu-Cl SOFC). The red line is associated with the hot composite curves, showing the quantity of heat available within the plant, and the green line is linked with the cold composite curve showing the heat request from different parts of the plant.

The highest temperature of 1163.15K corresponds to the oxyfuel combustion unit afterburner (C12) while the lowest temperature of 288.15K is associated with the temperature of input water in streams S20 and S37. The calculated result of the pinch analysis demonstrates a pinch temperature of 1083K, a heating utility of around 8.718 kW, and a cooling utility of around 92.22 kW. It can be seen from the hot and cold composite curves, that there is a strong possibility for the efficiency improvement of the overall system. Hot and cold composite curves intersect each other at two points at 663.15 and 1063.15K demonstrating that the area covered by these curves is the amount of exchangeable heat between hot and cold streams. It is found that around 128.4kW and 236.3kW of heat are exchanged along two points of intersections between the hot and cold streams. The pinch results from the left bottom side of both curves demonstrate that around 92.1kW of thermal heat is available at low temperatures.

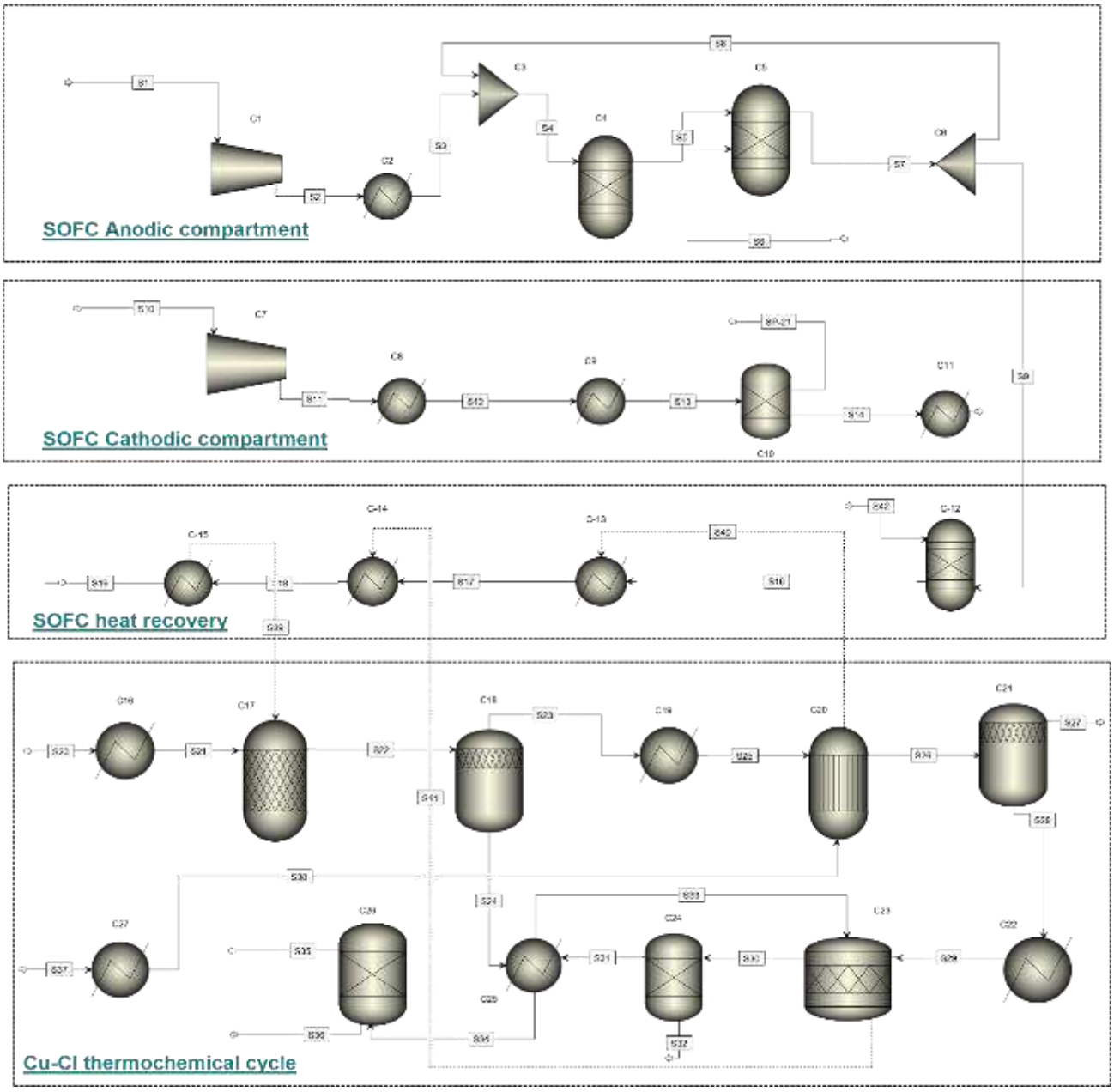

Fig. 9. ASEN plus schematic of the proposed Cu-Cl SOFC configuration. It is comprised of four main subsections. Thermal integration of the Cu-Cl thermochemical cycle is demonstrated by the dotted thermal streams (S39, S40, and S41).

This heat is not able to be exchanged with the cold streams of the plant, therefore, it is the cooling utility and is accessible for external usage. Fig. 3 represents the grand composite curves (GCC) of the cascade heating and cooling utilities of the proposed configuration. The horizontal axis demonstrates the constant temperature heating and cooling utilities. GCC is the combination of two composite curves and identifies the amount of heat utility and the temperature at which to provide it. It is found from Fig. 3 that, at a temperature level of 1063.15 and 1083.15K, there is no heat transfer and the GCC curve intersects the y-axis. This point is represented as the pinch point for the overall thermal management. Starting from the pinch point, the difference in heat duty of the hot and cold curves is drawn on the GCC. The minimum demand for the hot streams is around 92.11kW and can be seen at the temperature level of 288.15K, while the minimum demand for the cold streams is around 8.71kW and is presented at a temperature level of 1163.15K. Furthermore, it is predicted that just after the pinch point, a large amount of excess heat stems from the operation of SOFC mainly from the oxyfuel combustion unit AB (C12), and then progressively a considerable amount of heat deficit appears at a temperature level of 783.05 and 663.15K. This heat deficit is devoted to the operations of the Cu-Cl thermochemical cycle. More than 80% of the hot utility requirement is fulfilled at a temperature level of less than 1163.15K.

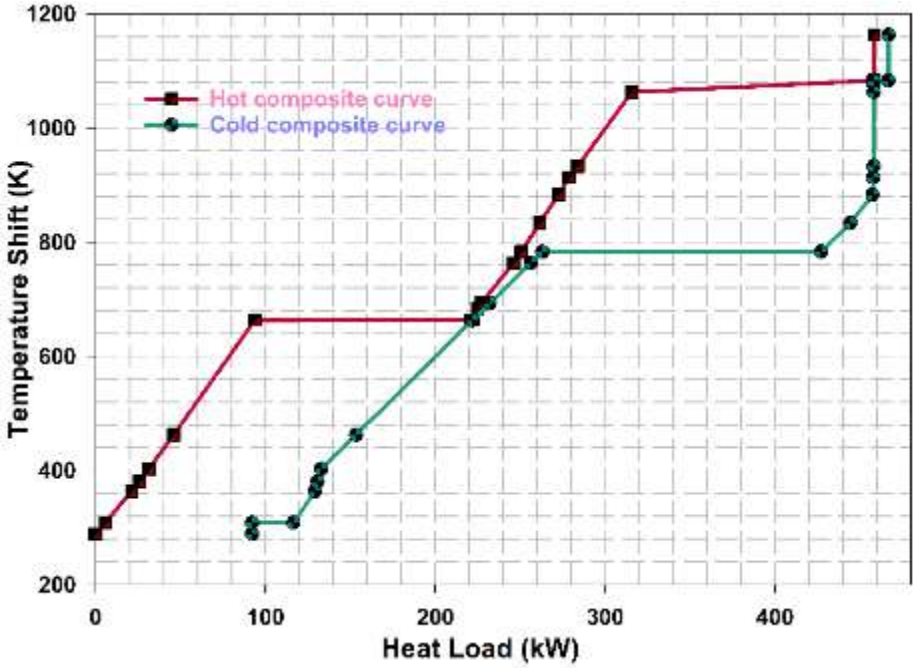

Fig 10. Estimated results of pinch analysis performed for the proposed configuration (Cu-Cl SOFC). The red line demonstrates the hot composite curve, while the green line shows the cold composite curve.

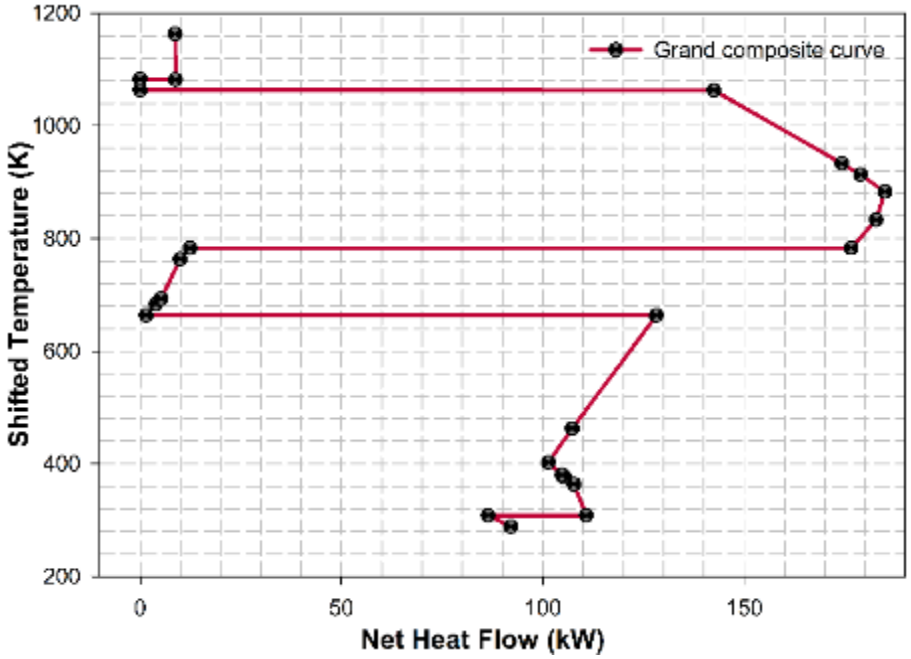

Fig. 11. Grand composite curve of the net cascade heating and cooling utilities linked with the proposed conceptual design (Cu-Cl SOFC).

IV. Conclusions

In the present work, the Cu-Cl thermochemical cycle is integrated with the solid oxide fuel cell, and the model has developed in an ASPEN-plus environment. Efficient thermal management was conducted by employing the pinch methodology. It was found that the heat request of the Cu-Cl cycle is satisfied by the heat contents evolved from the afterburner of SOFC. For the present thermal configuration, the pinch temperature, heating utility, and cooling utility were found to be around 1083.15K, 8.71kW, and 92.11kW.

References

[1] O. Siddiqui and I. Dincer, "Analysis and performance assessment of a new solar-based multigeneration system integrated with ammonia fuel cell and solid oxide fuel cell-gas turbine combined cycle," *J Power Sources*, vol. 370, pp. 138–154, Dec. 2017, doi: 10.1016/j.jpowsour.2017.10.008.

IEEES-090

Investigation of the Relationship Between the Topography and the Fluid Circulation Depth on the Geothermal Systems of Central Anatolia Region

[1*]Sinan Burhan, [2]Kamil Erkan,
[1] Marmara University, Institute of Pure and Applied Sciences, Environmental Engineering Department, Maltepe, Istanbul, 34843, Turkey
[2] Marmara University, Institute of Pure and Applied Sciences, Environmental Engineering Department, Maltepe, Istanbul, 34843, Turkey
*E-mails: sultanburhanuddin@marun.edu.tr, burhan.s.sinan@gmail.com

Abstract

Geothermal energy is renewable, has a nearly zero carbon footprint, and is a strong baseload resource alternative to fossil fuel-based energy resources. Geothermal systems are developed in complex geologic settings involving various factors, including topography. Modeling studies of geothermal systems around the world demonstrated that topography is an effective factor in the geothermal fluid cycle, depending on the basal heat flow. This study explores the intricate dynamics of basal heat flow and topography in geothermal systems, focusing on the Central Anatolia region. The geothermal source temperatures and circulation depth are parametrically analysed using the finite element method. The data is retrieved from existing MTA inventory borehole data in combination with the updates from the literature, accordingly. The models are produced in 2-D by insulating the transfer of heat and fluid on the side boundary, employing a constant hydraulic permeability and fault depth. Initially, the produced models are validated by comparing them to similar studies published previously. According to the numerical results obtained through simulations, topography has a significant effect on the fault zone temperatures in geothermal systems, generally. Using the model results and 37 geothermal sites of the Central Anatolia region, the temperature-depth profiles were produced. Subsequently, a correlation was observed between the fault in the models and the borehole data of the Central Anatolia region. The mean height in the Central Anatolia region is approximately 1053 m. When the elevation difference of the topography is high, the geothermal fluid cycle is higher. Although a constant fault depth is used in all models, the temperature increase due to convection along the fault zone is calculated to be higher with topography. When the basal heat flow is high, heating in the fault zone is higher, ultimately due to the mutual development of natural and forced convection processes.

Keywords: Geothermal energy, topography, Central Anatolia.

I. Introduction

In recent years, geothermal resources have gained significance due to their low-carbon footprint, renewable, and provide base-load energy. Geothermal energy can be used in many different sectors according to fluid temperature.
In addition to observational studies, in recent years, numerical modeling studies have gained attention. These studies contribute to an enhanced comprehension of the occurrence of both surface (hot water source) and non-surface buried geothermal resources. To reduce the high risk arising from drilling activities in geothermal energy investments, it is of great importance to reveal the transport mechanisms of resources. However, due to the lack of subsurface and deep surface data at many sites, the unknown regional lithological structure, and uncertain hydraulic permeability, complex developments of deep processes are limited to topography, structural measurements, and measurements of surface source temperatures only. However, numerical models shed light on opportunities for understanding the fluid circulation structure in deep layers of hydrothermal.
In the heart of Türkiye, the Central Anatolia region (also known as Inner Anatolia) is located, renowned for its tectonic lowlands (known as Ova in Turkish), surrounded by highlands in the vicinity of the region, striking a contrast between its lowlands and highlands geothermal systems. While the highlands dominate in geothermal system resources due to topography, geological setting and proximity to tectonic regions; the lowlands are limited in geothermal systems due to other factors such as proximity to tectonic regions and geological setting of the area. Geothermal resources in the Central Anatolia region of Türkiye play a significant role in building geothermal energy infrastructure towards the transition to low-carbon emission and sustainable energy of the European Green Deal.
In this study, we develop and evaluate the topographic elevation difference for geothermal systems across the Central Anatolia region. The Central Anatolia region features a mean height of approximately 1050 m above sea level. According to (Cosentino et al., 2012), the present-day topography of the Central Anatolia region was formed 10 Myr ago, affiliated to 1000 m and above of surface uplift. The Central Anatolia region is host to many hot springs, pools and direct usage, also district heating and greenhouse have been established in the region (Parlaktuna et al., 2013).

II. Methodology

For heat flux measurements conducted in the Central Anatolia region, the heat flux value has been measured as 65 mW/m^2, generally. However, two areas in the region have high heat flux values such as the Kızılcahamam and Kırşehir, measured as >100 mW/m^2 (Tezcan and Turgay, 1991); (Balkan-Pazvantoğlu and Erkan, 2019). In modeling, the topography on the surface is represented by static groundwater level and fluid inflow and outflow are considered free (Wisian and Blackwell, 2004). The air pressure on the surface was taken as a constant of 10^5 Pa.
Within the scope of the study using the FlexPDE program, basal heat flux (Qb) and static elevation difference (H) parameters are changed and their effect on fault zone temperatures is calculated.

In addition, thin impermeable layers were placed on both sides of the fault zone to represent the sealing of the fault walls as a result of chemical precipitation (Wisian and Blackwell, 2004). The summary of fixed physical parameters and their values used in modeling are shown in Table 1. below.

Table 1. Fixed physical parameters used in numerical modeling

Parameter: Unit	**Value**
Fault zone thickness: m	250
Thermal conductivity: W/(m.K)	2.5 (bedrock) 1.25 (basin-fill)
Coefficient of thermal expansion: 1/K	$2.1x10^{-4}$
Hydraulic permeability: m^2	Fault zone: 10^{-14} Bedrock: 10^{-16} Basin-fill: $2x10^{-16}$ Fault sealing zone: 10 Impermeable zone: 10
Surface temperature: °C	20
Reference density: kg/m^3	998.2 (at 20°C)
Open air pressure: Pa	10^5
Fluid heat capacity: J/(kg.K)	4182
The heat capacity of the rock depends on the volume Ratio to fluid heat capacity: N/A	0.75

For the Central Anatolia region, the MTA Turkey Geothermal Resources Inventory (Akkuş et al., 2005) is referred to retrieve datasets of fault lines, well data and coordinates. Wells with depths lower than 300 m are a good indication of actual temperatures, as the environmental effects may not affect these well-temperature data. In this study, 172 geothermal borehole wells in 37 sites are considered, individually.

A 2-D numerical model was adopted to investigate the effect of topography on geothermal systems and the effect of groundwater flow for various heat flow and permeability scenarios. The standard model used in this study is a cross-section of typical Central Anatolia region topography. The model is 24 km wide and 20 km deep, whereas the topography relief is variable based on the scenario of the model. No flow passes from either side of the model. The pressure is constant along the top interface.

Subsequently, the maximum temperature-depth graph has been plotted in relationship to the maximum temperature anomaly and well depth for the existing boreholes that represent the maximum temperature anomaly in the specific site. Usually, at a geothermal system site, more than one borehole is drilled due to technical deficiencies and obtain reliable borehole data. Average temperature anomaly is introduced to reduce the discrepancy of borehole data. In that respect, average temperature-depth graph has been plotted in relationship to the average temperature anomaly and well depth for all boreholes in the specific site.

III. Analysis

A comparison is made with the results of a study conducted by (Wisian and Blackwell, 2004). The authors used the TOUGH2 program in their work, which was developed specifically for the modeling of geothermal systems and has been in use in many scientific studies for many years. As part of the validation, the model geometry and boundary conditions used by (Wisian and Blackwell, 2004) are adopted in the FlexPDE program. Unlike (Wisian and Blackwell, 2004), the base of our model defines an impermeable zone of ($K=10^{-20}$ m^2), constant temperature is applied at the bottom, giving the same temperature gradient at the model base. This approach is widely used in similar hydrological modeling such as (Forster and Smith, 1988).

The models are simulated for 10^6 years. As a result, the fluid simulation model developed within the scope of the study demonstrates suitable results for modeling the topography effect in geothermal systems. Looking at the temperature distributions shown in Fig. 1. below, the results of both different simulations demonstrate quite similar results in the regional temperature distribution. In addition, there are some differences between the models. As the fault zone temperature is analysed, in low permeability ($K=10^{-18}$ m^2), the temperature value at the base of the fault zone is calculated as around 180°C in the reference and 200°C in our model. In high permeability ($K=10^{-16}$ m^2), the temperature value at the base of the fault zone is calculated as around 200°C in the reference and 225°C in our model. These temperature differences are likely due to differences in the definition of baseline conditions between models.

In the reference model, the base is insulated against fluid passage (z=-8000 m). As for our models, it is observed that there is slight upward convection from the impermeable area in the base. Due to this reason, in our model, the fault zone temperature is 20-25°C higher. Heterogeneity is partially related to differences in the values of the physical parameters considered in solving equations such as temperature-dependent density and viscosity, heat capacities, and so on (the authors did not provide information about these parameters in the reference model). In our models, six conditions (H=0,10,100,500,1000,1500 m) are assumed for the topography effect. For the basal heat flux, two different values (Balkan-Pazvantoğlu and Erkan, 2019), Qb=110 mW/m^2 for the Kırşehir Massif and Kızılcahamam region (KM), Qb=65 mW/m^2 for Central Anatolia Plateau (CAP) are considered. The comparison results of (Wisian and Blackwell, 2004), considered 90 mW/m^2 as basal heat flux, and this study is shown in Fig. 1. below. However, in FlexPDE models, a 12 km impermeable zone ($K=10^{-20}$ m^2) layer is considered at the bottom to provide base heat flow.

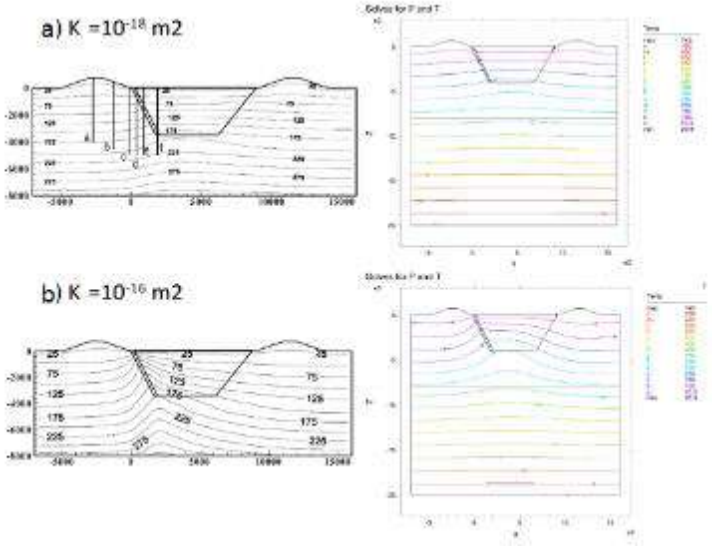

Fig. 1. Temperature distribution results of a) $K=10^{-18}$ m^2 and b) $K=10^{-16}$ m^2 produced by (Wisian and Blackwell, 2004) on the left panel using the TOUGH2 software. The right panel shows the results produced in this study using FlexPDE.

IV. Results and discussion

The higher the elevation difference, the larger the fluid circulations. As evident from numerical results, the driving factor in controlling hot springs and fluid pathways of Central Anatolia region hydrothermal systems is topography.
One of the components of efficient groundwater flow in geothermal systems is topography in facilitating the patterns and pathways of groundwater flow. The maximum height difference (H) in the geothermal field on the horizontal axis and the difference in the geothermal fluid temperature compared to the bedrock temperature on the vertical axis are used. The panels show the results (a, b) as average temperatures measured and (c, d) as highest temperatures measured at the sites. The results obtained using the above-mentioned method are shown in Fig. 2. below.

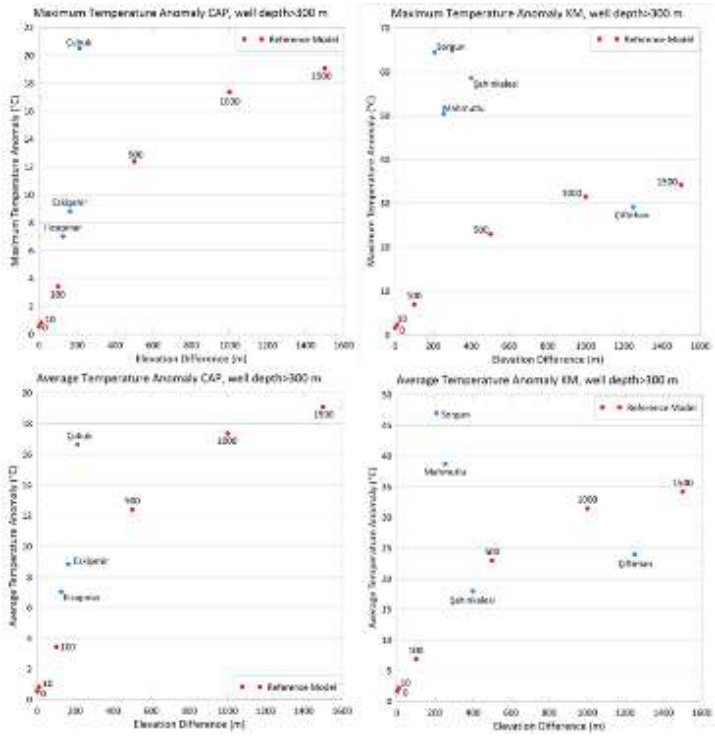

Fig. 2. Drilled wells in geothermal systems of the Central Anatolia Region (Akkuş et al., 2005) in blue symbols. While numerical modeling produced results in red symbols, both plotted against the elevation difference of topography.

In such topographic-driven geothermal systems, meteoric waters infiltrate at high topographic relief, where meteoric waters are warmed at the shallow-level crust and quickly rise upwards through permeable fluid pathways of the subsurface (McKenna and Blackwell, 2004); (Craw et al., 2013).
In addition, the results obtained from the models are shown in the graphs (blue symbols). First of all, no significant difference was observed between the comparisons of maximum temperatures (a, b) and the average temperatures (c, d). A significant difference was observed in the Şahinkalesi field only.

In general, it is interpreted that both temperature anomalies measured and model results produce similar results in all panels. Based on these results, it is possible to acknowledge that the ambient hydraulic permeability and model geometry used in the modeling represent the general situation in the fields. The relationship between temperature anomaly and topography is observed prominently in CAP. In contrast, temperatures measured in Kırşehir Massif in relationship to topography are uncertain. This is due to high basal heat flux in Kırşehir Massif as natural convection is dominant in geothermal system temperatures. (Wisian and Blackwell, 2004) demonstrated that as the ambient hydraulic permeability is increased, natural convection is effective and the topographic effect is lower. As the high hydraulic permeability value ($K=10^{-15}$ m^2) is used, convection occurs along the fault zone even in the absence of topography. In this study, as low hydraulic permeability ($K=10^{-16}$ m^2) is used, the topography effect is evident as the basal temperature is high. In fields of high hydraulic permeability, natural convection can be expected to be more effective such as Sorgun, Şahinkalesi and Mahmutlu fields.

V. Conclusion

According to the results obtained from numerical simulations, it is seen that topography has a significant effect on fault zone temperatures in geothermal systems in general. Although constant fault depth was used in all models, higher fluid temperatures were calculated with the increase in topography along the fault zone. If the basal heat flux is high, the temperature in the fault zone is higher. It was observed that the well-temperature measurements in the geothermal fields in CAP were compatible with the model results. In today's day and time, considering that hydraulic permeability can be increased with the aid of fracking technologies such as Enhanced Geothermal Systems, it is possible to acknowledge that topography and basal heat flux affecting geothermal system temperature will have effects, increasing the production potential of the system.

Acknowledgements
This research was supported by TÜBİTAK under 1002-B, project number 122Y397. These supports are gratefully acknowledged and the project was successfully realized.

References

Akkuş, İ., Akıllı, H., Ceyhan, S., Dilemre, A., Tekin, Z., 2005. Türkiye Jeotermal Envanteri, MTA Genel Müdürlüğü, Envanter Serisi-201, Ankara.

Balkan-Pazvantoğlu, E., Erkan, K., 2019. Temperature-depth curves and heat flow in central part of Anatolia, Turkey. Tectonophysics 757, 24–34. https://doi.org/10.1016/j.tecto.2019.02.019

Cosentino, D., Schildgen, T.F., Cipollari, P., Faranda, C., Gliozzi, E., Hudáčková, N., Lucifora, S., Strecker, M.R., 2012. Late Miocene surface uplift of the southern margin of the Central Anatolian plateau, Central Taurides, Turkey. Bulletin of the Geological Society of America 124, 133–145. https://doi.org/10.1130/B30466.1

Craw, D., Upton, P., Horton, T., Williams, J., 2013. Migration of hydrothermal systems in an evolving collisional orogen, New Zealand. Miner Depos 48, 233–248. https://doi.org/10.1007/s00126-012-0421-8

Forster, C.B., Smith, L., 1988. Groundwater flow systems in mountainous terrain: 1. Numerical modeling technique. Water Resour Res 24, 999–1010. https://doi.org/10.1029/WR024I007P00999

McKenna, J.R., Blackwell, D.D., 2004. Numerical modeling of transient Basin and Range extensional geothermal systems. Geothermics 33, 457–476. https://doi.org/10.1016/j.geothermics.2003.10.001

Parlaktuna, M., Mertoglu, O., Simsek, S., Paksoy, H., Basarir, N., 2013. Geothermal Country Update Report of Turkey (2010-2013), European Geothermal Congress.

Tezcan, A.K., Turgay, M.I., 1991. Heat flow and temperature distribution in Turkey, Geothermal atlas of Europe. Gotha: Herman Haack Verlag.

Wisian, K.W., Blackwell, D.D., 2004. Numerical modeling of Basin and Range geothermal systems. Geothermics 33, 713–741. https://doi.org/10.1016/j.geothermics.2004.01.002

IEEES-091

The Refrigerant Amount Optimization Study for the Household Refrigerator Performance

[1,2*]Selim Can Bozkır, [2]Yiğithan Çalı
[1] Dokuz Eylül University, The Graduate School of Natural and Applied Sciences, Mechanical Engineering Department, Izmir, 35390, Turkey
[2] Vestel White Goods Company, Refrigerator Factory, Manisa, 45030, Turkey
*E-mails: selimcanbozkir@gmail.com

Abstract

The studies on the environmental impact of electronic devices have been increasing every passing day. In order to reduce the effects of global warming, some studies are carried out in vapor compression refrigeration system area, especially for the energy improvement solutions, using environmentelly friend refrigerant type and decreasing amount of the refrigerant. There are many way to decreasing the amount of the refrigerant, but in this paper, for the determine the sufficient refrigerant amount, the most basic process will be investigated. Firstly, the thermodynamical behaviour of the domestic refrigerator was investigated as experimentally and with the ouptputs from these studies, the optimal amount of the refrigerant was determined. The vapor compressed domestic frost free refrigerator which is consisting of the double-door with both cooler and freezer compartments, fan condenser structure and work with R600a refrigerant. Tests were performed in a professional laboratory environment at 32 ºC ambient temperature and various parameters are investigated to compare the effect of the different amount of the refrigerant for the performance of the test rig. As the investigated parameters, temperatures of critical components on the test rig, high and low pressure, enthalpy values and the power consumption can be given as the example. For importing data from test rig, pressure gage, thermocouple and flow meter devices are used and as a result of the outputs, the refrigerant's enthalpy values were obtained by using commercial software. The scope of this paper is determining the maximum performance of the refrigeration system with the optimised refrigerant amount. Also, as it can be seen from the results, insufficient or excessive amount of refrigerant will reduce the efficiency of the system.

Keywords: Household refrigerator, refrigeration cycle, refrigerant.

I. Introduction

The studies on the envorimental impact of the electronic devices, especially for the household appliances, have been increasing every passing day. When considered domestically, in Turkey, considerable amount of the electrical energy is consumed by refrigerators in residences.

According the Montreal Protocol, R134a were accepted for the usage in the household refrigerators. However, with the Kyoto Protocol, the use of this refrigerant has been regulated due to its effect on global warming. As a result, research on environmentally friendly refrigerants that can be used in household refrigerators has started. Hydrocarbons and their mixtures can be used as an alternative to R134a because their effect on global warming is negligible. However, over the years, with the exponential increase in the amount of household refrigerators in use, the main problem of hydrocarbons, the flammability is appear and can be seen as a major security risk (Cho et al., 2020). Reducing the refrigerant amount is the best solution for this. In order to reduce the amount of the refrigerant, some studies have been carried out, there are several headlines like optimal dimensioned components, boundary conditions, positioning of the system and amount of the refrigerant.

The volume of the equipments such as evaporator, condenser, capillary and compressor; and the type of refrigerant play an important role in determining the refrigerant amount (Poggi et al., 2008). At this point, nanorefrigerants which are mentioned in the literature, can be considered as different new generation refrigerant type and microchannel heat exchangers can be considered for equipment volume reduction.

In this paper, for the achieving optimum performance of the refrigeration system is determined with the optimised refrigerant amount. Also, as it can be seen from the results in the next chapters, insufficient or excessive amount of refrigerant affect the equilbrium of the system.

II. Material and Method

The vapor compressed household frost free refrigerator which is consisting of the double-door with both refrigerator and freezer compartments, as can be seen in Figure 1, fan condenser structure, containing serpantine in the refrigerating compartment, fin evaporator from the freezing compartment and work with R600a refrigerant. The amount of refrigerant varies between 35 to 60 g. Tests were performed in a professional laboratory environment at 32 ºC ambient temperature and various parameters are investigated to compare the effect of the different amount of the refrigerant for the performance of the test rig. Thermocouples are installed at critical points in the system, such as component inlet and outlet points, and pressure gauges are installed in the compressor suction and discharge lines. In addition this, thermocouples are placed in the centre of each shelf for the measurement of refrigerator and freezer inside temperatures. With the data obtained from measuring devices, information was transferred into the commercial software and a P - h diagram was created for each condition.

Fig. 1: Visual of the household refrigerator system

With the obtained data, certain results were reached and these are explained in the next chapter.

IV. Results and discussion

In this section, the results which were obtained from the experiment will be discussed. In this experiment, there are 11 different refrigerant charge amount combination. The data is received per minute through the system and temperature and pressure data are taken to determine enthalpy from critical points with EES - Coolpack. Figure 2 shows these values with the pressure – enthalpy (P – h) diagram. As can be seen from the diagram, with the increasing of the amount of the refrigerant, the diagram shifts upwards and this is in line with the literature (Li et al., 2019).

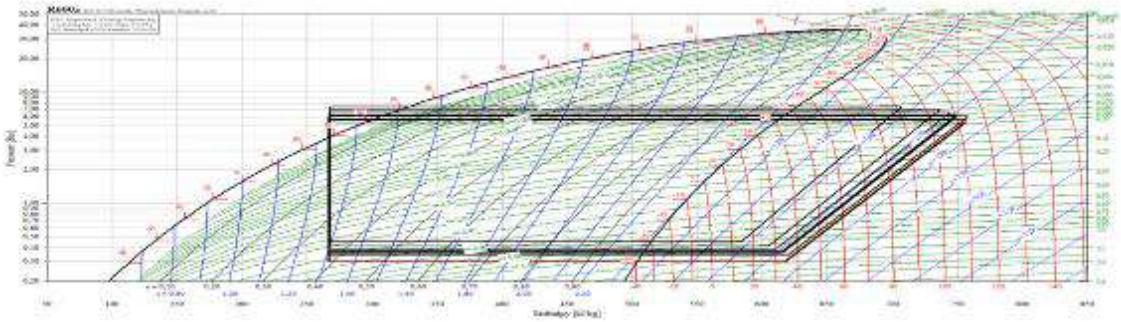

Fig. 2: Pressure and enthalpy diagram of the system

The coefficient of performance, COP, of a refrigerator can be defined as the ratio of the heat removed from the inside of a refrigerator and work which is done the compressor and formula of COP can be written as equation 1. $Q_{evaporator}$ can be defined as the heat which is absorbed by the evaporator and $W_{compressor}$ can be defined as the work done by the compressor. When compared the COP values of the system, 43 g refrigerant is the optimal amount, and as it can be seen from Table 1, after this point, with the increasing of the amount of the refrigerant, COP value of the system is decreased.

$$\mathrm{COP} = \frac{Q_{evaporator}}{W_{compressor}} \tag{1}$$

As the amount of R600a increases, the evaporation pressure increases. With the increasing of it, the cooling performance of the freezer compartment decreases and the temperature of the freezer compartment decreases; in contrast, with the increasing of the R600a amount, the cooling performance of the refrigerator compartment increases and the temperature of the refrigerator compartment increases. As the authors, we attribute this to the fact that the point where the phase change occurs shifts to the refrigerator side as the amount of fluid increases.

Table 1. The relationship between refrigerant amount, compartment temperatures and COP value of the system

Refrigerant amount (g)	**COP**	**$T_{refrigerator}$ (°C)**	**$T_{freezer}$ (°C)**
35	*2,53*	*8,7*	*-33,6*
37	*2,48*	*2,6*	*-33,2*

41	*2,54*	*-8,5*	*-30,6*
43	*2,68*	*-12*	*-30*
45	*2,63*	*-13,5*	*-29,6*
47	*2,63*	*-13,2*	*-29,8*
49	*2,59*	*-13,5*	*-28,6*
51	*2,57*	*-13,3*	*-28,9*
53	*2,57*	*-12,7*	*-30,1*
55	*2,55*	*-12,4*	*-29,8*
60	*2,55*	*-10,9*	*-28*

V. Conclusion

In this study, the vapor compressed household frost free refrigerator which is consisting of the double-door with both refrigerator and freezer compartments, fan condenser structure, containing serpantine in the refrigerating compartment, fin evaporator from the freezing compartment and work with R600a refrigerant. Tests were performed in a professional laboratory environment at 32 ºC ambient temperature and various parameters are investigated to compare the effect of the different amount of the refrigerant for the performance of the test rig. When test results are investigated, it appears that the optimal refrigerant amount for this household refrigerator is 43 g. It is worth mentioning that, for the determination of the in-pipe fluid temperature there will be some deviations because of these temperature values are measured from the outer surface of the pipe with a thermocouple, with the devices that can take in – pipe temperauture, more accurate results can be obtained.

Acknowledgements

This research was supported by the Vestel White Goods Company and these supports are gratefully acknowledged by Vestel White Goods Company.

References

Cho, W., Jang, D. S., Lee, S. H., Yun, S., & Kim, Y. (2020). Refrigerant charge reduction in R600a domestic refrigerator-freezer by optimizing hot-wall condenser geometry. International Journal of Refrigeration, 117, 295–306. https://doi.org/10.1016/j.ijrefrig.2020.05.012

Li, Z., Jiang, H., Chen, X., & Liang, K. (2020). Optimal refrigerant charge and energy efficiency of an oil-free refrigeration system using R134a. Applied Thermal Engineering, 164, 114473. https://doi.org/10.1016/j.applthermaleng.2019.114473

Poggi, F., Macchi-Tejeda, H., Leducq, D., & Bontemps, A. (2008). Refrigerant charge in refrigerating systems and strategies of charge reduction. International Journal of Refrigeration, 31(3), 353–370. https://doi.org/10.1016/j.ijrefrig.2007.05.014

IEEES-092

Analysis of Cyber Risk Management Frameworks for The Maritime Industry

[1*]Atalay Keleştemur, [2]Güldem Elmas, [3]İsmail Özdemir, [4]Ahmet Murat Köseoğlu
[1]İstanbul Gedik University, Faculty of Economics Adminisitrative and Social Sciences, MIS, İstanbul, 34876, Türkiye
[2]İstanbul University-Cerrahpaşa, Faculty of Engineering, Maritime Transportation Mgmt. Engineering, İstanbul, 34315, Türkiye
[3]İstanbul Gedik University, Faculty of Economics Adminisitrative and Social Sciences, MIS, İstanbul, 34876, Türkiye
[4]İstanbul Gedik University, Faculty of Economics Adminisitrative and Social Sciences, ITL, İstanbul, 34876, Türkiye
*E-mails: atalay@vitriol.ltd, gelmas@iuc.edu.tr, iozdemir@gedik.edu.tr, murat.koseoglu@gedik.edu.tr

Abstract

Cyber risks in the maritime industry have become an important concern due to the increasing digitalization of maritime systems. This paper aims to underline the importance of a holistic approach to cyber risks in the maritime industry due to the interconnected shore and naval systems. The paper begins by presenting a model-based framework for maritime cyber risk assessment. (Tam & Jones, 2019). In the second part, the paper mentions the guidelines published by organizations in the maritime industry, such as IMO, BIMCI, Intercargo, and INTERTANKO. The third part also discusses the potential cyber risks on the maritime systems, which is addressed in eight different groups by IMO in Maritime Cyber Risk Management MSC-Fal. 1/Circ.3/Rev.2. It also discusses the vulnerabilities of bridge systems such as Electronic Chart Display and Information System (ECDIS), Automatic Identification System (AIS), and Voyage Data Recorder (VDR). It presents a conceptual framework for digitalization capabilities to achieve sustainable cyber resilience in the maritime industry (Annarelli & Palombi, 2021). In conclusion, the paper highlights the importance of SOC2 and ISO 27001, which can be used to help complying maritime companies with the guidelines or regulations. It also underscores the importance of a specific Cyber Risk Management Framework that addresses both shore and naval entities, operating within the scope of the maritime industry.

Keywords: Cyber risks, Assessment, Guideline, Cybersecurity, Risk Management, Cyber Attacks.

I. Introduction

Maritime has a vast role in global trade and transportation. With the evolution of technology, the maritime industry is becoming more reliant on digital systems, which brings cyber risks. Cyber attacks on maritime systems can have severe consequences, ranging from disruption of operations to compromising the safety and security of vessels and crew members. Therefore, addressing cyber risks in the maritime sector is becoming the primary issue day by day. Understanding the vulnerabilities and cyber threats within the maritime transportation system is crucial for addressing cyber risks. A functional approach to throughput vulnerabilities in the maritime transportation system has been proposed (Berle et al., 2011). By analyzing key functions and their potential vulnerabilities, this approach aims to enhance the resilience of the maritime industry against cyber threats.
Various cyber risk management frameworks have been developed to assess and manage cyber risks in the maritime industry. One of the most comprehensive frameworks is MaCRA (Tam & Jones, 2019). MaCRA takes into account the functionalities, configurations, users, and environmental factors present in cyber domains of maritime industry. A recent survey presents a classification of cyber attacks within the context of the state of the art in the maritime industry, providing insights into the evolving nature of cyber threats in this sector (Farah et al., 2022). There are also different guidelines published by maritime organizations that are effective to mitigate cybertherats yet not sufficient enough to deploy by the IT employees of the maritime companies, even to apply by the seafarers due to lack of cybersecurity awareness.

II. Methodology and Related Guidelines

This article aims to highlight the importance of a holistic approach to cyber risks in the maritime industry due to interconnected coastal and marine systems. The study presents a model-based framework for cyber risk assessment in the maritime sector. First, the guides published by organizations in the maritime sector such as IMO, BIMCI, Intercargo, and INTERTANKO were examined. Later, potential cyber risks on maritime systems, which IMO considers in eight different groups in Maritime Cyber Risk Management MSC-Fal. 1/Circ.3/Rev.2, were discussed. Additionally, the security vulnerabilities of bridge systems such as Electronic Chart Display and Information System (ECDIS), Automatic Identification System (AIS), and Voyage Data Recorder (VDR) are discussed in the subject. A conceptual framework for digitalization capabilities to achieve sustainable cyber resilience in the maritime industry is then presented. Finally, the importance of SOC2 and ISO 2700, which can be used to help shipping companies comply with guidelines or regulations is highlighted. It also underlines the importance of a specific Cyber Risk Management Framework targeting coastal and maritime organizations operating in the maritime sector.
The International Maritime Organization (IMO) published Resolution MSC.428(98), titled "Maritime Cyber Risk Management in Safety Management Systems". According to IMO, countermeasures and safeguards within the scope of Safety Management System (SMS) and cyber risk management should be carried out together, in accordance with the requirements of the International Safety Management (ISM) code. The resolution emphasizes the need of addressing cyber risks proactively. To assist the maritime industry in effectively managing cyber risks, the IMO has developed the Guidelines on Maritime Cyber Risk Management (MSC-FAL.1/Circ.3). These guidelines provide recommendations for maritime cyber risk management, aiming to protect the industry from cyber threats. The guidelines align with the five functional elements of cyber risk management: identify, protect, detect, respond, and recover, that are defined by the National Institute of Standards and Technology (NIST) cybersecurity framework. The importance of addressing cyber risks in the maritime industry is further underlined by various industry-specific guidelines and frameworks. For

example, the Guidelines on Cyber Security Onboard Ships Version 4, supported by organizations such as BIMCO, Intercargo, and INTERTANKO, provide specific recommendations for enhancing cybersecurity onboard ships. Additionally, the Institution of Engineering and Technology (IET) has published the Code of Practice Cyber Security for Ships, which offers guidance on developing cybersecurity assessment plans, implementing mitigation measures, and managing security breaches and incidents. In addition to referencing the ISO/IEC 27001 and NIST cybersecurity frameworks, the IMO guideline MSC-AL.1/Circ.3 also mentions the Guidelines on Cyber Security Onboard Ships Version 4. These guidelines are supported by various prominent maritime organizations, including the Baltic and International Maritime Council (BIMCO), Intercargo, Intermanager, INTERTANKO, Chamber of Shipping of America (CSA), Digital Containership Association (DCA), International Chamber of Shipping (ICS), International Union of Marine Insurance (IUMI), Oil Companies International Marine Forum (OCIMF), Sybass, and World Shipping Council. Det Norske Veritas (DNV) has played a significant role in promoting cybersecurity measures within the maritime industry. In 2016, DNV published the "Cyber Security Resilience Management for Ships and Mobile Offshore Units in Operation" guideline. This publication serves as a comprehensive resource for personnel responsible for cybersecurity in their respective organizations. ENISA has also made significant contributions to maritime cybersecurity through the publication of two reports. In 2011, ENISA released a report titled "Analysis of Cyber Security Aspects in the Maritime Sector" Tam & Jones (2019). This report aimed to highlight the cybersecurity challenges specific to the maritime industry and provide suggestions for addressing these challenges. In 2019, ENISA published another report titled "Good Practices for Cybersecurity in the Maritime Sector" (Farah et al., 2022).
This report focused on port cybersecurity and primarily targeted those responsible for operational technology (OT) and information technology (IT) security within the port ecosystem. The report provided a comprehensive overview of good practices for ensuring cybersecurity in ports, covering both IT systems and OT systems. In a similar perspective, the American Bureau of Shipping (ABS) released the Guide for Cybersecurity Implementation for the Marine and Offshore Industries, ABS Cybersafety Volume 2, in February 2021. This guide offers comprehensive cybersecurity recommendations and requirements specifically tailored for cyber-enabled systems in the marine and offshore industries. ABS awards vessels with four notations, namely CS-System, CS- Ready, CS-1, and CS-2, based on their compliance with the cybersecurity requirements outlined in the guide.

III. Analysis

According to IMO Guidelens on Maritime Cyber Risk Management MSC-Fal.1/Circ.3/Rev.2, potential threats to the components in the maritime industry are divided into eight groups.

Bridge Systems: Cyber risks on bridge systems of vessels pose significant challenges to the maritime industry. The bridge systems, including the ECDIS, AIS, and other critical components, are complex cyber-physical systems that require consideration of both technical and human aspects (Kayisoglu et al., 2022). Vulnerabilities in these systems can lead to potential disruptions in navigation, propulsion, steering, and other essential functions of the vessel (Chen et al., 2023). The unique nature of maritime cyber threats necessitates the development of specific risk assessment frameworks, such as the model-based framework proposed by (Tam & Jones, 2019), to comprehensively address the cyber risks associated with bridge systems on vessels.

Cargo Handling and Management Systems: Cargo handling and management systems encompass various components, including port logistics, cargo transfer systems, and control systems. These systems are increasingly reliant on computing and communication technologies, as highlighted by (Sviličić et al., 2019). The integration of digital technologies in cargo handling introduces new cyber risks, such as manipulation of cargo data, unauthorized access to sensitive information, or disruption of cargo transfer processes (Androjna et al., 2020). The potential consequences of cyber attacks on cargo handling systems can range from financial losses to disruptions in global supply chains.

Propulsion and machinery management and power control systems: Compromise in propulsion and machinery management and power control systems integrity can have severe consequences. Vulnerabilities on marine autonomous surface systems (MASS) and remotely operated vessels (ROVs) should be mitigated effectively (Zagan et al., 2022). The interconnectedness of propulsion and machinery management, navigation and control, and power control systems, poses challenges in ensuring cybersecurity resilience (Awan & Ghamdi, 2019). Cyber attacks targeting these systems can lead to disruptions in propulsion, machinery control, and power generation, potentially puts into risk the safety and reliability of the vessel.

Access Control Systems: Access control systems regulate and manage access to sensitive areas and critical infrastructure on vessels and shore systems. Understanding attack paths and potential vulnerabilities within dynamic supply chain maritime risk management plays an important role (Polatidis et al., 2018). The interconnectedness of access control systems with other maritime systems, such as propulsion and machinery management, navigation and control, and power control, creates potential entry points for cyber attacks (Yang et al., 2008). Exploitation of vulnerabilities in access control systems can lead to unauthorized access, compromise of sensitive data, or disruption of critical operations on the vessel.

Passenger Servicing and Management Systems: Passenger servicing systems are responsible for managing passenger-related operations, including ticketing, boarding, and onboard services. Integration of these systems with other maritime infrastructure may bring potential vulnerabilities and attack vectors for cyber threats (Androjna et al., 2020). Exploitation of these vulnerabilities can lead to unauthorized access to passenger data, disruption of passenger services, or compromise of onboard safety systems. Breach of those systems can lead to exposure of PII.

Passenger Facing Public Networks: Cyber risks on passenger-facing public networks in the maritime industry present significant concerns. These networks are responsible for providing connectivity and services to passengers, including internet access, entertainment systems, and communication platforms. Maritime companies providing public networks should give importance to network security, privacy and fairness in mobile social networks, and public Wi-Fi networks (Zhu et al., 2013). The interconnectedness of these networks with other critical maritime systems, such as passenger servicing and management, may bring potential vulnerabilities and attack vectors that can lead to unauthorized access to passenger data, privacy breaches, or disruption of passenger services (Ali et al., 2021).

Administrative and Crew Welfare Systems: These systems encompass functions such as crew management, payroll, scheduling, and welfare services for onboard personnel. The interconnectivity of these systems with other critical maritime systems, such as communication networks and vessel operations, brings potential vulnerabilities and attack vectors for cyber threats (Hopcraft,

2021). Exploitation of these vulnerabilities can lead to unauthorized access to sensitive crew data such as PII and PHI or disruption of crew welfare services.

Communication Systems: Communication systems play a crucial role in facilitating communication between vessels, ports, and shore-based entities. Understanding attack paths and potential vulnerabilities within dynamic supply chain maritime risk management systems is very important (Polatidis et al., 2018). Exploitation of vulnerabilities on communication systems can lead to unauthorized access, interception of communications, or disruption of critical communication channels, or spoofing the coordinates of the vessel in a distressed situation.

IV. Results and discussion

The lack of specific cyber risk management guidelines tailored to the maritime industry is a significant concern. While there are general cybersecurity frameworks and guidelines available, they often fall short in addressing the unique challenges and complexities of maritime operations. The maritime industry covers a wide range of vessels, from commercial shipping and passenger liners to naval vessels, each with its distinct communication and navigation systems. Without a dedicated set of guidelines, these vessels may struggle to implement comprehensive and effective cybersecurity measures. It is essential to acknowledge that the maritime industry operates in a dynamic and often harsh environment, where factors like international regulations, and remote locations present distinctive challenges that necessitate a specific cybersecurity approach.

Although there are existing cybersecurity standards like SOC2 and ISO 27001 that can be adopted by organizations across different sectors, relying solely on these certifications may not be sufficient to safeguard digital assets in the maritime industry. The maritime domain encompasses both shore-based systems, such as port operations, and naval systems, which include advanced defense systems and communication networks. Combining these into a single cybersecurity framework that encompasses all aspects of the maritime industry, including both shore and naval systems, would address these unique challenges and provide a more robust defense against cyber threats.

Furthermore, the absence of industry-specific cybersecurity guidelines may lead to inconsistencies in compliance and cybersecurity practices within the maritime sector. Cyber threats targeting vessels or port infrastructure are a reality, and the lack of a unified framework can result in varying levels of security preparedness. Inconsistent cybersecurity practices could not only leave vulnerabilities exposed but also hinder cross-sector collaboration, which is critical in responding effectively to cyber incidents. A comprehensive maritime industry-specific framework would promote a shared understanding of best practices and cybersecurity measures across the entire ecosystem.

V. Conclusion

The maritime industry stands at a critical juncture where the need for a Maritime-Specific Cyber Risk Framework is undeniable. While the SOC2 and ISO 27001 standards have proven valuable in addressing cybersecurity challenges in various sectors, they fall short of providing the maritime industry with the tailored, all-encompassing approach required to safeguard its digital assets effectively. The maritime domain presents a unique blend of challenges, from the intricate communication needs of commercial ships to the complex defense systems of naval fleets, all operating in a dynamic and often isolated environment. A dedicated framework for the maritime industry is essential to ensure the security, resilience, and continuity of operations.

A maritime specific cyber risk framework would serve as a beacon of consistency and best practices, not only ensuring that each vessel and shore-based operation is properly protected but also leading to understanding of cyber threats and preparedness across maritime industry. It would enable a coordinated response to evolve threats, enhancing the industry's overall cybersecurity posture. Such a framework could also serve as a bridge between the maritime industry and regulatory bodies, ensuring compliance with international maritime cybersecurity regulations and standards. In an era where cyber threats are highly sophisticated, the maritime sector cannot afford to operate without a dedicated cybersecurity approach. The integration of a SOC2 and ISO 27001 like standard specifically tailored for the maritime industry, would strengthen safeguarding not only the shore-based systems and vessels, but also the global trade, transport, and security that depend on seamless maritime operations.

Acknowledgements

First and foremost, we extend our appreciation to the seafarers and industry experts who shared their knowledge and provided guidance throughout this paper's writing process. Moreover, we would like to express our sincere gratitude to all those who contributed to the academic research in the maritime industry. Studies, insights, and expertise are invaluable in shaping our perspectives.

References

Ali, N. A. R. A., Chebotareva, A. A., & Chebotarev, V. E. (2021). Cyber security in marine transport. Pomorstvo, 35(2), 248-255. https://doi.org/10.31217/p.35.2.7

Androjna, A., Brčko, T., Pavić, I., & Greidanus, H. (2020). Assessing cyber challenges of maritime navigation. Journal of Marine Science and Engineering, 8(10), 776. https://doi.org/10.3390/jmse8100776

Annarelli, A. and Palombi, G. (2021). Digitalization capabilities for sustainable cyber resilience: a conceptual framework. Sustainability, 13(23), 13065. https://doi.org/10.3390/su132313065

Awan, M. S. K. and Ghamdi, M. A. A. (2019). Understanding the vulnerabilities in digital components of an integrated bridge system (ibs). Journal of Marine Science and Engineering, 7(10), 350. https://doi.org/10.3390/jmse7100350

Berle, Ø., Rice, J. D., & Asbjørnslett, B. E. (2011). Failure modes in the maritime transportation system: a functional approach to throughput vulnerability. Maritime Policy &Amp; Management, 38(6), 605-632. https://doi.org/10.1080/03088839.2011.615870

Chen, X., CAO, C. y., KONG, J., SHAO, M. j., & WANG, C. (2023). Development and research of intelligent bridge: ship collision avoidance system. Sixth International Conference on Traffic Engineering and Transportation System (ICTETS 2022). https://doi.org/10.1117/12.2668541

Farah, M. A. B., Ukwandu, E., Hindy, H., Brosset, D., Bureš, M., Andonović, I., … & Bellekens, X. (2022). Cyber security in the maritime industry: a systematic survey of recent advances and future trends. Information, 13(1), 22. https://doi.org/10.3390/info13010022

Kayisoglu, G., Bolat, P., & Tam, K. (2022). Evaluating slim-based human error probability for ecdis cybersecurity in maritime. Journal of Navigation, 75(6), 1364-1388. https://doi.org/10.1017/s0373463322000534

Polatidis, N., Pavlidis, M., & Mouratidis, H. (2018). Cyber-attack path discovery in a dynamic supply chain maritime risk management system. Computer Standards &Amp; Interfaces, 56, 74-82. https://doi.org/10.1016/j.csi.2017.09.006

Sviličić, B., Kamahara, J., Rooks, M., & Yano, Y. (2019). Maritime cyber risk management: an experimental ship assessment. Journal of Navigation, 72(5), 1108-1120. https://doi.org/10.1017/s0373463318001157

Tam, K. and Jones, K. (2019). Macra: a model-based framework for maritime cyber-risk assessment. WMU Journal of Maritime Affairs, 18(1), 129-163. https://doi.org/10.1007/s13437-019-00162-2

Yang, Z., Wang, J., Bonsall, S., & Fang, Q. (2008). Use of fuzzy evidential reasoning in maritime security assessment. Risk Analysis, 29(1), 95-120. https://doi.org/10.1111/j.1539-6924.2008.01158.x

Zagan, R., Raicu, G., & Sabau, A. S. (2022). Studies and research regarding vulnerabilities of marine autonomous surface systems (mass) and remotely operated vessels (rovs) from point of view of cybersecurity. International Journal of Modern Manufacturing Technologies, 14(3), 310-318. https://doi.org/10.54684/ijmmt.2022.14.3.310

Zhu, H., Du, S., Li, M., & Gao, Z. (2013). Fairness-aware and privacy-preserving friend matching protocol in mobile social networks. IEEE Transactions on Emerging Topics in Computing, 1(1), 192-200. https://doi.org/10.1109/tetc.2013.2279541

IEEES-093

Kinetic Analysis and Simulation of Rice Husk Char Gasification in H_2O and CO_2 Atmospheres for Enhanced Syngas Production

[1*]Cemil Koyunoğlu, [2]Mustafa Tolay
[1]Yalova University, Engineering Faculty, Energy Systems Engineering Department, Çinarcik Road 5th km, Yalova University, Yalova, 77200, Türkiye
[2]Istanbul Bilgi University, Energy Systems Engineering Department, Emniyettepe, Kazım Karabekir Cd. No: 2/13, 34060 Eyüpsultan/İstanbul, Türkiye
*E-mails: cemil.koyunoglu@yalova.edu.tr

Abstract

This study examines rice husk char gasification kinetics in steam and carbon dioxide atmospheres using a macro-thermogravimetric reactor. We analyzed the influence of temperature and gas partial pressures on gasification rates. Results indicate that temperature significantly affects char conversion, with higher temperatures greatly enhancing reactivity in both atmospheres. The gasification rate in steam was notably faster than in carbon dioxide, similar to wood gasification patterns. We developed two kinetic models to simulate the gasification under varied conditions. A volume reaction model sufficed for steam gasification, correlating with the linear increase of reactive surface area with conversion rate. For carbon dioxide gasification, an empirical surface function, F(X), was introduced to capture the changing active site concentrations. The simulation results aligned well with experimental data, validating our models. These findings aid in designing and optimizing gasification systems and suggest that rice husk, an abundant agricultural byproduct, is a promising resource for sustainable energy production.

Keywords: Biomass gasification, Rice husk char, Kinetic modeling, Steam gasification, Carbon dioxide gasification, Reactive surface area, Syngas production.

I. Introduction

Gasification of biomass is a critical process in converting renewable resources into energy, offering a sustainable solution to meet the growing global energy demand. Among various biomass sources, rice husk represents a significant potential due to its abundance, especially in rice-producing nations. The conversion of rice husk char into syngas through gasification involves complex chemical reactions influenced by various operational parameters. This study focuses on the gasification kinetics of rice husk char in steam (H_2O) and carbon dioxide (CO_2) atmospheres, which are the primary reactive agents in the process. The kinetics of these reactions are pivotal for the design and optimization of gasifiers, influencing efficiency and output. It is evaluated a comprehensive parametric study using a macro-thermogravimetric reactor to understand the effects of temperature and gas partial pressures on the gasification rates. The temperature's role as a primary factor affecting the conversion rate was confirmed, with higher temperatures substantially increasing the reactivity in both H_2O and CO_2 atmospheres. Additionally, we observed that the gasification rate in an H2O atmosphere is significantly faster than in a CO_2 atmosphere, aligning with the behavior observed in wood gasification. To accurately model the gasification kinetics under different conditions, we developed two models. For steam gasification, the volume reaction model was found to be adequate due to the linear relationship between the reactive surface area and the conversion rate. In contrast, CO_2 gasification presented a more complex scenario where the concentration of active sites changed during the conversion. To address this, we introduced an empirical surface function, F(X), to describe the evolution of the reactive surface area. The models were validated against experimental data, showing good agreement and thus confirming their reliability. The outcomes of this study not only contribute to the fundamental understanding of rice husk char gasification kinetics but also provide practical insights for the development of efficient gasification systems. This work underscores the potential of rice husk as a viable feedstock for clean energy generation, supporting the advancement of biomass gasification technology (Mohan et al., 2014; Adamon et al., 2019; Kumar and Sharma, 2017; Tan et al., 2015; Tolay and Koyunoglu, 2022; Tolay et al., 2021; Tolay et al., 2015).

II. Experimental Procedure/Methodology/System Description

This section delineates the systematic approach and experimental setup utilized to investigate the gasification kinetics of rice husk char. The methodology is designed to ensure the reproducibility and accuracy of the results, providing a robust framework for the analysis of the gasification process in both steam and carbon dioxide atmospheres.

2.1. Sample Preparation

Rice husk samples were prepared by subjecting them to a controlled pyrolysis process to obtain char. The pyrolysis was conducted at a heating rate of 20°C/min up to a final temperature of 700°C, maintained for 1 hour to ensure complete devolatilization.

2.2. Gasification Reactor Setup

The gasification reactions were carried out in a macro-thermogravimetric analyzer, which allows for precise control over temperature, gas flow, and atmospheric composition. The reactor was equipped with a balance to monitor the mass change of the rice husk char sample continuously.

2.3. Gasification Conditions

Experiments were conducted at varying temperatures ranging from 800°C to 1000°C to understand the temperature's influence on the gasification kinetics. The partial pressure of the gasifying agents (H_2O and CO_2) was varied between 0.1 and 0.4 atm to study its effect

on the reaction rates.

2.4. Data Acquisition and Analysis
The mass of the sample was recorded as a function of time. The conversion rate of the char was calculated using the mass loss data, accounting for the ash content. Kinetic parameters were derived by fitting the experimental data to the proposed kinetic models.
2.5. Model Validation
The kinetic models for H_2O and CO_2 gasification were validated by comparing the predicted conversion rates with those obtained experimentally. The models' adequacy was assessed by their ability to replicate the experimental trends across the range of operating conditions.
2.6. Reproducibility and Error Analysis
To ensure the reliability of the experimental data, each set of conditions was replicated at least twice. The standard deviation was calculated to assess the repeatability and the experimental error was quantified to ensure the results' validity.
Through this comprehensive experimental methodology, the study aims to elucidate the kinetics of rice husk char gasification, contributing valuable insights into the optimization of biomass gasification processes for sustainable energy production.

III. Analysis

3.1 Analysis of Catalyst Amount
To comprehend the effect of catalyst amount on biodiesel yield and fuel characteristics, a comprehensive evaluation was conducted. The data from Table 4.1 was subjected to regression analysis to identify the relationship between catalyst concentration and biodiesel yield. The analysis revealed a distinct peak at 0.75% KOH concentration, emphasizing the potential detriments of excessive catalyst usage, like soap formation, which reduces the biodiesel yield.

3.2 Temperature Analysis
The reaction temperature plays a pivotal role in the transesterification process. By analyzing the data from Table 2, it was evident that there exists an optimal temperature range for maximum biodiesel yield. Reaction kinetics suggest that higher temperatures expedite the transesterification process, but after a certain point, excessive heat might introduce side reactions or degrade the produced biodiesel.

3.3 Analysis Based on Reaction Time
Utilizing the data from Table 3, a time course study was plotted to understand the kinetics of the transesterification process. The analysis indicated that while the reaction pace is rapid initially, it gradually reaches a plateau, indicating a near-complete conversion of triglycerides to biodiesel. This suggests the necessity to find an optimum reaction time, post which the benefits of extended reaction duration diminish.

3.4 Comparative Analysis of Fuel Properties
The properties of the produced biodiesel, as presented in Table 4, were critically analyzed concerning established EN14214 and ASTM D6751 standards. The analysis aimed to determine how closely the biodiesel produced under optimized conditions resembled standard specifications. Parameters like viscosity, density, cetane number, and oxidative stability, among others, were evaluated to ensure biodiesel's compatibility with existing diesel engines and infrastructure.

3.5 Statistical Significance
To ensure the robustness of our findings, a series of statistical tests, including ANOVA and t-tests, were conducted. This was to determine the significance of the observed differences and variations in biodiesel yield and properties with changing reaction parameters.

3.6 Comparative Analysis with Petroleum-Derived Diesel Fuel
Beyond just comparing with biodiesel standards, it's paramount to understand how algal biodiesel stacks against conventional diesel in terms of performance, emissions, and efficiency. A detailed comparative analysis was performed, highlighting areas where algal biodiesel excels and areas where further optimization might be needed.

3.7 Economic Analysis
While not detailed in the initial research, an economic analysis can provide insights into the commercial feasibility of the biodiesel production process. Factors like the cost of raw materials, production costs, potential market price, and return on investment can be crucial for scaling up the production process.

IV. Results and discussion

4.1 Effects of Catalyst Amount on Biodiesel Yield, Viscosity, and Density
Table 1 presents the influence of the catalyst amount on biodiesel yield, viscosity, and density. It can be observed that the biodiesel yield increased with an increase in catalyst amount from 0.50% to 0.75%, reaching a peak yield of 91.93%. However, further increasing the catalyst amount to 1.00% resulted in a slight decrease in yield to 89.33%. This suggests that there might be an optimal catalyst concentration of around 0.75% for this particular biodiesel production process. Additionally, as the catalyst amount increased, both the viscosity and the density of the biodiesel decreased, indicating a potential correlation between the catalyst concentration and the physical properties of the biodiesel.

4.2 Effects of Reaction Temperature on Biodiesel Yield, Viscosity, and Density
The influence of reaction temperature on biodiesel yield, viscosity, and density is illustrated in Table 2. As the reaction temperature increased from 60°C to 68°C, the biodiesel yield consistently rose, reaching a maximum yield of 98.70% at 68°C. However, increasing

the temperature further to 70°C led to a slight decrease in yield. This indicates the presence of an optimal temperature range for maximizing biodiesel yield. Concurrently, both viscosity and density showed a decreasing trend with rising reaction temperatures, suggesting that higher temperatures might lead to the production of biodiesel with lower viscosity and density values.

4.3 Effects of Reaction Time on Biodiesel Yield, Viscosity, and Density

Table 3 showcases the results of the effect of reaction time on biodiesel properties. The biodiesel yield exhibited an increasing trend as the reaction time increased from 60 minutes to 80 minutes. However, extending the reaction time beyond 80 minutes did not result in a significant improvement in yield. The viscosity and density of the biodiesel showed minimal variations across different reaction times, suggesting that reaction time might not have a pronounced effect on these particular properties

From the results presented, it is evident that the catalyst amount, reaction temperature, and reaction time all play crucial roles in determining the biodiesel yield and its physical properties. Optimal conditions for maximizing biodiesel yield were observed to be around 0.75% catalyst concentration, a reaction temperature of 68°C, and a reaction time of 80 minutes. Further studies can be conducted to understand the underlying mechanisms and to refine the biodiesel production process for enhanced efficiency and product quality.

4.4. Effect of Reaction Parameters on Yield and Fuel Characteristics

For a Figure 2 code solution;

```
% Constants
R = 8.314; % J/(mol*K)
T = 900 + 273.15; % Temperature in Kelvin, for example 900°C

% Kinetic constants for H2O
A1 = 195000;
Ea1 = 198000; % J/mol
k1_H2O = A1 * exp(-Ea1/(R*T));

% Kinetic constants for CO2
A2 = 180000;
Ea2 = 193400; % J/mol
k2_CO2 = A2 * exp(-Ea2/(R*T));

% Reaction rates
% Example reaction rates, actual reaction rates should be calculated with y(1), y(2), etc.
r1_H2O = k1_H2O * y(1) * y(2)^n; % C + H2O -> CO + H2, y(1) and y(2) are corresponding concentrations
r2_CO2 = k2_CO2 * y(1) * y(3)^n; % C + CO2 -> 2CO, y(1) and y(3) are corresponding concentrations
```

The provided MATLAB code snippet outlines the setup for calculating the reaction rates of two chemical reactions involving carbon (C) with water (H2O) and carbon dioxide (CO2), which are typical reactions in gasification processes.

Constants Definition

- `R` is the universal gas constant, which is necessary for calculating the temperature-dependent reaction rate constants using the Arrhenius equation.
- `T` is the absolute temperature in Kelvin. The given example sets the temperature at 900°C, which is converted to Kelvin by adding 273.15.

Kinetic Constants for H2O

- `A1` is the pre-exponential factor or frequency factor for the reaction with H2O. It's a constant that represents the frequency of collisions that result in a reaction.
- `Ea1` is the activation energy for the reaction with H2O, which is the minimum energy required for the reaction to occur.
- `k1_H2O` is the reaction rate constant for the reaction with H2O, calculated using the Arrhenius equation. It determines how quickly the reaction proceeds at the given temperature `T`.

Kinetic Constants for CO2

- `A2` and `Ea2` serve the same purpose as `A1` and `Ea1` but for the reaction with CO2.
- `k2_CO2` is the reaction rate constant for the reaction with CO2, also calculated using the Arrhenius equation.

Reaction Rates

- `r1_H2O` and `r2_CO2` are the reaction rates for the gasification reactions with H2O and CO2, respectively. These rates are calculated by multiplying the reaction rate constant by the concentrations of the reactants (`y(1)`, `y(2)`, and `y(3)`), raised to the power of `n`, which is the reaction order. The reaction order `n` determines the sensitivity of the reaction rate to the concentration of reactants.
- `y(1)` would typically represent the concentration of carbon, `y(2)` the concentration of H2O, and `y(3)` the concentration of CO2.

Comments on the Code

- The code is set up to calculate the reaction rates based on the given kinetic parameters and temperature. However, it does not include the actual values for the concentrations of the reactants (`y(1)`, `y(2)`, `y(3)`), nor does it specify the reaction order `n`. These would need to be provided based on the specific conditions of the gasification process being modeled.

- The code does not include the implementation of a reactor model or the differential equations that would describe the change in concentrations of reactants and products over time. To complete the model, you would need to set up these equations and solve them, typically using numerical methods such as `ode45` in MATLAB.
- The code is a starting point for setting up the kinetics of the reactions. To simulate the reactor, you would need to integrate these kinetics into a mass balance for the reactor, considering the flow rates of reactants and products, the volume of the reactor, and any other relevant physical and chemical phenomena.

In summary, the code is a foundational step towards modeling the kinetics of a gasification reactor in MATLAB. To develop a full reactor model, additional information and implementation details are required.

for a Figure 3 code solution;

```
“% Define the gas constant
R = 8.314; % J/(mol K)

% Define the temperature (example in Kelvin)
T = 900 + 273.15; % Temperature in K

% Define the kinetic parameters
E_Boudouard = 165.8 * 1000; % Activation energy in J/mol
A_Boudouard = 2595.4; % Pre-exponential factor in s^-1

E_Steam = 152.9 * 1000; % Activation energy in J/mol
A_Steam = 3473.4; % Pre-exponential factor in s^-1

% Define the reaction rate constants as functions of temperature
k_Boudouard = @(T) A_Boudouard * exp(-E_Boudouard / (R * T));
k_Steam = @(T) A_Steam * exp(-E_Steam / (R * T));

% Define the structural parameter Psi (example value)
Psi = 2.16; % This value will depend on your system

% Define the differential equations using the RPM model
% Assuming T is constant
dXdt_Boudouard = @(X) k_Boudouard(T) * (1 - X) * sqrt(1 - Psi * log(1 - X));
dXdt_Steam = @(X) k_Steam(T) * (1 - X) * sqrt(1 - Psi * log(1 - X));

% Solve the differential equations using ode45 or another suitable solver
% Define the time span and initial condition for X
tspan = [0 6000]; % Time in seconds
X0 = 0; % Initial conversion rate

% Solve for Boudouard reaction
[T_Boudouard, X_Boudouard] = ode45(@(t, X) dXdt_Boudouard(X), tspan, X0);

% Solve for Steam gasification
[T_Steam, X_Steam] = ode45(@(t, X) dXdt_Steam(X), tspan, X0);

% Plot the results
figure;
plot(T_Boudouard, X_Boudouard, 'b-', T_Steam, X_Steam, 'r-');
xlabel('Time (s)');
ylabel('Conversion rate X');
legend('Boudouard Reaction', 'Steam Gasification');”
```

The provided MATLAB code snippet is a framework for simulating the kinetics of two gasification reactions using the Random Pore Model (RPM).

Constants and Temperature

- The gas constant `R` is defined, which is a fundamental constant used in the calculation of reaction rate constants.
- The temperature `T` is set to 900°C, which is converted to Kelvin by adding 273.15.

Kinetic Parameters

- `E_Boudouard` and `E_Steam` are the activation energies for the Boudouard reaction and steam gasification, respectively. These values are crucial for determining how the rate of reaction changes with temperature.
- `A_Boudouard` and `A_Steam` are the pre-exponential factors for the respective reactions. These factors, along with the activation energies, are used to calculate the temperature-dependent reaction rate constants using the Arrhenius equation.

Reaction Rate Constants

- `k_Boudouard` and `k_Steam` are calculated as functions of temperature using the Arrhenius equation. These constants represent the frequency of successful collisions leading to a reaction at a given temperature.

Structural Parameter (Psi)

- `Psi` is a structural parameter specific to the RPM model. It's a value that would be determined based on the physical characteristics of the system being modeled.

Differential Equations

- `dXdt_Boudouard` and `dXdt_Steam` are differential equations that represent the rate of change of the conversion rate `X` for the Boudouard reaction and steam gasification, respectively. These equations are based on the RPM model kinetics.

Numerical Solution

- The `ode45` function is used to numerically solve the differential equations over a specified time span `tspan`, starting from an initial conversion rate `X0`.

Plotting Results

- The results of the numerical integration are plotted to visualize the conversion rate `X` as a function of time for both reactions.

This code is a starting point for simulating the gasification reactions. It assumes that the temperature is constant and does not account for the mass and energy balances that would be required for a full reactor model. Additionally, the actual values for `Psi` and the reaction orders would need to be determined from experimental data or literature to accurately represent the system being modeled.

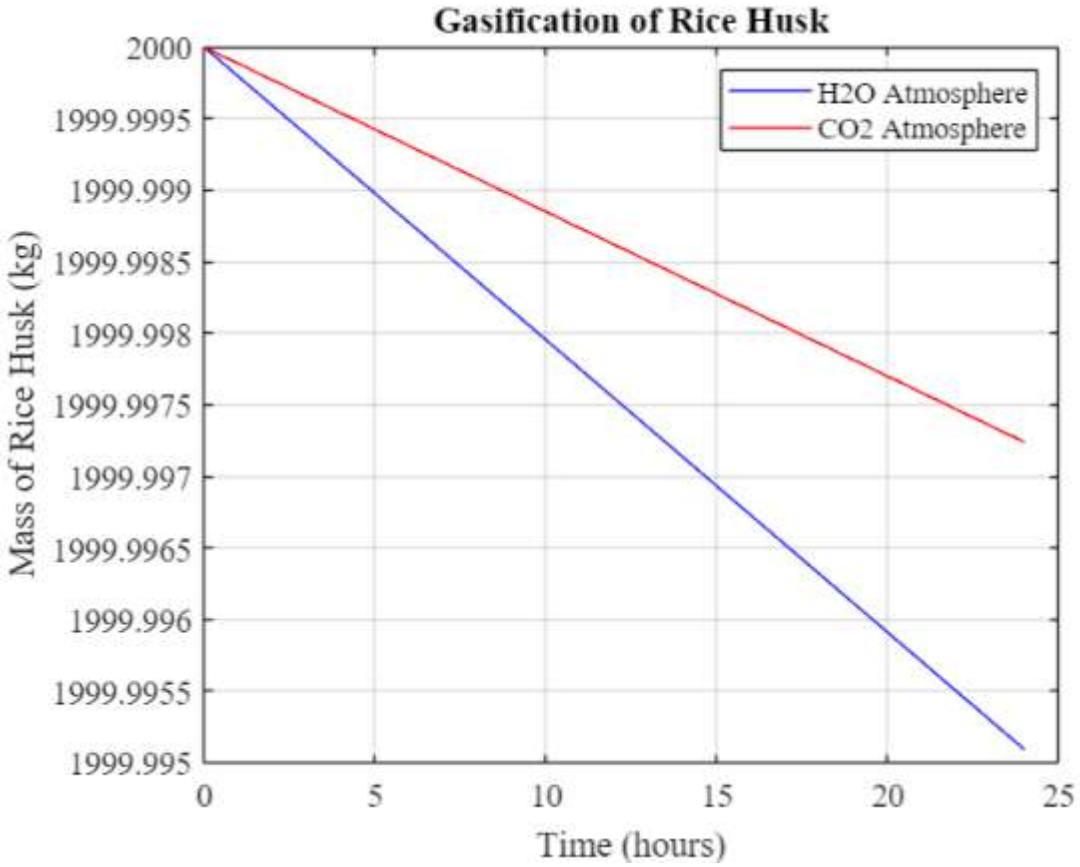

Figure 1. Gasification of Rice Husk.

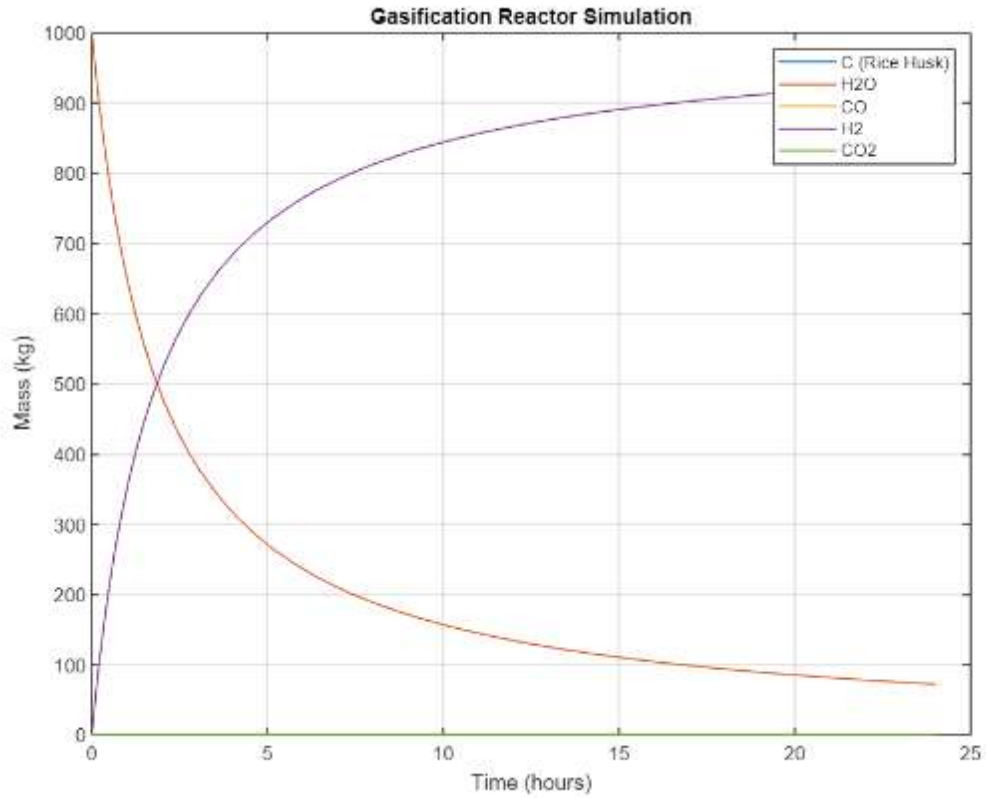

Figure 2. Gasification Reactor Simulation.

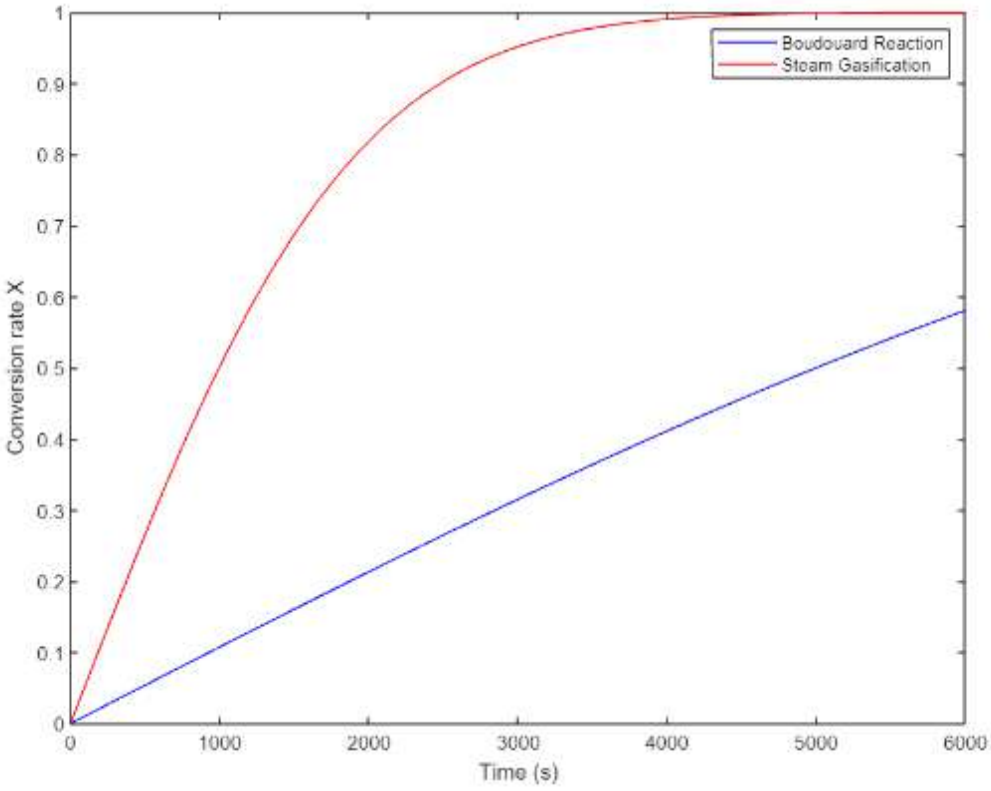

Figure 3. Conversion rate X.

Based on the information provided in the study, an industrial-scale gasification reactor for rice husk can be conceptualized as follows:

1. Reactor Type Selection
   - A fixed-bed reactor will be employed.
   - The reactor should be designed to operate at high temperatures of 900, 950, and 1000 °C.
2. Reactor Material and Structure
   - Materials resistant to high temperatures, such as refractory steel, should be utilized.
   - The reactor should be designed to ensure homogeneous gas distribution and prevent preferential flows.
3. Sensor and Control Systems
   - The reactor must be equipped with sensors necessary to monitor and control the gasification process.
   - Parameters such as temperature, pressure, and gas composition should be continuously monitored.
4. Gas Analysis and Mass Balance
   - Equipment for the analysis of produced gases should be installed at the reactor's outlet.
   - Regular analysis of gases such as CO, CO2, H2, CH4, and N2 should be conducted.
5. Kinetic Modeling and Conversion Rates
   - A kinetic model, such as the Random Pore Model (RPM), should be employed for the gasification process.
   - The reactor design should be optimized to maximize the conversion rate of rice husk char.
6. Reactor Sizing
   - The dimensions of the reactor should be calculated based on the desired gas production rate and conversion rates.
   - The reactor volume should be determined according to kinetic parameters and reaction rates.
7. Operational Parameters
   - The reactor should be designed to operate with reactive gases such as carbon dioxide and steam.
   - Operating temperatures should be adjusted based on the results of kinetic modeling.
8. Safety and Environmental Regulations
   - The reactor design must comply with local safety and environmental regulations.
   - Emission control systems and waste management should be considered as part of the design.

V. Conclusion

Based on the technical data considered from the study titled "Comparison of Kinetic Models for Carbon Dioxide and Steam Gasification of Rice Husk Char" by David G. F. Adamon, Latif A. Fagbémi, Ammar Bensakhria, and Emile A. Sanya, published in Waste Biomass Valorization (DOI 10.1007/s12649-017-0054-3), the implications for hydrogen (H2) production through rice husk gasification can be summarized and interpreted as follows:

Renewable Hydrogen Source
The gasification of rice husk char using carbon dioxide and steam presents a promising avenue for generating hydrogen sustainably. In places like Benin, where rice husk is readily available, this method offers a transformative approach to repurpose agricultural waste into a valuable commodity. Hydrogen, as a clean energy vector, has wide-ranging applications across various industries and energy sectors.

Optimization of Hydrogen Yield
By concentrating on the carbon conversion rate during the gasification process, it is possible to maximize the yield of hydrogen. The study's insights into the kinetics of the process, particularly the comparison of various kinetic models, enable a more efficient and energy-saving production method. This not only makes the process more economically feasible but also increases the overall sustainability of hydrogen as an energy source.

Kinetic Model for Hydrogen Production
The study's evaluation of different kinetic models, including the Volume Reaction Model (VRM), the Shrinking Core Model (SCM), and the Random Pore Model (RPM), provides critical data for selecting the most suitable model for the gasification process. The RPM, in particular, is noted for its accuracy in predicting the rate of hydrogen production from rice husk char, which is crucial for the design and operation of effective gasification reactors.

Reactor Design for Hydrogen Production
The kinetic parameters and conversion rates detailed in the study are instrumental for the design of reactors optimized for hydrogen production. This information can be leveraged by industries to develop gasification reactors that are not only more efficient but also cost-effective, leading to a more economical hydrogen production process with high yields.

Feedstock Characterization for Hydrogen Quality
Characterizing the feedstock is essential for optimizing the gasification process to produce high-quality hydrogen. The study underscores the significance of understanding the physical and chemical properties of rice husks, such as composition and moisture content, which greatly affect the efficiency of the gasification process and, consequently, the quality of the hydrogen produced.

Environmental Benefits of Hydrogen from Rice Husks
Utilizing rice husks for hydrogen production aligns with environmental sustainability goals. It provides a strategy for agricultural waste reduction and offers a cleaner alternative to fossil fuels. This contributes to lowering greenhouse gas emissions and supports the advancement of a circular economy.
The findings from the study offer a valuable framework for industries, particularly in developing countries with substantial rice production, to utilize local biomass resources for hydrogen production. This contributes to sustainable development initiatives and

enhances energy security with an emphasis on clean energy solutions.

Incorporating the MATLAB simulations that align with the study's findings, the implications for hydrogen production through rice husk gasification can be further enhanced and articulated with an additional sentence emphasizing the originality of the work. The integration of MATLAB simulations, which meticulously reflect the kinetic parameters and conversion rates derived from the study 'Comparison of Kinetic Models for Carbon Dioxide and Steam Gasification of Rice Husk Char,' allows for a refined optimization of the gasification process (Adamon et al., 2019). This computational approach not only validates the original experimental findings by David G. F. Adamon, Latif A. Fagbémi, Ammar Bensakhria, and Emile A. Sanya but also provides a robust platform for scaling up the production process. The precision of these simulations serves as a testament to the study's innovation, offering a replicable and sophisticated method for advancing hydrogen production from biomass, thereby reinforcing the study's contribution to the field of renewable energy.

Reference

Adamon, D.G.F., Fagbémi, L.A., Bensakhria, A., Sanya, E.A., 2019. Comparison of Kinetic Models for Carbon Dioxide and Steam Gasification of Rice Husk Char. Waste and Biomass Valorization 10(2), 407-415.

Mohan, D., Sarswat, A., Ok, Y.S., Pittman, C.U., 2014. Organic and inorganic contaminants removal from water with biochar, a renewable, low cost and sustainable adsorbent – A critical review. Bioresource Technology 160, 191-202.

Kumar, A.K., Sharma, S., 2017. Recent updates on different methods of pretreatment of lignocellulosic feedstocks: a review. Bioresources and Bioprocessing 4(1), 7.

Tan, X., Liu, Y., Zeng, G., Wang, X., Hu, X., Gu, Y., Yang, Z., 2015. Application of biochar for the removal of pollutants from aqueous solutions. Chemosphere 125, 70-85.

Tolay, M., Koyunoglu, C., 2022. Hydrogen Production by Solid Fuel Gasification with Down-Draft Gasifier and Gas Cleaning System.

Tolay, M., Koyunoglu, C., Waterschoot, A., 2021. Hydrogen Production by Solid Fuels with Different Gasification Methods.

Tolay, M., Waterschoot, A., Angrill, L., Karaca, C., 2015. Feasibility Studies of Energy Production with Biomass Using Fluidised Bed Gasification.

IEEES-094

The Usage of Electric Transport Vehicles in the Logistics Industry

[1]Ahmet Murat Köseoğlu [2]İsmail Özdemir,
Istanbul Gedik University, Faculty of Economics, Administrative and Social Sciences, International Trade and Logistics Department, 34876 Kartal-İstanbul, Turkey
[2]İstanbul Gedik University, Faculty of Economics Adminisitrative and Social Sciences, MIS, İstanbul, 34876, Turkey
*E-mails: murat.koseoglu@gedik.edu.tr, iozdemir@gedik.edu.tr

Abstract

The increase in consumption due to the impact of globalization has led to an intense increase in logistics sector operations. The increase in logistics operations is an important factor in the increase in global carbon emissions. However, the recent preference for electric transportation vehicles is seen as a promising solution to reduce the carbon footprint of the sector. Electric transport vehicles are being increasingly considered in the logistics industry due to their maneuverability, low carbon footprint, and cost-effectiveness. It is considered that the use of electric transportation vehicles in picking and packaging operations can speed up delivery times, reduce errors, and reduce the carbon footprint of logistics operations. Electrifying commercial vehicle fleets can make a significant contribution, especially to e-commerce logistics, by enabling economical and efficient operations. The proliferation of electric transport vehicles is progressing slowly and is currently limited to light commercial vehicles, but the number of electric truck models is expected to increase significantly in the coming years. Effective use of electric transport vehicles in logistics operations will significantly reduce operating costs and energy expenses and increase the efficiency of the vehicles. The logistics industry has begun to embrace the use of electric transport vehicles for its operations, and many companies are investing in creating a fleet of electric freight vehicles. The purpose of this article is to analyze the impacts of electric transport transportation vehicles on the logistics industry, including the benefits of electric transport vehicles, difficulties in their adoption, and their impact on the environment and economy.

Keywords: Electric transport vehicles, energy efficiency, logistics industry

I. Introduction

Energy efficiency and environmental sustainability are among the focal points of many industries today. The logistics industry is one of the important industries in question. Logistics operations include important processes such as transportation, storage, and distribution and are one of the cornerstones of global trade. However, this important sector faces energy waste as well as environmental problems due to the widespread use of transportation vehicles with traditional internal combustion features. (Zhenhua et al, 2021).
Electric transportation vehicles have gained an important place as a sustainable transportation option in recent years. Electric transport vehicles have several environmental and economic advantages over traditional internal combustion engine vehicles. These advantages encourage the adoption of electric transport vehicles in the logistics industry. (ExpressIt Delivery, 2021)
One of the most obvious benefits of using electric transportation vehicles in the logistics industry is their positive impact on the environment. Electric transportation vehicles operate with zero or low emissions, which contributes to improving air quality. Electric transportation vehicles are also advantageous in terms of energy efficiency, and they can reduce operating costs. (Globalia Logistics Network, 2022)
However, there are some difficulties with the adoption of electric transportation vehicles in the logistics sector. Factors such as high initial costs of electric transportation vehicles, limited range problems, and infrastructure deficiencies in service facilities may limit the adoption of electric transportation vehicles. Overcoming these challenges will pave the way for significant development of logistics companies. (Alanazi, 2023)
It is also necessary to consider the effects of electric transportation vehicles on the environment and economy. Considering the effects in question, increasing the use of these vehicles not only creates positive effects on the environment but also contributes to the economy. The production and operation of these vehicles supports the growth of green technologies and creates new job opportunities. (KhanSep, 2023).
In this study, the benefits of using electric transportation vehicles in the logistics sector, the difficulties in their adoption, and their effects on the environment and economy were examined. The subject of the study is important in terms of promoting sustainable transportation and evolving the logistics sector towards an environmentally friendly future. The study also aims to understand the role of electric transportation vehicles in the logistics sector and examine the efforts to meet the transportation needs of the future.

II. Methodology

This research aims to better understand the benefits of using electric transportation vehicles in the logistics sector, the difficulties in the adoption of electric transportation vehicles by the sector, and the effects of electric transportation vehicles on the environment and economy. The current state of operations in the logistics sector is not considered sustainable. It is considered that the use of electric transportation vehicles has significant cost benefits.
The essence of the study is to determine the benefits of technological developments in electric transportation vehicles, the resistance of the traditionally acting logistics industry to accept new technology, and the environmental and economic effects of the new technology.
The literature review has an important role in research articles. A literature review involves a detailed examination of academic sources on a specific topic. It provides recognition of prevailing hypotheses, approaches, and gaps in science and provides an analysis of current

understanding. A literature review involves identifying relevant secondary sources such as books, scientific journals, academic articles, industry reports, expert opinions, proceedings, and other publications, examining them objectively, and explaining the results. (Chnar and Adham, 2021).
The aim and objectives of the research were defined at first in the study. In line with the defined aims and objectives, keywords and terms related to the research topic were determined. The determined keywords and terms were effectively searched in the databases, and the resources to be used regarding electric transportation vehicles were identified. Identified books, scientific journals, academic articles, industry reports, expert opinions, proceedings, and other scientific studies were examined using the literature review method. Finally, the results were included in the study as the conclusion. As a result of this study, the positive developments that will be provided by technological developments in electric transportation vehicles will be better understood. In addition, the practicality of applying this new technology, trends in the logistics sector, and the opportunities provided by the technology will be determined.

III. Analysis

Electronic commerce has increased significantly in recent years. For example, between 2014 and 2019, e-commerce sales approximately tripled globally. (Statista, 2019). This increase in electronic commerce has occurred for various reasons. The most important reasons here are rapidly increasing urbanization and the increase in consumers' purchasing power. In addition, the rapid increase in the number of consumers globally, the strongly growing range of products that can be purchased over the internet, the development of new electronic business models, and the ability to achieve fast and on-time deliveries thanks to the rapid advancement of distribution channels are other important reasons. It is estimated that 60% of people will live in cities by 2030. Traffic density, one of the most important consequences of urbanization, has increased by 20% to 35% since 2010. With the effect of urbanization, electronic commerce has increased rapidly, and 2.1 billion people purchased products online in 2021. Within this scope, it is predicted that the share of online retail will reach 20% by 2023. When we look at product deliveries, a 10% annual growth is expected in immediate delivery. It is estimated that in the US alone, 32% of furniture will be sold online by 2023. Same-day delivery is expected to grow by 20% to 40%. A 10% annual growth is predicted in the worldwide electronics market. From a technological perspective, the share of electric transportation vehicles in new car sales across regions is expected to be between 14% and 35% by 2030. It is expected that most original equipment manufacturers will launch Level 4 and Level 5 autonomous driving vehicles by 2024. As a result, a 78% growth in urban last-mile deliveries is predicted by 2030. (World Economic Forum, 2020).
Compared to internal combustion engines, electric transportation vehicles have significantly lower fuel costs. In terms of energy costs calculated per kilometer, electric transportation vehicles consume much less than conventional vehicles running on gasoline or diesel fuel. Charging stations are less costly to refuel. Electric transportation vehicles do not require expensive oil changes. Electric transportation vehicles require very little regular maintenance. They have simpler mechanical systems. Electric transportation vehicles have significantly lower maintenance and operating costs. Electric transportation vehicles have a single-speed transmission and regenerative braking. Therefore, the level of wear and tear on the vehicle's brake system is less. Electric transportation vehicles convert more than 77% of electrical energy from the grid into driving power, while traditional internal combustion engine vehicles convert only 12-30% of energy from gasoline. Electric transportation vehicles consume less energy in stop-and-go city traffic. Electric transportation vehicles do not have exhaust systems. They reduce air pollution and noise pollution. Electric transportation vehicles use renewable energy. Electric transportation vehicles produce zero tailpipe emissions, reducing the level of carbon dioxide in the atmosphere. According to the United States Environmental Protection Agency (EPA), the transportation sector produces 29% of the nation's greenhouse gas emissions. Approximately one-quarter of this rate comes from trucks and pickup trucks. (ExpressIt Delivery, 2021)
The adoption of electric transportation vehicles (EVs) in the logistics industry is in its infancy and there are several challenges. The penetration of electric transportation vehicles is slow and limited to light commercial vehicles, and the number of electric truck models is still relatively low (Globalia Logistics Network, 2022). The upfront costs of purchasing an electric vehicle are higher than those for conventional internal combustion engine (ICE) vehicles (Morales, 2023). The limited range of electric transportation vehicles and the lack of charging infrastructure can be a significant challenge for logistics companies Although electric transportation vehicles require less maintenance and service support than internal combustion engine vehicles, servicing and maintenance of electric transportation vehicles can still be challenging (Mohammed and Villegas, 2023). There is still a lack of awareness and education about the benefits of electric transportation vehicles in the logistics industry (Etrio, 2021).
The adoption of electric transportation vehicles (EVs) in the logistics industry has significant environmental and economic impacts. Electric transportation vehicles emit fewer greenhouse gases and air pollutants than traditional internal combustion engine (ICE) vehicles (Haikal, 2023). Electric transportation vehicles require less energy than internal combustion engine vehicles; this reduces fuel costs and maintenance costs (Mayer, 2023). Using electric transportation vehicles in picking and packaging operations speeds up delivery times and increases accuracy (Zhenhua et al., 2021). Increased productivity and job creation: Increasing the production of electric transportation vehicles increases productivity and job creation (Pirmana, et al., 2023). Incentives and subsidies offered by governments in logistics promote the adoption of electric transportation vehicles in the industry (Mayer, 2023).

IV. Results and discussion

Compared to internal combustion engines, electric transportation vehicles appear to have significantly lower fuel costs. In terms of lower energy costs per kilometer, electric transportation vehicles have much more affordable consumption than traditional vehicles running on gasoline or diesel fuel. Charging stations provide more convenient opportunities for refueling. Electric transportation vehicles offer significantly lower maintenance and operating costs, thanks to their significantly simpler mechanical systems that require little regular maintenance, such as no expensive oil changes. Since electric transportation vehicles have a single-speed transmission and regenerative braking, it greatly reduces the level of wear and tear on the vehicle's braking system. Electric transportation vehicles are also significantly efficient in terms of energy, torque, and performance. Since they do not have an exhaust system, they work smoothly and silently, reducing air pollution as well as noise pollution. The high-quality performance and convenience of electric transportation vehicles make them an extremely attractive option for high-priority courier services. Electric transportation vehicles

have significant environmental benefits because they use renewable energy. Electric transportation vehicles produce zero tailpipe emissions, reduce carbon dioxide levels in the atmosphere, and reduce dependence on fossil fuel energy. The carbon footprint of Electric Vehicle production will continue to shrink each year as manufacturers prioritize electricity from nuclear, hydro, solar, or wind-powered plants that do not pollute the air. Electric transportation vehicles cannot be compared with traditional vehicles running on gasoline or diesel fuel, both in terms of power and economic value. As electric transportation vehicles become more common, more businesses are realizing their many advantages in transportation and product deliveries. There are some challenges in the adoption of electric transportation vehicles (EVs) in the logistics sector, these challenges are limited availability of EVs (ExpressIt Delivery, 2021), high upfront costs (Morales, 2023), limited range and charging infrastructure (Globalia Logistics Network, 2022), maintenance and service (Mohammed and Villegas 2023), and lack of awareness and training (Etrio, 2021).
The important effects of electric transportation vehicles on the environment and economy are as follows: Reduced carbon footprint reduces the carbon footprint of the logistics sector (EDF Energy, 2020). The adoption of electric transportation vehicles in logistics helps improve air quality, especially in densely populated urban areas and reduces greenhouse gas emissions and air pollution (Zhenhua et al, 2021). The reduced cost of energy consumption makes EVs a more economical alternative for last-mile logistics. Accurate tracking and optimization of electric transportation vehicles increases efficiency and reduces last-minute logistics costs (Mayer, 2023). Increasing the production of electric transportation vehicles increases gross added value and productivity through its indirect positive effects. Incentives and subsidies offered by governments enable the development of the logistics sector and increase investments (Pirmana et al. 2023).

V. Conclusion

There are great benefits to using electric transportation vehicles in the logistics industry and on the environment and economy**.** Thanks to the reduced carbon footprint, the carbon footprint of the logistics sector is reduced (Alternative Fuels Data Center, 2022). Electric transportation vehicles provide cost savings because their fuel costs and maintenance costs are low (Globalia Logistics Network, 2022). The use of electric transportation vehicles in picking and packaging operations in the logistics industry accelerates delivery times, increases accuracy, and reduces the carbon footprint of logistics (Alanazi, 2023). Gross added value and job creation increase thanks to the increased production of electric transportation vehicles (EDF Energy, 2020). Government support, incentives, and subsidies to encourage the adoption of electric transportation vehicles in logistics to improve the sector (Globalia Logistics Network, 2022), are the most important ones.
There are also some difficulties in the adoption of electric transportation vehicles: The penetration of electric transportation vehicles is slow and limited to light commercial vehicles. The number of electric truck models is still relatively low (Naveen et al. 2023). The initial costs of purchasing an electric vehicle are higher than those of conventional internal combustion engine vehicles (Khansep, 2023). Compared to internal combustion engine vehicles, electric transportation vehicles have limited range, and charging infrastructure is not yet as widespread as it should be. (Alanazi, 2023), The adoption of electric transportation vehicles in logistics has the potential to deliver significant environmental and economic benefits. (Pirmana et al., 2023) The logistics industry does not yet have sufficient maintenance and service support to ensure that electric transportation vehicles remain operational and efficient (Alternative Fuels Data Center, 2022). There is still a lack of awareness and education about the benefits of electric transportation vehicles in the logistics industry (EDF Energy, 2020).

References

Alanazi, F., (2023). Electric Vehicles: Benefits, Challenges, and Potential Solutions for Widespread Adaptation, Applied Sciences.; 13(10):6016. https://doi.org/10.3390/app13106016

Alternative Fuels Data Center (AFDC), (2022). Electric Vehicle Benefits and Considerations, https://afdc.energy.gov/fuels/electricity_benefits.html

Chnar M. and Adham A. M. (2021). Literature Review as a Research Methodology: An Overview and Guidelines, https://www.researchgate.net/publication/350581402_Literature_Review_as_a_Research_Methodology_An_overview_and_guidelines

EDF Energy, (2020). Benefits of Electric Cars on The Environment, https://www.edfenergy.com/energywise/electric-cars-and-environment

Etrio, (2021). How will Electric Vehicles Impact the Intra-city Logistics Industry?, https://etrio.in/how-will-electric-vehicles-impact-the-intra-city-logistics-industry/ExpressIt Delivery, (2021). The Impact of Electric Vehicles on the Logistics Industry, https://expressitdelivery.com/blog/the-impact-of-electric-vehicles-on-the-logistics-industry/

Globalia Logistics Network, (2022). Impact of Electric Vehicles on The Transportation and Logistics Industry, https://www.globalialogisticsnetwork.com/blog/2022/04/20/impact-of-electric-vehicles-on-the-transportation-and-logistics-industry/

Haikal, D., (2023). The Positive Impact of Electric Vehicles in Logistics Companies, https://www.linkedin.com/pulse/positive-impact-electric-vehicles-logistics-companies-diane-haikal/

Khansep, T., (2023). Rev. Thomson, L., Latest Research in the Environmental Benefits and Challenges of Electric Vehicles, https://www.azocleantech.com/article.aspx?ArticleID=1724

Mayer, M., (2023)., Electric Trucks Beginning to Show Signs of Cost Savings, Environmental Defense Fund (EDF), https://www.foodlogistics.com/sustainability/fuel-efficiency/news/22866651/environmental-defense-fund-edf-electric-trucks-beginning-to-show-signs-of-cost-savings

Morales, I., (2023). The Transformative Impact of Electric Vehicles on Logistics Operations, https://www.linkedin.com/pulse/transformative-impact-electric-vehicles-logistics-isaac-morales/?trk=pulse-article_more-articles_related-content-card

Mohammed J and Villegas J (2023). Total impact of electric vehicle fleet adoption in the logistics industry. Front. Sustain. 4:1158993. doi: 10.3389/frsus.2023.1158993, https://www.frontiersin.org/articles/10.3389/frsus.2023.1158993/full

Naveen, V., Vaishali A., Koppiahraj K., Satakshi A., Rakesh D. R., Sanjoy K. P., (2023). Mitigating Barriers to Adopting Electric Vehicles in An Emerging Economy Context, Journal of Cleaner Production, Volume 414, 137557, ISSN 0959-6526, https://doi.org/10.1016/j.jclepro.2023.137557, https://www.sciencedirect.com/science/article/pii/S0959652623017158

Pirmana, V., Alisjahbana, A.S., Yusuf, A. et al. (2023). Economic and environmental Impact of Electric Vehicles Production in Indonesia. Clean Techn Environ Policy 25, 1871–1885 https://doi.org/10.1007/s10098-023-02475-6

Statista, (2019). Retail e-commerce sales worldwide from 2014 to 2023, https://www.statista.com/statistics/379046/worldwide-retail-e-commerce-sales

World Economic Forum, (2020). The Future of the Last-Mile Ecosystem, https://www.weforum.org/publications/the-future-of-the-last-mile-ecosystem/

Zhenhua, C. et al, (2021). Environmental and Economic Impact of Electric Vehicle Adoption in the U.S, Environ. Res. Lett. 16, 045011, https://iopscience.iop.org/article/10.1088/1748-9326/abe2d0

IEEES-095

Thermodynamic Performance Analysis of Different Phase Change Materials for Cold Thermal Energy Storage

[1]Merve Altuntas, [2,3]*Dogan Erdemir, [1]Sebahattin Unalan
[1] Erciyes University, Department of Mechanical Engineering, Kayseri, Turkey
[2] Ontario Tech University, Clean Energy Research Laboratory, Oshawa, Ontario, Canada
[3] Yildiz Technical University, Department of Mechanical Engineering, Istanbul, Turkey
*Corresponding author e-mail: dogan.erdemir@ontariotechu.ca

Abstract

This study presents a comprehensive thermodynamic analysis to determine the effect of different phase change materials (PCMs) on the performance of the encapsulated cold thermal energy storage system. Twelve different PCMs, which have different melting points and latent heat, are evaluated based on the overall COP values of the cooling system. As a result of the study, it is observed that the COP has decreased as phase temperature decreases since the lower phase temperature requires lower heat transfer fluid temperature, which is performed in the evaporator of the chiller. Also, using lower phase change materials that have lower melting points causes higher heat gains (cold capacity lost), less efficient heat transfer and potential increases in thermal resistance.

Keywords: Cold thermal energy storage, phase change material, cooling load, cooling capacity, heat storage, COP.

I. Introduction

Cold thermal energy storage (TES) systems are gaining significant attention in the field of energy due to their potential to mitigate the effects of intermittent renewable resources and peak demands on the networks. These systems store cold energy in a medium, which can be used later when needed. They are particularly beneficial in controlling the timing of energy consumption, which can help shave peak loads in energy plants and district energy systems.

Cooling and air conditioning systems have become one of essential needs for people due to increasing ambient temperatures, rising time spent indoors, and increasing the number of activities performed indoors, along with the increasing need for thermal comfort conditions. Today, almost the half of the energy consumed in the buildings are used by heating, ventilating, and air conditioning (HVAC) systems. AC systems cause the peak loads at micro and macro scales as the time-of-use periods of air conditioning systems coincide because they are used simultaneously. When the duration of the peak cooling loads and levels are taken into consideration, they are quite higher than the average load and needed in a limited time period. That short period but relatively higher load requires higher capacity system equipment (chiller, backup power, etc.) and power supply. As a result, it is quite costly to meet peak loads. It is possible to manage cooling loads effectively through the use of thermal energy storage techniques, particularly cold thermal energy storage methods for cooling purposes. This can significantly reduce the operating cost, size, and capacity of the equipment by managing the cooling loads. Ice thermal energy storage systems, often named ice storage systems, are one of the most common practical applications of thermal energy storage systems for cooling applications due to the high latent heat capacity of water/ice phase changing, availability, cost, and relatively lower environmental impacts.

Latent heat storage using phase change materials (PCMs) is one of the most effective methods of storing thermal energy. Therefore, PCM has been applied to increase the thermal energy storage capacity of different systems. In PCM application, solid-liquid phase change is used to store large amounts of energy. The substances used may be organic, such as paraffin and fatty acids, or inorganic, such as aqueous salt solutions; both show a single melting temperature when pure and a melting range when mixed.

The importance of cold TES systems lies in their ability to efficiently utilize renewable or low-grade waste energy resources, or to use low-price electricity for energy storage during off-peak times. This can help bridge the gap between global energy demand and supply. Moreover, they can even reduce CO2 emissions and costs by ensuring energy is used when it is cheaper and there is more renewable energy in the mix. In summary, cold TES systems play a crucial role in managing future electricity supply/demand challenges, providing flexibility and ancillary services, and contributing to sustainability. This study deals with the performance assessment of twelve different PCMs which are used in cold thermal energy storage systems. The thermal properties of a large number of PCMs between -30°C and 0°C are studied. The performance of the system is assessed over the overall value of the cooling syste.

II. Material and Methods

Twelve different PCMs which can potentially be used in cold thermal energy storage systems are evaluated in the present study. The list of PCMs used in the present study is given with their thermodynamic properties in Table 1. As seen from Table 1, the phase change temperature of the materials varies from 0°C to -30°C. The different phase change temperatures have been studied to determine its impact on the thermodynamic performance of the system. The latent heat storage capacity of the PCMs varies from 50.6 to 335 kJ/kg. Fig. 1 demonstrates the schematic layout of the encapsulated heat storage system for their operating periods which are charging, storing and discharging periods. The temperature values highlighted in the Fig. 1 are for water/ice. 1 MWh of cooling capacity is considered. The system is consisted of chiller chiller group, packed-bed (encapsulated) storage tank, storage medium (PCM), heat exchanger, pumps, three-way valves, and installment equipment. As the heat transfer fluid (HTF), theethylene-glycol solution is considered. In this work, the ISS integrated AC and heat pump system has been thermodynamically assessed through based on the first and second laws of thermodynamic. A systematic energy and exergy analyses have been conducted.

Table 1. Thermophysical Properties of Phase Change Materials

	Materials	Phase Change Temperature (°C)	Latent Heat (kJ/kg)	Density (kg/m^3)	Thermal Conductivity (W/(m·K))	Specific Heat (kJ/(kg·K))	Kinematics Viscosity υ (/s)	Reference
PCM 1	5-Nonanone (C9H18O)	-3.84	175.3	915	0.5211	0.3057	0,000004172	[1][2][3][4]
PCM 2	Caproic acid (C6H12O2)	-4	146.18	915.1	0.5209	0.3057	0,000004195	[1][5][6]
PCM 3	n-Tridecane (C13H28)	-5.15	156.76	915.9	0.5193	0.3056	0,00000437	[1][15][7]
PCM 4	Butyric acid (C4H8O2)	-5.4	131.55	916.1	0.5189	0.3055	0,00000441	[1][15][16][17][8]
PCM 5	Heptanoic acid (C7H14O2)	-7	118.6	917.2	0.5167	0.3053	0,000004674	[1][16][17][9]
PCM 6	Triethylene glycol (C6H14O4)	-7	247	917.2	0.5167	0.3053	0,000004674	[1][16][10][11]
PCM 7	Tert-amyl alcohol (C5H12O)	-8.95	50.6	918.6	0.5139	0.3051	0,000005025	[1][12][13]
PCM 8	Diethylene glycol (C4H10O3)	-10.4	247	919.7	0.5119	0.3049	0,000005311	[1][16][3][5]
PCM 9	2-Octanone (C8H16O)	-21.55	190.4	927.5	0.4963	0.3036	0,000008448	[1][15]
PCM 10	n-Undecane (C11H24)	-25.75	143.9	930.4	0.4904	0.3031	0,00001026	[1][15][18][14]
PCM 11	n-Decane (C10H22)	-29.85	194	933.2	0.4847	0.3026	0,00001256	[1][15]
PCM 12	Water	0	335	998	0.6	4.186	0,000003657	[18]

Note: Density and specific heat values for the temperaute of 25 °C and 100 kPa of pressure.

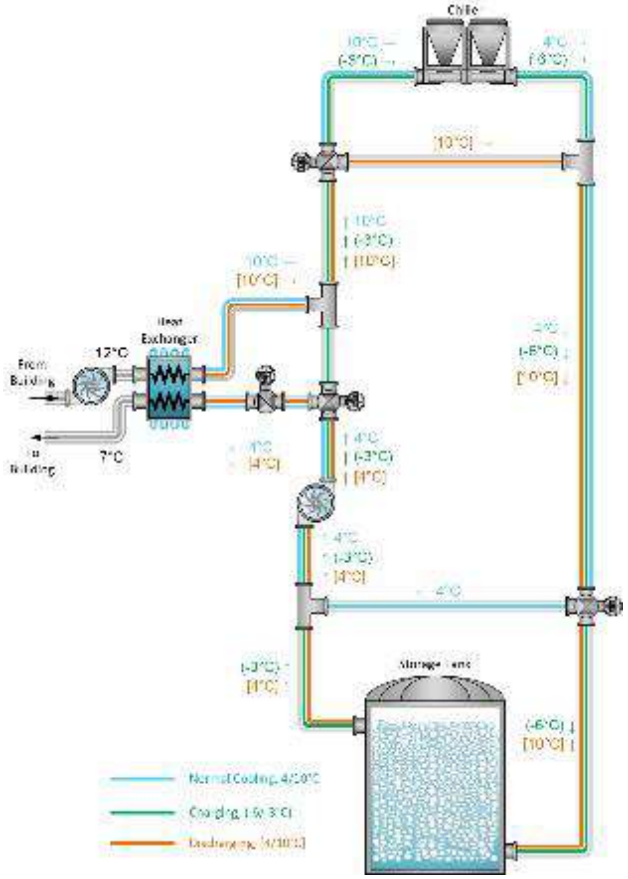

Fig. 1: Encapsulated Heat Storage System [19]

III. Results and Discussion

When different phase change materials are used in cold thermal energy storage applications, the COP value increases as the phase change temperature decreases. As seen in Figure 2, the COP value of n-decane material with the lowest melting temperature (-29.85°C) is 2.264, n-undecane (-25.75°C), 2-Octanone (-21.55°C). The COP values of diethylene glycol (-10.4°C), tert-amyl alcohol (-8.95°C), tri-ethylene glycol (-7°C), heptanoic acid (-7°C) materials are 2.493, 2.777, respectively. Calculated as 3.792, 3.962, 4.209, 4.209. As can be seen from the values, COP values increased as the temperature value of the materials increased. COP is a measure of how effectively a cooling system can transfer heat from a cold reservoir to a hot reservoir. As the temperature difference between cold and hot storages increases, the heat transfer ability of the system increases, and the COP also increases.
Similarly, in Figure 2, the COP values of the five highest melting temperature values are respectively; water (0°C) 5.351, 5-nonanone (-3.84°C) 4.661, caproic acid (-4°C) 4.636, n-tridecane (-5.15°C) 4.465, butyric acid (-5, 4°C) was found to be 4.429. In the case of PCMs, the heat loss from the system to the environment becomes more pronounced as the temperature value decreases. Thus, the temperature difference between the system and its surroundings becomes greater. As heat is lost to the environment, the system must work harder to maintain the desired low temperature, reducing its efficiency and COP.

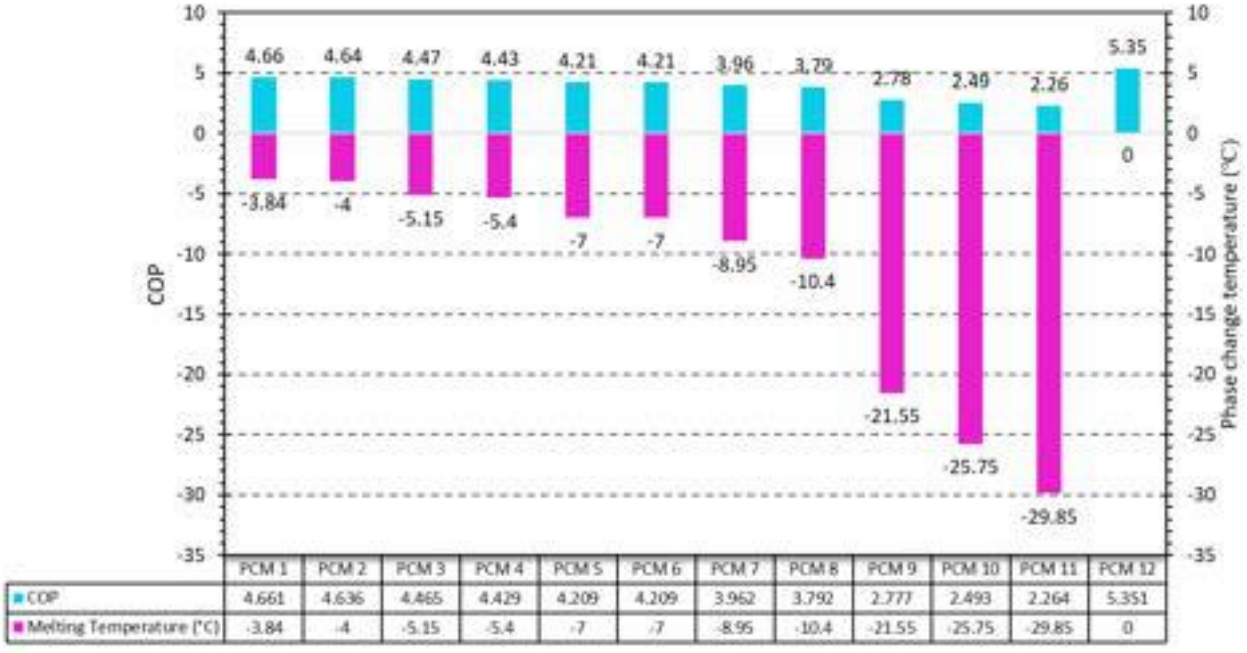

	PCM 1	PCM 2	PCM 3	PCM 4	PCM 5	PCM 6	PCM 7	PCM 8	PCM 9	PCM 10	PCM 11	PCM 12
COP	4.661	4.636	4.465	4.429	4.209	4.209	3.962	3.792	2.777	2.493	2.264	5.351
Melting Temperature (°C)	-3.84	-4	-5.15	-5.4	-7	-7	-8.95	-10.4	-21.55	-25.75	-29.85	0

Fig. 2. Comparison of the COPs and phase change temperatures for the PCMs studied.

IV. Conclusion

This research conducts a thermodynamic investigation to evaluate how twelve different phase change materials affect the efficiency of an encapsulated cold thermal energy storage system. This system has been evaluated thermodynamically based on the COP calculations. As a result of the present study, the highest COP value is observed to be 5.351 when water is used to be PCM. The lowest COP value is seen with n-decane (2.26). As seen from these results, the lower phase change temperature reduces the COP of the system. As the phase temperature of the materials decreases, the COP decreases because lower phase temperatures require a lower heat transfer fluid temperature managed in the cooler's evaporator.

References

Sanaye. S., and Shirazi. A., (2013). Thermo-economic optimization of an ice thermal energy storage system for air-conditioning applications, *Energy Build.*, vol. 60, pp. 100–109. doi: 10.1016/J.ENBUILD.2012.12.040.

Sanaye. S., and Hekmatian. M., (2016). Ice thermal energy storage (ITES) for air-conditioning application in full and partial load operating modes, *Int. J. Refrig.*, vol. 66, pp. 181–197. doi: 10.1016/J.IJREFRIG.2015.10.014.

Luo, N., Hong. T., Li. H., Jia. R., and Weng. W., (2017). Data analytics and optimization of an ice-based energy storage system for commercial buildings, *Appl. Energy*, vol. 204, pp. 459–475. doi: 10.1016/J.APENERGY.2017.07.048.

Erdemir, D., and Altuntop. N., (2018). Effect of encapsulated ice thermal storage system on cooling cost for a hypermarket, *Int. J. Energy Res.*, vol. 42, no. 9, pp. 3091–3101. doi: 10.1002/er.3971.

Talukdar. S., Afroz. H. M. M., Hossain. M. A., Aziz. M. A., and Hossain. M. M., (2019). Heat transfer enhancement of charging and discharging of phase change materials and size optimization of a latent thermal energy storage system for solar cold storage application, *J. Energy Storage*, vol. doi: 10.1016/j.est.2019.100797.

Yang. L., *et al.*, (2021). A comprehensive review on sub-zero temperature cold thermal energy storage materials, technologies, and applications: State of the art and recent developments, *Applied Energy*, vol. 288. Elsevier Ltd. doi: 10.1016/j.apenergy.2021.116555.

Li. G., Hwang. Y., Radermacher. R., and Chun. H. H., (2013). Review of cold storage materials for subzero applications," *Energy*, vol. 51. Elsevier Ltd, pp. 1–17. doi: 10.1016/j.energy.2012.12.002.

Xie. Z., Xue. W., Chen. H., and Huang. Y., (2011). Mechanical and thermal properties of 99% and 92% alumina at cryogenic temperatures, *Ceram. Int.*, vol. 37, no. 7, pp. 2165–2168. doi: 10.1016/j.ceramint.2011.03.066.

Andon. R. J. L., Counsell. J. F., Lees. E. B., and Martin. J. F., (1970). Thermodynamic properties of organic oxygen compounds. Part XXIII. Low-temperature heat capacity and entropy of C6, C7, and C9 ketones, *J. Chem. Soc. A Inorganic, Phys. Theor. Chem.*, pp. 833–837. doi: 10.1039/J19700000833.

Sharma. R. K., Ganesan. P., Tyagi. V. V., Metselaar. H. S. C., and Sandaran. S. C., (2015). Developments in organic solid-liquid phase change materials and their applications in thermal energy storage, *Energy Convers. Manag.*, vol. 95, pp. 193–228. doi: 10.1016/j.enconman.2015.01.084.

Yaws. C. L.,(1995). *Thermal conductivity graps for C5 to C7 compounds*.

Finke. B. H. L., *et al.*, (1953). LOW-TEMPERATURE THERMAL DATA FOR PARAFFIN HYDROCARBONS 333 Low-temperature Thermal Data for the Nine Normal Paraffin Hydrocarbons from Octane to Hexadecane.

Martin. J. F., and Andon. R. J. L., (1982). Thermodynamic properties of organic oxygen compounds Part LII .(') Molar heat capacity of ethanoic, propanoic, and butanoic acids.

Karimeh Labban. A., Francis Westrum. E., Antonio. J., and Cheda. R., (1991). Heat capacity and thermophysical properties of n-heptanoic acid from 5 to 350 K.

Oró. E., De Gracia. A., Castell. A., Farid. M. M., and Cabeza. L. F., (2012). Review on phase change materials (PCMs) for cold thermal energy storage applications, *Applied Energy*, vol. 99. Elsevier Ltd, pp. 513–533. doi: 10.1016/j.apenergy.2012.03.058.

Stephens. M. A., and Tamplin. W. S., (1979). Saturated Liquid Specific Heats of Ethylene Glycol Homologues.

Xu. X., Zhang. X., and Munyalo. J. M., (2019). Key technologies and research progress on enhanced characteristics of cold thermal energy storage, *Journal of Molecular Liquids*, vol. 278. Elsevier B.V., pp. 428–437. doi: 10.1016/j.molliq.2019.01.040.

Huffman. M., (1969). Capacities , Entropies and Free Energies of Ten Compounds, vol. 1969, no. 1.

Long Cheng. W., Ding. M., Dong YuanÇ X., and Han. B. C., (2017). Analysis of energy saving performance for household refrigerator with thermal storage of condenser and evaporator, *Energy Convers. Manag.*, vol. 132, pp. 180–188, Jan. doi: 10.1016/j.enconman.2016.11.029.

Yan. C., Shi. W., Li. X., and Zhao. Y., (2016). Optimal design and application of a compound cold storage system combining seasonal ice storage and chilled water storage, *Appl. Energy*, vol. 171, pp. 1–11. doi: 10.1016/J.APENERGY.2016.03.005.

Erdemir, D., et al., (2021). Experimental investigation on the effect of ice thermal storage system on electricity consumption cost for a hypermarket, *Int. J. Energy Storage*, vol. 251. doi: 10.1016/j.enbuild.2021.111368.

IEEES-096

Smart Greenhouse System and Control of Necessary Parameters for Accelerating Plant Growth-I

[1*]Nurdan Akdemir, [1]Yunus Babacan
[1]Erzincan Binali Yildirim Üniversity, Faculty of Engineering, Institute of Science and Technology, Erzincan, 24000, Türkiye
[*]Corresponding autor Email: nurdanozturk.eem@gmail.com

Abstract

To meet the increasing demand for agricultural products globally and in our country, it is necessary to facilitate the production of agricultural goods and ensure that production is carried out in a healthy manner. In line with this goal, agricultural fields need to be supported with automation techniques. In the conducted study, an automation system has been designed to address the significant issue of irrigation in agricultural areas. In this work, data obtained from a moisture sensor placed in the soil where the plant is cultivated have been processed by an Arduino Uno controller. Based on these data, when irrigation is needed, the solenoid water valve will automatically operate, and the irrigation process will be carried out according to the plant's requirements. Thus, automatic irrigation has been implemented to ensure the correct timing and amount of irrigation water, preventing excessive water waste and maximizing energy efficiency.

Keywords: Arduino, Plant Moisture Sensor, Automatic Watering, Proteus.

I. Introduction

In this conducted study, a system capable of autonomous agricultural irrigation with an embedded system has been designed. The soil moisture detection sensor on the system measures the soil moisture level, and it is controlled by an Arduino Uno microcontroller. Additionally, the designed system includes a DHT11 air humidity sensor and a soil moisture sensor to monitor humidity values.
The DHT-11 is a digital sensor that simultaneously measures both temperature and humidity values. It utilizes a capacitive humidity sensor and a thermistor inside to measure the surrounding air. The sensor transfers the data from these sensors to the digital output pin. The sensor provides an output every 2 seconds (Ersin, 2017).
Developed by General Instruments, the PIC microcontroller is a microcontroller that can perform input-output operations very quickly. Command and information storage memories are independent of each other and as a result, their cost is higher than microcontrollers of other architecture types, but with the help of technological developments, the price difference has disappeared over time (Çalışır, 2021).
A soil moisture sensor is a device used to measure the moisture content in the soil or the level of a low-scale liquid. The moisture meter is immersed in the environment where measurement will take place. Due to the resistance created by the soil or the immersed liquid, a voltage difference occurs between the probe terminals. The information obtained from this voltage difference allows the measurement of the moisture level. As the moisture content in the soil increases, the conductivity also rises. The sensitivity of the sensor can be adjusted using the trim pot located on the board (Altunbaş, 2018).

Advantages of Automatic Watering

Considering the findings obtained in previous studies, the three-month measurement results are shown in Figure 1. A three-month measurement has been conducted, and the water savings obtained by comparing the results on a monthly basis have been calculated. The water consumption of pepper, tomato, and eggplant plants irrigated with a plant moisture sensor and normal irrigation has been compared (Altunbaş 2018).

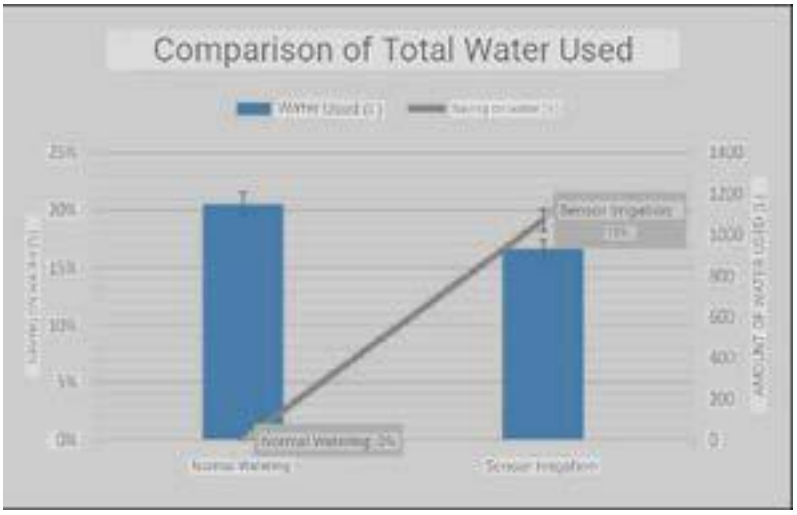

Figure 1. Total amount of water used and water savings achieved (%) (Altunbaş 2018).

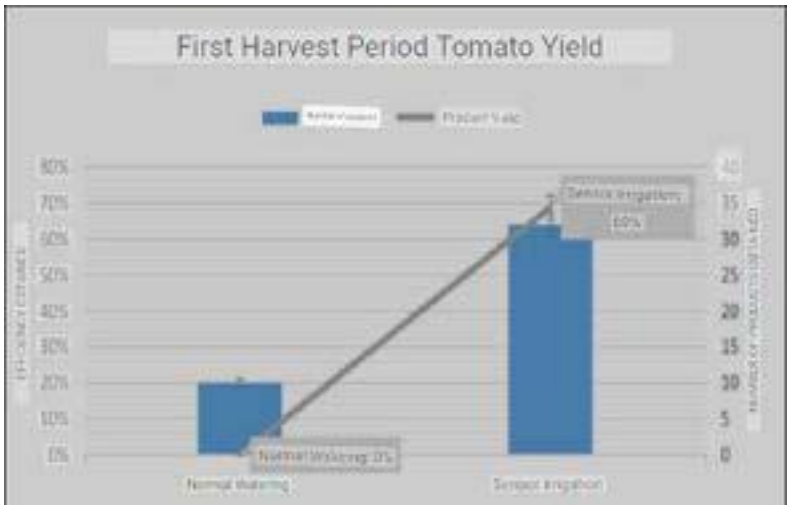

Figure 2. First harvest period tomato product yield (Altunbaş 2018).

As a result, when the products obtained from sensor-based irrigation are compared to conventional irrigation, an increase in both crop yield and product weight has been observed (Altunbaş 2018).

II. Material Method

The automation of the automatic irrigation system consists of two components: software and hardware.

- The hardware component comprises elements such as the Arduino Uno controller, a controller like a microcontroller or Programmable Logic Controller (PLC), and components like sensors and output devices such as relays and contactors.
- The software component is the part created to control the installed hardware in the desired manner and make decisions about the system's operation based on data.

In this study, an agricultural irrigation system was designed using an Arduino board that utilizes the Atmega328 microcontroller. The Arduino board provides more libraries and easy programming features compared to its counterparts. In Figure 3, the section displaying the program for the automatic irrigation system with sensors and motors is shown.

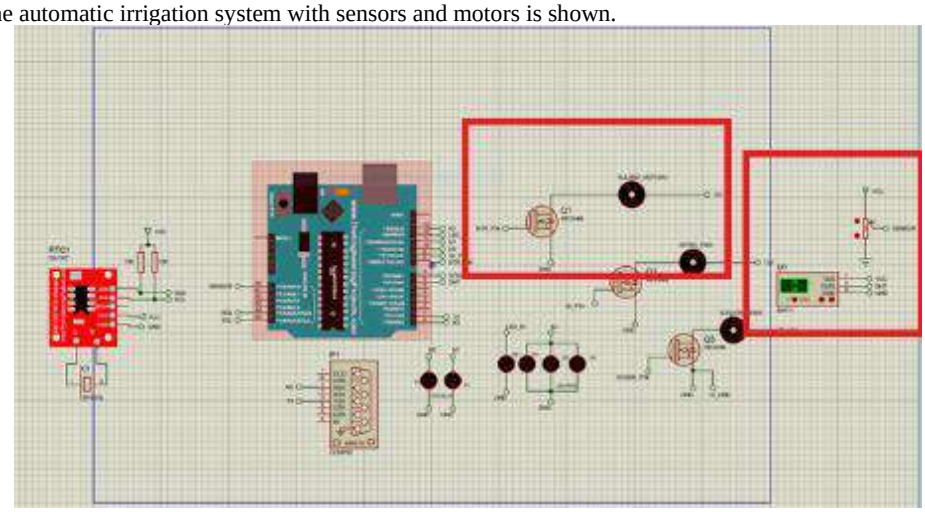

Figure 3. Automatic Irrigation System Circuit

The system operates according to a specific algorithm. An algorithm has been designed to carry out the irrigation process based on the moisture level of the plant. The flowchart of the system algorithm is illustrated in Figure 4.

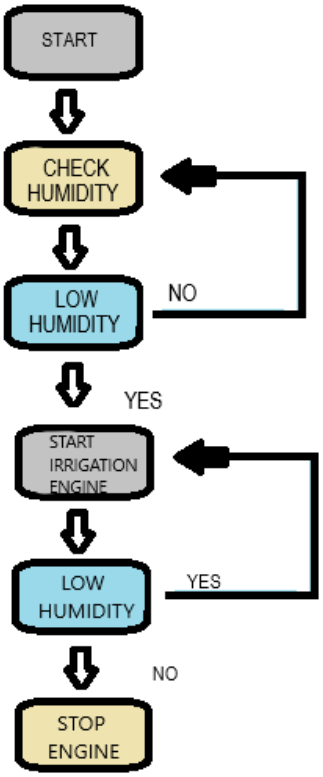

Figure 4. Flow chart of the system

III. Discussion and Conclusion

Irrigation is one of the most important elements of agricultural production. In this context, the use of water and saving water have become important in today's conditions. In the study, the water needs of the plants were determined in the light of literature research by using the plant moisture sensor, and irrigation was done depending on the amount of water needed by the plant. At the same time, the designed system can be monitored on the Liquid Crystal Display (LCD) screen.

In this context, the aim is to reduce operational and maintenance expenses such as personnel costs, energy costs, and maintenance and repair costs. Additionally, achieving equitable water distribution through drip irrigation is targeted. Accordingly, in the conducted study, the moisture level of the plant was determined with the help of a plant moisture sensor, the required water for the plant was provided, and water savings were achieved.

References

Çalışır, R., (2021), "Pic Mikrodenetleyici İle Çalışan Otomatik Bahçe Sulama Sistemi", master's thesis.
Altunbaş, Y., (2018), "Bitki Su İhtiyacına Göre Uzaktan Kontrollü Bahçe Sulama Sistemi", master's thesis.
Ersin, Ç.,(2017), "EJONS International Journal on Mathematic, Engineering and Natural Sciences", 131-143.

IEEES-097

Smart Greenhouse System and Control of Necessary Parameters for Accelerating Plant Growth-II

[1*]Nurdan Akdemir, [1]Yunus Babacan
[1]Erzincan Binali Yildirim Üniversity, Faculty of Engineering, Institute of Science and Technology, Erzincan, 24000, Türkiye
[*]Corresponding autor Email: nurdanozturk.eem@gmail.com

Abstract

Greenhouses are facilities where production is carried out by providing the most suitable environmental conditions for the development of the plant. Heating of greenhouses becomes mandatory to provide these suitable conditions, especially in cold seasons. For this reason, cooling and heating systems are applied in greenhouses in our country to protect them from extreme heat and cold. Lack of regular heating and cooling causes problems such as low efficiency, limitation in production type and the necessity of using hormones. In this study, the data received from the temperature-humidity sensor placed in the soil where the plant was grown was processed into the Arduino Uno controller. The system keeps the temperature of its environment between 19 - 23 C. As input variables, humidity and temperature values are taken from the external environment with the DHT11 sensor and transferred to the microcontroller. Depending on the output values, heating or cooling fans are operated to provide the necessary air conditioning.

Keywords: Arduino, Plant Moisture Sensor, Automatic Heating, Automatic Cooling, Air Conditioning, Proteus.

I. Introduction

Greenhouses are movable structures that enable the economic cultivation of cultivated plants and provide the development factors necessary for plant production in periods when climatic conditions are not suitable for growing plants outdoors(Sevgican and fri 2000). In this study, a system that can provide autonomous greenhouse heating and cooling with an embedded system was designed. The temperature of the environment was measured with the temperature humidity detection sensor on the system and controlled with the Arduino Uno microcontroller.

Arduino
Arduino is a tool that can perform tasks that a computer can do, such as detection and control of multiple devices in the real environment. It is an open source physical computing platform based on a simple microcontroller. There is a development environment for developing software. These development environments, which have become very popular recently, are used in various academic studies for different purposes. Atmega328 microcontroller was used in this study. (Şimşek and Taşdelen, 2015).

DHT-11 Humidity and Temperature Sensor
In indoor plants, the temperature and humidity of the environment are of critical importance for plant development. For this reason, these sensors are used for temperature and humidity control in systems such as greenhouse automation.(Çelik and Duran, 2022). The schematic representation of some sensors used in smart agriculture is as follows.

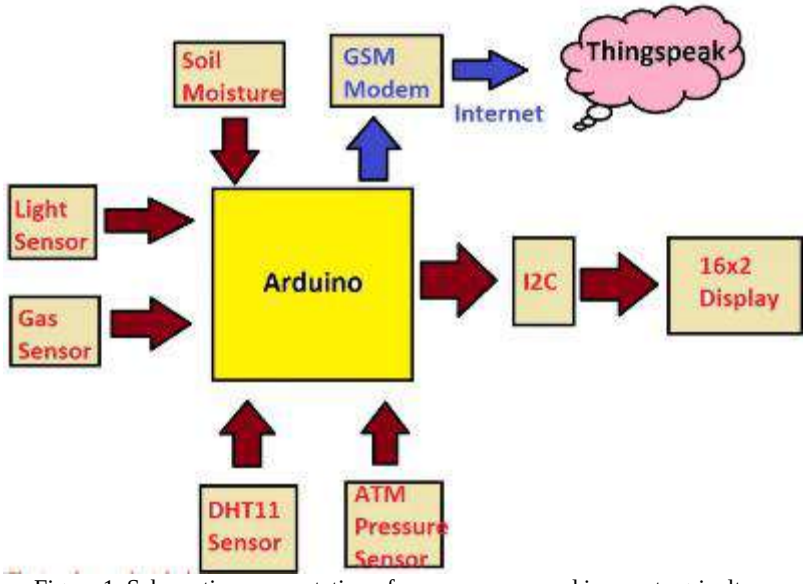

Figure 1. Schematic representation of some sensors used in smart agriculture

The sensor used in our system is DHT11. While the DHT 11 sensor shown in Figure 2 can measure ambient humidity and the analog signal produced by the moisture in the air reacting with the salts in the sensor and creating a conductivity difference, the humidity in the soil is measured by using the resistance difference or capacitive effect of the water density in the soil on the sensor (Novelan,2020).

Figure 2. DHT11 air humidity sensor

Advantages of Automatic Heating and Cooling Systems

In previous studies, cucumbers were planted in a normal non-automated greenhouse and an automated greenhouse at the same time. It has been observed that the product grown in the automated greenhouse develops more regularly than the product grown in the classical greenhouse. While cucumber seedlings developed slowly in the normal greenhouse, it was observed that faster growing and productive plants were formed in the automated greenhouse. While flowering is late in the normal greenhouse, flowering is faster in the automated greenhouse and it opens an average of 10-15 days earlier, and it has been observed that the leaves and branches grow more clearly. The main purpose is to keep the climate characteristics such as humidity and temperature inside the greenhouse constant at the desired values thanks to automation and to prevent external factors from affecting the development. In the experiments, it was observed that the humidity and temperature values were kept constant within the desired ranges thanks to the automation system. As a result, it has been observed that the products in the automated greenhouse develop faster, from seed to flowering, from seedling development to product formation, on average, 10-15 days, compared to the products in the normal greenhouse(Yılmaz 2016).

Şekil 3. Variation of greenhouse indoor and outdoor temperatures over time (Yılmaz 2016).

II. Material Method

Automatic heating and cooling system automation consists of two parts: software and hardware.

- Hardware part; Arduino Uno controller is the part consisting of a controller such as microcontrollers or PLC, sensors and output elements such as relays and contactors.
- Software part; It is the part that is created to control the installed hardware in the way we want and decides whether the system works or not according to the data.

In this study, an agricultural heating and cooling system was designed using Arduino board using Atmega328 microcontroller. Arduino board provides more libraries and easier programming features than its counterparts. Figure 4 is the part where the sensor, heating fan and cooling fans of the automatic heating and cooling system of the program are shown.

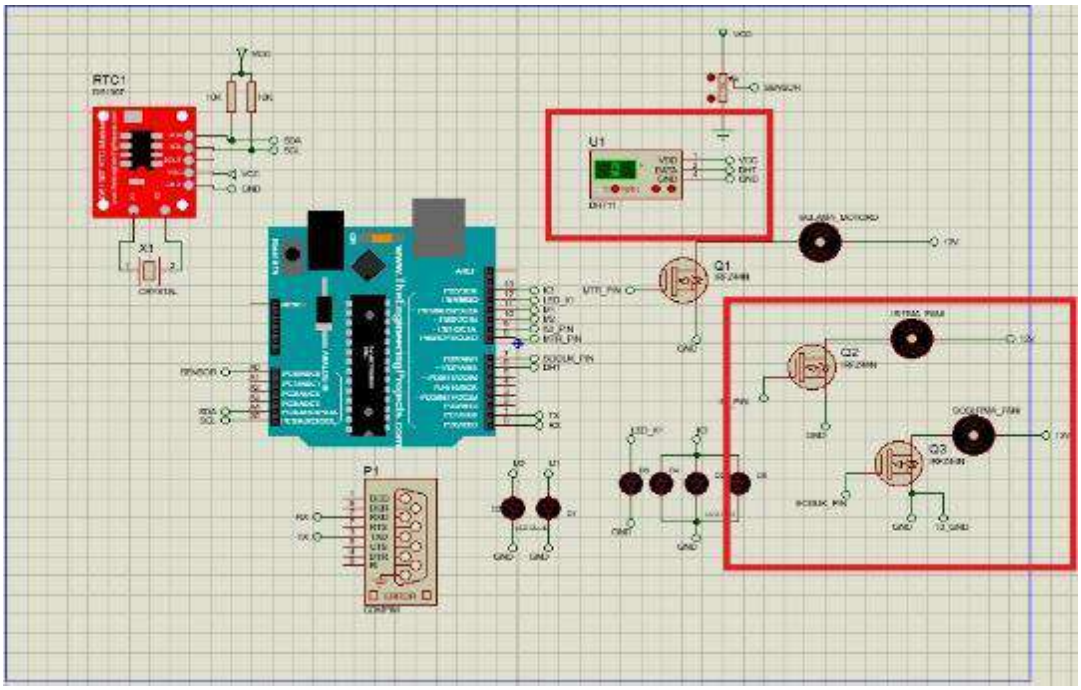

Figure 4. Automatic irrigation system

III. Discussion and Conclusion

As the world population increases, agricultural lands are gradually decreasing, and with this, some problems arise in accessing healthy and quality food. The production of healthy food is possible if the plants used in food production are healthy. The use of sensors in agricultural areas by taking advantage of developing technology to provide the necessary conditions for the plant is necessary for sustainable agriculture. In this study, the DHT 11 sensor, which can measure air humidity and air temperature, was used. As a result, within the scope of this article, a system that will benefit crop production has been designed with the help of sensors that measure air humidity and temperature.

Accordingly, in the study carried out, the environmental conditions required by the plant were provided with the help of the plant temperature and humidity sensor.

Resources

Şimşek M. ve Taşdelen K., 2015.” Denetleyici Alan Ağı Üzerinden Sensör Verilerinin İzlenmesi”, academic informatics journal, 945-950

Çelik K. ve Duran A,. 2022. ”Akıllı Tarımda Nem ve Sıcaklık Sensörleri Kullanılarak Tarımsal Verilerin Algılanması İşlenmesi ve Transferi”, ISPEC Journal of the Institute of Science and Technology, 17-26.

Yılmaz A. Ve Doğan H., 2016. “Sera İçi Hava Şartlarının Otomasyon Sistemi İle Üretim Kalitesinin Artırılması ile İlgili Bir Çalışma”, Journal of Life Sciences, 147-159.

Novelan, M.S., Amin, M., 2020. “Monitoring system for temperature and humidity measurements with DHT11 sensor using nodeMCU.” International Journal of Innovative Science and Research Technology, 5(10): 123-128.

IEEES-098

Smart Greenhouse System and Control of Necessary Parameters for Accelerating Plant Growth-III

[1*]Nurdan Akdemir, [2]Yunus Babacan
Erzincan Binali Yildirim Üniversity, Faculty of Engineering, Institute of Science and Technology, Erzincan, 24000, Türkiye
*Corresponding autor Email: nurdanozturk.eem@gmail.com

Abstract

Artificial lighting systems are used in greenhouses when plants cannot meet the light they need to grow and develop. LED (Light Emitting Diode) lamp technology has many uses and has also taken its place in the field of plant production. Studies are being carried out on its use in the field of plant production to increase photosynthesis. Although LED lamps can emit light in different wavelengths, they can only produce light in the blue and red regions of the typhoon, which are the most used by plants.. A system has been designed to investigate the effects of artificial lighting applications specifically on plant production. This system is very important in terms of providing significant advantages in artificial lighting applications and energy saving.

Keywords: LED (Light Emitting Diode) Lamp, Greenhouse, Lighting Automation System, Artificial Light Sources.

I. Introduction

In general, green plants need a certain amount of light at certain times to grow and develop. The increase in light intensity within certain limits and at a rate accelerates the growth and development of the plant, however, it plays a very important role in shaping some morphological characteristics of plants such as elongation, root shape, leaf anatomy and leaf size. (Vardar, 1973) In addition, light is the only energy that plants need to carry out photosynthesis, and it is also a source of information that provides seasonal changes in plants due to the difference in the length of day and night. (Yağcıoğlu 1996).

Led Grow Lights

The photosynthesis characteristics of plants give us important information about the use of artificial lighting sources. (Mcfate, 1989). The advantages of LED lamps created from LED light sources can be listed as follows; They have a small volume, are long-lasting, can emit light at the desired wavelength, have adjustable light intensity, can emit low heat to the environment, and are environmentally friendly.

LED lamps, which are created by combining many LEDs, are commercially produced in rectangular or round types. The power of LED grow lights used in agricultural applications varies depending on the number of LEDs they have. These LEDs are red and blue in color and are arranged in mixed proportions on a plate. This ratio varies depending on the need during the germination, growth and fruit periods, usually as intense red and less intense blue.

Figure 1. LED lighting systems in greenhouses

Plant Productivity Characteristics Of LED Light Source Applications

According to Efe, (2014), in the experiment conducted, all of the plants in the parcels were harvested on the 69th day because they reached harvest size. It is stated that the harvest period varies between 70-150 days according to Thompson and Kelly, (1957), and 106-124 days according to Karataş et al., (1995). Although the harvest time of the plants grown in the experiment was parallel to the literature, plant weights were found to be above the literature studies (Efe 2014).

In the research conducted, it has been confirmed that LED lighting application in addition to daylight in curly leaf salad cultivation has a positive effect on plant development, in the light of the findings below.

Led Light Source	Total Plant Weight (g)	Marketable Head Weight (g)	Number of Marketable Sheets (Piece)	Total Number of Leaves (Piece)	Marketable Yield (ton/ha)
RED	**940,04 cd**	**804,83 de**	**39,83 d**	**43,58 c**	**32,06 cd**
CONTROL	**1047,92 b**	**888,71 bc**	**43,92 bc**	**48,00 b**	**35,55 b**
BLUE	**1054,67 b**	**891,25 bc**	**45,00 b**	**49,08 b**	**35,65 b**
BLUE+RED	**1050,33 b**	**916,58 b**	**45,50 ab**	**48,67 b**	**36,40 b**

Figure 2. Effect of different colored LED light source applications on plant productivity characteristics (Efe, 2014).

II. Material Method

The aim of this study is to design a lighting automation system with LED lamps that can be adjusted according to the characteristics of vegetables and fruits, the environment and demand. Environmental factors have significant effects on plant development in the cultivation of vegetables and fruits. In cases where light is insufficient, problems with thin stem development, low number of flowers, weak cluster formation and poor root development occur (Sevgican, 1999).

Since the light intensity decreases in the winter months (December, January, February, March), the need for additional lighting comes to the fore when growing fruit and vegetables in greenhouses. (Köksal, İncesu, Teke,. 2013) For these reasons, an automation system with LED lamps was needed. In the system we designed, selection will be made by teaching the environmental values of the 3 most grown vegetables and 3 tropical fruits in Turkey to the system we designed. The selected vegetables are tomatoes, cucumbers, peppers and 6 tropical fruits: pineapple, kiwi and banana. The environmental values will be automatically adjusted according to the product selected from the touch screen, and the environmental values will be adjusted by the system according to the planting of the product in the same greenhouse.

The simulation environment was designed and implemented in the Proteus program. One of the best features of the Proteus program is its ability to simulate interaction between the software running on a microcontroller and any analog or digital electronics connected to it (Çalışır, 2021).

It provides constant information to the user and can be followed through the touch screen, which part of the program is in the program. The lighting of the LEDs that will provide illumination is possible with the signals coming from the output pins of the microcontroller. Microcontrollers' access to the codes written in visual studio code that determine how the simulation behaves is possible by including a hex file in the simulation environment.

Figure 3. LED lighting system simulation

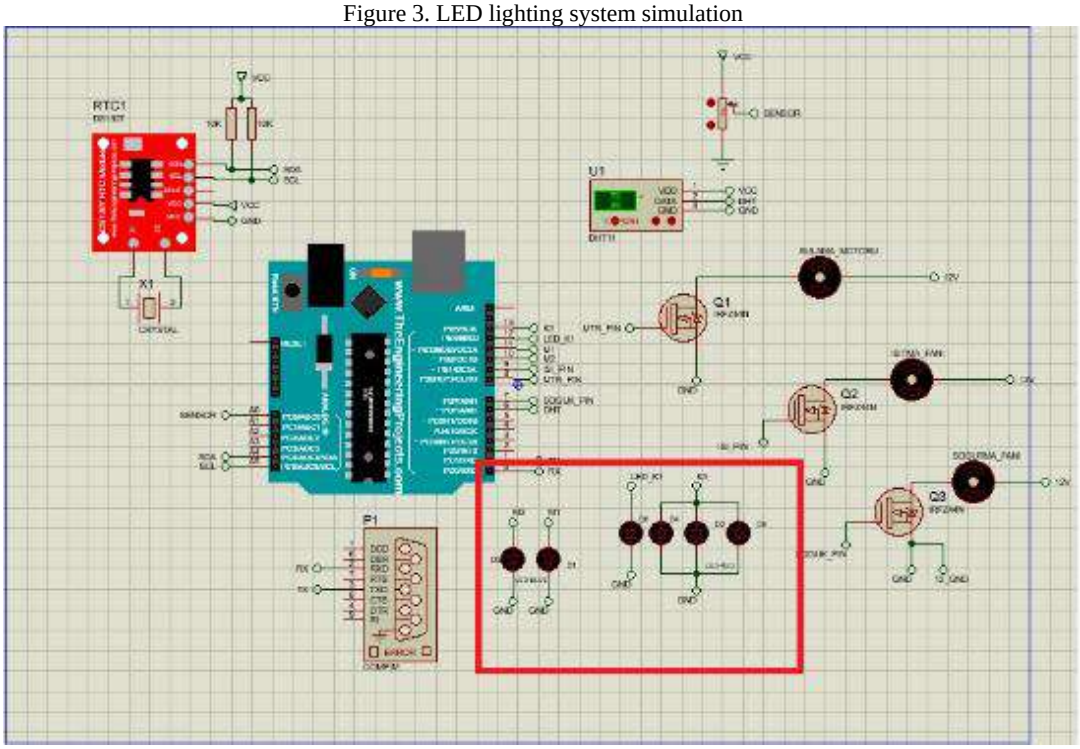

III. Discussion and Conclusion

As a result of the study, the design of a lighting automation system that can provide the lighting values needed in agricultural production has been successfully carried out. This study provides the opportunity to observe and examine the properties of LED light and its effects on plants. The opportunities provided by LED light sources will meet the increasing demand for high-quality greenhouse cultivation and protect the natural environment. In addition, these results will provide a very broad perspective and shed light on future studies in agricultural production research areas such as tissue culture and plant growth chambers. The lighting automation system implemented in this study is important in terms of providing observation and examination opportunities on the effects of LED light on plants, as well as contributing to the science and greenhouse cultivation of our country.

Resources

Vardar Y., 1973. "Phytochrome System in Plants", Turkish Journal of Biology, (23): 47-56.

Yağcıoğlu A., l996. "Agricultural Electrification". Ege University Faculty of Agriculture Publications. Bornova- İzmir, 280.

Efe H., 2014. "Cultivation of Curly Leaf Salad in Solid Media Culture Effects of Additional LED Lighting Applications on Yield, Quality and Plant Development" master's thesis.

McFate, K.L., 1989. "Electrical Energy in Agriculture". Elsevier Science Publishers, Netherlands.

Sevgican, A., 1999. "Greenhouse Vegetable Growing", Skin I, Ege University Faculty of Agriculture Publications: 538, Textbook: 302.

Köksal, N., İncesu, M., Teke, A., 2013, ""Effects of LED Lighting System on Tomato Plant Development", Journal of Agricultural Sciences Research 6, 72-75.

Çalışır, R., 2021 ""Automatic Garden Irrigation System Working with Pic Microcontroller", master's thesis.

IEEES-099

Potential Use of Hydrogen Pentoxide and Hydrogen Peroxide in Transportation Sector: An LCA Study

*[2]Assem Abdurakhmanova and [1,2]Ibrahim Dincer
[1]Ontario Tech University, Clean Energy Research Laboratory, Oshawa, Ontario, Canada
[2]Yildiz Technical University, Clean Energy Technologies Institute, Istanbul, Turkey
*E-mail: assem.abdurakhman@gmail.com

Abstract

In accordance with the analysis utilizing the GREET dataset, this study establishes three distinct pathways as a foundational framework for comparing hydrogen pathways for production of hydrogen pentoxide and hydrogen peroxide, with a specific focus on their implications for the transportation sector. These pathways are structured based on three primary criteria: 1 - Electricity, 2 - Natural Gas, and 3 - Gaseous Hydrogen. Varied values of these criteria were assigned to each pathway to facilitate the evaluation of their performance within a common framework. These pathways encompass diverse methodologies for electricity generation, including non-distributed coal-fired power generation, as well as the utilization of natural gas sourced from shale and conventional extraction techniques for the centralized production of gaseous hydrogen. Furthermore, these pathways incorporate the utilization of gaseous hydrogen generated from renewable natural gas, with a specific focus on its application in the production of liquid hydrogen (LH2). Compared to the conventional method of hydrogen peroxide production, the CO_2 emissions from conventional production of hydrogen peroxide are as high as 0.57 kg, while the alternative Pathways methods of hydrogen peroxide production reduce these emissions to a value between 0.006 kg and 0.003 kg.

Keywords: Hydrogen, hydrogen pentoxide, hydrogen peroxide, Transportation sector.

I. Introduction

This study delves into the intricate web of associations between a chemical catalyst and its repercussions on diverse renewable energy generation methods. It leverages data derived from the Greenhouse gases, Regulated Emissions, and Energy use in Transportation (GREET) program to scrutinize these complex relationships. Specifically, the investigation encompasses three distinct sectors, namely Electricity, Natural Gas, and Gaseous Hydrogen, as they converge along the pathway involving Unallocated Electricity from Biogenic Waste. This pathway integrates multiple facets, including electricity generation using hydro storage, the conversion of food waste into natural gas as an intermediate fuel, and the centralization of power plants in the production of compressed H_2 gas from coal. The comprehensive analysis of this study extends its purview to encompass the specific needs and objectives of the transportation sector, recognizing the critical role that hydrogen plays in addressing the sector's energy and environmental challenges. The results of this extensive analysis reveal that hydrogen produced from renewable sources emits the least amount of greenhouse gases, rendering it a promising candidate for a sustainable and environmentally friendly transportation fuel. Carbon dioxide emissions today account for 76% of total greenhouse gas emissions, and 65% of these emissions come directly from fossil fuels and industrial activities (Dincer and Aydin 2023). This study contributes valuable insights that could significantly influence the trajectory of the transportation sector, aligning it with the global shift toward cleaner and more efficient energy solutions. The implications of these findings extend far beyond the boundaries of the laboratory, promising to reshape the energy landscape and facilitate a more sustainable and environmentally responsible future.

II. Methodology

This research uses the Life Cycle Assessment (LCA) method to compare indicators of the studied processes (Lui 2022). LCA assesses environmental impacts of producing clean hydrogen from renewable energy sources (Iyer and Kelly 2022). This assessment considers a wide range of emissions, including carbon dioxide (CO_2), methane (CH_4), nitrogen oxides (NOx), volatile organic compounds (VOC), sulphur oxides (SOx) and nitrous oxide (N_2O). The methodology emphasises sustainability and the long-term well-being of ecosystems and society. The methodology emphasises sustainability and the long-term well-being of ecosystems and society. To improve accessibility and clarity of data presentation, a graphical approach is favoured in this paper. Graphical representations are used to communicate estimates of environmental effects associated with CO_2, CH_4, NOx, NOx, VOC, SOx and N_2O. These visual tools clearly present the results, focusing on their relevance to sustainable development. Playing an important role for transportation, this methodology extends its scope of inclusion, considering the specific needs and objectives of the transport sector.

III. Results and discussion

In line with the analyses carried out using the GREET dataset, this study identifies three different pathways as the fundamental basis for comparing pentoxide and hydrogen peroxide, with a particular focus on their impact on the transport sector. These pathways consist of:

- Pathway 1: Electricity: Generated through non-distributed coal-fired power generation. Natural Gas: Produced from shale and conventional recovery for central plant gaseous hydrogen production. Gaseous Hydrogen: Compressed gaseous hydrogen produced from renewable natural gas, specifically used for low-pressure hydrogen production.
- Pathway 2: Electricity: Generated through non-distributed electricity production from biogenic waste, along with pumped storage electricity production. Natural Gas: Conversion of food waste into natural gas, which serves as an intermediate fuel. Gaseous Hydrogen: Central plant production of compressed gaseous hydrogen from coal.

- Pathway 3: Electricity: Delivered from a grid-connected photovoltaic (PV) system without battery storage. Natural Gas: Utilisation of shale and conventional recovery natural gas as stationary fuels. Gaseous Hydrogen: Central plant production of gaseous hydrogen from electrolysis using a high-temperature gas-cooled reactor (HTGR) for process fuels.

Various values for these criteria have been assigned to each pathway to facilitate the evaluation of their performance within a single system. The study also considers CH_4, NOx, VOC, SOx and N_2O emissions, noting differences between pathways due to feedstock composition and production processes. The results of these studies are presented in Figures 1-2. This highlights the complex nature of the effect of the chemical catalyst. Figure 1 shows the hydrogen pentoxide and Figure 2 shows the hydrogen peroxide production, both figures show emissions of CO_2, these values are taken on a per kg basis. It is to be noted that the expected outcome of this study is to reveal the key role of chemical catalyst in the production of pure hydrogen and its extensive influences on the field of renewable energy. By combining LCA methods and detailed analyses of the data obtained, this study contributes to the current discourse on the integration of clean hydrogen production technologies by providing solid information for informed decision making. The results of our study should serve as a starting point for the transition to a sustainable and long-term energy future, including aspects related to the transport sector.

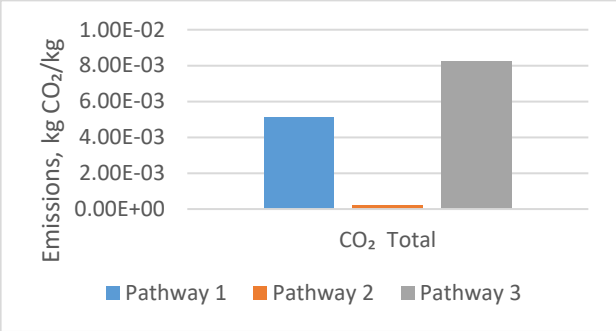

Fig. 1. Hydrogen in Pentoxide

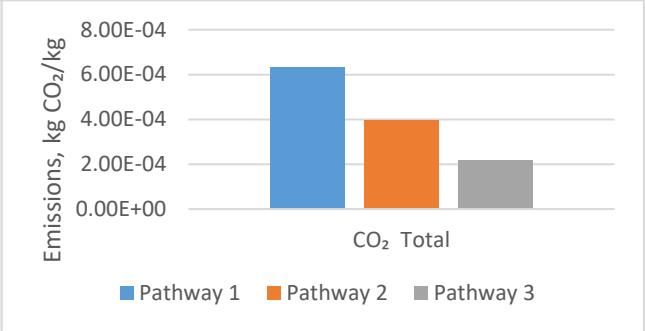

Fig. 2 Hydrogen in Peroxide

IV. Conclusions

The aim of this study is to systematically analyse the impact of a chemical catalyst on the production of pure hydrogen and its possible extension to more extensive renewable energy technologies. Using data from the GREET programme, the analysis covers both environmental and economic aspects of the subject area. The main point of emphasis of the study is to highlight the important role of hydrogen in the transport sector. The results reveal the potential of the catalyst in changing the structure of a sustainable transport sector and highlight its importance for the development of renewable energy technologies. This study provides an important scientific basis for understanding the complex interrelationships shaping the future of the renewable energy sector, particularly in the context of transport technologies.

References

Dincer, Ibrahim; Aydin, Muhammed Iberia (2023): New paradigms in sustainable energy systems with hydrogen. In *Energy Conversion and Management* 283, p. 116950. DOI: 10.1016/j.enconman.2023.116950.

Iyer, Rakesh; Kelly, Jarod (2022): Life-Cycle Inventory of Critical Materials: Nickel, Copper, Titanium, and Rare-Earth Elements.

Lui (2022): Life cycle assessment of waste-to-hydrogen systems for fuel cell electric buses in Glasgow. In *Scotland Bioresour Technol* 359.

IEEES-100

A Comprehensive Analysis of the Thermal and Heat Transfer Characteristics of the Melting of Capric Acid As A Phase Change Material In a Rectangular Thermal Storage Unit

[1] Md. Imran Alam, [1] Munawar Nawab Karimi, [1*] Osama Khan, [2] Ashok Kumar Yadav, [3*] Anoop Kumar Shukla, [4*] Sabri Alkan

[1] Department of Mechanical Engineering, Jamia Millia Islamia, New Delhi - 110025, India.
2 Department of Mechanical Engineering, Raj Kumar Goel Institute of Technology, Ghaziabad, India.
3 Department of Mechanical Engineering, Amity University Uttar Pradesh, Noida, 201313, India
[4] Department of Motor Vehicles and Transportation Technologies, Maritime Vocational School of Higher Education, Bandırma Onyedi Eylül University, Turkey
*E-mails: shukla.anoophbti@gmail.com; salkan@bandirma.edu.tr

Abstract

In order to optimize the cost and quality of TES systems, it is highly advised to study how PCMs perform in terms of the shape and structure of the container as well as the heat transfer mechanism. The study examines the behavior of PCMs, particularly Capric acid, while melting in a rectangular domain while examining several elements of heat transfer. An exte1nsive numerical analysis is carried out for this study utilizing a specialized two-dimensional finite volume model built using ANSYS Fluent CFD. The model uses an enthalpy-porosity method that allows for a thorough investigation of the PCM's thermal behavior and heat transfer properties during melting. To better comprehend the process, the researchers assessed eleven crucial parameters. Melting rate, melt front patterns, temperature distribution, PCM surface average temperature, total stored energy, Prandtl, Rayleigh, and Stefan numbers, velocity vector direction and contours, surface-averaged Nusselt number, and heat flux are some of these parameters. The study's findings provided significant novel insights into the melting process. The variations in the Nusselt number demonstrated that during the first melting process, heat conduction predominated overheat transfer. However, as the process advances, convection became the dominant heat transfer mechanism. Specific significant values were obtained at the conclusion of the melting process: the total energy stored was 187.32 kJ/kg, the melting time was 4536 s, the surface-average temperature reached 311.3 K, and the Prandtl, Rayleigh, and Stefan numbers were 41.8, 5.27×10^8, and 0.15, respectively. A significant novel finding of this study is that Capric acid is a viable option for low-temperature TES applications as it has favorable thermodynamic, kinetic, and thermophysical properties. These results pave the way for the development of effective TES systems based on organic PCMs, along with existing research on Capric acid.

Keywords: Hydrogen liquefaction, precooling, parameters, optimization, efficiency.

I. Introduction

The study discussed in the provided text focuses on the optimization of Thermal Energy Storage (TES) systems with a particular emphasis on the use of Capric acid as a Phase Change Material (PCM). The goal is to enhance both cost-efficiency and quality by investigating the performance of PCMs concerning container shape, structure, and heat transfer mechanisms. The research employs numerical analysis, utilizing a specialized two-dimensional finite volume model created with ANSYS Fluent Computational Fluid Dynamics (CFD) software. This model employs an enthalpy-porosity method to comprehensively explore the thermal behavior and heat transfer properties of Capric acid during the melting process.

II. Materials and Methods

The research delves into eleven critical parameters to gain insights into Capric acid's behavior during melting. These parameters include the melting rate, melt front patterns, temperature distribution, PCM surface average temperature, total stored energy, Prandtl, Rayleigh, and Stefan numbers, velocity vector direction and contours, surface-averaged Nusselt number, and heat flux. This comprehensive approach allows for a thorough examination of the melting process and its underlying mechanisms.

Table 1: Thermophysical parameters of lauric acid [8].

Property	Unit	Value
Temperature of melting, T_f	°C	48.2
Temperature of solidification, T_i	°C	43.5
Latent heat, LH	kJ/kg	187.21
Solidus specific heat capacity, c_{pi}	kJ/(kgK)	2.18

Liquidus specific heat capacity, c_{pf}	kJ/(kgK)	2.39
Solidus density, δ_i	kg/m^3	940
Liquidus density, δ_f	kg/m^3	885
Solidus thermal conductivity, θ_i	W/(mK)	0.16
Liquidus thermal conductivity, θ_f	W/(mK)	0.14
Coefficient of thermal expansion, α	1/K	0.0008

Table 2: Thermophysical parameters of capric acid [10].

Property	Unit	Value
Temperature of melting, T_f	°C	32
Coefficient of thermal expansion, α	1/K	0.001
Latent heat, *LH*	kJ/kg	152.7
Solidus specific heat capacity, c_{pi}	kJ/(kgK)	1.9
Liquidus specific heat capacity, c_{pf}	kJ/(kgK)	2.4
Solidus density, δ_i	kg/m^3	1018
Liquidus density, δ_f	kg/m^3	888
Solidus thermal conductivity, θ_i	W/(mK)	0.372
Liquidus thermal conductivity, θ_f	W/(mK)	0.153
Kinematic viscosity, ψ	m^2/s	3×10^{-6}

III. Results and Discussion

The study yields several noteworthy findings: Evolution of Heat Transfer Mechanisms: The study demonstrates that heat conduction initially dominates during the early stages of the melting process, but as the process progresses, convection becomes the dominant heat transfer mechanism. This insight is crucial for understanding the behavior of PCMs during phase transitions and optimizing TES systems accordingly.

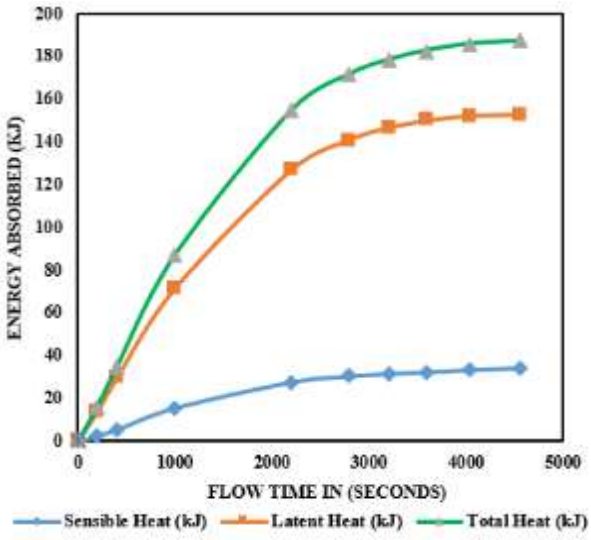

Fig. 1: Total, latent and sensible accumulated energies versus time of capric acid.

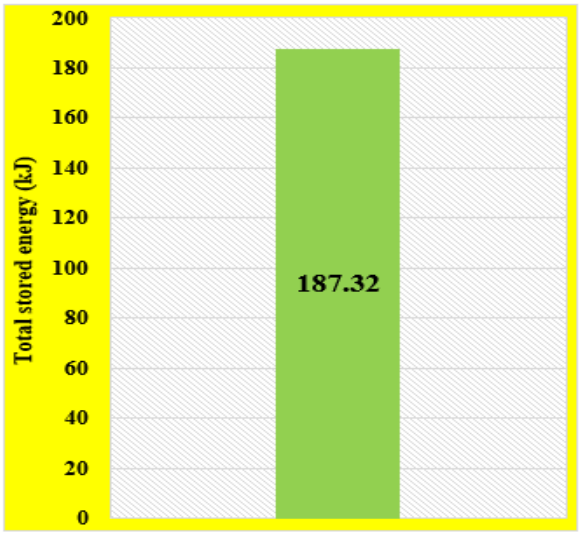

Fig. 2: Total energy stored, (Etot) for capric acid.

Performance Metrics: The research provides specific values that are crucial for evaluating Capric acid's suitability for TES applications. The total energy stored is found to be 187.32 kJ/kg, the melting time is 4536 seconds, and the surface-average temperature reaches 311.3 Kelvin. The Prandtl, Rayleigh, and Stefan numbers are calculated at 41.8, 5.27×108, and 0.15, respectively. These metrics offer valuable data for designing and fine-tuning TES systems. Capric Acid as a Viable Option: A significant and innovative contribution of this study is the affirmation of Capric acid as a viable option for low-temperature TES applications. The favorable thermodynamic, kinetic, and thermophysical properties of Capric acid make it a promising candidate for use in TES systems, thus opening up opportunities for further research and development.

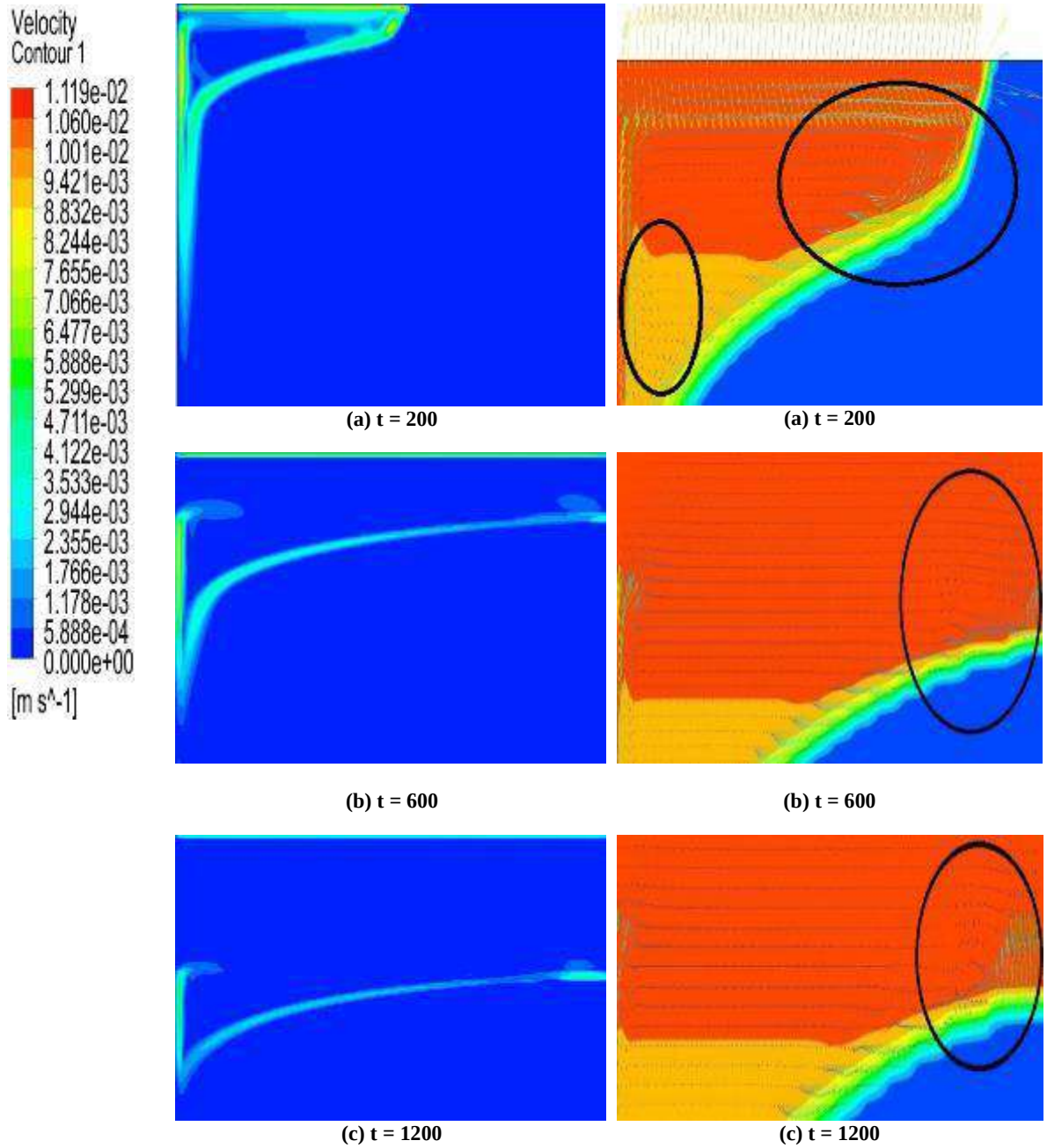

Fig. 3 Instantaneous velocity vector (contours and direction) of capric acid at different flow durations.

IV. Conclusions

In conclusion, the research discussed in the provided text presents a thorough analysis of Capric acid's thermal behavior during the melting process within a rectangular domain. The findings shed light on the heat transfer mechanisms involved and provide essential data for designing efficient TES systems. Moreover, the confirmation of Capric acid as a suitable PCM for low-temperature TES applications is a significant contribution that paves the way for the development of more effective and sustainable energy storage solutions. This study serves as a valuable resource for researchers and engineers working on TES system optimization and the utilization of organic PCMs like Capric acid.

- Based on the results of its thermodynamic, thermophysical, and kinetic characteristics in this novel study and also evident from the published literature, capric acid has a high potential for use in low-temperature TES.
- Analysis of the major mechanisms of heat transmission during the various phases of melting is done using recorded temperature fields and the melt front's progression. Heat conduction is shown to be the main methodology of heat transfer in the earliest melting stages, followed by a brief time of transition, and the remaining part of the melting is controlled by convection.
- The magnitude of the convection circulation at the initiation of the convection mode of heat transmission is significant, and when melt front approaches the opposite side, the convection current begins to weaken. When the melting process nears completion, disappearing convection circulation is observed.
- Also, the estimated Nusselt number provides a more comprehensive picture of the thermal transmittance of capric acid throughout melting by clearly illustrating the phases of heat transmission (conduction, transition, dominant convection, and weak

convection).

- The total energy stored, melting time, Prandtl, Rayleigh, and Stefan numbers are found to be 187.32 kJ/kg, 4536 s, 41.8, 5.27×108 and 0.15, respectively.

According to the results of this investigation, it is worthwhile to investigate incorporating low-temperature PCMs into solar photovoltaic air conditioning systems.

References

[1] F.S. Javadi, H.S. Metselaar, P. Ganesan, Performance improvement of solar thermal systems integrated with phase change materials (PCM): A review, Solar Energy, 206 (2020) 330–352. https://doi.org/10.1016/j.solener.2020.05.106

[2] A. Gani, Fossil fuel energy and environmental performance in an extended STIRPAT model, Journal of Cleaner Production, 297 (2021) 126526. https://doi.org/10.1016/j.jclepro.2021.126526

[3] X. Huang, C. Zhu, Y. Lin, G. Fang, Thermal properties and applications of microencapsulated PCM for thermal energy storage: A review, Applied Thermal Engineering, 147 (2019) 841–855. https://doi.org/10.1016/j.applthermaleng.2018.11.007

[4] Y. Zhao, X. Zhang, W. Hua, Review of preparation technologies of organic composite phase change materials in energy storage, Journal of Molecular Liquids, 336 (2021) 115923. https://doi.org/ 10.1016/j.molliq.2021.115923

[5] H. Liu, K. Sun, X. Shi, H. Yang, H. Dong, Y. Kou, P. Das, Z.- S. Wu, Q. Shi, Two-dimensional materials and their derivatives for high performance phase change materials: emerging trends and challenges, Energy Storage Materials, 42 (2021) 845–870. https://doi.org/10.1016/j.ensm.2021.08.022

[6] S.S. Magendran, F.S.A. Khan, N.M. Mubarak, M. Vaka, R. Walvekar, M. Khalid, E.C. Abdullah, S. Nizamuddin, R.R. Karri, Synthesis of organic phase change materials (PCM) for energy storage applications: A review, Nano-structures & Nano objects, 20 (2019) 100399. https://doi.org/10.1016/ j.nanoso.2019.100399

[7] S.M. Hasnain, Review on sustainable thermal energy storage technologies, Part I: heat storage materials and techniques, Energy Conversion and Management, 39 (1998) 1127–1138. https://doi.org/10.1016/S0196-8904(98)00025-9

[8] Z. Gu, H. Liu, Y. Li, Thermal energy recovery of air conditioning system–heat recovery system calculation and phase change materials development, Applied Thermal Engineering, 24 (2004) 2511–2526. https://doi.org/10.1016/j.applthermaleng.2004.03.017

[9] A. Hasan, S.J. Mccormack, M.J. Huang, B. Norton, Evaluation of phase change materials for thermal regulation enhancement of building integrated photovoltaics, Solar Energy, 84 (2010) 1601–1612. https://doi.org/10.1016/j.solener.2010.06.010

IEEES-101

Experiments review of solar wastewater treatment (SOWAT)

[1*]Sadek Igoud, [1]Belgassim Boutra, [1]Lamine Aoudjit, [1]Aïcha Sebti,
[2]Fatiha Souahi, [2]Chems-Eddine Chitour, [3]Djamel Zeriri and [3]Amel Mameche
[1] Unité de Développement des Equipements Solaires (UDES), Centre de Développement des Energies Renouvelables (CDER), 42415 Bou-Ismaïl, Algeria
[2] Département de Génie Chimique, Ecole Nationale Polytechnique (ENP), 16200 El Harrach, Algeria
[3] Division laboratoires/Activité Exploration et Production (DLAB), Sonatrach, 35000 Boumerdès, Algeria
*E-mails: s.igoud@udes

Abstract

Human well-being, agriculture and industry activities generate several types of wastewater whose treatment depends on their physicochemical and biological composition. The choice of the most efficient treatment requires coupling various processes but induces high electricity consumption, financial expenses and greenhouse gas emission. And this goes against the goals adopted by the United Nations in its 2030 Agenda for Sustainable Development.
The present paper suggests the use of solar evaporation-condensation process among new proposed solutions for wastewater treatment targeting sustainability but above all efficiency and ease of scaling up. The paper summarizes the several obtained results during domestic, urban and industrial wastewaters treatments. These later were conducted in a single stage of treatment by using single equipment: solar still.
The results showed that the same process allowed recording for domestic wastewater a removal of organic pollution estimated at 83.62% of BOD and 77.26 % of COD. High water sanitary quality was obtained by recording total absence of studied infectious organisms: Total and fecal coliforms also fecal streptococci. Urban wastewater treatment also recorded efficiency close to that conventional treatment applying activated sludge applied in Tipasa wastewater treatment plant. Turbidity was reduced by 99%; BOD between 86 and 90% and inactivation of infectious organisms has reached 99%. Industrial wastewater recorded better efficiency compared to conventional treatment applying coagulation-flocculation in Sonatrach de-oiling plant. In addition of total hydrocarbon removal estimated at 97.6% and total suspended solids at 86.8%; high salinity concentration was removed at 99.3%.
SOWAT results open promising perspectives for green hydrogen production using PV–water electrolysis system thus targeting carbon neutrality of all the chain production

Keywords: Solar wastewater treatment; Sustainability; Efficiency; Ease of use, green hydrogen.

I. Introduction

The response to the growing and vital needs of the world population as well as to the economic sectors has been undertaken according to development models based exclusively on non-renewable natural resources. These models have shown their limits and induced the fragility of the environmental balance materialized by global warming and the scarcity of natural resources as water, energy, minerals, bioproducts…
Facing these limits, a solution is worldwide adopted. It consists to move from conventional to sustainable development models. This direction has been taken since 2002 in the Johannesburg World Summit on Sustainable Development (Report of the World Summit on Sustainable Development, 2002). And it has constituted a challenge taken up by a large part of researchers and political deciders. This direction is maintained: 193 Member States of the United Nations General Assembly including Algeria have ratified the "Agenda 2030 for Sustainable Development" (UN General Assembly, 2015) targeting the preservation of natural resources and reduction of greenhouse gas emissions.
Water counts among natural and vital resources that need to be preserved but without depending on conventional energy. In Algeria as several other countries, a unique conventional model is applied for wastewater management. It applied in high urban density the activated sewage sludge process that is considered as an energy-intensive treatment (Igoud et al., 2015). Natural and aerated lagoons are applied in low urban density. But in contrary, industrial wastewater is not treated because it is specific to each type of industry. So it requires several and various treatment processes to treat diverse and complex substances often non-biodegradable, toxic; harmful… (Pesci Pereira et al., 2013).
What's better than nature to be inspired from to develop new sustainable water management?
Effectively, the hydrologic cycle shows that water in earth is treated and reused for millennia (Marshall S.J., 2013). Among natural phenomena contributing to it: solar evaporation-condensation. Its first application for potable water production at large scale was in 1872 at Las Salinas in Chile (Delyannis E., 2003). But its experimentation for wastewater treatment is recent. It dates from 1978 for domestic wastewater (Quasim, 2013; and 2000's for urban and industrial wastewaters (Zarasvand et al. , 2013; Igoud et al., 2017; 2022).
The present paper synthesizes all experiments of solar wastewater treatment (SOWAT) conducted at EVER's laboratory (Epuration et Valorisation des Eaux de Rejet) located at the Development Unit of Solar Equipment (UDES), Algeria, and compares obtained results.

II. Experimental Procedure/Methodology/System Description

SOWAT process

SOWAT is an evaporation-condensation process based on phase change of wastewater. It reproduces the hydrological cycle of water through: the evaporation of water, its condensation into water droplets and their precipitation in the form of rain. These stapes are reproduced in a closed enclosure where:

- wastewater is filled in a basin and heated by solar energy,
- heated wastewater evaporates and saturates the enclosure where it is imprisoned,
- produced vapor condenses into fine water droplets on contact with the cold upper part of the enclosure (double sloped glass roof),
- produced droplets trickles by gravity from glass roof thus forming treated wastewater.

SOWAT prototypes

SOWAT experiments applied three types of prototypes:

- a greenhouse solar still composed by a single-basin and covered by a double sloped glass roof (figure 1),
- a greenhouse hybrid solar still composed by a single-basin and covered by a double sloped glass roof. The laboratory prototype is heated by two hot plates maintained at 150 °C (figure 2),
- a greenhouse hybrid multi-sources solar still composed by a single-basin and covered by one glass roof. In real condition of use, the prototype is heated by butane gas burners (figure 3). This energy hybridization can also be powered by renewable energy.


Fig. 1: Greenhouse solar still


Fig. 2: Greenhouse hybrid solar still


Fig. 3: Greenhouse hybrid multi-sources solar still

Experimental designs

- SOWAT efficiency has been evaluated by treating domestic, urban and industrial wastewater using the three types of prototypes described above. The studied wastewater consisted on:
- domestic wastewater sampled from a septic tank at HBK life base (Sonatrach), Ouargla [10],
- urban wastewater sampled from an activated sewage sludge wastewater treatment plant, Tipasa [9],
- saline oily wastewater sampled from a coagulation-flocculation de-oiling-plant, at HBK oil field (Sonatrach), Ouargla [11],

III. Results and discussion

SOWAT results (figure 4) showed that domestic wastewater treatment recorded a removal of organic pollution estimated at 83.62% of BOD and 77.26 % of COD. High water sanitary quality was obtained by recording total absence of studied infectious organisms: Total and fecal coliforms also fecal streptococci.

Urban wastewater treatment also recorded efficiency close to that conventional treatment applying activated sludge applied in Tipasa wastewater treatment plant. Turbidity was reduced by 99%; BOD between 86 and 90% and inactivation of infectious organisms has reached 99%.

Industrial wastewater recorded better efficiency compared to conventional treatment applying coagulation-flocculation in Sonatrach de-oiling plant. In addition of total hydrocarbon removal estimated at 97.6% and total suspended solids at 86.8%; high salinity concentration was removed at 99.3%.


Fig. 4. Results of solar wastewater treatments

IV. Conclusion

SOWAT is a new sustainable wastewater treatment based on the hydrologic cycle that recycles water in earth for millennia. Thermal evaporation-condensation is applied by using solar energy with the opportunity to use renewable energies and natural gas.

Significant results of pollutants abatement have been obtained during all reported experiments conducted to treat domestic, urban and several types of industrial wastewaters.
SOWAT results open promising perspectives for green hydrogen production using PV–water electrolysis system thus targeting carbon neutrality of all the chain production

Acknowledgements
Authors thank all the staff of the institutions: UDES, ENP, ONA and DLAB-Sonatrach

References

Report of the World Summit on Sustainable Development (2002). Johannesburg, South Africa, 26 August-4 September 2002. Ed, United Nations, New York, NY, 2002. www.unmillenniumproject.org/projects/131302_wssd_report_reissued.pdf

UN General Assembly (2015). Transforming our world: The 2030 agenda for sustainable development. 21 October 2015, A/RES/70/1. https://www.refworld.org/docid/57b6e3e44.html

Igoud S., Souahi F., Chitour CE., Adjrad A., Habchi M., Chouikh A. (2015). Diagnostic of electricity consumption, its cost and greenhouse gas emissionin the wastewater treatment sector of Algeria. Desalination and Water Treatment 55(7): 1725–1734. ttps://doi.org/10.1080/19443994.2014.928236

Pesci Pereira C. João Pedro Neves Goldenstein, João Paulo Bassin. Industrial Wastewater Contaminants and their Hazardous Impacts, DOI:10.1002/9781119737629.ch1In book: Biosorption for Wastewater Contaminants (pp.1-22).

Marshall S.J. (2013). The global water cycle In Hydrology in Reference Module in Earth Systems and Environmental Sciences, 2013.

E. Delyannis – Historic background of desalination and renewable energies. Solar Energy 75 (2003) 357–366). https://doi.org/10.1016/j.solener.2003.08.002

Qasim, S. R. (1978) Treatment of domestic sewage by using solar distillation and plant culture. Journal of environmental science and health. Part a: Environmental science and engineering: Toxic/hazardous substances and. Environmental Engineering, 13(8), 615–627.

Zarasvand Asadi, R., Suja, F., Ruslan, M.H. and Abd Jalil, N. (2013). The application of a solar still in domestic and industrial wastewater treatment. Solar Energy, 93, 63–71.

Igoud, S., F. Souahi, and C. E. Chitour. 2017. Solar wastewater treatment (SOWAT) and reuse for agricultural irrigation. Irrigation and Drainage 66 (5):750–7. doi:10.1002/ird.2157.

Igoud, S., D. Zeriri, L. Aoudjit, B. Boutra, A. Sebti, F. Khene, and A. Mameche. 2021. Climate change adaptation by solar wastewater treatment (SOWAT) for reuse in agriculture and industry. Irrigation and Drainage 70 (2):243–53. ttps://doi.org/10.1002/ird.2540

Igoud S., Zeriri D., Boutra B., Mameche A., Benzegane Y., Belloula M., Benkara L., Aoudjit L., Sebti A. (2022). Compared efficiency of sustainable and conventional treatments of saline oily wastewater rejected by petroleum industry in Algerian Sahara, Petroleum Science and Technology 40(1),92-106. https://dOI: 10.1080/10916466.2021.2002358

IEEES-102

Intelligent Control of DC-DC Boost Converter for Hydrogen and Fuel Cell Systems: An Artificial Neural Network Approach

[1]Mustafa Özden, [2*]Davut Ertekin
[1] Electrical and Electronics Engineering Department of Bursa Technical University, 16310 Yıldırım, Bursa, Türkiye
[2] Power Electronics Center of Electrical and Electronics Engineering Research Laboratories, Bursa Technical University, 16310 Yıldırım, Bursa, Türkiye
*E-mails: davut.ertekin@btu.edu.tr

Abstract

The employment of Artificial Neural Network (ANN)-based controllers in the proposed DC-DC boost converter for fuel cell applications represents a groundbreaking advancement in power electronics. With a focus on achieving a high voltage gain and enhanced efficiency, the design incorporates a switched-inductor-capacitor cell at the input and a switched-capacitor cell at the output, minimizing current ripples and augmenting voltage gain for compatibility with low-input current ripple, high voltage and grid connections. The novel aspect of the ANN controller lies in its exclusive reliance on the circuit's intrinsic characteristics, eschewing dependence on mathematical models or external controller data. Through meticulous parameter tuning, conducted by systematically varying duty cycle values in MATLAB/Simulink program, the ANN controller ensures optimal performance within a specified input range and a reference output voltage. In contrast to existing converters and controllers, which often encounter challenges in mitigating current ripples and optimizing efficiency, the proposed system addresses these drawbacks by leveraging ANN-based control. This innovative approach demonstrates superior adaptability to the unique characteristics of the boost converter, marking a significant stride in the development of efficient and reliable fuel cell power systems.

Keywords: Artificial neural network, Hydrogen energy, DC-DC power boost converter.

I. Introduction

The field of power electronics is witnessing a transformative advancement through the integration of Artificial Neural Network (ANN)-based controllers into the design of power converters for renewable energy such the fuel cell (Sayed, 2023), photovoltaic (Srinivasan, 2021), and battery applications (Naguib, 2023). The innovative design focused on achieving heightened voltage gain and improved efficiency, incorporates a switched-inductor-capacitor cell at the input and a switched-capacitor cell (Ertekin, 2023) at the output that makes the proposed topology ready for applications such the high-voltage direct current (HVDC) transmission, electric vehicles (EVs) (Sah, 2021), electroplating, electrolysis, high-voltage power supplies, etc (Chen, 2020). This suggested configuration not only amplifies the voltage gain but also minimizes undesirable current ripples that is vital for fuel cells for their longer lifespan, rendering the system well-suited for applications requiring high voltage and grid connections (Baltacı, 2023).
Contrasting with conventional converters and controllers that grapple with challenges related to mitigating current ripples and optimizing efficiency, the proposed system strategically leverages ANN-based control to address these limitations. The ANN controller's distinctive feature lies in its exclusive reliance on the intrinsic characteristics of the circuit, bypassing the need for external mathematical models or controller data. Through meticulous parameter tuning, involving the systematic variation of duty cycle values within a simulation program, the ANN controller ensures optimal performance within a specified input range (22 V to 24 V) while maintaining a reference output voltage of 300 V. To further enhance the reliability of the proposed system, a refined ANN-based controller is introduced to mitigate identified drawbacks associated with conventional ANN controllers. This novel controller is meticulously designed to enhance the stability and convergence of the control system, overcoming challenges such as susceptibility to noise and suboptimal convergence.
Comprehensive simulation studies have been conducted to substantiate the efficacy of the proposed system, validating its performance under varying operational conditions. Additionally, experimental tests affirm the system's robustness and efficiency up to 500 W. The integration of ANN-based control into the DC-DC boost converter not only overcomes existing limitations but also establishes a foundation for reliable and efficient fuel cell power systems.

II. Proposed Artificial Neural Network controller-based DC-DC boost converter

A. Proposed converter

Figure 1 illustrates the converter in question. As outlined in the introduction, a key advantage of this proposed converter is its compatibility with low-voltage sources, such as fuel cells, photovoltaic energy systems, and batteries. The converter's primary goal is to initially minimize the fuel cell input current ripple to obtain a longer lifespan of the fuel cell systems and raise the voltage output from these sources, with further enhancement taking place within the converter itself. This initial voltage boost is accomplished through the application of the input switched-inductor-capacitor (SLC) cell, consisting of inductors L1 and L2, capacitor C1, and diodes D1 and D2. Following this stage, the voltage undergoes additional amplification through the switched-capacitor (SC) cell, formed by diodes D4, D5, and D6, as well as capacitors C3, C4, and C5.
Examining the configuration of the SC cell reveals that, over specific time intervals, the output voltage distributes itself among the capacitors and the power switch. This mechanism effectively mitigates voltage stress on the semiconductor devices.

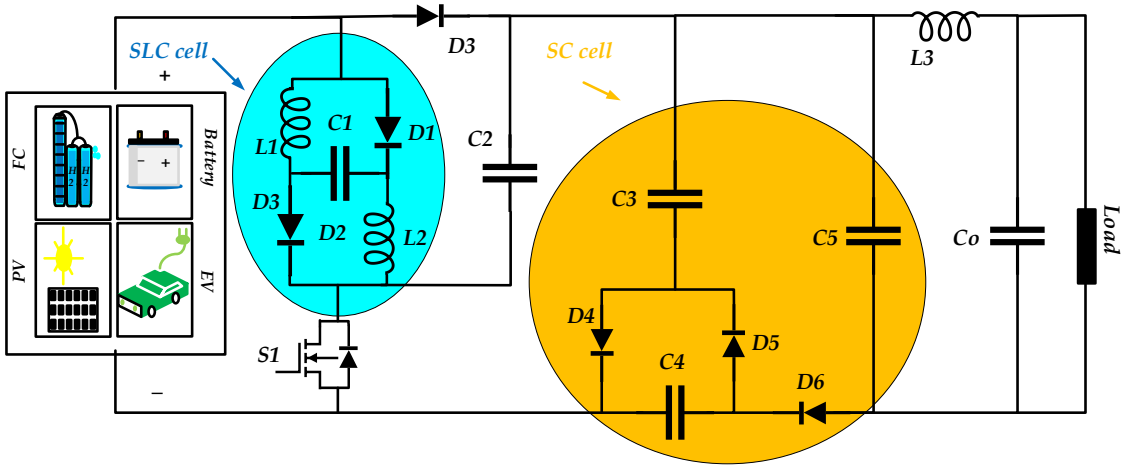

Fig. 1: The proposed SLC-SC boost converter

B. Gain calculation

Figures 2a and 2b provide a depiction of the state of semiconductor devices and the charging and discharging modes for the inductors and capacitors. During time intervals when the switch receives a positive voltage from the PWM switching signal, it is in a short-circuit state, as illustrated in Figure 2a.

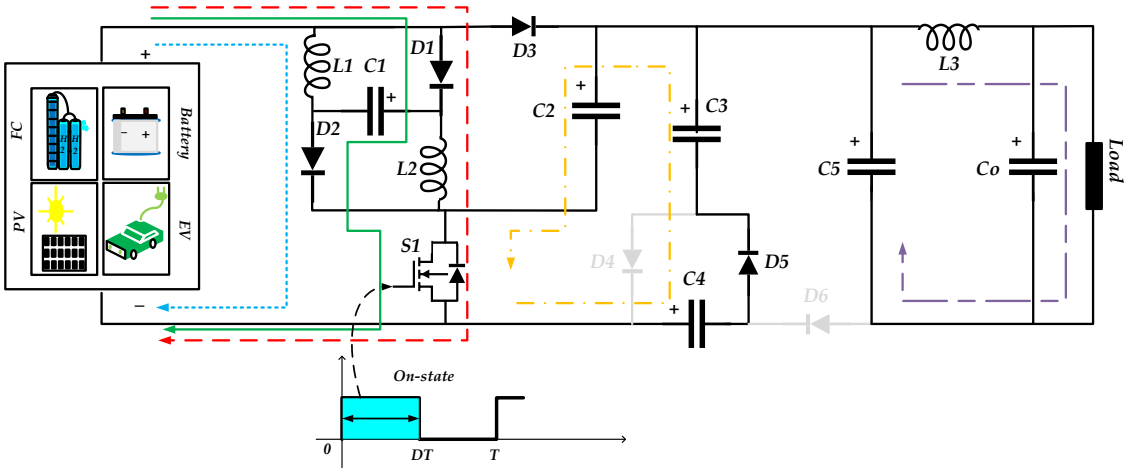

(a)

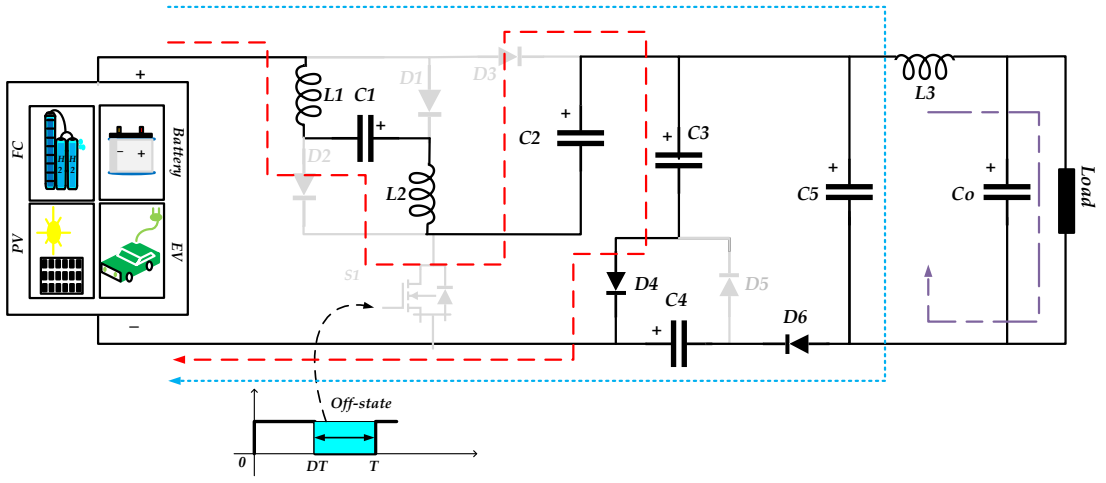

(b)

Fig. 2: The state of the semiconductor devices of the proposed boost converter when the switch S1 is (a) activated and (b) deactivated

In the subsequent time interval, when the switch is in the off state, both inductors L1 and L2 undergo a discharging process, creating a series circuit that includes capacitors C1, C2, and C3, along with diode D4. This state is evident from Figure 2b, where capacitors C1 and C2 are discharging, while capacitor C3 is being charged, in contrast to the previous operational mode. The gain in voltage for this converter can be determined by evaluating the voltage across the inductors during both the on and off states of switch S1, as well as by accounting for the voltage across all capacitors. The expression for the voltage gain is presented in Equation (1).

$$V_O = \frac{5\text{-}D}{1\text{-}D} V_{in} \rightarrow G = \frac{V_O}{V_{in}} = \frac{5\text{-}D}{1\text{-}D} \quad (1)$$

C. The artificial neural network based controller:

The presented approach employs a controller based on artificial neural networks to regulate the circuit. The input data for this controller is derived from the normalized difference between the reference value (V_{ref}) and the output voltage value (V_o) of the circuit. The controller's output is represented by the additional duty value ($\pm \Delta D$) applied to the PWM generator. When implementing a closed-loop control system with an artificial neural network, the conventional practice involves training the neural network using input-output values obtained from a different type of controller, such as a PID controller. Figure 3 illustrates the block diagram of the control methodology proposed for the boost converter.

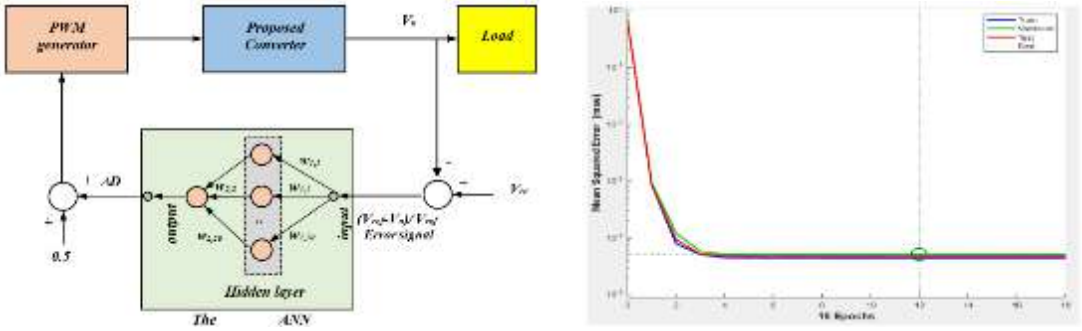

(a) (b)

Fig 3: (a) ANN-based controller design, (b) Training and test performans graph of the network.

This research introduces a distinctive approach where the design of an Artificial Neural Network (ANN)-based controller for the boost converter circuit is achieved solely through the circuit's inherent characteristics. Notably, no reliance is placed on the mathematical model of the circuit, and no data from any other controllers are utilized. To delineate the circuit's traits, duty cycle values were systematically altered between 0.4 and 0.8 in increments of 0.001 within a simulation program, yielding the output voltage values. The reference value is set at 300 V, and the input value spans the range of [22 V to 24 V].

Using the acquired training data, the network—configured with 1 input, 1 output, 1 hidden layer, and 20 neurons—underwent training employing the Levenberg-Marquardt learning algorithm. The training performance graph, depicted in Figure 3b, illustrates the convergence of the network's training error. Training, testing, and validation errors, measured in terms of Mean Squared Error (MSE), were determined as $4.42 \cdot 10^{-5}$, $5.14 \cdot 10^{-5}$ and $4.78 \cdot 10^{-5}$, respectively. Notably, Figure 3b indicates that the network's training error approaches its final value after only 3 epochs.

III. Results and discussion

The authenticated model underwent testing in the simulation framework, with the boost converter integrated into the circuit as depicted in Figure 3a. The simulation study encompassed diverse loads ranging from 700 Ω to 1 KΩ. Under a 1 KΩ load, both input inductor L1 and load currents were obtained, as reported in Figure 4a.

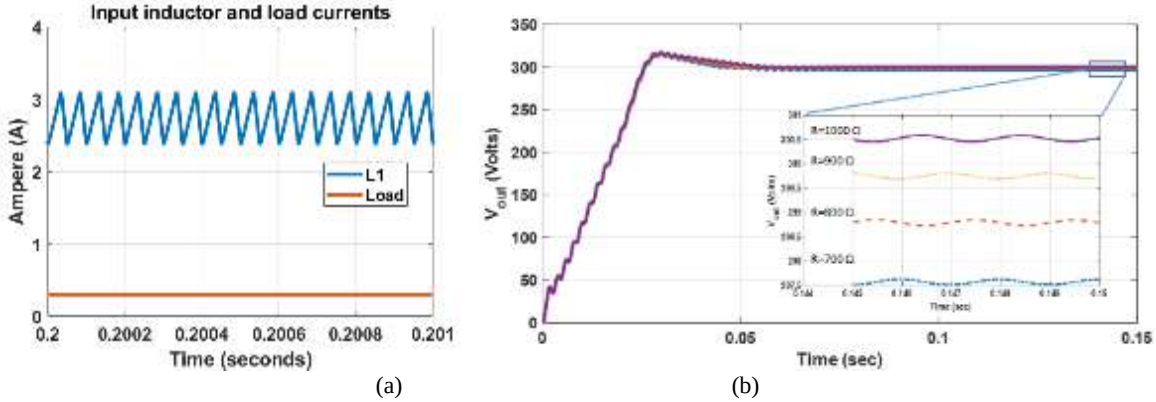

(a) (b)

Fig 4: Simulation result for controller, (a) input inductor and load currents under 1000 Ω resistive load, and (b) generated output voltage with different load values from 700 to 1000 Ω.

This figure highlights a prominent feature of the proposed converter topology, showcasing minimal fluctuations in the input inductor current. This characteristic directly contributes to an extended lifespan of the input voltage source and heightened reliability. The output voltage rapidly reached the predetermined value of 300 V in less than 0.05 seconds. In the most demanding load scenario, represented by the 700 Ω condition, the output voltage marginally decreased to 297.5 V. Detailed results are outlined in Figure 4b.

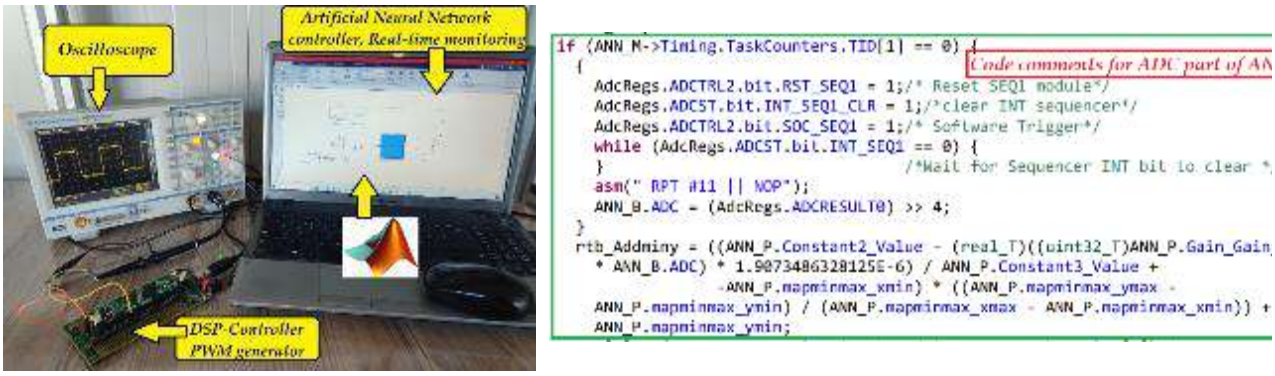

(a) (b)

Fig: 5. The experimental tests, (a) the evaluation of the proposed ANN controller using a DSP microcontroller, and (b) comments on the code for analog-to-digital conversion generated through the employed microcontroller.

Figure 5a showcases the laboratory workbench setup used to experimentally test the proposed ANN controller, employing the TMS320F28335 Digital Signal Processing-based microcontroller with a rapid analysis speed of 80 Mb/sec. The figure demonstrates the generated pulse width modulation (PWM) signals for an input voltage of 24 VDC and an anticipated output voltage of 300 VDC, revealing a duty ratio close to 0.55 on the oscilloscope. This observation aligns with the theoretical and simulation results. Figure 5b provides a sample of code comments generated by the TMS-DSP microcontroller, exemplified by the codes for analog-to-digital conversion.

IV. Conclusion

This research introduces a power boost converter featuring two switched-capacitor-inductor cells, specifically designed for applications involving low-voltage sources like fuel cells and photovoltaic systems. The primary advantage of this proposed converter lies in its capability to minimize input current ripple for fuel cells or photovoltaic panels, thereby enhancing the lifespan and overall reliability of these energy sources. Additionally, it increases the voltage gain, rendering them suitable for high-voltage applications such as electric vehicle charging, grid integration, and high-voltage direct current (HVDC) systems.

In the subsequent phase, a novel aspect is introduced through the proposition of an artificial neural network controller. This innovative controller design is characterized by its reliance solely on the inherent features of the circuit, excluding the use of the mathematical model or data from any other controllers. The proposed controller demonstrates swiftness and precision, effectively regulating the output voltage to 300 VDC within an input voltage range of 22 to 24 V and a duty ratio close to 0.55, as outlined in equation (1).

Author contirbutions

The structure and methodology of the proposed converter were devised by Davut Ertekin, while the design, simulation, and testing of the ANN controller were conducted by Mustafa Özden. Both authors collaborated on the simulation, experimental tests, and the composition and editing of the study.

References

Sayed, E. T., Rezk, H., Abdelkareem, M.A., Olabi, A. G., (2023): Artificial neural network based modelling and optimization of microalgae microbial fuel cell, International Journal of Hydrogen Energy, https://doi.org/10.1016/j.ijhydene.2022.12.081.

Srinivasan, S., Tiwari, R., Krishnamoorthy, M., Lalitha, M.p., Raj, K.K., (2021): Neural network based MPPT control with reconfigured quadratic boost converter for fuel cell application, International Journal of Hydrogen Energy,Pages 6709-6719,https://doi.org/10.1016/j.ijhydene.2020.11.121.

Naguib, M., Kollmeyer, P., and Emadi, A., (2023): Application of Deep Neural Networks for Lithium-Ion Battery Surface Temperature Estimation Under Driving and Fast Charge Conditions, IEEE Transactions on Transportation Electrification, pp. 1153-1165, doi: 10.1109/TTE.2022.3200225.

Ertekin, D., (2023): A high gain switched-inductor-capacitor DC-DC boost converter for photovoltaic-based micro-grid applications, CSEE Journal of Power and Energy Systems, doi: 10.17775/CSEEJPES.2022.08440.

Sah, B., Kumar, P., and Bose, S.K., (2021): A Fuzzy Logic and Artificial Neural Network-Based Intelligent Controller for a Vehicle-to-Grid System, IEEE Systems Journal, pp. 3301-3311, doi: 10.1109/JSYST.2020.3006338.

Chen, X., Cao, W., Zhang, Q., Hu, S., and Zhang, J., (2020): Artificial Intelligence-Aided Model Predictive Control for a Grid-Tied Wind-Hydrogen-Fuel Cell System, IEEE Access, vol. 8, pp. 92418-92430, doi:10.1109/ACCESS.2020.2994577.

Baltacı, K., Ertekin, D., Bayrak, G., (2023): Design and experimental validation of an artificial neural network-SVPWM controller for a novel micro grid-tied fuel cell-based 3-phase boost inverter, International Journal of Hydrogen Energy, https://doi.org/10.1016/j.ijhydene.2023.10.291.

IEEES-103

Active Balancing with Bidirectional Energy Transfer: A Flyback Converter Solution for Lithium-Ion Cells

[1,2]Eren Küpcü, [3*]Davut Ertekin
[1] Graduate School of Bursa Technical University, 16310, Yıldırım, Bursa, Türkiye
[2] TRON Elektronik Sistemler A.Ş., Ümraniye/İstanbul, Türkiye
[3] Power Electronics Center of Electrical and Electronics Engineering Research Laboratories, Bursa Technical University, 16310, Yıldırım, Bursa, Türkiye
*E-mails: davut.ertekin@btu.edu.tr

Abstract

Passive equilibrium in energy storage, dependent on dissipative components, leads to substantial power losses and thermal inefficiencies. Conversely, dynamic equilibrium, particularly with flyback converters, provides benefits by redistributing energy efficiently without the use of dissipative elements. This strategy heightens efficiency, minimizes thermal dissipation, and enhances the overall reliability of the system. Active approaches counter passive balancing limitations, optimizing energy storage system utilization and lifespan, propelling advancements in battery management technologies. In the present investigation, an active balancing system incorporating a bidirectional energy flow and utilizing a flyback converter is introduced. The proposed cell balancing system incorporates a snubber circuit to safeguard the Mosfet switching element from potential damage. This protective mechanism disperses the energy accumulated in the leakage inductance of the transformer, not involved in the energy transfer, as heat into the surroundings. The flyback converter facilitates energy transfer between cells and the battery pack bidirectionally, contingent upon the charge or discharge status of the battery pack. Notably, the energy transfer occurs in isolation, ensuring effective isolation between the battery pack and its constituent cells. The validity of the proposed system is substantiated through comprehensive simulation and laboratory studies, validating the accuracy of the theoretical calculations.

Keywords: Active balancing, Lithium-ion batteries, Flyback converter, Bidirectional power flow.

I. Introduction

Passive balancing systems, commonly employed in energy storage applications, exhibit notable drawbacks that impact their overall effectiveness. One primary limitation lies in their inherent reliance on dissipative elements, such as resistors or dissipative switches, to redistribute energy among individual cells within a battery pack (Baumhöfer, 2014). This approach results in significant power losses and thermal inefficiencies, compromising the overall efficiency of the energy storage system (De Rienzo, 2023).
Contrastingly, active balancing methods, particularly those utilizing flyback converters, present a promising alternative with distinct advantages (Yun, 2023). Active balancing employs power electronics to actively redistribute energy among cells, mitigating the need for dissipative elements and thereby minimizing energy losses. The flyback converter, a type of transformer-based converter, proves advantageous in this context due to its inherent ability to provide galvanic isolation and efficiently transfer energy between cells (Guo, 2021).
The key benefits of active balancing with flyback converters include enhanced efficiency, reduced thermal dissipation, and improved overall system reliability (Yau, 2022). By mitigating the drawbacks associated with passive balancing, active methods contribute to the optimal utilization and longevity of energy storage systems, thereby advancing the state-of-the-art in the domain of battery management technologies.
In this examination, we propose an active balancing system featuring bidirectional energy transfer and employing a flyback converter. The envisaged cell balancing system incorporates a snubber circuit to shield the Mosfet switching element from potential harm. This safeguard mechanism dissipates the energy accumulated in the leakage inductance of the transformer, uninvolved in the energy transfer, as heat into the surroundings. The flyback converter facilitates bidirectional energy transfer between cells and the battery pack, contingent upon the battery pack's charge or discharge status. Importantly, the energy transfer occurs in isolation, ensuring effective separation between the battery pack and its individual cells. The credibility of the proposed system is validated through comprehensive simulation and laboratory analyses, affirming the accuracy of the theoretical calculations.

II. The proposed topology and operational principles

The active cell balancing system proposed in this study, as illustrated in Figure 1, is centered around a flyback converter. Comprising 2n switching arrays designed for n cells, two snubber circuits, two Mosfet switching elements, and a flyback converter, this innovative balancing system facilitates effective energy redistribution within a battery pack.
The distinctive switching sequence orchestrates the connection of selected cells to the primary side of the transformer. Notably, the implementation features the use of Mosfet switching elements in the switching arrays, deviating from the conventional application of photoMOS relays. This deviation is motivated by the high cost, elevated power loss, and limited lifespan associated with photoMOS relays in comparison to the more efficient and durable MOSFET switching elements.
Within the proposed cell balancing system, a critical role is played by the snubber circuit, which serves to safeguard the Mosfet switching element from potential damage. In the realm of active balancing systems, particularly those utilizing flyback converters, the integration of snubber circuits stands as a pivotal design consideration. The indispensable function of a snubber circuit lies in addressing the potential adverse impacts stemming from swift switching transitions within power electronic devices, such as MOSFETs.

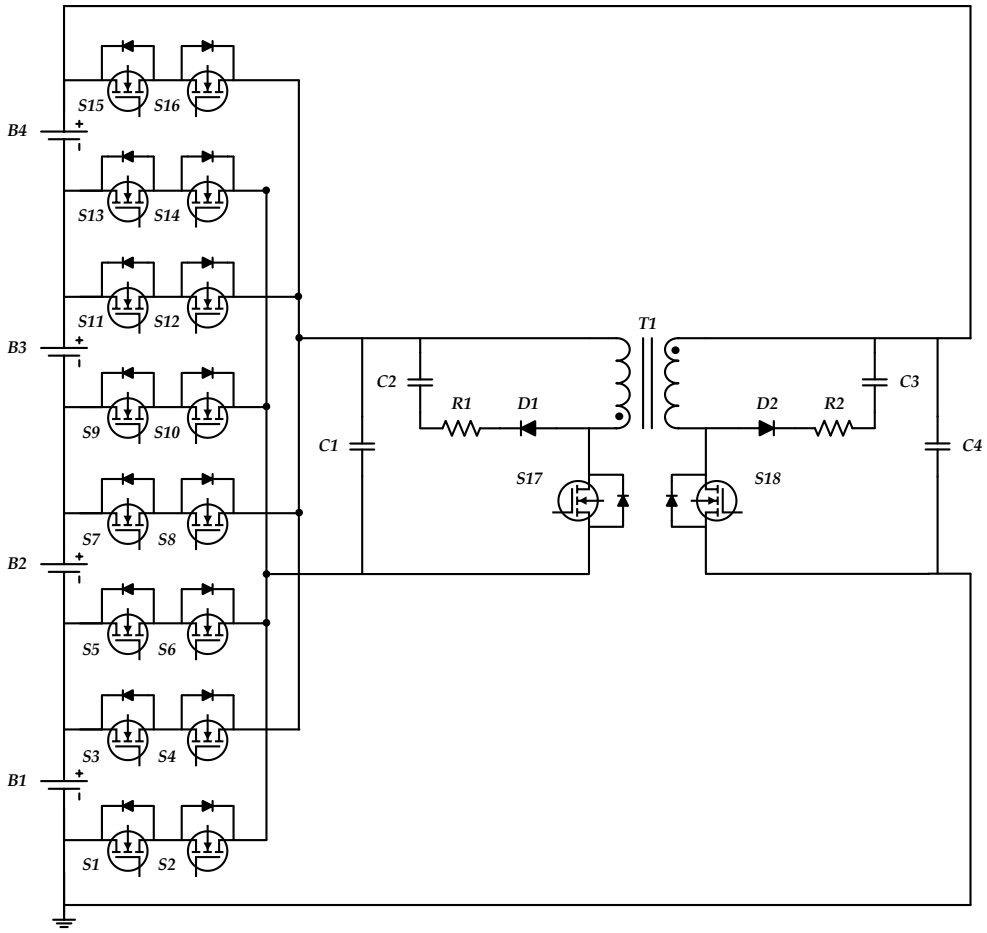

Fig. 1: Proposed cell balancing system

Within a flyback converter-based active balancing system, the dynamic nature of switching actions during cell connections and disconnections to and from the transformer introduces transient voltage spikes and ringing. In the absence of effective countermeasures, these transients pose risks of voltage stresses and oscillations, potentially causing harm to the switching elements and compromising the overall system efficiency.

A strategically implemented snubber circuit within the active balancing system emerges as a protective barrier against these undesirable effects. By furnishing a controlled discharge path for the energy stored in the leakage inductance of the transformer—energy not integral to the primary energy transfer—the snubber circuit adeptly dissipates this excess energy as heat into the surrounding environment. This dissipation serves to prevent voltage spikes and curtail ringing, thereby shielding the MOSFET switching elements from potential harm and augmenting the overall reliability and longevity of the system.

The imperative for a snubber circuit in a flyback converter-based active balancing system becomes conspicuous when scrutinizing the inherent traits of power electronic devices. The rapid switching dynamics inherent to such systems necessitate measures for transient control, fortifying the robustness of the overall system. The incorporation of a snubber circuit thus stands as a pivotal engineering decision, ensuring the optimal functionality and endurance of the active balancing system within the rigorous operational conditions of energy storage applications.

This protective mechanism efficiently disperses the energy accumulated in the leakage inductance of the transformer—energy not involved in the primary energy transfer—into the surrounding environment in the form of heat. The quantification of this energy accumulation in the leakage inductance is expressed through Equation 1.

This multifaceted design integrates advanced switching sequences, efficient energy transfer mechanisms, and protective circuits to enhance the overall performance, durability, and reliability of the active cell balancing system, thereby contributing to the advancement of battery management technologies.

$$P = \frac{1}{2} L_{leakage} I_{peak}^2 \frac{V_s}{V_s - V_R} f_s \quad (1)$$

The leakage inductance of the transformer is indicated by $L_{leakage}$, the primary peak current value of the transformer, I_{peak}, the voltage on the snubber capacitor V_s, the reflection voltage V_R formed by the effect of the winding ratio of the transformer, and the switching frequency f_s.

The flyback converter can transfer energy from cell to pack or from pack to cell, depending on the charge or discharge status of the battery pack. Energy transfer between the battery pack and the cells forming the battery pack is carried out in isolation thanks to the flyback converter.

The flyback converter has three different operating modes: continuous current mode, discontinuous current mode, and critical conduction mode. In the proposed balancing system, the operating mode of the flyback converter is determined as discontinuous current mode due to its lower-dimensional magnetic component, better electromagnetic input performance, and natural switching

advantages at zero current.
Figure 2 illustrates the schematic representation of the battery management system, encompassing the suggested cell balancing system. This system comprises a bidirectional flyback converter, a voltage and current detection mechanism with differential receiver opamp circuits, a switching array facilitating cell connections to the transformer's primary, isolated, and non-isolated drivers, and a microcontroller tasked with governing the switching elements.

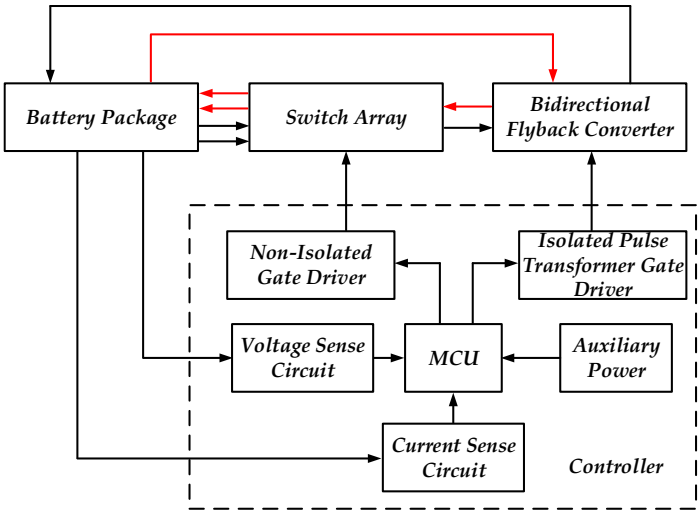

Fig. 2: Battery Management System (BMS) block diagram including the proposed cell balancing system

III. Results and discussion

Initially, the proposed cell balancing system underwent simulation studies using Matlab/Simulink software, and the simulation results were cross-verified against theoretical calculations.

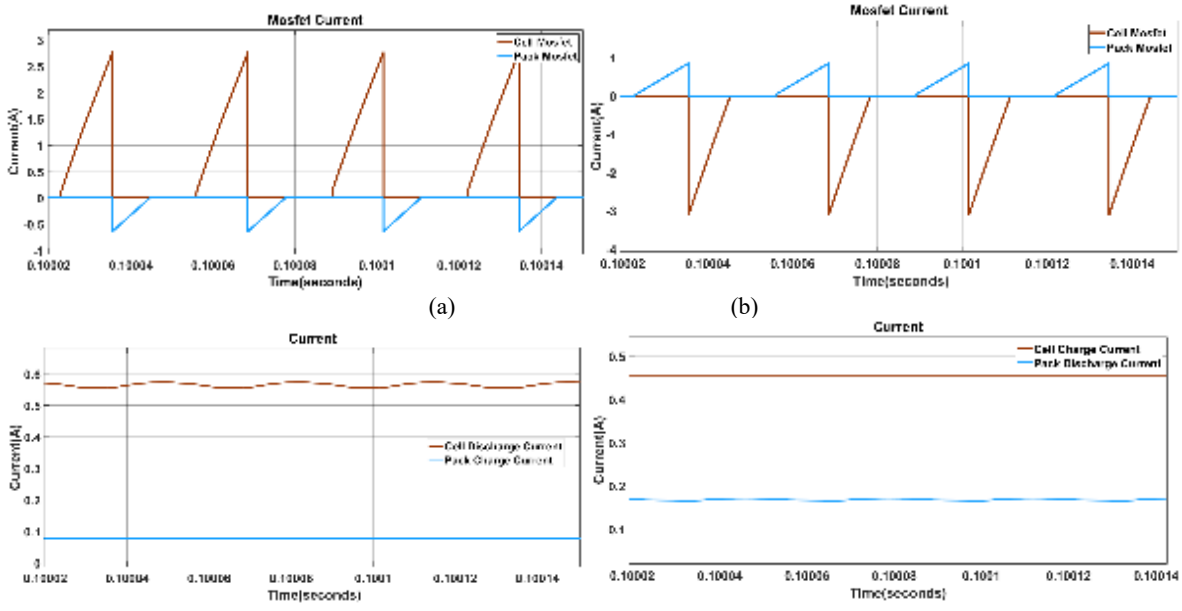

Fig. 3: (a) Current magnitudes of the switching elements linked to both the primary and secondary sides of the flyback transformer, and (c) the current during cell discharge and the current during battery pack charging. Simulation outcomes depicting the switching elements during the cell-to-pack balancing operation are presented. It illustrates (b) the magnitudes of current and (d) the charging current for the cell and the discharging current for the battery pack in the switching elements linked to the primary and secondary of the flyback transformer.

Upon applying a control signal to the switching elements linked to the transformer's primary and secondary, the current through the switches experiences linear increments. Conversely, when the control signal is terminated, the current rapidly decreases to zero. The peak and effective values of this current are contingent on both the input voltage and the power transmitted to the output, concurrent with the balancing process occurring bidirectionally between the cell and the package. The computation of the effective values of the current waveforms for Mosfet switching elements in Figures 5a and 6a reveals the corresponding current values in Figures 5d and 6d, respectively.

IV. Conclusion

The performance of individual cells within a battery pack undergoes alterations over time due to aging and environmental factors. These changes can lead to diminished energy storage capacity, posing safety risks such as overcharge or over-discharge. In response to these challenges, an innovative active cell balancing system featuring a flyback converter has been introduced. The flyback converter enhances the efficiency and speed of the balancing process by facilitating energy transfer bidirectionally between the cell and the pack, contingent upon the charge or discharge status of the battery pack.

A notable enhancement in system longevity and cost and energy savings has been achieved by opting for MOSFETs over the widely used photoMOS components in the switching array. This strategic substitution not only increases the lifespan of the balancing system but also contributes to overall cost-effectiveness and energy efficiency.

Within the encompassing battery management system, inclusive of the proposed balancing system, pertinent parameters gleaned through current and voltage monitoring circuits are collated by a microcontroller. Subsequently, the balancing procedure is executed by regulating the switching elements through isolated or non-isolated drive circuits. This comprehensive approach not only mitigates performance degradation in aging cells but also optimizes safety and efficiency in the battery pack, thus advancing the field of battery management technologies.

Acknowledgements

Conducted by Eren Küpcü, a Master's student at Bursa Technical University, and guided by his advisor, Associate Professor Davut Ertekin, this research project received partial funding from Bursa Technical University's Scientific Research Projects unit (Project No. 220Y028). The authors express their gratitude to this unit for its support. The experimental tests and measurements were performed within the Tron Electronic Systems Joint Stock Company where the student is employed. The researcher and his advisor extend their appreciation to the company for its financial support and for providing the necessary laboratory facilities for project implementation.

References

Baumhöfer, T., Brühl, M., Rothgang, S., Sauer, D. U., (2014). Production caused variation in capacity aging trend and correlation to initial cell performance: Journal of Power Sources, Pages 332-338, https://doi.org/10.1016/j.jpowsour.2013.08.108.

Di Rienzo, R., Nicodemo, N., Verani, A., Baronti, F., Roncella, R., Saletti, R., (2023). A novel methodology to study and compare active energy-balance architectures with dynamic equalization for second-life battery applications: Journal of Energy Storage, 108772, https://doi.org/10.1016/j.est.2023.108772.

Yun, Z., Qin, W., Shi, W., Wu, C., (2023). Research on active state of charge balance of battery pack based on two controllable flyback converters: Journal of Energy Storage, 106183,https://doi.org/10.1016/j.est.2022.106183.

Guo, X., Geng, J., Liu, Z., Xu, X., Cao, W., (2021). A Flyback Converter-Based Hybrid Balancing Method for Series-Connected Battery Pack in Electric Vehicles: IEEE Transactions on Vehicular Technology, pp. 6626-6635, doi: 10.1109/TVT.2021.3087320.

Yau, Y. T., Hung, T. L., (2022). A Flyback Converter With Novel Active Dissipative Snubber: IEEE Access, pp. 108145-108158, doi: 10.1109/ACCESS.2022.3204872.

IEEES-104

Fabrication of a Graphene-Based Nanohybrid Interlayer For Improved Li-S Cells Via Atomic Layer Deposition

[1*]Hazal Gergeroglu, [1,2]Mato Knez, [3]Mehmet Ziya Söğüt
[1] CIC nanoGUNE, Tolosa Hiribidea 76, E-20018, Donostia – San Sebastian, Spain
[2] IKERBASQUE, Basque Foundation for Science, E-48009, Bilbao, Spain
[3] Piri Reis University, Maritime Faculty, Marine Machinery Engineering Department, Tuzla, Istanbul,34940, Türkiye
*E-mails: h.gergeroglu@nanogune.eu

Abstract

Energy storage systems, including Lithium-sulfur (Li-S) and Li-ion batteries (LIB), are pivotal for the transition to a sustainable, low-carbon energy future. They enhance energy reliability, enable the widespread use of renewables, support the growth of electric mobility, and play a critical role in reducing greenhouse gas emissions and promoting environmental sustainability. While Li-S batteries have superior energy densities over the widely employed Li-ion technologies and are more sustainable solutions, various challenges, including mechanical fragility, the shuttle effect during operation, low electrical conductivity, suboptimal capacity retention, and the limited durability of sulfur cathodes, are obstacles to their immediate integration into commercial applications.
This study showcases the synthesis of a hybrid material as interlayer in Li-S batteries to address the critical challenges of this technology. In the first stage, three-dimensional graphene foam (3D GF), to be used as matrix of the nanohybrid, was obtained by chemical vapor deposition (CVD). The choice of 3D GF results from its low weight and the great potential for optimizing the overall energy density of high-performance Li-S cells. Then, thin films of aluminum oxide (Al_2O_3) were deposited on the 3D GF matrix via atomic layer deposition (ALD), which will improve polysulfide-blocking in the Li-S cell. The resulting 3D GF/Al_2O_3 nanohybrid was characterized by means of SEM, EDX, Raman spectroscopy, XRD, and XRR.

Keywords: atomic layer deposition, graphene foam, alumina, nanohybrid, interlayer.

I. Introduction

In response to escalating energy consumption and heightened global environmental apprehensions, substantial endeavors are underway to develop energy storage systems that are not only clean, renewable, sustainable, and cost-effective but also exhibit high performance (Lipu et al.,2022). Against this backdrop, commercially available Li-ion batteries (LIBs) have been extensively employed to fulfill fundamental energy requirements. However, LIBs approached their theoretical energy density limit, and pose significant environmental challenges due to the use of toxic materials, such as $LiFePO_4$ and $LiCoO_2$ (Zhang et al., 2021). In contrast, Li-S batteries, utilizing cost-effective, non-toxic sulfur as the cathode, can reduce the environmental burden associated with LIBs and other battery technologies containing transition metals (Chen et al., 2022). Moreover, Li-S batteries are most promising to replace traditional LIBs in the next-generation energy storage technologies due to their high performance. For instance, Li-S batteries, utilizing sulfur as cathode and lithium as anode, offer exceptional theoretical energy densities of up to 2600 $Wh \bullet kg^{-1}$ (Liu et al., 2021). The practical energy density of Li-S batteries can range from 400 to 600 $Wh \bullet kg^{-1}$ (Gu et al., 2016). However, for Li-S technology to compete with LIBs, significant challenges need to be overcome, such as detrimental mechanisms during operation (e.g., shuttle effect, low conductivity of sulfur ($5x10^{-3}$ $S \bullet cm^{-1}$), low-capacity retention, anode corrosion, etc.) and limitations in sulfur cathode processing (e.g., low mechanical stability of sulfur cathodes, defects, low sulfur loading, etc.) (Ye et al., 2020). Given these challenges, carbon nanomaterials have emerged as essential components in high-performance Li-S battery designs and have been widely adopted in the past decade. Notably, the introduction of graphene, a two-dimensional (2D) nanomaterial, has significantly influenced both the nanoelectronics industry and Li-S technology (Sundar et al., 2023).
Graphene is a single atomic layer of hexagonally arranged carbon atoms. It has exceptional properties, including a high surface area and excellent electronic behavior, making it paramount for high-performance Li-S battery designs. However, challenges like agglomeration, restacking, and difficulties in appropriate electrical contacting have limited its practical use. Three-dimensional graphene foam (3D GF), an interconnected network of continuous graphene sheets, offers solutions to these issues. Its highly porous macroscopic and microscopic structure, significant specific surface area, and ease of handling have contributed to its growing popularity in future practical applications, surpassing traditional 2D graphene. Particularly in the commercialization of Li-S batteries, 3D GF holds promise as a valuable material for enhancing the battery's electrochemical performance, prolonging its operational lifespan, mitigating anode degradation, and addressing the challenges associated with low energy density in practical applications (Oyedotun and Manyala, 2020). The utilization as composite with certain metal oxide-based adds value as those materials can function as efficient chemical absorption sites for polysulfides within Li-S batteries. Recent investigations have suggested that various metal oxides, including α-Fe_2O, MnO_2, TiO_2, Al_2O_3, and ZnO, can act as polysulfide scavengers (Deng et al..2023). Among these metal oxides, Al_2O_3 stands out for its remarkable polysulfide capture capability. Additionally, Al_2O_3 is the one of the most popular metal oxide for ALD-based surface coating due to its cost-effectiveness and ease of deposition. Nevertheless, Al_2O_3 is electrochemically inert and is insulating, limiting the battery's capacity. Moreover, a thick alumina layer can hinder Li^+ ion mobility and, consequently, reduce the overall capacity, rate capability, and long-term cycling life of a Li-S battery (Yu et al., 2014). Therefore, minimizing such loading is imperative to prevent an increase in impedance and a decrease in overall gravimetric capacity and energy density.
In this study, a nanohybrid interlayer was developed to enhance the conductivity and maintain the polysulfide capture capabilities in Li-S cells without increasing weight and volume. The 3D GF matrix material was obtained using the traditional catalytic CVD method. Subsequently, amorphous Al_2O_3 was deposited onto the surface of this matrix via ALD, followed by heat treatment to form alpha Al_2O_3. The structural, elemental, morphological, and crystallographic properties of the resulting 3D GF/Al_2O_3 nanohybrids were analyzed by SEM, EDX, Raman spectroscopy, XRD, and XRR, respectively.

II. Experimental Procedure

3D GF/Al_2O_3 Nanohybrid Synthesis: Initially the matrix, 3D GF, was obtained. The synthesis of 3D GF involved traditional catalytic CVD, performed at 1000 °C using a Ni-substrate. After CVD, PMMA was applied, and the nickel substrate was etched with 3M HCl at 50°C. Subsequent steps included multiple washes with deionized water and acetone, followed by drying at 70°C. Thereafter, the dried 3D GF was carefully placed into the ALD reactor. ALD of amorphous Al_2O_3 was conducted using Trimethylaluminum (TMA) and water (H_2O) as precursors. As a carrier and purging gas, high-purity nitrogen (99.9999%) at a flow rate of 20 standard cubic centimeters per minute (sccm) was used. After each precursor pulse time of 20 milliseconds, a TMA and H_2O exposure time of 8 seconds was given, followed by a nitrogen purge of 10 seconds. The 3D GF were coated by amorphous Al_2O_3 applying various numbers of ALD cycles (25, 50, 75, 100, 150, and 200 cycles) at an operating temperature of 200°C. The nomenclature for resulting nanohybrids corresponds to the number of ALD cycles, e.g., GA100 signifies 3D GF coated with Al_2O_3 via 100 ALD cycles.
Characterizations: Morphological investigation of the 3D GF and GA samples was performed via scanning electron microscopy (eSEM, FEI-QUANTA 250, equipped with EDX) with an accelerating voltage of 5 kV. In the SEM analysis, x100 magnifications were utilized to determine the survey image of the graphene foam skeleton. Additionally, energy dispersive X-ray (EDX) analysis was performed with the same device to measure the amount of elements quantitatively. Structural analysis was performed by Raman spectroscopy (alpha300 R, WITec Raman Imaging, Oxford Instruments) using a 532 nm wavelength laser. The phase composition and thickness determination of the samples were analyzed by X-ray diffraction (XRD) and X-ray reflectivity (XRR) through a PANalytical X'Pert Pro instrument with Cu-K radiation (~1.54 Å), operated at 40 mA and 45 kV. XRD was performed in increments of 0.015° and with a counting time of 8s per step in a grazing incidence configuration with grazing angles ranging from 0.5 to 2°, in the range of $10^o \leq 2\theta \leq 60^o$. The thicknesses of the Al_2O_3 films were determined by XRR using a reference sample with known thickness and recording in the range of $0.1^o \leq 2\theta \leq 2.5^o$, in steps of 0.003°and with a counting time of 2s per step. The HighScore Plus software was utilized to attain the relevant quantitative crystallographic information with the help of the databases PDF2 and ICCD.

III. Results and discussion

The structural characterizations of the 3D GF and GA samples are shown in Fig. 1. Raman spectra have shown that the 3D GF, synthesized by CVD, has very little sp^3 hybridization and a high crystallinity and quality. The finding of the G (1581 cm^{-1}) and 2D (2694 cm^{-1}) Raman peaks, exclusive to graphene, as well as the low intensity of the D band (1344 cm^{-1}), are attributable to defects and sp^3 hybridization of carbon. Additionally, the integral intensity ratio of the G band to the 2D band (I_G/I_{2D}) was calculated, yielding ratios ranging from 0.92 to 1.67, as illustrated in Fig. 1 (see inset table). This determination was corroborated through SEM, indicating that CVD-based 3D GF exhibited few-layer properties, as evidenced by various I_G/I_{2D} ratios (Figs. 2a-h). Notably, the Raman spectra did not show an obvious Al_2O_3 band due to the rather low content of Al_2O_3; however, the presence of Al_2O_3 was confirmed through EDX spectra, as depicted in Fig. 2h.
The morphological and elemental characterizations of 3D GF and GA samples are shown in Fig. 2. Fig. 2a illustrates the three-dimensional interconnected network structure of few-layer GF. The variation in the number of graphene layers is attributed to the porous Ni scaffold on which the graphene foam is synthesized. Ni metal foam exhibits diverse crystal orientations, making the rate of carbon solubility in the Ni grains variable. Consequently, during the CVD process, the carbon deposition results in graphene with varying numbers of layers. Fig. 2b-g confirms that the three-dimensional interconnected structure of the GF remains intact after the ALD process, irrespective of the number of applied ALD cycles. However, it is observed that the thickness of the walls increases proportionally with the number of ALD cycles. This is very clearly observable upon comparison of GA25 (Fig. 2b) and GA200 (Fig. 2g).

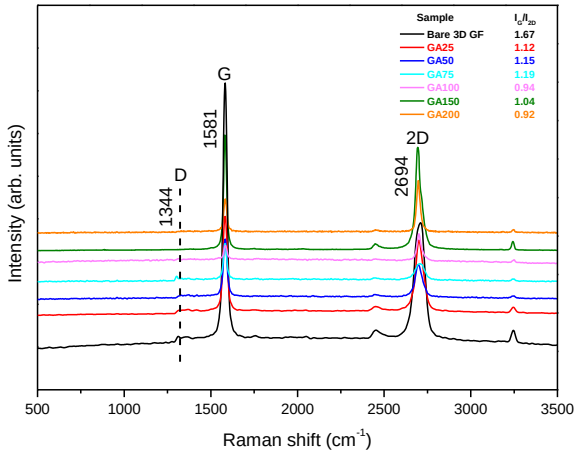

Fig 1. Raman spectra of CVD-based 3D GF and ALD-based GA nanohybrids

The chemical composition of ALD-based GA samples was investigated using EDX (Fig. 2h). The analysis confirms the presence of carbon (C), aluminum (Al), and oxygen (O) in all samples, with the peaks of O and Al corresponding to Al_2O_3, while the C signal is indicative of the CVD-based 3D GF. The ratio of aluminum and oxygen elements (weight percentages%) confirms the stoichiometry of aluminum oxide (O/Al~1.55) (see inset table in Fig. 2h).. Quantitative measurements, obtained from EDX, have reflected the purity of aluminum oxide, and no impurities or contaminations were observed in ALD-based GA nanohybrids.

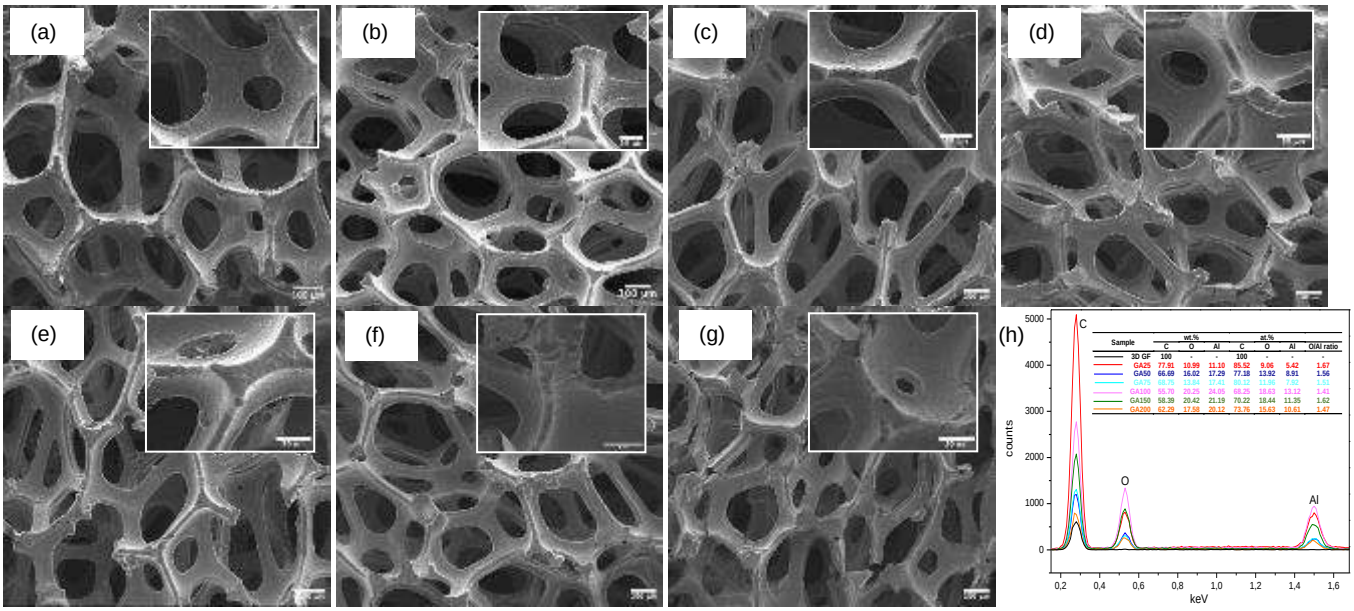

Fig. 2. SEM Images of (a) 3D GF, (b) GA25, (c) GA50, (d) GA75, (e) GA100, (f) GA150, (g) GA200; and (h) EDX spectra of bare 3D GF and ALD-based GA samples.

Depending on the number of cycles, the thickness of the ALD-based GA samples was estimated by measuring them on Si wafers used as reference samples during the ALD process. XRR scans of ALD-grown Al_2O_3 films using 25, 50, 75, 100, 150, and 200 cycles are shown in Fig.3a. The period of oscillation has gradually decreased with an increasing number of ALD cycles. The inset table in Fig. 3a shows the thickness determined from the oscillation of the curves in Fig. 3a and the growth per cycle (GPC), derived from dividing the total thickness by the number of applied ALD cycles. Consistent with the SEM observation, the layer thickness increased progressively as the number of ALD cycles was raised. For each sample, the expected growth per cycle of ALD-grown Al_2O_3 of about 1 Å/cycle at 200ºC was approximately verified.

Although transformation temperatures for bulk alumina are well known, heat treatment studies are required for films with nanometric thicknesses. For this reason, reference samples, subjected to the same ALD process parameters as the GA100 nanohybrid, were heat-treated in air for 30 minutes. To obtain alpha alumina and to observe the effect of different temperatures on ALD-based alumina thin films, heat treatment was applied between 600-1200ºC. Figure 3b shows the XRD patterns of post-heat treated and untreated reference samples. Similar to bulk alumina, thin film patterns at 600 and 700ºC indicate the presence of a dense amorphous alumina phase in the structure. However, when the temperature was increased to 1000ºC, low-intensity sharp peaks became evident and peaks attributed to α-Al_2O_3 were detected from samples trated at 1200ºC. It was found that the diffraction peaks at 2θ values of 24.93°, 35.65°, 37.07°, 43.03°, 51.25°, and 57.23 appeared, which are referred to (012), (104), (110), (113), (024), and (116) directions of Miller indices, respectively. These values match well the JPCDS # 00–010–0173 of α-Al_2O_3.

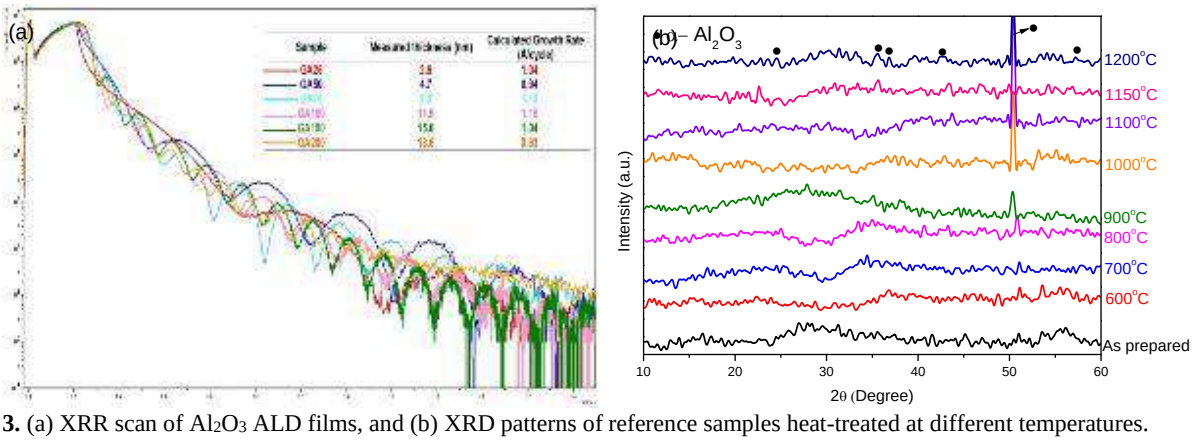

Fig. 3. (a) XRR scan of Al_2O_3 ALD films, and (b) XRD patterns of reference samples heat-treated at different temperatures.

IV. Conclusion

Al_2O_3 thin films were successfully deposited by ALD on 3D GF surfaces 3D GF@Al_2O_3 (GA) nanohybrids were obtained. The Raman spectra indicate that the CVD-based 3D GF exhibits minimal sp^3 hybridization and possesses high crystallinity and quality. SEM analyses show that the porous and interconnected 3D network of the GF was preserved even after the ALD process. Additionally, a systematic increase in the thickness of the 3D GF walls due to the increase in the number of ALD cycles was observed. EDX analyses confirmed the presence of C, Al, and O elements in all samples after ALD treatment, without any contamination or impurity. A Si wafer, placed as a reference sample in the ALD chamber next to each 3D GF, was used for determining the growth dynamics by XRR. The measurements showed thicknesses in the range of 2.5-20 nm linearly correlated with the number of applied ALD cycles. The reference samples were also heat treated in air for 30 minutes at temperatures between 600-1200ºC, and the effect of temperatures on the phase formation was examined by XRD. The XRD patterns confirmed the formation of α-Al_2O_3 at 1200ºC. Further studies will include verification of the intermediate layers by phase analysis and the application of the intermediate layer in the Li-S battery cell.

Acknowledgements
This research was supported by The Scientific and Technological Research Council of Türkiye (TÜBİTAK) with the project ID 1059B192201811.

References

Chen, J., Zhang, Y., Yang, J., Nuli, Y., & Wang, J. (2022). Post lithium-sulfur battery era: challenges and opportunities towards practical application. *Science China Chemistry*, 1-16. https://doi.org/10.1007/s11426-022-1421-7

Deng, S., Guo, T., Heier, J., & Zhang, C. (2023). Unraveling Polysulfide's Adsorption and Electrocatalytic Conversion on Metal Oxides for Li-S Batteries. *Advanced Science*, *10*(5), 2204930. https://doi.org/10.1002/advs.202204930

Gu, Xingxing, Zhang, S., & Hou, Y. (2016). Graphene-Based Sulfur Composites for Energy Storage and Conversion in Li-S Batteries. *Chinese Journal of Chemistry*, *34*(1), 13–31. https://doi.org/10.1002/cjoc.201500675

Hata! Köprü başvurusu geçerli değil. Lipu, M.S.H., Mamun, A. A., Ansari, S., Miah, M.S., Hasan, K., Meraj, S. T., A bdolrasol, G.M.M., Rahman, T., Maruf, H., Sarker, R.M., Aljanad, A., Tan, N.M. (2022). Battery management, key technologies, methods, issues, and future trends of electric vehicles: A pathway toward achieving sustainable development goals. *Batteries*, *8*(9), 119. https://doi.org/10.3390/batteries8090119

Liu, Y., Liu, S., Li, G., & Gao, X. (2021). Strategy of enhancing the volumetric energy density for lithium–sulfur batteries. *Advanced Materials*, *33*(8), 2003955. https://doi.org/10.1002/adma.202003955

Oyedotun, K. O., & Manyala, N. (2020). Graphene foam–based electrochemical capacitors. *Current Opinion in Electrochemistry*, *21*, 125–131. https://doi.org/10.1016/j.coelec.2019.12.010

Sundar, L. S., Mir, M. A., Ashraf, M. W., & Djavanroodi, F. (2023). Synthesis and characterization of graphene and its composites for Lithium-Ion battery applications: A comprehensive review. *Alexandria Engineering Journal*. https://doi.org/10.1016/j.aej.2023.07.044

Ye, H., Li, M., Liu, T., Li, Y., & Lu, J. (2020). Activating Li_2S as the lithium-containing cathode in lithium–sulfur batteries. *ACS Energy Letters*, *5*(7), 2234–2245. https://doi.org/10.1021/acsenergylett.0c00936

Yu, M., Yuan, W., Li, C., Hong, J.-D., & Shi, G. (2014). Performance enhancement of a graphene–sulfur composite as a lithium–sulfur battery electrode by coating with an ultrathin Al_2O_3 film via atomic layer deposition. *Journal of Materials Chemistry A*, *2*(20), 7360–7366. https://doi.org/10.1039/C4TA00234B

Zhang, J., Li, M., Younus, H. A., Wang, B., Weng, Q., Zhang, Y., & Zhang, S. (2021). An overview of the characteristics of advanced binders for high-performance Li–S batteries. *Nano Materials Science*, *3*(2), 124-139. https://doi.org/10.1016/j.nanoms.2020.10.006.

Simultaneous Biohydrogen Production from Energetic Poplar and Waste Minimization Using Membraneless Microbial Electrolysis Cell

[1*]A. Faruk Kılıcaslan, [1,2] A. Yagmur Goren, [1] Ibrahim Dincer and [3] Ali Khalvati
[1] Clean Energy Research Laboratory (CERL), Faculty of Engineering and Applied Science, Ontario Tech. University, 2000 Simcoe Street North, Oshawa, Ontario L1G 0C5, Canada
[2] Izmir Institute of Technology, Department of Environmental Engineering, Urla, Izmir 35430, Turkiye
[3] Viona Consulting INC., Agro-Environmental Innovation and Technology, Research and Development Company, Thornhill, Ontario L3T 0C6, Canada
*E-mail: ahmet.kilicaslan@ontariotechu.net

Abstract

Environmental concerns triggered by the emission of greenhouse gases (GHGs) from fossil fuels have revolutionized industrial business planning and resulted in the development of cutting-edge technology for the treatment of wastewater and the production of green bioenergy. In this regard, microbial electrolysis cells (MEC) have gained significant attention as a promising, useful, cutting-edge, and sustainable process. Therefore, biohydrogen ($bioH_2$) production from energetic poplar and anaerobic sludge mixture in a membrane-less single-cell microbial electrolysis cell (MEC) was evaluated in this study. The MEC system was performed with different voltage values (0.5-1.5 V) and in the presence of various metal oxide nanoparticles (Al_2O_3, MgO, and Fe_2O_3). The maximum production of 417 ppm was obtained at a voltage of 1.5 V. In addition, the $bioH_2$ production increased with increasing operating time. The $bioH_2$ production increased from 40 to 417 ppm with increasing operation time from 1 to 10 min.
Furthermore, the highest $bioH_2$ production value was 464 ppm in 7 min in the presence of Fe_2O_3. Overall, these results proved that the MEC process with the addition of metal oxides may provide promising results in overcoming fundamental problems such as the prevention of overpotential losses.

Keywords: Microbial electrolysis, poplar leaves, metal oxide, anaerobic sludge, biohydrogen.

I. Introduction

Energy and water are two essential resources that have a significant impact on the development of civilizations. Global energy consumption is predicted to surpass 736 quadrillion BTUs by 2040, while the global population is projected to reach 9.7 billion by 2050 (Baruah et al., 2018). Moreover, freshwater has become one of the most limited resources because of the increased global population and industrialization. Concerns about the environment forced on by the release of greenhouse gases (GHGs) from fossil fuels have caused a paradigm change in industrial business planning, leading to the development of innovative technologies for wastewater treatment and the production of green bioenergy (Dey et al., 2020). In the past, several thermochemical, electrolytic, and photo-based processes were used to produce H_2. Namely, thermochemical processes employ pressure and heat to break molecular bonds, while the process of dissolving water with the use of electricity is called electrolysis. Microorganisms release H_2 through photolytic-based processes. Moreover, thermochemical processes use fossil fuels as a base material, but electrolytic and photolytic-based processes are more expensive since they require a lot of energy.
In this regard, thermodynamic and environmental problems must be addressed by the biological production of H_2, which uses wastewater for H_2 synthesis while simultaneously treating the wastewater (Aydin et al., 2021). The raw materials used in the biological production of H_2, such as different kinds of wastewater, lignocellulosic biomass, and organic substances, are easily accessible, reasonably priced, and leftovers from other industries. In this context, microbial electrolysis cell (MEC) is regarded as a useful, cutting-edge method. The concept of MECs was first proposed in 2005 (Liu et al., 2005). In such circumstances, MEC technology offers simultaneous advantages, including gaseous energy production and organic waste treatment. Therefore, this study utilized the membrane-less MEC system for biohydrogen ($bioH_2$) production from poplar leaves and domestic anaerobic sludge mixture. To our knowledge, the energetic poplar leaves have not been utilized as biomass resources for the MEC process to produce $bioH_2$, especially $bioH_2$, during waste treatment. Moreover, the effects of voltage (0.5, 1, and 1.5 V) and metal oxide nanoparticles (Al_2O_3, MgO, and Fe_2O_3) on the $bioH_2$ production performance of the MEC process were investigated. Overall, the fundamental understanding of membrane-less MEC proposed in the study might guide the researchers to develop a sustainable and effective process to produce $bioH_2$ and provide waste minimization using various wastewater effluents. In addition, we believe that the current study is going to be valuable in overcoming the fundamental problems in the MEC process with the addition of metal oxides such as the prevention of overpotential losses.

II. Experimental

All experimental runs were performed in the single-cell membrane-less MEC system, which is constructed using a plexigasll material (Fig. 1). The stainless steel plates are used as an anode and cathode electrodes, and the electrodes were cleaned before all experiments. The MEC feed with 250 mL of anaerobic sludge from a wastewater treatment facility and acid-treated energetic poplar as a biomass source. The voltage applied from an adjustable DC power source was linked to the MEC using copper wire coupled with electrodes. The $bioH_2$ gas was collected in an external cylindrical container, which includes an MQ8 hydrogen sensor, and monitored during the experiments.

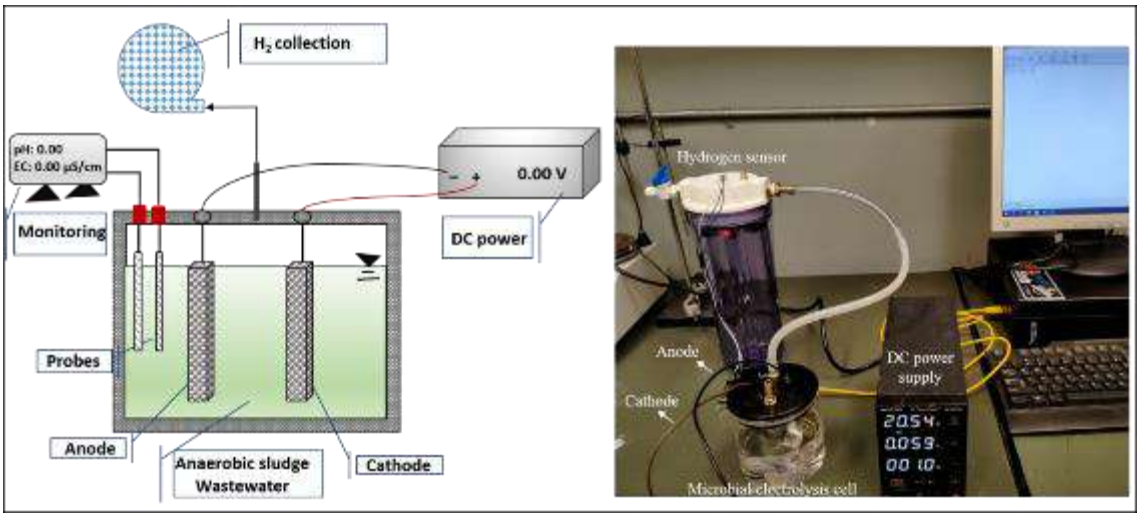

Fig. 1: Schematic diagram and lab-scale experimental set-up of the microbial electrolysis cell.

III. Analysis

The pH and electrical conductivity in the MEC were measured using a pH and conductivity meter at the end of the experiments, respectively. The produced H_2 gas from the MEC was analyzed with an MQ8-H_2 sensor. The total amount of H_2 produced for each time period was used to calculate the cumulative H_2 production as follows:

$$V_{H_{2,t}} = C_{H_{2,t}} \times V_{BG,t} + V_{HS} \times \left(C_{H_{2,t}} - C_{H_{2,t-1}}\right) \quad (1)$$

where $V_{H_{2,t}}$ is the volume of H_2 produced between t and t-1; $C_{H_{2,t}}$ and $C_{H_{2,t-1}}$ is the concentrations of H_2 measured at periods t and t-1, respectively; and $V_{BG,t}$ and V_{HS} is the volume of biogas produced from time t until time t-1 and headspace volume of the reactor, respectively. Then, the cumulative H_2 ($V_{H_{2,cum}}$) production was determined as a sum of H_2 productions between each measurement ($V_{H_{2,t}}$) during fermentation

IV. Results and discussion

This paper studied the effects of voltage and metal oxide nanoparticles at a temperature of 25 °C, initial pH of 5.5, and inoculum amount of 50 mL during the retention time of 10 min. The effect of the voltage on the bioH_2 production without metal oxide addition in the MEC is presented in Fig. 2a. As expected, the bioH_2 production enhanced with the increment in applied voltage. The lowest bioH_2 production of 109 ppm was observed at a voltage of 0.5 V in 10 min, while the maximum production (417 ppm) was obtained at a voltage of 1.5 V. In addition, the bioH_2 production increased with increasing operating time. For instance, bioH_2 production increased from 40 to 417 ppm with increasing operation time from 1 to 10 min. Moreover, the effects of various metal oxides were also considered and illustrated in Fig. 2b. The highest bioH_2 production values were 448 ppm in 9.5 min, 455 ppm in 8.5 min, and 464 ppm in 7 min using Al_2O_3, MgO, and Fe_2O_3, respectively. These results revealed that the bioH_2 production performance of the system improved in the presence of metal oxide nanoparticles. For instance, the bioH_2 production increased from 417 to 464 ppm in the presence of Fe_2O_3. Moreover, the addition of metal oxides decreased the operating time to achieve the maximum bioH_2 capacity.

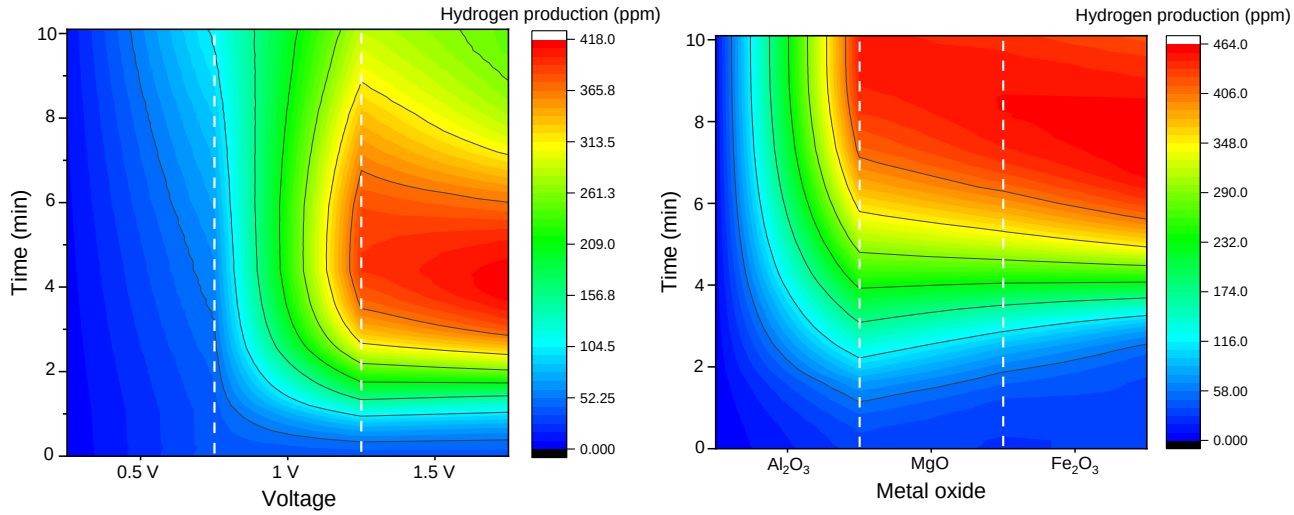

Fig. 2. H_2 production at various voltage values (a) and metal oxide types (b) in the MEC cell.

V. Conclusions

In this study, the membrane-less single-cell MEC process was performed for both sustainable bioH_2 production and waste minimization. Particularly, it was obtained that the applied voltage and metal oxide nanoparticles have significantly positive effects on bioH_2 production during the start-up of the process. At improved operating conditions (initial pH of 5.5, temperature of 25 °C, biomass hydrolysate volume of 200 mL, and anaerobic sludge volume of 50 mL), as the voltage value was increased from 0.5 to 1.5 V, the bioH_2 production was increased from 109 to 417 ppm without metal oxide nanoparticles. On the other hand, the bioH_2 production improved with the addition of the metal oxide nanoparticles, and the maximum production of 464 ppm was obtained using Fe_2O_3 nanoparticles in 7 min. Consequently, this study proved that the MEC is a sustainable and promising bioH_2 production process from energetic poplar biomass and anaerobic sludge mixture with concurrent waste minimization opportunity.

References

Aydin, M.I., Karaca, A.E., Qureshy, A.M.M.I., Dincer, I., 2021. A comparative review on clean hydrogen production from wastewaters. J. Environ. Manage. 279, 111793.

Baruah, J., Nath, B.K., Sharma, R., Kumar, S., Deka, R.C., Baruah, D.C., Kalita, E., 2018. Recent trends in the pretreatment of lignocellulosic biomass for value-added products. Front. Energy Res. 6, 141.

Dey, P., Pal, P., Kevin, J.D., Das, D.B., 2020. Lignocellulosic bioethanol production: prospects of emerging membrane technologies to improve the process–a critical review. Rev. Chem. Eng. 36, 333–367.

Liu, H., Grot, S., Logan, B.E., 2005. Electrochemically assisted microbial production of hydrogen from acetate. Environ. Sci. Technol. 39, 4317–4320.

IEEES-106

Exergy-Based Analysis of Polymer Recycling in the Automotive Sector

[1*]Cemil Koyunoğlu, [2]Tamer Çınar
[1]Yalova University, Engineering Faculty, Energy Systems Engineering Department, Çinarcik Road 5th km, Yalova University, Yalova, 77200, Türkiye
[2] SİGMA A.Ş., Teknopark İstanbul, Pendik, İstanbul, Turkey
*E-mails: cemil.koyunoglu@yalova.edu.tr

Abstract

The recycling of polymers is of paramount importance in addressing environmental concerns and resource conservation in the automotive sector. This study employs an exergy-based approach to assess the energy consumption associated with polymer recycling at different levels: primary, secondary, tertiary, and quaternary. Exergy consumption, measured in MJex/kg, quantifies the energy required or lost during each recycling process. The findings reveal significant variations in energy requirements among different polymer types, highlighting the need for informed decision-making in recycling methods and materials. This research contributes to a better understanding of the environmental and economic implications of polymer recycling, offering valuable insights for sustainable practices in the automotive industry.

Keywords: Polymer recycling, automotive sector, exergy-based analysis, energy consumption, sustainability, environmental impact, recycling levels, polymer types, resource conservation, sustainable practices.

I. Introduction

The automotive industry is increasingly recognizing the importance of sustainable practices, including the efficient recycling of materials. Polymer recycling plays a pivotal role in reducing waste, conserving resources, and mitigating environmental impacts associated with vehicle production. However, assessing the energy implications of polymer recycling processes remains a complex challenge.

This study addresses this challenge by adopting an exergy-based approach to analyze polymer recycling in the automotive sector. Exergy consumption, a measure of the energy quality, is used to quantify the energy required or lost during each recycling stage. The four recycling levels investigated—primary, secondary, tertiary, and quaternary—offer a comprehensive view of the energy demands associated with polymer recycling.

In the subsequent sections, we present a detailed analysis of the findings from each recycling level, highlighting the variations in exergy consumption among different polymer types. These insights will inform decision-makers in the automotive industry about the most energy-efficient and environmentally friendly recycling practices.

The significance of this research lies in its contribution to the sustainable development of the automotive sector. By understanding the energy implications of polymer recycling, industry stakeholders can make informed choices, balancing economic considerations with environmental responsibility. This study serves as a valuable resource for guiding future recycling practices in the automotive industry, aligning them with global sustainability goals.

II. Experimental Procedure/Methodology/System Description

2.1. Methodology

The data used in this study were obtained from the following source:

Citation: Russo, S.; Valero, A.; Valero, A.; Iglesias-Émbil, M. Exergy-Based Assessment of Polymers Production and Recycling: An Application to the Automotive Sector. Energies 2021, 14, 363. https://doi.org/10.3390/en14020363.

This information confirms that the data used in the analysis were derived from the specified academic paper published in the journal "Energies" in 2021, and the provided citation can be used to reference the source of the data in academic or research work.

The MATLAB codes have been prepared based on the article published in the "Energies" journal in 2021. The code encompasses exergy-based assessment of polymer production and recycling, and it has been used for the analysis of data presented in the mentioned article. The purpose of this code is to calculate the exergy consumption of different polymer types at primary, secondary, tertiary, and quaternary recycling levels and display the results.

The code uses data that includes polymer types and their corresponding exergy consumption values to perform these calculations and prints the results to the screen. It starts by calculating the values for primary recycling, followed by separate calculations for secondary, tertiary, and quaternary recycling.

This code may have been created to assist researchers or engineers interested in conducting exergy-based analyses based on the studies presented in the article. However, to fully understand how the code works and interpret the results, it may be necessary to review the article itself.

III. Analysis

3.1 MATLAB Code for Primary Recycling Analysis

This MATLAB code is used to analyze the exergy consumption values for different polymer types in the context of the primary recycling process and display the results. Such analysis helps assess the energy efficiency and environmental impact of polymer production and recycling processes. Here are academic explanations in English for the key components of the code:

1. `exergy_consumption_primary` Array: This array contains the exergy consumption values (in MJex/kg) for various polymer types in the primary recycling process. Exergy consumption values are determined separately for each polymer type and are used in the analysis.
2. `polimer_turleri` Cell Array: This cell array contains the names of different polymer types to be included in the analysis. The name of each polymer type is defined in this cell array and is used for better understanding and visualization of the results.
3. `for` Loop: This loop is used to perform individual analyses for each polymer type. It iterates through the `polimer_turleri` cell array and calculates and displays the exergy consumption value for each polymer type.
4. `fprintf` Function: This function is used to print the results to the screen. The name of each polymer type (`polimer_turleri{i}`) and the exergy consumption value (`exergy_consumption_primary(i)`) are displayed appropriately. Exergy consumption values are displayed with precision in MJex/kg.
This code is useful for evaluating the energy consumption of polymer production and recycling processes and understanding the differences in energy efficiency among different polymer types. It also serves as an important tool for environmental sustainability analysis.

```
"% Verilen exergy tüketim değeri
exergy_consumption_primary = [0.71, 0.23, 0.14, 2.3, 5.3, 10.3, 2.7, 16.8, 11.4]; % MJex/kg olarak
% Polimer türlerini tanımlayın
polimer_turleri = {'PE/PP', 'PE/PP (Tertiary)', 'PVC (Secondary)', 'PVC (Tertiary)', 'ABS (Secondary)', 'PU (Tertiary)', 'PA66 (Tertiary)', 'PET (Secondary)', 'PET (Tertiary)', 'SBR/EPDM (Tertiary)'};
% Sonuçları ekrana yazdırın
fprintf('Birincil (Primary) Geri Kazanım Analizi:\n');
for i = 1:numel(polimer_turleri)
    fprintf('%s:\n', polimer_turleri{i});
    fprintf('Exergy Consumption: %.2f MJex/kg\n', exergy_consumption_primary(i));
    fprintf('\n');
end"
```

3.2. MATLAB Code for Secondary Recycling Analysis
This MATLAB code is designed for the analysis of exergy consumption values associated with secondary recycling processes for various polymer types and presents the results. Secondary recycling involves steps such as cleaning, drying, shredding, contaminant separation, and pelletization after the collection of discarded polymers. The code provides insights into the energy efficiency and environmental impact of these recycling processes.
Here's an explanation of the key components of the code:
1. `exergy_consumption_secondary` Array: This array contains the exergy consumption values (in MJex/kg) for different polymer types in the context of secondary recycling processes. The exergy consumption values are determined separately for each polymer type and are used in the analysis.
2. `polimer_turleri` Cell Array: This cell array defines the names of various polymer types that are considered in the analysis. Each polymer type's name is specified in this cell array and is used for identification and reporting purposes.
3. `for` Loop: This loop is used to perform individual analyses for each polymer type. It iterates through the `polimer_turleri` cell array, calculates the exergy consumption value for each polymer type, and displays the results.
4. `fprintf` Function: This function is utilized to print the results to the screen. It displays the name of each polymer type (`polimer_turleri{i}`) and its corresponding exergy consumption value (`exergy_consumption_secondary(i)`) with precision in MJex/kg.
The code provides a valuable tool for assessing the energy consumption associated with secondary recycling processes for polymers. It helps researchers and practitioners understand the differences in energy efficiency among various polymer types and aids in making informed decisions regarding recycling methods and materials.

```
"% Verilen exergy tüketim değeri
exergy_consumption_secondary = [0.71, 2.2, 0.14, 1.1, 2.3]; % MJex/kg olarak
% Polimer türlerini tanımlayın
polimer_turleri = {'PE/PP', 'PE/PP', 'PVC', 'PVC', 'ABS'};
% Sonuçları ekrana yazdırın
fprintf('İkincil (Secondary) Geri Kazanım Analizi:\n');
for i = 1:numel(polimer_turleri)
    fprintf('%s:\n', polimer_turleri{i});
    fprintf('Exergy Consumption: %.2f MJex/kg\n', exergy_consumption_secondary(i));
    fprintf('\n');
end"
```

3.3. MATLAB Code for Tertiary Recycling Analysis
This MATLAB code is intended for the analysis of exergy consumption values associated with tertiary recycling processes for various polymer types and presents the results. Tertiary recycling involves processes such as depolymerization, solvolysis, thermolysis, and pyrolysis to recover monomers from discarded polymers. The code offers insights into the energy efficiency and environmental impact of these recycling methods.
Here's an explanation of the key components of the code:
1. `exergy_consumption_tertiary` Array: This array contains the exergy consumption values (in MJex/kg) for different polymer types in the context of tertiary recycling processes. The exergy consumption values are determined separately for each polymer type and are used in the analysis.

2. `polimer_turleri` Cell Array: This cell array defines the names of various polymer types that are considered in the analysis. Each polymer type's name is specified in this cell array and is used for identification and reporting purposes.
3. `for` Loop: This loop is used to perform individual analyses for each polymer type. It iterates through the `polimer_turleri` cell array, calculates the exergy consumption value for each polymer type, and displays the results.
4. `fprintf` Function: This function is utilized to print the results to the screen. It displays the name of each polymer type (`polimer_turleri{i}`) and its corresponding exergy consumption value (`exergy_consumption_tertiary(i)`) with precision in MJex/kg.
The code provides a valuable tool for assessing the energy consumption associated with tertiary recycling processes for polymers. It helps researchers and practitioners understand the differences in energy efficiency among various polymer types in the context of tertiary recycling and aids in making informed decisions regarding recycling methods and materials.

```
“% Verilen exergy tüketim değeri
exergy_consumption_tertiary = [0.23, 0.42, 0.11, 0.13, 5.3, 10.3, 16.8, 22, 11.4]; % MJex/kg olarak
% Polimer türlerini tanımlayın
polimer_turleri = {'PE/PP (Tertiary)', 'PE/PP (Tertiary)', 'PVC (Tertiary)', 'PVC (Tertiary)', 'PU (Tertiary)', 'PA66 (Tertiary)', 'PET (Tertiary)', 'PET (Tertiary)', 'SBR/EPDM (Tertiary)'};
% Sonuçları ekrana yazdırın
fprintf('Üçüncül (Tertiary) Geri Kazanım Analizi:\n');
for i = 1:numel(polimer_turleri)
    fprintf('%s:\n', polimer_turleri{i});
    fprintf('Exergy Consumption: %.2f MJex/kg\n', exergy_consumption_tertiary(i));
    fprintf('\n');
end”
```

3.4. MATLAB Code for Quaternary Recycling Analysis

This MATLAB code is designed for the analysis of exergy consumption values associated with quaternary recycling processes for various polymer types and presents the results. Quaternary recycling typically involves energy recovery from plastics through incineration. The code helps evaluate the energy efficiency and environmental impact of this recycling method.
Here's an explanation of the key components of the code:
1. `exergy_consumption_quaternary` Array: This array contains the exergy consumption values (in MJex/kg) for different polymer types in the context of quaternary recycling processes. In this case, the exergy consumption values are assumed to be zero for all polymer types, as quaternary recycling often focuses on energy recovery rather than material recycling.
2. `polimer_turleri` Cell Array: This cell array defines the names of various polymer types that are considered in the analysis. Each polymer type's name is specified in this cell array and is used for identification and reporting purposes.
3. `for` Loop: This loop is used to perform individual analyses for each polymer type. It iterates through the `polimer_turleri` cell array, assuming zero exergy consumption values for all polymer types in quaternary recycling, and displays the results.
4. `fprintf` Function: This function is utilized to print the results to the screen. It displays the name of each polymer type (`polimer_turleri{i}`) and its corresponding exergy consumption value (`exergy_consumption_quaternary(i)`), which is assumed to be zero in this case.
The code provides a tool for acknowledging that quaternary recycling is primarily focused on energy recovery rather than material recycling, and it helps researchers and practitioners understand the differences in energy efficiency among various polymer types in this context.

```
“% Verilen exergy tüketim değeri
exergy_consumption_quaternary = [0, 0, 0, 0, 0]; % MJex/kg olarak
% Polimer türlerini tanımlayın
polimer_turleri = {'PE/PP', 'PE/PP', 'PVC', 'PVC', 'Other'};
% Sonuçları ekrana yazdırın
fprintf('Dördüncül (Quaternary) Geri Kazanım Analizi:\n');
for i = 1:numel(polimer_turleri)
    fprintf('%s:\n', polimer_turleri{i});
    fprintf('Exergy Consumption: %.2f MJex/kg\n', exergy_consumption_quaternary(i));
    fprintf('\n');
end”
```

IV. Results and discussion

Below are the results of the exergy recovery analysis for each polymer
In this analysis, it is examined the exergy consumption values for different recycling levels: primary, secondary, tertiary, and quaternary. Exergy consumption is measured in MJex/kg, representing the energy required or lost during each recycling process. Let's break down the findings:

4.1. Primary Recycling Analysis

- PE/PP has an exergy consumption of 0.71 MJex/kg in primary recycling, indicating the energy needed to recycle this polymer.
- PVC (Secondary) and ABS (Secondary) also have relatively low exergy consumption values, 0.14 MJex/kg and 5.30 MJex/kg, respectively.
- On the other hand, PU (Tertiary) requires a significant amount of energy, with an exergy consumption of 10.30 MJex/kg.

4.1.1. Results

PE/PP:

Exergy Consumption: 0.71 MJex/kg
PE/PP (Tertiary):
Exergy Consumption: 0.23 MJex/kg
PVC (Secondary):
Exergy Consumption: 0.14 MJex/kg
PVC (Tertiary):
Exergy Consumption: 2.30 MJex/kg
ABS (Secondary):
Exergy Consumption: 5.30 MJex/kg
PU (Tertiary):
Exergy Consumption: 10.30 MJex/kg
PA66 (Tertiary):
Exergy Consumption: 2.70 MJex/kg
PET (Secondary):
Exergy Consumption: 16.80 MJex/kg
PET (Tertiary):
Exergy Consumption: 11.40 MJex/kg

4.2. Secondary Recycling Analysis

- PE/PP and PVC require 0.71 MJex/kg and 0.14 MJex/kg, respectively, for secondary recycling.
- ABS stands out with a higher exergy consumption of 2.30 MJex/kg.

4.2.1. Results

PE/PP:
Exergy Consumption: 0.71 MJex/kg
PE/PP:
Exergy Consumption: 2.20 MJex/kg
PVC:
Exergy Consumption: 0.14 MJex/kg
PVC:
Exergy Consumption: 1.10 MJex/kg
ABS:
Exergy Consumption: 2.30 MJex/kg

4.3. Tertiary Recycling Analysis

- PE/PP (Tertiary) and PVC (Tertiary) show lower exergy consumption values of 0.23 MJex/kg and 0.11 MJex/kg, respectively.
- On the other hand, PU (Tertiary) and PA66 (Tertiary) have higher values of 5.30 MJex/kg and 10.30 MJex/kg, respectively.
- PET (Tertiary) and SBR/EPDM (Tertiary) also require significant energy for tertiary recycling, with values of 16.80 MJex/kg, 22.00 MJex/kg, and 11.40 MJex/kg, respectively.

4.3.1.Results

PE/PP (Tertiary):
Exergy Consumption: 0.23 MJex/kg
PE/PP (Tertiary):
Exergy Consumption: 0.42 MJex/kg
PVC (Tertiary):
Exergy Consumption: 0.11 MJex/kg
PVC (Tertiary):
Exergy Consumption: 0.13 MJex/kg
PU (Tertiary):
Exergy Consumption: 5.30 MJex/kg
PA66 (Tertiary):
Exergy Consumption: 10.30 MJex/kg
PET (Tertiary):
Exergy Consumption: 16.80 MJex/kg
PET (Tertiary):
Exergy Consumption: 22.00 MJex/kg
SBR/EPDM (Tertiary):
Exergy Consumption: 11.40 MJex/kg

4.4. Quaternary Recycling Analysis

- In quaternary recycling, all polymer types, including PE/PP, PVC, and "Other," have zero exergy consumption values. This indicates that quaternary recycling primarily focuses on energy recovery, such as incineration, rather than material recycling.

4.4.1. Quaternary Recycling Analysis

PE/PP:
Exergy Consumption: 0.00 MJex/kg
PE/PP:
Exergy Consumption: 0.00 MJex/kg
PVC:
Exergy Consumption: 0.00 MJex/kg

PVC:
Exergy Consumption: 0.00 MJex/kg
Other:
Exergy Consumption: 0.00 MJex/kg"

The results highlight the varying energy requirements for different polymer types in recycling processes. While some polymers can be recycled with relatively low energy input, others, especially in tertiary recycling, demand higher energy consumption. Understanding these differences is crucial for making informed decisions regarding recycling methods and materials, taking into account both environmental and economic considerations.

V. Conclusion

The analysis presented in this study sheds light on the exergy consumption values associated with recycling polymers at different levels: primary, secondary, tertiary, and quaternary. Exergy consumption, measured in MJex/kg, quantifies the energy required or lost during each recycling process.
The findings reveal several key insights:
Primary Recycling Analysis
- PE/PP exhibits a relatively low exergy consumption of 0.71 MJex/kg during primary recycling.
- PVC (Secondary) and ABS (Secondary) also demonstrate relatively low exergy consumption values, at 0.14 MJex/kg and 5.30 MJex/kg, respectively.
- In contrast, PU (Tertiary) demands a significant amount of energy, with an exergy consumption of 10.30 MJex/kg.
Secondary Recycling Analysis
- PE/PP and PVC require 0.71 MJex/kg and 0.14 MJex/kg, respectively, for secondary recycling.
- ABS stands out with a higher exergy consumption of 2.30 MJex/kg.
Tertiary Recycling Analysis
- PE/PP (Tertiary) and PVC (Tertiary) exhibit lower exergy consumption values of 0.23 MJex/kg and 0.11 MJex/kg, respectively.
- PU (Tertiary) and PA66 (Tertiary) have higher values of 5.30 MJex/kg and 10.30 MJex/kg, respectively.
- PET (Tertiary) and SBR/EPDM (Tertiary) also require significant energy for tertiary recycling, with values of 16.80 MJex/kg, 22.00 MJex/kg, and 11.40 MJex/kg, respectively.
Quaternary Recycling Analysis
- In quaternary recycling, all polymer types, including PE/PP, PVC, and "Other," exhibit zero exergy consumption values. This suggests that quaternary recycling primarily focuses on energy recovery, such as incineration, rather than material recycling.
These results emphasize the varying energy requirements for recycling different polymer types. While some polymers can be recycled with relatively low energy input, others, especially in tertiary recycling, demand higher energy consumption. Understanding these differences is crucial for making informed decisions regarding recycling methods and materials, considering both environmental and economic considerations.
The study underscores the importance of assessing exergy consumption in polymer recycling processes to optimize resource utilization and minimize environmental impacts in the automotive sector and beyond. Further research and development in sustainable recycling practices are essential for a more environmentally friendly and energy-efficient future.

Reference

Adamon, D.G.F., Fagbémi, L.A., Bensakhria, A., Sanya, E.A., 2019. Comparison of Kinetic Models for Carbon Dioxide and Steam Gasification of Rice Husk Char. Waste and Biomass Valorization 10(2), 407-415.
Mohan, D., Sarswat, A., Ok, Y.S., Pittman, C.U., 2014. Organic and inorganic contaminants removal from water with biochar, a renewable, low cost and sustainable adsorbent – A critical review. Bioresource Technology 160, 191-202.

IEEES-107

Energy and Exergy Analysis of Steam Co-gasification of Olive Husk and Polypropylene: An Aspen Plus Modeling Study

[1*]Duygu GÜNDÜZ HAN, [1]Kaan ERDEM, [2]Adnan MİDİLLİ
[1] Medeniyet University, Faculty of Engineering and Natural Sciences, Mechanical Engineering Department, Ünalan Mah. Ünalan Sk. D100 Karayolu Yanyol 34700, Istanbul, Türkiye
[2] Istanbul Technical University, Faculty of Mechanical Engineering, Department of Mechanical Engineering, İnönü Caddesi, No. 65, Gümüşsuyu, 34437, İstanbul, Türkiye
*E-mail: duygu.gunduz@medeniyet.edu.tr

Abstract

This study utilizes Aspen Plus to explore the steam-assisted co-gasification of olive husk and polypropylene. The influence of varying plastic content ratios in the feedstock was assessed on the composition of the syngas and the performance of the gasifier. The findings indicate that an increased proportion of PP results in higher concentrations of CO and CH_4 in the syngas, accompanied by a decrease in CO_2 levels. Additionally, the research demonstrates a slight increasing-decreasing trajectory of H_2 content in syngas. Significant improvements in energy and exergy efficiencies of the gasifier are observed with the increasing PP content. Consequently, this study offers valuable insights into co-gasification systems aimed at sustainable energy production.

Keywords: Aspen plus, co-gasification, polypropylene, olive husk.

I. Introduction

Alternative energy sources and waste management strategies are gaining importance to meet the growing global energy demand. With the rise in waste production worldwide (Midilli et al., 2022), effective waste management has become a global concern. Co-gasification is a more promising solution, as it enhances the quality of producer gas when compared to the utilization of these feedstocks separately (Ajorloo et al., 2022) while gasification, a thermochemical technology, is considered environmentally friendly method for converting (He et al., 2020).
Equilibrium-based modeling, especially using Aspen Plus, has proven efficient and cost-effective for assessing process conditions. Several researchers documented numerical investigation of co-gasification process through the utilization of Aspen Plus previously (Ajorloo et al., 2022; Singh et al., 2022; Tian et al., 2022).
This paper addresses a notable gap in the existing literature by investigating the steam-assisted co-gasification of olive husk and polypropylene via the Aspen Plus simulator. The results provide valuable insights for co-gasification systems.

II. Methodology

Feedstock Properties

Olive husk (OH) and Polypropylene (PP) were selected as fuels for the steam co-gasification system. The feedstock characteristics were provided in Table 1.

Table 1. Properties of feedstocks (Kartal and Özveren 2020; Xiao et al., 2007)

Polypropylene			
Proximate Analysis (wt %, dry basis)		Ultimate Analysis (wt %, dry basis)	
Fixed Carbon	-	C	86.21
Volatile Matter	99.3	H	12.20
Ash	0.7	N	0.72
Moisture	0.41	S	0.17
HHV (MJ/kg)	44.7	O	-
Olive Husk			
Proximate Analysis (wt %, dry basis)		Ultimate Analysis (wt %, dry basis)	
Fixed Carbon	26.98	C	49.37
Volatile Matter	67.50	H	7.84
Ash	5.52	N	1.28
Moisture	9.48	S	0.11
HHV (MJ/kg)	19.2	O	35.88

Modeling

The steam co-gasification of OH and PP was thoroughly examined using Aspen Plus, where a comprehensive assessment of mass and energy balance, as well as chemical equilibrium, was conducted across the entire process as represented in Figure 1. To carry out this investigation, the proximate and ultimate analyses of the feedstocks, were retrieved from existing literature (Kartal and Özveren, 2020; Xiao et al., 2007).
In the modeling and analysis process, several key assumptions were made. Material streams were classified into three types by Aspen Plus: mixed, conventional solids, and nonconventional solids. The physical properties of conventional components involved in the gasification process were rigorously evaluated using the Peng-Robinson equation with Boston-Mathias modification (PR-MB), which

is a recommended approach for gasification processes (Pala et al., 2017). Within the kinetic-free numerical model, both stoichiometric and non-stoichiometric methodologies, employing Gibbs's free energy minimization, were applied to ensure thermodynamic equilibrium. The model was built with following assumptions including operating under steady-state, steady-flow conditions, maintaining isothermal temperature, neglecting pressure drops in the system, assuming ideal gas behavior for all gases, and considering char as pure carbon while excluding tar and other heavy hydrocarbons from the model (Marcantonio et al., 2020; Tauqir et al., 2019).

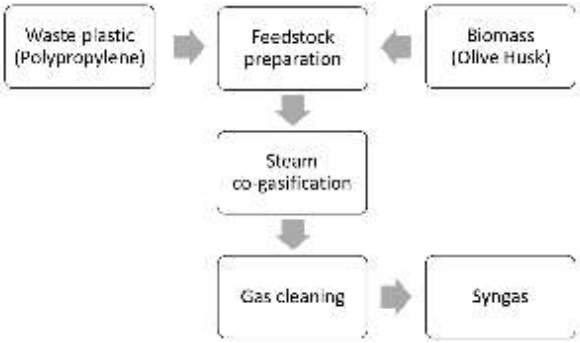

Fig.1. Illustrative diagram of the steam co-gasification process fueled by polypropylene and olive husk

III. Energy and Exergy Analysis of Gasifier

The energy and exergy efficiencies of the gasifier are defined as the useful output values divided by the total input values, as expressed below.

$$\eta_{\text{energy}} = \frac{\dot{E}_{\text{USEFUL,OUT}}}{\dot{E}_{\text{TOTAL,IN}}} \quad (1)$$

$$\eta_{\text{exergy}} = \frac{\dot{E}x_{\text{USEFUL,OUT}}}{\dot{E}x_{\text{TOTAL,IN}}} \quad (2)$$

where $\dot{E}$ and $\dot{E}x$ stands for energy rate and exergy rate respectively. The exergy rate was calculated as the sum of chemical exergy $\dot{E}x_{ch}$ and physical exergy $\dot{E}x_{ph}$ by neglecting kinetic and potential exergy rates.

$$\dot{E}x = \dot{E}x_{ph} + \dot{E}x_{ch} \quad (3)$$

IV. Results and discussion

This study looks into the impact of PP content within the feedstock on syngas composition and gasification efficiencies. The simulations were conducted under conditions of 850 °C and a steam-to-fuel ratio (S/F) of 1.25.

Table 2. Comparison of syngas composition for various PP contents in feedstock

Plastic content in feedstock	%0 PP (%100 OH)	%20 PP (%80 OH)	%40 PP (%60 OH)	%60 PP (%40 OH)	%80 PP (%20 OH)	%100 PP (%0 OH)
	Syngas composition (%v/v. dry)					
H_2	54.91	55.83	56.27	56.42	56.32	55.54
CO	11.94	15.40	18.55	21.42	24.02	26.23
CO_2	23.19	18.77	15.14	12.05	9.38	7.16
CH_4	9.96	10.00	10.04	10.11	10.28	11.07

As presented in Table 2, the syngas composition exhibits variations in response to differing PP content in the feedstock. It is noteworthy that PP contains a substantial hydrogen content in its feedstock, leading to elevated levels of both H_2 and CH_4 in the syngas as the PP proportion in the feedstock increases. Specifically, as the PP content within the feedstock blend escalates from 0% to 60%, the H_2 concentration increases from 54.91% to 56.42%. However, as the PP content surges from 60% to 100%, the H_2 concentration experiences a slight decline from 56.42% to 55.54%. This phenomenon can be attributed to the heightened PP content causing reduced moisture levels in the blends, which, in turn, hampers various critical reactions, including the reforming of hydrocarbons, the water gas reaction, and the water gas shift reaction. Furthermore, the escalation in PP content leads to an increase in CO concentration and a decrease in CO_2. This trend can be elucidated by the Boudouard reaction, which is promoted by the addition of a higher proportion of carbon-rich plastic in the feedstock.

The lower heating value (LHV) and exergy of syngas, which represent the predominant factors influencing energy and exergy efficiencies, exhibit notable enhancements with an increasing proportion of PP in the feedstock blend. As depicted in Figure 2, the energy and exergy efficiency trends closely mirror the corresponding LHV and exergy variations of the syngas. With the progression of PP content within the feedstock mixture, ranging from 0% to 100%, energy efficiency and exergy efficiency both undergo a substantial increase, transitioning from 78.91% to 89.82% and from 79.60% to 87.39%, respectively.

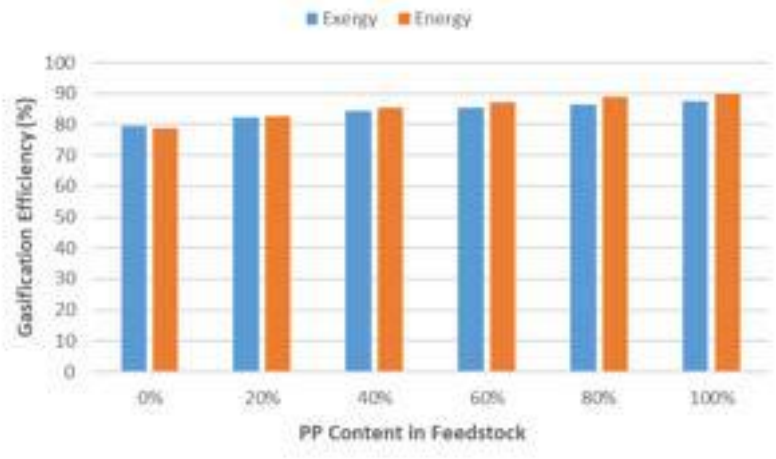

Fig. 2. Effect of plastic content in feedstock on energy and exergy efficiencies

V. Conclusion

The investigation concerning the co-gasification of OH and PP was undertaken employing the Aspen Plus simulation platform. The study aimed to examine the influence of the plastic content within the feedstock blend on gas composition, as well as energy and exergy efficiencies. As the proportion of plastic in the feedstock mixture increases, there is a significant increase in CO and CH_4 concentrations, conversely a decrease in CO_2 concentration. In addition, the H_2 content in the syngas follows a rising-falling pattern, with an initial rise and subsequent decline. The peaks of energy and exergy efficiency within the gasification process are observed in the case of 100% PP feedstock.

Acknowledgements
The authors acknowledge the support provided by Istanbul Medeniyet University (BAP Project number: F-GAP-2022-1782), as well as Istanbul Technical University.

References

Ajorloo, M., Ghodrat, M., Scott, J., & Strezov, V., (2022) Modelling and statistical analysis of plastic biomass mixture co-gasification. Energy 256, 124638.

He, J., Yang, Z., Xiong, S., Guo, M., Yan, Y., Ran, J., & Zhang, L., (2020) Experimental and thermodynamic study of banana peel non-catalytic gasification characteristics. Waste Management 113, 369-378.

Kartal, F., Özveren, U., (2020) A deep learning approach for prediction of syngas lower heating value from CFB gasifier in Aspen plus®. Energy 209, 118457.

Marcantonio, V., Bocci, E., Ouweltjes, J. P., Del Zotto, L., & Monarca, D. (2020). Evaluation of sorbents for high temperature removal of tars, hydrogen sulphide, hydrogen chloride and ammonia from biomass-derived syngas by using Aspen Plus. International journal of hydrogen energy, 45(11), 6651-6662.

Midilli, A., Kucuk, H., Haciosmanoglu, M., Akbulut, U., & Dincer, I., (2022) A review on converting plastic wastes into clean hydrogen via gasification for better sustainability. International Journal of Energy Research 46(4), 4001-4032.

Pala, L. P. R., Wang, Q., Kolb, G., & Hessel, V., (2017) Steam gasification of biomass with subsequent syngas adjustment using shift reaction for syngas production: An Aspen Plus model. Renewable Energy 101, 484-492.

Singh, M., Salaudeen, S. A., Gilroyed, B. H., & Dutta, A., (2022) Simulation of biomass-plastic co-gasification in a fluidized bed reactor using Aspen plus. Fuel 319, 123708.

Tauqir, W., Zubair, M., & Nazir, H. (2019). Parametric analysis of a steady state equilibrium-based biomass gasification model for syngas and biochar production and heat generation. Energy Conversion and Management, 199, 111954.

Tian, Y., Luo, Z., He, D., Yang, Y., Liang, S., Liu, W., & Yuan, L., (2022) Co-gasification of biomass and polyethylene: a simulation study by considering tar formation. Biomass Conversion and Biorefinery 1-9.

Xiao, R., Jin, B., Zhou, H., Zhong, Z., & Zhang, M., (2007) Air gasification of polypropylene plastic waste in fluidized bed gasifier. Energy Convers. and Manag. 48(3), 778-786.

IEEES-108

Smart Control for Sustainable Power: A Step-Up Converter with Artificial Neural Network Regulation in Hydrogen and Fuel Cell Technology

[1*]Davut Ertekin, [2]Mustafa Özden
[1] Power Electronics Center of Electrical and Electronics Engineering Research Laboratories, Bursa Technical University, 16310 Yıldırım, Bursa, Türkiye
[2] Electrical and Electronics Engineering Department of Bursa Technical University, 16310 Yıldırım, Bursa, Türkiye
*E-mails: davut.ertekin@btu.edu.tr

Abstract

The integration of switched-inductor and switched-capacitor cells into fuel cell systems, combined with artificial neural network (ANN) control, offers several benefits. This includes the optimization of voltage levels and reduction of energy losses, resulting in enhanced voltage boosting, greater power density, smaller input current ripple and higher reliability, and improved overall efficiency. Furthermore, the incorporation of ANNs facilitates a tailored and self-learning control strategy that aligns with the unique characteristics of the fuel cell system. This adaptability enhances reliability and tolerance to non-ideal conditions, such as variations in fuel quality and temperature. The collaborative approach also showcases potential for the seamless integration of energy storage, optimizing energy harvesting and advocating for the efficient utilization of fuel cells in sustainable energy applications. Collectively, these advantages position the proposed system as a promising advancement in fuel cell technology.
This investigation introduces an innovative configuration for a boost converter by incorporating switched-inductor and switched-capacitor cells at both the input and output terminals of a Luo converter, along with the utilization of an Artificial Neural Network (ANN) controller. The outcomes indicate a reduction in ripples in the fuel-cell input current and an improvement in the generated voltage of the converter. These enhancements establish the suitability of the topology for applications in high-voltage direct current and AC grid systems. The findings from simulations and experimental tests substantiate the theoretical analyses. A laboratory prototype converter with a power rating of 300 W underwent successful testing in the laboratory setting.

Keywords: Artificial neural network, Luo-based boost converter, fuel cell, Enhanced reliability.

I. Introduction

In fuel cell applications, the utilization of a Luo converter (Luo, 2004) equipped with switched-inductor cells offers significant advantages, particularly in mitigating fuel cell current ripplewhich is a pivotal parameter crucial for both the extended lifespan of the fuel cell and the overall system's reliability. This is achieved through the parallel-charging and series-discharging states of inductors in switched-inductor cells (Ertekin, 2023), which efficiently minimize current fluctuations. The reduction in fuel cell current ripple is instrumental in ensuring a prolonged operational life for the fuel cell and enhancing the reliability of the entire system. Moreover, the incorporation of switched-capacitor cells at the output of the Luo converter further amplifies the benefits (Qi, 2021). This augmentation can be accomplished seamlessly, without the need for additional auxiliary power switches or control mechanisms. The application of switched-capacitor cells serves to elevate the gain of the converter significantly. This enhancement is pivotal, as it contributes to improved overall efficiency and performance without introducing additional complexities to the control system. Adaptive learning, allowing for dynamic adjustments and improved performance in response are obtained by application of ANN as the controller in these converters (Kart, 2023).
In the present study, we have devised a switched-inductor-based Luo converter (Ghasemi, 2022) at the input side and integrated a switched-capacitor cell at the output nodes of the Luo converter. The primary objective is to diminish the input current ripples of the fuel cell and concurrently augment the voltage output of the fuel cell. Given that the generated voltage of a fuel cell is typically modest, necessitating a boost converter for enhancement, the introduced configuration proves instrumental in achieving these objectives. This approach not only optimizes the converter's efficiency but also addresses the intrinsic limitations associated with the voltage levels generated by fuel cells.
The suggested converter features a single power switch, thereby minimizing the intricacies associated with the control mechanism. Comprehensive evaluations, encompassing both simulation and experimental tests, have been conducted, affirming the theoretical foundations of both the proposed converter and controller.

II. The Proposed Boost Converter

Depicted in Figure 1 is the proposed power step-up converter, featuring a switched-capacitor and inductor cell at its input and a switched-capacitor cell at its output. The input side cell is composed of inductors L1 and L2, diodes D1 and D2, and capacitor C1. Conversely, the output side cell involves capacitors C3 and C4, along with diodes D4 and D6. Operational modes are elaborated in Figure 2, with the switch analyzed in both on and off modes.
During the on mode, as delineated in Figure 2a, both inductors L1 and L2 are aligned in parallel with the input voltage, instigating their charging process. Simultaneously, capacitor C1 undergoes charging through diodes D1 and D2. Furthermore, inductor L3 and capacitor C2 experience a charging phase, while capacitors C3 and C4 undergo a dynamic discharge and charge, respectively, forming a circuit path facilitated by diodes D5 and capacitor C2. In this mode, capacitor Co plays a crucial role in supplying the output load.

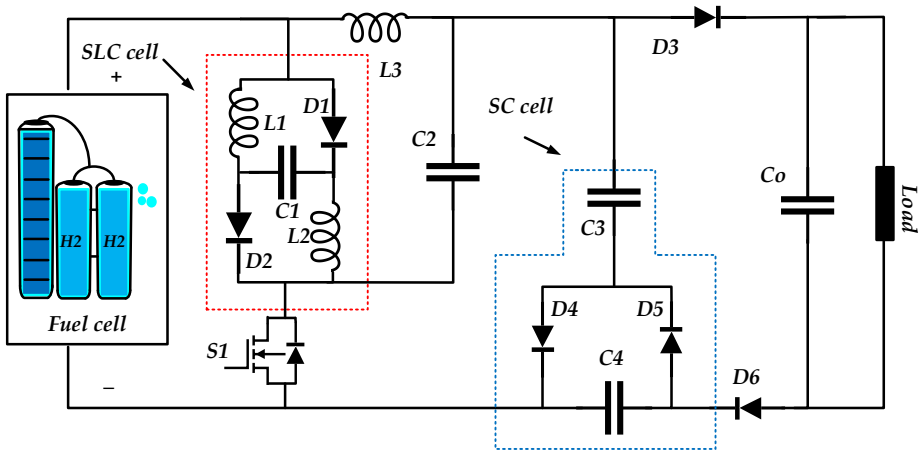

Fig. 1: The suggested boost converter integrated with a fuel cell.

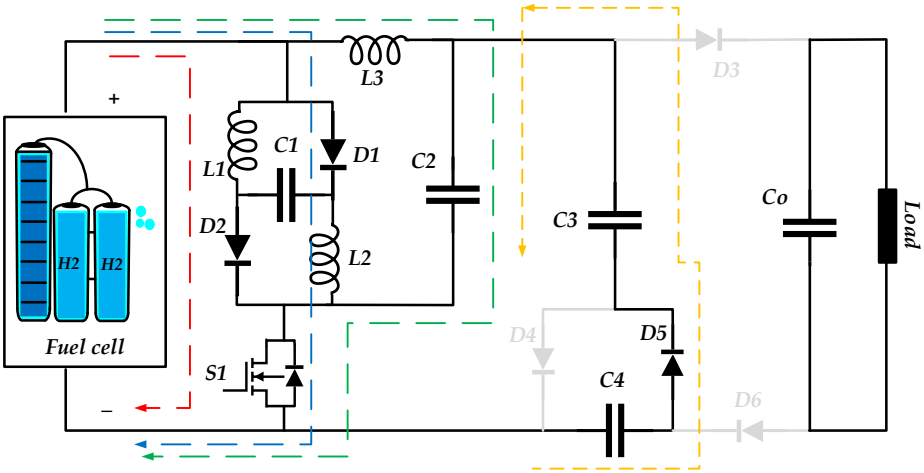

(b)

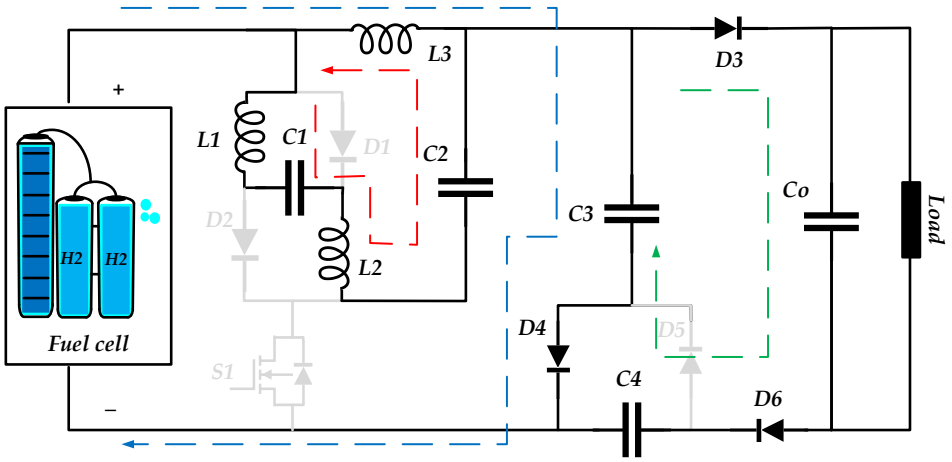

(b)

Fig. 2: The configuration of semiconductor components and charging-discharging states of passive elements in the proposed step-up converter during (a) switch S1 activation and (b) switch S1 deactivation.

Contrarily, in the second operational mode that is shown in Figure 2b, all inductors L1, L2, and L3 discharge, resulting in a reduction in the voltage on capacitors C1 and C2. Capacitor C3 is charged through the input voltage source and diodes D4, while capacitor Co is recharged via diodes D3 and D5. Simultaneously, capacitor C4 undergoes a discharge process.

This intricate operational design, characterized by the alternation of charging and discharging states, demonstrates the versatility of the proposed converter. The unique configuration efficiently manages energy flow, ensuring an optimized power conversion process with minimal current ripple and enhanced voltage stability, particularly essential for fuel cell applications where the reliability and longevity of the system are paramount. The described modes illustrate the dynamic nature of the proposed converter, showcasing its ability to adapt to varying operational requirements.

III. The Proposed ANN Controller

This proposed methodology employs a control system based on a 2-input-1-output artificial neural network (ANN) to govern the circuit. The input values for the first node of the network are normalized Vin values, while the second input node receives data derived from the normalized difference between the reference value (Vref) and the output voltage value (Vo) of the circuit. Subsequently, the ANN-based controller generates an additional duty value (± ΔD), which is then applied to the PWM generator. The block diagram of the control methodology proposed for the boost converter is depicted in Figure 3a.

For network training, exclusively the characteristic features of the circuit were utilized, devoid of any data from other controllers. To acquire the circuit's output values under varied duty and Vin conditions, duty values were systematically adjusted between 40% and 80% in 1% increments, while V_{in} values were modified at 11 V, 12 V, and 13 V using a simulation program. The Vref value is set at 115 V, the V_{inmax} value at 13 V, resulting in the acquisition of 2400 data points, encompassing [V_{err}, V_{in}] vs [± ΔD] values, utilized for network training. The hidden layer of the network consists of 25 neurons, and the Bayesian regularization method is employed for training. The training performance graph, illustrated in Figure 3b, demonstrates the convergence of the network's training error. After 55 epochs, both training and testing performances, measured in terms of Mean Squared Error (MSE), were determined as $9.83 \cdot 10^{-5}$, $14.64 \cdot 10^{-5}$, respectively.

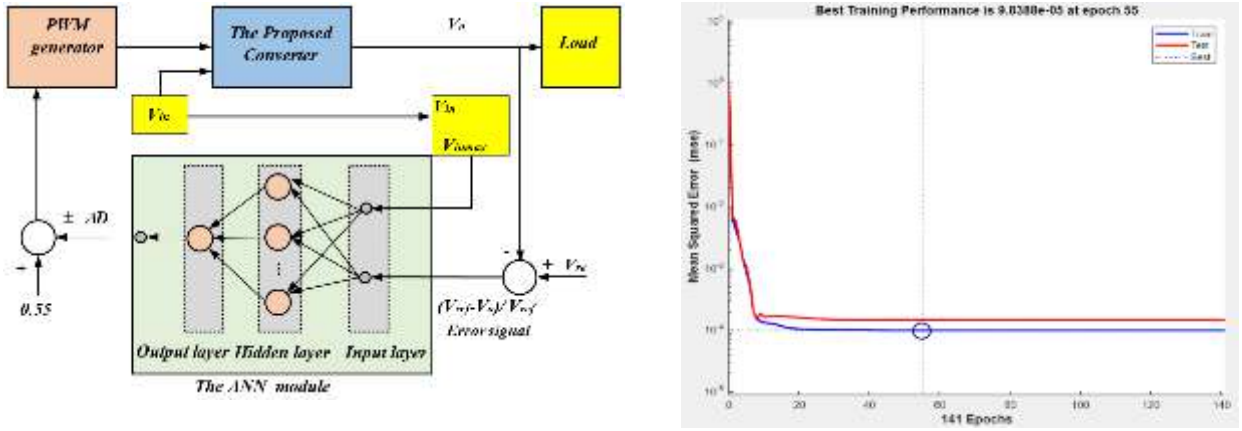

(a) (b)

Fig. 3: (a) Schematic representation of the control methodology, (b) Graph illustrating the training performance.

IV. Results and Discussion

Upon scrutinizing the simulation outcomes, the output voltage values corresponding to input voltages (Vin) of 11 V, 12 V, and 13 V are determined as 116.93 V, 115 V, and 111.68 V, respectively. Figure 4a illustrates that the circuit's output voltage attains its steady-state value at 0.2 seconds when the circuit's supply voltage is 13 V, decreases to 12 V at 0.3 seconds, and further decreases to 11 V at 0.8 seconds. The observed output voltage undergoes a 1.9 V deviation from the reference voltage and experiences a 3 V reduction due to the alteration in the supply voltage, as depicted in the results.

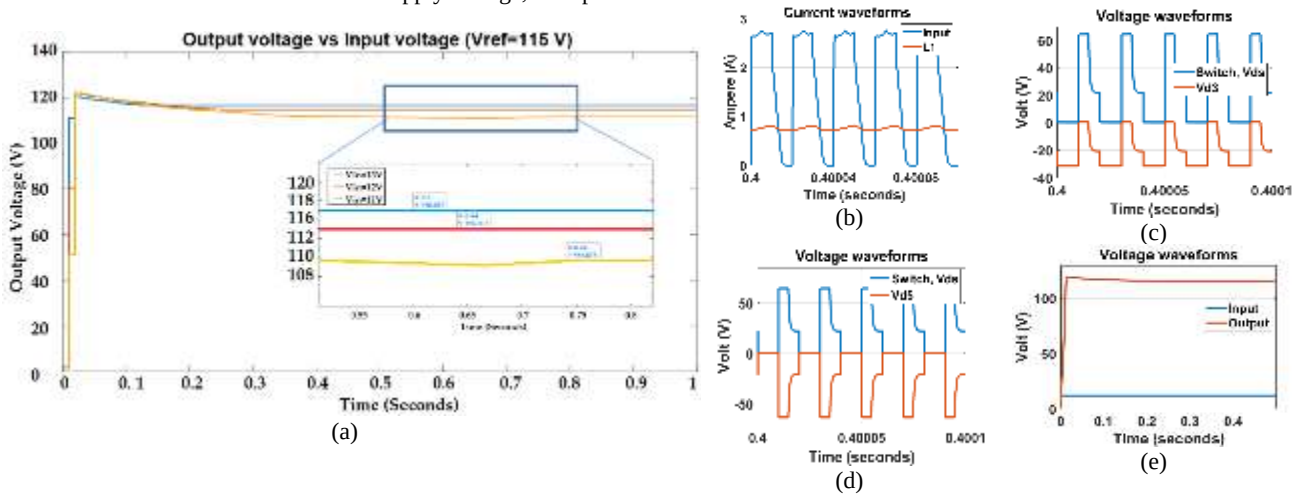

(a) (b) (c) (d) (e)

Fig. 4: (a) The effectiveness of the proposed ANN controller in producing output voltage under varying input voltages, (b) Current waveforms for the fuel cell and inductor L1, (c) Voltage across the drain-source terminals of switch S1 and biasing voltage on diode D3, and (d) D5, along with (e) Input-output voltage profiles.

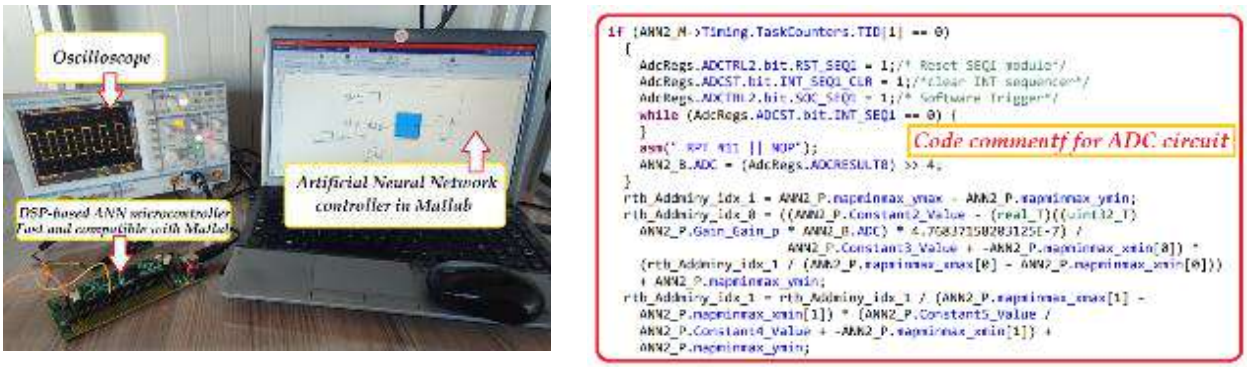

(a) (b)

Fig. 5: (a) Experimental evaluations to acquire PWM signals for switching facilitated by the proposed ANN controller, and (b) Exemplary generated code comments by the DSP controller for the Analog to Digital section of the controller.

Figure 4b illustrates the waveforms of the input source and inductor L1 current. Notably, the negligible current ripple in inductor L1 contributes to a reduction in the input source current duration. The depicted figure demonstrates an average current of approximately 2A for the fuel cell source at 115 V with a 1kΩ output load. Given the high voltage gain of the proposed converter, the input source side maintains a proportional ratio with the output voltage. This implies that for a tenfold increase in voltage, the input side current should be ten times greater than the output current.

The voltage across switch S1 and diodes D3 and D5 is showcased in Figures 4c and 4d, respectively. These figures serve to validate the theoretical analyses presented in Figures 2b and 2c, affirming that when the switch is activated, diode D3 is deactivated while diode D5 is activated. Figure 4e presents the input and output voltage for the proposed converter with a duty ratio of 0.5, clearly illustrating that the converter enhances the voltage at the load side by approximately tenfold.

Figure 5 showcases the experimental test setup designed for the proposed ANN controller. Employing a MATLAB-compatible DSP-based microcontroller, code comments are generated to facilitate understanding. The test bench configuration is depicted in Figure 5a, while Figure 5b illustrates sample code comments generated by the microcontroller, specifically addressing the analog-to-digital conversion process.

V. Conclusion

This study introduces a DC-DC power boost converter with a high voltage gain, designed for the integration of low-voltage fuel cells and controlled by an artificial neural network method. The proposed converter addresses the critical issue of minimizing input current ripple, a key parameter for prolonging the fuel cell's lifespan. Additionally, it achieves a substantial voltage gain suitable for integrating low-voltage fuel cells into grid systems or high-DC voltage applications. The artificial neural network controller, developed using a 2-input-1-output approach, relies solely on the circuit's characteristic features without utilizing data from similar controllers. Notably, the converter features a simplified control system with only one power switch, reducing overall complexity. Implementation of the control mechanism is facilitated through a digital signal processing-based Matlab-compatible microcontroller. Experimental results validate the accuracy of the simulation and theoretical outcomes.

Author Contirbutions

The structure and methodology of the proposed converter were devised by Davut Ertekin, while the design, simulation, and testing of the ANN controller were conducted by Mustafa Özden. Both authors collaborated on the simulation, experimental tests, and the composition and editing of the study.

References

Luo, F. L., Ye, H.,(2004). Positive output multiple-lift push-pull switched-capacitor Luo-converters: IEEE Transactions on Industrial Electronics, pp. 594-602, doi: 10.1109/TIE.2004.825344.

Ertekin, D., (2023): A high gain switched-inductor-capacitor DC-DC boost converter for photovoltaic-based micro-grid applications, CSEE Journal of Power and Energy Systems, doi: 10.17775/CSEEJPES.2022.08440.

Qi, Q., Ghaderi, D., Guerrero, J. M., (2021). Sliding mode controller-based switched-capacitor-based high DC gain and low voltage stress DC-DC boost converter for photovoltaic applications, International Journal of Electrical Power & Energy Systems:106496,https://doi.org/10.1016/j.ijepes.2020.106496.

Kart, S., Demir, F., Kocaarslan, I., Genc, N., (2023). Increasing PEM fuel cell performance via fuzzy-logic controlled cascaded DC-DC boost converter, International Journal of Hydrogen Energy: https://doi.org/10.1016/j.ijhydene.2023.05.130.

Ghasemi, F., Yazdani, M. R., Delshad, M., (2022). Step-Up DC-DC Switching Converter With Single Switch and Multi-Outputs Based on Luo Topology: IEEE Access, pp. 16871-16882, 2022, doi: 10.1109/ACCESS.2022.3150316.

IEEES-109

Life Cycle Analysis of Power Supply Selection for a Chloralkali Production Plant

*[2,3]Sümeyya Ayça and [1,2]Ibrahim Dincer
[1]Ontario Tech University, Clean Energy Research Laboratory, Oshawa, Ontario, Canada
[2]Yildiz Technical University, Department of Mechanical Engineering, Istanbul, Turkey
[3]Istanbul Health and Technology University, Faculty of Engineering and Applied Science, Sutluce, Istanbul, Türkiye
*Corresponding author's e-mail: smyayca@gmail.com

Abstract

This study involves the comparison of carbon emission rates of various power sources that can be used to meet the power required by the system in a chlor-alkali plant where H_2 production takes place. Greenhouse Gases, Regulated Emissions and Energy Use in Transport (GREET) programme was used to select the power source. In this programme, the emission values of carbon dioxide (CO_2), methane (CH_4), sulphur oxides (SO_x) and nitrogen oxides (NO_x) emitted by various renewable and non-renewable power sources were examined. The renewable energy source with the lowest emission rate was determined as Wind Power Generation. Among the non-renewable energy sources, Nuclear Power Generation has the lowest emission rate.

Keywords: GREET, life cycle analysis, carbon emission, methane emission, sulphur oxide emission, nitrogen oxide emission.

I. Introduction

One of the important factors that raise concerns about environmental impacts is the emission of toxic gases. Efforts to reduce these emissions, especially from the burning of fossil fuels and other industrial processes, are increasing day by day. One of the facilities used in the production of hydrogen, which can be produced using renewable energy sources and is a clean and reliable energy carrier, is the Chlor-alkali plant. During the production of H_2 in this plant, a power supply is required for the operation of the system. There are many alternative methods to meet this power requirement. When choosing the most appropriate method among these methods, LCA (Life Cycle Assessment) programmes are used to examine the environmental impacts of a product or process. One of these programmes is GREET (Greenhouse Gases, Regulated Emissions and Energy Use in Transportation). In this study, GREET programme is used to examine the emission rates of toxic gases emitted from an industrial production process. In this study, in which the emission rates of different power sources are analysed, it is tried to select the power source with the lowest emission rate to meet the power requirement of the chlor-alkali production plant, which is one of the hydrogen production plants. In the study, the data are shown graphically in the results section for a better understanding of the results obtained in the emission rate analyses of many renewable and non-renewable energy sources. With this study, it is aimed to provide alternative information on this subject while making power supply selection in a chlor-alkali production facility.

II. Methodology

In this study, a comparison of power sources for the emission rates that should be considered in the selection of the source to meet the power required in a chlor-alkali production facility where hydrogen production takes place. With the data obtained, mainly renewable and non-renewable energy sources are emphasised. The necessary data were obtained from GREET programme. In the programme, a new Pathway was designed for the investigation of the chlor-alkali production plant. Sodium chloride production, hydrochloric acid production and electricity were added as inputs and their definitions were made. As output, 1 kg H_2 value is defined. In the system, only the electricity Pathway section was changed and other Pathways and values were taken as fixed. In the modified electricity Pathway section, 8 different Pathways consisting of renewable and non-renewable energy sources were selected. Pathway1, Pathway2, Pathway3, Pathway4, Pathway5, Pathway6, Pathway7 and Pathway8 were selected as wind energy, grid-connected pv system, geothermal energy, biomass energy, nuclear energy, natural gas, coal and oil-fired system respectively. During the analysis, emission rates of CO_2, CH_4, SO_x and NO_x gases were examined.

III. Results and discussion

In this study, the emission rates of 8 different Pathways consisting of renewable and non-renewable energy sources that can be used as a power source were analysed. In this section, the results obtained from each Pathway are presented. The graphs given below with Figs 1, 2, 3 and 4 are obtained with the data of CO_2, CH_4, SO_x and NO_x emission rates, respectively. These are then listed as follows:
(a) Pathway 1: Wind Power Generation: This selected pathway is a renewable energy source. In this option, where the lowest emission rate was obtained, CO_2, CH_4, SO_x and NO_x emission rates were obtained as 1.65 kg, 0.003 kg, 0.003 kg and 0.005 kg, respectively. The use of this energy source in such a system seems to be advantageous compared to other sources in terms of meeting the power supply of the system as well as low gas emissions.
(b) Pathway 2: Electricity delivered from grid-connected PV system: This system is another renewable and reliable energy source. When compared to Pathway1, it is seen that it is a more advantageous option compared to other sources, although it has a higher emission rate. CO_2, CH_4, SO_x and NO_x emission rates respectively, 3.73

kg, 0.007 kg, 0.003 kg and 0.008 kg were obtained.

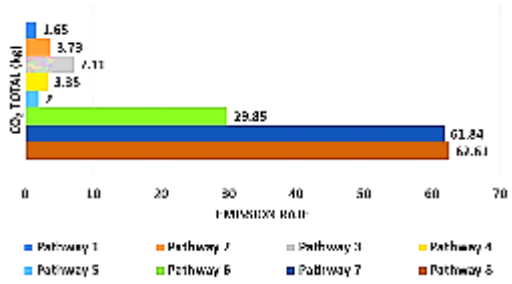

Fig. 1. CO_2 Emission rate

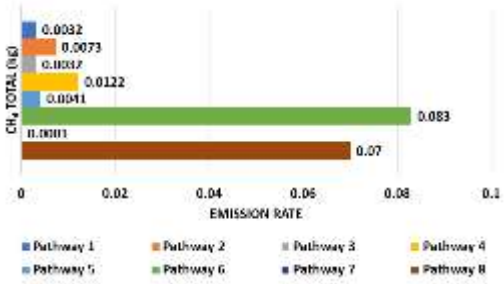

Fig. 2 CH_4 Emission rate

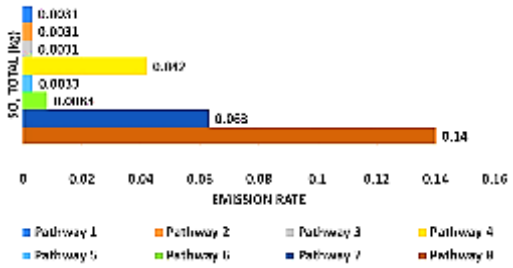

Fig. 3. SO_x Emission rate

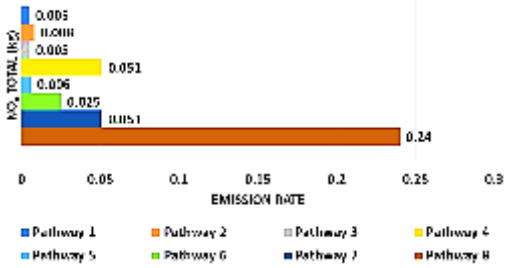

Fig. 4 NO_x Emission rate

(c) Pathway 3: Geothermal Electricity Production: This system is also a renewable energy source like the 2 Pathways given above. CO_2, CH_4, SO_x and NO_x emission rates were obtained as 7.11 kg, 0.003 kg, 0.003 kg and 0.005 kg, respectively. In this option, CO_2 emission rate is higher than Pathway1 and Pathway2, CH_4, SO_x emission rates are the same and NO_x emission rate is less than the other Pathway2.
(d) Pathway 4: Biomass Power Generation: In this option, which is another renewable energy source, CO_2, CH_4, SO_x and NO_x emission rates are 3.35 kg, 0.012 kg, 0.042 kg and 0.051 kg, respectively. In this option, where CO_2 emission is lower than Pathway2, SO_x and NO_x emission data are higher than the 3 Pathways mentioned above.
(e) Pathway 5: Nuclear Power Generation: In this option, which is a non-renewable energy source, CO_2, CH_4, SO_x and NO_x emission rates were obtained as 2 kg, 0.004 kg, 0.003 kg and 0.006 kg, respectively. These data are very important for this study. These data can be evaluated in terms of alternative source as a less emission source option.
(f) Pathway 6: Natural Gas-Fired Power Generation: When the data obtained from Natural Gas, which is a non-renewable energy source in this section, it is seen that CO_2, CH_4, SO_x and NO_x emission rates are 29.85 kg, 0.083 kg, 0.008 kg and 0.025 kg, respectively. Compared to the other Pathway options, a significant increase in CO_2 and CH_4 emission rates has been achieved.
(g) Pathway 7: Coal-Fired Power Generation: In this option, which is another non-renewable energy source, CO_2, CH_4, SO_x and NOx emission rates are 61.84 kg, 0.0001 kg, 0.063 kg and 0.051 kg, respectively. Although the low value of CH_4 emission is pleasing, the high emission rates in other gases are worrying.
(h) Pathway 8: Oil-Fired Power Generation: In this other option, which is one of the non-renewable energy sources, CO_2, CH_4, SO_x and NO_x emission rates were obtained as 62.61 kg, 0.007 kg, 0.14 kg and 0.24 kg, respectively. When the toxic gas emission results of all other Pathways are considered, it is seen that the other gas emissions are much higher in this Pathway except CH_4 emission.

IV. Conclusions

In this study, the emission rate of a power source to be determined for use in a chlor alkali plant was analysed. In order to determine this power source, the emission rates of 8 different renewable and non-renewable energy sources were analysed. When the results obtained are analysed, it is seen that the lowest emission rate is obtained from the Wind Power Generation system determined as Pathway1. Among the non-renewable energy sources, it is seen that the Nuclear Power Generation system, defined as Pathway5, has the lowest emission rate. In this study, Wind Power, a renewable and clean energy source, is proposed as a power source in a chlor-alkali system.

References

Dincer, Ibrahim; Aydin, Muhammed Iberia (2022): An assessment study on various clean hydrogen production methods. Energy. 245, p. 123090. doi.org/10.1016/j.energy.2021.123090

Dincer, Ibrahim; Aydin, Goren, Yagmur (2023): A comprehensive review on environmental and economic impacts of hydrogen production from traditional and cleaner resources. Journal of Environmental Chemical Engineering. 11, p. 111187. doi.org/10.1016/j.jece.2023.111187.

IEEES-110

Decarbonisation Targets and Actions in Turkish Maritime Sector Within the Framework of the Financing Agreement for the Annual Action Plan in favor of Türkiye for 2021

Dr. Halil Çeçen,
Nuh Naci Yazgan University, Faculty of Law, Department of the European Union Law, Ertuğrul Gazi Mah. Nuh Naci Yazgan Yerleşkesi Küme Evler, Kocasinan, Kayseri, 38170, Türkiye.
*E-mail: hcecen@nny.edu.tr

Abstract

One of the fields of action specified in the Financing Agreement for the Annual Action Plan in favor of Türkiye for 2021 (financing agreement) is the field of "Sustainable Green Energy and Transport". As stated in the relevant field of action, greenhouse gas emissions from maritime activities constitute 2.6% of total global emissions, and decarbonization in the maritime sector is a major challenge.
In this context, Türkiye approved MARPOL Annex VI in 2013, which set the limits for NOx and SOx emissions from ports and ship exhausts and prohibits the emissions of substances from ships that deliberately damage the ozone layer. In addition, the International Maritime Organization set a net zero target in greenhouse gas emissions from international maritime activities by 2050, in July 2023. In order to achieve these targets, the Turkish commercial fleet of vessels need to be modernized through the inclusion of new sustainable technologies.
The financing agreement specified three support fields which one of them is "decarbonization and green shipping program in maritime". This program will target the retrofitting of old vessels and inclusion of new vessels to support the transition to an environmentally friendly maritime fleet and to improve the supply of alternative fuel infrastructure.
In order to achieve these targets, grants will be provided by the European Bank for Reconstruction and Development (EBRD) to enable investments. EBRD, in coordination with the Turkish Ministry of Transport and Infrastructure, will prioritize the investments by determining a pilot project pool with the technical and administrative support of the EU Delegation. Therefore, the field of actions in the financing program will support the Turkish maritime operations to become environmentally friendly, by including the new green fleet of vessels and improving port facilities infrastructure and by increasing the effectiveness of the climate-related corporate governance of private sector.

Keywords: decarbonisation of Turkish maritime, sustainable green energy and transport, green ports, green fleet of vessels, financing agreement.

I. Introduction

The Paris Agreement entered into force in Turkish law by being published in the Official Journal of Turkish Republic dated 7 October 2021 and numbered 31621. In order to achieve the heat targets decided in the Paris Agreement, it will be necessary to act with a holistic approach, covering all sectors. This issue is also stated in the Turkish Green Deal Action Plan adopted by the Ministry of Commerce (Ministry of Commerce, 2021). In the Turkish Green Deal Action Plan, targets for decarbonization of the Turkish maritime sector are also determined. And policies regarding the decarbonisation of Turkish maritime sector such as introducing zero-emission vehicles in maritime transportation, increasing the production/use of sustainable and alternative fuels, developing green maritime and green port practices were set as targets. Key policy areas to achieve these targets such as the construction of new ships and retrofitting of existing ships were considered. In addition, once the Turkish Climate Change Bill prepared by the Ministry of Environment, Urbanization and Climate Change becomes law, significant powers and duties shall be given to the Ministry of Transport and Infrastructure to achieve these goals in Turkish maritime sector (Ministry of Environment, Urbanisation and Climate Change, 2022).

In the "Implementing Decision on the financing of the annual action plan in favor of Turkey for 2021" adopted by the European Commission, the actions and fund allocation to be carried out for the green conversion of and decarbonization in the Turkish maritime sector were arranged in detail. This decision of the Commission, which contributes to the European Green Deal in addition to the legal regulations in Turkish law, shall have an impact on the practices in the Turkish maritime sector.

In this research, the "Implementing Decision on the financing of the annual action plan in favor of Turkey for 2021" adopted by the European Commission is reviewed within the framework of the European Green Deal and the Turkish Green Deal Action Plan, and the green conversion of the Turkish maritime sector is discussed.

II. Methodology

In this research, the legal regulations in the *acquis communautaire*, the current documents in Turkish law, the works of Turkish administrative authorities and international law documents are reviewed as a methodology. Additionally, studies in the literature were also examined. The subject of the research concerns the current regulations and developments between the European Union (EU) and Türkiye. For this reason, the research, which reviews the current policies related to the decarbonisation of Turkish maritime sector within the framework of the relations between the EU and Türkiye, may contribute to the academic studies in the field of European Union studies in Türkiye.

III. Analysis

In accordance with the Article 9(1) of the "Regulation (EU) 2021/1529 of 15 September 2021 establishing the Instrument for Pre-Accession assistance (IPA III)", the annual or multi-annual action plans and measures and direct or indirect management of the "Regulation (EU, Euratom) 2018/1046 of the European Parliament and of the Council of 18 July 2018 on the financial rules applicable to the general budget of the Union" are regulated. The purpose of Regulation 2021/1529 is to provide political, institutional, legal, administrative, social and economic support to the candidate countries, including Türkiye, in order to comply with the Union values and "to progressively align to Union rules, standards, policies and practices in terms of future Union membership". In this context, "Implementing Decision of 10.12.2021 adopting the Instrument for Pre-Accession Assistance (IPA III) Programming Framework for the period 2021-2027" was adopted by the Commission.

The mentioned implementing decision includes the title "Window 3: Green Agenda and Sustainable Connectivity". In the relevant section, green conversion of the transportation sector, including maritime, and prevention of marine pollution are stated among the main targets. The financial framework of the implementing decision was set under the "Implementing Decision of 16.12.2021 on the financing of the annual action plan in favor of Turkey for 2021", also adopted by the European Commission. It was stated by the Commission that this decision would also contribute to the European Green Deal due to its content. The fifth annex titled "Sustainable Green Energy and Transport" section of the "Implementing Decision of 16.12.2021 on the financing of the annual action plan in favor of Turkey for 2021", includes important actions regarding green conversion of the Turkish maritime sector.

In the Commission's Implementing Decision dated 16.12.2021, "Maritime Decarbonisation and Green Shipping Program" was decided among the areas of support. As a target in the relevant area, the policies in regard to retrofitting of old vessels and the construction of new vessels were determined in order to own environmentally friendly, low-emission, energy-efficient maritime fleet, which requires significant investments in the Turkish maritime sector. In addition, improving the supply of alternative fuel infrastructure to power port activities is counted as another action. In this context, strategies for decarbonisation of Turkish maritime sector include reducing greenhouse gas emissions, deploying renewable energy sources, and supporting climate resilient investments to promote energy efficiency and circular economy.

Within the framework of the program, the required financial sources have been provided as grants and loans by the European Bank for Reconstruction and Development (EBRD). Additionally, technical support and capacity development is provided within the framework of the program. It is also necessary here to express the contributions of the EBRD to the country. EBRD invested in Türkiye more than €17.3 billion (Sari, 2023). Accelerating Turkey's Green Economy Transformation and Regional Energy Connectivity is also among EBRD's operational priorities. In addition to the EUR 20 million EU IPA contribution, the program is expected to raise additional investment of EUR 50 million in investment from the EBRD and co-financiers. The projects on the development of the bunkering of alternative fuel infrastructure with LNG, Bio-LNG, hydrogen and ammonia, the use of renewable equipment such as solar panels in port operations, and the use of zero or low emission vehicles in the coastal part of the port will be supported tith the funds provided by the EBRD. The retrofitting of existing vessels and the construction of new green vessels are also intended to accelerate the conversion into a low-carbon, energy-efficient maritime fleet and to create a sustainable marine environment. It has also been stated by the EBRD that projects that do not target green transformation measures will not be supported (European Commission, 2021b).

The contribution of the Commission's Implementing Decision to the policies of Türkiye in this context is also important. Firstly, Türkiye committed to reduce greenhouse gas emissions resulting from maritime activities at the international level. Türkiye approved MARPOL Annex VI in 2013, which set the limits for NOx and SOx emissions from ports and ship exhausts and prohibits the emissions of substances from ships that deliberately damage the ozone layer. The International Maritime Organisation (IMO)'s greenhouse gas emissions reduction strategy in 2023 set the indicative checkpoints as "to reduce the total annual GHG emissions from international shipping by at least 20%, striving for 30%, by 2030, compared to 2008; and to reduce the total annual GHG emissions from international shipping by at least 70%, striving for 80%, by 2040, compared to 2008" (International Maritime Organisation, 2023). Türkiye also signed "the Ministerial Declaration of the Union for the Mediterranean on sustainable blue economy" (Union for the Mediterranean, 2021) and "the Bucharest Ministerial Declaration on the Common Maritime Agenda for the Black Sea" (Common Maritime Agenda for the Black Sea, 2019) to support the policies for ensuring sustainable, climate-neutral and zero-pollution maritime transportation in both the Mediterranean and the Black Sea.

The relevant Implementing Decision of the Commission is also important in terms of providing the green maritime targets stipulated in the Eleventh and Twelfth Development Plans of Türkiye. In the Eleventh Development Plan, it was stated that Türkiye would follow the green growth policy and transform the vessels used in long-distance passenger and vehicle transportation into environmentally and energy-friendly electric ships and would expand the sustainable green port practices (Presidency of the Republic of Turkey Presidency of Strategy and Budget, 2019). The Twelfth Development Plan for the years 2024-2028 include the policies of Türkiye towards supporting the green port practices by encouraging the use of low-emission/zero emission machinery and equipment to minimize environmental impacts by increasing energy efficiency in port operations. These actions require investments by both the private and public sectors. In this context, the Commission's Implementing Decision directly supports the targets in the national strategy and policy documents and the current projects and programs carried out by public authorities (Presidency of the Republic of Turkey Presidency of Strategy and Budget, 2023).

Another contribution of the Commission's Implementing Decision is to the modernisation of Turkish fleet. A significant part of the vessels in Turkish fleet is more than 20 years old. In addition, vessels in the Turkish commercial fleet also need to be modernized by including new sustainable technologies. However, the Turkish maritime industry has a key role for economic growth and acts as a catalyst for global trade (European Commission, 2021b). At the same time, the transportation sector, including the maritime, constitutes 22.6% of the total greenhouse gas emissions in Türkiye in accordance with the National Inventory Report submitted to the UNFCCC in 2021 (Turkish Statistical Institute, 2021). And the maritime industry is considered to grow in the long term due to the increase in economic growth of Türkiye. Additionally, many sea ports in Türkiye are vulnerable to climate change risks and lack energy efficiency, causing local air and water pollution (European Commission, 2021b).

The maritime trade of Türkiye was approximately doubled from 2005 to 2015, and this growth constituted 6.27% of the annual growth rate. This is because Turkish ports constitute important pillars in international trade. However, Turkish ports are also at an early stage in the sector's green conversion. Since fossil fuels are used as a power source in Turkish maritime activities, energy efficiency measures are also important to reduce CO2 emissions from maritime activities. A few Turkish ports have alternative fuel bunkering infrastructure. In this context, the grants and credits of the EBRD under the Commission's Implementing Decision shall help to build infrastructure at the sea ports of Türkiye to use LNG, hydrogen, ammonia, electricity and biofuels (European Commission, 2021b).

Achieving the objectives within the framework of the Commission's Implementing Decision is only possible with the close cooperation of the Turkish authorities, which are committed to promoting climate change mitigation policies and initiatives in the maritime sector, and the financial support of the European Union. The projects to be implemented will contribute to the creation of Turkish fleet of green ships and the management of the private sector in a climate-related manner. And it will gradually contribute to the environmentally friendly conversion of Turkish maritime activities and significantly improve the environmental performance of the region. Performing the Commission's Implementing Decision will strengthen the integration of the EU and Türkiye in the field of transportation by ensuring progressively compliance of the Turkish maritime sector with the EU transportation policies, increase the sustainability and efficiency of Turkish maritime transportation.

IV. Results and discussion

Within the framework of the Regulation 2021/1529 of 15 September 2021 establishing the Instrument for Pre-Accession assistance (IPA III), the European Commission announced the IPA III Program covering the years 2021-2027 for Türkiye, which is a candidate country for the membership to the EU. One of the most important parts of the program is the fifth annex titled "Sustainable Green Energy and Transport", includes actions on green conversion of the Turkish maritime sector. In this context, the financement conditions of the program, which contributes to both the compliance of the Turkish maritime sector with the *acquis communautaire* and the implementation of the European Green Deal, were determined by the "Implementing Decision of 16.12.2021 on the financing of the annual action plan in favor of Turkey for 2021" by the European Commission. Therefore the financement program, which also supports the policies of Türkiye towards green maritime in the Mediterranean and the Black Sea, its commitments to the climate change mitigation and implementation of the strategies of IMO in Türkiye, will help decarbonising the Turkish maritime sector. In this context, retrofitting of the old Turkish vessels to be environmentally friendly, building new ships equipped with green technology, reducing greenhouse gas emissions in port activities, and increasing green port practices by using renewable energy sources in portside activities are stated among the actions to be taken.

The support provided to Turkish seaports, which considered an important pillar in international trade, by the Commission's "Implementing Decision of 16.12.2021 on the financing of the annual action plan in favour of Turkey for 2021" within the framework of the IPA III program, shall not only ensure the decarbonization of the Turkish maritime transportation, but shall also enable the performance of the targets in the Twelfth Development Plan for the years 2024-2028 of Türkiye. The mentioned decision of the Commission will also contribute to the achievement of the targets under the Paris Agreement and IMO strategies by reducing greenhouse gas emissions. Via the funds provided by EBRD under IPA III program, the compliance of the Turkish maritime transportation with the acquis communautaire will also be monitored.

V. Conclusion

In the research, the effects of the Commission's "Implementing Decision of 16.12.2021 on the financing of the annual action plan in favour of Turkey for 2021" and the policies of Türkiye in decarbonisation of the Turkish maritime sector are reviewed. As a conclusion, the financial support provided by the EBRD under the Commission's relevant decision to apply financing for the green conversion of the Turkish maritime sector shall increase the cooperation between the EU and Türkiye, accelerate compliance of Turkish policies with the acquis communautaire in the field of transportation and will contribute to the climate change mitigation by reducing greenhouse gas emissions under the framework of the Paris Agreement and decarbonizing the Turkish maritime sector which is considered an important pillar in international trade.

References

Annex 5 to the Commission Implementing Decision on the financing of the annual action plan in favour of Turkey for 2021. (2021). https://neighbourhood-enlargement.ec.europa.eu/system/files/2022-01/C_2021_9734_F1_ANNEX_EN_V1_P1_1671889.PDF.

Common Maritime Agenda for the Black Sea. (2019). the Bucharest Ministerial Declaration on the Common Maritime Agenda for the Black Sea. https://black-sea-maritime-agenda.ec.europa.eu/206/common-maritime-agenda-black-sea.

European Commission. (2021a). Commission Implementing Decision of 10.12.2021 adopting the Instrument for Pre-Accession Assistance (IPA III) Programming Framework for the period 2021-2027. Brussels, 10.12.2021 C(2021) 8914 final. https://neighbourhood-enlargement.ec.europa.eu/system/files/2022-01/C_2021_8914_COMMISSION_IMPLEMENTING_DECISION_EN.pdf.

European Commission. (2021b). Commission Implementing Decision of 16.12.2021 on the financing of the annual action plan in favour of Turkey for 2021. Brussels, 16.12.2021 C(2021) 9734 final. https://neighbourhood-enlargement.ec.europa.eu/system/files/2022-01/C_2021_9734_F1_COMMISSION_IMPLEMENTING_DECISION_EN_V4_P1_1671449.PDF.

International Maritime Organization. (2023). 2023 IMO Strategy on Reduction of GHG Emissions from Ships. https://wwwcdn.imo.org/localresources/en/MediaCentre/PressBriefings/Documents/Clean%20version%20of%20Annex%201.pdf.

Ministry of Environment, Urbanisation and Climate Change. (2022). Climate Change Bill. https://www.gebzeto.org.tr/wp-content/uploads/2022/10/TOBB-%C4%B0klim-De%C4%9Fi%C5%9Fikli%C4%9Fi-Kanunu-Tasla%C4%9F%C4%B1.pdf.

Presidency of the Republic of Turkey Presidency of Strategy and Budget. (2019). Eleventh Development Plan 2019-2023. https://www.sbb.gov.tr/wp-content/uploads/2022/07/Eleventh_Development_Plan_2019-2023.pdf.

Presidency of the Republic of Turkey Presidency of Strategy and Budget. (2023). Eleventh Development Plan 2024-2028. https://www.sbb.gov.tr/wp-content/uploads/2023/11/On-Ikinci-Kalkinma-Plani_2024-2028_17112023.pdf.

Regulation (EU) 2021/1529 of the European Parliament and of the Council of 15 September 2021 establishing the Instrument for Pre-Accession assistance (IPA III), Official Journal of the European Union, L 330, 20.9.2021, p. 1–26, https://eur-lex.europa.eu/legal-content/EN/ALL/?uri=CELEX:32021R1529.

Regulation (EU, Euratom) 2018/1046 of the European Parliament and of the Council of 18 July 2018 on the financial rules applicable to the general budget of the Union, Official Journal of the European Union, L 193, 30.7.2018, p. 1–222, https://eur-lex.europa.eu/legal-content/EN/TXT/?uri=CELEX:32018R1046.

Sari, D. (2023). "EBRD unveils plan for greener maritime sector in Türkiye", https://www.ebrd.com/news/2023/ebrd-unveils-plan-for-greener-maritime-sector-in-trkiye.html.

Turkish Statistical Institute. (2021). National Inventory Report for submission under the United Nations Framework Convention on Climate Change April 2021. https://unfccc.int/documents/271544.

Union for the Mediterranean. (2021). Ministerial declaration on Sustainable Blue Economy 2 February 2021. https://ufmsecretariat.org/wp-content/uploads/2021/02/Declaration-UfM-Blue-Economy-EN-1.pdf.

IEEES-111

Review of the Current Developments About Reducement of the Greenhouse Gas Emissions from Maritime Activities According to Turkish Climate Change Bill

Dr. Halil Çeçen
Nuh Naci Yazgan University, Faculty of Law, Department of the European Union, Ertugrul Gazi Mah. Nuh Naci Yazgan Yerleskesi Kume Evler Kocasinan, Kayseri, 38050, Türkiye
*E-mail: hcecen@nny.edu.tr

Abstract

This research delves into the regulations aimed at reducing greenhouse gas emissions from the maritime activities in the Climate Change Bill, which is expected to come into force in Turkish law. In this context, Turkish legal regulations are discussed together with the literature review.
Turkish Climate Change Bill, prepared in order to comply with the international commitments and acquis communautaire, comprises also the general framework of reducing greenhouse gas emissions from maritime activities, which constitute a sub-branch of the transport sector. The Climate Change Bill entrusts the Ministry of Transport and Infrastructure, as the competent ministry, the following tasks: to develop low or zero emission transport options in maritime; to work towards the decarbonization of ports and all components in the shipping value chain; to deploy low- or zero-emission vessels and to take the necessary measures to ensure the adaptation of the maritime activities to climate change by determining the negative effects of climate change on the maritime sector.
The relevant provisions of the Climate Change Bill regarding the maritime sector, comprehensively address the decarbonization of the maritime sector at the Ministry level. As the relevant provisions of the Turkish Climate Change Bill are reviewed together with the Green Deal prepared by the Turkish Ministry of Commerce in order to comply with the European Green Deal and the projects of the Directorate-General for Maritime Affairs of Türkiye funded by the European Commission for green maritime practices, it is concluded that in Turkish law, the numbers of primary and secondary regulations are currently increased for decarbonization process of the martime sector in order to comply with the international commitments regarding to global fight against climate change.

Keywords: Turkish maritime sector, green maritime, Turkish Climate Change Bill.

I. Introduction

Transport is among the sectors for reducing greenhouse gas emissions in combating climate change and is particularly emphasized in the renewable energy directives and regulations of the European Union. The Directive 2003/30/EC aimed to increase the use of biofuels in the transport sector by establishing the target was 5,75% at the Member States level by 2010 [Directive 2003/30; Article 3(1)(b)(ii)], while the Directive 2009/28/EC imposed on the EU Member States to achieve 10% renewable energy share in the energy consumption in transport [Directive 2009/28, Article 3(4)].

The target set in the Directive 2018/2001 was “to ensure that the share of renewable energy within the final consumption of energy in the transport sector at least 14 % by 2030” [Directive 2018/2001, Article 25(1)]. This target was increased to 29% by Directive 2023/2413 [Directive 2023/2413, Article 25(1)(a)(I)]. Both the International Maritime Organization and the European Union work on to reduce greenhouse gas emissions resulting from activities in the maritime sector, which is a sub-dimension of the transportation sector.

In this context, the International Maritime Organization (IMO) determined the target “to reduce CO2 emissions per transport work, as an average across international shipping, by at least 40% by 2030, compared to 2008” in its 2023 “Strategy on Reduction of GHG Emissions from Ships” (International Maritime Organisation, 2023). The efforts of the European Union and IMO to reduce greenhouse gas emissions resulting from activities in the maritime sector trigger the necessary studies in Turkish law.

The Climate Change Bill, which was prepared for the first time in Turkish law, is important in terms of fulfilling Turkiye’s commitments under the Paris Agreement and also complying with the acquis communautaire. In the draft text of Climate Change Bill, policy areas for reducing greenhouse gas emissions resulting from activities in the maritime transportation sector are expressed in a general framework. In addition, the General Directorate of Maritime Affairs of Türkiye is supported by the European Commission within the scope of the "Maritime Decarbonisation and Green Shipping Programme for Turkey" project.

II. Experimental Procedure/Methodology/System Description

In this research, the Turkish Climate Change Bill and the relevant documents in Turkish law were examined together with the acquis communautaire, international regulations and the work of the International Maritime Organization. There are limited number of studies in the literature related to the subject of the research. This situation constitutes the limitation of this research. The subject of the research is based on current regulations. For this reason, the research which reviews the current regulations in Turkish law may contribute to academic studies in Türkiye.

III. Analysis

By signing of the “United Nations Framework Convention on Climate Change (UNFCCC)” in 1992, the Parties agreed to combat

climate change globally. Although the Article 4(1)(c) fo UNFCCC regulated to reduce the greenhouse gases in transport, the Kyoto Protocol adopted at the 3rd Conference of the Parties to the UNFCCC built the cornerstone regulation in this regard. The Parties committed to "reduce greenhouse gas emissions in the transportation sector" [Kyoto Protocol, Article 2(1)(a)(vii)]. There was also a provision stating that "the Parties would work together with the International Maritime Organization (IMO) to reduce greenhouse gas emissions arising from international maritime activities" [Kyoto Protocol, Article 2(2)]. In this context, the European Union (EU) as a party of the Kyoto Protocol adopted regulations in the fields of green transformation and decarbonization of maritime activities.

Türkiye, which is a candidate country for the membership to the European Union, continues its work on the chapters of energy and climate change among its compliance policies with the acquis communautaire. In this context, Turkish Green Deal Action Plan was adopted by the Ministry of Commerce in accordance with the European Green Deal targets. Taking the targets of European Green Deal such as introduction zero-emission vehicles in the field of transport, development of electric vehicle infrastructure, increasing the production/use of sustainable and alternative fuels (European Commission, 2019), the Turkish Green Deal Action Plan determines the actions to perform in the Turkish maritime sector to combat climate change and reduce sector-related greenhouse gas emissions (Ministry of Commerce, 2021).

In this respect, the Turkish Green Deal Action Plan aims to implement actions in sustainable and smart transport and the objectives of extending green maritime and green port practices are also included. In addition, reducing harmful emissions arising from the maritime sector and supporting green maritime, environmentally friendly changes will be implemented by the construction of new vessels which use low-emission alternative fuels and the retrofitting of existing vessels. In accordance with the Turkish Green Deal Action Plan, creating a financial support mechanism for innovative technologies which will be used for sustainable and safe transport, is also considered by the Ministry of Commerce (Ministry of Commerce, 2021).

Within the scope of efforts to reduce harmful emissions of the maritime sector and to support green maritime, in line with the targets established in the Turkish Green Deal Action Plan, the "Regulation on the Promotion of the Construction of New Ships to Replace Scrapped Turkish Flag Ships" was published in the Official Gazzette of the Turkish Republic dated 28.04.2021 and numbered 31468. In accordance with the provisions of the relevant regulation, "a grant of 25% of the conversion cost is provided to ship owners who converts the power for the main engines of existing ships from fossil fuel to an alternative environmentally friendly energy source" (Ministry of Commerce, 2022).

Another important development in this regard is the European Commission's "Implementing Decision of 16.12.2021 on the financing of the annual action plan in favour of Turkey for 2021". The fifth action of the relevant decision is titled as "Sustainable Green Energy and Transportation". In the relevant part of the decision it is stated that Turkey is one of the fastest growing energy economies in the world and that the demand for energy and electricity is increasing rapidly in parallel with the growing economy. In this context, various action plans were determined to perform the green conversion in the Turkish maritime sector in order to reduce the increasing greenhouse gas emissions. These action plans include the retrofitting of existing ships and the incorporation of new ships to support the transformation to an environmentally friendly, low emissions carbon, energy and fuel efficient maritime fleet. It also aims to improve the supply of alternative fuel infrastructures to power port operations, focusing primarily on reducing greenhouse gas emissions, while supporting climate-resilient investments that promote energy efficiency (European Commission, 2021).

As a significant progress, Türkiye signed the declaration titled "Union for the Mediterranean (UfM) Ministerial declaration on Sustainable Blue Economy" dated February 2, 2021. By signing the relevant declaration, Türkiye undertakes important commitments regarding sustainable, climate-neutral and zero-pollution maritime transport and ports. Within the framework of the declaration, the goal is to ensure the potential role of the maritime transport sector in reducing global greenhouse gas emissions, taking into account the vital and strategic role of maritime transport in the Mediterranean (Union for the Mediterranean, 2021). In order to promote the transformation of ship vessels and ports in the Mediterranean towards carbon-neutrality and zero pollution, the Ministers calls for "the specific needs and priorities of Mediterranean countries, including investments in the provision of Onshore Power Supply" and "the development of alternative fuels for ships, as well as investments in energy-saving technologies for port activities and an increase in infrastructure investments". The Ministers envisage "encouraging Mediterranean countries to actively cooperate and contribute to the implementation of joint projects in the provision of clean energy and technology" (Union for the Mediterranean, 2021).

It should be stated here that Türkiye, which were criticized for a long time for not signing the Paris Agreement (Alan, 2021), became a party to the Agreement and the Paris Agreement came into force in Turkish law by being published in the Official Gazette of the Turkish Republic dated 7 October 2021 and numbered 31621. Therefore, the temperature targets in the Paris Agreement, which requires reducing greenhouse gas emissions within the framework of combating climate change, thus became a part of internal law of Türkiye.

In the 2023 Türkiye Progress Report published by the European Commission, it is stated that Türkiye was about to adopt a climate law (European Commission, 2023). The law mentioned by the European Commission is the Climate Change Bill prepared by the Ministry of Environment, Urbanization and Climate Change (Türkoğlu Üstün, 2021), and the draft text was submitted to the approval of the Turkish Grand National Assembly.

The Climate Change Bill includes the reduction of greenhouse gas emissions in combating and adaptation to climate change and planning and implementation tools for these issues in line with the green development vision and net zero emission target, and important provisions regarding activities in the maritime transport sector are also included in the Climate Change Bill. In particular, the Ministry of Transport and Infrastructure is delegated important powers and duties: In this context, with the provisions set out in the Climate Change Bill, the Ministry of Transport and Infrastructure shall have the authority to develop and extend the use of low or zero emission, energy efficient and alternative clean fuels in international and intercity passenger and freight transport by sea. The Ministry of Transport and Infrastructure also shall be responsible to work towards decarbonising ports, maritime transport activities and all elements in the shipping value chain, developing zero-emission refueling and charging capabilities, deploying low- or zero-emission

ships, creating green shipping corridors and taking the necessary measures for the adaptation of these sectors to climate change by determining the negative impacts of climate change on the transport and maritime sectors. As it is understood from the Climate Change Bill, the Ministry of Transport and Infrastructure is delegated important duties in taking actions and putting these actions into effect in order to achieve green conversion and decarbonization of the Turkish maritime sector (Ministry of Environment, Urbanisation and Climate Change, 2022).

In addition, in case the emissions trading system in the draft law is established, one of the sectors which will be included in the system within the framework of compliance with the acquis communautaire, may be the maritime sector. The European Union has already included the maritime activities into its Emissions Trading System and has adopted the Regulation 2023/957 which regulates the inclusion of maritime activities into EU Emissions Trading System. In this context, by including the activities in the Turkish maritime sector, Climate Change Bill shall contribute to the compliance of Turkish law with the acquis communautaire but including the Turkish maritime activities into the Emission Trading System, which is considered to be established in Türkiye, shall also contribute to fully comply with the European Union's related directives and regulations (Ministry of Environment, Urbanisation and Climate Change, 2022).

In the Twelfth Development Plan covering the years 2024-2028, there are important action plans regarding decarbonization and green conversion of the maritime activities in line with the provisions included in the Turkish Climate Change Bill. In this context, "green port practices will continue to be supported by encouraging the use of low-emission/non-emission-producing machinery and equipment to minimize environmental impacts by increasing energy efficiency in port operations" and "the R&D activities for extending the environmentally friendly, new generation marine vehicles shall be promoted" (Presidency of the Republic of Türkiye Presidency of Strategy and Budget, 2023).

In parallel with these current developments regarding the green conversion in Turkish maritime sector, the provisions of the Turkish Climate Change Bill, which regulate that the Ministry of Transport and Infrastructure is obliged with taking the necessary measures for the adaptation of maritime sectors to climate change by determining the negative effects of the climate change on maritime sector, extending the use of low or zero emission, energy efficient, alternative clean fuels, deploying low or zero emission ships and green port practices in international and intercity passenger and freight transport by sea, are important in order to comply with the acquis communautaire and international agreements. In this context, the authorities delegated to the Ministry Environment, Urbanisation and Climate Change shall also provide the necessary legal reform to implement regulations for compliance works regarding the decarbonization of the Turkish maritime sector.

IV. Results and discussion

The developments achieved at the international level and the European Union level regarding the green conversion in the maritime sector, which is one of the significant sectors that require international and national regulations to reduce greenhouse gas emissions in the combating climate change on the basis of the Paris Agreement, concern closely Turkish law, as it is binding in the internal law of Türkiye. In this context, international agreements - the Paris Agreement - to which Türkiye is a party, the International Maritime Organization works, the "Union for the Mediterranean (UfM) Ministerial declaration on Sustainable Blue Economy" declaration, and the regulations in the acquis communautaire required the adoption of a climate change law in Turkish law. In the Turkish Green Deal Plan prepared by the Ministry of Commerce in 2021 within the framework of compliance with the European Green Deal, increasing the production/use of sustainable and alternative fuels in maritime transport and extending green port practices are included. The duties and powers for performing the necessary policies to achieve the action plans are delegated to the Ministry of Transport and Infrastructure in the Climate Change Bill. Once the bill becomes law by the approval of the Turkish Grand National Assembly, decarbonizing the Turkish maritime sector and reducing the greenhouse gas emissions from maritime activities shall be among the priority policies of the Ministry of Transport and Infrastructure.

V. Conclusion

As a result of the research, the commitments given under the Paris Agreement in combating climate change and efforts to comply with the acquis communautaire triggered the adoption of regulations to reduce greenhouse gas emissions in all sectors with a holistic approach in Turkish law by drafting the text of Climate Change Bill, thus helping to implement the decarbonization policies in the Turkish maritime sector. Once the draft text of the Climate Change Bill is approved by the Turkish Grand National Assembly and becomes law after the legsilative procedures in national law, shall lead to the structual organisation to achieve the decarbonisation targets of the Turkish maritime sector under the management of the Ministry of Transport and Infrastructure.

References

Alan, Ilemin N., (2021). An Evaluation of Climate Change from a Legal Perspective of Turkey in the Scope of International Law. Proceedings of the 5th International Conference on Climate Change, 5(1), 74-85. https://doi.org/10.17501/2513258X.2021.5106

European Commission. (2019). Communication from the Commission: European Green Deal. Official Journal of the European Union, Brussels, 11.12.2019, COM(2019) 640 final, https://eur-lex.europa.eu/legal-content/EN/TXT/?uri=COM%3A2019%3A640%3AFIN.

European Commission. (2021). Commission Implementing Decision of 16.12.2021 on the financing of the annual action plan in favour of Turkey for 2021. Brussels, 16.12.2021 C(2021) 9734 final. https://neighbourhood-enlargement.ec.europa.eu/system/files/2022-01/C_2021_9734_F1_COMMISSION_IMPLEMENTING_DECISION_EN_V4_P1_1671449.PDF.

European Commission. (2023). Türkiye 2023 Report. https://neighbourhood-enlargement.ec.europa.eu/system/files/2023-11/SWD_2023_696%20T%C3%BCrkiye%20report.pdf.

International Maritime Organisation. (2023). 2023 Strategy on Reduction of GHG Emissions from Ships. https://wwwcdn.imo.org/localresources/en/OurWork/Environment/Documents/annex/MEPC%2080/Annex%2015.pdf.

Kyoto Protocol to the United Nations Framework Convention on Climate Change. (1997). https://unfccc.int/resource/docs/convkp/kpeng.pdf.

Ministry of Commerce. (2021). Turkish Green Deal Action Plan. https://ticaret.gov.tr/data/640f220d13b8761b449ccb42/YESIL%20MUTABAKAT%20Eylem%20Plan%C4%B1.pdf.

Ministry of Commerce Green Deal Working Group. (2022). Annual Activity Report. https://ticaret.gov.tr/data/643ffd6a13b8767b208ca8e4/YMEP%202022%20Faaliyet%20Raporu.pdf.

Ministry of Environment, Urbanisation and Climate Change. (2022). Climate Change Bill. https://www.gebzeto.org.tr/wp-content/uploads/2022/10/TOBB-%C4%B0klim-De%C4%9Fi%C5%9Fikli%C4%9Fi-Kanunu-Tasla%C4%9F%C4%B1.pdf.

Presidency of the Republic of Türkiye Presidency of Strategy and Budget. (2023). Twelfth Development Plan (2024-2028). https://onikinciplan.sbb.gov.tr/wp-content/uploads/2023/11/On-Ikinci-Kalkinma-Plani_2024-2028.pdf.

Regulation (EU) 2023/957 of the European Parliament and of the Council of 10 May 2023 amending Regulation (EU) 2015/757 in order to provide for the inclusion of maritime transport activities in the EU Emissions Trading System and for the monitoring, reporting and verification of emissions of additional greenhouse gases and emissions from additional ship types, Official Journal of the European Union, L 130, 16.5.2023, p. 105–114.

Türkoğlu Üstün, Kamile. (2021). Yeni Bir Dönemin Başlangıcı: Avrupa Yeşil Mutabakatı ve Türk Çevre Hukuku ve Politikalarına Etkileri. Memleket Siyaset Yönetim 16, 329-366.

Union for the Mediterranean. (2021). Union for the Mediterranean (UfM) Ministerial declaration on Sustainable Blue Economy. https://ufmsecretariat.org/wp-content/uploads/2021/02/Declaration-UfM-Blue-Economy-EN.pdf.

United Nations Framework Convention on Climate Change. (1992). https://unfccc.int/files/essential_background/background_publications_htmlpdf/application/pdf/conveng.pdf.

IEEES-112

Goal Programming-Based Bi-Objective Optimization Model in Empty Container Logistics

[1*]Hüseyin Gençer, [2]Sevda Dede,
[1]Piri Reis University, Faculty of Economics and Administrative Sciences, Maritime Business Management Department, Postane Mahallesi, Eflatun Sk. No:8, Istanbul, 34940, Türkiye
[2]Piri Reis University, Maritime Higher Vocational School, Logistics Programme, Postane Mahallesi, Eflatun Sk. No:8, Istanbul, 34940, Türkiye
*E-mails: hgencer@pirireis.edu.tr

Abstract

Nowadays, due to the decline in global trade, the demand for container shipping has decreased, and therefore the freight rates have also decreased. Moreover, the trade imbalances that always exist between regions and countries in world trade is also reflected in container shipping. As a result of this, the excess containers are repositioned to locations where they are needed, resulting in significant expenses. Empty container repositioning (ECR) results in a rise in overall transportation activity, hence contributing to elevated levels of carbon emissions that have detrimental effects on both society and the environment. One of the primary objectives of liner carriers is to provide the required number of containers at the right time and at the lowest cost to locations in need of containers. ECR costs are one of the variable costs that directly affect the total freight cost. The unit ECR cost of a location depends on many factors such as the number of empty containers sent to or from that location, feeder transportation costs, terminal handling chargers (THC), full container export and import rates. Therefore, the total ECR costs in a region and the unit ECR cost of a location in that region may conflict with each other. For this purpose, this study introduces a model that minimizes the total ECR costs in a region and provides control of unit ECR cost for the locations.

Keywords: Bi-objective optimization, empty container logistics, sustainability.

I. Introduction

Container shipping, which has made a significant revolution in the global supply chain (Levinson, 2006), can be seen as a mirror of international trade. The trade imbalance between regions and countries in world trade is also reflected in container shipping. As a result of this, the excess containers are repositioned to locations where they are needed, resulting in significant expenses. On the other hand, empty container repositioning (ECR) does not yield any additional value to customers. ECR results in a rise in overall transportation activity, hence contributing to elevated levels of carbon emissions that have detrimental effects on both society and the environment. One of the primary objectives of liner carriers is to provide the required number of containers at the right time and at the lowest cost to locations in need of containers. ECR costs are one of the variable costs that directly affect the total freight cost. ECR has garnered significant attention within the academic community as well. Especially after the 2000s, an increase in studies in this field has been observed.

ECR can be planned at various levels, including between warehouse and port, between locations, between regions and between continents. These planning levels can also be considered operational, tactical and strategic (Braekers et al., 2011). In research in the literature, mathematical programming models and meta-heuristic solution methods have generally been developed for minimizing the ECR costs. In these studies, costs such as maritime transportation costs, inland transportation costs, port handling costs, port storage costs, and container leasing costs were taken into account within the ECR costs. The literature reviews conducted by Theofanis and Boile (2008), Braekers et al. (2011), Lee and Song (2017), and Gençer and Demir (2019) provide comprehensive insights into the research on ECR. One of the understudied topics in the ECR-related literature is how to reflect the ECR cost to full container freight price.

II. Methodology

In this study, a lexicographic goal programming-based bi-objective mixed-integer linear programming (MILP) model has been developed. The first objective function minimizes the total ECR costs in a region, while the second objective function minimizes the deviation from the target unit ECR cost in the locations according to their priority level. Liner carriers carry out ECR operations with their own ships as well as with the feeder ships of other operators, especially in short distances. The model takes these into account, as well as third-party ECR by road and rail.

The first constraint in the model is to meet the weekly demand in export-dominant locations. The second constraint is that more than excess number of empty containers in cannot be shipped from import-dominant locations in that week. The third constraint is the weekly capacity constraint of transportation modes between locations, such as ship capacity. The model considers three types of containers and a four-week period. The other assumptions of the model are as follows:

- The number of containers required and the number of excess containers for each week and location are known.
- The capacities, arrival and transportation times of the ships, are known for each week.
- The weekly storage cost of the empty containers and the free storage time are taken into account in the locations.

III. Results and discussion

The model tested with the real data taken from a liner carrier's Eastern Mediterranean (EMED) and Black-Sea Region Agencies. The experimental studies are carried out via IBM ILOG CPLEX 12.6 on a computer of Intel(R) Core (TM) i5-4210U CPU 2.40 Ghz processor - 4 GB RAM. The model gives solutions for both the first and the second objective function in a very short computational time. The results of the first objective function, minimizing the total ECR costs, provide thousands of dollars in cost savings compared to the liner carrier's real-life applications. Moreover, the results determine that the unit ECR cost of the locations can vary considerably according to the ECR plans made within a region, and whether a full container shipment (booking) will be accepted or not. Furthermore, the results highlight the importance of connectivity and associated costs of third-party feeder transports.

IV. Conclusion

ECR operations and their associated costs will always remain one of the most important issues in container shipping. Moreover, ECR costs are one of the most important variable costs affecting the profitability or contribution of full container shipments. The bi-objective model proposed in this study can be used by the liner carriers for their real life ECR operations and cost calculations. By configuring the objective functions in a different way, the model can also find the maximum weekly number of empty containers to be sent to or from the locations depending on the minimum deviation from the unit ECR cost for each location. Therefore, the model can be used as a decision support tool in finding the highest profitability or contribution for full container shipments to be made between the locations where the liner carriers operate. As a result, the model developed in the study also prevents carbon emissions by preventing unnecessary ECR operations.

References

Braekers, K., Janssens, G.K. & Caris, A. (2011). Challenges in Managing Empty Container Movements at Multiple Planning Levels, Transport Reviews, 31 (6), 681-798.

Dong, J., Song, D. (2009). Container fleet sizing and empty repositioning in liner shipping systems, Transportation Research Part E, 45, 860–877.

Gençer, H.& Demir, H. (2019). An Overview of Empty Container Repositioning Studies and Research Opportunities, Business and Management Horizons, 7 (1), 1-22.

Gençer, H.& Demir, H. (2020). Optimization of Empty Container Repositioning in Liner Shipping, Business and Management Horizons, 8 (1), 1-18.

Lee, C. Y. & Song, D. P. (2017). Ocean container transport in global supply chains: Overview and research opportunities, Transportation Research Part B, 95, 442-474.

Levinson, M., (2006) The box : how the shipping container made the world smaller and the world economy bigger, Princeton University Press, N.J.

Theofanis, S. & Boile, M. (2009). Empty marine container logistics: facts, issues and management strategies, GeoJournal, 74, 51-65.

IEEES-113

Multi-Objective Optimization in Container Port Operations

[1*]Hüseyin Gençer,
[1]Piri Reis University, Faculty of Economics and Administrative Sciences, Maritime Business Management Department, Postane Mahallesi, Eflatun Sk. No:8, Istanbul, 34940, Türkiye
*E-mails: hgencer@pirireis.edu.tr

Abstract

The increase in demand for container transportation, growth in ship sizes and mergers in the sector have greatly affected container ports. In particular, the bargaining power and pressure of global container line operators, united in various alliances, on ports has increased. Some global operators impose conditions on hourly ship handling movements to ports when making agreements. In this regard, ports need to plan the operations of the services they provide to ships in the best possible way. Planning of gantry cranes, which are one of the most important resources of ports, includes crucial operations of the services provided to the ships. Managing the energy efficiency of gantry cranes in a container port is crucial to reducing operating costs, minimizing environmental impact and ensuring smooth operations. One of the most important points of crane energy efficiency is minimizing unnecessary crane movements. Namely, optimum planning of cranes will both shorten the service provided to ships and increase the energy efficiency of the port. This study proposes a multi-objective optimization model, which minimizes the total service time given to ships and gantry crane movements by considering desired handling movements per ship per hour. The model was tested with real data and provides optimum solution within a reasonable time. The results reveal that the model developed in the study can be used as an important decision support system in the operation planning of container ports.

Keywords: Container port operations, Multi-objective optimization, Port energy efficiency.

I. Introduction

The increase in demand for container transportation, growth in ship sizes and mergers in the sector have greatly affected container ports. In particular, the bargaining power and pressure of global container line operators, united in various alliances, on ports has increased. Some global operators impose conditions on hourly ship handling movements to ports when making agreements. In this regard, ports need to plan the operations of the services they provide to ships in the best possible way. Container terminal operations may generally be categorized into three primary categories. The initial category of activities takes place at the quayside, where boats dock and quay cranes are responsible for the loading and unloading of containers. Quayside operations serve as the interface between yard operations and container terminal activities. Yard side activities encompass the transfer of containers using trailers or straddle carriers, the stacking of containers using yard cranes, and the storage of containers inside the terminal's yard area. Land-side operations refer to a category of operations that often involve the loading and unloading of containers, and encompass both the terminal and its surrounding area. Numerous studies have demonstrated that operational research (OR) techniques may be effectively utilized across various operations inside container ports, including quayside, yard side, and land side activities. The first and most detailed survey in that area was conducted by Stahlbock and Voss in 2008. The authors reviewed the studies done on the subject in terms of each type of terminal operations including the equipment specifications. Detailed literature reviews on container port operations are available in the studies of Bierwirth and Meisel (2010), Bierwirth and Meisel (2015), Rodrigues and Agra (2022).
In our study, we are dealing with the quayside operations in container terminals that can be summarized as follows in the order of operations: A ship arrives at terminal and waits for her berthing position determined by terminal management. Once her position became available, the ship berths and the available gantry cranes are assigned to handle (load/unload) the containers related to the ship. Since moving the ship to different berths in later periods cause loss of time and cost, in general, a ship is served at the same berth until the end of her operations. On the other hand, the quay cranes are located on a parallel line to the berths and can be moved along different berths in order to serve another ships at different berths, but are not able to pass each other. After all the containers are handled, the ship leaves the berth and its berthing position becomes availabe for the next ships. In our study, we attempt to develop an integrated model, which considers the two processes – berth allocation and gantry crane assignment –simultaneously.

II. Methodology

This study proposes a multi-objective mathematical programming model. The first objective minimizes the total service time of ships arriving to the seaports. The second objective minimizes the total number of gantry crane movements. Unlike the models in researches such as Gençer and Özdemir (2014), Özdemir and Ursavaş (2015), in this study, the number of cranes to be assigned per ship, determined by liner operators depending on the hourly handling movement speed of the ships, was taken into account in the model. This is how applications are carried out in small and medium-sized ports where competition is intense. In this context, the model was developed for real-life operations in small and medium-sized ports. The basic assumptions of the model are as follows:

- The quay of consists of different berths at each only one ship can berth. A ship can berth at any of the berths unless her length is not longer than the berth and stays at the same berth during her process time.
- All the gantry cranes are identical.
- Depending on her length, each ship has a maximum number limit of gantry cranes to be served
- Gantry crane assignment is dynamic during the handling process meaning that a gantry crane which serves a ship at time t, can leave this ship and be moved to a different berth to serve anothership at time t+1.

- The impact of conditions related to other operations at terminal such as; deviation of berthing position to the container stacking area, number of trucks which transport containers to the stacking area etc. are assumed to be identical and have no influence on berth and crane assignment decisions.

III. Analysis

We performed a computational experiment on the data set, which has been used previously in the literature (Liang et al.2009; Han et al.2010; Liang et al.2011). The experimental studies are carried out via IBM ILOG CPLEX 12.6 on a computer of Intel(R) Core (TM) i5-4210U CPU 2.40 Ghz processor - 4 GB RAM. The model provides solution within a reasonable computational time. Thanks to the model, various solution options can be offered to decision makers in container ports. Moreover, it can be predicted at which hours there will be congestion and how much the port's inland capacity usage will be. As a result, more efficient use of the port's resources and capacity is ensured.

IV. Conclusion

Along with the increasing importance of container ports, novel approaches and optimization methods are being introduced to increase the efficiency of operations at container terminals. One of the overall objectives in container port operations is to minimize the service time of the ships. On the other hand, one of the other important objective of ports is the efficient use of gantry cranes, which are the sources where the port consumes the most energy. This study introdueced a multi-objective optimization model which minimizes the total service time given to ships and gantry crane movements by considering desired handling movements per ship per hour. The model was tested with real data and provides optimum solution within a reasonable time. The results reveal that the model developed in the study can be used as an important decision support system in the operation planning of container ports. Future research directions could include the development of models that take different objectives into account.

References

Bierwirth, C., Meisel, F. 2010. “A survey of berth allocation and quay crane scheduling problems in container terminals”, European Journal of Operational Research, 202 (3), 615-627.

Bierwirth, C. & Meisel, F. 2015. A follow-up survey of berth allocation and quay crane scheduling problems in container terminals”, European Journal of Operational Research, 244, 675-689.

Gençer, H. & Özdemir, D. (2014) Bi-objective Quay Crane Assignment Problem, 34. Ulusal Yöneylem Araştırması ve Endüstri Mühendisliği Kongresi, Bursa, 25-27 Haziran.

Goodchild, A., Zhao, W., Wygonik, E. 2010. “Decision Problems and Application of Operations Research at Marine Container Terminals”. Wiley Encyclopedia of Operations Research and Management Science, Cochran, J.J., John Wiley & Sons.

Han, X., Z. Lu, L. Xi (2010): A proactive approach for simultaneous berth and quay crane scheduling problem with stochastic arrival and handling time. European Journal of Operational Research, 207 1327–1340.

Liang, C., Y. Huang, Y. Yang. (2009): A quay crane dynamic scheduling problem by hybrid evolutionary algorithm for berth allocation planning. Computers & Industrial Engineering, 56 (3) 1021–1028.

Liang, C., J. Guo, Y. Yang. (2011): Multi-objective hybrid genetic algorithm for quay crane dynamic assignment in berth allocation planning. Journal of Intelligent Manufacturing, 22 471–479.

Özdemir, D. & Ursavaş, E. (2015). Bi-objective Berth–crane Allocation Problem in Container Terminals, in Global Logistics, Ed: Kara, B.Y., Sabuncuoğlu, İ., Bidanda, B., Taylor & Francis Goup, 83-104.

Rodrigues, F. & Agra, A. (2022). Berth allocation and quay crane assignment/scheduling problem under uncertainty: A survey, European Journal of Operational Reseacrh, 303, 501-524.

Stahlbock, R. and Voss, S. (2008): Operations Research at Container Terminals: A Literature Update, OR Spectrum.30(1), 1–52.

Energetic and Exergetic Performance Analysis of the Solar Tower-Based Integrated Plant Combined With Helium-Based Brayton Cycle and HTSE For Power and Hydrogen Generation

[1*]Fatih YILMAZ, [1]Murat OZTURK, [2]Resat SELBAS
[1] Isparta University of Applied Sciences, Faculty of Technology, Department of Mechatronics Engineering, 32200, Isparta/Turkiye
[2] Isparta University of Applied Sciences, Faculty of Technology, Department of Mechatronics Engineering, 32200, Isparta/Turkiye
*E-mail: fatihyilmaz@isparta.edu.tr

Abstract

Solar energy systems have gained more and more importance in the net-zero emission transition day by day. The combination of solar energy and other energy conversion technologies is important for the production of sustainable commodities. The developed combined plant is designed to generate power and hydrogen with a helium-based Brayton cycle and high-temperature steam electrolyzer (HTSE). A detailed thermodynamic performance analysis is conducted to determine the system performance using the energetically and energetically methods. In light of the analysis results, the overall energy and exergy efficiency of the entire plant is computed as 38.87% and 21.15%, respectively, at 650 W/m^2 solar radiation. Also, the system can generate 1480 kW net power and 0.01352 kg/s clean hydrogen.

Keywords: Energy, exergy, solar energy, HTSE, hydrogen, power.

I. Introduction

One of the most important problems of today is undoubtedly considered to be global warming, which increasingly affects the universe. This means that the average global temperature increase from 1880 to today has reached 1.18 ℃

(Kahraman and Dincer, 2022). This increasing temperature poses a serious problem for humanity. Therefore, it is inevitable for humanity to take important steps and impose sanctions to overcome this issue**.** At this point, to tackle the environmental problem and switch to a clean future, renewable energy sources, and also the integration of these sources into combined plants, which energy efficiency methods have gained importance. For a carbon-free future, the use of solar energy, which is the most important renewable energy source, is very important. Because these systems are an important technology considered in the energy efficiency method. In recent years, there have been many studies on solar energy systems, which are renewable energy sources, and combined energy conversion cycles obtained by integrating these systems.
Zare et al. (2016) developed an energy and exergy analysis of the solar energy-based Brayton cycle assisted (BC) combined plant for power generation. Their developed model had an exergy efficiency of higher than 70%. Yilmaz et al. (2022) posed a new multigeneration assisted by solar energy that generates clean multiple beneficial products. They computed that overall energy and exergy efficiency are 43.77% and 19.61%. A dynamic simulation and analysis of the solar and coal-based plant with supercritical CO_2 Brayton cycle is evaluated and examined by Wang et al. (2023). They used the CO_2 working fluid at the supercritical phase and then the system efficiency reached 43.19%. Additionally, some studies with solar-assisted helium fluid are given here (Khan et al. 2023; Khan and Mishra 2023; Zhou et al. 2023).
This study aims to comprehensively perform thermodynamic analysis of clean hydrogen and power production with a combined system supported by solar energy. In this context, energy and exergy efficiencies are examined according to different design parameters.

II. System description and methodology

This designed system consists of a solar tower cycle, a double-turbine helium fluid Brayton cycle, and a high-temperature electrolysis (HTE) for hydrogen production. Steam, which is more than needed for HTE, may be preferred for drying and heating purposes. Helium fluid rotates between points 6 and 10 components such as the compressor, high-pressure (HPT), and low-pressure turbines (LPT). The whole purpose is to produce clean hydrogen and electricity.

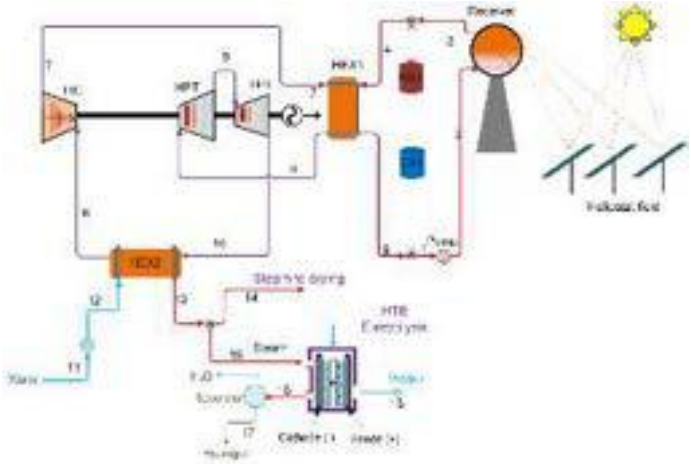

Fig.1 Solar energy based combined plant layout

The detailed energy and exergy efficiency of this designed system is examined by comprehensively considering the thermodynamic analysis method. For the analysis, assumptions are made such as the system is modeled as a steady-state flow, kinetic and potential energy changes are not taken into account, and pressure and heat losses are neglected. Here, the mass, energy, entropy, and exergy equations, which are generally the four-part equilibrium equation of thermodynamic analysis in its simplest form, can be written as follows. (Cengel et al. 2011; Dincer 2020);

$$\dot{m}_i = \dot{m}_e \quad (1)$$

$$\dot{Q}_i + \dot{W}_i + \sum \dot{m}_i h_i = \dot{Q}_e + \dot{W}_e + \sum \dot{m}_e h_e \quad (2)$$

$$\sum \left(\frac{\dot{Q}}{T}\right)_i + \sum \dot{m}_i s_i + \dot{S}_{gen} = \sum \left(\frac{\dot{Q}}{T}\right)_e + \sum \dot{m}_e s_e \quad (3)$$

$$\dot{E}x^{\dot{Q}_i} + \dot{E}x^{\dot{W}_i} + \sum \dot{m}_i ex_i = \dot{E}x^{\dot{Q}_e} + \dot{E}x^{\dot{W}_e} + \sum \dot{m}_e ex_e + \dot{E}x_{des} \quad (4)$$

The helium-based Brayton (HBC) and overall system (Sys) performance ratio can be developed as;

$$\eta_{HBC} = \frac{\dot{W}_{HPT}+\dot{W}_{LPT}-(\dot{W}_{HC})}{\dot{m}_7(h_8-h_7)} \quad (5)$$

$$\psi_{HBC} = \frac{\dot{W}_{HPT}+\dot{W}_{LPT}-(\dot{W}_{HC})}{\dot{m}_7(ex_8-ex_7)} \quad (6)$$

$$\eta_{sys} = \frac{\dot{W}_{net}+(\dot{m}_{H_2} LHV_{H_2})+(\dot{Q}_{steam})}{\dot{Q}_{solar}} \quad (7)$$

$$\psi_{sys} = \frac{\dot{W}_{net}+(\dot{m}_{H_2} ex_{H_2})+\dot{E}x_{Q,steam}}{\dot{E}x_{Q,solar}} \quad (8)$$

III. Results and discussion

In this section, comprehensive mathematical simulation results are discussed. The changes in energy and exergy efficiency occurring in the entire system are examined based on specific parameters. Moreover, some assumptions made to address the thermodynamic analysis of the system are given in Table 1. In light of the assumptions in Table 1, these simulation results are depicted in Table 2. According to Table 2, the net electricity generation capacity of the entire system is 1480 kW and clean hydropower production is 0.01352 kg/s. Moreover, this designed work has 38.87% energy efficiency and 21.15% exergy efficiency.

Table 1 Design and assumption parameters for the developed model

Parameters	**Value**
Solar radiation rate, W/m^2	650
Receiver inlet temperature, ℃	121
Receiver outlet temperature(calculated), ℃	720
Receiver inlet pressure, kPa	132
Solar cycle working fluid	Salt(60NaNO3_40KNO3
Power cycle working fluid	Helium
Helium compressor inlet temperature, ℃	32
Turbines isentropic efficiency	0.89
Helium compressor inlet pressure, kPa	2000
Helium compressor outlet pressure, kPa	6000
HTE inlet temperature, ℃	383.7
HEX effectiveness	0.8
Reference temperature, ℃	25
Reference pressure, kPa	101.325

Table 2. Case study results of the developed solar-based combined plant

Results	**Value**
$\dot{W}_{net}$	1480 [kW]
$\dot{m}_{hydrogen}$	0.01352 [kg/s]
η_{BC}	20.86 [%]
ψ_{BC}	35.87 [%]
η_{ov}	38.87 [%]
ψ_{ov}	21.15 [%]

Figs. 2 and 3 examine the effect of solar radiation on the system. According to Fig. 2, as solar radiation increases from 500 W/m^2 to 750 W/m^2, both net power production and hydrogen production increase. Moreover, (Figure 3) With Helium-based BC, the energy and exergy efficiency of the entire system increased linearly.

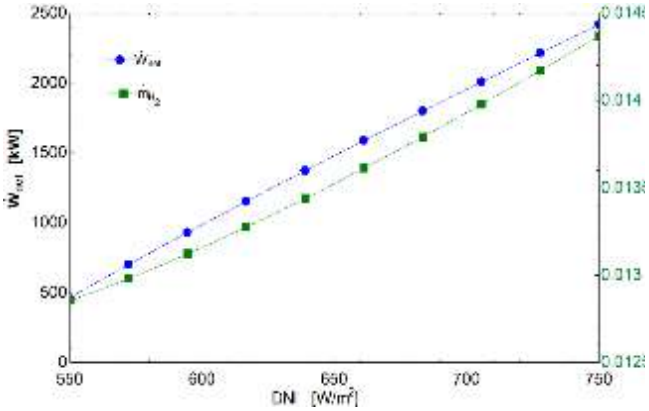

Fig. 2. Effect of solar radiation on the net power and hydrogen rate

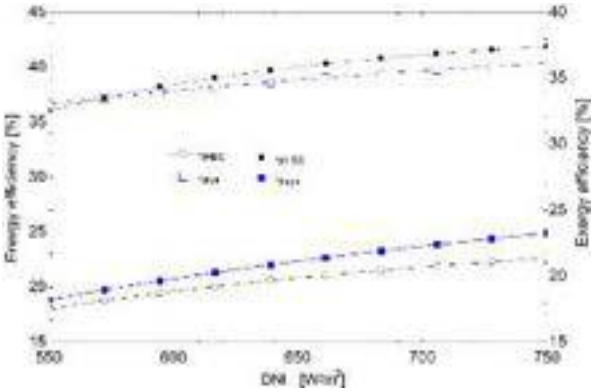

Fig. 3. Effect of solar radiation on the developed plant performance

Figure 4 shows the increase in system changes with heliostat number. As the number of mirrors increased from 200 to 550, this had a positive effect on the system efficiency, as the system reached higher temperatures.

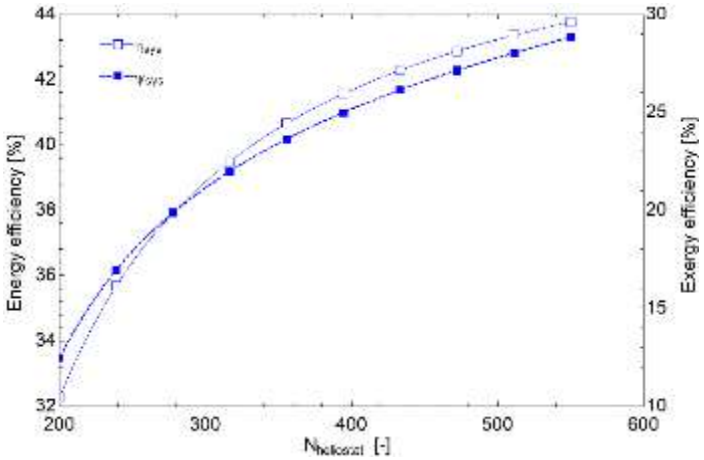

Fig. 4. Effect of heliostat number on overall plant's efficiency

The effect of changing the compression of the helium compressor between 1.5 and 4.5 on the system is presented in Figs. 5 and 6. Here, with the increase in compressor compression ratio, the system energy and exergy efficiency The energy and exergy efficiency of the entire system increases up to a certain rate and then begins to decrease. Net production showed a reverse change, that is, a decrease, after approximately 3.2, due to the higher work consumed by the compressor.

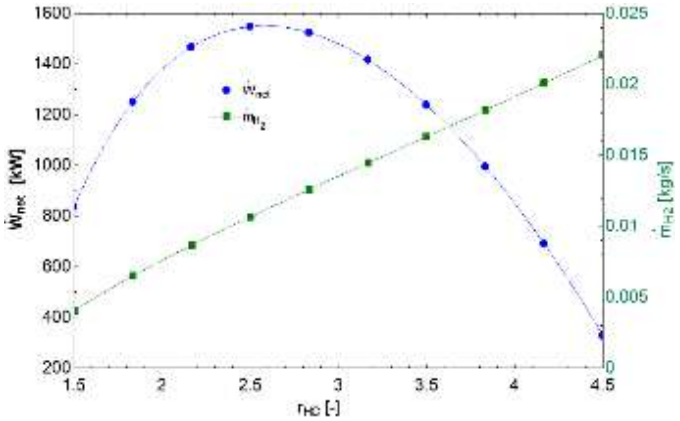

Fig. 5. Impact of Helium compressor compression ratio on the net power and hydrogen rate

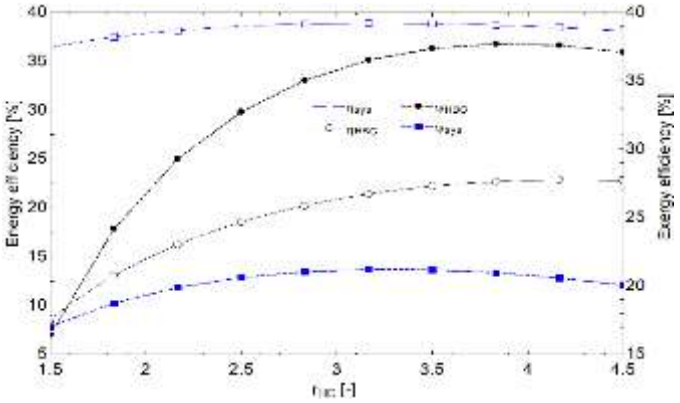

Fig. 6. Impact of Helium compressor compression ratio on the BC and overall system efficiency

Finally, Fig. 7 examines the effects of increasing the heat exchanger contact point on the system. Here, as the energy going to the subsystems decreases with the increase in compression point temperature, the system efficiency decreases negatively.

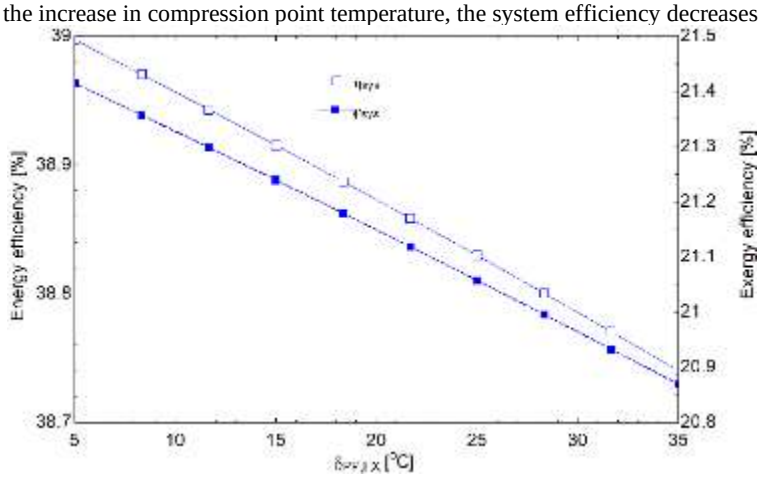

Fig.7. Chance in the overall system efficiency vs pinch point temperature of HEX

IV. Conclusion

The developed solar energy-based combined plant deals with detailed thermodynamic performance modeling based on energy and exergy efficiency that generates power, hydrogen, and steam. Energy and exergy analysis approaches are fulfilled to determine the system and subsystem efficiency. The results show that the newly developed model can be favorable based on the energy and exergy efficiency. Also, the system power generation capacity is computed as 1480 kW. Moreover, the green hydrogen generation is 0.01352 kg/s. For energy and exergy efficiencies, the HBC system has 20.86% and 35.87% while the entire system has 38.87% and 21.15%, respectively.

References

Cengel, Y. A., Boles, M. A., & Kanoğlu, M. (2011). *Thermodynamics: an engineering approach* (Vol. 5, p. 445). New York: McGraw-hill.

Dincer, İ. (2020). *Thermodynamics: a smart approach*. John Wiley & Sons.

Kahraman, U., & Dincer, I. (2022). Investigation of a Solar Energy-Based Trigeneration System. In *Renewable Energy Based Solutions* (pp. 537-557). Cham: Springer International Publishing.

Khan, Y., & Mishra, R. S. (2023). Performance analysis of a solar based novel trigeneration system using cascaded vapor absorption-compression refrigeration system. *International Journal of Refrigeration*, *155*, 207-218.

Khan, Y., Singh, D., Caliskan, H., & Hong, H. (2023). Exergoeconomic and Thermodynamic Analyses of Solar Power Tower Based Novel Combined Helium Brayton Cycle-Transcritical CO2 Cycle for Carbon Free Power Generation. *Global Challenges*, 2300191.

Wang, D., Han, X., Li, H., & Li, X. (2023). Dynamic simulation and parameter analysis of solar-coal hybrid power plant based on the supercritical CO2 Brayton cycle. *Energy*, *272*, 127102.

Yilmaz, F., Ozturk, M., & Selbas, R. (2022). Development and assessment of a solar-driven multigeneration plant with compressed hydrogen storage for multiple useful products. *International Journal of Hydrogen Energy*.

Zare, V., & Hasanzadeh, M. J. E. C. (2016). Energy and exergy analysis of a closed Brayton cycle-based combined cycle for solar power tower plants. *Energy conversion and management*, *128*, 227-237.

Zhou, J., Ali, M. A., Zeki, F. M., & Dhahad, H. A. (2023). Thermoeconomic investigation and multi-objective optimization of a novel efficient solar tower power plant based on supercritical Brayton cycle with inlet cooling. *Thermal Science and Engineering Progress*, *39*, 101679.

IEEES-115

Assessment of the Current Developments Regarding the Reduction of Maritime Transport CO2 Emissions Within the Framework of the Acquis Communautaire

Dr. Halil Çeçen
Nuh Naci Yazgan University, Faculty of Law, Department of the European Union, Ertugrul Gazi Mah. Nuh Naci Yazgan Yerleskesi Kume Evler Kocasinan, Kayseri, 38050, Türkiye
*E-mail: hcecen@nny.edu.tr

Abstract

In this research, the provisions of Regulation 2023/957 adopted by the European Union (EU) on the extension of the emission trading system to maritime activities are examined.
Regulation 2023/957, which includes provisions to ensure the inclusion of maritime activities in the EU Emissions Trading System (ETS) and the monitoring, reporting and verifying of additional greenhouse gas emissions and emissions from additional ship types, was published in the Official Journal of the European Union (OJEU) dated 16 May 2023. As decided in the regulation, it is necessity all sectors of the economy to contribute to achieve to reduce emissions targeted by the European Climate Law numbered 2021/1119, and therefore maritime activities should also contribute to this targets. The amended Article 2(1) of the Regulation shall apply to the greenhouse gas emissions released during their voyages for transporting for commercial purposes cargo or passengers from such ships' last port of call to a port of call under the jurisdiction of a Member State and from a port of call under the jurisdiction of a Member State to their next port of call, as well as within ports of call under the jurisdiction of a Member State.
In addition, Directive 2023/959 regulates the provisions applicable to voyages between the ports of call of the Member States or from ships performing voyages departing from a port of call under the jurisdiction of a Member State and arriving at a port of call outside the jurisdiction of a Member State in the allocation of allowances in respect of maritime transport activities.
The EU, which adopted the European Green Deal and the European Climate Law, proves that it attaches importance to combating climate change both in the EU level and globally by regulating the inclusion all sectors of the economy, including the maritime transportation activities, which is the subject of this research.

Keywords: maritime transport CO_2 emissions, Regulation (EU) 2023/957, Directive (EU) 2023/959.

I. Introduction

One of the most important policies followed by the European Union to reduce greenhouse gas emissions for combating climate change is the establishment of Emissions Trading System (ETS). In this regard, in accordance with the provisions of the "Directive 2003/87/EC establishing a scheme for greenhouse gas emission allowance trading within the Community", it is necessary to obtain allowance from the national competent authority before performing an activity which produces greenhouse gas emissions. These allowances and necessary conditions are subject to certain criterias in the Directive 2003/87/EC.

After the Paris Agreement entered into force, the European Commission announced the European Green Deal, which requires the involvement of all sectors in combating climate change. Based on the European Green Deal, Regulation 2021/1119 (the European Climate Law) was adopted in order to become a climate neutrality by 2050. In order to achieve the targets of the Regulation 2021/1119, it is required to determine policies to reduce greenhouse gas emissions in all sectors with a holistic approach.

Special attention were given to the transport sector in the Directive 2003/30/EC and the renewable energy Directives numbered 2009/28/EC and 2018/2001, and it was aimed to increase the use of renewable energy in the transport sector in a given year. In this context, since the activities in the maritime transportation sector constitute a significant part of global greenhouse gas emissions, studies on the extending the EU ETS into the maritime have thus led to the adoption and entry into force of Regulation 2023/957. In addition, the Directive 2023/959 amended the Directive 2003/87/EC, and the conditions and criterias for reducing greenhouse gas emissions in maritime transportation activities, which were included in the emission trading system, were determined.

In this research, Regulation 2023/957 and Directive 2023/959 are reviewed within the framework of the European Union's policies towards combating climate change.

II. Methodology

In this research, legal documents in the acquis communautaire, international law documents and studies in the literature were examined. Since the subject of the research deals with current developments, the research may contribute to the literature.

III. Analysis

Maritime transport constitutes 75% of the Union's foreign trade and 31% of its domestic trade in terms of volume (European Commission, 2023). One of the reasons for including maritime transportation activities in the EU ETS is the increase in greenhouse gas emissions resulting from activities in this sector. It was found out that there was a 36% increase in emissions resulting from fossil fuels sold within the Union on voyages from one Member State to another Member State or to a third country since 1990 (Directive 2023/959, Recital 17). In addition, carbon dioxide emissions from maritime transportation constitute 3-4% of the Union's total emissions (Directive 2023/959, Recital 20). If this rate increases, the Union's goal of becoming a climate neutral continent by 2050 is at risk. For this reason, it was also stated in the Commission's European Green Deal that maritime transportation activities should be included in the EU ETS (European Commission, 2019).
The action to include the emissions from the maritime sector from 2023 by the EU or IMO was stated in the Directive 2018/410 (Lighthouse Swedish Maritime Competence Center, 2020). Following the works on the inclusion of the emissions from maritime activities into the EU ETS, the "Regulation (EU) 2023/957 of the European Parliament and of the Council of 10 May 2023 amending Regulation (EU) 2015/757 in order to provide for the inclusion of maritime transport activities in the EU ETS and for the monitoring, reporting and verification of emissions of additional greenhouse gases and emissions from additional ship types" entered into force by being published at the OJEU dated 16 May 2023 and numbered L 130/105.

As stated in the Regulation 2023/957, "all sectors of the economy need to contribute to global efforts in order to achieve the emission reductions established by the Regulation 2021/1119 (European Climate Law) by ensuring that maritime activities contribute to the Union's climate targets as well as the goals of the Paris Agreement". In addition to the to Article 1 of the Regulation 2015/757 with the amendment by the Regulation 2023/957, the Regulation was amended as to "lay down rules for the accurate monitoring, reporting and verification of greenhouse gas emissions and of other relevant information from ships arriving at, within or departing from ports under the jurisdiction of a Member State, in order to promote the reduction of greenhouse gas emissions from maritime transport in a cost effective manner." The other greenhouse gases, such as methane gas (CH_4) and nitrous oxide (N_2O), besides carbon dioxide (CO_2) emissions released from 2024 onwards were also included in the scope of Regulation 2023/957 upon the finding that an increase in the emissions of methane gas and nitrous oxide in maritime transportation activities.

Another legal instrument, which has entered into force yet, is the "Directive 2023/959 amending Directive 2003/87/EC establishing a system for greenhouse gas emission allowance trading within the Union and Decision (EU) 2015/1814 concerning the establishment and operation of a market stability reserve for the Union greenhouse gas emission trading system". In accordance with the Article 1(7) of the Directive 2023/959; "the allocation of allowances and the application of surrender requirements in respect of maritime transport activities" shall apply as following:

- "50% of the emissions from ships departing from a port of call under the jurisdiction of a Member State and arriving at a port outside the jurisdiction of a Member State
- 50% of emissions from ships departing from a port of call outside the jurisdiction of a Member State and arriving at a port under the jurisdiction of a Member State,
- 100% of emissions from ships departing from a port of call under the jurisdiction of a Member State and arriving at a port under the jurisdiction of another Member State,
- 100% of emissions from ships within a port of call under the jurisdiction of a Member State."

In accordance with the relevant article, not only voyages between ports of call located in the EU, but also voyages departing from a port of call located outside the EU and arriving to a port of call located in the EU and voyages departing from a port of call located in the EU Voyages to a port of call outside the EU are also included in the emissions trading system. The Directive 2023/959 also includes a rule that "in case a global market-based measure is adopted by IMO to reduce greenhouse gas emissions from the international maritime transport sector, the Commission will consider amending the Directive in the light of the adopted measure of IMO in case that this global market-based measure is ambitious to achieve the targets of the Paris Agreement, covers the environmental integrity and is coherent with the EU ETS".

Following the entry into force of the Directive 2023/959, the IMO adopted the "2023 Strategy on Reduction of Greenhouse Gas Emissions from Ships" on 7 July 2023. In the relevant strategy, "reducing CO_2 emissions per transport work, as an average across international shipping, by at least 40% by 2030, compared to 2008" was targeted. In addition, "reaching net-zero greenhouse gas emissions by 2050", in line with the Article 2 of the Paris Agreement, is also another target of the IMO's Strategy.

In addition, the legislative procedures for the use of renewable fuels in maritime transport was brought into end and the Regulation 2023/1805 was published in the OJEU dated 22 September 2023. The Regulation regulates "uniform rules to limit the greenhouse gas intensity of the energy used on board by ships leaving, arriving at, or staying within ports under the jurisdiction of Member States, and to impose an obligation to use on-shore power supply or zero-emission technology in these ports". To achieve this target, the regulation sets a limit on the greenhouse gas concentrations of fuels used by ships as "2% from 1 January 2025, 6% from 1 January 2030, 14.5% from 1 January 2035, 31% from 1 January 2040, 62% from 1 January 2045 and 80% from 1 January 2050".

With the current developments and the adoption of new Directives and Regulations related to the reduction of the greenhouse gas emissions from maritime activities, the EU consistently follows the policies to fully implement the Paris Agreement and to include all the sectors of the economy by triggering the third countries to comply with the international commitments to the climate change mitigation (Dobson, 2017).

IV. Results and Discussion

Due to the increase in greenhouse gas emissions resulting from activities in the maritime transportation sector and the fact that maritime transportation has a significant share in the EU's internal and external trade, important developments in the acquis communautaire have been provided. The Regulation 2023/957 extended the EU ETS to activities in the maritime transportation sector. The Directive 2023/959 amended the Directive 2003/87/EC and established the strategies and principles for reducing greenhouse gas emissions from the activities in the maritime transport sector. And by adopting the Directive 2023/1805, spesific binding and ambitious targets were set for the Member States to reduce greenhouse gas emissions until 2050.
In order to achieve the targets of the Paris Agreement, the EU has been expanding the content of its emission trading system in such a way which have an impact on international maritime transportation activities, with the policies it follows to reduce greenhouse gas emissions. Following these policies of the EU, IMO also announced its greenhouse gas emissions reduction strategy in 2023, thus it can be seen that the EU has also triggered the IMO to determine a strategy for reducing greenhouse gas emissions from the international maritime transport sector.

V. Conclusion

The European Union adopts regulations related to climate change mitigation based on its international commitments. The Regulation 2021/1119 aims to create a climate neutrality by 2050, covering all sectors of the economy. For this reason, reducing greenhouse gas emissions from activities in the maritime transport sector were included in the EU ETS to achieve these targets. The provisions of the Regulation 2023/957, Directive 2023/959 and Directive 2023/1805 affect not only the EU's internal trade but also its external trade with the third countries. Therefore, the EU follows a stable policy in the combating climate change and triggers all parties to give efforts for the implementation of the Paris Agreement.

References

Directive 2003/87/EC of the European Parliament and of the Council of 13 October 2003 establishing a scheme for greenhouse gas emission allowance trading within the Community and amending Council Directive 96/61/EC (Text with EEA relevance) Official Journal of the European Union L 275, 25.10.2003, p. 32–46.

Directive (EU) 2018/410 of the European Parliament and of the Council of 14 March 2018 amending Directive 2003/87/EC to enhance cost-effective emission reductions and low-carbon investments, and Decision (EU) 2015/1814 (Text with EEA relevance.), OJ L 76, 19.3.2018, p. 3–27.

Directive (EU) 2023/959 of the European Parliament and of the Council of 10 May 2023 amending Directive 2003/87/EC establishing a system for greenhouse gas emission allowance trading within the Union and Decision (EU) 2015/1814 concerning the establishment and operation of a market stability reserve for the Union greenhouse gas emission trading system (Text with EEA relevance), Official Journal of the European Union, L 130, 16.5.2023, p. 134–202.

European Commission. (2019). The European Green Deal. Brussels, 11.12.2019 COM(2019) 640 final. https://eur-lex.europa.eu/resource.html?uri=cellar:b828d165-1c22-11ea-8c1f-01aa75ed71a1.0002.02/DOC_1&format=PDF.

European Commission. (2023). European Green Deal: Agreement reached on cutting maritime transport emissions by promoting sustainable fuels for shipping. Press release. 23 March 2023. Brussels. https://ec.europa.eu/commission/presscorner/detail/en/ip_23_1813.

International Maritime Organisation. (2023). 2023 IMO Strategy on Reduction of GHS Emissions from Ships. https://wwwcdn.imo.org/localresources/en/OurWork/Environment/Documents/annex/MEPC%2080/Annex%2015.pdf.

Lighthouse Swedish Maritime Competence Center. (2020). Including maritime transport in the EU Emission Trading System – addressing design and impacts. https://ivl.diva-portal.org/smash/get/diva2:1549488/FULLTEXT01.pdf.

Nobson, N. L.; Ryngaert, C. (2017). Provocative Climate Protection: EU "Extraterritorial" Regulation of Maritime Emissions, The International and Comparative Law Quarterly 66, 295-333. doi: 10.1017/S0020589317000045.

Regulation (EU) 2015/757 of the European Parliament and of the Council of 29 April 2015 on the monitoring, reporting and verification of carbon dioxide emissions from maritime transport, and amending Directive 2009/16/EC (Text with EEA relevance), Official Journal of the European Union, L 123, 19.5.2015, p. 55–76.

Regulation (EU) 2021/1119 of the European Parliament and of the Council of 30 June 2021 establishing the framework for achieving climate neutrality and amending Regulations (EC) No 401/2009 and (EU) 2018/1999 ('European Climate Law'), Official Journal of the European Union, L 243, 9.7.2021, p. 1–17.

Regulation (EU) 2023/957 of the European Parliament and of the Council of 10 May 2023 amending Regulation (EU) 2015/757 in order to provide for the inclusion of maritime transport activities in the EU Emissions Trading System and for the monitoring, reporting and verification of emissions of additional greenhouse gases and emissions from additional ship types (Text with EEA relevance), Official Journal of the European Union, L 130, 16.5.2023, p. 105–114.

Regulation (EU) 2023/1805 of the European Parliament and of the Council of 13 September 2023 on the use of renewable and low-carbon fuels in maritime transport, and amending Directive 2009/16/EC (Text with EEA relevance), Official Journal of the European Union, L 234, 22.9.2023, p. 48–100.

IEEES-116

Demoeconomics: The Relationship Between Energy and Demoethical Values

[1*]Rinat A. Zhanbayev, [2,3]Muhhamad Irfan, [4]Daniil G. Maksimov, [5,6]Anna V. Shutaleva, [1]Makpal Kozhakanova
[1] National Engineering Academy of the Republic of Kazakhstan, Department of Sciences and Technology, Almaty, 050010, Kazakhstan
[2] Beijing Technology and Business University, School of Economics, Beijing, 100048, China
[3] Ilma University, Department of Business Administration, Karachi, 75190, Pakistan
[4] Udmurt State University, Department of Public Service and Personnel Management, Izhevsk, 426034, Russia
[5] Department of Philosophy, Ural Federal University Named after the First President of Russia B.N. Yeltsin, Ekaterinburg, 620002, Russia
[6] Ural State Law University Named after V.F. Yakovlev, Department of Social and Humanitarian Disciplines, Ekaterinburg, 620137, Russia
*E-mails: zhanbayevrinat@gmail.com

Abstract

This article is devoted to the conceptual analysis of the relationship with energy resources, in the context of demoeconomics based on demoethical values as a tool for transforming the sustainable development of society. The purpose of the research is to establish the possibilities of applying demoethical values in the demoeconomic component of the economy within the framework of the relationship of energy resources that can contribute to sustainable development. The work uses a general methodological approach to research, that is, a systematic approach, within which methods of logical synthesis, goal setting, and goal decomposition are provided. The research demonstrates that the correlation between demoethical values and water and energy resources is established within the framework of "spirituality and morality", "responsibility", "justice", "rationality", and "security". It is posited that achieving sustainable societal development necessitates adherence to ethical principles that can effectively balance humanity's economic, social, and environmental requirements. The study's findings suggest that the value-based approach of demoethics assists in molding individuals, fostering virtuous behavior, and cultivating capable leaders who can make ethical, rational decisions. These decisions, in turn, facilitate a harmonious equilibrium between the economic, social, and environmental demands of society. Additionally, the demonstration of moral conduct in various life situations enhances the population's quality of life and enhances societal competitiveness. By employing the principles of demoethics, society can foster both personal growth and societal advancement.

Keywords: sustainable development goals (SDG), sustainable development of society, energetic resources, demoeconomics, demoethical values, spirituality, moral, responsibility, justice, rationality, safety, ethical rational decisions.

I. Introduction

Energy consumption, climate change, and environmental degradation are global issues (Lin & Li, 2022), which have created new research directions for the efficient operation and development of the energy system. The development of vehicles powered by new fuel cells is one of the important strategies to solve the problems associated with environmental pollution and climate change (AlHajri et al., 2021; Saatloo et al., 2022). The reason is that changing climate conditions and an increase in the frequency of natural disasters are circumstances that have a significant impact on the economic and social spheres, while they also create new problems in the field of energy security and sustainable development of states and society.

Population growth and increased consumption mean that energy issues are becoming increasingly important. Projections for 2035 (Shang et al., 2018) indicate a potential 40% increase in water demand and a 30% increase in energy demand. Of particular relevance are the issues of finding new energy sources, reducing energy dependence, and increasing energy efficiency. Water treatment facilities currently account for approximately 8% of global electricity consumption, underscoring the intricate interdependence between water and energy systems (Connor, 2015). As the need for water treatment escalates, this percentage could rise, further exacerbating the energy-water nexus. One approach that aims to exploit the synergies between different factors influencing sustainable development is the "nexus" approach, which allows identifying and resolution of emerging uncertainties (Sharmina et al., 2016; Hoolohan et al., 2019). The existence of many environmental, social, economic, and technological uncertainties at the micro- and macroeconomic levels creates difficulties in meeting the demand for water and energy resources. Water scarcity influences climate change (Byers et al., 2014; Naughton et al., 2012), which has led to an increase in overall water demand, as evidenced by the installation of carbon capture and storage systems in coal-fired power plants that will have global impacts on water and energy resources (Rodriguez et al., 2013).

Addressing these challenges and ensuring a sustainable future requires a comprehensive approach. Besides encouraging the adoption of environmentally friendly vehicles, initiatives to enhance water and energy efficiency are paramount. This achievement is possible through the development of advanced water treatment technologies that consume less energy, as well as by promoting water conservation practices and promoting the use of renewable energy sources in energy production. The consequences of water and energy shortages extend beyond national borders. This circumstance necessitates international cooperation to solve these problems on a global scale.

The water cycle and its changes raise valid concerns, particularly about water resource management in developing countries amidst cultural, social, political, and technological transitions (Sedláček, 2014). The availability of resources directly impacts

the energy sector, wherein successful decarbonization and energy supply decentralization are dependent factors (Helm, 2007). Renewable energy, while promising, also faces challenges, predominantly its susceptibility to weather conditions (Pryor et al., 2020). Consequently, numerous sectors within the economy are compelled to upgrade their conventional infrastructure in ways that enhance resilience towards evolving climatic conditions (Koh et al., 2009).
However, when studying the scientific works carried out to date, no studies were identified on the relationship between energy resources and demoethical values. It is necessary to use demoeconomics based on demoethical values as one of the main tools for transforming the sustainable development of society. Thus, it is necessary to note the importance of transdisciplinary and demoeconomic research based on demoethical, human-centered principles that emphasize the necessary values and needs of people in managing the demoethical components of the economy.
The purpose of the research is:
– identifying and analyzing the causes, trends, and forecasts in the field of energy resource use, offering recommendations to future researchers on this topic;
– application of demoethical values in the demoeconomic component of the economy within the framework of the relationship of energy resources that can contribute to sustainable development.

II. Methodology

This study presents integrated tools that include the connection between water and energy resources within the framework of the “demo-economic management concept based on demo-ethical values” to solve energy and water problems. We have outlined recommendations and some strategies that are used to define the relationship between water and energy resources. building on the Sustainable Development Goals (SDG), in particular SDG 3 (healthy lives and promoting well-being), SDG 6 (clean water and sanitation), SDG 7 (affordable clean energy), SDG 10 (reduced inequalities), SDG 7 (affordable clean energy), SDG 10 (reduced inequality), SDG 13 (climate action and peace) and SDG 16 (peace, justice and strong institutions). The focus on creating long-term sustainable solutions to increase stakeholder participation in decision-making processes was the methodological basis for this study for the formulated provisions of the presented recommendations.

III. Analysis

The main goal of sustainable development is the need to achieve a balanced development of technological and ethical rationalities in society, which should be aimed at increasing the competitiveness of a region or country and improving the quality of life of the population. Already in 1968, G. Hardin drew attention to the fact that humanity, while solving technical issues, does not solve issues in the field of improving moral and ethical relationships between people.
One dominant approach to understanding demand focuses on the individual as the unit of analysis and uses models that seek to understand pro-environmental behavior and motivation and their impact on energy and water demand (Frederiks, et al.,2015). This approach typically examines how attitudes, beliefs, and values shape human behavior, with particular emphasis on human free will. The rational choice model and theories of planned behavior and reasoned action present people as independent decision-makers. Others, such as the norm activation model, attribute a level of activation to social norms because a person's behavior is influenced by their awareness of the consequences of their actions and acceptance of personal responsibility (Abrahamse, et al., 2009).
Although research has increasingly recognized the gap between attitudes and behavior in environmental decision-making, the rational choice model has implications for both environmental economics and policy. This point of view is associated with the information deficit model, which is that to make a rational choice, people need information that would allow them to make the right decision. The described approach is useful for identifying the driving forces aimed at changing behavior, studying routines and traditions of resource use, and considering “rebound effects” (Herring, 2006), for example, if a person is motivated to implement environmental actions by values rather than money, the rebound effect may be smaller (Kaklamanou, et al., 2013).
To resolve the issue of social, economic, environmental, and technological uncertainties, a “demo-economics” component is proposed, based on the principles of demo-ethics, which means the individual satisfaction of the basic needs of society and man. By demoethics, we understand a section of ethics aimed at revealing general ideas about the essence of the world and man’s place in it based on the ideas and principles of sustainable development of society. The theoretical foundations of demoethics, such phenomena as education, reason, knowledge, science, and honest work, were developed since the principles of Abu Nasr al-Farabi, A. Kunanbaev, Y. Balasaguni, and it is they that today in the methodology of demoethics ensure the effective implementation of socially sustainable best available technologies. We consider demoethics as “a fundamental factor in the functioning of the proposed social development model. Demoethics can be defined as the ethical framework that governs the application of ethical principles in society, particularly concerning open interdisciplinary problems. It serves as a bridge between the aspirations of individuals and the norms and values of society” (Zhanbayev et al., 2023, p. 5-6).
The concept of demoeconomics is grounded upon principles and values of demoethics, such as "spirituality and morality," "responsibility," "justice," "rationality," and "safety." It assists in the cultivation of moral behavior, virtue, and leadership qualities in individuals and governing bodies, irrespective of the circumstances.
In the realm of energy, spiritual and moral values can serve as a foundation for the development and implementation of practices that promote the sustainable and ethical utilization of energy resources, while considering the needs and well-being of society as a whole. For instance, these values can be utilized to conduct educational campaigns, encourage the adoption of renewable energy sources, and initiate public infrastructure projects that foster energy efficiency.
The significance of "spiritual and moral" values in the energy and water resource sectors stems from fostering an understanding of the importance of adhering to ethical principles and exhibiting a responsible attitude towards the environment.
Within the energy sector, spiritual and moral values may encompass:
1. Ensuring equitable access to energy resources for all societal segments, while considering the needs and capacities of each individual.

2. Conservation of natural resources, reducing the reliance on fossil fuels and promoting the development of alternative energy sources aimed at mitigating the adverse environmental and biodiversity impacts.
3. Embracing accountability for the selection of energy technologies by assessing and mitigating potential risks and consequences associated with their use, such as in the case of nuclear energy.

IV. Results and Discussion

Demoeconomics is a section of economics in which, based on ideas about the sustainable development of society, issues of improving the quality of life of the population through freedom of social choice, consumption, and restrictions are considered in the aspect of modern directions of development of the digital and green economy. The main idea of demoeconomics is that economic and social processes should consider the interests and needs of the population, and not just the interests of economic and political elites. The key factors in demoeconomics are environmental sustainability, social justice, and innovative development potential. In demoeconomics, significant emphasis is placed on the digital economy and the green economy, which are integral to contemporary progress and increasingly influential in public affairs. The digital economy facilitates the emergence of novel prospects for economic and social advancement while enhancing production and consumption efficiency.
A fundamental principle of demoeconomics involves the engagement of the population in decision-making processes pertaining to the economy and social sphere. This principle can be implemented through diverse means, ranging from continuous exchange of perspectives and consultations to direct involvement of the population in decision-making via various mechanisms of civic participation. In totality, demoeconomics has the potential to invigorate economic development and foster the establishment of a more equitable and sustainable society. It allows formulating fresh models of economic progress that account for the interests of all societal segments and the environment. Thus, sustainable development is a model of social development that is based on an effective state strategy, which includes demographic, democratic, demo-economic, and demo-ethical components. The main goal is to achieve a balanced development of technological and ethical rationalities in society, aimed at improving the quality of life of the population and increasing the competitiveness of the region.
The value of responsibility plays a key role in ensuring sustainable, efficient, and environmentally friendly use of energy resources. We believe that energy must be responsible, which means energy must comply with a balance between the needs of the current generation and the ability of future generations to meet their needs. Therefore, an important requirement of responsible energy is the use of resources in a way that preserves their availability for future generations, it is important to integrate environmentally friendly and energy-efficient technologies into production and life support systems and minimize the negative impact on nature since they are necessary for the development of society and the well-being of humanity as a whole. The reason is that responsible use of energy resources is a fundamental factor in environmental protection, as it is based on respect for environmental principles and recognition of potentially harmful impacts. human factor on the environment.
In the energy sector, the value of "equity" assumes particular significance. It encompasses the concept of energy justice, which provides an analytical framework for evaluating the outcomes of decision-making during the energy transition. Energy equity is reflected in the fair sharing of costs and benefits, equal opportunity, recognition, and participation in energy processes. It highlights the need for access to safe, affordable, and sustainable energy.
Justice is a comprehensive framework applicable to decision-making processes. It is often evaluated using three fundamental principles: distributive justice, procedural justice, and recognition justice (McCauley et al., 2013). These principles have become prevalent in policy analysis, programs, and academic research, effectively shaping the discourse surrounding energy justice.
Overall, embracing the values of responsibility and equity within the energy sector enables us to foster sustainable and inclusive practices. By upholding these principles, we can ensure the equitable distribution of energy resources, promote environmental preservation, and work towards the betterment of both present and future generations.
Energy justice is a comprehensive framework applicable to decision-making processes. It is often evaluated using three fundamental principles: distributive justice, procedural justice, and recognition justice. These principles have become prevalent in policy analysis, programs, and academic research, effectively shaping the discourse surrounding energy justice.
Overall, embracing the values of responsibility and equity within the energy sector enables us to foster sustainable and inclusive practices. By upholding these principles, we can ensure the equitable distribution of energy resources, promote environmental preservation, and work towards the betterment of both present and future generations.
Within the “three principles” model, distributive justice considers the benefits and costs of the energy transition. The expansion of wind energy raises concerns about the benefits and challenges of each source, such as environmental impacts and development costs. The distribution of these costs may be uneven based on geographic proximity and the availability of benefits such as workforce training (Hu, 2020).
In addition, procedural justice examines how policies and decisions are implemented and how various stakeholders are included in energy development decision-making processes. This requires inclusive and meaningful access for all stakeholder communities to have a say at every stage of the process (Hazrati & Heffron, 2021).
Recognition equity seeks to recognize all individuals or communities affected by changes in the energy system and values understanding the social, political, and cultural implications of energy policies or decisions for all people. Understanding that energy systems and transitions can disproportionately impact certain marginalized communities is a key component of recognizing equity. Recognition and procedural justice often go hand in hand, as the energy transition considers both the value of who is represented in decision-making processes and the measures that enable or discourage that representation (Lee & Byrne, 2019).
The role of the value “rationality” in the energy sector is as follows. Public-Private Energy and Energy Efficiency Partnership (REEEP) CEO Marianne Moscoso-Osterkorn describes the complexity of assessing and measuring the overall effectiveness of energy efficiency measures (Interview, 2016). The results of the measures taken are mixed, as they are influenced by many different factors, such as economic growth, the way energy is used, available technologies, mentality, and the “rebound effect”, among others. Regrettably, it is challenging to corroborate all the provisions stated in the report, thereby diminishing the

conclusiveness of its findings. Undoubtedly, the efficacy of energy efficiency measures, designed to curtail greenhouse gas emissions, may be subject to scrutiny when considering both direct and indirect rebound effects. Nevertheless, it is vital to acknowledge that energy efficiency encompasses numerous additional advantages beyond climate change mitigation. Through judicious energy consumption, labor productivity and production capacity can increase, electricity usage can decrease, household expenditures can be reduced, and, notably, power supply reliability can be enhanced.

Practice shows that measures to improve energy efficiency are most successful if they are part of a set of general measures, including the introduction of new technologies, an incentive system, training, as well as mobilization of forces, and propaganda among the population. The result of such comprehensive programs is a significant reduction in energy consumption. According to a September 2009 assessment by the Asia-Pacific Economic Community, Thailand's standards and labeling program resulted in 10,175 gigawatt-hours of electricity savings, 1,725 megawatts of peak load reduction, and 6 million tons of carbon emissions savings. gas In the Philippines, air conditioner labeling and standards reduced total power consumption by 6 MW during the first year of the program. Another example is the national program for the transition to energy-saving lamps, launched in 2007 in the Republic of Ghana. The program has reduced the peak load on the nation's strained power grid and lowered energy costs for most low-income residents. After replacing six million lamps, the peak load on the country's electricity grid fell by 124 MW per year, and carbon dioxide emissions into the atmosphere decreased by 112,320 tons. Energy costs decreased by $33 million (Making It, 2011).

The role of the value of “security” in the energy sector is as follows. Traditionally, energy security has been defined as an adequate, affordable, and reliable supply of energy. Energy is essential for both economic development and human security. Reliable energy supply can be seen as a public good for society for which governments must ultimately take responsibility to minimize market supply failures. Disruptions in the supply of oil, gas, and electricity can have serious consequences for societies, economies, and individuals.

Unlike energy security and its vulnerabilities, climate change is a more recent issue but is closely related to energy policy and energy security. Thus, energy supply disruptions also result from extreme weather conditions or accidents: in August and September 2005, hurricanes Katrina and Rita shut down 27 percent of US oil production and 21 percent of oil refining in the Gulf of Mexico, with worldwide implications for oil prices, energy policy, climate change, strategic oil reserves and perceptions of security of supply. Decision-makers need to address the twin challenges of energy security and climate change to ensure the security of our global energy system and reduce greenhouse gas emissions as part of an overall human security strategy (Umbach, 2008).

V. Conclusion

Strategic energy planning has long-term and significant implications, as the long life of these infrastructures determines demand and consumption patterns for many decades to come. From a demand perspective, it appears to be fairly stable, but ongoing and major changes in climate, society, and technology are creating an increasingly dynamic environment with diverse effects that interact to drive demand in different ways. This is particularly relevant for energy and water resources, which must be explored under rapidly changing conditions and deep uncertainty. This changing view requires new types of research questions and appropriate approaches to address them.

This paper proposes a concept of the principles and values of demoethics, which allows each member of society to adapt to various negative consequences and which will be used as tools of stabilization in the conditions of the “emerging” climate reality, which is emerging at the current time and affects issues of sustainable development of states. The approach of the concept of values of demoethics, which highlights “spirituality and morality”, “responsibility”, “justice”, “rationality” and “safety” helps to form a person, virtues, a city ruler capable of making ethical rational decisions, capable of ensuring a balance between economic, social, and environmental needs of humanity, as well as the manifestation of moral behavior in any life situation.

It is also important to note that when adapting members of society to negative consequences, it is necessary to teach them to possess the qualities of demoethics, such as education, good manners, reason, knowledge, science, and honest work. As a result, the synthesis of education, upbringing, developed intelligence, acquisition of knowledge, scientific principles, and honest work will play an important role in sustainable development.

To implement SDG 13 (action to combat climate change and its impacts), SDG 6 (ensure access to water and sanitation for all), SDG 7 (ensure access to clean and affordable energy), SDG 3 (healthy lifestyles and promoting well-being), SDG 11 (make cities and human settlements inclusive, safe, resilient, and sustainable) measures are proposed to develop the demo-economy component. With the observance and implementation by society and the state of the concept of demoeconomics, which is based on demoethical values, the implementation of the interconnections of the concept of the “water-food-energy-ecosystems”, “water-soil-waste” systems could help increase the interconnection between various sectors of the economy, which, in turn, turn, would make it possible to achieve consistency in the efficient use of resources.

Acknowledgments: This study was funded and supported by the Science Committee of the Ministry of Education and Science of the Republic of Kazakhstan No. AP13068164 “Development of tools aimed at modeling socio-economic systems for sustainable development of society”.

References

Abrahamse, W., Steg, L., (2009) How do socio-demographic and psychological factors relate to households’ direct and indirect energy use and savings? J. Econ. Psychol. 30 (5), 711–720. https://doi.org/10.1016/j.joep.2009.05.006

AlHajri, I., Ahmadian, A., Elkamel, A., (2021) Techno-economic-environmental assessment of an integrated electricity and gas network in the presence of electric and hydrogen vehicles: A mixed-integer linear programming approach. Journal of Cleaner Production 319, 128578. https://doi.org/10.1016/j.jclepro.2021.128578

Byers, E., Hall, J., Amezaga, J., (2014) Electricity Generation and Cooling Water Use: UK Pathways to 2050. Global

Environmental Change. Part A 25, 16–30. https://doi.org/10.1016/j.gloenvcha.2014.01.005
Connor, R., (2015) The United Nations world water development report 2015: Water for a sustainable world. UNESCO Publishing, Paris, France.
Frederiks, E.R., Stenner, K., Hobman, E.V., (2015) Household energy use: applying behavioural economics to understand consumer decision-making and behaviour. Renew. Sustain. Energy Rev. 41, 1385-1394. https://doi.org/10.1016/j.rser.2014.09.026
Hazrati, M., Heffron, R.J., (2021) Conceptualising restorative justice in the energy transition: changing the perspectives of fossil fuels. Energy Research & Social Science 78, 102115. https://doi.org/10.1016/j.erss.2021.102115
Helm, D., (2007) The New Energy Paradigm. Oxford University Press, Oxford, UK,
Herring, H., (2006) Energy efficiency-a critical view. Energy 31 (1), 10–20. https://doi.org/10.1016/j.energy.2004.04.055
Hoolohan, C., Soutar, I., Suckling, J., et al., (2019) Stepping-up innovations in thewater-energy-food nexus: A case study of anaerobic digestion in the UK. Geogr.J. 185, 391–405. https://doi.org/10.1111/geoj.12259Howarth
Howard, D., Sharmina, M., Hoolohan, C., Larkin, A., Burgess, P., Colwill, J., Gilbert, P., Knox, J., Anderson, K., (2016) A nexus perspective on competing land demands: Wider lessons from a UK policy case study. Environmental Science & Policy 59, 74-84. https://doi.org/10.1016/j.envsci.2016.02.008
Hu, Z. (2020). When energy justice encounters authoritarian environmentalism: the case of clean heating energy transitions in rural China. Energy Research & Social Science 70, 101771. https://doi.org/10.1016/j.erss.2020.101771
Interview: Moscoso-Osterkorn on the future of renewable energy. May 13, 2016. Available from: https://executiveacademy.at/en/news/detail/moscoso-osterkorn-on-the-future-of-renewable-energy (access date: 10.10.2023).
Kaklamanou, D., Jones, C.R., Webb, T.L., Walker, S., (2013) Using public transport can make up for flying abroad on holiday: compensatory green beliefs and environmentally significant behavior. Environ. Behav. 47 (2), 184–204. https://doi.org/10.1177/0013916513488784
Koch, H., Vögele, S., (2009) Dynamic modelling of water demand, water availability and adaptation strategies for power plants to global change. Ecol. Econ. 68 (7), 2031–2039. https://doi.org/10.1016/j.ecolecon.2009.02.015
Lee, J., Byrne, J., (2019) Expanding the conceptual and analytical basis of energy justice: beyond the three-tenet framework. Frontiers in Energy Research 7, 99. https://doi.org/10.3389/fenrg.2019.00099
Lin, B., Li, Z., (2022) Towards world's low carbon development: The role of clean energy. Applied Energy 307, 118160. https://doi.org/10.1016/j.apenergy.2021.118160
Liu, J., Yang, H., Zhou, Y., (2021) Peer-to-peer trading optimizations on net-zero energy communities with energy storage of hydrogen and battery vehicles. Applied Energy 302, 117578. https://doi.org/10.1016/j.apenergy.2021.117578
Making It. № 6, II quarter 2011. Available from: https://www.unido-russia.ru/archive/num6/art6_17/ (access date: 10.10.2023).
McCauley, D.A., Heffron, R.J., Stephan, H., Jenkins, K., (2013) Advancing energy justice: the triumvirate of tenets. International Energy Law Review 32(3), 107–110.
Naughton, M., Darton, R., Fung, F., (2012) Could climate change limit water availability for coal-fired electricity generation with carbon capture and storage? A UK case study. Energy Environ. 23 (2–3), 265–282. https://doi.org/10.1260/0958-305X.23.2-3.265
Pryor, S.C., Barthelmie, R.J., Bukovsky, M.S., Leung, L.R., Sakaguchi, K., (2020) Climate change impacts on wind power generation. Nat Rev Earth Environ 1, 627–643. https://doi.org/10.1038/s43017-020-0101-7
Rodriguez D.J., Delgado, A., DeLaquil, P., Sohns, A., (2013) Thirsty Energy. Water Papers. The World Bank. Available from: http://hdl.handle.net/10986/16536 (access date: 10.10.2023).
Saatloo, A.M., Mehrabi, A., Marzband, M., Aslam, N., (2022) Hierarchical user-driven trajectory planning and charging scheduling of autonomous electric vehicles. IEEE Transactions on Transportation Electrification, 1. https://doi.org/10.1109/TTE.2022.3196741
Sedláček, J., Knutti, R., (2014) Half of the world's population experience robust changes in the water cycle for a 2°C warmer world. Environ. Res. Lett. 9 (4), 044008. https://doi.org/10.1088/1748-9326/9/4/044008
Shang, Y., Hei, P., Lu, S., Shang, L., Li, X., Wei, Y., Jia, D., Jiang, D, Ye, Y., Gong, J., Lei, X., Hao, M., Qiu, Y, Liu, J., Wang, H., (2018) China's energy-water nexus: Assessing water conservation synergies of the total coal consumption cap strategy until 2050. Applied energy 210, 643–660. https://doi.org/10.1016/j.apenergy.2016.11.008
Umbach, F., (2008) German Debates on Energy Security and Impacts on Germany's 2007 EU Presidency. In: Marquina, A. (eds) Energy Security. Palgrave Macmillan, London. https://doi.org/10.1057/9780230595002_1
Zhanbayev, R.A., Irfan, M., Shutaleva, A.V., Maksimov, D.G., Abdykadyrkyzy, R., Filiz, S., (2023) Demoethical Model of Sustainable Development of Society: A Roadmap towards Digital Transformation. Sustainability 15, no. 16, 12478. https://doi.org/10.3390/su151612478.

IEEES-117

Electrochemical Disinfection of Secondary Effluent Using a Low Cost Stainless Steel Electrodes

[1*] Hafida Lebik, [2] Rafik Elhadi, [1] Sarah Mahidine, [1] Wassila Yazid, [1] Sarah Djelti, [1] Belgassim Boutra
[1] Unité de Développement des Equipements Solaires, UDES, Centre de Développement des Energies Renouvelables, CDER, 42415, Tipaza, Algeria.
[2] Centre De Recherche Scientifique et Technique en Analyses Physico – Chimique, CRAPC, 42415, Tipaza, Algeria.
*E-mails: lebikhafida@yahoo.com

Abstract

The global water crisis has led to the development of research in unconventional water resources areas, such as wastewater reclamation and reuse. However, enabling the safe reuse of water requires a reliable disinfection process to ensure efficient inactivation of pathogens. In recent years, electrochemical disinfection (ED) has gained great interest, as it enables the design of compact, portable devices, particularly for remote communities. The main objective of this research is to demonstrate the feasibility of ED applied to the disinfection of real wastewater effluent using low-cost stainless steel electrodes. The effect of varying treatment durations (5, 15, and 30 minutes) on the reduction of coliforms, used as an indicator bacteria, was investigated. The results show that a total reduction (meaning 6 Log reduction) of the initial bacterial load is achieved regardless of the electrolysis time.
However, an examination of energy consumption revealed high values of a minimum value of about 1kwh /m3 per log reduced coliforms. In order to optimise energy consumption, the addition of electrolyte (0.1N NaCl) has been examined. The results obtained showed that the addition of electrolytes helps to reduce energy consumption by half, but is accompanied by the production of sludge, the quantity of which increases with the increase in electrolysis time. The results allowed us to highlight potential applications of electrochemical disinfection and permit to give an operational approach to the system.

Keywords: Electrochemical disinfection, coliforms reduction, energy consumption, sludge generation.

I. Introduction

Climate change that causes scarcity of rain or heavy rainfall out of season, combined with a growing population and an increasing demand for water, are all contributing factors to the water crisis in several countries. Indeed, according to UNICEF, half of the world's population is facing water scarcity by 2025 (UNESCO World Water Assessment Programme, 2018). On the other hand, rapid urbanization in conjunction with the high cost of wastewater treatment has led to the generation of increasingly large volumes of untreated wastewater, most of which is discharged into the receiving environment without prior treatment (Boretti and Rosa, 2019). Hence, exploring the use of unconventional sources of water has become a necessity.
However, wastewater recycling implies using an effective disinfection treatment to ensure a safe and reliable water source for reuse. Several disinfection processes are commonly used in tertiary treatment for inactivating pathogens such as chlorine, ultraviolet irradiation, filtration and ozonation (EPA, 2004). The importance of disinfection has led to ongoing research into developing new processes more efficient, easier to maintain and, above all, more versatile and modular. In this context, the electrochemical disinfection (ED) technique can play a crucial role. Indeed, ED is particularly promising for decentralized small-scale systems and represents a compelling alternative to chemical disinfection, as it eliminates the need to handle hazardous chemicals. It offers potential advantages such as scalability, the ability to create compact, portable devices, versatility, environmental compatibility, automation, inherent safety, and cost savings (Martínez-Huitle and Brillas, 2021).
The effectiveness of electrochemical disinfection has been extensively documented (Cotillas et al., 2018; Hand and Cusick, 2021; Isidro et al., 2020; Zhang et al., 2013). However, the majority of the studies deal with synthetic solutions, where disinfection tests are conducted within controlled matrix compositions (Jin et al., 2019; Rahmani et al., 2019; Zhang et al., 2023). Unfortunately, these studies often overlook the interferences that may be present in real wastewater, characterized by a high concentration of organic matter and the presence of pathogen mixtures, thereby limiting the practical applicability of such systems (Forés et al., 2023). Similarly, the unavailability of cost-effective electrode materials crucial for efficient Electrochemical Disinfection (ED) impedes the widespread development of the system at a large scale.
In this study, we examine the disinfection potential of cost-effective stainless steel electrodes (316L type, commonly used in marine applications) in treating a real treated wastewater effluent.
The aim of the process evaluation is to reduce coliforms, taken as an indicator microorganism, with the objective of meeting the reuse compliance standards set at the national level. An attempt to minimize energy consumption has been incorporated through the introduction of electrolytes.
The novelty of this research lies in its approach, which considers both energy consumption and sludge production, alongside using wasted materials as electrodes and real wastewater.

II. Experimental Procedure /Methodology/System Description

The experiments were conducted using a sample of real treated wastewater, obtained directly from the clarification basin of the Beni Merad wastewater treatment plant in Algeria. Importantly, no prior pretreatment was administered to the sample, as it inherently represents a secondarily treated wastewater and is deemed ready for tertiary treatment. This unaltered nature of the wastewater sample ensures that the experimental conditions closely mimic real-world scenarios, allowing for a more

accurate assessment of the disinfection process.
All electrochemical disinfection experiments were performed in a batch reactor. As shown in Fig. 1, the reactor consists of 500ml container with five pairs of parallel plate electrodes with dimensions of (4.5 cm × 9 cm); electrodes are made of stainless steel 316L, which contains a maximum carbon rate of 0.03%, reducing the risk of carbon precipitation and ensuring maximum corrosion resistance. The electrodes were used with an electrode distance of 1 cm.

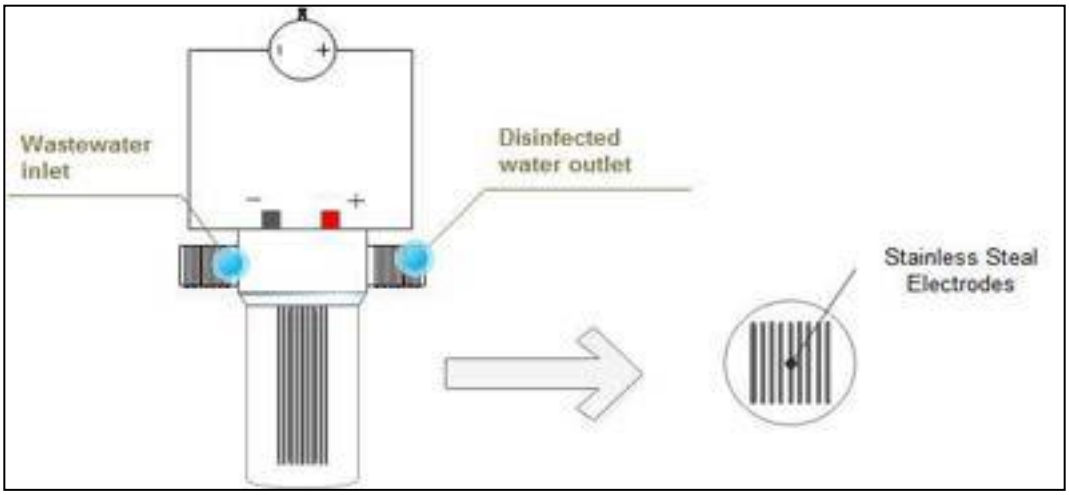

Fig. 1: Schematic diagram of the electrochemical cell

Experiments were conducted in duplicate, at a constant current of 3A, provided by a digital direct current power supply (Peak Tech-1885).
During electrolysis, the voltage of the cell was taken as a function of time. In electrolyte experiments, 0.1N NaCl was added and mixed into wastewater before electrolysis.
For sludge quantification, each sample was filtered, and the filtrate was collected and subjected to oven drying until a constant weight was achieved. The weighing process was executed using an analytical balance with a precision of 0.0001 g.
Immediately after treatment, sodium thiosulfate (0.1 mL of 3% solution) was added into the medium to stop the dechlorination and ensure accurate results in the enumeration of coliforms in wastewater (American Public Health Association, 2017).

III. Analysis

In the present work, coliforms were used as indicators of microbiological contamination. Coliform enumeration in wastewater was performed using membrane filtration methods and incubation on Lactose TTC Agar with Tergitol® 7 medium.
A sample of 100 ml is filtered on sterile cellulose-nitrate filters of 0.45µm. After filtration the filter is transferred, under aseptical conditions, to the agar surface and incubated for 21 ± 3 hours at 36 ± 2 °C. After that, the typical colonies were counted.
To estimate the amount of initial coliform bacteria load, sequential decimal dilutions from 1/10 to $1/10^7$ were performed on the initial raw sample.
In order to identify any potential contamination, an ultra-pure white is filtered and incubated for each series of analyses in the same way as the sample being examined.
The results are expressed as the decimal logarithmic number of units forming colonies (UFC) per 100 ml.

The energy consumption (EC) for the electrochemical disinfection treatment was calculated in kWh m^{-3} per log removal of coliform, according to Eq1 adapted from (Li et al., 2010):

$$EC = \frac{E_{cell}\ I\ t}{1000\ Vs\ \Delta(Log_{10}\ C)} \quad (1)$$

where Ecell is the the cell voltage (V), I is the current (A), t is treatment time in (h), Vs is the treated volume (m^3) and Δlog10 NC is the log inactivation of coliforms corresponding to tcalculated as follows:

$$\Delta Log_{10}\ C = Log\ \frac{N}{N_0} \quad (2)$$

where N is the number of units forming colonies at t electrolysis time (UFC/ml), and N_0 is the initial coliform load (UFC/ml).

IV. Results and discussion

The study aimed to explore the impact of different treatment durations (5, 15, and 30 minutes) on the reduction of coliforms, employed as indicator bacteria. The outcomes of the investigation revealed a consistent and substantial total reduction, equivalent to a 6 Log reduction, in the initial bacterial load. This suggests that the treatment time exceeded the required duration for electrochemical disinfection within the system. However, it's important to note that the treatment duration was deliberately chosen to facilitate energy consumption tests and assess the evolution of sludge production.

The analysis of energy consumption revealed elevated values, with a recorded values variying from 1 to 7 kWh/m³ per log reduction of coliforms. It was also observed that an extended treatment time led to higher energy consumption.
In order to maximize energy efficiency, the introduction of electrolyte (0.1N NaCl) was investigated, the results showed that the electrolyte addition reduced energy consumption by half.
However, this energy-saving enhancement came at the expense of increased sludge production, a quantity of which escalated with extended electrolysis times. These findings not only shed light on potential applications of electrochemical disinfection but also provide operational approaches for the system, offering valuable insights into the delicate balance between energy efficiency and sludge management in wastewater treatment.

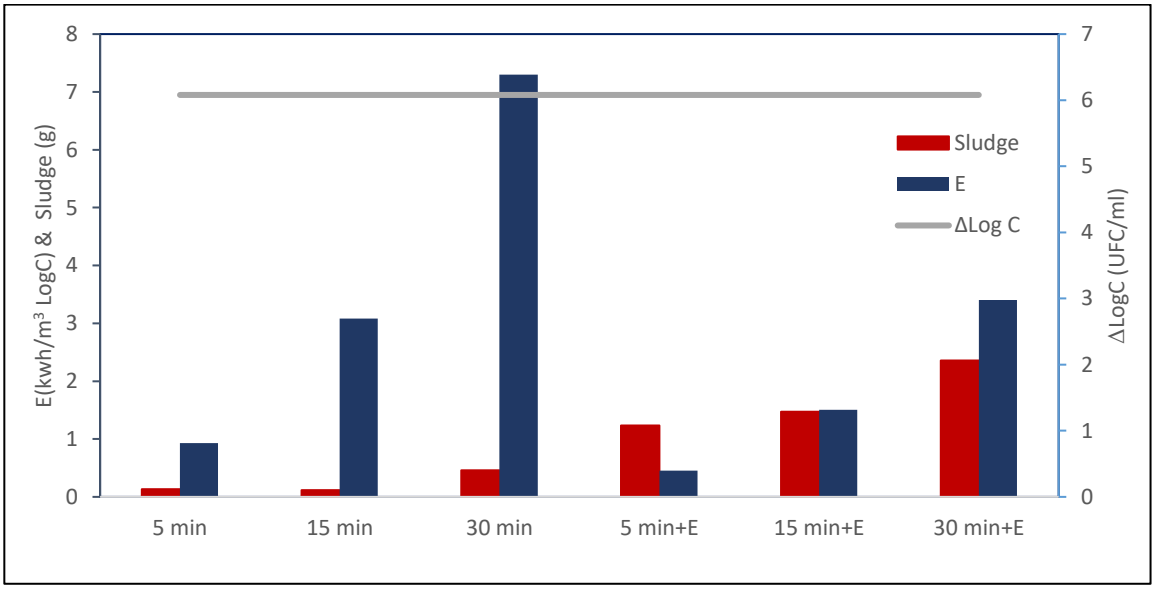

Fig. 2. : Energy consumption, sludge production and coliforms reduction in ED system for different treatment time with (E) and without electrolyte addition

V. Conclusion

The investigation centered on electrochemical disinfection (ED) as a promising solution for treating secondary treated wastewater. Notably, the study employed cost-effective stainless steel electrodes (316L type), commonly used in marine applications, presenting a pragmatic approach to developing efficient and sustainable disinfection processes.
The evaluation of treatment durations demonstrated a remarkable and consistent total reduction of 6 Log units in coliforms across varying timeframes, signaling the efficacy of the electrochemical disinfection process. Exceeding the necessary duration for disinfection, was intentionally chosen to facilitate comprehensive assessments of energy consumption and sludge production evolution. The analysis of energy consumption reveals elevated values, emphasizing the energy-intensive nature of electrochemical disinfection. To address this, the addition of electrolyte (0.1N NaCl) effectively reduced energy consumption. However, this commendable reduction came at the cost of increased sludge production, particularly noticeable with extended electrolysis times.
In order to find abalance between sludge production, energy consumption, and treatment efficiency, it is crucial to optimize the electrolyte dosage.

References

American Public Health Association, 2017. Standard methods for the examination of water and wastewater, 23rd ed. APHA American Public Health Association, Washington, D.C.
Boretti, A., Rosa, L., 2019. Reassessing the projections of the World Water Development Report. npj Clean Water 2, 15. https://doi.org/10.1038/s41545-019-0039-9
Cotillas, S., Lacasa, E., Sáez, C., Cañizares, P., Rodrigo, M.A., 2018. Disinfection of urine by conductive-diamond electrochemical oxidation. Appl. Catal. B Environ. 229, 63–70. https://doi.org/https://doi.org/10.1016/j.apcatb.2018.02.013
EPA, U., 2004. Primer for municipal wastewater treatment systems. OoW Manag.
Forés, E., Mejías-Molina, C., Ramos, A., Itarte, M., Hundesa, A., Rusiñol, M., Martínez-Puchol, S., Esteve-Bricullé, P., Espejo-Valverde, A., Sirés, I., Calvo, M., Araujo, R.M., Girones, R., 2023. Evaluation of pathogen disinfection efficiency of electrochemical advanced oxidation to become a sustainable technology for water reuse. Chemosphere 313, 137393. https://doi.org/https://doi.org/10.1016/j.chemosphere.2022.137393
Hand, S., Cusick, R.D., 2021. Electrochemical disinfection in water and wastewater treatment: identifying impacts of water quality and operating conditions on performance. Environ. Sci. Technol. 55, 3470–3482.
Isidro, J., Brackemeyer, D., Sáez, C., Llanos, J., Lobato, J., Cañizares, P., Matthée, T., Rodrigo, M.A., 2020. Electro-disinfection with BDD-electrodes featuring PEM technology. Sep. Purif. Technol. 248, 117081. https://doi.org/https://doi.org/10.1016/j.seppur.2020.117081

Jin, Y., Shi, Y., Chen, R., Chen, X., Zheng, X., Liu, Y., 2019. Electrochemical disinfection using a modified reticulated vitreous carbon cathode for drinking water treatment. Chemosphere 215, 380–387. https://doi.org/https://doi.org/10.1016/j.chemosphere.2018.10.057

Li, H., Zhu, X., Ni, J., 2010. Inactivation of Escherichia coli in Na2SO4 electrolyte using boron-doped diamond anode. Electrochim. Acta 56, 448–453. https://doi.org/https://doi.org/10.1016/j.electacta.2010.08.055

Martínez-Huitle, C.A., Brillas, E., 2021. A critical review over the electrochemical disinfection of bacteria in synthetic and real wastewaters using a boron-doped diamond anode. Curr. Opin. Solid State Mater. Sci. 25, 100926. https://doi.org/https://doi.org/10.1016/j.cossms.2021.100926

Rahmani, A.R., Samarghandi, M.R., Nematollahi, D., Zamani, F., 2019. A comprehensive study of electrochemical disinfection of water using direct and indirect oxidation processes. J. Environ. Chem. Eng. 7, 102785. https://doi.org/https://doi.org/10.1016/j.jece.2018.11.030

UNESCO World Water Assessment Programme, 2018. The United Nations world water development report 2018: nature-based solutions for water. UNESCO, Paris.

Zhang, C., Jiang, Y., Li, Y., Hu, Z., Zhou, L., Zhou, M., 2013. Three-dimensional electrochemical process for wastewater treatment: A general review. Chem. Eng. J. 228, 455–467.

Zhang, J., Su, P., Xu, T., Yuan, L., Qiao, M., Yang, B., Zhao, X., 2023. Comprehensive study on the role of reactive oxygen species and active chlorine species on the inactivation and subcellular damage of E.coli in electrochemical disinfection. Sep. Purif. Technol. 304, 122408. https://doi.org/https://doi.org/10.1016/j.seppur.2022.122408.

EEES-118

Re-defining and conceptualizing the Energy Footprint as a Sstandalone Indicator

[1*]Abdullah Muratoglu,
[1] Batman University, Civil Engineering Department, Batman, 72100, Türkiye
*E-mails: abdmuratoglu@gmail.com

Abstract

Footprinting methods are employed to assess the influence of human activities on natural resources. The prominent footprint methods include ecological (ECF), carbon (CF), water (WF), and energy footprints (ENF). The term "energy footprint" has been employed in previous academic studies, primarily referring to ecological land area and carbon emissions, without a distinct methodology of its own. Previous research has endeavored to enhance the methodology from different angles. Nonetheless, a standalone methodology that explicitly illustrates the quantification steps and measurement of the ENF remains undeveloped. The main objective of this study is to refine the definitions and methodology of the ENF, transforming it into a standalone technique that is separate from the ecological footprint. Consequently, the concept, dimensions, and units of the energy footprint have been reconsidered. This new approach is inspired by the water footprint methodology that has emerged and systemized in recent years. The inclusion of the primary source of energy is also one of the key innovations of this approach. This new concept considers the comparability and standardization of energy-intensive products and processes, ranging from various fossil fuels to renewable energy sources. Consequently, this study undertook a review of existing approaches to the energy footprint and the main pillars of redefined methodology inspired from the modern water footprint indicator.

Keywords: energy, footprint, management, virtual, novel approach.

I. Deficiencies in Portraying the Energy Footprint

There is a lack of agreement among researchers regarding the definition and methodology of the energy footprint. The Global Footprint Network defines it as the combined land area utilized for generating non-food and non-feed energy (Čuček et al., 2012). Jones et al. (2015) employed the term "energy footprint" to refer to the ecological impacts caused by energy resources, rather than treating it as a standalone metric. Likewise, the Ecological Footprint Standards (GFN, 2009) do not classify the energy footprint as an independent indicator. Hoekstra & Wiedmann (2014) acknowledged various types of footprint measurements like ecological, carbon, material, and water footprints. Nevertheless, they did not present a scientific explanation for the energy footprint. The majority of previous investigations into the energy footprint have utilized the ecological footprint approach. (Chen et al., 2007; Čuček et al., 2012; Fang et al., 2014; Jones et al., 2015; Stoeglehner & Narodoslawsky, 2009; Zhang et al., 2016).

Despite the term "embedded energy" being introduced in the 1980s (Costanza, 1980; Odum et al., 1978), the progress in energy footprint research has been limited for over four decades due to various limitation about conceptualization and methodization. On the contrary, the concept of "virtual water," put forward by Allan (1993), has witnessed significant advancements in the field of water footprinting. Then, numerous research studies on water footprinting worldwide have adopted a similar methodology proposed by Hoekstra et al. (2011), demonstrating its widespread application. The standardization of the water footprint methodology, along with the widespread use of a common technical language, has improved the control, verification, and dissemination of international research. Similarly, this study aims to take an initial step in systematizing the methodology of the energy footprint by differentiating it from the ecological footprint.

The analysis of energy footprints has been carried out using various methods such as ecological footprint, input-output analyses, and life cycle assessment (Tian et al., 2019). However, the author believes that the method lacks a proper conceptualization with its own methodology. Regrettably, previous studies have mostly utilized their own approaches when quantifying the energy footprint, which undermines the comparability of the results being universally accepted.

The initial approach to assessing the energy footprint has received criticism for its static nature, lacking explicit consideration of the connections between final consumption and primary energy requirements (Ferng, 2002). In response, Ferng (2002) underscored the importance of a distinct energy footprint that incorporates input-output analyses, separate from the ecological footprint (Fang et al., 2014). The definition put forth by Tian et al. (2019) contributes to the modern understanding of the energy footprint as an indicator that accounts for the direct and indirect consumption of energy resources in the production of goods and services for the final consumer. However, their conceptualization is somewhat constrained in terms of accommodating various units of energy footprint, and further research is necessary to delve into the methodology employed for calculating the energy footprint. There have been previous studies on other energy types such as nuclear, renewables, wind and solar (Čuček et al., 2012). However, many of these studies have relied on ecological footprints and the associated land area as indicators.

II. Energy footprint should be distinguished from ecological footprint

It is reported that, the ecological footprint term has been firstly proposed by Wackernagel and Rees (Wackernagel & Rees, 1996) showing a sustainable development index for calculating human dependency on the land and water ecosystem (Ferng, 2002). The ecological footprint analyses try to calculate the amount of biologically productive area that is needed to produce

the annual resource flows that is consumed by a population of a region (Haberl et al., 2001). Stöglehner (2003) linked the ecological footprint to the energy supplies of regions, households, and companies. It can be said that the previous studies on footprinting of energy is based on ecological considerations, rather than being an independent indicator for measuring and comparing the different type of energy use. Earlier studies on ecological footprint are based on a land use matrix of several consumption categories (Bicknell et al., 1998). The land use types are; energy land, built environment, gardens, croplands, pasture and forests. On the other hand, the consumption categories are food, domestic use, transportation, trade goods and services (Bicknell et al., 1998).

III. A Novel Approach to Energy Footprint: Concept and Initial Methodology

Definition and Concepts

The concept, definitions, and models brought by this study are listed below:

1. Energy footprint (ENF) is an indicator that quantifies the human consumption of energy resources naturally available on Earth. This indicator encompasses all types of energy resources, including fossil fuels, renewables, and nuclear energy, that are utilized in human activities.

2. The Energy Footprint (ENF) is defined as the total energy consumption in the production or supply chain of goods and services. The total ENF of a final product or process is the sum of all direct and indirect energy-using processes throughout its life cycle. The ENF of a region or corporation is the sum of the ENF of all its sub-processes and products.

3. The primary aim of ENF studies is to improve the environmental sustainability of energy resources by providing an objective measure and comparison of different products, tools, services, processes, and organizations.

4. The ENF framework is intended to facilitate effective energy management, specifically targeting the enhancement of energy efficiency and conservation through the mitigation of energy losses.

5. The ENF metric does not incorporate the energy consumed in the formation of natural materials, such as the embedded energy in raw materials and other sources. For instance, fossil fuels are concentrated forms of solar energy and do not possess any ENF until they are utilized in human activities. ENF solely originates after the implementation of anthropogenic activities.

Quantifying the Energy Footprint at Different Scales

The energy footprint can be assessed by considering various levels of human activities, as depicted in Figure 1. These scales have been categorized as below;

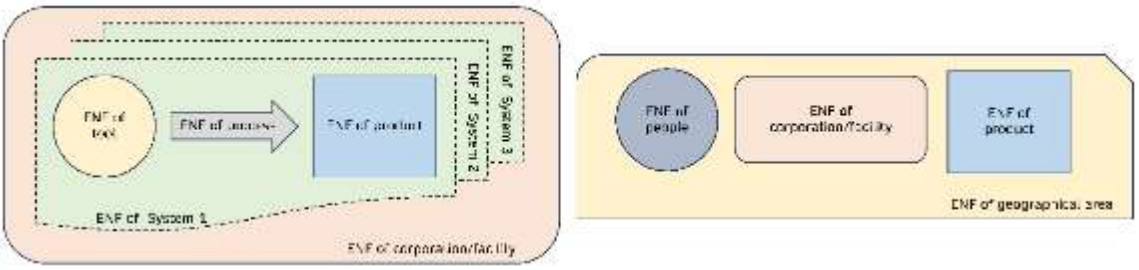

Figure 1. Energy footprint at different anthropogenic scales

•The energy footprint of a **tool** is calculated by summing up the energy consumed by the tool over a given time period.
•The energy footprint associated with a **process** is the cumulative energy consumption of all the tools and equipment utilized within that process. This type of energy footprint can be quantified using various units of time, including seconds, hours, days, years, and more.
•The energy footprint of a **product** is determined by aggregating the energy footprints of all the tools and processes employed in its supply chain.
•The energy footprint of a **work** or **system** is the cumulative energy usage of all the products, processes, and tools utilized during its entire lifecycle.
•The energy footprint of a **facility** is calculated by summing up the energy footprints of all the products, processes, departments, and tools used throughout the organization.
•The energy footprint of a **corporation** is calculated by adding up the energy footprints of all its subsidiary processes and products.
•The energy footprint of **individuals** or **a group of people** (e.g., per capita, district, country, or any other collective) is calculated by aggregating the energy footprints of all energy-intensive goods and services utilized by the inhabitants of the group.
•The energy footprint within **a defined geographic area** (e.g., district, country, or land area) refers to the cumulative energy footprint of all the individuals, organizations, products, processes, tools, and other components utilized within that particular region.

Dimensions and Units

The ENF indicator is a dimensional parameter, with a primary representation of [ML2T-2] or [FL]. Henceforth, the dimension [E] will serve as the basis for defining the energy footprint. It is imperative for all ENF indicators to maintain this dimension as the numerator. Diverse units, such as kWh, J (joule), cal (calorie), Btu (British Thermal Unit), koe (kilograms of oil equivalent), and others, can be employed to quantify the ENF.

The ENF can also be expressed as the energy footprint per unit, such as per area, time, mass, or production quantity, to facilitate better comparability across different sectors. In this scenario, the dimension should be reflected in the denominator. Table 1 provides a list of dimensions and typical units for various sub-indicators of the energy footprint.
Unit energy footprint indicators enable us to compare energy intensity of independent products and processes. Accordingly, a person can prefer to minimize its energy use, or an organization or country may try to reduce its energy consumption by comparing the processes involved in.

The use of unit ENF indicators enables the comparison of energy intensity between distinct products and processes. In turn, individuals can opt to minimize their energy usage, while organizations and countries can endeavor to lower their energy consumption by evaluating the involved processes.

Table 1. Dimensions, typical units and example of various sub-indicators of ENF

Unit indicators of energy footprint	Abbreviation	Dimension	Typical unit	Example
Energy footprint per unit product	ENF_u	[E]	kWh, MJ, etc.	ENF of a dress, automobile, etc.
Energy footprint per area	ENF_a	$[EL^{-2}]$	kWh/m^2, MJ/m^2 MW/ha	ENF to harvest crop per hectare, ENF to produce one meter square of plasterboard or steel plate
Energy footprint per time of process	ENF_t	$[Et^{-1}]$	kW, kWh/day, J/s, MJ/day	ENF per one hour of flight, ENF of a water pump working one day, ENF of a typical home per day, etc.
Energy footprint per mass of product	ENF_m	$[EM^{-1}]$	kWh/kg, MWh/ton, MJ/kg	ENF of a kilo of sugar production, ENF per ton of steel production, etc.
Energy footprint per volume of product	ENF_v	$[EL^{-3}]$	kWh/lt, MWh/m^3	ENF of one m^3 of concrete production, ENF of oil one gallon of oil production
Energy footprint per distance	ENF_d	$[EL^{-1}]$	kWh/km, Wh/m	ENF of standard container transportation per distance, etc.
Energy footprint per capita	ENF_p	$[Et^{-1}]$	kWh/person per time, MJ/capita per time	ENF of average people living in the USA, etc.

Virtual energy
The definition of virtual energy used in this study is closely resembles the previous approximations of Odum et al. (1978) and Costanza (1980). Accordingly, virtual energy can be characterized as the overall energy consumed during anthropogenic activities. This term can also be used interchangeably with embodied energy, embedded energy, or shade energy. Consequently, all human activities inherently incorporate a virtual energy component, which we refer to as virtual energy content (VEC). Table 1 provides examples of VEC for unit indicators.

Colors of energy
Footprint studies not only focus on the overall energy content of various processes, products, or systems, but also emphasize the significance of considering the type and source of energy to mitigate the environmental impact of production. In this study, the primary energy resource is taken into account by assigning a specific color to each energy type during the analyses. These colors are chosen based on the associated production risks and to provide a clearer representation of the energy used. Regardless of having the same ENF, different types of energy can lead to diverse environmental consequences and varying economic values.

Table 2. The colors attributed to the different energy sources by ENF methodology presented in this study

Color of energy	Type of energy	Classification	Conversion technologies
White energy	Wind energy	Renewable energy	Wind turbines
Yellow energy	Solar energy	Renewable energy	Photovoltaic and solar thermal energy.
Green energy	Biomass, biofuels	Renewable energy	Thermochemical, biochemical processes
Blue energy	Hydroelectricity	Renewable energy	Hydrostatics, hydroelectric power plants, hydrokinetics, tidal and wave power, etc.
Brown energy	Geothermal	Renewable energy	Geothermal heating, cooling, power
Red energy	Nuclear energy	Fossil energy	Nuclear reactors

*The term "green energy" should not be used interchangeably with the broader category of renewable and sustainable energy sources, which encompasses solar, hydroelectric, wind, and other forms.

IV. Conclusion

The main objective of this study is to redefine and conceptualize the Energy Footprint (ENF) as a standalone indicator, separate from the ecological footprint. The paper highlights the deficiencies in previous approaches to assessing the energy footprint and emphasizes the need for a distinct methodology. The authors propose a novel approach to the ENF, refining its definitions, methodology, and dimensions inspired from the water footprint methodology and highlight the concept of virtual energy. The paper also discusses the quantification of the energy footprint at different scales and explores the dimensions and units associated with the ENF.

Additionally, in this study, various colors of energy are attributed to different types of energy footprints. Wind energy is represented by "White energy," solar energy is denoted by "Yellow energy," biomass and biofuels are associated with "Green energy," hydroelectricity is linked to "Blue energy," geothermal energy is related to "Brown energy," nuclear energy is represented by "Red energy," and fossil fuels are responsible for "Black energy". Each color of energy corresponds to a specific type of energy source or technology used in energy production.

In conclusion, this research contributes to the field of energy footprint assessment by proposing a refined and standalone methodology for quantifying the Energy Footprint (ENF). By differentiating the ENF from the ecological footprint, this study introduces a new approach to understanding and measuring the human consumption of energy resources. The redefined concept, dimensions, and units of the ENF provide a comprehensive framework for assessing energy intensity, enhancing energy management, and promoting environmental sustainability. Further research can be conducted to explore spatial and temporal boundaries, international policy implications, and the development of standards to support the implementation and adoption of the ENF methodology.

References

Allan, J. A. (1993). Fortunately there are substitutes for water otherwise our hydropolitical futures would be impossible. In *Overseaes Development Administration, Priorities for Water Resources Allocation and Management* (pp. 13–26). Overseas Development Administration.

Bicknell, K. B., Ball, R. J., Cullen, R., & Bigsby, H. R. (1998). New methodology for the ecological footprint with an application to the New Zealand economy. *Ecological Economics*, *27*(2), 149–160. https://doi.org/https://doi.org/10.1016/S0921-8009(97)00136-5

Chen, B., Chen, G. Q., Yang, Z. F., & Jiang, M. M. (2007). Ecological footprint accounting for energy and resource in China. *Energy Policy*, *35*(3), 1599–1609. https://doi.org/https://doi.org/10.1016/j.enpol.2006.04.019

Costanza, R. (1980). Embodied Energy and Economic Valuation. *Science*, *210*(4475), 1219–1224. https://doi.org/10.1126/science.210.4475.1219

Čuček, L., Klemeš, J. J., & Kravanja, Z. (2012). A Review of Footprint analysis tools for monitoring impacts on sustainability. *Journal of Cleaner Production*, *34*, 9–20. https://doi.org/https://doi.org/10.1016/j.jclepro.2012.02.036

Fang, K., Heijungs, R., & de Snoo, G. R. (2014). Theoretical exploration for the combination of the ecological, energy, carbon, and water footprints: Overview of a footprint family. *Ecological Indicators*, *36*, 508–518. https://doi.org/https://doi.org/10.1016/j.ecolind.2013.08.017

Ferng, J.-J. (2002). Toward a scenario analysis framework for energy footprints. *Ecological Economics*, *40*(1), 53–69. https://doi.org/https://doi.org/10.1016/S0921-8009(01)00270-1

GFN. (2009). *Ecological Footprint Standards 2009*.

Haberl, H., Erb, K.-H., & Krausmann, F. (2001). How to calculate and interpret ecological footprints for long periods of time: the case of Austria 1926–1995. *Ecological Economics*, *38*(1), 25–45. https://doi.org/https://doi.org/10.1016/S0921-8009(01)00152-5

Hoekstra, A. Y., Chapagain, A. K., Aldaya, M. M., & Mekonnen, M. M. (2011). The Water Footprint Assessment Manual. In *Water Footprint Network*. https://doi.org/978-1-84971-279-8

Hoekstra, A. Y., & Wiedmann, T. O. (2014). Humanity's unsustainable environmental footprint. *Science*, *344*(6188), 1114–1117. https://doi.org/10.1126/science.1248365

Jones, N. F., Pejchar, L., & Kiesecker, J. M. (2015). The Energy Footprint: How Oil, Natural Gas, and Wind Energy Affect Land for Biodiversity and the Flow of Ecosystem Services. *BioScience*, *65*(3), 290–301. https://doi.org/10.1093/biosci/biu224

Odum, H. T., Wang, F. C., Alexander, J., & Gilliland, M. (1978). *Energy analysis of environmental values: A manual for estimating environmental and societal values according to embodied energies*.

Stoeglehner, G., & Narodoslawsky, M. (2009). How sustainable are biofuels? Answers and further questions arising from an ecological footprint perspective. *Bioresource Technology*, *100*(16), 3825–3830. https://doi.org/https://doi.org/10.1016/j.biortech.2009.01.059

Stöglehner, G. (2003). Ecological footprint — a tool for assessing sustainable energy supplies. *Journal of Cleaner Production*, *11*(3), 267–277. https://doi.org/10.1016/S0959-6526(02)00046-X

Tian, X., Chen, B., Geng, Y., Zhong, S., Gao, C., Wilson, J., Cui, X., & Dou, Y. (2019). Energy footprint pathways of China. *Energy*, *180*, 330–340. https://doi.org/https://doi.org/10.1016/j.energy.2019.05.103

Wackernagel, M., & Rees, W. (1996). *Our Ecological Footprint: Reducing Human Impact on the Earth*. New Society Publisher.

Zhang, B., Qiao, H., Chen, Z. M., & Chen, B. (2016). Growth in embodied energy transfers via China's domestic trade: Evidence from multi-regional input–output analysis. *Applied Energy*, *184*, 1093–1105. https://doi.org/https://doi.org/10.1016/j.apenergy.2015.09.076.

IEEES-119

Insights Into a Sustainable Campus: Piri Reis University

[1]Duygu Erten, P.E.AIA, BREEAM Fellow
[1,2] Sustainability Advisor, Adjunct Faculty at Boğaziçi University
[1] Sustainability Advisor, IMAK Chamber of Shipping, Meclis-I Mebusan Cad. No 22, Beyoğlu, İstanbul, Türkiye
[2] Boğaziçi University, Adjuncy Faculty(2012-2014), Civil Engineering Department, Bebek, Istanbul, 34342, Türkiye

*E-mail: duyguerten2050@gmail.com

Abstract

In recent years, energy efficient university campuses with certified green buildings are becoming a reality that are setting construction and energy benchmarks for the industry. Sustainable design and construction was prioritized in the planning of the new Piri Reis University campus. As part of this significant effort, in 2014, Piri Reis University was completed on a campus composed of 8 blocks totaling 60,000 m^2 interconnected by open-air public spaces in Tuzla, İstanbul, Türkiye; becoming Türkiye's first green campus with all its buildings certified with BREEAM system. The buildings integrated a high-efficiency design, construction materials, and technologies; as well as the natural gas-powered trigeneration system providing 45% of the campus's electricity needs. Furthermore, the campus was also designed as a living lab where students, faculty, researchers, and industry are able to monitor and validate the performance of this state-of-the-art facility. Three of the buildings received BREEAM-Very Good certification and Applied Marine Training Center (UDEM)- Building A, received BREEAM Excellent certification-the first green ratingat excellent level in Türkiye. This article will discuss some of the architectural and building system design features that paved the way for a sustainable campus. The analysis of the Piri Reis University Green Campus case indicates that a dedicated client with a strict environmental policy and green rating goal is the fundamental reason to reach the sustainability goals set at the planning phase of the project. Commitment of the owners, university management support, and collaborative work through integrated design among project parties have been the most important reasons among many on the project's success.

Keywords: Sustainability, Green Campus, Integrative Design, Energy Efficiency.

I. Introduction

Piri Reis Maritime University provides higher maritime education and applied training in Tuzla district of Istanbul, Türkiye. Its model is very unique since it is founded by the support and sponsorship of the whole maritime sector, namely IMEAK Chamber of Shipping (IMEAK) through Turkish Maritime Education Foundation (TUDEV). TÜDEV, IMEAK and the University Management had a common organizational strategy about creating a new campus so they wrote environmental responsibility policies. Once the campus program is established and the design team is selected, the sustainability goal for the new campus buildings is set for British Research Establishment (BRE)'s Environmental Assessment Method. Bespoke BREEAM is part of the BREEAM family of environmental assessment methods. It is a voluntary scheme that aims to quantify and reduce the environmental burdens of buildings by rewarding those designs that take positive steps to minimise their environmental impacts. With a Bespoke BREEAM assessment BRE developed criteria specific to the building and the functions within it. Information to develop the criteria is collected via a building questionnaire for the design team to complete and also a kickoff meeting is held. Due to the nature of Bespoke BREEAM projects not every credit is applicable to all function areas. To reflect this, credit scores are area weighted according to the floor area within the building that the credits have been achieved for. This recognises the environmental benefits of achieving a credit in an area that represents a large proportion of the building compared to where a credit is achieved in only a small proportion of the building. Projects are assessed using a system of credits. The credits are grouped within the 10 categories (Figure 1).

II. Experimental Procedure/Methodology/System Description

With the support from TÜDEV and University management, the project team accepted the campus sustainable development as its basic strategy. There is no "one size fit all" approach for sustainable development strategy for campuses, whose disparity range from culture and society to GDP per province, geological and climatic location, government policies and technological advancement. Based on the practical applications reviewed globally, using green rating system in the design/build process can produce significant benefits that are not likely to result from standard practices. Though they are not perfect, assessment measurements based on building life cycle can produce significant long-term benefits for building owners and occupants as these systems helps for solving existing building problems, limiting environmental impacts, creating healthier and more productive places, and reducing building operations cost (1,2,3). This paper presents approaches used to create a sustainable campus.

Figure 1: BREEAM Score chart and certification for Block A (UDEM building)

III. Analysis

The important parameters leading to a sustainable campus are summarized below:
Land Use: With the decision for creating a Green Campus with certified buildings, the area adjacent to water was designated as a "green area". A well-known naval terminology was projected as the design concept keyword (Neta: "neat, safe, efficient"). Simplicity, plainness, and efficiency are fundamental for spatial planning and operation principles of ships and dockyards, functionalist simplicity of the overall layout was combined with worn out looking materials with high recycled content. During the design phase, the views and how user will take the greatest advantage of the sea views were discussed with precision. Instead of mono-block mass, the eight blocks, two of which were buried under the ground, were gradually placed on the land, taking advantage of the slope of the land. With the parallel use of the blocks in the land parallel to the sea, the prevailing wind was also blocked, making it possible to create internal gardens protected from hard lodos and hubris.
Heating System & Thermal Zoning: Heating and cooling of the areas have by four pipe induction units. System operates as induction logic. Fresh air is supplied via air handling units, cooling and heating is supplied via coils in the induction units. In permanently occupied operational spaces local occupant control is available for temperature adjustment in each occupied space (space that is expected to be occupied by a user for more than 30 min.) to reflect differing user demands. However, in large spaces where someone is in charge of the heating but individual users do not expect to control the heating, is zoned for the purpose of heating and cooling but controls which allow independent adjustment of heating/cooling systems within the building are not required in these types of spaces. Manual control is available by means of the room thermostat which wirelessly (or via a wired connection) communicates with the controller. The clear display in combination with a clear and user friendly key pad will enable the user to easily change the room temperature and airflow.

Absorption Cooling: The cooling energy of the buildings are supplied by 2 units absorption chillers which work with cogeneration system with cooling capacity (each):560 kW (2 units) and generator working temperature 95–75 °C. Lighting, heating-cooling and electricity expenditures are kept to minimum levels with the designed building automation.

Ventilation: a) Air Handling Units: The air handling units are in moduls. All the air handling units are suitable for EN 1886 standarts. Fitler by-pass leakage in the panel connection spaces is suitable for F9 standart and panel leakages are according to L1 class. Mechanical resistance is suitable for D1 class **b) Galvanised air ducts:** Galvanized steel air ducts are manufactured in factories, no manual duct manufacturing is allowed. Flanged and joint assemblaged duct joint system is used all air ducts and fittings.

Air Quality Sensors: Fresh air is provided in accordance with the national best practice ventilation standart TS EN 13779 "Ventilation for non-residential buildings-Performance requirements for ventilaton and room conditioning systems**.** Duct type CO_2 and temperature transmitter (aqtt) is installed in all occupied spaces. This air quality sensor changes the outlet signal acoording to the CO_2 concentration of the air and according to temperature changes. This sensor is connected to BMS. All the air handling units" aspirators are VSD (variable speed drive) controlled, so that the fresh air rate could be adjusted.
Water: The usage water of the entire campus is obtained by converting sea water into fresh water. With the pipes laid in the sea, both the use water and fire water tanks of all wet volumes and the water needed by the trigeneration center are supplied. Rain and gray water, on the other hand, are saved by using toilet toilets and landscaping irrigation.
Trigeneration System: The natural gas-powered trigeneration system installed provides 45% of the campus's electricity needs and 50% of the cooling and heating needs are met with the energy released during electricity generation. The system meets the minimum standards defined in EU CHP directive. Trigeneration usage meant campus facilities moved beyond the traditional way of separate energy production.
Solar Panels for Domestic Hot Water Heating: Panel's optic efficiency was tested according to EN 12975 and absorber surface area was higher than %75. Domestic hot water is supplied by solar panels that are located on the roofs.
Microbial contamination: Design teams and construction contractors ensured that building services are designed to reduce the risk of legionellosis in operation, through a robust risk analysis process that the risk of waterborne and airborne legionella contamination has been minimised.

Figure 2: Trigeneration system

Figure 3: 120 solar collectors the roof

Figure 4: Reverse Osmos system

Figure 5: Usage of perforated corten plates

Construction Site

By implementing the site waste management plan, the amount of waste has been reduced on site. The amounts and proportions of wastes reused, recycled, and sent to the landfill are monitored monthly and measures have been taken for waste reduction accordingly. All energy and water consumptions are monitored regularly on a monthly basis, and the amounts of CO_2 emissions linked to energy are calculated and measures are taken accordingly. Electric and gas consumptions vs targets are plotted o charts in figures 6 and 7.

Commissioning: In order to encourage a properly planned handover and commissioning process that reflects the needs of the building occupants, testing and commissioning of all systems were carried out. The scope included programme of seasonal commissioning for one year following Project completion.

IV. Results and Discussion

The sustainability approaches integrated to design and construction which helped the project succeed are summarized below: The owner hired a project management firm to faciliate the integrated design process.One of the goals was to reduce the CO_2 emissions resulting from transportation. 175 bicycle parking spaces were provided for employees and students to benefit from alternative means of transportation. Showers and changing rooms are designed as part of the BREEAM requirements.

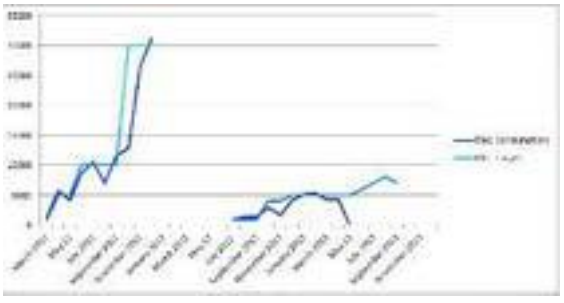

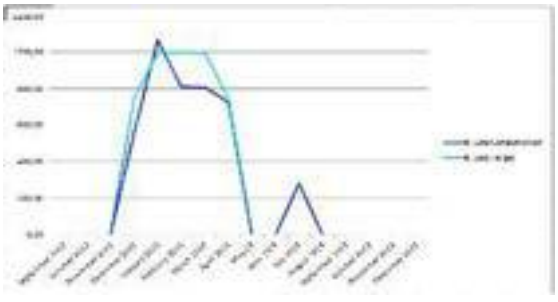

Figure 6: Electric consumption vs targets

Figure 7: Gas consumption vs targets

Building heating and cooling energy needs are met by a trigeneration system. The condenser water required for 'absorbent chiller', 'heat pump chiller' and trigeneration gas engines is supplied not with classical cooling towers, but directly from the sea. Thus, 40% savings are obtained from the need for electricity.Domestic cold water is provided by 'reverse osmos' and seawater undergoing the necessary treatment processes.Hot Water Supply is provided by Solar Collectors installed on the roof. Thus, 12% energy savings are achieved. All sinks, shower trays and gray water collected from shower boats are used in reservoirs with on-site treatment. In this way, the use of gray water is ensured.The rainwater from the roof is collected and purified and is used for garden irrigation.The goal was maximizing the benefits from the daylight. Lighting levels; designed to meet standards to provide the best visual performance and comfort in a cost-saving way.Healthy and comfortable working environments were provided by using harmful volatile organic compound-free materials with the environmental / sustainable purchasing policy applied. 100% recycled perforated corten plates with no mercury were used to absorb the sun's ultraviolet rays and reduce mechanical cooling loads indoors.Energy and water consumptions are monitored and recorded with the Building Management System (BMS) and savings studies are carried out in this directionLighting, heating-cooling and electricity expenditures can also be kept to minimum levels with the designed building automation.By collecting and storing recyclable waste seperately, diversion from landfills are reached.The use of products that provide low water consumption is procured.The usage water of the entire campus is obtained by converting sea water into fresh water. With the pipes laid in the sea, both the use water and fire water tanks of all wet volumes and the water needed by the trigeneration center are supplied. Rain and gray water, on the other hand, are saved by using toilets and landscaping irrigation. So the campus is off the grid when it comes to water usage.

V. Conclusion

The analysis of the Piri Reis University Green Campus case indicates that a dedicated client with a strict environmental policy is a fundamental reason to reach the sustainability goals set at the planning phase of the project. Commitment of the owners, university management support, and collaborative work among project parties to complete the project based on international standards have been the most important reasons among many on the project's success.

Acknowledgements

The author wants to thank to IMEAK Chamber of Shipping (IMEAK) for their support of the sustainability consultancy and research work.

References

2. Fowler KM (2006) Sustainable building rating systems – summary. (The Pacific Northwest National Laboratory DOI:10.2172/926974

3. Cam C.N., Ong B.L. (2005) Building environmental assessment tools and the multi-dimensional pathways towards sustainable architecture, The 2005 World Sustainable Building Conference, Tokyo, 27-29 September 2005 (SB05Tokyo)

Cooper I. (1999), Which focus for building assessment methods – environmental performance or sustainability? Building Research & Information.

IEEES-120

Exergy-based Performance Analysis and Assessment of Geothermal District Cooling Systems

[1*]Nurdan Yildirim, [2]Arif Hepbasli,
[1]Yaşar University, Faculty of Engineering, Department of Mechanical Engineering, 35100 Bornova, Izmır, TURKIYE
[2]Yaşar University, Faculty of Engineering, Department of Energy Systems Engineering, 35100 Bornova, Izmır, TURKIYE
*E-mail: nurdan.yildirim@yasar.edu.tr

Abstract

Space cooling and heating is responsible for a huge amount of energy consumed worldwide. Based on the recent literature review, there has been a particular interest in renewable energy-based district heating and cooling systems. Considering geothermal energy, most applications are related to district heating while only few installations regard for district cooling. The main objectives of this contribution are to exergetically, exergoeconomically and lowexergetically model, analysis and evaluate a geothermal district cooling system (GDCS) along with its main components based on the real measurement values for the first time to the best of the authors' knowledge. In this regard, the Balcova GDCS, the first geothermal cooling system in Turkey, was considered as an application place. This GDCS was commissioned at the end of May 2018 and since then, the system has been operated successfully. The whole system consists of a heat exchanger, a chiller, a cooling tower and circulating pumps. Space cooling is accomplished from geothermal energy through a LiBr-water absorption cycle. In this study, energy and exergy efficiencies as well as exergy destructions and exergoeconomic factor values of each component and the entire system were determined to present possible improvements first. The exergy efficiency value of the whole system on the product/fuel basis was then calculated to be 49.4% at a dead (reference) state temperature of 19 ^{o}C while the minimum and maximum thermodynamic loss rates belonged to the chiller and heat exchanger, respectively.

Keywords: Geothermal, geothermal district cooling, exergy, exergoeconomics, lowex, exergy efficiency.

I. Introduction

Buildings consume huge amount of energy and are responsible for one-third of world greenhouse gas emissions (Soltania et al., 2019). A significant share of this energy consumed has been used for cooling and heating purposes. District cooling systems (DCSs) have been widely in use for providing the necessary cooling comfort in commercial, residential, institutional, and industrial customers from one central source and developed as a very important technology because of their high-quality cooling and high effectiveness. The energy supplied from DCS is used in space cooling and dehumidification. DCSs can also be integrated with renewable energy in an economically feasible manner when compared to conventional cooling systems (Gang et al., 2016: Wang et al., 2017; Inayat and Raza, 2019; Anderson and Rezaie, 2019). In this context, low-cost resources for buildings can be provided through geothermal heating and cooling systems, which generally have greater lifespans, temporal consistency, reliability, and resilience, compared to other renewable energy sources, such as wind and solar (Dincer and Acar, 2015).

As far as recent studies conducted on GDCSs are concerned and as also highlighted by Modi et al. (2017), in the last decades, an impressive number of studies has been performed by many researchers to explore various aspects of absorption refrigeration system (ARS), which have become more important because of their fueling by renewable energy other than electricity. In this regard, Ma et al. (2010) explained an absorption refrigeration system, namely a two-stage LiBr/H_2O absorption chiller driven by hot water, used for exploiting mid low temperature geothermal resources. Based on their experimental data, the COP values for this chiller varied between 0.38 and 0.42 with heat source temperature values of 63-65 ^{o}C. This system also reduced the power consumption to 62% compared to a traditional air-conditioner while the payback period of the investment was less than four years. Sikorska-Bączek (2015) studied a hybrid absorption-compression refrigerator powered by geothermal energy used for the production of ice slurry for air-conditioning refrigeration. It was concluded that absorption refrigerators were particularly economically attractive when there was a free energy source having temperature values between 50 and 200°C. Modi et al. (2017) modeled and analyzed an absorption refrigeration system using LiBr-H_2O solution through energy and exergy analysis methods while they applied an optimization criterion to the generator temperature for enhancing energy and rational efficiencies and identifying the exergy destruction values of each system component. They proposed that generator and absorber were the essential components from the design point of view while COP and rational efficiency values were fluctuated with respect to the component temperature of the system. The COP value for heating increased with increment in the generator temperature while the circulation ratio indicated the inverse pattern. Inayat and Raza (2019) reviewed possible potential of DCSs with various renewable energy technologies and highlighted that the most suitable renewable energy technologies that could e integrated with DCSs seemed to be biomass energy, solar thermal energy, geothermal energy, surface water energy, solar photovoltaic energy, and waste heat energy. They reported that DCSs had strong budding with these renewable energies for supplying sustainable and clean cooling energy options in the future world. Ozcan et al. (2019) designed a geothermal assisted cooling system with a vapor absorption chiller using water and ammonia as an absorbent and a refrigerant, respectively, for meeting the demand of a 140 m^2 detached single-family house in the city of Izmir, Turkey. They used energy and exergy analysis methods for evaluating the performance of the whole system along with its main components while undertaking some parametric studies. The system had a coefficient of performance (COP) value of 0.30 with a simple payback period of 6.4 years. The highest exergy destruction was due to the absorber with a rate of 38.2%, followed by the solution heat exchanger and rectifier.

The present contribution differs from the previously conducted ones as follows: (i) It performs exergetic and exergoeconomic analyses of the Balcova GDCS, which is the first GDCS in Turkey, based on the actual operational data for the first time, and (ii) It also applies the Low-Ex approach to the building where the GDCS was installed for investigating the exergetic efficiencies of the overall system from the primary energy source to the building envelope.

II. System description

The Balcova GDCS was commissioned at the end of May 2018 and since then, the system has been operated successfully. The whole system consists of a heat exchanger (I), a chiller (II), a cooling tower (III) and circulating pumps (P1-3), as shown in Fig. 1.

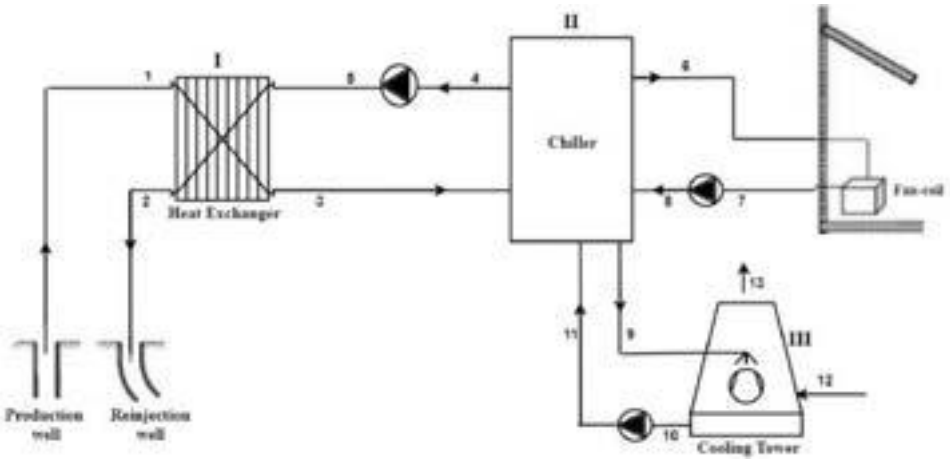

Fig. 1. A schematic diagram of the Balcova geothermal district cooling system

In the Balcova geothermal field, there are various wells, which form a ring line. The geothermal water enters the primary loop (state 1) of the heat exchanger (I) and is then reinjected. The geothermal water temperatures vary between 95 °C and 118 °C, keeping at 98 °C during the summer season while the geothermal water is reinjected at 75 °C (state 2) with a pressure of 2.1 bar. On the secondary loop of the heat exchanger, the hot water is circulated at flow and return temperatures of 100 °C (state 3) and 70 °C (state 4), respectively to supply the heat flux to the chiller (II), namely a LiBr-water absorption cycle. It is then routed through the refrigeration circulation to the building where the chilled water enters fan-coils at 7 °C (state 6) and leaves it at 12 °C (state 7) while flow and return cooling water temperatures at the cooling tower (III) are 32 °C (state 9) and 28 °C (11), respectively (Yigit, 2019).

III. Analysis

General mass, energy and exergy balance equations are given in more detail elsewhere (Hepbasli, 2010). The following relations used for the main components of the Balcova GDCS illustrated in Figure 1.

Relative irreversibility (RI) is calculated by

$$RI = \dot{E}x_{dest,i}/\dot{E}x_{dest,total} \quad (1)$$

In this study, we used the **Ex**ergy **C**ost **E**nergy **M**ass (EXCEM) analysis, which was proposed by Rosen and Dincer (2003) and dictates mass, energy, exergy and cost balance equations while the EXCEM method was applied to an energy supply chain for space heating in a building (Yucer and Hepbasli, 2013). The EXCEM parameter $\dot{R}_{ex}$, which is defined as the ratio of thermodynamic loss rate $\dot{L}_{ex}$ to cost *K*, may be written as follows:

$$\dot{R}_{ex} = \dot{L}_{ex}/K \quad (2)$$

Yucer and Hepbasli (2013) also proposed a new definition "**Ex**ergetic **C**ost **E**ffectiveness (ExCE)" to include both the effects of equipment's exergy destruction and cost figure to the overall system, as given below:

$$ExCE = a.b \quad (3)$$

where *a* and b are the contribution of a stage or a component to the total cost and to the total exergy destruction, respectively.

IV. Results and discussion

The values for exergy destruction rates, relative irreversibility rates and exergy efficiencies are calculated at a reference state temperature of 19 °C and listed in Table 1. As can be seen from the table, the greatest exergy destruction (irreversibility) on the main system components of I-III occurs in the cooling tower, followed by the chiller and the heat exchanger.

Table 1. Values of exergy destruction rates, relative irreversibility rates and exergy efficiencies for one representative unit of the Balçove GDCS at a dead state temperature of 19 °C

	T_0 = 19 °C					
Component no.	$\dot{E}x_{dest}$ (kW)	ε (%)	Ḟ	Ṗ	*RI*	*RI*
I	3.02	91.42	35.21	32.19	6.7	4.7
II	11.41	12.4	13.03	1.62	25.2	17.7
III	30	42.6	52.24	22.24	68.1	46.5
P1	0.74	29.2	1.04	0.30		1.1
P2	2.69	17.4	3.25	0.56		4.2
P3	16.61	26.5	22.61	6.00		25.8
Total (I+II+III)	*45.19*		*127.38*	*62.91*	*100*	*100*
Grand total	*64.47*		*127.38*	*62.91*	*100*	*100*

EXCEM analysis is applied to the main components and results are presented in Table 2. The chiller has the minimum EXCEM ratio as 0.114 W/US$ because its capital cost is higher than that of other components on the components I-III basis. One can see from the table that the chiller represents the maximum *ExCE* value among all components, meaning that it needs to be firstly improved before other components. On the components I-III basis, if one considers the exergy destruction rate or RI values, more attention for improvement should be paid to the cooling tower while in case of using the ExCE, the chiller should have a priority. This clearly indicates that exergy analysis needs to be combined with economic analysis tools.

Table 2. Exergoeconomic results of the Balcova GDCS

Component no.	T_0= 19 °C					
	$\dot{E}x_{dest}$ (kW)	*K* US$	$\dot{R}_{ex}$ (W/ US$)	*a*	*B (or RI)*	*ExCE*
I	3.02	500	6.04	0.0038	0.047	0.00018
II	11.41	100,000	0.114	0.7604	0.177	0.13459
III	30	30,000	1	0.2247	0.465	0.10449
P1	0.74	300	2.467	0.002	0.011	0.00002
P2	2.69	500	5.38	0.0038	0.042	0.00016
P3	16.61	700	23.73	0.0053	0.258	0.00137
Total	*64.47*	*131,500*		*1*	*1*	

V. Conclusion

Most of the modelling and analysis of geothermal district systems are based on heating and energetic evaluations while there are very limited studies focusing on exergetic assessment of GDCSs. Especially, no studies using the actual operational data for an exergetic holistic approach have appeared in the open literature. This study contributed to the literature in terms of this approach. The main concluding remarks we have drawn from the results of the present contribution may be listed as follows:

- Exergy is a way to sustainable development. In this regard, exergy analysis is a very useful tool, which can be successfully used in the performance evaluation of GDCSs as well as all energy-related systems while it helps determine the locations, types, and true magnitudes of energy losses, guiding the design of more efficient energy systems.
- The overall exergy efficiency value on the product/fuel basis was determined to be 49.4% at a dead (reference) state temperature of 19 °C.

- Considering exergy efficiencies, the heat exchanger had the highest value of 91.42%.
- The greatest exergy destruction (irreversibility) on the main system components of I-III were due to the cooling tower, followed by the chiller and the heat exchanger.
- The minimum and maximum thermodynamic loss rates belong to the chiller and heat exchanger on the components I-III, respectively.
- The chiller represents the maximum exergetic cost effectiveness value among all components in the system.
- The application of GDCSs should be widespread throughout the country because Turkey has an attractive and huge geothermal energy utilization potential.
- The results are expected to be beneficial to the researchers, government administration, and engineers working in the field of geothermal energy systems.
- For future studies, performing the comprehensive transient advanced exergetic. exergoeconomic and exergoenvironmental analyses of the system is proposed.

Acknowledgements
The authors would like to thank the former managers of Izmir Geothermal Energy Inc., Mr. Erkal Sinan Arslan. Mr. Hasan Çığ Sezer and Mr. Koray Yigit worked at. for allowing to visit the Balcova Geothermal District Cooling System and providing the necessary data utilized in the analyses and calculations of this study.

References

Anderson, A., Rezaie, B., (2019). Geothermal technology: Trends and potential role in a sustainable future. Applied Energy 248, 18-34.
Dincer, I., Acar, C., (2015). A review on clean energy solutions for better sustainability. International Journal of Energy Research 39, 585-606.
Gang. W., Wang. S., Xiao. F., Gao. D., (2016). District cooling systems: Technology integration. system optimization. challenges and opportunities for applications. Renewable and Sustainable Energy Reviews 53, 253-264.
Hepbasli, A., (2010). A review on energetic, exergetic and exergoeconomic aspects of geothermal district heating systems (GDHSs), Energy Conversion and Management 51(10), 2041-2061.
Inayat, A., Raza, M., (2019). District cooling system via renewable energy sources: A review. Renewable and Sustainable Energy Reviews 107, 360-373.
Ma, W., Luo, C., Gong. Y., (2010). An absorption refrigeration system used for exploiting mid-low temperature. Geothermal Resource. Proceedings. World Geothermal Congress 2010. Bali, Indonesia.
Modi, B.. Mudgal, A., Patel, B., (2017). Energy and exergy investigation of small capacity single effect lithium bromide absorption refrigeration system. Energy Procedia 109, 203-210.
Ozcan, B., Aykurt, I., Akpak, M., Tacer, T., Yildirim, N., Hepbasli, A., Ozcan, H.G., (2019). Thermodynamic analysis and assessment of a geothermal cooling system for a House. Int. J. Exergy 29 (2/3/4), 350-369.
Rosen, M.A., Dincer, I., (2003). Exergy–Cost–Energy–Mass Analysis of Thermal Systems and Processes. Energy Conversıon and Management 44(10), 1633-1651.
Sikorska-Bączek, R., (2015). The use of geothermal energy in absorption refrigeration circuits. Technical Transactions Environment Engineering, 1-Ś.
Soltania, M., Kashkoolia, F.M., Dehghani-Sanijd, A.R., Kazemia, A.R., Bordbara, N., Farshchia, M.J., Elmia, M., Gharalif, K., Dusseaultd, M.B., (2019). A comprehensive study of geothermal heating and cooling systems. Sustainable Cities and Society 44, 793-818.
Wang, S., Xiao, F., Gang, W., Wang, S., Xiao, F.U., (2017). District cooling systems and individual cling systems: comparative analysis and impacts of key factors. *Sci Technol Built Environ* 23, 241-250.
Yigit, K., (2019). Personal Communication. Izmir Geothermal Inc., Balcova, Izmir, Turkey.
Yucer. C., Hepbasli. A., (2013). Exergoeconomic analyses of an energy supply chain for space heating in a building. Energy and Buildings 62, 343-349.

IEEES-121

Evaluating Sustainable Aviation Fuels: A Comparative Analysis of Expert Groups

Omar ALHARASEES[1]*, Serdar SANLI, Utku KALE[1]
[1]Budapest University of Technology and Economics, Faculty of Transportation Engineering and Vehicle Engineering, Department of Aeronautics and Naval Architecture, Address: Budapest, 1111, Hungary

*E-mail: oalharasees@edu.bme.hu

Abstract

Employing sustainable aviation fuels (SAFs) stands as a pivotal stride in mitigating aviation's ecological footprint and realizing carbon neutrality. Yet, discerning the optimal SAF option demands a judicious evaluation encompassing economic feasibility, technical viability, and social acceptability. A multifaceted decision-making approach rooted in the Analytic Hierarchy Process (AHP) underpins a comprehensive methodology for tackling this hurdle. This entailed engagement from three distinct expert cohorts: aviation operators, managers, and researchers. Their collective involvement ensured an exhaustive assessment of each component's significance in SAF selection. The AHP framework seamlessly orchestrated component prioritization based on their relative import, enabling decision-makers to reconcile divergent stakeholder objectives. The upshot of this appraisal is that it empowers policymakers and decision-makers to pinpoint the SAF variant aligning with their precise aims. The study's revelations underscore the paramount significance of evaluating environmental impact criteria, notably carbon emissions. Moreover, economic and technical viability emerged as pivotal factors in this selection juncture.

Keywords: Sustainable Aviation Fuels, Multi-Criteria Decision-Making, Analytic Hierarchy Process, Environmental Impact, Economic Feasibility.

I. Introduction

The aviation sector significantly contributes to greenhouse gas emissions, particularly carbon dioxide, posing a substantial challenge to environmental mitigation in aviation (Perea-Moreno *et al.*, 2022). Global aviation emissions, as reported by the International Civil Aviation Organization (ICAO), comprised about 2.4% of the total CO2 emissions in 2018 and are anticipated to escalate due to the expanding demand for air travel (Gössling and Humpe, 2020). Thus, mitigating aviation's environmental impact stands pivotal in attaining international climate objectives.

One promising avenue to confront this challenge involves the advancement of sustainable aviation fuel (SAF), holding the potential to curtail aviation's carbon footprint while satiating escalating fuel requisites (Bergero *et al.*, 2023). SAF is derived from varied feedstocks like plant oils, municipal waste, and agricultural residues, substantially reducing carbon emissions by nearly 80% compared to traditional fossil fuels (Sharma *et al.*, 2021). Moreover, SAF seamlessly integrates with prevailing aviation infrastructure, encompassing aircraft, engines, and fueling systems, and can be blended with conventional fuels. Nevertheless, the development of SAF is influenced by multifaceted factors, encompassing economic, technical, and socio-cultural acceptability considerations. Effectively navigating these hurdles necessitates a collaborative approach involving industry stakeholders, policymakers, and the public.

A primary obstacle in sustainable aviation fuel (SAF) advancement is production cost, notably surpassing traditional fossil fuels, primarily due to feedstock scarcity and costly conversion technologies (Tanzil *et al.*, 2021). The International Energy Agency (IEA) underscores this cost differential, indicating SAF production costs are presently two to six times higher than conventional jet fuel (Ng, Farooq and Yang, 2021). The absence of a definitive regulatory framework and carbon pricing mechanism further impedes SAF development and integration. Technical feasibility and social acceptability are pivotal considerations in SAF maturation (Lai, Karakaya and Björklund, 2022). Adhering to fuel specification requisites, encompassing energy density and combustion characteristics, is critical for technical feasibility, ensuring safety and efficacy. Simultaneously, modifying extant infrastructure for SAF storage and handling, necessitated by disparate freezing points compared to traditional jet fuel, poses an additional cost facet (Kramer *et al.*, 2022).

Addressing social acceptability becomes imperative, entailing public perception and acceptance of SAF (Anderson *et al.*, 2022). Health ramifications from SAF production and utilization, alongside community engagement, necessitate careful consideration (Xu *et al.*, 2022). Moreover, concerns regarding specific SAF feedstocks, like palm oil, and their adverse impacts on biodiversity and deforestation underscore the significance of responsible sourcing (Kurzawska, 2021). Furthermore, elevated particulate emissions from certain SAFs underline potential air quality and public health concerns.

Addressing these challenges necessitates multifaceted solutions, notably alternative feedstocks and innovative conversion technologies (Schmidt *et al.*, 2018). Establishing a transparent regulatory framework, implementing a carbon pricing mechanism, and fostering public awareness are pivotal components. The European Union's Renewable Energy Directive stands as a prime example, offering regulatory clarity and market signals promoting SAF development.

Sustainable aviation fuel (SAF) stands out as a promising remedy to mitigate aviation-related greenhouse gas emissions. However, the scarcity of raw materials and concerns about technical feasibility and social acceptability hamper its uptake.Thus, discerning preferences across various job categories and experience tiers regarding SAF is paramount for informed decision-making and policy sculpting within the aviation domain. The Analytic Hierarchy Process (AHP) presents a structured avenue, enabling a comprehensive evaluation of stakeholder SAF preferences (Saaty, 1990). By utilizing the "Saaty Scale" and AHP methodologies (Saaty, 2002), this study endeavors to unravel nuanced insights into diverse stakeholder orientations towards SAF, substantially contributing to strategic policy frameworks and

promoting SAF integration, thus advancing sustainability in aviation.

II. Methodology

The Analytic Hierarchy Process (AHP), a systematic, integrative approach by Saaty integrated for comprehensive evaluation (Omar and Utku, 2022), blends mathematical and psychological principles for complex decision-making. Pioneered by Thomas L. Saaty in the 1980s, AHP enables thorough evaluation and finds extensive use across various sectors (Saaty and Vargas, 2012).
An essential hierarchical model takes shape to delineate critical aspects of sustainable aviation fuel (SAF) and pinpoint the most pivotal constituent (Saaty, 2008). This model forms a structured tree-like representation, with the objective at the top, criteria, and sub-criteria in the middle, and alternatives at the base. Figure 1 illuminates the AHP decision-making process through a succinct flowchart.

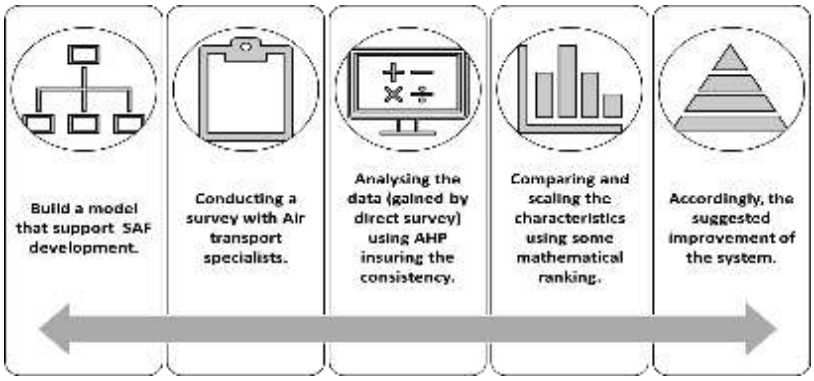

Fig. 1 The steps of the AHP framework in SAF evaluation

A crucial step in this process is the creation of Pairwise Comparison Matrices (PCM), showcasing decision-makers preferences for specific option pairs. The Saaty scale (Table 1) ensures PCM elements are positive, transitive, and reciprocal, signifying consistency. Specialized aviation experts, well-versed in decision criteria, contribute through a thoughtfully designed questionnaire survey. Ongoing scrutiny of the consistency ratio (CR) is essential, rectifying any excess over 0.1 by reviewing judgments, scrutinizing inconsistencies, gathering more data, or seeking expert advice. This meticulous approach significantly enhances the understanding of critical SAF elements.

Table 1 Saaty scale (Saaty, 1977)

Mathematical representation	1	2,4,6,8	3	5	7	9
Meaning	Both aspects are equally important	Values between moderate and strong importance	One aspect is moderately more important than the other	One aspect is strongly more important than the other	One aspect is very strongly more important	One aspect is extremely more important than the other

Lastly, individual PCMs within each group amalgamate using the geometric mean aggregation method, culminating in a singular PCM epitomizing the group's preferences. The eigenvector method calculates model component weights. Utilizing the weighted sum method, prioritization unveils the paramount component in SAF selection. These meticulous AHP steps adeptly discern pivotal aspects and components steering SAF implementation within the contemporary aviation industry. Figure 2 delineates this hierarchical structure, offering a visual elucidation.

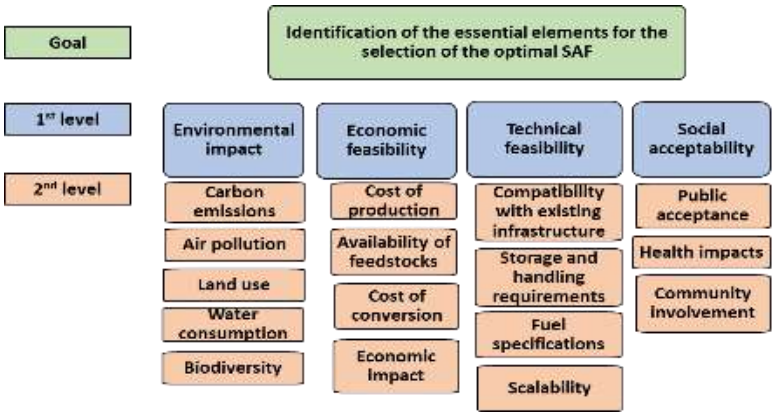

Fig. 2 The SAF Hierarchal structure

The SAF hierarchical approach provides a structured evaluation framework. Four levels assess environmental impact, economic and technical feasibility, and social acceptability. Next, Pairwise Comparison Matrices (PCMs) will assess model parameters and define critical model aspects.

III.Results and Discussion

The study utilized AHP, surveying 13 global aviation experts. Expertise-based segmentation provided varied industry perspectives. Job roles guided classification into aviation operators, managers, and researchers. The study quantified SAF evaluation challenges and aimed to enhance sustainability. Methodologically, participants were classified based on roles, and averages were derived using geometric mean. Weights and rankings for the SAF model's first-level elements were calculated for each group (see Table 2).

Table 2 AHP-comparison weights and priority ranking for experts' groups.

CRITERIA	AVIATION OPERATORs		MANAGEMENT		RESEARCHERs		AVERAGE	
	Weights	Rank	Weights	Rank	Weights	Rank	Weights	Rank
Environmental impact	45.23%	1	35.96%	1	39.90%	1	40.36%	1
Economic feasibility	18.38%	3	24.65%	2	28.58%	2	23.87%	2
Technical feasibility	20.97%	2	16.13%	4	15.87%	3	17.66%	4
Social acceptability	15.42%	4	23.25%	3	15.65%	4	18.11%	3

The table summarizes the criteria (environmental impact, economic feasibility, technical feasibility, social acceptability) for sustainable aviation fuel (SAF) as assessed by aviation operators. Environmental impact is the prime concern, emphasizing a growing awareness of environmental issues within the aviation industry. Conversely, social acceptability holds lesser weight, indicating lower priority for operators. Implementing these findings involves developing SAF with a reduced environmental impact while ensuring technical and economic feasibility. Effective communication and stakeholder engagement may address any social acceptability concerns. Management also emphasizes environmental impact, followed by economic feasibility, social acceptability, and technical feasibility. This balance suggests a conscious effort to integrate environmental concerns with economic and social considerations. Among researchers, environmental impact takes precedence, followed by economic and technical feasibility, with social acceptability noted as essential but less emphasized. These weightings reveal relationships between SAF production and the aviation system, highlighting the need to reduce environmental harm while considering practical limitations and aiming for public acceptance.

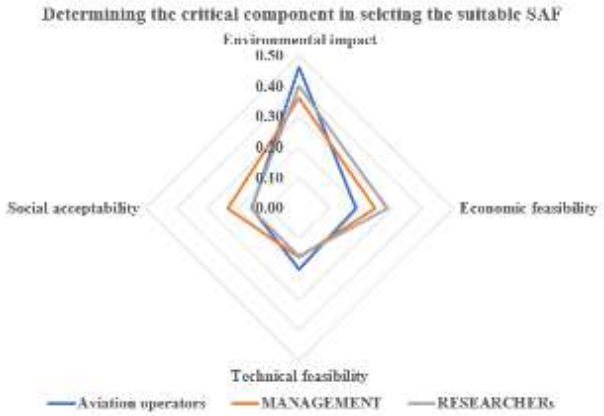

Fig 3. The hierarchal model comparison for all groups.

In order to gain a comprehensive overview of the survey results and discern key aspects from all experts' perspectives, a detailed model comparison is crucial. Figure 3 offers an extensive cross-group analysis, sorting aviation groups by participant experience levels. This figure facilitates the examination of diverse criteria across various perspectives, emphasizing pivotal factors. Across all groups, the environmental impact criterion consistently emerges as the most critical, with economic feasibility following, albeit with slight variations in the aviation operators' group. The overarching goal is to identify critical factors and their influence on the dynamic and stochastic aviation system.

IV. Conclusion

Sustainable aviation fuels (SAFs) represent a promising remedy for the aviation industry's environmental impact. However, choosing the optimal SAF demands a comprehensive economic feasibility assessment, technical viability, and social acceptance assessment. Employing a multi-criteria decision-making (MCDM) approach via the Analytic Hierarchy Process (AHP), this study facilitated prioritization based on relative significance, enabling informed decisions that reconcile diverse and often conflicting stakeholder objectives. The results underscore the paramount importance of evaluating environmental impact criteria, particularly carbon emissions. Additionally, economic and technical feasibility are pivotal in the selection process. Policymakers and decision-makers can use these findings to pinpoint the most fitting SAF alternative aligned with their objectives. Overcoming challenges like production costs, feedstock limitations, high conversion technology expenses, regulatory gaps, and a lack of carbon pricing mechanisms is crucial for SAF development and adoption. Technical feasibility, ensuring compliance with fuel specifications for safety and performance, is equally vital. Fostering SAF demands a collaborative, multi-stakeholder effort involving industry, policymakers, and the public. The AHP method emerges as a valuable framework for prioritizing critical SAF selection factors, empowering decision-makers to harmonize diverse stakeholder objectives. SAF adoption stands pivotal in realizing global climate objectives, with this study's insights poised to guide policymakers and stakeholders in promoting sustainability within aviation.

References

Anderson, B.J. *et al.* (2022) 'Social Science Applications in Sustainable Aviation Biofuels Research: Opportunities, Challenges, and Advancements', *Frontiers in Energy Research*, 9, p. 946. Available at: https://doi.org/10.3389/FENRG.2021.771849/BIBTEX.

Bergero, C. *et al.* (2023) 'Pathways to net-zero emissions from aviation', *Nature Sustainability 2023*, pp. 1–11. Available at: https://doi.org/10.1038/s41893-022-01046-9.

Gössling, S. and Humpe, A. (2020) 'The global scale, distribution and growth of aviation: Implications for climate change', *Global Environmental Change*, 65, p. 102194. Available at: https://doi.org/10.1016/J.GLOENVCHA.2020.102194.

Kramer, S. *et al.* (2022) 'Perspectives on Fully Synthesized Sustainable Aviation Fuels: Direction and Opportunities', *Frontiers in Energy Research*, 9, p. 1040. Available at: https://doi.org/10.3389/FENRG.2021.782823/BIBTEX.

Kurzawska, P. (2021) 'Overview of Sustainable Aviation Fuels including emission of particulate matter and harmful gaseous exhaust gas compounds', *Transportation Research Procedia*, 59, pp. 38–45. Available at: https://doi.org/10.1016/J.TRPRO.2021.11.095.

Lai, Y.Y., Karakaya, E. and Björklund, A. (2022) 'Employing a Socio-Technical System Approach in Prospective Life Cycle Assessment: A Case of Large-Scale Swedish Sustainable Aviation Fuels', *Frontiers in Sustainability*, 3, p. 55. Available at: https://doi.org/10.3389/FRSUS.2022.912676.

Ng, K.S., Farooq, D. and Yang, A. (2021) 'Global biorenewable development strategies for sustainable aviation fuel production', *Renewable and Sustainable Energy Reviews*, 150, p. 111502. Available at: https://doi.org/10.1016/J.RSER.2021.111502.

Omar, A. and Utku, K. (2022) 'Air Transport Projects Quality Assessments by Analytical Hierarchy Process (AHP)', *Repüléstudományi Közlemények*, 34(2), pp. 73–82. Available at: https://doi.org/10.32560/RK.2022.2.6.

Perea-Moreno, A.-J. *et al.* (2022) 'Use of Sustainable Fuels in Aviation—A Review', *Energies 2022, Vol. 15, Page 2440*, 15(7), p. 2440. Available at: https://doi.org/10.3390/EN15072440.

Saaty, T.L. (1977) 'A scaling method for priorities in hierarchical structures', *Journal of Mathematical Psychology*, 15(3). Available at: https://doi.org/10.1016/0022-2496(77)90033-5.

Saaty, T.L. (1990) 'How to make a decision: The analytic hierarchy process', *European Journal of Operational Research*, 48(1). Available at: https://doi.org/10.1016/0377-2217(90)90057-I.

Saaty, T.L. (2002) 'Decision making with the Analytic Hierarchy Process', *Scientia Iranica*, 9(3). Available at: https://doi.org/10.1504/ijssci.2008.017590.

Saaty, T.L. (2008) 'Decision making with the analytic hierarchy process', *International journal of services sciences*, 1(1), pp. 83–98. Available at: https://www.inderscienceonline.com/doi/abs/10.1504/IJSSci.2008.01759 (Accessed: 15 February 2022).

Saaty, T.L. and Vargas, L.G. (2012) 'The possibility of group choice: Pairwise comparisons and merging functions', *Social Choice and Welfare*, 38(3). Available at: https://doi.org/10.1007/s00355-011-0541-6.

Schmidt, P. *et al.* (2018) 'Power-to-Liquids as Renewable Fuel Option for Aviation: A Review', *Chemie Ingenieur Technik*, 90(1–2), pp. 127–140. Available at: https://doi.org/10.1002/CITE.201700129.

Sharma, B.P. *et al.* (2021) 'Economic Analysis of Developing a Sustainable Aviation Fuel Supply Chain Incorporating With Carbon Credits: A Case Study of the Memphis International Airport', *Frontiers in Energy Research*, 9, p. 802. Available at: https://doi.org/10.3389/FENRG.2021.775389/BIBTEX.

Tanzil, A.H. *et al.* (2021) 'Strategic assessment of sustainable aviation fuel production technologies: Yield improvement and cost reduction opportunities', *Biomass and Bioenergy*, 145, p. 105942. Available at: https://doi.org/10.1016/J.BIOMBIOE.2020.105942.

Xu, B. *et al.* (2022) 'Sustainable commercial aviation: What determines air travellers' willingness to pay more for sustainable aviation fuel?', *Journal of Cleaner Production*, 374, p. 133990. Available at: https://doi.org/10.1016/J.JCLEPRO.2022.133990.

IEEES-122

Hydrogen-Powered Aviation: Shaping Sustainable Future Skies

Omar ALHARASEES[1]*, Serdar SANLI, Utku KALE[1]
[1] Budapest University of Technology and Economics, Faculty of Transportation Engineering and Vehicle Engineering, Department of Aeronautics and Naval Architecture, Address: Budapest, 1111, Hungary
*E-mail: oalharasees@edu.bme.hu

Abstract

Within aviation sustainability, hydrogen has emerged as a frontrunner, promising a paradigm shift towards greener skies and a cornerstone for future sustainable air travel. The world, grappling with climate change, is keen on adopting hydrogen as an aviation fuel, envisioning a transformative shift. However, this necessitates a profound understanding of stakeholder perspectives on hydrogen's potential and safety. This in-depth survey delves into stakeholders' opinions concerning hydrogen as a green energy source for the aviation sector. It navigates the landscape of views by analyzing attitudes towards hydrogen's potential to reduce emissions, revolutionize sustainability, and enhance safety. Understanding the public's knowledge and confidence levels concerning hydrogen systems is vital for future integration. These invaluable insights can guide strategic decisions, enabling the industry to harness hydrogen effectively, thus curbing aviation's environmental impact and fostering a sustainable future.

Keywords: Hydrogen System, Aviation Sustainability, Environmental Impact, Safety Assessment, Air Travel Transformation.

I. Introduction

The aviation industry, a significant contributor to global carbon emissions, stands at a critical crossroads. The urgency to mitigate climate change propels the search for alternative, sustainable aviation fuels (Hasan *et al.*, 2021). Hydrogen emerges as a promising candidate, potentially revolutionizing aviation and aligning it with environmental objectives. Its high energy density and clean combustion profile render it an attractive option, capable of significantly reducing greenhouse gas emissions (Yusaf *et al.*, 2022). Initiatives like the European Clean Sky project and Airbus' hydrogen-fueled concept aircraft pave the way (Benítez, Martinez and Nuñez, 2023), showcasing real progress towards a sustainable aviation future.

Transitioning to hydrogen-powered aviation demands an interdisciplinary approach, integrating technological innovation with policy frameworks (Hoelzen *et al.*, 2022). Initiatives like the Hydrogen Council, a global CEO-led coalition, advocate for hydrogen as a key solution (Baquero and Monsalve, 2022). This collective effort emphasizes collaboration between industries, governments, and academia to expedite the development and implementation of hydrogen technologies. Strategic partnerships and funding mechanisms, as exemplified by the U.S. Department of Energy's Hydrogen and Fuel Cells Program (Miller *et al.*, 2016), underscore the role of governmental support in driving this transformative change.

Hydrogen's potential in aviation extends beyond propulsion, influencing auxiliary systems. Innovative projects such as the Hydrogen OnSite Generation for Aircraft Services (H2OGAS) program explore on-site hydrogen production at airports (Gaubatz *et al.*, 2023), enhancing the viability of hydrogen-based aviation. Moreover, advancements in hydrogen fuel cell technology are manifest in the ZEROe aircraft concept by Airbus, demonstrating the feasibility of long-range hydrogen-powered flights (Yusaf *et al.*, 2023). These real-world endeavors highlight the promising trajectory of hydrogen integration in aviation.

Safety stands as a paramount concern in the deployment of hydrogen technology. As seen in NASA's safety protocols for hydrogen fueling and storage, comprehensive safety assessments are instrumental in instilling confidence (Degirmenci *et al.*, 2023). Technological solutions, such as intelligent hydrogen sensors like those deployed by Boeing, further bolster safety measures (Shen *et al.*, 2023). The stringent safety measures and ongoing research within the aviation sector lay the foundation for safe and responsible hydrogen integration.

Public acceptance and understanding are linchpins for successfully adopting hydrogen in aviation. For example, there is increasing engagement in initiatives like the European Union's Clean Sky 2 Joint (Onorato, Proesmans and Hoogreef, 2022). Educational campaigns and outreach initiatives resembling Hydrogen Education are vital in dispelling misconceptions and fostering awareness (Bridgeland *et al.*, 2022). Prominent figures and organizations openly supporting hydrogen technologies, like the endorsement from environmental activists, play a crucial role in shaping public perception and encouraging collective action toward sustainable aviation.

In this transformative journey, research and development serve as the cornerstone. Partnerships between academia and industry, reminiscent of the collaboration between the National Renewable Energy Laboratory (NREL) and industry leaders, drive innovation. Research institutions like the DLR Institute of Engineering Thermodynamics in Germany conduct pioneering studies to optimize hydrogen combustion and address technological challenges (Kallo, 2015). These collaborative research endeavors substantiate the concerted effort toward sustainable hydrogen-powered aviation.

An essential facet of this transition is understanding the viewpoints of stakeholders. Insights garnered from comprehensive surveys are fundamental in tailoring strategies. Engaging with various stakeholders, from passengers to industry professionals, ensures a complete understanding of expectations and concerns, facilitating informed decision-making.

The imperative to act against climate change, as emphasized in international agreements like the Paris Agreement, propels the aviation industry to embrace hydrogen as a path to sustainable skies (Benítez, Martinez and Nuñez, 2023; Tanaka *et al.*, 2023). Governmental mandates, similar to the European Green Deal's commitment to making Europe the world's first climate-neutral continent, set a bold agenda.

These regulatory frameworks position hydrogen as an imperative and signal a global shift toward sustainable aviation, compelling stakeholders to contribute actively to the realization of this vision.

II. Methodology

Exploring public perceptions and attitudes toward hydrogen-powered aerial systems involves a comprehensive analysis of safety, environmental considerations, economic viability, and societal readiness. In the context of the aviation sector, notable organizations such as ZeroAvia and Airbus have made strides in demonstrating the feasibility of hydrogen fuel cells for aircraft propulsion ('ZeroAvia completes first hydrogen-electric passenger plane flight', 2020). Collaborative programs like the Clean Sky 2 Joint Undertaking in the European Union reflect a broader commitment to innovative technologies for environmentally friendly aviation (Tanaka *et al.*, 2023).
By using the questionnaire, this research captures diverse viewpoints on the broader application of hydrogen in aviation. The findings, as illustrated in Figure 1, depicting age and gender distribution among participants, provide valuable insights into the demographic landscape shaping these perspectives.

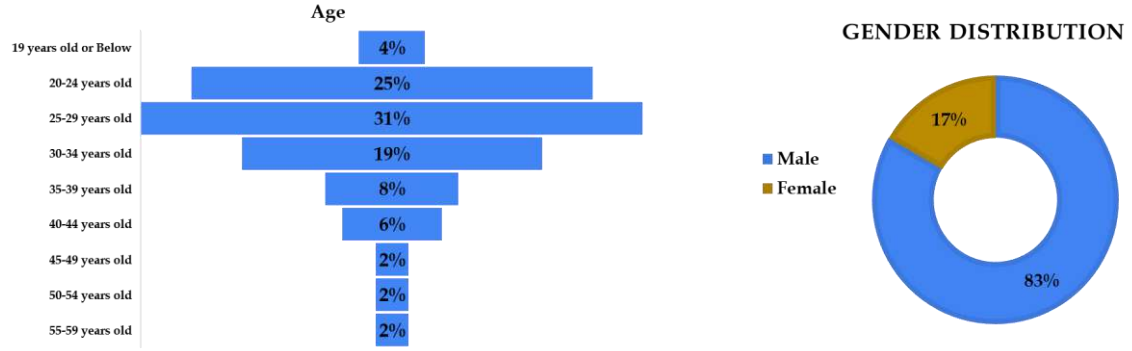

Figure 1 Participants Age & Gender Distribution.

Recent advancements in hydrogen-powered aviation, distinct from previously mentioned examples, include milestone test flights like Boeing's 2008 Two-seater test near Madrid (Alves *et al.*, 2022), and the 2016 four-seater aircraft flight developed by the German aeronautical research agency DLR, in the framework of HY4 (Kallo, 2015). These achievements signal progress in hydrogen plane technology, reinforcing the transformative potential of hydrogen in the aviation industry.
The survey, which explores participant perspectives on safety, environmental impact, economic viability, and societal acceptance, serves as a vital tool for informing policy decisions and technological advancements. This ensures a nuanced understanding of public expectations, a critical factor in achieving a seamless integration of hydrogen technology into the future of aviation.

III.Results & Discussion

Exploring perceptions and attitudes toward hydrogen-powered aerial systems encompasses various aspects, including safety, environmental considerations, economic viability, and societal readiness. An online survey was employed to gather diverse viewpoints on hydrogen in aviation, specifically focusing on its broader application in aerial systems.
Respondents' views on the environmental impact of hydrogen-powered aerial systems are encapsulated in Figure 2, illustrating a spectrum from "Strongly Disagree" to "Strongly Agree" across several environmental statements. The data reflects diverse perspectives on hydrogen's potential to reduce aviation emissions significantly, the necessity for extensive research to comprehend its full environmental benefits, its capacity to revolutionize aviation sustainability, the recommendation for prioritizing hydrogen as a green energy source in the aviation industry, and the belief in its ability to mitigate aviation's environmental impact. This array of viewpoints highlights varying perceptions, providing a nuanced understanding of hydrogen technology's role in addressing environmental concerns.
Regarding safety and security concerns, Figure 2 also depicts participants' varying perceptions and confidence levels. The assessments include confidence in critical safety measures, the role of scientific research in safety protocols, the necessity of safety advancements for public acceptance, the essentiality of public trust for wider adoption, and diversified confidence levels in the safety measures and research supporting hydrogen aviation. These results distinctly illustrate the spectrum of viewpoints, reflecting respondents' differing levels of assurance and trust in the safety aspects of hydrogen-powered aviation.
Societal acceptance and economic viability play crucial roles in integrating hydrogen-powered aerial systems, as demonstrated in Figure 3. This figure provides insight into respondents' perspectives on elements related to societal acceptance and economic viability, including the role of public opinion, the influence of open discussions, the impact of public perception on project feasibility, the aviation industry's focus on educating the public about hydrogen's benefits, and the overall importance of public perception in advancing hydrogen technology in aviation.

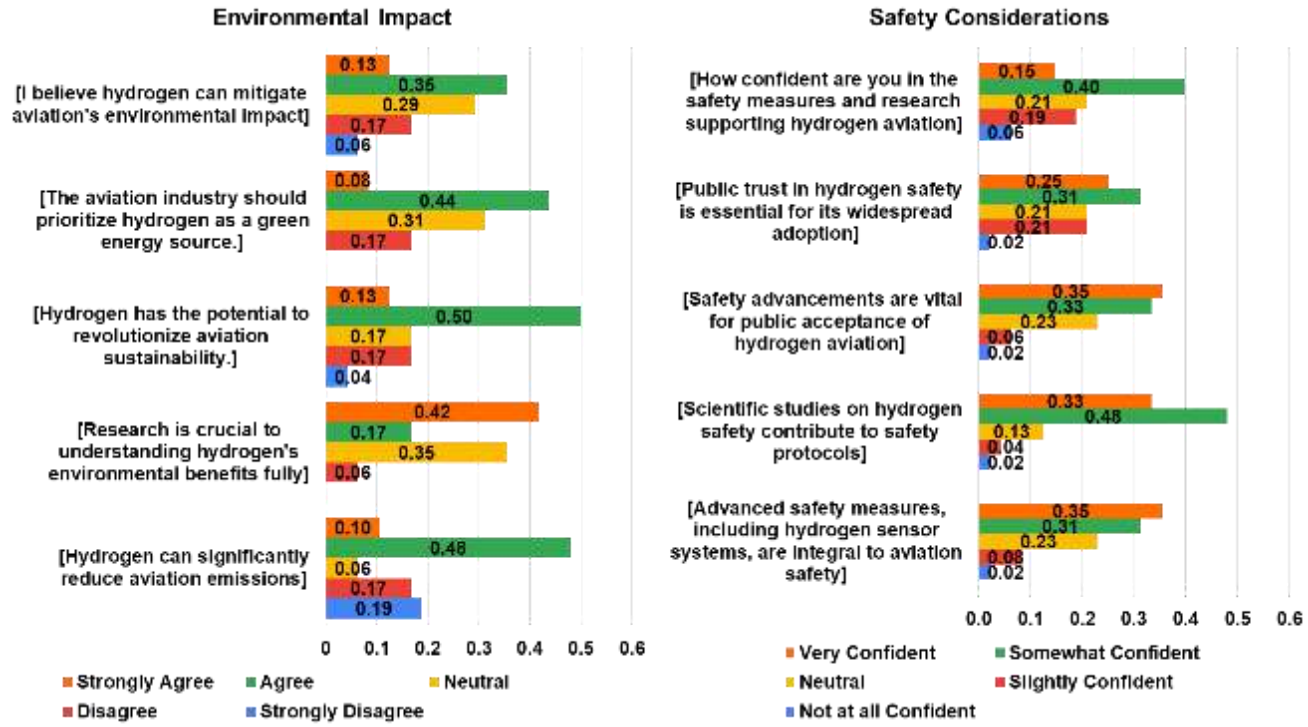

Figure 2 Environmental Impact & Safety Considerations Outcomes.

Examining economic and social considerations in Figure 3 also yields essential insights into the broader socio-economic landscape of hydrogen-powered aerial systems. Participants' feedback underscores critical aspects such as the profitability of investments, emphasizing the need for a longer-term outlook to assess economic sustainability. They also stressed the importance of technological development, indicating that investment decisions are contingent upon the advancement and reliability of hydrogen-related technologies. Moreover, there was a strong emphasis on aligning hydrogen technology investments with broader sustainability goals within the aviation industry.

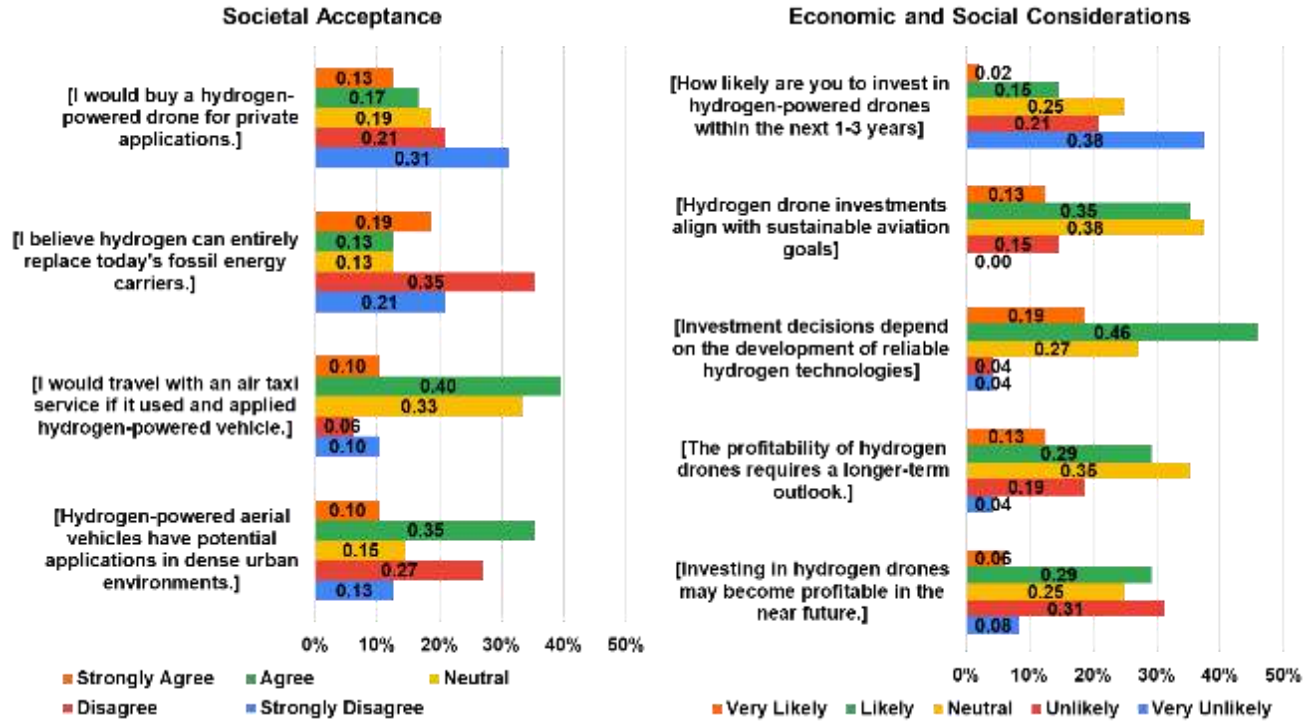

Figure 3 Societal Acceptance & Economic and Social Considerations Outcomes.

Participants' likelihood of investing in hydrogen-powered aerial systems within the near future varied, illustrating diverse and

comprehensive concerns regarding the economic and social implications associated with the adoption of hydrogen technology.

IV.Conclusion

The integration of hydrogen technology in aviation signifies a leap toward sustainable practices. Survey insights from experts across diverse backgrounds reveal nuanced considerations on safety, environmental impact, societal acceptance, and economic viability. While there's enthusiasm for hydrogen-powered aviation's potential, various concerns demand thoughtful addressing.

Survey results reveal different perspectives on environmental expectations, safety, societal acceptance, and economic viability. Confidence in hydrogen's potential coexists with the need for comprehensive research. Safety, public perception, and societal readiness require collaborative attention.

Recommendations encompass evolving safety standards, ongoing research, and robust educational initiatives. Addressing safety, promoting education, and fostering collaborative efforts are crucial for successfully integrating hydrogen technology in aviation, paving the way for a sustainable future.

References

Alves, M.P. *et al.* (2022) 'A Review on Industrial Perspectives and Challenges on Material, Manufacturing, Design and Development of Compressed Hydrogen Storage Tanks for the Transportation Sector', *Energies 2022, Vol. 15, Page 5152*, 15(14), p. 5152. Available at: https://doi.org/10.3390/EN15145152.

Baquero, J.E.G. and Monsalve, D.B. (2022) 'From Fossil Fuel Energy To Hydrogen Energy: Transformation of Fossil Fuel Energy Economies Into Hydrogen Economies Through Social Entrepreneurship', *Proceedings of WHEC 2022 - 23rd World Hydrogen Energy Conference: Bridging Continents by H2*, pp. 1256–1259. Available at: https://doi.org/10.1016/j.ijhydene.2023.06.123.

Benítez, L., Martinez, M. and Nuñez, M. (2023) 'Regional Multi-Mission Aircraft in Clean Sky 2: Environmental Impact and Actual Technologies Evaluation from Flight Tests', *Journal of Physics: Conference Series*, 2526(1), p. 012010. Available at: https://doi.org/10.1088/1742-6596/2526/1/012010.

Bridgeland, R. *et al.* (2022) 'Challenges toward achieving a successful hydrogen economy in the U.S.: Potential end-use and infrastructure analysis to the year 2100', *Cleaner Production Letters*, 3, p. 100012. Available at: https://doi.org/10.1016/J.CLPL.2022.100012.

Degirmenci, H. *et al.* (2023) 'Analyzing the hydrogen supply chain for airports: Evaluating environmental impact, cost, sustainability, viability, and safety in various scenarios for implementation', *Energy Conversion and Management*, 293, p. 117537. Available at: https://doi.org/10.1016/J.ENCONMAN.2023.117537.

Gaubatz, J. *et al.* (2023) 'Estimating the Energy Demand of a Hydrogen-Based Long-Haul Air Transportation Network', *2023 International Conference on Future Energy Solutions, FES 2023* [Preprint]. Available at: https://doi.org/10.1109/FES57669.2023.10182543.

Hasan, M.A. *et al.* (2021) 'Climate Change Mitigation Pathways for the Aviation Sector', *Sustainability 2021, Vol. 13, Page 3656*, 13(7), p. 3656. Available at: https://doi.org/10.3390/SU13073656.

Hoelzen, J. *et al.* (2022) 'Hydrogen-powered aviation and its reliance on green hydrogen infrastructure – Review and research gaps', *International Journal of Hydrogen Energy*, 47(5), pp. 3108–3130. Available at: https://doi.org/10.1016/J.IJHYDENE.2021.10.239.

Kallo, J. (2015) 'DLR leads HY4 project for four-seater fuel cell aircraft', *Fuel Cells Bulletin*, 2015(11), p. 13. Available at: https://doi.org/10.1016/S1464-2859(15)30362-X.

Miller, E.L. *et al.* (2016) 'U.S. Department of Energy Hydrogen and Fuel Cells Program: Progress, Challenges and Future Directions', *MRS Advances*, 1(42), pp. 2839–2855. Available at: https://doi.org/10.1557/ADV.2016.495/METRICS.

Onorato, G., Proesmans, P. and Hoogreef, M.F.M. (2022) 'Assessment of hydrogen transport aircraft: Effects of fuel tank integration', *CEAS Aeronautical Journal*, 13(4), pp. 813–845. Available at: https://doi.org/10.1007/S13272-022-00601-6/TABLES/11.

Shen, C. *et al.* (2023) 'Review of the Status and Prospects of Fiber Optic Hydrogen Sensing Technology', *Chemosensors 2023, Vol. 11, Page 473*, 11(9), p. 473. Available at: https://doi.org/10.3390/CHEMOSENSORS11090473.

Tanaka, K. *et al.* (2023) 'Environmental-impact assessments at airport level of Clean Sky 2 technologies', *Journal of Physics: Conference Series*, 2526(1), p. 012012. Available at: https://doi.org/10.1088/1742-6596/2526/1/012012.

Yusaf, T. *et al.* (2022) 'Sustainable Aviation—Hydrogen Is the Future', *Sustainability 2022, Vol. 14, Page 548*, 14(1), p. 548. Available at: https://doi.org/10.3390/SU14010548.

Yusaf, T. *et al.* (2023) 'Sustainable hydrogen energy in aviation – A narrative review', *International Journal of Hydrogen Energy* [Preprint]. Available at: https://doi.org/10.1016/J.IJHYDENE.2023.02.086.

'ZeroAvia completes first hydrogen-electric passenger plane flight' (2020) *Fuel Cells Bulletin*, 2020(10), p. 6. Available at: https://doi.org/10.1016/S1464-2859(20)30444-2.

IEEES-123

Adaption of Fuel-Cell Energy in Aviation Infrastructure

Omar ALHARASEES[1]*, Utku KALE[1]
[1]Budapest University of Technology and Economics, Faculty of Transportation Engineering and Vehicle Engineering, Department of Aeronautics and Naval Architecture, Address: Budapest, 1111, Hungary
*E-mail: oalharasees@edu.bme.hu

Abstract

This study meticulously analyzes the integration of fuel cell technology in aviation infrastructures and airports, employing the robust Analytical Hierarchy Process (AHP) methodology. The investigation encompasses vital criteria such as environmental impact, technological feasibility, economic viability, and reliability, considering factors like carbon emissions reduction potential, air and noise pollution mitigation, resource sustainability, existing infrastructure compatibility, technological maturity, energy efficiency, initial investment costs, operational and maintenance expenses, long-term cost savings, system reliability, energy source stability, and grid connectivity. By applying the AHP model, this comprehensive assessment provides nuanced insights for aviation stakeholders, facilitating informed decisions toward sustainable energy choices.

Keywords: Fuel Cell Technology, Analytical Hierarchy Process (AHP), Aviation Sustainability, Environmental Impact, Energy Source Integration.

I. Introduction

In an era marked by intersecting environmental, technological, economic, and reliability considerations, the aviation industry confronts an imperative to reassess its energy sources (Jia, Macário and Buyle, 2023). A pivotal player in global transportation, commerce, and connectivity (Kelemen, 2009), the aviation sector, comprising aircraft, airports, and airfields, simultaneously contributes significantly to greenhouse gas emissions and environmental pollution (Hasan *et al.*, 2021). Tackling these challenges necessitates profoundly exploring diverse energy types and their seamless integration into aviation and airport infrastructures.

The aviation industry's carbon footprint stands as a critical concern, with sustainable energy solutions promising to mitigate its environmental impact (Zhang, Gudmundsson and Oum, 2010). This study delves into how distinct Factors can effectively reduce carbon emissions, mitigate air and noise pollution, and foster resource sustainability within aviation. Real-world instances, such as adopting electric ground support vehicles at airports and using sustainable aviation fuels in commercial flights, underscore the industry's dedication to sustainable practices.

Integrating new energy sources into aviation necessitates technological feasibility and compatibility with existing infrastructure. Governed by stringent regulations and characterized by intricate operational dynamics, the aviation industry demands energy solutions that seamlessly align with its complex ecosystem (Rojas-Michaga *et al.*, 2023). Technological advancements, exemplified by integrating solar panels into airport structures for electricity generation and the ongoing development of battery-electric aircraft, showcase efforts to make aviation more sustainable (Yıldız *et al.*, 2023).

The economic dimension is pivotal, and sustainability should not compromise profitability. This analysis will scrutinize the financial aspects of adopting various energy types, considering initial investment costs, operational and maintenance expenditures, and the potential for long-term cost savings. Initiatives like deploying electric ground vehicles at airports and investing in hydrogen infrastructure projects illuminate the economic dynamics within aviation's sustainable energy landscape.

Uninterrupted and dependable energy supply is paramount for aviation operations, where disruptions can have severe consequences. This article evaluates the reliability and resilience of different energy sources, encompassing system reliability, energy source stability, and grid connectivity options. The presence of cogeneration systems supplying electricity and heat to airport facilities underscores the importance of resilient energy solutions.

The aviation industry is constantly evolving, with increasing air travel demand and evolving operational needs. Energy solutions must be scalable to accommodate this growth and flexible to adapt to changing circumstances. We will investigate the critical factors in investing in the suitable energy type adaptability while considering its capacity to integrate with other energy sources. Solutions like grid-connected systems with energy storage capabilities exemplify adaptations to the dynamic aviation landscape (Rupcic *et al.*, 2023).

In this article, we explore diverse factors that affect fuel cell technology within the aviation and airport infrastructure context, subsequently conducting an Analytical Hierarchy Process (AHP) analysis (Alharasees and Kale, 2023). This analysis provides a panoramic understanding of the relevance and applicability of fuel cell technology in the aviation industry and airport infrastructures.

II. Methodology

In undertaking a meticulous evaluation of diverse fuel cell technology energy types for integration into aviation infrastructures and airports, this study adopts the Analytical Hierarchy Process (AHP) methodology. Recognized for its capacity to handle complex decision-making scenarios, AHP systematically structures the hierarchy of criteria and facilitates a comprehensive analysis (Saaty, 1980).

The foundation of our evaluation lies in the insights of 18 Aviation Experts, strategically categorized into two groups—aviation operators and managers. This grouping ensures a holistic perspective, incorporating the aviation industry's operational and managerial facets. These

experts, possessing profound knowledge and experience, played a pivotal role in providing nuanced judgments on the criteria under consideration.

The Saaty scale was employed to capture the qualitative judgments of the expert panel. This scale, a proven tool in decision-making processes, assigns numerical values to verbal judgments, allowing for a nuanced yet quantifiable representation of expert opinions. Table 1 delineates the Saaty scale as a reference guide for the experts in expressing their preferences and comparisons.

Table 1 Saaty Scale (Saaty, 2008)

Intensity of Importance	1	3	5	7	9	2, 4, 6, 8
Definition	Equal Importance	Moderate Importance	Strong Importance	Very Strong Importance	Extremely Strong Importance	Intermediate Values

Figure 1 presents the Aviation Infrastructure Fuel-Cell Hierarchical Model, representing the structured hierarchy of criteria. This visual aid showcases the interconnections and dependencies among the various criteria, providing a holistic view of the analytical framework.

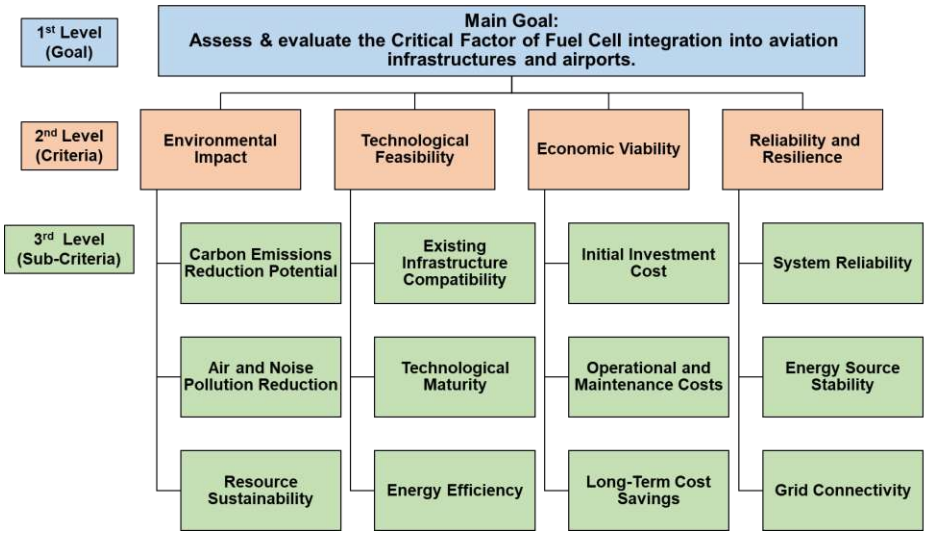

Figure 1 Fuel-Cell Hierarchal Model.

Within this model, the hierarchical arrangement encapsulates four key strata, each probing a distinct facet of the integration of fuel cell technology energy types:

- Environmental Impact Assessment: The first stratum of the evaluation centers on the environmental impact of different energy types. Within this context, the current researcher meticulously scrutinizes the potential for reduction of carbon emissions, air and noise pollution, and the overarching theme of resource sustainability. Real-world implementations, such as the adoption of electric ground support vehicles at airports and the integration of sustainable aviation fuels in commercial flights, serve as benchmarks to elucidate the palpable impact on the industry's environmental stewardship.
- Technological Feasibility Examination: The second tier delves into the technological feasibility of incorporating diverse energy types into the aviation ecosystem. We assess their compatibility with existing infrastructure, gauging technological maturity and energy efficiency. Illustrations abound, including the integration of solar panels into airport structures for electricity generation and the ongoing development of battery-electric aircraft, signaling a pivotal leap in technological advancements tailored to render aviation more sustainable.
- Economic Viability Analysis: Financial considerations form the bedrock of our third tier of analysis. Economic viability encompasses a discerning examination of initial investment costs, operational and maintenance expenditures, and the prospect of long-term cost savings. Instances such as deploying electric ground vehicles at airports and investing in hydrogen infrastructure projects illuminate the economic dynamics underpinning aviation's sustainable energy landscape.
- Reliability and Resilience Assessment: The fourth stratum evaluates the reliability and resilience embedded within different energy sources. This encompasses an in-depth system reliability analysis, energy source stability, and grid connectivity options. Noteworthy deployments of cogeneration systems, adept at supplying electricity and heat to airport facilities, underscore the strategic imperative of resilient energy solutions within aviation operations.

The holistic evaluation conducted through the Analytical Hierarchy Process (AHP) methodology, considering the insights of 18 Aviation Experts, provides a comprehensive understanding of the multifaceted dimensions surrounding integrating diverse fuel cell technology energy types in aviation and airport infrastructures. By navigating through the environmental, technological, and economic aspects, this analysis illuminates a pathway for informed decision-making in pursuing sustainable energy solutions within the aviation industry.

III. Results & Discussion

The evaluation of fuel cell technology energy types within the context of aviation and airport infrastructures was conducted through the Analytical Hierarchy Process (AHP) in this research. In this section, we present the weighted criteria evaluations by aviation managers and operators, shedding light on their distinctive perspectives. The Saaty scale served as the foundation for pairwise comparisons, ensuring a systematic and reliable assessment.

As depicted in Table 2, aviation managers prioritize reliability and resilience (33.20%) as the top concern, emphasizing the need for a dependable energy supply. Environmental impact follows closely at 29.71%, showcasing a commitment to sustainability. Economic viability holds the third spot (27.44%), highlighting financial considerations. Technological feasibility receives the lowest weight (9.65%), indicating relatively lower importance in their considerations. This nuanced hierarchy provides critical insights into their decision-making dynamics.

Table 2 PCM of Aviation Managers

Aviation Managers					
Criteria	Environmental Impact	Technological Feasibility	Economic Viability	Reliability and Resilience	Weights
Environmental Impact	1.00	2.00	3.00	2.00	29.71%
Technological Feasibility	0.50	1.00	2.00	2.00	9.65%
Economic Viability	0.33	0.50	1.00	2.00	27.44%
Reliability and Resilience	0.50	0.50	0.50	1.00	33.20%
CR=0.05263	Sum=				100%

Turning to Table 3, which outlines the weighted criteria evaluation by aviation operators, a divergent perspective emerges. Environmental impact holds the highest weight at 39.27%, signifying a heightened focus on minimizing the environmental footprint within this expert group. Technological feasibility, economic viability, reliability, and resilience are assigned weights of 18.30%, 13.81%, and 28.62%, respectively. This distribution underscores aviation operators' distinctive emphasis on environmental considerations, echoing the broader industry trend.

Table 3 PCM of Aviation Operators.

Aviation Operators					
Criteria	Environmental Impact	Technological Feasibility	Economic Viability	Reliability and Resilience	Weights
Environmental Impact	1.00	4.00	4.00	1.00	39.27%
Technological Feasibility	0.25	1.00	2.00	0.50	18.30%
Economic Viability	0.25	0.50	1.00	0.50	13.81%
Reliability and Resilience	1.00	2.00	2.00	1.00	28.62%
CR=0.0745	Sum=				100%

Comparing these expert perspectives, it becomes evident that while both groups prioritize environmental impact, aviation managers allocate relatively higher importance to reliability and resilience, constituting 33.20% of their considerations. In contrast, while still valuing reliability and resilience, aviation operators place a more substantial emphasis on environmental impact, accounting for 39.27% of their weighted criteria. These nuanced differences highlight the varied perspectives and priorities within the aviation industry concerning sustainable energy adoption.

Figure 2 further illustrates the comparative analysis between aviation managers and aviation operators. The radar graph visually reinforces the distinct weightings assigned by each group to environmental impact, technological feasibility, economic viability, reliability, and resilience. This graphical representation offers a succinct overview of the varying emphases and provides a foundation for more in-depth discussions on the implications of these distinct perspectives.

The weighted criteria evaluations underscore the multifaceted considerations concerning sustainable energy solutions within the aviation industry. The differing emphases of aviation managers and operators illuminate the complex decision-making landscape, providing valuable

insights for stakeholders navigating the path toward a more sustainable aviation future.

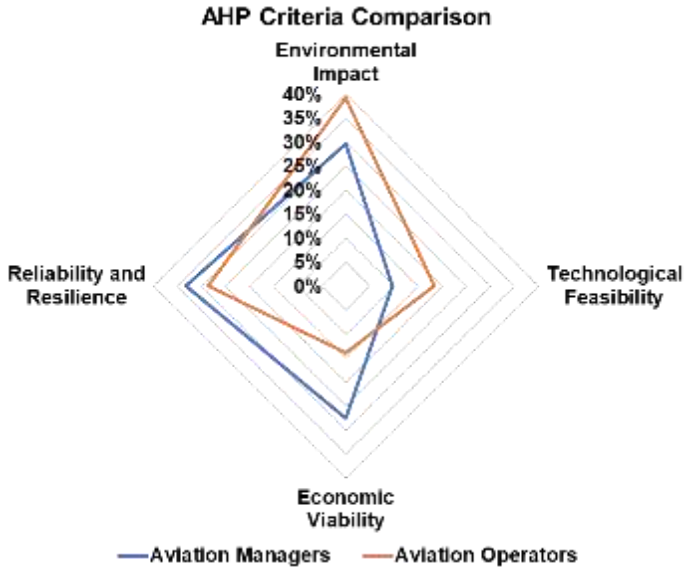

Figure 2 AHP Main Criteria Comparison.

IV. Conclusion

This comprehensive study delves into the intricate landscape of integrating fuel cell technology into aviation infrastructures and airports, employing the robust Analytical Hierarchy Process (AHP) methodology. The exploration considers critical criteria such as environmental impact, technological feasibility, economic viability, and reliability, providing nuanced insights for aviation stakeholders. The industry's commitment to sustainability is evident, particularly emphasizing reducing environmental impact and adopting diverse energy types.

Aviation managers prioritize reliability and resilience, emphasizing the need for a dependable energy supply, while environmental impact closely follows, showcasing a commitment to sustainability. Economic viability holds the third spot, and technological feasibility is less critical. In contrast, aviation operators prioritize environmental impact, highlighting their focus on minimizing the industry's ecological footprint.

These findings illuminate the complex decision-making dynamics within the aviation industry, providing valuable insights for stakeholders navigating toward a sustainable aviation future. As the industry grapples with evolving demands, the study informs strategic choices, fostering a more sustainable and resilient aviation landscape for the future.

References

Alharasees, O. and Kale, U. (2023) 'Applying AHP for supplier selection in aviation: a multi-criteria decision-making approach', *International Journal of Sustainable Aviation*, 9(4), pp. 293–313. Available at: https://doi.org/10.1504/IJSA.2023.134344.

Hasan, M.A. *et al.* (2021) 'Climate Change Mitigation Pathways for the Aviation Sector', *Sustainability 2021, Vol. 13, Page 3656*, 13(7), p. 3656. Available at: https://doi.org/10.3390/SU13073656.

Jia, X., Macário, R. and Buyle, S. (2023) 'Expanding Horizons: A Review of Sustainability Evaluation Methodologies in the Airport Sector and Beyond', *Sustainability 2023, Vol. 15, Page 11584*, 15(15), p. 11584. Available at: https://doi.org/10.3390/SU151511584.

Kelemen, Z. (2009) 'Airport information system integration by using message broker', *Periodica Polytechnica Transportation Engineering*, 37(1–2), pp. 15–21. Available at: https://doi.org/10.3311/PP.TR.2009-1-2.03.

Rojas-Michaga, M.F. *et al.* (2023) 'Sustainable aviation fuel (SAF) production through power-to-liquid (PtL): A combined techno-economic and life cycle assessment', *Energy Conversion and Management*, 292, p. 117427. Available at: https://doi.org/10.1016/J.ENCONMAN.2023.117427.

Rupcic, L. *et al.* (2023) 'Environmental impacts in the civil aviation sector: Current state and guidance', *Transportation Research Part D: Transport and Environment*, 119, p. 103717. Available at: https://doi.org/10.1016/J.TRD.2023.103717.

Saaty, T.L. (2008) 'Decision making with the analytic hierarchy process', *International journal of services sciences*, 1(1), pp. 83–98. Available at: https://www.inderscienceonline.com/doi/abs/10.1504/IJSSci.2008.01759 (Accessed: 15 February 2022).

Yıldız, M. *et al.* (2023) 'Solar energy for the airport ground support equipment – a quantitative study', *Aircraft Engineering and Aerospace Technology*, 95(5), pp. 831–837. Available at: https://doi.org/10.1108/AEAT-08-2022-0211/FULL/PDF.

Zhang, A., Gudmundsson, S.V. and Oum, T.H. (2010) 'Air transport, global warming and the environment', *Transportation Research Part D: Transport and Environment*, 15(1), pp. 1–4. Available at: https://doi.org/10.1016/J.TRD.2009.07.011.

IEEES-124

A Strategy on Off-Shore Alternative Fuel Production

[1*]Onur Otlu, [2]Adnan Midilli, [3]Zehra Yumurtacı
[1] Yıldız Technical University, Faculty of Science and Literature, Mechanical Engineering Department, Barbaros Bulvarı Yıldız, Istanbul, 34349, Türkiye
[2] Istanbul Technical University, Energy Institute, İTÜ Ayazağa Campus Maslak, Istanbul, 34469, Türkiye
[3] Yıldız Technical University, Faculty of Science and Literature, Mechanical Engineering Department, Barbaros Bulvarı Yıldız, Istanbul, 34349, Türkiye
*E-mails: onur.otlu@std.yildiz.edu.tr amidilli@itu.edu.tr zyumur@yildiz.edu.tr

Abstract

Wind power, one of the most plentiful renewable energy sources, holds even greater resources in open seas and deep waters, but these areas bring many technical challenges for energy production and its transmission to land. Open sea offshore wind farms have started energy production in the last decade. In the same period, the maritime sector has set for itself ambitious targets, aiming to become carbon neutral around 2050. This necessitates a significant increase in the production of alternative fuels such as hydrogen, methanol and ammonia. With the advances in off-shore construction and alternative fuel production technologies, it can be possible to combine these two areas and establish off-shore platforms where electricity from wind turbines can be transformed into hydrogen and then into alternative fuels. With the inclusion of nitrogen and carbon dioxide, these platforms can contribute to green fuels production, decarbonization, and the supply of future manned or autonomous fleets with alternative fuel to extend their ranges in long journeys. This study focuses on the thermodynamic, economic, environmental and sustainability analysis of such platforms and determine their sustainability indicators to determine if these can assist the transformation of energy and maritime sectors.

Keywords: Green hydrogen, offshore, marine fuels, methanol, sustainability indicators

I. Introduction

The share of renewable energy resources in global electricity production is rising every year. Certain European countries have achieved renewable electricity production in excess of 50% of their daily consumption, with the EU-wide average reaching %22 (Eurostat, 2022) Wind power is one of the most abundant renewable energy sources in the world, and this resource is most plentiful on the seas, where higher power densities and capacity factors can be obtained compared to land, and there are less restrictions in terms of space and noise. Open seas and deeper waters hold greater resources still, but establishing wind farms in deep waters brings many technical challenges, such as establishing foundations for the turbines and transmitting the produced electricity back to land. (Diaz, Soares, 2020) Though HVAC and HVDC cable connections have proliferated in the last decades, it is sometimes infeasible to bring the electricity produced offshore to land via cable connections, especially in deep water locations far from shore. Here, hydrogen pipelines to shore are being considered, but even farther, the products will need to be transported on vessels to land (Calado and Castro, 2021).

At the same time, the maritime sector is undergoing a profound transition. The goals set by the International Maritime Organization to achieve 50% reduction in greenhouse gas emissions from the maritime sector have been updated in 2023, and now the sector aspires to be carbon neutral “around 2050” (International Maritime Organization, 2023). This requires a strong shift to alternative fuels such as hydrogen, methanol, ethanol and perhaps ammonia, and adds to the already high forecasts for alternative fuels for the upcoming decades (DNV, 2023). Production and supply of these fuels to ships across the world are expected to require significant investments and effort.

As offshore construction, water electrolysis and alternative fuel reactor technologies mature, it could be possible to combine these in an off-shore platform to convert the electricity produced by off-shore wind turbines into green hydrogen. This produced hydrogen can be stored as compressed gas, or liquified, and loaded on carrier ships to be transported to the coast. It can also be transformed into alternative fuels such as methanol, formic acid, DME or ammonia with the addition of carbon dioxide or nitrogen. This area has already received attention in literature, with studies to assess the technical and economic aspects of sustainable fuel production from far-offshore wind resources (Babarit, Body et al, 2019), techno-economic analysis of hydrogen production from the WindFloat Atlantic offshore wind farm (Lucas, Ferreira et al, 2022), techno-economic feasibility of energy converter fleets (Babarit, Gilloteaux et al, 2018) and assessment of off-shore platforms for novel methanol synthesis processes including exergetic and exergoeconomic analyses resources (Crivellari, Cozzani and Dincer, 2019). With many countries incorporating significant off-shore wind energy investments and green hydrogen transformation into their roadmaps, this area continues to receive academic and sectoral interest.

II.Main Considerations

The study commences with the establishment of a target production rate for hydrogen and methanol, set as the amount necessary to provide two 5.000 tonnes ships with enough methanol to sail from the Black Sea to Italy and back. This leads to specifying the wind turbines necessary to provide enough electricity to produce green hydrogen, sea water reverse osmosis treatment, hydrogen compression, conversion into methanol or e-fuels and delivery to pipelines or carrier ships including auxiliary equipment. This step allows for the determination of the other equipment necessary for the production and conversion, the installation requirements of the plant -which is currently planned as a 40x60 m offshore platform with two levels - the amount of nitrogen and carbon dioxide that needs to be added into the plant and electricity and chemical efficiencies of every subcomponent present.

Fig. 1: Off-Shore Alternative Fuel Production Plant Layout

At the next step, every production and conversion method on the plant are put through an energy and exergy efficiency analysis using software such as EES, Aspen or Homer. This step establishes an efficiency analysis of the plant processes from beginning to end as well as the necessary data for the determination of sustainability indicators. This step is followed by an economic analysis, using the installation, production, and delivery costs for the various fuels and the NPV and pay-back period of the facility and comments on the most favorable method to bring the produced alternative fuels to land, or to supply them for fleets of manned or autonomous fleets on long journeys.
Environmental and sustainability analyses of the plant and processes follow to determine the effects on local life, sea and air environments and socio-economic activity in the area. The final step is the determination of sustainability indicators to provide solid results for the assessment of the soundness of the plant and investment.

III. Strategic Approach

The plant is proposed to be able to output four different chemicals which can be used as fuel or chemical feedstock: hydrogen, methanol, DME and ammonia. These four production branches are to be investigated for thermodynamic and economic efficiencies, including the market and demand for these products. The ability to produce different chemicals according to demand provides flexibility and versatility to the plant.
While the original concept is deep-water wind turbines and an offshore chemical conversion and production plant in the vicinity, at the current conjecture there are four different approaches for hydrogen production using offshore wind. These are:

- Offshore turbines, transmitting the produced electricity to an onshore chemical plant for hydrogen production and conversion to other chemicals
- Offshore turbines with a central offshore platform, which collects the produced electricity and converts it into hydrogen. Then, this hydrogen is transported by pipeline to the shore.
- Offshore turbines, each with hydrogen production equipment, which directly convert the produced electricity into hydrogen. This hydrogen is then collected from each turbine and transported by pipeline to shore.
- In even deeper waters, offshore floating turbines produce electricity, which is collected in a central offshore platform to be converted into hydrogen (and possibly alternative fuels), then transported by sea vessels

These lead to many different combinations that need to be assessed to find the optimum method for different wind regimes and demand patterns. Three locations on sea trade routes with high levels of offshore wind have been chosen, and simulations are expected to locate the most favourable choices for these locations.

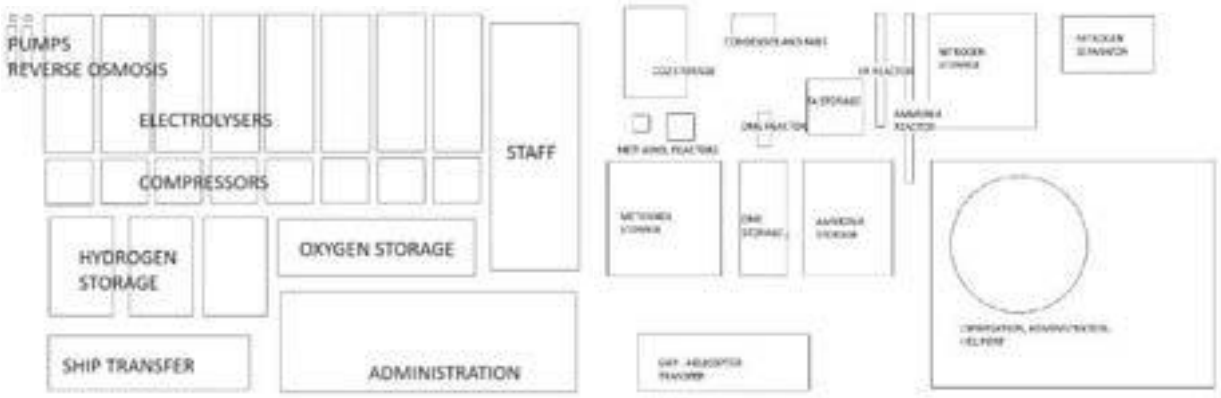

Fig. 2. Platform and level layout of the alternative fuel production plant

The efficiency and economic data received from the study, together with its environmental and sustainability implications, make it possible to determine whether such plants can be expected to be profitable and sustainable. These plants need to sustain themselves, make sense from an economic point of view, provide the alternative fuels at competitive prices and cause no harm to the local environment. Current equipment and construction costs, already assessed to a degree, allow for the determination of the CAPEX and OPEX of the investment, and electricity and fuel prices worldwide can be used to determine if the plant can be expected to survive economically.

IV. Results and discussion

Such offshore platforms could lead to the accomplishment of the below objectives:

- Harnessing the wind energy potential in the open seas and allowing it to be supplied to shore or to travelling ships as valuable alternative fuels,
- Facilitating the green and carbon-neutral transformation of the maritime industry by producing and supplying alternative fuels at competitive prices,
- Extending the operational range of commercial manned or autonomous ships by locating such facilities in critical waterways and trade routes,
- Contributing to carbon neutrality by incorporating carbon dioxide brought from shore of from travelling ships.

If the results are positive, we could expect such offshore platforms to be a common sight in the future and provide significant benefits to the energy and shipping sectors. This can transform the future of sea transport and increase the strategic value of locations where such plants can be set up to support sea trade routes.

V. Conclusion

With the ambitious roadmaps set by countries worldwide and energy and maritime sector unions, it is obvious that significant investments will be made in offshore turbine and platform constructions as well as manyfold increases in alternative fuels production. The authors believe that such an offshore production plant can satisfy the requirement of both sectors and hopefully provide an economical, environmentally friendly, and sustainable solution for the future of global sea transport.

Acknowledgement

The study has not received any external contributions. The authors would like to thank Yıldız Technical University and Istanbul Technical University in Türkiye for their technical support.

References

Babarit, A.,(2019). Energy and economic performance of the FARWIND energy system for sustainable fuel production from the far-offshore wind energy resource, Fourteenth International Conference on Ecological Vehicles and Renewable Energies

Lucas,T. R., (2022). Hydrogen production from the WindFloat Atlantic offshore wind farm: A techno-economic analysis, Applied Energy 310

Babarit, A.,(2018). Techno-economic feasibility of fleets of far offshore hydrogen-producing wind energy converters, International journal of hydrogen energy 43

Crivellari, A., Cozzani, V., Dincer, I. (2019) Exergetic and exergoeconomic analyses of novel methanol synthesis processes driven by offshore renewable energies, Energy 187

Diaz, H., Guedes Soares, C., (2020) Review of the current status, technology and future trends of offshore wind farms, Ocean Engineering 209

Calado, G., Castro, R., (2021) Hydrogen Production from OffshoreWind Parks: Current Situation and Future Perspectives, Applied Sciences 2021, 11, 5561

Eurostat Renewable energy statistics, data extracted January 2023, Renewable energy statistics - Statistics Explained (europa.eu)

International Maritime Organization, IMO's work to cut GHG emissions from ships, IMO's work to cut GHG emissions from ships

DNV, Maritime Forecast to 2050, Maritime Forecast to 2050 - DNV.

IEEES-125

Thermal Analysis for Different Discharge Rates in A Li-Ion Battery Package

[1]Büşra Namaldı Kömürcü, [2*]Muhammet Çelik, [3]Gülşah Elden, [3]Mustafa Serdar Genç.
[1] Erciyes University, Graduate School of Natural and Applied Sciences, Kayseri, 38000, Turkey
[2] Aksaray University, Engineering Faculty, Mechanical Engineering Department, Aksaray, 68100, Turkey
[3] Erciyes University, Engineering Faculty, Energy Systems Engineering Department, Kayseri, 38000, Turkey

*celik@aksaray.edu.tr

Abstract

Lithium-ion batteries have become one of the most popular energy storage systems in recent years, thanks to their advantages such as high power density, long cycle life, and fast charging capability. Lithium-ion batteries require excellent temperature control to ensure that all these benefits last. Low temperature drastically reduces battery capacity and power, while high temperature causes degradation. As a result, battery life may be reduced, and thermal runaway may occur. For all these reasons, thermal analysis for lithium-ion batteries should be investigated. This study presents the thermal analyses for different discharging rates (0.5 C, 1.0 C, 1.5 C, and 2. C) in a Li-Ion battery pack to explore the effects of discharge rate on temperature and heat generation revealed in the battery pack. In order to achieve these analyses, a 3-D battery pack in a cubic arrangement was designed using 25 cylindrical types of 18650 Li-Ion batteries in total with 5 series and 5 parallel configurations. The numerical results show that the temperature difference in the battery pack is 7.7 K when the battery pack is discharged at 0.5 C, while the temperature difference is 29.8 K when it is discharged at 2.0 C. Furthermore, it can be seen that the distribution of heat production within the battery decreases from the center of the battery to the outside.

Keywords: Lithium-ion cell, Battery pack configuration, Thermal analysis, Discharge rate.

I. Introduction

Today, although renewable energy technologies are developing and becoming widespread, approximately 60% of the energy production in the world originates from fossils. One of the reasons why countries cannot give up fossil fuel-based energy production is that renewable energy sources cannot provide uninterrupted power. To prevent this situation, energy storage technologies are used. Energy can be stored in different forms to be converted into electrical energy and used when necessary [1]. Methods used and developed for energy storage are called energy storage technologies. One of the most popular energy storage technologies in recent times is lithium-ion batteries. The working principle of batteries is based on the charge/discharge mechanism. Electrochemical reactions during charging/discharging only occur within a certain temperature range, so it is very important for batteries to operate within a certain temperature range. Studies [2, 3] have shown that lithium-ion batteries should operate between 293.15 K- 328.15 K. In addition, a high-temperature difference between the batteries in a battery system negatively affects the performance of the battery, so the temperature difference between the batteries should not exceed 5 K. While low temperature significantly reduces battery capacity and power, high temperature causes degradation, reducing battery life and thermal runaway may occur [4, 5]. Therefore, thermal analysis for lithium-ion batteries should be analyzed in depth.

II. System Description

The purpose of this study is to investigate the effects of different discharge rates on temperature and heat generation revealed in the battery package because of electrochemical reaction and charge transfer. In line with this purpose, a battery pack consisting of 25 lithium-ion batteries having a power of 323.75 Wh and a capacity of 17.5 Ah was modeled by exposure to ambient air for different discharge rates (0.5 C, 1.0 C, 1.5 C, and 2.0 C). In order to perform thermal analysis, time-dependent solutions were performed using Comsol Multiphysics software. Figure 1 shows the 3-D geometry of the battery package. Furthermore, the numerical analyses were carried out at 296.15 K under 1 atm air pressure using model parameters given in Table 1.

Table 1. Model Parameters

Parameter	Value
Size	18650
Shape	Cylindrical
Capacity	3.5 Ah (12 Wh)
Nominal Voltage	3.6 V
Charge Voltage	4.2 V
Discharge Voltage	2.5 V
Operating Temperature Range	233.15 K-333.15 K
Thermal conductivity,in plane	30 W/mK
Thermal conductivity,through plane	1 W/mK

Figure 1. The 3-D geometry of the Battery Package

III. Mathematical Modeling

The designed battery package contains 25 batteries, 5 in series and 5 in parallel, connected to each other with connectors. In order to calculate the voltage and the temperature distribution, Comsol Multiphysics software was used. The governing equations used in the battery pack during discharge are as follows:

$$E_{cell} = E_{OCV}\ (SOC,T)\ \eta_{IR} + \eta_{act}$$

$$\eta_{IR} = \eta_{IR,1C}\ \frac{I_{cell}}{I_{1C}}$$

$$\eta_{act} = \frac{2RT}{F}\text{asinh}\frac{I_{cell}}{2J_0\ I_{1C}}$$

where E is potential, OCV is open circuit voltage, SOC is state of charge, η_{IR} is ohmic overpotential, η_{act} is activation overpotential, F is Faraday constant, J_0 is current density.

Energy Conservation Equation:

$$\rho_b\ C_b\ \frac{\partial T_b}{\partial_t} = \nabla\ .(k_b\ \nabla T_b) + \dot{Q_g}$$

Here ρ is density, C_b is battery-specific heat capacity, T is temperature, k is thermal conductivity, $\dot{Q}g$ is heat generation. Each of the cells inside the battery package was considered as homogenous structure includes internal heat source. With this context, the heat generation was calculated for each battery by using following expressions:

$$\dot{Q_g} = \dot{Q_r} + \dot{Q_j}$$

$$\dot{Q_r} = -T_b\ \Delta S\ \frac{I}{nF}$$

$$Q_j = I\ (E-V) = I^2\ R_e$$

where $\dot{Q_r}$ is reaction heat, $\dot{Q_j}$ is joule heat, I is current, R is heat resistance and S is entropy value.

IV. Results and Discussion

The battery pack in 5S5P configuration was solved numerically at different discharge rates of 0.5 C, 1.0 C, 1.5 C, and 2.0 C, separately. Figures 2-4 are based on the hottest cell in the battery package. Figure 2 shows the variations of potential with time at different discharge rates. As can be seen in this figure, as the discharge rate increases, the discharge time decreases. The slowest discharge occurs at 0.5 C, while the fastest discharge occurs at 2 C. The variations of heat generation with time at different discharge rates are presented in Figure 3. Cells generate heat as a result of electrochemical reactions during discharge, heating both themselves and the cells around them. While most heat generation occurs at a discharge rate of 2.0 C due to the increase in electrochemical activity and kinetic energy of ions with increasing discharge rate, the least heat production occurs at a discharge rate of 0.5 C. Figure 4 depicts the variations of temperature with time at different discharge rates. In this figure, the increase in discharge rate causes an increase in temperature because of increasing heat generation in the battery package. It is observed that there is a temperature difference of 7.7 K at 0.5 C discharge rate, 15.2 K at 1.0 C discharge rate, 18.8 K at 1.5 C discharge rate, and 29.8 K when 2.0 C discharge rate is applied, respectively.

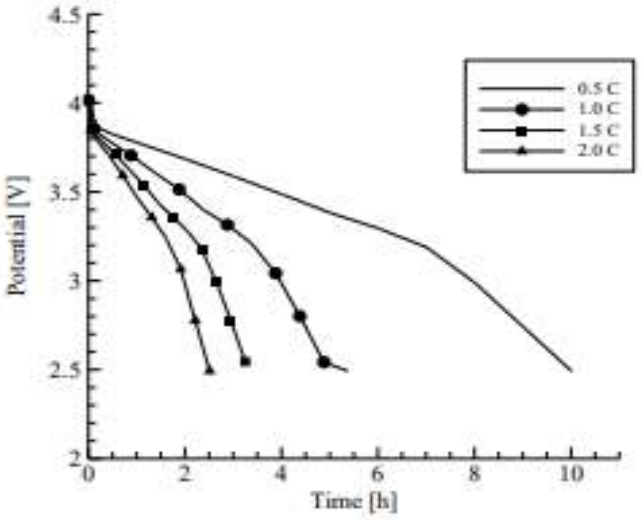

Figure 2. The variations of potential with time at different discharge rates

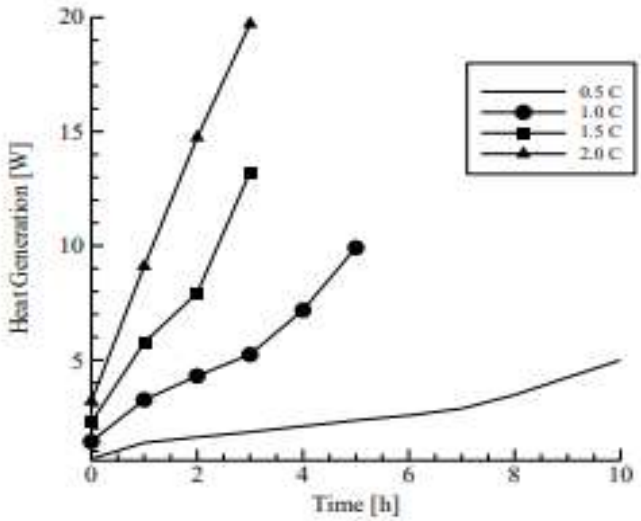

Figure 3. The variations of heat generation with time at different discharge rates

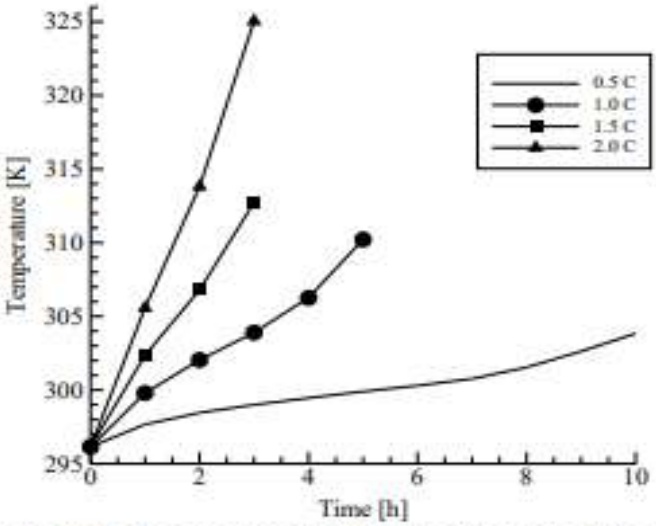

Figure 4. The variations of temperature with time at different discharge rates

Figure 5 and Figure 6 present the temperature distributions along in-plane and through-plane in the battery package at different discharge rates, respectively. It can be seen that the distribution of heat generation within the battery package decreases from the center of the battery to the outside for all discharge rates.

V. Conclusion

In this study, the effects of different discharge rates on temperature and heat generation revealed in the battery package are numerically examined in detail. The obtained numerical results are as follows: While the battery package was discharged at 0.5 C, it was discharged in approximately 11 hours. On the other hand, when it was discharged at 2.0 C, it was discharged in 3 hours. The heat generation within the battery package increases with increasing discharge rates and discharge time. While the temperature difference in the battery package is 7.7 K at 0.5 C discharge rate, it is 29.8 K at 2.0 C discharge rate. Moreover, for all discharge rates, the heat generation distribution within the battery package decreases from the center to the exterior. Consequently, 1.0 C discharge rate is the most suitable discharge rate for this battery package, considering the temperature and time balance.

Acknowledgement

This study was supported by Tübitak, 2210-D Master's Program for National Industry. Project/Application Number:1649B022113465

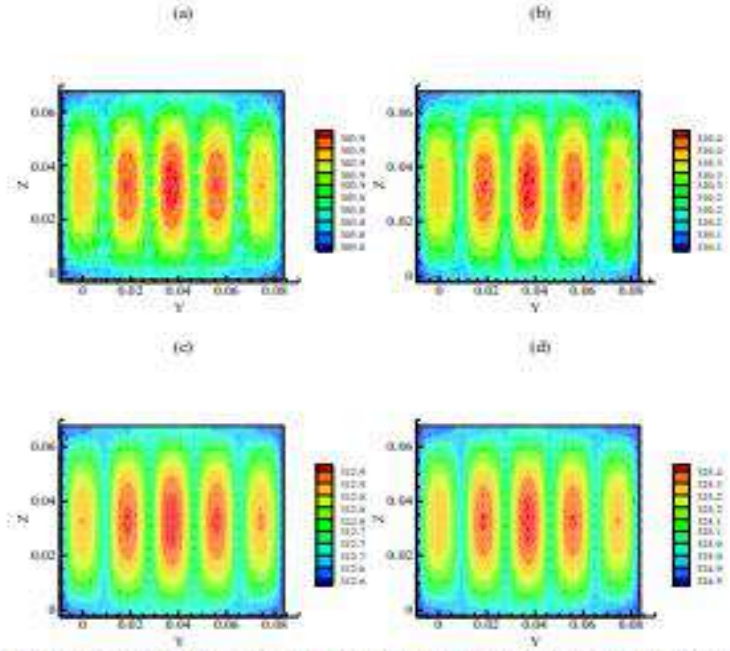

Figure 5. Temperature distributions at in-plane in the battery pack for different discharge rates a) 0.5 C b) 1.0 C c) 1.5 C d) 2.0 C.

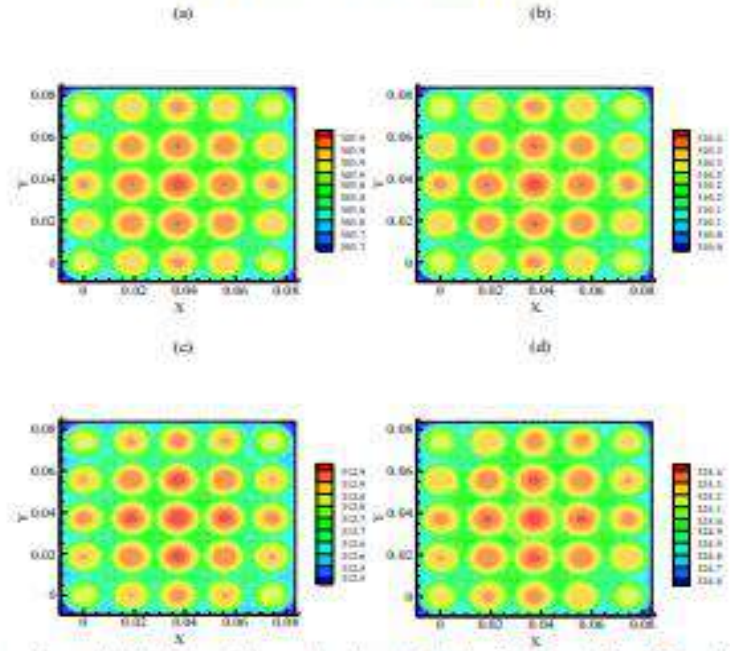

Figure 6. Temperature distributions at through-plane in the battery pack for different discharge rates a) 0.5 C b) 1.0 C c) 1.5 C d) 2.0 C.

References

[1] Kocaman, B.,*The Technologies of Energy Storage on Smart Grids and Microgrids.*

[2] Zhao, Y., et al., *Active cooling based battery thermal management using composite phase change materials.* Energy Procedia, 2019. 158: p. 4933-4940.

[3] Kizilel, R., et al., *An alternative cooling system to enhance the safety of Li-ion battery packs.* Journal of Power Sources, 2009. 194(2): p. 1105-1112.

[4] Shabani, B. and M. Biju, *Theoretical modelling methods for thermal management of batteries.* Energies, 2015. 8(9): p. 10153-10177.

[5] Smart, M., et al., *Effect of electrolyte type upon the high-temperature resilience of lithium-ion cells.* Journal of the Electrochemical Society, 2005. 152(6): p. A1096.

IEEES-126

Design and Analyses of Double Flash Geothermal Power Plant Combined ith Reheat-Transcritical CO2 Rankine Cycle for Power, Hydrogen, Hot Water, and Freshwater Generation

[1*]Fatih Yılmaz, [1]Murat Ozturk, [2]Resat Selbas
[1] Isparta University of Applied Sciences, Faculty of Technology, Department of Mechatronics Engineering, 32200, Isparta/Turkiye
[2] Isparta University of Applied Sciences, Faculty of Technology, Department of Mechatronics Engineering, 32200, Isparta/Turkiye
*E-mail: fatihyilmaz@isparta.edu.tr

Abstract
Renewable energy technologies are critical models for the clean and sustainable future transition to net-zero emission. In this developed study, a combined multigeneration plant-driven geothermal energy for power, hydrogen, hot water, and freshwater is proposed and analyzed. This plant comprises a double-flash geothermal cycle with two turbines, a re-heat transcritical Rankine cycle, a PEM electrolysis, and a multi-effect desalination unit. To determine the system efficiency, a comprehensive parametric analysis is carried out by energy and exergy efficiency methods. Furthermore, a sustainability index assessment and exergy destruction evaluation are conducted. Based on the thermodynamic analysis, the combined plant can generate 1686 kW net power. The energy and exergy efficiency of the overall plant are determined as 13.76% and 18.18%, respectively.
Keywords: Energy, exergy, geothermal, combined plant, fresh water, hydrogen

I. Introduction

Increment in energy consumption especially fossil-based fuels by day by gives rise to environmental challenges, for example, global warming, acid rain, ozone depletion, etc. (Yilmaz 2022). One of the main solutions is the renewable energy sources to change this situation. Among renewable energy sources, geothermal energy has great potential and, unlike solar and wind sources, is almost least affected by environmental conditions. Geothermal energy, which has great potential to produce heat, electricity, and cooling, is already used around the world and can be integrated with other renewable energy sources and contribute to reducing CO2 in the atmosphere (Bozgeyik et al. 2022). Another important point is that to use this energy source more effectively, it is important to integrate it with different thermal systems in terms of efficiency. There are many studies on this subject in the literature.
Liu et al. (2023) developed a comprehensive analysis of a multigeneration system driven by geothermal sources and oxyfuel combustion. The energy and exergy efficiency of their paper are 47.2% and 40.34%, respectively. Furthermore, Yuksel et al. (2023) examined a new design multigeneration plant that generates beneficial products. The system is driven by a geothermal source and integrated with different thermal systems. Energetic and energetic performance ratio values are determined as 46.87% and 44.13%, respectively. In continuation, Hai et al. (2023) examined an exergo economic and exergo environmental evaluation of the geothermal sourced multigeneration plant. They calculated that the thermal and energetic performance values of the developed model are 24.4% and 32.1%, respectively. Again, Siddiqui and Ishaq (2023) developed an original geothermal energy-based combined plant for the production of power and other outputs. Their developed plant has a 23.5% energetic performance ratio.
In general, it should be noted that integrated power plants based on geothermal energy have gained much more importance in recent years. This study deals with the thermodynamic analysis of a geothermal-motivated integrated plant consisting of a double flash geothermal cycle, a reheat transcritical CO2 Rankine cycle (tRC), a PEM electrolyzer, and a multi-effect desalination (MED) unit. For this reason, comprehensive energy and exergy analyses are conducted to determine the system's performance

II. System design and analysis

This designed work consists of a double flash geothermal cycle, a reheat tRC , a PEM electrolysis, and a MED unit for the production of clean and sustainable power, hydrogen, hot, and clean water, as shown in Fig. 1. The geothermal source temperature enters the system at 180 ℃ and finally returns to the underground at approximately 60 ℃. The subsystems are thermally integrated and work simultaneously.

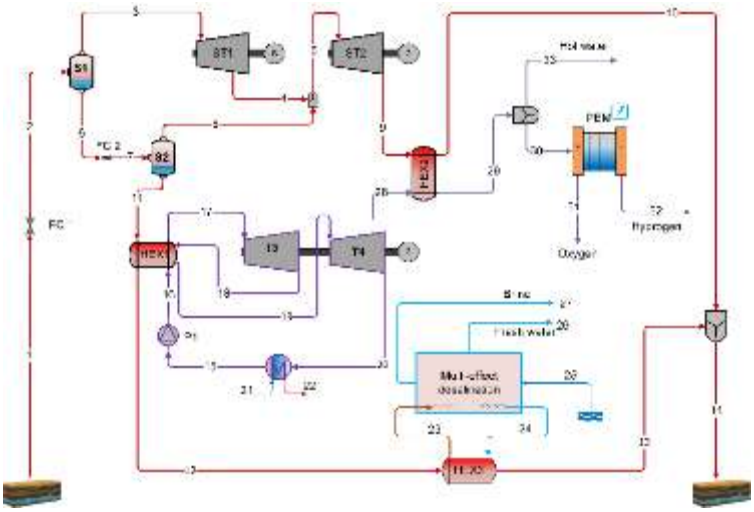

Fig.1. The schematic layout of the developed geothermal-based combined plant

Assumptions considered in system modeling; the system kinetic and potential energy changes are neglected, pressure and temperature changes are not taken into account, and it is modeled as a steady state flow. When analyzing this system, the four general equilibrium equations of thermodynamics can be formulated as follows (Dincer 2020);

$$\dot{m}_{in} = \dot{m}_{out} \quad (1)$$

$$\dot{Q}_{in} + \dot{W}_{in} + \sum \dot{m}_{in} h_{in} = \dot{Q}_{out} + \dot{W}_{out} + \sum \dot{m}_{out} h_{out} \quad (2)$$

$$\sum \left(\frac{\dot{Q}}{T}\right)_{in} + \sum \dot{m}_{in} s_{in} + \dot{S}_{gen} = \sum \left(\frac{\dot{Q}}{T}\right)_{out} + \sum \dot{m}_{out} s_{out} \quad (3)$$

$$\dot{E}x^{\dot{Q}_{in}} + \dot{E}x^{\dot{W}_{in}} + \sum \dot{m}_{in} ex_{in} = \dot{E}x^{\dot{Q}_{out}} + \dot{E}x^{\dot{W}_{out}} + \sum \dot{m}_{out} ex_{out} + \dot{E}x_{des} \quad (4)$$

The overall system performance ratio can be developed as;

$$\eta_{sys} = \frac{\dot{W}_{net} + (\dot{m}_{H_2} LHV_{H_2}) + (\dot{Q}_{hotwater}) + (\dot{m}_{fw} h_{fw})}{\dot{Q}_{in,geothermal}} \quad (5)$$

$$\psi_{sys} = \frac{\dot{W}_{net} + (\dot{m}_{H_2} ex_{H_2}) + (\dot{E}x_{Q,hotwater}) + (\dot{m}_{fw} ex_{fw})}{\dot{E}x_{Q,in,geothermal}} \quad (6)$$

III. Results and discussion

This paper investigates the thermodynamic performance analysis of the geothermal-based combined plan. To conduct the thermodynamic simulation, the assumptions and the system's design indicators are presented in Table. Based on the Table 1 values, detailed energy and exergy analyses are fulfilled and case study results are tabulated in Table 2. Herein, the net power generation capacity of the developed plant is 1686 kW.

Table 1. The analysis and assumptions parameters of the geothermally driven combined plant

ıeters		
Geothermal unit		
T[1]	℃	180
P[1]	kPa	1003
$\dot{m}_{geo}$	kg/s	200
T[14]	℃	50.65
Re-heat t-RC		
T[15]	℃	24.44
P[15]	kPa	6500
P[17]	kPa	19500
P[19]	kPa	9750
$\dot{m}_{CO2}$	kg/s	82.83
PEM inlet temperature	℃	76.5
PEM inlet pressure	kPa	101.3
Reference temperature	℃	25
Reference pressure	kPa	101.3

Table. 2 Simulation results of the developed combined plant

Systems and products	η (%)	ψ (%)
Single generation	3.06	13.44
tRC	14.67	77.33
MED	51.52	30.16

Overall system	13.76	18.18	water	, kg/s
System products			ɔgen	921 kg/s
Net power rate	1686, kW			
Hot water	2721, kW			

Figs. 2, and 3 examine the effects of the change in geothermal source temperature on the system and subsystems, respectively. Fig. 2 depicts the increase in energy and exergy efficiency of the SG and the entire system. Fig. 3 shows the increase in net power production from the system.

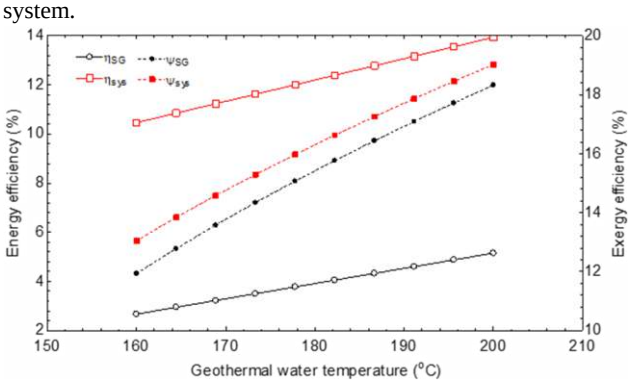

Fig. 2. Effect of the geothermal water temperature on the SG and overall system performance

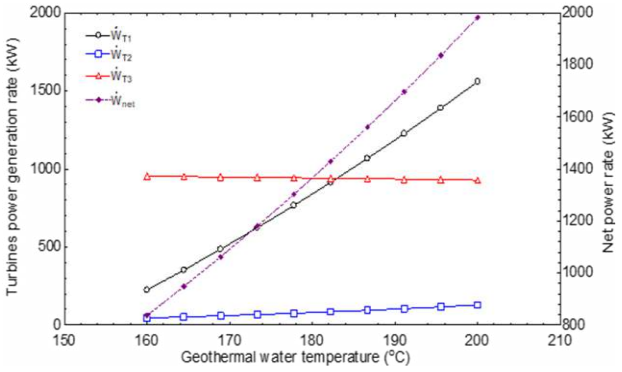

Fig. 3 The relationship between the geothermal source temperature and power production rates

Finally, Fig. 4 depicts the increase in hot water and freshwater production with increasing geothermal source temperature. As a result, the increase in geothermal source temperature has a positive effect on the system. To continue, the generated hydrogen rate and SI value are increased geothermal source temperature rises, as shown in Fig.5. Raising the geothermal source temperature has a positive effect on the system performance and also the system's efficiency.

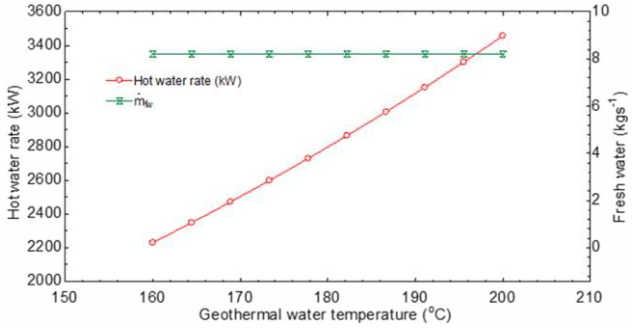

Fig. 4 The relationship between the geothermal source temperature and hot and fresh water rate

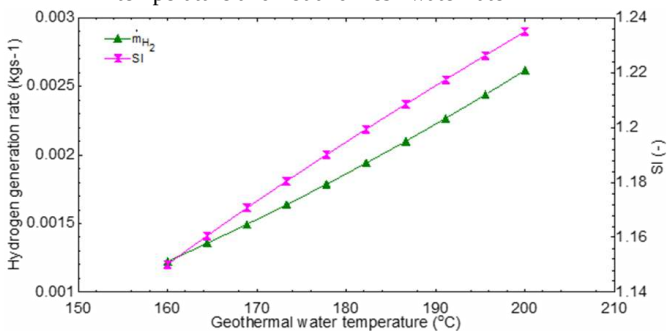

Fig. 5 The relationship between the geothermal source temperature and hydrogen rate and SI value

While Figure 6 shows the negative effect of the increase in geothermal mass flow rate on the system performance, Figure 7 shows the increase in the amount of hydrogen to be obtained from the system with the increasing mass flow rate. Here, it is seen that the mass flow rate and the amount of energy entering the system are higher, thus negatively affecting the system's efficiency.

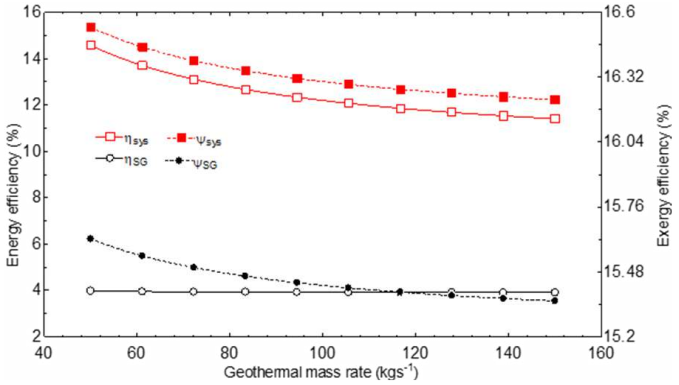

Fig. 6. The impact of the geothermal water mass rate on the SG and overall system performance rates

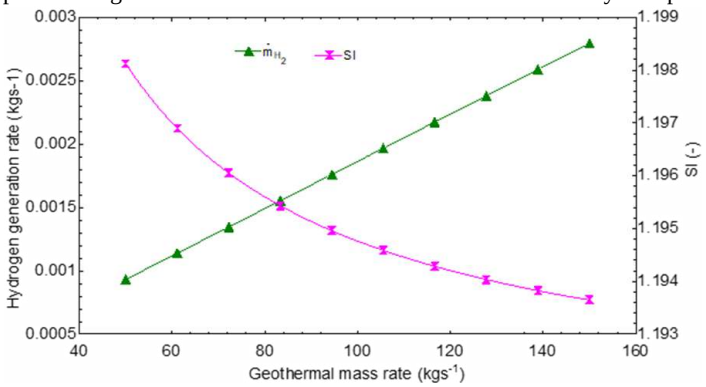

Fig. 7. The impact of the geothermal water mass rate on the hydrogen generation rate and SI value

In conclusion, Figures 8 and 9 examine the pressure ratio of Flash-chamber 1. The increase in pressure ratio, from 1 to 4, increases the efficiency up to approximately 1.8 and then decreases it (Figure 8). The amount of hydrogen produced and the change in SI value similarly increase at first and then decrease (Figure 9).

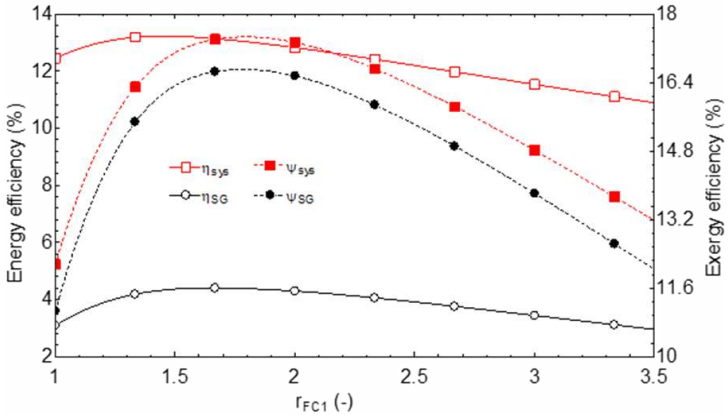

Fig. 8. Effect of the FC1 expansion ratio on the SG and overall system performance.

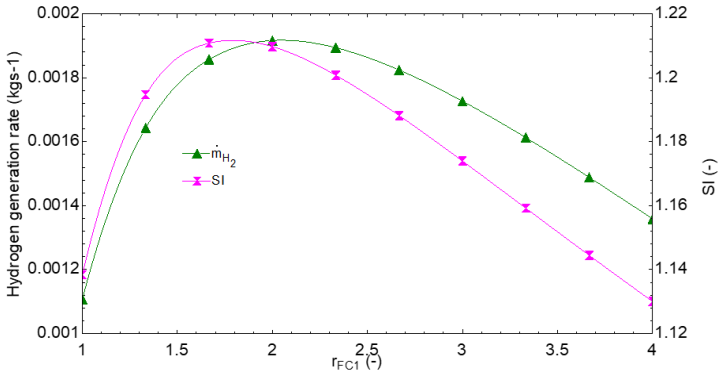

Fig. 9. Effect of the FC1 expansion ratio on the hydrogen rate and sustainable index value.

IV. Conclusion

The newly developed geothermal energy-based combined plant for the production of clean power, hot water, freshwater, and hydrogen is proposed and evaluated. In this regard, detailed thermodynamic analysis is employed through the energetic and energetic analyses approaches. The following important results can be achieved;

- The proposed system can generate 1686 kW of power, 2721 kW of hot water, 22.28 kg/s of fresh water, and finally 0.003921 kg/s of clean hydrogen.
- The energy and exergy efficiency of the SG system is 3.06% and 13.44%, respectively. These values increased by approximately 346% and approximately 35.26%, resulting in 13.76% energy efficiency and 18.18% exergy efficiency for the entire system.
- An increment in the geothermal water temperature has a positive effect on the system's performance. However, a rise in the mass flow rate of the geothermal source has a negative effect on the system's efficiency.

References

Bozgeyik, A., Altay, L., & Hepbasli, A. (2022). A sub-system design comparison of renewable energy based multi-generation systems: A key review along with illustrative energetic and exergetic analyses of a geothermal energy based system. *Sustainable Cities and Society*, *82*, 103893.

Dincer, İ. (2020). Thermodynamics: a smart approach. John Wiley & Sons.

Hai, T., Radman, S., Abed, A. M., Shawabkeh, A., Abbas, S. Z., Deifalla, A., & Ghaebi, H. (2023). Exergo-economic and exergo-environmental evaluations and multi-objective optimization of a novel multi-generation plant powered by geothermal energy. Process Safety and Environmental Protection, 172, 57-68.

Liu, X., Zhao, H., Huang, Z., Shi, S., Guo, R., Ding, P., & Xie, S. (2023). A comprehensive study of a novel multigeneration system using a combined power plant based on geothermal energy and oxyfuel combustion. Journal of Cleaner Production, 408, 137098.

Siddiqui, O., & Ishaq, H. (2023). A geothermal energy driven integrated energy system for fresh water and power production. International Journal of Hydrogen Energy.

Yilmaz, F. (2022). Development and modeling of the geothermal energy based multigeneration plant for beneficial outputs: Thermo-economic and environmental analysis approach. Renewable Energy, 189, 1074-1085.

Yuksel, Y. E., Ozturk, M., & Dincer, I. (2023). Development and analysis of geothermal energy-based low-grade heat utilization in an integrated form for multigeneration with hydrogen. Sustainable Energy Technologies and Assessments, 57, 103176.

IEEES-127

Experimental and Numerical Analysis on Prismatic LFP Battery Surface Temperature Distribution

[1,2*]Oya Bakar, [2]Murat Uysal, [1,3]Barış Yılmaz
[1] Marmara University, Faculty of Engineering, Mechanical Engineering Dept., Maltepe, Istanbul, 34854, Turkiye
[2] Teksan A.Ş, Sancaktepe, Istanbul, 34791, Turkiye
[3] Lakehead University, Faculty of Engineering, Mechanical Engineering Dept., Thunder Bay, ON, P7B 5E1, CA

* E-mails: oyabakar@teksan.com

Abstract

Lithium iron phosphate (LFP) batteries have gained widespread popularity as a promising energy storage for their high energy density. However, the elevated energy density presents a challenge in terms of heat generation increase within the battery, necessitating an effective temperature management system. The skepticism regarding battery heat generation value arises from the absence of battery temperature tests conducted by battery suppliers. 280 Ah LFP batteries are new and current technology and have started to become prevalent battery types in the energy storage system sector, yet there is a notable scarcity of comprehensive studies on this specific battery type. Understanding the battery's temperature response during operation is crucial for determining the most appropriate method for a battery temperature management system and applying adequate cooling to the appropriate surface of the batteries. Without recognizing the battery's thermal features will mislead the thermal management studies, and risk the battery's life and performance. Therefore, both numerical and experimental studies were accomplished for a single battery in this work. The battery modeling tool in ANSYS-Fluent software was utilized after obtaining the characteristic voltage graph of the battery at different state-of-charge (SOC) levels. Temperature distributions on the battery surface and the heat generation results were obtained with the MSMD method. Afterward, using the heat generation value found by the MSMD method as input to the CHT coupling method has also been used to compare temperature distributions predicted by the two methods. Furthermore, the experimental study was conducted for the modeled package and results are compared to the numerical predictions. Good agreement has been observed between the numerical and experimental results in which the minimum and maximum differences are obtained to be 0.06% and 2.07%, respectively.

Keywords: Energy storage system, prismatic LFP battery, heat generation

I. Introduction

LFP batteries are the most preferred lithium-ion battery type. Besides being safer compared to other lithium-ion battery types, they have longer cycle life, higher power density, wider operating temperature range and lower self-discharge rate. These features make LFP batteries more environmentally friendly and suitable for applications in renewable energy storage systems (Fan and Zhang,2019). Prismatic LFP batteries are commonly used in energy storage systems due to simple installation, easy maintenance, high energy density, and good heat dissipation characteristics thanks to their flat design.

Controlling the temperature of the battery is crucial for sustaining the battery's performance, lifecycle, and state of health. Keeping the battery's temperature in its optimal range, between 15 and 35 degrees, is necessary (Mei and Xu, 2020). Elevated temperatures accelerate aging, contribute to capacity fade, lead to higher self-discharge rate, and pose thermal runaway while low temperatures increase the internal resistance, and lead to capacity loss and dendrite formation. Therefore, the thermal management system is vital for batteries. To design a correct and an efficient thermal management system, it is required to ensure the heat generation value. Battery manufacturers are usually lack of experiments regarding the battery thermal performance and heat generation value in their catalogs. They commonly use the Bernardi equation to calculate the heat generation value. However, Bernardi's expression is not sufficient enough to calculate heat generation rate. Therefore, ANSYS-Fluent battery modeling tool has been used in this study to obtain reliable heat generation value by using the MSMD and CHT coupling solution approaches and then numerical results have been validated with experimental measurements. Temperature distribution contours were obtained by considering anisotropic thermal conductivity of battery active material in which the different thermal conductivity values were defined in different coordinate directions (Zhang and Feng, 2022).

II. Experimental Methodology

In experimental studies, a single battery was fully charged first with a power supply. Afterward, temperature measurement was conducted at points located on the front, left, top, and bottom sides of battery unit. Thermocouples were placed at 25 points on the front side, 15 thermocouples were used on the left side, and 6 thermocouples were used for both top and bottom surfaces as can be seen on Figure 1. The utilized experimental devices, data loggers and the photo of the experimental setup can be seen on Figure 2.

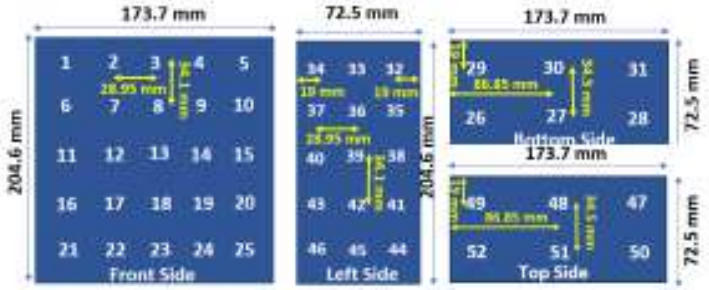

Fig. 1. Temperature Measurement Points

Fig. 2. Experimental Setup

A power supply device, a load bank, HIOKI LR8402-20, and HIOKI CT9692 sensor were used in the experiments. HIOKI LR8402-20 was used to record the temperature, ampere, and voltage data. The load bank enabled a battery to discharge at a 0.5C discharge rate. HIOKI CT9692 sensor measured the current value by connecting it to the load bank's cable.

In the experimental analysis, the Hybrid Pulse Power Characterization (HPPC) test was initially completed to obtain the voltage–time graph of the battery. Six voltage-time graphs were obtained for six different state of charge (SOC) levels by means of the HPPC test. Voltage graphs were obtained for 95%, 85%, 75%, 65%, 55%, and 45% SOC values. Beginning from the 95% capacity level, the battery was discharged up to 85% level, and then, the battery was left at that state until reaching the relaxation point which means reaching a constant level. Afterward, the battery was discharged to the next SOC level and then, the battery was left at that state again until it reached a constant voltage level. These voltage-time data were arranged in a file and then used as an input to the Fluent battery modeling tool. A power supply is utilized for charging the battery to the desired capacity before starting the experiment. Then, the temperature measurements were carried out at 23 C° ambient temperature. The battery was kept in the room for a while to make sure that thermal equilibrium between the battery and the room air was established. At a constant 0.5C discharge rate meaning 140 A, the battery was discharged to its minimum voltage level of 2.5 V for 2 hours, and temperature, ampere, and voltage data were recorded.

$$q = I\,(V_{OC} - V) - I\,(T\frac{dV_{OC}}{dT}) = I^2(R_O + R_P) - I\,(T\frac{dV_{OC}}{dT}) \qquad (1)$$

where I is current, V_{OC} is open circuit voltage, R_O is the ohmic resistance, and R_P is the polarization resistance. The I (V_{OC} -V) term in the Eq. 1 represents the irreversible heat generation, and the I ($T\frac{dV_{OC}}{dT}$) is the reversible heat generation (Jindal and Katiyar, 2022). This formulation is known as the Bernardi equation. Battery manufacturer calculates their battery's heat generation value by using this expression. However, that formulation is not sufficient and deviates significantly from the numerical CFD results (Wu, and Qiu, 2023).

After finishing the HPPC tests, results were implemented in the battery modeling tool of ANSYS-Fluent. Two different battery modeling methods have been utilized in this work, namely; MSMD and CHT methods. Firstly, heat generation was calculated using the MSMD method. Secondly, the heat generation value found by the MSMD solution method in the first step was used as an input to the CHT coupling method to compare the temperature distribution predictions of the two methods. Thirdly, the CHT coupling method was used for two different heat generation data: 4.9 W and 11.76 W. 4.9 W were calculated considering ohmic resistance. 11.76 W was calculated considering the sum of the ohmic resistance and polarization resistance at 140 A. The max. ohmic resistance of the battery is 0.25 mohm. Polarization resistance during discharge is 0.35 mohm. Total resistance is 0.6 mohm. The purpose of the third step was to compute and compare the temperature distribution results using the battery manufacturer's heat generation data and their calculation method.

III. Numerical Analysis

In the Fluent battery modeling tool, the MSMD solution method and ECM e-chemistry model have been utilized (Trinuruk and Onnuam, 2023). Measured nominal battery capacity and C discharge rate were implemented into the battery modeling tool. Active components, busbars, and tabs as passive components and external connectors were selected. The initial state of charge representing the current capacity at the beginning of the experiment was specified. Reference capacity indicating the ampere value by which the experiment was performed was entered into the tool. Levenberg-Marquardt (LM) algorithm and the 6-parameters method were used to estimate the parameters of the equivalent circuit model. Transient analysis was chosen. Material properties, that can be seen in Table 1, were defined for the battery as active material, busbar, and tab. The surrounding heat transfer coefficient was assumed to be 5 W/m^2.K. SIMPLE pressure-velocity coupling scheme and second-order upwind discretization scheme were set up. The environment temperature was 23 degrees used for standard initialization.

Table 1. Material Properties

Text	Active Material	Busbar	Tab	
Density (kg/m^3)	2154	8978	2700	
Specific Heat (J/kg.K)	1000	381	871	
Thermal Conductivity (W/m.K)	2 (X),11(Y),11(Z)	387.6	234	
Electrical Conductivity (S/m)	Uds-0 1.19e+06 Uds-1 9.83e+05	5.8e+07	3.541e+07	

IV. Results and discussion

The experimentally obtained HPPC test results versus time can be seen in Figure 3. This graph includes 6 SOC levels. The beginning voltage level is 3.33 V. Battery was discharged to 3.13 V.

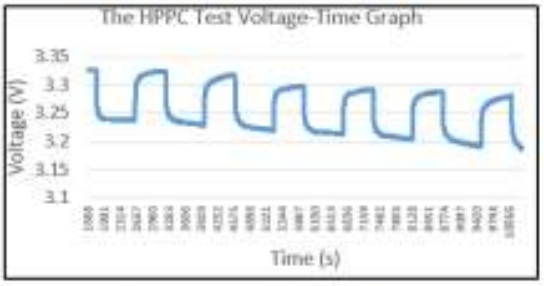

Fig. 3. The HPPC Test Voltage Graph

The heat generation value of the LFP 280 Ah battery was obtained numerically using the Fluent battery modeling tool. The comparison of the measured and the predicted voltage graphs can be seen in Figure 4. It was clearly observed that the LM method predicted voltage change in time better than the JH method since the LM method showed better agreement with experimental data.

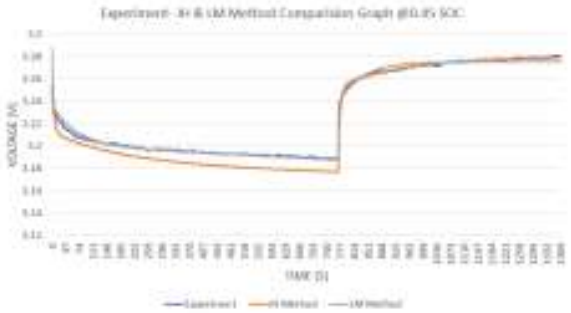

Fig. 4. Battery Modeling Voltage Curve Comparison

After running the simulation, the temperature contour of the MSMD method was obtained. In Fig. 5. temperature contours predicted by the MSMD solution method, 4.9 W CHT Coupling solution method, 11.76 W CHT Coupling method and 5.1 W CHT Coupling method can be seen respectively.

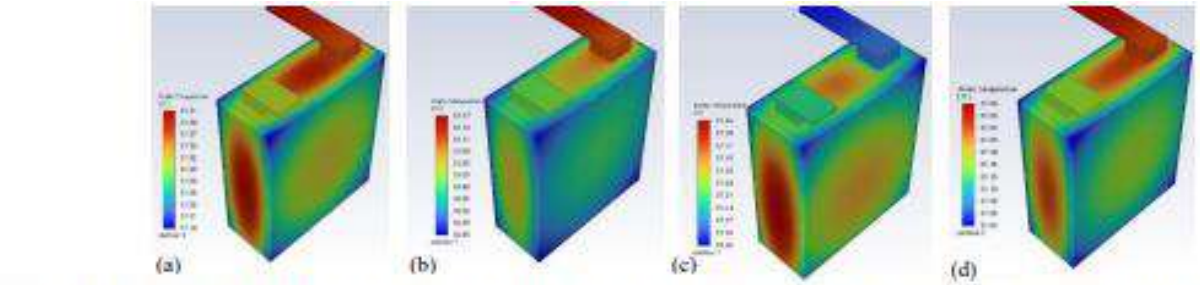

Fig. 5. (a)MSMD Method Temperature, (b)4.9 W CHT Coupling, (c) 11.76 W CHT Coupling, (d) 5.1 W CHT Coupling Contours

The locations of the measurement points were defined on the battery surfaces to monitor and compare the computed temperature results. Experiments were repeated 3 times and the average result was used for comparison. The comparison of the temperature measurements and the computations done using the MSMD method can be seen in Figure 6a. In Figure 6b, the comparison of the predictions by both numerical methods can be seen. It is seen that the temperature results are in good agreement with experiments where the maximum deviation is found to be about 2%. MSMD and CHT methods computed almost similar results since the difference is less than 1% between the predictions of two methods.

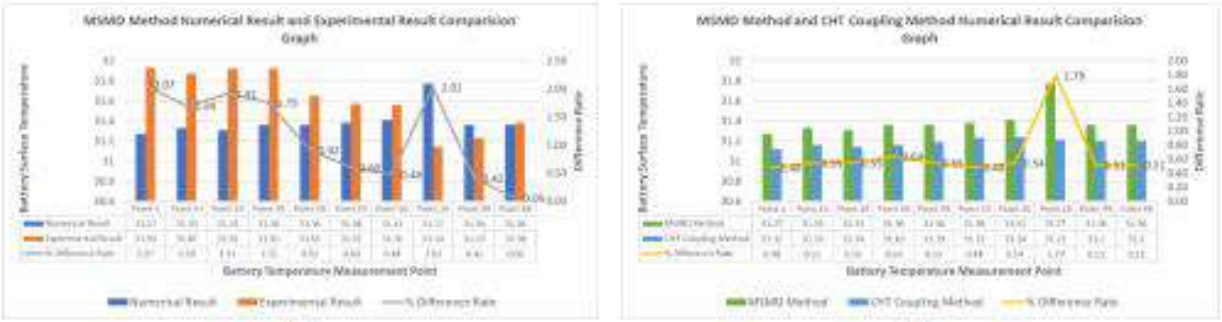

Fig.6.(a) MSMD Method Numerical Result and Experiment Result Comparison Graph & (b) MSMD Method and CHT Coupling Method Comparison Graph

V. Conclusion

In this study, a 280 Ah LFP battery has been examined experimentally and numerically. Studies are done for a single batter unit. Initially, experiments were conducted to obtain the voltage discharge characteristics of the battery. Then the obtained results were implemented to the battery modeling tool of Fluent to examine the temperature distribution on the battery. Two different battery models have been utilized, namely; MSMD and CHT coupling methods. The comparison of the experimental and numerical results showed a good agreement and the maximum difference was found about 2%. Therefore, it is concluded that battery modeling can be a promising tool to understand and reveal the temperature variations on the battery surface for large-scale applications.

Acknowledgements

I would like to thank the Teksan Generator for allowing me to use its laboratory facilities and giving support. I would like to thank Furkan Dilbaz and Recep Uysal for their technical guidance.

References

Wu, C., Wu, L., Qiu, C., Yang, J., Yuan, X., Cai, Y., Shi, H., (2023) Experimental and numerical studies on lithium-ion battery heat generation behaviors. Energy Reports, 5064-5074. https://doi.org/10.1016/j.egyr.2023.04.021

Jindal, P., Katiyar, R., Bhattacharya, J., (2022) Evaluation of accuracy for Bernardi equation in estimating heat generation rate for continuous and pulse-discharge protocols in LFP and NMC based li-ion batteries. Applied Thermal Engineering, 117794. https://doi.org/10.1016/j.applthermaleng.2021.117794

Trinuruk, P., Onnuam, W., Senanuch, N., Sawatdeejui, C., (2023) Experimental and numerical studies on the effect of lithium-ion batteries's shape and chemistry on heat generation. Energies, 264. https://doi.org/10.3390/en16010264

Mei, N., Xu, X., Li, R., (2020). Heat dissipation analysis on the liquid cooling system coupled with a flat heat pipe of a lithium-ion battery. ACS Omega 2020, 17431-17441. https://doi.org/10.1021/acsomega.0c01858

Zhang, F., Feng, X., Xu, C., Jiang, F., Ouyang, M., (2022). Thermal runaway front in failure propagation of long shape lithium-ion battery. International Journal Heat and Mass Transfer, 121928.

https://doi.org/10.1016/j.ijheatmasstransfer.2021.121928

Fan, R, Zhang, C., Wang, Y, Ji, C., Meng, Z., Xu, L., Ou, Y., Chin, C., S., (2019). Numerical study on the effects of battery cold climate. Journal of Energy Storage, 1200969. https://doi.org/10.1016/j.est.2019.100969

IEEES-128

Green synthesis of ZnO Nanoparticles for effective photocatalytic degradation of Malachite Green under UV light and Sun-light : a comparative study

Mohamed AIT OUMERACI[1], Tarek BERRAMA[1], Hayet TIZI[1], Feriel SAHOUI[1],
[1]*Laboratory of Industrial Process engineering sciences, University of Sciences and Technology Houari Boumediene, BP 32, El-Alia, 16111, Bab-Ezzouar, Algiers, Algeria.*

* E-mails: m.aitoumeraci@gmail.com

The aim of this study is the synthesize of Zinc oxide nanoparticles (ZnO-NPs) from the aqueouse extract of Rosmarinus Officinalis. For achieving this aim, aqueous extract and Zinc sulfate, used as a precursor, are mixed in batch reactor. To chatacterize the (ZnO-NPs), spectroscopy (UV-VIS) and X-ray diffraction are used. The results of X-ray diffractometry (XRD) analysis showed that hexagonal structure. Due of their high power of excitement at ambient temperature level, UV-Vis ranges presented normal absorption comes to a head around 375 nm. The photocatalytic study demonstrated the capability of ZnO-NPs to degrade a dye contaminant (MG) under UV light and Sun-light, the degradation yield for afetr one hour is relatively high, going beyond 99% and 90% respectivly.

Keywords: ZnO-Nanoparticles, Green Synthesis, UV light, Photocatalytic activity, degradation unser Sun light

I. Introduction

The contamination of water by organic pollutants, particularly textile dyes, remains a problem that is causing serious damage to the ecosystem in both the short and long term, mainly due to the industrialization of developing countries (Shekhar et al. 2008). To overcome this critical situation, various technologies have been developed, such as adsorption, biodegradation, advanced oxidation processes, etc. The photocatalytic method for degrading polluting materials is one of the techniques that has been gaining in importance in recent times (Varjani and Sudha, 2018) (Zhu and Wang, 2017); Different types of materials with a photocatalytic function, called photocatalysts, are produced. Oxides including metal have wide-band gap and excitation properties based on their size, shape, structure, and electron filling (Bjaalie et al., 2014) (Hao and Lang, 2019). The semiconductor, zinc oxide, has been studied for these properties and has found have 3.37 eV of energy band gap and 60 meV of binding energy of exciton which accounts as a potential photocatalyst (Vaiano et al., 2018). Nanotechnology is the most advanced technology for nanoscale manipulation in a wide range of scientific fields. Recent studies are focusing on how to improve and synthesize nanoscale photocatalysts. The green synthesis of nanoparticles with photocatalytic activity from plant extracts to degrade hazardous pollutants has been studied (Rupa et al. 2019). Thus, the aim of this study is to synthesize zinc oxide nanoparticles using a plant-derived reducing agent for the photocatalytic degradation of malachite green in aqueous solution.

II. Experimental Procedure

Rosmarinus officinalis leaves have been washed and dried. Extraction was carried out under heat, using water as the extraction solvent.

Fig.1 : ZnO-NPs synthesized by Green method

Biosynthesis was carried out in several stages. The extract is mixed with a zinc sulfate solution at a volume ratio of 1:1.The reaction was carried out under reflux. The reaction was carried out under stirring for 2 hours. After reaction, soda is added until a precipitate is formed, which is separated by centrifugation. The recovered precipitate is washed with an alcoholic solution, dried for 24 hours in an oven at 105°C and ground to a powder, which is then calcined (see fig.1). For photocatalysis, 0.2 g of ZnO-NP was introduced into 200 mL of 25 ppm malachite green solution, at room temperature with stirring and either under UV light or sunlight irradiation. The concentration of the dye was measured before and after treatment with a UV spectrophotometer. A duration of 30 minutes of adsorption in the absence of light is essential before photocatalysis. The reaction takes place in a photocatalysis reactor.

III. Results and discussion

III.1. XRD

XRD pattern of synthesized ZNPs is givern in Fig.2. It clearly indicates crystalline structure for the synthesized nanoparticles.

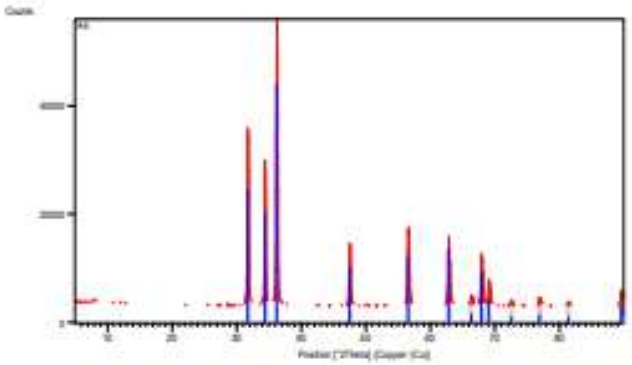

Fig. 2. XRD results for the synthesized ZnO-NPs

The sharp diffraction peaks were observed at 2θ values 31.5; 34.3; 36.5; 47.5; 56.5 ; 62.9 ;67.5; 68.0; 69.0 degrees. These peaks are indexed by (100), (002), (101), (102), (110), (103), (112) and (202) diffraction grating planes respectively, confirming the hexagonal structure of wurtzite for the synthesized nanoparticles. This pattern is consistent with the standard peaks displayed by the International Center for Diffraction Data [Shabnam et al. 2019)

III.2. UV–Visible spectroscopy

UV–Visible absorption spectrum of synthesized nanoparticles is shown in Figure 3. It is well known from absorption spectroscopy that the band gap increases with decreasing particle size. There is also an opposite dependency between the band gap and the absorption wavelength. There is also an opposite dependency between bandgap and absorption wavelength. The absorption of ZnO powder has been shown to occur around 375 nm.

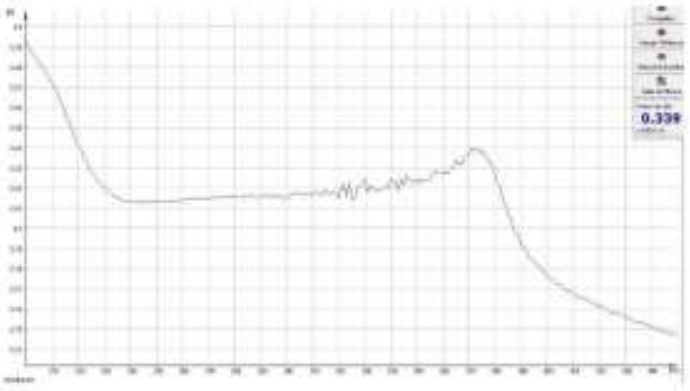

Figure 3. UV–Visible spectrum of the synthesized ZNOPs

III.4. Photocatalysis

In this reaction process, semiconducting metal oxide nanostructures (ZnO) are activated with direct sunlight, ultraviolet (UV), and in absence of any source of light, separately. The photogenerated charge carriers are excited from the valence band to the conduction band, creating electron/hole pairs. To study the photocatalysis of Zno-NPs,

MG solutions are prepared and the variation in MG concentration is monitored. Fig. 4 shows the effect of treatment on MG degradation. No significant effect is obtained in the case of photolysis, but in presence of UV-light and sun-light, the degradation achieves 90%.

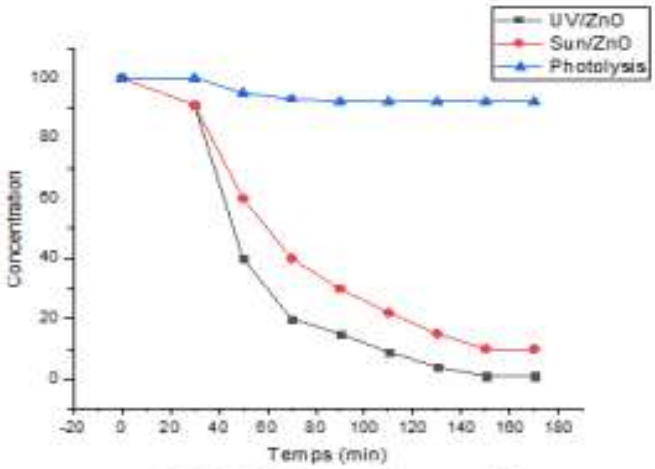

Fig. 3. ZnO-Nps test in photocatalysis

V. Conclusion

In this study, ZnOPs was synthesized by Rosmarinus officinalis leaves aqueous extract using zinc sulfate. UV–Visible spectrum showed a distinct peak around 375 nm, which is specific for ZnOPs. The XRD results confirmed the efficiency of the synthesis process.

References

BjaalieL, Himmetoglu B, Weston L, Janotti A, Van de Walle C. Oxide interfaces for novel electronic applications, New J. Phys. 16 (2014) 025005.

Hao H, Lang X. Metal sulfide photocatalysis: visible-light-Induced organic transformations, ChemCatChem 11 (2019) 1378–1393.

Rupa, E.J.; Kaliraj, L.; Abid, S.; Yang, D.-C.; Jung, S.-K. Synthesis of a Zinc Oxide Nanoflower Photocatalyst from Sea Buckthorn Fruit for Degradation of Industrial Dyes in Wastewater Treatment. *Nanomaterials* **2019**, *9*, 1692. https://doi.org/10.3390/nano9121692

Shabnam F., Mina J., Hassan K F (2019) Green synthesis of zinc oxide nanoparticles: a comparison, Green Chemistry Letters and Reviews, 12:1, 19-24, DOI:10.1080/17518253.2018.1547925.

Shekhar T.S, Kiran B., Puttaiah E., Shivaraj Y., Mahadevan K. Phytoplankton as index of water quality with reference to industrial pollution, J. Environ. Biol. 29 (2008) 233.

Vaiano V., Matarangolo M., Murcia J. Rojas H., Navío J.A, Hidalgo M. Enhanced photocatalytic removal of phenol from aqueous solutions using ZnO modified with Ag, Appl. Catal. B 225 (2018) 197–206.

Varjani S.J., Sudha M.C. Treatment technologies for emerging organic contaminants removal from wastewater, Water Remediation, Springer, 2018, pp. 91–115.

Zhu S, Wang D. Photocatalysis: basic principles, diverse forms of implementations and emerging scientific opportunities, Adv. Energy Mater. 7 (2017) 1700841.

IEEES-129

Energetic and Exergetic Analysis of a Marine-Type ORC WHRS Using Zeotropic Mixtures

[1]Mehmet Akman, [2*]Selma Ergin
[1] Muğla Sıtkı Koçman University, Department of Motor Vehicles and Transportation Technologies, 48420, Muğla, Turkiye
[2] Istanbul Technical University, Faculty of Naval Architecture and Ocean Engineering, Department of Naval Architecture and Marine Engineering, 34469 Maslak, Istanbul, Turkiye

* E-mails: ergin@itu.edu.tr

Abstract

Energy efficiency and decarbonization have been the primary concerns for the shipping industry, recently. Organic Rankine Cycle-based waste heat recovery systems, on the other hand, propose challenging solutions for increasing energy efficiency and decreasing ships' emissions. In this study, a marine-type and recuperative ORC system using zeotropic mixtures is modelled to recover a methanol-fueled marine engine's exhaust gas waste heat. Firstly, the waste heat potential of the exhaust gas is calculated at different engine operating conditions. Then, zeotropic mixtures are designed to be used for the modelled marine-type ORC WHRS. Very low GWP (<10) and zero ODP working fluids from the latest hydrofluoroolefins; R1336mzz(Z) and R1234ze(Z) are employed in pure form and mixed in various compositions. Subsequently, energetic and exergetic analyses are conducted to show the effects of temperature glide, mass fraction and evaporation pressure of the mixtures. Finally, the debatable research questions regarding the design and application of zeotropic mixtures are tried to be answered.

Keywords: Energy efficiency, Waste heat recovery, ORC, Zeotropic mixture, Methanol

I. Introduction

Energy-efficient shipping and decarbonization have been key concerns of the maritime industry in recent times. The Fourth IMO GHG Study underlines that the share of ship-based greenhouse gas emissions in 2018 is 2.89% of global GHG emissions and it can rise between 90% and 130% of the 2008 level by 2050 unless the required measures are taken (IMO, 2020). Hence, IMO has developed a strategy to cut down the carbon intensity by at least 20% by 2030 and 70% by 2040 baselining the carbon intensity level of 2008 (IMO, 2023). Enforced measures of the Energy Efficiency Design Index (EEDI) and Ship Energy Efficiency Management Plan (SEEMP) with emission regulations have been effective since 2013. In addition, IMO also amended MARPOL Annex VI to widen the scope of reducing the carbon footprint of ships by the enforcement of the Energy Efficiency Existing Ship Index (EEXI), Carbon Intensity Indicator (CII) and enhanced SEEMP (IMO, 2020).

Organic Rankine Cycle (ORC) technology has been one of the most challenging alternatives for increasing the energy efficiency of ships, recently. Parallel to the International Maritime Organization's emission targets and energy-efficient shipping mission, ORC-based WHR systems provide remarkable solutions. The studies and applications regarding ORC WHR systems are ongoing and the focus for the researchers is mainly based on increasing the thermodynamic, economic and environmental performance of integrated marine power generation systems (Akman & Ergin, 2019, 2021, 2023; Hwang et al., 2023). One of the most effective ways to increase the performance of an ORC WHR system is a high-performance working fluid selection. The working fluids for an ORC system are mainly classified into hydrocarbons, hydrofluorocarbons and hydrofluoroolefins which have offered promising performances, recently (Jovell et al., 2022). The basic principles for the selection of a working fluid are high thermo-economic performance, low flammability, toxicity, and instability as well as low global warming potential (GWP) and ozone depletion potential (ODP). Therefore, the applications are focusing on the replacement of hydrofluorocarbons which have relatively high GWP and ODP (Mondejar et al., 2018).

Zeotropic mixtures, on the other hand, provide solutions for better energetic and exergetic performance as well as environmentally friendly operation (Zhai et al., 2018). A zeotropic mixture consists of pure fluids and has a temperature glide meaning that the phase change occurs within a temperature range which is based on the thermo-physical properties and mass fractions of the components. The latest studies also show that zeotropic mixtures can be used as an alternative to using the high GWP and ODP working fluids which are restricted or not recommended for thermal systems. For instance, Song et al. (2015) used R141b (ODP>0, GWP=700) as the retardant in the mixture and stated that the net power output of the system operated with the designed mixture is 13.3% higher than that of the system operated with the pure fluid. In this study, R1336mzz(Z) and R1234ze(Z) from hydrofluoroolefins are mixed in various compositions to obtain zeotropic mixtures to be used in an ORC waste heat recovery system driven by the exhaust gas of a methanol-fueled marine engine. Firstly, the exhaust gas waste heat potential of the engine is calculated and a recuperative ORC system is configurated. Then, low GWP (<10) and zero ODP working fluids are mixed to obtain energetic and exergetic performances under various mass fractions and temperature glides as well as evaporation pressures. The net power output, thermal and exergy efficiency and exergy destruction rate of zeotropic mixtures are presented and finally, the highlights are drawn for future studies.

II. Waste Heat Recovery Model

The model of the dual-fuel engine used in this study is MAN B&W 5S50ME-C9.6 which is operable under Tier II and Tier III modes burning methanol and marine diesel oil (MDO) (MAN, 2014). The engine has an exhaust gas recirculation (EGR) system to minimize the NO_X emission under Tier III mode. Besides, MDO is used as pilot oil to

avoid knocking and to control ignition during the gas injection mode (Babicz, 2015). The engine properties and exhaust gas data are obtained using Computerized Engine Application System (CEAS) software (MAN, 2020). According to CEAS calculations, the mass flow rate of exhaust gas is between 7.9 kg/s and 15.2 kg/s at 50% MCR and 100% MCR, respectively. The exhaust gas temperature is between 484 K and 492 K. The specific gas consumption (SGC) and specific pilot oil consumption (SPOC) with exhaust gas data are obtained from the authors' previous study (Akman & Ergin, 2022).

The proposed ORC WHR system and temperature-entropy diagram are schematically shown in Fig. 1 (a-b). The exhaust gas after the turbocharger enters the boiler of ORC to evaporate the mixtures. After the expansion process, the fluid is sent to the recuperator to increase the enthalpy of the fluid coming from the pump. After the recuperator, the fluid is cooled down in a condenser where fresh water is used for cooling then the liquid mixture is recirculated. The temperature glide occurs in the condenser and evaporator based on the zeotropic mixture composition which has different boiling and dew point temperatures.

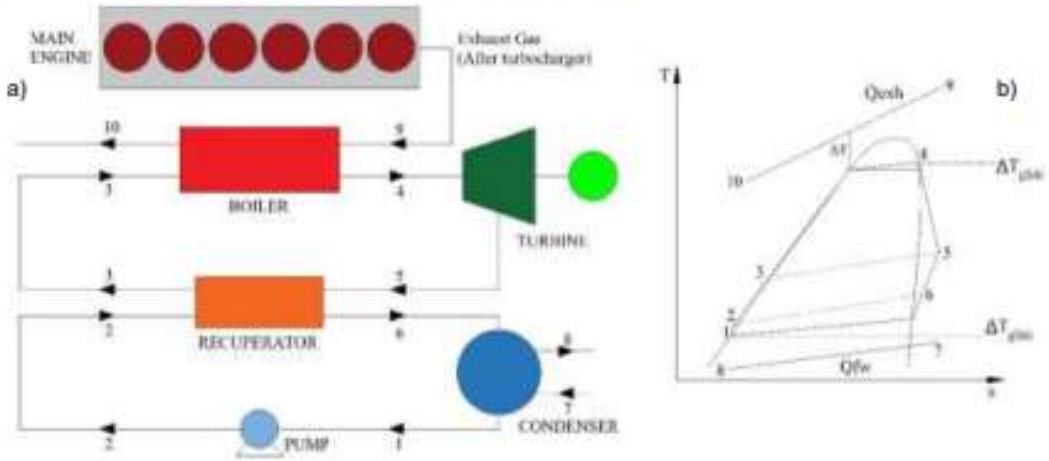

Fig. 1: Schematic diagrams of recuperative ORC (a) and T-s diagram (b)

The selection of a marine-type working fluid is an important step for an ORC WHRS. Not only the thermo-economic performance but also the regulations must be considered for an onboard system. MARPOL Annex VI regulation directs that the fluids to be used onboard ships must have zero ozone depletion potential. Moreover, according to the European Regulation; substances with a global warming potential of 2500 or more have been banned since 1st January 2020 (JSRAE, 2016). In this study, the properties of the working fluids used for forming zeotropic mixtures are shown in Table 1.

Table 1. The properties of selected working fluids for forming zeotropic mixtures

Fluids	Boiling point (°C)	Critical temperature (°C)	Critical pressure (kPa)	GWP	ODP
R1336mzz(Z)	33.45	171.35	2903	2	0
R1234ze(Z)	9.73	150.12	3530	7	0

III. Methodology

The mathematical model of energetic and exergetic analyses is based on the first and second laws of thermodynamics. A computer code is written in MATLAB for the parametric analysis based on the following equations. The working fluids' thermodynamic and transport properties are obtained and integrated into the code using Refprop 10. The heat transfer from the exhaust gas boiler, recuperator and condenser can be calculated by;

$$\dot{Q}_{in} = \dot{m}_{exh} c_{p\_exh} (T_9 - T_{10}) = \dot{m}_f (h_4 - h_3) \quad (1)$$

$$\dot{Q}_{out} = \dot{m}_{fw} c_{p\_fw} (T_7 - T_8) = \dot{m}_f (h_6 - h_1) \quad (2)$$

$$\dot{Q}_{rec} = \dot{m}_f (h_5 - h_6)\epsilon = \dot{m}_f (h_3 - h_2) \quad (3)$$

where *exh*, *fw*, and *f* subscripts indicate exhaust gas, freshwater and working fluid, respectively. The effectiveness and enthalpy (kJ/kg) are symbolized with ϵ and h, respectively. The power output from the turbine *(t)* is calculated by the inlet and outlet enthalpy difference of the turbine:

$$\dot{W}_t = \dot{m}_f (h_4 - h_3)\mu_t \quad (4)$$

The pump power, net power and cycle thermal efficiency are calculated as:

$$\dot{W}_p = \frac{\dot{m}_f (h_2 - h_1)}{\eta_p} \quad (5)$$

$$\dot{W}_{net} = \dot{W}_t - \dot{W}_p \quad (6)$$

$$\eta_{th\_ORC} = \frac{\dot{W}_{net}}{\dot{Q}_{in}} \quad (7)$$

The heat loss factor for the evaporator and condenser is 0.95 and the recuperator effectiveness is 0.8 (Akman & Ergin, 2022). The minimum temperature of the exhaust gas after the turbocharger is 100 °C. The pinch point temperature differences in the evaporator and condenser are 30 K and 5 K, respectively (Zhai et al., 2018). The isentropic efficiency of the turbine and pump is 0.75 (Akman & Ergin, 2022). The reference state for exergy analysis is T_0=293.15 K and P_0=100 kPa. The exergy of a state in the cycle can be written as follows:

$$x_i = (h_i - h_0) - T_0(s_i - s_0) \qquad i = \{1,2,\ldots\ldots,10\} \quad (8)$$

After the calculation of exergy at each state, the exergy obtained and destructed in the heat exchangers, pump and turbine are defined and exergy efficiency can be calculated as follows,

$$\sum \dot{X}_{in} - \sum \dot{X}_{out} = \dot{X}_{dest} \quad (9)$$

$$\eta_{ex\_ORC} = \frac{\dot{W}_{net}}{\dot{Q}_{in}\ (1 - \frac{T_0}{T_{hs}})} \quad (10)$$

where $\dot{X}_{in}$, $\dot{X}_{out}$ and T_{hs} represent the inlet and outlet exergy rates and source temperature, respectively. As can be understood from the equations, temperature glide minimizes the exergy losses based on that the working fluid inlet and outlet temperatures get closer to those of the source temperatures.

IV. Results

The thermodynamic performance of mixtures is analyzed at varying evaporation pressures (P_{eva}), mass fractions (Ψ) and glide temperatures. The mass fractions range from 0 to 1 with an increment of 0.1. When the mass fraction is zero, the working fluid is pure R1234ze(Z) and when it is 1 the working fluid is pure R1336mzz(Z). Therefore, the zeotropic mixtures form in the range of 0.1 to 0.9 compositions. Besides, the evaporation pressure ranges from 1400 kPa to 2800 kPa with an increment of 140 kPa. Fig. 2 (a-b) shows the net power output and thermal efficiency of the ORC WHR system at different evaporation pressures and mass fractions under 85% MCR engine loading conditions. The net power output surface remarks that the higher mass fraction of R1336mzz(Z) results in a higher net power output. However, the evaporation pressure of the zeotropic mixture should be adjusted following the mass fractions. According to the calculations, it is possible to generate 173.1 kW net power when the engine is operated at 85% MCR and Tier II mode. When the engine is at full load, the net power output rises to 235.5 kW which corresponds to about 2.7% increase in the thermal efficiency of the power generation system. The calculated maximum thermal efficiency is 13.36% at 2800 kPa when R1336mzz(Z) is purely used. However, it is possible to obtain high thermal efficiency by adjusting the mass fraction 0.9/0.1 R1336mzz(Z)/ R1234ze(Z) at 2000 kPa—the lower evaporation pressure and mass fraction result in lower thermal efficiency.

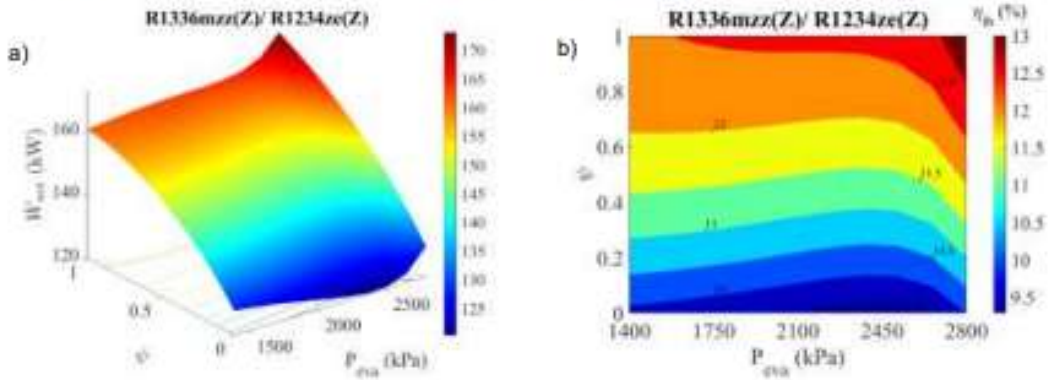

Fig. 2: The change of net power output (a) and thermal efficiency (b)

The exergy analysis of the zeotropic working fluids reveals that the mass fraction and temperature glide have substantial effects on the exergetic performance. Fig 3 (a-b) shows the change in exergy efficiency and exergy destruction with respect to mass fractions and temperature glide in the condenser. The maximum temperature glide is 5.07 K when the composition of the mixture is 0.7/0.3 R1336mzz(Z)/R1234ze(Z). The higher temperature glide lowers the condensation exergy losses in the condenser. The calculated maximum exergy efficiency is 43.52% at 2800 kPa when the mass fraction is 1 at 85% MCR. The analysis also shows that at lower loads (50% - 70% MCR) and lower mass fractions, it is possible to increase the exergy efficiency up to 44%. Besides, the calculated maximum exergy destruction rate is 215.6 kW when R1234ze(Z) is purely used at 2800 kPa.

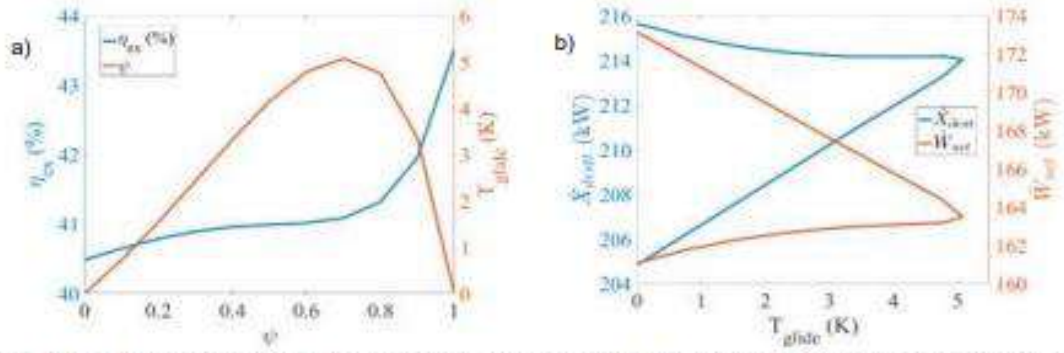

Fig. 3: The effect of mass fraction (a) and temperature glide (b) on the exergy efficiency and exergy destruction

V. Conclusions

In this study, a marine-type and recuperative ORC system using zeotropic mixtures is modelled to recover a methanol-fueled marine engine's exhaust gas waste heat. R1336mzz(Z) and R1234ze(Z) are employed in pure form and mixed in various compositions. The energetic and exergetic analyses underline that the temperature glide, mass fraction, and evaporation pressure have remarkable effects on the cycle performance. Using zeotropic mixtures instead of pure fluid can increase the thermal and exergy efficiency by more than 3% and 7%, respectively. The different types of working fluids can be mixed and thermo-economic performance optimization studies of zeotropic mixtures can be conducted in future studies. Zeotropic mixture design approaches can also be developed for marine ORC WHR systems.

Acknowledgements

The authors would like to express their gratitude to Istanbul Technical University Scientific Research Projects (BAP) Department for their financial support to the project numbered MGA-2023-44648, which is currently being carried out at Istanbul Technical University Naval Architecture and Marine Engineering Department.

References

Akman, M., & Ergin, S. (2019). An investigation of marine waste heat recovery system based on organic Rankine cycle under various engine operating conditions. *Proceedings of the Institution of Mechanical Engineers Part M: Journal of Engineering for the Maritime Environment*, 233(2), 586–601. https://doi.org/10.1177/1475090218770947

Akman, M., & Ergin, S. (2021). Thermo-environmental analysis and performance optimisation of transcritical organic Rankine cycle system for waste heat recovery of a marine diesel engine. *Ships and Offshore Structures*, *16*(10), 1104–1113. https://doi.org/10.1080/17445302.2020.1816744

Akman, M., & Ergin, S. (2023). Thermo-economic optimization of an ORC system for a dual-fuel marine engine. *Proceedings of the Institution of Mechanical Engineers Part M: Journal of Engineering for the Maritime Environment*. https://doi.org/10.1177/14750902231207128

Akman, M., & Ergin, S. (2022). Greener shipping: An investigation of an ORC-based waste heat recovery system for a methanol-fueled marine engine. *4th International Meeting - Ship Design & Optimization and Energy Efficient Devices for Fuel Economy*.

Babicz, J. (2015). *Wärtsilä Encyclopedia of Ship Technology*. https://www.wartsila.com/encyclopedia

Hwang, D. J., Jee, J. H., Kim, J. S., Kim, S., & Oh, C. (2023). A study on the design of Waste Heat Recovery Unit (WHRU) for 30kW Organic Rankine Cycle (ORC) power system for ships. *Journal of International Maritime Safety, Environmental Affairs, and Shipping*, *7*(1). https://doi.org/10.1080/25725084.2023.2184603

IMO. (2020). *Fourth IMO GHG Study 2020 Executive Summary*. https://www.imo.org/en/OurWork/Environment/Pages/Fourth-IMO-Greenhouse-Gas-Study-2020.aspx

IMO. (2023). *2023 IMO Strategy on Reduction of GHG Emissions From Ships—MEPC.377(80)*. https://www.imo.org/en/MediaCentre/PressBriefings/pages/Revised-GHG-reduction-strategy-for-global-shipping-adopted-.aspx

Jovell, D., Gonzalez-Olmos, R., & Llovell, F. (2022). A computational drop-in assessment of hydrofluoroethers in Organic Rankine Cycles. *Energy*, *254*, 124319. https://doi.org/10.1016/j.energy.2022.124319

JSRAE. (2016). *Risk Assessment of Mildly Flammable Refrigerants*. https://www.jsrae.or.jp/committee/binensei/final_report_2016r1_en.pdf

MAN. (2014). *Using Methanol Fuel in the MAN B&W ME-LGI Series*. https://www.mandieselturbo.com/docs/default-source/shopwaredocuments/using-methanol-fuel-in-the-man-b-w-me-lgi-series.pdf

MAN. (2020). *CEAS engine calculations*. https://www.man-es.com/marine/products/planning-tools-and-downloads/ceas-engine-calculations

Mondejar, M. E., Andreasen, J. G., Pierobon, L., Larsen, U., Thern, M., & Haglind, F. (2018). A review of the use of organic Rankine cycle power systems for maritime applications. In *Renewable and Sustainable Energy Reviews* (Vol. 91, pp. 126–151). Elsevier Ltd. https://doi.org/10.1016/j.rser.2018.03.074

Song, J., & Gu, C. (2015). Analysis of ORC (Organic Rankine Cycle) systems with pure hydrocarbons and mixtures of hydrocarbon and retardant for engine waste heat recovery. *Applied Thermal Engineering*, *89*, 693–702. https://doi.org/10.1016/j.applthermaleng.2015.06.055

Zhai, H., An, Q., & Shi, L. (2018). Zeotropic mixture active design method for organic Rankine cycle. *Applied Thermal Engineering*, *129*, 1171–1180. https://doi.org/10.1016/j.applthermaleng.2017.10.027

IEEES-130

Comparison study of four typical ORC configurations integrated with hydrogen production unit for the exploitation of medium temperature geothermal sources

Taha Aydin[1], Hadi Genceli*[1], Parisa Heidarnejad[2]
[1] Yıldız Technical University, Department of Mechanical Engineering, Istanbul, Turkey
[2] İstanbul Gedik University, Department of Mechanical Engineering, Istanbul, Turkey
*E-mails: hgenceli@yildiz.edu.tr

Abstract
The organic Rankine cycle (ORC), as the most prospective technology for low/moderate temperature geothermal sources, has different configurations available to match these kind of sources. This paper is aimed at revealing the condition for which different ORC configurations are matched to the medium temperature geothermal sources thermodynamically so as to give selection guidance. Four mostly investigated configurations including the subcritical ORC (ORC), the ORC with internal heat exchanger (ORC-IHE), the ORC with open feed heater (ORC-OFH), and the partially evaporated ORC (PEORC) are selected to enable efficient utilization of low temperature geothermal sources. All these cycles are integrated to proton exchange membrane electrolyzer unit (PEM) with the purpose of hydrogen production. Their thermodynamic performance is analyzed and compared from the viewpoint first and second law efficiencies. The results indicate that, ORC-IHE has maximum net power output, hydrogen production energy and exergy efficiencies by 382 kW, 0.062 kg/h, 17% and 46% among other ORC configurations. Also, subcritical ORC has maximum heat source utilization and exergetic heat source utilization by about 45% and 67% among remaining ORC configurations.

Keywords: Organic Rankine Cycle, Geothermal, Thermodynamic analysis, Hydrogen production

I. Introduction

Global energy demand can only be met sustainably by decreasing our reliance on fossil fuels. Implementing a structural transformation in energy infrastructure involves transitioning seamlessly from traditional energy providers to novel, environmentally friendly, and renewable energy sources. The initial and subsequent stages of this process involve investigating sustainable energy sources and generating environmentally friendly hydrogen fuel, which can serve as a substitute for fossil fuels in the worldwide energy provision. Geothermal energy has a remarkably high Capacity Factor of over 98%, which is one of the greatest among both standard and alternative energy resources [1]. The primary technological limitation hindering the extensive use of geothermal energy is the restricted efficiency of existing power generation systems that rely on geothermal flows at temperatures that are both low and moderate [1]. The majority of geothermal resources that are easily obtainable and can be reached without difficulty are restricted to low to moderate temperatures. This indicates the necessity for innovative technologies such organic Rankine cycles to convert the energy at better efficiency.

Various configurations can be derived by modifying the fundamental design of the ORC system, which primarily comprises a condenser, an evaporator, a turbine, and a pump,. Several works have examined how adjustments to the setup of an ORC system affect its overall performance. Pastor-Martinez et al. [3] found that when comparing series and parallel topologies, the use of an internal recuperator is beneficial for serial applications, but it does not considerably increase the achievable net power output in parallel setups. In their study, Sun et al. [4] conducted a comparison of three different configurations of the ORC system. The aim was to determine the design that would be the most efficient in recovering both the thermal energy from a low/medium grade heat source and the cold energy from the LNG stream. In their study, Nondy and Gogoi [5] conducted a comparison and analysis of various ORC setups for the purpose of generating power by harnessing the energy from the exhaust gas of a gas turbine. The exergo-economic study encompassed four types of Organic Rankine Cycle (ORC) systems: simple ORC, regenerative ORC, recuperative ORC, and recuperative-regenerative ORC (RR-ORC). Ganjehsarabi [6] proposed an integrated system with the aim of achieving similar goals, which combines a geothermal assisted ORC with a PEM electrolyzer. The suggested working fluids yielded exergy efficiencies of roughly 40%.

In tis study, four different ORC configurations (subcritical, with IHE, with OFH and partially evaporated) integrated with hydrogen production plant are compared thermodynamically for medium-grade geothermal sources. This study evaluates the net power output, hydrogen production, energy efficiency, exergy efficiency, heat source utilization, and the exergetic heat source utilization as the performance indicators.

II. System Description

Figure 1 showcases designs of four distinct geothermal energy facilities that are capable of producing hydrogen and electricity. Case (a) depicts a basic subcritical ORC including a turbine, a pump, an evaporator, a condenser and a PEM electrolyzer unit. In all configurations, the geothermal fluid coming from the producing well enters the evaporatorin order to produce vapor of R113 organic working fluid with the purpose of generating mechanical power through turbine. Leaving stream from turbine goes to condenser and pump in order to complete the cycle. On the other hand, a predefined share of electricity power by the generator is utilized to run the PEM electrolyzer, producing hydrogen. In case (b) (ORC-IHE), the oulet stream of the turbine is utilized for preheating the fluid before entering the evaporator. In case (c) (ORC-OFH), a partly expanded stream of the turbine is fed to a heater to transfer thermal energy to the outlet of the pump2. In case (d), the stream leaving the evaporator, partially evaporates into the liquid–vapor mixture and then enters the expander to generate power.

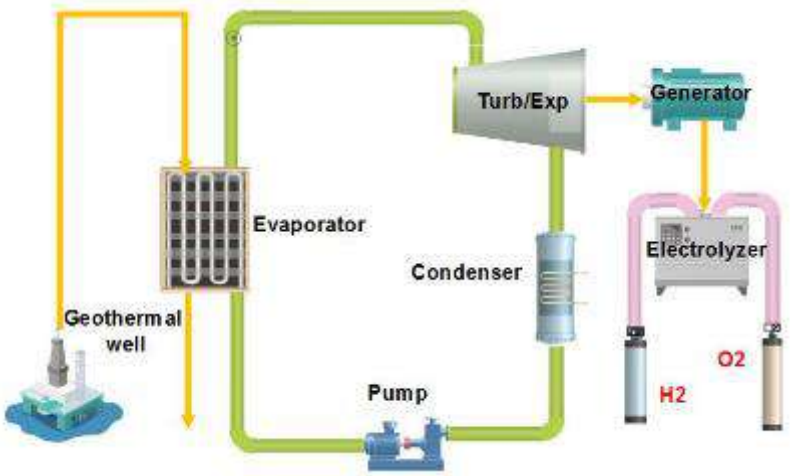

Fig. 1: Schematic diagram of the basic ORC system incorporated with PEM electrolyzer.

III. Analysis

The performance assessment of the different configurations of the proposed system from thermodynamic viewpoints is conducted through applying first and second laws of thermodynamics to all components. The analysis that follows relies on several simplifying assumptions. These assumptions include treating the operation of the ORC cycle as steady-state, considering the geothermal fluid as water. The reference temperature (T_o) and pressure (P_o) values are 20 ℃ and 101.325 kPa, respectively. With these considerations in mind, the general equations for mass, energy, and exergy balances are expressed as follows:

$$\sum \dot{m}_i - \sum \dot{m}_e = 0 \quad (1)$$

$$\sum \dot{m}_i h_i + \sum \dot{Q}_i + \sum \dot{W}_i = \sum \dot{m}_e h_e + \sum \dot{Q}_e + \sum \dot{W}_e \quad (2)$$

$$\sum \dot{m}_i ex_i - \sum \dot{m}_e ex_e + \sum \dot{E}x_i^Q + \sum \dot{E}x_i^W = \sum \dot{E}x_e^Q + \sum \dot{E}x_e^W + \dot{E}x_D \quad (3)$$

Six performance indicators such as net power output, hydrogen production, energy efficiency, exergy efficiency, heat source utilization, and the exergetic heat source utilization are determined through equations (4-7) as well [6-7]:

$$\eta = \frac{W_{net} + m_{H_2} \times LHV_{H_2}}{Q_{in}} \quad (4)$$

$$\varepsilon = \frac{W_{net} + m_{H_2} \times HHV_{H_2}}{Ex_{in}} \quad (5)$$

$$HSU = \frac{h_{geo,in} - h_{geo,out}}{h_{geo,in} - h[0]} \quad (6)$$

$$ESU = \frac{Ex_{geo,in} - Ex_{geo,out}}{Ex_{geo,in}} \quad (7)$$

where η is the energy efficiency, ε is the exergy efficiency, W_{net} is the net power output of the system (kW), HSU is the heat source utilization and ESU is the exergetic heat source utilization.

IV. Results and discussion

In order to validate the modeling results of the present research, the entire system under consideration is divided into two components: the ORC and the PEM electrolyzer. The simulation outcomes for the PEM electrolyzer are compared with published experimental data by Ioroi et al. [8], and a substantial agreement between the two sets of data is obtained.

The comparison study of the four proposed configurations were performed through considering some design parameters listed in

Table 1. The obtained results are also presented in this Table as well.

Table 1. Design parameters and thermodynamic performances of the four studied configurations of ORC

	ORC	ORC-IHE	ORC-OFH	PEORC
Turbine inlet temperature (◦C)	*120*	*120*	*120*	*114*
Condenser temperature (◦C)	*35*	*35*	*35*	*60*
Geothermal water temperature (◦C)	*140*	*140*	*140*	*140*
The mass flow rate of geothermal water (kg/s)	*10*	*10*	*10*	*10*
Evaporator pinch point (◦C)	*5*	*5*	*5*	*5*
Condenser pinch point (◦C)	*10*	*10*	*10*	*10*
Electrolyzer temperature (◦C)	*80*	*80*	*80*	*80*
Net power output (kW)	*326.3*	*382*	*153.9*	*135.7*
Hydogen mass flow rate (kg/h)	*0.05333*	*0.06209*	*0.02578*	*0.02282*
Energy efficiency (-)	*0.1445*	*0.1703*	*0.1566*	*0.08087*
Exergy efficiency (-)	*0.3931*	*0.4602*	*0.1854*	*0.1786*
Heat source utilization (-)	*0.4517*	*0.4513*	*0.1994*	*0.3480*
Exergetic heat source utilization (-)	*0.6709*	*0.6704*	*0.3364*	*0.5477*

Figure 2 depicts the variation of the hydrogen production and exergy efficiency of the four ORC-PEM systems with the turbine inlet temperature (T_1). As the turbine inlet temperature, T_1, increases, the interaction between net output power and heat supply exergy causes the exergy efficiency of all four systems to initially rise and then smoothly decline. Among them, ORC-IHE exhibits the highest exergy efficiency, followed by ORC, PEORC, and ORC-OFOH in sequential order.

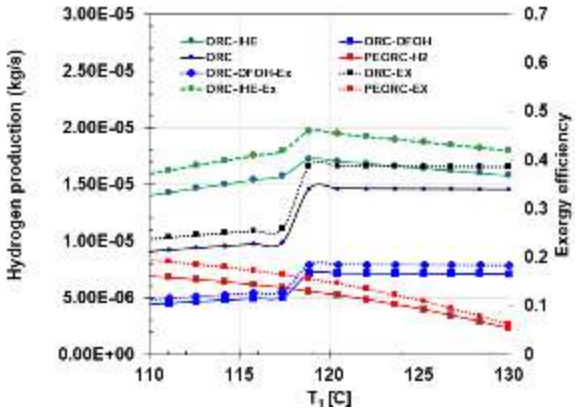

Fig. 2. Effect of turbine inlet temperature (T_1) on the exergy efficiency and hydrogen generation of four ORC based integrated PEM electrolysis systems.

V. Conclusions

This study utilized a thermodynamic comparative assessment to evaluate several configurations of a geothermal-driven system that produces both hydrogen and power. This inquiry assesses the performance of the geothermal-based energy system that has been mentioned through six performance indicators namely, the net power output, hydrogen production, energy efficiency, exergy efficiency, heat source utilization, and the exergetic heat source utilization. The obtained results present that, ORC-IHE has maximum net power output, hydrogen production energy and exergy efficiencies by 382 kW, 0.062 kg/h, 17% and 46% among other ORC configurations. Also, subcritical ORC has maximum heat source utilization and exergetic heat source utilization by about 45% and 67% among remaining ORC configurations.

References

[1] S.J. Zarrouk, H. Moon, Efficiency of geothermal power plants: A worldwide review Geothermics, 51 (2014), pp. 142-153.
[2] A. Franco, Power production from a moderate temperature geothermal resource with regenerative Organic Rankine Cycles, Energy Sustain Dev, 15 (2011), pp. 411-419.

[3] E. Pastor-Martinez, C. Rubio-Maya, V.M. Ambriz-Díaz, J.M. Belman-Flores, J.J. Pacheco-Ibarra, Energetic and exergetic performance comparison of different polygeneration arrangements utilizing geothermal energy in cascade, Energy Convers. Manag., 168 (2018), pp. 252-269.

[4] Z. Sun, H. Zhang, T. Zhang, L. Lin, K. Lin, Optimizations and comparison of three two-stage Rankine cycles under different heat source temperatures and NG distribution pressures, Energy Convers Manag, 209 (2020), Article 112655.

[5] J. Nondy, T.K. Gogoi, Exergoeconomic investigation and multi-objective optimization of different ORC configurations for waste heat recovery: A comparative study, Energy Convers Manag, 245 (2021), Article 114593.

[6] Ganjehsarabi, H. (2019). Mixed refrigerant as working fluid in Organic Rankine Cycle for hydrogen production driven by geothermal energy. Int. J. Hydrogen Energy Energy 44, 18703–18711

[6] Ibrahim Dincer, Marc A. Rosen, Chapter 7 - Exergy Analysis of Heat Pump Systems,

Editor(s): Ibrahim Dincer, Marc A. Rosen, Exergy (Second Edition), Elsevier, 2013.

[7] Dawo, F., Buhr, J., Schifflechner, C., Wieland, C., & Spliethoff, H. (2023). Experimental assessment of an Organic Rankine Cycle with a partially evaporated working fluid. *Applied Thermal Engineering*, *221*, 119858.

[8] Ioroi, T., Yasuda, K., Siroma, Z., Fujiwara, N., Miyazaki, Y. (2002). Thin film electrocatalyst layer for unitized regenerative polymer electrolyte fuel cells. *Journal of Power Sources*112.

IEEES-131

Adsorption of Co (II) ions onto NaX and NaA zeolites

*Ferhat Djawad, Nibou Djamel, Hadj Mekatel, Amokrane Samira.
Laboratoire de Technologie des Matériaux, Université des Sciences et de la Technologie Houari Boumediene, B.P. 32, El-Alia, Bab-Ezzouar, Alger, Algérie

* E-mails: * ferhat_djawed@hotmail.fr

Abstract

The present work objective to eliminate Co^{2+} heavy metals on molecular sieves of zeolite types. The study carried out in this article as a first step in of the hydrothermal elaboration of zeolite materials of the NaX and NaA types. The prepared sieves were characterized by X-ray diffraction (XRD) and scanning electron microscopy (SEM) The second part of this work is devoted to the study of the elimination of metal ions on elaborated zeolites. The effect of certain physical parameters such as the pH of the solution, the solid/liquid ratio, the initial concentration of the metal ion and the temperature were studied. The best interpretation of the experimental data was obtained by the Langmuir isotherm with a maximum adsorption capacity of 96.72 and 90.19 mg/g for cobalt on both NaX and NaA zeolites.

Keywords: Adsorption; Cobalt ions; Zeolite; isotherm; Lagmuir.

I. Introduction

Nowadays, the protection of the environment has become a major societal challenge. The problem of heavy metals has become a concern. A common feature of industrial effluents is related to the fact that they almost always contain toxic metals. The protection of the environment imposes to limit the contents of these metals to the maximum allowed (Woumfo et al. 2007; Glatz, 2012). The toxicity of a metal is directly related to its reactivity with living matter. In the trace state, most metals considered toxic are in fact essential to life and therefore, the control of heavy metal emissions in the environment must refer to a toxicity scale (Mourad, 2012). Among these processes, adsorption is one of the most efficient techniques owing to its various advantages such as high relatively easy regeneration, adsorption capacity, fast kinetics and the use of a large variety of adsorbent materials (clays , zeolites …)(Nibou et al. 2010; Izidoro et al. 2013).

Microporous solid materials such as zeolites have a certain economic impact by their use in various industries especially the treatment of aqueous effluents (Co^{2+}, Ni^{2+} and Zn^{2+} ...) and the petroleum industry. In the present work, we chose two types of solid microporous materials most used in different industries namely, NaA zeolites and NaX faujasites for the demonstration of their surface reactivity. Thereby, we have synthesized zeolites of the NaA and NaX types. They were prepared by hydrothermal crystallization in a teflon-jacketed steel autoclave from gels of molar compositions ((x) Al_2O_3 (y) SiO_2 (z) Na_2O (w) H_2O). Various reaction parameters such as temperature, the solid / liquid ratio, the initial concentration of the cation and the pH of the solution have been optimized (Breck, 1984; Khemaissia et al. 2007),.The kinetics of fixation has also an important impact on the evaluation of the performance of the adsorbent. The fixation contains three phases of transfer of the material and a reaction phase. The first represents the migration of the solute from the aqueous phase to the surface of the solid (external diffusion).The second related to intra-particle diffusion, and finally the surface chemical reaction between these functions of the adsorbent and the metal ions (Khambhaty et al. 2012). The results indicating that the zeolite is an open structure whose cations are readily exchangeable with the ions present in the solution. Therefore, chemical exchange is slow comparing to other diffusion processes, which involve the determination step of the mechanism (Ltaief et al.2015). Several mathematical models describing a system of a particle at constant pressure and volume have been used in the literature such as those found (Blanchard et al.1984) and Holfferich (Helfferich, 1962). We have focused on the use of models based on Fick laws, during the analysis of the data obtained experimentally and for determining the step, which describes the mechanism of the reaction, pH solution, and adsorbent dose, initial concentration of ions and the temperature were studied. The present paper consisted of: 1) Investigation of some NaA and NaX characteristics (XRD and SEM). 2) Optimization of parameters influencing the adsorption phenomenon. 3) Study of isotherm models in order to identify the adsorption mechanism.

II. Experimental Procedure

We have elaborate two types of faujasite NaX and NaA zeolites using the following conditions: Two gels of molar composition are prepared for the both zeolites [NaX (4.8Na_2O; 1Al_2O_3; 3.8SiO_2; 224H_2O), NaA (1.1 Na_2O 1 Al_2O_3 1.26 SiO_2 92 H_2O)]. Then, 2.70 and 1.28 g of NaOH are mixed with 23.34 and 21.74 g of distilled water under magnetic stirring until complete dissolution for NaX and NaA respectively. 5.47 g of aluminum source are then gradually added for each gel and 1.32, 3.97 g of silicon source for NaX and NaA respectively. The mixtures are stirred until homogeneous gels are obtained, the latter are maturing for 24 hours at room temperature and then placed in a reactor heated at 100 ° C for 24 hours. After crystallization, the crystals must be recovered by washing, filtration and drying (Nibou et al. 2010; Amokrane et al. 2007).

The identification of the phases was carried out using brand powder diffractometer (Panalytical X'Pert PRO, using CuKα radiation) at a scan range 2θ from 5 to 50°. All samples were observed using branded scanning electron microscopy SEM (JEOL 6360) equipped with energy dispersive spectrometry for chemical analysis. The infrared adsorption spectra were recorded between 4000 and 400 cm-1 using an infrared spectrometer of the type Perkin Elmer Spectrum (version 10.03.06).

Batch adsorption manipulations of Co^{2+} ions were carried out in a double-walled Pyrex reactor of capacity 200 cm^3 whose temperature was regulated by a thermostat bath. Preparation of the Co^{2+} solutions between (50–200 mg/L) were started by diluted of stock solution of (1000 mg/L). The effect of pH was studied in the range of 3 to 11 with optimizing condition such as 0.2 g of our adsorbent with 200 mL of Co (II) ions (100 mg/L) at room temperature solution. We use NaOH (0.1 M) or HCl (0.1 M) to

adjust our pH. The adsorption kinetics and isotherms of the solutions between (50–200 mg/L) have been performed at different temperatures (25, 30, 40, and 55 °C).

III. Analysis

The final Co (II) concentration is determined using UV–Vis spectrophotometer (Optizen 2120 UV–Visible, max = 465 nm) (Fedailaine et al. 2016).

Using the following relationship, we calculated the removal percentage of Co (II) ions.

$$\text{Removal of } Co^{2+}(\%) = \frac{(C_o - C_e)}{C_o} x100 \quad (1)$$

Where C_o and C_e are the initial and equilibrium Co (II) concentrations (mg/L) respectively. The adsorption capacity of the samples, q_t (mg/g), were determined using the relationship:

$$q_t = \frac{(C_o - Ce)V}{C_o\, m} \quad (2)$$

where ***V*** is the volume of the Co (II) solution and ***m*** is the weight of our adsorbent. The equilibrium constant K_c is given by:

$$K_c = \frac{(C_o - C_e)}{C_e} \quad (3)$$

IV. Results and discussion

The X-ray diffraction spectra (XRD) of the elaborated zeolites (NaX and NaA) are shown in Fig. 1 (a, b). All inter-reticular distances as well as the relative intensities of all the diffraction peaks obtained were compared to the zeolite ASTM file (Nibou, 1999). These spectra show the presence of all crystallization planes having NaX and NaA type structures. On the other hand, the NaX sample exhibits a strong peak compared to those of NaA showing a good crystallinity.

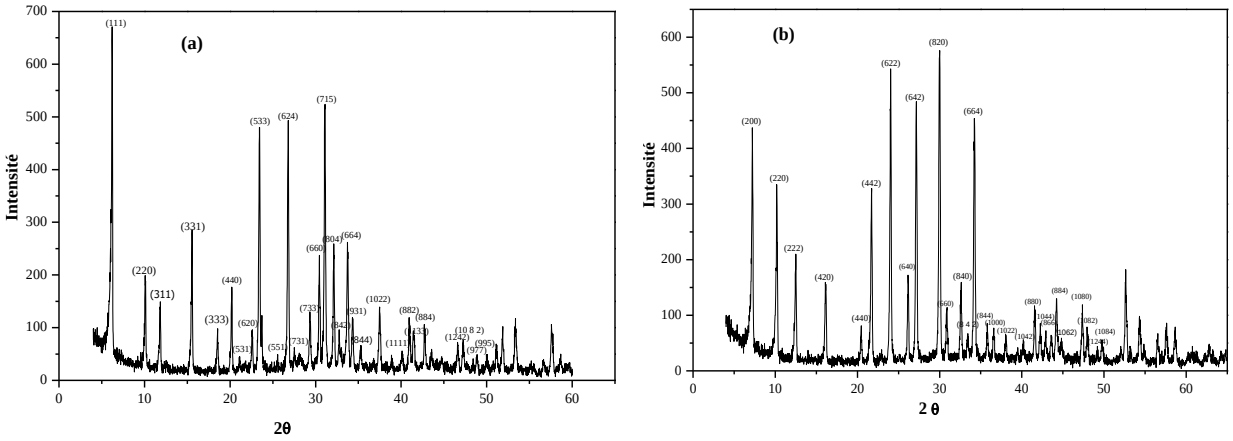

Fig. 1. XRD patterns of NaX (a) and NaY (b) zeolites.

The scanning electron microscope (SEM) observation shows the morphology of the crystals which have a very homogeneous and regular cubic form for the two zeolites (NaX and NaA) Fig. 2 (a, b). The qualitative analysis by dispersive energy spectroscopy allowed the identification of the main elements of the framework of each zeolite. From the results, the values of Si/Al atomic ratio of NaX and NaA samples are 1.5 and 1.3 respectively. It can be observed that the value of the Si/Al ratio of NaX is greater than NaA. The NaA ratio directly influences the atomic percentage of the cations compensating (11.39) compared to the NaX sample (10.15) as shown in Fig 2 (a, b).

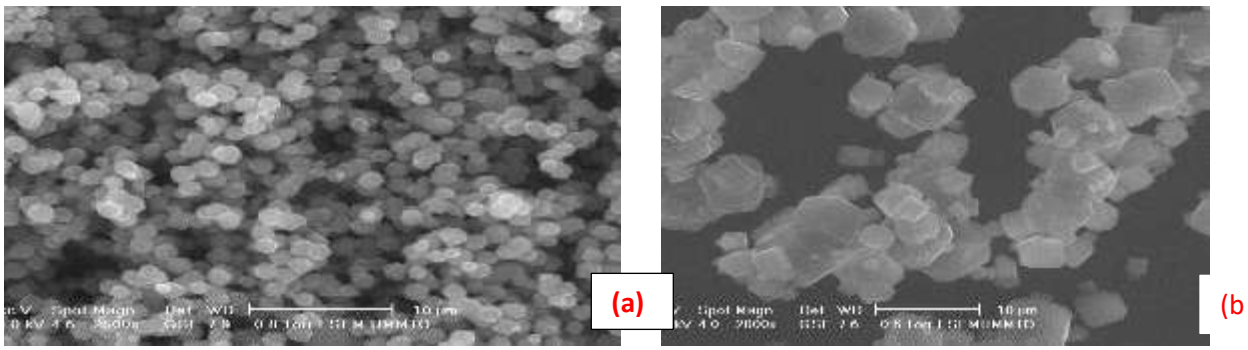

Fig. 2. SEM micrographs of NaX (a) and NaA (b) zeolites.

Effect of experimental conditions on adsorption processes

Effect of the pH value

To observe the effect of pH on the cobalt adsorption by the two zeolites elaborated (NaX and NaA) Fig 3 (a) and determining the optimum adsorption pH of each adsorbent, an initial concentration solution of 100 mg/L was used. The initial pH of the solutions is adjusted to different values in a range of 2 to 8. The elaborated zeolites (NaX and NaA) are brought into contact with a volume

of metallic solution for a ratio of S / L = 1 g/L and subjected to a stirring speed of 300 rpm for 5 hours at room temperature. From the results shown in Fig.3 (a) showing a maximum removal of Co (II) ions (90% NaX and 81% NaA) at pH ~ 6. At lower pH, the percentage is low, this is due to the competing H^+ ions which are present in the solution and which are therefore more adsorbed than the cobalt ions, because of their small size and high mobility they are privileged to occupy the active sites, this reduces the adsorption of cobalt (Habiba et al. 2018).

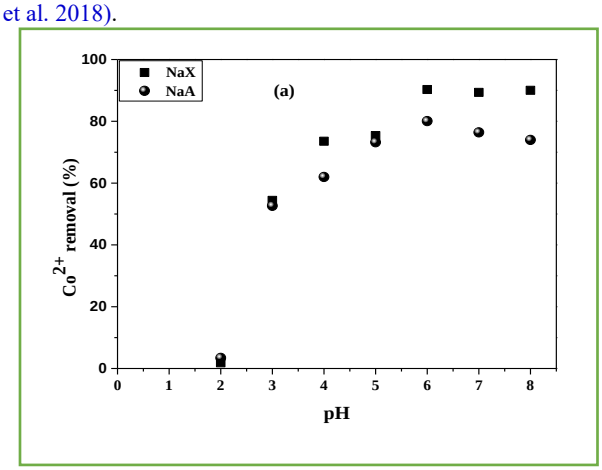

Fig. 3. Effect of pH on the adsorption uptake of Co (II) from aqueous solutions onto zeolites NaA and NaX.

([Co^{2+}] = 100 mg/L, T = 25 °C and S/L = 1 g/L).

Effect of initial concentration

To study the influence of concentration, we varied the range from 50 to 200 mg/L. The results obtained are shown in Fig 4. We note that the adsorption rate of the ions on the two zeolites NaX and NaA decreases with the increase of the initial concentration of the ions Co^{2+} (97,79 à 48,36%), (98,70 à 45,09 %) respectively. By cons, the adsorbed quantity records a respective increase of (48,90 à 96,72 mg/g), (49,35 à 90,19 mg/g), for Co^{2+} ions. This behavior is explained by the fact that the higher the C_o concentration of the ions, the more the number of ions in solution increases, implying a higher adsorption capacity. These results are in agreement with the work obtained in the literature (Abbas et al. 2014).

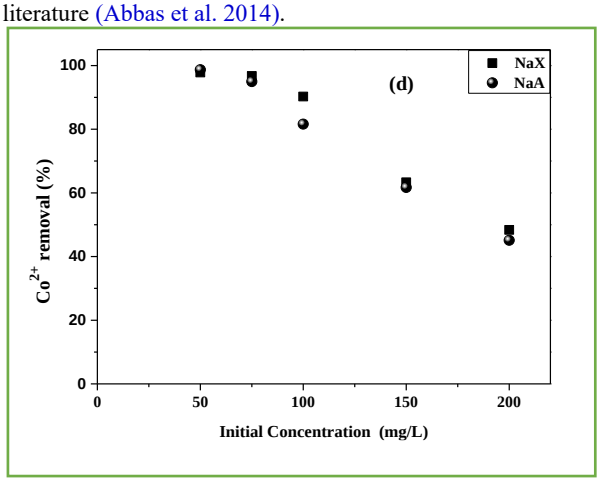

Fig. 4. Effect of initial concentration on the adsorption uptake of Co (II) from aqueous solutions onto zeolites NaA and NaX.

(pH = 6, T = 25 °C and S/L = 1 g/L).

Adsorption isotherms

Many theoretical models have been developed to describe adsorption isotherms such as the Langmuir model, the Freundlich model and the Temkin model. Equations (4), (5) and (6) were used for each model, respectively.

$$\frac{C_e}{q_e} = \frac{1}{q_m b} + \frac{C_e}{q_m} \quad (4)$$

q_e is the amount of adsorbed Co^{2+} (mg/g). The monolayer adsorption capacity q_m (mg/g) and the Langmuir constant related to the free adsorption energy b (L/mg) (Table 1) were evaluated from the slope and intercept of the linear plots of C_e/q_e versus Ce respectively.

The linear form represents the Freundlich adsorption model as follows:

$$\ln q_e = \ln K_F + \frac{1}{n} \ln C_e \quad (5)$$

where K_F (mg/g) and n are the Freundlich constants related to adsorption capacity and adsorption intensity respectively. The values of K_F and n (Table 1) were determined from the intercept and slope of the linear plot of ln qe versus ln C_e.

According to the results presented in Table 1, taking into consideration the values of the correlation factors (R^2), we deduce that. The adsorption isotherms of Co^{2+} ions by the two NaX and NaA zeolites are well represented by the Langmuir model, with maximum adsorption capacity values of 97.46 mg / g for the NaX zeolite and 90.91 mg / g for the NaA zeolite. It is known that any adsorption represented by the Langmuir model, is in monolayer and reflects a chemical phenomenon. Therefore, we can see that Cobalt adsorption by these two adsorbents is chemical in nature. The mechanism involved would be a monolayer adsorption involving identical and independent site.

Table 1. Results of the equilibrium isotherm models of NaX and NaA.

Text	Langmuir Parameters			Freundlich Parameters		
	$_m$ (mg/g)	(L/mg)	R^2	k_F	1/n	R^2
NaX	*97.46*	*1.020*	*0.9999*	*57.47*	*0.129*	*0.6962*
NaA	*90.91*	*0.794*	*0.9997*	*55.89*	*0.114*	*0.8948*

V. Conclusion

All the experiments and observations made in this work allow us to draw the following conclusions.

The development of different zeolites has made it possible to better understand the preparation steps and in particular to control the procedure for the preparation of different zeolites by hydrothermal route. Fauasite type zeolites X and A of starting molar 4,8 Na_2O 1 Al_2O_3 3,8 SiO_2 224 H_2O; and 1.1Na_2O ; 1Al_2O_3 ; 1.26 SiO_2 ; 92H_2O; respectively are obtained for 24h crystallization times and a heating temperature of 100 ° C and a cure time 24h and autogenous pressure. The use of aluminum in the form of isopropoxide Al $[(CH3)_2 CHO]_3$ has made it possible to obtain faujasite NaX and zeolite NaA. The spectra obtained by X-ray diffraction were compared with those of the literature. This comparison allowed us to identify the synthesized materials. Observation using scanning electron microscopy made it possible to determine the morphology as well as the grain size. The adsorption of Co^{2+} ions on the elaborated zeolites allowed us to study the influence of several physical parameters as the pH of the solution and the initial concentration of the metal ion. The adsorption experiments carried out in batch mode have shown that the zeolites produced are effective adsorbents for the removal of these metal ions. The adsorption rates obtained are: 97,79% (for 50 mg /L) in the case of the NaX zeolite. They are of the order of 98.70% in the case of the NaA zeolite. The modeling of adsorption isotherms of metal ions was undertaken using different models from the literature (Langmuir and Freundlich). The Langmuir model found a satisfactory correlation.

Acknowledgements

This work was financially supported by the Faculty of Mechanic and Engineering Process (USTHB, Algiers).

References

Abbas, M.; Kaddour, S.; Trari, M. (2014) Kinetic and equilibrium studies of cobalt adsorption on apricot stone activated. Journal of Industrial and Engineering Chemistry, 20(3), 745-751. https://doi.org/10.1016/j.jiec.2013.06.030.

Amokrane, S.; Rebiai, R.; Nibou, D. (2007) Behaviour of Zeolite A, Faujasites X and Y Molecular Sieves in Nitrogen Gas Adsorption. Journal of Applied Sciences, 7: 1985-1988. DOI: 10.3923/jas.2007.1985.1988.

Blanchard, G.; Maunaye, M.; Martin, G. (1984) Removal of heavy metals from waters by means of natural zeolites. Water research, 18(12): 1501-1507. https://doi.org/10.1016/0043-1354(84)90124-6

Breck, D.W. (1984) Zeolite molecular sieves: structure, chemistry and use;Krieger.

Fedailaine, M.; Berkani, S.; Trari, M. (2016) Ni^{2+} reduction under solar irradiation over $CuFe_2O$ 4/TiO_2 catalysts. Korean Journal of Chemical Engineering, 33(7): 2027-2033. https://doi.org/10.1007/s11814-016-0054-1

Glatz, J.-P. (2012) Spent fuel dissolution and reprocessing processes.

Habiba, U.; Siddique, T.A.; Lee, J.J.L.; Joo, T.C.; Ang, B.C.; Afifi, A.M. (2018) Adsorption study of methyl orange by chitosan/polyvinyl alcohol/zeolite electrospun composite nanofibrous membrane. Carbohydrate polymers, 191: 79-85. https://doi.org/10.1016/j.carbpol.2018.02.081

Helfferich, F. Ion exchange; Courier Corporation, 1962.

Izidoro, J.d.C.; Fungaro, D.A.; Abbott, J.E.; Wang, S. (2013) Synthesis of zeolites X and A from fly ashes for cadmium and zinc removal from aqueous solutions in single and binary ion systems. Fuel, 103: 827-834. https://doi.org/10.1016/j.fuel.2012.07.060

Khambhaty, Y.; Mody, K.; Basha, S. (2012) Efficient removal of Brilliant Blue G (BBG) from aqueous solutions by marine Aspergillus wentii: Kinetics, equilibrium and process design. Ecological Engineering, 41: 74-83. https://doi.org/10.1016/j.ecoleng.2012.01.002

Khemaissia, S.; Nibou, D.; Amokrane, S.; Lebaili, N. (2007) Elaboration and characterization of high silica ZSM-5 and mordenite solid microporous materials. Journal of Applied Sciences, 7(5): 720-723. DOI: 10.3923/jas.2007.720.723

Ltaief, O.O.; Siffert, S.; Fourmentin, S.; Benzina, M. (2015) Synthesis of Faujasite type zeolite from low grade Tunisian clay for the removal of heavy metals from aqueous waste by batch process: Kinetic and equilibrium study. Comptes Rendus Chimie, 18(10): 1123-1133. https://doi.org/10.1016/j.crci.2015.03.013

Nibou, D.; Mekatel, H.; Amokrane, S.; Barkat, M.; Trari, M. (2010) Adsorption of Zn^{2+} ions onto NaA and NaX zeolites: kinetic, equilibrium and thermodynamic studies. Journal of Hazardous Materials, 173(1-3): 637-646. https://doi.org/10.1016/j.jhazmat.2009.08.132

NIBOU, D. Doctoral thesis. USTHB, Alger, 1999.

Woumfo, D.; Kamga, R.; Figueras, F.; Njopwouo, D. (2007) Acid activation and bleaching capacity of some Cameroonian smectite soil clays. Applied Clay Science, 37(1-2): 149-156. https://doi.org/10.1016/j.clay.2006.12.008

IEEES-132

Development of a Dynamic t-CO2 Rankine Cycle Model with Heat Recovery System for Daily-Based Performance Assessment

[1]Tunahan Akış*, [1]Mehmet Akif Ezan, [1]Nuri Kayansayan, [2]Önder Kızılkan, [3]Çağla Cergibozan, [1]Can Özgür Çolpan
[1] Dokuz Eylül University, Engineering Faculty, Mechanical Engineering, Buca, İzmir, 35390, Türkiye
[2] Isparta University of Applies Sciences, Faculty of Technology, Mechanical Engineering, Bahçelievler, Isparta, 32200, Türkiye
[3] Dokuz Eylül University, Engineering Faculty, Industrial Engineering, Buca, İzmir, 35390, Türkiye
* E-mail: tunahan.akis@deu.edu.tr (Corresponding Author)

Abstract

This study performs the first-law and second-law analyses of a solar-assisted transcritical CO_2 (tCO_2) Rankine power cycle. The power cycle consists of five main components: (i) solar collector, (ii) turbine, (iii) condenser, (iv) pump and (v) heat recovery system. The cycle is modeled in the MATLAB environment and investigated with experimental solar irradiation values on a summer day in Izmir, Türkiye, and parametric analyses are performed. The output temperature of the flat plate solar collector has been calculated iteratively, and the input enthalpy values of the turbine are determined based on the measured pressure values in previous studies. In conclusion, the water outet temperature of heat recovery system, the thermal efficiency, second law efficiency, and total power generation of the cycle throughout the day are calculated.
Keywords: Rankine Cycle, Transcritical CO_2 Rankine Cycle, Solar Assisted CO_2 Power Cycle

I. Introduction

In line with climate change, which has recently come to the fore with global warming, research on the efficient use of energy resources and the tendency to use alternative energy sources are being attracted. Conventional power cycles used from the Industrial Revolution until today consume fossil fuels, and the products of this consumption create greenhouse gas effects (Hu et al., 2000). This situation has led researchers to examine alternative systems. Supercritical and transcritical carbon dioxide (sCO_2 - tCO_2) systems, an alternative power generation cycle, are among the alternatives mentioned. On the other hand, using solar thermal energy as an energy source in power generation systems is among the important topics discussed in the literature. Since the sun is an easily accessible and cost-effective thermal energy source, research on solar energy-assisted power generation systems has gained popularity in the last quarter century. The integration of solar energy into these systems is not limited to power generation cycles but is also addressed in cooling cycles. A detailed study of solar energy integration into this system can be found in (Mody et al., 2017).

Literature investigation shows that two CO_2 power cycle types are generally considered (White et al., 2021). In both cycles, the high-pressure value of the power cycle rises beyond the supercritical point, and the low-pressure value falls below the critical point only in transcritical cycles. The critical point pressure value for CO_2 is 7.38 [MPa]. For this reason, power cycles designed with CO_2 are called supercritical or transcritical cycles. This feature of CO_2 makes it possible to design an efficient power generation system. Because the amount of power that is consumed to reach the pressure level required to operate the turbine in the system is lower according to other working fluids (White et al., 2021). On the other hand, it is also possible to use it in low and medium-grade temperature applications (Yamaguchi et al., 2019). The literature discusses three types of analyses in power cycles that work with CO_2. The perspective of the first type of analysis is first law analysis, and it examines maximizing cycle performance. Studies that have achieved this have also dealt with second-law analyses in parallel and assessed the irreversibilities in the systems. Some studies have carried out Levelized Cost of Electricity (LCOE) analyses. Most studies that include first law analysis have directly included solar thermal energy in the cycle. In one of these studies (Song et al., 2012), the power generation cycle of the system used to cool the liquefied natural gas system is examined. The cycle is a transcritical CO_2 power generation cycle, and solar collectors provide the energy required to produce power. In addition, a thermal energy storage tank is used in the system to ensure the continuity and stability of the cycle. In the study, for conducting first law analysis, turbine inlet pressure, turbine inlet temperature, and condensation temperature are considered as key parameters, and cycle efficiency is examined. In another study (Yamaguchi et al., 2019), an experimental examination of a transcritical CO_2 power cycle was carried out by incorporating vacuum tube solar collectors into the cycle, and the system's performance in the summer and winter seasons was examined. First and second law analyses are carried out with the data obtained from the experimental system. There is also a heat recovery system in the system. The system's overall efficiency is achieved as 61.4% for wintertime and 37.2% for summertime. In parallel, the second law efficiency is calculated as 7.63% for summertime and 4.08% for wintertime. In the study, the other result is reported that the exergy destruction level of evacuated tube solar collectors is at a high level (96.32% in summer season, 93.58% in winter season) and showed that this situation negatively affected the cycle second law efficiency. Pan et al. (2019) conducted a theoretical study examining the tCO_2 power generation cycle integrated with the Rankine and Brayton cycles. They found the maximum thermal efficiency of the Rankine cycle 0.3463 and observed that it was 3% less than the Brayton cycle. They also reported that the thermal efficiency of the cycle showed a peak value at different cooling water inlet temperatures and, therefore, at different condensation temperatures, and they observed that this peak value occurred at 11 MPa condensation pressure. Sarimento et al. (2018) carried out parametric analyses of the solar energy-assisted tCO_2 Rankine cycle. They examined the regenerator and solar energy collector components in detail. As a result of parametric studies, they optimized the solar energy collector according to the maximum second law efficiency, and they determined the heat transfer area of the solar collector that produces minimum exergy destruction. Their findings reported that using regenerators increased the second law efficiency by 38.21%, which reduced the required solar collector surface area by 34.46%.

Current work aims to conduct first and second-law analyses of the solar energy-assisted tCO2 Rankine power cycle and examine the system's annual energy and exergy efficiency. A literature survey shows limited studies focus on parametric analyses of solar energy-assisted tCO_2 Rankine cycles. Many studies have emphasized that the second law efficiency of this cycle is low. This is basically because of the heat losses in solar collectors and collector efficiencies. The solar collector efficiency value is examined iteratively depending on the inlet and outlet temperatures, and the first and second law efficiency obtained from the cycle for a day is examined daily.

II. Model and Solution Method

In this study, the solar-assisted tCO2 Rankine cycle is examined parametrically. The system consists of five main components: (i) Solar collector, (ii) Turbine, (iii) Heat recovery system, (iv) Condenser, and (v) Pump. The schematic representation of the system is given in Fig. 1(a). The pump pressurizes the liquid CO_2 (1), and supercritical high-pressure CO_2 gains energy from the solar collector and becomes the supercritical-state before entering the turbine (2). CO_2 expands in the turbine (3), generating mechanical power through the shaft and leaving the turbine in the supercritical state. CO_2 then enters the heat recovery system (HRS) to produce hot process water. In this way, the system is able to produce hot water and recovers some of the heat that the condenser needs to reject. CO_2 leaves the HRS (4), condenses in the condenser, and returns to the pump (5). A representative T-s diagram of the cycle is given in Fig. 1 (b). Validation of the analysis with literature is given separately for winter and summer seasons in Figs. 1(c-d) .The equations required to perform the energy and exergy analyses are given in Table 1.

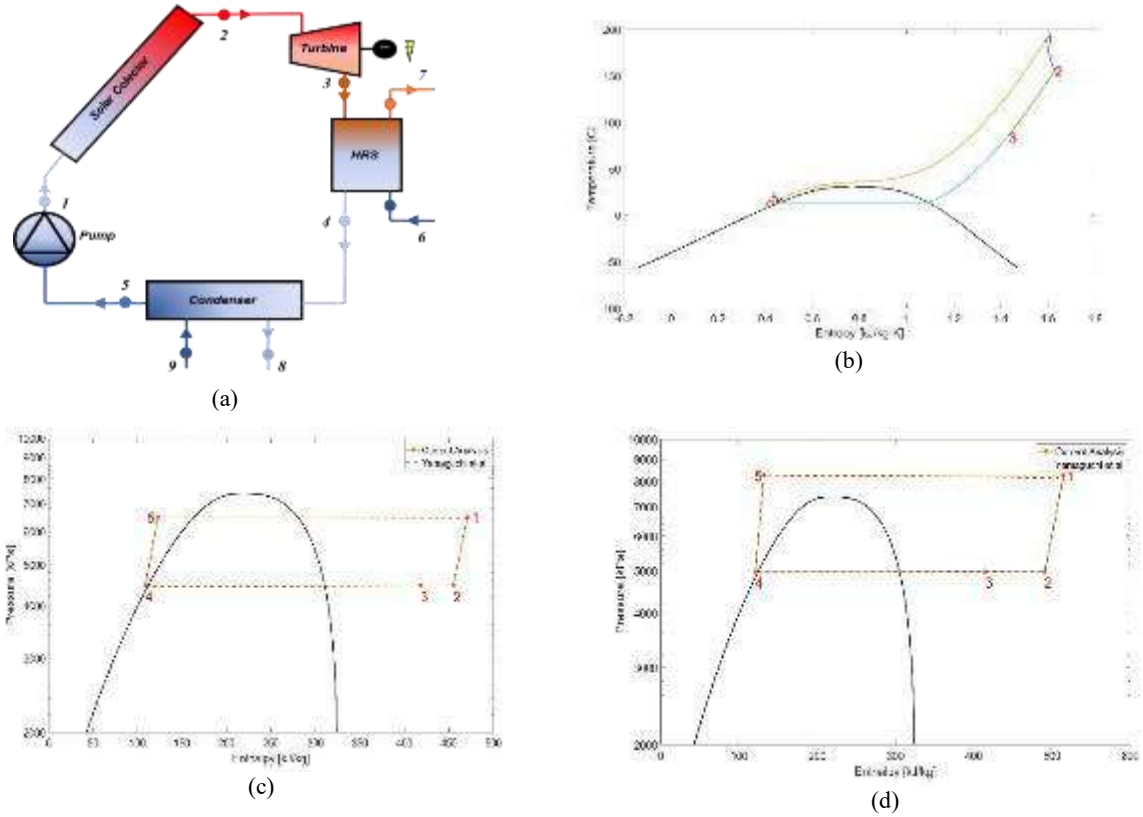

Fig. 1: (a) Schematic Diagram of Solar Assisted tCO_2 Rankine Cycle, (b) Representative T-s diagram of the cycle, (c) Validation on winter season of analysis, (d) Validation on summer season of analysis

Table 1. Balance equations for power cycle components

Component	1st-Law	2nd-Law
Turbine	$\dot{W}_t = \dot{m}_{ref}\,(h_3\text{-}h_2)$	$\dot{E}x_{dest,t} = \dot{m}_{ref}(h_1\text{-}h_2\text{-}T_0(s_1\text{-}s_2))\text{-}\dot{W}_t$
HRS	$\dot{Q}_{HRS} = \dot{m}_{ref}\,(h_4\text{-}h_3)$	$\dot{E}x_{dest,HRS} = \text{-}\dot{m}_{ref}\,\Delta\psi_{ref}\text{-}\dot{m}_w\,\Delta\psi_w$
Condenser	$\dot{Q}_c = \dot{m}_{ref}\,(h_5\text{-}h_4)$	$\dot{E}x_{dest,c} = \text{-}\dot{m}_{ref}\,\Delta\psi_{ref}\text{-}\dot{m}_w\,\Delta\psi_w$
Pump	$\dot{W}_p = \dot{m}_{ref}\,(h_1\text{-}h_5)$	$\dot{E}x_{dest,p} = \dot{m}_{ref}(h_4\text{-}h_5\text{-}T_0(s_4\text{-}s_5))\text{-}\dot{W}_p$
Solar Collector	$\dot{Q}_s = \dot{m}_{ref}\,(h_2\text{-}h_1)$	$\dot{E}x_{solar} = G_T A\left(1+\frac{1}{3}\left(\frac{T_0}{T_{sun}}\right)^4 \text{-}\frac{4}{3}\left(\frac{T_0}{T_{sun}}\right)\right)$

Solar collector efficiency curves taken from Gomariz et al. (2019) are used to determine the efficiency as a function of the inlet and outlet temperatures of the working fluid, ambient air, and instantaneous solar radiation, and an iterative procedure is coded to evaluate the state properties with the efficiency of the collector. For the current analysis, 15 flat plate solar collectors with a heat transfer surface area of 0.64 m^2 are considered. The generalized form of energy efficiency is defined by Gomariz et al. (2019) as

$$\eta = \eta_0 - \frac{k_1(T_m - T_a)}{G_T} - \frac{k_2(T_m - T_a)^2}{G_T} \quad (1)$$

where η_0 is the reference efficiency, T_m is the average CO_2 temperature inside the solar collector, T_a is the outdoor air temperature and G_T is the instantaneous solar radiation value in W/m^2. Hourly average solar irradiation data is obtained from meteorological data for Izmir, Türkiye. For determining the pressure at the turbine outlet, a constant expansion ratio is defined in Eq. 2 is used to determine the outlet pressure of the fluid in the turbine,

$$R_t = \frac{P_{high}}{P_{low}} \quad (2)$$

where P_{high} and P_{high} are high and low pressures of the working fluid. The heat recovery system is analyzed with the epsilon-NTU method. In the first step, the possible maximum capacity values in the system is calculated with the approach given in Eq. 3.

$$\begin{aligned} \dot{Q}_1 &= \dot{m}_{ref}(h_4 - h_3), \text{assume } T_3 = T_7 \\ \dot{Q}_2 &= \dot{m}_{w\_HRS}(h_7 - h_6), \text{assume } T_4 = T_6 \\ Q_{max} &= \min(Q_1, Q_2) \end{aligned} \quad (3)$$

By taking into account the smaller of the two separate Q values calculated with Eq. 3, the outlet temperatures on the CO_2 and water side can be determined with Eq. 4.

$$\epsilon_{HRS} = \frac{\dot{m}_{ref}(h_4 - h_3)}{\dot{Q}_{max}} = \frac{\dot{m}_{w,HRS}(h_7 - h_6)}{\dot{Q}_{max}} \quad (4)$$

Here ϵ_{HRS} is the effectiveness value of the exchanger.1st law and 2nd law efficiencies are through the following equations (Yamaguchi et al., 2019):

$$\eta_{cycle} = \frac{\dot{W}_t + \dot{Q}_{HRS}}{\dot{W}_p + \dot{Q}_s} \quad (5)$$

$$\epsilon_{cycle} = \frac{\dot{W}_t + \dot{m}_{w,HRS}\,\Delta\psi_{w,hrs}}{\dot{E}x_{solar} + \dot{W}_p} \quad (6)$$

The parameters required to perform the first law analysis are given in Table 2.

Table 2. Input Values

Parameter	Unit	Value
Turbine inlet Pressure	MPa	8.15
R_t	-	1.64
HRS Water Inlet Temperature	°C	70
Condenser Water In. Temperature	°C	8
Turbine Isentropic Efficiency	%	61.8
Pump Isentropic Efficiency	%	35.4
Condenser Water Mass Flow Rate	kg/s	0.2
HRS Water Mass Flow Rate	kg/s	0.01
Outdoor Temperature	K	303
Sun Surface Temperature (Petala, 2005)	K	5739

IV. Results and discussion

Fig. 2 shows the results of the analyzed power cycle. The thermal efficiency of the cycle decreases with increasing CO_2 mass flow rate, and the maximum efficiency value is determined as 29.7% for a mass flow rate of 0.0025 kg/s CO_2 around noon (Fig. 2(a)). On the contrary, the second law efficiency of the cycle increased with increasing mass flow rate, and its maximum value is determined as 1.6% for a mass flow rate of 0.004 kg/s CO_2 around 7 am in the morning (Fig. 2(b)). Outlet water temperatures in the heat recovery exchanger can be seen at different times for different mass flow rates at Fig. 2(c). The system can produce hot water for a mass flow rate of 0.004 kg/s CO_2, with a maximum temperature difference of 8 °C around noon. As can be seen in Fig. 2(d), the system produces a maximum power of 92.3 W at around noon for a CO_2 mass flow rate of 0.004 kg/s.

V. Conclusions

A pseudo-transient model is developed for a solar collector integrated t-CO2 Rankine cycle. Concluding remarks are listed below:

- Transcritical CO_2 power cycles are promising and can replace traditional power generation systems with similar or improved efficiency values.
- The efficiency of the system increases with increasing solar radiation values. The current study determines the maximum thermal efficiency value to be 29.7%. The system's efficiency can be further increased by improving the efficiency of solar collectors.

- Due to the intermittent nature of the solar power, the system examined in the current study operates between 7 am and 5 pm in the conditions of Izmir City, Türkiye. Thermal energy storage mechanisms can be included in the cycle in order for the system to operate continuously.

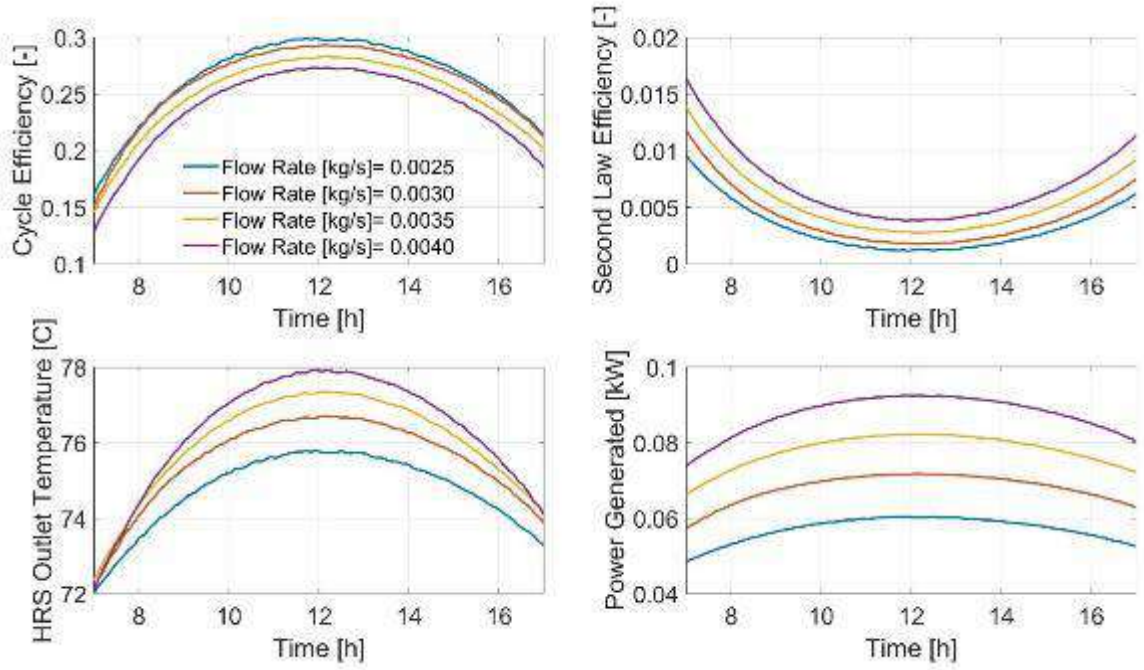

Fig. 2: Results of Solar Assisted tCO_2 Rankine Cycle, (a) T-s diagram, (b) Thermal efficiency of the cycle during the day, (c) Heat Recovery System Water Outlet Temperature, (d) Generated Power

References

Hu Y, Naito S, Kobayashi N, Hasatani M. CO2, NOx and SO2 emissions from the combustion of coal with high oxygen concentration gases. Fuel. 2000;79(15):1925-1932

Modi A, Bühler F, Andreasen JG, Haglind F. A review of solar energy based heat and power generation systems. Renewable and Sustainable Energy Reviews. 2017;67:1047-1064

White, M. T., Bianchi, G., Chai, L., Tassou, S. A., & Sayma, A. I. (2021). Review of supercritical CO2 technologies and systems for power generation. Applied Thermal Engineering, 185, 116447.

Yamaguchi, H., Yamasaki, H., & Kizilkan, O. (2020). Experimental investigation of solar-assisted transcritical CO2 Rankine cycle for summer and winter conditions from exergetic point of view. International Journal of Energy Research, 44(2), 1089-1102.

Song, Y., Wang, J., Dai, Y., & Zhou, E. (2012). Thermodynamic analysis of a transcritical CO2 power cycle driven by solar energy with liquified natural gas as its heat sink. Applied energy, 92, 194-203.

Pan L, Li B, Shi W, Wei X. Optimization of the self-condensing CO2 transcritical power cycle using solar thermal energy. Applied Energy. 2019;253:113608.

Sarmiento C, Cardemil JM, Díaz AJ, Barraza R. Parametrized analysis of a carbon dioxide transcritical Rankine cycle driven by solar energy. Applied Thermal Engineering. 2018;140:580-592.

Gomariz, F. P., López, J. M. C., & Munoz, F. D. (2019). An analysis of low flow for solar thermal system for water heating. Solar Energy, 179, 67-73.

Petela R. Exergy analysis of the solar cylindrical-parabolic cooker. Solar Energy. 2005;79(3):221-233.

IEEES-133

Thermodynamic analysis of the parabolic dish collector based hydrogen production system

[1*]Arif Karabuga, [2]Zafer Utlu
[1] Sustainable Energy Systems Application and Research Center, Haliç University, 34445, Istanbul, Turkey
[2] Faculty of Engineering, Mechanical Engineering, Haliç University, 34445, Istanbul, Turkey

* E-mails: arif.karabuga@gmail.com

Abstract
In this study, the energy analysis of the parabolic dish solar collector (PDSC) supported hydrogen production system, where solar energy is used for green hydrogen production, is presented. To benefit from solar energy, a PDSC with a 1.54 m2 opening is used, an organic Rankine cycle (ORC) with a capacity of 1 kW is used for electricity production, and a proton exchange membrane (PEM) electrolyzer is used for hydrogen production. As a result of thermodynamic analysis, ORC and the energy efficiency of the entire system were calculated as 32.93% and 3.54%, respectively.

Keywords: Hydrogen production, Parabolic dish collector, ORC

I. Introduction

To cope with the global climate crisis, countries are basing their energy policies on decarbonization. Hydrogen, considered as an energy carrier, is a prominent alternative for countries' decarbonization policies. For this reason, R&D and P&D studies on hydrogen attract great attention. In particular, hydrogen production obtained by splitting water using renewable energy sources, in other words green hydrogen production, is of critical importance for decarbonization policy. In recent years, there has been a significant increase in the number of studies addressing solar energy-supported hydrogen production, which is a type of renewable energy. The hydrogen production system from ammonia using various collectors to utilize solar energy was studied by (Andriani and Bicer, 2023). A road map for hydrogen production as an alternative to natural gas for clean energy or decarbonization targets has been put forward. Technical, economic and environmental review of the green hydrogen production system from various renewable energy sources such as wind and solar is presented by (Garcia and Oliva, 2023). As a result of the study, it was found that the cost of hydrogen production was between 2.09$/kgH2 - 3.28$/kgH2. In the study prepared by (Bozgeyik et al. 2023), they presented the energy, exergy, economic and environmental analysis of the multi-energy production system by utilizing different renewable energy sources. In the study, hydrogen, electricity, heating, cooling and fresh water were produced using solar, geothermal and biomass. As a result of the study, electricity production, hydrogen production, energy and exergy efficiency of the system were calculated as 7.76 MW, 3.52 kg/h, 65.55% and 27.09%, respectively.

The main purpose of this study is to experimentally examine the thermodynamic analysis of PDSC-assisted electricity and hydrogen production. It is aimed to determine the parameters that affect the energy efficiency and hydrogen production of the entire system and to reveal ideal operating conditions.

II. System Description

In this study, the PDSC supported electricity and hydrogen production system is examined experimentally. It is covered with a stainless steel metal reflective surface with a mouth opening of 1.54 m2. Radiation from the sun is focused on a point between 1000-3000 times, depending on the radiation intensity. R134a working fluid is used in the receiver tank located at the focal point. The fluid temperature at the PDSC outlet was measured as 113°C (point 2) and the thermal energy obtained from the collector enters the turbine directly. At the turbine exit (point 3), the fluid is cooled with air through the condenser. The temperature difference in the condenser is measured as approximately ΔT=45°C. At the condenser exit, the fluid enters the pump in liquid phase (point 4). Turbine capacity is measured as approximately 1.5 kW. The electricity obtained from the turbine is used in the proton exchange membrane (PEM) electrolyzer for hydrogen production.

It enters the purification system used to prevent clogging of the electrolyzer pores in hydrogen production. Ultrapure water is used in the PEM electrolyzer. Figure 1 shows the flow chart of the PDSC based electricity and hydrogen production system. Table 1 gives the design parameters of the system.

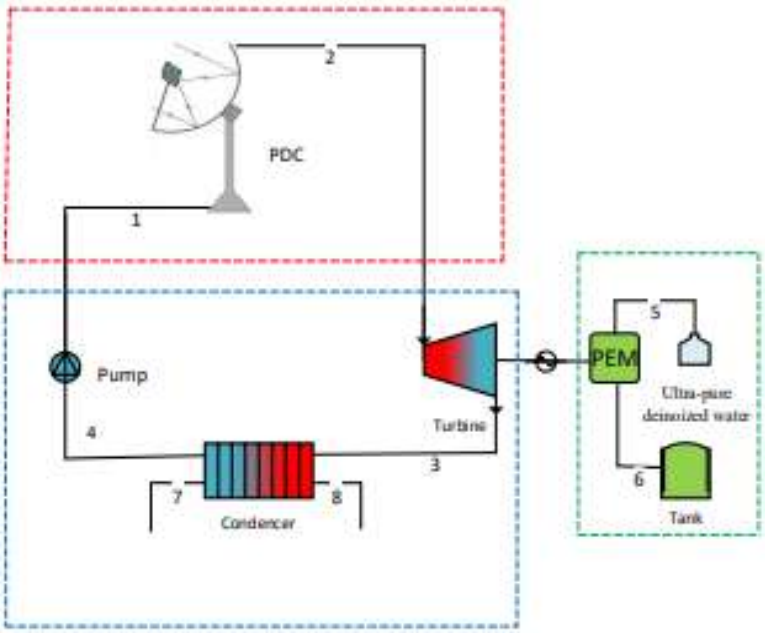

Fig. 1:PDSC based hydrogen production system

Table 1. Design parameters of the PDSC based hydrogen production system

Parameter	Value
PDSC area	1.54 m^2
Working fluid	R134a
PDSC output temperature	90-130°C (constant 113°C)
PDSC output pressure	28 bar
PDSC input temperature	53°C
ORC mass flow rate	0.03 kg/s
Isentropic efficiency of turbine	0.87

III. Analysis

The equilibrium equations used for the thermodynamic analysis of the experimental system examined in this section are given below. The presented PDSC based hydrogen production system inculed of three main parts. These are PDSC, ORC and PEM electrolizer. The first laws of thermodynamics are applied to each component in these three parts with a holistic approach. Engineering equation solver (EES) software is used for thermodynamic analysis and graphs are obtained depending on the results of this analysis.Bir sistemin verimliliğinin hesaplanabilmesi için termodinamiğin birinci yasası olan enerji analizi yapılmalıdır (Utlu and Hepbasli, 2010; Sogut and Erdogan, 2022). The energy balance equations applied to the PDSC based hydrogen production system are given below (Sorgulu and Dincer, 2023);

$$\sum \dot{m}_{in} = \sum \dot{m}_{out} \tag{1}$$

$$\dot{Q}_{in} + \dot{W}_{in} + \sum(\dot{m}_{in} h_{in}) = \dot{Q}_{out} + \dot{W}_{out} + \sum(\dot{m}_{out} h_{out}) \tag{2}$$

$$\dot{Q}_U = A_c F_R [I\varepsilon\rho - U_L(T_{in} - T_{amb})] \tag{3}$$

$$\dot{Q}_{solar} = IA\varepsilon\rho \tag{4}$$

$$\eta_{col} = \frac{\dot{Q}_U}{\dot{Q}_{solar}} \tag{5}$$

where $\dot{m}$ is the mass flow rate (kg/s), h is the specific enthalpy (kJ/kg), s is the specific entropy (kJ/kg K), $\dot{Q}$ is the heat transfer rate (kW), $\dot{W}$ is the work rate (kW), T is temperature (°C), A is PDSC area (m^2), F is the removal factor and η is the energy efficiency. Furthermore, subscripts in, out, U and amb is input, output, usefull heat and ambient, respectively.

IV. Results and discussions

The results of the presented study and thethermodynamic analysis evaluation of the solar-assisted hydrogen production have been discussed in this section. The experiments have been carried out for different parameters considered under different solar radiations and collector output temperature conditions. Furthermore, this section presents the energy efficiency of the investigated solar-based hydrogen production system. In addition, parametric analyses are presented to investigate the solar radiations and collector output temperature conditions, which are effective on the whole system's performance. In Figure 2, energy efficiency and hydrogen production amount values are shown depending on the PDSC outlet temperature. If the collector outlet temperature changes between 60°C-150°C, the change in the energy efficiency obtained from the whole system and hydrogen production amount is shown. It is observed that there is a remarkable resonance in the energy efficiency and hydrogen production amount of the entire system depending on the increase in the PDSC outlet temperature. While a notable increase is recorded between the collector outlet temperature between 80°C and 95°C, a notable decrease is observed at temperatures above 95°C.

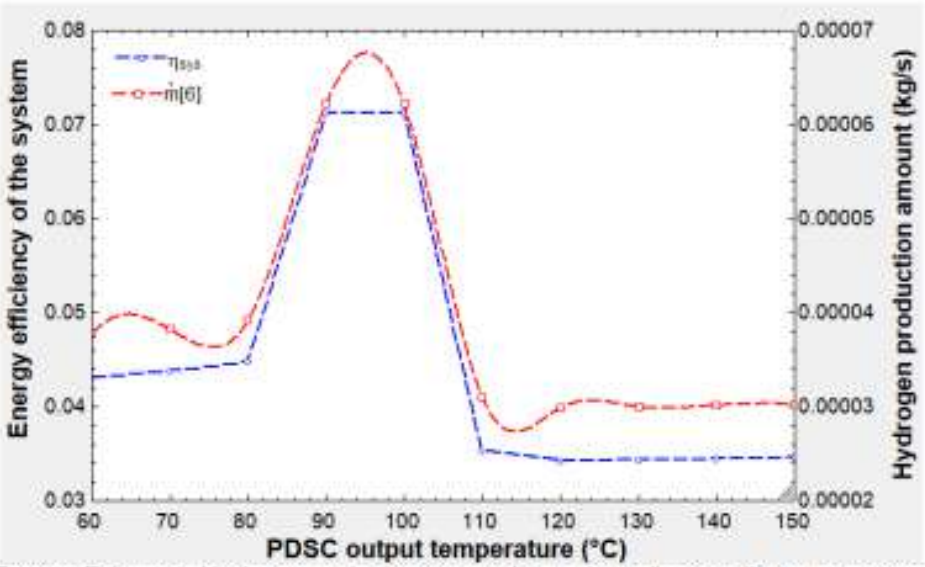

Fig. 2. Energy efficiency and hydrogen production amount change depending on collector output temperature

Thermodynamic analysis results obtained as a result of the study are given in table 2. As a result of the analysis, collector capacity, turbine capacity and electrolyzer capacity were calculated as 2.788 kW, 0.929 kW and 0.918 kW, respectively. In addition, the hydrogen production amount was measured as 0.000031 kg/h and the energy efficiency of the system was measured as 3.54%. Of the amount of work obtained from the turbine, 0.01093 kW is consumed as pump work. If pump consumption increases, the net amount of work to be achieved decreases.

Table 1. Thermodynamic results of the present study

Component	Result
PDSC capacity	*2.788 kW*
Pump capacity	*0.01093 kW*
Turbine capacity	*0.929 kW*
PEM electrolizer capacity	*0.9181 kW*
Energy efficiency of the ORC	*%32.9*
Energy efficiency of the whole system	*%3.54*
Hydrogen production amount	*0.000031 kg/s*

V. Conclusions

In this study, the experimental analysis of the PDSC solar collector system integrated hydrogen generation system is investigated. The thermodynamic analysis of the system designed according to the actual operating conditions is discussed. The important results obtained in the study are presented below;

- The energy efficiency of PDSC is calculated as 9.278%.
- The energy efficiency of the ORC system is calculated as 32.93%.
- The energy efficiency of the turbine is measured as 0.929 kW.
- According to the actual operating conditions, the energy efficiency of the whole system is calculated as 3.549% respectively.

References

Andriani, D., Bicer, Y., 2023. A Review of Hydrogen Production from Onboard Ammonia Decomposition: Maritime Applications of Concentrated Solar Energy and Boil-Off Gas Recovery. Fuel 352, 128900. https://doi.org/10.1016/j.fuel.2023.128900

Garcia, M.G., Oliva, S.H., 2023. Technical, economic, and CO2 emissions assessment of green hydrogen production from solar/wind energy: The case of Chile. Energy 278 (Part B), 127981. https://doi.org/10.1016/j.energy.2023.127981

Bozgeyik, A., Altay, L., Hepbasli, A., 2023. Energetic, exergetic, exergoeconomic, environmental and sustainability analyses of a solar, geothermal and biomass based novel multi-generation system for production of power, hydrogen, heating, cooling and fresh water. Process Safety and Environmental Protection 177, 400-415. https://doi.org/10.1016/j.psep.2023.07.018

Utlu, Z., Hepbasli, A., 2010. Comparison of Turkey's Sectoral Energy Utilization Efficiencies between 1990 and 2000, Part 1: Utility and Industrial Sectors. Energy Sources 26, 1331-1344. https://doi.org/10.1080/00908310490441629

Sogut, M.Z., Erdogan, O., 2022. An investigation on a holistic framework of green port transition based on energy and environmental sustainability. Ocean Engineering 266(Part 3), 112671. https://doi.org/10.1016/j.oceaneng.2022.112671

Sorgulu, F., Dincer, I., 2023. A solar energy driven thermochemical cycle based integrated system for hydrogen production. Energy 269, 126834. https://doi.org/10.1016/j.energy.2023.126834

IEEES-134

Smart micro-grids as improving solution for supplying agriculture farms

H. Belmili[1], S. Boulouma[1], L. Baghli[2], B. Bendib[1], A. Mecharnane[3]
N. Kibir[4], R. Cheikh[1], Abdelilah Rochd[5]
[1]Unité de Développement des Équipements Solaires, UDES, Centre de Développement des Énergies Renouvelables, CDER, 42415, Tipaza, Algérie, Hocine.belmili78@gmail.com, h.belmili@cder.dz
[2]Université de Lorraine, GREEN, F54000 Nancy, France, Lotfi.Baghli@univ-lorraine.fr
[3]Université de Tlemcen, LAT (UT), Tlemcen, Algérie, mechernene_aek@hotmail.com
[4]MicroEnergy International GmbH, Germany, noara.kebir@microenergy-consulting.com
[5]Green Energy Park IESI Lab, ENSET Mohammedia Benguerir, Morocco, rochd@greenenergypark.ma

Abstract:
This paper presents a pilot study to supplying agriculture farms with stand-alone micro-grids (MG). Actually, micro-grids based on renewable energy resources have recently emerged as a very interesting solution for different domains. Agriculture is one of these domains that is meant to be supplied with MGs. The objective is to develop smart MG based on the production of renewable energy in order to support the sustainable development nexus based on the three sectors: energy, water and agriculture. The power transported through this MG will be used for water pumping, irrigation systems, and for supplying farm loads. Low-cost solar water pumps, photovoltaic (PV) systems and energy storage batteries will be combined in this new system. The management and optimization of the operation will be carried out by an intelligent control system based on artificial intelligence. The power of the PV generator, the batteries and the volume of the water storage tank will be sized according to the overall energy consumption of the area. Field sensors and weather stations will be involved in order to have quantitative data stored in databases and used for the study. The control and optimization will be based on smart solutions. The use of the internet of things (IoT) is a critical feature for monitoring, supervising, and performance evaluation of this MG and in best practice agriculture activities. Furthermore, it improves the long-term viability, efficiency, control the energy flow, water management and maintenances facilities.

Keywords: *Smart micro-grids, agriculture, artificial intelligence, water pumping, irrigation systems, IoT.*

I. Introduction:

In many areas, particularly the Algerian Sahara Desert, the lack of access to dependable and sustainable energy sources in rural farming communities has been a huge problem. This problem not only has an impact on food security and agricultural output, but it also has a negative impact on the possibility for rural economic growth (SDG, 2023). The MG-FARM project was started to construct smart microgrids based on renewable energy sources that are specifically made to promote the sustainable growth of the energy, water, and agricultural sectors in order to meet this challenge (mgfarm, 2023). Using specially designed microgrids systems that can adjust to load profiles and storage methods. The ideal of microgrids remote area farms is a critical research subject that must be addressed in this situation. This study proposal's goal is to look at the design and optimization of micro-grids for farming operations in the Algerian Sahara Desert, and remote areas, with a particular emphasis on how big the micro-grid should be to accommodate the energy requirements of contemporary and sustainable agricultural techniques. This study will explore the possibilities of renewable energy sources for rural economic development while also bridging the gap between electricity availability and food security. Additionally, this research will produce solutions for farmers, stakeholders, and rural communities that are both commercially viable and environmentally sustainable. The literature on micro-grids, renewable energy, and sustainable agriculture practices will be reviewed as part of this study project. Fieldwork in Saharan farms, data collection on energy use and weather patterns are all part of the research technique.

II. Water-Energy-Food Nexus: Implications and Interdisciplinary Approaches

The complex interdependence between water, energy, and food systems, often referred to as the "Water Energy-Food Nexus," highlights the necessity of an integral approach to sustainable agriculture. Recognizing the linked nature of these three essential sectors, the Nexus approach stresses the need for collaborative and inter-disciplinary efforts in decision-making, especially within the realm of sustainable farming. Given the importance of this integrated approach, sustainable agricultural practices can be best understood through a sequential interdisciplinary methodology (SDG and economy, 2023).
At first, the Determination of optimal crops for the specific region's soil and climate conditions. This step is foundational, ensuring that subsequent decisions align with the agricultural potential of the region. As their outcomes is the identification of the most suitable crops and an understanding of their water requirements (Filza Fatima Rizvi,

2020). Secondary, Hydraulics/Water Engineering Role as once the crops and their water needs are established, the next step involves designing irrigation systems that efficiently cater to these demands, taking into consideration local water availability (Manjari Sharma, 2019). As consequences an optimal design of irrigation infrastructure, selection of appropriate pumps, and other relevant hydraulic systems. At last, the energy engineering roles, that working in accordance with the hydraulic requirements in place, energy engineering comes into play to meet the energy demands of these systems and other farm operations. So, like outcomes, the designing of microgrids and/or energy system that ensures consistent, sustainable power to meet the farm's requirements (Liang Tao, 2011 and Y.J. Acosta-Silva, 2019).

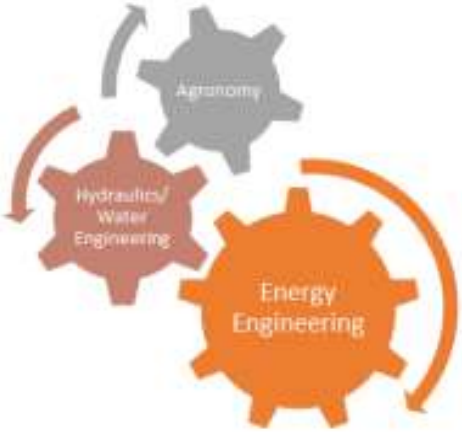

Fig. 1. The Integrated approach for sustainable agricultural practices

III. Case Study: Algeria Pilot Farm Experimental practices

Situated in the heart of Algeria's agricultural belt, the UDES Pilot Farm, situated in Cherchell, Algeria, represents a nexus of traditional farming practices and emerging energy solutions. Selected for its emblematic representation of Algerian farms and its potential for sustainable transformation, the Cherchell Pilot Farm serves as a pertinent case study for this research. The primary goal of the UDES pilot farm is to amplify and refine agricultural support mechanisms through the integration of PV solar energy production, advanced energy storage, and effective water management techniques. This paradigm not only aligns with top-tier agricultural practices but also heralds the incorporation of new entrepreneurial avenues within the agrarian sector. The introduction of digitized microgrids and smart storage systems within this farm endeavors to establish a blueprint for Algerian farmers contemplating similar transitions (Hakim Azoug, 2021), the figure 2 gives a photo and the satellite view of the farm. Acting as a pivotal resource, the pilot farm illuminates innovative pathways for Algerian agriculturists, proffering insights into avant-garde water and energy consumption and storage strategies. The assessments emanating from this locale elucidate the multifaceted challenges inherent in the chosen case studies. Furthermore, they demarcate prospective solutions meriting deeper exploration within this project's ambit (Saba, D., 2015). A holistic appraisal of optimal strategies to counter these challenges will be rigorously dissected, culminating in actionable recommendations and transformative strategies for enhanced agricultural modalities.

The components of this pilot farm include:

- 05 kW to supplying: water pumping and automated drip irrigation system,
- 08 kW to the electrification of: a multi-span greenhouse, a small cold storage room system, lighting and all powering farm electrical equipment, through a central inverter.
- Technical local: for data acquisition and control based (IoT and IA) technology.
- 06 KVA backup diesel generator.

Fig. 2. Pilote farm Activities around solar PV power plant

IV. MGFARM platform

Smart farms use modern technologies such as the Internet of things (IoT), artificial intelligence (AI), and renewable energy (RE) based microgrids to enhance productivity, reduce costs, and minimize environmental impact. In the context of the MGFARM, the pilot farms situated in Algeria and Morocco mainly focus on renewable energy systems, which provide clean, reliable, and sustainable energy for farms. However, microgrids require efficient monitoring and supervision to ensure optimal performance, energy flow, reliability, and safety. In addition, irrigation, greenhouse, and crops have several parameters that need to be supervised and monitored to ensure optimal production and water efficiency in the whole farm. This report provides an overview of monitoring and supervision strategies in the framework of MGFARM.

In the frame of the MGFARM project, one of the main objectives is to develop a sophisticated and holistic platform for being adopted by different farmers. The platform (figure 5) consists of a closed-loop system where real-time soil and crop sensing, weather conditions, as well as predictive water map, drive the pumping and irrigation process. Test sites will be set-up, up as living laboratories, using solar-powered pumps and sensors for extracting different factors, such as soil salinity, temperature, humidity, wind speed and direction, and solar radiation to compute and predict the volume of water required by crops, expect generated solar energy and then optimize pumping/irrigation schedules accordingly. A geographical water map overplayed by the prediction of renewable energy production will be used to develop better water pumping/irrigation schedules. In summary, the major goals are:

- *Develop and deploy the sensors (i.e., SW/HW solutions) that measure and extract accurate data (i.e., measurement of soil properties) within-field conditions,*
- *Sensors' placement (e.g., location and number) taking into consideration the field variability, which is required to establish the prescription map,*
- *Investigate the best suitable technologies to be used for data communication, in particular for the irrigation system monitoring and water rates control,*
- *Design and develop an embedded decision-support software tool, which can accomplish data sensing and data processing/aggregation, and input rate adjustment in real-time while preserving high precision,*
- *Develop and integrate a green energy solution (e.g., solar photovoltaic) into the irrigation system to power all power-hungry devices and equipment.*

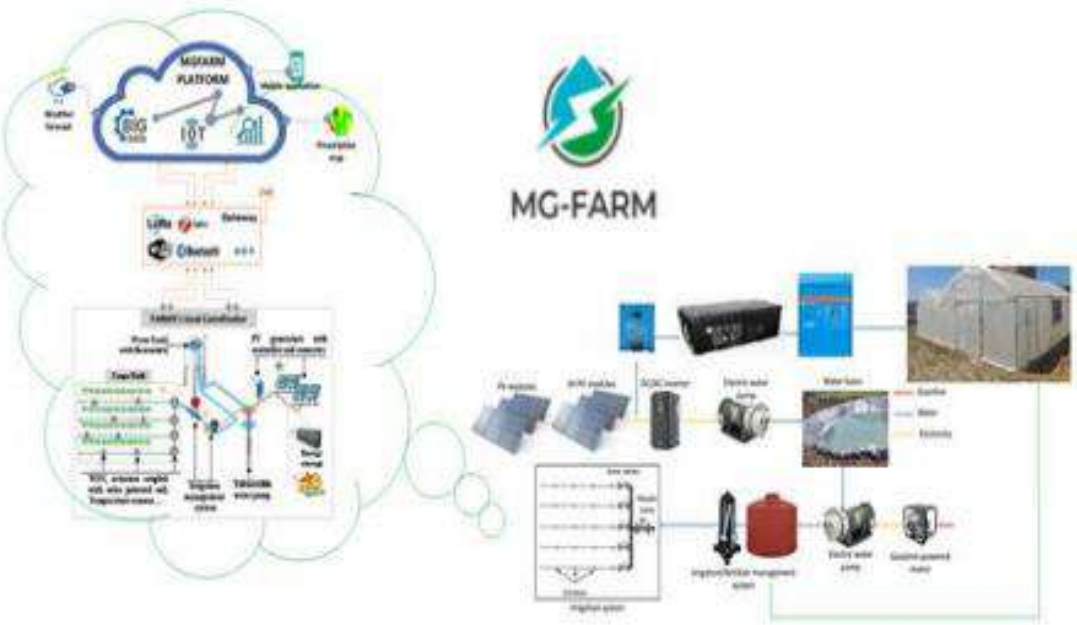

Fig. 3. MGFARM holistic platform

1. **Sensor-based Monitoring:** *Sensor-based monitoring involves the use of sensors to collect data on the performance of renewable energy systems. For instance, sensors can be installed to monitor the energy output of solar PV panels, wind turbines, or micro-hydro generators. Sensors can also monitor the temperature, humidity, and other environmental factors that affect the performance of renewable energy systems. The data collected by sensors can be used to identify potential problems, optimize system performance, and ensure safety.*
2. **Wireless Monitoring:** *Wireless monitoring involves the use of wireless sensors and communication systems to transmit data to a central monitoring system. Wireless sensors can be installed in different locations to monitor the performance of renewable energy systems. The data collected by wireless sensors can be transmitted to a central monitoring system via wireless communication systems such as Wi-Fi, Bluetooth, or Zigbee. Wireless monitoring systems can provide real-time data on the performance of renewable energy systems, which can be used to detect faults, optimize system performance, and ensure safety.*
3. **Cloud-based Monitoring:** *Cloud-based monitoring involves the use of cloud computing to store and analyze data from renewable energy systems. Data from sensors or wireless monitoring systems can be transmitted to a cloud-based platform where it is stored, analyzed, and visualized. Cloud-based monitoring systems can provide real-time data on the performance of renewable energy systems, which can be accessed remotely by farmers, technicians, or managers. Cloud-based monitoring systems can also use machine-learning algorithms to analyze data and predict potential problems or faults.*

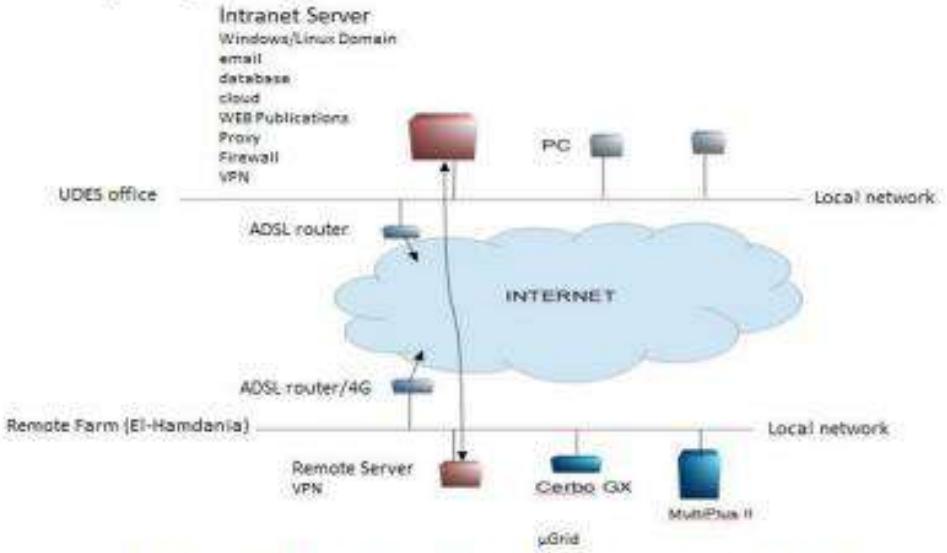

Fig. 4. MGFARM and the ITC uses to control and collect data from remote area.

V. Conclusion

Around this project MGFARM, that presented briefly in this paper, we have to make research, development, deployment, and integration of the micro-grids and the new smart technologies based on renewable energy solutions by the application of modern photovoltaic panels, new irrigation techniques, and water extraction by solar pumping, also new controls and management techniques, to economize in the same time the energy and the water. Consequently, the MGFARM is a nexus water-energy-agriculture, which is a solution that permits the promotion of sustainable social practices to the local population (water management, energy efficiency). This nexus solution is based on smart technics to water and electricity intelligent management and storage.

Acknowledge

LEAP-RE *MG-FARM project is part of the LEAP RE programme. LEAP RE has received funding from the European Union's Horizon 2020 Research and Innovation Program under Grant Agreement 963530.*

References

SDG. 2023. https://sdgs.un.org/goals.

https://www.leap-re.eu/mg-farm/, 2023.

Agriculture takes up food security challenge of independent Algeria. 2023, https://www.aps.dz/en/economy/44284-agriculture-takes-up-food-security-challenge-of-independent-algeria.

Filza Fatima Rizvi et al. "Review of Energy Consumption and Potential of Renewable Energy in Agriculture Sector: A Case Study of Pothohar Region of Pakistan". Pakistan Journal of Agricultural Research (2020). doi: 10.17582/journal.pjar/2020/33.2.280.288.

Manjari Sharma and Samiksha Mehra. "Advanced Irrigation System Using Solar Energy and Pivot Control Panels". Invertis Journal of Renewable Energy (2019). doi: 10.5958/2454-7611.2019.00022.5.

Liang Tao et al. "From laboratory Microgrid to real markets — Challenges and opportunities". 8th International Conference on Power Electronics - ECCE Asia (2011). doi: 10.1109/icpe.2011.5944600.

Y.J. Acosta-Silva et al. "Applications of solar and wind renewable energy in agriculture: A review:" Science Progress (2019). doi: 10.1177/0036850419832696.

Hakim Azoug, Hocine Belmili, Grid-connected control of (PV-Wind) Hybrid Energy System, International Journal of Power Electronics and Drive Systems (IJPEDS), Vol 12, No 2: June 2021.

Saba, D., Laallam, F.Z., Belmili, H., Hadidi, A.: Contribution of renewable energy hybrid system control based of multi agent system coordination. In: The Symposium on Complex Systems and Intelligent Computing, CompSIC 2015.

IEEES-135

Comparative Evaluation of Solar Exergy Models for Various Regions in Turkey

[1*]Seyed Hamed Pour Rahmati Khalejan
[1]Hidropar Motion Control Technology Center (HKTM) Inc, R&D Center, Gebze 41400 Kocaeli, Turkey

* E-mails: Hamed.pourrahmati@hktm.com.tr

Abstract
For design, installation and optimization of solar photovoltaic (PV) power systems, it is important to determine the maximum useful solar radiation energy, or solar exergy, of the mounted area according to the months and seasons. This study examines four distinct solar exergy models—Petela, Spanner, Parrott, and Jeter—as means to determine the utilizable solar energy output within seven distinct geographical regions in Turkey, namely Eastern Anatolia, Central Anatolia, Black Sea, Mediterranean, Aegean, Marmara, and South-eastern Anatolia. Each region encompasses unique environmental parameters. Over the course of 12 months, the research systematically evaluates the solar exergy potential of these regions. Ultimately, the findings derived from the application of these models are rigorously compared and contrasted, thereby contributing to an enhanced understanding of the most effective approaches to harnessing solar energy across diverse geographic contexts.

Keywords: Photovoltaic power system, solar radiation energy, solar exergy, comparative analysis.

I. Introduction

Solar-based energy sources are the most promising choice for the future of our world due to their cleanliness and unlimited availability (Hepbasli ,2008). Solar PV power technology is an effective and fast- developing means of collecting solar irradiation (Mustafa et al, 2020).

For design, install and optimize solar PV power systems, it is important to determine the maximum useful solar radiation energy (solar exergy) of the mounted area according to the months and seasons. In practical terms, the exergy of solar radiation incorporates both qualitative and quantitative data related to global solar radiation, allowing for the determination of the maximum available output work that can be derived from it (Rawat et al, 2017).

A multitude of both theoretical and experimental investigations are dedicated to the exploration and analysis of exergy within the context of solar radiation, reflecting a substantial body of research aimed at comprehensively understanding and harnessing the potential of solar energy;

Petla (1964) derived a formula to calculate the exergy of solar radiation taking into account the radiation that is emitted from sun and reaches the Earth's surface. In this formula, a relationship based on the temperature of both exposed surfaces was proposed. Spanner (1964) considered the value of solar radiation exergy as work potential of the system. Parrott (1978) expanded upon Petela's proposed solar exergy model by incorporating the geometric considerations of the sun-earth axis motion, specifically in relation to the incoming solar radiation. Departing from Spanner's methodology, Jeter (1981) introduced the Carnot heat engine model as a novel framework for assessing the exergetic aspects of solar radiation. Bejan's seminal work (Bejan, 1987) delved into an examination of the theories put forth by Petela, Spanner, and Jeter, affirming the individual validity of each of these theories. The foundational premise of these theories revolves around a high-temperature isotropic radiation source that receives heat from a correspondingly high-temperature heat reservoir. Bejan's scrutiny provided affirmation to the theoretical underpinnings of these models, contributing to the broader understanding of high-temperature isotropic radiation sources and their interactions with heat reservoirs as postulated by Petela, Spanner, and Jeter. Wurfel (2002) delved into the thermodynamic constraints affecting solar energy conversion across various solar cell types, concluding that efficiency could be enhanced by minimizing thermal losses. Zamfirescu and Dincer (2009) presented a thermodynamic model specifically crafted to examine the exergetic content of solar radiation arriving at the Earth's surface, with the potential for work generation through a dual cascaded thermodynamic cycle. Alta et al. (2010) conducted an extensive analysis by utilizing solar radiation data obtained from 152 meteorological stations distributed across diverse geographical areas in Turkey. By incorporating data from a wide range of meteorological stations, the research aimed to provide a detailed and region-specific understanding of the exergetic characteristics of solar radiation.Their study involved the computation of solar radiation exergy based on global solar radiation, ambient temperature, and the exergy/energy ratio. Hepbasli et al. (2014) determined the value of solar exergy for specific regions in Saudi Arabia and Turkey. Meanwhile, Jamil and Beloes (2019) devised empirical models outlining the value of solar exergy in different regions of India.

In this study, examination of solar exergy models of Petela, Spanner, Parrott and Jeter was performed for determine usable solar energy for seven geographical regions (Eastern Anatolia, Central Anatolia, Black-sea, Mediterranean, Aegean, Marmara, South-eastern Anatolia) with different environmental parameters in Turkey for the period between 1990 and 2020. Finally, a comparative analysis was conducted on the acquired results.

II. Materials and Methods

The analysis of solar exergy was calculated under weather conditions of seven geographical regions in Turkey. Figure 1 shows the map of these regions (Önçel et al, 2018).

The data for this study were collected from 1991 to 2020. In this study, the parameters for calculation of solar exergy are; solar irradiation, ambient temperature (*Ta*) and surface temperature of sun (*Ts*) which it is 5772 K.

In order to the applicability of the models, the measurements of monthly average global solar radiation and ambient temperature derived from geographical and meteorological data (https://climateknowledgeportal.worldbank.org/country/turkiye/climate-data-historical of Turkey) were used.

Fig. 1: The map of seven geographical regions in Turkey.

III. Theoretical Analysis

Energy analysis of solar radiation ($\dot{E}_S$), which considered as the first law of thermodynamics, is given as:

$$\dot{E}_{Solar} = AI_S \tag{1}$$

where I_S is the solar radiation and A is the surface of unit area that sun's radiant reach on it.

Using the second law of thermodynamics solar exergy is performed. Petela, Jeter, Parrott, and Spanner primarily conducted the calculation of solar radiation exergy.

Petela's theorem states that the solar exergy including solar radiation intensity can be expressed as follows:

$$\dot{E}x_{petela} = AI_S\left[1 - \frac{4}{3}\left(\frac{T_a}{T_s}\right) + \frac{1}{3}\left(\frac{T_a}{T_s}\right)^4\right] \tag{2}$$

Spanner considered the solar exergy as the work potential;

$$\dot{E}x_{Spaner} = AI_S\left[1 - \frac{4}{3}\left(\frac{T_a}{T_s}\right)\right] \tag{3}$$

Jeter consider solar exergy as Carnot heat engine:

$$\dot{E}x_{Jeter} = AI_S\left[1 - \left(\frac{T_a}{T_s}\right)\right] \tag{4}$$

The calculation of solar exergy, taking into account the geometry of the incoming radiation, follows the formulation provided in Parrott's model and can be expressed as:

$$\dot{E}x_{Parrott} = AI_S\left(1 - \frac{4}{3}\left(\frac{T_a}{T_s}\right)(1 - cos\,\sigma)^{\frac{1}{4}} + \frac{1}{3}\left(\frac{T_a}{T_s}\right)^4\right) \tag{5}$$

Considering the equations related to solar exergy models, the calculation of solar exergy was performed for seven geographical regions in Turkey. This methodological approach aimed to derive comprehensive insights into the solar energy potential specific to each region, thus contributing to a nuanced understanding of the exergetic aspects of solar radiation in the Turkish context.

IV. Results and discussion

The primary objective of this research endeavor was to systematically examine the solar exergy across diverse regions of Turkey, thereby furnishing a pragmatic viewpoint that proves invaluable for both industrial applications and the scientific community, fostering a comprehensive understanding of the solar energy landscape within the context of the specific geographical nuances of the country.

Table 1 indicates the mean values of solar radiation exergy for a period of 30 years for seven geographical regions in Turkey.

The ambient temperature is one of the most important parametrs in determantion of solar exergy. As shown in Table 1, Eastern Anatolia (E-Anatolia) with a temperature value of 283.7K and the Mediterranean with a temperature

value of 289.4K respectively, have the lowest and hieghst average temperatures over the 30-years period.

As illustrated in Table1, the mean value of solar energy various between 1120 kWh/m^2 and 1460 kWh/m^2 for seven regions over a long period of time. In addition, using Petela and Spanner models for these regions, the average solar exergy varies within the range of 1046 kWh/m^2 to 1364 kWh/m^2. While in the Jeter approach the mean values of solar exergy range from 1064 kWh/m^2 to 1386 kWh/m^2, in the Parrott model they vary from 1109 kWh/m^2 to 1444 kWh/m^2 in seven different regions.

Table 1. The mean values of the solar exergy models over a period of 30 years for different regions in Turkey.

Regions	*Ta* (K)	Sun Hours (hours/year)	$\dot{E}_S$ (kWh/m^2)	$\dot{E}x_{petela}$ (kWh/m^2)	$\dot{E}x_{Spaner}$ (kWh/m^2)	$\dot{E}x_{Jeter}$ (kWh/m^2)	$\dot{E}x_{Parrott}$ (kWh/m^2)
Marmara	286.5	2409	1168	1091	1091	1110	1156
Aegean	288.4	2738	1304	1218	1218	1238	1291
Mediterranean	289.4	2956	1390	1298	1298	1320	1376
Black Sea	285.3	1971	1120	1046	1046	1064	1109
C-Anatolia	283.6	2628	1314	1229	1229	1249	1301
E-Anatolia	282.7	2664	1365	1277	1277	1298	1351
SE- Anatolia	289.5	2993	1460	1364	1364	1386	1444
Mean of Turkey	286.5	2640	1311	1225	1225	1245	1298

The mean ratio of solar exergy to solar radiation energy for the seven regions is calculated at 0.93, consistent with Petela and Spanner's model. Furthermore, this ratio is noted to extend to 0.95 and 0.99 for the Jeter and Parrott models, respectively, across these regions.

Figure 2 shows variation of the mean annual values of the global solar energy and solar radiation exergy for seven geographical regionso of Turkey for a 30 years period.

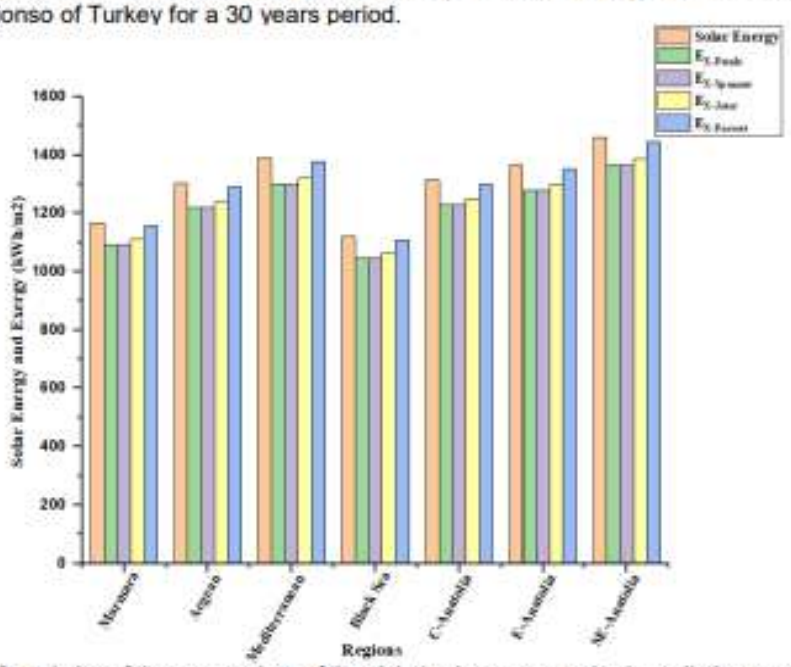

Fig. 2: variation of the mean values of the global solar energy and solar radiation exergy.

From Figure 2, it can be seen that the calculation of solar radiation exergy efficiency based on the Spanner and Petela models gives very similar results. In addition, the solar exergy values are lower than the solar energy values for all models. This is due to the fact that the exergy analysis gives a realistic value by considering environmental parameters. Finally, it can be seen that the South-east Anatolia region has the highest potential and the Black Sea region has the lowest solar energy potential in terms of solar radiation energy and exergy.

V. Conclusion

In conclusions, utulizing the first and second laws of thermodynamics, this study systematically computed and compared the solar radiation energy as well as the solar exergy approach examined by Parrott, Spanner, Jeter, and Petela. This comparative analysis contributes to a deeper understanding of the thermodynamic characteristics inherent in solar energy models, thereby enhancing our capacity to assess and optimize the utilization of solar resources. The summarized results are as follows:

- The calculated average ratio of solar exergy to solar radiation energy across the seven regions is established at 0.93, aligning with the model proposed by Petela and Spanner. Notably, for the Jeter and Parrott models, this ratio extends to 0.95 and 0.99, respectively, within the specified regions. The South-east Anatolia region exhibits the highest potential, while the Black Sea region demonstrates the

lowest solar energy potential, considering both solar radiation energy and exergy.

- The average annual solar energy varies between 1120 kWh/m² and 1460 kWh/m² across seven regions over a period of 30 years.
- The mean annual solar energy for Turkey is calculated as 1311 kWh/m² for a 30-years period.
- The mean annual solar exergy values for Turkey are 1225 kWh/m² for both the approaches of Petela and Spanner. This value is 1245 kWh/m² for Jeter model and 1298 kWh/m² for the Parrott model.

Acknowledgements

I would like to extend my deepest appreciation to the Research and Development Center of Hidropar Motion Control Technology Center (HKTM). Their unwavering support and generous provision of resources were instrumental in making this study possible

References

Alta, D., Ertekin, C., Evrendilek, F. (2010). Quantifying Spatio-temporal dynamics of solar radiation exergy over Turkey. Renew. Energy 35 (12), 2821–2828.

Bejan, A. (1987). Unification of three different theories concerning the ideal conversion of enclosed radiation.

Hepbasli, A. (2008). A key review on exergetic analysis and assessment of renewable energy resources for a sustainable future. Renewable and sustainable energy reviews, 12(3), pp.593-661.

Hepbasli, A., and Z. Alsuhaibani (2014). "Estimating and comparing the exergetic solar radiation values of various climate regions for solar energy utilization." Energy Sources, Part A: Recovery, Utilization, and Environmental Effects 36(7) (2014), pp. 764-773.

Jamil, B. and Bellos, E. (2019). Development of empirical models for estimation of global solar radiation exergy in India. Journal of Cleaner Production, 207, pp.1-16.

Jeter, S.M. (1981). Maximum conversion efficiency for the utilization of direct solar radiation. Solar energy, 26(3), pp.231-236.

Mustafa, R. J., Gomaa, M. R., Al-Dhaifallah, M., & Rezk, H. (2020). Environmental impacts on the performance of solar photovoltaic systems. Sustainability, 12(2), 608.

Önçel, S. İ. B. E. L., Güldemir, O. S. M. A. N., & Yayla, Ö. N. D. E. R. (2018). Geographical exploration of vegan dishes from Turkish cuisine. GeoJournal of Tourism and Geosites, 23(3).

Petela, R. (1964). Exergy of heat radiation.

Parrott, J.E. (1978). A theoretical upper limit to the conversion efficiency of solar energy. Solar Energy, 21(3), pp.227-229.

Rawat, R., Lamba, R., & Kaushik, S. C. (2017). Thermodynamic study of solar photovoltaic energy conversion: An overview. Renewable and Sustainable Energy Reviews, 71, 630-638.

Spanner, D.C. (1964). Introduction to thermodynamics. Introduction to thermodynamics.

Wurfel, P. (2002). Thermodynamic limitations to solar energy conversion. Physica E: Low-dimensional Systems and Nanostructures, 14(1-2), 18-26.

Zamfirescu, C., & Dincer, I. (2009). How much exergy one can obtain from incident solar radiation?. Journal of Applied Physics, 105(4).

IEEES-136

Efficiency Optimization of Solar Assisted Absorption Refrigeration Systems

Gülçin Yıldırım Çimşir[1], Tuba Okutucu Özyurt[2]
[1]Istanbul Technical University, Graduate School, Energy Science and Technology Program
[2]Istanbul Technical University, Energy Institute, Renewable Energy Division
34469, Sarıyer, İstanbul

Abstract
Since refrigeration systems have high energy costs and electricity consumption, absorption refrigeration systems which have high initial investment costs but low operating expenses appear as an alternative to refrigeration systems. In refrigeration cycles supported by renewable energy, efficiency studies have great importance for the electrical power to be sufficient. In the literature, efficiency studies cover topics such as system performance coefficient, exergy and energy efficiency, or system geometries. Accordingly, it is aimed to achieve maximum efficiency by taking an optimal value for all variables considered. The objective of this study is to examine a solar absorption cooling system with four different collector types and corresponding solar radiation values. Collector area and collector inlet temperatures are varied. System performance is evaluated based on thermal efficiency and solar coefficient of performance (SCOP) using an alternative working pair, namely, LiCl-H_2O. The optimum system parameters yielding maximum SCOP are determined.

Keywords: Renewable energy, Solar power, Absorption refrigeration systems, Efficiency, Efficiency optimization, Solar coefficient of performance.

I. Introduction
In today's world, the limited nature of energy resources and their environmental impacts are increasingly being discussed. In this context, solar energy holds great potential for countries that are exposed to abundant sunlight, such as Turkey. However, the development and widespread implementation of solar energy projects in the country are facing certain regulatory and geographical limitations. Particularly in the northern regions of Ankara, the capital of Turkey, the use of solar energy systems is restricted due to specific licensing regulations. In these areas, the installation of solar energy plants beyond a certain capacity is prohibited. As Turkey aims for sustainability in the energy sector, it is essential to consider such limitations.

In the literature various studies about optimization of solar assisted absorption refrigeration systems were conducted on a multitude of different working pairs using several different programs.
One of the studies focuses on the optimization of designs and phase change materials. It explores a solar-powered ammonia water absorption refrigeration system that utilizes waste heat from a ship engine or economizer. The study emphasizes that a heat pump facilitates the refrigeration process, contributing to an overall efficiency improvement. Additionally, it highlights the crucial role of the absorbing plate's location in increasing the system's Coefficient of Performance (COP). (Dhindsa, 2021)
Another study investigates plate heat exchanger (PHE) absorbers, known for their ability to provide substantial heat transfer coefficients within compact dimensions. The study focuses on the geometric optimization of PHE design, specifically involving increases in channel width, channel height, and the number of plates. The outcome of this geometric optimization is noted to result in both high efficiency and compactness, showcasing the potential for an effective balance between performance and space utilization in plate heat exchanger systems. (Zhai, 2021)
Another study describes an experimental system with a PTC array, hot water storage tank, lithium bromide absorption chiller, cooling tower, and blower coils. It finds that increasing hot water temperature enhances the system's Coefficient of Performance (COP). The study recommends shortening pipes to minimize heat loss. (Li, 2016)
Another study introduces a prototype of an innovative ammonia-water absorption refrigeration system with a unique generator structure, designed to efficiently utilize various waste heat sources. Economic analysis highlights improved performance and economic advantages over compressor-based pre-cooling systems. The findings suggest that the proposed system significantly lowers specific power consumption in liquified natural gas plants, making it a competitive and economically viable alternative for natural gas pre-cooling compared to traditional compressor refrigeration systems. (Lu, 2021)
Another research delves into assessing the efficacy of the LiCl-H_2O working combination as opposed to the standard LiBr-H_2O in a solar absorption cooling arrangement. Employing a straightforward solar cooling configuration comprising flat plate collectors and a storage tank, the investigation systematically examines both pairs across different heat source and ambient temperature ranges. The primary objective is to reduce the required collection area while maximizing exergetic efficiency. Findings reveal that, across all scenarios, LiCl-H2O demonstrates superior performance compared to LiBr-H_2O, necessitating approximately 8% less collection area for the same cooling demand. (Bellos, 2016)
Another study estimates the operating temperatures of an LiCl-H_2O vapor absorption refrigeration system (VARS) using an inverse technique with weak solution concentration as the objective function and a differential evolution (DE) optimization algorithm. The research explores 34 temperature combinations, presenting the energetic and exergetic performance for each. Parametric analysis reveals how component temperatures impact system performance. A comparison with the LiBr-H_2O system highlights that the coefficient of performance (COP) increases with evaporator temperature, while exergy efficiency decreases, and total system irreversibility increases. Lower condenser and absorber temperatures result in a higher COP, but exergy efficiency decreases, and total system irreversibility increases. (Gogoi, 2016)

This study relies on a unique methodology to examine the solar energy potential and limitations in Turkey. Using the LiCl-H_2O

working pair, the thermal efficiencies of four different solar energy collectors are investigated based on 34 different collector inlet temperatures (T_{col_in}). Additionally, for each of these collector areas ranging from 0.4 -0.5 m^2, the values of Solar Coefficient of Performance (SCOP) and solar radiation (Qs) were evaluated. These collectors include the flat plate collector (FPC), the compound parabolic collector (CPC), evacuated tube collectors (ETC), and the parabolic trough collector (PT). The obtained results are based on the annual solar radiation data in Istanbul. This methodology illustrates the potential for optimizing geographical conditions and collector types for solar energy systems.

II. Methodology

Within the scope of this study, a solar-powered cooling system has been examined under steady-state conditions for the purpose of comparison. Simultaneously, the system operation was optimized to evaluate each working pair under suitable operating conditions. The main components of the scrutinized system include the solar collector field, storage tank, and absorption chiller, which are interconnected according to Figure 1. The study focuses on the conditions where solar energy is captured by four different collector types, and the working fluid LiCl-H_2O is heated in the system.

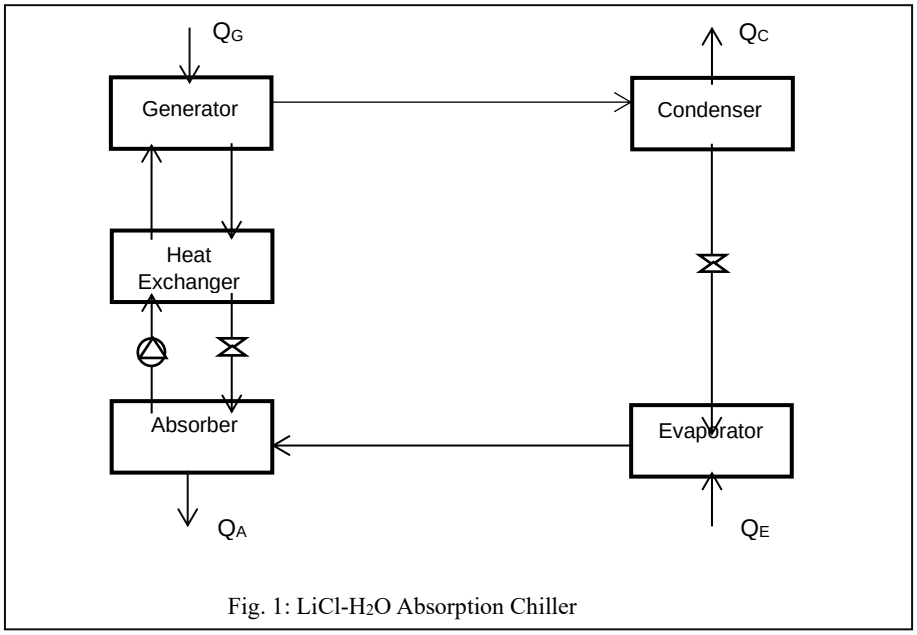

Fig. 1: LiCl-H_2O Absorption Chiller

III. Analysis

The SCOP calculations for four different collector types, parabolic trough collectors (PTC), evacuated tube collectors (ETC), compound parabolic collectors (CPC), and flat plate collectors (FPC), are conducted based on the following equations. (Bellos, 2016)

PTC: $SCOP_{PT}=Q_E/Q_{solar\_PT}$ (1)

CPC: $SCOP_{CP}=Q_E/Q_{solar\_CP}$ (2)

ETC: $SCOP_{ETC}=Q_E/Q_{solar\_ETC}$ (3)

FPC: $SCOP_{FPC}=Q_E/Q_{solar\_FPC}$ (4)

$Q_{\_solar}=A_c \times G$ (5)

Collector areas have been taken as 34 different values in the range of 0.4 - 0.5 m^2. Solar energy and geographical parameters (G) values for collectors are obtained according to Table 1. (Bellos, 2016) Solar radiation and SCOP are then analyzed.

Table 1. Solar energy and geographical parameters

Collector Type	Parameter	Value (W/m^2)
PTC	G_b	600
CPC	G_{cpc}	941
ETC, FPC	G_T	973

When examining the inlet temperature of the working fluid from the generator to the collector (T_{col_in}) for 34 different situations, the thermal efficiency calculation (n_{th}) for four different collector types is conducted based on the following equations.

PTC: $n_{th\ col\_PT}=0,762-(0,2125*((T_{col\_in}-T_{am}))/G_b)-(0,001672*G_b*(((T_{col\_in}-T_{am}))/G_b))^2$ (6)

CPC: $n_{th\ col\_CP}=0,7-(3,4*((T_{col\_in}-T_{am}))/G_{cpc})$ (7)

ETC: $n_{th\ col\_ETC}=0,82-(2,19*((T_{col\_in}-T_{am}))/G_T)$ (8)

FPC: $n_{th\ col\_FPC}=0,75-(5*((T_{col\_in}-T_{am}))/G_T)$ (9)

IV. Results and discussion

Our analysis demonstrates the impact of collector areas on performance. Specifically, when different collector areas were used, ETC and FPC stood out with high solar radiation values. These results emphasize the importance of geographical locations and environmental conditions in solar energy projects. However, it is essential to note that high solar radiation does not always equate to a high solar coefficient of performance value. In particular, we observed that the solar coefficient performance values of PT were higher than other collectors. (Figure 2.) This indicates that PT can operate more effectively under low light intensity conditions. The flexibility of PT may enhance its usability in different geographical regions and climate conditions.

In terms of thermal efficiency, the highest value was determined for the PT collector. (Figure 3.) These results highlight PT as a preferred choice, especially for systems operating at high temperatures. However, while evaluating these results, one must consider the geographical location, climate conditions, and other factors specific to solar energy projects.

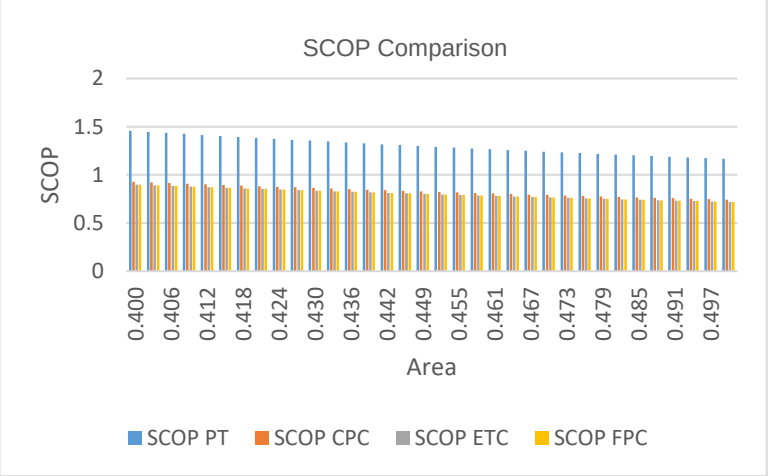

Figure 2: SCOP results according to area

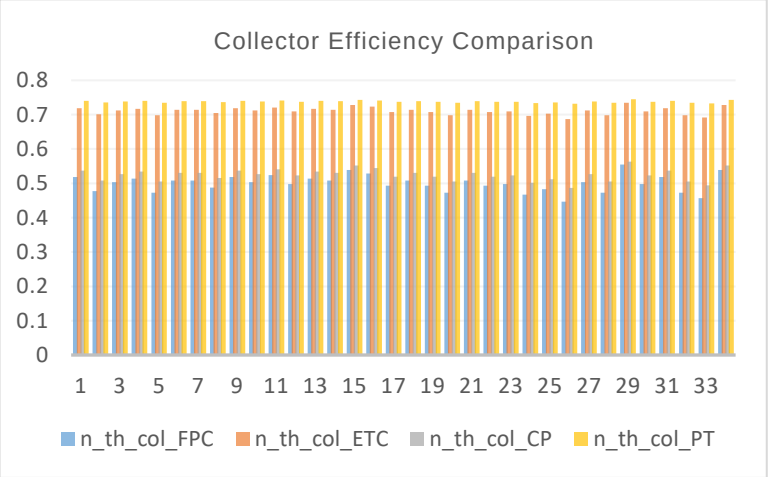

Figure 3: Thermal efficiency results according to Tcol_in

V. Conclusion

Choosing the right collector is crucial considering geography. This study guides future research on solar energy systems. Despite regulatory constraints, solar energy holds promise in Turkey. In Ankara's northern regions, solar energy systems are restricted by licensing regulations but Istanbul, while not ideal for solar projects, has significant potential. Challenges in this densely populated metropolis include limited space. Efficient solar panel placement is vital for maximizing energy production.

In this study, solar radiation was calculated for 34 different cases with collector areas in the range of 0.4 - 0.5 m^2 considering 4 different collector types using predetermined Solar Energy and geographical parameters. The evaporator cooling load was set at 350 kW, and the resulting SCOP values were compared. PTC was identified as the collector type with the lowest solar radiation and the highest SCOP value. When the collector inlet temperature is considered as a variable, PTC had the largest collector area, while FPC and ETC had the smallest areas. Additionally, ETC and PTC demonstrated the highest thermal efficiency. Taking into account both thermal efficiency and SCOP values, it was concluded that PTC is the most suitable collector type, and the optimum collector inlet temperature was determined accordingly.

The examination of the dynamics and limitations of the solar energy sector in Turkey is the aim of this study, as the country seeks to increase energy production sustainably. Solar energy, being both environmentally friendly and renewable, offers a promising solution to Turkey's energy needs.

References

Bellos, E.; Tzivanidis, C.; Antonopoulos, K. A., (2016). Exergetic and energetic comparison of LiCl-H2O and LiBr-H2O working pairs in a solar absorption cooling system. Energy Conversion and Management, 2016, 123: 453-461.

Bellos, E.; Tzivanidis, C.; Antonopoulos, K. A., (2016). Exergetic, energetic and financial evaluation of a solar driven absorption cooling system with various collector types. *Applied Thermal Engineering*, 102: 749-759.

Dhindsa, G. S., (2021). Review on performance enhancement of solar absorption refrigeration system using various designs and phase change materials. *Materials today: proceedings*, 37: 3332-3337.

Gogoi, T. K.; Konwar, D., (2016). Exergy analysis of a H2O–LiCl absorption refrigeration system with operating temperatures estimated through inverse analysis. *Energy Conversion and Management*, 110: 436-447.

Li, M., (2016). Experimental investigation on the performance of a solar powered lithium bromide–water absorption cooling system. *International journal of refrigeration*, 71: 46-59.

Lu, D., (2021). Experimental study and economic analysis of an absorption refrigeration system with new generator structure applied for pre-cooling in liquefied natural gas plant. *International Journal of Refrigeration*, 129: 78-87.

Zhai, C.; Sui, Z.; Wu, W., (2021). Geometry optimization of plate heat exchangers as absorbers in compact absorption refrigeration systems using H2O/ionic liquids. *Applied Thermal Engineering*, 186: 116554.

Robust Grid Synchronization PLL Algorithms for Harmonic Distorted and Unbalanced 3-Phase Grid Conditions.

[1*]Smail Toufik, [1]Boulouma Sabri, [1]Seddaoui Nawel, [1]Rahmani Hachemi

[1]Unité de Développement des Equipements Solaires UDES EPST/Centre de Développement des Energies Renouvelables, Bou-Ismail, 42415, Tipaza, Algeria.

* smail.toufik77@gmail.com

Abstract

In renewable energy systems (RES), grid synchronization is an important factor involved in the operation and control coordination of grid-connected power electronic converters. Phase locked loop (PLL) is an essential part of the control unit of the grid-connected power electronic converters it synchronizes the input signal with the output signal in both frequency and time. In this paper, a three-phase phase-locked loop (PLL) is proposed, which operates fast and accurately for grid synchronization under unbalanced grid conditions. A synchronous reference frame (SRF-PLL) algorithm with Proportional Integral (PI) control calculated with the symmetrical optimum method (SO) has been designed. The performances of the (PLL) system have been verified for non-ideal grid conditions in phase jump using Matlab. Also, according to the bode plots, the stability of the designed system has been analyzed. Finally, the simulation results demonstrated the effectiveness of the proposed (PLL) in terms of unsteady state performance and dynamic response.

Keywords: renewable energy systems, Phase locked loop (PLL), Proportional Integral (PI) control, symmetrical optimum method (SO).

I. Introduction

Power electronic converters play a fundamental role in the grid-connected renewable energy sources. They are used for various purposes such as power quality improvement (Kashif et al., 2018), grid-integration of distributed energy resources (Aourir et al., 2020; Benyamina et al., 2021; Chishti et al., 2020; Chowdhury et al., 2022; Meral and Çelik, 2019) charging electric vehicles (Mishra et al., 2021) and supplying domestic and industrial loads (Lucía et al., 2011). These applications require grid-synchronous operation of the converter with the grid. This process is commonly known as grid- synchronization. Grid synchronization necessitates the real-time extraction of unknown grid voltage parameters. As a result, Significant research attention has been given to this problem in the last years. Efficient, fast, and accurate techniques are reported in the literature. Out of them, phase-locked loop (PLL) (Bierhoff, 2017; Chedjara et al., 2018; Sadeque et al., 2021; Shah et al., 2020) and its various variants are particularly popular. The Phase Locked Loop (PLL) structure consists of the voltage-controlled oscillator (VCO) blocks, the loop filter (LF) and the phase detection (PD). The (PD) block determines the phase difference between output signal and input signal (Vin). Moreover, it produces a proper error signal (Rajan et al., n.d.). This error signal is transferred to the (LF) block. The (LF) demonstrates the low-pass-filter (LPF) characteristic to provide stability of the system. In addition, it typically comprises of the first-order (LPF) or a proportional and integral (PI) controller. In other words, the loop filter (LF) specifies the dynamics of the system (Amin and Mohammed, 2010). The signal at the output of the loop filter (LF) generates the output signal in the same phase as the input signal by driving the voltage-controlled oscillator (VCO). Thereby, the output signal follows the input signal (Vin) (Teodorescu et al., 2011). Figure 1 shows the block structure of the PLL. This structure automatically synchronizes the phase of the output signal to the phase of the input signal as it is a feedback system.

Fig. 1: Block structure of the PLL (Giotopoulos and Korres, 2023)

This paper proposes a Phase locked loop (PLL) method for renewable energy sources. An error signal corresponding to this difference in amplitudes is fed to a Proportional Integral (PI) Control which forces the error to zero over time. This method is as simple and easy to apply as it is robust. Therefore, even under voltage-unbalanced conditions, it is still able to estimate the phase angle and frequency of the grid voltage. On the other hand, the presence of distortions in the grid voltage does not impede the performance of the (PLL) method as it would be seen in the simulation results.

II. Synchronous Reference Frame-PLL (SRF-PLL)

The Synchronous Reference Frame-PLL (SRF-PLL) operates as a feedback system to instantaneously detect the phase angle (θ) of the grid voltages. In this (SRF-PLL) algorithm, the three-phase grid voltages (Va, Vb,Vc) are firstly measured. Then, the three-phase grid voltages are transformed to the stationary frame variables (Vα, Vβ) by Clarke rotation matrix given in Eq (1). After, the Vα and Vβ voltages are converted to the synchronous frame variables (Vd, Vq) by Park rotation matrix in Eq (2). The estimated phase angle (θ*) of the grid voltage is fed back to operate the abc to dq block so that the Park rotation can be performed.

$$\begin{bmatrix} V_\alpha \\ V_\beta \end{bmatrix} = \frac{2}{3}\begin{bmatrix} 1 & -\frac{1}{2} & -\frac{1}{2} \\ 0 & \frac{\sqrt{3}}{2} & \frac{\sqrt{3}}{2} \end{bmatrix}\begin{bmatrix} V_a \\ V_b \\ V_c \end{bmatrix} \quad (1)$$

$$\begin{bmatrix} V_d \\ V_q \end{bmatrix} = \begin{bmatrix} \cos(\theta^*) & \sin(\theta^*) \\ -\sin(\theta^*) & \cos(\theta^*) \end{bmatrix}\begin{bmatrix} V_\alpha \\ V_\beta \end{bmatrix} \quad (2)$$

In ideal grid conditions, the estimated phase angle (θ*) equals to the phase angle (θ) of the grid voltage. As given from Eq. 2 and Eq. 3, while Vd is equal to peak voltage of the grid, Vq becomes zero. In Fig. 2, basic block diagram of SRF-PLL is shown.

$$V_q = V_m \sin(\theta - \theta^*) \quad (3)$$

$$V_d = V_m \cos(\theta - \theta^*) \quad (4)$$

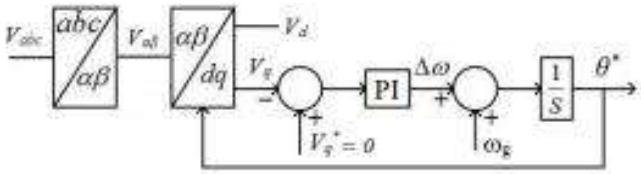

Fig 2: Basic block structure of PLL

Open-loop and the closed-loop transfer function of the proposed system are given as Eq.(5) and Eq. (6):

$$G_{cl} = \frac{G_{ol}}{1 + G_{ol}} \quad (5)$$

$$G_{ol} = \left(K_p \frac{1 + s\tau}{s\tau}\right)\left(\frac{1}{1 + sT_s}\right)\left(\frac{V_m}{s}\right) \quad (6)$$

The bode diagram of open loop and closed loop PLL are shown in the Fig 3 (a) & (b) respectively. The result shows that the PLL loop bandwidth is 314(rad/s) and phase margin is 86.4 degree which indicates that the transfer function is working correctly and the system is stable.

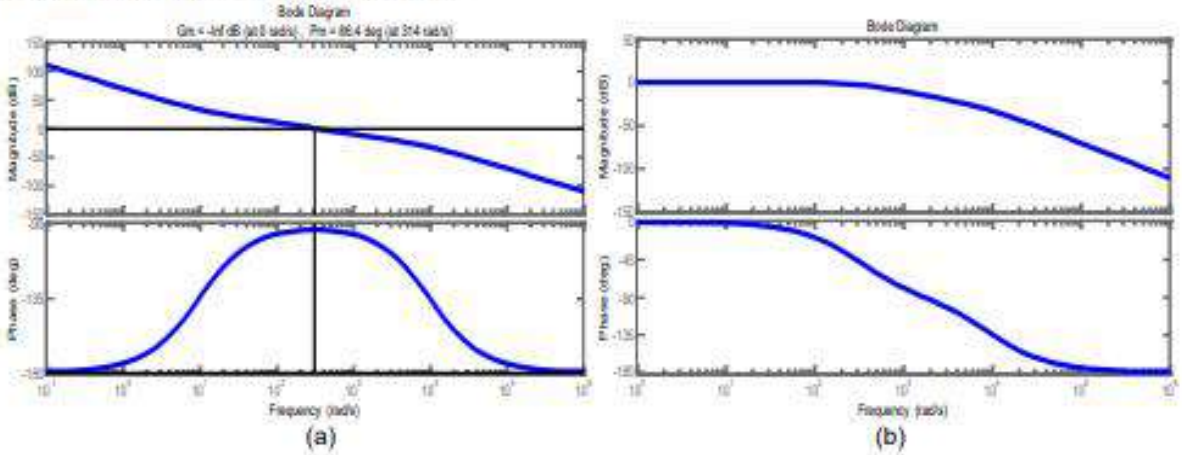

Fig 3: (a) Bode plot of open-loop proposed PLL, (b) Bode plot of closed-loop proposed PLL

II. Results and discussion

In this section, a series of simulations have been carried out to establish the capability of the proposed technique. The proposed PLL parameters are summarized as follows: natural frequency is ωn=314 rad/s, the damping ratio of the loop filter is ξ = 0.10142 and the PI coefficients are calculated (KP=0.8263, KI=49298). The control algorithm is implemented using Matlab environment with the sampling frequency set to 10 kHz. Fig 4, shows the grid response of the proposed (PLL) to phase jump. It is observed that the input signals making a phase jump were simultaneously applied to all three phases as presented in Fig 4. It can be seen that the phase jump occurs between the 5 and 6 cycles while the proposed (PLL) synchronizes the two phases together after the sixth cycle. Based on the simulation, the output of PLL is in synchronism with the grid as shown in Fig 4 (d). It can be seen in Fig 4 (e) that the voltage error becomes zero after many periods. The grid voltages estimating frequency and phase angle are shown in Fig 4 (f), (g), respectively.

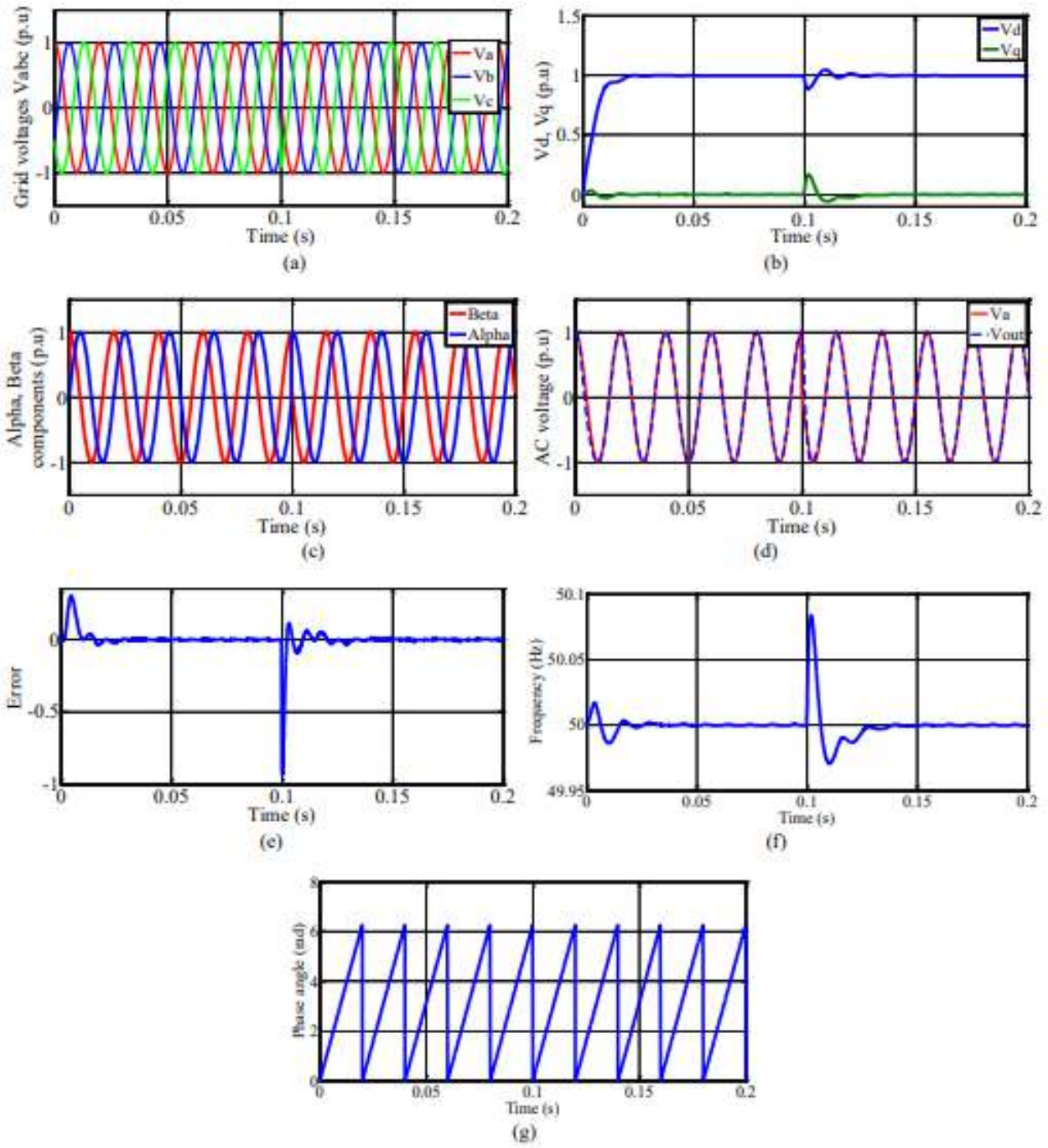

Fig. 4 Response of the proposes (PLL) under phase jump grid condition (a) grid voltage (b) change of the Vd and Vq voltage, (c) Alpha and Beta components voltage, (d) Va and Vout voltage, (e) Phase error, (f) frequency and (g) phase angle

III. Conclusion

In this paper, a Phase locked loop (PLL) algorithm is proposed for renewable energy sources (RES). A synchronous reference frame (SRF-PLL) algorithm with Proportional Integral (PI) control calculated with the symmetrical optimum method has been designed. The proposed method achieves robust tracking of the phase angle under phase jump. In addition, the Phase Lock Loop (PLL) method has high error rejection capability and oscillations which is an indication of the speed of response and stability. The Proportional Integral (PI) control designed using the symmetrical optimal method (SO) seems to work quite well and the results indicate its ability to optimize the phase margin. Finally, all simulation results show the grid synchronization capability of the (PLL) proposed in non-ideal grid conditions.

References

Amin, M.M., Mohammed, O.A., 2010. Software Phase Locked Loop technique for grid-connected wind energy conversion systems, in: 2010 IEEE 12th Workshop on Control and Modeling for Power Electronics (COMPEL). IEEE, pp. 1–8. https://doi.org/10.1109/COMPEL.2010.5562424

Aourir, M., Abouloifa, A., Lachkar, I., Aouadi, C., Giri, F., Guerrero, J.M., 2020. Nonlinear control and stability analysis of single stage grid-connected photovoltaic systems. International Journal of Electrical Power & Energy Systems 115, 105439. https://doi.org/10.1016/j.ijepes.2019.105439

Benyamina, F., Benrabah, A., Khoucha, F., Zia, M.F., Achour, Y., Benbouzid, M., 2021. An augmented state observer-based sensorless control of grid-connected inverters under grid faults. International Journal of Electrical Power & Energy Systems 133, 107222. https://doi.org/10.1016/j.ijepes.2021.107222

Bierhoff, M.H., 2017. A General PLL-Type Algorithm for Speed Sensorless Control of Electrical Drives. IEEE Transactions on Industrial Electronics 64, 9253–9260. https://doi.org/10.1109/TIE.2017.2711568

Chedjara, Z., Massoum, A., Massoum, S., Wira, P., Safa, A., Gouichiche, A., 2018. A novel robust PLL algorithm applied to the control of a shunt active power filter using a self tuning filter concept, in: 2018 IEEE International Conference on Industrial Technology (ICIT). IEEE, pp. 1124–1131. https://doi.org/10.1109/ICIT.2018.8352336

Chishti, F., Murshid, S., Singh, B., 2020. Weak Grid Intertie WEGS With Hybrid Generalized Integrator for Power Quality Improvement. IEEE Transactions on Industrial Electronics 67, 1113–1123. https://doi.org/10.1109/TIE.2019.2898598

Chowdhury, V.R., Singh, A., Mather, B., 2022. Internal Model-Based Active Damping Strategy for a Back-to-Back Modular Multilevel Converter System for Advanced Grid Support: Preprint.

Giotopoulos, V., Korres, G., 2023. Implementation of Phasor Measurement Unit Based on Phase-Locked Loop Techniques: A Comprehensive Review. Energies (Basel) 16, 5465. https://doi.org/10.3390/en16145465

Kashif, M., Hossain, M.J., Zhuo, F., Gautam, S., 2018. Design and implementation of a three-level active power filter for harmonic and reactive power compensation. Electric Power Systems Research 165, 144–156. https://doi.org/10.1016/j.epsr.2018.09.011

Lucía, Ó., Barragán, L.A., Burdío, J.M., Jiménez, Ó., Navarro, D., Urriza, I., 2011. A Versatile Power Electronics Test-Bench Architecture Applied to Domestic Induction Heating. IEEE Transactions on Industrial Electronics 58, 998–1007. https://doi.org/10.1109/TIE.2010.2048840

Meral, M.E., Çelik, D., 2019. A comprehensive survey on control strategies of distributed generation power systems under normal and abnormal conditions. Annu Rev Control 47, 112–132. https://doi.org/10.1016/j.arcontrol.2018.11.003

Mishra, D., Singh, B., Panigrahi, B.K., 2021. Adaptive Current Control for a Bidirectional Interleaved EV Charger With Disturbance Rejection. IEEE Trans Ind Appl 57, 4080–4090. https://doi.org/10.1109/TIA.2021.3074612

Rajan, M., Devi, J., Supriya, M., Kadam, S., n.d. Phase Locked Loop for synchronization of Inverter with Electrical grid: A Survey.

Sadeque, F., Benzaquen, J., Adib, A., Mirafzal, B., 2021. Direct Phase-Angle Detection for Three-Phase Inverters in Asymmetrical Power Grids. IEEE J Emerg Sel Top Power Electron 9, 520–528. https://doi.org/10.1109/JESTPE.2020.2977398

Shah, S., Koralewicz, P., Gevorgian, V., Parsa, L., 2020. Small-Signal Modeling and Design of Phase-Locked Loops Using Harmonic Signal-Flow Graphs. IEEE Transactions on Energy Conversion 35, 600–610. https://doi.org/10.1109/TEC.2019.2954112

Teodorescu, R., Liserre, M., Rodríguez, P., 2011. Grid Converters for Photovoltaic and Wind Power Systems. Wiley. https://doi.org/10.1002/9780470667057

Study the flame characteristics of gasoline propanol blends for SI engine

Kumaravel S [a], Saravanan C.G [a], Premkumar P [a], Edwin Geo [b] V, Manoj Babu A [c] ElayaPerumal A [d]

[a]Department of Mechanical Engineering, Annamalai University, Annamalainagar, Tamilnadu, India.
[b]Department of Mechanical Engineering, IstinyeUniversity, Isatnbul, Turkey
[c]Department of Mechanical Engineering, Dr.MGR Educational and Research Institute, chennai, Tamilnadu, India.
[d]Department of Mechanical Engineering, Anna University, Guindy Chennai, Tamilnadu, India.,

Abstract

Propanol has similar physiochemical properties with gasoline, there is no any distraction while blend propanol with gasoline. In this study carried out the performance and emission characteristics of MPFI engine fuelled by gasoline propanol blend. Propanol was blended with gasoline by volume of 10%, 20% and 30% namely 1-PRL10, 1-PRL20, and 1-PRL30. The fuel properties were analysed by CHNS, FTIR and TGA. At the same time to focused the study the flame propagation of gasoline propanol blend, the cylinder combustion flame was captured by using AVL Visio scope camera. Flame characteristics such as spatial flame distribution evaluated from the captured flame images for propanol blends and compared with neat gasoline it resulted 1-PRL30 were captured more area. NOx emission was increased while increasing the volume of propanol but HC and CO was decreased. Brake thermal efficacy of the engine was increased for each fuel blends compared than sole gasoline.

Keywords: Gasoline, Propanol, Emission, Alternative fuel, Endoscope visualization,

1. Introduction

Biofuels are one of the most promising alternative to the fossil fuels, the inadequacy of fossil fuel demand and supply and automotive emission forcing to identifying the good alternative. Alcohol fuels like ethanol and methanol, Propanol and other higher order alcohols gave the good result while adding with fossil fuels like gasoline and diesel. Alcohol additives are more reliable and less toxic than others it gives notable efficiency too. Ethanol already being commercialized(Uslu & Celik, 2020) (Zhou et al., 2015). Octane number of alcohol fuel and oxygen content improve the performance of the IC engine(Mourad & Mahmoud, 2018). While blended alcohol fuels with gasoline, it has resulted more stability because of it properties. Propanol having low carbon chain and high heating value and its hygroscopic behaviour is less (Mehmet, 2019). Ethanol has been proven it can be used with gasoline and diesel with blended state and the researches revels ethanol is the one of the promising biofuel, Pollution is one of the major reason for alternative the fossil fuel into bio fuels, bio fuels are less toxic, and renewable at the same time it easy to manufacture(Hu et al., 2020). Higher order alcohol fuels are elevated the level of oxygen content while blende fossil fuel alcohols are most reliable and renewable fuel as well as it's can be made locally from various sources. Alcohols makes less impact on the environmental, highly oxygenated fuels are more suitable for spark ignition engine (Awad et al., 2018). (Geo et al., 2019) Investigate the performance and emission parameters of twin cylinder MPFI engine, which is fuelled by lower and higher order alcohol blends like ethanol and benzyl, both the alcohol fuels are blended with gasoline by the volume of 10% and 20% the engine was run on various load conditions like 20%, 40%, 60%, 80% and 100%, in this study registered ethanol 10% and 20% has 30.41% and 31.1% brake thermal efficiency, benzyl 10% and 20% has 32.8% and 33.2% Brake thermal efficiency, here both alcohol blends has more brake thermal efficiency than sole gasoline. (Huang et al., 2020) Examined the evaporation characteristics of soybean biodiesel it's blended with n-propanol with various temperature rage authors found the evaporations capacity was increased while increasing the propanol volume in the blend and the combustion characteristics also increased. (Fulzele, 2015) et al. reviewed the various higher order alcohol fuels fuelled in gasoline engine, from their report the Propanol has strong potential to use as alternative fuel. Physical and chemical characteristics of alcohol can be play the roll on engine performance, combustion process, emission output and octane number, carbon content, oxygen content and also the boiling point and latent heat of evaporation. (Qian et al., 2018) was conducted experiment on gasoline direct engine maintain constant speed of 2000 rpm the blend volumes of 10%, 20% and 50% named as PRTRF0.1, PRTRF0.3, and PRTRF0.5, respectively, the test result was showed the higher proportion of Propanol has improved the in cylinder pressure and heat release rate of the engine at the same time reduce the period of rapid combustion, The 50% propanol gasoline blend showed higher brake thermal efficiency than other fuel blends, the thermal efficiency was increased where propanol was increase. In this study examined the combustion and emission characteristics of gasoline propanol blend, however number of engine studies are reported on propanol fuels but there is minimum studies reported on visioscopic technic, here the combustion events of various propanol gasoline blends are compared with sole gasoline by using endoscopic technic.

2.Research Setup and Procedure

2.1 Experimental Engine

The experimental investigation on twin cylinder TATA NANO engine with multi point port fuel injection system, the engine has loaded by eddy current dynamometer. Electronic control unit (ECU) has monitoring the quantity of fuel injection respected to input signals of engine speed, throttle position and manifold pressure. At every load condition, fuel consumption was measured by using electronic weighing machine within the time interval of 60 second, Every 100 cycle in cylinder pressure were measured with respect to crank angle with help of pressure transducer which is mounted on the head of the engine cylinder. The one end of AVL digas analyser probe was connected to tail pipe of the engine which is used to measure the exhaust emission like HC, CO and NO. Initially

the engine was operated in without any load to ensure the steady state condition of the engine, in initial stage engine was ran by neat gasoline for removing the last experiment fuel residual and it will be repeated for every test at before change the fuel. Experiment was initiate after confirming the engine condition. The engine was operated at various load conditions like as1.6, 3.2, 4.8, 6.4 and 8 kW. AVL Visio scope analyser captured the flame propagation, which captured at maximum load condition. There was maintaining two hours interval for each test purpose to cooling of Visio scope window and engine. The constant speed was maintain at entire experiment.

Table. 1 specifications of Experimental Engine.

Bore & Stroke	73.5mm (square engine)
Compression ratio	9.5:1
Fuel injection type	MPFI
Maximum Engine output Power	25 kW @ 5250 rpm
Maximum Torque	48 Nm @ 3000 rpm
Number of cylinder	2
Cycle	4-stroke
Cooling system	Water

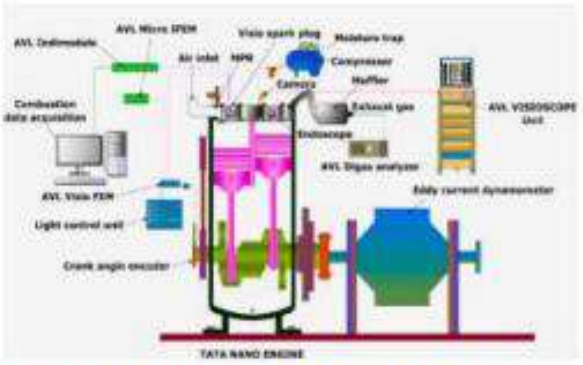

Fig 1. Schematic view of Test engine with endoscopic

Table 2. Fuels Properties

Sl No	Fuel Properties	Gasoline	n- Propanol	1-PRL10 (90% gasoline + 10% n-Propanol)	1-PRL20 (80% gasoline + 20% n-Propanol)	1-PRL30 (70% gasoline + 30% n-Propanol)
1	Viscosity at 25° C (mm^2)	0.5-0.6	1.74	0.714	0.828	0.942
2	Density kg (m^3)	734	803.7	740.9	747	754.7
3	Flash Point (°C)	-36 to -45	15	-37.2	-31.40	25.60
4	Calorific value (Kj/kg)	45000	30000	42500	40500	39400

3. Result and discussion

3.1 Flame Propagation

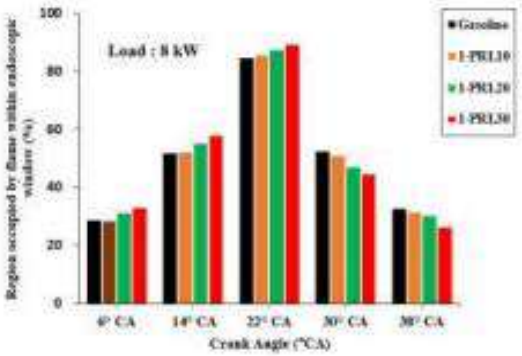

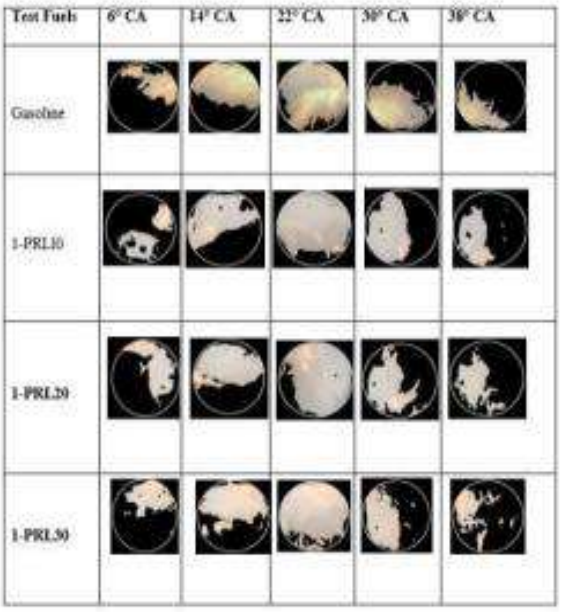

Fig 2. Region occupied flame within endoscope widow at various crank angle

Fig 3. Photo graphic view of flame propagation with respect to various Crank Angle (°CA)

The combustion process was elevated from the spark plug location, images captured 5 times with respect to crank angle position for every propanol gasoline blends, from analysis of image processing a more diffusion flame in nearby the spark plug location. In this study the gasoline propanol blends combustion images were captured the crank angles of 6° 14° 30° 38° and 8°. The images were captured at only maximum load condition here is the maximum load is 8kW. From the processed images resulted while increasing the blend proportion with gasoline the flame propagation and capturing area was increase as well as the flame speed also increased slightly for every fuel blends. Fig 2 and 3 proven the above-mentioned statements. The captured images processed by using MATLAB tools and compared with 100% gasoline, for every fuel blends are showed higher flame propagation area. During the combustion due to diffusion flame to seen a highly improper flame front in spark plug region because of these reason the flame observed highly luminance. A flame front was rapidly travelled across the combustion chamber. Propanol is a higher order alcohol, It's higher carbon and inherent oxygen content was increased the combustion capacity of the fuel while blended with gasoline, there is a marginal difference in the percentage of flame propagation area in every fuel blends a captured images are visually showed that. To increase Propanol gasoline blend ratio the flame luminosity also increase because the higher carbon chain and higher oxygenated content will increase the flame speed than sole gasoline flame speed. A high luminance flame was captured at 8kW means maximum load condition because of the large quantity of fuel was injected on the time its leads to producing more heat energy on the time of combustion, propanol has oxygen content but in this study seen more diffusion flame for the reason is when engine was operated at maximum speed and maximum load condition there is no enough time to ensure the homogeneous form of air fuel mixture. Because of these reason on the maximum load condition the fuel was in rich condition thus resulted the diffusion flame at maximum load condition. Diffusion flames are contributing the more flame luminosity. Among the fuel blends 1-PRL10, 1-PRL20 and 1-PRL30 blend 1-PRL30 occupies more region at 22° crank angle.

3.2 Combustion characteristics.

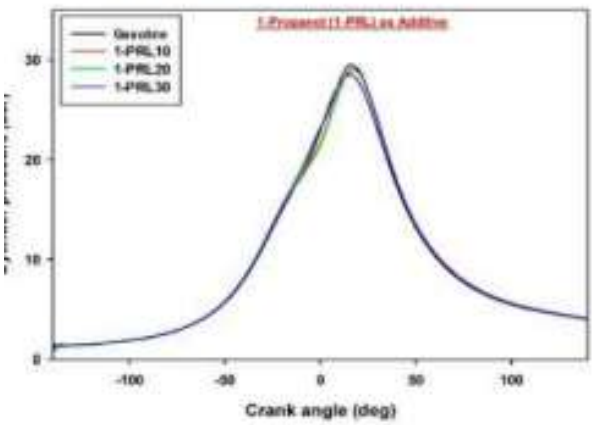

Fig.4. In cylinder Pressure with respect to Crank Angle

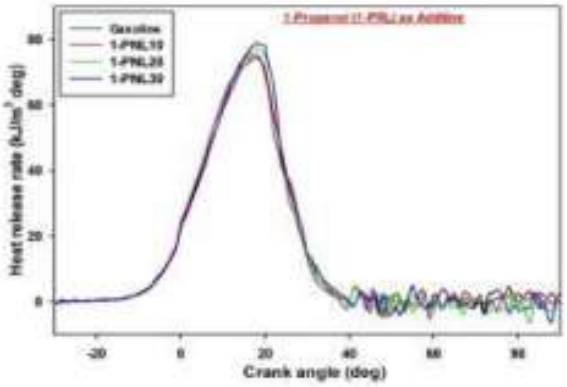

Fig.5. Heat release rate with respect to Crank Angle

The combustion parameters can improve while increasing the oxygen content in the fuel and OH content might improve the burn rate of the fuel. In this study the in cylinder pressure were calculated for 100% gasoline and 1-PRL10, 1-PRL20, 1-PRL30. Fig 4 clearly showed the pressure variation for each fuel blend every propanol gasoline fuel blend in cylinder pressure compared with neat gasoline. Fuel blends 1-PRL10, 1-PRL20, 1-PRL30 are showed more in cylinder pressure than 100% gasoline 1-PRL30 showed higher pressure than all fuel blends. The alcohol fuels role vital role at combustion while mixed with gasoline because of it single boiling point and higher oxygen content than gasoline. Oxygenated fuels are helped to complete the combustion with maximum level. For its higher latent heat of vaporization provide higher the volumetric efficiency for engines. Alcohol fuels can be used directly in spark ignition engines it will directly influence the structure of flame and increase the speed of the flame (Awad et al., 2017). Presence of oxygen content and OH group increased the rate of burning for fuel blends, which leads to increase the speed of flame. Higher speed flam was increase the pressure inside the combustion chamber. The maximum in cylinder pressure is 28.511, 29.06, 29.42 and 29.56 bar for gasoline, 1-PRL10, 1-PRL20 and 1-PRL30 respectively. The same trend was continued in heat release rate, When propanol was blended with the gasoline the physio chemical properties were nearly close to the gasoline like calorific value reach closer value to the sole gasoline. In this respect HRR rate was calculated for maximum load condition for all fuel bled and compared to sole gasoline. Fuel blends of 1-PRL10, 1-PRL20 and 1-PRL30 heat release rate were measured, all fuel blends shows higher HRR than sole gasoline, 1-PRL30 showed higher heat release rate than all fuel blends.

3.3 Performance and Emission analysis

Below graphical images showed the performance and emission characteristics of propanol gasoline blends

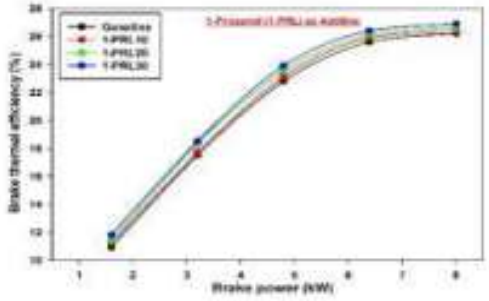

Fig.6. BTE with Respect to various Brake Power.

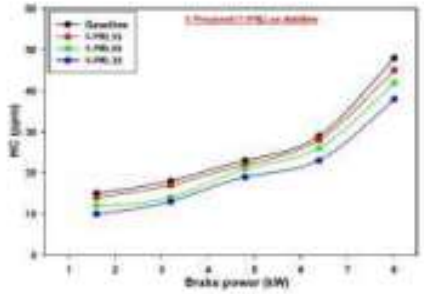

Fig.7. HC Emission with Respect to various Brake Power.

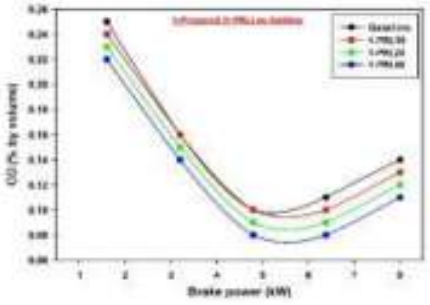

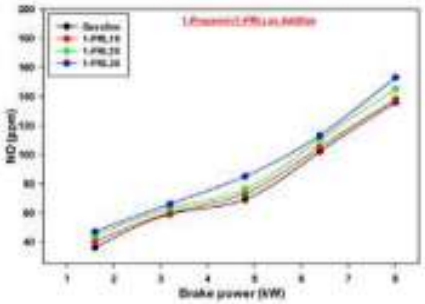

Fig.8. CO Emission with Respect to various Brake Power. Fig.9. NO Emission with Respect to various Brake Power

4. Conclusion.

1. The higher flame propagation was captured while increasing the Propanol with gasoline. 30% Propanol gasoline blend showed higher flame propagation than other fuel blends and gasoline, the endoscopic visualization results showed that. Propanol gasoline blend showed higher in cylinder pressure and heat release rate than sole gasoline, from all the blends 30% Propanol gasoline blend was showed higher pressure as well as higher HRR rate.
2. In 1-PRL30 fuel blend results showed 2% higher brake thermal efficiency than sole gasoline from among the blends, From the graphical results exhaust emission like CO and HC were reduced 20.83% and 32.14% respectively. But 11.11% NO emission was increased for than sole gasoline. From the experimental work propanol can be used as alternative fuel for gasoline engine upto 30% blend volume, here any engine modification is not required.

References

Awad, O. I., Mamat, R., Ali, O. M., Sidik, N. A. C., Yusaf, T., Kadirgama, K., & Kettner, M. (2017). Alcohol and ether as alternative fuels in spark ignition engine : A review. *Renewable and Sustainable Energy Reviews*, *May*, 0–1. https://doi.org/10.1016/j.rser.2017.09.074

Awad, O. I., Mamat, R., Ibrahim, T. K., Thaeer, A., Yusri, I. M., Adnin, M., Humada, A. M., & Yusop, A. F. (2018). Overview of the oxygenated fuels in spark ignition engine : Environmental and performance. *Renewable and Sustainable Energy Reviews*, *91*(March), 394–408. https://doi.org/10.1016/j.rser.2018.03.107

Fulzele, S. D. (2015). *HIGHER ALCOHOL BLEND WITH PETROL : ALTERNATIVE FUEL FOR SI*. *5*, 598–601.

Geo, V. E., Godwin, D. J., Thiyagarajan, S., Saravanan, C. G., & Aloui, F. (2019). E ff ect of higher and lower order alcohol blending with gasoline on performance , emission and combustion characteristics of SI engine. *Fuel*, *256*(February), 115806. https://doi.org/10.1016/j.fuel.2019.115806

Hu, J., Abubakar, S., & Li, Y. (2020). A novel reduced i -propanol- n -butanol-ethanol (IBE)/ diesel mechanism for engine combustion and emissions prediction. *Fuel*, *278*(April), 118291. https://doi.org/10.1016/j.fuel.2020.118291

Huang, X., Wang, J., Wang, Y., Qiao, X., & Ju, D. (2020). Experimental study on evaporation and micro-explosion characteristics of biodiesel / n-propanol blended droplet. *Energy*, *205*, 118031. https://doi.org/10.1016/j.energy.2020.118031

Mehmet, Ş. (2019). *The e ff ect of the injection pressure on single cylinder diesel engine fueled with propanol – diesel blend*. *254*(March). https://doi.org/10.1016/j.fuel.2019.115617

Mourad, M., & Mahmoud, K. R. M. (2018). Performance investigation of passenger vehicle fueled by propanol / gasoline blend according to a city driving cycle. *Energy*, *149*, 741–749. https://doi.org/10.1016/j.energy.2018.02.099

Qian, Y., Guo, J., Zhang, Y., Tao, W., & Lu, X. (2018). Combustion and Emission Behavior of N-propanol as Partially Alternative Fuel in a Direct Injection Spark Ignition Engine. *Applied Thermal Engineering*. https://doi.org/10.1016/j.applthermaleng.2018.08.044

Uslu, S., & Celik, M. B. (2020). Combustion and emission characteristics of isoamyl alcohol-gasoline blends in spark ignition engine. *Fuel*, *262*(September 2019), 116496. https://doi.org/10.1016/j.fuel.2019.116496

Zhou, X., Chen, Y., Wang, C., Guo, J., & Wen, C. (2015). (Liquid + liquid) equilibria for (water + 1-propanol + diisopropyl ether + octane, or methylbenzene, or heptane) systems at T = 298.15 K. *Journal of Chemical Thermodynamics*, *87*, 13–22. https://doi.org/10.1016/j.jct.2015.03.003.

A Concept Design Study for the Energy-Efficiency of Bulk Carriers

[1*] Mehmet Akman, [2]Bülent İbrahim Turan, [3]Ahmet Taşdemir, [4]Mehmet Ziya Söğüt
[1] Muğla Sıtkı Koçman University, Motor Vehicles and Transportation Technologies Department, Bodrum, Muğla, 48420 Türkiye
[2] Muğla Sıtkı Koçman University, Motor Vehicles and Transportation Technologies Department, Bodrum, Muğla, 48420 Türkiye
[3] Piri Reis University, Maritme Faculty, Department of Marine Engineering, Tuzla, İstanbul, 34940, Türkiye
[4] Piri Reis University, Maritme Faculty, Department of Marine Engineering, Tuzla, İstanbul, 34940, Türkiye

* E-mails: mehmetakman@mu.edu.tr

Abstract
The pressure on low-carbon and energy-efficient shipping is growing and the time is running out for acting. Alternative fuels, optimized hull form, light structural design, waste heat recovery, establishing highly efficient propulsion systems and energy-efficient devices onboard stand out as the key applications for greener shipping. In this paper, a benchmark study is conducted to obtain the main characteristics and propulsion trends of handymax class bulk carriers. Then a concept design process is carried out for the bulk carrier with 178 m overall length and 32000 DWT capacity. The Energy Efficiency Design Index is calculated for the base design with conventional diesel prime mover. Subsequently, the application of LNG and methanol-fueled dual-fuel engines for the base design is investigated and compared with conventional diesel propulsion in terms of energy efficiency and environmental impacts. Additional measures which can be implemented during the design stages of bulk carriers are discussed. According to the results, the concept design with LNG-fueled dual-fuel engines has the lowest EEDI while methanol fuel has promising potential as a marine fuel.

Keywords: Energy efficiency, Ship design, Methanol, LNG, Bulk carrier

INTRODUCTION

Ship design is a multidisciplinary process comprising a wide range of iterant analyses. The concept, contract and detail designs are the main phases of a ship design where the dimensional characteristics, stability, strength manoeuvrability and propulsion properties are defined (Turan, 2023). The ship to be designed should fulfil the mission requirements as well as comply with the International Maritime Organization regulations. Energy efficiency and emission control have been the major concerns of the IMO and maritime-based greenhouse gas emissions (GHGs) are aimed to be reduced gradually. The process has started with the enforcement of the Energy Efficiency Design Index (EEDI) and Ship Energy Efficiency Management Plan (SEEMP) and the scope has enlarged with the adoption of the Energy Efficiency Existing Ship Index, Carbon Intensity Indicator (CII) and enhanced SEEMP (IMO, 2023b). In this context, IMO has developed a strategy to decrease the carbon intensity by at least 20% by 2030 and 70% by 2040 compared to the carbon intensity of 2008 (IMO, 2023a). The measures that can be taken consist of various operational actions such as slow-steaming (Dere et al., 2022), route planning (Yercan & Sogut, 2023), trim and ballast optimization, planned maintenance and onboard energy management; or design-oriented practices such as hull form optimization, weight reduction by improved structural design (Taşdemir et al., 2021), waste heat recovery (Akman & Ergin, 2023) and carbon capture and storage (Güler & Ergin, 2021).

The determination of propulsion and electricity power requirements and then the selection of a high-performance power generation system steps in a design process, on the other hand, is directly related to energy efficiency and emission control. The latest studies focus on alternative fuels which have relatively less GHG emissions compared to Heavy Fuel Oil (HFO) or Marine Diesel Oil (MDO) (Akman, 2023). Therefore, dual-fuel engines which are capable of burning liquified natural gas (LNG) or methanol (MeOH) have been started to be used onboard as the prime movers. Propulsion trend reports for merchant ships underline that complying with the regulations and tackling environmental problems are procurable with LNG or MeOH-fueled dual-fuel engines which are operable by tuning under various emission control modes (MAN, 2022). Besides, not only the GHG emissions but also the sulphur oxides (SO_X) and particulate matter (PM) as well as nitric oxides (NO_X) by selective catalytic reduction (SCR) or exhaust gas recirculation (EGR), substantially decrease when LNG or MeOH are used as the primary fuels onboard (IMO, 2023b).

In this study, a benchmark study for handymax size bulk carriers is carried out to obtain the general characteristics at first. Then a concept design of a 32000 DWT bulk carrier is performed including hydrostatic calculations, resistance and power estimations as well as general arrangement. The Energy Efficiency Design Index of the designed bulk carrier is calculated under a conventional configuration – a single main engine with no shaft generator and auxiliary engines fueled by MDO, LNG or MeOH. The effects of using LNG or MeOH as an alternative to MDO are shown in terms of energy efficiency and environmental impacts. Moreover, available technologies for bulk carriers are presented and possible contributions of these systems to the energy efficiency of bulk carriers are discussed.

2. General Characteristics of Bulk Carriers

Bulk carriers in the world merchant fleet are one of the dominant ship types which transport 43% of total goods in terms of tonnage and the capacity of these ships ranges from a few hundred to 400000 DWT (MAN, 2022). Depending on the size and capacity, bulk carriers are classified into small, handysize, handymax, panamax, capsize and very large bulk carriers (VLBC), whose typical overall length ranges from about 115 m to 360 m (MAN, 2022; Taşdemir et al., 2023). On the other hand, the typical overall length and DWT ranges of handymax bulkers are 150

m – 200 m and 35000 DWT – 50000 DWT, respectively (MAN, 2022). Before modelling and analyzing the hull forms, the general characteristics of 50 handymax bulk carriers that were built after 2013 are obtained using the VF database (Taşdemir et al., 2023). Fig. 1 shows the moulded beam/draft and overall length (L_{OA})/moulded beam (B); DWT and brake horsepower (BHP) of ships with respect to overall length. There are sister ships in the analyzed group, therefore, repetitive data are filtered. According to the plots, the average B/T and L_{OA}/B ratios are 3 and 6; DWT and BHP are 35000 and 10000, respectively. The ships have one conventional main engine and two or three auxiliary engines fueled by HFO and MDO.

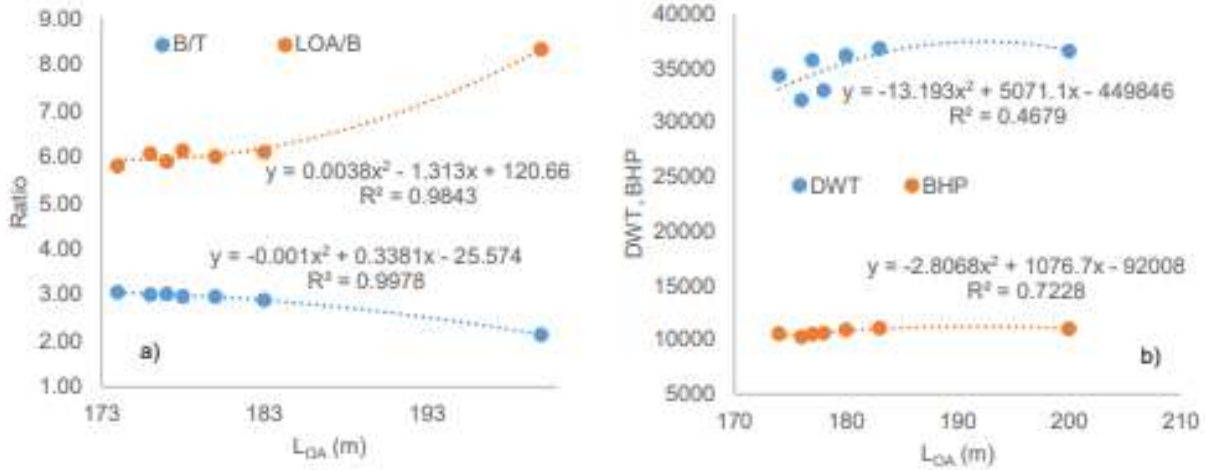

Fig. 1: Dimensional ratios (a) and DWT-BHP (b) of the investigated bulk carriers

3. Concept Design of the Bulk Carrier

The concept design of bulk carrier consists of hull modelling based on the agreed dimensions and capacity, preliminary hydrostatic and resistance calculations, planning of general arrangement, determination of the power requirements, main and auxiliary engines, making of equipment lists, preliminary cost calculations and rendering steps before contract and detail design phases. Based on the benchmark study and agreed properties the main characteristics of the conceptually designed bulk carrier are shown in Table 1.

Table 1. The main characteristics of the designed bulk carrier

Length overall (L_{OA})	178.00 m
Length waterline (L_{WL})	174.75 m
Breadth (moulded) (B)	29.12 m
Breadth (waterline) (B_{WL})	29.12 m
Depth (D)	15.00 m
Design draught (T)	9.70 m
Design freeboard (f)	5.30 m
Displacement tonnage (Δ)	40676 ton
Deadweight tonnage (DWT)	32000 DWT (@ design draught)
Cargo capacity	43000 m^3
Gross tonnage	24000 GT
MDO tank capacity	1500 m^3
LNG/MeOH tank capacity	600 m^3-3000 m^3
Crew	30
Design speed	14 knots
Navigation speed	12 knots
M/E power	7900 kW (1 set M/E)
A/E power	1500 kW + 150 kW (3 set A/E + 1 set E/G)

Before estimating the main propulsion power, the hull resistance and effective power are calculated for the modelled hull. Fig. 2 shows the concept design and the effective power change of the agreed hull at different speeds. According to the resistance calculations using the Holtrop-Mennen method, the effective power of the hull is about 5500 HP at design speed. This value is valid for full load with sea and machinery margins, and the brake power value obtained for 12 knots is approximately 7400 HP.

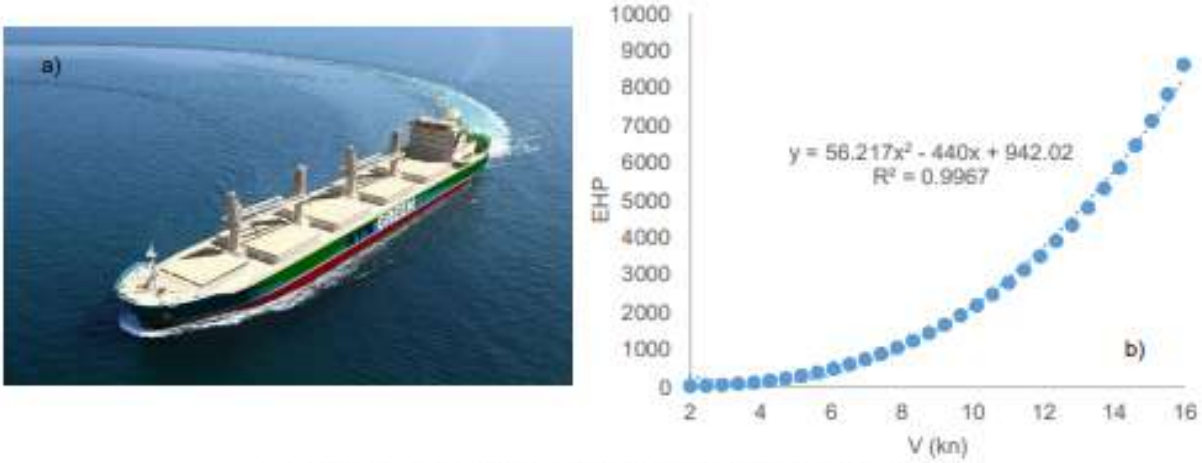

Fig. 2: Render of concept design (a) and the effective power change (b)

3. Calculation of EEDI for the Concept Design

The selection of engines which will meet the power requirements as well as comply with regulations is crucial. Nowadays, LNG and MeOH-fueled engines integrated with NOx reduction devices are proposed for onboard powering systems. Hence, after the estimation of main engine brake power, an engine selection process is conducted: The market-ready engines with the same power output and fueled with MDO, LNG and MeOH are investigated. Using the CEAS database (MAN, 2020), six-cylinder and 45 cm bore with ultra-long stroke 6G45ME-GI and 6G45ME-LGIM dual-fuel engines capable of generating 7900 kW at full load are selected for EEDI calculations. EEDI calculations are carried out using the guidelines of IMO (MEPC.308(73), 2018).

The chemical and physical properties of LNG and MeOH are remarkably different from MDO which results in varieties in thermal, economic, environmental performance and safety along with design. Carbon factor (t-CO2/t-fuel) and lower heating values (MJ/kg) of MDO, LNG and MeOH are 3.206, 2.75 and 1.375; 42.7, 48 and 19.9, respectively (MEPC.308(73), 2018). During calculations, only M/E and A/E are considered and there is no energy efficiency device integrated into these engines. The attained EEDI values of the bulk carrier installed with the main and auxiliary engines fueled with MDO, LNG and MeOH are shown in Fig. 3. According to the results, LNG and MeOH-fueled engines fulfil the reference EEDI. The bulk carrier with conventional MDO-fueled engines cannot comply with the limit unless additional energy-efficient systems or operations are conducted. Besides, the phase 3 reduction factor is defined as 20% for bulk carriers to be built, therefore, systems applied for the studied design cannot solely comply with the target EEDI. The LNG-fueled engines seem more feasible in terms of EEDI than MeOH, however, the volume occupied by the LNG-fueled propulsion systems is reported to be about 2 times higher than that occupied by MeOH-fueled system (Akman, 2023).

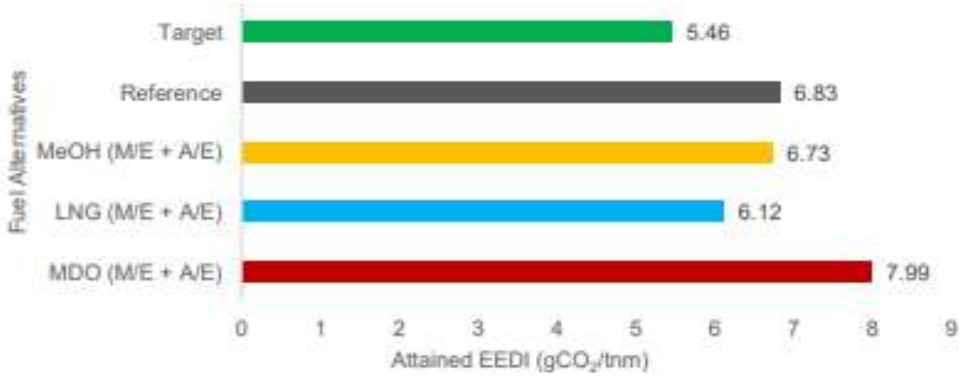

Fig. 3: Attained EEDI of bulk carrier fueled with MDO, LNG and MeOH

There are effective methods which can be applied in the design phase of bulk carriers to decrease the attained EEDI. Hull form optimization/modification or waste heat recovery systems are reported to be used to decrease the reference EEDI by up to 15%; integrating wind-assisted propulsion and PV panels are reported to decrease the annual fuel consumption about by 22% and 7%, respectively (Barreiro et al., 2022). Besides, using efficient propellers combined with rudder bulbs and flow regulators can reduce fuel consumption about by 12% (MAN, 2016).

4. Conclusions

In this study, handymax class bulk carriers' dimensional characteristics are presented and a concept design of a 32000 DWT bulk carrier is carried out including hydrostatic calculations, resistance and power estimations as well

as general arrangement. The Energy Efficiency Design Index of the designed bulk carrier is calculated installed with the dual-fuel engines powered by MDO, LNG or MeOH. The effects of using LNG or MeOH as an alternative to MDO are shown in terms of energy efficiency and emissions. According to the obtained data and calculation results, the attained EEDI of LNG-fueled bulk carriers is the lowest and complies with the reference value. Besides, methanol is a promising option in terms of design requirements and well-to-wake emissions. The stricter regulations are forcing the designers and engine manufacturers to install devices that increase energy efficiency and develop new technologies to comply with the limits set by IMO. In future studies, the combination of the aforementioned energy efficiency applications integrated with the LNG or MeOH-fueled systems can be investigated.

References

Akman, M. (2023). A Techno-Environmental and Energy Efficiency Investigation of Marine Dual-Fuel Engines. *Marine Science and Technology Bulletin*, *12*(2), 128–141. https://doi.org/10.33714/masteb.1247489

Akman, M., & Ergin, S. (2023). Thermo-economic optimization of an ORC system for a dual-fuel marine engine. *Proceedings of the Institution of Mechanical Engineers Part M: Journal of Engineering for the Maritime Environment*. https://doi.org/10.1177/14750902231207128

Barreiro, J., Zaragoza, S., & Diaz-Casas, V. (2022). Review of ship energy efficiency. *Ocean Engineering*, *257*, 111594. https://doi.org/10.1016/j.oceaneng.2022.111594

Dere, C., Zincir, B., Inal, O. B., & Deniz, C. (2022). Investigation of the adverse effects of slow steaming operations for ships. *Proceedings of the Institution of Mechanical Engineers, Part M: Journal of Engineering for the Maritime Environment*, *236*(4), 1069–1081. https://doi.org/10.1177/14750902221074191

Güler, E., & Ergin, S. (2021). An investigation on the solvent based carbon capture and storage system by process modeling and comparisons with another carbon control methods for different ships. *International Journal of Greenhouse Gas Control*, *110*. https://doi.org/10.1016/j.ijggc.2021.103438

IMO. (2023a). *2023 IMO Strategy on Reduction of GHG Emissions From Ships—MEPC.377(80)*. https://www.imo.org/en/MediaCentre/PressBriefings/pages/Revised-GHG-reduction-strategy-for-global-shipping-adopted-.aspx

IMO. (2023b). *Improving the energy efficiency of ships*. https://www.imo.org/en/OurWork/Environment/Pages/Improving%20the%20energy%20efficiency%20of%20ships.aspx

MAN. (2016). *MAN Alpha Unique Kappel Propellers – Radical Fuel Savings*.

MAN. (2020). *CEAS engine calculations*. https://www.man-es.com/marine/products/planning-tools-and-downloads/ceas-engine-calculations

MAN. (2022). *Propulsion trends in bulk carriers*. https://www.man-es.com/docs/default-source/marine/tools/propulsion-trends-in-bulk-carriers.pdf?sfvrsn=d851b1c6_14

MEPC.308(73). (2018). *Guidelines on The Method of Calculation of The Attained Energy Efficiency Design Index (EEDI) for New Ships*.

Taşdemir, A., Nohut, S., & Akman, M. (2021). Analytical and Numerical Analysis of the Strength Performance of a Novel Ship Construction Profile. *Journal of ETA Maritime Science*, *9*(3), 200–209. https://doi.org/10.4274/jems.2021.87049

Taşdemir, A., Nohut, S., & Akman, M. (2023). *Gemi Türleri—Ticari Gemilerin Karakteristik Özellikleri* (1st ed.).

Turan, B. İ. (2023). Design framework for sail & rigging parameters of Bodrum Gulets: Comparison of schooner and ketch configurations. *Ships and Offshore Structures*, *18*(11), 1582–1593. https://doi.org/10.1080/17445302.2022.2129918

Yercan, F., & Sogut, M. Z. (2023). Comparative analysis of entropy and environmental impacts of shipping operations on arctic and international routes. *Applied Ocean Research*, *139*, 103707. https://doi.org/10.1016/j.apor.2023.103707

IEEES-140

Analysis of Thermally Coupled Fuel Cell and Metal Hydride Hydrogen Storage Tank System for Lightweight Vehicles

[1*]Sera Ayten Çetinkaya, [2]Mehmet Akif Ezan, [2]Mustafa Umut Karaoğlan, [2]C. Ozgur Colpan
[1]The Graduate School of Natural and Applied Sciences, Dokuz Eylul University, Izmir, Türkiye
[2]Department of Mechanical Engineering, Faculty of Engineering, Dokuz Eylul University, Izmir, Türkiye

*E-mails: sera.acetinkaya@gmail.com

Abstract

Hydrogen technologies are now more widely used thanks to hydrogen's growing significance in recent years. These technologies include metal hydride (MH) tanks, which chemically store hydrogen, and fuel cells, which utilize hydrogen to produce electricity. However, MH tanks' either charge or discharge require thermal management during their operation. This study aims to develop a 1D mathematical model to examine the thermal interaction between the fuel cell and the MH tank system for their incorporation in lightweight vehicles. Mass balance, energy balance, and kinetic reaction equations for the MH tank were solved using the MATLAB/Simulink program. The hydrogen consumption amount of the fuel cell under different power outputs is defined in the model, and the hydrogen need of the fuel cell under a certain driving cycle is given as input to the MH tank model. To ensure thermal management, a controller is designed between the fuel cell and the tank, depending on the temperature variations of the MH tank during desorption and the operating pressure of the fuel cell. Analyses were carried out for 2 different scenarios: Scenario-1 (without thermal coupling and controller) and Scenario-2 (with thermal coupling and without controller).

Keywords: Fuel Cell Vehicle, Metal Hydride Hydrogen Storage, Thermal Coupling, Thermal Management

I. Introduction

In the literature, numerous studies have investigated the thermal interaction of proton exchange membrane fuel cell (PEMFC) and metal hydride (MH) hydrogen storage systems employing various cooling methods, both experimentally and theoretically. Zhu et al. (2019) integrated a PEM fuel cell and an MH hydrogen storage tank thermally using a heat exchanger and control system. They employed a liquid coolant in the cooling system, where the heat generated by the fuel cell was directed to the fluid that facilitated the heating of MH tanks with the assistance of a fan. Subsequently, they developed a mathematical model to analyze the dynamic behavior of the system and experimentally validated the model. Omrani et al. (2019) theoretically examined the thermal connection in a system comprising an open-cathode PEMFC and an MH tank. They constructed a mathematical model to simulate the heat transfer between PEMFC waste heat and MH storage. Rahimi and Mahmoodi (2019) utilized heat pipes to transfer heat from the fuel cell to the MH tank and conducted analyses using Computational Fluid Dynamics (CFD) simulations. Alam et al. (2020) investigated waste heat recovery from PEMFC using thermally coupled Thermoelectric Generators (TEG) and MH tanks. They proposed a strategy involving the thermal integration of PEMFC, TEG, and MH for efficient waste heat recovery from PEM fuel cells. They developed a mathematical model for the theoretical prediction of the system's dynamic performance. Chabane et al. (2021) presented the thermal interaction topology of an MH tank and PEMFC for vehicle applications. They designed the system using MATLAB/Simulink and conducted analyses to examine its performance.

In this study, a 1D mathematical MH tank desorption model was developed in Matlab/Simulink using the finite volume method. The model was validated using data from the literature. The FC-MH model was created by combining the MH model with the power output of the fuel cell. By examining the operating conditions of the FC-MH system under two different scenarios (Scenario-1 (without thermal coupling and controller) and Scenario-2 (with thermal coupling and without controller), it is aimed to determine the most suitable system for lightweight vehicles.

II. System Description and Mathematical Model

The FC-MH system planned to be designed is for lightweight vehicles. The schematic of the system is given in Fig. 1. The specifications of the fuel cell and metal hydride tank planned to be used in the system are given in Table 1. It is planned to use 3 metal hydride tanks in the system. The geometry of the hydrogen tank was determined by considering commercial hydrogen tanks in the literature. The drive cycle given in Fig. 2(a) was used for the calculation of the power requirement to be supplied by the fuel cell (Fig. 2(b)). This cycle is approximately 8 km long. The amount of hydrogen required to complete a cycle is calculated as approximately 15 g. Accordingly, the driving cycle was repeated 12 times to completely run out of hydrogen in the tank.

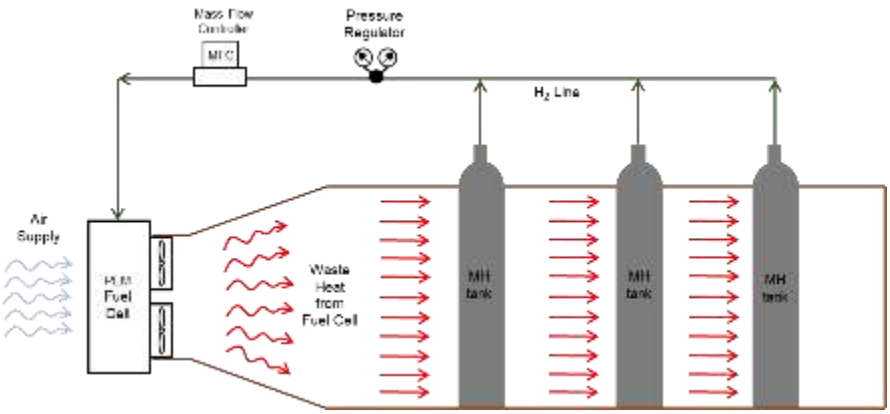

Fig. 1. Schematic of the FC-MH System for Lightweight Vehicles

Table 1. Specifications of the PEM Fuel Cell and the Metal Hydride Tank

Vehicle	Weight	365 kg
	Battery Capacity	0.6 kWh
	Maximum Speed	64 km/h
H2000 Fuel Cell [7]	Type of Fuel Cell	PEM
	Number of Stack	48
	Dimensions	30.3 cm × 35 cm × 18.3 cm
	Rated Power	2000 W
	H_2 Pressure at the Inlet	0.45 – 0.55 bar
	Reactants	Hydrogen and Air
	Maximum Stack Temperature	65 °C
Metal Hydride Hydrogen Storage Tank [8]	Material	$LaNi_5$
	Maximum Hydrogen Capacity	63 g
	Height	26 cm
	Diameter	10 cm
	Charging Pressure	5 - 12 bar
	Maximum Pressure	30 bar

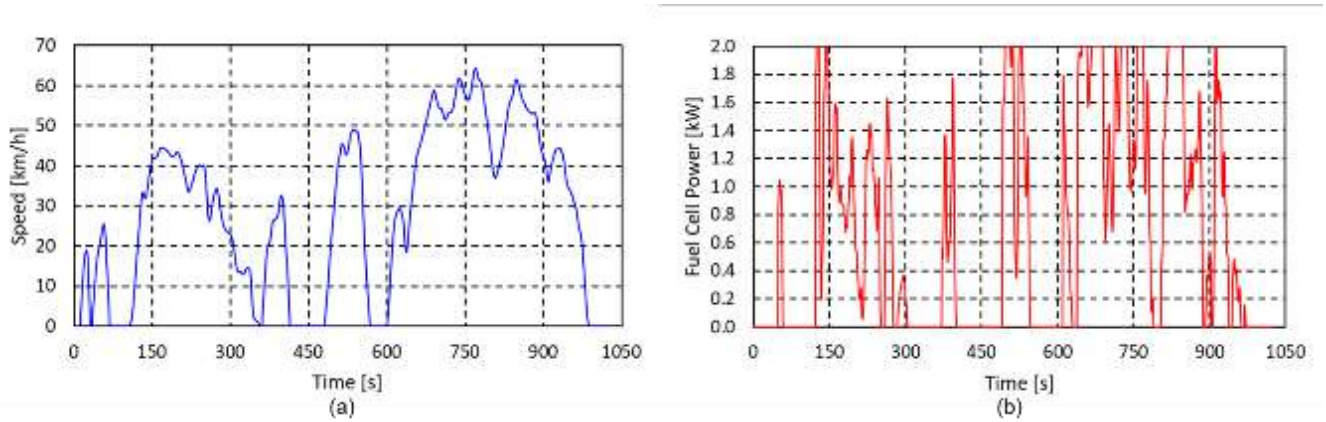

Fig. 2. Profiles used in the model: (a) driving cycle and (b) power input required for fuel cell operation

Two different scenarios were determined to examine the effect of thermal management in the FC-MH system. In Scenario-1, it is assumed that there is no thermal management and the hydrogen flow rate provided to the fuel cell is provided by the simultaneous

operation of 3 MH tanks. In Scenario-2, MH tanks operate simultaneously as in Scenario-1, but it is planned to create thermal management between the fuel cell and MH tanks by transmitting the waste heat of the fuel cell onto the tanks.

The 1D mathematical model was developed in Matlab/Simulink. The hydrogen flow rate determined according to the power need of the fuel cell is given by the demand block subsystem (Fig. 3). The metal hydride model was divided into two subsystems as mass balance/density equations subsystem and energy balance subsystem (Fig. 4). The detailed information can be found in Ref. [9] for modeling of MH hydrogen storage system.

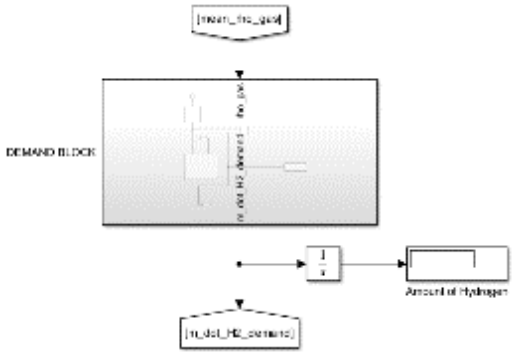

Fig. 3. Demand Block Subsystem

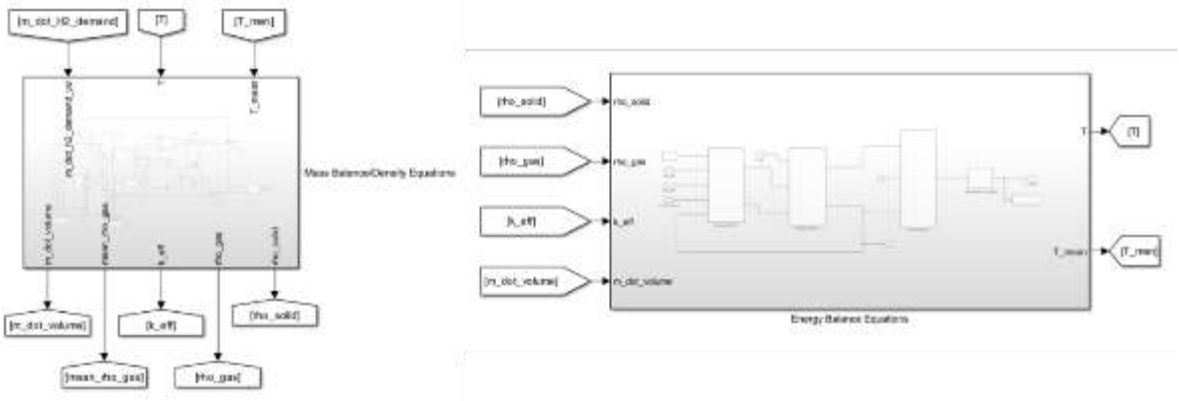

Fig. 4. Mass Balance/Density Equations Subsystem and Energy Balance Subsystem

III. Results and Discussion

In this section, analyses were carried out for Scenario-1 at constant ambient temperature (25 °C) and different heat transfer coefficients where the air was assumed to be stagnant. Table 2 examines the amount of hydrogen consumed by the MH tanks until the surface temperature drops to 5 °C. Results are given in terms of the travel duration and range of the vehicle for each heat transfer coefficient. Increasing the convective heat transfer slightly extends the range and travel range yet considering the length of the driving cycle, Scenario-1 looks insufficient to provide the required hydrogen discharge rate from the MH tank. However, it has been observed that this scenario is insufficient considering the length of the driving cycle and the amount of hydrogen that the tanks can store.

Table 3. Hydrogen consumption, duration, and range in different heat transfer coefficients for Sc-1 at 25°C

Heat Transfer Coefficient [W/m^{2}K]	Hydrogen Consumption [g]	Duration [s]	Range [m]
3	1.946	748	1410
4	1.951	749	1415
5	1.956	750	1419
6	1.961	751	1423
7	1.966	752	1427

In Table 3, the results of the analyses performed at different temperatures (25 °C - 55 °C) and different heat transfer coefficients for Scenario-2 are presented. In Scenario-2, it is aimed to examine the forced convection effect by using higher heat transfer coefficient values compared to Scenario-1 and using different ambient temperatures. Table 3 shows that the increases in hydrogen consumption, simulation time, and range in which the vehicle can move depend on the increase in convection coefficient and temperature. Compared to Scenario-1, it can be said that Scenario-2 is better, but in this case, it is not sufficient considering the driving cycle and the hydrogen that the tanks can store.

Table 3. Hydrogen consumption, duration, and range under different heat transfer coefficients and temperature for Sc-2

Temperature [°C]	Hydrogen Consumption [g] / Duration [s] / Range [m]		
	10 W/m^{2}K	20 W/m^{2}K	30 W/m^{2}K
25	1.98 / 755 / 1441	2.027 / 761 / 1466	2.073 / 766 / 1489
30	2.025 / 760 / 1465	2.112 / 770 / 1510	2.225 / 814 / 1683
35	2.07 / 765 / 1488	2.223 / 814 / 1682	2.358 / 830 / 1735
40	2.115 / 770 / 1512	2.316 / 825 / 1718	2.495 / 844 / 1799
45	2.163 / 779 / 1555	2.412 / 835 / 1760	2.662 / 878 / 1947
50	2.226 / 815 / 1683	2.511 / 846 / 1808	2.295 / 1220 / 2543
55	2.276 / 821 / 1703	2.628 / 871 / 1918	4.211 / 1681 / 3282

IV. Conclusion

In this study, it is aimed to thermally couple a fuel cell and metal hydride hydrogen storage tanks. Using the Matlab/Simulink program, the hydrogen flow rate that the 2 kW fuel cell should use for the power requirement under a certain driving cycle was given as input to the 1D mathematical metal hydride tank model. To examine the effect of thermal management, the model was tested for two different scenarios. For Scenario-1, where there is no thermal management, the results showed an increase depending on the convection coefficient, but it could not complete the driving cycle. Although the results of Scenario-2 with thermal management were better than Scenario-1, they were still insufficient to meet the driving cycle. These results show the necessity of thermal management for effective operation in the FC-MH system. In the continuation of the study, it is planned to design a controller that controls the hydrogen flow rate for MH tanks and to conduct parametric studies under different scenarios.

Acknowledgements

This work has been supported by Dokuz Eylül University Scientific Research Projects Coordination Unit under grant number FBA-2023-2996.

References

[1] Zhu, D., Ait-Amirat, Y., N'Diaye, A., & Djerdir, A. (2019). Active thermal management between proton exchange membrane fuel cell and metal hydride hydrogen storage tank considering long-term operation. Energy Conversion and Management, 202, 112187.

[2] Omrani, R., Nguyen, H. Q., & Shabani, B. (2019). Open-cathode PEMFC heat utilisation to enhance hydrogen supply rate of metal hydride canisters. Energy Procedia, 160, 542-549.

[3] Rahimi, R., & Mahmoodi, F. (2019). Transient three-dimensional simulation of a metal hydride hydrogen storage tank interconnected to a PEM fuel cell by heat pipes. Iranian Journal of Hydrogen & Fuel Cell, 6(2), 117-132.

[4] Alam, M., Kumar, K., & Dutta, V. (2020). Dynamic modeling and experimental analysis of waste heat recovery from the proton exchange membrane fuel cell using thermoelectric generator. Thermal Science and Engineering Progress, 19, 100627.

[5] Chabane, D., Iqbal, M., Harel, F., Djerdir, A., Candusso, D., Elkedim, O., & Fenineche, N. E. (2021). Coupling a metal hydride tank with a PEMFC for vehicular applications: A simulations framework. International Journal of Energy Research, 45(11), 16511-16523.

[7] Horizon PEM Fuel Fell h-2000 Manual, 2013. https://www.fuelcellstore.com/manuals/horizon-pem-fuel-cell-h-2000-manual.pdf (Date of Access: 12.05.2023)

[8] Busqué, R., Torres, R., Grau, J., Roda, V., & Husar, A. (2017). Effect of metal hydride properties in hydrogen absorption through 2D-axisymmetric modeling and experimental testing in storage canisters. international journal of hydrogen energy, 42(30), 19114-19125.

[9] Disli, T., Çetinkaya, S. A., Ezan, M. A., & Colpan, C. O. (2023). Numerical investigations on the absorption of a metal hydride hydrogen storage tank based on various thermal management strategies. International Journal of Hydrogen Energy.

Structural and thermal characterization of polyethylene-based nanocomposites containing multi-walled carbon nanotubes.

[1]*SororSaadallah,[2]Kelthoum Saadallah,[1]Mohamed CherifBouleklab,[1]Smail Hamamda

[1] Laboratory of Thermodynamics and Surface Treatment of Materials, Constantine 1 University, P.O. Box, 325 Route Ain el Bey, Constantine, Algeria

[2] Laboratory of process engineering, Amar TelidjiUniversityofLaghouat, BP37G, Laghouat 03000, Algeria

*E-mails:sororsaadallah@yahoo.com

Abstract

High-density polyethylene (HDPE) is a widely used thermoplastic polymer that is produced through the polymerization of ethylene. Polymer-based composites, such as HDPE, play an important role in daily life and have social and economic importance. This study focuses on evaluating the effect of multi-walled carbon nanotubes (MWNTs) as fillers in HDPE with specific properties sourced from "Ufa Org Synthesis" in Russia. Different mixtures with varying MWNT fractions were prepared for analysis, resulting in four types of samples. The samples were characterized using X-ray diffraction (XRD), differential scanning calorimetry (DSC), and FT-IR analysis. X-ray diffraction showed that the nanocomposites were well crystalline, particularly in the PE+0.04%MWNT and PE+0.01%MWNT samples. The FT-IR spectra revealed that the presence of MWNTs with HDPE could be identified through characteristic peaks in the spectrum, indicating the successful incorporation of MWNTs in the matrix itself. Additional evaluation of the thermal properties of the composites was performed using DSC. The results confirmed that MWNTs have a positive effect on the physicochemical properties of HDPE-MWNTs nanocomposites, particularly enhancing thermal resistance compared to HDPE. This finding suggests that the potential applications of polymer/carbon nanotube nanocomposites are broad, ranging from energy storage and environmental protection to medicine.

Keywords: Polymeric matrix composites (PMCs), Nano-structures, Thermal properties, Physical properties.

I. Introduction

Recent years have seen a significant increase in interest in polyethylene-based nanocomposites because of their special combination of characteristics, which include improved mechanical, thermal, and electrical capabilities. Particularly, high-density polyethylene (HDPE) is commonly utilized in diverse applications. It is initially produced through the high-pressure polymerization of ethylene. Because of its high degree of branching, which forces the molecules to be loose rather than packed, this polymer forms a low-density material that is ideal for sterile medical packaging films, plastic bags, and wraps due to its great flexibility and chemical resistance(DB, 2010; Khelil et al., 2023; Omar et al., 2012). A wide range of potential solutions in numerous disciplines have become possible due to the capacity to build and modify materials at the nanoscale.In the last few decades, a vast array of nanomaterials have been produced(Zakaria et al., 2019).Multiwalled carbon nanotubes (MWCNTs) have demonstrated significant promise in strengthening polymer matrices, mechanical characteristics, and high aspect ratios(Zhang & Jiang, 2011).The improvement of the mechanical characteristics of polymeric matrices mainly relies on the exceptional mechanical properties of MWCNTs, such as their high strength, stiffness, and aspect ratio. The incorporation of multi-walled carbon nanotubes (MWCNTs) into High-density polyethylene (HDPE) nanocomposites presents the potential to exploit the complimentary interactions, resulting in enhanced material characteristics.The distinct combination of HDPE's with MWCNT's remarkable mechanical, electrical, and thermal characteristicspresents a favorable option for the advancement of advanced nanocomposites in diverse industrial sectors. The objective of this paper is to analyze the structure and thermal properties of nanocomposites made fromhigh density polyethylene (HDPE) and multi-walled carbon nanotubes (MWCNTs).

II.Experimental Procedure/Methodology/System Description

The high-density polyethylene (HDPE) with a density of 918.5 ± 1.5 kg/m3 produced by "Ufa Org Synthesis" (Russia) and multi-walled carbon nanotubes (MWCNTs) were utilized in the sample preparation. The nanotubes were synthesized using the chemical vapor deposition (CVD) technique within a spinning reactor. The catalyst used was a powder combination of Al_2O_3, MoO_3, and Fe_2O_3(Zhang et al., 2003).The propylene was just used as a source of carbon (Revo S, (2015)).

The samples underwent a multi-step preparation process. Initially, the HDPE and MWCNT powders were combined in a revolver-type rotational for 4 hours and 120 revolutions per minute. After thorough mixing, the resulting isotropic mixtures were collected. Next, these mixtures were loaded into an extruder vacuum cylinder and subjected to heat. The temperature was raised to 120 °C and maintained for 40 minutes, while the pressure inside the cylinder reached 103 Pa. As a result, the mixture underwent a process of forced extrusion through a die. The final step involved shaping the composites into cylindrical form. These cylinders had a uniform diameter of 3 mm and a height of approximately 5 mm. In total, four different types of samples were generated for further investigation. The types were identified by the different proportions of MWCNTs (0.01%, 0.04%, 0.07%, and 10%) in the initial mixtures.

III. Characterization methods

A range of experimental methods, including differential scanning calorimetry (DSC), infrared spectroscopy, and X-ray diffraction (XRD), were used to characterize the samples.

Cuk α radiation (copper anode, wavelength λ cuk α =1.541838 Å) was used in the Xpertpro diffractometer XRD examination at 45 kV and 40 mA, with a scanning range of 2θ = 20-100°. The analysis was carried out at a temperature of 25 °C.

The thermal characteristics of the nanocomposites were evaluated using a Jupiter STA 449 F3 calorimeter manufactured by Netzsch in Selb, Germany. DSC measurements were employed for this purpose. The samples were subjected to heating in an Al2O3 crucible, with a temperature range of 30-160 °C and a heating rate of 10 °C per minute. The DSC measurements were conducted using a regulated flow rate of 20.0 ml/min in an argon atmosphere.

The Jasco FT/IR-6300 spectrometer was chosen to produce infrared spectra in the mid-infrared region, specifically within the wavelength range of 2.5 to 25 micrometers (400-4000 cm-1). This instrument was selected for its ability to detect changes in functional groups as well as investigate the functionality and molecular bonding of the composite material.

IV. Results and discussion

IV.1. XRD

Xray diffraction was used to further investigate the structural analysis of the HDPE+X%MWCNT sample (X=0.01%, 0.04%, 0.07%, and 10%); Figure 1 depicts the model used for this study.

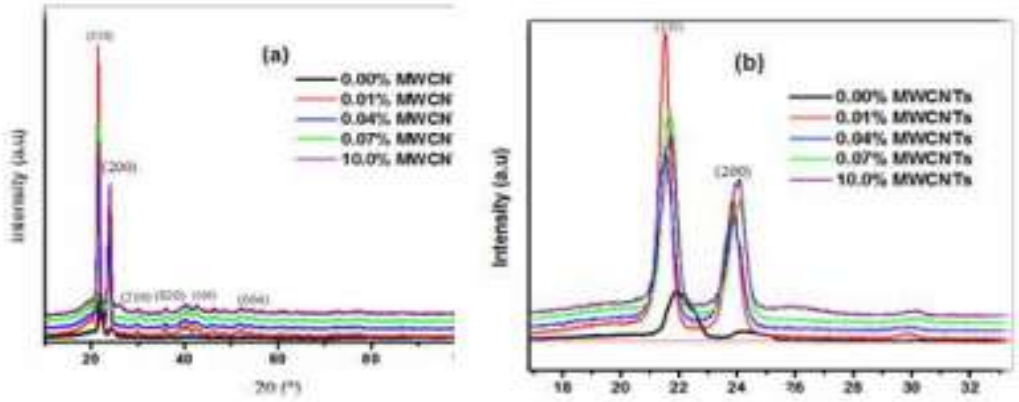

Fig.1. X-ray diffraction spectra of the pure HDPE and the HDPE +X%MWCNTs Nanocomposites.

Figure 1-(a) shows five diffraction peaks with intensities corresponding to the (110),(200),(210),(020),(100), (004) planes. This proves that the nanocomposites are well crystallized, especially in the HDPE+0.04%MWCNT and HDPE+0.01%MWCNT sample. Each peak corresponds to a family of reticular plane (hkl). No characteristic peak of impurities was detected. There are two peaks (110) and (004) which come from carbon nanotubes, observed by (Fouad & Elleithy, 2011)when the concentration of MWCNTs is high in polyethylene, an increase in the intensity of the peaks is observed.X-ray diffraction characterization showed that the intensities of all peaks of the nanocomposite are clearly higher than those of pure polyethylene,this is well evident in Figure 1-(b) .Thus, the introduction of multi-walled carbon nanotubes is responsible for a strong increase in the intensities of the X-ray diffraction peaks of the nanocomposites.

IV.2. DSC

Heat flux is a quantitative measure of the amount of heat that is transferred between a substance and its surrounding environment. Differential scanning calorimetry (DSC) is a measurement technique used to assess the thermal properties of a substance, including heat capacity, melting point, glass transition, and more. Polymers, such as polyethylene, serve as a prime example due to their widespread utilisation in diverse industries owing to their exceptional mechanical and thermal characteristics. The process of self-organization into crystalline structures results in the liberation of heat and the generation of an exothermic peak.

DSC curves are shown for HDPE +X% MWCNTs samples with varying concentrations of carbon nanotubes Fig.2.

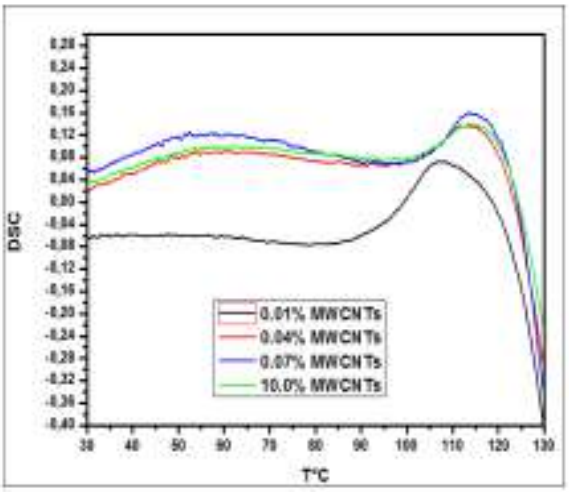

Fig. 2.Differential scanning calorimetric diagrams for the PE + X%MWCNTs Nanocomposites.

Figure 2 demonstrates that all the curves exhibit identical forms until reaching an angle of 90°. Furthermore, the differential scanning calorimetry (DSC) intensity of the sample having the lowest concentration of carbon nanotubes, specifically 0.01%, exhibits the lowest value across the whole range of temperatures. The HDPE+0.07%MWCNT sample exhibits a significantly higher DSC (differential scanning calorimetry) value in comparison to the other two nanomaterials. A sharp drop in heat flux is seen, along with many oscillations close to the melting point.
Therefore, the three curves representing 0.04%, 0.07%, and 10% exhibit nearly identical levels of intensity. At a temperature of 115°C, there is a noticeable exothermic peak, which suggests a transition in the material, perhaps associated with its breakdown. In general, the calorimetric curves exhibit similar appearance. This is most likely related to carbon nanotubes' high dispersion. This finding is consistent with that of (Khelil et al., 2023), who investigated polyethylene containing significant concentrations of multi-walled carbon nanotubes.

IV.2. Infrared spectroscopy

Figure 4 presents the transmission infrared (FTIR) spectra of HDPE + x% MWCNT (carbon nanotube) samples.

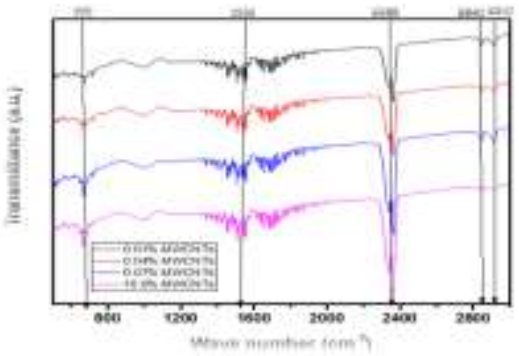

Fig. 4.Fourier Transform Infra-Red spectroscopy for the PE + X%MWCNTs Nanocomposites.

There is a direct correlation between wave number and intensity, as the graphic illustrates. The infrared spectrum indicates the existence of several domains.
Pure HDPE polyethylene contains CH_2 groups and displays absorption bands of high, medium, and low intensity associated with these groups. The spectra exhibit distinct absorption bands that correspond to the polyethylene molecules, particularly the bands centred at 660 cm^{-1}, which are associated with the vibration modes γ (C-H) of both the crystalline and amorphous phases. The absorption bands at around 1540 cm^{-1} correspond to the δ (C-C) vibration modes of both the crystalline and amorphous phases. In addition, the υ (C-H) bond exhibits symmetric and asymmetric vibrations at 2841 cm^{-1} and 2917 cm^{-1}, respectively. Theresults are comparable to the findings reported by (Bajer et al., 2005; Boudrahem M, (2014); Stark & Matuana, 2004)
The infrared spectra exhibit varying intensities of different vibration modes, which are contingent upon the inclusion of carbon nanotubes.

v. Conclusion

The findings of this research are substantial, as they demonstrate the improvement of thermostructural characteristics and validate the advantageous effects of integrating multi-walled carbon nanotubes

within the domain of materials science. Nanocomposites composed of polyethylene and multi-walled carbon nanotubes possess the ability to substitute heavy and expensive materials. This advantage enables significant advancement in diverse sectors of the business.

References

Bajer, D., Kaczmarek, H., Buffeteau, T., & Sourisseau, C. (2005). Photo- and Bio-Degradation Processes in Polyethylene, Cellulose and their Blends Studied by ATR-FTIR and Raman Spectroscopies. *Journal of Materials Science*, *40*, 4189-4198. https://doi.org/10.1007/s10853-005-2821-y

Boudrahem M, B. A., Kirati O. ((2014)). Etude de Vieillissement d'un Polyethylene de haute Densite (PEHD 100) Utilise dans les Conduites a Gaz Sous Pressions., *2*, 20–26.

DB, M. (2010). *Downstream aspects of polyethylene. In: Introduction to industrial polyethylene, pp 99–115*.

Fouad, H., & Elleithy, R. (2011). High density polyethylene/graphite nano-composites for total hip joint replacements: Processing and in vitro characterization. *Journal of the Mechanical Behavior of Biomedical Materials*, *4*(7), 1376-1383. https://doi.org/https://doi.org/10.1016/j.jmbbm.2011.05.008

Khelil, S., Barama, N., Naoui, Y., Bouleklab, M. C., Dorbani, T., Nedilko, S., Revo, S., & Hamamda, S. (2023). Influence of the MWCNTs on the properties of the HDPE + X% MWCNTs nanocomposites. *Applied Nanoscience*, *13*, 6849-6858. https://doi.org/10.1007/s13204-023-02802-9

Omar, M. F., Akil, H. M., & Ahmad, Z. A. (2012). Effect of molecular structures on dynamic compression properties of polyethylene. *Materials Science and Engineering: A*, *538*, 125-134. https://doi.org/https://doi.org/10.1016/j.msea.2011.12.111

Revo S, H. S., Ivanenko K et al. ((2015)). Thermal analysis of Al + 0.1% CNT ribbon. *Nano Res Lett* https://doi.org/https:// doi. org/ 10.1186/ s11671- 015- 0878-3

Stark, N. M., & Matuana, L. M. (2004). Surface chemistry changes of weathered HDPE/wood-flour composites studied by XPS and FTIR spectroscopy. *Polymer Degradation and Stability*, *86*(1), 1-9. https://doi.org/https://doi.org/10.1016/j.polymdegradstab.2003.11.002

Zakaria, M. R., Md Akil, H., Abdul Kudus, M. H., Ullah, F., Javed, F., & Nosbi, N. (2019). Hybrid carbon fiber-carbon nanotubes reinforced polymer composites: A review. *Composites Part B: Engineering*, *176*, 107313. https://doi.org/https://doi.org/10.1016/j.compositesb.2019.107313

Zhang, J., & Jiang, D. (2011). Interconnected multi-walled carbon nanotubes reinforced polymer-matrix composites. *Composites Science and Technology*, *71*(4), 466-470. https://doi.org/https://doi.org/10.1016/j.compscitech.2010.12.020

Zhang, M., Rong, M., Zhang, H., & Friedrich, K. (2003). Mechanical Properties of Low Nano-Silica Filled High Density Polyethylene Composites. *Polymer Engineering & Science*, *43*, 490-500. https://doi.org/10.1002/pen.10040

IEEES-142

Polystyrene ZIF-8 Metal-Organic Framework Composite Nanofibrous Membrane for Oil/Water Separation

Kamala Thota, ,Ramya Araga, Manohar Kakunuri, Sharath babu Anne*.
National Institute of Technology Warangal, Department of Chemical Engineering, Warangal, 506004, India
* E-mail: sarat@nitw.ac.in

Abstract
Efficient separation of oil/water is essential for mitigating oil pollution stemming from both oil spills and industrial oily wastewater. This has led to the development of highly efficient superhydrophobic and superoleophilic membranes. The surface morphology, area, and functional groups are pivotal in fine-tuning the surface wettability of these membranes. Frequently, nanofibrous membranes with high surface areas incorporate materials with low surface energy and extensive surface area to amplify wettability. In this study, zeolite imidazole framework (ZIF-8) particles exhibit strong hydrophobic and oleophilic characteristics, boasting a high surface area as well as excellent thermal and chemical stability were embedded into polystyrene precursor to fabricate superhydrophobic/superoleophilic composite nanofibrous membrane using electrospinning technique. This composite membrane exhibited outstanding oil sorption capability for both miscible and immiscible oil/water mixtures. The electrospun composite nanofibrous membrane surface morphology, wettability, oil sorption capacity, separation efficiency, thermal stability, and oil permeate flux were examined meticulously. The composite membrane proliferated WCA, oil permeate flux, separation capacity, and absorption capacity values compared to the pristine membrane attributed to the incorporation of ZIF-8 particles. The fabricated composite nanofibrous membrane exhibited a high-water contact angle (WCA) of ≈155^{o}± 1.5^{o} and an oil contact angle of 0^{o}. The oil permeate flux for surfactant stabilized W/O peanut emulsion (1896±81 L/m^2.h) and immiscible oil/water separation (2936±108 L/m^2.h). The composite membrane successfully separated the oil from water in sunflower oil, water in bean oil, and water in diesel emulsions. Furthermore, the separation efficiency of the composite membrane was determined and found to be 99±0.5%. The fabricated composite membrane was an excellent promising material separating the oil from the emulsion.

Keywords: Zeolite imidazole framework (ZIF-8), emulsion separation, superhydrophobicity, electrospinning, and polystyrene.

Introduction

Oil pollution poses a significant challenge, with enduring and severe consequences for the environment (Rasouli, 2021). The continuous occurrence of oil pollution is primarily attributed to incidents like oil spills, oil transportation, petrochemical industries, chemical industries, textile industries, and daily life activities (Wang, 2015). This results in a devastating impact on the ecological environment and substantial economic losses (Zhang, 2020). Current approaches for oil/water separation, including skimming, gravity separation, sedimentation, and biological methods, have limitations such as secondary pollution, low oil absorption capacity, high economic costs, and low separation efficiency (Zhang, 2020; Sarbatly, 2016).

Additionally, these conventional methods are effective for separating immiscible oil/water mixtures but prove inadequate for emulsified miscible oil/water mixtures (emulsions). Therefore, there is a pressing need to develop innovative materials for oil/water separation to overcome these drawbacks. Emulsified oil/water mixtures, especially those with water droplet sizes less than 20 μm, present a significant challenge for separation (Zhang, 2022). Membrane materials emerge as a promising solution due to their small pore sizes, effectively hindering the penetration of emulsified water droplets and enabling the separation of emulsion oil/water mixtures (Thota, 2023).

Electrospun fibrous membranes are most suitable for miscible emulsion separations due to their eminent features like high porosity, surface morphology, low fabrication cost, high oil absorption capacity, high separation efficiency, easy fabrication method, etc. (Zhang, 2020). Membranes are fabricated by different methods such as electrospinning, template synthesis, self-assembly, etc. (Deng, 2023). Nanofibrous membranes well known for various applications due to their unique properties such as high surface-to-volume ratio, high surface area, high porosity, economically feasible, flexibility, etc. (Ma, 2016). However, nanofibers have demerits such as low separation efficiency, low mechanical strength, reusability, temperature sensitivity, etc. (Moatmed, 2019). To surpass these demerits as well as to increase the roughness, WCA, separation efficiency, chemical stability, and absorption capacity of fibrous membranes different materials are incorporated into the polymer matrix such as nanoparticles (SiO_2, Al_2O_3, Fe_3O_4), metal-organic frameworks (MOF), etc. (Jiang, 2020).

Recently, MOFs are prominent materials for various applications such as water purification, gas separation, catalysis, and energy storage devices, owing to their eminent features like high surface area, high porosity, high water contact angle, thermally and chemically stable, selective oil/water separation, etc. MOFs are available in different types based on the type of metal ions and organic linkers used in the synthesis, ZIF-8 was one of the MOF material . ZIF-8 was synthesized by combining the zinc metal ions with a 2-methyl imidazolate organic linker which has hydrophobic properties (Li, 2021). ZIF-8 is an outstanding material for oil/water separation owing to its low cost of synthesis, facile preparation, high surface area, and hydrophobic behavior.
Herein, we demonstrated the facile fabrication of a ZIF-8 incorporated PS fibrous membrane that exhibits excellent w/o emulsion separation with a high oil permeate flux, superhydrophobicity, and oil absorption capacity. However, few studies are available on ZIF-8-based sponges, meshes, and aerogel oil/water separation. But, as far as concerned to our knowledge no reported data is available on ZIF-8 incorporated PS fibrous membrane for surfactant stabilized w/o emulsion separation. The prepared composite fibrous membrane's morphology, WCA, immiscible and emulsion oil/water separation, oil permeate flux, oil absorption capacity, thermal stability, and chemical stability were studied thoroughly. This composite membrane displayed excellent features compared to the pristine fibrous membrane.

II. Experimental Procedure

Fabrication of ZIF-8 incorporated PS composite membrane

Firstly, for the synthesis of ZIF-8 nanoparticles, Zinc nitrate hexahydrate was dissolved in 200 ml of methanol (solution-I) stirred for 15 min and organic linker 2-methylimidazole was dissolved in 100 ml of methanol (solution-II) stirred for 15 min. Solution-I was added to solution-II slowly and stirred for 3 hours using a magnetic stirrer. The solution mixture color will change from colorless to a turbid white color solution. ZIF-8 nanoparticles were collected after centrifugation (7000 rpm) of 3 times (10 min) and washed with methanol several times. The nanoparticles were dried in a vacuum oven at 70 ^{o}C for 12 hours. After drying nanoparticles were used in the fabrication of the composite membrane.

First, 0.8g of ZIF-8 nanoparticles was dissolved in 10 ml of N, N-dimethylformamide (DMF) using a magnetic stirrer with a speed of 800 rpm for 3hrs. To this solution, 0.8g of PS was added to the ZIF-8 dispersion and magnetically stirred for 10 hours to form a uniform solution. This solution was loaded into a 10 ml syringe and arranged in the electrospinning setup. The humidity and temperature of the electrospinning setup were 45% and 25^{o}C respectively. The voltage, rotating drum speed, drum collector distance from the needle tip, and flow rate of the precursor solution were 16 kV, 250 rpm, 12cm, and 0.8 ml/hr. respectively. An 18-gauge needle was used for discharging the precursor solution. For the pristine PS fibrous membrane first, 0.8 g of PS was dissolved in DMF solvent using a magnetic stirrer with a speed of 400 rpm for 8 hr. The operating conditions for electrospinning were voltage, rotating drum speed, drum collector distance from the needle tip and PS solution flow rate were 16 kV, 12 cm, and 0.8 ml/hr. respectively.

III. Oil/water separation studies

In this work to explore the w/o miscible oil/water separation different types of emulsion are prepared. First, 0.1 g of span 80 emulsifier was added to the 50 ml of oil and stirred with a speed of 1200 rpm. A 2 ml of water was slowly added to the oil and stirred at a high speed for 4 hours to prepare a stable emulsion for the separation experiments. Four emulsions were prepared using different oils such as sunflower oil/water, bean oil/water, diesel/water, and peanut oil/water. The surfactant-stabilized emulsion was poured into the gravity-based oil/water separation device. The surfactant-stabilized emulsion images were captured in an optical microscope before separation and after separation. The ZIF-8 composite fibrous membrane and pristine PS oil permeate flux were calculated using the below expression.

$$\text{Oil permeate flux (L/(m}^2\text{.hr.))} = \left(\frac{\text{Volume of the oil permeate}}{\text{Membrane surface area*Separation time}}\right) \quad (1)$$

The separation efficiency was calculated for four different oil emulsions determined by using the following equation

$$\text{Separation efficiency of the fibrous membrane (\%)} = \left(\frac{\text{Volume of oil separated}}{\text{Total amount of oil added}}\right)\times 100 \quad (2)$$

IV. Results and discussion

The ZIF-8 composite PS and pristine fibrous surface morphologies were examined by using FESEM. Fig. 1 illustrate fibrous membrane morphology at different magnifications. FESEM pictures reveal the pristine PS fibers have very smooth surfaces compared to the ZIF-8 composite PS fibers. The composite fibers have rough surfaces attributed to the ZIF-8 nanoparticles which are protruded and stacked on the fiber surface as shown in Fig. 1 a, b, and c.

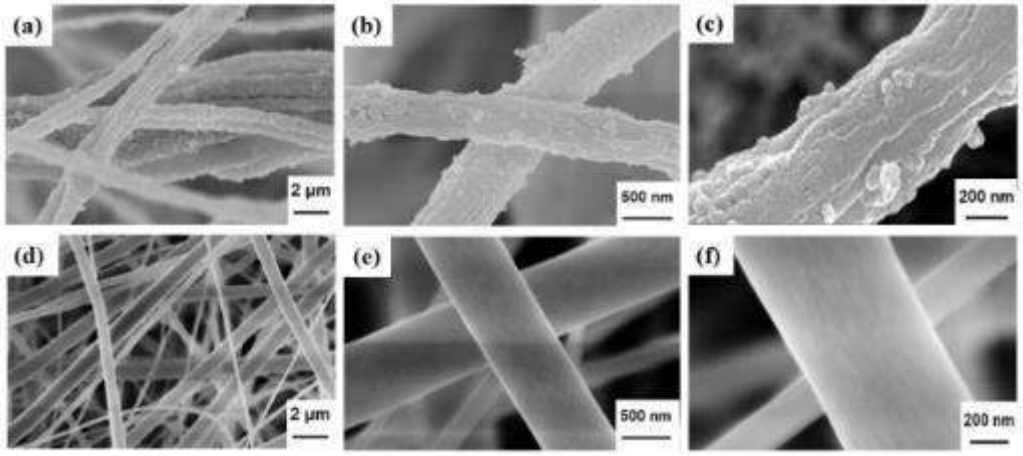

Figure 1. FESEM images of a-c) ZIF-8 incorporated PS; d-h) pristine PS fibrous membranes at different magnifications

The oil permeability of the ZIF-8 incorporated PS and pristine PS fibrous membranes was investigated using the gravity-assisted oil/water separation setup as shown in Fig.2b. First, the emulsion mixture was slowly transferred into the oil/water separation setup as shown in Fig. 2b. The oil was allowed to pass through the membrane, and water droplets were rejected from the membrane due to the superhydrophobic behavior of the composite membrane as shown in Fig.2c. The highest emulsion oil permeate flux and separation efficiency of the ZIF-8 incorporated PS fibrous membrane were 1896±72 L/m^2.h and 99 ± 0.2%. For pristine PS fibrous

membrane, the highest oil permeate flux and separation efficiency were 1264±68 L/m^2.h and 85 ± 0.1%. The oil permeate flux and separation efficiency was enhanced for the ZIF-8 incorporated PS membrane for emulsion separation was attributed to its improved surface area, and the superhydrophobic feature of the ZIF-8 nanoparticles.

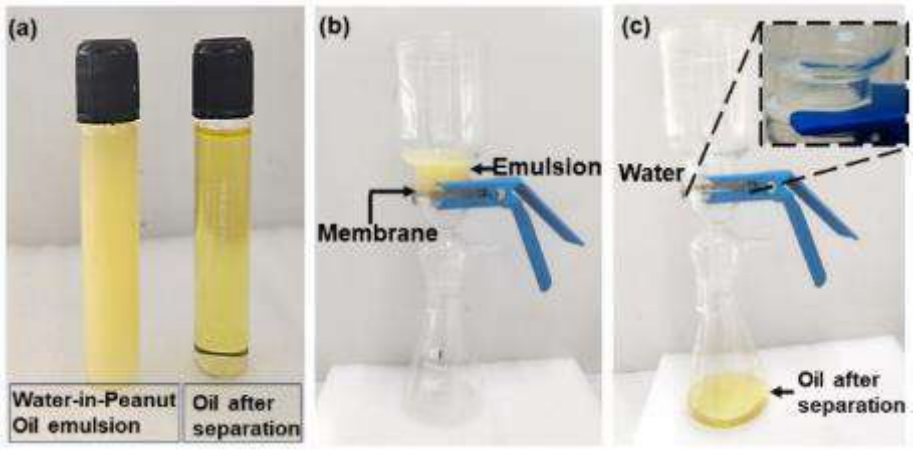

Figure 2. a) Image of w/o (Peanut oil) emulsion before separation and oil collected after separation. b and c) the photographs of the before and after separation of the w/o emulsion mixture.

Given the outcomes highlighted earlier, the PS fibrous membrane incorporating ZIF-8 exhibited remarkable effectiveness in separating surfactant-stabilized emulsions. A comprehensive presentation of the study's detailed findings will be available in the complete manuscript.

V. Conclusion

This study involved the creation of a ZIF-8 incorporated PS fibrous membrane through a straightforward one-step electrospinning technique. The WCA for the ZIF-8 composite fibrous membrane reached 155±1.5°. Remarkably, this composite fibrous membrane demonstrated effective separation capabilities for both immiscible and surfactant-stabilized emulsion oil/water mixtures. In terms of performance, the membrane achieved the highest oil permeate flux of 2936±108 L/m^2.h for immiscible oil/water mixtures and 1896±72 L/m^2.h for emulsions. The introduction of ZIF-8 nanoparticles into the fiber matrix contributed to increased surface area and roughness in the fiber surface morphology, enhancing superhydrophobic and superoleophilic features.

Acknowledgments
Financial support for this study was funded by a grant from the Science and Engineering Research Board (SERB)-SRG (File number SRG/2019/001113), Govt. of India.

References

Deng, Y. (2022). Multi-Hierarchical Nanofiber Membrane with Typical Curved-Ribbon Structure Fabricated by Green Electrospinning for Efficient, Breathable and Sustainable Air Filtration. J. Memb. Sci. 660, 120857. https://doi.org/10.1016/j.memsci.2022.120857

Jiang, S. (2020). Electrospinning Superhydrophobic–Superoleophilic PVDF-SiO_2 Nanofibers Membrane for Oil–Water Separation. J. Appl. Polym. Sci. 137, 1–10. https://doi.org/10.1002/app.49546

Li, Y. (2021) High-Hydrophobic ZIF-8 @ PLA Composite Aerogel and Application for Oil-Water Separation. Sep. Purif. Technol. 270, 118794. https://doi.org/10.1016/j.seppur.2021.118794

Ma, W. (2016). Electrospun Fibers for Oil-Water Separation. RSC Advances. 6,12868–12884. https://doi.org/10.1039/c5ra27309a

Moatmed, S. M. (2019). Highly Efficient and Reusable Superhydrophobic/Superoleophilic Polystyrene@ Fe_3O_4 Nanofiber Membrane for High-Performance Oil/Water Separation. J. Environ. Chem. Eng. 7, 103508. https://doi.org/10.1016/j.jece.2019.103508

Rasouli, S. (2021). Superhydrophobic and Superoleophilic Membranes for Oil-Water Separation Application: A Comprehensive Review. Mater. Des. 204, 109599. https://doi.org/10.1016/j.matdes.2021.109599

Sarbatly, R. (2016). A Review of Polymer Nanofibres by Electrospinning and Their Application in Oil-Water Separation for Cleaning up Marine Oil Spills. Mar. Pollut. Bull. 106, 8–16. https://doi.org/10.1016/j.marpolbul.2016.03.037

Thota, K. (2023). Candle Soot Nanoparticle Embedded Nanofibrous Membrane for Separation of Miscible and Immiscible Oil/Water Mixtures. Polym. Compos. 44, 4243–4251. https://doi.org/10.1002/pc.27394

Wang, X. (2015). Electrospun Nanofibrous Materials: A Versatile Medium for Effective Oil/Water Separation. Mater. Today. 19, 403–414. https://doi.org/10.1016/j.mattod.2015.11.010

Zhang, J. (2019). Electrospun Flexible Nanofibrous Membranes for Oil/Water Separation. J. Mater. Chem. A. 7 ,20075–20102. https://doi.org/10.1039/c9ta07296a

Zhang, N. (2020). A Review on Oil/Water Emulsion Separation Membrane Material. J. Environ. Chem. Eng. 10, 107257. https://doi.org/10.1016/j.jece.2022.107257

Zhang, N. (2020). A Review on Oil/Water Mixture Separation Material. Ind. Eng. Chem. Res. 59, 14546–14568. https://doi.org/10.1021/acs.iecr.0c02524

IEEES-143

Assessment of the Life Cycle and Energy, Exergy use of Various Tomato Products Supply Chain in the Food Sector Under Various Improvement Scenarios

[1]Samiye Adal, [2]Zafer Erbay
[1]Afyon Kocatepe University, Engineering Faculty, Food Engineering Department, Afyonkarahisar, Turkey
[2]Adana Alparslan Türkeş Science and Technology University, Engineering Faculty, Food Engineering Department, Adana, Turkey, * E-mails: [1]smy.akn@gmail.com, [2]zafererbay@yahoo.com

Abstract

This study examines the energy, exergy, CO_2 emission analyses, and life cycle assessment in retail tomato, tomato juice, and tomato paste production, encompassing the complete supply chain from farm to fork and farm to gate. The production method for each product was divided into three key steps: fresh tomato agriculture, factory processing, and packaging and transportation. The cumulative analysis method was employed to calculate energy, exergy, and CO_2 emissions, and the system was evaluated exergetically. The OpenLCA 1.11.0 software, Agribalyse 3.1 database, and CML-IA baseline technique were used to select impact assessment categories, and three improvement scenarios were evaluated in addition to the base case. The largest impact on tomato farming is caused by the use of diesel oil, the excessive use of chemical fertilizers, and the use of electricity. CEnC, CExC, and CCO_2C were 3320.12 MJ/ton, 3501.53 MJ/ton, and 224.20 kg/ton, respectively, in the base case scenario for fresh tomato production. In the biodiesel scenario, these values decreased to 1380.40 MJ/ton, 1250.27 MJ/ton, and 66.69 kg/ton, respectively. Hotspot impact categories were determined as Abiotic (fossil) depletion (AFDP), Global warming (GWP100a), and human toxicity. In the tomato paste GP-BD scenario, AFDP was estimated to be 3.2E+03 (MJ), which is lower than the base case. Among the scenarios examined, the "Biodiesel scenario" shows the best results in terms of decreased energy and exergy values, reduced CO_2 emissions, and minimized environmental impacts. The utilization of non-renewable energy resources in manufacturing processes and the energy-intensive nature of inputs employed in specific production processes contribute significantly to the observed high environmental consequences.

Keywords: Exergy, life cycle, tomato products, biodiesel

I. Introduction

The food industry is one of the major consumers of energy in processes as well as fossil fuels, which emit a substantial amount of greenhouse gases (GHGs) into the water and air, thereby contributing to environmental contamination. The food industry has been reported to be responsible for between 20% to 33% of the overall greenhouse gas (GHG) emissions (Groth et al., 2023). Approximately 33% of the overall greenhouse gas emissions in the food chain are estimated to be related to energy usage (Crippa et al., 2021). The lack of adequate environmental care has led to a multitude of global environmental challenges pertaining to food security, global warming, carbon emissions, and waste produced along the supply process (Türkten and Ceyhan, 2023). Due to the significant energy inputs in this industry, there has been a growing concern in utilizing energy evaluation and modeling methodologies for the purpose of conducting energy utilization evaluations, with the aim of achieving energy conservation and subsequent financial benefits. The application of thermodynamic analysis is of utmost importance in the examination of energy efficiency within industrial processes. Exergy analysis has emerged as a crucial tool for the purpose of designing, analyzing, and optimizing thermal systems. Life Cycle Assessment (LCA), on the other hand, is a widely used tool for examining the environmental implications of the food system. This method is becoming more common for examining the environmental effects of agricultural productions. Assessments of the life cycle environmental impacts of the production of food, including agriculture and processing, along the supply chain, enhance knowledge of the environment and highlight critical production systems (Ghnimi et al., 2021).

Tomatoes are widely used in human diets due to their rich content of lycopene (Alda et al., 2009), vitamins A, B, and C, as well as minerals iron, calcium, and magnesium (Srivastava and Kulshreshtha, 2013). Additionally, tomatoes are a good source of dietary fiber (Frusciante et al., 2007). However, due to its high-water content, fresh harvested tomatoes are perishable. Therefore, a large portion of the tomatoes grown around the world are processed to create new durable-longer shelf life-products like tomato paste, tomato pulp, tomato juice, diced tomatoes, tomato powder, well-known ketchup, dried tomato, etc. (Soufiyan et al., 2016). Numerous studies have been conducted to examine the processes in the food industry. These topics are typically examined independently under specific fields of energy studies, exergy studies, or life cycle assessments. Moreover, it is worth noting that these studies typically concentrate on a specific component of a process, such as a single component of equipment or a particular production stage. This study includes a thorough analysis of energy, exergy, CO_2 emissions, and LCA, while also comparing various scenarios within cradle to gate approach. The environmental hotspots of the study have been discovered, and various scenarios have been tested by modifying the variables that have the greatest impact on the investigated metrics. The objective of this study is to provide researchers and stakeholders in the food business with a holistic view on optimizing all phases of production processes using tomato products. The implications of this study can also be extended to comparable operations within the food sector, adopting the same approach also.

II. Experimental Design and Methodology

The present study examines the assessment of energy, exergy consumption and CO_2 emission with LCA in the manufacturing of retail tomato, tomato juice, and tomato paste. The initial step of the study involves assessing the process design and providing a comprehensive system description. The production method for each product was divided into three key stages: fresh tomato

agriculture (TF), factory processing (FP), and packaging-transportation (PT). The basis for all calculations was the production or processing of one metric ton (1000 kg) of fresh tomatoes. The functional unit for LCA was chosen as 1 kilogram of unit product. For the whole system and each component of the production system, mass balances based on dry matter and water contents were established. The cultural practices pertaining to tomato cultivation in Turkey have been documented from the literature (Engindeniz, 2006; Esengun et al., 2007; Yelmen et al., 2019). The technical spesifications of equipment utilized for every step of production, including conveying, concentrating, canning or bottling, sterilizing, packaging, etc., has been collected from the websites of leading national and international equipment suppliers within the tomato-processing sector such as Frumak Food Technologies Machinery, Shangai Chengdong Co. Ltd., Shangai Honest Machinery Co., Ltd., Dongguang Xinglong Packacing Machinery Co., Ltd., Jiangsu Ketchview Machinery Technology Co., Ltd., Shase Machiney, Shangai LWT Machinery Co., Ltd., Zhangjiagang Fillex Beverage Machinery Co., Ltd.

The cumulative exergy consumption method was employed to determine the values of energy (CEnC), exergy (CExC) and CO_2 (CCO_2C) emissions (Degerli et al., 2015; Karakaya and Özilgen, 2011; Özilgen and Sorgüven, 2011; Sorgüven and Özilgen, 2012; Szargut et al., 1988). LCA methodology was used to assess the environmental implications of the processes according to ISO 14040 (ISO, I., 2006) and ISO 14044 (ISO, E., 2006). The fundamental stages of LCA include goal and scope definition, life cycle inventory, life cycle impact assessment, and improvement assessment (Farahani et al., 2019). The goal of this LCA research is to assess the environmental implications of retail tomato, tomato juice and tomato paste. All steps of production are considered, including TF, FP and PT stages. Another important objective is to evaluate the potential impact of different strategies in enhancing the overall environmental sustainability of the entire supply chain.The LCA study was carried out using OpenLCA 1.11.0 (Green Delta GMBH, Berlin, 2021) software, and the impact asessment categories were chosen using CML-IA baseline technique (Guinée, 2002). The backdrop system data, which included agrochemical manufacturing, electricity, transportation, and so on, were obtained from the Agribalyse 3.1 and Ecoinvent 3.9.1. For LCA inventory, data sources including the Türkiye Development Agency report (Development, 2021; Hacıbekoğlu et al., 2013; Industry, 2021; Türkiye Republic Ministry of Industry and Technology, 2021),Türkiye Statistical Institute report (TÜİK, 2023), International Energy Agency Report (IEA, 2022) and Republic of Türkiye Ministry of Agriculture and Forestry Report (Development, 2021) were used. Abiotic depletion (ADP), Abiotic (fossil) depletion (AFDP), acidification (AP), eutrophication (EP), global warming potential (GWP), ozone layer depletion (ODP), human toxicity (HTP), freshwater aquatic ecotoxicity (FWEP), terrestrial ecotoxicity (TEP), and photochemical oxidation (POCP) are the impact categories calculated via CML-IA baseline method. A sensitivity test was carried out to determine how the output parameter (i.e., environmental impact) varies when the input values change. Morris' one-at-a-time strategy was used to modify input parameters (Groen et al., 2014; Shimako et al., 2018; Sun et al., 2012). The following scenarios were used in the study to conduct sensitivity analysis in the context of tomato processing: BC: The baseline scenario, BD: Use of biodiesel instead of diesel and natural gas with conversion, GP: Use of glass packaging instead of steel packaging, PF: Precision farming of tomato growing and GP-BD: Glass packaging and biodiesel usage combination.

III. Results and discussion

As seen from Figure 1. (b) the results showed that the biggest energy consumers in tomato agriculture are chemical fertilizers, electricity, and transportation, which requires the use of diesel oil. According to Esengun et al.(Esengun et al., 2007) the usage of chemical fertilizers is likely far more than what is truly required and is not based on soil study. Applying effective fertilizer management techniques will lower energy consumption and give the chemicals to the soil in precisely the right amounts for the plants. On the contrary, the implementation of energy-efficient trucks and the optimization of delivery schedules have the potential to reduce diesel use (Karakaya and Özilgen, 2011).

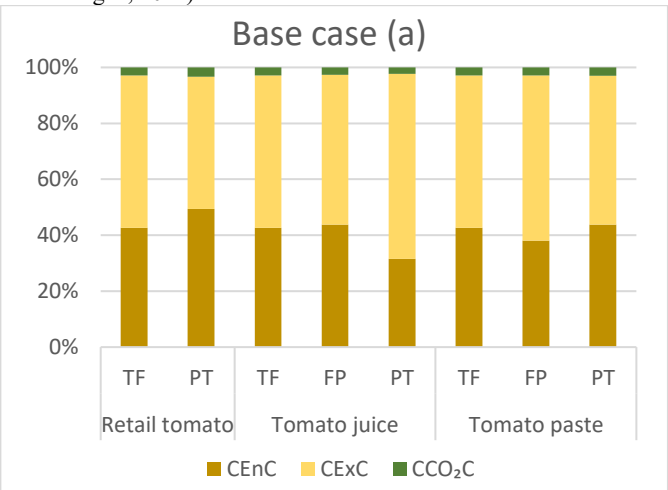

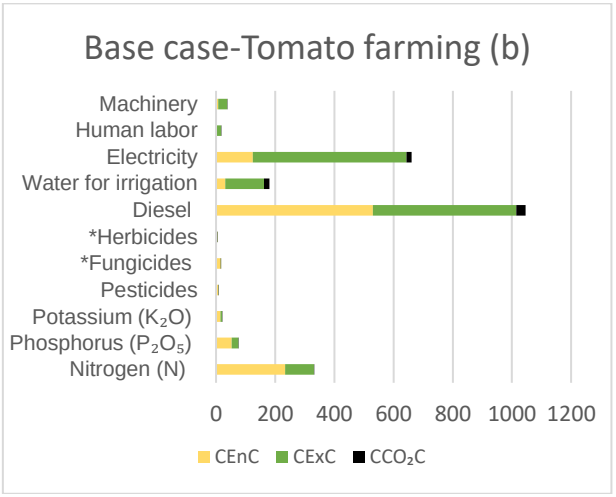

Figure 1. CEnC, CExC and CCO_2C results of retail tomato, tomato juice and tomato paste within BC (a) and BC-TF (b) results **TF:** Tomato Farming, **PT:** Packaging and transportation

Additionally, the utilization of a renewable fuel such as biodiesel holds the potential for even greater reductions. All cases and scenarios, except for BD, the packaging and transport stage has emerged as an important contributor to the CEnC, CExC and CCO_2C in the retail tomato, tomato juice and tomato paste production. By reducing the impact in the PT step, the usage of biodiesel in the BD scenario has directed attention to the effects of tomato farming. The main contributing steps on the estimated parameters in the base case were PT step for retail tomato, FP and TF steps for tomato juice and tomato paste. In the PT step of tomato juice production, the GP and GP-BD scenarios have demonstrated higher values than the BC. In the tomato juice-FP step, it is observed that tubular sterilization equipment exhibits the highest values for CEnC, CExC and CCO_2C. On the other hand, during the PT step of BC, the primary factors contributing to these values are steel, cardboard, and diesel. The CO_2 emissions resulted from steel (BC) and glass (GP) are 47.5 kg/ton and 163.80 kg/ton, respectively. The tomato paste production provided the best results in both the BD scenario and the GP-BD scenario, with the BC scenario exhibiting comparatively lower values than the GP scenario. The largest contributors to the CEnC, CExC, and CCO_2C values in tomato paste-BC are the evaporator and tubular sterilization equipment, which is followed by electricity consumption. The substitution of natural gas with biodiesel in the FP stage resulted in a significant reduction of around 68% in the CEnC value of the evaporator, tubular sterilization machine, and aseptic filling machine. Using glass packaging-GP, on the other hand, increases the values of CEnC, CExC, and CCO_2C. However, when GP is combined with biodiesel utilization (GP-BD), the outcomes are better for both BC and GP.

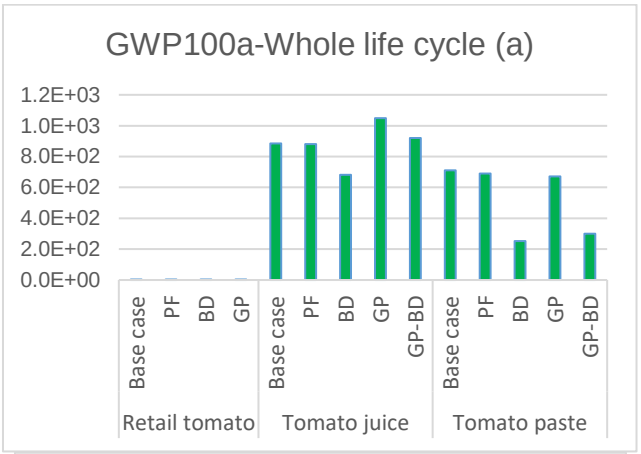

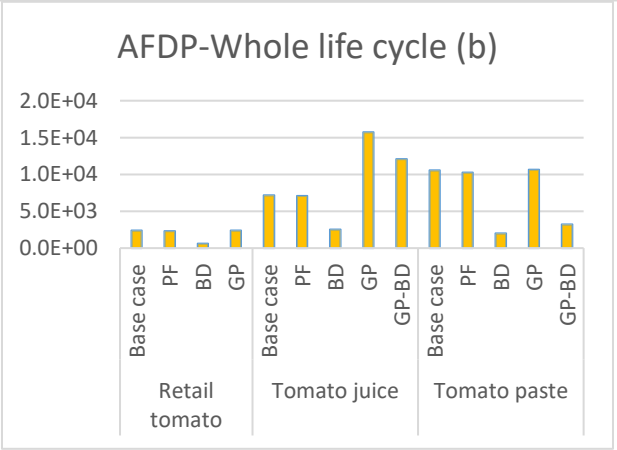

Figure 2. Whole life cycle GWP(a) and AFDP(b) impact category results of retail tomato, tomato juice and tomato paste
GWP: Global warming (GWP100a) (kg CO_2 eq), **AFDP**: Abiotic (fossil) depletion potential (MJ)

Upon conducting an analysis of the LCA, it was observed that the impact categories of AFDP, GWP, HTP, and FWEP exhibited the greatest values for retail tomatoes, tomato juice, and tomato paste. The GWP (Figure 2. (a)) and FWEP impact categories in retail tomato production obtained the highest value in the PT step, whereas the HTP value obtained a greater value in the TF step. In all cases, except for the TF step, it is evident that PF didn't demonstrate a noticeable change compared to BC, and BD has reduced the impact categories effect on all processes.
The AFDP impact category in tomato juice production had the highest value at the FP step in the BC, PF, and GP scenarios as seen from Figure 2. (b) The usage of biodiesel in the BD and GP-BD scenarios resulted in a decrease in the values due to the elimination of diesel use which is a non-renewable fossil fuel. When analyzing the outputs of OpenLCA, it becomes apparent that transportation, diesel and natural gas consumption, as well as electricity usage, emerge as the primary factors influencing the environmental impact of AFDP retail tomato production.
The highest values have been seen in the BC, FP, and GP scenarios in the tomato paste production-FP step. This conclusion is not surprising, given that the FP step consumes electricity and natural gas for various operations, especially for evaporation and sterilization processes. The utilization of glass packaging, disregarding the recycling aspect, as an alternative for tin cans has resulted in an increased adverse effect across all environmental categories. The utilization of glass packaging in combination with biodiesel, referred to as the GP-BD scenario, yields favorable results in impact categories, leading to reduced values in comparison to BC.

When analyzing the graphical outcomes of OpenLCA, the transportation, diesel and natural gas consumption, steel production, pesticide, as well as electricity emerge as the top five primary factors influencing the environmental impact of BC productions of retail tomato, tomato juice and tomato paste. In accordance with our study, (Del Borghi et al., 2014) stated that the agricultural step and packaging production were found to have the greatest impact in all the categories under consideration throughout the life cycle of tomato products. According to (Ghnimi et al., 2021), the findings of their study revealed that the tin production step emerged as the primary source of environmental impact in the appertization system used for chopped tomato production. Additionally, the agricultural step was identified as the secondary significant contributior to the overall environmental impact. The global warming potential (GWP) associated with tomato production and tin packing constituted 54.33% and 45.00% respectively of the overall GWP in their study.

IV. Conclusion

The establishment and maintenance of a sustainable food supply chain require a systematic approach. The involvement of various stakeholders, including farmers, manufacturing companies, policymakers, retailers, consumers, and investors, is crucial for the agri-food sector. These stakeholders must collaborate to develop and implement sustainable agri-food production processes and environmentally friendly products. Based on the results of this study, some steps of the tomato products' life cycles have been determined to be of utmost importance in terms of their overall environmental impact, with potential options for enhancement. In most impact categories, the tomato farming and packaging-transportation steps were identified as significant areas of concern primarily due to their substantial reliance on fossil fuel usage. The utilization of renewable energy sources like biodiesel has a significant positive impact on the environmental effects of food processing. Improvement strategies can be designed during the agriculture and packaging stages to mitigate the adverse environmental effects of food supply chains. These efforts include optimizing renewable fuel alternatives, enhancing fertilization practices, and optimizing the use of environmentally friendly or recyclable packaging materials. By focusing on these areas, the overall environmental impact of food supply chains can be reduced.

Acknowledgements

This work was supported by the Scientific Research Project Fund of Adana Alparslan Türkeş Science and Technology University under the Project Number 23832001.

References

Alda, L.M., Gogoasa, I., Bordean, D.-M., Gergen, I., Alda, S., Moldovan, C., Nita, L., 2009. Lycopene content of tomatoes and tomato products. Journal of Agroalimentary Processes and Technologies 15(4), 540-542.
Crippa, M., Solazzo, E., Guizzardi, D., Monforti-Ferrario, F., Tubiello, F.N., Leip, A., 2021. Food systems are responsible for a third of global anthropogenic GHG emissions. Nat Food 2(3), 198-209.
Degerli, B., Nazir, S., Sorgüven, E., Hitzmann, B., Özilgen, M., 2015. Assessment of the energy and exergy efficiencies of grain cultivation and bread making processes in Turkey and Germany. Energy 93, 421-434.
Del Borghi, A., Gallo, M., Strazza, C., Del Borghi, M., 2014. An evaluation of environmental sustainability in the food industry through Life Cycle Assessment: the case study of tomato products supply chain. Journal of Cleaner Production 78, 121-130.
Development, T.I.o.E.a.P., 2021. Agricultural Products Market, Tomato Report.
Esengun, K., Erdal, G., Gündüz, O., Erdal, H., 2007. An economic analysis and energy use in stake-tomato production in Tokat province of Turkey. Renewable Energy 32(11), 1873-1881.
Farahani, S.S., Soheilifard, F., Raini, M.G.N., Kokei, D., 2019. Comparison of different tomato puree production phases from an environmental point of view. Int J Life Cycle Ass 24(10), 1817-1827.
Frusciante, L., Carli, P., Ercolano, M.R., Pernice, R., Di Matteo, A., Fogliano, V., Pellegrini, N., 2007. Antioxidant nutritional quality of tomato. Mol Nutr Food Res 51(5), 609-617.
Ghnimi, S., Nikkhah, A., Dewulf, J., Van Haute, S., 2021. Life cycle assessment and energy comparison of aseptic ohmic heating

and appertization of chopped tomatoes with juice. Sci Rep 11(1), 13041.
Groen, E.A., Heijungs, R., Bokkers, E.A., de Boer, I.J., 2014. Sensitivity analysis in life cycle assessment, Proceedings of the 9th international conference on life cycle assessment in the agri-food sector. ACLCA Vashon, WA, USA, pp. 8-10.
Groth, C., Wegmann, C., Meyerding, S.G., 2023. Perception of product sustainability: The case of processed tomatoes–A qualitative study in Germany. Journal of Retailing and Consumer Services 71, 103214.
Guinée, J.B., 2002. Handbook on life cycle assessment: operational guide to the ISO standards. Springer Science & Business Media.
Hacıbekoğlu, A., Hacıbekoğlu, M., Çetinel, S., Ülver, M., 2013. Tomato Paste Production Facility Investment Feasibility.
IEA, 2022. World energy outlook 2022. IEA Paris, France.
Industry, G.C.o.C.a., 2021. Fruit and Vegetable Processing (Canned and paste) Production Feasibility Report.
ISO, E., 2006. 14044: Environmental Management, Life Cycle Assessment, Requirements and Guidelines, DIN Deutsches Institut für Normung e. V. Beuth Verlag, Berlin.
ISO, I., 2006. 14040. Environmental management—life cycle assessment—principles and framework, 235-248.
Karakaya, A., Özilgen, M., 2011. Energy utilization and carbon dioxide emission in the fresh, paste, whole-peeled, diced, and juiced tomato production processes. Energy 36(8), 5101-5110.
Özilgen, M., Sorgüven, E., 2011. Energy and exergy utilization, and carbon dioxide emission in vegetable oil production. Energy 36(10), 5954-5967.
Shimako, A.H., Tiruta-Barna, L., Bisinella de Faria, A.B., Ahmadi, A., Sperandio, M., 2018. Sensitivity analysis of temporal parameters in a dynamic LCA framework. Sci Total Environ 624, 1250-1262.
Sorgüven, E., Özilgen, M., 2012. Energy utilization, carbon dioxide emission, and exergy loss in flavored yogurt production process. Energy 40(1), 214-225.
Soufiyan, M.M., Dadak, A., Hosseini, S.S., Nasiri, F., Dowlati, M., Tahmasebi, M., Aghbashlo, M., 2016. Comprehensive exergy analysis of a commercial tomato paste plant with a double-effect evaporator. Energy 111, 910-922.
Srivastava, S., Kulshreshtha, K., 2013. Nutritional content and significance of tomato powder. Annals of Arid Zone 52(2), 121-124.
Sun, X.Y., Newham, L.T.H., Croke, B.F.W., Norton, J.P., 2012. Three complementary methods for sensitivity analysis of a water quality model. Environmental Modelling & Software 37, 19-29.
Szargut, J., Morris, D.R., Steward, F.R., 1988. Exergy analysis of thermal, chemical, and metallurgical processes. Springer.
TÜİK, 2023. Dış Ticaret İstatistikleri, Mart 2023 Raporu. Türkiye İstatistik Kurumu.
Türkiye Republic Ministry of Industry and Technology, E.M.D.A., 2021. Hatay Province Tomato Paste Production Facility Pre-Feasibility Report.
Türkten, H., Ceyhan, V., 2023. Environmental efficiency in greenhouse tomato production using soilless farming technology. Journal of Cleaner Production 398, 136482.

IEEES-144

A Study on the Elimination of Heavy Metal Pollution with Soma Thermal Power Plant Fly Ash

[1*]Nagihan Ersoy, [2]İsmail Ekmekçi,
[1] Manisa Celal Bayar Üniversitesi, Soma Meslek Yüksekokulu, İş Sağlığı ve Güvenliği, Manisa, 45500, Türkiye
[2] İstanbul Ticaret Üniversitesi, Mühendislik Fakültesi, Endüstri Mühendisliği, İstanbul, 34840, Türkiye
* E-mails: nagihanersoy89@gmail.com

Abstract

Fly ash generated during the combustion of coal for electricity generation in coal-fired thermal power plants is a serious threat to the environment. The problem of accumulation of fly ash in a sustainable way needs to be solved urgently. There are many ways to resource fly ash, but high value-added applications are rare. Many researchers have turned to carrying out studies to eliminate heavy metal pollution by using natural and inexpensive adsorbents. In this study, the chemical composition of the ashes belonging to the Soma Thermal power plant and Scanning Electron Microscope (SEM) analysis images were given. The optimum conditions under which the ashes will be activated at different calcined temperatures (200ºC, 400ºC, 600ºC, 800ºC) and adsorb heavy metals have been determined. In the optimization studies, the change of adsorption capacities of fly ash depending on the adsorbed grain size, pH and temperature was studied. The adsorption capacity and the amount of adsorbed substance were determined using polarographic methods. The high adsorption capacity of fly ash, which is a solid waste problem around the Soma thermal power plant, has increased its importance in terms of using ash in the treatment process.

Keywords: Adsorbent, heavy metal pollution, environmental pollution, fly ash

I. Introduction

Fly ash causes serious pollution to the soil, water and atmosphere. The reuse of fly ash instead of disposal and storage is the best option for ecological balance. Therefore, the use of fly ash has been used in construction, agriculture, mining and environmental protection areas, fertilizer or soil modification and mine filling, used as cement and concrete additive. In addition, there are various high value-added applications, such as the extraction of rare metal, cenosphere or magnetic beads and the production of molecular sieves, ceramic Octobers or catalyst supports (Wang, 2021). The comprehensive utilization rate of fly ash in China is more than 70%. However, high value-added applications account for only about 5% of overall usage. Therefore, it is important to develop and disseminate high value-added applications of fly ash. Due to the porous structure of fly ash, its use in adsorption and pollution removal is important in practice.

Only ¼ of the total fly ash production is recovered. Europe takes the first place with 47%, followed by the United States with 39%(Gollakota, 2019). Fly ash, which is not usually used, is stored in ash dams with a hydraulic system. These dams cause water pollution by storing about several million tons of fly ash. Fly ash escaping from electro filters creates air pollution. In addition, only 12% of the fly ash in these settlements is recycled into useful products, while the rest is unused and left exposed, causing ecological imbalances and increasing natural disasters (Gollakota, 2019).

Today, heavy metals are a source of pollution for water and soil. It is formed by this pollution when industrial waste reaches water and soil. Other morbidities caused by exposure to volatile ash may also be present, including metallic components such as lead, arsenic and mercury. Other chemicals used in different coal power plant operations can also negatively affect human health. Heavy metals are the pollutants that cause the most serious health problems (Ersoy, 2022).

Fly ash has also been used for the removal of copper from aqueous solution. It has been found that the adsorption efficiency depends on the concentration, pH and temperature (Pandey,1985). It has been found that fly ash can be considered as a potential adsorbent for the removal of copper and cadmium from wastewater. Equilibrium studies for the adsorption of zinc and copper from aqueous solutions were carried out using sugar beet pulp and fly ash (Pehlivan,2006). The removal properties of Pb (II) and Cu (II) Fromaqueous solution with fly ash have been investigated by Alinnor (Alinnor,2007).

The presence of organic pollutants has significantly affected the removal of heavy metals from wastewater. Wang et al; investigated the adsorption of heavy metals by using fly ash as an adsorbent (Wang,2008).

Fly ash has also been used for the removal of toxic heavy metals, namely Cu (II), Pb (II) and Cd (II) from water (Apak,1998).

It has been found that fly ash is a good adsorbent for the removal of zinc from aqueous solutions (Prabhu,1981) Gashi et al reported that fly ash shows good adsorptive properties for the removal of lead, zinc, cadmium and copper from wastewater in the battery and fertilizer industries (Gashi,1988).

II. Experimental Procedure/Methodology/System Description

The fly ash was first washed 2-3 times with pure water and dried at 105^{O}C in the oven. Then it was divided into 60,100,200,400 mesh sizes with the Octagon Digital CE device. The SEM (Scanning Electron Microscopy) images of the fly ash adsorbent used are given in Figure 1. Figure 2 shows the SEM image of heavy metal adsorbed Soma thermal power plant ash.

Figure 1: SEM image of untreated fly ash

Figure 2: SEM image of heavy metal adsorbed fly ash

The chemical composition and percentages of Soma thermal power plant fly ash are shown in Table 1.

Table1: Analysis results of fly ash

Contents	Percent
SiO_2	10.84
Al_2O_3	8.217
Fe_2O_3	16.25
SO_3	33.40
Cao	60.15

The excess of CaO in the fly ash of Soma thermal power plant makes the ash basic. These properties of ashes are used in the design of combustion equipment. In the experiments, standard solutions with a concentration of Zn^{+2}=119.1mg/L Cd^{+2}=112.4mg/L Pb^{+2}=108.3mg/L Cu^{+2}=106.5mg/L were used. Particle size, glow temperature and mixing speed, etc. for fly ash in polarographic analysis. optimum conditions have been determined by conducting experiments on parameters such as.

III. Analysis

III.I. Effect of the Adsorbent Amount

3g, 4g,5g were taken from fly ash adsorbents calcined at 800oC with a grain size of 200mesh, each remained in 100ppm 50ml (Zn^{+2}, Cd^{+2}, Pb^{+2}, Cu^{+2}) solution for 2 hours and mixed at a speed of 800 Frpm. Polarographic analyses were performed with 5 ml samples from the solution. In Table 2 and Figure 2, the effect of 3g, 4g, 5g Fractions of fly ash on the adsorption of %Zn^{+2}, %Cd^{+2}, % Pb^{+2}, % Cu^{+2} is seen.

Table 2: The effect of the amount of adsorbent on the adsorption of %Zn^{+2}, %Cd^{+2}, %Pb^{+2}, %Cu^{+2}

Beginning	Zn^{+2}=139.1mg/L						Cd^{+2}=108.7mg/L					
Minute	15	30	45	60	90	120	15	30	45	60	90	120
5g	20.16	10.20	4.30	1.50	1.38	0.00	23.47	19.00	14.43	11.30	10.47	8.53
4g	30.21	25.10	15.07	10.02	5.30	2.35	35.16	22.14	17.30	10.09	12.30	14.15
3g	40.54	30.25	17.03	22.14	15.07	10.24	50.84	45.13	40.04	30.27	18.92	17.02
Beginning	Pb^{+2}=122.5mg/L						Cu^{+2}=161.2mg/L					
Minute	15	30	45	60	90	120	15	30	45	60	90	120
5g	10.50	1.06	1.00	0.8	1.15	1.03	0.00	0.00	0.00	0.00	0.00	0.00
4g	18.02	12.60	7.30	3.40	2.01	1.31	30.25	15.03	5.02	0.00	0.00	0.00
3g	30.23	27.54	18.03	9.07	7.02	6.03	60.25	50.15	35.03	27.12	18.09	15.03

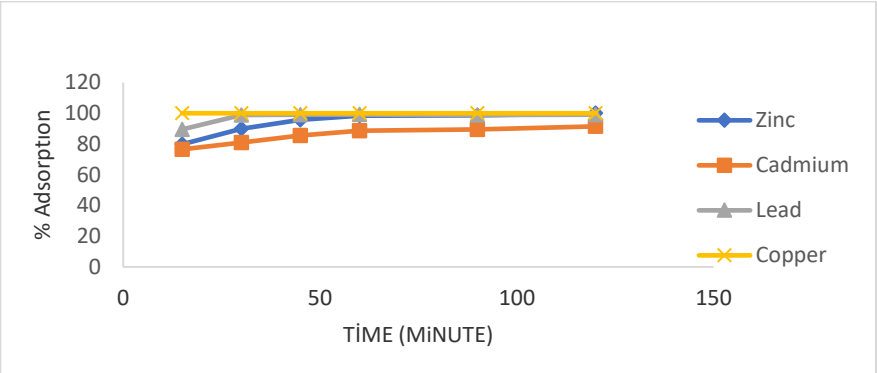

Figure 3: Adsorption of % (Zn^{+2}, Cd^{+2}, Pb^{+2}, Cu^{+2}) 5g Ash in time

III.II. Effect of Grain Size

Fly ash of 60 mesh, 100mesh, 200mesh, 400mesh grain sizes were used. 5g fly ash was left in 100ppm 50ml solution and mixed at a speed of 800rpm. Samples were taken from the solution in 5 ml volumes, centrifuged and analyzed polarographically. In the polarographic analysis, a suspended mercury drop electrode (HMDE) was used as the working electrode, an Ag/AgCl electrode was used as the reference electrode, and a Pt electrode was used as the auxiliary electrode. 20 mL bidistilled water, 0.1mL sample to be analyzed and 1.25mL support electrolyte (0.7mL KCI+ 0.5mL CH3COONa) were added to the sample container of the device. 300s N_2 gas was passed to provide an inert environment. For example, after the polarogram was taken, 0.1mL 100 Frpm (Zn^{+2}, Cd^{+2}, Pb^{+2}, Cu^{+2}) standard was added to the sample chamber and after the measurement was taken, 10 s N_2 gas was passed and 0.1mL 100 Frpm (Zn^{+2}, Cd^{+2}, Pb^{+2}, Cu^{+2}) standard was added again. The Fractions of (Zn^{+2}, Cd^{+2}, Pb^{+2}, Cu^{+2}) in the sample were determined in ppm. Table 3 shows the effect of different grain sizes on the adsorption of Zn^{+2}, Cd^{+2}, Pb^{+2}, Cu^{+2}.

Table 3: Effect on adsorption % Zn^{+2}, % Cd^{+2}, % Pb^{+2}, % Cu^{+2} the size of the grain in time

Beginning	Zn^{+2}=139.1mg/L						Cd^{+2}=108.7mg/L					
Minute	15	30	45	60	90	120	15	30	45	60	90	120
60Nm	48.10	27.95	24.13	21.03	33.74	50.24	15.56	4.10	3.57	10.09	14.41	4.02
100Nm	28.86	20.21	10.12	9.67	17.07	6.88	19.43	17.06	10.05	1.58	1.19	1.31
200Nm	10.12	9.67	6.88	5.39	2.30	3.30	1.67	1.58	1.19	1.42	1.31	1.07
400Nm	27.8	25.88	24.13	12.10	10.00	17.42	8.5	2.7	2.5	1.5	1.25	2.93
Beginning	Pb^{+2}=122.5mg/L						Cu^{+2}=161.2mg/L					
Minute	15	30	45	60	90	120	15	30	45	60	90	120
60Nm	30.08	29.66	27.98	23.82	25.34	30.67	6.35	0	0	0	0	0
100Nm	16.71	14.24	12.03	10.85	7.23	9.28	0	0	0	0	0	0
200Nm	15.94	14.58	14.27	14.26	10.07	6.03	0	0	0	0	0	0
400Nm	23.5	16.9	10.43	12.25	7.05	6.08	0	0	0	0	0	0

III.III. Effect of Superheat Temperature

Fly ashes of different grain sizes were heated for 2 hours at 200^{0}C, 400^{0}C, 600^{0}C, 800^{0}C and brought to room temperature in a desiccator. 5g was taken from the fly ash, 100ppm remained in 50mL (Zn^{+2}, Cd^{+2}, Pb^{+2}, Cu^{+2}) solution for 2 hours and mixed at a speed of 800 Frpm. Samples of 5 ml of the solution were taken at intervals of 15 minutes and centrifuged. The samples were analyzed by polarographic technique. Table 4 shows the effect of ash at 200^{0}C, 400^{0}C, 600^{0}C, 800^{0}C on the adsorption of Zn^{+2}%, Cd^{+2}%, Pb^{+2}%, Cu^{+2}% in time.

Table 4: Effect on adsorption % Zn^{+2}, % Cd^{+2}, % Pb^{+2}, % Cu^{+2} The temperature of the glow in time

Beginning	Zn^{+2}=139.1mg/L						Cd^{+2}=108.7mg/L					
Minute	15	30	45	60	90	120	15	30	45	60	90	120
200^{0}C	40.93	33.17	30.10	28.14	15.27	24.42	5.44	3.21	3.02	1.87	1.02	2.41
400^{0}C	25.19	20.17	17.49	13.09	15.07	12.03	8.92	6.30	3.30	2.01	1.51	2.31
600^{0}C	18.78	11.28	10.20	8.64	5.32	7.21	6.66	4.02	3.22	1.25	3.02	2.50
800^{0}C	11.3	8.89	5.75	5.04	3.02	2.01	3.51	2.78	1.12	2.93	1.02	2.10
Beginning	Pb^{+2}=122.5mg/L						Cu^{+2}=161.2mg/L					
Minute	15	30	45	60	90	120	15	30	45	60	90	120
200^{0}C	15.4	14.2	12.9	10.09	6.04	9.72	2.21	1.02	0	0	0	0
400^{0}C	14.94	10.21	8.75	6.54	3.52	4.75	0	0	0	0	0	0
600^{0}C	17.73	16.09	10.94	10.02	15.75	10.03	0	0	0	0	0	0
800^{0}C	14.97	10.27	8.64	6.51	9.31	5.03	0	0	0	0	0	0

III.IV. pH Effect

The grain size is 200mesh and the glow temperature is 800^{0}C in the first of three separate ashes in a solution of 100ppm 50mL (Zn^{+2}, $Cd^{+2,}$ Pb^{+2}, Cu^{+2}) with a pH of CH3COOH/CH3COONa buffer set to 3, the second is 100ppm 50mL with a pH of CH3COOH/CH3COONa buffer set to 4 (Zn^{+2}, Cd^{+2}, Pb^{+2}, Cu^{+2}) From100mesh and a glow temperature of 800^{0}C. The first is 100ppm 50mL with a pH of CH3COOH/CH3COONa buffer set to 400ppm (Zn^{+2}, Cd^{+2}, Pb^{+2}, Cu^{+2}). The second is 100ppm 50mL

with a pH of CH3COOH/CH3COONa buffer set to 400ppm from100 in the solution, the third one remained for 2 hours in 100ppm 50mL (Zn^{+2}, Cd^{+2}, Pb^{+2}, Cu^{+2}) solution with CH_3COOH/CH3COONa buffer with pH set to 5 and mixed at a speed of 800rpm. Polarographic analyses were performed with 5 ml samples to show the change in the amount of Zn^{+2}, Cd^{+2}, Pb^{+2}, Cu^{+2} depending on time. Table 5 shows the effect of pH on the adsorption of Zn^{+2}%, Cd^{+2}%, Pb^{+2}%, Cu^{+2}% in time.

Table 5: Effect on adsorption % Zn^{+2}, % Cd^{+2}, % Pb^{+2}, % Cu^{+2} pH in time

Beginning	Zn^{+2}=139.1mg/L						Cd^{+2}=108.7mg/L					
Minute	15	30	45	60	90	120	15	30	45	60	90	120
pH 3	19.74	23.06	33.09	30.12	27.00	26.28	16.69	12.25	8.75	5.41	8.02	7.67
pH 4	17.09	19.01	14.02	9.08	7.02	6.00	14.13	10.08	7.03	4.09	2.01	1.55
pH 5	15.54	8.55	6.51	4.25	4.35	4.13	8.13	6.14	5.31	3.22	2.75	2.86
Beginning	Pb^{+2}=122.5mg/L						Cu^{+2}=161.2mg/L					
Minute	15	30	45	60	90	120	15	30	45	60	90	120
pH 3	25.51	40.91	63.06	40.21	38.12	18.08	28.91	30.13	34.19	32.13	38.23	35.98
pH 4	30.01	26.26	22.13	17.01	15.25	12.14	25.04	20.13	17.09	14.15	12.03	10.09
pH 5	27.54	25.14	24.14	22.17	19.53	17.01	20.18	17.01	14.53	12.10	6.81	3.25

IV. Results and discussion

Zinc (II), cadmium (II), lead (II), copper (II) ions in a mixed solution medium were observed on the amount of adsorbent we used between 3g and 5g when they were left for 2 hours, the optimal adsorption of both materials was observed as seen when the amount of 5g adsorbent was used. Decoction of zinc (II), cadmium (II), lead (II), copper (II) ions were left in the mixed solution environment for 2 hours. the amount of 5g fly ash adsorbed zinc (II) around 85%-90%, cadmium (II) around 87%-92%, lead (II) around 55%-60%, copper (II) around 90%-99%, respectively. In addition, 5g fly ash maintains zinc (II), cadmium (II), lead (II), copper (II) adsorption at the end of 24 hours and 36 hours.

When the effect of the particle size of ash on adsorption was investigated, the optimum adsorption was observed with a grain size of 200 mesh. As the particle size decreased, the percentage adsorption increased because the surface area increased. The optimum temperature for ash has been determined to be 8000C. The pH of the solution medium also affects the adsorption. The pH of the prepared 100ppm zinc (II), cadmium (II), lead (II), copper (II) standard is about 3.5. The optimum adsorption was observed at pH 4 in the studies. When looking at the SEM images of the ash, it is seen that the pore diameters are very small, and it is seen that the pores of the untreated ash are hollow. The filling of the pores of the ash in the SEM images after the adsorption process is evidence of adsorption. Figure 2 shows the SEM image of heavy metal adsorbed Soma thermal power plant ash.

V. Conclusion

In adsorption studies on fly ash in Zn^{+2}, Cd^{+2}, Pb^{+2}, Cu^{+2} mixed solution environment, various parameters such as the amount of adsorbent, particle size, glow temperature and pH effect were investigated, and it was determined what the optimal conditions required for adsorption to occur depend on pH. As a result, since fly ash is economical, it can be used for removing and recovering heavy metals by placing it at the discharge points of industrial enterprises with a high content of heavy metals.

Acknowledgements

References

Alinnor, I. J. (2007). Ağır metal iyonlarının sulu çözeltiden uçucu kül ile adsorpsiyonu. *Yakıt*, 86(5-6), 853-857.

Apak, R., Tütem, E., Hügül, M., & Hizal, J. (1998). Heavy metal cation retention by unconventional sorbents (red muds and fly ashes). *Water research*, *32*(2), 430-440.

Ersoy, N., Bingöl, N., & Ekmekci, İ. (2022). Kömürlü Termik Santrallerdeki İSG Çalışmalarının Değerlendirilmesi. *OHS ACADEMY*, *5*(2), 103-130.

Gashi, S. T., Daci, N. M., Ahmeti, X. M., Selimi, T. J., & Hoca, E. M. (1988). Endüstriyel atık sulardan ağır metallerin uzaklaştırılması. *Çevre Bilimi Çalışmaları* (Cilt 34, s. 91-97). Elsevier.

Gollakota, A. R., Volli, V., & Shu, C. M. (2019). Progressive utilisation prospects of coal fly ash: A review. *Science of the Total Environment*, *672*, 951-989.

Pandey, K. K., Prasad, G., & Singh, V. N. (1985). Copper removal from aqueous solution by fly ash. *Water Res*, *19*(7), 869-873.

Pehlivan, E., Çetin, S., & Yanık, B. H. (2006). Şeker pancarı posası ve uçucu kül kullanılarak sulu çözeltilerden çinko ve bakırın emilimi için denge çalışmaları. *Tehlikeli maddeler dergisi*, *135*(1-3), 193-199.

Prabhu, P. V. S. S., Swamy, M. N., & Raju, T. S. S. N. (1981). Adsorption of zinc from aqueous solutions by flyash. *IAWPC TECH. ANN.*, *8*, 46-52.

Wang, S., Terdkiatburana, T., & Tadé, M. O. (2008). Single and co-adsorption of heavy metals and humic acid on fly ash. *Separation and Purification Technology*, *58*(3), 353-358.

Wang, C., Xu, G., Gu, X., Gao, Y., & Zhao, P. (2021). Gözenekli malzemeler şeklinde kömür uçucu külünün yüksek katma değerli uygulamaları: Bir inceleme. *Seramik Uluslararası*, *47*(16), 22302-22315.

EVALUATION OF WIND ENERGY AND ATMOSPHERIC STABILITY IN EDINCIK

*[1]Sevinc A. Sirdas, [2]Kemal Ege Sural
[1] Istanbul Technical University, Faculty of Aeronautics and Astronautics
Department of Meteorological Engineering, Maslak 34469 Istanbul, Turkey

* E-mails: sirdas@itu.edu.tr, ssirdas@gmail.com, kegesural@gmail.com*

Abstract
Meteorological conditions have a large impact on wind energy output; thus, they need to be carefully considered during the installation phase of wind turbines to maximize efficiency. It is critical to assess the stability or instability of the atmosphere, since turbulence inside the atmospheric boundary layer has a substantial impact on wind energy generation. The purpose of this research is to give a thorough examination of the influence of meteorological conditions in wind energy generation. The findings of this study show that energy generation varies significantly depending on weather conditions and turbulence levels. A more precise assessment of energy output may be accomplished by taking atmospheric stability, turbulence characteristics, and aerodynamic equations into account, allowing for enhanced wind farm design and operating techniques. In this study, wind data from ECMWF (European Centre for Medium-Range Weather Forecasts) has been utilized. Additionally, observational data from a wind turbine installed in the Edincik region has been incorporated. This observation dataset contains measurements of wind speeds, wind directions, and exported energy values from a turbine with a height of 100 meters. Based on data, turbulence calculation was performed using turbulence kinetic energy, horizontal turbulence intensity, vertical turbulence intensity, power law expression, and Reynold's decomposition methods. Higher energy export results from decreased turbulence intensity and Turbulent Kinetic Energy (TKE). The rate of turbulence dissipation does not necessarily affect energy export. With a few exceptions, lower TKE typically delivers greater energy. Daily changes in turbulence, wind speed, atmospheric stability, and terrain all have an impact on energy export. Seasonal fluctuations in turbulence intensity are seen, owing mostly to atmospheric instability and wind shear.

Keywords: Wind Energy, Atmospheric Boundary Layer Stability, Turbulence Kinetic Energy, Horizontal and Vertical Turbulence Intensity, Power Law Expression

I. Introduction

The escalating global demand for energy presents environmental challenges, prompting a shift towards cleaner, sustainable sources like wind and solar power. These renewables, driven by technological advancements, are subject to weather dynamics, necessitating precise wind forecasting for effective wind farm operation. As highlighted by Asilhan Sirdas (2005 and 2018), depleting fossil fuel reserves and the associated environmental consequences underscore the need for sustainable alternatives, such as wind power. Short-term wind predictions, with timeframes ranging from 5 minutes to 1 hour, are critical for optimizing wind turbine performance and capacity utilization. Atmospheric stability significantly influences wind energy systems, impacting electricity generation by affecting wind speed and direction (Clara et al, 2016). This study aims to explore the interplay between atmospheric stability and wind energy, particularly their effects on wind characteristics and energy production. It contributes to the ongoing quest for enhanced reliability and efficiency in renewable energy sources, aligning with the overarching goal of advancing sustainability and cleaner energy solutions.

II. Experimental Procedure/Methodology/System Description

a) Turbulent Kinetic Energy (TKE)

In fluid dynamics, turbulence kinetic energy (TKE) is defined as the average kinetic energy per unit mass associated with the vortex in the turbulent flow. As a result of the interplay between turbulent eddies and the mean flow, TKE is produced by the shear creation of Reynolds stress (Craft & Launder, 1992). The rate at which energy is transferred from large-scale motion to small-scale motion is related to the rate of viscous dissipation of TKE (Elghobashi & Truesdell, 1993). In conclusion, TKE is a crucial factor in comprehending fluid motion and how it interacts with the environment.

$$TKE = \frac{1}{2}\left(\sigma_u{}^2 + \sigma_v{}^2 + \sigma_w{}^2\right) \quad (1)$$

Where $\sigma_u{}^2$ $\sigma_v{}^2$and $\sigma_w{}^2$ are variance in latitudinal (u), longitudinal (v), and vertical (w) velocities (m s^{-1}). TKE is a direct measure of the intensity of three-dimensional turbulence.

b) Horizontal Turbulence Intensity

Turbulence intensity (I_u) is calculated by dividing the standard deviation of wind speed by the average wind speed using a specified formula (Clara et al, 2016). The standard deviation and turbulence level significantly influence the resulting value. Turbulence intensity is typically considered low when it equals or is below 1%, and severe when it exceeds 10%. Studies, such as Hui, Larsen, and Xiang (2009), suggest that this parameter provides insight into the prevailing turbulence level. Additionally, the value of I_u is calculated by dividing the value of the standard deviation of the mean horizontal wind speed (u) at a specific height (z) by u for each u speed u(z).

$$I_u = \frac{\sigma_u}{u(z)} \quad (2)$$

c) Vertical Turbulence Intensity

Vertical turbulence intensity is a metric that quantifies the turbulence within the vertical component of wind. It is typically assessed by calculating the standard deviation of vertical wind speed fluctuations in relation to the mean wind speed. Much like horizontal turbulence intensity, vertical turbulence intensity serves as an indicator of turbulence magnitude in the vertical dimension, and its value is directly linked to the standard deviation of wind speed variations. This metric holds significance in various applications, such as the design of tall structures and bridges, as well as the assessment of wind turbine efficiency.

$$I_W = \frac{\sigma_W}{u(z)} \tag{3}$$

d) Power Law Equation

The relationship between wind speed and altitude is often represented using the power-law equation in wind energy research. This mathematical model is commonly applied to simulate wind speed profiles in flat, uniform terrains. However, due to the complex and diverse nature of turbulent flows, the power-law equation is subject to unpredictability, as noted by Kikumoto et al. (2017). The exponent, denoted as alpha (), within this equation signifies the wind shear between wind speeds at different heights. In essence, the wind speed increases with altitude in an inversely proportional manner to the height above the ground. The formula used to express the equation is

$$u(z) = u_R \left(\frac{z}{z_R}\right)^{\alpha} \tag{4}$$

where u is the wind speed at height z, uR is the reference wind speed at height zR, and α is the power law exponent. The value of α depends on the atmospheric stability and surface roughness (Gül and Asilhan Sirdas; 2020).

III. Analysis

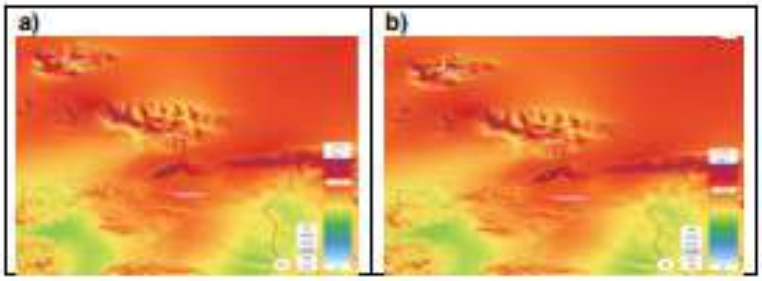

Fig.1. a) Average Wind Speeds b) Average Power Density (Global Wind Atlas, n.d.)

This study assesses the wind energy potential in Bandirma's Edincik area, affected by both Mediterranean and Black Sea climates. The region benefits from consistent, strong winds, particularly along the coast, making it an ideal site for wind energy generation. Predominantly, precipitation occurs in winter, and north-northeast winds prevail at an average speed of 15 km/h. Annual average rainfall is approximately 703.3 kg/m² (Bandirma University, 2023). The Global Wind Atlas indicates that coastal areas in Bandırma, especially Edincik, experience high average wind speeds. These wind speeds greatly impact power density, a crucial factor directly linked to a wind farm's energy potential as it is proportionate to the cube of wind speed. This study integrates ECMWF wind data with observations from a 100-meter-height wind turbine in Edincik (Durak, 2018), enabling a comprehensive analysis of wind characteristics in the region and a more precise assessment of wind resource, turbine performance, and overall wind energy potential in Edincik.

IV. Results and discussion

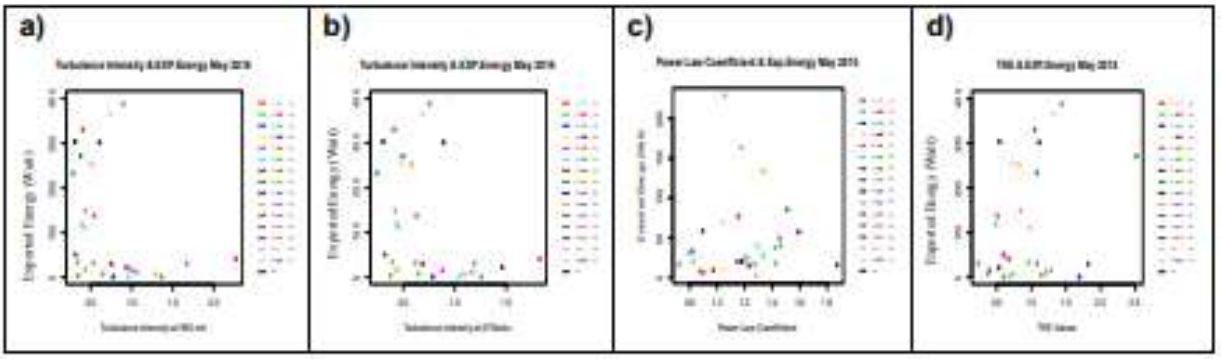

Fig. 2. a) Comparison of Turbulence Intensity at 950 mb and Exported Energy in May 2015, b) Comparison of Turbulence Intensity at 975 mb and Exported Energy in May 2015, c) Comparison of Alfa Values and Exported Energy in May 2015, d) Comparison of Turbulence Kinetic Energy and Exported Energy in May 2015.

In May, an inverse relationship is observed between turbulence intensity and exported energy levels at the 950mb and 975mb. Lower turbulence intensity is associated with higher exported energy, signifying increased energy export during periods of reduced turbulence. Conversely, no significant correlation is evident when examining alpha values in relation to exported energy. Notably, lower TKE levels exhibit clustering of data points, indicating that higher levels of exported energy tend to concentrate during periods of diminished TKE.

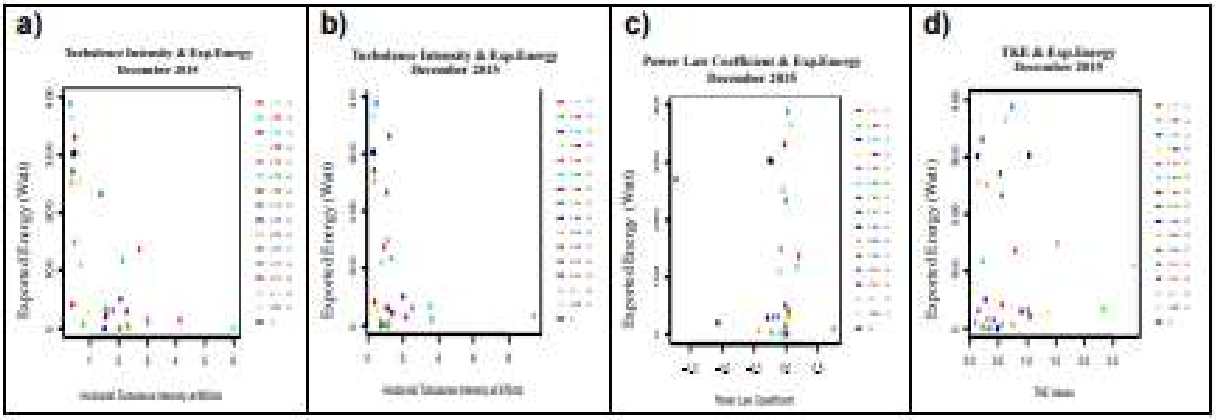

Fig. 3. a) Comparison of Turbulence Intensity at 950 mb and Exported Energy in December 2015, b) Comparison of Turbulence Intensity at 975 mb and Exported Energy in December 2015, c) Comparison of Alfa Values and Exported Energy in December 2015, d) Comparison of Turbulence Kinetic Energy and Exported Energy in December 2015.

When analyzing December data, a distinct relationship emerges between horizontal turbulence intensity and exported energy. Lower turbulence intensity consistently corresponds to higher exported energy levels, indicating an inverse correlation. However, the connection with exported energy becomes less clear when considering alpha values. On the other hand, low Turbulent Kinetic Energy (TKE) values are associated with increased exported energy.

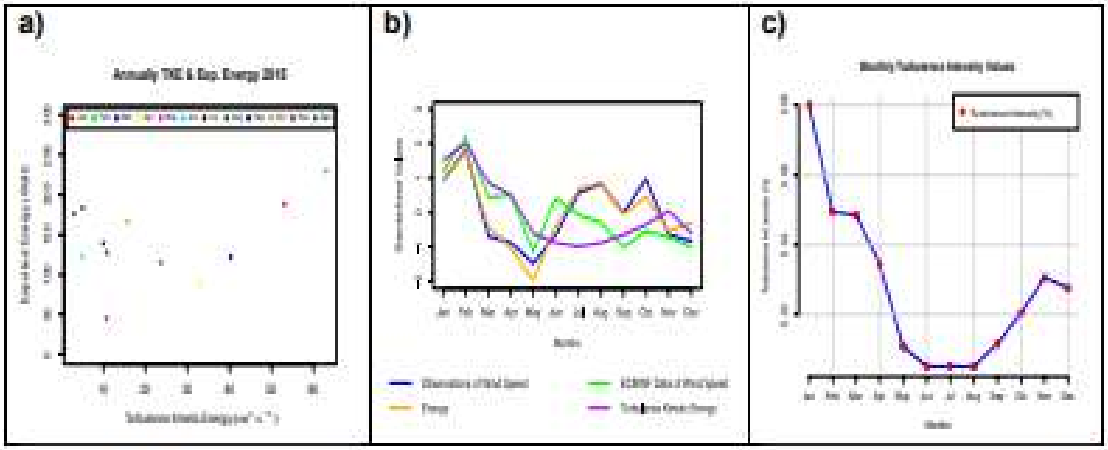

Fig. 4. a) Annually Turbulence Kinetic Energy and Exported Energy comparison in 2015. b) Comparison of Observations of Wind Speed, ECMWF Data of Wind Speed, Exported Energy and Turbulence Kinetic Energy for Edincik in 2015. c) Monthly Turbulence Intensity Values for Edincik in 2015.

Analysis of monthly Turbulent Kinetic Energy (TKE) and energy patterns reveals an inverse relationship. Lower TKE months correlate with higher energy values, with February showing the highest TKE and energy levels. Surprisingly, May, despite low TKE, exhibits low energy levels. This relationship is supported by a graph of ECMWF wind data, observed wind speed, exported energy, and TKE, indicating that high TKE periods generally coincide with increased energy exports. However, it's noteworthy that reduced TKE in specific months leads to higher energy exports, suggesting additional factors beyond turbulence, such as atmospheric stability, local terrain, and climatic conditions influencing wind energy conversion. A 2015 monthly analysis of turbulence intensity identifies January as the most turbulent month, with summer months showing the lowest turbulence intensity, attributed to factors like atmospheric instability, wind shear, and seasonal variations.

V. Conclusion

In summary, this thesis has yielded valuable insights into the relationship between atmospheric turbulence parameters and exported energy. We have observed a consistent inverse correlation between turbulence intensity and Turbulent Kinetic Energy (TKE) with exported energy, indicating that reduced turbulence leads to higher energy export. However, when considering alpha values, which gauge turbulence dissipation rate, the connection with exported energy remains less conclusive. This suggests that while turbulence is significant in energy export, its rate of dissipation doesn't consistently influence the process. Monthly analysis of TKE values and energy export supports these findings, revealing that lower TKE months generally yield higher energy levels. Notably, February, despite its turbulence, exhibits greater energy production. Exported energy increases during periods of reduced turbulence kinetic energy, suggesting the influence of other factors like atmospheric stability, local terrain, and climate on wind energy conversion. Seasonal trends in turbulence intensity levels show higher values in January and lower values in summer months, attributed to atmospheric instability, wind shear, and seasonal factors. In conclusion, this research underscores the intricate connection between turbulence characteristics and energy export within the atmospheric boundary layer. It emphasizes the roles of turbulence intensity and TKE in shaping energy export levels, while acknowledging the potential impact of other variables. These findings lay a foundation for future research to enhance renewable energy systems' efficiency and effectiveness, particularly those reliant on atmospheric conditions.

References

Albornoz, C. P., Soberanis, M. E., Rivera, V. R., & Rivero, M. (2022). Review of atmospheric stability estimations for wind power applications. Renewable and Sustainable Energy Reviews, 163, 112505.

Bandırma University. (n.d.). Bandırma İklim. Retrieved April 25, 2023, from https://www.bandirma.edu.tr/tr/www/Sayfa/Goster/Bandirmada-iklim-1084

Clara M. St. Martin; Julie K. Lundquist; Andrew Clifton; Gregory S. Poulos; Scott J. Schreck, 2016. Wind turbine power production and annual energy production depend on atmospheric stability and turbulence. 10.5194/wes-2016-21

Craft, T. J., & Launder, B. E. (1992). New wall-reflection model applied to the turbulent impinging jet. AIAA journal, 30(12), 2970-2972.

Durak, M. (2018). Rüzgar enerji santrallan üretim ve işletme değişkenlerinin çoklu- yarıvariogram yöntemi ile alansal tahmini.

Elghobashi, S., & Truesdell, G. (1993). On the two-way interaction between homogeneous turbulence and dispersed solid particles. I: Turbulence modification. Physics of Fluids A: Fluid Dynamics, 5(7), 1790-1801.

Global Wind Atlas. (n.d.). Global Wind Atlas. https://globalwindatlas.info

Hui, M. C. H., Larsen, A. X. H. F., & Xiang, H. F. (2009). Wind turbulence characteristics study at the Stonecutters Bridge site: Part I—Mean wind and turbulence intensities. Journal of Wind Engineering and Industrial Aerodynamics, 97(1), 22- 36.

Kikumoto, H., Ooka, R., Sugawara, H., & Lim, J. (2017). Observational study of power-law approximation of wind profiles within an urban boundary layer for various wind conditions. Journal of Wind Engineering and Industrial Aerodynamics, 164, 13- 21.

Sirdas, S., 2005. Daily wind speed harmonic analysis for Marmara region in Turkey, Energy Conversion and Management 46(7):1267-1277, DOI:10.1016/j.enconman.2004.06.020

Sirdas, Asilhan S. and Akatas, N., and İzgi, E., 2018. Improved wind speed prediction results by Artificial Neural Network Method, Book Chapter of Springer Nature, Green Energy and Technology: Exergy for A Better Environment and Improved Sustainability, Volume 2 – Applications, Editors: Fethi Aloui; Ibrahim Dincer, Hardcover ISBN: 978-3-319-62574-4, Series ISSN: 1865-3529, DOI: 10.1007/978-3-319-62575-1

Gül, F. B. and Asilhan Sirdas, S., 2020. Boundary Layer Stability Impact on Wind Power, International Conference on Sustainable Energy and Energy Calculations, ICSEEC, Istanbul, Turkey, September 4 – 5, 2020, Sustainable Energy and Energy Calculations Proceedings, ISBN: 978-605-65842-3-7.

Stull, R. B. (2015). Practical meteorology: an algebra-based survey of atmospheric science. University of British Columbia.

Van den Berg, G. P. (2008). Wind turbine power and sound in relation to atmospheric stability. Wind Energy: An International Journal for Progress and Applications in Wind Power Conversion Technology, 11(2), 151-169.

GLOBAL WARMING AND THUNDERSTOMS IN SOUTH AEGEAN REGION OF TURKIYE

[1*]Sevinc A. Sirdas, [2]Kemal Ege Sural
[1] Istanbul Technical University, Faculty of Aeronautics and Astronautics
Department of Meteorological Engineering, Maslak 34469 Istanbul, Turkey

* E-mails: sirdas@itu.edu.tr, ssirdas@gmail.com, kegesural@gmail.com*

Abstract
Complex convective storms with strong updrafts and thunderstorms are hazardous natural events for every alive, it can cause many damages for properties, transportation so they can be detrimental for economies; furthermore, they are harmful for human health, evenly it can finalize to deaths. Besides, lightning and thunderstorm, are one considered as one of the financial losses and accidents in airspace, coastal areas, agricultural fields, urban areas and effected regions every year. In this study strong thunderstorms with electrical discharge will be investigated in İzmir and Antalya. In this study, especially six indexes, Lifted Index, K index, CAPE, Total Totals Index, SWEAT index and Bulk Richardson Number were analyzed in each other. Trend analysis was performed between 2005 and 2015 depending on the frequency of the severe electrical storm. With the effect of global warming, the intensity of thunderstorm was evaluated using different indices. As a result, in general, Lifted Index is indirectly proportional to other indexes because it is an indicator of possibility of thunderstorm if it is below 2, and also negative values; on the other hand, the other indexes have positive values when they show possibility of thunderstorms. The 2015–2049 CMIP6 climate predictions show different trends in temperature and precipitation by using SSP1-2.6 and SSP2-7.0 climate change seniors with Mann-Kendall test.

Keywords: Climate Change, Extreme Weather, Electrical Storm, Thunderstorm, Weather Indexes, CAPE

I. Introduction

Lightning and thunderstorms have been more frequent in the past several years; this rise has been attributed mainly to certain meteorological conditions and global warming. Significant financial losses and safety problems in Turkish airspace have resulted from these thunderstorms (Sirdas et al., 2018). According to scientific studies, global warming is linked to an increase in thunderstorm frequency, which is especially bad for coastal regions like the Mediterranean, Aegean Sea, and Black Sea. These areas are vulnerable to flash floods caused by intricate convective storm systems. Every day, between 2,000 and 2,500 thunderstorms occur worldwide, resulting in a variety of risks such flash floods, lightning damage, interruptions to transportation, and fatalities. More people die each year from flash floods caused by thunderstorms than from hurricanes, tornadoes, and lightning all together. Risks from complex convective events, which are frequent in the spring and summer, include hail, tornadoes, severe winds, and flash flooding (Sirdas et al., 2016). People who live in high-risk locations ought to be on guard, keep an eye on the weather, and have emergency preparations. In conclusion, communities can lessen the effects of severe storms by being more aware of the situation and prepared. A severe mesoscale complex convective system's possible effect was evaluated using indicators including the Showalter, K, and Lifted indexes, which shed light on atmospheric stability (Miglietta, 2019; NOAA, 2022).

II. Methodology

A key statistical technique for lowering the dimensionality of big datasets, enhancing interpretability, and facilitating the presentation of intricate, multidimensional data is principal component analysis, or PCA. Two sets of variables were subjected to PCA in this investigation. PCA identifies linear combinations of variables, termed principal components, which are orthogonal and capture the maximum data variability (Royal Society Publishing, 2015). When dealing with a dataset comprising p numerical variables for each of n entities, PCA aims to determine a set of k < p linear combinations that account for the highest data variability. Each linear combination is represented by a vector $z = [z_1, z_2, \ldots, z_k]$, and is given by:

$$z = a_1x_1 + a_2x_2 + \ldots + a_px_p \quad (1)$$

where $x = [x_1, x_2, \ldots, x_p]$ is the original data vector and $a = [a_1, a_2, \ldots, a_p]$ are constants that satisfy the constraint $a_1^2 + a_2^2 + \ldots + a_p^2 = 1$. The first principal component (z_1) captures the most significant data variation, while subsequent components capture the remaining variation, remaining uncorrelated with the prior ones. (Royal Society Publishing, 2015) The PCA algorithm works by computing the covariance matrix of the data, which is given by:

$$Cov(X) = (1/n) * X^T * X \quad (2)$$

For the data's covariance matrix, represented by the letter X, which is a n x p data matrix with n observations, eigenvectors and eigenvalues are calculated. Principal components are represented by eigenvectors, and their explanatory ability is measured by eigenvalues. The most significant principal components are those with the greatest eigenvalues. (2015) Royal Society Publishing

Equation 3 allows the original data to be transformed into the principal component space.

$$Z = X * V \quad (3)$$

This results in a transformed matrix Z, where Z is n×k and V is p×k. Visualization of the transformed data can be

performed through a scatter plot, utilizing the principal components as axes (Royal Society Publishing, 2015). PCA is a potent tool for exploratory data analysis, unveiling patterns and relationships in high-dimensional datasets. Additionally, it's widely used for dimensionality reduction and data compression, effectively preserving crucial information (Royal Society Publishing, 2015; Jolliffe, 2002).

III. Analysis

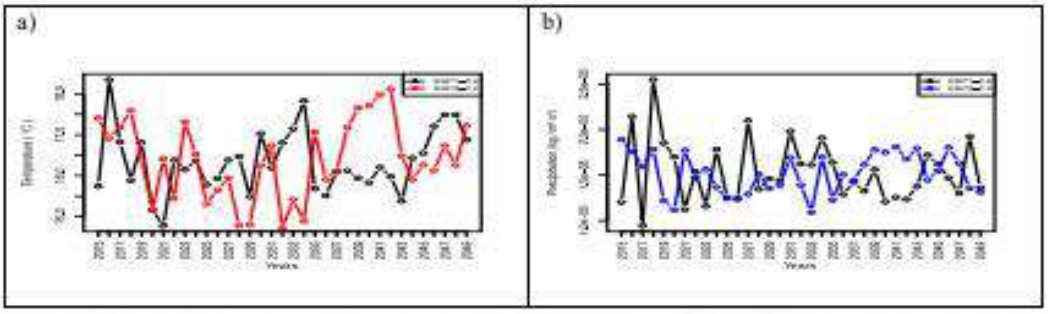

Fig. 1. a) Temperature Projections b) Precipitation Projections Between 2015 and 2049 (*Copernicus Climate Data Store,2023*

Table 1. Mann-Kendall trend analysis results

Data	SSP1-2.6 Temperature	SSP1-7.0 Temperature	SSP1-2.6 Precipitation	SSP1-7.0 Precipitation
z	1.3917	0.73847	-0.22722	0.65327
n	35	35	35	35
p-value	0.164	0.4602	0.8203	0.5136
S	99.00	5.300000e+01	-17.00	47.00
varS	4958.33	4.958333e+03	4958.33333333	4958.3333333
tau	0.1663866	8.907563e-02	-0.02857143	0.0789916

The 2015–2049 CMIP6 climate predictions show different trends in temperature. Temperatures under SSP1-2.6 drop sharply between 2024 and 2043 before increasing once again. SSP3-7.0 predicts 2042 to be the highest temperature. SSP1-2.6 predicts a falling trend in precipitation until 2049, but SSP3-7.0 predicts a declining trend until 2037, after which there will be an increase. The findings of the Mann-Kendall trend analysis are non-significant, indicating the absence of statistically significant trends.

IV. Results and discussion

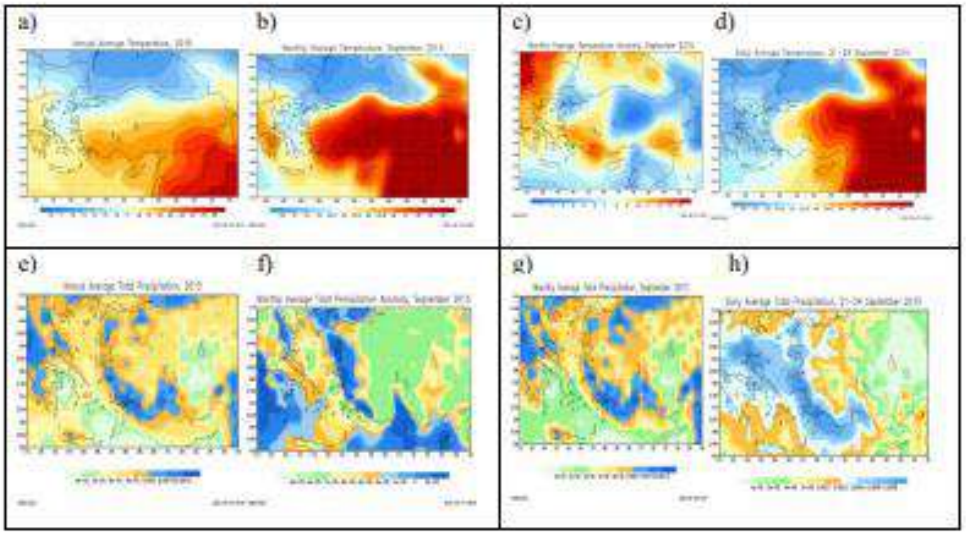

Fig. 2. a) Annual Average Temperature,2015 b) Monthly Average Temperature, September 2015 c) Monthly Average Temperature Anomaly, September 2015 d) Daily Average Temperature 21-24 September 2015 e) Annual Average Total Precipitation,2015 f) Monthly Average Total Precipitation, September 2015 g) Monthly Average Total Precipitation Anomaly, September 2015 and h) Daily Average Total Precipitation 21-24 September 2015

Turkey has a variable climate, with hot summers and mild coastal winters and harsher winters with a lot of snowfall in the interior. The average temperature in coastal regions, such as the Mediterranean and Aegean shores, often stays between 15 and 22°C. On the other hand, interior areas with average temperatures between 13 and 17°C,

such as Eastern Anatolia, have a colder climate. However, from September 21 to 24, Turkey's Aegean and Mediterranean shores witnessed weather anomalies from the regular monthly trend, which included cooler temperatures and more precipitation.

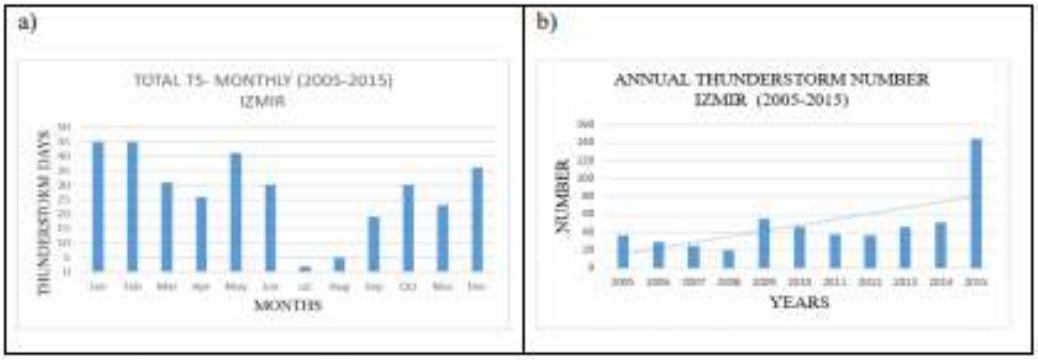

Fig. 3. The number of monthly and annual thunderstorms in airports of Turkey (2005-2015) (Sirdas Asilhan et al., 2018).

The monthly distribution of thunderstorm activity in Izmir from January 2005 to December 2015 is analyzed in this study. The results show that thunderstorm activity varies seasonally in the area, occurring more frequently in the spring and fall and less frequently in the summer. This pattern is in line with earlier studies that link the reduction in summertime convective potential to warm air mass subsidence and the increase in springtime convective instability. 2015 saw the most of the thunderstorms in Izmir.

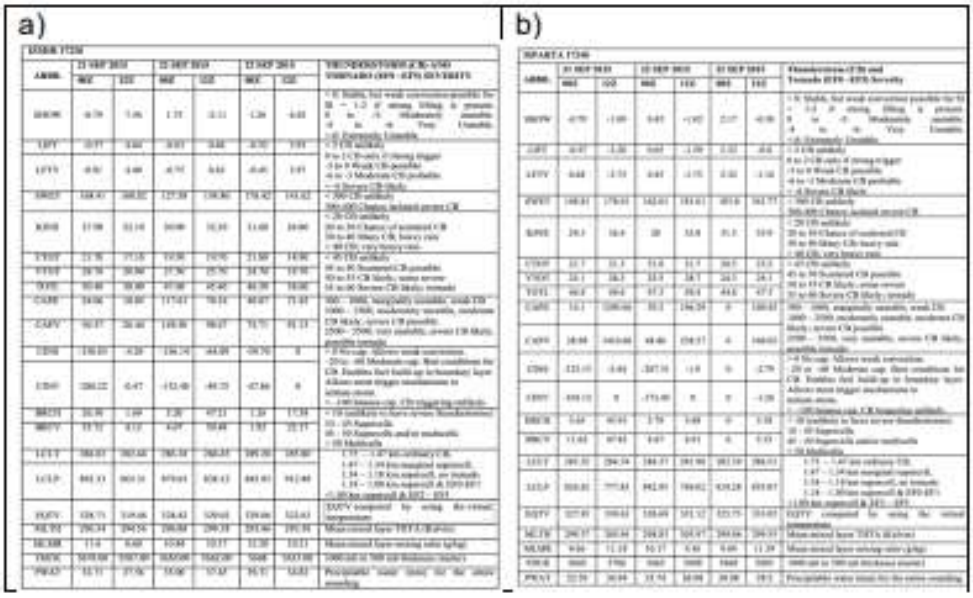

Fig. 4. Classification of thunderstorm indexes for each case for a) Izmir and b) Isparta observations (based on to Stull, 2000).

In Isparta, on certain days, the range of CAPE values from 14.1 to 1295.06 J/kg suggested there was enough energy for the development of thunderstorms. On specific days, negative CIN levels indicated an unstable atmosphere that was favorable for thunderstorms. All days showed a higher chance of severe weather despite low SWET values; this was corroborated by PWAT values more than 20 mm, which indicates substantial atmospheric moisture. There was a strong chance of thunderstorm development on days with LCLT values over 280 K, and the atmospheric instability was highlighted by TOTL on many days, which also suggested the possibility of thunderstorm formation. Compared to September 21 and 23, Izmir's CAPE and CAPV readings on September 22 were much higher, indicating increasing instability. Convection inhibition is absent, as shown by negative CINS and CINV values, which supports the generally unstable atmospheric conditions.

In Izmir and Isparta, PCA investigated the relationships between climatic variables and found significant connections. Cross Total and K Index have a substantial negative correlation (-0.77) in Izmir, indicating a negative link. In 00Z data, there is a strong positive correlation (0.81) between LCL Temperature and CAPE. Cross Total and SWEAT Index showed a strong positive association (0.81) in 12Z observations. There is a significant negative correlation (-0.73) between the Showalter Index and the Lifted Index in Isparta's 00Z data. An adverse relationship is revealed by a substantial negative correlation (-0.82) between the SWEAT Index and LCL temperature during 12Z

measurements. These results provide important new understandings of the intricate relationships between meteorological factors.

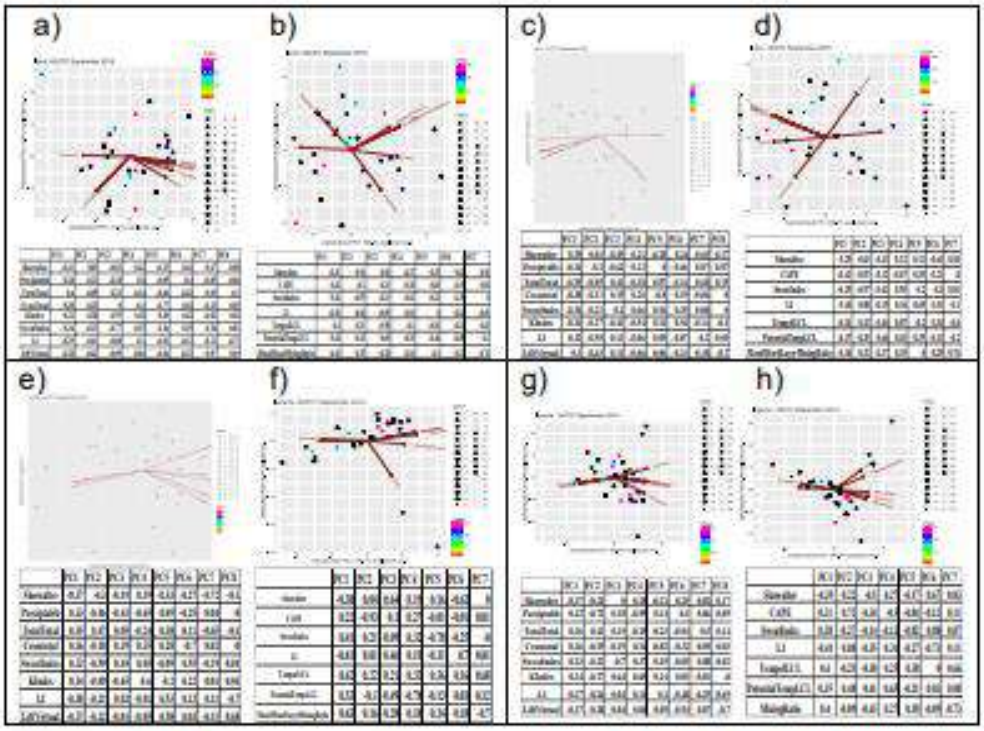

Fig. 5. a and b) Izmir 00Z September 2015. c and d) Izmir 12Z September 2015. e and f) Isparta 00Z September 2015. g and h) Isparta 12Z September 2015

V. Conclusion

Over a period of a month, this study examined the impact of meso-scale convective complex storms on floods, lightning, and heavy rainfall in Turkey's South Aegean area. Multilinear regression research, using meteorological indices and vertical atmospheric variables, showed an inverse association (-0.74) between lifted index (LI) and convective available potential energy (CAPE), with LI decreasing as CAPE increases. The complex nature of convective complex storm systems was highlighted by the positive correlations observed between CAPE and the Mean mixed layer mixing ratio and the Equivalent potential temperature [K] of the Lifted Condensation Level (LCL). Climate projections show that temperatures and precipitation will fluctuate dynamically over time, emphasizing the need for adaptable solutions. The lack of apparent trend underlines the need to manage the difficulties caused by the unpredictability of changing weather patterns. These storms pose challenges in prediction due to their dynamic nature and can lead to various risks, including heavy rainfall, flooding, and property damage. Effective strategies for mitigating their impact in the South Aegean region involve enhancing early warning systems, disaster response preparedness, and sustainable land planning.

References

Copernicus Climate Data Store (no date) Copernicus Climate Data Store | Copernicus Climate Data Store. Available at: https://cds.climate.copernicus.eu/cdsapp#!/dataset/projections-cmip6?tab=form (Accessed: 15 October 2023).

Freedman, D.A. (2009). Statistical Models: Theory and Practice. Cambridge University Press. p. 26. Miglietta, M.M. (2019). Mediterranean Tropical –Like Cyclones (Medicanes). Atmosphere. 10,206. doi:10.3390/atmos10040206

Jolliffe, I. T. (2002). Principal Component Analysis. Springer.

Sirdas, A.S., Diriker, A.B., and Kumar, V., 2016. Heavy Precipitation Events in Marmara Region and connections with the North Atlantic and Arctic Oscillation Patterns, Environment and Natural Resources Research, Vol. 6, No. 4, DOI: http://dx.doi.org/10.5539/enrr.v6n4p1

Sirdas Asilhan, Ikizceli, A. and Kumar, V., 2018. Evaluation of Thunderstorms and Associated Hazards in the Air traffic over Turkey, July 30-August 1, 2018, Tokyo, Japan, ICENS, ISSN 2313-7827

Stull, R. B. (2015). Practical meteorology: an algebra-based survey of atmospheric science.

IEEES-147

Natural gas production by anaerobic digestion process from different food wastes : A simulation study

Chandra Prakash Gupta, Naresh Thota*
Chemical Engineering Department, National Institute of Technology Warangal, Warangal, 506004, India

* E-mail: naresht@nitw.ac.in

Abstract
Anaerobic digestion (AD) is a complex biological process involving multiple reactions. There are four steps involved in the complete AD process viz. hydrolysis, acidogenesis, acetogenesis, and methanogenesis. The extent of the reaction controls the first step and the other steps are kinetically controlled. A process simulation model (PSM) to represent all the reactions involved was developed using Aspens plus Software using the NRTL model. Three types of Food waste viz. Mesophilic, Thermophilic, and Psychrophilic were used as feed to the AD process and produced Natural gas. All three Feeds contained different compositions of carbohydrates, proteins, and fats. The effect of all these compositions were studied and compared their effects on Natural gas production. Increasing the temperature and pressure for all three feeds viz. mesophilic, thermophilic, and psychrophilic food waste increased the production of natural gas but after reaching the maximum limit, further increase in temperature resulted in a continuous decrease in the production of natural gas. However, It was found that thermophilic food waste is more temperature-sensitive as compared to mesophilic and psychrophilic food waste. At 4 % protein in all the three types of feed, the production of natural gas was maximum and a further increase of protein percentage in feed resulted in a decrease in the production of natural gas. Further effect of hydraulic retention time, feed to water ratios were studied for the maximum production of natural gas. By comparing all the three types of feed for the production of natural gas, it is observed that thermophilic food waste produced more natural gas followed by mesophilic and psychrophilic food wastes keeping all other variables as constant.

Keywords: Food waste, natural gas, anaerobic digestion, process model, .

I. Introduction

One major challenge looming for the world in the near future is the issue of energy. Currently, global attention is increasingly turning towards renewable energy sources, and rightfully so. The Anaerobic Digestion (AD) process emerges as a promising avenue within the realm of renewable energy, particularly harnessed from food waste. An inherent advantage of this method is the mitigation of pollution associated with food waste, as it is efficiently converted into energy. Anaerobic Digestion is a controlled Process involving microbial decomposition of organic matter in absence of oxygen. Anaerobic digestion involves the process of decaying biodegradable material in the absence of any terminal electron acceptors like; sulfate, nitrate, or oxygen. Anaerobic digestion consists of several complex biochemical reactions carried out by several types of microorganisms that survive in oxygen-free conditions. During this process, Natural gas is produced which is mainly composed of methane (CH_4) and carbon dioxide (CO_2) (Methane being the primary component) as major gases with a trace amount of hydrogen sulfide(H_2S), nitrogen(N_2), and water vapors (Yuanyuan et al., 2018). Natural gas is a renewable energy source that can be used as a fuel or can be used in a variety of ways for the production of heat and/or electricity. Natural gas directly can be used in the kitchen for cooking purposes. We can use it without any separation, with the only problem of carbon dioxide being a highly corrosive gas. If the percentage of carbon dioxide is low, we can use directly Natural gas for cooking purposes. It is possible to produce sufficient heat for cooking purposes through the Bio-methanation process. Without the separation of carbon dioxide from Natural gas, we are getting 90% to 95% of methane, we call it Bio CNG. Chemically produced CNG contains 95% to 98% methane which is close to that being produced by the Bio-methanation process. We can remove the carbon dioxide from the Natural gas and other gases like H_2, H_2S, and NH_3 and come up with a methane percentage of 95% to 98%, it can be used as fuel and the same Natural gas can also be used for electricity or power production.

Numerous prior studies have demonstrated the efficacy of Continuous Stirred Tank Reactors (CSTR) in managing organic waste like grass, chicken manure, corn stover, vegetable waste, and sewage sludge. In China, the predominant approach in many large-scale anaerobic digestion facilities involves the utilization of two-stage digesters. The intricate microbial process involved in the anaerobic digestion of food waste in these two-stage reactors is subject to various influencing factors. Of these, Hydraulic Retention Time (HRT) stands out as a critical parameter among the key operational conditions, necessitating regular monitoring in anaerobic reactors. Natural gas plants in the agricultural area mostly apply long HRT to allow sample time for the optimal degradation of complex compounds (Shi et al., 2017). the methane content exhibited a notable decrease, ranging from 14.2% to 28.5%, with an HRT of 20 days, which was the lowest among the three reactors. Several studies have explored the inclusion of co-digestion feed, such as cattle manure, alongside food waste to enhance methane yield. The aim was to investigate the anaerobic co-digestion of food waste and cattle manure, identifying key parameters influencing biogas and methane yield. Both batch and semi-continuous tests consistently revealed improved total methane production through co-digestion, with an optimal food waste (FW) to cattle manure (CM) ratio identified as 2. At this specific ratio, batch tests demonstrated a remarkable 41.1% increase in total methane production, reaching a

corresponding methane yield of 388 mL/g-VS (Zhang et al., 2013). The current simulation efforts involve modeling the anaerobic digestion process for various food waste types namely characterized by diverse compositions, utilizing the Aspen Plus software. Additionally, the investigation encompasses the analysis of how key parameters such as temperature, pressure, fat composition, protein composition, feed-to-water ratio, and hydraulic retention time (HRT) impact natural gas production. The ultimate focus is on comprehensively understanding the interplay of these variables and their collective influence on achieving optimal natural gas production.

II. Modelling and simulation methodology

Figure 1 illustrates the process simulation model for the anaerobic digestion process is developed using Aspen Plus software. This tool has a rigorous method that can be used to estimate the properties of the components and detail thermodynamic calculations (Harun et al., 2019). The thermodynamic properties package used in this simulation is the non-random-two-liquid (NRTL). The technique simulation version divides the digestion reaction into groups of reaction sets. The hydrolysis reactions in anaerobic digestion are entirely dependent on the extent of the reaction, while other stages, namely acidogenic, acetogenic, and methanogenic reactions, are controlled by kinetics. (Rajendran et al., 2014). The process flow diagram for anaerobic digestion comprises a mixer, two reactors (Stoichiometric and CSTR), a Heat Exchanger, and a Separator, as illustrated in Figure 1. The anaerobic digestion of food waste, which consists of carbohydrates, proteins, and fats, involves hydrolysis reactions operating within a reaction extent range of 0.0-1.0. Distinct temperature and pressure conditions are specified for different digestion phases: Mesophilic conditions: Temperature at 35°C and pressure at 0.7 atm, Thermophilic conditions: Temperature at 50°C and pressure at 1 atm, Psychrophilic conditions: Temperature at 18°C and pressure at 1 atm.

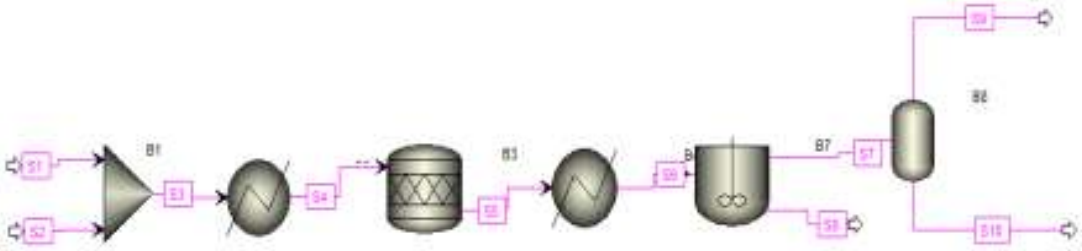

Figure 1. Process simulation model for the anaerobic digestion process

There are four stages of AD process. The four stages of reaction involved are mentioned below ((Rajendran et al., 2014).

1. **Hydrolysis:** This stage involves the breakingup of complex organic matter into simple materials as shown in reactions below. In this step, insoluble complex organic materials such as protein, carbohydrates, and fats are converted to soluble monomers such as Peptides, Fatty acids, and saccharides. It is a slow process. This stage is a rate-limiting stage in the AD process.

$$C_5H_8O_4 + H_2O \rightarrow 2.5C_2H_4O_2 \quad (1)$$

$$C_5H_8O_4 \rightarrow C_5H_4O_2 + 3H_2O \quad (2)$$

$$C_5H_8O_4 + H_2O \rightarrow C_5H_{10}O_5 \quad (3)$$

$$C_6H_{12}O_6 \rightarrow 2C_2H_6O + 2CO_2 \quad (4)$$

$$2C_2H_6O + CO_2 \rightarrow 2C_2H_4O_2 + CH_4 \quad (5)$$

$$C_{13}H_{25}O_7N_3S + 6\,H_2O \rightarrow 6.5CO_2 + 6.5CH_4 + 3\,H_3N + H_2S \quad (6)$$

$$C_{51}H_{98}O_6 + 8.436\,H_2O_4 \rightarrow C_3H_8O_3 + 2.43\,C_{16}H_{34}O \quad (7)$$

$$C_{37}H_{70}O_5 + 4.1H_2O \rightarrow 2.1C_3H_8O_3 + 0.9C_{16}H_{34}O + 0.9C_{18}H_{34}O_2 \quad (8)$$

$$C_{37}H_{68}O_5 + 4.3H_2O \rightarrow 2.2C_3H_8O_3 + 0.9C_{16}H_{34}O + 0.9C_{18}H_{32}O_2 \quad (9)$$

$$C_{57}H_{104}O_6 + 3H_2O \rightarrow C_3H_8O_3 + 3C_{18}H_{34}O_2 \quad (10)$$

2. **Acedogenesis:** This is also called the fermentation process. In the Acidogenesis step majorly all basic monomers get converted into volatile fatty acids, but these volatile fatty acids are mostly propionic acid, butyric acid, and large carbon-containing fatty acids. This stage is affected by a diverse group of bacteria that are capable of bringing down the pH up to 4 inside the digester.

$$C_2H_5NO_2 + H_2 \rightarrow C_2H_4O_2 + NH_3 \quad (11)$$

$$C_2H_5NO_2 + 0.5H_2O \rightarrow 0.75C_2H_4O_2 + NH_3 + 0.5CO_2 \quad (12)$$

$$C_6H_{12}O_6 + 0.1115NH_3 \rightarrow 0.1115C_5H_7NO_2 + 0.744C_2H_4O_2 + 0.5C_3H_6O_2 + 0.4409C_4H_8O_2 + 0.6909CO_2 + 1.0254H_2O \quad (13)$$

$$C_3H_8O_3 + 0.4071NH_3 + 0.0291CO_2 + 0.005H_2 \rightarrow 0.04071C_5H_7NO_2 + 0.94185C_3H_6O_2 + 1.09308H_2O \quad (14)$$

3. **Acetogenesis:** In this stage, propionic acid, and butyric acid will be broken down and converted into acetic acid, and from acetic acid, we get methane and carbon dioxide

$C_{18}H_{34}O_2 + 15.2396H_2O + 0.2501CO_2 + 0.1701NH_3 \rightarrow 0.1701C_5H_7NO_2 + 8.6998C_2H_4O_2 + 14.4978H_2$ (15)

$C_3H_6O_2 + 0.06198NH_3 + 0.314336H_2O \rightarrow 0.06198C_5H_7NO_2 + 0.9345C_2H_4O_2 + 0.660412CH_4 + 0.160688CO_2 + 0.00055H_2$ (16)

$C_4H_8O_2 + 0.0653NH_3 + 0.8038H_2O + 0.0006H_2 + 0.5543CO_2 \rightarrow 0.0653C_5H_7NO_2 + 1.8909C_2H_4O_2 + 0.446CH_4$ (17)

$C_5H_{10}O_2 + 0.0653NH_3 + 0.5543CO_2 + 0.8044H_2O \rightarrow 0.0653C_5H_7NO_2 + 0.8912C_2H_4O_2 + C_3H_8O_2 + 0.4454CH_4 + 0.0006H_2$ (18)

$C_{18}H_{32}O_2 + 15.356H_2O + 0.482CO_2 + 0.1701\ H_3N \rightarrow 0.1701\ C_5H_7NO_2 + 9.02C_2H_4O_2 + 10.0723\ H_2$ (19)

$C_{18}H_{34}O + 15.253\ H_2O + 0.482\ CO_2 + 0.1701\ H_3N \rightarrow 0.1701C_5H_7NO_2 + 8.4402C_2H_4O_2 + 14.9748\ H_2$ (20)

4. **Methanogenesis:** This is the final step of the AD process in which methanogens create methane (CH_4) from the final products of acetogenesis as well as from some of the intermediate products from hydrolysis and acidogenesis. There are two pathways in general known to utilize acetic acid and CO2 to create CH4 and their biochemical reactions are given below

$C_2H_4O_2 + 0.022NH_3 \rightarrow 0.022C_5H_7NO_2 + 0.945CH_4 + 0.066H_2O + 0.945CO_2$ (21)

$14.49H_2 + 3.83CO_2 + 0.083NH_3 \rightarrow 0.083C_5H_7NO_2 + 3.41CH_4 + 7.49H_2O$ (22)

Results and discussion

1. **Effect of Temeperature:** The methane production observations for various types of feed revealed a temperature-dependent trend. Specifically, at lower temperatures, methane production was observed to be low. However, as the temperatures increased, methane production also increased, reaching a peak before subsequently decreasing. This suggests a temperature-dependent relationship where methane production is influenced by the prevailing temperatures, with an optimal range for maximizing methane production.

2. **Effect of Pressure:** The observations for methane production across all types of feed indicated a relationship with varying pressure. Specifically, at low pressures, methane production was observed to be low. However, as the pressure increased, methane production also increased, reaching a peak before subsequently decreasing. This suggests a pressure-dependent trend, where methane production is influenced by the prevailing pressure conditions, with an optimal range for maximizing methane production.

3. **Effect of fat composition:** All three feeds exhibited an initial rise in methane production with increasing fat composition, followed by a decline after reaching an optimum point. Mesophilic feed showed a linear increase initially, while Thermophilic and Psychrophilic feeds demonstrated a sharp initial rise in methane production.

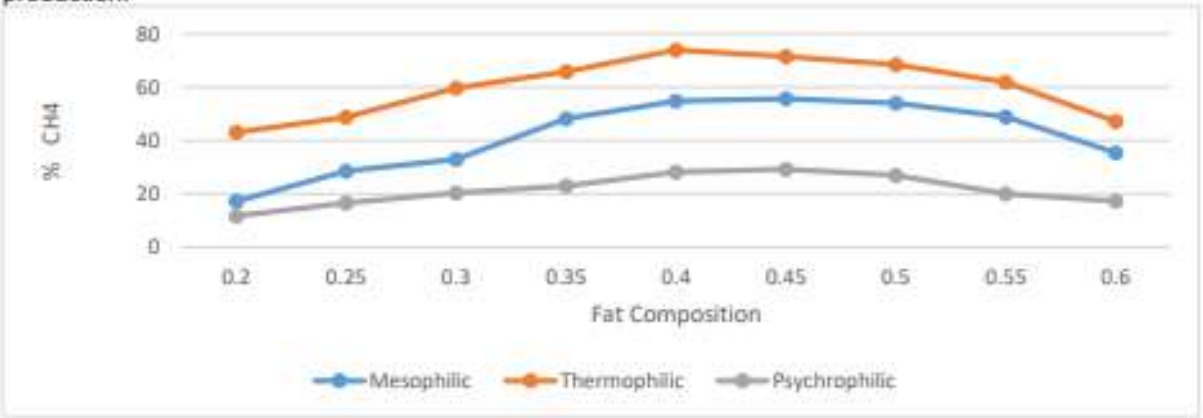

Figure 2. Effect of fat composition on all type of feed for natural gas production

4. **Effect of protein composition:** All three feeds demonstrated peak methane production at minimal protein levels. Increasing protein in the feed resulted in a gradual slowdown of methane production across Mesophilic, Thermophilic, and Psychrophilic feeds. In conclusion, high protein content in the feed is unfavorable for methane production.

5. **Effect of feed to water ratio:** Across all three feeds, the optimal Feed to Water ratio for maximum methane production was observed at 1:10 for Mesophilic and Thermophilic feeds and 1:12 for Psychrophilic feed. Mesophilic and Psychrophilic feeds exhibited a linear increase in methane production with an increasing Feed to Water ratio, while the Thermophilic feed maintained constant production up to a 1:10 ratio.

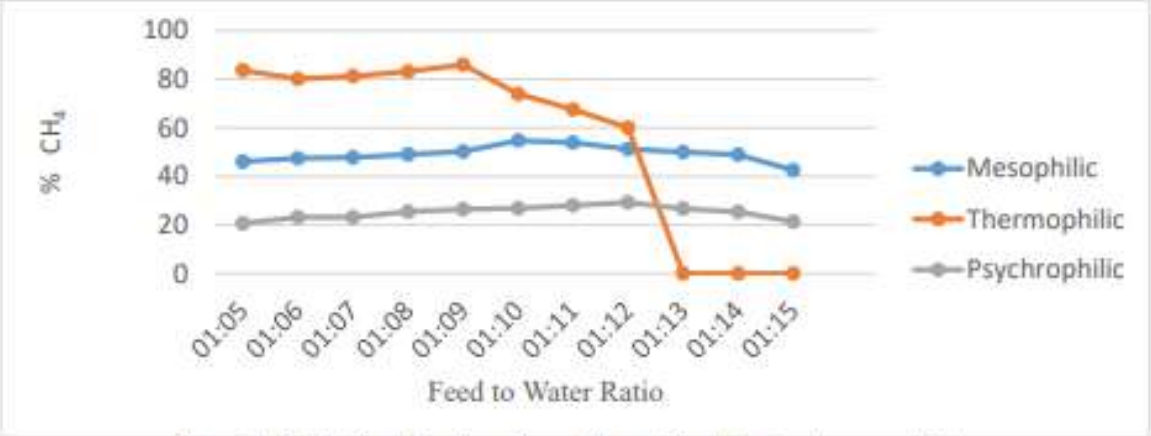

Figure 6. Effect of feed to water ratio on all type of feed for natural gas production

6. **Effect of Hydraulic retention time:** Across all three feeds, a consistent pattern was observed with a linear increase in methane production as the Hydraulic Retention Time (HRT) values increased. However, this upward trend eventually reached a point where further increases in HRT did not result in additional methane production, indicating a plateau or constant level of methane production at longer HRT values.

In a comparative analysis of the three feed types for natural gas production, it is observed that thermophilic food waste yielded the highest natural gas production, followed by mesophilic and psychrophilic food waste. This observation held true when all other variables, including temperature, pressure, HRT, etc., were kept constant. The optimum conditions were mentioned in the below table.

Table 1: Optimum condition for natural gas production for all types of feed

Type of Waste Food	Mesophilic	Thermophilic	Psychrophilic
Operating Temperature	35 ℃	50 ℃	18 ℃
Operating Pressure	0.7 atm	1 atm	2 atm
% CH_4	54.74	73.93	29.24
% CO_2	35.19	11.90	48.01

IV. Conclusions

Anaerobic digestion was simulated using Aspen Plus software, modeling the four sequential steps of the process. The hydrolysis step, based on the extent of the reaction, was represented by a stoichiometric reactor unit. The remaining three steps of anaerobic digestion were simulated using a kinetic reactor, specifically a Continuous Stirred Tank Reactor (CSTR). Raising the temperature and pressure enhanced natural gas production in mesophilic, thermophilic, and psychrophilic food waste. After reaching the peak, further temperature increase led to a decline in natural gas production. Notably, thermophilic food waste exhibited greater sensitivity to temperature changes compared to mesophilic and psychrophilic food waste. Increasing fat composition initially boosted natural gas production in all three feeds, but beyond a certain point, production declined. This decrease was attributed to the fact that the primary component of natural gas is formed through the breakdown of carbohydrates. Notably, at 4% protein content in all three feed types, natural gas production reached its maximum, and any further increase in protein percentage led to a decline in natural gas production. the optimal Feed to Water ratio for maximum natural gas production was observed at 1:10 for both mesophilic and thermophilic food waste, in line with literature data. For psychrophilic food waste, the maximum natural gas production was observed at a 1:12 Feed to Water ratio. Additionally, increasing the Hydraulic Retention Time (HRT) for all three feed types led to an increase in natural gas production. However, beyond a certain point, further increases in HRT resulted in constant natural gas production.

Acknowledgements

Authors thank the financial support given by ministry of education, INDIA and national institute of technology Warangal to carry out this study.

References

- Harun, N., Hassan, Z., Zainol, N., Ibrahim, W.H.W. and Hashim, H. (2019), Anaerobic Digestion Process of Food Waste for Biogas Production: A Simulation Approach. Chem. Eng. Technol., 42: 1834-1839.
- Rajendran K, Harshavardhan R. K.,, Magnus L, Mohammad J. T., (2014) A novel process simulation model (PSM) for anaerobic digestion using Aspen Plus, Bioresource Technology, 168, 7-13.
- Shi X.S., Dong J.J., Yu J.H., Yin H., Hu S.M., Huang S.X., Yuan X.Z.,(2017) Effect of Hydraulic Retention Time on Anaerobic Digestion of Wheat Straw in the Semicontinuous Continuous Stirred-Tank Reactors. Biomed Res Int.,2017:2457805.
- Yuanyuan R, Miao Y, Chuanfu W, Qunhui W, Ming G, Qiqi H, Yu L, (2018) A comprehensive review on food waste anaerobic digestion: Research updates and tendencies, Bioresource Technology, 247, 1069-1076.
- Zhang C, Gang X, Liyu P, Haijia S, Tianwei T, (2013) The anaerobic co-digestion of food waste and cattle manure, Bioresource Technology, 129, 170-176.

IEEES-148

Thermodynamic Analysis of Multi-Energy Integrated System Combining Geothermal, Green Hydrogen, and Cold Energy Storage

[1*]Onder Kizilkan, [1]Gamze Soyturk
[1]Isparta University of Applied Sciences, Faculty of Technology, Department of Mechanical Engineering, 32200, Isparta, Turkey

* E-mails: onderkizilkan@isparta.edu.tr

Abstract

This study presents a comprehensive performance assessment of an innovative integrated energy system that combines geothermal energy utilization for cooling, power generation, and freshwater production, along with incorporating a green hydrogen production subsystem. The synergy between these components offers a promising pathway toward sustainable energy solutions. The geothermal-based combined cooling, power generation, and freshwater system harnesses the Earth's heat to provide cooling and electricity generation, reducing the dependency on conventional fossil fuels. Furthermore, the freshwater generation aspect addresses the critical issue of water scarcity in arid regions. In addition to these benefits, integrating a green hydrogen production subsystem enhances the overall sustainability of the system. The hydrogen production subsystem utilizes excess energy to produce green hydrogen, which can be used as a clean fuel or stored for later use. This research evaluates the performance and efficiency of the overall system. Additionally, the effects of essential system parameters on system performance were examined by performing parametric analysis. The results of this study demonstrate the feasibility and benefits of applying geothermal-based combined systems with green hydrogen production, paving the way for a more sustainable and cleaner energy future.

Keywords: Geothermal energy, hydrogen, cold energy storage, energy, exergy.

I. Introduction

In the search for sustainable and efficient energy systems, the integration of multiple energy sources has emerged as a promising approach. One such innovative paradigm is multi-energy integrated systems that combine geothermal, green hydrogen, and cold energy storage (He, 2020). This comprehensive study aims to explore the synergies and interactions between geothermal energy, green hydrogen production, and cold energy storage within a unified framework. As global energy demands continue to increase and environmental concerns intensify, the need for cleaner, more resilient energy systems becomes imperative. With its low carbon footprint and consistent availability, geothermal energy offers a viable option for baseload energy production. Simultaneously, interest in green hydrogen as a clean fuel source as an alternative to traditional fossil fuels has also gained momentum. Integrating these resources with cold energy storage technologies can increase overall system efficiency and contribute to a more sustainable energy environment. This research aims to conduct a thermodynamic analysis to evaluate the performance and interactions of the integrated system. Combining geothermal, green hydrogen and cold energy storage technologies, this study attempts to determine optimum operating conditions and energy conversion efficiencies. The information gained from this analysis is expected to provide valuable guidance for the design and implementation of multi-energy integrated systems and contribute to the ongoing transition towards a more sustainable and resilient energy future.

II. System Description and Analysis

Fig.1 shows a schematic representation of a multi-integrated system combining geothermal, green hydrogen, and cold energy storage. The system includes geothermal energy as the primary source for energy production. The consistent and renewable nature of geothermal energy provides a reliable and continuous power supply, providing a stable foundation for the integrated system. Green hydrogen, produced through the electrolysis of water using electricity produced from renewable sources, plays a crucial role in the integrated system. Electrolyzers split water molecules into hydrogen and oxygen, producing a clean and sustainable hydrogen fuel. This hydrogen can be stored and used for a variety of applications such as power generation, transportation, and industrial processes; this contributes to the decarbonization of multiple sectors. Cold energy storage technologies are integrated to increase overall system efficiency. Using excess energy generated during periods of high availability, the system uses cold storage solutions such as cryogenic storage or advanced refrigeration methods. This stored cold energy can be used strategically during periods of peak demand or to increase the efficiency of specific processes, further optimizing the overall energy use of the integrated system.

In this subchapter, a detailed definition of the thermodynamic methodology utilized in this paper is introduced. First and second law analyses are conducted using the MATLAB software program for the performance evaluation of the arrangement. In this research, the thermodynamic analysis is made under the following assumptions:

- Steady-state and continuous-flow conditions have been selected for all components within the system.
- The alterations in potential and kinetic energy are not considered in the energy analysis.
- The thermal dissipation from the turbine and pumps is neglected.
- Pressure drops within the pipelines, and heat exchangers are not considered.
- The reference state properties are set at 20°C and 101.325 kPa.

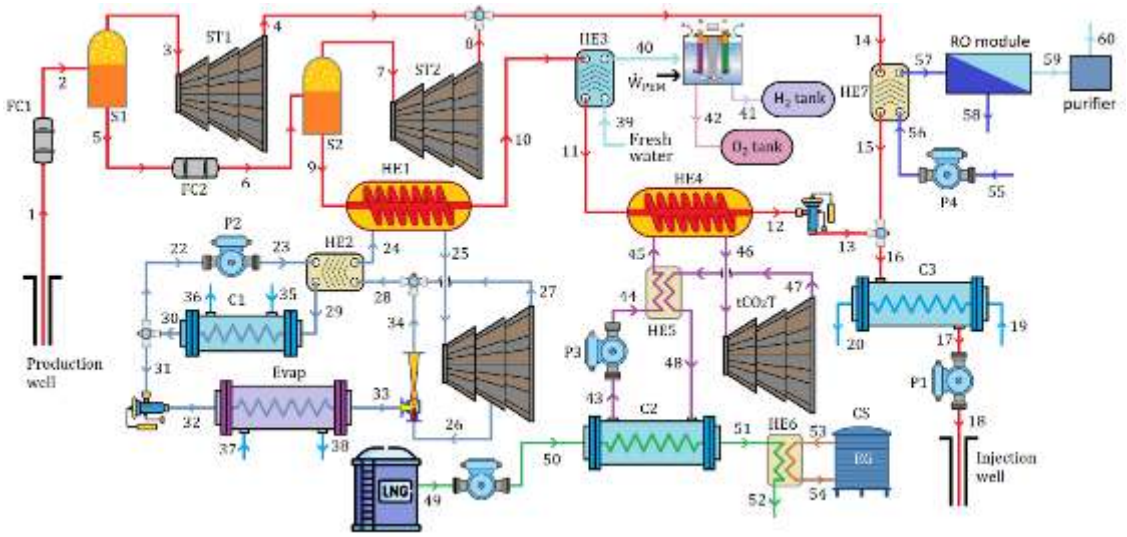

Fig. 1. Schematic representation of the integrated system with multi-outputs

The equation for mass balance in continuous, steady-state processes can be articulated in the following manner (Cengel, 2010):

$$\sum \dot{m}_{in} = \sum \dot{m}_{out} \quad (1)$$

Here, *ṁ* represents the mass flow, *in* signifies the inlet while *out* displays the outlet. The energy balance is articulated as follows:

$$\dot{Q} + \sum \dot{m}_{in} h_{in} = \dot{W} + \sum \dot{m}_{out} h_{out} \quad (2)$$

Within this mathematical expression, $\dot{Q}$ stands for the rate of heat transfer, $\dot{W}$ symbolizes the work, and *h* signifies the enthalpy. When conducting an exergy analysis, the equation for conservation is established as follows (Dincer and Rosen, 2013).

$$\dot{E}x_Q - \dot{E}x_W = \sum \dot{E}x_{in} - \sum \dot{E}x_{out} + T_0 \dot{S}_{gen} \quad (3)$$

where the initial and subsequent components pertain to the exergetic value of thermal energy and mechanical energy, respectively. *Ėx* denotes the exergy flow rate, T_0 represents the reference state temperature, and the final term corresponds to entropy generation. Within the provided equation, each term can be defined as follows:

$$\dot{E}x_{dest} = T_0 \dot{S}_{gen} \quad (4)$$

$$\dot{E}x_Q = \dot{Q}\left(\frac{T-T_0}{T}\right) \quad (5)$$

$$\dot{E}x_W = \dot{W} \quad (6)$$

$$\dot{E}x_W = \dot{m}\, ex \quad (7)$$

In Eq. (7), ex denotes the specific flow exergy and can be calculated through the subsequent equation:

$$ex = (h-h_0) - T_0(s-s_0) \quad (8)$$

For the modeling of the double flash geothermal power plant, the formulation was adapted from Toker et al. (2023), whereas for the hydrogen, the modeling of Soyturk et al. (2023), and for the combined cooling and power system, equations from Kizilkan and Khanmohammadi (2023) were used.

III. Results and discussion

In this study, a comprehensive performance evaluation of an innovative integrated energy system that combines geothermal energy utilization for cooling, power generation, and freshwater production, along with the incorporation of a green hydrogen production subsystem, is carried out. The analyses of the engineered system were conducted using MATLAB software. Fig.2 shows the integrated system's power generated, cooling capacity, and cold storage capacity. From the figure, the highest power production is in the steam turbine with 25128 kW.

Fig.3 shows the amount of hydrogen, oxygen, clean water, and ethylene glycol stored in the system. The figure shows the hydrogen flow rate is 2.3252 kg/h, and the oxygen flow rate is 13.368 kg/h. In addition, the flow rate of clean water produced in the system was 9.3152 m^3/h, and the flow rate of stored ethylene glycol was calculated as 4.7798 m^3/h.

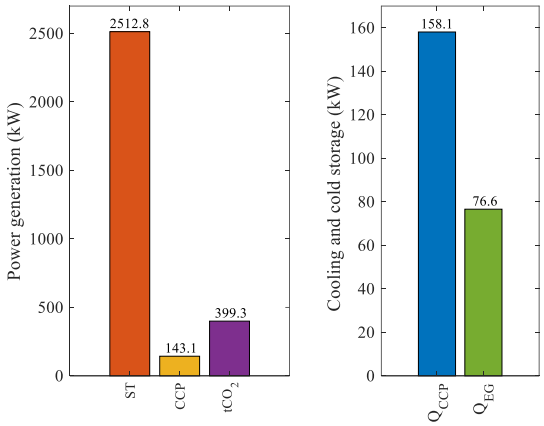

Fig. 2. Useful outputs of the integrated system

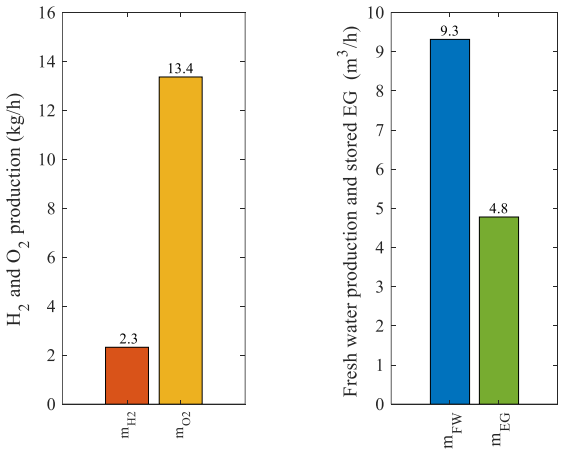

Fig. 3. The amount of hydrogen, oxygen, clean water produced, and EG stored in the integrated system

Parametric studies were carried out to examine the effects of some basic parameters on the system performance. Fig.4 shows the impact of geothermal water temperature on the net power and energy efficiency produced in the system. As seen in the figure, when the geothermal water temperature increases from 180°C to 250°C, the net power and energy efficiency produced in the system increases. This increase is due to higher geothermal water temperatures causing larger temperature differences and increasing the efficiency of the energy conversion process. Fig.5 shows the cooling, cold storage capacity, hydrogen, and freshwater production change with geothermal water temperature. As seen in the figure, as the geothermal water temperature increases, the cooling capacity remains almost constant while the coolant storage capacity decreases. In addition, it is seen that as the geothermal water temperature increases, the production of hydrogen and freshwater remains almost constant.

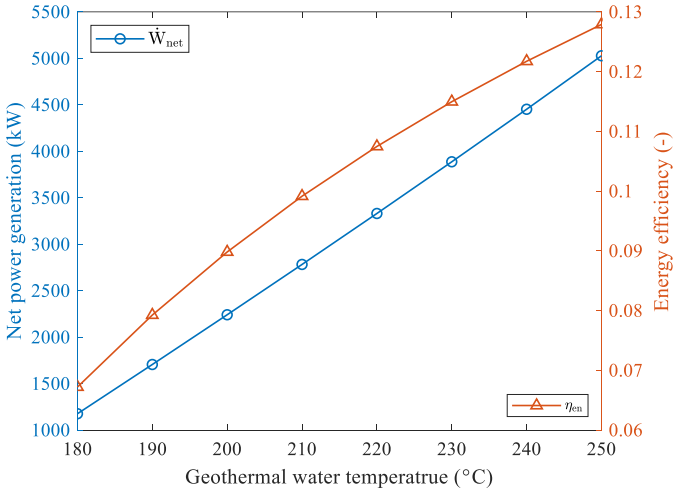

Fig. 4. Variation of net power production and energy efficiency with geothermal water temperature

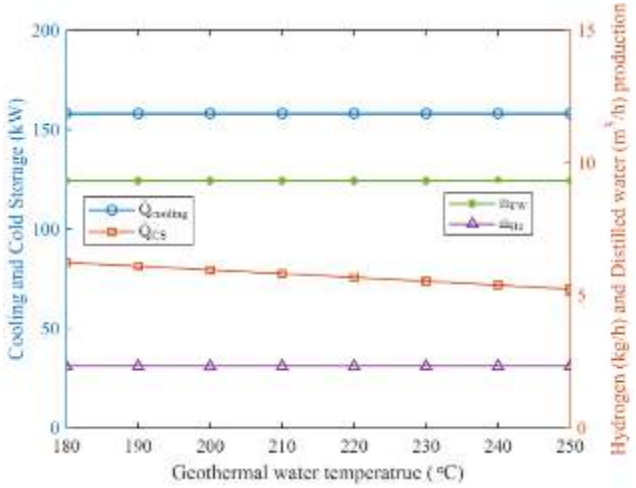

Fig. 5. Variation of cooling, cold storage capacity, hydrogen, and distilled water production with geothermal water temperature

IV. Conclusion

This research offers a thorough evaluation of the effectiveness of a novel integrated energy system. This system integrates geothermal energy for cooling, power generation, and freshwater production alongside the integration of a subsystem dedicated to green hydrogen production. According to the analysis results, the net power produced in the geothermal power plant was calculated as 2512.8 kW, and the net power produced in the combined cooling power plant was calculated as 143.07 kW. Additionally, the net power produced in the transcritical Rankine cycle turbine is 399.3 kW. In the integrated system, the hydrogen flow rate for production is 2.3252 kg/h, and the oxygen flow rate is 13.368 kg/h. In addition, the flow rate of clean water produced in the system was calculated as 9.3152 m^3/h, and the flow rate of stored ethylene glycol was calculated as 4.7798 m^3/h. According to calculations, the total energy efficiency of the system is 10.342%. Moreover, parametric studies were carried out to examine the effects of some basic parameters on the system performance. It has been observed that as geothermal water temperature increases, net power production and energy efficiency increase, while hydrogen and clean water production remain almost constant.

References

Cengel, YA., Boles, MA., (2010). Thermodynamics: An Engineering Approach.

Dincer, I., Rosen, M.A., (2013). Exergy: Energy, Environment and Sustainable Development, 2nd Ed. Oxford, UK: Elsevier; 576 p.

He, T., Lv, H., Shao, Z., Zhang, J., Xing, Xialian., Ma, H., (2020). Cascade utilization of LNG cold energy by integrating cryogenic energy storage, organic Rankine cycle and direct cooling, Applied Energy, 277, 115570. https://doi.org/10.1016/j.apenergy.2020.115570.

Kizilkan, O., Khanmohammadi, S., (2023). Design a novel solar based system integrated with humidification-dehumidification unit and re-compression sCO2 cycle for sustainable development. Journal of Cleaner Production, 407, 137117. https://doi.org/10.1016/j.jclepro.2023.137117

Li, M., Zhu, K., Lu, Y., Zhao, Q., Yin, K., (2023). Technical and economic analysis of multi-energy complementary systems for net-zero energy consumption combining wind, solar, hydrogen, geothermal, and storage energy. Energy Conversion and Management, 295, 117572. https://doi.org/10.1016/j.enconman.2023.117572

Soyturk, G., Kizilkan, O., Ezan, M.A., Colpan, C.O., (2023). PVT integrated hydrogen production with small-scale transcritical power cycle. Process Safety and Environmental Protection, 180, 351-360. https://doi.org/10.1016/j.psep.2023.10.017

Toker, S.C., Kizilkan, O., Nižetić, S., (2023). Design and evaluation of an innovative double-flash geothermal power plant combined with reheat tCO2 Rankine cycle, Kalina cycle, desalination, and H2 generation. 2023 8th International Conference on Smart and Sustainable Technologies (SpliTech), Split/Bol, Croatia, 2023, pp. 1-5, doi: 10.23919/SpliTech58164.2023.10192946.

IEEES-149

Conceptual Design and Analysis of a Solar Energy Based Multi-Generation System with Helium Gas Cycle, Green Ammonia and Hydrogen Production

[1*]Gamze Soyturk, [1]Onder Kizilkan
[1]Isparta University of Applied Sciences, Faculty of Technology, Department of Mechanical Engineering, 32200, Isparta, Turkey

* E-mails: gamzeyildirim@isparta.edu.tr

Abstract
This abstract introduces an approach to harnessing renewable energy sources for enhanced sustainability by combining a solar tower-based helium gas cycle with green ammonia and hydrogen production. The integration of these technologies represents a promising solution to address the world's growing energy needs while minimizing environmental impacts. The solar tower-based helium gas cycle is at the heart of this innovative system, utilizing concentrated solar power to generate high-temperature helium. The helium gas is subsequently directed into a closed cycle, driving turbines to produce electricity efficiently. This approach offers a sustainable and clean energy source, reducing the dependence on fossil fuels and mitigating greenhouse gas emissions. The system's uniqueness lies in its synergy with green ammonia and hydrogen production. Excess energy from the solar tower is diverted into chemical processes for green ammonia synthesis and water electrolysis to produce green hydrogen. Both ammonia and hydrogen serve as versatile energy carriers and feedstocks for various industrial applications, offering a sustainable alternative to traditional, carbon-intensive production methods. This paper highlights this integrated system's technical aspects and advantages, including the versatility of green ammonia and hydrogen as clean fuels and feedstocks. It also highlights the vital role of this technology in advancing sustainability goals and contributing to a more environmentally friendly energy environment. The solar tower-based helium gas cycle with green ammonia and hydrogen production offers a path to a more sustainable energy future. The system's efficient use of renewable resources, reduced environmental impact, and versatile green energy carriers position it as a promising solution to meet the world's energy demands while promoting environmental stewardship.

Keywords: Solar tower, helium gas cycle, hydrogen, ammonia, energy, exergy.

I. Introduction

In pursuing sustainable and environmentally friendly energy solutions, integrating solar energy into multi-generation systems has emerged as a promising avenue for meeting the increasing global demand for power, heat, and fuel. This undertaking involves harnessing the immense potential of solar radiation to drive a sophisticated energy conversion system that produces electricity and generates valuable commodities such as green ammonia and hydrogen (Tesio, 2021). This research delves into the conceptual design and analysis of a solar energy-based multi-generation system. Central to this system is incorporating a helium gas cycle, presenting a unique approach to enhance overall efficiency and performance. Helium, with its exceptional thermodynamic properties, plays a pivotal role in optimizing the energy conversion process, ensuring maximum utilization of solar resources. The inclusion of green ammonia and hydrogen production within the multi-generation framework adds a transformative dimension to the project. Green ammonia, synthesized using renewable energy sources, emerges as a versatile carrier of energy, contributing to the decarbonization of various sectors, including agriculture and transportation (Wang and Dai, 2016; Wang, 2022). Simultaneously, the production of hydrogen, a clean and efficient fuel, serves as a critical element in the transition towards a hydrogen economy (Dincer, 2011; Dincer and Acar, 2015). This research aims to comprehensively analyze the thermodynamic aspects of the proposed solar energy-based multi-generation system. By exploring the synergy between the helium gas cycle, green ammonia, and hydrogen production, the study seeks to contribute valuable insights into the development of sustainable energy solutions that align with the goals of mitigating climate change and ensuring a resilient and low-carbon energy future. As the world grapples with the challenges of transitioning to renewable energy, this research endeavors to provide a holistic understanding of a novel and integrated approach toward harnessing solar power for a cleaner and more sustainable tomorrow.

II. System Description

Fig.1 shows the schematic representation of a solar energy-based multiple-generation system with a helium gas cycle, green ammonia, and hydrogen production. The system includes high-efficiency solar concentrators to focus sunlight onto solar receivers. These concentrators include parabolic troughs, heliostats, or other advanced solar tracking technologies to maximize solar energy collection. A closed-loop helium gas loop is used to transfer heat from the solar receivers to a high-efficiency helium gas turbine (Yari and Mahmoudi, 2010). High-temperature helium heated by concentrated solar radiation drives the turbine to produce electricity. The system uses advanced materials and design optimization to achieve high thermal efficiency. Excess solar energy is used to produce green ammonia through the Haber-Bosch process. This environmentally friendly approach involves the synthesis of ammonia using nitrogen and hydrogen. The hydrogen required for this process is obtained from the electrolysis of water powered by excess electricity produced by solar concentrators. The system includes an electrolysis unit to produce hydrogen using excess electricity generated during periods of high solar radiation. This hydrogen can serve as a clean fuel for various applications, such as transportation, industrial processes, and energy storage.

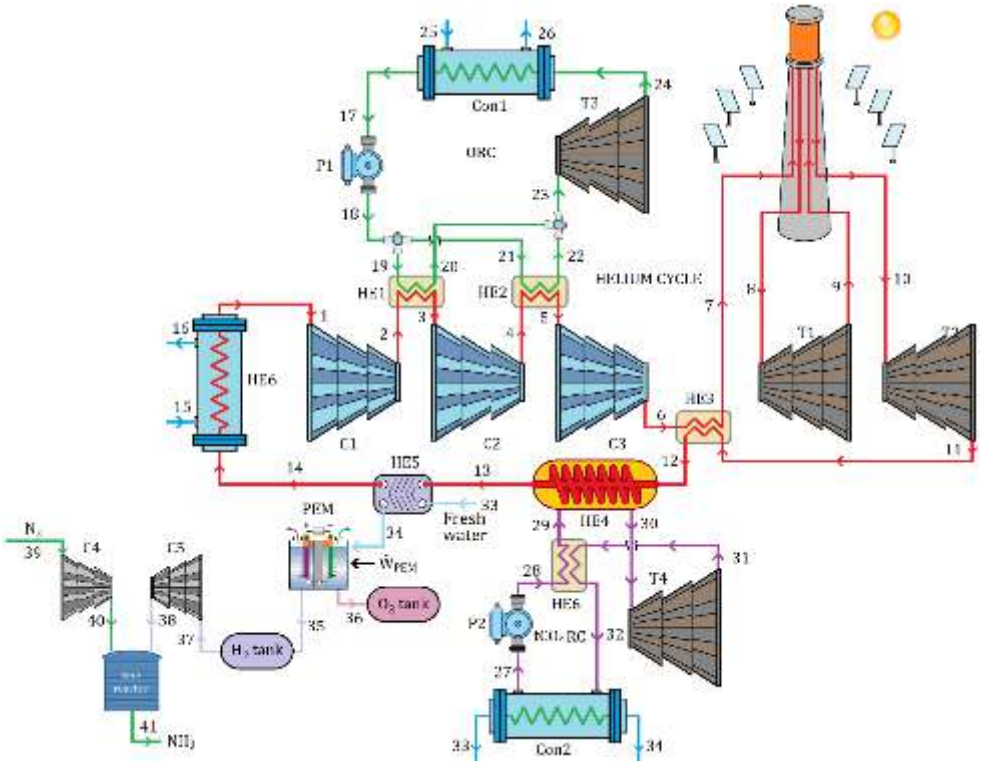

Fig. 1. Schematic illustration of the solar-based multi-generation system with green ammonia and hydrogen production

III. Analysis

Energy and exergy analyses are performed using the EES (Engineering Equation Solver) program for the performance evaluation of the system. In this paper, the thermodynamic analysis is made under the following assumptions:

- The steady-state and steady-flow conditions are chosen for all system elements.
- The energetic and exergetic changes for kinetic and potential energies are neglected.
- The heat losses from the pump and turbine are neglected.
- The pressure drops through the pipelines, and heat exchangers are neglected.

For the performance assessment of the solar-driven system, the first and second laws of thermodynamics and the principles of conservation of mass are applied to each system element. The mass and energy balance equations for steady-state and steady-flow processes are written as (Cengel and Boles, 2015):

$$\sum \dot{m}_{in} = \sum \dot{m}_{out} \tag{1}$$

Here, $\dot{m}$ is the mass flow rate and subscripts "*in*" and "*out*" are the input and output states. Energy balance equality in a general method is written as (Bejan and Moran, 1996):

$$\sum \dot{m}_{in}\left(h + \frac{v^2}{2} + gz\right)_{in} + \sum \dot{Q}_{in} + \sum \dot{W}_{in} = \sum \dot{m}_{out}\left(h + \frac{v^2}{2} + gz\right)_{out} + \sum \dot{Q}_{out} + \sum \dot{W}_{out} \tag{2}$$

Here, $\dot{Q}$ is the heat energy transfer rate, $\dot{W}$ is the power transfer rate, h is the specific enthalpy, v is the velocity, z is the elevation, and g is the gravitational acceleration. Entropy balance equality is given as:

$$\sum \dot{m}_{in} s_{in} + \sum \frac{\dot{Q}}{T} + \dot{S}_{gen} = \sum \dot{m}_{out} s_{out} \tag{3}$$

Here, s is the specific entropy, and $\dot{S}_{gen}$ stands for entropy generation rate. An exergy balance equality of any system can be described as (Dincer and Rosen, 2013):

$$\sum \dot{m}_{in}\dot{e}x_{flow} + \sum \dot{E}x^{Q}_{in} + \sum \dot{E}x^{W}_{in} = \sum \dot{m}_{out}\dot{e}x_{flow} + \sum \dot{E}x^{Q}_{out} + \sum \dot{E}x^{W}_{out} + \dot{E}x_{dest} \quad (4)$$

Where $\dot{e}x_{flow}$ is the flow exergy, $\dot{E}x^{Q}_{in}$ is the exergy associated with heat flow across the control volume of the process, $\dot{E}x^{W}_{in}$ is the exergy associated with work and $\dot{E}x_{dest}$ is the exergy destruction. In the above equation, each term is defined as follows:

$$\dot{e}x_{flow} = (h\text{-}h_0)\text{-}T_0(s\text{-}s_0) \quad (5)$$

$$\dot{E}x^{Q} = \dot{Q}\left(\frac{T\text{-}T_0}{T}\right) \quad (6)$$

$$\dot{E}x^{W} = \dot{W} \quad (7)$$

$$\dot{E}x_{dest} = T_0\dot{S}_{gen} \quad (8)$$

For the calculation of hydrogen and ammonia production, the references Yilmaz and Ozturk (2022) and Siddiqui and Dincer (2019) were used.

IV. Results and discussion

In this study, the thermodynamic performance of the solar energy-based multi-generation system with helium gas cycle, green ammonia, and hydrogen production is investigated. At the same time, parametric studies were carried out to examine the effects of solar radiation and helium cycle pressure ratio on cycle performance. Fig.2 shows the effect of solar radiation and the He cycle pressure ratio on the net power produced in the system and energy efficiency. As seen in the figure, as solar radiation increases, net power production and energy efficiency increase.

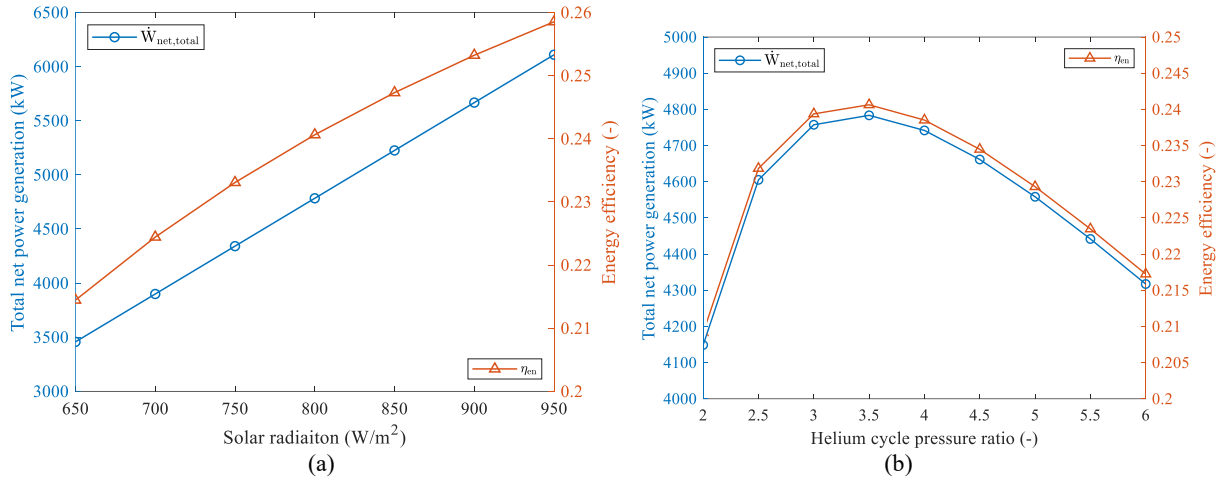

Fig. 2. Impact of (a) solar radiation and (b) He cycle pressure ratio on the total power generation and energy efficiency

Fig.3 shows the effect of solar radiation and the He cycle pressure ratio on the power produced in the helium cycle, the tCO_2 cycle, and the ORC cycle. As seen in the first figure, the power produced in the Helium cycle and tCO_2 cycle increases as it increases from 650 W/m^2 to 950 W/m^2. It is seen that the power produced in the ORC cycle remains almost constant as solar radiation increases. With the cycle pressure ratio, the power generation of the ORC cycle increases while others decrease. Fig.4 shows the effect of solar radiation and the He cycle pressure ratio on hydrogen and ammonia production. As seen in the figure, hydrogen production increases from 0.55 kg/h to 0.64 kg/h as solar radiation increases from 650 W/m^2 to 950 W/m^2. Likewise, ammonia production increases from approximately 3.1 kg/h to 3.55 kg/h.

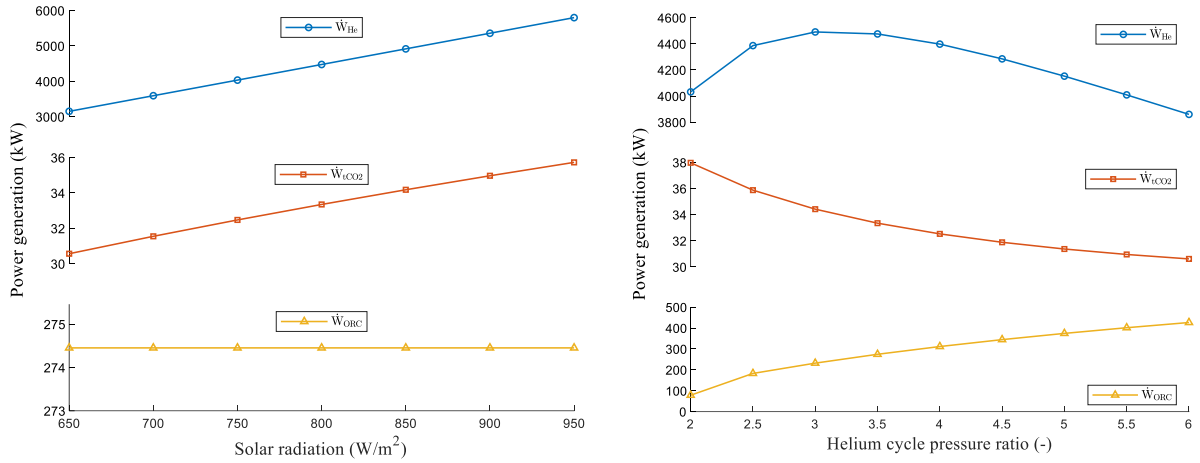

(a) (b)

Fig. 3. Impact of (a) solar radiation and (b) He cycle pressure ratio on the power generation of subcycles

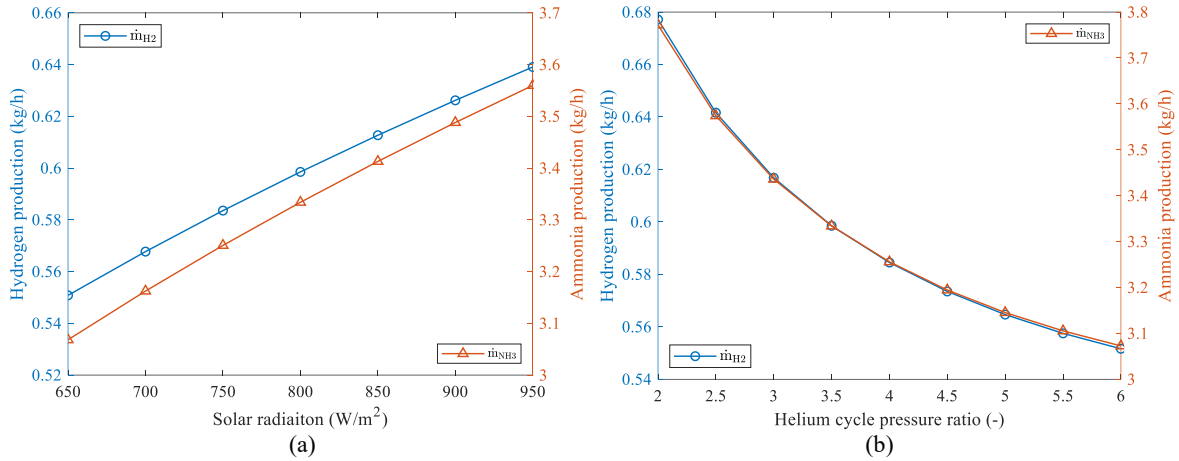

(a) (b)

Fig. 4. Impact of (a) solar radiation and (b) He cycle pressure ratio on the hydrogen and ammonia production

V. Conclusion

In this study, the conceptual design and analysis of the helium gas cycle, green ammonia and hydrogen production, and solar energy-based multiple-generation systems were carried out. Energy and exergy analyses were carried out using the EES software program to evaluate the system's performance. At the same time, parametric studies were carried out to examine the effects of solar radiation and helium cycle pressure ratio on system performance. According to the analysis results, the system's overall energy efficiency was calculated to be 24.06%, and the net power produced in the system was calculated to be 4783.6 kW. Additionally, the amounts of hydrogen and ammonia produced are 0.59853 kg/h and 3.3339 kg/h, respectively. According to the parametric analysis results, it was concluded that as solar radiation increases, net power production and energy efficiency increase.

References

Bejan, A., Moran, M.J., (1996). Thermal Design and Optimization, New York: John Wiley & Sons.

Cengel, Y.A., Boles, M.A., (2015). Thermodynamics: An Engineering Approach 8th Edition.

Dincer, I., Rosen, M.A., (2013). Exergy: Energy, Environment and Sustainable Development.

Dincer, I., Acar, C., (2015). A review on clean energy solutions for better sustainability. International Journal of Energy Research, 39, 585–606. https://doi.org/10.1002/er.

Dincer, I., (2011). Green methods for hydrogen production. Int J Hydrogen Energy, 37, 1954–71. https://doi.org/10.1016/j.ijhydene.2011.03.173.

Siddiqui, O., Dincer, I., (2019). Design and analysis of a novel solar-wind based integrated energy system utilizing ammonia for energy storage. Energy Conversion and Management, 195, 2019, 866-884. https://doi.org/10.1016/j.enconman.2019.05.001

Tesio, U., Guelpa, E., Verda, V., (2021). Multi-objective optimization of helium power cycle for thermo-chemical energy storage in concentrated solar power. Energy Conversion and Management. 12, 100116. https://doi.org/10.1016/j.ecmx.2021.100116

Yari, M., Mahmoudi, S.M.S., (2010).Utilization of waste heat from GT-MHR for power generation in organic Rankine cycles. Applied Thermal Engineering, 30(4), 366-375. https://doi.org/10.1016/j.applthermaleng.2009.09.017

Yilmaz, F., Ozturk, M., (2022). Design and modeling of an integrated combined plant with SOFC for hydrogen and ammonia generation. International Journal of Hydrogen Energy, 47(74), 31911-31926. https://doi.org/10.1016/j.ijhydene.2022.01.249

Wang Q. Thermodynamic analysis and optimization of the combined supercritical carbon dioxide Brayton cycle and organic Rankine cycle-based nuclear hydrogen production system 2022:832–59. https://doi.org/10.1002/er.7208.

Wang, X., Dai, Y., (2016). An exergoeconomic assessment of waste heat recovery from a Gas Turbine-Modular Helium Reactor using two transcritical CO 2 cycles. Energy Convers Management, 126, 561–72. https://doi.org/10.1016/j.enconman.2016.08.049.

IEEES-150

Performance Assessment of Power and Synthetic Methane Production from Geothermal Energy

[1,2*]Dogukan Suleyman Mızrak, [3]Yagmur Nalbant Atak, [4,5]Anil Erdogan, [5]C. Ozgur Colpan
[1] Dokuz Eylul University, The Graduate School of Natural and Applied Sciences, Izmir, Türkiye
[2] Vestel Home Appliances, R&D Department of Refrigerator Factory, Manisa, Türkiye
[3] Atılım University, Faculty of Engineering, Department of Mechanical Engineering, Ankara, Türkiye
[4] Vestel Home Appliances, Technology Development Department, Manisa, Türkiye
[5] Dokuz Eylul University, Faculty of Engineering, Department of Mechanical Engineering, Izmir, Türkiye

*Corresponding Author: dogukanmizrak4@gmail.com

Abstract

In this study, a synthetic methane production system integrated into a geothermal power plant is presented. The process of capturing and converting CO_2, found in the non-condensable gas stream in a geothermal power plant, into synthetic methane gas is thermodynamically analyzed. For this purpose, it is considered that all the CO_2 captured is reacted with hydrogen in a Sabatier reactor where the methanation reaction occurs. Considering the chemical equilibrium for this reaction, the amount of methane produced is found. For the amount of hydrogen needed in this reaction, the power requirement for the electrolyzer required in the system is determined. The effect of the working fluid type of the organic Rankine cycle, the operating temperature of the Sabatier reactor, and the capacity factor of the PEM electrolyzer on the amount of methane obtained and the thermal efficiency of the integrated power and methane production system are assessed. The results show that R290 gives the highest thermodynamic performance among the other working fluids studied.

Keywords: Geothermal Power Plant, Synthetic Fuel, Electrolysis, Sabatier Reactor

I. INTRODUCTION

The continuous growth of the world's population and economy has led to a parallel increase in the energy requirements. As a result of this increase, air pollution and greenhouse gases have increased, the quality of life of living beings has been affected and the effects of climate change have increased significantly. Obtaining the energy needed by humanity in a renewable, sustainable, low-carbon emission, and clean way has gained great importance (Guo et al., 2023; Bertani, 2016). According to the International Energy Agency (IEA), global energy demand is expected to increase by 2.4% (approx. 29.2 trillion BOE) in 2023 compared to the previous year (IEA, 2023). Electricity generated from geothermal resources has become an important alternative to the increasing energy demand due to its renewable and low carbon emission. As proof of this, especially in the 5 years between 2018 and 2023, there has been an increase of 2.7 GW of installed capacity, which corresponds to 17% in energy from geothermal resources worldwide (IRENA, 2023). Although geothermal power plants are known as renewable and clean energy sources, they also have some challenges due to geological and climatic reasons. Geothermal fluid contains non-condensable gases such as CO_2, H_2S, NH_3, and CH_4, and some of these gases, especially CO_2 and H_2S, can cause environmental problems as a result of their release into the atmosphere (Yousefi et al., 2010). A large-scale study by Bartani et al. (2002) revealed that 112 kg of CO_2 is produced for every 1 MWh of energy production from geothermal energy. With the emergence of such a high amount of CO_2 gas from geothermal energy production sites, studies have started to be carried out to capture CO_2 gas, to use it for different resources, or to re-inject it (Guo et al, 2023). In geothermal power plants, non-condensable gases are present in the geothermal brine coming from the reservoir at an average rate of 3%, depending on the region (Guo et al, 2023). Reinjecting NCG gases in geothermal power plants not only supports the operation of these plants with zero emissions but also supports the formation of steam by supporting the refilling and pressurization of the reservoir together (Kaya et al., 2018). Kaya and Zarrouk (2017) showed that the presence of CO_2 in the reservoir, which contains 95% of the reinjected NCG gas content, reduces the flash-point pressure in the geothermal fluid mixture, promotes boiling and increases the enthalpy of the fluid entering the geothermal system.

Hydrogen is the most common and simplest element in our world and has a high energy content (Zhang et al., 2016). Hydrogen is clean, efficient, reliable, and offers significant social benefits with the potential to provide cost-effective solutions in the future (Kalinci et al., 2015). From the past to the present, researchers have increasingly focused on hydrogen and considered hydrogen as the world's future energy carrier (Yuksel et al., 2018a; Acar and Dincer, 2019). Among renewable energy sources, geothermal energy has a great potential for hydrogen production. The electrical energy and geothermal heat obtained from geothermal power plants can be used in the process of producing hydrogen by electrolyzing water (Yılmaz and Kanoglu, 2014). Nowadays, Proton Exchange Membrane (PEM) electrolyzers are widely used in the electrolysis of water. Yuksel et al. (2018b) showed that the exergy efficiency of the system increases from 38% to 64% as the temperature of the geothermal fluid increases from 130 degrees to 180 degrees. In addition, the production efficiency of hydrogen increases from 39% to 44% by increasing the temperature of the PEM electrolyzer from 60 degrees to 85 degrees. In addition to obtaining hydrogen gas by using the electrical energy and geothermal heat obtained from the geothermal power plant, capturing the CO_2 in the geothermal fluid and reacting it with the produced hydrogen gas emerges as a way to obtain synthetic fuel. In

this process, the Sabatier reaction discovered by French chemist Paul Sabatier in 1910 is important because it is the simplest way to convert hydrogen and CO_2 gases into methane gas with high efficiency and selectivity (Moioli et al., 2019). The aforementioned Sabatier equation is shown in Eq. (1). Although it is preferable to carry out the Sabatier reaction at low temperatures, the use of a catalyst is necessary due to kinetic limitations. Gao et al. (2012) showed that CH_4 selectivity and production efficiency decrease when the reaction temperature is higher than 400°C. In addition, the efficiency of CH_4 production increased when the reaction pressure was increased from 1 atm to 30 atm, but significant yield increases could not be obtained at higher pressures.

$$CO_2 + 4H_2 \leftrightarrow CH_4 + 2H_2O \quad (1)$$

The literature review discussed shows that there are multiple factors in the conversion of hydrogen obtained from electrolyzers integrated into geothermal power generation plants and CO_2 separated from the geothermal fluid into CH_4, a synthetic fuel. In this study, the amount of CO_2 to be obtained from the geothermal system for a certain electrolyzer power is determined. The effects of some important parameters (organic fluid type, operating temperature of Sabatier reactor, and the capacity factor of PEM electrolyzer) on the energy efficiency of the integrated system areanalyzed.

II. Mathematical Modeling

The schematic of the integrated system providing power and synthetic methane production from geothermal energy is given in Fig.1. This system includes an organic Rankine cycle, a carbon dioxide capture system, a PEM electrolyzer for hydrogen production, and a Sabatier reactor for the synthetic methane production. The geothermal fluid extracted from the production well (State a), first enters the CO_2 capture system to separate CO_2 (State 9), after that the rest of the geothermal fluid (State a1) goes to the heat exchanger group, and finally, the rest fluid heats the working fluid in the ORC system. The working fluid in ORC enters the turbine to produce power (State 1), then it is sent to the regenerator (State 2), air-cooled condenser (State 3), pump (State 4), the regenerator again (State 5), and the heat exchanger group (State 6) to complete the cycle. On the other side, geothermal fluid without CO_2 leaving the heat exchanger group is sent to the mixer to return to the reinjection well. A part of separated CO_2 (State 9a) enters the CO_2 compressor to combine with hydrogen (State 17) coming from the H_2 compressor and produced from the PEM electrolyzer; whereas the other part of CO_2 (State 21) is sent to the Brayton cycle to increase the pressure for mixing the rest of geothermal fluid that enters to the reinjection well. H_2 and CO_2 (State 18) are sent to the Sabatier reactor to produce synthetic methane in the presence of a catalyst, and the synthetic methane (State 19) is produced. In addition, the required heat for water used in the electrolyzer (State14) is provided from the heat of synthetic methane using a heat exchanger. Table 1 shows the operating parameters for the integrated system.

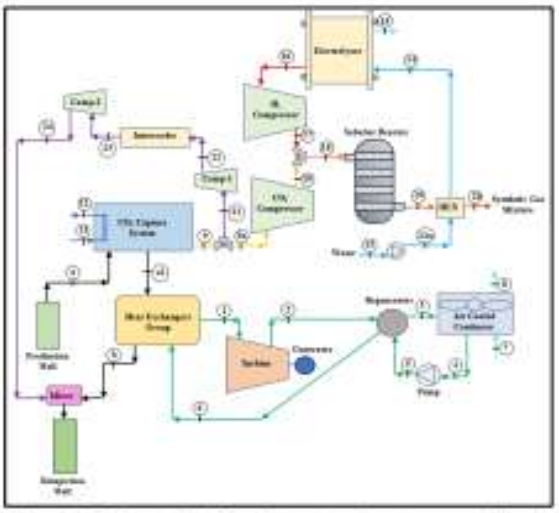

Fig. 1: Schematic of the integrated system providing power and synthetic methane production from geothermal

Table 1. Operating parameters used in the mathematical modeling.

Parameter	Value	Parameter	Value
Geothermal powered ORC		**Heat exchanger group**	
Inlet temperature of geothermal fluid	160.6 °C	Type of HEX	Shell and tube
Inlet pressure of geothermal fluid	780 kPa	Number of passes and tubes	1 pass and 4000 tubes
Mass flow rate of geothermal fluid	120.7 kg/s	Overall heat transfer coefficient	1 kW/m^{2}K
Type of working fluid in ORC	R134a	**Sabatier Reactor**	
Mass flow rate of working fluid	213.4 kg/s	Operating temperature	200°C
PEM Electrolyzer		Operating pressure	635 kPa
Operating temperature	60°C	Catalyst type	Nickel-based catalyst

In this study, a detailed mathematical model is formed for the integrated system providing power and the synthetic methane production from the geothermal energy. In this regard, thermodynamic balances (mass and energy balances) are applied for all components in this system. The modeling approach and equations used are given as follows. These equations were solved using the EES program. The general form of an open system mass and energy balance equations enclosing the control volume of each component under the steady-state conditions are given in Eqs. (2) and (3), respectively (Moran et al., 2010).

$$0 = \sum \dot{m}_i - \sum \dot{m}_e \quad (2)$$

$$0 = \dot{Q}_{cv} - \dot{W}_{cv} + \sum \dot{m}_i \cdot h_i - \sum \dot{m}_e \cdot h_e \quad (3)$$

where $\dot{Q}_{cv}$ is rate of heat transfer between the component and the environment, $\dot{W}_{cv}$ is the power, $\dot{m}_i$ and $\dot{m}_e$ are the mass flow rates of inlet and exit streams.

In recent years, research has been conducted on technologies for the production of synthetic fuels from carbon dioxide to reduce emissions. One of these technologies is the reaction of hydrogen and carbon dioxide to methane and water in a reactor using a catalyst. This reaction is called the Sabatier reaction (Eq. (1)). The methane produced by this reaction can be used as a fuel or liquefied and stored as LNG. This will partially solve the problem of carbon dioxide storage. The equilibrium constant for Sabatier reaction is calculated using Eq. (4).

$$K_{sab} = exp\left(\frac{-\Delta \bar{g}}{\bar{R}\,T}\right) = \frac{x_{CH_4,out}\cdot\left(x_{H_2O,out}\right)^2}{x_{CO_2,out}\cdot\left(x_{H_2,out}\right)^4}\cdot\left(\frac{P_{subatier}}{P_{ref}}\right)^{-2} \quad (4)$$

where, $\Delta \bar{g}$ is the change in Gibbs free energy, $\bar{R}$ is the universal gas constant, T is the operating temperature of the reactor, x is the molar fraction of each species exiting the reactor. After solving the above equation iteratively, the molar flow rates of each species can be found according to the reaction rates.

III. Results and discussion

In this section, the results and discussion for the integrated system are presented. Table 2 shows the state properties of the integrated system.

Table 2. Thermophysical properties of the integrated system

State Number	Fluid Name	Pressure (kPa)	Temperature (K)	Specific Enthalpy (kJ/kg)	Specific Entropy (kJ/kg·K)
1	R134a	4370	422.9	356.5	1.058
2	R134a	947	363	325.1	1.080
3	R134a	947	346.2	307.8	1.031
4	R134a	947	310.5	104.3	0.3825
5	R134a	4370	313.2	108	0.3849
6	R134a	4370	325	125.3	0.4391
7	Air	624.8	433.6	677.6	1.947
8	Air	624.8	337.3	268.9	0.8823
9	Carbondioxide	624.8	433.6	-8818	4.85
10	Carbondioxide	634.8	473.2	-8779	4.933
11	Water	100	298.2	104.8	0.367
12	Water	100	338.2	272.1	0.8935
13	Water	100	298.2	104.8	0.3669
14	Water	110	333.2	251.2	0.8311
15	Oxygen	110	333.2	32.15	6.488
16	Hydrogen	110	333.2	503.2	66.02
17	Hydrogen	634.8	473.2	2524	63.86
18	Mixture	634.8	473.2	-7029	14.06
19	Mixture	634.8	473.2	-10337	10.92
20	Syngas Mixture	634.8	378.7	-10539	10.45
21	Carbondioxide	624.8	433.6	-8818	4.85
22	Carbondioxide	1936	553.8	-8696	4.883
23	Carbondioxide	1936	473.8	-8778	4.723
24	Carbondioxide	6000	601.2	-8646	4.757

The fluid selection for ORC systems involves choosing the most frequently used, innovative, and ecologically friendly fluids outlined in the literature. The following refrigerants were chosen: R134a, R124, R142b, Isobutane, R227ea, R1234yf, R290, and R1234ze. The effect of ORC working fluid type on the energy efficiency and the net power output of the integrated system is presented in Fig. 2. The results illustrate that when R290 is utilized as the ORC working fluid, it attains the highest net power output and energy efficiency among the other working fluids that were examined.

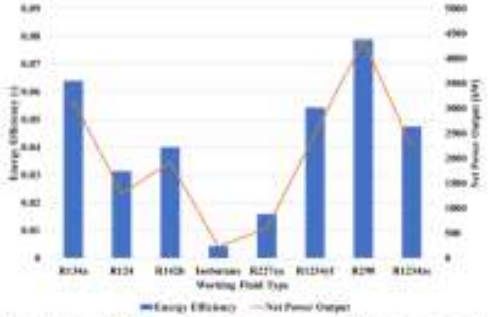

Fig. 2. The effect of different ORC working fluids on the energy efficiency and net power output of the integrated system

Fig. 3(a) demonstrates the effect of Sabatier reactor temperature on the molar fraction of the species. As the temperature increases, the molar fraction of methane and water in the mixture decreases. On the other hand, the molar fractions of hydrogen and carbon dioxide decrease with an increase in the temperature. It was found that the

Sabatier reactor, which operates at a higher temperature, reduces the yield of methane production. Fig. 3(b) illustrates the effect of PEM electrolyzer load on the mass flow rate of hydrogen and methane. When the load capacity of PEME increases by 0% to 200%, there is a significant decrease in the mass flow rate of both hydrogen and methane production.

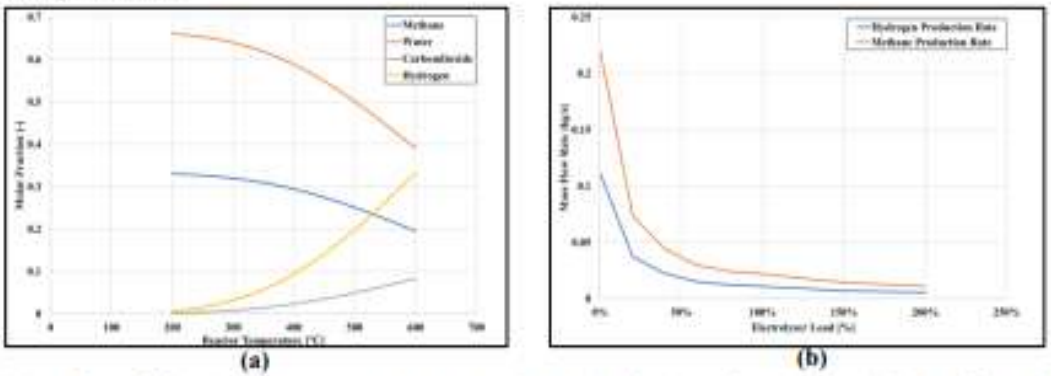

Fig. 3. (a) the effect of Sabatier reactor temperature on the molar fraction of species and (b) the effect of PEME load capacity on the hydrogen and methane production rates

IV. Conclusion

In this study, a comprehensive mathematical model is formed for the integrated system that generates both power and synthetic methane from geothermal energy. To achieve this, thermodynamic balance equations including mass and energy balances, are applied to all components within the system. The modeling equations used in the integrated system are solved utilizing EES software. The main results derived from the study conducted are given as follows.

- Among the other investigated working fluids, R290 exhibits the highest energy efficiency and net power output.
- As the reactor temperature increases, the molar fraction of water and methane decreases. In contrast, the molar fraction of carbon dioxide and hydrogen increases.
- Methane and hydrogen production decreases with an increase in electrolyzer load capacity.

References

Acar, C., & Dincer, I. (2019). Review and evaluation of hydrogen production options for better environment. Journal of cleaner production, 218, 835-849.

Bertani, R. (2016). Geothermal power generation in the world 2010–2014 update report. Geothermics, 60, 31-43.

Bertani, R., & Thain, I. (2002). Geothermal power generating plant CO2 emission survey. IGA news, 49, 1-3.

Gao, J., Wang, Y., Ping, Y., Hu, D., Xu, G., Gu, F., & Su, F. (2012). A thermodynamic analysis of methanation reactions of carbon oxides for the production of synthetic natural gas. RSC advances, 2(6), 2358-2368.

Guo, P., Kumar, N. B., Elmasry, Y., Alanazi, A., Alanazi, T. I., Armghan, A., ... & Wae-hayee, M. (2023). CO2 hydrogenation for geothermal energy storage through synthetic natural gas production and byproduct of refrigeration and freshwater using solid oxide electrolyzer cell (SOEC) and methanation reactor; Techno-economic evaluation and multi-objective optimization. Journal of CO2 Utilization, 69, 102395.

IEA (2023), World Energy Outlook 2023, IEA, Paris, France.

IRENA (2023), Energy Transition Outlook 2023.

Kalinci, Y., Hepbasli, A., & Dincer, I. (2015). Techno-economic analysis of a stand-alone hybrid renewable energy system with hydrogen production and storage options. International Journal of Hydrogen Energy, 40(24), 7652-7664.

Kaya, E., & Zarrouk, S. J. (2017). Reinjection of greenhouse gases into geothermal reservoirs. International Journal of Greenhouse Gas Control, 67, 111-129.

Kaya, E., Callos, V., & Mannington, W. (2018). CO2–water mixture reinjection into two-phase liquid dominated geothermal reservoirs. Renewable Energy, 126, 652-667.

Moioli, E., Mutschler, R., & Züttel, A. (2019). Renewable energy storage via CO2 and H2 conversion to methane and methanol: assessment for small scale applications. Renewable and Sustainable Energy Reviews, 107, 497-506.

Moran, M. J., Shapiro, H. N., Boettner, D. D., & Bailey, M. B. (2010). *Fundamentals of Engineering Thermodynamics*. John Wiley & Sons, Ltd.

Yilmaz, C., & Kanoglu, M. (2014). Thermodynamic evaluation of geothermal energy powered hydrogen production by PEM water electrolysis. Energy, 69, 592-602.

Yousefi, H., Ehara, S., Yousefi, A., & Seiedi, F. (2010). Rapid Environmental Impact Assessment of Sabalan Geothermal Power Plant, NW Iran. In World Geothermal Congress, Bali, Indonesia.

Yuksel, Y. E., Ozturk, M., & Dincer, I. (2018a). Thermodynamic analysis and assessment of a novel integrated geothermal energy-based system for hydrogen production and storage. International Journal of Hydrogen Energy, 43(9), 4233-4243.

Yuksel, Y. E., Ozturk, M., & Dincer, I. (2018b). Analysis and performance assessment of a combined geothermal power-based hydrogen production and liquefaction system. International Journal of Hydrogen Energy, 43(22), 10268-10280.

Zhang, F., Zhao, P., Niu, M., & Maddy, J. (2016). The survey of key technologies in hydrogen energy storage. International journal of hydrogen energy, 41(33), 14535-14552.

IEEES-151

An Investigation of Heat Transfer in the Heat Exchanger of a Condenser Tumble Dryer

[1] Vasıf Can YILDIRAN, [1] Hasan Güneş
[1]İstanbul Technical University, Department of Mechanical Engineering, İstanbul, 34437, Türkiye

* E-mails: yildiranv@itu.edu.tr, guneshasa@itu.edu.tr

Abstract
In this study, the focus has been on the tumble dryer among the white goods product group. Electric tumble dryers primarily come in three different types; vented, condenser, and heat pump dryers. Within the scope of this study, heat transfer in the region named condenser, which serves as the heat exchanger of a condenser dryer, has been investigated. The efficiency of heat transfer in the condenser directly influences the condensation capability which affects the drying and energy performance of the machine directly. Both numerical and experimental methods have been employed to examine the heat transfer in the condenser. The drying and cooling cycles of the condenser dryer have been modeled according to specific assumptions. The grid design causing pressure loss in the cooling cycle has been altered to increase the spaces through which air can pass. With this modification, the mass flow rate of cooling air has increased by approximately 9 %. Along with the increase in mass flow rate, the temperature difference of the drying air in the condenser has been raised from 5.1 °C to 7.1 °C according to CFD results. This corresponds to an improvement of approximately 40 % in temperature difference.

Keywords: Tumble Dryer, Computational Fluid Dynamics, Conjugate Heat Transfer

I. Introduction

In the context of this study, the condenser product under investigation has a condenser with two different air cycles, where heat transfer occurs between these two air streams. One of these cycles is related to the drying air. The drying air cycle is a closed system; the air, heated in the heater to increase its moisture absorption capacity, is directed into the drum with the help of a fan. The air that removes the moisture from the laundry is then directed to the channels of the condenser. The drying air, whose temperature decreases in the channels of the condenser, leaves moisture in the condenser channels. The other cycle is related to the cooling air. The cooling air is drawn into the system from the ambient environment with the help of a fan. Subsequently, the air separated from the fan is directed to the condenser fins through diffusers. The cooling air passing through the fins of the condenser, where the heat of the drying air is given, absorbs the heat of the condenser, and the drying air is cooled. Both cycles continue until the drying cycle is complete.

With the increasing daily energy consumption, the importance of system efficiency is growing. Like other white goods products, the energy consumption of clothes dryers is at a noticeable level (To et al., 2007). The most crucial outputs of tumble dryers are energy consumption, drying rate, and water collection rate. Among these outputs, customers pay the most attention to energy consumption when purchasing a clothes dryer (Stawreberg and Wikström, 2011). Although heat pump dryers are the most efficient products in terms of energy consumption, condenser dryers still maintain their place in the market.

Within the scope of this study, the heat transfer and fluid dynamics in the heat exchanger region directly influencing the drying system of the condenser dryer have been investigated. Increasing heat transfer enhances drying performance, and improved drying performance directly affects energy consumption. Both numerical and experimental methods have been employed in this study.

II. Methodology

This study initially commenced with energy performance tests conducted in the laboratory. The machine was tested at the Haier Europe Energy Performance Laboratory according to EN 60456 and IEC 61121 standards. Based on the results of these tests, the machine's energy consumption, drying performance, and water collection rate were determined. Data such as temperature and air flow rate of cooling and drying air, to be used in the numerical analysis, were also measured in laboratory tests. The flow rates of the drying and cooling air in the machine were measured with an anemometer. Temperatures from significant areas on the machine were collected throughout the entire drying cycle via thermocouples.

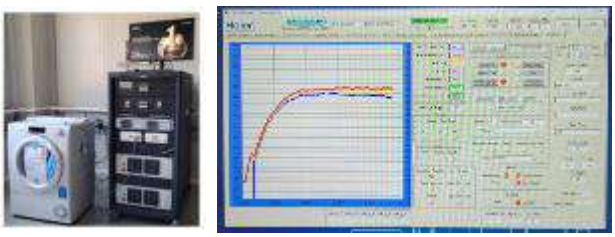

Fig. 1: Test Corner of Energy Performance Laboratory and DAQ Screen of Measurements

Anemometer and some specialized equipment are used for measuring the flow rates of cooling air and drying air.

Fig. 2: Anemometer and Flowmeter Devices

To understand the temperature variations during the drying cycle thermocouples were placed at the condenser inlet and outlet for the cooling air, and at the inlet, outlet, and heater exit for the drying air.

Fig. 3: Thermocouple Positions of Cooling Air Condenser Inlet and Outlet

Fig. 4: Thermocouple Positions of Drying Air Condenser Inlet, Outlet and Heater Outlet

The creation of the numerical model involves four stages. Firstly, the fluid volumes of the model to be worked on were extracted using SpaceClaim software. Subsequently, a mesh was generated for the fluid volumes using Fluent Mesh software. After the mesh was created, the Ansys Fluent software was employed as the solver. Once the solution was completed, the results were examined using Ansys Fluent (ANSYS User Guide).
In this study, before creating the CFD model of the condenser dryer, the CAD model of the machine was examined. The upcoming CFD model includes the condenser, where the cooling air and drying air perform heat transfer without mixing with each other.

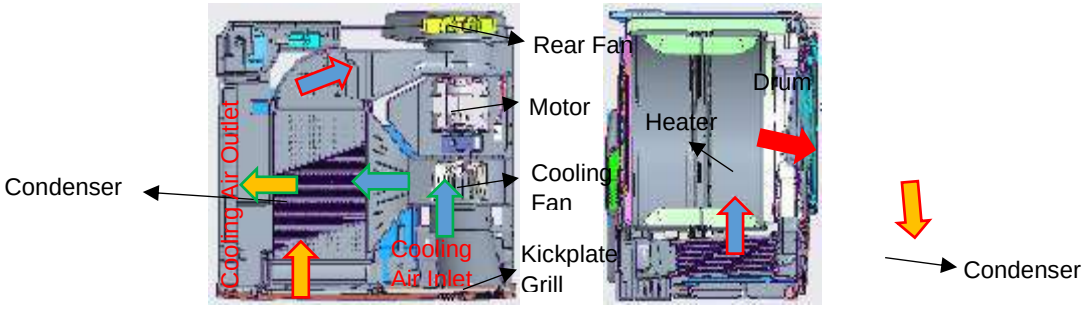

Fig. 5: Drying System of Condenser Tumble Dryer

Geometries were created to form the fluid volumes for modeling both the drying and cooling air.

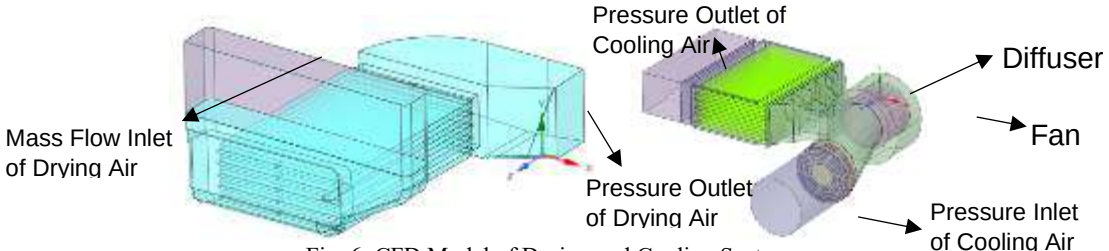

Fig. 6: CFD Model of Drying and Cooling System

Condenser is a multi-layered heat exchanger composed of fins and channels. As the drying air flows through the channels, it transfers heat to the channels and then to the fins. The cooling air, in turn, passes through the fins, effectively removing the heat and releasing it outside the machine.

Fig. 7: Condenser and Condenser Model for CFD

The heat transfer in the system occurs between the cooling air modeled as a porous medium inside the condenser and the drying air passing through the condenser channels (ANSYS User Guide). This approach is based on the pressure drop graph dependent on velocity for the finned region, where the fin thickness is below 1 mm, making it challenging to mesh in the solution network. The fins of the condenser have a direct impact on pressure drop and heat transfer (Khande et al., 2018). In this study, while modeling the porous medium approach for pressure loss induced by fins, the fins themselves have not been included in the modeling.
A study on the decoupling of the number of cells was conducted during the establishment of the solution network. The experimental measurement of the mass flow rate of the cooling air was considered as the reference. The number of cells was increased until the flow rate in the numerical study was stabilized. Ultimately, with 4.5 million cells (Study Number 4), the mass flow rate of the cooling air was obtained with a 2% margin of error.

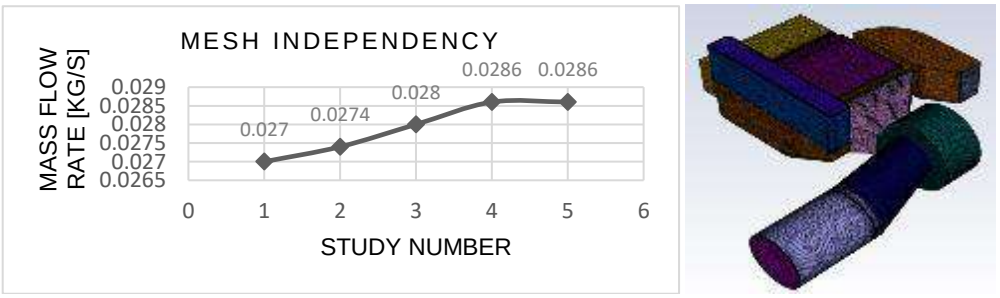

Fig. 8: Pressure Drop - Freestream Velocity Graph for Porous Media Approach and Meshed Geometry

The meshing process, completed with Fluent Mesh software using a polyhedral structure, enhances analysis accuracy and solution speed (Chen et al., 2022). Following geometry preparation, meshing, and experimental investigations, the simulation transitioned to the Ansys Fluent solver. The Coupled solution method addressed pressure-velocity coupling in the Navier-Stokes equations (Wilcox, 1998). The Reynolds-Averaged Navier-Stokes (RANS) approach, known for its cost-effectiveness, was selected. Within Ansys Fluent CFD software, the k-ω SST (Shear Stress Transport) turbulence model from the RANS family was chosen for precise results (Menter, 1994).
In this study, boundary conditions for the numerical model were established based on experimental data. The drying side was modeled with a fixed flow rate input and pressure outlet, while the cooling side utilized pressure inlet and outlet. The cooling fan was simulated using the Moving Reference Frame (MRF) method (Gullberg et al., 2011). Temperature boundary conditions were determined from thermocouple results. The CFD model incorporated the energy equation and represented single-phase flow without moisture, treating the fluid as an ideal gas to analyze heat transfer in the condenser with two different temperatures. The cooling fan speed is 2750 rpm. The inlet temperature of the cooling air is 38 °C, and the drying air is 71.7 °C. The drying air is characterized by a mass flow rate of 0.0434 kg/s. Pressure outlets and inlet are set at 101325 Pa.
The CFD analysis has been completed for the the current model. The post-process procedures are as follows.

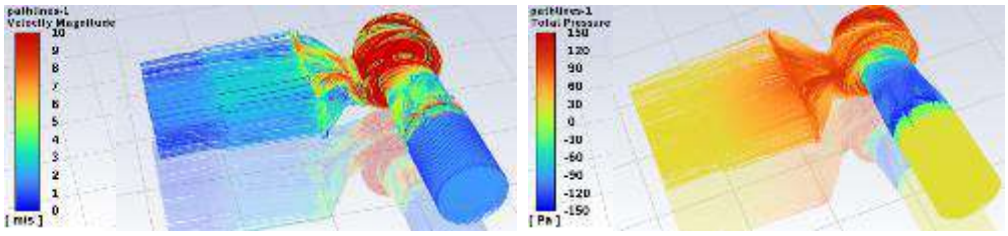

Fig. 9: Velocity and Total Pressure Distribution for Cooling Air

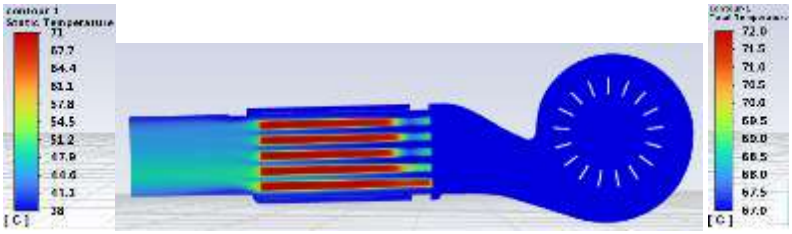

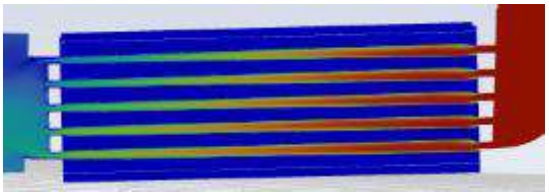

Fig. 10: Temperature Distribution for Middle Section of Cooling Air and Drying Air

As a result of the CFD analysis, temperature variations have been examined. A previous one-dimensional simulation study concluded that an increase in the cooling air flow rate positively affects heat transfer (Yıldıran, V.C., & Güneş, H., 2023). In another study, it was noted that a decrease in the cooling air flow rate extended the drying time (Do et al., 2013). Therefore, the number of holes in the cooling channel grid has been increased to increase cooling flow rate. CFD analysis has been conducted again with the modified grid.

III. Results and Discussion

By 27 % increasing the air intake holes on the grid located at the cooling fan inlet, the resistance in the grid area has decreased. This reduction in resistance has led to an increase in the flow rate of the cooling air. This increase has resulted in approximately a 9% flow gain. With the increase in the cooling flow, the temperature of the drying air leaving the condenser has decreased by 2 °C compared to the current condition.

Table 2. CFD Results of Current and Modified Model

Drying Cycle	Current	Modifed
Cooling Mass Flow Rate [kg/s]	*0.0285*	*0.0312*
Drying Mass Flow Rate [kg/s]	*0.0434*	*0.0434*
Drying Air Inlet	*71.69*	*71.69*
Drying Air Outlet	*66.6*	*64.6*
ΔT [°C]	*5.1*	*7.1*

While the increase in cooling flow may increase the temperature difference of the drying air, especially after CFD analyses, flow-related problematic areas have been observed, particularly in the lower tier of the condenser. The structure of the baffle can be studied to direct the cooling air to the fins below the condenser. Additionally, it has been observed that the flow distribution in the diffuser region can be improved. Another subject of study could be the redesign of the diffusers. Improvements in these areas could enhance heat transfer.

IV. Conclusion

The CFD analysis of the condenser-type drying machine has been completed. The analysis was repeated by the surface area of the suction holes of the cooling channel has been increased by 27 %. Additionally, the mass flow rate of the cooling air has increased by 9%. Due to increased flow rate, drying air exits the condenser 2°C cooler.

Acknowledgements

For their contributions to my master's thesis, we extend our thanks to Renta Electric Home Appliances Industry and Foreign Trade Ltd. and our affiliated company, Haier Europe.

References

ANSYS User Guide

Chen, H., Zhou, X., Feng, Z., & Cao, S. J. (2022). Application of polyhedral meshing strategy in indoor environment simulation: Model accuracy and computing time. Indoor and Built Environment,31(3), 719-731.

Do, Y., Kim, M., Kim, T., Jeong, S., Park, S., Woo, S., ... & Ahn, Y. (2013). An experimental study on the performance of a condensing tumbler dryer with an air-to-air heat exchanger. Korean Journal of Chemical Engineering, 30, 1195-1200.

EN 60456 and IEC 61121

Gullberg, P., Lo¨ fdahl, L., & Nilsson, P. (2011, January). Fan modeling in CFD using MRF model for under hood purposes. In Fluids Engineering Division Summer Meeting (Vol. 44403, pp. 931-942).

Khande, A.R., Pandhare, A.P., Ghavate, R.D. (2018). CFD Analysis of Air Cooled Condenser in Tumble Cloth Dryer, Journal of Emerging Technologies and Innovative Research, Vol 5 Issue 11, (pp 706-717).

Stawreberg, L., & Wikström, F. (2011). Does the energy labelling system for domestic tumble dryers serve its purpose? Journal of Cleaner Production,19(12), 1300-1305.

To, W. M., Yu, T. W., Lai, T. M., & Li, S. P. (2007). Characterization of commercial clothes dryers based on energy-efficiency analysis. International Journal of Clothing Science and Technology.

Wilcox, D. C. (1998). Turbulence modeling for CFD (Vol. 2, pp. 103-217). La Canada, CA: DCW industries.

Yıldıran, V.C., & Güneş, H.. (2023). Effects Of Coolıng Aırflow Rate And Temperature On The Water Collectıon In Condenser Dryers: One-Dımensıonal Modelıng Approach. In 10th International Congress on Engineering and Technology Management (pp. 463-477). Academic Press.

IEEES-152

Effects of Climate Change and Global Oscillations on Probable Maximum Precipitation

Ömer Oğuzhan Arabacı[1] and Sevinc Asilhan Sirdas[1,*]
[1,*] Istanbul Technical University, Faculty of Aeronautics and Astronautics
Department of Meteorological Engineering, Maslak 34469 Istanbul, Turkey

* E-mails: sirdas@itu.edu.tr, ssirdas@gmail.com, oguzhanarb@hotmail.com

Abstract

Water has this immeasurable importance; extreme minimum and extreme maximum precipitations are also very critical for the continuation of life on earth. Because of the global climate change, increase in the number of extreme weather phenomes observed all over the world, but the intensity and magnitude of warming impact change locally. In this study, the five provinces of Türkiye, Adana, Ankara, Isparta, Izmir and Samsun were used; precipitation, dew temperature and average humidity, maximum humidity, minimum humidity and soil moisture data were collected evaluated and analyzed. The data obtained from the automatic stations is hourly data and contains years between 2010 and 2014 and the data from The European Centre for Medium-Range Weather Forecasts (ECMWF) used for modeling as 6-hour data, Mann-Kendall (MK) trend analysis and monthly average and total values, increase and decrease trends are examined. The correlation between 3 important oscillations (Arctic Oscillation (AO), El Nino South Oscillation (ENSO) and North Atlantic Oscillation (NAO)) was analyzed and the correlation between them was examined. As a result, it was determined that there were occasional correlations with these oscillations in 5 provinces analyzed and they were affected by these oscillations, but a statistical correlation was not found most of the time. In general, while the average humidity values are in the 40-80% band, it is determined that there are trends of both serious drought and serious precipitation in these humidity values. As a result, drought periods and occasional maximum precipitation periods were observed in these 5 provinces, and occasionally correlated with dew temperature and occasional average humidity, minimum humidity, maximum humidity and soil moisture. However, it has been observed in cases of sudden drought to maximum precipitation or vice versa.

Keywords: Climate Change, Water, Probable Maximum Precipitation, Flood, Drought, Mann-Kendall, ENSO, NAO, AO, PMP

I. Introduction

There has been a lot of destruction caused by meteorological natural disasters, both loss of life and loss property from past to present in our country and in the world. Especially in the last century, with climate change, the incidence and occurrence of these disasters have changed and have closely affected everyone's lives. Only 3 of the 31 natural disasters that occur in the world are caused by non-meteorological reasons (Kadıoğlu, 2008). Since meteorology is so related to natural disasters, meteorology has a lot of work to do in predicting these natural disasters and taking the necessary precautions. Over the past few decades, dangerous weather events such as heavy rain, heavy snowfall, drought, and heat waves caused by climate change have been concentrated in densely populated urban and industrial areas (Jee & Kim, 2017). Therefore, it is a very important task for meteorology to predict the encounter of such natural disasters in important and dense cities in our country and in the world and to take precautions against these disasters. According to the World Meteorological Organization (WMO), 700,000 people lost their lives due to meteorological disasters in the 1980s alone (WMO, 1999). In Korea, for example, local downpours sometimes cause floods and landslides, resulting in heavy casualties and loss of property (Korea Meteorological Administration, 2011). As in many countries in the world, serious loss of life and property occurs in our country due to natural disasters. Especially when there is no rainfall, drought, heavy precipitation, floods, heat waves are gradually becoming a part of our lives today and this situation is expected to be much more in the future. The decrease in water resources in Turkey is an indication that desertification and related ecological deterioration have started to be affected by the negative aspects of global warming, and according to the scenarios, drought in Turkey will increase between the next 2080-2099 years (Sirdas Asilhan, 2017). Sirdas et al., 2013 is mentioned that therefore, being more successful in forecasts with modeling and making more accurate analyzes for future weather forecasting by interpreting the model outputs with the right analysis methods both minimizes the loss of property and life and eliminates the economic slowdown caused by natural disasters such as droughts and floods. Storms have increased most in tropical regions of the world, but there is also a noticeable increase outside the tropics. Due to the intensified thunderstorms in countries outside the tropics, such as Turkey, there is also an increase in the number and severity of flash floods in cities (Sirdas et al., 2013). In rainy years, flood disasters are common in general, leading to loss of life and property, and in dry years, many agricultural products do not grow due to lack of water and access to water becomes difficult for many people. In addition, in dry years, there are vital water deficit in terms of agriculture and people's access to water. Drought is also considered to be a huge problem in supplying the water needs of big cities. A decrease in precipitation of 13 percent to 20 percent in Istanbul may cause severe drought as a result of global warming, but this problem can be prevented when planning and sustainable management are made for drought (Sirdas, 2017). Therefore, damages can be minimized when the data is analyzed correctly for both drought and probable maximum precipitation and necessary precautions are taken (Sirdas et al., 2013).

II. Methodolgy and Data

In this study, the observed data of temperature; average, minimum and maximum humidity; precipitation, snow and soil moisture are obtained from Turkish State Meteorological Directorate (MGM) between 2010-2014 as hourly data and from the European Medium-Range Weather Forecasting Center (ECMWF) between 2015-2020 (until February) as six hours time range. Reanalysis data from ECMWF is a global atmospheric reanalysis data as grib or netcdf data. ECMWF Reanalysis data was read from the grib format and transferred to the notebook, and from the notebook to ascii. Mann-Kendall test monotonic trend analysis was done with RStudio program and values such as standard deviation, tau, p-value were obtained. While conducting the trend analysis, since the data were 4-year station data and 6-year model data, trend analysis was carried out on a year-by-year basis for a total period of 10 years.

Fig. 1: Locations of the stations to be analyzed on the map

In this study, the ground base stations are selected as Adana (17351), Ankara (17130), Isparta (17240), Izmir (17220) and Samsun (17030) which are together with the station coordinate of the cities to be analyzed shown in Fig.1.

III. Analysis

The 10-year distribution graphs of the monthly average data of Adana, Ankara, Isparta, Izmir and Samsun provinces were examined in this area Fig. 2.

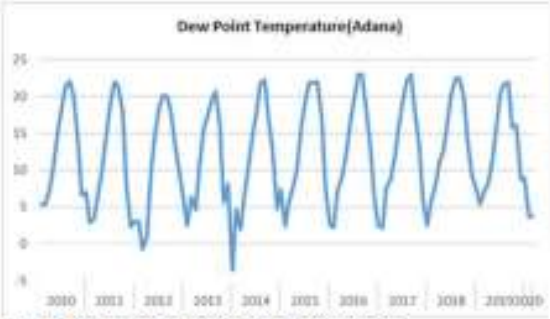

Fig. 2: Dew Point Temperature of Adana

Mann-Kendall test for trend analysis method was used for trend analysis for ECMWF reanalysis data, the RStudio program was used and since the data were 6 hours of data between 2015-2020 (until February), they were calculated together. When performing the Mann-Kendall test trend analysis, a positive S and tau value indicates that the trend is in an upward trend, and a negative trend indicates a downward trend. The p-value value was used as 0.05 for this analysis and it was accepted that there was statistical significance for less than this value.

Global circulations in the atmosphere have an important role in the long-term weather events around world. Therefore, the circulations in the world significantly affect the climatic variability of many areas. The term El Niño has been used by indigenous people for centuries to describe the abrupt change in the direction of ocean currents and the temperature of surface waters on the west coast of South America every 2-5 years as a result of warm surface waters flowing eastward from the equatorial western Pacific Ocean replacing the nutrient-rich cold waters of the coastal Humbolt Current (Türkeş, Sumer, & Kılıç). Extreme weather events are influenced by many distant atmospheric circulations, from topography to local strain, such as the El Niño Southern Oscillation (ENSO), Arctic Oscillation (AO) and the North Arctic Oscillation (NAO) (Sirdas, Diriker, & Kumar, 2016). Since the El Niño Southern Oscillation (ENSO), Arctic Oscillation (AO) and North Atlantic Oscillation (NAO) indices significantly affect the climate so that a comparison analysis of the standardized precipitation data with the indices was performed in Fig. 3.

Also, probable maximum precipitation is calculated for floods, torrent, intense extrem precipitation and heavy rain by using daily total precipitation.

PMP and K_m formulas;

$$K_m = \frac{X_m - \overline{X}_{n-1}}{\sigma_{n-1}} \qquad \text{PMP} = \overline{X}_n + K_m\sigma_n = \overline{X}(1 + K_m C_v)$$

where X_m is the maximum observed value, X_{n-1} is the mean value average excluding maximum data, σ_{n-1} is standard deviation excluding maximum data.

IV. Results and discussion

As a result, when all the data were analyzed, it was determined that maximum heavy rains fell in January 2012 and 2013 and the 2013-2017 period was dry. It has been analyzed that the trend, which was on an upward trend until 2010-2014, was in a downward trend in the 2015-2020 period. When examined with the ENSO index, there was a correlation with ENSO in 2010, and in 2019, it was similar to ENSO, that is, it showed the effect of El Niño Southern Oscillation in Fig. 3. When the humidity and heat temperatures were analyzed by value, the trend analyzes were also examined and the heavy rains in Adana province tended to increase in the 2012-2013 period, confirming the first hypothesis, while the years 2013-2017 were determined as drier years. When we look at the province of Ankara, Ankara, which received heavy rainfall in 2010, has tended to be dry in terms of precipitation in the 10-year period.

Fig. 3: Comparison of provinces standardized data with ENSO, NAO and AO (2011,2018 and 2019)

Table 1: Annual trend analysis of study areas.

Precipitation	2010	2011	2012	2013	2014	2015-2020
Adana	↑	—	↑	—	↑	↓
Ankara	↑	—	↑	—	—	—
Isparta	—	—	—	—	—	—
İzmir	—	—	—	—	—	—
Samsun	↑	—	↑	↑	↑	—

There is an upward trend in the trend analysis in the years when there is extreme rainfall in Adana (2010-2013), and there is a downward trend in the dry years (2013-2017). While there was an upward trend in the trend analysis of heavy rainfall in Ankara in 2010, there was no trend in other years. While there was heavy rainfall in Samsun in 2010 and 2013, there was an upward trend in the trend analysis, and since 2014, there has been no trend in drought years. Compared to the ENSO index, it was analyzed that it had the most impact on Ankara in 2017 and 2019. When analyzed with moisture values, it indicates that there is a tendency towards drought, taking into account the moisture values corresponding to 40-80% values throughout the analysis. Considering Isparta, it has been analyzed that precipitation has been at seasonal normal for 10 years and it has been proven that there is no trend because the p-value value is constantly greater than 0.05 in the trend analysis.

V. Conclusion

Isparta precipitation data, which was parallel to the NAO index in 2010, is correlated with the NAO as a decreasing and increasing trend in 2016. When the precipitation data of İzmir was examined, it was seen that the precipitation tended to decrease in the trend analysis of İzmir, which received heavy rainfall starting from 2010. In particular, it was observed that the years 2016 and 2018 were quite dry compared to other years. When analyzed according to the AO index, it was seen that there was a correlation in 2010 and 2011. Finally, when Samsun was analyzed, it was observed that Samsun, which received heavy rainfall in 2010 and 2013, was dry compared to previous years, especially for the last 5 years. In Samsun, where there is a tendency to decrease in Dew point temperatures, the precipitation trend tends to decrease in general. Samsun, which is highly correlated with the

ENSO index, especially for the year 2010, shows the effect of this oscillation. When the relationship between ENSO, AO and NAO standardized data and standardized precipitation data of 5 provinces is interpreted with correlation; In 2014, there is a strong correlation between Samsun precipitation and ENSO value, this year is the beginning of drought in Samsun and warming has started with ENSO. In 2012 and 2015, there is a strong inverse proportion between Isparta and ENSO, and in these years, Isparta received above-average rainfall. In 2016, there is a strong correlation between the data of Adana, Ankara, Isparta and Izmir and ENSO, and in these years, these 4 provinces experienced the driest years in 10 years. In 2010, while the AO value received negative values, Adana, Izmir and Isparta received heavy rains, although they were strongly inversely proportional to the AO value. In 2013, while the AO value was generally negative, it was strongly inversely proportional to Ankara and Ankara received very little rainfall. In 2015, AO values were generally positive and Samsun province received little rainfall and was dry because it was correlated with AO. In 2019, the NAO value is negative and precipitation increases the system, since there is a strong correlation in Adana, it seems that Adana has come out of drought in 2019 and precipitation tends to increase. In the same year, there is a correlation between Isparta and Izmir and it seems that precipitation has started to increase in these provinces from drought. In 2015, rainfall in Samsun was low and dry. Since NAO is generally positive for this year and there is a strong correlation between NAO and Samsun, rainfall in Samsun is low and dry. As a result, both extreme rainfall and extreme droughts were observed in the 5 analyzed provinces within 10 years, and their decreasing and increasing tendencies were determined by trend analysis. When PMP is examined, the margin of value is calculated as 5.44% for Adana, 19.10% for Ankara, 0.36% for Isparta, 6.20% for Izmir and 23% for Samsun. In general, although PMP values calculated with 48-year maximum data vary for each cities, they are generally consistent.

References

Heavy Rainfall Events Top 10 (in Korean); KMA Registered PUB, No. 11-136000-000833-01; Korea Meteorological Administration: Seoul, Korea, 2011.

Jee, J., & Kim, S. (2017). Sensitivity Study on High-Resolution WRF Precipitation Forecast for a Heavy Rainfall Event. *Atmosphere*, *8*(12), 96. doi:10.3390/atmos8060096

Kadıoğlu, M. (2008). Sel, Heyelan ve Çığ için Risk Yönetimi; Kadıoğlu, M. ve Özdamar, E., (editörler), "Afet Zararlarını Azaltmanın Temel İlkeleri"; s. 251-276, JICA Türkiye Ofisi Yayınları No: 2, Ankara.

MMO. (1999). Meteorolojik Karakterli Doğal Afetler ve Meteorolojik Önlemeler Raporu, TMMOB Meteoroloji Mühendisleri Odası

Sırdas, A. S., Diriker, A. B., & Kumar, V. (2016). Heavy Precipitation Events in Marmara Region and connections with the North Atlantic and Arctic Oscillation Patterns. *Environment and Natural Resources Research*, *6*(4), 1. doi:10.5539/enrr.v6n4p1

Sirdas S, Sen Z, Oztopal A (2013) Climate Change Expectations in the Next Half Century of Turkey. . Causes, Impacts and Solutions to Global Warming pp 103-127. https://doi.org/10.1007/978-1-4614-7588-0 6

Sırdas, A. S. (2017, June 9). *Türkiye'de Kuraklık 2080-2099 Yılları Arasında Artacak*. Retrieved from https://www.ekoyapidergisi.org/3530-turkiyede-kuraklik-2080-2099-yillari-arasinda-artacak.html.

Türkeş, M., Sümer, U. M., & Kılıç, G. (n.d.). El-Nino-Güneyli Salınım: Küresel Bir Okyanus/Atmosfer Olayı. Retrieved from https://www.mgm.gov.tr/FILES/iklim/yayinlar/elnino.pdf

Entropy Generation Induced by AC and DC Magnetic Fields on MWCNT-Fe_3O_4/Water Hybrid Nanofluid Flowing in U-tube

[1*]Emrehan Gürsoy, [2]Engin Gedik
[1] Karabük University, Institute of Graduate Programs, Energy Systems Engineering Department, Karabük, 78050, Türkiye
[2] Karabük University, Engineering Faculty, Mechanical Engineering Department, Karabük, 78050, Türkiye

* E-mail: emrehangursoy@gmail.com

Abstract
U-tube flow geometry is used in shell and tube heat exchangers as both horizontal and vertical directions. In this study, entropy generations induced by alternating current (AC) and direct current (DC) magnetic fields ($\dot{S}'''_{gen,\,mf}$) analyses of U-tube were computationally investigated for both U-tube geometries. The analyses were computed for Dean number (Dn) of 117.1, 175.6, and 234.2 correspond the laminar flow regime. MWCNT-Fe_3O_4/water hybrid nanofluid, which has two volume fractions (φ=0.001% and 0.003%), was used as working fluid. While the strengths of AC and DC magnetic field were applied as B= 0.16T and 0.30T, frequency and wave form of AC magnetic field were determined as f= 2 Hz and square, respectively, for both strengths. The results were presented under the three focuses: effect of magnetic field strength, effect of MWCNT-Fe_3O_4/water hybrid nanofluid volume fraction, and effect of magnetic field type. According to the results, it was found that as decreasing of magnetic field strength, $\dot{S}'''_{gen,\,mf}$ shows a decrement. While the lowest $\dot{S}'''_{gen,\,mf}$ was obtained in B=0.16T of DC at Dn=117.1. On the other hand, it was concluded that volume fraction increment of MWCNT-Fe_3O_4/water hybrid nanofluid negatively affect the $\dot{S}'''_{gen,\,mf}$. There is a difference between the AC and DC magnetic field types. The lowest $\dot{S}'''_{gen,\,mf}$ was obtained in DC magnetic field and irreversibility reduced in the rate of 99.45% and 99.55% in B= 0.16T and 0.30T, respectively, at Dn=117.1.

Keywords: U-tube, entropy generation, DC and AC magnetic field, laminar flow regime.

I. Introduction

Shell and tube heat exchangers one of the most used heat exchangers in industrial process due to provide high pressure and temperature resistance. U-tube flow geometry is generally used in rear side of shell and tube heat exchanger and constructed according to Tubular Heat Exchanger Manufacturer Association (TEMA). Many researchers spent time to enhance the performance of U-tube by benefiting heat transfer enhancement techniques. Kaya et al., (2020) performed a numerical study for determining the efficiency of U-tube benefit from Al_2O_3/water nanofluid with different volume fractions of φ=1.0%, 2.0%,3.0%, and 4.0% and shapes of blade, brick, and platelet. They reported that the highest efficiency is resulted as 67.1% in Al_2O_3/water nanofluid with φ=4.0 vol% and brick shape. Jahanbin et al., (2022) examined the performance of U-tube by using seven different nanofluid included Cu, Ag, Al_2O_3, Fe_2O_3, SiO_2, CuO, and TiO nanoparticles in the volume fraction of ranging from 0.1% to 2.0%. It is clearly shown that the heat transfer enhancement in all nanofluids is greater than the pressure drops. Entropy generation analysis is one of the most popular way to measure the effectiveness of the thermal system and there are many studies investigated the entropy generation U-tube in literature by using the heat transfer enhancement techniques. One of them is realized by Feizabadi et al., (2019). The researchers have carried out an experimental study on U-tube, inserted a twisted tape, and measured the entropy generation. Experiment has been carried out for turbulence flow regime (3843<Re<11436) and twisted tape ratios of 2 and 6. The results shows that twist ratio and entropy generation is direct proportion with each other. Gürsoy et al., (2023) investigated the entropy generation in U-tubes, enhanced with spherical dimple fin and included four different curvature radiuses, under between of Dn= 9.1 and 301.2. Fe_3O_4/water, which have three volume fractios, has been used as working fluid and the pitch ratio of dimple shows a variation (P/d=6.0, 7.5, and 9.0). The researchers presented that increasing of volume concentration negatively affect the total entropy generation due to excessive increment of pressure drop. Besides, curvature radius is inverse proportion with total entropy generation. Finally, as decreasing of pitch ratio provided a decreasing in total entropy generation.
In the literature, entropy generations due to heat transfer and pressure drop irreversibilities have been utilized to evaluate the effectiveness of passive heat transfer enhancement techniques in the U-tube. However, the magnetic field applying, which take part of active heat transfer enhancement techniques, is tackled in this study. Because of this, entropy generation induced by magnetic field (also known as Joule dissipation irreversibility) has been numerically investigated in this study. Alternative (AC) and direct (DC) magnetic fields have been applied on the certain surface of U-tube at B= 0.16T and 0.30T strengths. In addition, frequency (f) and wave form of AC magnetic field is considered as f= 2 Hz and square. Besides, MWCNT-Fe_3O_4/water hybrid nanofluid with φ=0.001% and 0.003% has been used as working fluid.

II. System Description

Flow domain and boundary conditions of U-tube aligned both horizontally and vertically have been presented in Fig. 1. Diameter and curvature radius of U-tube has been considered as D=20.57 mm and R_c=0.75 m. This determination has been done according to results of Gürsoy et al., (2023) study and represented the highest performance. AC and DC magnetic field, which strengths are B= 0.16T and 0.30T, have been applied at θ=90° where cover the 100 mm length surface. Besides, AC magnetic field has f=2 Hz and square wave form for both strengths. Magnetic field characteristics have been determined according to study of Gürsoy et al., (2023a) and (Tekir et al., 2020) due to provide the highest performance.
Working fluid enters the inlet section at Dn= 117.1, 175.6, and 234.2 correspond the laminar flow regime under constant temperature of T_{inlet}=300 K. The thermophysical properties of working fluid are determined in Table 1. Rheological properties of

working fluid have been identified as incompressible and Newtonian fluid. Besides, it has been assumed that flow is fully developed hydrodynamically and developing thermally under steady-state conditions. Constant heat flux of q"=1000 W/m^2 has been applied on entire walls. Furthermore, certain assumptions such as zero heat transfer via radiation, neglecting of buoyancy force, single phase, and constant thermo-physical properties have been considered.

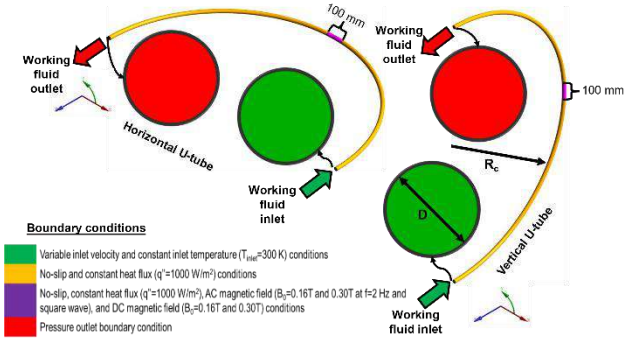

Fig. 1: Fluid domain and boundary conditions of the study.

Table 1. Thermophysical properties of MWCNT+Fe_3O_4/water hybrid nanofluid for two volume concentration (Izadi et al., 2018).

Working Fluid	Thermophysical Properties					
	Density, ρ (kg/m^3)	Specific heat, C_p (W/kgK)	Thermal conductivity, k (W/mK)	Dynamic viscosity, μ (kg/ms)	Electrical conductivity, σ (S/m)	Magnetic permeability, μ_{mp} (H/m)
0.001% MWCNT+Fe_3O_4/water	1002.34	4182.66	0.6734	0.00091	0.299	1.25006E-06
0.003% MWCNT+Fe_3O_4/water	1010.04	4183.99	0.6856	0.00101	0.799	1.25006E-06

III. Analysis

Within the scope of this study, 24 numerical analyses were carried out on the 3D numerical model using the governing equations required for heat transfer and flow characteristic analysis and given as Eq. (1)-(5) (Jiji, 2009).

Continuity equation:

$$\frac{\partial\rho}{\partial t}+\frac{1}{r}\frac{\partial}{\partial r}(r\rho V_r)+\frac{1}{r}\frac{\partial(\rho V_\theta)}{\partial\theta}+\frac{\partial(\rho V_z)}{\partial z}=0 \quad (1)$$

r-component of the momentum equation;

$$\rho\left(V_r\frac{\partial V_r}{\partial r}+\frac{V_\theta}{r}\frac{\partial V_r}{\partial\theta}-\frac{V_\theta^2}{r}+V_z\frac{\partial V_r}{\partial z}\right)=-\frac{\partial P}{\partial r}+\rho g_r+\mu\left(\frac{\partial^2 V_r}{\partial r^2}+\frac{1}{r}\frac{\partial V_r}{\partial r}-\frac{V_r}{r^2}+\frac{1}{r^2}\frac{\partial^2 V_r}{\partial\theta^2}-\frac{2}{r^2}\frac{\partial^2 V_\theta}{\partial\theta}+\frac{\partial^2 V_r}{\partial z^2}\right)+q(E_0+V_rB_0)B_0 \quad (2)$$

θ-component of the momentum equation;

$$\rho\left(V_r\frac{\partial V_\theta}{\partial r}+\frac{V_\theta}{r}\frac{\partial V_\theta}{\partial\theta}-\frac{V_rV_\theta}{r}+V_z\frac{\partial V_\theta}{\partial z}\right)=-\frac{1}{r}\frac{\partial P}{\partial\theta}+\rho g_\theta+\mu\left(\frac{\partial^2 V_\theta}{\partial r^2}+\frac{1}{r}\frac{\partial V_\theta}{\partial r}-\frac{V_\theta}{r^2}+\frac{1}{r^2}\frac{\partial^2 V_\theta}{\partial\theta^2}+\frac{2}{r^2}\frac{\partial^2 V_r}{\partial\theta}+\frac{\partial^2 V_\theta}{\partial z^2}\right)+q(E_0+V_\theta B_0)B_0 \quad (3)$$

z-component of the momentum equation;

$$\rho\left(V_r\frac{\partial V_z}{\partial r}+\frac{V_\theta}{r}\frac{\partial V_z}{\partial\theta}+V_z\frac{\partial V_\theta}{\partial z}\right)=-\frac{\partial P}{\partial z}+\rho g_z+\mu\left(\frac{\partial^2 V_z}{\partial r^2}+\frac{1}{r}\frac{\partial V_z}{\partial r}+\frac{1}{r^2}\frac{\partial^2 V_z}{\partial\theta^2}+\frac{\partial^2 V_z}{\partial z^2}\right)+q(E_0+V_zB_0)B_0 \quad (4)$$

The energy equation;

$$\rho c_v\left(V_r\frac{\partial T}{\partial r}+\frac{V_\theta}{r}\frac{\partial T}{\partial\theta}+V_z\frac{\partial T}{\partial z}+\frac{\partial T}{\partial t}\right)=k\left(\frac{\partial^2 T}{\partial r^2}+\frac{1}{r}\frac{\partial T}{\partial r}+\frac{1}{r^2}\frac{\partial^2 T}{\partial\theta^2}+\frac{\partial^2 T}{\partial z^2}\right)+\mu\Phi+\frac{1}{\sigma}\vec{j}^2 \quad (5)$$

On the other hand, as the data reductions, Eq. (6) is given to describe the flow regime in U-tube.

$$Dn=Re\sqrt{\left(\frac{D}{2R_c}\right)} \quad (6)$$

where Dn is the dimensionless Dean number, Re specifies the dimensionless Reynolds number, D shows the diameter (mm) of U-tube, and R_c describes the curvature radius (m) of U-tube.

$$Re=\frac{\rho UD}{\mu} \quad (7)$$

where ρ is the density (kg/m^3), U identifies the velocity (m/s), and μ is the dynamic viscosity (Pa.s) of working fluid. Furthermore, Eq. (8) is used to calculate the entropy generation induced by AC and DC magnetic fields. This equation has been identified in ANSYS Fluent with the help of Custom Field Function.

$$\dot{S}'''_{gen,mf}=\frac{\sigma_{eff}\times\vec{B}^2\times\vec{U}^2}{T} \quad (8)$$

where $\dot{S}'''_{gen,mf}$ describes the volumetric entropy generation (W/m^{3}K) arising from magnetic field, σ_{eff} is the effective electrical conductivity (S/m) of working fluid, B shows the magnetic field strength (T), T identifies the temperature (K) of working fluid. Numerical analyses have been computed with ANSYS Fluent 19.2 software according to the finite volume method. To form a mesh structure on fluid domain, general and local mesh settings have been used and the mesh quality metrics (orthogonal and skewness) have been considered. Besides, the mesh convergence has been done under Dn= 117.1 for MWCNT-Fe_3O_4/water hybrid nanofluid with φ=0.001% in Fig. 2 (a) and element number of 1033047 is selected as optimum. Subsequently, the optimum mesh structure given in Fig. 2 (b) has been formed. Pressure-based solver, absolute velocity formulation, and stead-state have been selected for analyses. SIMPLE algorithm and second order spatial discretization have been used to solution of governing equations.

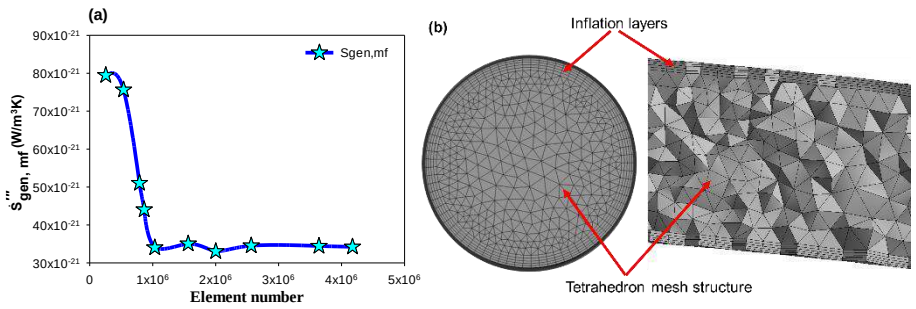

Fig. 2. (a) Convergence analysis results and (b) optimum mesh structure of the numerical study.

IV. Results and discussion

Prior to performing numerical analyses, validation with the literature is required to evaluate the suitability of the results. For this purpose, the friction factor phenomenon has been considered to validate the results with the experimental study of White (1929) in Fig. 3. Analysis has been carried out for water at Dn=117.9, 131.8, 152.2, and 186.4 and performed harmony at the error rate of 7.10% with the literature.

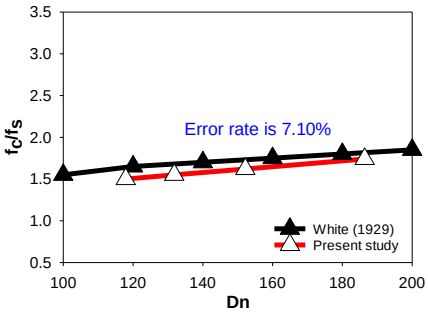

Fig. 3. Validation of the numerical study with literature.

Effect of AC and DC magnetic fields on $\dot{S}'''_{gen,mf}$ have been investigated as a function of Dn in Fig. 4. The figure has presented a general outcome about irreversibility of magnetic fields in terms of magnetic field types, magnetic field strengths, hybrid nanofluid fractions and position of U-tube. When a general observation is done on flow regime, increment of Dn negatively affect the system performance particularly in AC magnetic fields. Besides, increment of magnetic field strengths applied as DC is not considerable effected the irreversibility. However, increment of AC type magnetic field strength is extremely affected the $\dot{S}'''_{gen,mf}$ for both fractions. According to the results, applying of AC magnetic fields increased the irreversibility in the system up to 99.45% and 99.55% for B= 0.16T and 0.30T compared to DC magnetic fields. Look results from a different perspective, magnetic field strength of B= 0.16T is less affect the irreversibility compared to B= 0.30T for both magnetic field types.

Compared to effect of MWCNT-Fe_3O_4/water hybrid nanofluid volume fractions, φ=0.001% provided a decreasing down to 75.48% in AC magnetic field, particularly. Increment of Dn adversely affected this decreasing. On the other hand, position of U-tube has considerable effect on $\dot{S}'''_{gen,mf}$. According to the results, vertical U-tube causes more less irreversibility compared to horizontal one. This irreversibility reduction is reached down to 100% in both magnetic field strengths and magnetic field types.

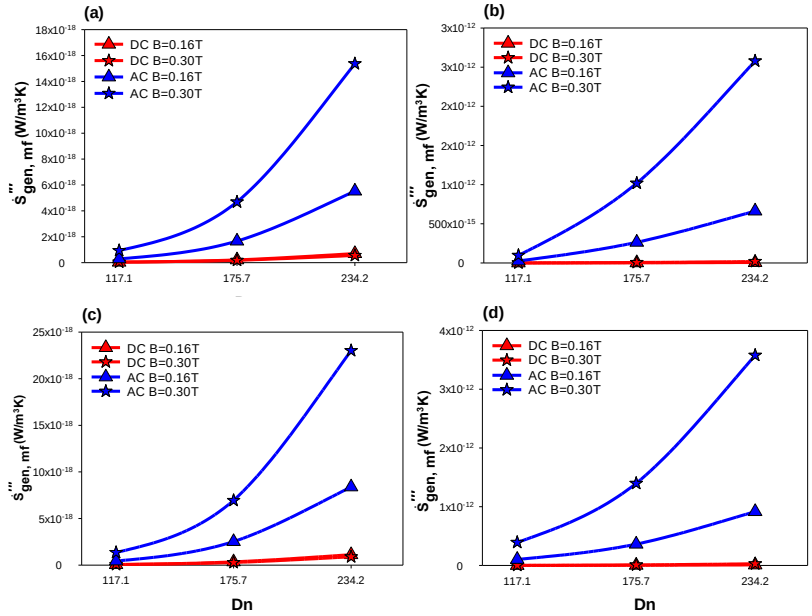

Fig. 4. The result of $\dot{S}'''_{gen,mf}$ as a function of Dn for; (a) φ= 0.001% vertical U-tube, (b) φ= 0.001% horizonal U-tube, (c) φ= 0.003% vertical U-tube, and (d) φ= 0.003% horizonal U-tube.

V. Conclusion

The entropy generation induced by AC and DC magnetic fields in U-tube with MWCNT-Fe_3O_4/water hybrid included φ=0.001% and 0.003% have been examined at Dn= 117.1, 175.6, and 234.2 in this numerical study. AC (with characteristic f = 2 Hz and square wave) and DC magnetic fields, which have strengths of B= 0.16T and 0.30T have been performed on the certain surface of U-tube. In addition, frequency (f) and wave form of AC magnetic field is considered as f= 2 Hz and square. Subsequent to the 24 numerical analyses, the acquired results are specified below:

- Increment of Dn negatively affect the $\dot{S}'''_{gen,mf}$ particularly in AC magnetic fields.
- DC magnetic field is more effective than AC magnetic field in terms of $\dot{S}'''_{gen,mf}$ without noticing strength magnitude.
- B= 0.16T is more suitable than B= 0.30T due to has less irreversibility.
- MWCNT-Fe_3O_4/water hybrid nanofluid volume fraction of φ=0.001% caused less $\dot{S}'''_{gen,mf}$ compared to φ=0.003%.
- Vertical position of U-tube exhibited less irreversibility compared to horizontal position.

Acknowledgement

The authors would like to thank Karabük University under the KBÜBAP-23-DR-044 scientific research project.

References

Feizabadi, A., Khoshvaght-Aliabadi, M., Rahimi, A.B., 2019. Experimental evaluation of thermal performance and entropy generation inside a twisted U-tube equipped with twisted-tape inserts. International Journal of Thermal Sciences 145, 106051. https://doi.org/10.1016/J.IJTHERMALSCI.2019.106051

Gürsoy, E., Gürdal, M., Kadir Pazarlıoğlu, H., Dağdeviren, A., Tekir, M., Arslan, K., Gedik, E., Adriana Minea, A., Kurt, H., 2023a. Effect of magnetic field locations on thermo-magnetic convection performance of Fe3O4/H2O ferrofluid flowing in a novel dimpled tube: An experimental study. Appl Therm Eng 226, 120305. https://doi.org/10.1016/J.APPLTHERMALENG.2023.120305

Gürsoy, E., Pazarlıoğlu, H.K., Gürdal, M., Gedik, E., Arslan, K., 2023b. Entropy generation of ferronanofluid flow in industrially designed bended dimpled tube. Thermal Science and Engineering Progress 37, 101620. https://doi.org/10.1016/J.TSEP.2022.101620

Izadi, M., Mohebbi, R., Karimi, D., Sheremet, M.A., 2018. Numerical simulation of natural convection heat transfer inside a ⊥ shaped cavity filled by a MWCNT-Fe3O4/water hybrid nanofluids using LBM. Chemical Engineering and Processing - Process Intensification 125, 56–66. https://doi.org/10.1016/J.CEP.2018.01.004

Jahanbin, A., Semprini, G., Pulvirenti, B., 2022. Performance evaluation of U-tube borehole heat exchangers employing nanofluids as the heat carrier fluid. Appl Therm Eng 212, 118625. https://doi.org/10.1016/J.APPLTHERMALENG.2022.118625

Jiji, L.M., 2009. Heat Convection, Second Edi. ed. Springer, New York.

Kaya, H., Alkasem, M., Arslan, K., 2020. Effect of nanoparticle shape of Al2O3/Pure Water nanofluid on evacuated U-Tube solar collector efficiency. Renew Energy 162, 267–284. https://doi.org/10.1016/J.RENENE.2020.08.039

Tekir, M., Taskesen, E., Aksu, B., Gedik, E., Arslan, K., 2020. Comparison of bi-directional multi-wave alternating magnetic field effect on ferromagnetic nanofluid flow in a circular pipe under laminar flow conditions. Appl Therm Eng 179, 115624. https://doi.org/10.1016/J.APPLTHERMALENG.2020.115624

White, C.M., 1929. Fluid Friction and Its Relation to Heat Transfer. Transactions of Institution of Chemical Engineering 10, 66–86.

IEEES-154

A Case Study: Energy and Efficiency Analysis for Hybrid System Consisting of SMR and Solar PTC

[1*]Gülcan Koca
[1] Gazi University, Faculty of Technology, Energy System Engineering, Ankara, Turkiye

* E-Mail: gulcankc@gmail.com

Abstract
Most of the world has faced climate change problem which is main problem today. Many countries are trying to deal with the problem. As known, greenhouse gases (GHG) especially carbon which makes atmosphere warmer and causes temperature rise, are undesirable element. Thus, industrial sector particularly energy sector is struggling to eliminate using of fossil fuels consisting of carbon. GHG emissions will be eliminated until 2050 defined as "Net Zero" focusing firstly on digitalization, electrification and sustainability. Thus, energy generation which is essential and indispensable for technological age shall be clean, affordable, uninterrupted and sustainable. Since energy sector has focused on carbon-free systems regarded as clean energy, renewable energy systems (RES), natural gas and nuclear energy systems are prominent in the sector. However, capacity factor of RES is not high depending on geography condition and it has intermittent generation. For natural gas, most countries are is typically imported. Nuclear investment cost is notably high and not affordable. In the paper, one of the new nuclear technologies and one of the solar technologies have been combined as a hybrid system to get more efficiency as a research study. As there are more than 80 small modular nuclear reactor (SMR) designs, studies on SMR regarded as one of the solutions have been ongoing to acquire proven technology. In the study, HTR PM design developed and started to operate by China as a SMR design and parabolic trough collector (PTC) as solar system have been selected. In proposed system, PTC is used for heating of main flow (water) coming from condenser instead of heating with extraction steam taking from HP/LP turbine. After analysing of energy and efficiency, it is obtained more efficiency around %1.4 in HP and LP Turbine including district heating. No 6-7-11-13 of the UN-17 Sustainable Development Goals can be obtained via hybrid system.

Keywords: Energy, efficiency, SMR, hybrid, integration, PTC, solar.

I. Introduction

Energy is essential of the human life and energy demand is increasing day by day. As it is vital for our world, all of users expect uninterrupted, stable, safe, reliable, cheap electricity to be supplied. Furthermore, because of climate change problem, energy generation must be provided from clean and sustainable energy sources. The reason of the climate change problem is due to greenhouse gasses (GHG) which are covering our planet as a blanket and then are helping to maintain atmosphere warmer temperature. Thus, main target is to eliminate the greenhouse gasses especially in every sector. For energy sector, renewable and clean energy will be replaced with fossil fuels due to having high carbon content by giving up of using. However, renewable energy sources (RES) have low-capacity factor depend on geography conditions. Additionally, base load operation is quite important in energy market because of uninterrupted supply. On the other hand, natural gas and nuclear energies regarded as clean energy are effective energy sources in terms of capacity factor and base load. Because of high capital cost of nuclear energy and importing of natural gas, benefit from the energies can be difficult. Therefore, hybrid energy systems are becoming prominent. Hybrid energy systems especially focusing on nuclear and RES will be played complementary roles to obtain net zero targets for climate change struggling. Hybrid systems can be used for district heating, hydrogen production, desalination, other industrial process. In this study focusing on hybrid system, one of the RES technologies and one of the new nuclear technologies are combined and analysed in order to obtained more efficient system and to benefit more from RES. Nuclear-Renewable Hybrid Energy Systems (N-R HES) can be regarded as integrated or combined system.

Nuclear-Renewable Hybrid Energy Systems (N-R HES) has been studied and analysed by many sorts of universities and institutions. The system has been interpreted as a valuable technical concept that can potentially diversify and leverage existing energy technologies (Green, 2013). This report has focused on NHES design that combines multiple energy systems including a nuclear reactor, energy storage system, variable renewable generator and additional process heat applications. After this starting, updated or new reports and master thesis have been performed (Mikelson, 2015, Rabiti, 2017 and Redfoot, 2018). USA Department of Energy has prepared Quadrennial technology review report and studied nuclear and renewable energy system together with energy storage (DOE, 2015). International Atomic Energy Agency has published a special TecDoc focusing on hybrid systems. Oak Ridge National Laboratory has analysed nuclear hybrid energy system to show enhanced performance of integrated systems relative to independent stand-alone systems (ORNL, 2016). Opportunities and challenges for N-R-HES have been analysed and summarized to quantify the economic potential (Ruth, 2018). Energy and exergy analysis have been performed for proposed hydrogen production combined with nuclear cogeneration system (Kowalczyk, 2019). Another hybrid system focusing on nuclear and solar-based energy has been designed and analysed in terms of food, fuel, and water production system for an indigenous community (Temiz and Dinçer, 2021). A nuclear-hydrogen hybrid energy system with large-scale storage has been studied in optimal dispatch and economic performance in a real-world market (Ho, 2022)

II. System Description and Methodology

Nuclear power technology has different types such as pressured water reactor (PWR) and boiling water reactor (BWR) regarded as large-scale plants. On the other hand, small modular nuclear reactors (SMR) have been tried to developed specially to replace coal-fired power plants in scope of net zero targets. There are more than 80 SMR designs all of the world. China completed one of the Generation-IV (Gen-IV) reactors as a demonstrator, High-Temperature Gas-cooled Reactor Pebble-bed Module (HTR-PM) and

reached criticality in September 2021 (WNA, 2022). After connection to the national grid, the first reactor began to produce power in 2022. Because of the first demonstration of Gen-IV SMRs, this study has grounded on the HTR-PM as a nuclear technology.
As for RES, there are many different solar technologies from solar thermal systems to photovoltaic technology using in different area. Parabolic Trough Collector (PTC) produces heat and is used in industrial area. PTC as solar technology and HTR-PM (SMR) as nuclear technology are selected and analysed.
Conventional thermal power plants (TPP) such as coal-fired and nuclear plants generate typically electricity via steam turbine and generator by benefitting from steam power obtained from pre-heated water. After exiting of the turbine, the steam goes to condenser, then to heat exchangers to be heated the condensed water. Extraction steam taking from system turbines is used to heat the water. In this study, PTC system is utilized to heat the water instead of extraction steam taking from turbines. Conventional system and proposed system are shown in Figure-1 and 2 respectively.

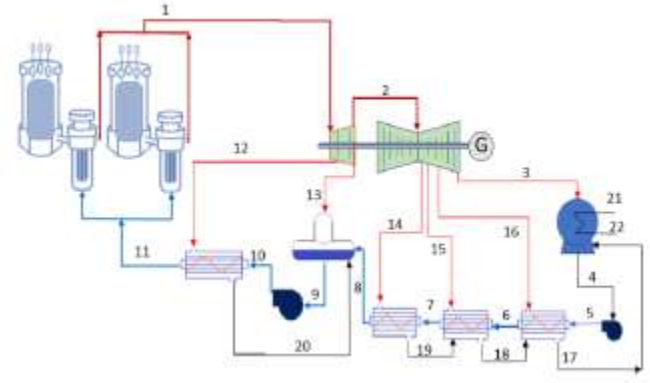

Figure 12: Conventional SMR steam cycle based on ref.: IAEA Status Report

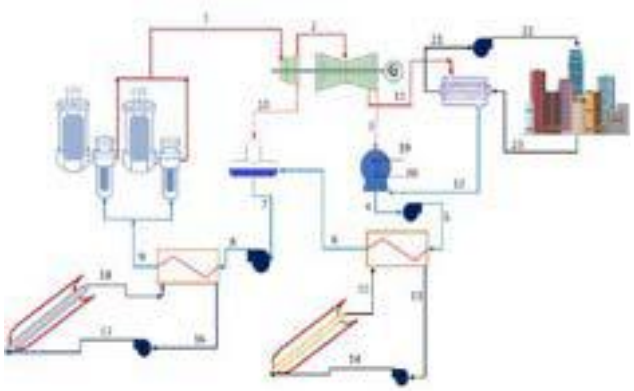

Figure 2: Proposed N-R-HES system steam cycle based on ref.: IAEA Status Report

There are two PTC systems in the proposed systems. One of them is integrated with heat exchanger used before deaerator and the other is integrated with the second heat exchanger used after main system pump. In the PTC systems, oil- Therminol-66 as a heat transfer fluid is used in the former to reach required temperature and solar salt (molten salt) mixing of 60% NaNO3 - 40% KNO3 as a heat transfer fluid is used in the latter to reach required high temperature. Therminol 66 is liquid-phase heat transfer fluid offering high-temperature thermal stability.
Aiming of the proposed system is to generate electricity via SMR system by benefitting from parabolic trough collector to obtaining more efficiency system and also, to provide required heat for district heating system.
Marmara Region in Turkiye is selected for the proposed system since there are some big industrial cities in the region such as Istanbul, Kocaeli, Bursa, Tekirdağ demanding high electricity capacity. In order to benefit from wind and solar at the same area, Balıkesir-Edremit site is analysed. Furthermore, earthquake value, near the water source for cooling, near the grid connection and population are taken into consideration for site selection.
System Advisor Model-SAM developed by National Renewable Energy Laboratory (NREL) is used for solar calculations. In the model, Model EuroTrough ET150 width of 5.75 m and length of 15m as parabolic trough is chosen. Schott PTR 70receiver with length of 4.06 m is used as glass cover coated by anti-reflective to reduce thermal losses by making vacuum space between the absorber tube coated by high absorbance material with low emittance and the glass cover. For district heating system, 17000 equivalent dwelling (each of one 100 m2) are heated by the steam taking from LP Turbine. Engineering Equation Solver-EES is used for thermodynamic calculations.

III. Analysis

Proposed N-R-HES system is analysed investigated thermodynamically in terms of energy and efficiency. The thermodynamic analyses are carried out for steady-state conditions in order to determine system performance. First of all, according to HTR-PM system cycle, conventional system shown in Figure-1 is analysed.

HTR-PM design has two-module reactors coupled to one steam turbine and the features of HTR- PM are shown in Table 1 (IAEA, Status report, 2011). Then, proposed system is analysed according to the Figure-2. For each state point shown in the figures, energy balance and mass balance are performed. Efficiency of some critical component is obtained according to the results of the energy balance figures. For calculations, some assumptions are considered. The balance equations applied for some components are shown in Table-2. The PTC system with oil and molten salt is simulated via SAM software for Balıkesir-Edremit.

Table 1. SMR (HTR-PM) Features

Installed capacity (thermal/electric)	*2x250 MWth / 211 MWe*
Primary coolant material	*Helium*
Primary coolant flow rate	*96 Kg/s*
Core coolant inlet temperature	*250 °C*
Core coolant outlet temperature	*750 °C*
Reactor operating pressure	*7.0 MPa*
Steam Generator İnlet/outlet temperature	*205/570 C (Zhang, 2016)*

Rated inlet steam pressure	*13.25 MPa*
Rated inlet steam temperature	*566 °C*
Steam flow rate	*671 t/h*
Rated discharge pressure	*4.5 kPa*
Thermodynamic cycle	*Rankine*

Mass Balance $\sum \dot{m}_{in} = \sum \dot{m}_{out}$

Energy Balance $\sum E_{in} = \sum E_{out}$

Efficiency $\eta = \frac{\sum E_{out}}{\sum E_{in}}$

Table 2. Balance Equations

Component	**Energy**		**Efficiency**
	Conventional System	**Proposed System**	
HTR-PM Steam Generator	$\dot{m}_1 h_1 = \dot{m}_{11} h_{11}$	$\dot{m}_1 h_1 = \dot{m}_9 h_9$	$\frac{\dot{m}_9 h_9}{\dot{m}_1 h_1}$
HP Steam Turbine	$\dot{m}_1 h_1 = \dot{m}_2 h_2 + \dot{m}_{12} h_{12} + \dot{m}_{13} h_{13} + W_{ST}$	$\dot{m}_1 h_1 = \dot{m}_2 h_2 + \dot{m}_{10} h_{10} + W_{ST}$	$\frac{\dot{m}_2 h_2 + \dot{m}_{10} h_{10}}{\dot{m}_1 h_1}$
LP Steam turbine	$\dot{m}_2 h_2 = \dot{m}_3 h_3 + \dot{m}_{14} h_{14} + \dot{m}_{15} h_{15} + \dot{m}_{16} h_{16} + W_{ST}$	$\dot{m}_2 h_2 = \dot{m}_3 h_3 + \dot{m}_{11} h_{11} + W_{ST}$	$\frac{\dot{m}_3 h_3 + \dot{m}_{11} h_{11}}{\dot{m}_2 h_2}$
Heat Exchanger-1	$\dot{m}_5 h_5 + \dot{m}_{16} h_{16} + \dot{m}_{18} h_{18} = \dot{m}_6 h_6 + \dot{m}_{17} h_{17}$	$\dot{m}_5 h_5 + \dot{m}_{15} h_{15} = \dot{m}_6 h_6 + \dot{m}_{13} h_{13}$	
Main Pump	$\dot{m}_9 h_9 + W_P = \dot{m}_{10} h_{10}$	$\dot{m}_7 h_7 + W_P = \dot{m}_8 h_8$	$\frac{\dot{m}_8 h_8}{\dot{m}_7 h_7}$

IV. Results and discussion

Conventional HTR-PM system design capacity is 211 MW, but in the study, it generates approximately 202 MW according to the assumptions. The proposed system integrated district heating system generates approximately 205 MW. Around increase of %1.4 MW energy together with HP and LP turbine is obtained. Furthermore, approximately 75% of exhausted steam generated in the proposed system is used in the district heating. Thereby 17000 equivalent dwelling each of the 100 m2 are heated via waste steam.

V. Conclusions

Clean, affordable, uninterrupted and sustainable energy generation must be provided for net zero target. Nuclear energy is impervious to weather conditions or geographic limitations and offers base load power so it should be evaluated together with RES. N-R HES systems support intermittent generation of RES as a suitable option. N- R HES is a clean system especially in terms of GHG emissions, so it will play role in energy transition from fossil fuels to climate-neutral energy. N-R HES technologies can be used for district heating, H2 generation, food drying, green house, water desalinization and other industrial process heating. For obtaining the UN Sustainable Development Goals, N-R-HES emerges as a rational solution. It will help to procure some of UN Sustainable Development Goals such us No:6 clean water and sanitation, No:7 affordable and clean energy, No:11 Sustainable cities and communities and No:13 climate action.

Efficiency is so important in struggling of the global warming. To increase the efficiency in every point, it will contribute to increase of life quality. Therefore, performance analyses, efficiency analyses, exergy studies should be performed through the industrial systems.

Acknowledgements

This research studying is still ongoing under PhD. End of the study, it will be achieved exact results. Additionally, due to limited access to the nuclear energy data, some data are assumed.

References

Department of Energy-DOE, (2015), Quadrennial technology review an assessment of energy technologies and research opportunities, Chapter 4, Technology Assessment, Hybrid Nuclear-Renewable Energy Systems, USA

Green, M., Sabharwall, P., Mckella, M. G., Yoon, S., Abel, C., Petrovic, B., Curtis, D., (2013), Nuclear-Hybrid Energy System: Molten salt energy storage, Idaho National Laboratory, USA

IAEA, Status Report, https://aris.iaea.org/PDF/HTR-PM.pdf, accessed November 2023

Ho, A., Hill, D., Hedengren, J., Powell, K. M., (2022), A nuclear-hydrogen hybrid energy system with large-scale storage: A study in optimal dispatch and economic performance in a real-world market, Journal of Energy Storage, 51 (2022) 104510.

Idaho National Laboratory-INL, (2015), Small modular reactor modeling using modelica for nuclear-renewable hybrid energy systems applications, Idaho National Laboratory, USA

Idaho National Laboratory-INL, (2017), Status report on modelling and simulation capabilities for nuclear-renewable hybrid energy systems, USA

Kowalczyk, T., Badur, J., Bryk, M., (2019), Energy and exergy analysis of hydrogen production combined with electric energy generation in a nuclear cogeneration cycle, Energy Conversion Department, 198 (2019) 111805

Oak Ridge National Laboratory (ORNL), (2016) Nuclear Hybrid Energy System FY16 Modeling Efforts at ORNL, ORNL/TM-2016/418, US Department of Energy.

Redfoot, E. K., (2018), Allocating heat and electricity in a nuclear renewable hybrid energy system coupled with a water purification system, master thesis, University of Idaho, USA,

Ruth, M., Spitsen, P., Boardman, R., (2019), Opportunities and Challenges for Nuclear-Renewable Hybrid Energy Systems: Preprint. Golden, CO: National Renewable Energy Laboratory. NREL/CP-6A20-72004. https://www.nrel.gov/docs/fy19osti/72004.pdf

Temiz, M., Dinçer, İ., (2021), Design and analysis of nuclear and solar-based energy, food, fuel, and water production system for an indigenous community, Journal of Cleaner Production, 314 (2021) 127890.

World Nuclear News-WNN, (2022), https://world-nuclear-news.org/Articles/China-s-demonstration-HTR-PM-reaches-full-power, accessed Now 2023

Zhang, Z., Dong, Y., Li, F., Zhang, Z., Wang, H., Huang, X., Li, H., Liu, B., Wu, X., Wang, H., Diao, X., Zhang, H., Wang, J., (2016), The Shandong Shidao Bay 200 MWe High-Temperature Gas-Cooled Reactor Pebble-Bed Module (HTR-PM) Demonstration Power Plant: An Engineering and Technological Innovation, Engineering, Vol 2, Issue 1 Pages 112-118.

IEEES-155

Assessment of the economic and environmental impacts of circular processes in green port transition and entropy management

[1*]M:Ziya Sogut and [2]Oral Erdogan
[1] Piri Reis University, Tuzla, Istanbul Türkiye

*E-mails:mzsogut@gmail.com

Abstract
Despite many different functions, port operations have continuous and energy-intensive processes. Considering the mobility of maritime trade today, the responsibility of ports is also developing in the concept of decarbonization, which has a global awareness. In this context, the roles of change in this process in ports should be evaluated together with the concept of green concept. This concept directly targets the smart transition in energy along with energy efficiency. In this study, firstly, the operational efficiency was evaluated on a reference port and the entropy production due to port energy consumption was calculated. The efficiency potential based on the developed environmental indicators was evaluated and its economic and environmental effects were examined separately. Exergy destruction in the study was found as 66.15%, while the energy efficiency potential due to the entropy approach is 36.64% approximately. In this context, some evaluations regarding the economic and environmental sustainability of the port were presented.

Keywords: Ports, Energy management, Efficiency, Entropy, Decarbonization

I. Introduction

Due to their prominent role in global climate change, the maritime sector has prioritized the conceptual development of green growth as a part of the circular economy it has created within itself, including maritime transportation, logistics management, ports, and port management. This has become a part of sustainability, which is one of the institutional frameworks of sectoral stakeholders (WG150, 2013). The concept of green ports, especially for national strategies, is a value that has developed in recent years and has found a place in the literature under different disciplines (Lei et al., 2020). Another dimension of the green port concept has developed among the principles of sustainability, and the difficulty of such a change has become significant, especially despite the environmental code developed by the European Sea Ports Organization (ESPO) (European Sea Ports Organization, 2003; Aneta Oniszczuk et al., 2018). The green port concept should be seen as an urgent action that supports the sustainability of ports and envisages healthy growth as a component of circular economies. Achieving sustainable economic growth in ports is, above all, a holistic approach that ensures the development of environmental awareness (Moon et al., 2018).

Today, ports, which are catalysts in the development of urban culture, can also be shaped as port cities and pioneers of green growth (Badurina et al., 2017). Although many environmental criteria are shaped as a criterion for a changing role in port management, the most important indicator is the entropy management resulting from energy-based consumption. This study presents an analysis of why energy is used in ports, which deals with economic and environmental sustainability based on entropy, and evaluates its managerial impact. Exergy destruction, which develops due to the concept of exergy, basically refers to the potential of the entropy formed for all systems depending on the environmental conditions in which it is located. For this reason, the impact that occurs is an environmental loss due to irreversibility as well as an economic loss caused by inefficiency.

II. Green port transition

Maritime transport carries approximately 90% of world trade through ports, and ports are one of the key points of economic sustainability caused by transportation. Ports are basically structures that need to be evaluated in a multidisciplinary manner, not only for ship transportation but also for related land elements. For this reason, it can act as one of the dynamics of environmental sustainability together with economic frameworks as a model. However, external pollutant effects along with operational processes also pose problems in the development of sustainability in port management. For this reason, the environmental impacts of ports in institutional structures also develop as a subject for national action plans. All these processes, directly or indirectly, also show that energy as a basic component in ports requires conceptual management tools (Ng et al., 2013). Countries that consider this development demand as a growth tool have developed an approach defined as green growth. This conceptual demand, especially in European countries, European Union Directives, and international agreements and regulations, aims to improve the environmental awareness of ports in green port policies. This situation has also developed as a perspective that supports the development of continuous improvement and growth models in ports. This approach, which is actually dimensioned with six basic components, also supports structural sustainability in ports, as can be seen in Figure 1.

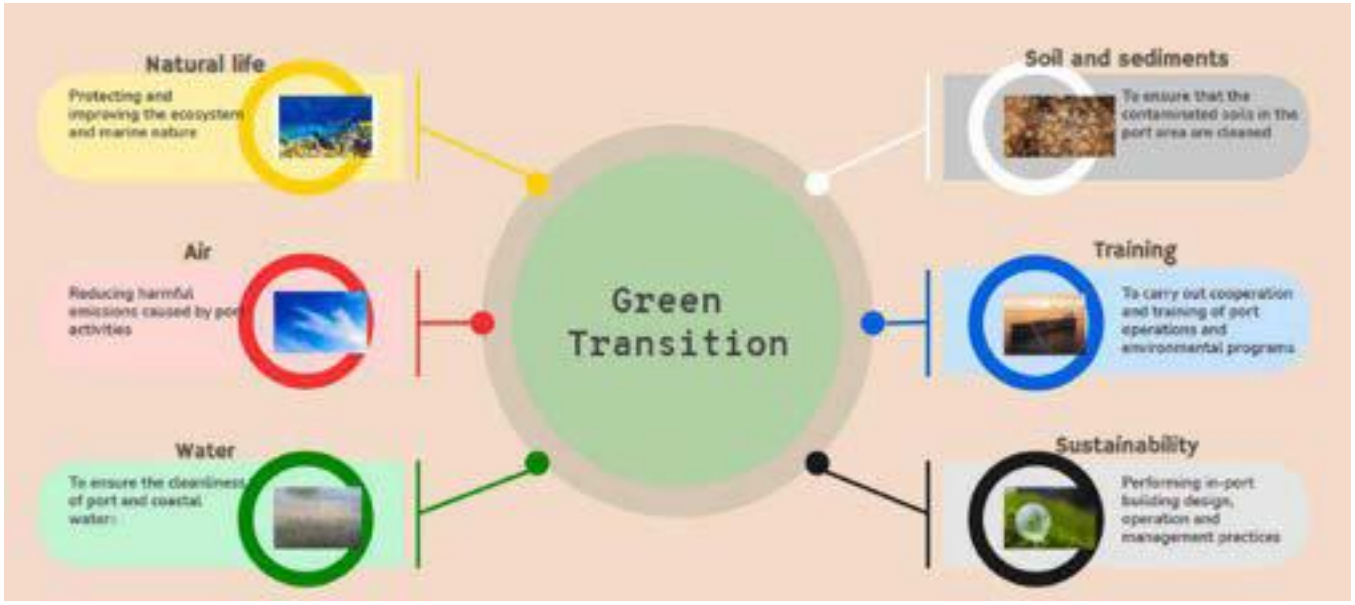

Fig. 1 Green transition in ports (Modified from TURKLIM, 2020)

III. Methodology

Improving economic and environmental sustainability in ports is primarily related to the manageability of entropy in energy, environment and related instruments for port operators. As a matter of fact, Sogut and Erdoğan (2022) presented the framework of the green port concept seen in Figure 2 with this approach.

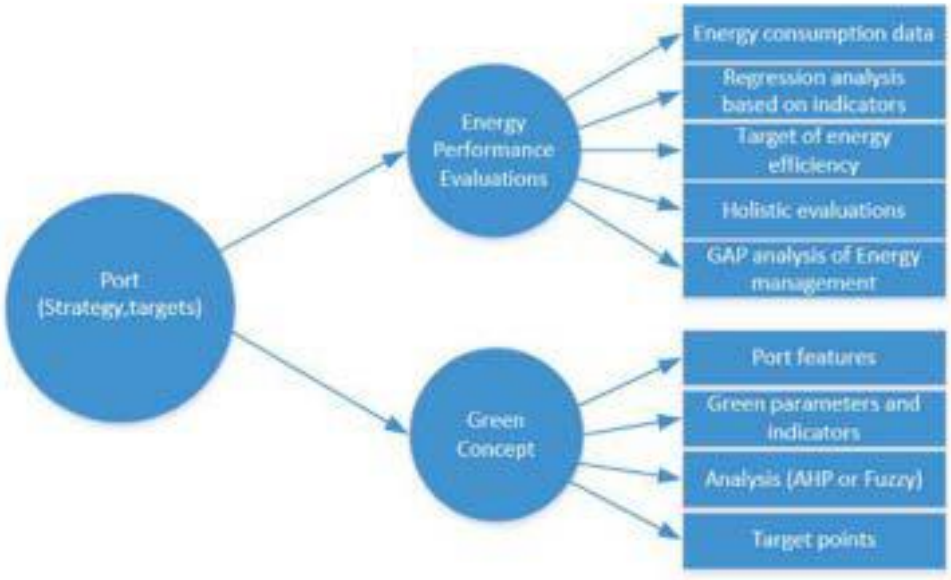

Fig. 2 Methodologic flow of green transition concept for ports

2

In the green port approach, while a managerial model is presented, entropy production due to exergy destruction in operational resources can also be developed within this structural model. This directly reveals the exergetic potential of energy in terms of performance management and also enables us to define the extent of port-related environmental pollution through entropy management. Therefore, first of all, defining entropy production for environmental sustainability is an engineering solution based on thermodynamics. However, its economic framework is a managerial framework of potential.

IV. Results and discussion

Ports, as living organisms, are regions with different structural areas and energy consumption behaviors depending on the load profile handled. Today, port authorities operate with different administrative structures and different systems, including the state and the private sector. Although energy consumption processes show different distributions according to port operations, sample consumption distributions are given in Figure 3.

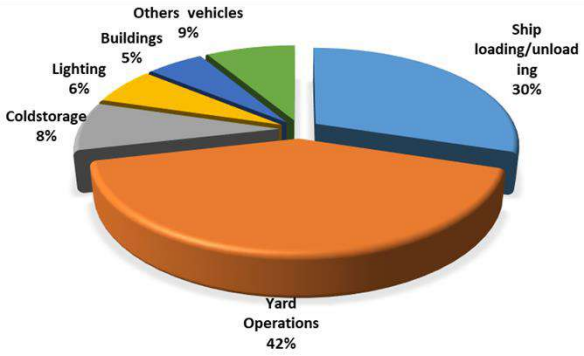

Fig. 3 Energy consumption distributions depending on functional structures in ports

Ports' energy consumption distributions are discussed together with their capacity loads. Exergy efficiencies based on the correlation between actual consumption data and demand consumption were examined. Due to their characteristics, ports have consumption differences in energy consumption depending on cargo handling. An approach was developed based on the boundary conditions for eight reference ports. For this purpose, the holistic annual consumption of each port for low and high conditions was taken as a basis and the efficiency in the ports was shaped as the ratio of demand to consumption. For this purpose, the calculated energy and exergy efficiency were evaluated separately and their distributions are given in Figure 4.

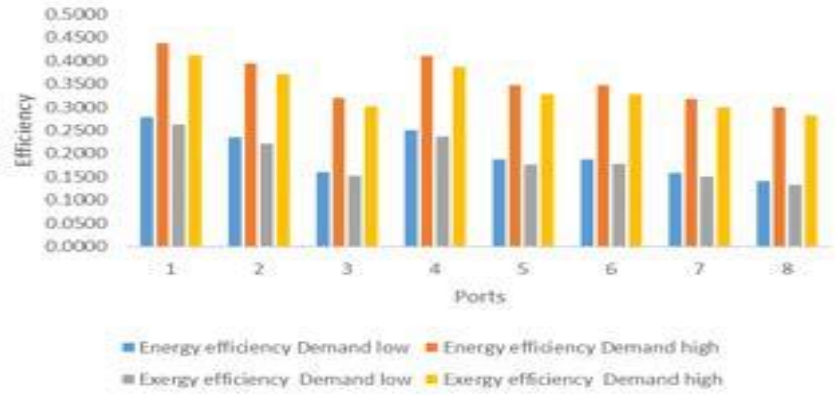

Fig.4 Energy and exergy efficiencies of on-demand ports

The main focus should be on inefficiencies in efficiency values, which should be taken into account in terms of energy costs and environmental impacts. In this context, the rates due to irreversibility were found to be 81.07% in the low-demand condition, while this value was found to be 66.15% in the high-demand condition. Although this process and its reasons represent a separate evaluation area, the main reason for irreversibility, especially in port operations, can be seen as operational problems. Exergy destruction caused by irreversibility is also the main reason for the entropy produced for such systems. This effect is the cause of both economic and environmental problems. Environmental impacts based on two parametric indexes developed for this purpose were examined and the results are given in Figure 5.

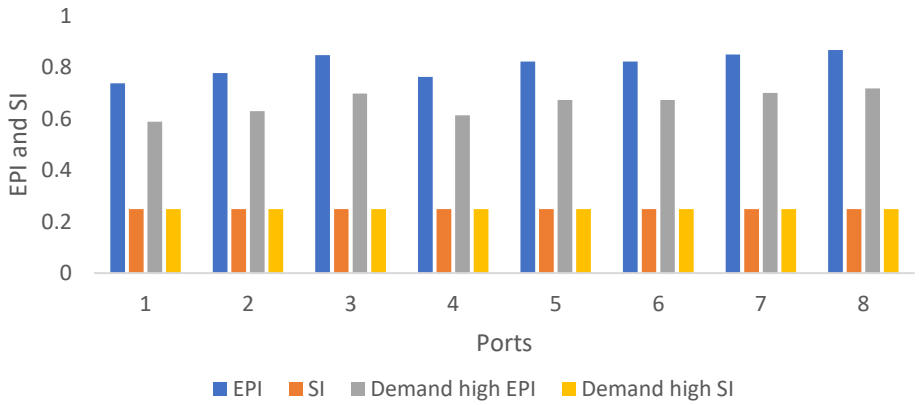

Fig. 5 EPI and SI distributions

The SI value developed according to the reversibility limit shows the boundary conditions for environmental impact. According to this degree, while low-demand management pollutes the environment 2.26 times more, this effect was found to be 1.66 in high-demand conditions. This situation shows the entropy effect, especially in terms of the environmental impact of energy. It shows

that they have the opportunity to improve this through institutional measures. This situation. In particular, it shows the energy efficiency rate that will be defined as a corporate target. The energy efficiency rate that will be defined as a corporate target against the total improvement potential in both conditions is given in Figure 6.

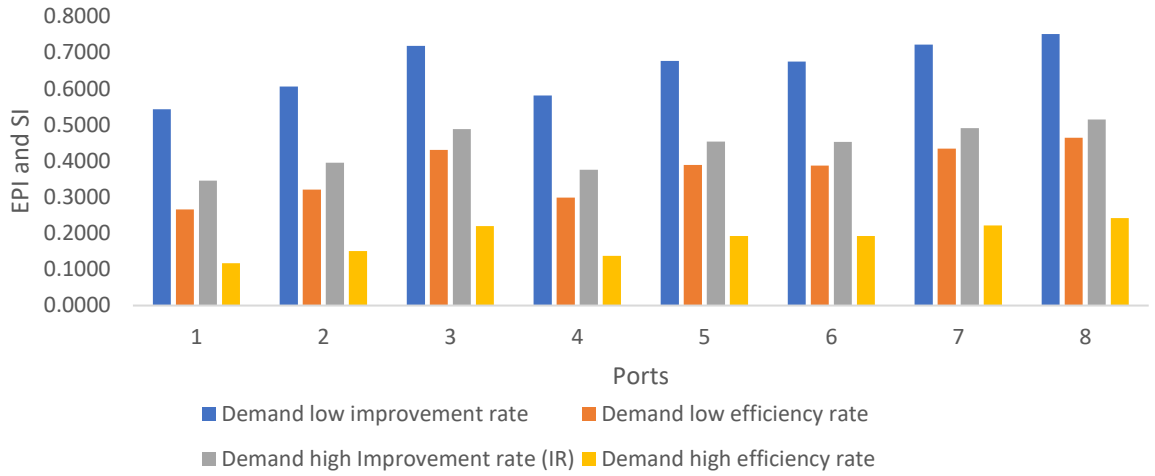

Fig. 6 Improvement and Efficiency rates

The analyses were examined in terms of consumption cost effects with 10-year scenarios for each port. According to the average inflation effect, price increases were taken as 50% and the inflation effect was taken as 40%. The increase in energy consumption in the business was evaluated as 17% by examining literature examples. In this context, while the total entropy cost for the ports region covers approximately 64.12% of the total cost, the cost impact of the possible efficiency rate was found to be 32.89%. This should be seen as the effect on the cumulative total. As a matter of fact, it should be seen as an effective efficiency approach despite the 17% consumption increase for the 10 years.

V. Conclusion

This study provides a framework for improving the economic and environmental manageability of energy in ports. In particular, it includes a potential evaluation of the energy consumption behavior of ports based on entropy over boundary conditions. Indeed, the average total exergy efficiency was found to be 19.14% and 34.06% in low and high-demand conditions. On the other hand, the environmental pollution potential due to entropy production was found to be 2.26 times higher than normal. Depending on energy and environmental sustainability, the energy efficiency potential for energy management in ports shows an average potential of 36.63%. An approach based on energy efficiency in port operations will provide significant gains.

References

Wg150, 2013. 'Sustainable Ports' A Guidance for Port Authorities. The World Association for Waterborne Transport Infrastructure Revision, 6.

Lei, W., Zhixiang, Z., Yang, Y., Jie, W., 2020. Green efficiency evaluation and improvement of Chinese ports: a cross-efficiency model. Transport. Res. Transport Environ. 88, 102590 https://doi.org/10.1016/j.trd.2020.102590. ISSN 1361-9209.

Oniszczuk-jastrząbek, A., Pawłowska, B., ve Czerma´nski, E., 2018. Polish sea ports and the Green Port concept. SHS Web of Conf. 57, 01023. September 18-20. Gdansk, Poland.

Moon, D.S.H., Woo, J.K., Kim, T.G., 2018. Green ports and economic opportunities. In: Froholdt, L. (Ed.), Corporate Social Responsibility in the Maritime Industry, WMU Studies in Maritime Affairs, 5. Springer, Cham. https://doi.org/10.1007/978-3-319-69143-5_10.

Badurina, P., Marijan, C., ˇCedomir, D., 2017. Contribution to the implementation of "Green Port" concept in Croatian seaports. Sci. J. Maritime Res. 31, 10–17. © Faculty of Maritime Studies Rijeka.

Ng, Adolf K.Y., Shu-Ling, C., Stephen, C., Ben, B., Zaili, Y., 2013. Climate change and the adaptation strategies of ports: the Australian experiences. Res. Transp. Bus. Manag. 8, 186–194. Oct.

TURKLIM, 2020. Green Port Policy. Regulation and Applications. TÜRKL˙IM - Turkey Port Operators Association. http://www.turklim.org/kport/yesil_liman/upload/Yesil-Liman-Turklim-Raporu.pdf.

Sogut. M: Z., Erdoğan O., An investigation on a holistic framework of green port transition based on energy and environmental sustainability, Ocean Engineering, Volume 266, Part 3, 2022, 112671, ISSN 0029-8018, https://doi.org/10.1016/j.oceaneng.2022.112671.

IEEES-156

Assessment of environmental pollution entropy-based approach of container ships in the ice-covered Arctic Ocean Route

[1]Oktay Cetin, [2]M. Ziya Sogut*, [3]Funda Yercan
[1,2,3]Piri Reis University, Tuzla, Istanbul Türkiye

*E-mails: ocetin@pirireis.edu.tr
mzsogut@gmail.com
fyercan@pirireis.edu.tr

Abstract

Maritime transportation, which is the basic building block of world trade, directly affects the global economy by meeting energy needs and sustainable environmental aspects. Ship technologies that generate power based on piston engine technology directly affect this process with their fossil fuel-based consumption. Arctic routes, which have emerged as an advantageous option in maritime transportation due to the effect of global warming, are an important issue that needs to be examined in terms of their effects on environmental sustainability due to pollution caused by irreversibility. This study, developed in this context, revealed the possible effects on the environment of an entropy-based evaluation in possible Arctic route preference. In the study, environmental impact assessment was discussed through two basic indicators developed based on entropy production. According to the current route features, the average energy efficiency was found to be 36.62%, while the exergy efficiency was found to be 33.60%. On the other hand, the impact of possible entropy production on environmental sustainability is approximately 1.65 times higher than it should be. Both indicators show that environmental degradation cannot be prevented, therefore improvement requires a process focused on decarbonization. At the end of the study, suggestions regarding route effects for sectoral decarbonization were developed.

Keywords: Maritime Management, Arctic Shipping, Efficiency, Environment, Sustainability.

I. Introduction

In parallel with the increase in environmental awareness, people's attention has started to focus on the Arctic Ocean region, where the ice has melted due to the effect of global warming in the last 50 years. With the acceleration of melting, it is predicted that the ice may completely melt in the summer months by 2040 and northern European countries may face the risk of flooding due to rising water levels by 2050 (Aksenov et al., 2017; Cheng et al., 2019). If the effects of global warming increase according to this forecast, new maritime trade routes in the Arctic Ocean, which can be used only in the summer months and limitedly with the help of nuclear icebreakers today, will continue to be used more intensively. The melting of sea ice in the Arctic Ocean has created new commercial opportunities for shipping companies, but also environmental problems. Melting ice in some parts of the Arctic Ocean that have been covered by sea ice for most of the year for centuries has opened up new shipping routes (Figure 1). The efforts of the countries in the region to have a say on new shipping routes are frequently on the agenda (Lasserre, 2014).

New maritime trade routes significantly shorten transportation distances. For example, ships currently sail approximately 10,850 nautical miles (20,100 km) between Asia (Busan) and Northern Europe (Rotterdam). If Arctic routes are used, this distance can be reduced to approximately 6,860 nautical miles (12,700 km). In this case, shipping companies will be able to make more trips (as ships will be able to complete their voyages in less time) and save fuel. This great economic advantage is attracting shipping companies to focus their attention on this region. The need for the support of icebreaker class ships may slightly reduce the possible profits of shipping companies (Zhang et al., 2016; Çetin and Büyüksağnak, 2021).

On the other hand, the use of Arctic routes may have some environmental impacts. There are many environmental problems related to oceans and seas. The most important ones are climate change, plastic pollution, overfishing, general marine pollution, oil spills, destruction of habitats, acidification of the seas, ship accidents, hunting of endangered species, and the failure to implement marine protected areas. However, it is clear that the public is not informed accurately and sufficiently about the importance of these hazards to which the marine environment is exposed, and the activities that need to be carried out regarding marine protection and sustainability (Easman et al., 2018). To prevent humanity from facing major disasters in the future, it is necessary to implement sustainable and consistent policies to first reduce and then eliminate these threats. Some studies on this subject in recent years suggest that ecosystem management should be addressed with a more holistic approach within the scope of marine environmental protection studies (Easman et al., 2018; Blau et al., 2015, Çetin, 2021).

This study presents a framework that evaluates the environmental impacts of energy-induced entropy production based on a container ship. In particular, the environmental impact of energy is discussed through two basic indicators.

II. Arctic route

"Arctic-Route" has developed as an alternative route and a solution that expresses change for many types of transportation, especially container transportation. Today, the competitive criteria of maritime transportation create significant problems in terms of time and energy costs in transportation costs. For this purpose, it is a sectoral choice. The Arctic solution developed as a transformation tool. Figure 1 shows the evolving Arctic shipping routes.

Figure 1. Arctic Shipping Routes (Humpert & Raspotnik, 2012)

Due to the increase in Arctic shipping, the number of ships and sailing hours in the Arctic Ocean are increasing. However, there are sectoral predictions that these newly opened routes may not be sustainable due to their high pollutant effects due to fuel and energy consumption.

III. Methodology

To address this issue, Sogut's (2021) Environmental Performance Index (EPI) and Sustainability Index (SI) were utilized to assess the potential environmental impacts. These indices consider the possibility of entropy caused by reversible and irreversible actions. In this context, the EPI is employed as follows:

$$EPI = \left(\frac{\sum S_{gen}}{\sum \dot{E}x_{in}}\right) * T_0 \quad (1)$$

The EPI is considered acceptable when it falls within the range of zero to one. A value near zero is beneficial in terms of environmental sustainability but zero cannot represent a true lower bound, as it does not consider the continuity of entropy generation or the requirement for the environment to be in a dead state for reversible processes to occur. The potential for improvement, which has been traditionally used, has been modified in this instance. The revised relationship is a result;

$$IP = (\eta_{Carnot} - \eta_{II}).(\dot{E}x_{in} - \dot{E}x_{out}) \quad (2)$$

The Sustainability Index (SI) employed in the research is a gauge of the entropy generated and the reversibility constraints of the system or process under scrutiny. SI; in this instance, is;

$$SI = \left(\frac{\sum S_{gen,c}}{\sum \dot{E}x_{in}}\right) * T_0 \quad (3)$$

This makes reducing entropy a crucial objective for supporting valid justifications for improving energy system efficiency, as represented by the energy efficiency ratio proposed in this study:

$$\theta = \frac{\sum (EPI\text{-}SI).IP}{\sum Ex_{in}} \quad (4)$$

The efficiency ratio derived from this formula can serve as a valuable target for companies or energy management units and can be based on more precise and accurate data. Additionally, it can function as institutional data to ensure that entropy is kept under control.

IV. Results and Discussions

In this study, the environmental sustainability effects of 11 container ships, which are taken as reference for Arctic routes that emerged due to global climate change, were examined. In the study, unlike environmental emission assessments, an entropy-based analysis was taken into account in terms of environmental impacts on ships. In this context, fuel consumption, energy and exergy efficiency and related entropy-based environmental indicators of the defined Arctic routes were evaluated for the reference ships. The reference ships are container ships engaged in international transportation with a capacity range between 18,000 DWT and 230,000 DWT and are actively operated in sectoral processes. In this study, the relationship between the power distributions of ships and their maximum speed distributions is stated partially proportionally. In contrast, the distributions do not conform directly to the parametric distribution associated with power. The power performance of ships is directly related to fuel consumption, and thermal efficiency is the quantitative measure based on the first law of thermodynamics. Exergy efficiency is a qualitative criterion that depends on environmental conditions and should be taken into account in terms of the irreversibility they cause. Holistic evaluation on ships is important in terms of environmental sustainability. In particular, efficiency effects related to engine power consumption also define the extent of fuel-induced irreversibility.

Although Arctic Ocean routes provide advantages in maritime transportation in terms of shortening the total range and voyage time, the average energy efficiency in terms of reference consumptions is 35.62%, while the exergy efficiency is found to be 33.60%. In the 10th container ship with a capacity of 24,765 DWT, where the highest efficiency was seen, energy and exergy efficiency were found to be 49.44% and 46.64%, respectively. This situation shows that it is a feature independent of load distributions. Although it is seen as an effect related to the icebreaker ship, the exergy destruction on the route and the entropy production caused by it also play a critical role. These inefficiencies are essentially a fuel-related polluting effect and rely on fossil-based consumption. Unlike the classical emission approach, entropy-based pollution dimensions were evaluated using two basic indices developed by Söğüt (2021). EPI evaluates the environmental extent of the impact relative to normal operating parameters, while SI takes into account Carnot values. Figure 2 shows the distribution of possible impacts of ships on routes based on these data.

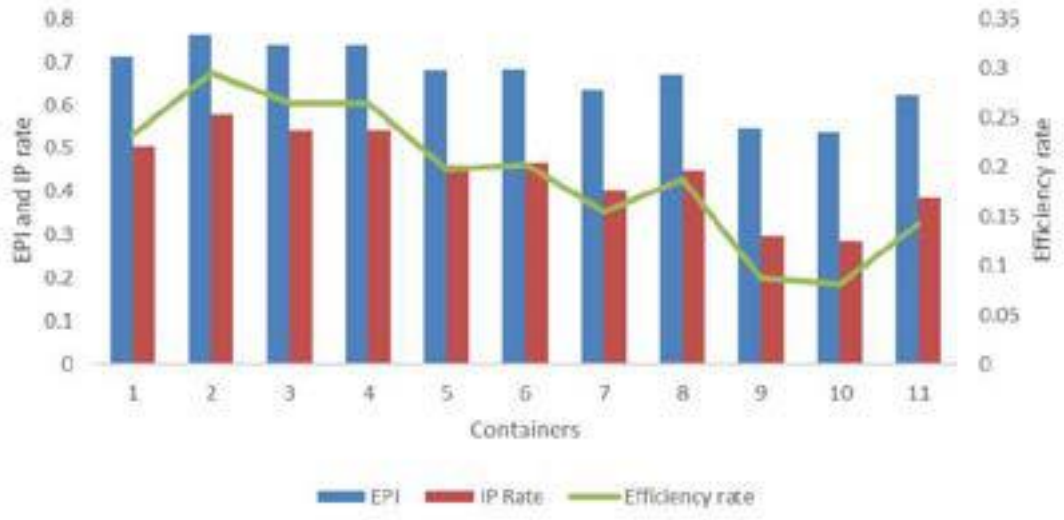

Fig.2 EPI and SI distributions with route-dependent Entropy generation

In the context of structures utilising fossil fuels, their potential environmental impact needs to be assessed. The EPI provides insight into the potential inefficiency of such structures, while the SI defines the boundary conditions to be considered. It can be seen that the utilisation of maritime trade routes in the Arctic Ocean by container ships would result in a significant pollution potential in terms of environmental impact due to the average EPI value of 0.66. Especially considering that the SI value is 0.25, it is seen that the pollution effect is approximately 1.66 times higher than the reference value.

V. Conclusion

Entropy analyzes based on the exergetic approach referenced in this study have revealed a framework for Arctic Ocean routes. The examined indicators show that, based on an exergy efficiency of 33.60%, the environmental sustainability impact creates a higher pollution level of 1.65 based on the direct irreversibility criterion. The approach developed in this study can be considered a direct entropy-based impact analysis. For this reason, the two indicators examined in terms of environmental impact can be seen as a new

approach framework.Entropy analyses based on the exergetic approach referenced in this study provided a framework for Arctic routes. The examined indicators show that due to an exergy efficiency of 33.60%, the environmental sustainability impact creates a higher pollution of 1.65 depending directly on the irreversibility criterion The approach developed in this study can be considered as a direct entropy-based impact analysis. For this reason, two indicators examined in terms of environmental impact can be seen as a new approach framework.

References

Aksenov, Y., Popova, E., Yool, A., Nurser, A., Williams, T., Bertino, L., & Bergh, J. (2017), On The Future Navigability of Arctic Sea Routes: High-Resolution Projections of the Arctic Ocean and Sea Ice. *Marine Policy*, 75, 300-317.

Blau, J., Green, L. (2015). Assessing the impact of a new approach to ocean management: evidence to date from five ocean plans, Marine Policy 56 (2015) 1–8, doi.org/10.1016/j.marpol.2015.02.004.

Cheng, L., Abraham, J., Hausfather, Z., & Trenberth, K. (2019), How fast are the oceans warming? *Science*, 363(6423), p.128-129.

Çetin and Büyüksağnak (2021), Turkey's interest in the Arctic region: the evaluation of being a party to the Svalbard Treaty. International Journal of Environment and Geoinformatics (IJEGEO), 8(3):350-358. doi. 10.30897/ijegeo.887540

Çetin, O. (2021). Relationship with Marine Environmental Consciousness and Maritime Culture in Turkey. International Journal of Environment and Geoinformatics (IJEGEO), 8(3):245-255. doi. 10.30897/ijegeo.862055

Easman, Emily S., Abernethy, Kirsten E., Godley, Brendan J. (2018). Assessing public awareness of marine environmental threats and conservation efforts. Marine Policy, 234-240.

Humpert and Raspotnik (2012). Arctic Year Book. Retrieved (15 November 2023) from https://arcticyearbook.com/images/yearbook/2012/Scholarly_Papers/14.Humpert_and_Raspotnik.pdf

Lasserre, F. (2014), Case studies of shipping along Arctic routes. Analysis and profitability perspectives for the container sector. *Transportation Research Part A: Policy and Practice*, 66, p.144-161.

Cabal, C., (2008), Optimisation energetique de l'etage d'adaptation electronique dedie a la conversion photovoltaique, UPS. Toulouse III, These.

Challa, D., Raghavendar, I., (2012), Implementation of Incremental Conductance MPPT With Direct Control Method Using Cuk Converter, Intern. J. of Mod. Eng. Res., Vol.2 Issue 6.

Dolara, A., Faranda, R., Leva, S., (2009), Energy comparison of seven MPPT techniques for systems" J.Electromagnetic Analysis & Application, 3:152-162.

Hussein, K.H., Muta, I., Hoshino, T., Osakada, M., (1995), Maximum photovoltaic power tracking: an algorithm for rapidly changing atmospheric conditions", IEE Proc. Generation Transmission Distrib. 142 (1), pp. 59–64

Kim, I. S., Kim, M. B., Youn, M. J., (2006), New maximum power point tracker using sliding-mode observer for estimation of solar array cu in the grid-connected photovoltaic system, IEEE Trans. on Ind. Elect., vol. 53, no. 4, pp. 1027-1035.

Rifa, I., Ratnaıka, Pemodelandan, P., (2012), Analisis Panel Photovoltaik, Conf. Inf., Telecom. Elec. Eng. UGM Yogyakarta.

Sera, D., Kerekes, T., Teodorescu, R., Blaadjerg, F., (2006), Improved MPPT Algorithms for rapidly Changing Environmental Conditions, Pow. Elect. and Motion Control Conf. , EPE-PEMC 2006. 12th Inter., pp. 1614-1619, Aug. 2006. 1, 3–13.

Sogut M. Ziya (2021) New approach for assessment of environmental effects based on entropy optimization of jet engine, Energy, Volume 234, 2021, 121250, ISSN 0360-5442, https://doi.org/10.1016/j.energy.2021.121250.

Veerachary, M., Shinoy, K.S., (2005), V2 nonlinear PV sources, IEE Proceedings vol. 152, no. 5, pp. 1263-1270.

IEEES-157

Heavy Metal Phytoremediation Using Energy Crops in Surface Soil of an Industrial Zone

1*Muhammed Baştuğ, 1Hatice Eser Ökten, 1Hale Demirtepe
1 İzmir Institute of Technology, Faculty of Engineering, Urla, İzmir, 35430, Türkiye
* E-mails: muhammedbastug@iyte.edu.tr, haticeokten@iyte.edu.tr, haledemirtepe@iyte.edu.tr

Abstract

Industrialization has caused heavy metal contamination of soil due to direct discharges of wastes and wastewater and atmospheric deposition of particles. To eliminate heavy metal pollution in the soil, phytoremediation has emerged as a sustainable removal technology since it is more economical and less destructive compared to physical and chemical remediation technologies. Moreover, phytoremediation using energy crops provides an opportunity to achieve soil remediation and bio-based energy production at the same time. However, studies on comparing the heavy metal removal potential of different plants and the simultaneous removal of several heavy metal species remained limited. Hence, this study aims at identifying the potential of three energy crops to remediate soils contaminated by eight heavy metals. In the 61-day pot study, Common Reed, Canola, and Safflower were used to remove heavy metals from the surface soils taken from Izmir Aliağa Industrial Zone. Soils with different pollution levels were used in the study to see the effect of plants on different pollution conditions. Heavy metal concentrations in soil and plants were determined by inductively coupled plasma with mass spectrometry (ICP-MS). The highest average removal efficiencies of Cr, Mn, Ni, Co, Cu, Zn, Cd, and Pb metals in the soil were found to be 13.55%, 15.75%, 12.87%, 7.48%, 17.81%, 46.64%, 15.23%, and 16.6%, respectively. Additionally, the highest average bioconcentration factors were 8.62, 5.67, 8.46, 5.53, 8.52, 28.59, 2.54, and 2.84, respectively. When the success of the studied plants in removing 8 heavy metals under different pollution conditions was scored, safflower received the highest score in total and common reed the lowest score. To conclude, the energy crops used in the study removed heavy metals remarkably in a short period, revealing their potential for sustainable phytoremediation of contaminated soils. Further studies are needed to investigate their energy production potential.

Keywords: energy crops, heavy metals, phytoremediation, soil, sustainability

I. Introduction

Soil heavy metal pollution is a significant environmental issue with far-reaching impacts for food safety, human health, and ecological balance. The effects of soil heavy metal pollution are seen more frequently, especially in regions where heavy industry and mining activities occur, and in agricultural areas where pesticide use is intensive. Various methods are employed to remediate soil contaminated by heavy metals, each having its own approach and effectiveness. These methods include physical, chemical, and biological remediation techniques, as well as innovative approaches such as phytoremediation and electrokinetic remediation (Akhtar et al., 2020). Phytoremediation, a technique that uses plants to remove pollutants, has gained attention as a green and cost-effective method for remediating heavy metal-polluted soils. Phytoremediation encompasses various mechanisms, including phytoextraction, phytostabilization, phytovolatilization, and rhizofiltration, which contribute to the removal and containment of heavy metals in the soil (Shi et al., 2023). The use of energy crop plants in the phytoremediation of heavy metals is a crucial strategy for the remediation of contaminated soils. Several plant species have been identified for their potential in phytoremediation due to their ability to absorb and eliminate heavy metals from the soil. Some of the notable energy crop plants used in phytoremediation include sunflower (*Helianthus annuus*), canola (*Brassica napus*), willow (*Salix spp*), and common reed (*Phragmites australis*) (Pandey et al., 2016; Šyc et al., 2012; Yazdanbakhsh et al., 2020). The limited studies on heavy metal phytoremediation using energy plants have hindered the advancement of this field. This lack of research has resulted in a limited understanding of the potential of energy plants in effectively removing heavy metals from contaminated soils.

Studies on safflower heavy metal phytoremediation potential has yielded promising results as both a bioenergy product and a good accumulator of heavy metals such as Cd, Pb, Ni, and Zn (Ciaramella et al., 2022). Moreover, Safflower presents itself as a viable alternative for cultivation in dry agricultural regions, owing to its exceptional resistance to both cold and heat stress. In addition, canola has an inherent capacity to uptake and accumulate heavy metals from the soil. These metals include but are not limited to Cd, Zn, and Cu (Rossi et al., 2002). Canola oil, derived from canola seeds, serves as the primary raw material for biodiesel production (Qiu et al., 2011). Common reed has also been studied extensively for its ability to remove heavy metals from soil and water. It showed higher accumulative capacities for heavy metals such as Cu, Cd, Cr, Ni, Fe, and Pb compared to another plant species (Prica et al., 2019).

The aim of the current work is to determine an ideal plant species that can be used in the remediation of multiple heavy metals, especially in industrially polluted soils, using energy crop plants. In this context, three energy crops known as safflower (*Carthamus tinctorius*), canola (*Brassica napus*), and common reed (*Phragmites australis*) were used. These plants were potted for 61 days using soils with varying contamination level. In the study, bioconcentration factors (BCF) and translocation factors (TF) of plants for Cr, Mn, Ni, Co, Cu, Zn, Cd, and Pb, heavy metal accumulation in roots and aboveground parts, and heavy metal removal efficiencies were examined. By this way, among the three energy plants, the most ideal plant for multiple heavy metal remediation was proposed.

II. Experimental Procedure/Methodology/System Description

Soil samples with 3 different heavy metal concentrations were used in the pot experiments, namely X, Y, and Z. Soil X was the soil taken from the Kozak plateau, İzmir, which was considered as a background area of industrial contamination. Soil Z was taken

from the Aliağa industrial zone, İzmir. Soil Y was the soil obtained by mixing the soil taken from the X and Z points in equal proportions. In each soil type, three different plants were studied as triplicates. In the study, pots with a diameter of 20 cm and a height of 17 cm were used. Each of the 27 planted pots contained 850 gr soil. A total of 30 pots were left outdoors for a 61-day growing period. During this process, all 3 control pots were left in the same conditions as the other plants, and they were irrigated with tap water with together other pots at each time. Figure 1 shows the layout of the pot experiment.

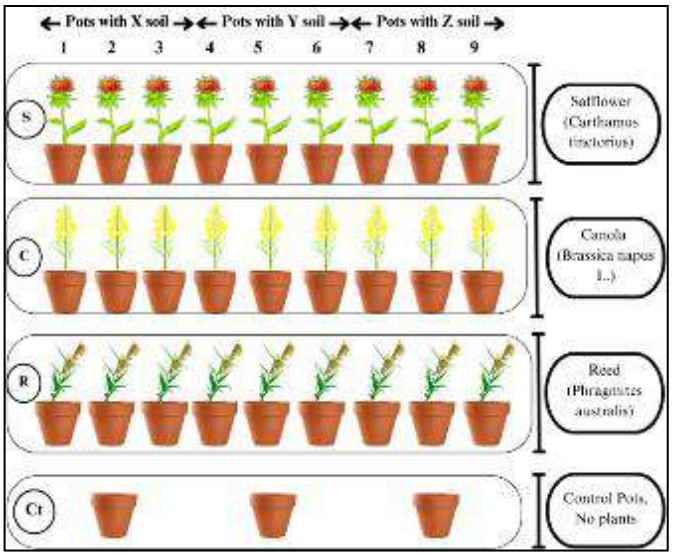

Fig. 1: The Layout of The Pot Experiment
(S: Safflower, C: Kanola, R: Reed, Ct: Control, X: Kozak Plateau Soil, Y: Aliağa Soil, Z: Equal Portion Mixture of X and Y)

At the end of the 61-day growth period, the plants were harvested to take samples of the roots and above-ground parts of the plants. The plant samples brought to the laboratory after the harvest were washed with tap water and distilled water, then wrapped with aluminum foil and dried at 60 °C for 36 hours. Then, the plant samples were passed through a hand rondo to make the digestion process of the samples more efficient. For the digestion of plant samples, a 0.5 g sample in Teflon containers was microwaved at 200 °C for 20 minutes with 10 ml of 65% HNO_3 (Merck-100456.2500). For the digestion of soil samples, 10 mL of nitric acid and 2 mL of hydrogen peroxide were used. The digested samples were centrifuged with a Hettich Rotina 38R centrifuge at 9000 RCF for 30 minutes and then the supernatant was collected. The heavy metal concentrations of soil and plant samples were determined by Agilent 7850 Inductively Coupled Plasma Mass Spectrometry (ICP-MS).

III. Analysis

In the study, translocation factor (TF) and bioconcentration factor (BCF) were used to determine whether plants are phytostabilizers or phytoextractors (Ang et al., 2023). The bioconcentration factor expresses the ratio of the metal concentration in the above-ground parts of the plant to the metal concentration in the soil. A BCF value greater than 1 generally indicate the potential of a plant species for phytoremediation, while plants with both BCF and TF values greater than 1 can be considered as phytoextractors. However, plants with a BCF value greater than 1 and a TF value less than 1 are classified as phytostabilizers (Ma et al., 2020). The calculation of BCF is shown in equation (1) (Ciaramella et al., 2022). The translocation factor is the ratio of the metal concentration in the plant green part to the root metal concentration as stated in Equation 2 (Ciaramella et al., 2022).

$$\mathrm{BCF} = \left(\frac{\text{Metal Concentration in the Plant}}{\text{Metal Concentration in the Soil}}\right) \quad (1)$$

$$\mathrm{TF} = \left(\frac{\text{Metal Conc.in the Above Ground Parts of the Plant}}{\text{Root Metal Conc.}}\right) \quad (2)$$

The results of the study were given as mean±RSD. In addition, Pearson correlation between heavy metal uptake of different plant parts and soil characteristics parameters were determined by using OriginPro 2023b along with 'Correlation Plot App', and correlation matrices were constructed in this regard.

IV. Results and discussion

Among the soils used in pots, the soil from the Aliağa region had the highest organic matter percentage and nutrient content. Since the plants used in the study are hyperaccumulator plants that are tolerant to heavy metals, the highest biomass production was achieved in pots using soil from the Aliağa region. As seen in Figure 2 the plant that produced the highest biomass was canola, with an average of approximately 106.7 g.

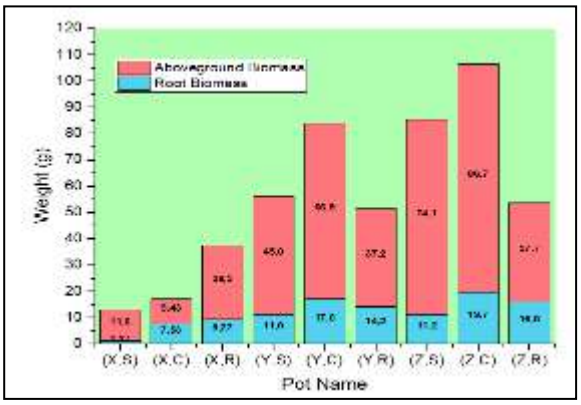

Fig. 2. Average Dry Weight of Plants in Pot Study
(S: Safflower, C: Kanola, R: Reed, X: Kozak Plateau Soil, Y: Aliağa Soil, Z: Equal Portion Mixture of X and Y)

Table 1 shows the highest removal efficiencies, BCF, and TF values of 8 heavy metals removed in the pot study for 3 different plant species. As seen in Table 1, when a comparison was made based on heavy metal removal efficiency, canola and safflower performed better in terms of removing multiple heavy metals. Safflower showed the best performance in terms of accumulation in roots and aboveground parts in general. As a result of the phytoremediation performance evaluation using BCF and TF, safflower revealed to be a good option for the removal of multiple metals from soil. It was also revealed that all three plants have phytostabilizing properties in general. Figure 3 a) shows the correlation matrix showing the relationship between heavy metal accumulation in the aboveground parts of the plants used in the study and soil properties. It was revealed that there was a positive relationship between the conductivity of the soil, the percentage of organic matter, the percentage of nitrogen, the amount of lime, phosphorus, and potassium, and the copper accumulation in the aboveground parts of the plant. It was also revealed that there was a positive relationship between pH in the soil and the concentration of chromium accumulated in the aboveground parts of the plant.

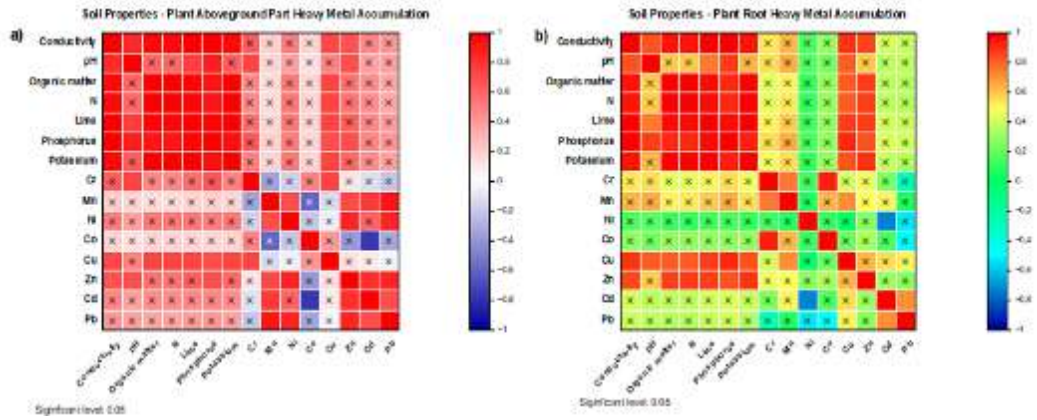

Fig. 3. Soil Properties and Heavy Metal Uptake of the Plants Correlation Matrix
(x sign: insignificant relationship)

Figure 3 b) shows the correlation matrix showing the relationship between heavy metal accumulation in the roots of the plants used in the study and soil properties. it was also revealed that there was a positive relationship between soil conductivity, organic matter percentage, nitrogen percentage, pH, amount of lime, phosphorus and potassium, and copper accumulation in the roots of plants.

Table 1. Highest Removal Efficiency, BCF, and TF Values for Heavy Metals in Pot Study
(S: Safflower, C: Kanola, R: Reed, X: Kozak Plateau Soil, Y: Aliağa Soil, Z: Equal Portion Mixture of X and Y)

Heavy Metals	**The Highest BCF**		**The Highest TF**		**The Highest Removal Efficiency**	
Text	**Pot Name**	**Mean Value**	**Pot Name**	**Mean Value**	**Pot Name**	**Mean Value**
Cr	*(X, C)*	*8,6*	*(X, R)*	*6,4*	*(Y, C)*	*13,5*
Mn	*(X, S)*	*5,67*	*(X, C)*	*1,08*	*(Z, S)*	*15,7*
Ni	*(X, R)*	*8,45*	*(Z, S)*	*0,67*	*(Y, R)*	*12,9*
Co	*(X, C)*	*5,53*	*(Z, R)*	*1,36*	*(Z, C)*	*7,5*
Cu	*(X, C)*	*11,1*	*(X, C)*	*0,27*	*(Z, C)*	*27,5*
Zn	*(Z, S)*	*28,6*	*(Y, S)*	*3,11*	*(X, C)*	*46,6*
Cd	*(X, S)*	*2,54*	*(Z, S)*	*1,19*	*(Z, S)*	*15,2*
Pb	*(X, S)*	*2,8*	*(Z, S)*	*0,99*	*(Z, S)*	*18,7*

V. Conclusion

The results revealed that when three energy crops were compared, safflower showed the highest performance under multiple heavy metal pollution. The fact that safflower can be used in biodiesel production and is highly resistant to drought conditions indicated that it might be an ideal plant for the sustainable remediation of multiple heavy metal pollution, especially in places under the influence of the Mediterranean climate, such as İzmir. From this perspective, the use of energy crops such as safflower, especially in areas affected by heavy industrial zones, can help obtain energy raw materials from soils that are not suitable for food production.

Acknowledgments
The authors would like to acknowledge the Environmental Development, Application, and Research Center, for the analysis of heavy metals.

References

Akhtar, F.Z., Archana, K.M., Krishnaswamy, V.G., Rajagopal, R., 2020. Remediation of heavy metals (Cr, Zn) using physical, chemical and biological methods: a novel approach. SN Appl Sci 2. https://doi.org/10.1007/s42452-019-1918-x

Ang, S.Y., Goh, H.W., Mohd Fazli, B., Haris, H., Azizan, N.A., Zakaria, N.A., Johar, Z., 2023. Heavy Metals Removal from Domestic Sewage in Batch Mesocosm Constructed Wetlands using Tropical Wetland Plants. Water (Switzerland) 15. https://doi.org/10.3390/w15040797

Ciaramella, B.R., Corinzia, S.A., Cosentino, S.L., Testa, G., 2022. Phytoremediation of Heavy Metal Contaminated Soils Using Safflower. Agronomy 12. https://doi.org/10.3390/agronomy12102302

Ma, H., Shi, G., Cheng, Y., 2020. Accumulation characteristics of metals and metalloids in plants collected from ny-Ålesund, arctic. Atmosphere (Basel) 11. https://doi.org/10.3390/atmos11101129

Pandey, V.C., Bajpai, O., Singh, N., 2016. Energy crops in sustainable phytoremediation. Renewable and Sustainable Energy Reviews 54, 58–73. https://doi.org/10.1016/j.rser.2015.09.078

Prica, M., Andrejić, G., Šinžar-Sekulić, J., Rakić, T., Dželetović, Ž., 2019. Bioaccumulation of heavy metals in common reed (Phragmites australis) growing spontaneously on highly contaminated mine tailing ponds in Serbia and potential use of this species in phytoremediation. Bot Serb 43, 85–95. https://doi.org/10.2298/BOTSERB1901085P

Qiu, F., Li, Y., Yang, D., Li, X., Sun, P., 2011. Biodiesel production from mixed soybean oil and rapeseed oil. Appl Energy 88, 2050–2055. https://doi.org/10.1016/j.apenergy.2010.12.070

Rossi, G., Figliolia, A., Socciarelli, S., Pennelli, B., 2002. Capability of Brassica napus to accumulate cadmium, zinc and copper from soil. Acta Biotechnol 22, 133–140. https://doi.org/10.1002/1521-3846(200205)22:1/2<133::AID-ABIO133>3.0.CO;2-3

Shi, J., Qian, W., Jin, Z., Zhou, Z., Wang, X., Yang, X., 2023. Evaluation of soil heavy metals pollution and the phytoremediation potential of copper-nickel mine tailings ponds. PLoS One 18. https://doi.org/10.1371/journal.pone.0277159

Šyc, M., Pohořelý, M., Kameníková, P., Habart, J., Svoboda, K., Punčochář, M., 2012. Willow trees from heavy metals phytoextraction as energy crops. Biomass Bioenergy 37, 106–113. https://doi.org/10.1016/j.biombioe.2011.12.025

Tallapragada, S., Lather, R., Vandana, Singh, G., 2021. Scope and future perspectives of phytoremediation. Int J Plant Sci 16, 77–85. https://doi.org/10.15740/has/ijps/16.aaebssd/77-85

Yazdanbakhsh, A., Alavi, S.N., Valadabadi, S.A., Karimi, F., Karimi, Z., 2020. Heavy Metals Uptake of Salty Soils by Ornamental Sunflower, Using Cow Manure and Biosolids: A Case Study in Alborz city, Iran. Air, Soil and Water Research 13. https://doi.org/10.1177/1178622119898460

Zhang, M., Wang, X., Yang, L., Chu, Y., 2019. Research on progress in combined remediation technologies of heavy metal polluted sediment. Int J Environ Res Public Health 16. https://doi.org/10.3390/ijerph16245098

IEEES-158

Simplified Method for Predicting Hourly Global Solar Radiation Distribution

[1*] Can Coskun, [1]Görkem Berkay Ergeç, [1]Didem Sena Aksu, [1]Zuhal Oktay
[1] Mechanical Engineering Department, Faculty of Engineering, İzmir Democracy University, İzmir, Turkey

* E-mails: dr.can.coskun@gmail.com, ergec293@hotmail.com, didemaksu.06.13@gmail.com, zuhal.oktay@gmail.com

Abstract

Until recently, long-term solar radiation data were needed to determine the hourly solar radiation distribution. With a new approach introduced in the literature, it is possible to reach the desired solar radiation distribution for that region by knowing only the annual total solar radiation amount. The method of calculating hourly solar radiation amounts using the distribution function created for Turkey is presented in this study. The calculation methodology is very easy and allows people with limited knowledge about solar energy to use it easily.

Keywords: Solar radiation, Solar energy, Synthetic Hourly Solar Radiation

I. Introduction

The increasing use of solar power as a source of electricity has led to increased interest in forecasting short time solar radiation. Forecasted short time solar radiation data is generally used for simulation of the solar power plants such as photovoltaic and concentrating solar power systems (Reikard, 2009, Laslett et al., 2014). The hourly solar-radiation amount is one of the important parameters for design and efficient operation of solar-energy systems. Forecasting short time solar radiation is neither completely random nor deterministic. It is necessary to know the possible short time trend of weather data such as solar radiation, outdoor temperature and wind speed for solar power plant simulations of energy and economics (Knight et al., 1991). In this respect, many researchers have focused on new models to generate synthetic hourly data. Laslett et al. (Laslett et al., 2014) developed an algorithm to generate synthetic hourly cloudiness data for any time of the year at any location in the southwest region of Western Australia (WA). In their study, hourly cloudiness data was generated from the daily values using a first order auto regression algorithm with time varying mean and standard deviation. Yang and Koike (Yang and Koike, 2002) developed a numerical model to estimate global solar irradiance from upper-air humidity. In their study, a sky clearness indicator was parameterized from relative humidity profiles. Numerical model was tested at 18 sites in Japan, and hence the relationship between global solar radiation and sky clearness indicator was investigated. They found that global solar radiation strongly depends on the sky clearness indicator. Gordon Reikard (Reikard, 2009) compared the Autoregressive Integrated Moving Average (ARIMA), Unobserved Components models, transfer functions, neural networks, and hybrid models to predict solar radiation at high resolution. He noticed that the best results are obtained using the ARIMA in logs, with time-varying coefficients. Chandel and Aggarwal (Chandel and Aggarwal, 2011) tested two models for estimation of hourly solar radiation in Western Himalayas. Many individual studies (Singh et al., 1997, Parishwad et al., 1997, Hussein, 2012, Yang and Koike, 2005) have been carried out in recent years on testing current models for different locations of the world.

Many models proposed to literature for the prediction of solar radiation are utilized existing climatic-parameters, such as cloud cover, sunshine duration, relative humidity and outdoor temperatures. Controversially, Can and Oktay (Can and Oktay, 2019) have been developed a model for prediction hourly and daily solar radiation based on total annual global solar radiation parameter. In the present study, we tested the reliability of the model by utilizing actual solar data available for Turkey.

II. Coskun and Oktay Model for Hourly Solar Radiatio

The hourly average global solar radiation of any time on a horizontal surface (I_H) in kW/m^2 can be estimated using the following equation;

$$I_H(t, dy, I_T) = a \cdot b \cdot \exp\left(\frac{-[t-c]^2}{2 \cdot d^2}\right) \quad (1)$$

In Equation (1), dy is the number of the day with count starting on January 1st. While the first day of January is dy =1, for the last day of December this value is 365 in the formula t indicates hour of the day. I_T is annual total solar radiation amount in kWh/m^2.year. The daily total global solar radiation on a horizontal surface (I_D) in kWh/m^2 can be estimated using the following equation;

$$I_D = \int_5^{21} I_H \cdot dt = \int_5^{21} a \cdot b \cdot \exp\left(\frac{-[t-c]^2}{2 \cdot d^2} \right) \cdot dt \quad (2)$$

Model paremeters for Turkey can be found by the equations below:

$$a = -6.47255533646 + 2.64499284473 \cdot 10^{-2} \cdot SR_{AA} - 3.68859978191 \cdot 10^{-5} \cdot SR_{AA}^{\ 2} + 2.53327237263 \cdot 10^{-8} \cdot SR_{AA}^{\ 3} - 8.56828030062 \cdot 10^{-12} \cdot SR_{AA}^{\ 4} + 1.14215701185 \cdot 10^{-15} \cdot SR_{AA}^{\ 5} \quad (3)$$

$$b = g + h \cdot \mathrm{Cos}(j \cdot dy + k) \quad (4)$$

$$g = 1.80300324597 \cdot 10^{4} - 46.6876827855 \cdot SR_{AA} + 4.56058396451 \cdot 10^{-2} \cdot SR_{AA}^{\ 2} - 1.93807902043 \cdot 10^{-5} \cdot SR_{AA}^{\ 3} + 3.04217557074 \cdot 10^{-9} \cdot SR_{AA}^{\ 4} \quad (5)$$

$$h = 1.68824486203 \cdot 10^{3} - 8.03193915952 \cdot SR_{AA} + 1.09963388231 \cdot 10^{-2} \cdot SR_{AA}^{\ 2} - 5.61575281081 \cdot 10^{-6} \cdot SR_{AA}^{\ 3} + 9.75941791105 \cdot 10^{-10} \cdot SR_{AA}^{\ 4} \quad (6)$$

$$j = 0.164780150638 - 3.69286290098 \cdot 10^{-4} \cdot SR_{AA} + 3.33562517725 \cdot 10^{-7} \cdot SR_{AA}^{\ 2} - 1.29948799213 \cdot 10^{-10} \cdot SR_{AA}^{\ 3} + 1.83616202997 \cdot 10^{-14} \cdot SR_{AA}^{\ 4} \quad (7)$$

$$k = 3.07186731215 - 7.29057853188 \cdot 10^{-3} \cdot SR_{AA} + 2.22327251699 \cdot 10^{-6} \cdot SR_{AA}^{\ 2} \quad (8)$$

$$c = 12.6921252445 + 0.21148171825 \cdot \mathrm{Cos}(0.0207537604614 \cdot dy - 3.73567688657) \quad (9)$$

$$d = l + m \cdot \mathrm{Cos}(n \cdot dy + p) \quad (10)$$

$$l = -42.3695859121 + 0.121453134826 \cdot SR_{AA} - 1.21712391834 \cdot 10^{-4} \cdot SR_{AA}^{\ 2} + 5.33992381107 \cdot 10^{-8} \cdot SR_{AA}^{\ 3} - 8.63315621218 \cdot 10^{-12} \cdot SR_{AA}^{\ 4} \quad (11)$$

$$m = -26.8947926096 + 7.27191943559 \cdot 10^{-2} \cdot SR_{AA} - 7.15213685864 \cdot 10^{-5} \cdot SR_{AA}^{\ 2} + 3.07986310837 \cdot 10^{-8} \cdot SR_{AA}^{\ 3} - 4.88955117317 \cdot 10^{-12} \cdot SR_{AA}^{\ 4} \quad (12)$$

$$n = 0.555251443826 - 1.40928564028 \cdot 10^{-3} \cdot SR_{AA} + 1.36740867243 \cdot 10^{-6} \cdot SR_{AA}^{\ 2} - 5.81017686505 \cdot 10^{-10} \cdot SR_{AA}^{\ 3} + 9.10938734424 \cdot 10^{-14} \cdot SR_{AA}^{\ 4} \quad (13)$$

$$p = -112.640927302 + 0.28162712307 \cdot SR_{AA} - 2.67400324374 \cdot 10^{-4} \cdot SR_{AA}^{\ 2} + 1.11034109891 \cdot 10^{-7} \cdot SR_{AA}^{\ 3} - 1.6998037957 \cdot 10^{-11} \cdot SR_{AA}^{\ 4} \quad (14)$$

III. Implementation of the model for Turkey

By using the hourly solar energy distribution function (Eq.1), the total amount of solar energy could be determined in 10 W intervals depending on the amount of solar radiation. Distribution of solar energy amount for 10 W solar radiation interval is given in Fig.1 for Turkey.

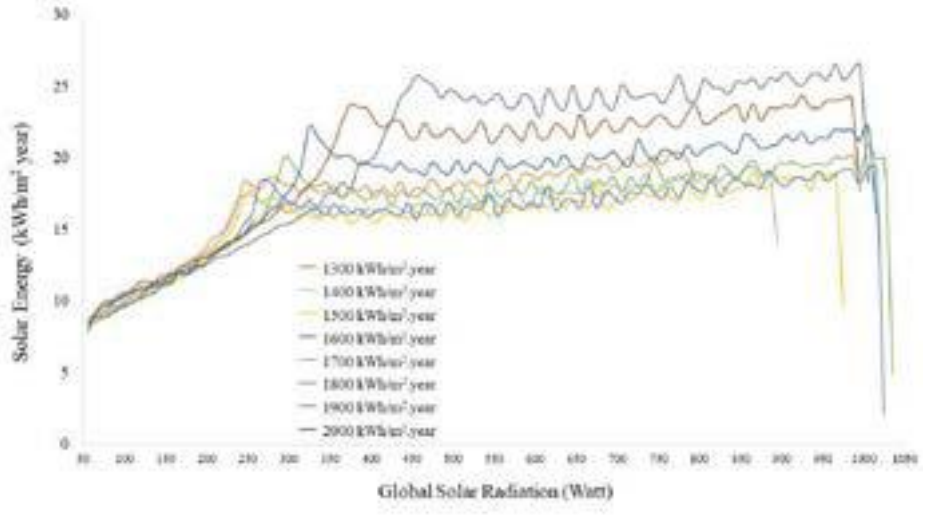

Fig. 1. Distribution of solar energy amount for 10 W solar radiation interval

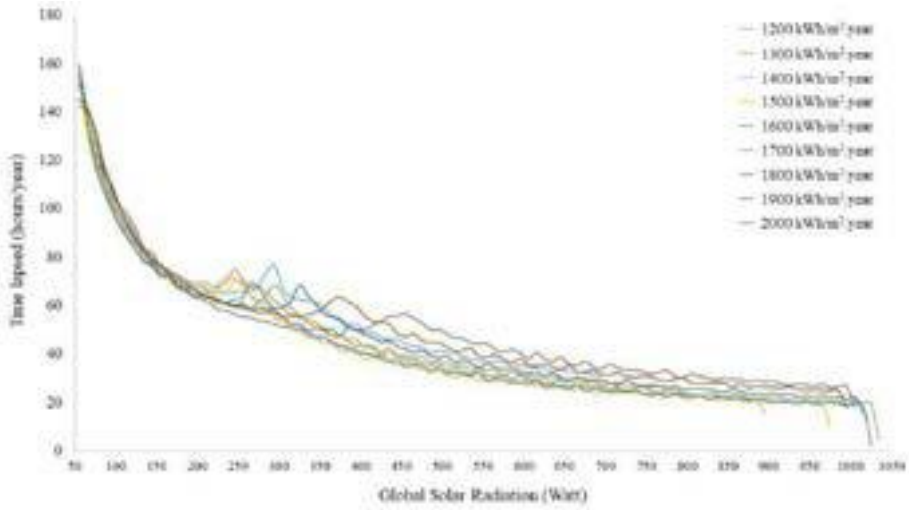

Fig. 2. Distribution of lapsed time for 10 W global solar radiation intensity interval

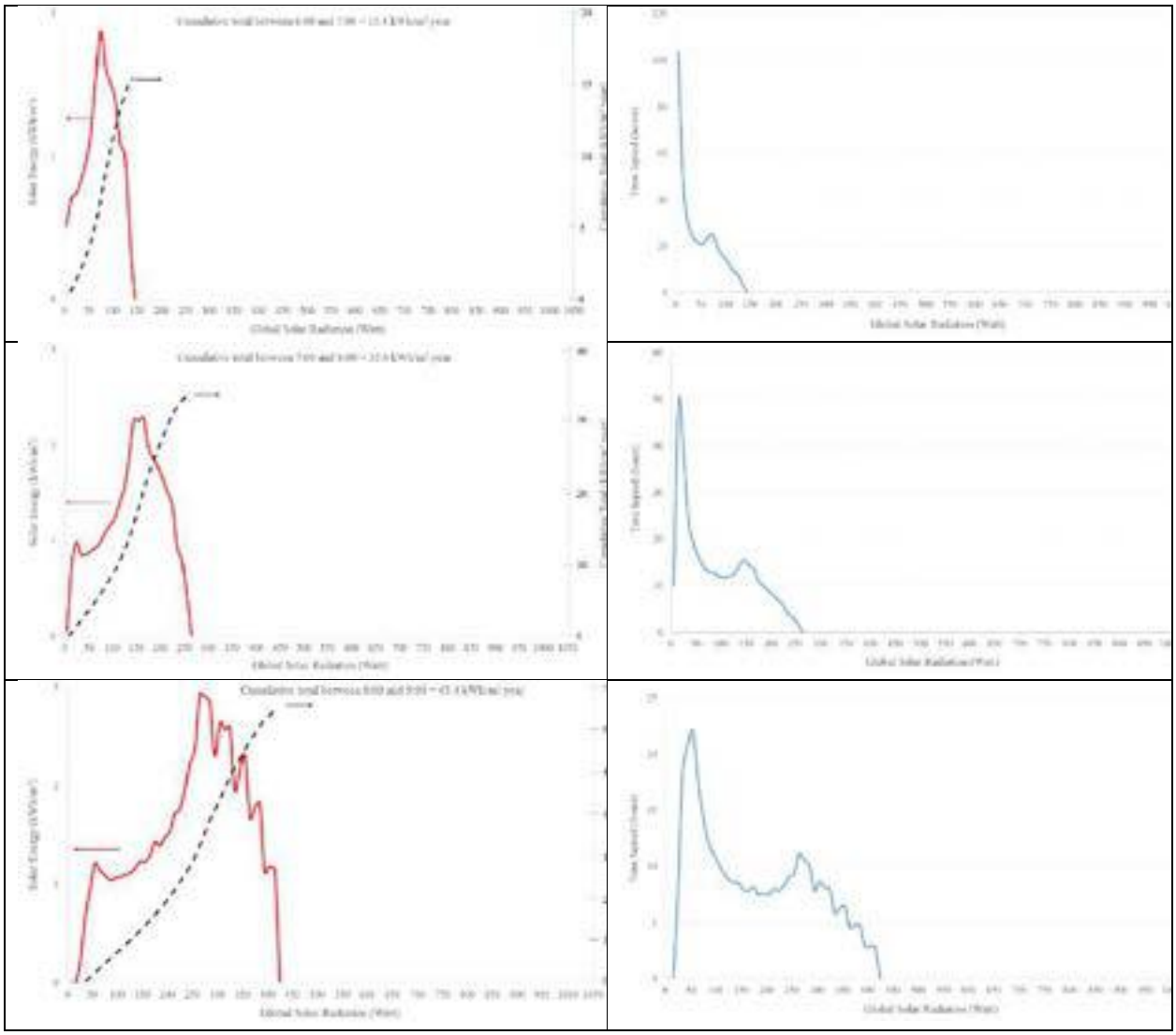

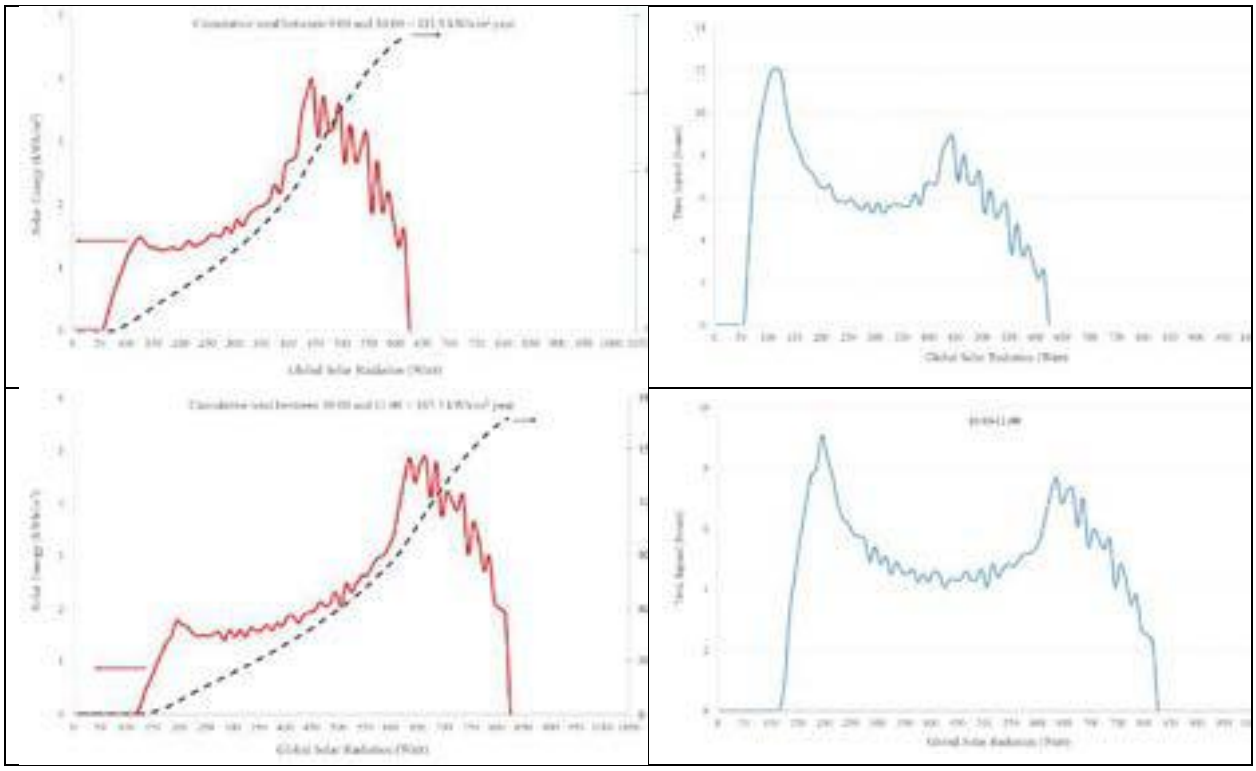

Fig. 3. Distribution of lapsed time and solar energy for 10 W global solar radiation intensity interval

Coskun and Oktay model for hourly global solar-radiation was implemented for Turkey. The average total global solar radiation is taken as 1750 kWh/m^2 year for this case study. Distribution of total falling solar energy amount and lapsed time for 10 W solar radiation interval between 06:00 and 11:00 is given in Fig. 3. The annual amount of solar energy realized under a certain solar radiation can be easily determined from Fig.3.

IV. Conclusion

Coskun and Oktay model can be utilized to simulate solar irradiance on an hourly time scale for any location in Turkey. The model can generate synthetic hourly horizontal radiation data. Using this method, we can determine which solar radiation values provide more solar energy. The amount of solar energy on an annual basis can be easily determined from these graphs. The model generated hourly solar radiation data with reasonably similar statistical characteristics. New model has direct applicability to use for simulation of both thermal and PV concentrating solar power systems.

References

Reikard, G. (2009). "Predicting solar radiation at high resolutions: A comparison of time series forecasts". Solar Energy. 83. 342–349

Laslett, D., Creagh, C., Jennings, P. (2014). "A method for generating synthetic hourly solar radiation data for any location in the south west of Western Australia, in a world wide web page". Renewable Energy. 68:87-102

Knight, K.M., Klein, S.A., Duffie, J.A. (1991). "A methodology for the synthesis of hourly weather data". Solar Energy. 46(2):109–120

Yang, K., Koike, T. (2002). "Estimating surface solar radiation from upper-air humidity". Solar Energy. 72(2):177–186

Chandel, S.S, Aggarwal, R.K. (2011). "Estimation of Hourly Solar Radiation on Horizontal and Inclined Surfaces in Western Himalayas. Smart Grid and Renewable Energy. 2:45-55

Singh, O.P., Srivastava, S.K, Pandey, G.N. (1997). "Estimation of hourly global solar radiation in the plane areas of Uttar Pradesh, India". Energy Conversion and Management. 38(8):779–785

Parishwad, G.V., Bhardwaj, R.K., Nema, V.K. (1997). "Estimation of hourly solar radiation for India". Renewable Energy. 12(3):303-313

Hussein, T.A.T. (2012). "Estimation of Hourly Global Solar Radiation in Egypt Using Mathematical Model". Int. J Latest Trends Agr. Food Sci. 2(2):74-82

Yang, K., Koike, T. (2005). "A general model to estimate hourly and daily solar radiation for hydrological studies". Water Resources Research. 41(10):1-13 doi/10.1029/2005WR003976/full

Coskun, C., Oktay, Z. (2019). An Advanced Simple Method for Generating Synthetic Average Instant Hourly Solar Energy. Journal of Management Science & Engineering Research, 1(1), 1–6.

IEEES-159

Prediction of Thermodynamic Properties for Compressed Natural Gas Mixtures

[1]Fatih Ozcan, [2]Muhsin Kiliç,
[1] Bursa Uludağ University, Orhangazi Yeniköy Asil Çelik Vocational School, Mechanical and Metal Technologies Department, Orhangazi/BURSA, 16810, Türkiye
[2] Bursa Uludağ University, Faculty of Engineering, Department of Mechanical Engineering, Nilüfer/BURSA, 16059, Türkiye

* E-mails: fatihozcan@uludag.edu.tr ; mkilic@uludag.edu.tr

Abstract
Pressures are changed during the transfer of compressed natural gas (CNG). In order to compute the thermodynamic properties of natural gas under these pressure changes, the compressibility factor (Z) must be found. AGA8 equation of state is one of the equations used to find the compressibility factor for different natural gas mixtures. In this study, this equation is scripted in MATLAB. The compressibility factor of the natural gas mixtures is calculated according to pressure and temperature. This calculation is used to compute the thermodynamic properties. To validate the procedure, the numerical values are compared with available measured values (%91 Methane) for density.

Keywords: Compressed Natural Gas, AGA8 Equation of State, Numerical Method, Matlab

I. Introduction

Compressed natural gas (CNG) is a clean-burning alternative to gasoline or diesel used in transportation. CNG contains methane and also other hydrocarbons such as butane, propane and ethane. Accurate prediction of thermodynamic properties for CNG is an essential requirement in optimum design and operation of most process equipment involved in storage and transportation. Accurate value of CNG compressibility factors is crucial in custody transfer operations.

An Equation of State (EOS) can describe the thermodynamic state of a fluid mixture. The AGA8-DC92 EOS and ISO-12213-2 is currently the industry standard to predict the density or compressibility factor of natural gas with an acceptable accuracy. The AGA8 EOS has been developed by American Gas Association. It contains both theoretical and empirical elements. It performs well and high accuracy for the temperature range between 143.15 K and 676.15 K, and pressure up to 280 MPa. The AGA8 has been also subject to various researches for thermodynamic property calculation. (AGA8-DC92 EoS, 1992). (Farzaneh-Gord et al., 2010) developed computer program to use The AGA8 EOS to find thermodynamic properties for natural gas such as internal energy and entalphy. (Farzaneh-Gord and Rahbari, 2012) used the AGA8 EOS to find thermodynamic properties for natural gas such as density, entalphy, speed of sound and Joule–Thomson coefficient. (Farzaneh-Gord et al., 2018) compare AGA8 and GERG2008 equation of state for flow meters in custody transfer.

II. The Numerical Method

The equation of state for the compressibility factor Z for the Detail Characterization Method is given in its condensed form by the following equations (Equations (1)-(14)) (AGA8-DC92 EoS, 1992):

$$Z = 1 + \frac{DB}{K^3} - D\sum_{n=13}^{18} C_n^* T^{-u_n} + \sum_{n=13}^{58} C_n^* T^{-u_n}(b_n - c_n k_n D^{k_n}) D^{b_n} \exp(-c_n D^{k_n}) \quad (1)$$

where *D* is reduced density defined as follow:

$$D = K^3 d \quad (2)$$

where, *K* is the mixture size parameter calculated using the following equation

$$K^5 = \left[\sum_{i=1}^{N} x_i K_i^{\frac{5}{2}}\right]^2 + 2\sum_{i=1}^{N-1}\sum_{j=i+1}^{N} x_i x_j \left(K_{ij}^5 - 1\right)\left(K_i K_j\right)^{\frac{5}{2}} \quad (3)$$

In Eq. (3), x_i is the mole fraction of component i in the mixture, x_j is the mole fraction of component j in the mixture, K_i is the size parameter of component i, K_j is the size parameter of component j, K_{ij} is the binary interaction parameter for size, and N is the number of components in the gas mixture.

The second virial coefficient B is given by the following equations, where N is the number of components in the gas mixture and the values of i and j both range from 1 to N:

$$B = \sum_{n=1}^{18} a_n T^{-u_n} \sum_{i=1}^{N} \sum_{j=1}^{N} x_i x_j E_{ij}{}^{u_n} \left(K_i K_j\right)^{\frac{3}{2}} B_{nij}^{*} \quad (4)$$

In Equation (4), B_{nij}^{*} and $E_{ij}{}^{u_n}$ are defined by the following equations:

$$B_{nij}^{*} = \left(G_{ij} + 1\text{-}g_n\right)^{g_n} \left(Q_i Q_j + 1\text{-}q_n\right)^{q_n} \left(F_i^{\frac{1}{2}} F_j^{\frac{1}{2}} + 1\text{-}f_n\right)^{f_n} \left(S_i S_j + 1\text{-}s_n\right)^{s_n} \left(W_i W_j + 1\text{-}w_n\right)^{w_n} \quad (5)$$

The binary parameters E_{ij}, and G_{ij}, are calculated using the following equations:

$$E_{ij} = E_{ij}^{*} \left(E_i E_j\right)^{\frac{1}{2}} \quad (6)$$

$$G_{ij} = \frac{G_{ij}^{*}\left(G_i + G_j\right)}{2} \quad (7)$$

In Equations (4) – (7), T is the temperature, N is the number of components in gas mixture, a_n, f_n, g_n, q_n, s_n, u_n, and w_n are the equation of state parameters, E_i, F_i, G_i, K_i, Q_i, S_i, and W_i are the corresponding characterization parameters.

In Equation (1), C_n^{*}, n = 13, . . ., 58, are temperature-dependent coefficients defined by the following equation:

$$C_n^{*} = a_n (G + 1\text{-}g_n)^{g_n} (Q^2 + 1\text{-}q_n)^{q_n} (F + 1\text{-}f_n)^{f_n} U^{u_n} \quad (8)$$

The mixture parameters U, G, Q, and F are calculated using the following equations, where in the double sums, i ranges from 1 to N-1 and, for each value of i, j ranges from i+1 to N:

$$U^5 = \left[\sum_{i=1}^{N} x_i E_i^{\frac{5}{2}}\right]^2 + 2 \sum_{i=1}^{N-1} \sum_{j=i+1}^{N} x_i x_j \left(U_{ij}{}^5\text{-}1\right) \left(E_i E_j\right)^{\frac{5}{2}}$$

$$G = \sum_{i=1}^{N} x_i G_i + \sum_{i=1}^{N-1} \sum_{j=i+1}^{N} x_i x_j \left(G_{ij}^{*}\text{-}1\right)\left(G_i + G_j\right) \quad (10)$$

$$Q = \sum_{i=1}^{N} x_i Q_i \quad (11)$$

$$F = \sum_{i=1}^{N} x_i{}^2 F_i \quad (12)$$

In the computation of the compressibility factor Z using the Detail Characterization Method, the composition of the gas and the absolute temperature T of the gas are known, and the absolute pressure P is known. The problem then is to compute the molar density d using the equation of state expression for the pressure P. For this purpose, Equation (1) is substituted into Equation (13) to obtain an equation for the pressure:

$$P = ZdRT \quad (13)$$

In Equation (13), P is pressure (kPa), Z is compressibility factor, d is molar density (kmol/m^3), R is universal gas constant (J/mol-K), and T is temperature (K). The molar density is calculated using Newton–Raphson iterative method in Matlab.

The density of natural gas (kg/m^3) is calculated by using the following equation:

$$\rho = M_w d \quad (14)$$

where M_w and d are molecular weight (kg/kmol) and molar density (kmol/m^3), respectively. The AGA8 model is intended for a specific range of the gas components. It is not recommended for
the gases with mole percentages outside of the value given (AGA8-DC92 EoS, 1992).

III. Composition of Natural Gas

Natural gas may contain up to 21 components. (ISO-12213-2, 2006) The primary component is Methane (CH_4) in the mixture. It also contains heavier hydrocarbons such as Ethane (C_2H_6), Propane (C_3H_8) and Butane (C_4H_{10}). Table 1 shows an experimental analysis of natural gas composition of %91 Methane (Patil,2007).

Table 1. Mole percent of natural gas component used in density calculation

Component	NG Experimental (%)
Methane (CH_4)	*90.991*
Nitrogen (N_2)	*2.031*
Carbon Dioxide (CO2)	*0.403*
Ethane (C_2H_6)	*2.949*
Propane (C_3H_8)	*1.513*
i-Butane (i-C_4H_{10})	*0.755*
n-Butane (n-C_4H_{10})	*0.755*
i-Pentane (i-C_5H_{12})	*0.299*
n-Pentane (n-C_5H_{12})	*0.304*

IV. Results and discussions

Figure 1 and figure 2 show effects of pressure and temperature on natural gas compressibility factor for experimental natural gas. The compressibility factor decreases as pressure increases and increases as temperature increases. The value of compressibility factor approaches to 1 as pressure decreases for all temperatures.

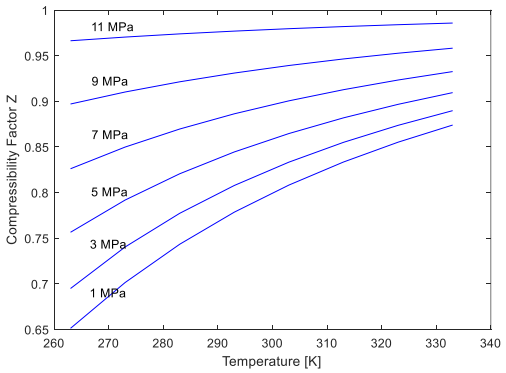

Fig. 1. Effects temperature on compressibility factor

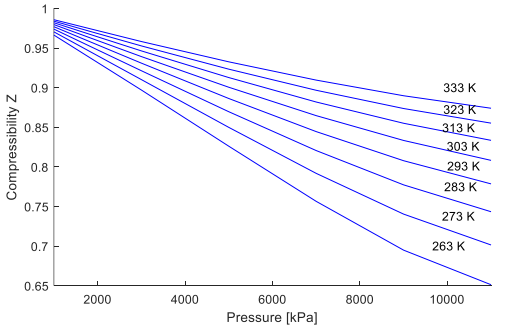

Fig. 2. Effects pressure on compressibility factor

Numerical method predicts the natural gas density in addition of compressibility factor. To validate the results, the numerical and available experimental values (Patil,2007) have been compared. The percent error and average absolute percent deviation (AAPD) have been employed as comparisons tools:

$$\% \text{ Error } = \frac{\text{Property}_{\text{Cal}} - \text{Property}_{\text{Exp}}}{\text{Property}_{\text{Exp}}} * 100 \quad (15)$$

$$\% \text{ AAPD } = \frac{1}{n} \sum \left| \frac{\text{Property}_{\text{Cal}} - \text{Property}_{\text{Exp}}}{\text{Property}_{\text{Exp}}} * 100 \right| \quad (16)$$

Density is calculated by utilizing Eq. (14). Table 1 shows mole percent of natural gas used in density calculation. Considering the experimental values, one could conclude that the density calculation has high accuracy with AAPD of 0.1787%.

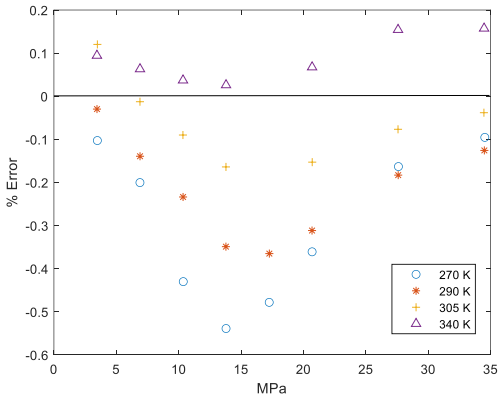

Fig. 3. Error percent in density calculation

Figure 3 illustrates error percent for density calculations. According to Figure 3, as temperature increases or pressure decreases, error percent decreases. This shows that as the natural gas behavior approaches closer to an ideal gas, accuracy of the AGA8 EOS for prediction density.

V. Conclusion

Accurate prediction of thermodynamic properties for CNG is an essential requirement in optimum design and operation of most process equipment involved in compressed, storage and transfer. In current study, Matlab program has been developed to calculate the property of natural gas mixture such as density in addition of the compressibility factor. To validate the numerical procedures, the numerical values have been compared with natural gas composition of %91 Methane mixture density values. The validations show that the average absolute percent deviation (AAPD) for density calculation is 0.1787%.

References

AGA8-DC92 EoS, 1992. Compressibility and Super Compressibility for Natural Gas and Other Hydrocarbon Gases, Transmission Measurement Committee Report, no. 8, AGA Catalog no. XQ 1285, Arlington, VA.

Farzaneh-Gord, M., Khamforoush, A., Hashemi, S., Pourkhadem, H., 2010. Computing thermal properties of natural gas by utilizing AGA8 equation of state. Int. J. Chem. Eng. Appl. 1, 20.

Farzaneh-Gord M., Rahbari HR., 2012. Numerical procedures for natural gas accurate thermodynamic properties calculation. Journal of Engineering Thermophysics; 21(4). https://doi.org/10.1134/S1810232812040017

Farzaneh-Gord M., Mohseni-Gharyehsafaa B., Toikkab A., Zverevab I., 2018. Sensitivity of natural gas flow measurement to AGA8 or GERG2008 equation of state utilization. Journal of Natural Gas Science and Engineering 57 305–321. https://doi.org/10.1016/j.jngse.2018.07.014

ISO-12213-2, 2006. Natural Gas-Calculation of Compression Factor, pt. 2: Calculation Using Molar Composition Analysis, ISO, Ref. no. ISO-12213-2:1997(E).

Patil, P., Ejaz, S., Atilhan, M., Cristancho, D., Holste, J.C., Hall, K.R., 2007. Accurate density measurements for a 91% methane natural gas-like mixture. J. Chem. Thermodyn. 39, 1157–1163.

IEEES-160

Combined effects of nozzle hole variation and piston bowl geometry modification on performance characteristics of a diesel engine with energy and exergy approach

[1*]Ozum Calli, [2]Vedagiri Praveena, [3]Edwin Geo Varuvel
[1,3] Istinye University, Faculty of Engineering and Natural Sciences, Department of Mechanical Engineering, Vadi Campus, Ayazağa District, Azerbaycan Street (Vadistanbul 4A Blok) Sarıyer, İstanbul, 34396, Turkey
[2] Dept. of Mechanical Engineering, SRM Institute of Science and Technology, Potheri, Kattankulathur 603203, Chengalpattu District, Tamilnadu, India

* E-mails: ozum.calll@istinye.edu.tr

Abstract
This experimental work aims to address the challenges of waste management. Biomass waste is converted into useful fuel and considered as a replacement to conventional fuel in CI engines. In this context, the grape marc and grape pomace are crushed and further processed to produce grapeseed oil. The grapeseed oil is further trans esterified to produce grapeseed seed oil methyl ester. The present study aims in examining the effect of varying piston shapes and nozzle profile on energy and exergy rates of a CI engine run with grapeseed oil methyl ester (GSME) blended with cerium oxide nano particles. The CeO2 nano particles were suspended in the base fuel at a concentration of 100 ppm and stability tests were conducted. The experiments were performed on a single cylinder, water cooled diesel engine with rated power of 5.2 kW. The research work includes two additional piston shapes namely, toroidal and shallow deep and two additional nozzle profiles viz. 4 hole and 5-hole nozzle. The hemispherical shape and 3-hole nozzle were considered as the standard one. Energy and exergy analysis were done on the experimental data to understand the exergy associated with cooling water, exhaust gas and unaccounted losses. The energy and exergy rates show that increase in nozzle hole number, decreases the destructive availability of the system. The exergetic efficiency of 32.8% is higher proving that toroidal shape and 5-hole nozzle profile is comparatively better and suitable for effective engine operation. HC, CO and smoke emissions reduced considerably by 14.4% to 30% by the engine modification. Brake thermal efficiency was improved from 28.2% to 31.02% for CI engine with biodiesel. The paper addresses the gap in fuel modification clubbed with engine modification using biomass waste derived fuel. Exergy and energy analysis further add value to this current experimental work.

Keywords: Piston bowl geometry, diesel engine, energy analysis, exergy analysis

I. Introduction

Wide range of applications such as agriculture, industrial fields, automotive and heavy-duty vehicles makes diesel engines unavoidable in the modern society (Dabi and Saha, 2018). Their high thermal efficiency and stability makes them suitable and sustainable over many decades (Thiyagarajan et al., 2019). Different additives blended with diesel and biodiesel results in multi-phase emulsion fuels that produces similar performance as that of diesel. Biodiesel stability and emulsion stability studies helps to understand better the property of biodiesel (Varuvel et al., 2018). However, problems incurred such as hazardous emissions and limitations in the fossil reserves, has created the necessity in exploration of renewable and alternative fuels that are suitable for CI engines. The heterogeneous mode of diesel combustion produces excessive NOx and smoke emissions (Ospina et al., 2019). To overcome these challenges, many researchers have carried out works on low temperature combustion techniques to minimize the adiabatic flame temperature. Combination of gasoline and iso-butanol blended with diesel were tested in a diesel engine at low and high rates of EGR. The fuel properties highly influence the emissions and it is found that small EGR rates provide high nucleation mode of the particulate numbers (Li et al., 2020). Homogenous charge compression ignition, gasoline direct ignition and premixed charge compression ignition are some of the methods through which low temperature combustion can be attained. This is achieved through low in-cylinder pressure, heat release rate and NOx emissions but with a simultaneous increase in hydrocarbon emissions (Pachiannan et al, 2019).

II. Experimantal Procedure

The experimentation was carried out with GSME blended with CeO2 nano particles as the operating fuel. The CeO2 nano particles were suspended in the base fuel at three different concentrations of 50, 100 and 200 ppm. Stability tests showed that the dosage level of 100 ppm was stable for 7 days. As a preliminary study, experiments were carried out with 100 ppm concentration. Visual Stability tests (ASTM D3707-89) were carried out on both the nano emulsion blends. The blend did not disintegrate for three days. Hence it was considered as a homogeneous mixture with good quality.

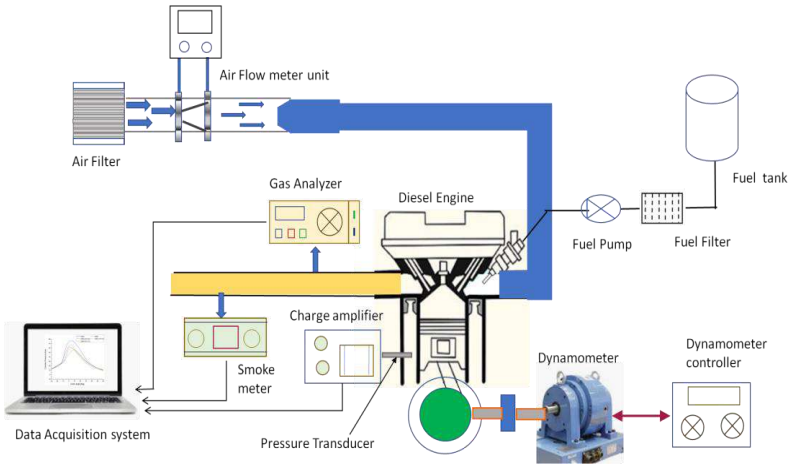

Fig. 1 Representation of experimental set up

III. Analysis

III. I. Energy analysis

It is the performance analysis carried out on a control volume based on the First law of thermodynamics. The steady flow (SF) energy equation for the above system is simplified as follows in equation

$$\dot{Q_{in}} = BP + \dot{Q_{cw}} + \dot{Q_{eg}} + \dot{Q_{un}} \quad (1)$$

Energy loss by circulated cooling water is given in equation

$$\dot{Q_{cw}} = \dot{m}_{cw} \times c_{pcw} \times (T_{wo}\text{-}T_{wi}) \quad (2)$$

Energy loss by exhaust gases from the engine is calculated ted cooling water is given in equation

$$\dot{Q_{eg}} = \dot{m}_{eg} \times c_{peg} \times (T_{eq}\text{-}T_{amb}) \quad (3)$$

Where $\dot{m}_{eg}$– total mass flow rate of exhaust gases = $\dot{m}_a + \dot{m}_{fu}$

c_{peg} - Specific heat capacity of exhaust gases

T_{eg}, T_{amb}- Exhaust gas temperature and ambient temperature

The steady flow energy equation (4) is rearranged to calculate the unaccounted energy loss

$$\dot{Q_{un}} = \dot{Q_{in}}\text{-}(BP + \dot{Q_{cw}} + \dot{Q_{eg}}) \quad (4)$$

III. II. Exergy analysis

Exergy is the maximum available work in a system calculated using II law of thermodynamics.

In a control volume system,

$$\frac{d(Exr_{sys})}{dt} = \frac{Exr_{in}\text{-}\ Exr_{out}}{dt}\text{-}Exr(dest) \quad (5)$$

Where $\frac{d(Exr_{sys})}{dt}$ – rate of change in exergy (6)

$(Exr_{in}\text{-}\ \ Exr_{out})$- Change in exergy transfer between the concerned system and its surrounding

$Exr(dest)$- exergy destruction with respect to time

The following equation denotes the relation between entropy generation and exergy destruction.

Exd = To * Sgen (7)

IV. Results

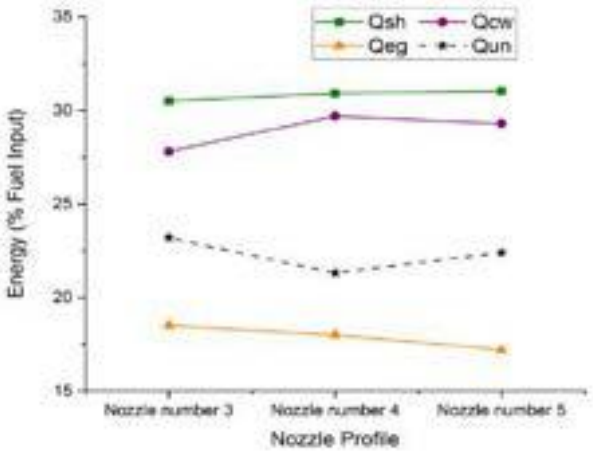

Fig 1 Effect of nozzle profile on energy distribution

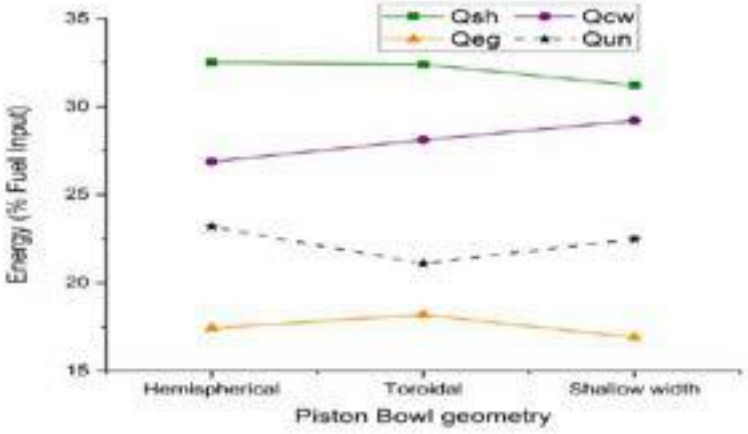

Fig. 2 Effect of piston geometry on energy distribution

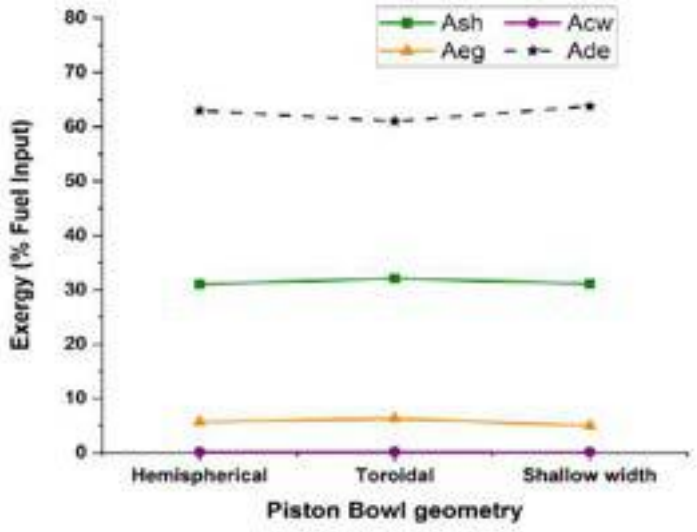

Fig. 3 Effect of piston geometry on exergy distribution

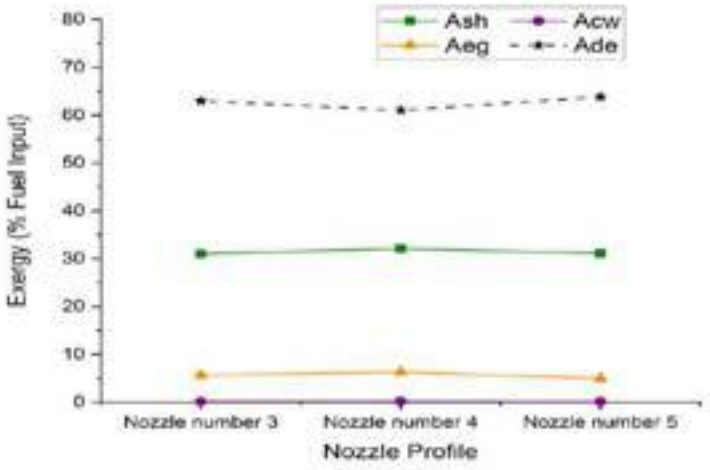

Fig. 4 Effect of nozzle profile on exergy distribution

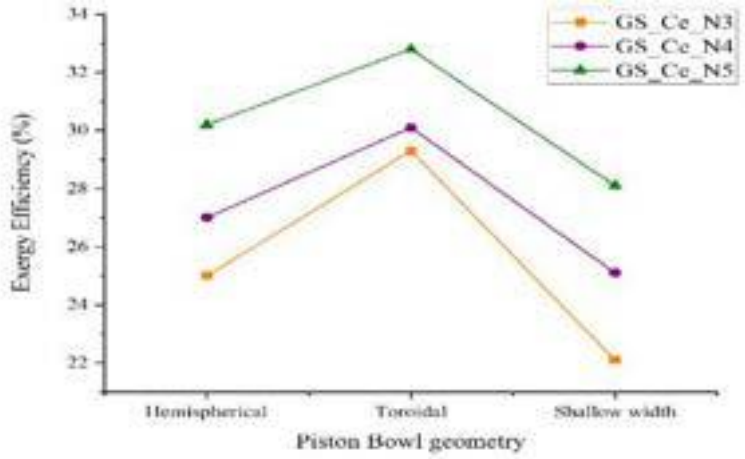

Fig. 17 Effect of piston geometry and nozzle profile on exergy efficiency

V. Conclusion

The analysis showed that GS_Ce fueled in CI engine can recover 30.5% of the total energy produced by the fuel. The remaining energy is lost to cooling water, exhaust gases and frictional losses. A slight increase in cooling water energy and reduction on exhaust gases energy rate is attained with GS_Ce_N5 profile. The shaft energy rate appears to increase from 31.2% to 32.4% for GS_Ce_TP profile.

Availability analysis shows that 32.8% of fuel exergy was convertible into useful exergy. The improved combustion process and fuel air mixing in GS_Ce_TP and N5 profile has decreased the destructive availability to 61%. The exhaust gas availability was 6.3% for the above modification.

References

Dabi, M., Saha, U. K., 2019. Application potential of vegetable oils as alternative to diesel fuels in compression ignition engines: A review. Journal of the Energy Institute, 92(6), 1710-1726.

Subramanian Thiyagarajan., Mohammad R Herfatmanesh., V Edwin Geo., Zhijun Peng., 2019. Experimental investigation into the effect of magnetic fuel reforming on diesel combustion and emissions running on wheat germ and pine oil. Fuel Processing Technology, 186, 116-124.

Edwin Geo Varuvel., Ankit Sonthalia., Thiyagarajan Subramanian., &Fethi Aloui., 2018. NOx-smoke trade-off characteristics of minor vegetable oil blends synergy with oxygenate in a commercial CI engine. Environmental Science and Pollution Research, 25(35), 35715-35724.

Ospina, G., Selim, M. Y., Al Omari, S. A., Ali, M. I. H., &Hussien, A. M., 2019. Engine roughness and exhaust emissions of a diesel engine fueled with three biofuels. Renewable Energy, 134, 1465-1472.

Li, S., Liu, J., Li, Y., Wei, M., Xiao, H., & Yang, S., 2020. Effects of fuel properties on combustion and pollutant emissions of a low temperature combustion mode diesel engine. Fuel, 267, 117123.

Pachiannan, T., Zhong, W., Rajkumar, S., He, Z., Leng, X., & Wang, Q., 2019. A literature review of fuel effects on performance and emission characteristics of low-temperature combustion strategies. Applied Energy, 251, 113380.

Debnath, B. K., Sahoo, N., &Saha, U. K., 2013. Thermodynamic analysis of a variable compression ratio diesel engine running with palm oil methyl ester. Energy conversion and management, 65, 147-154.

IEEES-161

Investigating Fuel Consumption Disparities Between Nonstop and Connecting Flights

[1*] Murat AYAR, [2]Selcuk EKİCİ, [1, 3]T. Hikmet KARAKOC
[1] Eskişehir Technical University, Faculty of Aeronautics and Astronautics, Eskişehir, 26555, Türkiye
[2] Igdir University, Department of Aviation, Igdir, 76000, Türkiye
[3] Istanbul Ticaret University, Information Technology Research and Application Center, Istanbul, 34445, Türkiye

* E-mails: muratayar@eskisehir.edu.tr

Abstract
This study delves into the exclusive examination of fuel consumption disparities between nonstop and connecting flights on a single air travel route while considering the influence of various flight phases. In a continually evolving industry that seeks to boost operational efficiency and mitigate environmental impact, this research offers a comprehensive view of fuel consumption patterns across specific flight phases. Utilizing data solely from one route and employing a diverse array of aircraft models, the findings underscore the substantial influence of aircraft selection and individual flight phases on fuel utilization. Through the comparative analysis of nonstop and connecting flights, this study unveils pronounced variations in fuel consumption during different stages of the journey. This emphasizes the potential for significant reductions in fuel consumption, and consequently, a diminished carbon footprint within the aviation industry. The insights from this research provide valuable guidance for aviation stakeholders, policymakers, and researchers who aim to make informed decisions for a more sustainable and efficient aviation sector.

Keywords: Fuel Consumption, Flight Phases, Air Travel Efficiency

I. Introduction

As the global population expands and economic activities continue to burgeon, there is a concurrent escalation in the demand for air transportation. While aviation serves as a crucial facilitator in connecting individuals and fostering international trade, its ecological ramifications cannot be understated (Youssef et al., 2020). Emissions from aircraft, primarily comprising carbon dioxide (CO_2), nitrogen oxides (NO_x), and water vapor, represent a substantial contributor to climate change, accounting for an estimated 2% of global energy-related CO_2 emissions (Cao et al., 2023; Masiol & Harrison, 2014). Furthermore, the aviation sector grapples with challenges related to aircraft engine noise and air pollution, posing consequential environmental and public health concerns (Baer, 2019). Amid mounting apprehensions regarding climate change and the imperative of ecological sustainability, the aviation industry faces escalating pressure to mitigate its emissions footprint. This necessitates a comprehensive comprehension of the origins and nature of aircraft emissions, along with their ecological ramifications. Through an in-depth analysis of fuel consumption trends and the exploration of alternative technological advancements, the aviation sector endeavors to advance towards the adoption of more sustainable practices in air transportation(Payán-Sánchez et al., 2018).

Despite the continuous evolution of aircraft technology, the aviation industry remains confronted with a pressing concern regarding fuel consumption (Payán-Sánchez et al., 2018). This factor significantly impacts operational expenses, environmental sustainability, and the operational range of aircraft. A comprehensive analysis of fuel usage across diverse flight configurations is imperative to pinpoint potential areas for enhancement and optimize the judicious utilization of resources (Singh et al., 2018). This research endeavors to scrutinize the variations in fuel consumption exhibited between non-stop and connecting flight alternatives operating between identical departure and arrival points. Specifically focusing on the route originating from Istanbul Airport to Heathrow Airport, a comparative analysis will be conducted between a direct flight option and a connecting flight route via Schiphol Airport. Through the meticulous examination of gathered data and the consideration of diverse determinants influencing fuel usage, the objective is to procure comprehensive insights into the fuel efficiency distinctive to various flight configurations. Ultimately, this study aims to contribute to the advancement of sustainable practices within the realm of aviation.

Despite the extensive body of research delving into fuel utilization within aviation, considerable knowledge gaps persist regarding the specific discrepancies between direct and connecting flights across diverse flight distances and configurations (Baumeister, 2017). While existing studies indicate potential fuel conservation in long-haul connecting flights, the evidence concerning shorter routes remains inconclusive, necessitating further investigation. Furthermore, the intricate influence of variables such as aircraft models, precise flight paths, and passenger capacity on fuel consumption warrants deeper scrutiny to foster a more comprehensive and nuanced comprehension of this matter. The dearth of data and comprehensive analysis impedes the formulation of efficacious strategies aimed at optimizing fuel efficiency and curbing environmental impact across the spectrum of flight configurations.

Consequently, this study endeavors to fill these lacunae in the scholarly discourse by conducting a comparative examination of fuel consumption and emissions between direct and connecting flights operating along the Istanbul-London route. Through the meticulous collection and analysis of pertinent data, this research seeks to offer valuable insights into the intricacies of fuel efficiency dynamics inherent in these distinct flight configurations, thereby contributing to the progression of sustainable practices within the aviation industry.

The primary objective of this study is to conduct a comprehensive investigation into the fuel consumption and associated emissions of both direct and connecting flights operating along the Istanbul-London route. Specifically focusing on a case study that compares a direct flight departing from Istanbul Airport (IST) to Heathrow Airport (LHR) with a connecting flight routed through Schiphol Airport (AMS), this research aims to delve into the nuanced differences in fuel usage between these distinct flight configurations. The study intends to analyze and elucidate the factors contributing to the observed variations in fuel consumption, thereby evaluating the potential for fuel savings and emission reductions associated with different flight options along this route. Ultimately, this investigation seeks to provide valuable insights that contribute to the existing body of research on aviation fuel consumption while offering practical recommendations geared toward optimizing fuel efficiency and minimizing environmental

impact within the aviation industry, especially concerning shorter flight distances.

The examination of fuel consumption differences between direct and connecting flights holds significant promise for the aviation industry and environmental conservation. Through a specific case study analysis, this research aims to provide crucial insights into how these flight configurations impact fuel efficiency and emissions. These findings can drive advancements in sustainable aviation by enabling airlines to optimize routes and configurations, resulting in reduced fuel usage, lower CO_2 emissions, cost savings, and improved passenger satisfaction. Moreover, the study offers airlines invaluable data for strategic decision-making, empowering them to make informed choices towards a greener and more sustainable future for air travel.

II. Methodology

This research delves into the discernible variations in fuel consumption and emissions between direct and connecting flights along the Istanbul-London route, employing EUROCONTROL's Integrated Aircraft Noise and Emissions Modelling Platform (IMPACT) alongside its expansive database.

IMPACT harnesses a sophisticated array of tools designed for comprehensive analysis of aircraft performance and environmental impact. Leveraging BADA 4 and cutting-edge aircraft databases, it facilitates precise calculations pertaining to fuel flow based on diverse engine types, operational conditions, and aircraft configurations. Advanced noise prediction models enable precise assessments of noise emissions for varied aircraft categories and operational scenarios (Cavadini & Lépinay, 2016). Additionally, CO_2 emissions are meticulously computed using globally recognized emission factors and fuel burn data. The platform allows the importation of real-time flight data sourced from air traffic control systems or model-based simulations for rigorous analysis. Furthermore, IMPACT enables the meticulous definition of flight procedures, simulation of diverse aircraft types and configurations for specific flight scenarios, and the generation of comprehensive reports detailing fuel consumption, noise emissions, and other performance metrics.

To ensure a comprehensive and representative dataset, information was collected for both direct and connecting flights operating between Istanbul Airport and Heathrow Airport, with connecting flights routed through Schiphol Airport. Data collection spanned three months, encompassing diverse flight conditions and operational scenarios. Collected data points encompassed flight details such as origin, destination, date, time, flight number, aircraft type, and flight distance, as well as operational data including fuel burn, flight duration, average altitude, average speed, and meteorological information. Additionally, aircraft specifications such as maximum takeoff weight, seating capacity, engine type, and engine performance data were recorded.

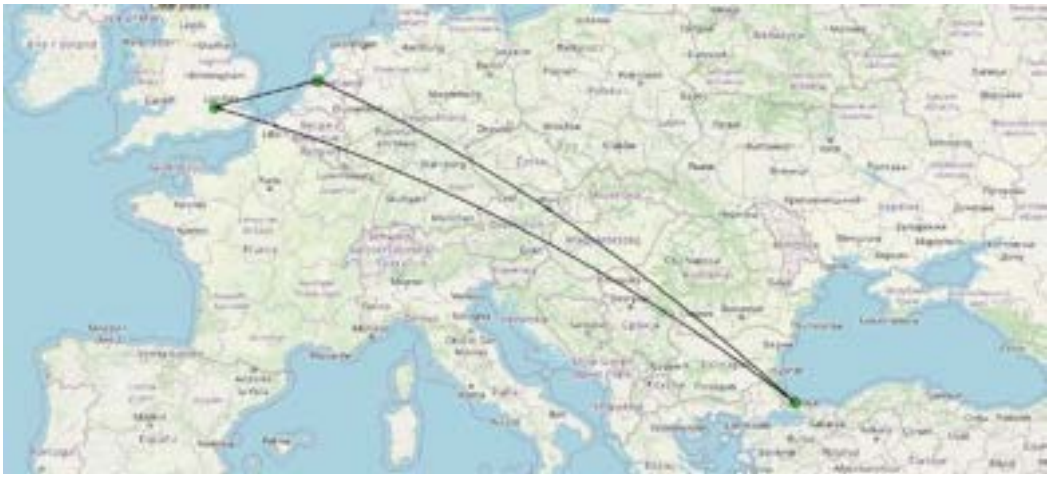

Figure 13 Nonstop and Connected Route

While this study focused exclusively on the Istanbul-London route and examined fuel consumption and CO_2 emissions for both direct and connecting flights, the methodologies and findings, while insightful, might not be universally applicable to other routes with differing distances, aircraft configurations, or operational factors. Further extensive research is imperative to generalize conclusions regarding fuel efficiency across diverse flight scenarios and configurations.

III. Results

This study investigated the fuel consumption and CO_2 emissions of direct and connecting flights on the Istanbul-London route. The results are summarized in the following table:

Flight Type	Distance (NM)	Fuel Burn (KG)	CO_2 Emissions (Tons)
Nonstop	1346.52	7241.84	22884.21
Connected	1381.72	9011.17	28475.28

As can be seen from the table, connecting flights consume significantly more fuel and emit more CO_2 than direct flights. The mean fuel burn for connecting flights is 19.4% higher than that of direct flights. The mean CO_2 emissions for connecting flights are 28.0% higher than that of direct flights.

The dataset analysis reveals several salient observations concerning the comparison between direct and connecting flights.

Firstly, it emerges that connecting flights, on average, traverse a slightly longer distance than direct flights, manifesting an average difference of 35.2 nautical miles. This disparity might be attributed to additional navigational considerations such as regional airspace constraints or prescribed arrival and departure protocols enforced by the connecting airports.

Figure 14 Distance Comparison - Nonstop vs. Connected Flights

Moreover, a substantial disparity in fuel consumption between the two flight types becomes apparent. Connecting flights exhibit a notable escalation in fuel burn compared to their direct counterparts. On average, the fuel burn for connecting flights surpasses that of direct flights by approximately 1769.33 kg, marking a 24.4% increase. This heightened fuel consumption can be attributed to the increased frequency of takeoffs and landings inherent in connecting flights, alongside potential elongation of flight durations.

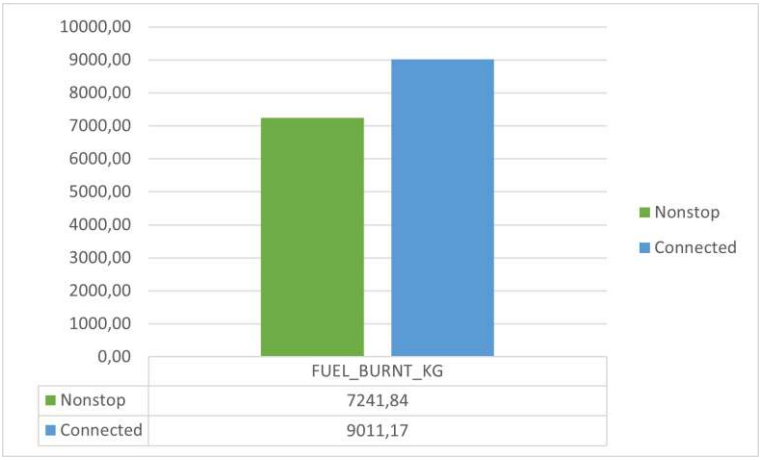

Figure 15 Fuel Burn Comparison - Nonstop vs. Connected Flights

Correspondingly, the analysis unveils a noteworthy trend in CO_2 emissions. Connecting flights demonstrate a considerably higher rate of CO_2 emissions vis-à-vis direct flights, with an average elevation of approximately 5591.07 tons increase. This upsurge in CO_2 emissions aligns directly with the observed augmented fuel consumption characteristic of connecting flights.

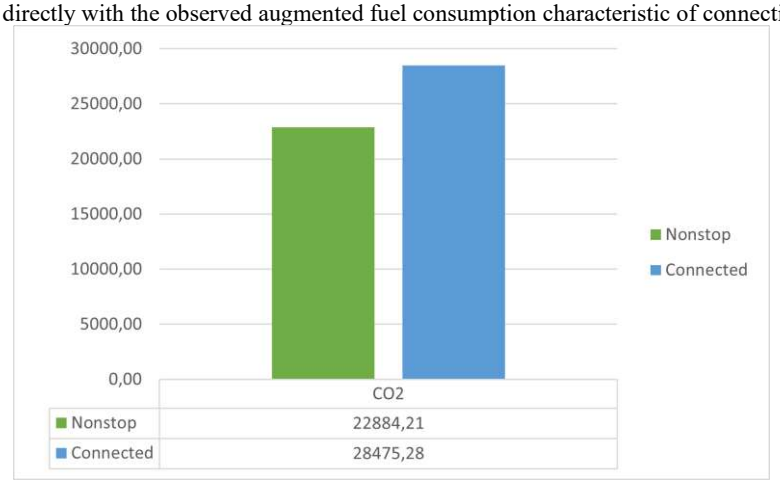

Figure 16 CO_2 Emissions Comparison - Nonstop vs. Connected Flights

In summary, the analysis unequivocally highlights the detrimental impact of connecting flights on both fuel efficiency and environmental sustainability when juxtaposed with direct flights. This knowledge holds substantial relevance for airlines and passengers alike, empowering them to prioritize choices that endorse efficient and eco-friendly air travel practices.

These findings are consistent with previous research that has shown that connecting flights are less fuel-efficient than direct flights. There are several reasons for this. First, connecting flights typically involve more takeoffs and landings, which are the most fuel-intensive phases of a flight. Second, connecting flights often involve longer flight times, which increases fuel burn. Third, connecting flights often involve higher altitudes, which also increases fuel burn.

This study is limited in several ways. First, it only focused on a single route, the Istanbul-London route. It is possible that the findings would be different for other routes with different distances, aircraft types, or operational factors. Second, the study only used data from a three-month period. It is possible that the findings would be different over a longer period of time. Third, the study did not account for other factors that could affect fuel consumption, such as weather conditions or passenger load.

The study's outcomes are explicable through two causal arguments. Firstly, the fuel-intensive nature of takeoffs and landings significantly contributes to increased fuel consumption during flights. Connecting flights, by their nature, involve a greater frequency of takeoffs and landings compared to direct flights, thereby amplifying overall fuel burn. Additionally, flight duration is another determinant, with longer flight times correlating with heightened fuel consumption. Connecting flights often encompass prolonged flight durations compared to direct flights, consequently escalating fuel usage. Moreover, altitude plays a pivotal role as fuel burn escalates at higher altitudes. Connecting flights frequently operate at elevated altitudes compared to direct flights, thereby contributing to increased fuel consumption.

Furthermore, deductive reasoning elucidates the study's findings. If connecting flights inherently involve more takeoffs and landings, this characteristic inherently implies higher fuel consumption. Given the empirical observation that connecting flights indeed encompass more takeoffs and landings than direct flights, the deduction follows that connecting flights consume more fuel than their direct counterparts. Thus, the study underscores that connecting flights tend to exhibit lower fuel efficiency compared to direct flights. These revelations bear significant implications for the aviation industry. Optimizing route networks to minimize the reliance on connecting flights stands as a viable strategy for airlines to curtail fuel consumption and consequent CO_2 emissions.

Acknowledgements

The authors would like to express their appreciation to EUROCONTROL for granting access to the database and the IMPACT platform, which significantly facilitated this research.

References

Baer, H. A. (2019). *Airplanes, the environment, and the human condition*. Routledge.

Baumeister, S. (2017). 'Each flight is different': carbon emissions of selected flights in three geographical markets. *Transportation Research Part D: Transport and Environment*, *57*, 1-9.

Cao, F., Tang, T.-Q., Gao, Y., You, F., & Zhang, J. (2023). Calculation and analysis of new taxiing methods on aircraft fuel consumption and pollutant emissions. *Energy*, *277*, 127618.

Cavadini, L., & Lépinay, I. (2016). Assessing trends in aviation noise and emissions in Europe using advanced modelling capabilities. 2nd ECATS Conference Proceedings: Making Aviation Environmentally Sustainable, Athens,

Masiol, M., & Harrison, R. M. (2014). Aircraft engine exhaust emissions and other airport-related contributions to ambient air pollution: A review. *Atmospheric Environment*, *95*, 409-455.

Payán-Sánchez, B., Plaza-Úbeda, J. A., Pérez-Valls, M., & Carmona-Moreno, E. (2018). Social embeddedness for sustainability in the aviation sector. *Corporate Social Responsibility and Environmental Management*, *25*(4), 537-553.

Singh, J., Sharma, S. K., & Srivastava, R. (2018). Managing fuel efficiency in the aviation sector: Challenges, accomplishments and opportunities. *FIIB Business Review*, *7*(4), 244-251.

Youssef, D., Gomes De Oliveira, F., Centeno, J., Figueiredo, L., & Halawi, L. (2020). Contingency Fuel Reduction in Brazil. *International Journal of Aviation, Aeronautics, and Aerospace*, *7*(3), 9.

IEEES-162

Power Grid Schemes of Marine Vehicles with Electric Propulsion

[1*]Taha Buğra Sari, [1]Orçun Şenler, [2]Murat Mustafa Savrun
[1] BMA Technology 41420, Kocaeli, Turkey
[2] Adana Alparslan Türkeş Science and Technology University, Department of Electrical & Electronics Engineering, 01250, Adana, Turkey

* E-mails: bugra.sari@bma.com.tr, orcun.senler@bma.com.tr, msavrun@atu.edu.tr

Abstract

In the international maritime sector, intensive studies have been carried out on environmental solutions and efficient use of energy in line with future goals. In line with these studies, alternative energy sources and propulsion systems that provide more efficient use of energy come to the fore. This paper presents AC and DC grid schemeswith fixed/variable diesel generator sets for marine vessels with electric propulsion. The distribution grid configuration and fixed/variable frequency operation determined for vessel loads typically fed by diesel generatorsdirectly affect the efficiency, fuel consumption, size, and cost of the system. In this regard, single-line diagrams of fixed/variable frequency AC grid and fixed/variable frequency DC grid which are used in practice are detailed and evaluated in terms of advantages/disadvantages.

Keywords: Marine vehicles, AC grid, DC grid, future aspects.

I. Introduction

Marine vessels play a significant role in global trade. Updates have been performed in the relevant sector regulations in order to reduce the use of fossil fuels and negative environmental impacts caused by traditional systems powered by internal combustion engines in marine vehicles. In parallel, the importance of electrification inmarine vessels has been increased (Chen et al., 2022). These innovative electric propulsion systems for marine vessels have the potential (I) to increase energy efficiency, (ii) to reduce carbon emissions, and (iii) to contribute to a cleaner and more sustainable future for maritime transport compared to conventional systems.

In this regard, several studies have been performed on electrically propelled ships. The related studies have examined power grids in two categories such as: AC and DC power systems (Ghimire et al., 2021). The AC powergrid system has become the most widely used power system in maritime vessels (Skjong et al., 2016). Traditional ship power systems are typically based on low-voltage alternating current (LVAC) distribution systems. These systems involve the use of separate diesel generators for ship propulsion systems and service loads, including heating, ventilation, and air conditioning pumps and compressors, control and communication systems loads and crane motors. In this context, various AC grid configurations have been designed. In the structure presented in the(Jayasinghe et al., 2017) article, the propulsion system and service loads are operated by separate generators. With the increasing controllability in power electronics, a common power system has been implemented for both propulsion and load systems. The current trend in power systems adopts a radial power distribution scheme, ensuring high efficiency, reliability, and stability through a regional approach to electrical distribution (Rose and Cunzer, 2015). Medium voltage AC distribution systems are frequently employed, in large ships. The related type systems are employed with constant speed generators and operate at a fixed frequency. Thus, the propulsion motors are operated at a constant speed. In this fixed-speed operation, slope angle control is utilized to adjust the inefficient propulsion power under low-load conditions (Hansen and Wendt, 2015). Additionally, the use of variable- speed drives enables the control of the propulsion motor speed, leading to performance improvements in the system (Jayasinghe et al., 2017).

Another grid scheme that has become increasingly important in recent years is the DC-based one. (Satpathi et al., 2019). With power electronics and other technological developments, DC grid integration has become advantageous. It makes it possible to reach higher energy dynamics by reducing power losses by eliminating many power converter components compared to the AC grid structure. In addition, frequency changes and harmonics inthe distribution of loads and generation sources with power electronic interfaces also decrease significantly with the reduction of converter units. Additionally, the absence of reactive currents due to the lack of frequency increases the power-carrying capacity. (Skjong et al., 2016). While voltage magnitude, phase sequence, and frequency synchronization are required for external sources in AC grids, frequency matching is not necessary in DC grids. Thus, it provides a faster response time for power generation (Kim et al., 2018). Consequently, the infrastructure is provided for the easy integration of next-generation studies such as battery (Lin et al., 2020) and fuel cell (Haxhiu et al., 2021) units.

This article presents conceptual designs for possible AC and DC grid schemes that can be used in marine vessels. In this context, (I) AC grid with constant frequency diesel generators (DGs), (ii) AC grid with variable frequency DGs, (iii) DC grid with constant frequency DGs, and (iv) DC grid with variable frequency DGs schemes have been presented and detailed. The rest of the article is organized as follows: Section II introduces conceptual AC and DC power schemes. Section III presents future applications involving possible integrations into grid schemes and system developments. Section IV presents the results with relevant discussions.

II. Grid Schemes

The primary objective of designing electrical grid schemes for maritime vessels is to ensure uninterrupted power to prevent the blackout of the vessel. In addition to this, electrical energy needs to be supplied for various on-board systems such as lighting, air conditioning, water pumps, and electronic equipment. For these purposes, the power plant on the ship is designed similar to an industrial power plant with various generator sets, which is not connected to an external power grid. This means that the power plant operates as a dedicated configuration with short distances from producers to consumers. To ensure the continuity of service in maritime vessels designed forthese purposes, the number, sizes, and locations of generators, as well as the type and components of the electrical distribution system, vary.

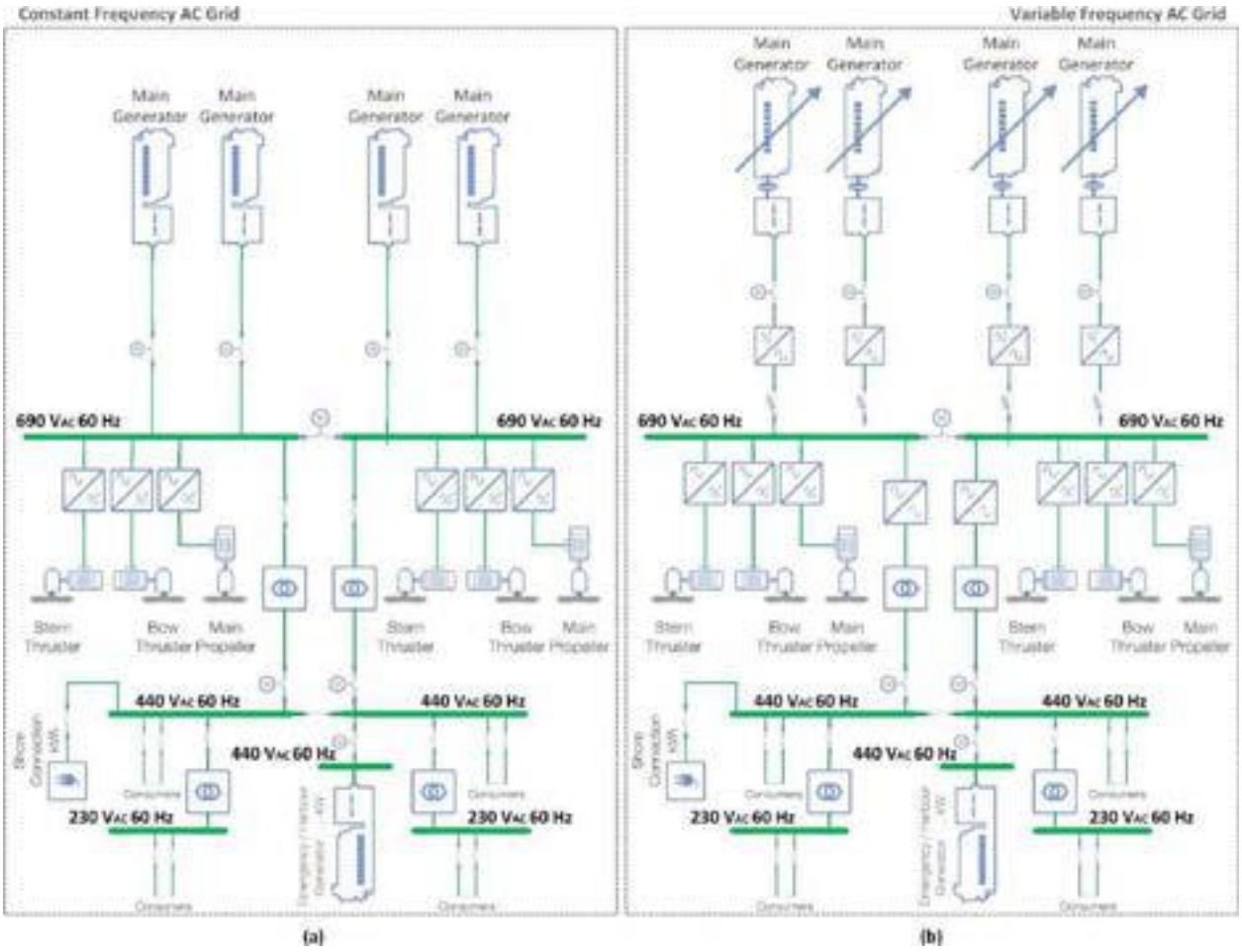

Fig. 1: AC grid schemes with constant (a) and variable (b) frequency DGs

Figure 1 illustrates AC grid configurations equipped with variable and constant frequency DGs. As seen in thefigure, the AC grid with constant frequency DGs (Fig. 1(a)) is equipped with a constant speed generator system. This eliminates the need for additional converters and an additional LCL filter to prevent Total Harmonic Distortion(THD) induced by the converters, providing benefits in terms of weight, volume, and cost. It also reduces the number of interfaces between systems, simplifying the overall system. However, the use of constant speed generators causes some disadvantages: (i) higher fuel consumption due to the constant rotation of the generators, (ii) shorterlifespan of generators as they experience increased stress, (iii) the need for an additional converter in front of the inverter drive and an additional LCL filter to prevent THD, leading to drawbacks in terms of weight, volume, and cost, (iv) lower power factor due to the absence of generator and converter drive, and (v) higher greenhouse gas emissions compared to applications involving variable frequency generators.

On the other hand, the AC grid structure with variable frequency DGs presented in Fig. 1(b) is equipped with a variable speed generator system. This reduces fuel consumption and extends the lifespan of generators. The use of generator and converter drive results in a higher power factor for the system. However, the use of a variable speed generator requires regulation with the converter unit of the system. This necessity leads to an increase in weight, volume, and cost due to the need for additional converters and an additional LCL filter to prevent THD induced by the converters.

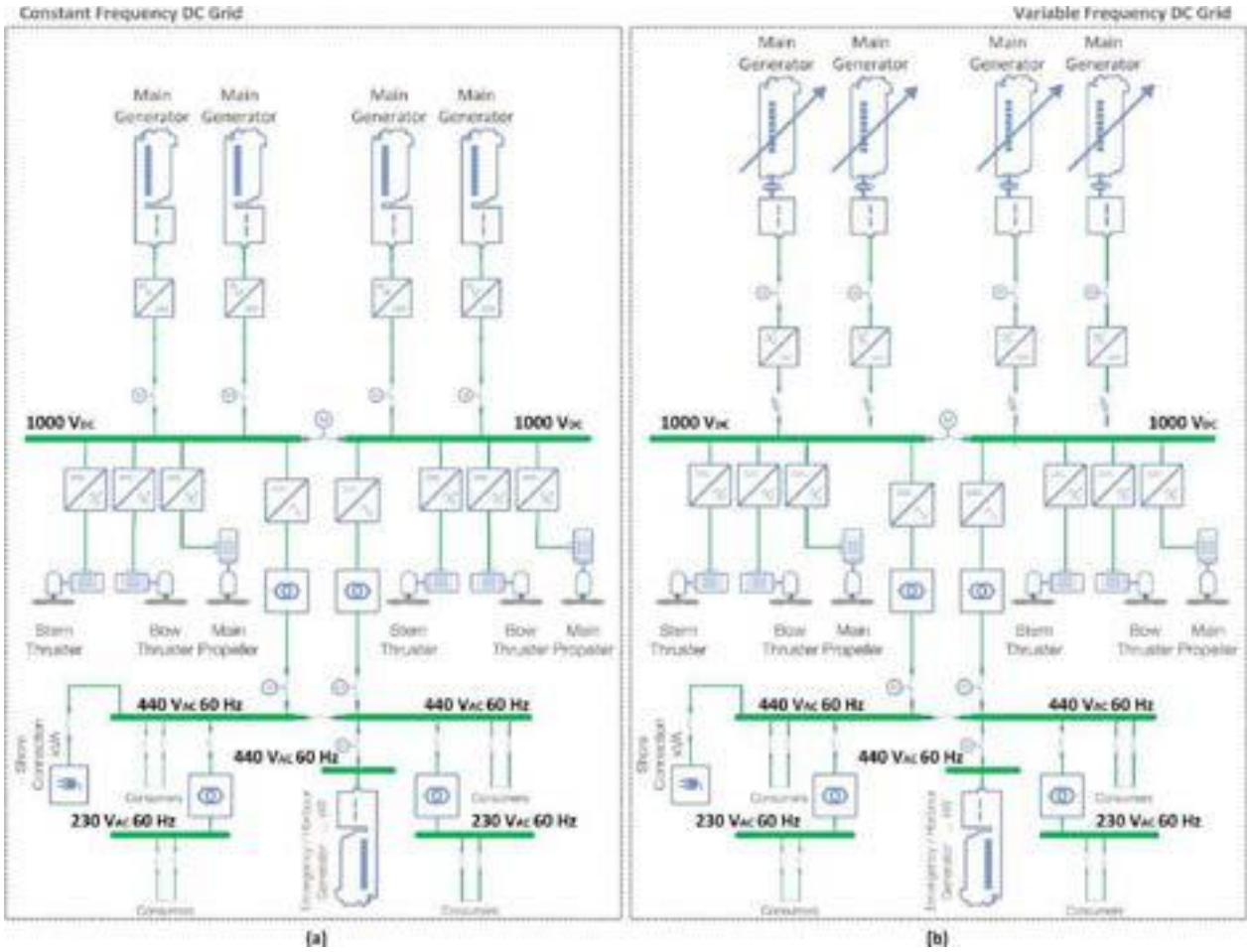

Fig. 2: DGs based DC grid schemes constant (a) and variable (b) frequency DGs

Fig. 2 depicts DC grid configurations equipped with variable and constant frequency DGs. Due to the use of aDC grid, there is no reactive power in the system. Compared to AC grid systems, DC grids require fewer converters, reducing the system's control complexity, weight, volume, and cost. As shown in Fig.2, the DC grid with constant frequency DGs (Fig. 2(a)) is equipped with a constant speed generator system. Continuous rotation of generators at a constant speed leads to higher fuel consumption, accelerating the aging of the relevant units. On the other hand, the DC grid structure with variable frequency DGs, equipped with a variable speed generator system, provides additional benefits by optimizing the use of the generator, resulting in higher performance, efficiency, and cost effectiveness, in addition to the advantages of DC grid structures.

III. Discussion and Future Grid Aspects

In comparison to the AC grid, a DC grid enables the integration of DC and AC power systems through a common DC bus, allowing for frequency-independent operation. Multiple DC-DC converters and AC-DC converterconnected to the common DC bus manage efficient and flexible power flow between AC and DC power systems. This configuration separates both DC and AC power sides, achieving independent and asynchronous operation. The mentioned power electronic converters not only handle power flow management but also perform voltage/current regulations for DC and AC power systems. The DC bus can be buffered by a battery unit to absorbor inject excessive power from DC or AC loads based on operating conditions. These features enable efficient and flexible power conversion/distribution, as well as better control and management of power flows. Additionally, the absence of synchronization issues in the DC grid facilitates the integration of renewable energy sources such as photovoltaic panels and fuel cells.

When examined in terms of fixed and variable frequency networks; In case of significant power fluctuations such as low partial loading, DGs are likely to lose efficiency and their fuel consumption to increase. Thanks to variable speed operation, DGs are operated at the optimum point and low fuel consumption is achieved.

IV. Conclusion

This study provides a detailed examination of the AC and DC power grid architectures in contemporary electrically propelled maritime vehicles. The grid structures are illustrated in detail using single-line diagrams, emphasizing the advantages and disadvantages of these configurations. Particularly noteworthy are the fuel emission advantages offered by variable frequency grids

Additionally, the flexibility provided by DC power grid structures and the ease of integrating new energy sources contribute to making these network configurations more attractive in modern times.

References

Chen, W., et al., (2022). DC-Distributed Power System Modeling and Hardware-in-the-Loop (HIL) Evaluation of Fuel Cell-Powered Marine Vessel. IEEE Journal of Emerging and Selected Topics in Industrial Electronics, vol. 3, no. 3, pp. 797-808, July 2022, doi: 10.1109/JESTIE.2021.3139471.

Ghimire, P., Zadeh, M., Pedersen, E., Thorstensen, J., (2021). Dynamic Modeling, Simulation, and Testing of a Marine DC Hybrid Power System. IEEE Transactions on Transportation Electrification, vol. 7, no. 2, pp. 905-919, June 2021, doi: 10.1109/TTE.2020.3023896.

Hansen, J. F., Wendt, F., (2015). History and State of the Art in Commercial Electric Ship Propulsion, Integrated PowerSystems, and Future Trends. Proceedings of the IEEE, vol. 103, no. 12, pp. 2229-2242, Dec. 2015, doi: 10.1109/JPROC.2015.2458990.

Haxhiu, A., Kyyrä, J., Chan, R., Kanerva, S., (2021). Improved Variable DC Approach to Minimize Drivetrain Losses in Fuel Cell Marine Power Systems. IEEE Transactions on Industry Applications, vol. 57, no. 1, pp. 882-893, Jan.-Feb. 2021,doi: 10.1109/TIA.2020.3035337.

Jayasinghe, S.G., Meegahapola, L., Fernando, N.; Jin, Z., Guerrero, J.M., (2017). Review of Ship Microgrids: System Architectures, Storage Technologies and Power Quality Aspects. Inventions , 2, 4. https://doi.org/10.3390/inventions2010004

Kim, k., Park, K., Roh, G., Chun , K., (2018). DC-grid system for ships: a study of benefits and technical considerations, Journal of International Maritime Safety, Environmental Affairs, and Shipping, 2:1, 1-12, DOI: 10.1080/25725084.2018.1490239

Lin, P., Zhao, T., Wang, B., Wang, Y., Wang, P., (2020). A Semi-Consensus Strategy Toward Multi-Functional Hybrid Energy Storage System in DC Microgrids. IEEE Transactions on Energy Conversion, vol. 35, no. 1, pp. 336-346, March 2020, doi: 10.1109/TEC.2019.2936120.

Rose M. W., Cuzner, R. M., (2015). Fault isolation and reconfiguration in a three-zone system. 2015 IEEE Electric ShipTechnologies Symposium (ESTS), Old Town Alexandria, VA, USA, 2015, pp. 409-414, doi: 10.1109/ESTS.2015.7157927.

Satpathi, K., Ukil, A., Nag, S. S., Pou, J., Zagrodnik, M. A., (2019). DC Marine Power System: Transient Behavior and Fault Management Aspects. IEEE Transactions on Industrial Informatics, vol. 15, no. 4, pp. 1911-1925, April 2019, doi: 10.1109/TII.2018.2864598.

Skjong, E., Volden, R., Rødskar, E., Molinas, M., Johansen, T. A., Cunningham, J., (2016). Past, Present, and Future Challenges of the Marine Vessel's Electrical Power System. IEEE Transactions on Transportation Electrification, vol. 2,no. 4, pp. 522-537, Dec. 2016, doi: 10.1109/TTE.2016.2552720.